TAYLOR'S UNIVERSITY

Wisdom · Integrity · Excellence

IT'S IN YOU TO **OWN THE FUTURE**

PROCEEDINGS OF

8th eureca 2017

INTERNATIONAL ENGINEERING RESEARCH CONFERENCE

TAYLOR'S UNIVERSITY, LAKESIDE CAMPUS

12th of JULY 2017

Proceedings of the International Engineering Research Conference - 8th eureca 2017

12th of July 2017,
Taylor's University, Lakeside Campus.

Proceedings of the International Engineering Research Conference - 8th eureca 2017

12th July 2017, Taylor's University, Lakeside Campus.

Editors

Satesh Narayana Namasivayam

Mohammad Hosseini Fouladi

Chong Chien Hwa

Chua Bee Lin | Hoo Choon Lih | Se Yong Eh Noum

Abdulkareem Shafiq | Viknesh Andiappan Murugappan | Chow Yin Hui

Yoon Li Wan

Published By

School of Engineering

Taylor's University

ISBN 978-967-0173-48-1

eISSN 2590-3845

© 2017. All Rights Reserved.
No print of this publication may be reproduced in any form or by any means without the prior permission of the publisher in writing.

Preface

The International Engineering Research Conference - 8th eureca 2017 was organised and hosted by Taylor's School of Engineering from the 12th of July 2017. In this conference, 50 technical papers were presented with an additional of 2 keynote presentations being delivered. The theme of the conference centered around the 14 Grand Challenges for Engineering of the 21st Century. A total of 120 participants were part of the event. The 50 papers represent peer-reviewed research articles that are mostly undergraduate final year projects that address one or more grand challenges for engineering. This conference also provides a platform for engineering students and researchers to showcase their ability in being interested in life-long learning as well as in enhancing their affective learning. This event also aims to address the Washington Accord Graduate Profile element 10 – "*WA10: Communicate effectively on complex engineering activities with the engineering community and society at large, such as being able to comprehend and write effective reports and design documentation, make effective presentations and give and receive clear instructions*" (source: ieaagreements.org). This conference is held twice a year and brings together engineering undergraduates, international delegates, practising engineers and industry from various fields of engineering. The conference provides an avenue for the exchange of research knowledge and information. Opportunities were also provided to network and develop collaborative linkages and discussions throughout the conference.

This event would have not been made possible without the tireless efforts and support of the organising committee, which consisted of staff and students of Taylor's School of Engineering, as well as our sponsors. I would like to take this opportunity to express my sincere thanks for the services and financial support rendered.

I look forward to the 8th eureca.

Associate Professor Ir. Dr. Satesh Narayana Namasivayam

Head of School,
School of Engineering,
Taylor's University.

Table of Contents

No.	Description of Paper	Page No.
1	**Degradation Studies of Durian Husk-filled Polyactic Acid Composites** *(Paper 2CE01)* Aaron Yesudian William Yesudian, M.M. Pang, S.C. Koay, Albert Tshai	1
2	**Biomass Derived Synthesis of Nanoparticles Using Hydrothermal Process and Deep Eutectic Solvents** *(Paper 2CE02)* Aatif Shafqat, R. Walvekar, V. Doshi, W.Y. Wong, K. Shahbaz	11
3	**Investigation of Palm Fibre-derived Activated Carbon in Water Filtration System** *(Paper 2CE03)* Chia Ying Yin, L.W. Yoon, R.Y. Teh	23
4	**Drying Characteristics and Retention Rate of Aloe-Emodin of Casia Alata During Processing** *(Paper 2CE04)* Choo Choon Oon, C.H. Chong, B.L. Chua	39
5	**Temperature Effect on Natural Hydroxyapatide Extraction from Fish Bones Tissue Engineering** *(Paper 2CE05)* Danial Aminin Zairin, Eunice S.W. Phang, T.S. Lee	54
6	**Influence of Different Oven-drying Temperature on the Antioxidant Activity of Betel Leaves (Piper Betlel)** *(Paper 2CE06)* Ginisha Ashok, B.L. Chua	68
7	**Wastewater De-fluoridation Using Traditional Coagulation instead of Ammonia Nitrogen Removal** *(Paper 2CE07)* Goh Zhen Jie, C.H. Chong, R. Rajasekaran, C.L. Goh	84
8	**Degradation Studies of Corn Husk-filled Polylactic Acid Composites** *(Paper 2CE08)* Lee Kim Weng, M.M. Pang, S.C. Koay, Albert Tshai	104
9	**Effect of Radiation Energy on Crystallisation Kinetics of Ethylene Vinyl Acetate (EVA)** *(Paper 2CE09)* Lim Khai Ming, Suganti Ramarad	117
10	**Optimisation of Extraction Condition of Avocado Fruit using Response Surface Methodology** *(Paper 2CE10)* Nassor Ali Seif Hemed, R. Rajasekaran	128
11	**Ammonical Nitrogen Removal in Synthetic Wastewater using Seaweed-Based Ionic Liquid and *Bacillus spp.*** *(Paper 2CE11)* Nazween Adrynna Ahmad Nazri, C.H. Chong, R. Rajasekaran	143
12	**Primary Recovery of Amylase from Pitaya (Hylocereus Polyrhizus Peels by using Alcohol/Salt Aqueous Two-Phase System (ATPS)** *(Paper 2CE12)* Ow Jun Leong, Chow Yin Hui	155

13 **Thermal Characterisation of Recycled Waste Tire Rubber/EVA Blends** *(Paper 2CE13)* 166
Sier Sue Ting, Suganti Ramarad, R. Walvekar

14 **Life Cycle Assessment of Direct Carbon Fuel using Rice Husk as a Fuel Source** *(Paper 2CE14)* 177
Tan Yong De, Viknesh Andiappan, Edwin C.Y Chung

15 **Debottlenecking Biofuel Process Plants via Simulation-based Tool** *(Paper 2CE15)* 190
Mark Leong Tin Wai, Viknesh Andiappan, Edwin C.Y. Chung

16 **Integration of Pre-treatment and In-situ Enzymatic Saccharification of Lignocellulosic Biomass for Sugar Production** *(Paper 2CE16)* 200
Ang So Khai, L.W. Yoon

17 **Bentonite-cement Mixes as Electrical Grounding Improvement Material** (*Paper 2EE01)* 212
Andrew Yap Khin Mann, Mohsen Nabipoor

18 **Artificial Neural Network Based (ANNB) Load Flow Method for Distribution Network with Distributed Generation** *(Paper 2EE02)* 222
Mohammad Hafizuddin Ameruddin, C.R. Sarimuthu, Aravind C.V.

19 **Controller Design for Load Frequency Control in Deregulated Environment** *(Paper 2EE03)* 236
Ser yi Heng, Aravind C.V., C.R. Sarimuthu

20 **Assessment of Taylor's University Electrical Distribution System** *(Paper 2EE04)* 248
Tee Ting Yong, R.A. Gamboa, C.R. Sarimuthu

21 **Effects of Manganese Oxide on the Sintered Properties of Alumina Ceramics** *(Paper 2ME01)* 267
Andrew Ng Kwong Weng, Kelvin W.J. Chew, Ramesh Singh

22 **Upper Limb Tracking System** *(Paper 2ME02)* 279
Arif Akmal Kamarudin, M. Farid

23 **Autonomous Water Quality Monitoring Unit for Autonomous Lake Improvement System (ALIS)** *(Paper 2ME03)* 296
Chua Yong Hong, M.T. Hajibeigy, Se Yong E.N., S.Y. Ch'ng

24 **Properties of Differently Sintered Commercial Y-TZP Ceramics** *(Paper 2ME04)* 310
Dharuna Raj Rajandran, Kelvin W.J. Chew, Ramesh Singh

25 **Improving the Accuracy of Taylor's Wind Tunnel Measurements** *(Paper 2ME05)* 322
Hutomo Wibowo, Abdulkareem S. Mahdi

26 **Numerical Investigation on Two-wheeler Bias Tyre Impact using Various Material Models** *(Paper 2ME06)* 342
Jane Lee Song Ern, Felicia Y.M. Wong

27 **Oil Solube Graphene for Thermal Conductivity Enhancement of PCM** *(Paper 2ME07)* 364
Jeremy Jude Fernandez, Azadeh Ghadimi, Henk Metselaar

28 **Reduction of Artefacts Caused by Implant in a #D Model** *(Paper 2ME08)* 376
Karthik Mayakrisenan, K.H. Cheah, W.Y. Leong

29 **A Numerical Assessment of Microtopographies with Varied Geometries in Relation to Biofouling Control** *(Paper 2ME09)* 390
Lam Kuo Min, Felicia Y.M. Wong, C.H. Lim

30 **Energy Harvesting of Air Conditioning Outdoor Unit** *(Paper 2ME10)* 405
Lee Kian Leng, Ghafour A.M., Azadeh Ghadimi

31 **Design and Development of a Multi-Element Active Aerodynamic Package to Enhance the Performance of Taylor's Formula SAE Car** *(Paper 2ME11)* 415
Lee Wen Yew, Abdulkareem S. Mahdi, Satesh Namasivayam

32 **Modification and Validation of Tensile Testing Method for Biaxial Loading on Cord Ply Layer in Two-wheeler Bias Tire** *(Paper 2ME12)* 429
Mah Weng Onn, S.C. Koay, C.K. Thein

33 **Finite Element Analysis on Human Spine Images** *(Paper 2ME13)* 444
Melvin Mok Poh Chuen, K.H. Cheah, W.Y. Leong

34 **Studying the Effect of Pitch Ratio on Sheet Cavitation in Marine Propellers** *(Paper 2ME14)* 455
Mohamed Ehab Elsayed Mohamed Aly Abdou, Abdulkareem S. Mahdi

35 **Reduction of Local Pressure Loss at 90^{o} Bends in Pipes using Swirl Flow** *(Paper 2ME15)* 466
Mohanad Mohammed Saleh Bajunaid, Abdulkareem A. Mahdi, C.H. Chong, Kelvin Ho

36 **Electrical Conductivity Enhancement of Graphene Oxide Nanofluid** *(Paper 2ME16)* 480
Muhammad Affiq M. Isa, Azadeh Ghadimi, Taghi Hajibeigy

37 **Preparation and Characterisation of Plastic Wood Composites from Recycled Polystyrene Foam and Corn Husk Fiber** *(Paper 2ME18)* 494
Nur Muhammad Yusuf Fahmy Idzehar, S.C. Koay, M.M. Pang, Albert Tshai

38 **Development of an Airborne Traffic Monitoring System** *(Paper 2ME19)* 506
Aaron Gayvin, K.H. Cheah

39 **Airflow Study of a Split-type Outdoor Unit Subjected to Near Wall Effect using Computational Fluid Dynamics (CFD) Simulation** *(Paper 2ME20)* 514
Syed Ahmad Fahmi Syed Ibrahim, Douglas Tung, W.M. Chin

40 **Design and Development of EEG Controlled Robotic Prosthetic Arm** *(Paper 2ME21)* 527
Tan Zhe Xin, C.L. Hoo, W.J. Chew

41 **Design of an Air Blower Mechanism for the Cassette Air-conditioner** *(Paper 2ME22)* 544
Wen Yong Xiang, Azadeh Ghadimi, W.M. Chin

42 **Optimisation of Torsional Thrust Stand for Sub-micronewton Thrust** *(Paper 2ME23)* 556
Wong Shin Chien, K.H. Cheah, E.V. Lau

43	**Assessing Flow Over Patterned Surfaces of Varied Sizes in Relation to Biofouling Control** *(Paper 2ME24)* Yap Yi Wei, Felicia Y.M. Wong, C.H. Lim	571
44	**A Numerical Study on Examining the Effects of Flooding on Train Tracks** *(Paper 2ME25)* Sathweer Roopah, Satesh Namasivayam	589
45	**Numerical Modal Analysis and Design of Piezoelectric Energy Harvester** *(Paper 2ME26)* M. Hosseini Fouladi, Satesh Namasivayam	604
46	**Batch Removal of Manganese Using Modified Palm Kernel Shell** *(Paper CE-UG001)* Ayu Haslija A.B, Trilokesh R.M, Rajesh Nithyanandam	620
46	**Effective extraction of natural antioxidants from Piper betle with the aid of ultrasound: Temperature extraction kinetics** *(Paper PG1)* Ameena Ali, Bee Lin Chua, Chien Hwa Chong, Siau Hui Mah	633
47	**Acoustic Absorption Performance of Coir Fiber- Rice Husk and Coir Fiber-Polystyrene Fibro-Granular Composites** *(Paper PG2)* Hasina Mamtaz, Mohammad Hosseini Fouladi, Satesh Narayana Namasivayam	645

Degradation Studies of Durian Husk-Filled Polylactic Acid Composites

Aaron Yesudian[1*], Pang Ming Meng[2], Koay Seong Chun[3] , Tshai Kim Yeow[4]
[1-3]*School of Engineering, Taylor's University, Malaysia*
[4]*Nottingham University Malaysia*

[*]*aaronyesudian@gmail.com*

Abstract
Durian husk is the waste product resulting from the consumption of the durian fruit *(Durio zibethinus Murray)*. The durian husk is seen as a potential new natural fibre reinforcementto be incorporated within a polymer matrix. The durian husk fibre can be used to reinforce polylactic acid (PLA) through an extrusion process. This study investigated the possibility of incorporating durian husk/skin fibre(DSF) into the PLA matrix to investigate its degradation properties of the PLA biocomposite. The PLA/DSF biocomposite was prepared using the melt blending technique. The samples was prepared at a temperature of 180^{o}C with a speed of 150 rpm in the internal mixer. The composite was then compression moulded to a thickness of 1 mm at 180^{o}C with a pressure of 150 bar. A pure PLA sample was also prepared to be used as control. The samples that contained the DSF had a higher degradation rate as compared to that of pure PLA. The thermogravimetric analysis(TGA) showed that the 5% sodium hydroxide(NaOH) pretreatment had improved the thermal stability of the PLA/DSF biocomposites. The hygrothermal test showed that the degradation of the PLA/DSF biocomposites was greater as compared to that of the soil burial test as the samples were susceptible to attack by both water and heat which makes it a more hostile environment. SEM micrographs showed that alkali pretreatment had brought about better adhesion between the DSF and the polymer matrix.

Keywords : polylactic acid , durian skin fiber , soil burial , hygrothermal degradation.

1.0 INTRODUCTION

Man's unsustainable quest to live a quality life with no regard for the environment has brought about staggering amounts of environmental disasters such as overflowing landfills to polluted riverbanks and beaches. This has motivated manufacturers to look for alternatives in producing more environmentally friendly items. The use of biodegradable polymers is viewed as one of the possible ways to lower down the impact brought about by petroleum based plastics. Biodegradable polymers are most of the time non-toxic and biodegradable due to the fact that they are generated from natural sources that are renewable. Biodegradable materials are materials that can be broken down by living organisms that produces biomass, hydrocarbons and methane under anaerobic conditions or carbon dioxide, water and biomass when in aerobic conditions [1].

The most common biopolymer is polylactic acid(PLA) which is a corn-based biodegradable thermosplastic aliphatic polyester that has been studied and researched for the past few years. PLA has widely been used PLA for decades in the biomedical field to make scaffolds and artificial bones [2].PLA is also used for various other application such as the manufacturing of food take away trays , bottles and also to make furniture. The increasing availability of PLA together with the increasing petroleum cost has spurred on the use of PLA as a suitable replacement for petroleum based products. PLA however does have its disadvantages such as having a low thermal stability, has a 10% elongation at break and weak softening properties[3]. There is a need to further improve and eliminate this disadvantages so that it can be suited for many other applications.

In recent times, PLA has widely been used as a matrix in biocomposites with natural fibres as reinforcement. Natural fibres are suitable as filler material to be incorporated within the PLA matrix as it has more advantages compared to synthetic fibres. This is because natural fibres are renewable and have lower weights.

Durian husk is a plant waste that is due to the durian fruit consumption. Durian is a very popular fruit in South East Asia namely in Malaysia, Indonesia and Thailand. Nevertheless, only 1/3 of the durian fruit can be consumed whereas the husk and seeds are waste products. The waste of the durian fruit is usually sent to the landfills or is burnt. This in turn causes harm to the environment. For this study, the durian husk was used as the filler that will be introduced into the PLA matrix. The aim of this study is to study the PLA durian skin fibre(DSF) composites degradation behavior when subjected to hygrothermal, soil burial and thermal testing.

2.0 Methodology

2.1 Durian Skin Fibers (DSF)

The durian skin was obtained from a local seller at no cost and was then cut into smaller pieces. The smaller pieces were then dried in the oven at 70^{o}C for 24 hours. The dried durian skin was then grinded into fibers and these durian skin fibers(DSF) were then pretreated with alkali.

2.2 Alkali Pretreatment

Alkali pretreatment was done to help improve the interfacial adhesion between the PLA matrix and the DSF. Dried DSF was initially soaked and stirred for one hour with 5% sodium hydroxide (NaOH) solution that was provided by Taylor's University. After an hour, the DSF was filtered out and soaked in water to reduce its alkalinity. The DSF in water was filtered out and soaked in water multiple times until a neutral solution was obtained. The DSF was then filtered out and dried in the oven at 80^{o}C for 24 hours to remove moisture[4].

Pretreatment was done to remove hemicellulose, pectin, lignin and wax as well as to enhance the surface roughness of the DSF. This will enhance the bonding capabilities between the PLA matrix and the DSF by exposing more reaction sites on the DSF for the polymer[5].

2.3 Preparation of Samples

The preparation of the DSF filled PLA biocomposites was done using the melt blending technique. The HAAKE internal mixer model Polylab System E93 was used for the melt blending. The biocomposite was formed at a temperature of 180^{o}C, at a speed of 50-100 rpm for a period of about 7-10 minutes[6]. The composite prepared has a composition varying from 0-40 wt% of DSF both treated and untreated and is shown in Table 1 below. The next part of the preparation process was to obtain the polymer sheets. The biocomposite went through a compression moulding process where it was preheated for a period of 5 minutes. The composite was then pressed for 1 minute at 180^{o}C under a pressure of 150 bar. The sheet was then cooled for 8 minutes to reduce it to a temperature of 60^{o}C[7]. A pure PLA sheet was also made in the same way and used as reference.

Table 1: Weight percentages of samples to be prepared.

Samples	Weight of treated DSF (grams)	Weight of untreated DSF (grams)	Weight of PLA (grams)	Total weight of biocomposite (grams)
Pure PLA	0	0	100	100
PLA/15% treated DSF	15	0	85	100
PLA/25% treated DSF	25	0	75	100
PLA/40% treated DSF	40	0	60	100
PLA/30% untreated DSF	0	30	70	100

2.4 Biodegradation Tests

2.4.1 Soil Burial Test

The soil burial test was done to test the biodegradability of the biocomposite towards the microorganisms present in the soil. Three pieces(to get an average) of each sample was buried with a depth of 7 cm with a separating distance of 2 cm in garden soil placed in a large pot[8]. The biocomposites buried were completely covered with soil and the composite were not visible. The weight loss of the buried samples was tested after the 1st, 2nd, 5th, 7th, 14th, 21st, 28th ,45th ,60th, 70th and 90th day. Throughout this period, the soil was sprayed with tap water to create a moist condition to promote microbial activity[9].Each sample was dug out and wiped before being dried at 45^{o}C – 55^{o}C until a constant weight is obtained. The weight of the samples were taken for every 10 minute interval up till a constant weight was achieved. All the data obtained was collected ,tabulated and analysed.

2.4.2 Hygrothermal Test

Hygrothermal test investigates the changes a sample undergoes under environmental conditions which are water and heat. The samples were immersed in a water bath at a set temperature of 58 ^{o}C , Giuliana Gorrasi et al. [10] research had concluded that the PLA degradation is best around its glass transition temperature which is around 55^{o}C to 65^{o}C. Before the test is carried out, the initial weights of the samples were weighed and noted down. The samples were then weighed again at intervals of 1, 2, 5, 7 and 14 days. This is done in order to investigate the degradation of the composite material[11]. All the data obtained were collected, tabulated and analysed.

3.0 Results and Discussions

The soil burial and hygrothermal test carried out will help give a clearer understanding on how the pretreatment impacts the biodegradation as well as whether the biodegradation increases with the weight percent of DSF within the biocomposite matrix.

3.1 Soil Burial Test

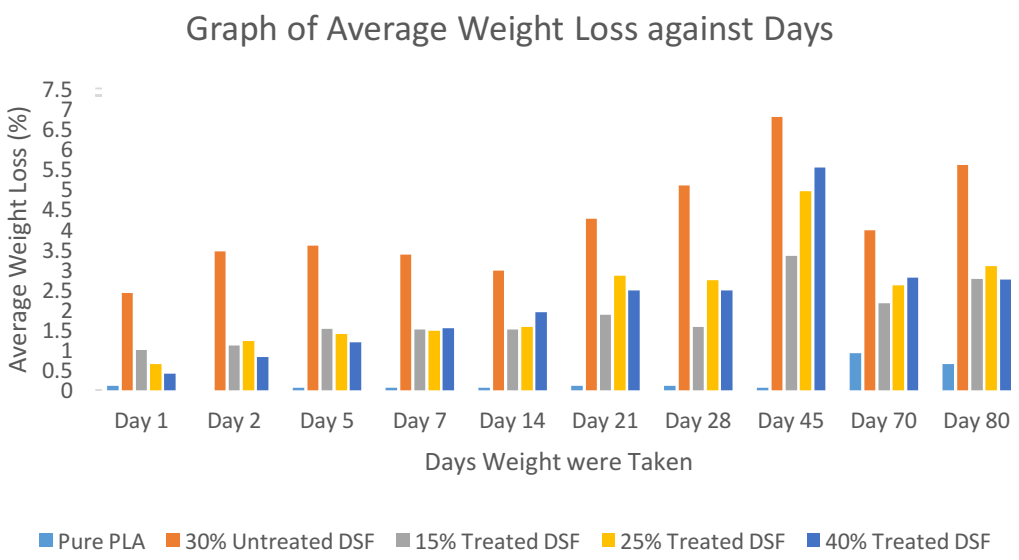


Figure 1 : Percentage weight loss for soil burial test.

The percentage weight loss of the samples were calculated using the following Equation 1.

$$\text{Percentage Weight Loss (\%)} = \frac{W1-W2}{W1}\ x\ 100 \quad (1)$$

Figure 1 illustrates the effect of the durian skin fibre on the biodegradability of PLA/DSF biocomposite when put through the soil burial test. The soil burial test was done on a laboratory scale to investigate the biodegradability properties of the PLA/DSF composite. From Figure 1 it can be seen that the untreated 30% DSF/PLA biocomposite had the highest percentage weight loss for all the days the weights were measured with pure PLA having the least percentage weight loss over all the other samples being tested. The treated DSF/PLA composite with fibre loadings 15% ,25% and 40% showed an average percentage weight loss between 0.4% to 6%. The pretreated PLA/DSF biocomposites had biodegraded slower than that of the untreated DSF/PLA biocomposites. This is because alkali pretreatment helps to increase the affinity between the pure PLA resin and the natural fibre [12] which in this study is the durian skin fibre (DSF). Numerous other studies had also concluded that alkali pretreatment lead to greater mechanical interlocking as surface roughness in increased with the treatment[13].

3.2 Hygrothermal Test

Due to the intrinsic property of naturally available fibres and the degradability of PLA in nature, the durability of such composites has become a point of concern. Nevertheless, most studies carried out today tend to focus more on further enhancing the mechanical properties of biocomposites. There is minimal amount of research done on the ageing behavior of PLA reinforced with natural fibres in a hygrothermal environment[11].

Figure 2 illustrates the percentage weight loss (%) as a function of time (days). After 14 days, the sample with 40% treated DSF had the highest weight loss 16.6% which was followed by the sample with 25% treated DSF and 15% treated DSF. It can be seen that pure PLA has the lowest percentage of weight loss of about 2% which is about the same of that of the soil burial test.

The overall trend shows that the degradation rate of the samples has increased with time. The percentage weight loss of the samples that underwent the hygrothermal test is greater than that of the samples that went through the soil burial test. This is because the samples in the hygorthermal test was susceptible to attack by both water and heat which is a more aggressive form of testing. During the hygrothermal test, the colour of the water in the beaker in which the samples were placed could be seen to be turning brown except for that of the pure PLA. As the time progressed the samples started becoming soft and more brittle. The pure PLA sample as seen in Figure 3 to be turning into a more obvious white colour and was not transparent anymore. For all the samples that contain the DSF, it can be seen that the sample that has 30% untreated DSF has a higher percentage weight loss up till day 7. This is due to the removal of lignin from the untreated DSF as the other samples containing the DSF had lignin removed during the pretreatment. The increase in percentage weight loss for the treated DSF on the 14th day may be due to the removal of the cellulose which would have been in greater amounts as compared to that of the untreated DSF biocomposite sample [1].

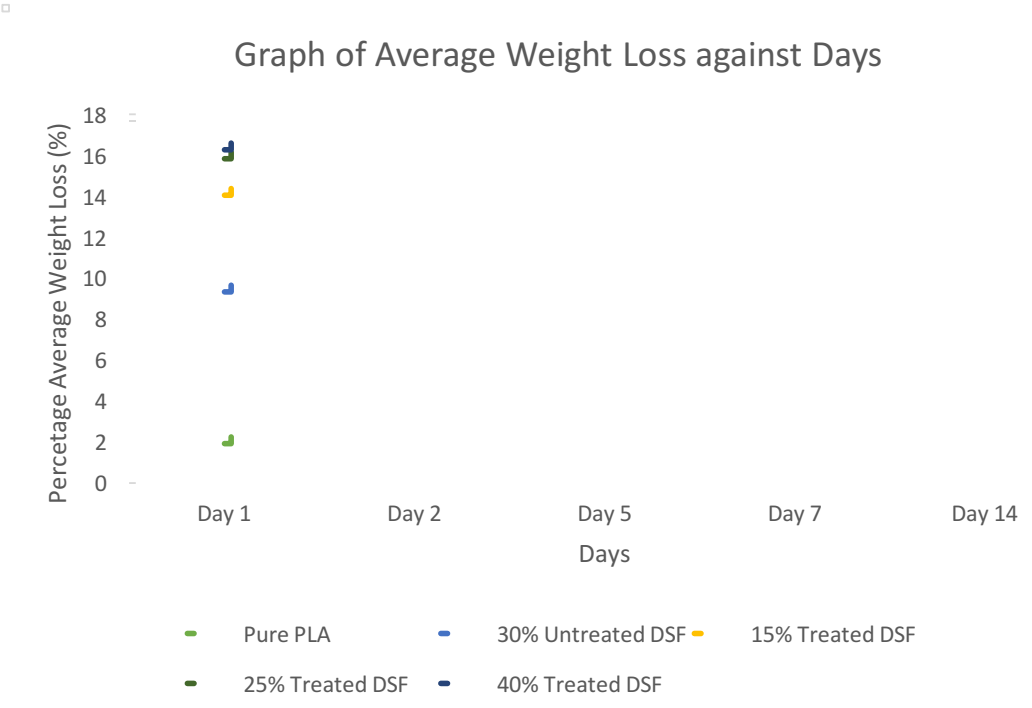


Figure 2: Percentage weight loss for hygrothermal test.

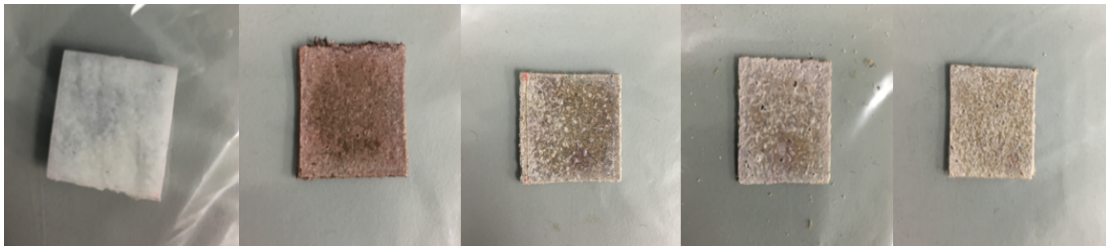


Figure 3 : Sample conditions after 14 days of hygrothermal test. Left to right : Pure PLA, 30% untreated DSF/PLA, 15% treated DSF/PLA, 25% treated DSF/PLA and 40% treated DSF/PLA.

The significantly higher percentage weight loss for the samples containing the DSF as compared to that of pure PLA may be caused by the hydrophilic property of the natural fibres that is caused by the hydroxyl group (-OH) present on the cellulose molecules[14]. The hydroxyl groups forms a hydrogen bond with the water molecules that can be easily removed when heated[15]. From Figure 2 it can be observed that the samples that underwent pretreatment had a higher percentage weight loss at the end of the test period. These results are as expected as pretreatment has brought about the removal of the non-cellulosic covering the cellulose (-OH) groups as well as increasing the surface roughness which in turn helps in increasing the surface area of the fibre[16]

3.3 Scanning Electron Microscope (SEM) Test

SEM micrographs of the surface of both the treated and untreated durian skin fibre composites can be seen in Figures 4 to 7. The fibers pullouts that are visible on the micrographs shows the poor adhesion between the untreated durian skin fibre(DSF) with the polylactic acid(PLA) matrix. The SEM micrographs of the treated DSF composites shows a better adhesion between the fibre and the matrix of the PLA. This strongly implies that the alkali pretreatment has brought about the strong adhesion between the fibre and the PLA matrix. The SEM micrographs also show that the durian skin fibres are not dispersed evenly around the composite matrix. Previous studies that have been carried out indicated that the performance of a biocomposite was directly linked to the dispersion of the natural fibres within the biocomposite matrix[17]. The properties of a biocomposite will significantly be less favourable in the event that bad dispersion of fibres were to occur. The SEM micrographs also shows that the roughness of the surface of the biocomposite had increased after going through 60 days of soil burial test. The SEM micrographs after 60 days of soil burial shows the presence of voids and crack lines indicating degradation.

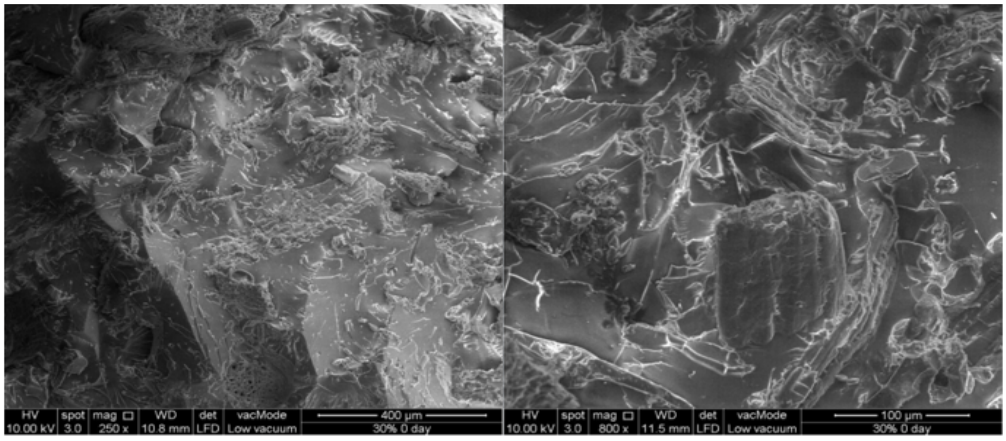


Figure 4: SEM image of 30% untreated DSF/PLA biocomposite before soil burial.

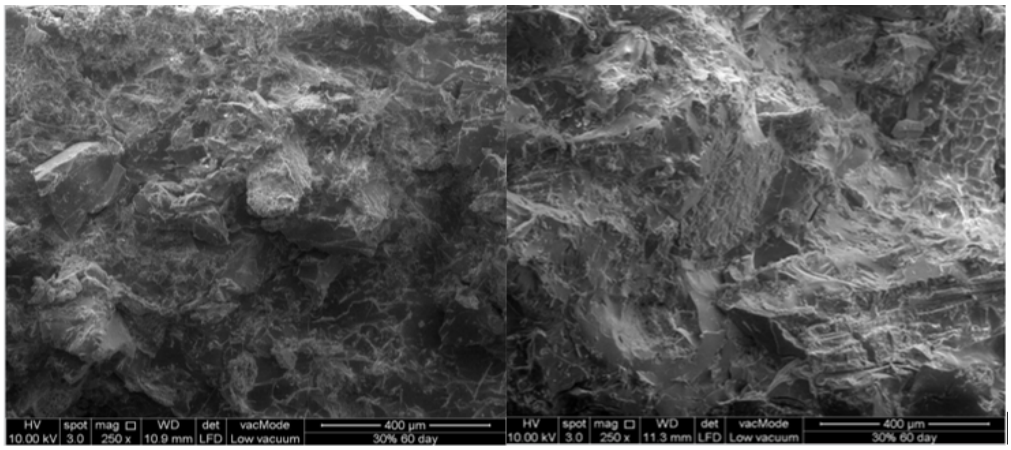


Figure 5: SEM image of 30% untreated DSF/PLA biocomposite after 60 days of soil burial.

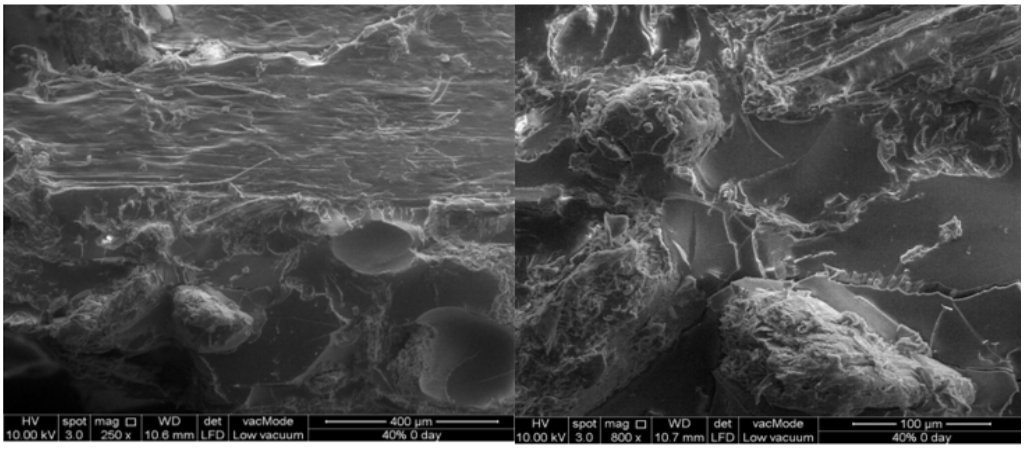


Figure 6: SEM image of 40% treated DSF/PLA biocomposite before soil burial.

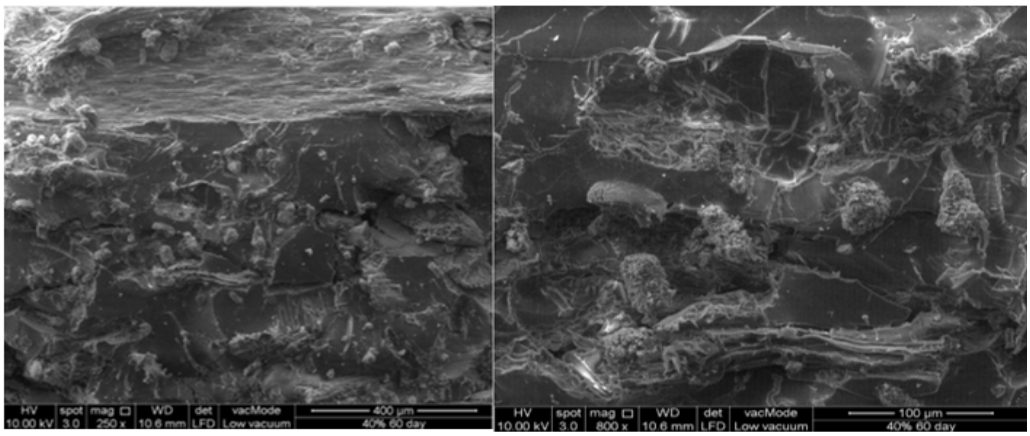


Figure 7: SEM image of 40% treated DSF/PLA biocomposite after 60 days of soil burial.

4.0 Conclusions

The presence of the durian husk/skin fibre (DSF) did improve the degradation of PLA. A higher percentage weight loss (%) was observed with the samples that contained the DSF. The thermogravimetric analysis(TGA) showed that the alkali pretreatment had improved the thermal stability of the PLA/DSF biocomposites. The hygrothermal test showed that the degradation of the PLA/DSF biocomposites was greater as compared to that of the soil burial test as the samples were susceptible to attack by both water and heat. SEM micrographs showed that alkali pretreatment had brought about better adhesion between the DSF and the polymer matrix. Therefore, more research and testing needs to be carried out to further test the capabilities of using the PLA/DSF composites in everyday applications.

References

[1] M. R. Nurul Fazita, K. Jayaraman, D. Bhattacharyya, M. K. Mohamad Haafiz, C. K. Saurabh, M. Hazwan Hussin, and H. P. S. Abdul Khalil, "Green composites made of bamboo fabric and poly (lactic) acid for packaging applications-a review," *Materials (Basel).*, vol. 9, no. 6, 2016.

[2] K.L.Pickering, *Properties and performance of natural-fibre composites*. Woodhead Publishing Limited, 2008.

[3] "Natural Fibers, Plastics and Composites," *J. Chem. Inf. Model.*, p. 370, 2004.

[4] S. Lee, "Influence of Chemical Modification and Filler Loading on Fundamental Properties of Bamboo Fibers Journal of Composite Materials," no. October 2015, 2009.

[5] M. Ayd, H. Tozlu, and S. Kemaloglu, "Effects of Alkali Treatment on the Properties of Short Flax Fiber – Poly (Lactic Acid) Eco-Composites," pp. 11–17, 2011.

[6] S. Matsumura, *Biodegradable Polymers for Industrial Applications*. 2005.

[7] N. Ploypetchara, P. Suppakul, D. Atong, and C. Pechyen, "Blend of polypropylene/poly(lactic acid) for medical packaging application: Physicochemical, thermal, mechanical, and barrier properties," *Energy Procedia*, vol. 56, no. C, pp. 201–210, 2014.

[8] M. Arena, C. Abbate, K. Fukushima, and M. Gennari, "Degradation of poly

(lactic acid) and nanocomposites by Bacillus licheniformis," *Environ. Sci. Pollut. Res.*, vol. 18, no. 6, pp. 865–870, 2011.

[9] M. Karamanlioglu, A. Houlden, and G. D. Robson, "Isolation and characterisation of fungal communities associated with degradation and growth on the surface of poly(lactic) acid (PLA) in soil and compost," *Int. Biodeterior. Biodegrad.*, vol. 95, no. PB, pp. 301–310, 2014.

[10] G. Gorrasi, A. Sorrentino, and R. Pantani, "Modulation of Biodegradation Rate of Poly (lactic acid) by Silver Nanoparticles," 2015.

[11] V. S. Raja and T. Shoji, *Stress corrosion cracking; Theory and Practice*. 2011.

[12] T. Yu, J. Ren, S. Li, H. Yuan, and Y. Li, "Effect of fiber surface-treatments on the properties of poly(lactic acid)/ramie composites," *Compos. Part A Appl. Sci. Manuf.*, vol. 41, no. 4, pp. 499–505, 2010.

[13] X. Liu, S. Lv, Y. Jiang, J. Shi, H. Tan, J. Gu, and Y. Zhang, "Effects of alkali treatment on the properties of WF/PLA composites," *J. Adhes. Sci. Technol.*, vol. 4243, no. November, pp. 1–11, 2016.

[14] R. H. Hu, M. young Sun, and J. K. Lim, "Moisture absorption, tensile strength and microstructure evolution of short jute fiber/polylactide composite in hygrothermal environment," *Mater. Des.*, vol. 31, no. 7, pp. 3167–3173, 2010.

[15] Z. Leman, S. M. Sapuan, A. M. Saifol, M. A. Maleque, and M. M. H. M. Ahmad, "Moisture absorption behavior of sugar palm fiber reinforced epoxy composites," *Mater. Des.*, vol. 29, no. 8, pp. 1666–1670, 2008.

[16] M. S. Islam, K. L. Pickering, and N. J. Foreman, "Influence of Hygrothermal Ageing on the Physico-Mechanical Properties of Alkali Treated Industrial Hemp Fibre Reinforced Polylactic Acid Composites," *J. Polym. Environ.*, vol. 18, no. 4, pp. 696–704, 2010.

[17] M. S. Salit, M. Jawaid, N. Bin, and E. Hoque, *Manufacturing of Natural Fibre Reinforced Polymer Composites*. .

Thermogravimetric Analysis of Pretreated Cow Dung Biomass Using Deep Eutectic Solvent

Aatif Shafqat[1], Rashmi Walvekar[1*], Mohammad Khalid[2], Kaveh Shahbaz[3]

[1]*School of Engineering, Taylor's University, Malaysia*

[2]*Nottingham University, Malaysia*

[3]*University of Auckland, New Zealand*

[*]*rashmigangasa.walvekar@taylors.edu.my*

Abstract

Cow dung biomass (CDB) was pretreated using choline chloride: oxalic acid deep eutectic solvent (DES). The three biomass to DES ratio chosen were 1g biomass to 50g DES, 1g biomass to 100g DES and 1g biomass to 150g DES. Each of the mass ratio were pretreated using three different times, 30 minutes, 60 minutes and 120 minutes. The temperature was kept constant for all the experiments at 90°C. The structure and morphology of the pretreated biomass were studied using EDX, FESEM and TGA analysis. EDX results showed a decrease in carbon content as well as an increase in oxygen content, while demonstrating that the best pretreatment time for obtaining the highest carbon content to be 30 min regardless of DES mass used. FESEM results for cow dung biomass showed a compact rough short fibre surface indicating the presence of lignin and lacking pores. Once pretreatment was performed, the surface turned into long fibres with a smoother structure and presence of pores. Finally, TGA was conducted for temperature range of 30°C to 600°C at 10°C/min on all biomass samples. about 38% of weight degrades in temperature range of 200°C and 400°C indicating degradation of cellulose and hemicellulose. The weight percentage remained same for unpretreated cow dung and ChOx5030 samples. The conclusion being, DES pretreatment does not result in heavy removal of cellulose and hemicellulose. Weight percentage degrading in temperature range of 450°C and 550°C increased from 5.5% of cow dung biomass to 19% for ChOx5030, indicating that DES pretreatment made the biomass more accessible to thermal effects.

Keywords: Cow Dung Biomass, Deep Eutectic Solvent, Pretreatment, Thermogravemteric Analysis, Field Electron Scanning Electron Microscopy.

1. Introduction

Dairy cows are one of the most populous animals in the world with more than 265 million [1]. Each cow produces up to 3 kg of dung every day, taking the amount of cow dung produced to 795 million per day [2]. Cow dung always had an application in agriculture but recently have found way as means to produce biogas [3], generating energy by direct combustion [4] and also in manufacturing bio-composites [2]. With the quantity of cow dung generated each year and the difficulty of their disposal, there can be even more applications in the field of engineering and science, as not all of the cow dung is currently utilized.

Besides the applications mentioned, cow dung biomass can be applied in manufacturing carbon based materials, however the structure and contents of cow dung will play major role in deciding what material can be synthesized from it, although it can be hypothesized that carbon based materials can be manufactured by altering the contents of cow dung similarly to the other biomass available [5]. Typical cow dung composition is mentioned in Table 1. Like other biomass, cow dung also consist of varying lignocellulose, cellulose, hemicellulose and lignin, as well as other materials in small quantities called extractives [6]. The cellulosic content is lower than other biomass because the biomass is already treated during the digestion process of the cow. Therefore, pretreatments are applied to alter the structure and composition of cow dung biomass.

Table 1. Composition of Cow Dung Biomass (CDB) [2]

Component	Weight %
Carbon	56.29
Oxygen	37
Fiber	40.4
Cellulose	27.4
Hemicellulose	12.2
Lignin	13

Cheap acidic pretreatments on biomass are done using sulfuric acid and phosphoric acid, while pretreatments using hydrochloric acid and nitric acids are more potent but relatively expensive due to higher cost of acids. The treatment is flexible enough for the process to be carried out at different temperatures and acid concentrations. Sulfuric acid pretreatment is applied to wheat straw biomass at a temperature of 90°C for 10 hours and the result is hemicellulose hydrolyzing while cellulose and lignin are unaffected [7]. The second type of pretreatment is performed using alkaline solutions of either sodium, potassium or ammonia at specific temperatures and pressures. Switchgrass biomass was pretreated using potassium hydroxide at a temperature of 121°C for 1 hours resulting in heavy delignification of switchgrass, however the application of potassium hydroxide for pretreatment is expensive [8]. Both acid and alkaline pretreatments attack the lignocellulose in a unique manner resulting in different final structure and content of the biomass [9] but researchers are still looking for alternatives to these pretreatments due to their high costs.

Recently ionic liquids (ILs) have been explored to replace existing conventional pretreatment methods. ILs have been used for pretreatment of corn stover [10] and wood chips biomass [11]. 1-methyl-3octylimidazolium IL was used as pretreatment in extraction of lignin from rice straw with a success of 50% lignin removal [12]. However, ILs are expensive and not environmentally favorable. Recently, a new type of solvent, very similar in function to ILs called deep eutectic solvents (DES), were discovered [13]. DES are better than IL, they are able to counter the disadvantages of ionic liquids such as toxicity and high cost. Preparation of DES is also very flexible requiring material that are renewable, can be tuned based on the application and they can be utilized as solvents for a number of extraction processes [14].

DES system is comparable to ionic liquids in the sense it has low melting points and performs similar reactions. The DES is a combination of an organic salt and hydrogen bond donor (HBD). The hydrogen bond donors (HBD) selected was oxalic acid, also having environmental friendly status as stated in the literature review, both of them are in solid state before the mixing process.

DES pretreatment was performed on corncob and the result was strong lignin removal. The best performing DES, consisting of choline chloride salt and oxalic acid HBD, was able to extract 98.5% lignin from corncob [15]. Although some research has been conducted in utilizing DES as pretreatment of biomass [15–17], it has never been conducted on cow dung and therefore provide an opportunity for exploration.

Since literature review on cow dung as potential biomass and its pretreatment technique has not been researched, it provided a strong opportunity for a novel research and explore a new dimension. The use of cow dung is vast but the main focus of this report is to understand the structure and morphology before and after pretreatment with choline chloride: oxalic acid, deep eutectic solvent. The factors studied during pretreatment are mass ratio of cow dung biomass to DES and the reaction time for the mixture.

2. Materials and Methods

2.1 Materials

Cow dung was obtained from farm in UPM, Serdang, and was sun dried followed by oven dried, then powdered using home grinder Panasonic. Choline chloride was purchased from Merck Sdn. Bhd. with a purity of 99% and is in solid state. Oxalic acid was purchased from SYNERTEC ENTERPRISE with a purity of 99.5% and is in solid state.

2.2 Experimental methodology

2.2.1 Synthesis of DES

Choline chloride was pre-dried for two (2) hours in oven before the preparation of DES to remove any moisture content, as moisture content interferes with the DES formation. DES with the molar ratio of 1:1 was synthesized. Time and temperature for mixing of DES was 2 hours and 80°C, respectively. A colorless solution with no crystals is observed once synthesis is complete.

2.2.2 Pretreatment of Cow Dung

Once the DES solution is prepared, pretreatment process can be conducted. 1 g of CDB was taken as standard for all the experiments performed. Pretreatment temperature was kept constant at 90°C for all the samples. The parameters that were altered were the CDB to DES mass ratios utilized for pretreatment and the pretreatment time. Mass of DES utilized were 50g, 100g and 150g. Mass ratio and pretreatment time as well as sample codes are provided in Table 2. The cow dung biomass sample not pretreated is referred to as cow dung biomass (CDB) throughout the study.

Magnetic stirrer was placed inside Schott bottle and the required mass of DES and cow dung biomass was transferred in the bottle. The bottle was then placed on a hot plate stirrer to begin pretreatment. Once the pretreatment was over, the mixture was allowed to cool down and the change of colorless DES to dark red brown was noted.

The sample contents were washed with ethanol twice to remove the DES and dissolved solids followed by water washing until a clear colorless distilled water containing the pretreated biomass is observed. The biomass is collected and oven dried at 100°C for 2 hours.

Table 2. Parameters of Original CDB and DES Pretreated CDB Samples

Mass of DES Used (g)	CDB:DES Mass Ratio	Pretreatment Time (minutes)	Sample Code
n/a	n/a	n/a	Cow Dung (CDB)
50	1:50	30	ChOx5030
50	1:50	60	ChOx5060
50	1:50	120	ChOx50120
100	1:100	30	ChOx10030
100	1:100	60	ChOx10060
100	1:100	120	ChOx100120
150	1:150	30	ChOx15030
150	1:150	60	ChOx15060
150	1:150	120	ChOx150120

3 Results and Discussion

3.1 Energy-Dispersive X-ray (EDX)

EDX was performed on cow dung biomass and the pretreated cow dung samples using EDX-Zeis Supra 35 VP equipment. All the samples were sent to Nottingham University, Malaysia for analysis. The aim of this analysis is to observe and understand the elemental weight percentage changes after each pretreatment. From a sample view, it can be noted that DES has strong potential to change the composition of carbon and oxygen present in the biomass. This is confirmed by various studies [14, 15, 18] and so is confirmed in during this research.

Cow dung biomass contains 56.29% carbon initially and the weight percentage drops after each pretreatment regardless of DES mass and pretreatment time. This is due to removal of high fraction of lignin and even small amount of cellulose and

hemicellulose. Absorption of each lignocellulose content by DES is also reported in various studies, whereas also reporting higher lignin absorption than cellulose and hemicellulose [14, 15, 18].

Table 3. Carbon and Oxygen Weight% of All Samples

Sample Code	Carbon Weight %	Oxygen Weight %
Cow Dung (CDB)	56.29	37
ChOx5030	52.1	42.04
ChOx5060	50.7	41.91
ChOx50120	50.57	43.21
ChOx10030	51.77	44.05
ChOx10060	49.62	41.87
ChOx100120	48.79	42.27
ChOx15030	52.1	42.79
ChOx15060	48.4	39.89
ChOx150120	48.05	45.08

Next, the weight of oxygen change is crucial in determining the behavior of DES. Table 3 and Figure 1, highlight the increase in oxygen weight percentage after each pretreatment. The increase can be related to the basic chemical formulas of cellulose, hemicellulose and lignin. Cellulose and hemicellulose molecules contain more oxygen than lignin molecules, while lignin contains more carbon [20] therefore, the increase in oxygen weight percentage after pretreatment in noted. However, the case is not straightforward for all pretreatments.

During the 30 min pretreatment of all mass ratios, the weight percentage of oxygen increases when compared to the original biomass sample. Oxygen weight percentage then decreases for all 60 min reaction time. Comparing oxygen weight percentage of ChOx10030 to ChOx10060, a notable decrease from 44.05% to 41.87% is observed. The situation is similar for other cases. When pretreatment time is further increased to 120 min, oxygen content can be seen increasing. This increase is interesting and highlights the important factor of DES pretreatment in delignification of biomass. More lignin can be accessed due to breaking of lignin layer.

It can be hypothesized that initially DES is dissolving all lignocellulose constituents, with lignin dissolved most, therefore increase in oxygen content. As pretreatment time is increased, more cellulose and hemicellulose get dissolved, reducing the oxygen content. Once pretreatment time is increased to 120 min, DES once again dissolves more lignin, increasing the cellulose and hemicellulose content and hence, the oxygen content.

The conclusion made from EDX analysis based on Table 3 and Figure 1 is that increasing DES mass does have not effect on the carbon content, since ChOx5030, ChOx10030 and ChOx15030 all result in the same carbon content of approx. 52%. However, with respect to time, the carbon content reduces, as shown by ChOx5060, when carbon content reduces to 50.7% and also ChOx150120, when carbon content reduced to 48.05%. It can be theorized that DES only attacks lignin during the first 30 min. As time is increased to 60 min, DES starts to attack cellulose and hemicellulose

structure and dissolves them as well. This can be confirmed by reduction in oxygen weight percentage. When time is increased to 120 min, DES dissolves almost all the available lignin as well as some cellulose and hemicellulose, until a saturation point is reached.

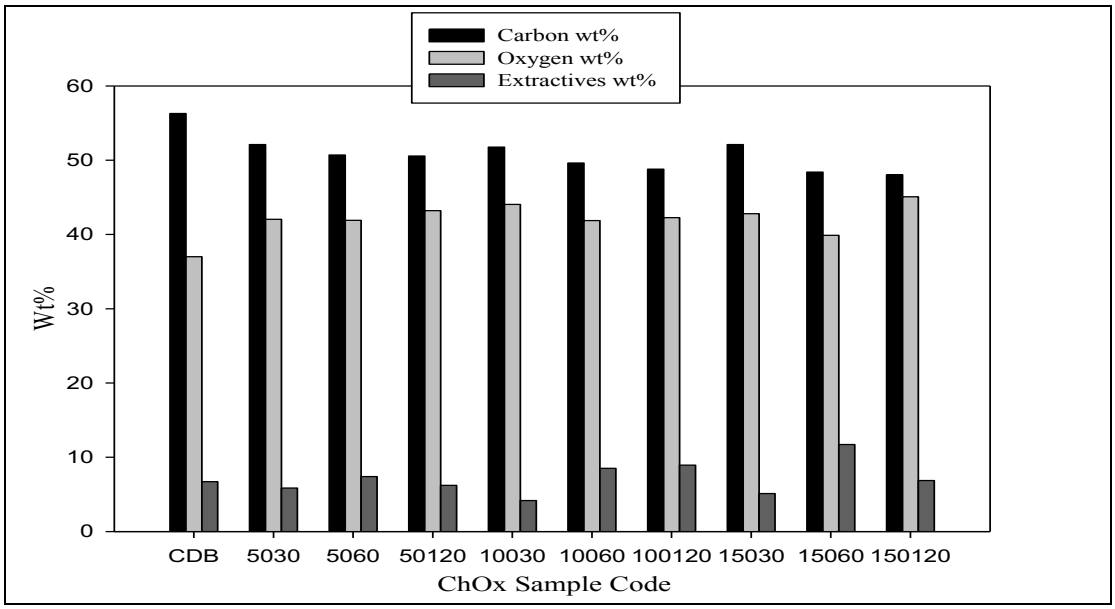


Figure 1. Weight Percentage of Carbon and Oxygen in Each Pretreated Sample

3.2 Field Emission Scanning Electron Microscopy (FESEM)

FESEM analysis was conducted using Ultra 55 FESEM from Chicago, USA with accelerating voltage of 20kV, to understand the structure and morphology of cow dung biomass before and after pretreatment. Once again, all the samples were sent to Nottingham University, Malaysia. From the initial observation of cow dung biomass at 1600x magnification, it can be seen the structure is a cluster of small, strongly linked fiber, Figure 2. Linkage results in a haphazard styled, rough solid surface, containing very little pores. The structure appears to be hard, which is a clear indication of lignin. Lignin contains a strong interlinking molecular structure, providing a hard rough surface good for protecting the biomass [6].

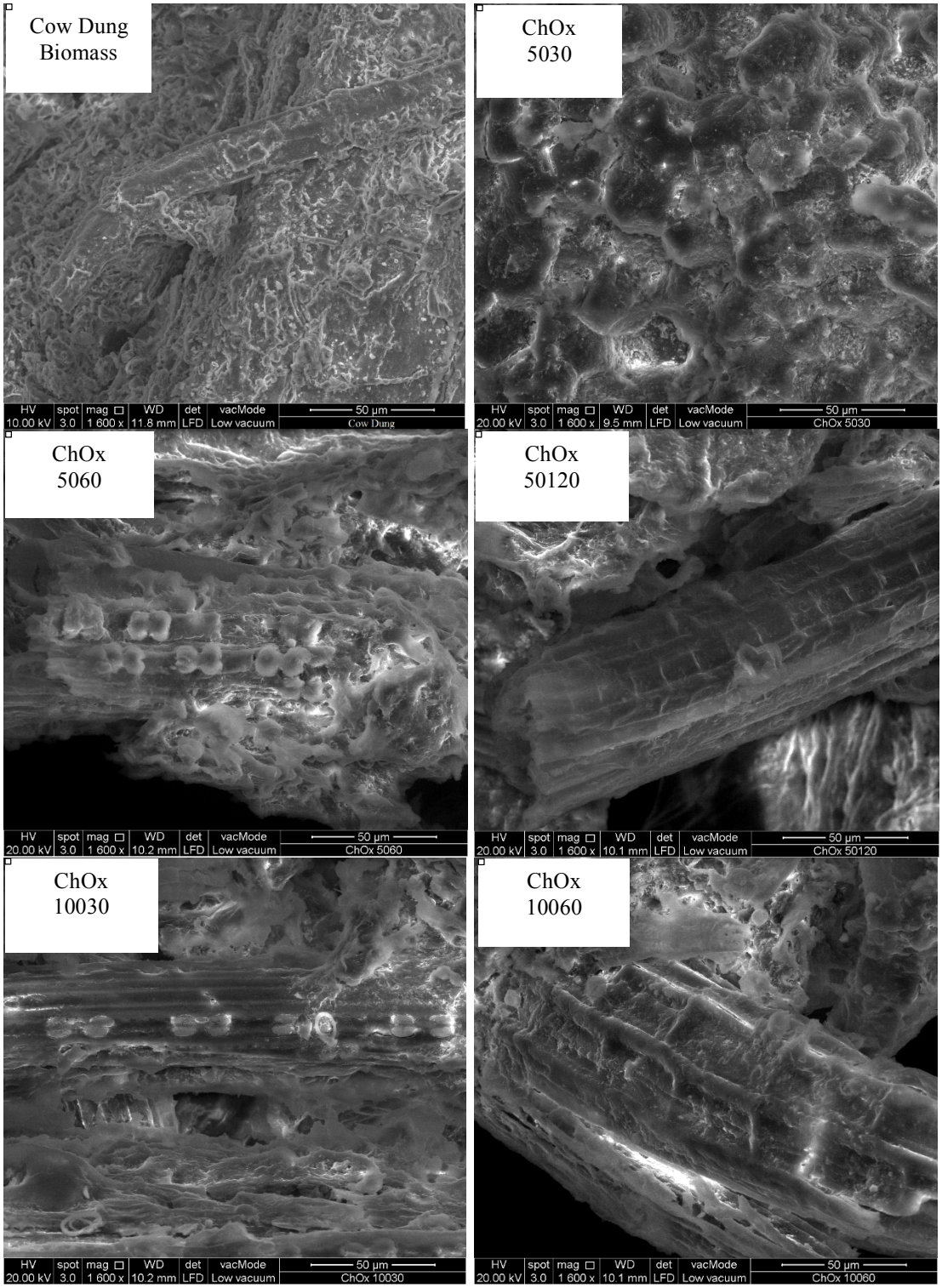


Figure 2: CDB Structure Before and After Pretreatment

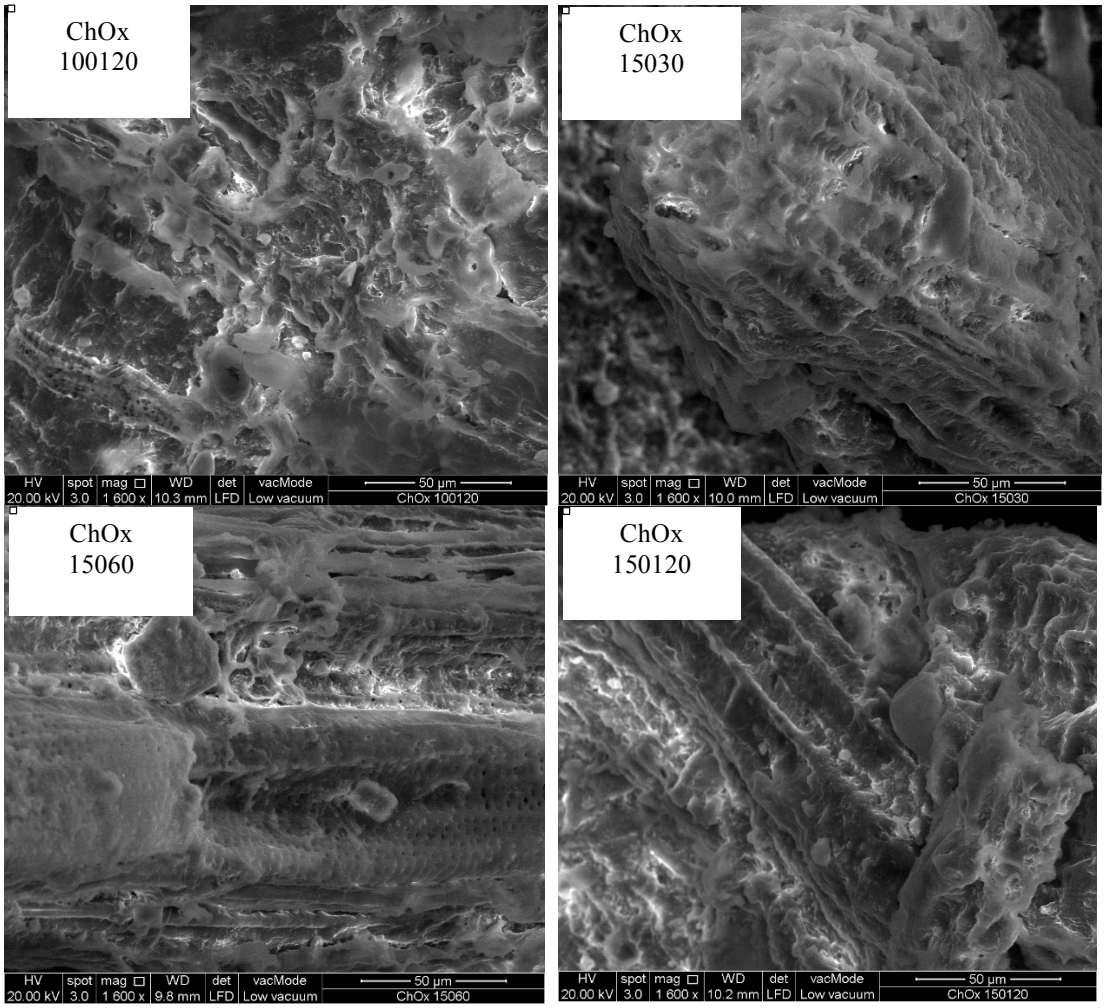


Figure 2: CDB Structure Before and After Pretreatment (Continued)

Pretreatment alters the structure of the biomass considerably. After all pretreatments, the biomass displays a heavy presence of long fibers, with a much smoother surface compared to original cow dung biomass. Long strands of these fiber can be seen clearly in the images and appears to be much softer in nature. The fiber exposure can be due to removal of lignin, since lignin is a hard solid structure that covers the biomass. Removal of lignin results in exposure of cellulose, hemicellulose and fiber, which have a much delicate and simple molecular structure consisting of straight chains as compared to lignin's crosslinking structure.

Finally pores between the strands are clearly visible. Breaking of bonding between cellulose, hemicellulose and lignin can result in pores within the structure, due to the disappearance of strong linkage between the three lignocellulose components. Difference between the structures of pretreated biomass is not subtle in these pictures, it is highly possible that a stronger magnification can outline the details for each pretreated sample.

3.3 Thermogravimetric Analysis (TGA)

TGA was performed using PerkinElmer TGA 8000. TGA is the main analysis for this research as it provides strong analysis for the presence of cellulose, hemicellulose and lignin. TGA was conducted for temperature range of 30°C to 600°C at 10°C/min. 5-10 mg of cow dung biomass samples was placed on platinum crucibles and the crucible were placed on the Perkin Elmer TGA 8000 trays for TGA. The conditions for analysis were set under an inert environment of 40 mL/min constant flow of nitrogen purge gas, to avoid any oxidation of the samples. Thermal degradation curves for cow dung biomass and all pretreated samples are provided Figure 3. There is an initial degradation occurring between temperature range of 60°C to 110°C. At this temperature, moisture evaporation is taking place and results in the first degradation dip.

Thermal degradation of hemicellulose starts at 180°C and ends around 340°C. Cellulose degradation begins at 280°C, peaking at 400°C when all cellulose is degraded. Lignin degrades slowly over the range of 200°C up until 600°C. Finally, fiber has a degradation temperature range of 150°C to 650°C [21]. This can be confirmed by the TGA curves for all the pretreated samples. The main degradation for all samples starts at 250°C, as it continues until 400°C with a very sharp gradient. As the temperature increases further, the gradient sharpness drops, however degradation continues as lignin or exposed fiber has not been decomposed yet.

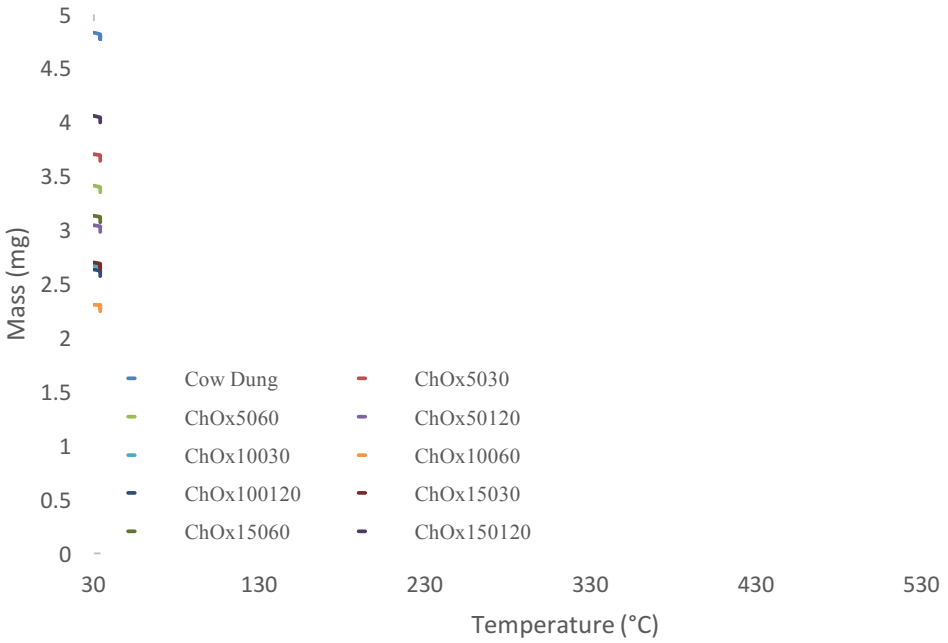


Figure 3: Accumulative Thermogravimetric Analysis

Analysis of cow dung from Figure 3, leads to the conclusion about the first weight loss of 12% and degradation starting at temperature of 34°C and completing at 110°C. This mass is the moisture content evaporating from the cow dung biomass. Furthermore, about 38% of weight degrades in temperature range of 200°C and 400°C, which links strongly with the combined mass of cellulose and hemicellulose from

Table 1, as well as falls in the degradation temperature of the two components. The final weight loss can be seen with a small onset starting at about 500°C and continuing until 570°C. Weight of 5.5% decomposes in this range, which can be final mass lignin or fiber degrading, while the remaining mass decomposes at steady state.

Comparison of analysis of cow dung to that ChOx5030 begins with the comparison of moisture content, as only 6.7% weight degrades in the range of 30°C to 110°C for ChOx5030. A simple reason for this reduction in moisture content can be due to pretreatment absorbing some of the moisture from the biomass, providing a positive point for pretreatment because the pretreated biomass does require a lot of energy to remove moisture content. A second weight loss missing cow dung but present in ChOx5030 is due to pretreatment, and it is highly possible a fiber structure with a decomposition temperature of 150°C has been exposed and can now easily degrade, which was not possible before pretreatment.

The most important degradation occurs in the range of 200°C to 400°C, that is the degradation temperature of cellulose and hemicellulose. Comparing the weight percentage degradation occurring for cow dung biomass and ChOx5030, there is not much difference. Both samples have around 38% degradation in that temperature range. This is an indication that DES did not dissolve much cellulose and hemicellulose. And last but not the least, weight percentage degrading in temperature range of 450°C and 550°C has increased from 5.5% to 19%. Component degrading within this range are most likely fibers and remaining lignin, however they degrade with much ease, not seen in TGA of cow dung biomass.

4. Conclusion

The focus of this research paper was to determine the change in structure and elemental composition of cow dung biomass after it undergoing DES pretreatment with three varying biomass parameters: DES mass ratios and reaction time. The pretreated biomass was subjected to EDX analysis, which indicated a reduction in carbon and oxygen weight percentage after pretreatment. Residence time of 60 min of all mass ratios indicated the least about of oxygen weight percentage. The SEM results showed drastic change in the structure of the pretreated biomass, since after pretreatment the structure was smoother and contained long strands of fiber as well as pores. Furthermore, thermogravemetric analysis determined the change occurring in degradation temperatures of the cow dung biomass and pretreated samples. TGA analysis of all samples resulted in ease of degradation of pretreated samples.

DES pretreatment proved to be strong enough in changing and allowing the biomass structure become more accessible. Although, further testing and analysis need to be done to understand the full extent the DES pretreatment had on cow dung biomass, as well as comparisons of choline chloride: oxalic acid DES with other DES and also conventional pretreatment methods need to be made.

References

[1] Pietro Gennari, “Statistics : Dairy cows,” pp. 1–8, 2012.
[2] M. Yusefi, M. Khalid, F. M. Yasin, L. C. Abdullah, M. R. Ketabchi, and R. Walvekar, “Performance of Cow Dung Reinforced Biodegradable Poly(Lactic

Acid) Biocomposites for Structural Applications," *J. Polym. Environ.*, vol. 0, no. 0, pp. 1–13, 2017.
[3] S. Abdulsalam, J. Mohammed, C. E. Programme, E. Technology, J. O. Etim, and A. I. State, "Production of Biogas From Cow and Elephant Dung," vol. 5, no. 1, pp. 51–56, 2012.
[4] M. Parsamehr, "Heat generation by cow dung incineration in the north of Iran," 2012.
[5] M. Guiotoku, C. M. B. F. Maia, C. R. Rambo, and D. Hotza, "Synthesis of Carbon-Based Materials by Microwave Hydrothermal Processing," *Chem. Eng.*, p. 19, 2003.
[6] H. Chen, "Chemical Composition and Structure of Natural Lignocellulose," *Biotechnology of lignocellulose: Theory and practice*, Chapter 2, 2014.
[7] G. González, J. López-Santín, G. Caminal, and C. Solà, "Dilute acid hydrolysis of wheat straw hemicellulose at moderate temperature: A simplified kinetic model," *Biotechnol. Bioeng.*, vol. 28, no. 2, pp. 288–293, 1986.
[8] R. Sharma, V. Palled, R. R. Sharma-Shivappa, and J. Osborne, "Potential of potassium hydroxide pretreatment of switchgrass for fermentable sugar production," *Appl. Biochem. Biotechnol.*, vol. 169, no. 3, pp. 761–772, 2013.
[9] V. Chaturvedi and P. Verma, "An overview of key pretreatment processes employed for bioconversion of lignocellulosic biomass into biofuels and value added products," *3 Biotech*, vol. 3, no. 5, pp. 415–431, 2013.
[10] S. Singh, G. Cheng, N. Sathitsuksanoh, D. Wu, P. Varanasi, A. George, V. Balan, X. Gao, R. Kumar, B. E. Dale, C. E. Wyman, and B. A. Simmons, "Comparison of Different Biomass Pretreatment Techniques and Their Impact on Chemistry and Structure," *Front. Energy Res.*, vol. 2, no. February, pp. 1–12, 2015.
[11] M. Zavrel, D. Bross, M. Funke, J. Büchs, and A. C. Spiess, "High-throughput screening for ionic liquids dissolving (ligno-)cellulose," *Bioresour. Technol.*, vol. 100, no. 9, pp. 2580–2587, 2009.
[12] G. Gogoi and S. Hazarika, "Coupling of ionic liquid treatment and membrane filtration for recovery of lignin from lignocellulosic biomass," *Sep. Purif. Technol.*, vol. 173, pp. 113–120, 2017.
[13] A. P. Abbott, G. Capper, D. L. Davies, H. L. Munro, and R. K. Rasheed, "Preparation of novel, moisture-stable, Lewis-acidic ionic liquids containing quaternary ammonium salts with functional side chains†," pp. 2010–2011, 2011.
[14] G. H. Yang, T. Y. Wu, Y. Loow, and L. Y. Ang, "Application of deep eutectic solvents in biomass valorization," pp. 1–20.
[15] C. Zhang, S. Xia, and P. Ma, "Bioresource Technology Facile pretreatment of lignocellulosic biomass using deep eutectic solvents," *Bioresour. Technol.*, vol. 219, pp. 1–5, 2016.
[16] Z. Maugeri, "Deep Eutectic Solvents: Properties and Biocatalytic Applications," p. 109, 2014.
[17] Shinya Yokoyama, "Part 2. Biomass resources," *Asian Biomass Handb.*, pp. 12–80, 2008.
[18] A. Abo-hamad, M. Hayyan, M. Abdulhakim, and M. Ali, "Potential applications of deep eutectic solvents in nanotechnology," vol. 273, pp. 551–567, 2015.
[19] Y. Zhang, X. H. Lu, X. Feng, Y. J. Shi, and X. Y. Ji, "Properties and Applications of Choline-Based Deep Eutectic Solvents," *Prog. Chem.*, vol. 25, no. 6, pp. 881–892, 2013.
[20] P. de Wild, H. Reith, and E. Heeres, *Biomass pyrolysis for chemicals*, vol. 2, no. 2. 2011.

[21] M. Brebu and C. Vasile, “Thermal degradation of lignin—a review,” *Cellul. Chem. Technol.*, vol. 44, no. 9, pp. 353–363, 2010.

Investigation of Palm Fibre- Derived Activated Carbon in Wastewater Treatment

Ying Yin Chia[1*], Li Wan Yoon[1]

[1]*School of Engineering, Taylor's University, Malaysia*

[*]*yingyin.chia02@sd.taylors.edu.my*

Abstract

Raw industrial wastewater has high concentration of hazardous pollutants which will affect human health as these pollutants infiltrate into human basic necessities such as water and food. Adsorption using activated carbon (AC) is a commonly used technique in wastewater treatment for removal of organic and inorganic pollutants. Current AC production from biomass usually uses strong acid or alkali as pretreatment agent. This research aims to study the AC production using a lower concentration of sulphuric acid (H_2SO_4) and potassium hydroxide (KOH). Deep eutectic solvent (DES), the reported environmental friendly pretreatment agent for biomass was also investigated. The AC produced were characterised by using Brunauer, Emmett and Teller (BET) and Fourier Transform Infrared Spectrometry (FTIR). Adsorption process on the effects of initial concentration of lead and nitrate were investigated. Adsorption isotherm studies were carried out and the data were analysed using Langmuir and Freundlich isotherms. The maximum micropore percentage was achieved by DES pretreated AC which has 91%. All samples were successfully converted to AC because they have similar functional groups as commercial activated carbon (CAC) based on FTIR results. AC undergoes DES pretreatment showed the highest removal of NO_3 and Pb(II). It removed NO_3 and Pb(II) up to 19.85% and 95.29% respectively. The Freundlich isotherm was found to best described for NO_3 removal with R^2 value of 0.9471, whereas Pb(II) fit into the Langmuir isotherm with R^2 value of 0.9836. This study shows the potential of reducing the concentration of acid and alkali in AC production. Moreover, the usage of DES as pretreatment agent is discovered not only effective in AC production but also reduce environmental issue as DES is a less hazardous and reusable chemical. In future, the recyclability of DES could be investigated to improve the economic feasibility of AC production.

Keywords: Empty Fruit Bunch, Pretreatment, Deep Eutectic Solvent, Activated Carbon, Adsorption

1. Introduction

Modernisation is a double- edged sword. Civilisation cannot move forward without industrial advancement. However, such advancement jeopardises the environment stability. Water bodies such as river, lake and sea are polluted due to industrial waste. In 2014, there was 70% industrial wastewater discharged without treatment, reported by United Nation Water [1]. Raw industrial wastewater has a high concentration of hazardous pollutants which will adversely affect human health as these pollutants infiltrate into human basic necessities such as water and food. Therefore, wastewater treatment processes are important to ensure the pollutants are discharged at an acceptable level. Adsorption process has been widely employed by industries as part of the treatment due to its simple design, ease of operation and convenience [2]. With adsorption process in wastewater treatment, the pollutants in wastewater will be adsorbed onto the surface of activated carbon (adsorbent) and removed from the wastewater before discharging into water bodies.

Commercial activated carbon (CAC) is usually made from coal which is a non-renewable resource [3]. The increasing demand of activated carbon (AC) causes the increasing need of non-renewable raw material. Hence, it is crucial to explore renewable carbon sources to produce AC. Lignocellulosic biomass has been explored to produce AC due to its carbonaceous characteristic. Empty fruit bunch (EFB) is used in this research to produce AC as it is available in abundance, low commercial value and initiating environment problem. Based on Hidayu and co-workers [4], it is concluded that EFB can be converted into activated carbon and proven to have a comparable characteristic with CAC based on FTIR examination.

AC is produced by going through two main processes; namely carbonisation and activation [2]. In carbonisation, the process decomposes the non- carbon components to produce char. After carbonisation, the char is activated using an activating agent to give the characteristics such as pore structure and surface functional group to an AC [2,5]. There are three types of activation process which are physical, chemical and physio-chemical activation. Physical activation is done after carbonisation; however for chemical activation, the raw material is impregnated with chemical activating agent prior to carbonisation. Physiochemical activation is combination of both physical and chemical activation. A research reported on the pore structure of raw EFB and EFB- derived AC has shown that carbonisation and activation processes are important to produce AC with porous structure [6].

The performance and effectiveness of an AC are greatly affected by carbonisation and activation process. There are many research investigating the effects of carbonisation and activation condition on the AC produced from biomass [7,8]. As reported by Abdullah et al. [9], the yield of AC increases as the concentration of $ZnCl_2$ increases but it drops after 15% of $ZnCl_2$. It has reported that the concentration of $ZnCl_2$ affects the surface area of AC produced. Apart from that, the comparison of combustion, pyrolysis and the acid treatment sequence has only done by [5] on the quality and properties of AC. Thus far, research on how the concentration of alkali and acid pretreatment affects the production of AC from EFB fibre is limited. Besides using acid and alkali as agent, another type of chemical agent called deep eutectic solvent (DES) could be explored. In recent years, a research uses DES in production of porous carbon monolith and the resulting carbon has porous structure [10]. Thus far, no research uses

DES as pretreatment agent in the production of AC. Since DES able to produce porous structure, DES can be one of the pretreatment agent in this study.

AC in adsorption process is widely used in wastewater treatment. Pollutants in industrial wastewater generally categorised as inorganic and organic compounds. Inorganic compounds are such as cations (copper, lead, mercury) and anions (nitrate, phosphate). Whereas phenolic compounds, dyes and pesticides fall into the organic compound category. Surface functional groups on activated carbon play a major role in wastewater treatment. Certain functional groups must exist on AC in order to remove the pollutants effectively. For instance, oxygen functional groups with proton donor must exist in order to remove heavy metal effectively as metal ions have the ability to form complex with the charged acid group [11]. The coconut based AC is widely used in wastewater treatment and gives promising results; however the investigation of EFB-derived AC in wastewater treatment is not well established yet. Thus far, only a few research had been done on using EFB- derived AC in wastewater treatment and the pollutants removal that had been investigated are such as dye [12], phenol [13] and heavy metals [14].

In this study, EFB has been chosen as the precursor for the production of AC due to its substantial amount generated in Malaysia. To date, the application of EFB-derived AC in wastewater treatment is not well established and the removal of anionic pollutants has not been done using EFB- derived AC. Hence, the removal of lead and nitrate will be studied using EFB- derived AC. To the best of our knowledge, limited research has been carried out on comparing different concentration of pretreatment agent on the production of AC from EFB. This research is also to identify if a lower concentration of acid and alkali pretreatment agent can be used. Furthermore, DES as pretreatment agent has not been investigated in the production of AC. This study mainly focuses on investigating the suitable operating condition for the production of AC which enhances lead and nitrate removal from wastewater.

2. Methodology

2.1 Material

Empty fruit bunch (EFB) fibre obtained from Furniu Fibre Sdn. Bhd was used as the raw material. The EFB fibre was washed and cleaned using distilled water to remove impurities on the fibre. Based on ASTM D2867-99, the cleaned EFB fibre was dried in an oven at a temperature of 110°C overnight to reduce the moisture content of the fibre [15]. Sulphuric acid (H_2SO_4) and potassium hydroxide (KOH) and Deep eutectic solvent (DES) were used as pretreatment agents. For adsorption study, lead (Pb(II)) and nitrate (NO_3) stock solutions were prepared from lead nitrate and potassium nitrate, which were purchased from Merck. The lead and nitrate test kit for heavy metal adsorption study were also purchased from Merck.

2.2 Sample Preparation

Total 6 sets of samples were produced. 5 sets were chemically pretreated sample and 1 set was the control sample which was the non-pretreated sample.

2.2.1 Pretreatment of EFB Fibre

15g of cleaned EFB fibre were pretreated with 85% H_2SO_4, 50% H_2SO_4, 50% KOH, 25% KOH with a ratio of 3:4 (Chemical: fibre) separately [5]. For DES, the ratio is 5:1 (Chemical: Fibre) [10]. For H_2SO_4 and KOH pretreatment, the fibre was placed to the split tube furnace immediately after pretreatment process. However, for DES, the fibre was pretreated for 4 hours at 110°C and was required to wash and dry the pretreated fibre before pyrolysis process [10]. The pretreated fibre was placed in crucible before placing it into the split tube furnace. Ensure only one type of sample was placed in the furnace to avoid cross contamination. An inert condition for carbonisation was created by flowing nitrogen (N_2) gas with a flow rate of 1 L/min. The sample was pyrolysed at 400 °C for 1 hour with heating rate ramping at 10 °C/min [5]. After carbonisation, the char was cooled down and rinsed with distilled water and dried in an oven at 110°C overnight. The dried char then proceeded to activation process with carbon dioxide (CO_2) gas.

2.2.2 Control Sample without Pretreatment

A control sample was synthesised to provide a baseline comparison for the chemical pretreated samples. The preparation methods of control sample were similar but without chemical pretreatment. No rinsing and drying steps were required to remove the chemical on the surface.

2.2.3 Activation Process

For activation process, the furnace was heated up to 900 °C with heating rate ramping at 10 °C and N_2 gas flowing at 1 L/min. When the furnace reached 900 °C, the N_2 gas was stopped and changed to CO_2 gas for 1 hour with flow rate 1 L/min. After 1 hour, the furnace was cooled down to room temperature by flowing N_2 gas at 1 L/min. After activation, the sample was rinsed and dried. The list of samples with sample codes was tabulated in Table 1.

Table 1: List of samples.

Condition	Code
Pretreatment with 85% H_2SO_4	P85SA-AC
Pretreatment with 50% H_2SO_4	P50SA-AC
Pretreatment with 50% KOH	P50PH-AC
Pretreatment with 25% KOH	P25PH-AC
Pretreatment with DES	PDES-AC
Without pretreatment (Control sample)	WP-AC

2.3 Characterisation of Activated Carbon (AC)

All EFB- derived AC samples were characterised using Brunauer, Emmett and Teller (BET) and Fourier Transform Infrared (FTIR) spectrometer. Nitrogen adsorption isotherm was carried out using Micromeritics Instrument system at 77 K. Prior to analysis, the sample was degassed at 300 °C for 5 hours. BET model was used to determine the pore characteristics such as surface area, pore volume and pore size from

the nitrogen adsorption isotherms. The nitrogen adsorption was carried out from relative pressure (P/P_o) of 0.01 to 0.99 [16].

FTIR spectrometer (Perkin Elmer Spectrum 100) was used to study the surface chemistry of the activated carbon. For this analysis, approximately 1g of powdered AC produced was required. FTIR spectra were measured with transmittance range from 4000 to 650 cm^{-1} with 16 attenuated total reflectance (ATR) unit scans with 4 cm^{-1} resolution. All sample spectra were baseline corrected and the transmittance value was normalized to the range from 0 to 100% [16].

2.4 Lead and Nitrate Adsorption Process

The adsorption study was carried out with different concentration of Pb(II) and NO_3 solution. The Pb(II) concentration used for adsorption process were range from 3 ppm to 0.5 ppm. The lead stock solutions were prepared from lead nitrate, $Pb(NO_3)$. As for NO_3, the concentration used were range 80 ppm to 30 ppm. The nitrate stock solutions were prepared from potassium nitrate, KNO_3.

0.1 g of AC sample with 50 ml of the stock solution was placed in a conical flask. The mixture was regulated at pH 7 by adding HCl or NaOH. The conical flask was placed in an incubating shaker with rotating speed of 150 rpm for 24 hours [17]. After 24 hours, the mixture was withdrawn and filtered. The concentration of the solution after adsorption was determined with test kit and was measured using Spectroquant ®. The amount of Pb(II) and NO_3 uptake were calculated using Eq. (1):

$$q_e = \frac{V\,(C_0 - C_e)}{W} \tag{1}$$

Where Q is mass (mg) of adsorbed component per g of AC, C_0 is the initial concentration (mg/l), C_e is the equilibrium concentration of the component (mg/l), W is the weight of AC used (g) and V is the volume of solution (L).

2.5 Adsorption Isotherm Model

Adsorption isotherm was used to study the behaviour of adsorbent (AC) in adsorption process and to identify the adsorption capacity of AC. This analysis of isotherm data is important to find the best fit model that can be used to explain the Pb(II) and NO_3 adsorption by AC [17]. Adsorption isotherm study was carried out using Langmuir and Freundlich isotherm. The linear equation for Langmuir isotherm is expressed as Eq. (2) [17]:

$$\frac{C_e}{q_e} = \frac{C_e}{Q_m} + \frac{1}{Q_m b} \tag{2}$$

Where q_e is the amount of component adsorbed on AC (mg/g), C_e is the equilibrium concentration (mg/L), Q_m is the adsorption capacity (mg/g) and b is the adsorption energy (L/mg). Q_m and b constant can be identified through the intercept and gradient of the linear graph of $\frac{C_e}{q_e}$ against C_e. Another feature of the Langmuir isotherm can be expressed with dimensionless constant separation factor or equilibrium parameter (R_L). The dimensionless was calculated with Eq. (3) as follows [18]:

$$R_L = \frac{1}{1+bC_e} \quad (3)$$

The Freundlich isotherm is expressed as follows:

$$logq_e = \log k_f + \frac{1}{n} logC_e \quad (4)$$

Where k_f and n are the Fruendlich constant which representing the adsorption capacity and adsorption intensity. These constant can be identified through the intercept and gradient of the linear graph of log q_e against log C_e.

3. Results and Discussion

3.1 Pore Development and Structure of Activated Carbon

Nitrogen adsorption isotherm is carried out for each AC samples from different route to study the pore characteristics. Pore characteristics such as surface area, pore size distribution, pore volume and etc. are obtained from nitrogen adsorption isotherm by using Branaeuer- Emmett- Teller (BET) model. Table 2 shows the pore characteristics of each EFB derived AC from different route.

Table 2: Pore characteristics of EFB- derived AC samples.

Sample	BET Surface Area (m2/g)	Micropore Suface Area (m2/g)	Average Pore Diameter (nm)	Micropore (%)
P85SA-AC	887.0664	734.4532	2.1054	82.80
P50SA-AC	739.9068	662.2668	2.4801	89.51
P50PH-AC	-	-	-	-
P25PH-AC	860.7611	590.5898	2.2838	68.61
PDES-AC	722.7199	660.7205	1.9133	91.42
WP-AC	800.0812	638.4178	1.9884	79.79

There is no data obtained for P50PH-AC as the structure collapsed and disintegrated due to high concentration of alkali used. This is probably caused by excessive potassium hydroxide (KOH) molecules which decomposed into water during heat treatment. The water molecules brought in gasification process to the carbon at high temperature as shown below [19]:

$$2KOH \rightarrow K_2O + H_2O$$
$$H_2O + C \rightarrow CO + H_2$$

Therefore, the carbon reacts to form carbon monoxide (CO) and hydrogen gas (H_2). This explained why there was no carbon left after activation process. This phenomenon was observed by Chai and co-workers [16] where no residue was left for 85% concentrated KOH sample. P25PH-AC has lower micropore surface area compared to other pretreated samples. This might be due to the phenomenon explained above which cause widening of micropore to mesopore. Hence, micropore surface area decreases. This can be correlated using the pore diameter as the average pore diameter is in mesopore range (2 nm- 50 nm) [20].

For acid pretreated AC, the BET surface area and micropore surface area are higher for P85SA-AC. It is suggested that the sulphuric acid (H_2SO_4) intercalated into

the EFB fibre. During pyrolysis process, the H_2SO_4 decomposed into water and sulphur trioxide and these products intercalate and force the crystalline layers in carbon apart [21]. At higher concentration, more H_2SO_4 molecules intercalate into EFB fibre; hence, improve the development of porous structures in AC and increase the surface area. This is in good agreement with Guo and Lua [22]. Table 2 shows that the BET surface area for P50SA-AC and PDES-AC are lower compared to WP-AC. Generally, chemically pretreated AC should have higher BET and micropore surface area than untreated AC [22,23]. During pretreatment process, chemical agent increases the surface area through creation of new micropores and increase the surface area [9]. However, the result from this paper is not following the trend. This might be due to during the heat treatment, some of the inorganic oxide may redeposit back and block some of the pores [24]. Further analysis using scanning electron microscopy (SEM) and x-ray diffraction (XRD) must be done to justify this. It can only be concluded that the results are dependent on the heat treatment combination (pyrolysis temperature, nitrogen air flow rate, activation temperature) and type of chemical used.

For PDES-AC, it has comparable BET surface area as the other samples. Although it has the lowest BET surface area (722.72 m^2/g), it has high micropore surface area (660.72 m^2/g) which is important for good adsorption. This implies that DES can be used as pretreatment agent in AC production to give porous structure. DES is usually used in pretreatment of biomass to improve sugar production by removing silica on biomass [10]. However, DES on AC production is still limited and the effect of DES on AC surface is not yet identified. Further analysis on surface morphology using SEM should be carried out. AC prepared from acid and DES pretreatment has shown to be different from WP-AC. Both of these treatment shows positive contribution to the development of porosity. From Table 2, it shows that the micropore percentage from these pretreatments are higher than WP-AC (80%). This concluded that acid and DES pretreatment were better than alkali pretreatment in term of producing microporous structure.

3.2 Surface Chemistry of Activated Carbon

The FTIR spectra of raw EFB and all the EFB- activated carbon samples are as shown in Figure 1. Based on Figure 1, raw EFB shows the most complicated spectrum compared to the others. The peak intensity of 3374 cm^{-1} for raw EFB spectrum is high due to the moisture content in raw EFB. This peak is not intensified in other AC samples as it has been removed during pyrolysis and activation process.

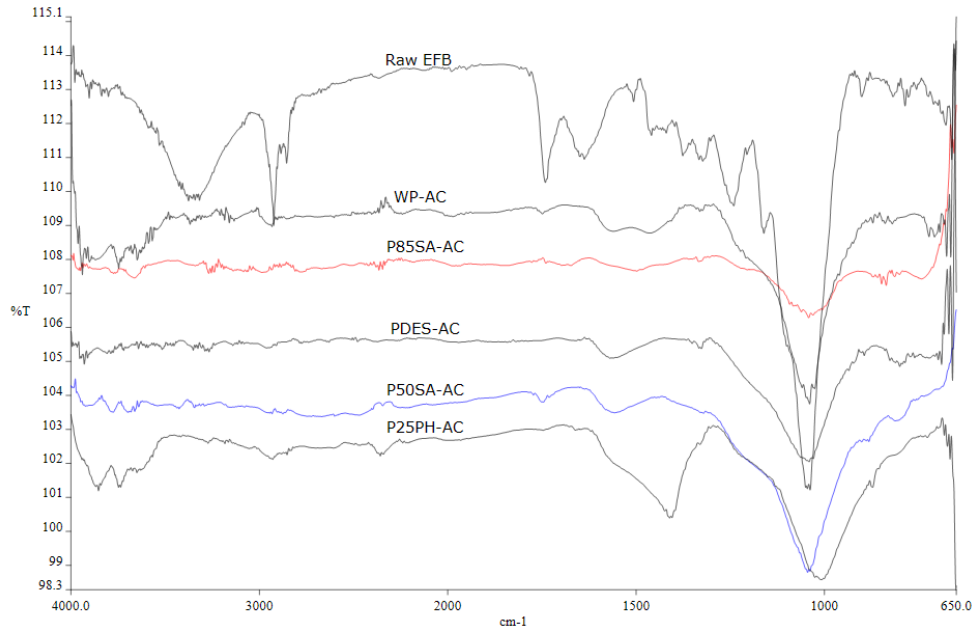


Figure 1: FTIR spectra of raw EFB and AC samples.

From Figure 2, the spectra trend of all the EFB AC is quite similar to the commercial activation carbon (CAC) spectrum. Hence, it shows that each sample successfully transformed into AC after pyrolysis and activation process. Table 3 shows the detailed peak positions and assignments of raw EFB and EFB-AC samples.

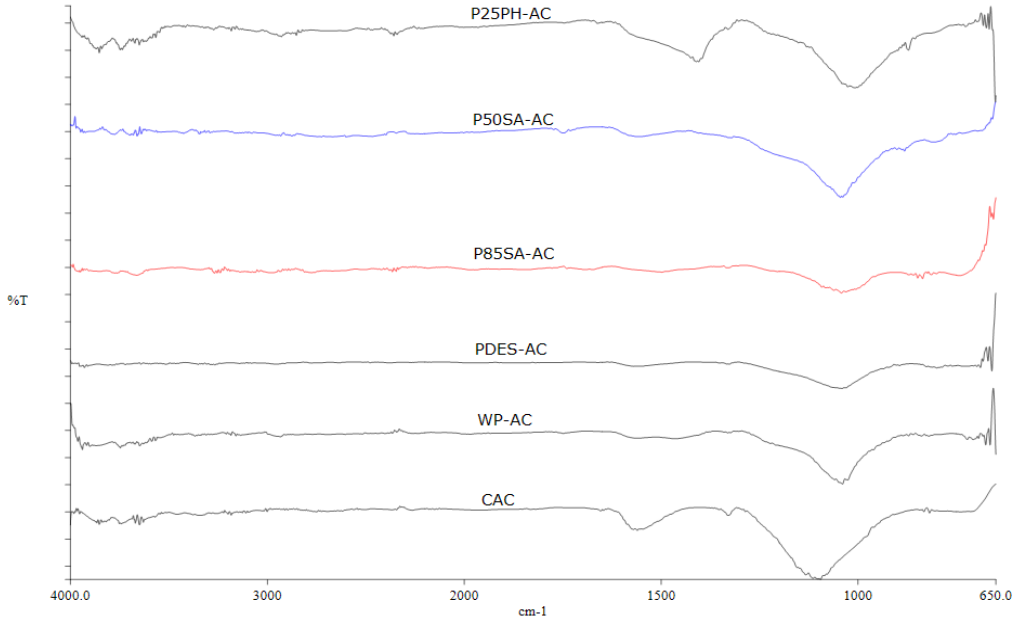


Figure 2: FTIR spectra of CAC and AC samples.

Table 3: Detailed peak positions and assignments.

Wave Number (cm^{-1})	Functional Group	1	2	3	4	5	6
3374	Stretching vibration of O-H hydroxyl group	•					
2923 & 2849	Stretching of C-H of lignocellulosic component	•					
1738	C=O stretching of hemicellulose (acetyl content) [25]	•	•		•	•	
1641	C=O stretching vibration in conjugated carbonyl of lignin [26]	•					
1515	C=C stretching vibration of aromatic rings of lignin [25,26]	•	•	•	•		•
1400- 1480	Aromatic skeletal with C-H in plane deforming and stretching [26]	•	•			•	
1243	Syringyl ring breathing and C-O stretching in lignin and xylan [26]	•					
1158	C-O-C asymmetric stretching in cellulose I and cellulose II [26]	•					
1041	C-O stretching vibration (cellulose, hemicellulose & lignin) [26]	•	•	•	•	•	•
880, 870, 810	C-H aromatic out of plane [27]	•	•	•	•	•	•

*1: Raw EFB; 2: WP-AC; 3: P85SA-AC; 4: P50SA-AC; 5: P25PH-AC; 6: PDES-AC

Based on Table 3, most of the adsorption peaks such as O-H at 3374 cm^{-1}, C-H at 2923 cm^{-1} and C=O at 1641 cm^{-1} in raw EFB are not visible in all the AC samples. The disappearance of these peaks as reported by Yacob et.al [28] where these functional groups vaporised as volatile matters when heat is applied. With this, it proved that pyrolysis and activation process have taken place. This is in good agreement with Hidayu and co-workers [4]. The C=O group of hemicellulose is not visible in P85SA-AC. It can be observed that C=O peak at 1738 cm^{-1} completely disappeared in P85SA-AC but not in P50SA-AC. This might be due to the concentration of H_2SO_4 used. At higher concentration of acid, it initiates more bond cleavage of C=O which leads to elimination reaction where volatile and light products are released. As reported by Nasser et.al, acid breaks several bonds in aliphatic and aromatic groups which initially appear in raw EFB. This finding is consistent with the disappearance of C=O group [27].

Lignin structure which characterised by peak 1515 cm^{-1} [25] on aromatic C=C stretching disappeared at P25PH-AC but visible in WP-AC, P85SA-AC, P50SA-AC and PDES-AC. This shows that lignin still intact even after acid and DES pretreatment which are favorable in AC production. As reported by Nor and friends [10], the type of DES used (Urea: Choline Chloride) does not show much delignification on EFB; hence this explained the lignin peak around 1515 cm^{-1} is still visible. The FTIR trend reported by [10] on DES pretreated EFB is not similar to this research. This might be due to high temperature pyrolysis and activation which is not done in [10].

Another observation made on the intensity of C-O stretching vibration peak at 1041 cm^{-1} based on Figure 1. The intensity of this peak for P85SA-AC and P50SA-AC is much lower than P25PH-AC. This might be due to the overall content of cellulose,

hemicellulose and lignin. Pretreatment of biomass using acid breaks cellulose and hemicellulose structure effectively; whereas alkali breaks lignin [29]. The overall C-O stretching vibration intensity was much reduced for acid pretreated sample as the cellulose and hemicellulose content takes up 81.1% of EFB components. Lignin content only takes up 18.1% [30]. P85SA-AC has lower intensity for peak 1041 cm^{-1} as compared to P50SA-AC. This might be due to high concentration acid that breaks cellulose and hemicellulose structure more effectively; hence resulting in less cellulose and hemicellulose content. For P25PH-AC, the cellulose and hemicellulose structure still intact together; hence C-O stretching vibration peak at high intensity. As for aromatic skeleton with C-H in crystalline cellulose at peak around 1400 cm^{-1} to 1480 cm^{-1}, it was not found in P85SA-AC and P50SA-AC. This peak can only be found in WP-AC and P25PHAC, where it indicates the cellulose content still available.

3.3 Lead and Nitrate Adsorption Study

Adsorption process carried out in two stages. The 1st stage is to identify the AC sample which results in highest adsorption for Pb(II) and NO_3. The 2nd stage is to study the effects of initial concentration of Pb(II) and NO_3 using the identified AC from 1st stage. Pb(II) adsorption by using EFB- derived AC has already been researched by Wahi and co-workers [6]. However, the preparation of the AC in [6] is different with the preparation method in this paper. Currently, there is no study done on NO_3 adsorption using EFB- derived AC. Thus, Pb(II) and NO_3 are chosen in the adsorption process.

3.3.1 1st Stage Adsorption Process

Pores act as active sites which played a major role in adsorption process. Hence, pores development in AC is crucial [6]. After BET analysis, AC samples which have higher micropore surface area percentage than WP-AC are investigated for 1st stage adsorption process. These AC samples are P85SA-AC, P50SA-AC and PDES-AC. The outcome of Pb(II) and NO_3 removal by each AC sample is shown in Figure 3.

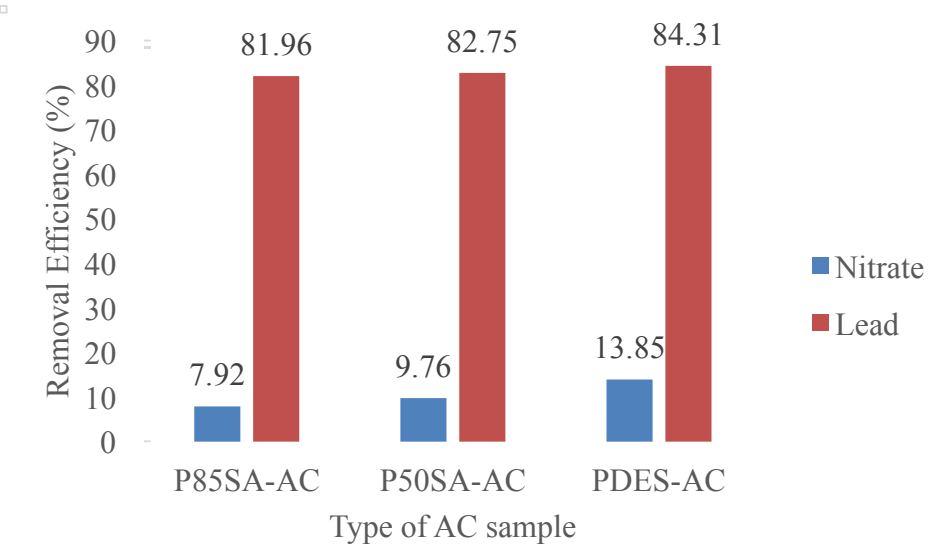


Figure 3: Removal efficiency of each AC for lead and nitrate adsorption.

The result shows that each AC sample is able to adsorb Pb(II) and NO_3. Since it is able to adsorb pollutants, it is concluded that these AC act like CAC and can relate to the similar trend obtained from FTIR for these AC with CAC. Based on Figure 3, Pb(II) and NO_3 removal are more effective using PDES-AC; hence it is used in 2nd stage adsorption process. PDES-AC is able to give the highest removal of Pb(II) and NO_3 despite having lowest BET surface area (722.72 m^2/g). However, PDES-AC has the highest micropore surface area percentage (91.4%) among all. Another observation is made on acid pretreated AC where P50SA-AC has higher adsorption capacity for both Pb(II) and NO_3 compared to P85SA-AC. P50SA-AC has micropore surface area percentage of 89.5%, whereas P80SA-AC has micropore surface area percentage of 82.8%. This suggests that the adsorption capacity is determined by the micropore surface area instead of BET surface area. Furthermore, it is concluded that a lower concentration of sulphuric acid (50%) can be used to pretreat EFB in AC production which is less hazardous to the environment.

3.3.2 2nd Stage Adsorption Process- Effect of Initial Concentration

The effect of initial Pb(II) and NO_3 concentration on removal percentage by PDES-AC is tabulated as shown in Figure 4.

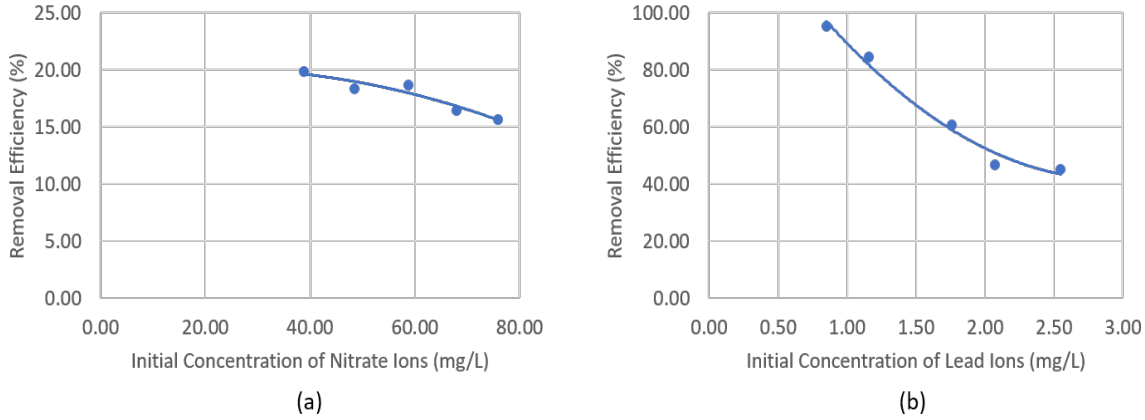


Figure 4: (a) Nitrate removal using PDES-AC (b) Lead removal using PDES-AC

Based on Figure 4, the removal percentage of NO_3 and Pb(II) decreases when the initial concentration of NO_3 and Pb(II) increase. This phenomenon is due to the reducing number of active sites on AC used for NO_3 and Pb(II) removal. At lower initial concentration, there are more adsorption sites available on the AC [31] and facilitate almost 100% adsorption. At high initial concentration, most of the active sites are saturated as the amount of AC remain unchanged [6]. Thus, left most of the NO_3 and Pb(II) ions unabsorbed in the solution. The Pb(II) result is with good agreement with Wahi et.al where it uses EFB to prepare AC [6].

Overall, it can be observed that NO_3 removal is not as effective as Pb(II). This might due to the number of positively charged sites on AC. As reported Demiral et. al, it suggests that positively charged site favors the NO_3 adsorption due to electrostatic attraction [17]. In this paper, PDES-AC might have lesser positively charged site compared to negatively charged site; hence resulting lesser NO_3 removal. The removal percentage of NO_3 was relatively lower compared to using zinc chloride ($ZnCl_2$) pretreated AC as reported by [17] which has removal percentage of 41%. This might

due to the type of pretreatment agent used. Acid pretreatment would protonate –OH group and give positive site which increases the electrostatic adsorption of anion [32].

3.4 Adsorption Isotherm

Adsorption isotherm is an indication on how molecules distribute during adsorption process between the liquid and solid phase at equilibrium state. Isotherm data analysis is important to develop a suitable model which accurately represents the results and can be used for design purposes. Langmuir isotherm and Freundlich isotherm are selected to analyse. Table 4 shows the adsorption coefficients and the correlation coefficients for both isotherms on removal of Pb(II) and NO_3.

Table 4: Adsorption isotherm parameters.

Type of Pollutants	Langmuir				Freundlich		
	Q_m (mg/g)	b	R_2	R_L	k_f	n	R_2
NO_3	8.7184	0.4266	0.7133	0.035 to 0.0700	0.4640	1.6124	0.9471
Pb(II)	0.5509	0.0975	0.9836	0.8800 to 0.9960	0.5532	12.9702	0.7561

In Langmuir isotherm, the assumption made is that the adsorption takes place at specific homogeneous sites [17]. The value of adsorption capacity (Q_m) and adsorption energy (b) for NO_3 removal are 8.7187 mg/g and 0.4266 L/mg respectively. For Pb(II), the values are 0.5509 mg/g and 0.0975 L/mg. The values R_L indicates the favorability of adsorption process. By considering the value of R_L, adsorption can be unfavorable ($R_L>1$), linear ($R_L=1$), favorable ($0<R_L<1$) and irreversible ($R_L<0$) [17]. The value of R_L for NO_3 onto PDES-AC changed from 0.035 to 0.07 and Pb(II) changed from 0.880 to 0.996. These values indicates that the adsorption of Pb(II) and NO_3 on PDES-AC are favorable.

In Freundlich isotherm, the assumption made is that a heterogeneous surface with a non-uniform distribution of heat adsorption over the AC surface [17]. The value n is an indication of favorability of adsorption. The value n greater than unity shows that the adsorption is favorable [17]. From Table 4, the n values suggest that Pb(II) and NO_3 are favorable adsorbed by PDES-AC. This shows that Pb(II) and NO_3 are favorable adsorbed by AC from EFB. Based on correlation coefficient, R^2, it suggests that Freundlich isotherm is best fit for NO_3 removal and Langmuir isotherm is best fit for Pb(II) removal.

4. Conclusion

EFB- derived activated carbon produced through acid pretreatment (85% and 50% H_2SO_4), alkali pretreatment (25% KOH) and DES pretreatment were successfully converted to AC as they have similar trend as CAC based on FTIR results. Acid and DES pretreated AC samples resulted in higher micropore percentage than the control sample. However, alkali pretreated AC resulted in lower micropore percentage than control sample and hence, it is not suitable for adsorption. In terms of removing Pb(II) and NO_3, P50SA-AC has higher removal efficiency than P85SA-AC and this indicates that lower concentration of acid can be used for pretreatment in AC production. DES pretreated AC showed highest adsorption of Pb(II) and NO_3 due to its high micropore percentage among all samples. The highest removal efficiency of NO_3 and Pb(II) using PDES-AC were 19.85% and 95.29% respectively. NO_3 can only be removed at lower

percentage which might be due to lack of positively charged surface on AC. It can also be concluded that removal of NO_3 and Pb(II) were dependent on the initial concentration of NO_3 and Pb(II). The Freundlich isotherm was found to provide best fit for NO_3 removal, whereas Pb(II) fit to the Langmuir isotherm. From this study, DES which is a less hazardous chemical and reusable is proven to be a potential pretreatment agent in AC production. For future study, different type of DES can be investigated in AC production.

References

[1] "UN-Water: Statistics detail," 2014. [Online]. Available: http://www.unwater.org/statistics/statistics-detail/en/c/211800/. [Accessed: 29-Sep-2016].

[2] R. C. Bansal and M. Goyal, *Activated Carbon Adsorption*. Boca Raton, FL: CRC Press, 2005.

[3] S. M. Anisuzzaman, C. G. Joseph, Y. H. Taufiq-Yap, D. Krishnaiah, and V. V. Tay, "Modification of commercial activated carbon for the removal of 2,4-dichlorophenol from simulated wastewater," *J. King Saud Univ. - Sci.*, vol. 27, no. 4, pp. 318–330, 2015.

[4] A. R. Hidayu, N. F. Mohamad, S. Matali, and A. S. A. K. Sharifah, "Characterization of activated carbon prepared from oil palm empty fruit bunch using BET and FT-IR techniques," *Procedia Eng.*, vol. 68, pp. 379–384, 2013.

[5] T. Lee, Z. A. Zubir, F. M. Jamil, A. Matsumoto, and F. Y. Yeoh, "Combustion and pyrolysis of activated carbon fibre from oil palm empty fruit bunch fibre assisted through chemical activation with acid treatment," *J. Anal. Appl. Pyrolysis*, vol. 110, no. 1, pp. 408–418, 2014.

[6] R. Wahi, Z. Ngaini, and V. Jok, "Removal of mercury, lead and copper from aqueous solution by activated carbon of palm oil empty fruit bunch," *World. Appl. Sci. J.*, vol. 5, pp. 84–91, 2009.

[7] G. O. El-Sayed, M. M. Yehia, and A. A. Asaad, "Assessment of activated carbon prepared from corncob by chemical activation with phosphoric acid," *Water Resour. Ind.*, vol. 7–8, pp. 66–75, 2014.

[8] C. Bouchelta, M. S. Medjram, O. Bertrand, and J. P. Bellat, "Preparation and characterization of activated carbon from date stones by physical activation with steam," *J. Anal. Appl. Pyrolysis*, vol. 82, no. 1, pp. 70–77, 2008.

[9] F. A. and O. S. W. Abdul Halim Abdullah, Anuar Kassim, Zulkarnain Zainal, Mohd Zobir Hussien, Dzulkefly Kuang, "Preparation and Characterization of Activated Carbon from Gelam Wood Bark (Melaleuca cajuputi)," *Malaysian J. Anal. Sci.*, vol. Vol. 7, no. No. 1, pp. 65–68, 2001.

[10] N. A. M. Nor, W. A. W. Mustapha, and O. Hassan, "Deep Eutectic Solvent (DES) as a Pretreatment for Oil Palm Empty Fruit Bunch (OPEFB) in Sugar Production," *Procedia Chem.*, vol. 18, no. Mcls 2015, pp. 147–154, 2016.

[11] A. Bhatnagar, W. Hogland, M. Marques, and M. Sillanpää, "An overview of the modification methods of activated carbon for its water treatment applications," *Chem. Eng. J.*, vol. 219, pp. 499–511, 2013.

[12] K. Y. Foo and B. H. Hameed, "Microwave-assisted preparation of oil palm fiber activated carbon for methylene blue adsorption," *Chem. Eng. J.*, vol. 166, no. 2, pp. 792–795, 2011.

[13] B. H. Hameed, I. A. W. Tan, and A. L. Ahmad, "Preparation of oil palm empty fruit bunch-based activated carbon for removal of 2,4,6-trichlorophenol:

Optimization using response surface methodology," *J. Hazard. Mater.*, vol. 164, no. 2–3, pp. 1316–1324, 2009.
[14] S. Daneshfozoun, A. Bawadi, and M. A. Abdullah, "Heavy Metal Removal by Oil Palm Empty Fruit Bunches (OPEFB) Biosorbent," *Appl. Mech. Mater.*, vol. 625, pp. 889–892, 2014.
[15] A. R. Hidayu, N. F. Mohamad, S. Matali, and A. S. a. K. Sharifah, "Preparation and characterization of activated carbon made from oil palm," *Procedia Eng.*, vol. 68, pp. 379–384, 2013.
[16] I. Chai, L. Ting, and L. Xiao Yien, "Creatinine Adsorption by Activated Carbon Fibre derived from Empty Fruit Bunch," 2016.
[17] H. Demiral and G. Gündüzoğlu, "Removal of nitrate from aqueous solutions by activated carbon prepared from sugar beet bagasse," *Bioresour. Technol.*, vol. 101, no. 6, pp. 1675–1680, 2010.
[18] M. Ali Khan, Y.-T. Ahn, M. Kumar, W. Lee, B. Min, G. Kim, D.-W. Cho, W. Bae Park, and B.-H. Jeon, "Adsorption Studies for the Removal of Nitrate Using Modified Lignite Granular Activated Carbon," *Sep. Sci. Technol.*, vol. 4616, no. January 2015, pp. 2575–2584, 2011.
[19] I. A. W. Tan, A. L. Ahmad, and B. H. Hameed, "Preparation of activated carbon from coconut husk: Optimization study on removal of 2,4,6-trichlorophenol using response surface methodology," *J. Hazard. Mater.*, vol. 153, no. 1–2, pp. 709–717, 2008.
[20] P. T. Williams and A. R. Reed, "Development of activated carbon pore structure via physical and chemical activation of biomass fibre waste," *Biomass and Bioenergy*, vol. 30, no. 2, pp. 144–152, 2006.
[21] W. C. Tan, R. Othman, A. Matsumoto, and F. Y. Yeoh, "The effect of carbonisation temperatures on nanoporous characteristics of activated carbon fibre (ACF) derived from oil palm empty fruit bunch (EFB) fibre," *J. Therm. Anal. Calorim.*, vol. 108, no. 3, pp. 1025–1031, 2012.
[22] J. Guo and A. C. Lua, "Textural and chemical characterisations of activated carbon prepared from oil-palm stone with H2SO4 and KOH impregnation," *Microporous Mesoporous Mater.*, vol. 32, no. 1, pp. 111–117, 1999.
[23] A. Gundogdu, C. Duran, H. B. Senturk, M. Soylak, M. Imamoglu, and Y. Onal, "Physicochemical characteristics of a novel activated carbon produced from tea industry waste," *J. Anal. Appl. Pyrolysis*, vol. 104, pp. 249–259, 2013.
[24] R. M. Suzuki, A. D. Andrade, J. C. Sousa, and M. C. Rollemberg, "Preparation and characterization of activated carbon from rice bran," *Bioresour. Technol.*, vol. 98, pp. 1985–1991, 2007.
[25] L. W. Yoon, T. N. Ang, G. C. Ngoh, A. Seak, and M. Chua, "Regression analysis on ionic liquid pretreatment of sugarcane bagasse and assessment of structural changes," *Biomass and Bioenergy*, vol. 36, pp. 160–169, 2011.
[26] J. Shi and J. Li, "Metabolites and Chemical Group Changes in the Wood-Forming Tissue of Pinus Koraiensis Under Inclined Conditions," *BioResources*, vol. 7, no. 3, pp. 3463–3475, 2012.
[27] A. N. A. El-Hendawy, "Variation in the FTIR spectra of a biomass under impregnation, carbonization and oxidation conditions," *J. Anal. Appl. Pyrolysis*, vol. 75, no. 2, pp. 159–166, 2006.
[28] A. R. Yacob, Z. A. Majid, R. Sari, and D. Dasril, "Comparison of Various Sources of High Surface Area Carbon Prepared by Different Types of Activation," *J. Anal. Sci.*, vol. 12, no. 1, pp. 264–271, 2008.
[29] P. Kumar, D. M. Barrett, M. J. Delwiche, and P. Stroeve, "Methods for

pretreatment of lignocellulosic biomass for efficient hydrolysis and biofuel production," *Ind. Eng. Chem. Res.*, vol. 48, no. 8, pp. 3713–3729, 2009.

[30] A. Geng, "Conversion of Oil Palm Empty Fruit Bunch to Biofuels," *Liq. gaseous solid biofuels*, pp. 479–490, 2013.

[31] M. Imamoglu and O. Tekir, "Removal of copper (II) and lead (II) ions from aqueous solutions by adsorption on activated carbon from a new precursor hazelnut husks," *Desalination*, vol. 228, no. 1–3, pp. 108–113, 2008.

[32] S. Kilpimaa, H. Runtti, T. Kangas, U. Lassi, and T. Kuokkanen, "Removal of phosphate and nitrate over a modified carbon residue from biomass gasification," *Chem. Eng. Res. Des.*, vol. 92, no. 10, pp. 1923–1933, 2014.

Drying Kinetics of *Cassia Alata*

Choong Oon Choo*, Chien Hwa Chong, Bee Lin Chua

School of Engineering, Taylor's University Lakeside Campus

**Corresponding Author: ChienHwa.Chong@taylors.edu.my*

Abstract

The objective of this research is to study the drying characteristic and the drying kinetics of *Cassia Alata* and to compare different drying methods to improve drying performance through reducing the drying duration and energy required for the drying process to reach it equilibrium moisture content. The drying methods used were oven drying, sun drying and combination of sun drying and oven drying. The drying temperature used in oven drying were 50^{o}C, 60^{o}C,70^{o}C, 80^{o}C and 90^{o}C. Six semi-theoretical and empirical thin layer drying models were used to compare the experimental result with the predicted data. 3 evaluation criteria were used to determine the goodness fitting which are determination coefficient (R^2), root mean square error (RMSE) and chi-square (χ^2). It was found that high drying temperature can increase the moisture diffusion during the falling rate period. Furthermore, page model was found to be the best fitted model to the experimental data. The correlation coefficient (R^2), chi-square ($\boldsymbol{\chi^2}$) and RMSE of Page model were 0.995 to 0.9493, 0.0001 to 0.0077 and 0.01 to 0.0876 respectively. Besides, by introducing the combination of sun drying and oven drying, the energy consumption reduced as high as 33 %. It also shortens the drying duration of sun drying from three days to six hours.

Keywords: *Cassia Alata*, herb drying, drying characteristic, mathematical modeling

1. Introduction

Cassia Alata is a well-known medicinal plant and it also categorized as *Fabaceae* in the plant family. *Cassia Alata* contained rich amount of nutrients such as anthraquinones, phenol and others which shows a positive result for antifungal, anitimicrobial and anticancer. Few applications have claimed an anti-aging function by using the different parts of *Cassia Alata* [1].

Drying is one of the oldest method to preserve fruits, vegetables and herbs. Drying is also a major role in manufacturing of foods, medicines and etc. By reducing the moisture content to a desired level is important to conserve the quality of the products [2]. Sun drying (SD), is a traditional method of drying herbs and fruits. It has some disadvantages such as dependents on weather, large area requirement, and long drying duration [3]. However, it is considered as free resources for the people to preserve foods, fruits as well as herbal [4]. Oven drying (OD), a most popular drying method to remove moisture content of the fruits and herbs. The design of oven dryer gave the equal heat for each of the trays and hence the drying is uniform [4].

Drying behavior of herbal is unable to be predicted and can only determine through experiment. The results obtained from the drying process such as weight loss, moisture content and etc are later converted into the drying rate versus free moisture content to explain the drying behavior of herbal [5]. Mathematic modeling of drying curve is used to better control of drying and obtain a high-quality product [6]. Besides, modeling of drying curve can optimize the drying parameter such as drying coefficient (k) and drying constant (a,b) [7]. Furthermore, modeling is based on fitting or describing the drying behavior of the foods or agricultural by using a set of mathematical equations. A thin layer drying models are suitable to describe the drying behavior of foods or agricultural such as tea, bay leaves, jackfruit and others [7, 8, 9].

In the twenty-first century, traditional medicine needed to be modernised. However, modernisation of herbal medicine should not be simply westernisation [1]. The purpose of studying herbal medicines is not only to determine the bioactive compounds from the herbal extracts to develop new drugs, but also standardise and control the quality of raw herbal material and to reveal their preventative and therapeutic mechanisms hence the objective of this research is to study the drying characteristic and the drying kinetic of *Cassia Alata*. Furthermore, drying is the one most commonly used to preserve fruit and vegetables. It helps to reduce the moisture content in the food matrix to a level that is safe for storage and transportation in process engineering [10]. However, the energy consumption is the problem relevant in drying as drying is the one most energy intensive unit operations in the industries [11]. Therefore, the second objective of this research is to compare different drying methods to improve drying performance through reducing the drying duration and energy required for the drying process to reach it equilibrium moisture content.

2. Material and methods

2.1 Sample preparation

Cassia Alata was purchased from a local nursery (Klang, Selangor, Malaysia). Leaves of *Cassia Alata* were harvested and the dirt is cleaned off using distillation water. 200 g of *Cassia Alata* leaves were weighted using a weight balance (A&D, HR250AZ, USA) and used to determine the bone drying weight using an oven dryer (Memmert, UN75, Germany). The operating condition to obtain the bone-dry weight is 105^{o}C for 24 hours.

2.2 Drying procedure

2.2.1 Oven drying

The procedure of oven drying has been modified from Khaw et al [5]. *Cassia Alata* leaves were dried in an oven dryer (Memmert, UN75, Germany) at 50^{o}C, 60^{o}C, 70^{o}C, 80^{o}C and 90^{o}C. 200 g of sample leaves was used for each test. The weight loss of the sample was measured using a weight balance (A&D, HR250AZ, USA). The measurement was conducted every 15 min interval for the first 60 min of drying and continue hourly until the weight loss of the sample leaves were constant.

2.2.2 Sun drying

200 g of sample leaves were sundried from 10:00 am to 4:00 pm and tempered from 4:00 pm to 10:00 am. The experiment was carried out for 3 days until the weight loss of the sample leaves were constant [12]. The weight loss of the sample leaves was measured using a weight balance (A&D, HR250AZ, USA) at 15 min interval for the first hour of drying, followed by hourly intervals. The average temperature and air velocity are 31.7^{o}C and 1.02 m/s respectively.

2.2.3 Combination of sun drying and oven drying

200 g of sample leaves were sundried for 2 hours. After 2 hours of sun drying, the sample leaves were sent to an oven dryer (Memmert, UN75, Germany) to dry at temperature of 90 ^{o}C, 80 ^{o}C and 70 ^{o}C. The weight loss of the sample leaves was measured using weight balance (A&D, HR250AZ, USA) at 15 min interval for the first hour of drying, followed by hourly intervals until the weight loss of the sample leaves were constant.

2.2.4 Drying characteristic

The moisture content (MC) can be calculated using Eq. (1):

$$MC = \frac{W_o - W_b}{W_b} \quad (1)$$

Where W_o is the initial weight of leaves (g) and W_b is the bone-dry weight (g).

The moisture ratio was determined with Eq. (2):

$$M_R = \frac{M_i - M_e}{M_o - M_e} \quad (2)$$

The drying rate was calculated using Eq. (3):

$$D_R = \frac{M_t - M_{t+\Delta t}}{\Delta t} \tag{3}$$

To calculate the effective diffusivity, Fick's second law of diffusion is used and shown in Eq. (4) [13]:

$$M_R = \frac{8}{\pi^2} \exp\left[D_{eff} t \left(\frac{\pi}{2l}\right)^2\right] \tag{4}$$

Taking ln from both sides:

$$lnM_R = ln\frac{8}{\pi^2} - D_{eff}\left(\frac{\pi}{2l}\right)^2 t \tag{5}$$

The slope of logarithmic M_R as a function of t is:

$$slope = -D_{eff}\left(\frac{\pi}{2l}\right)^2 \tag{6}$$

2.2.4 Mathematical Modeling

Thin layer drying models have been found often applicate to describe/fit most of fruits, vegetables and herbs products. Thin layer drying models consists of two models which are semi-theoretical model and empirical model. Where semi-theoretical model is derived from Fick's second law of diffusion. The thin layer drying models are listed in Table 1.

Table 1: Thin layer models

Model Name	Model	Reference
Newton	$MR = \exp(-kt)$	[14]
Page	$MR = \exp(-kt^n)$	[15]
Modified Page	$MR = \exp((-kt)^n)$	[16]
Henderson-Pabis	$MR = a\exp(-kt)$	[17]
Diffusion	$MR = a\exp(-k_1 t) + (1-a)\exp(-k_2 t)$	[18]
Modified Henderson-Pabis	$MR = a\exp(-k_1 t) + b\exp(-k_2 t) + c\exp(-k_3 t)$	[19]

Where k, k_1, k_2, k_3 is the drying coefficient, a, b, c, n is the drying constant.

3 evaluation criteria which are determination coefficient (R^2), root mean square error (RMSE) and chi-square (χ^2) were used to evaluate the fitness of the thin layer drying model.

$$R^2 = \frac{\sum_{i=1}^{n}\left(M_{Ri} - M_{Rpre,i}\right) * \sum_{i=1}^{n}(M_{Ri} - M_{Rexpi})}{\sqrt{\left[\sum_{i=1}^{n}\left(M_{Ri} - M_{Rpre,i}\right)^2 * \sum_{i=1}^{n}(M_{Ri} - M_{Rexpi})^2\right]}} \tag{7}$$

$$\chi^2 = \frac{\sum_{i=1}^{n}\left(MR_{Rexp,i} - M_{Rpre,i}\right)^2}{N_v - N_c} \quad (8)$$

$$RMSE = \sqrt{\frac{1}{N}\sum_{i=1}^{n}(M_{Rpre,i} - M_{Rexp,i})^2} \quad (9)$$

3. Results and discussion

3.1 Drying characteristics

3.1.1 Oven drying

The drying curve of *Cassia Alata* leaves dried using an oven dryer has been shown in Figure 1. The equilibrium moisture content of *Cassia Alata* leaves at temperature 90^{o}C was found to be 0.039 g H_2O/g DM which has a lowest equilibrium moisture content than dried leaves sample 50^{o}C, 60^{o}C, 70^{o}C and 80^{o}C with the equilibrium moisture content of 0.077 g H_2O/g DM, 0.079 g H_2O/g DM, 0.090 g H_2O/g DM and 0.068 g H_2O/g DM respectively. However, dried leaves sample 60^{o}C (0.079 g H_2O/g DM) and 70^{o}C (0.090 g H_2O/g DM) had the higher moisture content than dried sample 50^{o}C (0.077 g H_2O/g DM) which may be caused by the water residual on the surface of the leaves at the beginning of the drying process. This behavior was also being found from *Moringa Oleifera* sample leaves [20]. The drying rate at the initial period is not stable as shown in Figure 1. This may be mainly the retained moisture between the leaves' surface when the leaves were overlapping to each other. Furthermore, the descending of drying rate at the falling rate period was very similar to other research materials such as red bell pepper and plums [21, 22]. During this period, the change of drying rate and the moisture loss from the leaves were slowed due to the leaves surface is no longer capable to supply free moisture to the saturated air in contact with it [23]. In this condition, the rate of drying is mainly depending on the diffusion of the moisture inside the sample leaves to the surface [23].

The moisture ratio as a function of time is plotted and shown in Figure 2. The moisture ratio of the sample leaves decreased exponentially with respective of time until it reached the constant moisture ratio of 0.013 g H_2O/g DM, 0.023 g H_2O/g DM, 0.030 g H_2O/g DM, 0.027 g H_2O/g DM and 0.026 g H_2O/g DM for 50^{o}C, 60^{o}C, 70^{o}C, 80^{o}C and 90^{o}C respectively.

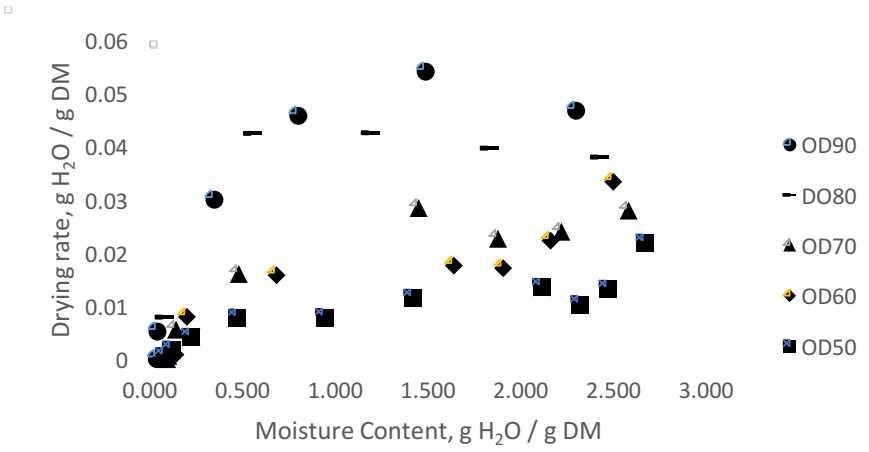


Figure 1: Drying rate as a function of moisture content for oven drying

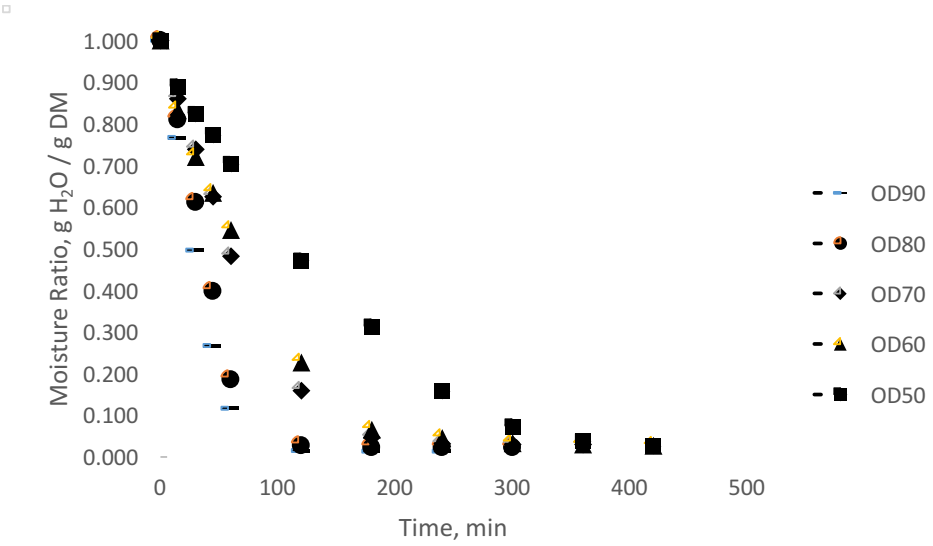


Figure 2: Moisture rate as a function of time for oven drying

The effective diffusivities were determined by the slope of a linear line obtained from the ln (M) as a function time and shown in Figure 3. The slope for 50°C, 60°C, 70°C, 80°C and 90°C were -0.009 min^{-1}, -0.0097 min^{-1}, -0.0135 min^{-1}, -0.0181 min^{-1} and -0.027 min^{-1} respectively. Hence, the effective diffusivities for 50°C, 60°C, 70°C, 80°C and 90°C were 2.9545 x 10^{-7} m^2/s, 3.1843 x 10^{-7} m^2/s, 4,4318 x 10^{-7} m^2/s 5.9419 x 10^{-7} m^2/s and 8.8636 x 10^{-7} m^2/s respectively. The obtained results show that the effective diffusivities elevated with the drying temperature due to the high evaporation of water molecules from the internal of the leaves sample [24]. As a comparison to other food and agricultural samples such as coconut coir pith (1.18 x 10^{-8} to 1.37 x 10^{-8} m^2/s), Grape (7.91 x 10^{-10} to 2.50 x 10^{-10} m^2/s) and tomato (3.09 x 10^{-9} to 9.28 x 10^{-9} m^2/s), the effective diffusivities of *Cassia Alata* is higher this is due to the outer surface texture of the leaves is more porous than other agricultural and food [25, 26, 27].

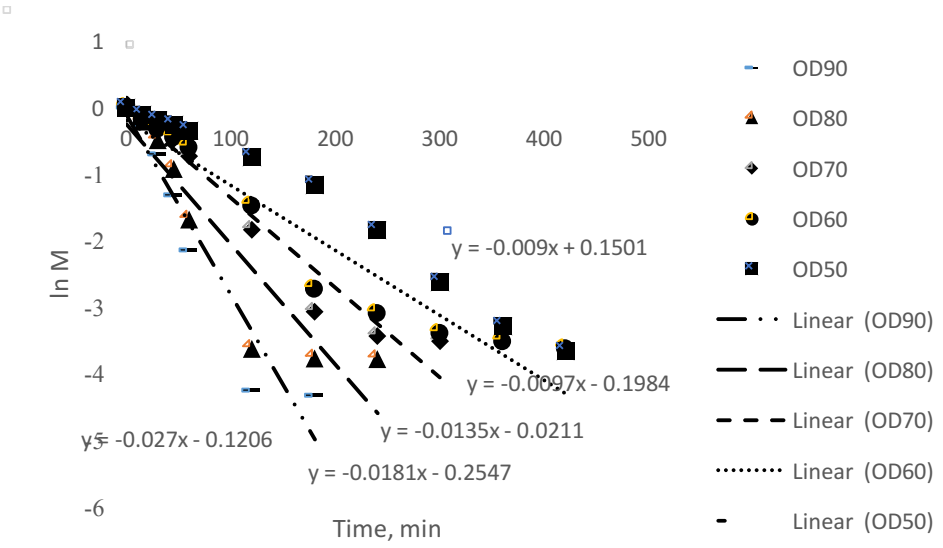
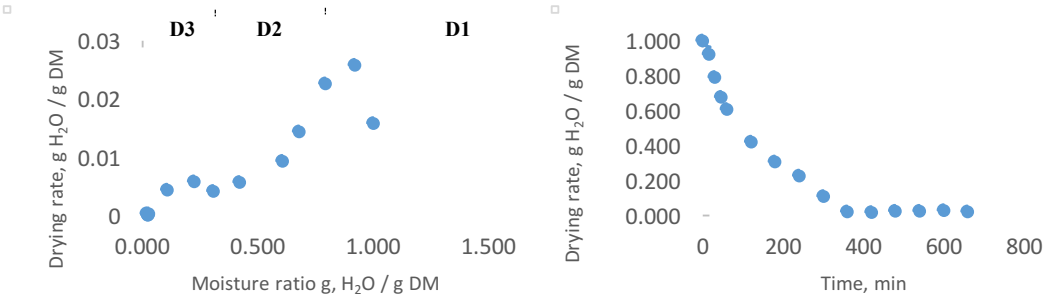


Figure 3: Logarithmic of moisture ratio as a function of time

3.1.2 Sun drying

The drying kinetic of *Cassia Alata* dried using sun drying method is shown in Figure 4a. The initial period (D1) (1.0 to 0.792 g H_2O / g DM) occurred in the first 30 min. The highest dry rates (0.02581 to 0.02265 g H_2O / g DM) have the highest moisture content of 2.997 to 2.3740 g H_2O / g DM. Then the drying rate of sample leaves were consistently dropping at the first falling rate period (D2) (0.679 to 0.307 g H_2O / g DM). Furthermore, in the second falling rate period (D3), the moisture ratio was 0.225 to 0.0025 g H_2O / g DM. The tempering period had the lowest drying rate of 0.00013 to 0.00009 g H_2O / g DM compared to initial, first falling rate and second falling rate regions (D1, D2, D3).

The moisture ratio as a function of time was also plotted and shown in Figure 4b. The moisture content of the sample leaves decreased exponentially with respective of time. There was a fluctuation at the time of 420 min to 660 min, the moisture ratio increased from 0.018 g H_2O / g DM to 0.022 g H_2O / g DM due to the relative humidity started to increase from 55.7% to 63%. Same phenomena also reported by Chong at el [12], where the relative humidity increases, the moisture ratio increase too.



(a) (b)

Figure 4: The relationship of drying rate and moisture ratio (a) and time (b)

3.1.3 Combination of sun drying and oven drying

The drying curve of *Cassia Alata* dried using CSOD is shown in Figure 5. During the sun drying period (SD), the drying rate was gradually increased from 0.00519 to 0.00769 g H_2O / g DM, 0.00550 to 0.00713 g H_2O / g DM for SDOD90 and SDOD80 at the first 15 min of the drying process. However, for SDOD70 the drying rate decreased from 0.00550 to 0.00713 g H_2O / g DM this is due to the relative humidity is relatively high (67%) compared to SDOD90 (55.7%) and SDOD80 (60%). Then the drying rate continuously decreased to 0.00160, 0.00558 and 0.0025 g H_2O / g DM for SDOD90, SDOD80 and SDOD70 respectively. At the oven drying period (OD), the drying rate rapidly increased from 0.00160 to 0.00878 g H_2O / g DM, 0.00435 to 0.00570 g H_2O / g DM and 0.00245 to 0.00594 g H_2O / g DM for SDOD90, SDOD80 and SDOD70 respectively. This is due to the uniform heating from the oven dryer to consistently dried the sample leaves. Furthermore, at the falling period the drying rate and the moisture loss started to slowdown and it is similar to oven drying in section 3.1.1.

The moisture ratio with respective of time is shown in Figure 6. The moisture ratio decreased linear during the first 60 min of the drying process. At 120 min, the moisture ratio of SDOD90 is slightly off to the drying trend, this might be due to the transferring period took too long from sun drying to oven drying and hence, the internal moisture of the leaves will be diffusive to the surface of the leaves [23]. Besides, SDOD90 had the lowest moisture ratio of 0.00253 g H_2O / g DM followed by SDOD80 and SDOD70 of 0.00347 g H_2O / g DM and 0.0162 g H_2O / g DM moisture ratio respectively.

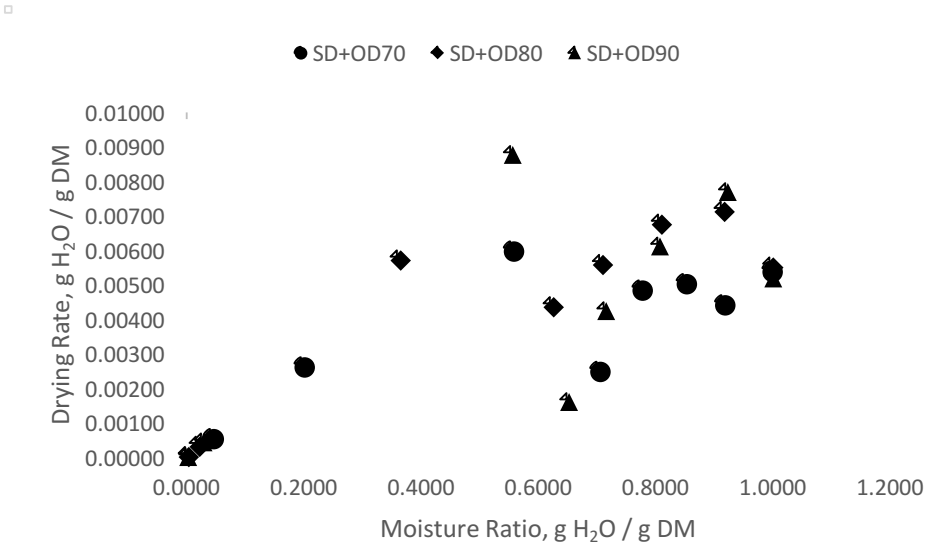


Figure 5: The relationship of drying rate and moisture ratio

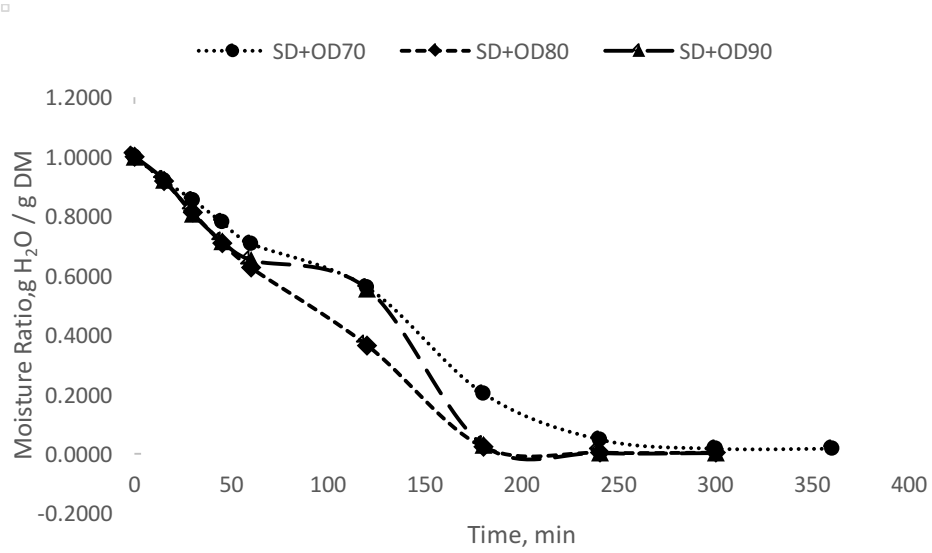


Figure 6: The relationship of moisture ratio and time

3.2 Empirical modeling

The best model that describing the drying characteristic was chosen by identifying the highest R^2 value and the lowest chi-square (χ^2) and root mean square (RMSE) value. In this case, all the model constant/ parameter, R^2, χ^2 and RMSE were tabulated in Table 2. The range of R^2, χ^2 and RMSE were 0.9382 to 0.9995, 0.0165 to 0.0001 and 0.01 to 0.01. Hence, the model that fitted to the drying curve was Page model which had a R^2, χ^2 and RMSE range of 0.9963 to 0.9995, 0.0005 to 0.0001 and 0.0226 to 0.01. In Figure 7 shows the comparison of model using experimental and predicted moisture ratio. The page model could fit into the drying process quite accurately.

Table 2: Results of curve fitting using various of thin layer model

Model	Temp (^oC)	Parameter	R^2	χ^2	RMSE
Henderson-Pabis	50	k = 0.0071, a = 1.0215	0.9931	0.0010	0.0320
	60	k = 0.0117, a = 1.0151	0.9940	0.0008	0.0276
	70	k = 0.0132, a = 1.0424	0.9912	0.0012	0.0346
	80	k = 0.0222, a = 1.0515	0.9807	0.0025	0.0499
	90	k = 0.0280, a = 1.0467	0.9826	0.0023	0.0474
Page	50	k = 0.0033, n = 1.1487	0.9965	0.0005	0.0222
	60	k = 0.0069, n = 1.1181	0.9963	0.0005	0.0226
	70	k = 0.0041, n = 1.2673	0.9983	0.0003	0.0175
	80	k = 0.0027, n = 1.5505	0.9974	0.0005	0.0219
	90	k = 0.0042, n = 1.5102	0.9995	0.0001	0.0100
Newton	50	k = 0.0069	0.9941	0.0011	0.0336
	60	k = 0.0110	0.9938	0.0009	0.0294
	70	k = 0.0124	0.9913	0.0015	0.0388
	80	k = 0.0209	0.9802	0.0029	0.0537
	90	k = 0.0267	0.9827	0.0026	0.0508
Modified Page	50	k = 0.0259, n = 0.2652	0.9941	0.0011	0.0336
	60	k = 0.0334, n = 0.3424	0.9941	0.0008	0.0282
	70	k = 0.0349, n = 0.3570	0.9913	0.0015	0.0387
	80	k = 0.0452, n = 0.4627	0.9802	0.0029	0.0537
	90	k = 0.0511, n = 0.5230	0.9827	0.0026	0.0508
Diffusion	50	k = 0.0069, a = 0.0298, b = 1.0001	0.9941	0.0011	0.0336
	60	k = 0.0114, a = 0.0313, b = 1.0000	0.9941	0.0008	0.0282
	70	k = 0.0124, a = 0.0313, b = 1.0000	0.9913	0.0015	0.0387
	80	k = 0.0315, a = 0.0315, b = 1.0599	0.9676	0.0056	0.0745
	90	k = 0.0177, a = 0.0315, b = 0.9419	0.9382	0.0165	0.1283

Cont. of Table 2

Model	Temp (^oC)	Parameter	R^2	χ^2	RMSE
Modified Henderson-Pabis	50	k_1 = 0.0071, k_2 = 0.0063, k_3 = 0.0004, a = 1.0211, b = 0.0004, c = 0.0004	0.9931	0.0010	0.0320
	60	k_1 = 0.0117, k_2 = 0.0117, k_3 = 0.0003, a = 1.0146, b = 0.0005, c = 0.0003	0.9940	0.0008	0.0276
	70	k_1 = 0.0132, k_2 = 0.0131, k_3 = 0.0003, a = 1.0419, b = 0.0005, c = 0.0003	0.9912	0.0012	0.0346
	80	k_1 = 0.0222, k_2 = 0.0171, k_3 = 0.0003, a = 1.0515, b = 0.0005, c = 0.0003	0.9807	0.0025	0.0499
	90	k_1 = 0.0279, k_2 = 0.0078, k_3 = 0.0047, a = 1.0463, b = 0.0005, c = 0.0047	0.9825	0..0022	0.0474

Table 3: Result of curve fitting using CSOD

Model	Temp (^oC)	Parameter	R^2	χ^2	RMSE
Newton	SDOD90	k = 0.0086	0.9387	0.0113	0.1062
	SDOD80	k = 0.0097	0.9776	0.0058	0.0764
	SDOD70	k = 0.0073	0.9709	0.0063	0.0795
Henderson-Pabis	SDOD90	k = 0.0092, a = 1.0573	0.9336	0.0105	0.1024
	SDOD80	k = 0.0105, a = 1.0706	0.9727	0.0047	0.0687
	SDOD70	k = 0.0079, a = 1.0612	0.9664	0.0054	0.0736
Page	SDOD90	k = 0.0014, n = 1.3846	0.9493	0.0077	0.0876
	SDOD80	k = 0.0015, n = 1.4145	0.9885	0.0018	0.0423
	SDOD70	k = 0.0009, n = 1.4160	0.9835	0.0025	0.0504
Modified Page	SDOD90	k = 0.0289, n = 0.2960	0.9397	0.0113	0.1062
	SDOD80	k = 0.0307, n = 0.3145	0.9776	0.0058	0.0764
	SDOD70	k = 0.0267, n = 0.2737	0.9709	0.0063	0.0795
Diffusion	SDOD90	k = 0.0086, a = 0.0301, b = 1.0000	0.9387	0.0113	0.1062
	SDOD80	k = 0.0097, a = 0.0300, b = 1.0000	0.9776	0.0058	0.0764
	SDOD70	k = 0.0073, a = 0.0296, b = 1.0000	0.9709	0.0063	0.0795
Modified Henderson-Pabis	SDOD90	k_1 = 0.0092, k_2 = 0.0088, k_3 = 0.0004, a = 1.0568, b = 0.0004, c = 0.0004	0.9336	0.0105	0.1024
	SDOD80	k_1 = 0.0085, k_2 = 0.1031, k_3 = 0.0216, a = 1.0408, b = 0.0000, c = 0.0216	0.9820	0.0026	0.0514
	SDOD70	k_1 = 0.0058, k_2 = 0.01031, k_3 = 0.0221, a = 1.0259, b = 0.0000, c = 0.0221	0.9790	0.0030	0.0549

The model for CSOD was tabulated in Table 3. The range of R^2, χ^2 and RMSE were 0.9885 to 0.336, 0.0018 to 0.0105 and 0.0423 to 0.1024 respectively. Besides that, the page model could fit into the drying process quite accurately due to the higher R^2 and lower χ^2 and RMSE value which had a range of 0.9885 to 0.9493, 0.0018 to 0.0077 and 0.0423 to 0.0876 respectively

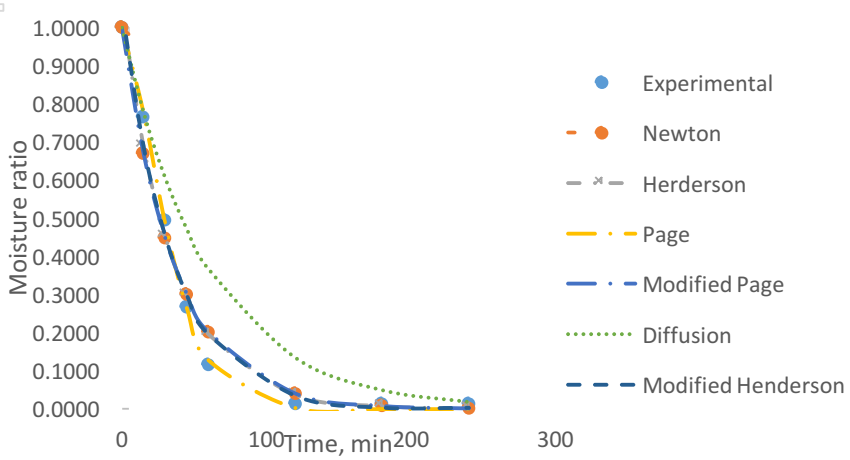


Figure 7: Comparison of model with moisture ratio as a function of time

3.5 Comparison of drying methods through energy consumption

In this project, a combination of sun drying and oven drying was used to dry *Cassia Alata* leaf to improve the drying performance through reducing the energy consumption as well as the time usage during the drying process. In figure 8 shows the energy consumption of each drying method. As the duration of oven drying increases, the energy consumption will eventually increase. By introducing sun drying into the drying process, it had an improvement of reducing the energy consumption as sun drying is a free energy that provide heat to reduce the moisture content. Furthermore, the reduction of energy consumption is increased from 25 % to 33 % as the drying temperature decrease from 90 to 70 ^{o}C. This behavior also been found in pumpkin slice using combination of microwave-air drying [28]. Besides, reducing the energy consumption during the drying process, it indirectly reducing the gas emission of greenhouse gases as well as the usage of fuel/coal that generate power. Furthermore, introducing oven drying to sun drying had shorten the drying duration as well as increase the drying efficiency of the entire drying process. In addition, combination of sun drying and oven drying will be able to overcome the disadvantage of sun drying because, oven drying provided uniform drying rate as well as shorten the drying duration of sun drying. On the other hand, sun drying reduced the energy consumption of oven drying.

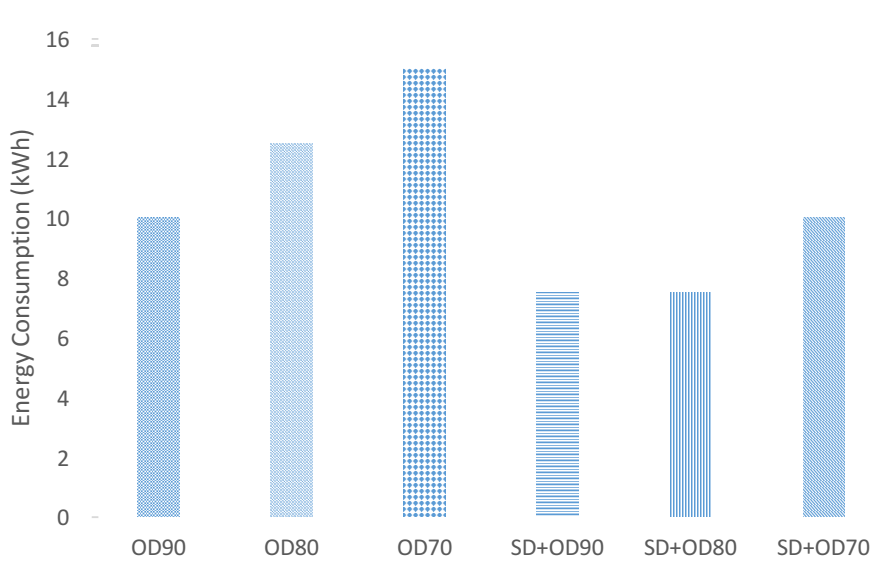


Figure 8: Energy consumption of drying methods

4. Conclusion

In this study, it found that oven drying with high temperature will enhance the moisture diffusion from the internal of the leaves to the surface during the falling rate period. Besides, in sundry method it was found that the relative humidity is the factor that effect the moisture content in the drying process. Furthermore, the Page model is the best fit model in comparison to five others thin layer drying models. The correlation coefficient (R^2), chi-square (χ^2) and RMSE of Page model were 0.995 to 0.9493, 0.0001 to 0.0077 and 0.01 to 0.0876 respectively. In addition, by implementing multiunit drying technology in *Cassia Alata* it reduces the drying duration as well as the energy consumption of oven drying. CSOD had reduce 25 % to 33 % energy consumption when the oven temperature decreases from 90 ^oC to 70 ^oC

Nomenclature

SD	***Sun drying***	D_R	***Drying rate***
OD	***Oven drying***	M_R	***Moisture ratio***
k, k_1, k_2, k_3	***Drying coefficient***	M_i	***Moisture content at respective time***
a, b, n	***Drying constant***	M_o	***Initial moisture content***
MC	***Moisture content***	M_e	***Equilibrium moisture content***
W_o	***Initial weight***	D_{eff}	***Effective diffusivity***
W_b	***Bone dry weight***	l	***Thickness***
DM	***Dry mass***	N_v	***Number of variables***
N_c	***Number of constant***		

CSOD	***Combination of sun drying and oven drying***
SDOD	***Sun drying and oven drying***

References

[1] W.J.H. Liu, "Traditional Herbal Medicine Research Methods". 2011.
[2] M. Abad, P. Noguera, R. Puchades, A. Maquieira, V. Noguera, "Physico-Chemical and Chemical Properties of Some Coconut Coir Dust for Use as A Peat Substitute For Containerized Ornamental Plants". J Bioresour Technol, vol. 82, pp. 241–245, 2002.
[3] I. Domaz, O. Ismail, "Drying Characteristics of Sweet Cherry". J Food Bioprod Process vol. 89, pp. 31–38, 2002.
[4] S. Kooli, A. Fadhel, A.Farhat, A.Belghith, "Drying of Red Pepper in Open Sun and Green House Conditions Mathematical Modeling and Experimental Validation". J Food Eng,vol. 79, pp. 1094–1103, 2007.
[5] C. W. Khaw, C. H. Chong, and J. M. Jee, "Drying Kinetics and Effect of Different Drying Temperature on Retained Chlorophyll Content of Cassia Alata Leaves," 2016.
[6] E. Meisami-asl, S. Rafiee, A. Keyhani, A. Tabatabaefar, "Mathematical Modeling of Moisture Content of Apple Slices During Drying". *Pak J* Nutr, vol. 8, pp. 804–809, 2009.
[7] V. Demir, T. Gunhan, A. K. Yagcioglu, A. K. Degirmencioglu, A. Degirmencioglu, "Mathematical Modeling and The Determination of Some Quality Parameters of Air Dried Bay Leaves," *J Biosyst Eng*, vol. 88, pp. 325–335, 2004.
[8] K. Raveendran, A. D. U. S. Amarasinghe, W. S. Botheju, "Drying Characteristics of Orthodox Broken Type Tea," *Trans Inst Eng Sri Lanka,* vol. 1, pp. 432–437, 2013.
[9] P. Kaushal, H. K, Sharma, "Osmo-Convective Dehydration Kinetics of Jackfruit," *J Saudi Soc Agric Sci*, 2014.
[10] E. Betoret, L. Calabuig-Jiménez, C. Barrera, and M. D. Rosa, "Sustainable Drying Technologies for the Development of Functional Foods and Preservation of Bioactive Compounds," J. del R. B. T.-S. D. T. Olvera, Ed. Rijeka: InTech, 2016, p. Ch. 03.
[11] D. Mierzwa, S. J. Kowalski, and J. Kroehnke, "Hybrid Drying of Carrot Preliminary Processed with Ultrasonically Assisted Osmotic Dehydration," *Food Technol. Biotechnol.*, vol. 55, no. 2, pp. 197–205, 2017.
[12] C. H. Chong, C. L. Law, M. Cloke, L. C. Abdullah, and W. R. W. Daud, "Drying Kinetics, Texture, Color, and Determination of Effective Diffusivities During Sun Drying of Chempedak," *Dry. Technol.*, vol. 26, no. 10, pp. 1286–1293, 2008.
[13] R. S. Aware and B. N. Thorat, "Garlic Under Various Drying Study and Its Impact on Allicin Retention," *Drying Tech*, pp. 1510–1518, 2011.
[14] A. Ayensu, "Dehydration of Food Crops Using a Solar Dryer with Convective Heat Flow," *SolarEnergy,* vol. 59, pp. 121–126, 1997.
[15] G. E. Page, "Factors Influencing the Maximum Rates of Air Drying Shelled Corn in Thin Layers," USA: Purdue University, 1949.

[16] G. M. White, I. J. Ross, Ponelert, "Fully Exposed Drying of Popcorn," *Transactions of ASAE*, vol. 24, pp. 466–468, 1981.
[17] E. K. Akpinar, Y. Bicer, C. Yildiz, "Thin layer drying of red pepper". *J. Food Eng.*, vol. 59 (1), pp. 99–104, 2013.
[18] O. Yaldız, C. Ertekin, H. I. Uzun, "Mathematical modeling of thin layer solar drying of sultana grape," *Sq. Energy*, vol. 26 (5), pp. 457–465, 2011.
[19] V. T. Karathanos, V. G. Belessiotis ,"Application of Thin-Layer Equation to Drying Data of Fresh and Semi-Dried Fruits," *J.Agric. Eng.Res.*, vol. 74 (4), pp. 355–361, 1999.
[20] M. A. Ali, Y. A. Yusof, N. L. Chin, M. N. Ibrahim, and S. M. A. Basra, "Drying Kinetics and Colour Analysis of *Moringa Oleifera* Leaves," *Agric. Sci. Procedia*, vol. 2, pp. 394–400, 2014.
[21] A. Vega, P. Fito, A. Andres, R. Lemus "Mathematical Modeling of Hot Air Drying Kinetics of Red Bell Pepper (Var. Lamuyo)," *J Food Eng*, vol. 79(4), pp. 1460–1466, 2007.
[22] R. K. Goyal, A. R. P. Kingsly, M. R. Manikantan, S. M. llyas, "Mathematical Modeling in Thin Layer Drying Kinetics of Plum in a Tunnel Dryer," *J Food Eng*, vol. 79(1), pp. 176–180, 2007.
[23] F. M. Botelho, P. C. Corrêa, A. L. D. Goneli, M. A. Martins, F. E. A. Magalhães, and S. C. Campos, "Periods of Constant and Falling-Rate For Infrared Drying of Carrot Slices," *Rev. Bras. Eng.*, vol. 67, pp. 845–852, 2011.
[24] Q. Chen, J. Bi, X. Wu, J. Yi, L. Zhou, and Y. Zhou, "Drying Kinetics and Quality Attributes of Jujube (*Zizyphus Jujuba Miller*) Slices Dried by Hot-Air and Short-Wave and Medium-Wave Infrared Radiation," *LWT - Food Sci. Technol.*, vol. 64, no. 2, pp. 759–766, 2015.
[25] J. A. K. M. Fernando and A. D. U. S. Amarasinghe A, "Drying Kinetics and Mathematical Modeling of Hot Air Drying of Coconut Coir Pith," *Springerplus*, vol. 5, no. 1, p. 807, 2016.
[26] I. Doymaz, M. Pala, "The Effects of Dipping Pretreatments on Air Drying Rates of The Seedless Grapes," *Journal of Food Engineering,* vol. 52, pp. 413–417, 2002.
[27] P. Rajkumar; S. Kulanthaisami; G. S. V. Raghavan, Y. Gariepy, V. Orsat, "Drying Kinetics of Tomato Slices in Vacuum Assisted Solar and Open Sun Drying Methods," *Drying Technology*, vol. 25, pp. 1349– 1357, 2007.
[28] I. Alibas, "Microwave, air and combined microwave-air-drying parameters of pumpkin slices," *LWT - Food Sci. Technol.*, vol. 40, no. 8, pp. 1445–1451, 2007.

eureca 2017 – Conference Paper
Paper Number 2CE05

Temperature Effect on Natural Hydroxyapatite Obtained from Fish Bones for Bone Tissue Engineering

Danial Aminin bin Zairin[1*], Eunice, Phang Siew Wei [1,2]

[1&2]*School of Engineering, Taylor's University, Malaysia*

[2]*Faculty of Engineering and Science, Department of Chemical Engineering, Universiti Tunku Abdul Rahman, Malaysia*

[*]*danialaminin@hotmail.com*

Abstract

Natural hydroxyapatite obtained from fish bones was preferred rather than synthetic due to better biocompatibility in bone tissue engineering. This research involved studying heating treatment effect, where calcination temperature and holding time were the two main parameters, on hydroxyapatite from fish bones as well as identifying its best conditions. In this research, fish bones, mackerel and herring based to be precise, were selected as hydroxyapatite source because of abundancy, availability and ease of acquiring in Malaysia. The particle structure, phase composition and crystallinity of hydroxyapatite from fish bones were analysed. The procedures to obtain hydroxyapatite involved pre-treatment – bone cleansing to remove organic substances and impurities, calcination – heating up fish bones at high temperature, and characterization processes. X-ray diffractometer (XRD) and Fourier-transform infrared spectrometer (FTIR) were included in characterization process to study and analyse the hydroxyapatite particle structure, phase composition or elements, crystallinity and such. XRD results showed that higher temperature shows better crystallinity and particle structure of hydroxyapatite. However, regardless of holding time, reaching temperature of 1000 °C slightly lowered the hydroxyapatite crystallinity. FTIR results showed the presence of phosphate, carbonate and hydroxyl groups after calcination. Besides, traces of biological elements were detected by FTIR on fish bones exposed to only elevating calcination temperature. Small traces of elements such as magnesium, sodium and such are detected from characterization. Comparing the two fish bones, herring resulted in overall better hydroxyapatite properties than in mackerel. The best temperature and calcination holding time to obtained exceptional overall hydroxyapatite properties from mackerel and herring would be 800 °C and 4 hours, respectively. These results proved to be promising for future medical application where bone restoration is heavily involved.

Keywords: Hydroxyapatite, Fish Bones, Calcination,

1. Introduction

Skeletal system of the human body comprises of bones connecting one another through joints, mainly serves for support and mobility. Similar to any other organ in the human body, bones are made out of cells combining together to form tissues. In this case, they are made out of bone tissues and bone marrow. Besides, it has a unique regeneration and healing abilities once its architecture disrupted. In an event where the bone experiences huge architecture lost due to trauma, bone infection or disease or such, this healing ability can fail. As a result, it will leave a permanent bone defect. Moreover, this self-heal rate decreases with aging. In order to counter this, new medical treatments that heavily involve bone regeneration or grafting must be implemented. According to statistics, there is a high demand of bone treatments as bone is the most transplanted tissue after blood [1, 2].

Natural hydroxyapatite (HA) is mineral found in human bone – calcium phosphate based compound, that promotes bone regeneration. This mineral can be found in the human body and teeth. Natural hydroxyapatite has been widely used for bone implantation due to similarity in composition. Unlike synthetic hydroxyapatite, it contains not only calcium phosphate element but other minerals and organic compounds in small amounts – magnesium, zinc and such. Implementing natural hydroxyapatite rather than synthetic is desirable for implant material as it results in exceptional bioactivity and osteointegration [3], [4]. On top of that, unlike synthetic, hydroxyapatite is non-toxic and will not be rejected by the human immune system [3].

Natural hydroxyapatite can be found in living organisms. Fish bones and scales, sea corals, egg shells and bovine are few of the sources that have been reported of natural hydroxyapatite extraction [5]–[12]. Fish bone is the ideal medium for natural hydroxyapatite extraction. Globally, approximately 18 to 30 million tons per annum of fish waste is removed [13]. Acquiring fish bones to extract hydroxyapatite could be economically viable – cheap source. Besides, selecting fish or any organisms that derived from ocean – corals, jellyfishes and such, grant easy access and comes in abundant. Moreover, it brings no religious conflicts, in terms of animal selection. In this research, mackerel and herring, locally known as *ikan tenggiri* and *ikan parang*, respectively, are chosen mainly because their availability and ease acquiring in Malaysia. Mackerel and herring are few of the fishes that are selected to make other food applications and products, discarding the bones as wastes.

There are few methods or techniques used to obtained hydroxyapatite from living organisms. Currently, methods that have been applied are calcination or thermal decomposition method, alkaline hydrothermal hydrolysis and subcritical water process [14]. However, out of the methods mentioned, calcination process is considered the cheapest as it only involves decomposition of bones at high temperature. On top of that, no chemicals are involved in calcination method.

There are two objectives to achieve in this research. The first objective is to study and analyze the calcination effect, where calcination temperature and holding time are the two main parameters, of natural hydroxyapatite from mackerel and herring bones. The range of calcination temperature and holding time are selected at 600 °C to 1000 °C and 2 hours to 6 hours, respectively. The second objective is to identify the

best conditions – calcination temperature and holding time, to obtain exceptional overall natural hydroxyapatite properties from mackerel and herring bones.

2. Methodology

2.1 Fish Bones Preparation

Two types of fishes were chosen; mackerel and herring. Bones of mackerel and herring were acquired from local market - Pasar Tani at Setiawangsa, Kuala Lumpur. The bones were freshly acquired, with organic substances and impurities present, since the fishes were cut or fillet as soon as the food products are displayed and ready to be sold. Firstly, the bones were washed using small brush or any means of tools to remove organic substances and impurities. Next, the fish bones were boiled in water for 1 hour to further remove the organic substances and impurities, where simple brushing is futile. The bones were then dried at room temperature. Once dried, the bones were placed in the furnace for calcination process – sample will undergo heating treatment at high temperature. The furnace will heat up the bones at 10 °C/min between 600 °C to 1000 °C [6], [15]–[17]. Once the desired calcination temperature has achieved, the bones continued to be heated with holding time between 2 to 6 hours [6], [15]–[17]. Once the holding time is completed, the calcinated bones were cooled in the furnace. The calcinated bones were then grinded to powder form for characterization and analyzation. Powdered form samples were required so that more surface areas can be analyzed and studied.

2.2 Sample Characterization

2.2.1 X-Ray Diffractometer (XRD)

The x-ray diffractometer (XRD, Bruker D8 Discover) was used to study and analyze the phase composition and crystallinity of the sample – verifying its purity and stability [6], [15]–[17]. Including x-ray diffractometer in the study account was essential as it identifies any thermal decomposition product of the sample [18]. The scanning was carried out with angle 2θ range from 10 to 70° with step size of 0.1° [6], [15]–[17]. The x-ray diffractometer was operated using Cu Kα radiation (λ = 1.540 Å) with operating voltage and current of 40 kV and 30 mA.

2.2.2 Fourier-Transform Infrared Spectrometer (FTIR)

The Fourier-transform infrared spectrometer (FTIR, Perkin Elmer Spectrum 100) was used to study and analyze the functional groups of the sample by interpreting the absorption through its chemical bonds [6], [15]–[17]. Functional groups of phosphate, hydroxyl and carbonates can be detected through the spectrometer. For each sample, the conditions were set for 4 cm^{-1} resolution with frequency range between 650 to 4000 cm^{-1} [6], [15]–[17].

2.3 Design of Experiments

Design of experiment was conducted by using commercialized software called Minitab. Taguchi method was implemented in order to estimate the optimization of calcination temperature and holding time. Table 1 below displays the Taguchi design

generated by Minitab software. Calcium phosphorus (Ca/P) ratio based on previous reports was used to estimate the optimum calcination temperature and holding time. This is because other characterization resulted more to qualitative than quantitative.

Table 1: Taguchi design generated by Minitab software

Calcination Temperature (°C)	Holding Time (hr)	Ca/P ratio
600	2	1.50
600	4	1.63
600	6	2.04
800	2	1.81
800	4	1.78
800	6	1.65
1000	2	1.67
1000	4	1.70
1000	6	1.72

Once Minitab analyzed the design of experiments, two graphs generated which displays on Figure 2. It was found that based on Ca/P ratio from previous reports, optimum calcination temperature and holding was 800 °C and 6 hours, respectively. However, analyzing one sample, on each species, with calcination temperature and holding time of 800 °C and 6 hours will not be sufficed to achieve the project objectives. In order to verify the calcination temperature and holding time effects, mild and extreme calcination conditions were devised based on project objectives and scope, for each fish species, which is designed on Table 2. In calcination temperature of 800 °C, holding time effect of 4 hours was selected as there were two samples selected for same holding time at different temperatures. On top of that, due to high characterization expense, all 18 samples were not sent for analysis. Instead, 10 samples are sent.

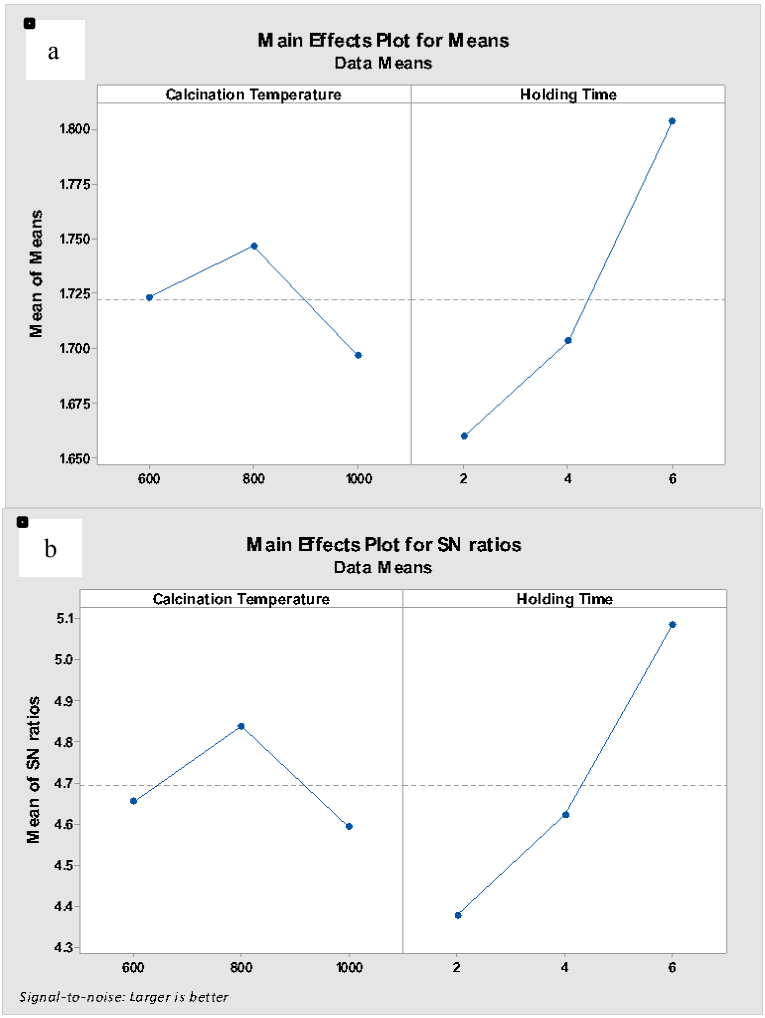


Figure 2: Graph plot generated by Minitab with (a) and without (b) signal to noise

Table 2: Experiment design for each fish species (sample preparation)

		Calcination Temperature (°C)		
		600	800	1000
Holding Time (hr)	2			
	4			
	6			

3. Results & Discussion

3.1 General Description

Figure 3 display the raw bones of mackerel and herring after cleansing and before calcination. The color of the bones for mackerel and herring were yellow-brown and yellow-white, respectively. These colors represent the organic elements or biological composition present in and around the bones [19]. Different species of fish may contain different elements in their respective bones. One of the properties that can be identified easily regarding the removal of organic elements or biological composition is the bone color. The bone started with its raw color and continued transforming to black, blue and white. This applies to both mackerel and herring.



Figure 3: Raw mackerel (left) and herring (right) bones

Figure 4 display the mackerel and herring bone where it only exposed to elevating calcination temperautre. These samples, labelled as preliminary, were prepared to observed the appearance of the bone during elevating calcination temperature. Based on Figure 2, both mackerel and herring have lost their raw color. However, black, blue and white can be seen clearly. The color transformation sequence can be deduced with aid of Table 3 and 4. Herring resulted pure white appearance after between 600 °C, 800 °C and 1000 °C, regardless of holding time. However, at 600 °C, mackerel bone contained blue and white color. This suggested that organic elements or biological composition was still present, which agreed with the previous author [19]. Besides, comparing the two bone type, mackerel contained more organic elements than in herring, since pure white color appearance was detected at lower calcination temperature of 600 °C.

After calcination process, the residue obtained were little. This trend applied to both mackerel and herring. The residue range from 24% to 36%. This supported the color factor as most of the mackerel and herring bones were made out of organic elements or biological composition. At blistering high temperatures, most of the elements were removed leaving hydroxyapatite as major component [12]. Small traces of elements were detected which will discussed in the next section.



Figure 4: Mackerel (left) and herring (right) after elevating calcination temperature

Table 3: Color and Residue of Mackerel Bone After Calcination

Calcination Temperature (°C)	Holding Time (hr)	Initial Mass (g)	Final Mass (g)	Residue (wt %)	Color
600	2	16.10	3.98	24.72	Blue & White
600	6	15.00	3.91	26.07	Blue & White
800	4	16.56	4.13	24.94	White
1000	2	16.60	5.82	35.06	White
1000	6	16.24	4.06	25.00	White

Table 4: Colour and Residue of Herring Bone After Calcination

Calcination Temperature (°C)	Holding Time (hr)	Initial Mass (g)	Final Mass (g)	Residue (wt %)	Color
600	2	11.50	3.68	32.00	White
600	6	9.13	3.11	34.06	White
800	4	12.40	3.68	29.68	White
1000	2	5.28	1.72	32.58	White
1000	6	8.25	2.40	29.09	White

3.2 FTIR Spectra Results

Four samples were selected for FTIR analysis; mackerel and herring exposed to elevating calcination temperature and mackerel and herring exposed to 1000 °C for 6 hours. Extreme condition was selected to demonstrate the functional group and elements or composition difference with samples exposed to elevating calcination temperature. Figure 3 display the FTIR spectra results for samples exposed to elevating calcination temperature. The main functional groups to be identified are phosphate, hydroxyl and carbonate as they reflect the hydroxyapatite trait.

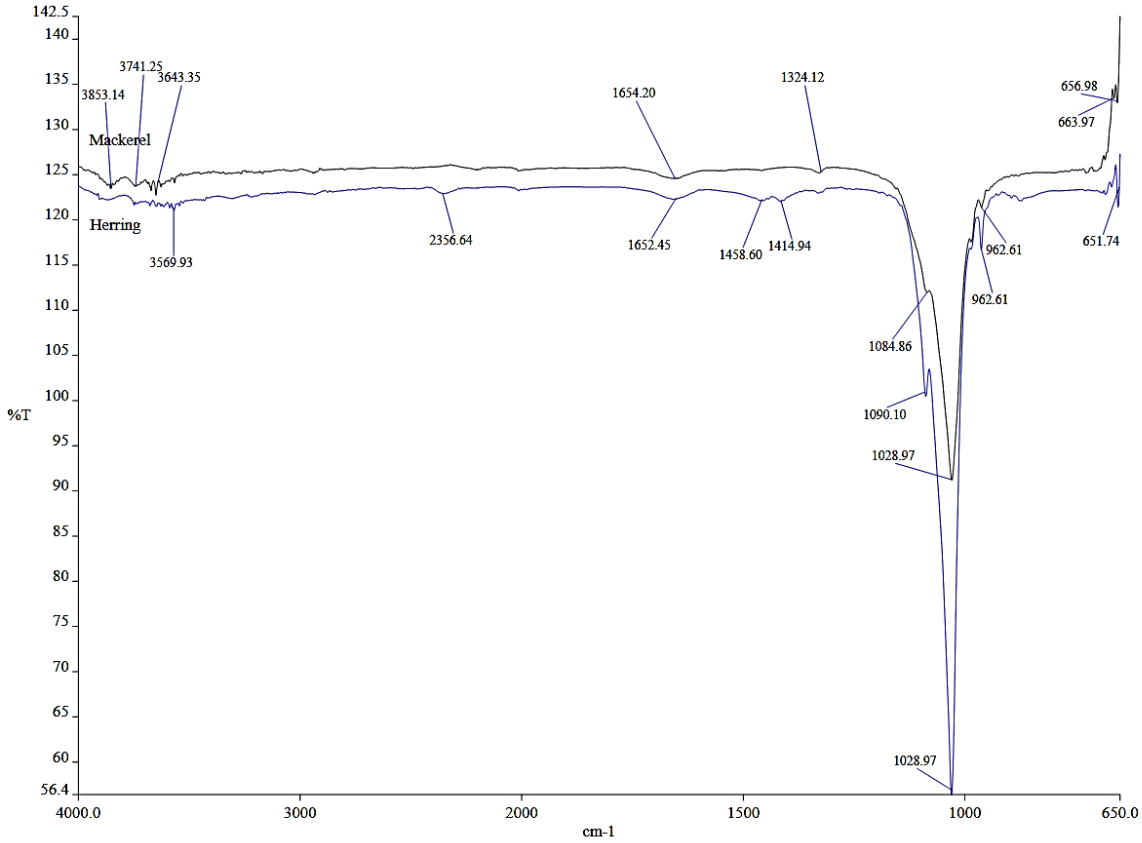


Figure 5: FTIR results of fish bones exposed to elevating calcination temperature

Based on Figure 5, mackerel and herring displayed similar peak trend. Narrow bands suggested good crystallization of sample [5]. Phosphate (PO_4^{3-}) group was detected between bands of 900 cm^{-1} and 1100 cm^{-1}. Carbonate (CO_3^{2-}) group was detected with small intensity at bands between 1300 cm^{-1} and 1660 cm^{-1}. Like carbonate group, hydroxyl (OH^-) group was detected with small intensity between bands of 3500 cm^{-1} and 3900 cm^{-1}. Organic materials can be detected at small intensity with bands of 2356.64 cm^{-1}. The results applied to both mackerel and herring. The results displayed agreed with previous authors as it showed similar results [5], [11], [14], [15], [19]–[21]. Comparing the fish bones, herring showed better crystallinity than in mackerel.

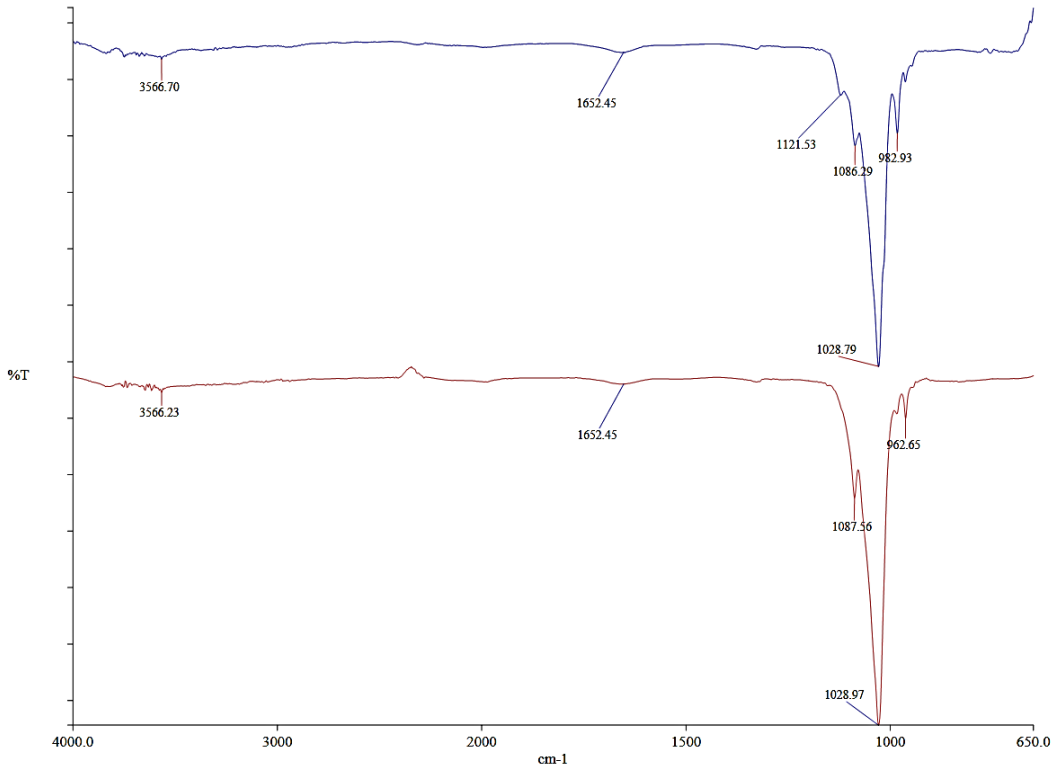


Figure 6: FTIR results of mackerel (blue) and herring (red) at 1000 °C for 6 hours

The results displayed on Figure 6 showed similar trend as one in Figure 5. At higher temperature and longer holding time, phosphate group resulted in higher intensity with sharper peak, suggesting higher crystallinity than preliminary samples. On top of that, organic elements have been decomposed resulting in smaller and broader bands at around 2000 cm^{-1}. Nevertheless, hydroxyl and carbonate groups can be detected but in much smaller intensities, comparing to the previous two samples. This can be concluded that at higher temperature with longer holding time, overall hydroxyapatite properties will be better.

The peaks around 1650 cm^{-1} were associated with carbonate ions while peaks between 1400 and 1460 cm^{-1} were associated with B-type hydroxyapatite due to substitution of phosphate and carbonate groups [6], [22], [23]. The carbonate groups between 1400 and 1460 cm^{-1} decreases or removed as calcination temperature elevates due to decomposition to carbon dioxide which usually occur at temperature above 600 °C, regardless of the holding time [24]. Bands around 960 cm^{-1} indicated the presence of β-type tricalcium phosphate (TCP) [25]. On the other hand, hydroxyl group band intensity grew smaller and broader as temperature elevates due to weaken of intermolecular hydrogen bonding of water molecules [20]. Carbonate ions should be conserved to enhance the hydroxyapatite property and hence, calcination temperature must be controlled – selecting lower calcination temperature and holding time. B-type tricalcium phosphate and non-resorbable hydroxyapatite has been reported as appropriate compound for bone regeneration as it provides permanent scaffold for bone formation via osteoconduction and speeds up the regeneration through resorption [26], [27].

3.3 XRD Results

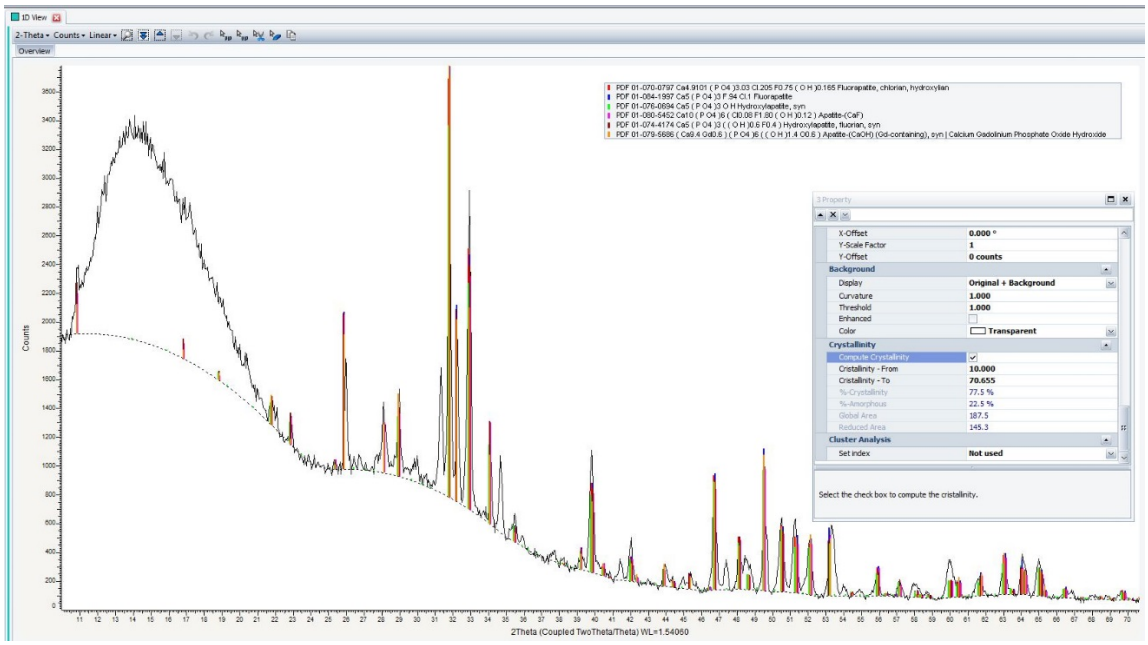


Figure 7: Herring bone at 1000 °C for 6 hours

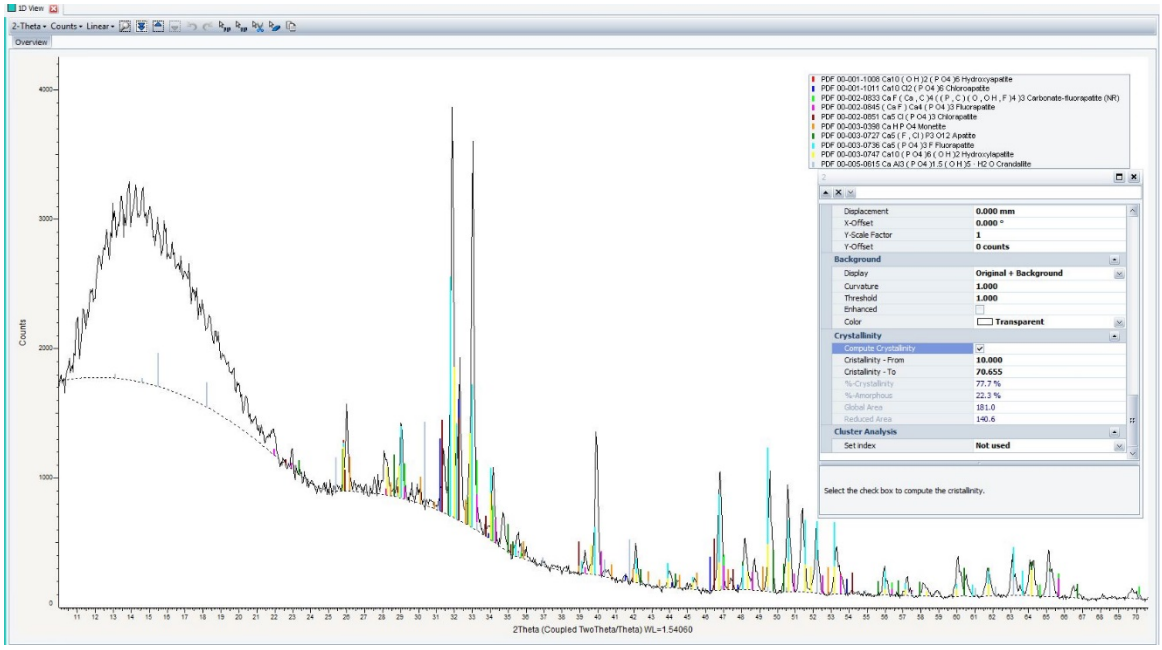


Figure 8: Herring bone at 800 °C for 4 hours

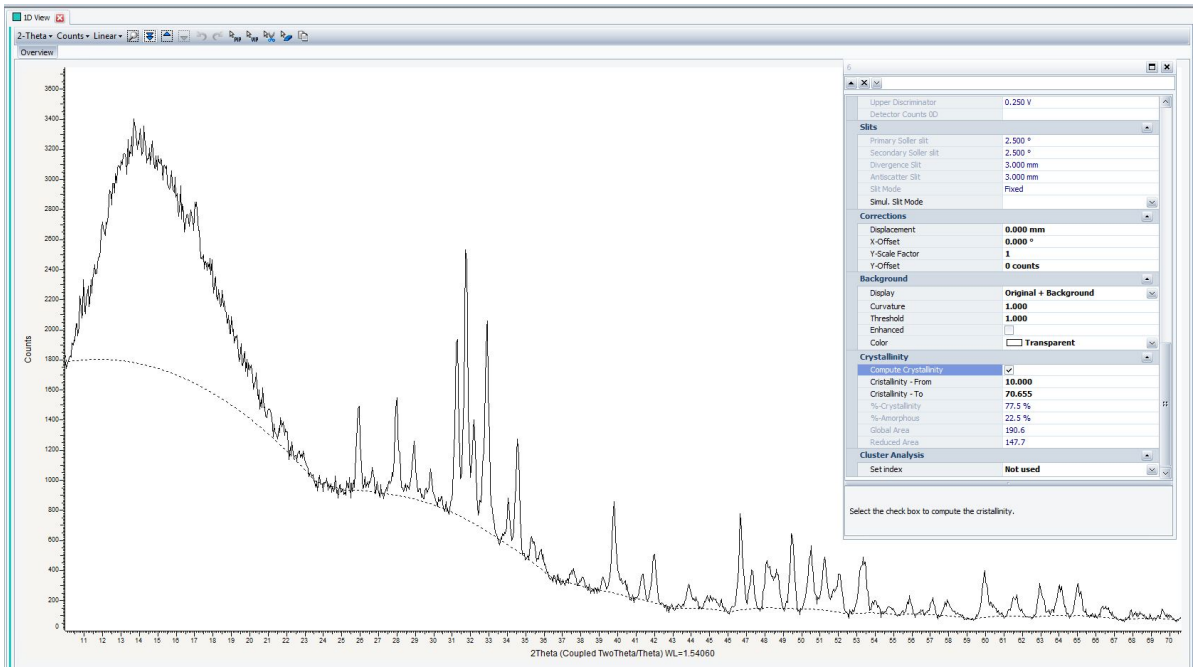


Figure 9: Mackerel bone at 800 °C for 4 hours

The crystallinity phase and purity of hydroxyapatite derived from fish bones were confirmed with XRD analysis. Figure 7, 8 and 9 displays the XRD patterns of different calcination temperature with its respective holding time. Despite the type of fish, calcination temperature and holding time, the patterns displayed are similar and no new peaks are generated. The XRD pattern indicated the hydroxyapatite structure is not affected, resulting in matrix stability and enhancement of crystallinity [19], [28]. Based on the results, both Mackerel and Herring resulted in same XRD trend. The intensity increased with decrease peak width as calcination temperature and holding time elevates. Besides, highly intense and sharp peaks suggested the removal of organic matters present in the fish bones [29]. This also indicated that the fish bones were made of organic matters or biological content. Minor presence of organic matters in both mackerel and herring resulted on XRD patterns on Figure 5 and 6 which is excellent for bioactivity, biocompatibility and osteoconductivity, increasing the osteoblast functions [5]. Both mackerel and herring contained minor of beta tricalcium phosphate (β-TCP) at temperatures 800 °C and 1000 °C which agrees with previous authors, regardless of fish type [5], [20], [30]. Minor presence of sodium, magnesium, potassium and other compounds is essential for biocompatibility as it contributes to metabolism in human body. Sodium and magnesium are responsible for bone metabolism but also result in osteoporosis – bone fragile [31], [32]. Magnesium is responsible for bone proliferation and function to enhance synthesis of protein [33]. Strontium is responsible for reducing bone resorption and enhance bone formation to prevent fractures [34].

What sets the difference, in terms of XRD results, between mackerel and herring is their respective intensities. Based on Figure 6 and 7, herring showed overall higher peak intensities than in mackerel, resulting in better hydroxyapatite crystallinity. In calcination of 600 °C, herring dominated over mackerel, regardless of holding time. Similar peak intensities were resulted in both calcination of 1000 °C. However, herring, with holding time of 6 hour of 1000 °C calcination temperature, resulted in better overall peak intensities than in mackerel. Hydroxyapatite property gave high result in

temperature of 800 °C with 4 hours of holding time as it displayed the highest intensity counts. This suggested that lower temperatures preserve better overall hydroxyapatite properties than intense temperatures such as 1000 °C [5]. Calcination temperature of 800 °C with 4 hours of holding time would preserve better overall hydroxyapatite property.

4. Conclusions

Natural hydroxyapatite was obtained from fish bones, specifically mackerel and herring, through calcination or thermal decomposition method. Based on results, herring resulted in better overall hydroxyapatite properties than in mackerel. Calcination temperature of 800 °C and holding time of 4 hours resulted in exceptional overall hydroxyapatite properties. Presence of minor elements or biological composition were detected, giving excellent biocompatibility and bioactivity. Hydroxyapatite derived from fish bones showed promising future for biomedical field, where bone regeneration is heavily involved as the raw materials are cheap and easy to acquire.

Acknowledgment

The authors gratefully acknowledged *Pasar Tani*, Setiawangsa (Kuala Lumpur, Malaysia) for providing fish bones and school of engineering from Monash University, Malaysia, for X-Ray Diffractometer analyzation of fish bones.

References

[1] J. K. Leach and D. J. Mooney, “Bone engineering by controlled delivery of osteoinductive molecules and cells.,” *Expert Opin. Biol. Ther.*, vol. 4, no. 7, pp. 1015–27, Jul. 2004.

[2] A. Oryan, S. Alidadi, A. Moshiri, and N. Maffulli, “Bone regenerative medicine: classic options, novel strategies, and future directions.,” *J. Orthop. Surg. Res.*, vol. 9, no. 1, p. 18, 2014.

[3] S. Samavedi, A. R. Whittington, and A. S. Goldstein, “Calcium phosphate ceramics in bone tissue engineering: A review of properties and their influence on cell behavior,” *Acta Biomater.*, vol. 9, no. 9, pp. 8037–8045, 2013.

[4] W. Suchanek and M. Yoshimura, “Processing and properties of hydroxyapatite-based biomaterials for use as hard tissue replacement implants,” *J. Mater. Res.*, vol. 13, no. 1, pp. 94–117, Jan. 1998.

[5] M. Boutinguiza, J. Pou, R. Comesaña, F. Lusquiños, A. De Carlos, and B. León, “Biological hydroxyapatite obtained from fish bones,” *Mater. Sci. Eng. C*, vol. 32, no. 3, pp. 478–486, 2012.

[6] N. Mustafa, M. H. I. Ibrahim, R. Asmawi, and A. M. Amin, “Hydroxyapatite Extracted from Waste Fish Bones and Scales via Calcination Method,” *Appl. Mech. Mater.*, vol. 774, pp. 2–6, 2015.

[7] S. Kongsri, K. Janpradit, K. Buapa, S. Techawongstien, and S. Chanthai, “Nanocrystalline hydroxyapatite from fish scale waste: Preparation, characterization and application for selenium adsorption in aqueous solution,” *Chem. Eng. J.*, vol. 215–216, pp. 522–532, 2013.

[8] Y. C. Huang, P. C. Hsiao, and H. J. Chai, “Hydroxyapatite extracted from fish scale: Effects on MG63 osteoblast-like cells,” *Ceram. Int.*, vol. 37, no. 6, pp. 1825–1831, 2011.

[9] E. M. Rivera, M. Araiza, W. Brostow, V. M. Castaño, J. R. Díaz-Estrada, R. Hernández, and J. R. Rodríguez, "Synthesis of hydroxyapatite from eggshells," *Mater. Lett.*, vol. 41, no. 3, pp. 128–134, 1999.

[10] M. Sivakumar, T. S. Sampath Kumar, K. L. Shantha, and K. Panduranga Rao, "Development of hydroxyapatite derived from Indian coral," *Biomaterials*, vol. 17, no. 17, pp. 1709–1714, 1996.

[11] D. C. Greenspan and D. Ph, "Comparison Of A Synthetic And Bovine Derived Hydroxyapatite Bone Graft Substitute," *Zimmer Dent.*, 2013.

[12] W. Khoo, F. M. Nor, H. Ardhyananta, and D. Kurniawan, "Preparation of Natural Hydroxyapatite from Bovine Femur Bones Using Calcination at Various Temperatures," *Procedia Manuf.*, vol. 2, no. February, pp. 196–201, 2015.

[13] E. O. Elvevoll and D. James, "The emerging importance of dietary lipids, quantity and quality, in the global disease burden: the potential of aquatic resources.," *Nutr. Health*, vol. 15, no. 3–4, pp. 155–67, 2001.

[14] N. A. M. Barakat, M. S. Khil, A. M. Omran, F. A. Sheikh, and H. Y. Kim, "Extraction of pure natural hydroxyapatite from the bovine bones bio waste by three different methods," *J. Mater. Process. Technol.*, vol. 209, no. 7, pp. 3408–3415, 2009.

[15] D. S. Seo, K. H. Hwang, S. Y. Yoon, and J. K. Lee, "Fabrication of hydroxyapatite bioceramics from the recycling of pig bone," *J. Ceram. Process. Res.*, vol. 13, no. 5, pp. 586–589, 2012.

[16] M. Supova, G. S. Martynkova, and Z. Sucharda, "Bioapatite made from chicken femur bone," *Ceram. - Silikaty*, vol. 55, no. 3, pp. 256–260, 2011.

[17] M. Ozawa and S. Suzuki, "Microstructural Development of Natural Hydroxyapatite Originated from Fish-Bone Waste through Heat Treatment," *J. Argent. Chem. Soc.*, vol. 17, no. 188335, pp. 2000–2002, 2002.

[18] A. M. Sofronia, R. Baies, E. M. Anghel, C. A. Marinescu, and S. Tanasescu, "Thermal and structural characterization of synthetic and natural nanocrystalline hydroxyapatite," *Mater. Sci. Eng. C*, vol. 43, pp. 153–163, 2014.

[19] J. Venkatesan and S. K. Kim, "Effect of temperature on isolation and characterization of hydroxyapatite from tuna (thunnus obesus) bone," *Materials (Basel).*, vol. 3, no. 10, pp. 4761–4772, 2010.

[20] K. Prabakaran and S. Rajeswari, "Development of hydroxyapatite from natural fish bone through heat treatment," *Trends Biomater. Artif. Organs*, vol. 20, no. 1, pp. 20–23, 2006.

[21] J. Venkatesan, B. Lowe, P. Manivasagan, K. H. Kang, E. P. Chalisserry, S. Anil, D. G. Kim, and S. K. Kim, "Isolation and characterization of nano-hydroxyapatite from salmon fish bone," *Materials (Basel).*, vol. 8, no. 8, pp. 5426–5439, 2015.

[22] I. Mayer, S. Schneider, M. Sydney-Zax, and D. Deutsch, "Thermal decomposition of developing enamel.," *Calcif. Tissue Int.*, vol. 46, no. 4, pp. 254–7, Apr. 1990.

[23] R. Zapanta LeGeros, "Apatites in biological systems," *Prog. Cryst. Growth Charact.*, vol. 4, no. 1–2, pp. 1–45, Jan. 1981.

[24] S. M. Barinov, J. V. Rau, S. N. Cesaro, J. Ďurišin, I. V. Fadeeva, D. Ferro, L. Medvecky, and G. Trionfetti, "Carbonate release from carbonated hydroxyapatite in the wide temperature rage," *J. Mater. Sci. Mater. Med.*, vol. 17, no. 7, pp. 597–604, Jul. 2006.

[25] Q. Zhu, Z. Ablikim, T. Chen, Q. Cai, J. Xia, D. Jiang, and S. Wang, "The preparation and characterization of HA/?-TCP biphasic ceramics from fish

bones," *Ceram. Int.*, 2017.
[26] M. Vallet-Regi and J. M. González-Calbet, "Calcium phosphates as substitution of bone tissues," *Prog. Solid State Chem.*, vol. 32, no. 1–2, pp. 1–31, 2004.
[27] E. Goyenvalle, E. Aguado, J.-M. Nguyen, N. Passuti, L. Le Guehennec, P. Layrolle, and G. Daculsi, "Osteointegration of femoral stem prostheses with a bilayered calcium phosphate coating.," *Biomaterials*, vol. 27, no. 7, pp. 1119–28, Mar. 2006.
[28] K. Sasaki and T. Goto, "Immobilization of Sr2+ on naturally derived hydroxyapatite by calcination of different species of fish bones and influence of calcination on ion-exchange efficiency," *Ceram. Int.*, vol. 40, no. 8 PART A, pp. 11649–11656, 2014.
[29] M. J. Glimcher and M. J., "Molecular Biology of Mineralized Tissues with Particular Reference to Bone," *Rev. Mod. Phys.*, vol. 31, no. 2, pp. 359–393, Apr. 1959.
[30] B. R. Sunil and M. Jagannatham, "Producing hydroxyapatite from fish bones by heat treatment," *Mater. Lett.*, vol. 185, no. August, pp. 411–414, 2016.
[31] I. R. Gibson and W. Bonfield, "Preparation and characterization of magnesium/carbonate co-substituted hydroxyapatites," *J. Mater. Sci. Mater. Med.*, vol. 13, no. 7, pp. 685–693, 2002.
[32] M. ?ari?, M. Piasek, M. Blanu?a, K. Kostial, and J. Z. Ilich, "Sodium and calcium intakes and bone mass in rats revisited," *Nutrition*, vol. 21, no. 5, pp. 609–614, May 2005.
[33] R. K. Rude and H. E. Gruber, "Magnesium deficiency and osteoporosis: animal and human observations," *J. Nutr. Biochem.*, vol. 15, no. 12, pp. 710–716, Dec. 2004.
[34] P. Ammann, "Strontium ranelate: A physiological approach for an improved bone quality," *Bone*, vol. 38, no. 2, pp. 15–18, Feb. 2006.

Influence of Oven-Drying temperature on the antioxidant activity of betel leave

Ginisha a/p Ashok[1*], Chua Bee Lin[2]

[1,2]*School of Engineering, Taylor's University*

[*]*ginisha027@hotmail.com*

Abstract

The *Piper betle* Linn, or more commonly know as *Sirih Melayu* by the locals, is part of the Piperacea family of the vast types of betel leaves vines available in the forests of Malaysia. The main purpose of this research is to study the effect of drying kinetics of betel leave by obtaining high antioxidants of betel leave and the best drying model of betel leave. The betel leave is dried by using an over dryer at temperature varying from 40^{o}C to 80^{o}C at 10^{o}C intervals. Next, the extraction process is carried out at temperature 40^{o}C where other parameters are the extraction time, ultrasound power and ratio of betel leave are at 60 minutes, 70W and 1:20 ratio respectively. The results obtain indicates that temperature is higher than shorter drying period is needed. The antioxidants extracted from the betel leave has a yield of 93% at 50^{o}C. Five different drying model were used to study the drying process, which includes Where Logarithmic Model, Page's Model, Henderson and Pabris Model, Two term model and Lewis's Model. These models were used in order to obtain the best model or the closest mathematical model that compliments the experimental data.

Keywords: Betel Leave, Drying Kinetics, Mathematical modelling, Antioxidant

1. Introduction

The herbal industry in Malaysia has been identified as a new foundation in expanding the economic growth of the country under economic transformation programme (ETP) which begun in early months of 2011 [1]. First few purpose of herbs includes medicinal purposes, where medicines can be found from numerous parts of the plant such as the seeds, roots, leaves or even flowers. Healthcare system based on herbs were developed thousands of years ago, through the Ayurveda medications and as well as the Traditional Chinese Medications [1]. Based on the estimation obtained from the World Health Organization (WHO), an average of 80% citizens worldwide depend on herbal medications predominantly for their daily health well-being.

Herbal products are frequently contrived by extracting bioactive essence from the existing medicinal plants. In order to obtain the bioactive extract several process was involved such as drying, solid-liquid extraction and as well as drying of the extract. Drying process is mainly known to remove moisture and it is normally known as the dehydration process as it involves in the removal of moisture [2]. Normally drying process incorporates heat on the raw material and this may be the essence of the reduction in moisture content or even the loss in quality. Phytochemicals adds to the constructive activity of medicinal plants. Hence, the main aspect that needs to be taken into consideration in the process of drying is to shorten the drying period while maintaining the active phytochemicals [2].

Antioxidant activity is generally defining as the capabilities of a substance to deactivate free activists which may cause various other diseases specifically human diseases. It protects human from diseases that causes death such as cancerous disease, Parkinson's and cardiovascular disease [3]. Besides that, the method used in this research is generally the DPPH assay method where it is used in the *in vitro* system for the purpose of evaluation where else the LPO is normally found in the *in vivo* antioxidant assay. Then, the solvent used for the purpose of has high frequency where ethanol is the most suitable stated by Choudhary & Kale (2002) [4].

Solid- liquid extraction (SLE) is acknowledged as a method to separate the medicinally active portion from the plant tissues using solvents such as ethanol or even water. The extract acquires consist of valuable ingredients of the experimented plant. These techniques include ultrasound-assisted or microware-assisted extraction, batch SLE, supercritical fluid and accelerated solvent extraction. Because of its low operation and as well as low capital cost therefore Batch SLE is the most appropriate or commonly used technique [5].

The herbal products that are produced varies in terms of usage namely, these bioactive essence extracts are being applied in herbal medicines, nutritional supplement and cosmetic products [1]. These products have seen a progress in sales is due to consumers particularly being aware of its medicinal possessions, providing safety declaration in usage, not forgetting that it is a relatively a reasonable alternative to its counterpart, the modern pharmaceuticals [5].

The objective of this research to determine the influence of different oven-drying temperature from 40^{o}C to 80^{o}C with 10^{o}C interval on the antioxidant activity of Betel Leaves using 1,2-diphenyl-2-picrylhydrazyl (DPPH) assay and to select the best

drying kinetic model with highest Coefficient determination (R^2) that represents the drying process of Betel Leaves based on the temperature that gives the highest antioxidant activity.

2. Methodology

2.1 Chemical Reagents

Ethanol (99.8% AR grade), 2, 2-Diphenyl-1-Picrylhydrazyl (DPPH), Fast Blue BB reagent and Gallic acid

2.2 Drying and Extraction of betel leave

The process starts with the drying process of betel leave using an Oven-dryer. The drying oven comprises of a temperature controller and a suction fan where the temperature and the speed of the fan can be adjusted accordingly but the main focus in this research is the temperature of the drying process. Hence during the experiment, the speed of the suction fan was adjusted to this maximum at all time. Under various temperature, the experimental leave was set to dehydrate. The temperature chosen includes a range from 40^{o}C to 80^{o}C with 10^{o}C interval [6]. The drying process carries on until there is no change in weight of the betel leave. Using an electronic balance, weight loss of the betel leave with the was measured with 10 minutes of interval. The ambient air temperature is said to be between 26 to 28^{o}C and the relative humidity is between 80 to 88% Wt% [6].

In the initial stage, the moisture content of the betel leave was determined using a moisture analyser. Followed by grounding of the dried betel leave which can be done using a cutting mill and the next process includes sonication of the mixture where 2g of betel leave is well mixed with 40ml of Ethanol of a ratio of 1g:20ml and an Ultrasonic bath (Elmasonic Model P120H, Singen, Germany) is used to prompt up the extraction process of the phytochemical [7].

This process is carried out within a timeframe of 90 minutes with temperature at 40^{o}C using an input power of 70 W and frequency of 37kHz [7]. The sample obtained after sonication, were then filtered using Whatman filter paper no.1 in a rotary flask in order to obtain supernatants of the sample. The filtrate was then dried in the rotary vacuum evaporator (Heidolph Model Hei-VAP Precision (HL), Schwabach, Germany) in order to remove the ethanol content at a bath temperature of 55^{o}C and cooling temperature 15^{o}C and the obtained vacuum pressure at approximately 253 mbar [7].

2.3 Antioxidant assay of betel leave using DPPH Radical Scavenging Capacity

The antioxidant activity of betel leave was using DPPH solution. 1mg of extract was reacted with 2ml of 80% ethanol [8]. Next, 2mg of DPPH was reacted with 5ml of 80% methanol and this solution were prepared in a schott bottle wrapped with aluminium foil in order to reduce the light exposure. The reaction mixture was placed in the ultrasound bath for 5 minutes to complete the reaction. Add 160µL of extract and 40µL of DPPH into a microplate and kept to settle for 3 minutes. The prepared sample were measured under an absorbance value of 520nm [8]. The test were done triplicate in order to reduce any offset. The equation used to calculate the scavenging activity:

$$\text{Scavenging activity } (\%) = [\frac{A_{sample}}{A_{control}}] \times 100\% \quad (1)$$

Therefore, $A_{control}$ is he absorbance of the DPPH solution at 0 minutes and A_{sample} is the absorbance of the sample [9].

2.4 Mathematical modelling of Drying of the Betel leave

Based on this research, five mathematical models were used to evaluate the drying process. Where Logarithmic Model, Page's Model, Henderson and Pabris Model, Two term model and Lewis's Model. These models were used in order to obtain the best model or the closest mathematical model that compliments the experimental data.

Table 2.4.1: Thin layer models for mathematical modelling

Model	Model name	Reference
$MR=\exp(-kt)$	Lewis	[10]
$MR=\exp(kt^n)$	Page	[10]
$MR=a\exp(-kt)$	Henderson and Pabris	[10]
$MR=a\exp(-kt)+c$	Logarithmic	[10]
$MR=a\exp(-k_0t)+b\exp(-k_1t)$	Two term	[10]
$MR=(1-(1-L_2)L_1t)^{(1/(1-L_2))}$	Chavez-Mendez	[10] [11]
$MR=a\exp(-(kt^n))+bt$	Midilli & Kucuk	[10] [11]

Where: t is the drying time where else a,c, k and n are the drying constants

2.5 Gallic Acid calibration curve

Gallic acid stock solution was prepared in a range of 20 to 500 mg/ml in deionizer water in a borosilicate tube. 100µL of Fast Blue BB reagent were added into all Gallic acid standard tubes and left to settle for 1 minute [12]. Next, 100µL of 5% NaOH was added. The reaction were allowed to settle for 90 minutes. Then, 200µL of the mixture were transferred to a microplate and the optical density used to measure was 420nm [12]. Lastly, the Gallic acid concentrations were then plotted against the density.

2.6 Analysis of Betel leave using Fast Blue BB reagent

1mg of extract were added to 1ml of 80% ethanol. 100µL of Fast Blue BB reagent were added into all extract tubes and left to settle for 1 minute. Next, 100µL of 5% NaOH was added [12]. The reaction were allowed to settle for 90 minutes. Then, 200µL of the mixture were transferred to a microplate and the optical density used to measure was 420nm [12].

2.7 Analysis using R^2 and RSME

Each experimental data was conducted triplicate and the results were shown based on the form of mean ± standard deviation. The values were calculated using a Microsoft Excel Solver 2016. The parameters that were used to validate the experimental data are the coefficient determination (R^2), root mean square error (RMSE) and as well as reduced chi-square (x^2). The coefficient determination which is the R^2 are normally used to determine the closeness of the experimental data to the fitted regression line. Formula are as below:

$$R^2 = 1 - \frac{\sum_{i=1}^{n}(C_{exp,i} - C_{pre,i})^2}{\sum_{i=1}^{n}(C_{exp,i} - \overline{C})^2} \quad (2)$$

$C_{exp,i}\ and\ C_{Pre,i}$ are experimental and predicted value of betel leave and $\bar{C}$ is the experimental data mean value.

Root mean square error (RSME) is another method used to evaluate the validation of the experimental data by comparing it with a model as shown in equation below:

$$RMSE = \sqrt{\frac{1}{N}\sum_{i=1}^{N}(C_{pre,i} - C_{exp,i})^2} \quad (3)$$

$C_{exp,i}\ and\ C_{Pre,i}$ are experimental and predicted value of betel leave and N is number of observations.

Where else, the Reduced Chi-square (x^2) is another method used as a comparison based on equation below:

$$x^2 = \sum \frac{(C_{exp,i} - C_{Pre,i})^2}{N - n} \quad (4)$$

$C_{exp,i}\ and\ C_{Pre,i}$ are experimental and predicted value of betel leave, n is the number of constants and N is number of observations.

3.Results and Discussion

3.1 Drying kinetics and mathematical modelling

The equilibrium moisture content was achieved when there was no change in the weight of the sample. The time needed to reach this equilibrium point differs based on the temperature. At temperature 40, 50, 60, 70 and 80 the betel leaves took respectively to reach equilibrium. This results shows that if the temperature is higher then shorter drying period is needed. When the drying temperature speeds up the drying process then the will be an increase in the rate of drying. Based on the observation done, the drying process took place in the falling rate period and short constant rate period were observed in the middle of the drying process and this has been similar observe in the drying rate of spinach by Doymaz in 2009.

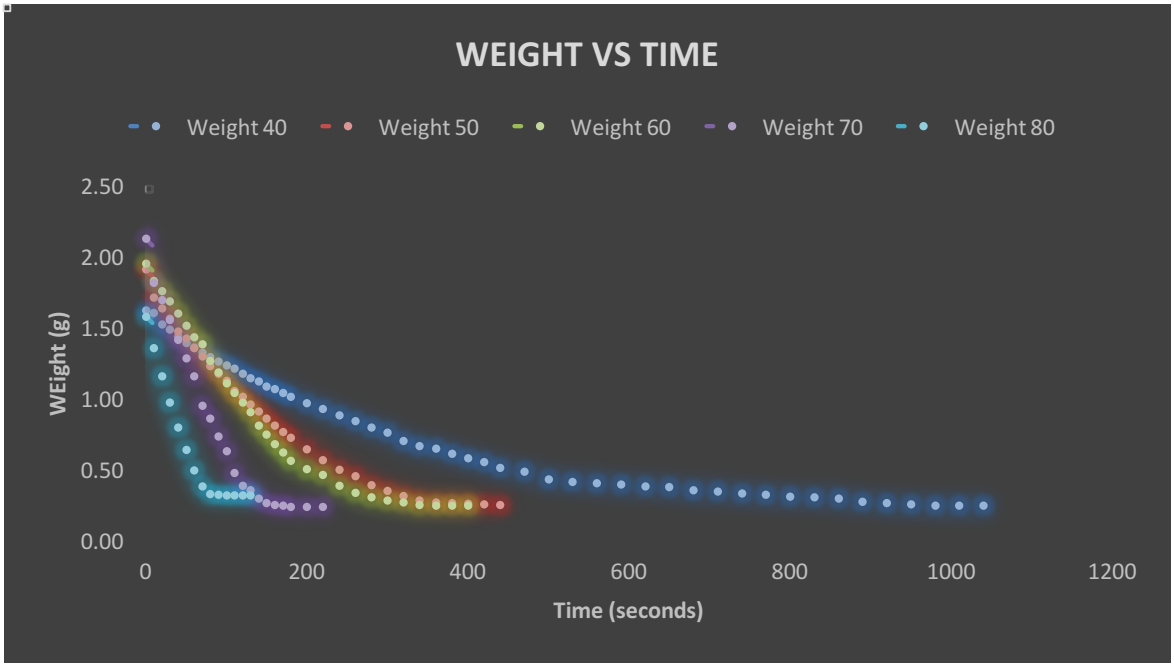


Figure 3.1: shows the drying weight against time at various temperature (40^{o}C, 50 ^{o}C, 60 ^{o}C, 70 ^{o}C and 80 ^{o}C)

Figure 3.1 proves the statement above where as the temperature increases, shorter drying period is needed. Therefore, high temperature has higher drying rate.

3.2 Fitting in the Drying Models for Betel Leave

The study of the drying kinetic models of the betel leave were carried out at drying temperature of 50^{o}C due to its high antioxidant activity. There are seven drying kinetic models that were chosen to study the behavior of the drying of betel leave as shows below.

3.2.1 Lewis model of betel leave

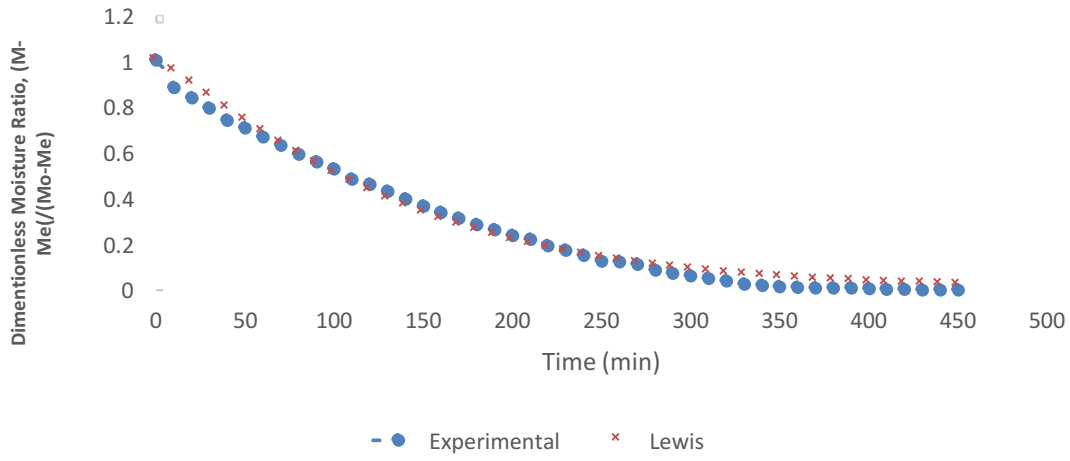


Figure 3.2.1: Curve Fitting for Lewis Model

Table 3.2.1: Optimum value for Lewis model

Model Name	Model	k	n	R^2	X^2	RMSE
Lewis	MR=exp(-kt)	0.003	1	0.98901	0.00095	0.03016

Table 4.2.1 shows the optimum value of the Lewis model constants which the corresponding value that includes the R^2, X^2 and RMSE values. The mass transfer coefficient value obtained is 0.003 min^{-1} which were determined using Microsoft Excel SOLVER. Besides that, the R^2 value obtained were approximately around 0.989 and the RMSE and X^2 are 0.03016 and 0.00095 respectively which shows that the results obtained were reliable.

3.2.2 Page Model for Betel leave

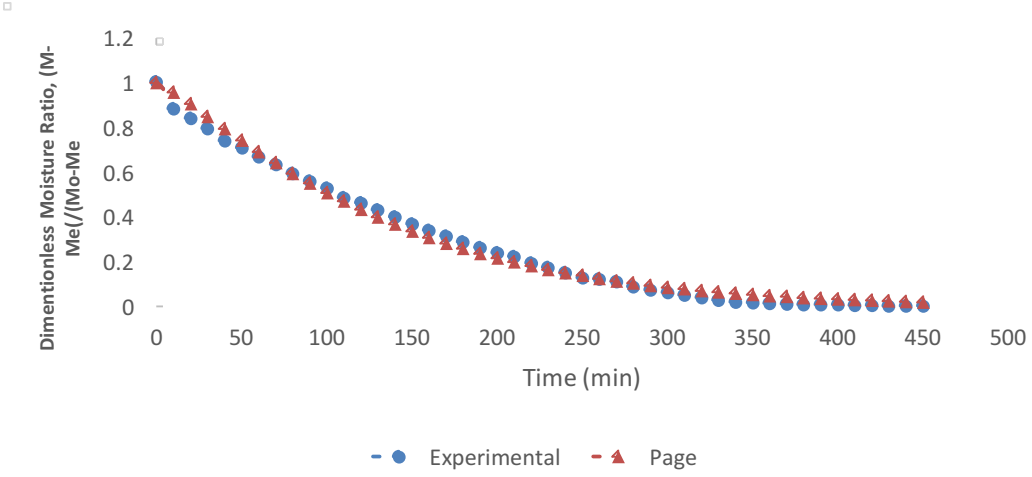


Figure 3.2.2: Curve Fitting for Page Model

Table 3.2.2: Optimum value for Page Model

Model Name	Model	k	n	R^2	X^2	RMSE
Page	$MR=\exp(kt^n)$	0.003	1.176	0.98901688	0.00095113	0.0301624

Table 3.2.2 shows the optimum value of the Page model constants which the corresponding value that includes the R^2, X^2 and RMSE values. The mass transfer coefficient value obtained is 0.003 min^{-1} which were similar to the Lewis model which were determined using Microsoft Excel SOLVER and n is the exponent and the value obtained is 1.176. Besides that, the R^2 value obtained were approximately around 0.989 and the RMSE and X^2 are 0.03016 and 0.00095 respectively which shows that the results obtained were reliable and highly similar to the Lewis Model.

3.2.3 Henderson & Pabis Model for Betel leave

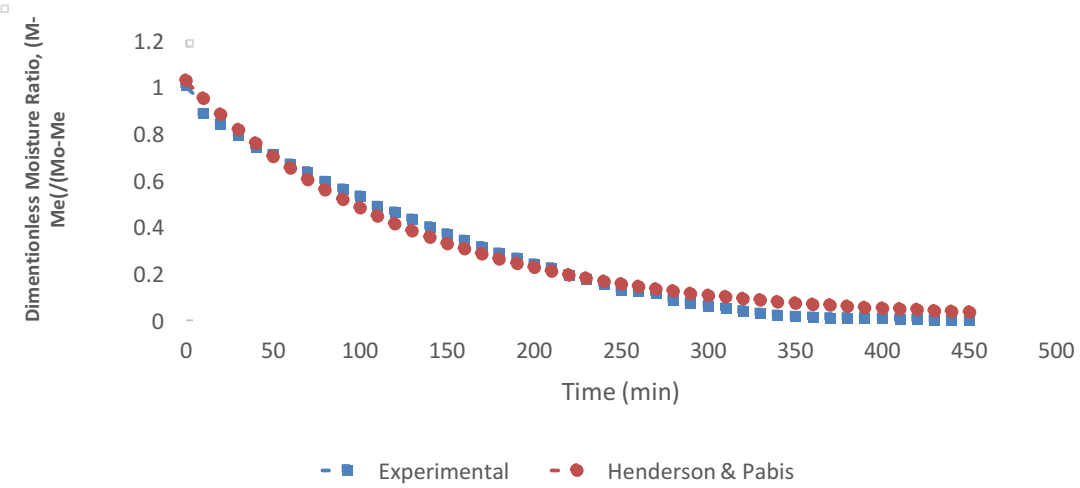


Figure 3.2.3: Curve Fitting for Henderson & Pabis Model

Table 3.2.3: Optimum value for Henderson & Pabis Model

Model Name	Model	k	a	R^2	X^2	RMSE
Henderson and Pabis	$MR=a\exp(-kt)$	0.0076	1.0239	0.981672929	0.0015871	0.0389628

Table 3.2.3 shows the optimum value of the Henderson and Pabis model constants which the corresponding value that includes the R^2, X^2 and RMSE values. The mass transfer coefficient value obtained is 0.0076 min^{-1} which were determined using Microsoft Excel SOLVER and a is the coefficient value which is 1.0239. Besides that, the R^2 value obtained were approximately around 0.9816 and the RMSE and X^2 are 0.0389 and 0.00158 respectively which shows that the results obtained were reliable. Based on the peppermint leave, the mass transfer coefficient value obtained is 0.0102 and coefficient a value of 1.015 which were closely related to the value obtained from the Henderson and Pabis model for betel leave.

3.2.4 Logarithmic Model for Betel Leave

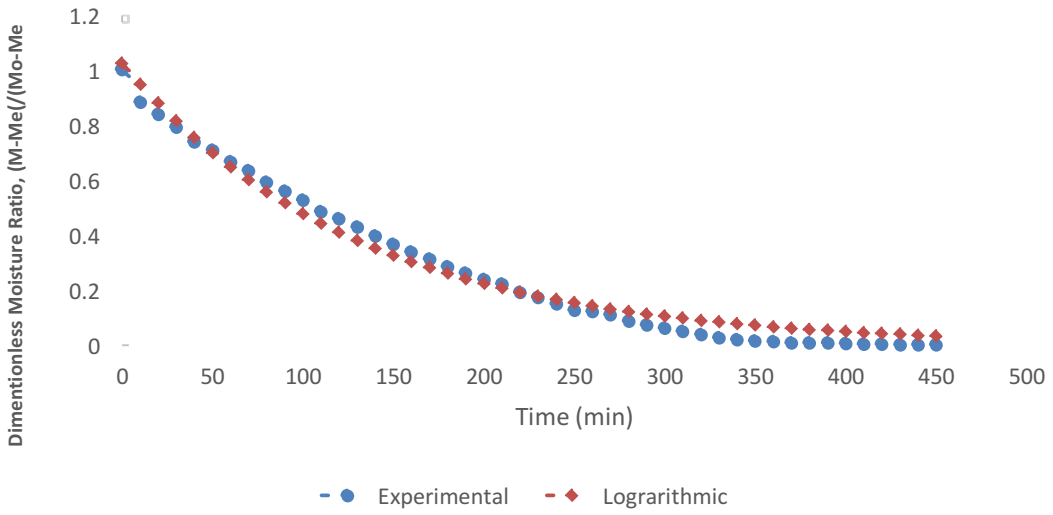


Figure 3.2.4: Curve Fitting for Logarithmic Model

Table 3.2.4: Optimum value for Logarithmic Model

Model Name	Model	k	a	c	R^2	X^2	RMSE
Logarithmic	MR=a exp(-kt)+ c	0.0076	1.0239	0.00	0.981672929	0.0015871	0.0389628

Table 4.2.4 shows the optimum value of the Logarithmic model constants which the corresponding value that includes the R^2, X^2 and RMSE values. The mass transfer coefficient value obtained is 0.0076 min^{-1} which were determined using Microsoft Excel SOLVER and a is the coefficient value which is 1.0239 and the c coefficient value is 0.00, therefore the value obtained for the mass transfer coefficient were similar as the Henderson & Pabis model. Besides that, the R^2 value obtained were approximately around 0.9816 and the RMSE and X^2 are 0.0389 and 0.00158 respectively which shows that the results obtained were reliable. Based on research done on fresh bay leave, the coefficient a obtained is 1.038 and the c coefficient is -0.019, which is close to the value obtained from the Logarithmic model of betel leave.

3.2.5 Two term Model for Betel Leave

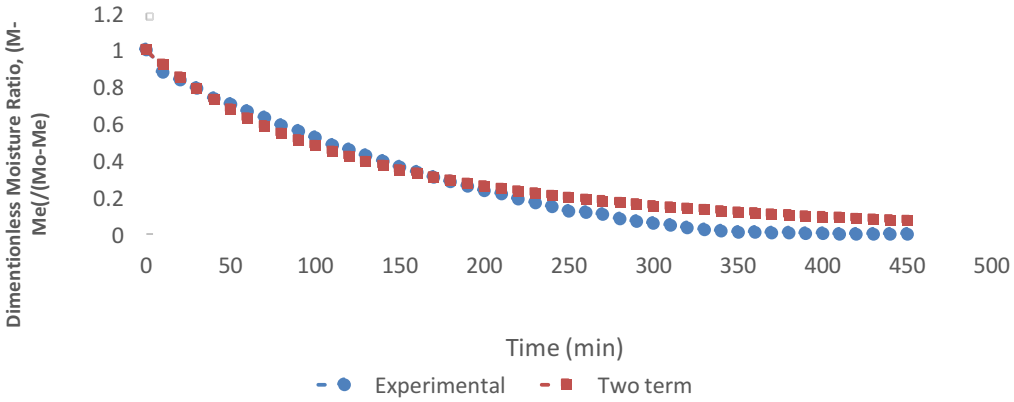


Figure 3.2.5: Curve Fitting for Two term Model

Table 3.2.5: Optimum value for Two term Model

Model Name	Model	k_0	k_1	a	b	R^2	X^2	RMSE
Two term	MR=a exp(-k_ot)+b exp(-k_1t)	0.00462	0.0134	0.5902	0.4118	0.946513221	0.00463189	0.0665621

The R^2 value obtained were approximately around 0.9465 and the RMSE and X^2 are 0.0665 and 0.0046 respectively which shows that the results obtained were less reliable in comparison to other drying models as it has the lowest coefficient correlation value.

3.2.6 Chavez-Mendez Model for Betel Leave

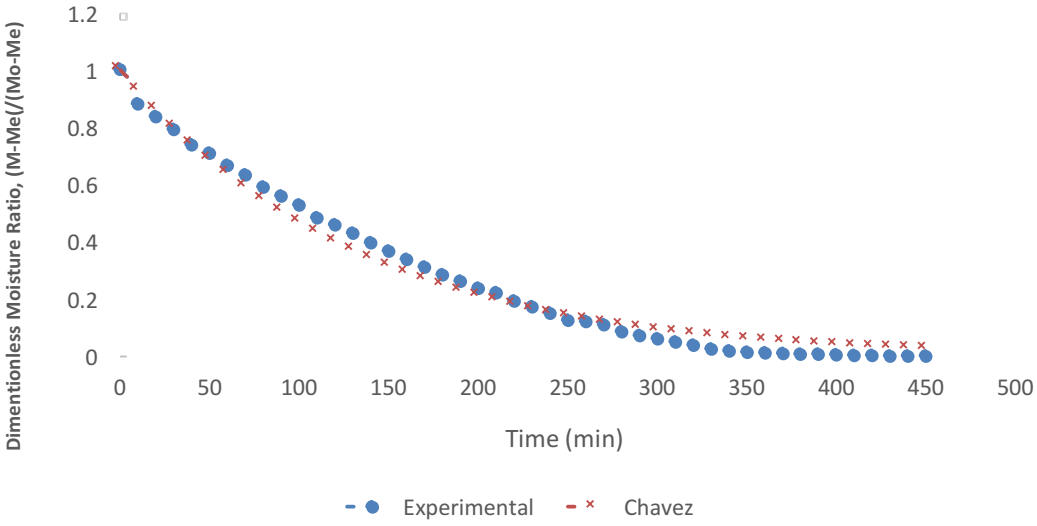


Figure 3.2.6: Curve Fitting for Chavez-Mendez Model

Table 3.2.6: Optimum value for Chavez-Mendez Model

Model Name	Model	L_1	L_2	R^2	x^2	RMSE
Chavez-Mendez	MR= (1-(1-L_2)L_1t)(1/(1-L_2))	0.00738994	0.92313419	0.984481403	0.001343893	0.035853347

Table 3.2.6 shows the optimum value of the Chavez-Mendez model constants which the corresponding value that includes the R^2, X^2 and RMSE values. The mass transfer coefficient value obtained is 0.0076 min^{-1} which were determined using Microsoft Excel SOLVER and a is the coefficient value which is 1.0239 and the c coefficient value is 0.00. Besides that, the R^2 value obtained were approximately around 0.984 and the RMSE and X^2 are 0.0358 and 0.00134 respectively which shows that the results obtained were reliable.

3.2.7 Midilli & Kucuk Model for Betel Leave

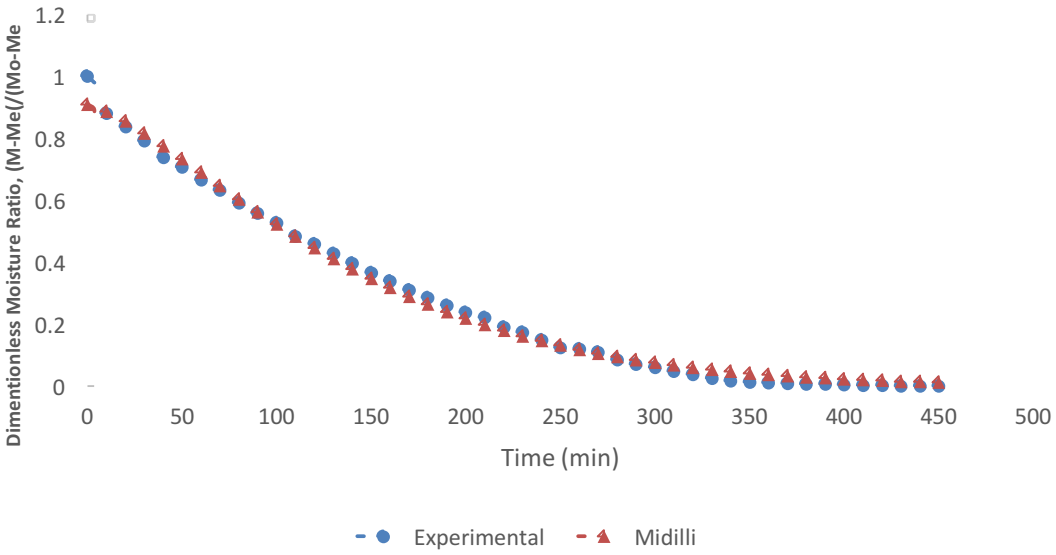


Figure 3.2.7: Curve Fitting for Midilli & Kucuk Model

Table 3.2.7 Optimum value for Midilli & Kucuk Model

Model Name	Model	k	n	a	b	R^2	X^2	RMSE
Midilli & Kucuk	MR=aexp(-(kt^n)) + bt	0.00102	1.3659	0.91008	0	0.993576369	0.000556279	0.023067141

Table 3.2.7 shows the optimum value of the Midilli & Kucuk model constants which the corresponding value that includes the R^2, X^2 and RMSE values. The mass transfer coefficient value obtained is 0.00102 min^{-1} which were determined using Microsoft Excel SOLVER and a is the coefficient value which is 0.910, the exponent n value of 1.365 and the b coefficient value is 0.00. Besides that, the R^2 value obtained

were approximately around 0.993 and the RMSE and X^2 are 0.02306 and 0.00055 respectively which shows that the results obtained were the most reliable as it has the highest coefficient correlation value.

Table 3.2.8: Drying Thin layer model

Model Name	Model	R^2	x^2	RMSE
Lewis	MR=exp(-kt)	0.9890169	0.0009511	0.0301624
Page	MR=exp(kt^n)	0.9890169	0.0009511	0.0301624
Henderson and Pabris	MR=a exp(-kt)	0.9816729	0.0015871	0.0389628
Logarithmic	MR=a exp(-kt)+ c	0.9816729	0.0015871	0.0389628
Two term	MR=a exp($-k_0t$)+b exp($-k_1t$)	0.9465132	0.0046319	0.0665621
Chavez-Mendez	MR= $(1-(1-L_2)L_1t)^{(1/(1-L_2))}$	0.9844814	0.0013439	0.0358533
Midilli & Kucuk	MR=aexp(-(kt^n)) + bt	0.9935764	0.0005563	0.0230671

By using SOLVER in Microsoft Excel 2016, the parameters of all the thin layer model were solved based on all the model listed in Table 16. The R^2 values calculated were all above 0.99 and RMSE value were below 0.02 and hence this shows that the selected model fits well with the experimental data. Drying temperature of 50^{o}C were selected to be evaluated is due to its high DPPH radial scavenging activity. By evaluating the R^2 and the RMSE values, the Midilli & Kucuk shows the most suitable model to fit the drying kinetics for temperature 50^{o}C. The plot of experimental data the best-fitted model was shown by the Midilli & Kucuk model. The variation in value between the most suitable model and as well as the least suitable model are approximately 3.5%. Therefore, Midilli & Kucuk were are appropriate for this drying process due to the R^2 value were closest to unity.

3.3 Effects of Temperature on the DPPH Radial Scavenging Activities

DPPH radial method were commonly used in order to estimate the free radial scavenging activities where the DPPH reagents changes color from purple to yellow and the change of color shows the impending of free radical scavenging of the sample antioxidants. Table 3.2.1 shows the results obtained from temperatures 40^{o}C to 80^{o}C of the percentage of radical scavenging activity.

Table 3.3.1: Shows the Percentage of Radial Scavenging activity

Temperature (^{o}C)	Radical Scavenging activity (%)
40	90.31 ± 0.17
50	93.22± 0.21
60	92.87± 0.17
70	92.53± 0.23
80	91.61± 0.19

The DPPH radical scavenging activities of the antioxidant of betel leave increases when the drying temperature increased from 40 to 50. This may be due to the increased in solubility and the diffusion coefficient of antioxidant compounds in the betel leave. From temperature 50°C to 80°C, a further decrease was observed in the DPPH radical scavenging activities which may cause by the thermo-sensitivity of the betel leave compound and therefore it reduces its activities at higher temperature. Based on Table 3.3.1, drying temperature 50°C provides the highest DPPH radical scavenging activities which is at 93.22% for betel leave. The absorbance used to measure the sample radical scavenging activity were as low as 0.052nm. The low absorbance used were mainly because of the high radical scavenging by the hydrogen donation.

3.4 Total phenolic content using Fast Blue BB reagent

The total phenolic content was determine using a microplate reader and Fast Blue BB reagent. Gallic acid calibration curve was used as a reference standard with different concentration and absorbance value as per Figure 3.3.1.

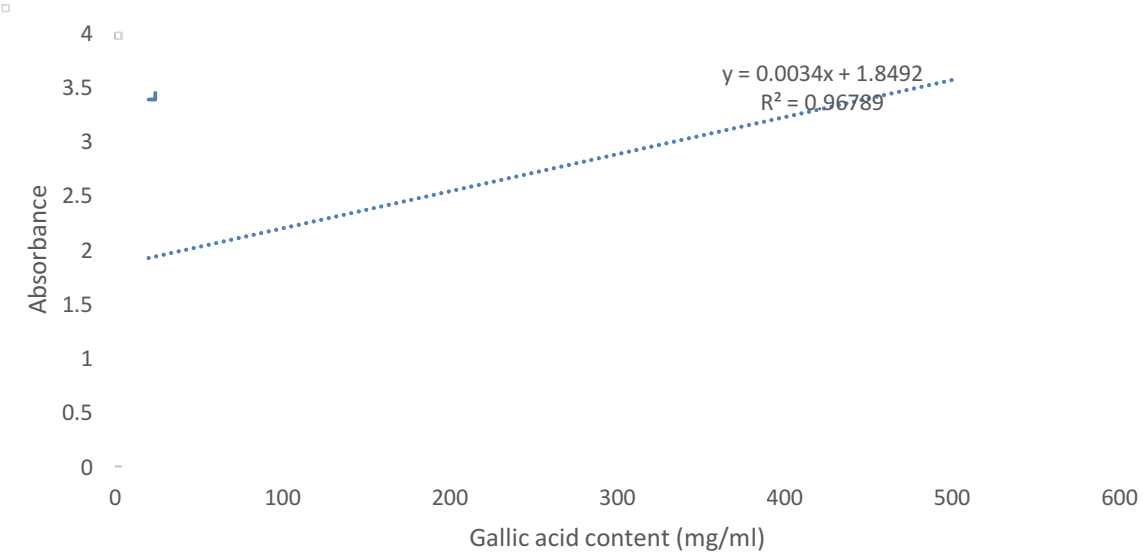


Figure 3.4.1: Gallic acid standard curve

The relationship of the absorbance as well as the concentration of the Gallic acid (mg/ml) were expressed in terms of the equation Y= 0.0034x + 1.8492. The Gallic acid calibration curve were used to determine the total phenolic content.

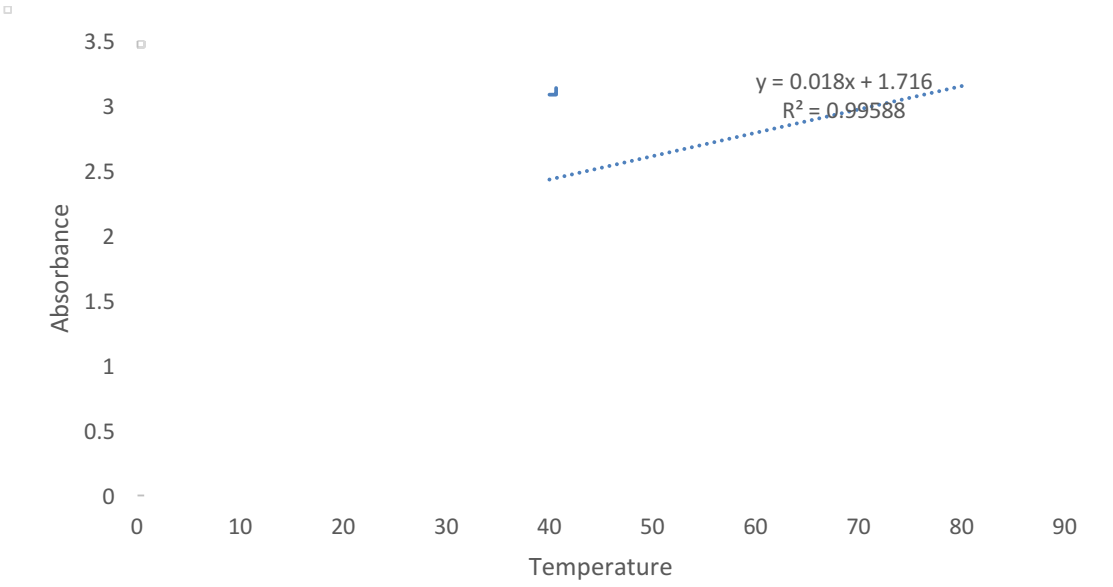


Figure 3.4.2: Experimental value using FBBB reagent to determine the total phenolic content

Figure 3.4.2 shows that as the temperature increases, the absorbance value rises which directly relates to the Gallic acid calibration curve. The R^2 value obtained from this calibration curve using the FBBB reagent is approximately 0.99 which is close to unity. The FBBB reaction with substrate Gallic acid were highly linear.

Table 3.4.1: Shows the concentration obtain from the experimental data using the Gallic acid calibration equation

Temperature	Absorbance	Concentration (mg/ml)
40	2.416	166.7
50	2.632	230.23
60	2.792	277.29
70	2.991	335.82
80	3.134	374.94

Table 3.4.1 shows that, higher absorbance value obtains higher concentration based on the calibration standard of Gallic acid. FBBB reagent directly detects the phenolic substances and therefore its proven to be more accurate in terms of measuring the total phenolic concentration.

Phenolic compounds are usually very effective antioxidants, due to its protective behavior, which again adds an advantage to its ability in scavenging free radicals. Free radicals are known as harmful components if its exist in an exposed or unprotected body. Phenols usually produces toxic compounds and undergoes oxidation, which stimulates inhibitory properties on pathogenic microorganisms.

Extract that has high antioxidant activity and high phenolic content shows high a-amylase inhibitory activity at diverse dilutions [21]. Increase of the dilution of the extract directly increases the activity of the a-amylase inhibitor. Where it indicates that,

high concentration of the phenolic compounds would have higher activity of the a-amylase inhibitor [21]. Therefore, if less phenolic compounds were introduced, then the decrease of the a-amylase inhibitory activity can be observed.

Nevertheless, methanol as well as ethanol were used in this process as it controls the uptake of glucose which then relates to hyperglycemia [21]. Based on studies done, it can be seen that the in vitro analysis perform shows additional awareness in the inhibitory properties of the significant enzymes which directly relates to hyperglycemia and type 2 diabetes [21]. Where, these effects related to diabetes can be credited to the antioxidant activity as well as the total phenolic content of the medicinal herbs or plants. Based on research done, it can be seen that 80^{o}C shows the highest total phenolic content concentration and therefore exhibits high a-amylase inhibitory activity [21].

4.0 Conclusions

This research was done in order to investigate the effect of temperature on the quality and drying kinetics of betel leave. The antioxidants of betel leave have higher yield at drying temperature of 50. This results shows that as the temperature increases the yield of the antioxidants increases but when the temperature reaches 60 here is a decrease in the yield of the antioxidants this is due to the degradation of the betel leave due to the high drying temperature. Therefore, most of the antioxidants has approximately similar results hence it can be concluded that betel leave is a good source of producing antioxidants.

In order, to study the effect of temperature on the drying of betel leave, mathematical modelling was used. Where Logarithmic Model, Page's Model, Henderson and Pabris Model, Two term model and Lewis's Model were used to fit the experimental data. Based on the value calculated, Logarithmic and as well as the Henderson & Pabris were are appropriate for this drying process due to the R^2 value were closest to unity.

Based on the Fast Blue BB analysis, as the temperature increases, the absorbance value rises which directly relates to the Gallic acid calibration curve. The R^2 value obtained from this calibration curve using the FBBB reagent is approximately 0.99 which is close to unity. Higher absorbance value obtains higher concentration based on the calibration standard of Gallic acid.

Reference

[1] "Medical plant conference", *Soci* by Frank Waimer, [Online], Available: http://www.soci.org/~/media/Files/Conference%20Downloads/2011/Medicinal%20Plants%20Mar%2011/Frank_Waimer.ashx [Accessed: 17 Sept 2016]
[2] World Health Organization (2000). General guidelines for methodologies on research and evaluation of traditional medicine. Geneva, World Health Organization.
[3] Nouri, L., Naftchi, A.M and Karim, A.A (2014) Phytochemical, antioxidant, antibacterial, and a-amylase inhibitory properties of different extracts from betel leaves. Industrial Crops and Products 62(10) page 47-52
[4] Ramlan, A.Z., Mohamad Roji, S., Sulaiman, N., and Sivakumar, K. (2000). Processing of herbs and herbal products. In: *Proceedings of the Seminar on Medicinal*

*Plant*s 12-13 September 2000 edited by Chang, Y.S., Mastura, M., Vimala, S. & Zainon, A.S. pp. 1–8. Kepong: Forest Research Institute Malaysia (FRIM)
[5] Wang, L. & Weller, C.L. (2006). Recent advances in extraction of nutraceuticals from plants. *Trends in Food Science & Technology* 17: 300–312
[6] PIN, K.Y. et al. "SOLID-LIQUID EXTRACTION OF BETEL LEAVES (PIPER BETLE L.)". *Journal of Food Process Engineering* 34.3 (2009): 549-565.
[7] J. W. LI, S. DONG DING, AND X. L. DING, "OPTIMIZATION OF THE ULTRASONICALLY ASSISTED EXTRACTION OF POLYSACCHARIDES FROM ZIZYPHUS JUJUBA CV. JINSIXIAOZAO," J. FOOD ENG., VOL. 8
[8] Djeridane, A. et al. "Antioxidant Activity Of Some Algerian Medicinal Plants Extracts Containing Phenolic Compounds". *Food Chemistry* 97.4 (2006): 654-660.
[9] Dasgupta, N., and De, N. (2004). Antioxidant activity of Piper betle L. leaf extract in vitro. Food Chemistry 88: 219–224.
[10] Ozdemir, M. A., and Onur Devres, Y. (1999). The thin layer drying characteristics of hazenults during roasting. Journal of Food Engineering 42: 225–233.
[11] Yaldiz, O., and Ertekin, C. (2001a). Thin layer solar drying of some vegetables. Drying Technology 19: 583 – 597.
[12] Medina, M.B., 2011a. Simple and rapid method for the analysis of phenolic compounds in beverages and grains. Journal of Agricultural and Food Chemistry 59, 1565–1571.
[13] Medina, M.B., 2011b. Determination of the total phenolics in juices and superfruits by a novel chemical method. Journal of Functional Foods 3, 79–87
[14] Slinkard, K., Singleton, V.L., 1977. Total phenol analysis: automation and comparison with manual methods. American Journal of Enology and Viticulture 28, 49– 55.
[15] By Novel Chemical Method". *Journal of Functional Foods* 3.2 (2011): 79-87
[16] Yaldiz, O., Ertekin, C., and Uzun, H.I (2001b). Mathematical modeling of thin layer solar drying of sultana grapes. Energy 26: 457– 465.
[17] Vimala,S., Mohd Ilham, A., Abdul Rashid, A., and Rohana, S. (2003) Nature's Choice to Wellness: Antioxidant Vegetables/Ulam. Kuala Lumpur: Forest Research Institute Malaysia (FRIM).
[18] Nalina, T., and Rahim, Z.H.A. (2007). The crude aqueous extract of Piper betle L. and its antibacterial effect towards *Streptococcus mutans*. *American Journal of Biotechnology and Biochemistry* 3(1): 10-15.
[19] Dr G. Palaniappa., Dr A. Sengottiyan., T. Sarvanan. (2012). Betel leaf: The green gold of India.
[20] Parmar, V.S., Jain, S.C., Bisht, K.S., Jain, R., Taneja, P., Jha, A., Tyagi, O.D., Prasad, A.K., Wengel, J., Olsen, C.E., and Boll, P.M. (1997). Phytochemistry of the genus *Piper*. *Phytochemistry* 44(4): 597-673.
[21] Nouri, Leila, Abdorreza Mohammadi Nafchi, and A.A. Karim. "Phytochemical, Antioxidant, Antibacterial, And A-Amylase Inhibitory Properties Of Different Extracts From Betel Leaves". *Industrial Crops and Products* 62 (2014): 47-52

Wastewater De-Fluoridation Using Traditional Coagulation

Goh Zhen Jie[1], Chong Chien Hwa[2], Rajesh Nithyanandam[3], Winston Lim[4], Nicholas Ong Tze Kai[5], Nurasatifah binti Kahar[6], & Hew Wee Seong[7].

[1]zhenjie.goh@sd.taylors.edu.my

Abstract
Excessive fluoride intake in human body causes dental and skeleton problems, and soft tissue disease especially fluorosis. Through establishing the fact that no proven treatment for fluorosis disease is presence up to date, prevention serves as the best approach by ensuring wastewater effluent from industries always meet the standard. This research aims to achieve final fluoride concentration of 5.0 ppm (standard B) through studying the effect of coagulant dosage, coagulant type, pH effect after de-fluoridation, and improvement of fluoride removal efficiency using fibrous thin film by coagulation. This study was done using poly-aluminium chloride (PAC) and mixture of sodium aluminate (SA) with sodium hydroxide (NaOH) as chemical coagulant and *Moringa oleifera* with *Okra mucilage* as natural coagulants to treat 100 ppm of synthetic wastewater sample as benchmark at respective studied condition. It proved that increasing coagulant dosage enhances de-fluoridation performance but in reducing rate due to inhibition of aluminium-fluoride formation. 85.9 % of de-fluoridation efficiency was achieved using 3 g/L of PAC with mixture of SA with NaOH by coagulation at optimum pH of 7. 65.8 % of de-fluoridation efficiency was achieved using 2.5g of ground *M. oleifera* in micro- size due to elevated contact area and natural coagulant characteristic. pH was increased from 2.86 ± 0.04 to 3.15 ± 0.41 and 4.5 ± 0.26 to 6.3 ± 0.53 for *M. oleifera* and *Okra mucilage* respectively due to elevated OH^- ions released after coagulation and vice versa to chemical coagulant due to elevated acidity by Al composition increased. 85.3 % of aluminium removal rate was achieved using 2.5g of ground Okra seeds in micro-size. With the presence of fibrous thin film, de-fluoridation performance has dropped from 65.8 % to 42.6% using 2.5 g of blended *M. oleifera* which might due to the inconsistency of pore sizes at surface of fibrous thin film. Statistical analysis using ANOVA one-way test showed p value of 5.53×10^{-12} ($p < 0.05$) which concluded coagulant dosage provides significant effect on de-fluoridation performance.

Keywords: De-fluoridation, Coagulant, Fluoride, pH, and Concentration.

1.0 Introduction

Fluoride shows to have both positive and negative effects on human. It is widely used in dental application for tooth decay prevention especially in higher sugar intakes areas. It is often presented in the form of tablets, mouthwashes, toothpastes, and other soluble gels with respective applications. It is evidently shown that at low concentrations of fluorides, human can benefit from its bone and tooth strengthening effect [1]. However, upon excessive intake via drinking water in the long run can lead to wide occurrence of dental and skeletal fluorosis diseases. In worldwide, there are approximately 500 million people are contracted to suffer fluorosis and these phenomena had been considered as major issues which would eventually affect the global population of people, economic and social aspect [1]. Hence, the removal of fluoride from portable water has received great attention in the past few years.

The existence of fluoride content in the environment occurs through natural presence in the earth's crust and industrial activities during disposal of waste products, especially semiconductor, electroplating, glass, steel etc. which lead to fluoride contamination on the surface and ground water. Hence, fluoride removal in wastewater treatment technologies has become popular topic and draw much interest by society nowadays. Water scarcity has been known as one of the greatest global challenges because of the rapid elevation in world's population which leads to continuous growth of water consumption rates [2]. Current wastewater treatment could be categorized into three main groups: Physical, chemical, or biological processes; and a typical wastewater treatment consists of combination of all wastewater treatment types to maximise de-fluoridation performance. According to World Health Organization (WHO) standard, the optimum fluoride level in portable water is between 0.5 mg/L to 1.0 mg/L and the effluent discharges standard for fluoride in wastewater industries are different with respect to countries. For instances, the wastewater effluent discharge standard for fluoride content in Malaysia is 5 ppm (standard B), whereas United State (US) recently established the effluent charge standard of 4 ppm for fluoride content in wastewater treatment [4, 5]. The general fluoride concentration in actual industrial wastewater ranged between 250 ppm to 1500 ppm, depending on operating condition. A polishing step might be necessary which mainly depends on respective discharge standard.

De-fluoridation was being accomplished by various techniques such as adsorption, electro-coagulation, membrane separation, ion-exchange, and the Nalgonda technique. Among the techniques used for fluoride removal, coagulation has been widely used due to its simplicity and high effectiveness of removing the fluoride content. In general, coagulation can be classified into two types which are chemical and natural coagulation. Aluminium chloride ($AlCl_3$), aluminium sulfate which known as alum and poly-aluminium chloride (PAC) are commonly used as the chemical coagulants, and have been proposed and well investigated with respect to the study of fluoride removal. While *Moringa oleifera* and *Okra mucilage* have been investigated and studied for exploring these seeds as potential natural coagulants for treating wastewater in the future [6].

Extensive studies were discovered by researchers and scientists regarding chemical coagulation for de-fluoridation. Gong *et al*. stated that the formation of Al-F complexes involves the fluoride removal using $AlCl_3$, and this effect improves the de-fluoridation efficiency to a large extent compared to aluminium hydroxide, $Al(OH)_3$ adsorption [7]. Bi *et al*. concluded that Al-F complexation influenced the hydrolysis of

aluminium salts and their respective distribution and transformation afterwards as the hydrolysis of Al salts tended to form a series of Al composition with respective structures, charges, and polymerization characters [8]. However, limited studies had been made on the effects of Al species distribution whereas the transformation on fluoride removal performance using Al coagulation is more focused and evaluated in this research. There were few studies focusing on the usage of natural coagulant for improvement of de-fluoridation. *Moringa* seeds are the most common natural coagulants used for investigating coagulation performance. *Moringa oleifera* can be derived as tropical plant which is highly available in Asia region especially in Indonesia and Malaysia due to their typical hot weather which promotes its growth [9]. Besides, *M. oleifera* and *Okra mucilage* were claimed to be non–toxic and recommended as coagulant in developing countries as they are effective as bio-coagulant to improve physio–chemical properties of contaminated water [9]. In general, turbidity reduction of more than 80 % had been reported to be achieved when plant-based coagulants like *Prunus armeniaca* seeds were used under optimised operating conditions, with the exception of few rare cases [10]. Abidin *et al*. reported that natural coagulants especially plant-based coagulants are having their unique coagulation mechanism [10]. For instance, the coagulation mechanisms in the seeds of *J. curcas* were predicted to behave as similar as adsorption and charge neutralization due to close similarities of cationic active coagulation agent to that in *Moringa oleifera* [11]. Despite various indigenous plant extracts were being observed to possess coagulation properties in removing turbidity for improvement of fluoride removal performance [12], the achievement of commercialization phase using plant-based coagulant were rather scarce. Financial, research and development, market awareness as well as the regulatory approval which has well documented in literature for the case of *M. oleifera* seeds were claimed to be the constraints that hindering the commercialization of natural coagulant in the future [12].

Despite coagulation provides cost effective performance with low equipment and capital costs, the main drawback using this conventional method is its low efficiency on removing contaminations which causes severe environmental issues such as water pollution which endangered marine habitants. Hence, many researchers and scientists were investigating on methods to improve efficiency of de-fluoridation either in portable water or wastewater effluent. One of the methods in optimising fluoride removal performance was membrane separation otherwise known as nanofiltration (NF) as it could achieve high inorganic removal like fluoride due to the involvement of combination of separation mechanisms including solution diffusion, size exclusion, and charge repulsion adsorption [13]. Ayoob *et al.* reported that improvement of fluoride removal using nanofiltration (NF) and reverse osmosis (RO) was successful as total of more than 96 % and 90 % of fluoride rejections were being accomplished respectively. Pontie *et al*. claimed that fluoride removal performance by NF/RO could reduce fluoride concentration in wastewater effluent up to 15 mg/L to meet WHO guideline with lower energy consumption [13]. Possible drawbacks of using NF such as membrane fouling and scaling which were inherent in fluoride removal through separation process. However, they could be significantly reduced by improving operating condition [13]. As nanotechnologies remain sophisticated in current studies, more research and investigation are necessary to explore the potential of using nanofiltration in improving fluoride removal performance and efficiency.
Further studies conducted on chemical and natural coagulants suggested sodium aluminate ($NaAlO_2$) with poly-aluminium chloride (PAC) as the representative of

chemical coagulants; while *Moringa oleifera* and *Okra mucilage* being selected as the studied natural coagulants to study their effects on fluoride removal efficiency. The research objectives are as followed:

1. To study the effect of coagulant dosage, coagulant types on fluoride removal performance and pH effect after coagulation at studied condition,
2. To achieve final fluoride concentration of 5.0 ppm (standard B of wastewater effluent discharge) using 100.0 ppm of hydrofluoric acid as synthetic wastewater sample.

The research topic mainly focuses on the report submitted by actual wastewater industry located in Russia [14]. This creates a benchmark of initial fluoride concentration of 100 ppm based on the characteristics of the studied wastewater sample. The actual characteristics of studied industrial wastewater are summarized in Table 1.

Table 1. Actual Industrial Wastewater Characteristics [14]

Parameters	Unit	Concentration
pH	-	2.95 ± 0.3
COD		1857 ± 69
SS		28.4 ± 2.6
Phosphorus		0.077 ± 0.07
Fluoride	mg/L	105.3 ± 21.2
Nitrate		3.25 ± 0.8
Sulfate		457.6 ± 28
Chloride		19,035 ± 2710

2.0 Methodology

In this research, quantitative types of research would be implemented to achieve research objectives whereby analysis and evaluation made determine the pathway to enhance fluoride removal efficiency using coagulation. Thus, validations and verifications regarding materials and test preparation were explained as follow in accordance to experimental and theoretical results.

2.1 Material Preparation

2.1.1 Synthetic Wastewater, Hydrofluoric Acid (HF)

Hydrofluoric acid, HF was used as the synthetic wastewater sample for de-fluoridation purpose by chemical and natural coagulation. HF 55% has been purchased from *Platinum Strike Sdn Bhd*, Malaysia which provided a concentration of 550000 ppm with 97% of purity. 148 microliters of HF 55% was taken out from the concentrated stock solution and is diluted with distilled water which added up together to from 1000 ml of diluted HF stock solution.

2.1.2 Chemical Coagulants, Poly-Aluminium Chloride (PAC) and Sodium Aluminate (SA)

Coagulants used for the study of the chemical coagulant dosage on de-fluoridation performance were poly-aluminium chloride (PAC) and sodium aluminate, $NaAlO_2$ (SA). PAC 30 % (clear yellowish solution, 15000 ppm, 95% purity, boiling point of 100-120˚C with complete solubility in water at 20˚C) and $NaAlO_2$ (white powder, minimum of 80% purity, optimal range of more than pH 12) had been supplied by *Platinum Strike Sdn Bhd* as well and used for the following tests. The mixture coagulation solution with 1 g/L has been prepared as 1 g of $NaAlO_2$ powder was weighed and diluted with 1000 ml of distilled water together with 1 g of NaOH powder and same steps were repeated for preparation of 2 g/L, 3 g/L and 0.5 g/L of mixture coagulant solution according to the formulation provided by [15].

2.1.3 Natural Coagulants, Moringa Oleifera and Okra Mucilage

Dried *Moringa oleifera* seeds were purchased from a local market with the coordination of (3.193587, 101.680083) located in Selangor. The dryness of *M. oleifera* seeds is 97.0 % and *M. oleifera* seeds was initially undergo washing process to remove unwanted impurities from it which might affected results obtained to achieve research objectives. Washed *M. oleifera* seeds were put into oven to reduce moisture content up to 97 % for following grounding process. Dried *M. oleifera* seeds were then ground into fine powder with micro-size particle (10^{-6} m) for increasing contact area between coagulants with fluoride ions during coagulation for the study using a domestic grinder (*Lebensstill* stainless Steel Coffee Grinder with series number of LKCG4012SS, Germany). After grinding process, *M. oleifera* in micro-size dimension was ready to be used for further analysis and evaluation in this research topic.

Okra mucilage was purchased from a local market with coordination of (3.193587, 101.680083) located in Selangor as well. The preparation of *Okra mucilage* was proceeded according to the research reported by Kwaambwa *et al*. with some modifications [16]. At first, *Okra* samples were cut longitudinally to obtain the pods. Then, these seed pods were separated from the seeds, and rinsed in proper ways ensuring no impurities was existed during coagulation. After rinsing process, the seed pods were then dried in the micro-oven (*Memmert* brand with series number of UN 70, Germany) at 70 ˚C for 14 hours. The dried *Okra* seeds were then ground into fine powder using domestic grinder (*Lebensstill* stainless Steel Coffee Grinder with series number of LKCG4012SS, Germany).

2.1.4 Fibrous Thin Film

Fibrous thin film was purchased from *Platinum Strike Sdn Bhd*. The characteristic of studied fibrous thin film consisted of random pore sizes ranges from micro-pore size (μm) to milli-pore size (mm) to study effect of pore size of film on coagulation performance *using Moringa oleifera* and *Okra mucilage* as natural coagulants. 2.5 g of *M. oleifera* and *Okra mucilage* were initially ground respectively into micro-size and filled into fibrous thin film and conduct coagulation process using Jar test.

2.2 Methods

There were tests required to be conducted to achieve the seeks of objectives. In this study, jar test is recommended to be used as the coagulation process for

enhancement of mixing process. pH test and fluoride concentration test were necessary as well to evaluate the physical parameter effect on de-fluoridation performance.

2.2.1 Jar Test

The coagulation tests were conducted using a jar tester (Lovibond® ET 750, USA) at ambient condition (25 ± 2 ˚C) with optimum pH value of 7 based on the findings from [17]. The procedure of this test was modified according to the journal reported by Aoudj *et al.* [80]. 148 microliters of synthetic wastewater, hydrofluoric acid (550000 ppm) was transferred into 2000 ml corrosive resistant beaker and diluted with distilled water with a total volume of 1000 ml. Chemical coagulant, PAC with mixture of $NaAlO_2$ and NaOH were added to the diluted HF solution with respective studied concentration. After addition of aluminium-based coagulant, the following steps consisted of 2 minutes of standard mixing at 100 rpm with an adjustment of desired initial pH value, then 15 minutes of slow mixing at 40 rpm, and 30 minutes of settling for stabilization. [17] Once the settling period had passed, the supernatants were filtered through a 0.45 μm thickness of sensitive membrane to analyse the final concentration of fluoride and aluminium residues in the filtrate. The filtered product is ready for the following tests and analysis. Same procedure has been applied to natural coagulant by replacing it from chemical coagulant with the preparation explained in section 2.1.3.

2.2.2 pH test

The pH meter (Eutech PC 700, Insearch Scientifix Sdn Bhd, Malaysia) is being used to test the final pH of the filtered substance from the jar test. The procedure was conducted according to manual provided by Hu *et al*. with some modification applied [81]. Before measuring the pH of the solution after coagulation, the indicator was required to be cleansed with distilled water. After rinsing process, the mercury was then immersed to the sample provided together with pH meter in a pH condition of 4.0. Once pH meter was successful in measuring the sample by showing the sign of "Ready for sample 2" on the monitor, the indicator was taken out and rinsed with distilled water for the second pH measurement from sample 2 at neutral pH condition (7). When the monitor of pH meter showed sign of "Ready to be used", the indicator was taken out again and cleansed with distilled water and the samples are ready for analysis.

2.2.3 Fluoride Concentration Test

A spectrophotometer (Spectroquant® Prove 300 UV/VIS, Merck KGaA, Germany) was used to determine the final concentration of fluoride content within the filtered product. A test kit with full set of reagents, corrosive resistant test tube and stirrer would be supplied by Merck company for fluoride concentration test. The procedure proceeded based on journal provided by He *et al*. with some adjustments [18]. At first, 2 ml of reagent 1 was being pipetted out and added into 25 ml of test tube. 5 ml of distilled water was then withdrew using pipette as well and added into the test tube. Then, 0.5 ml of the stock solution, HF after coagulation was taken out and mixed with the reagent within the test tube. Lastly, one scoop of reagent powder 2, 0.1 g was added into the test tube and shake the test tube using gloves for even mixing without precipitation. After settling time of 5 mins, the mixture was then poured into cuvette and was ready to be measured using spectrophotometer. Initial fluoride concentration

of synthetic wastewater sample was measured using similar procedure as mentioned above. However, 0.5 ml of synthetic wastewater sample was initial taken out and added into 3.5 ml of distilled water in ratio of 1:7 for dilution purpose to ensure the fluoride concentration measured by the spectrophotometer stayed within intended ppm range.

2.2.4 Aluminium Concentration Test

A spectrophotometer (Spectroquant® Prove 300 UV/VIS, Merck KGaA, Germany) was used to determine the final concentration of aluminium content within synthetic wastewater sample. A test kit with full set of reagents, corrosive resistant test tube and stirrer would be supplied by Merck company for fluoride concentration test. The procedure proceeded based on journal provided by He *et al*. with some adjustments [18]. At first, 5 ml of pre-treated sample was being pipetted out and added into 25 ml of test tube. 1 level of blue micro-spoon of reagent Al-1, 1 μm was added into the test tube, close the test tube with hand covered by gloves, and then shake vigorously for few seconds until reagent is completely dissolved. Then, 1.2 ml of reagent Al-2 was added with another syringe, then close the tube and mix. Lastly, 0.25 ml of reagent Al-3 was added into the same test tube, close test tube and started to mix and left it to stand for 7 minutes. After reaction time of 7 minutes, blank solution was being prepared by adding 5 ml of pre-treated sample in another 25 ml of test tube. Slide the colour card through to the left side until the closest possible colour was achieved between 2 open test tubes when viewed from above. Then, read off the result n mg/L Aluminium from the colour at lower right-hand edge of the comparator block within the bottom part of the box from spectrophotometer. Initial aluminium concentration of synthetic wastewater sample was measure using similar procedure as mentioned above.

3. Results and Discussion

With respect to the methodology mentioned from previous section, the evaluation and analysis of the result would be obtained and divided into three parts which were regarding to the effect of coagulant dosage towards de-fluoridation, comparison of fluoride removal rate using natural and chemical coagulant as well as the effect of pH after de-fluoridation process and optimisation of de-fluoridation.

3.1. Effect of Chemical Coagulant Dosage on De-Fluoridation Efficiency

The effect of chemical coagulant dosage on fluoride removal performance was studied with the methodology provided. The mixture of 5 g of sodium aluminate ($NaAlO_2$), 5 g of sodium hydroxide (NaOH) diluted with 1 litre of distilled water and poly-aluminium chloride (PAC) were used as the chemical coagulants involved to investigate how coagulant dosages affected rate of fluoride removal. The study of coagulant dosages towards the efficiency of removing fluoride focused on the studied condition (fluoride concentration range of 0.2 ppm to 20.0 ppm) at neutral pH [18]. Chen *et al.* reported that the composition of aluminium ions, Al_3 showed high positive charge, most stable structural basis, and strong binding affinity as well as most active Al species in Al salts responsible for chemical coagulation [19]. He *et al*. claimed that neutral pH remains the optimum acidity for most of the Al species (Al_2, Al_3, Al_4, Al_7 etc.) for de-fluoridation [18], which prompted this experiment of removing fluoride using Al based coagulant to be performed under a pH value of 6-7 [6, 13, 14]. The

coagulant dosage used for removing fluoride from the stock solution (100 ppm of Hydrofluoric acid, HF) is one of the most crucial physical parameter to be evaluated for ensuring the effectiveness and efficiency of removing fluoride through coagulation whereby it was being limited to have minimum coagulant dosage of 1 g/L due to the studied condition (fluoride concentration range which has been mentioned above). Hence, to have sufficient data to proceed the coagulation for de-fluoridation describes in Table. 2., four sets of different coagulant dosages had been synthesized based on formulation provided by [18] with three sets of average values and de-fluoridation efficiencies provided. With respect to that, Figure 1 was provided to have further investigations regarding the effect of coagulant dosages on efficiency of fluoride removal.

Table 2. Fluoride Removal Efficiency at Respective Coagulant Dosage
*HI indicates fluoride concentration which exceeds from 20.0 ppm

Coagulant Dosage, g/L	Final Fluoride Concentration, ppm			Fluoride Removal Efficiency, %		
	1st Average Value	2nd Average Value	3rd Average Value	1st Average Value	2nd Average Value	3rd Average Value
0.5	HI	HI	HI	>80.0	>80.0	>80.0
1.0	19.2 ± 1.2	19.0 ± 1.1	18.5 ± 1.0	80.8	81.0	81.5
2.0	14.7 ± 1.5	15.8 ± 1.6	14.2 ± 1.2	85.3	84.2	85.8
3.0	14.5 ± 2.3	14.4 ± 2.0	14.5 ± 1.3	85.5	84.4	85.9

Coagulant dosage showed significant effect on de-fluoridation efficiency. With respect to Table 2., the final fluoride concentration at coagulant dosage of 0.5 g/L showed "HI" symbol for three average reading which indicated that the remaining fluoride content after chemical coagulation still exceeded the amount of 20.0 ppm. This occurrence is explainable through the possible lack of aluminium compositions (Al_3, Al_7 etc.) binding with fluoride ions within the stock solution, HF to form aluminium-fluoride complexes which were commonly known as flocs [20]. As a result, incomplete de-fluoridation process might have occurred causing high fluoride contents contamination at the surface of stock solution, HF after settlement which caused failure to achieve the standard of industrial effluent from wastewater (5.0 ppm for Standard B and 2.0 ppm for Standard A) [21]. The fluoride concentration was reduced from more than 20.0 ppm to a range of 18.5 ppm – 19.2 ppm with average deviation of ± 1.5 at coagulant dosage of 1.0 g/L. Error existed in final fluoride concentration measurement might cause by the exposure of concentrated synthetic wastewater sample to the surrounding air for long period of time as well as different positioning to take measurement. This data was revealing the possibility of higher Al-F complexes being produced and settled down with the given settling time, 10 minutes. Thus, lower fluoride contents remained within the Synthetic wastewater sample (HF) and the efficiency of removing fluoride eventually increased. Referring to Table 2., the coagulant dosage of 2.0 g/L and 3.0 g/L provided final fluoride concentration of (14.7 ± 1.5 g/L, 15.8 ± 1.6 g/L and 14.2 ± 1.2 g/L) and (14.4 ± 2.3 g/L, 14.5 ± 2.0 g/L and 14.4 ± 1.3 g/L) respectively. It could be observed that the remaining fluoride content after coagulation had been lowered down when coagulant dosage increased from 1.0 g/L to 2.0 g/L and then 3.0 g/L but with a slower reducing rate. It was notably observed that the elevated coagulant dosage will become less significant to the changes on the

final remaining fluoride, until a point where the effect became non-apparent when a constant value is observed despite the continuous increased of the coagulant dosage. Due to lack of fluoride ions, F^- to bind with aluminium composition, Al to form Al-F complexes as the initial concentration of stock solution was fixed to have 100.0 ppm and hence will eventually act as the limiting substances for the formation of Al-F complexes after coagulation [5]. Hence, fluoride removing rate would eventually achieve a constant value even though the coagulant dosage kept increased. However, Liu *et al*. claimed that the elevated Al concentration might inhibit the attachment of fluoride ions, F^- onto Al flocs to form Al-F complexes and adversely inhibited fluoride removal by Al coagulation thereafter [22]. Hence, a statement could be predicted as the efficiency of fluoride removal would increase with a slower increasing rate and held constant at coagulant dosage of 3.0 g/L to 4.0 g/L and then tended to lower down when the coagulant dosage is kept elevated after 4.0 g/L due to the inhibition of F^- attached onto Al flocs to form Al-F complexes for maximising fluoride removal rate. Lastly, the coagulant dosage of 0.5 g/L to 3.0 g/L were still unable to achieve standard A and B from industrial effluent of wastewater treatment which are 2.0 ppm and 5.0 ppm respectively.

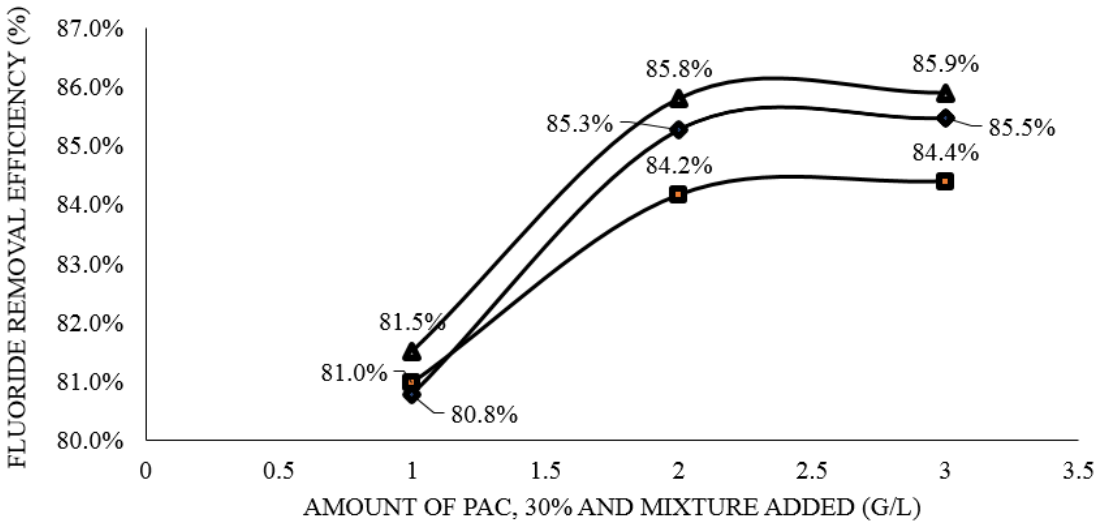


Figure 1: Fluoride Removal Efficiency at Respective Coagulant Dosage, —◆— 1st Average Reading, —■— 2nd Average Reading, and —▲— 3rd Average Reading

The trend of de-fluoridation efficiency with respective chemical coagulant dosage was studied. As shown in Figure 1, first average reading presented the efficiency of removing fluoride was increased from 80.8 % to 85.3 % and eventually to 85.5 % when coagulant dosage increased linearly from 1.0 g/L to 3.0 g/L. The efficiency of fluoride removal using chemical coagulation for second and third set of average data had similar behaviour and trend with the first set of average reading, with a value from 81.0 % to 84.2 % and elevated to 84.4 % as well as from 81.5 % to 85.8 % and increased to 85.9 %, respectively. It was clearly observed that at higher fluoride removal efficiency, further increment of the coagulant dosage produces less drastic changes on the removal rate. It is also shown clearly that the maximum curve of the data lies between the ranges of 2.0 g/L to 2.5 g/L of coagulant dosage, where the fluoride removal efficiency will start to decrease with further addition of the coagulant. The trend of the results above showed similar agreement with the journal provided by Liu

et al. [22]. Hence, it can be concluded that results obtained were legit and suitable to be evaluated and discussed.

3.2 Study of Natural Coagulant, *Moringa Oleifera* towards De-Fluoridation Process

Moringa oleifera (*M. oleifera*) is the most common natural coagulant used for fluoride removal either in lab-scale or industrial scale. Ndabigengesere *et al*. claimed that de-fluoridation process using natural coagulant would produce bio-degradable sludge which having relatively smaller volume compared to chemical coagulant especially aluminium based coagulant [23]. The report provided by Okuda *et al*. stated that with the use of *M. oleifera* seed as coagulant would be less affected by the water pH after de-fluoridation process [24]. The study of *M. oleifera* towards efficiency of de-fluoridation was presented as Table 3. as shown below with the average initial and final fluoride concentration of the synthetic wastewater sample, Hydrofluoric acid (HF) and hence, efficiency of fluoride removal was determined and tabulated.

Table 3. Study of *M. oleifera* towards fluoride removal efficiency

Average [F_i], ppm	Average [F_f], ppm	Fluoride Removal Efficiency, %
91.0 ± 15.25	31.1 ± 17.93	65.8

* 2.5 g of *M. oleifera* seed was grounded manually and used as initial coagulant dosage
* [F_i] – Initial Fluoride Concentration
* [F_f] – Final Fluoride Concentration

Different type of coagulant produced varying fluoride removal performances.

Referring to Table 3., it was clearly seen that the initial fluoride concentration of stock solution, HF was having 91.0 ppm with deviation of ± 15.25. Deviation existed might cause by quality of *M. oleifera* used for de-fluoridation study. The freshness of *M. oleifera* were not analyzed before conducting the experiment and this would affect the initial and final measured fluoride concentration within synthetic wastewater sample and different freshness of natural coagulant would provide different fluoride removal performance. Since the initial fluoride concentration of synthetic wastewater sample was prepared manually to have 100.0 ppm with some deviations, the average reading of initial fluoride concentration was still within acceptable range and was safe to be used. Before initiating de-fluoridation process, *M. oleifera* was initially ground into powder with micro-size of particle size to increase the contact area between coagulant and synthetic wastewater sample for enhancing de-fluoridation efficiency [22]. The fluoride concentration after coagulation process using *M. oleifera* was found to be 31.1 ppm with deviation of ± 17.93 and the efficiency fluoride removal rate was determined to be 65.8 %. De-fluoridation performance using chemical coagulant with formulation was ranged from 80.8 % to 85.9 % at coagulant dosage of 1.0 g/L to 3.0 g/L. However, Choy *et al*. reported that chemical coagulant would generally provide a higher efficiency of removing fluoride content compared to natural coagulant as the aluminium composition, Al in chemical composition was more concentrated and higher compared to natural coagulant [25]. Choy *et al*. claimed that average aluminium concentration in natural coagulant like *M. oleifera* was 150 mg of Al per 1 kg of *M. oleifera* [25]. Although chemical coagulant provided a greater impact on removing fluoride content from either wastewater or drinking water, the higher Al composition in chemical coagulant provided higher chances of aluminium residuals after settlement

and this caused another environmental issue [22]. Residual aluminium in treated water had been the center of debate as it was linked to serious health problem such as development of Alzheimer's disease (AD) [26]. In contrast, natural coagulant like *M. oleifera* was safe to use, eco-friendly and are mostly toxic-free. As such, sludge treatment or post-treatment as well as the handling cost were much lower to provide a more sustainable option. One of the studies reported by Govindan *et al*. stated most of natural coagulants possessed non-corrosive properties which eradicate the concern of pipe corrosion [25]. Hence, less maintenance and equipment costs were required for securing the sustainability of the process. Despite most of the natural coagulants were environmental friendly and were known for their effectiveness in reducing the turbidity flow, the knowledge about characteristics and properties of the resultant flocs formed are limited and the studies as well as research regarding this field are rather scarce [27]. In addition to that, even though most of the natural coagulant are green to nature and can be used without hazard, the use of crude extract for extracting the organic matter into wastewater treatment would produce various inorganic and organic biomolecules like lipids which inhibits the coagulation process [27]. The organic matter produced from leeching and crude extraction would also turn into precursor to the formation of trihalomethanes (THMs), a form of carcinogenic which elevated the chlorine demand for proper disinfection [91]. Lower fluoride removal efficiency, 65.8% was determined using 2.5 g of ground *M. oleifera* compared to 85.9 % of de-fluoridation performance achieved using 3 g/L of poly-aluminium chloride and mixture of sodium aluminate and sodium hydroxide. However, there are pros and cons using chemical or natural coagulant to treat wastewater using coagulation. Chemical coagulant provides higher efficiency of removing fluoride, thus improved the economic values. However, its higher efficiency questioned the overall profit as its low sustainability required higher maintenance cost, not to mention that chemical coagulants proved to be less eco-friendly compared with natural coagulant, hence environmental handling fees would be necessary, thus further increased the overall cost. In contrast, natural coagulant is safe, and provides the least harm to environment aspect. However, in-depth, and extensive knowledges regarding the characterization and properties of the natural coagulants remained limited and unknown up-to-date, hence potential disadvantages may yet be uncovered by modern scientists.

3.3 Study of Natural Coagulant, Okra mucilage towards Aluminium Removal Efficiency

Okra is previously called as *Hibiscus esculentus* which belonged to Malvaceae family. It is a perishable fruit with relatively short for post – harvesting period and its skin is very susceptible to browning due to loss of water, whereby depressing economical value of *Okra mucilage* for consumption in nature [28]. *Okra* seeds (*Okra mucilage*) also known as one of the most widely used natural coagulant used for wastewater treatment in both lab and industrial scale. The study of *Okra mucilage* towards efficiency of de-fluoridation was presented as Table 4. as shown below with the average initial and final fluoride concentration of the synthetic wastewater sample, hydrofluoric acid (HF) and hence, efficiency of aluminium removal was determined and tabulated as Table 4. below.

Table 4. Study of *Okra mucilage* towards Aluminium Removal Efficiency

Average [Al_i], mg/L	Average [Al_f], mg/L	Aluminium Removal Efficiency, %
3.49 ± 0.64	0.59 ± 0.04	87.3

* 2.5 g of *Okra mucilage* seeds were ground manually into micro-size (μm) and used as initial coagulant dosage at operating pH of 4.42 ± 0.26
* [Al_i] – Initial Aluminium Concentration
* [Al_f] – Final Aluminium Concentration

Okra mucilage provided significant effect on reducing aluminium concentration through coagulation process by referring to Table 4. In this study, 87.3 % of aluminium removal rate was achieved using 2.5 g of *Okra mucilage* ground into micro-size (μm) on synthetic wastewater sample with average initial aluminium concentration of 3.49 ± 0.64 mg/L at operating pH of 4.42 ± 0.26. Deviation in aluminium concentration existed might cause by quality of *Okra mucilage* used for aluminium removal study. The freshness of *Okra mucilage* was not analysed before conducting the experiment and this would affect the initial and final measured fluoride concentration within synthetic wastewater sample and different freshness of natural coagulant would provide different aluminium removal performance. This high aluminium removal efficiency phenomena was supported with the claim made by Sher *et al*., where the ground micro-size of the *Okra mucilage* would cause a substantial impact towards the coagulation efficiency. This is because by reducing particle size into micro-size, or even smaller, nano-size would increase the contact surface between the coagulant and the aluminium particles, thus enhancing the contact time between them. [29]. Eckenfelder reported that a natural coagulant dosage lower than optimal condition might not have sufficient charges to provide destabilization for effective homogeneous removal [30]. The occurrence of having such high removal rate of aluminium would be because of the natural characteristic of *Okra* seed. Miller *et al*. claimed that *Okra mucilage* consisted of galacturonic acid component which was likely active for observed coagulation activity [31]. Besides, such high aluminium removal efficiency might produce because of the optimum operating pH (optimum pH ranges from 4.5 to 6). Freista *et al*. studied the effect of operating pH on coagulation efficiency using *Okra* seeds and reported that 92.05 % of turbidity removal rate was achieved at optimum pH range from 5 to 6 which was almost similar to the operating pH in this study [32]. Stephenson *et al*. also supported the claim made from [32] and reported when pH was too low, protons outcompete metal hydrolysis products for organic ligands and the removal rate was poor due to failure of precipitation; while under more alkaline conditions, coagulating species tended to be less positively charged which would diminish their attraction to anionic organic compound, leading to enhancement of coagulation efficiency [33]. Mishra *et al*. reported that maximum coagulation efficiency could achieved at pH 6 because of the precipitation of metal ions into hydroxide form when pH increased near to neutral pH (7) [34].

3.4 Effect of Coagulant Types on pH Parameter After De-Fluoridation Process

The pH effect after coagulation for de-fluoridation is one of the important parameters required to be evaluated to decide whether post-treatment of maintaining the pH to neutral condition is necessary or not. If there were some changes in pH value

after de-fluoridation process, post-treatment like neutralization is required for maintaining pH back to neutral state. This particular unit was highly sensitive and required detailed specifications for one particular process, hence its construction and maintenance cost are very expensive. Therefore, it is crucial to evaluate the significant of varying pH value after coagulant on the de-fluoridation process. To have sufficient data for the evaluation, the average readings of de-fluoridation process from three individual sets were proceeded using 2.5 g of each natural coagulant, *Moringa oleifera* and *Okra mucilage* with and without thin fibrous film and tabulated as Table 5. Fibrous thin film, also known as the common tea bag, was used to improve the fluoride removal efficiency which would be further discussed in the next section.

***Table 5. pH Effect after Coagulation by Using* M. oleifera *and* Okra mucilage**

Coagulation Specification	*Okra mucilage*		*M. oleifera*	
	Initial pH	**Final pH**	**Initial pH**	**Final pH**
Without fibrous thin film	4.5 ± 0.26	6.3 ± 0.53	2.86 ± 0.04	3.15 ± 0.41
With fibrous thin film	4.67 ± 0.10	5.83 ± 0.65	2.78 ± 0.12	3.0 ± 0.82

The effect of natural coagulation with fibrous thin film was studied. According to Table 5., it was clearly seen that the pH after de-fluoridation process using *Okra mucilage* without fibrous thin film was increased from 4.5 ± 0.26 to 6.3 ± 0.53. The pH after wastewater treatment also showing an increasing of pH value from 2.86 ± 0.04 to 3.15 ± 0.41 by using *M. oleifera* as the natural coagulant without fibrous thin film. This occurrence could be explained by the fact that the stock solution, hydrofluoric acid with 100.0 ppm tended to be more alkaline due to the capability of natural coagulant, *M. oleifera* and *Okra mucilage* lied in the presence of cationic water-soluble protein found in their respective skin and seeds [35]. This ability would eventually lead to the acceptance of proton within the water by alkaline amino acids existed in both natural coagulant which resulted in the release of hydroxyl group ions, OH^- to increase the pH of stock solution [35]. Referring to Table 5., the pH value was increased 10 % after coagulation using *M. oleifera* as the natural coagulant, while *Okra Mucilage* showed 40 % of elevated pH value after de-fluoridation process. *Okra mucilage* provided a greater pH change because the composition of water-soluble protein was higher compared to *M. oleifera* which attracted more proton to be received by the protein to produce OH^- ions [35]. By referring to Table 5., the pH value using *M. oleifera* as natural coagulant with fibrous thin film changes from 2.78 ± 0.12 to 3.0 ± 0.82 and 4.67 ± 0.10 to 5.83 ± 0.65 for natural coagulant, *Okra mucilage*. It was additionally to be observed that the pH changes before and after coagulation with fibrous thin film for both natural coagulants (24 % and 8 % respectively) are much lower compared to de-fluoridation process without fibrous thin film (40 % and 10%). This could be explained by the fact that fibrous thin film was used to capture insoluble amino acid from the stock solution and only soluble amino acid was able to diffuse into synthetic wastewater from the fibrous thin film. Hence, lower amount of amino acid was released from the tea bag and lower proton was attracted by amino acid to produce less amount of OH^- ions. As a result, lower pH was formed as the synthetic wastewater, HF with fibrous thin film was less alkaline compared with the presence of fibrous thin film. In contrast, Sutherland *et al*. claimed that the pH of the medium will increases when the chemical coagulant dosage like poly-aluminium chloride increased due to elevated H^+ ions

released from hydrolysis [98]. The deviations existed in pH value for this experiment might due to freshness of natural coagulant used (*M. oleifera* and *Okra seeds*) for the study of pH effect after de-fluoridation process. Freshness of natural coagulants used might reduce as time passed, led to different coagulant performance.

3.5 Improving Wastewater Treatment Using Fibrous Thin Film

Extensive studies had been done by researchers and scientists for optimising the fluoride removal efficiency with the use of various techniques such as membrane separation [36]. Lhassani *et al*. claimed that nanofiltration is the most effective among membrane separation processes to provide a partial de-fluoridation with an optimal fluoride content within the permeate by adjusting the operating condition [36]. However, studies regarding nanofiltration performance on fluoride removal in wastewater are rather scarce. The works presented by Lhassani *et al*. was based on pilot studies [36]. Detail studies on the effect of membrane intrinsic properties on fluoride removal efficiency were limited as well. Therefore, evaluation on the effect of membrane separation on fluoride removal performance was necessary to be done to discover the potential of membrane separation technique on improving the wastewater de-fluoridation efficiency. Upon to this study, a fibrous thin film was used as the medium to investigate its effect towards fluoride removal efficiency in wastewater using *Moringa oleifera* as the natural coagulant. The result of fluoride removal performance with and without fibrous thin film was recorded and tabulated as Table 6. for comparison purpose. Coagulation with fibrous thin film provided different fluoride removal performance compared to coagulation without permeate.

Table 6. De-Fluoridation Process using *M. oleifera* as Natural Coagulant with and without Fibrous Thin Film

The Existence of Fibrous Thin Film	Fluoride Removal Efficiency, %
Presence	42.6
Absence	65.8

According to Table 6., the efficiency of fluoride removal with fibrous thin film was found to be 42.6 % which is lower compared to fluoride removal performance without fibrous thin film. This totally violated the theoretical principle, which stated that the presence of permeate (in our case, the fibrous thin film) will generate a concentration gradient between the bulk concentration from synthetic wastewater sample (HF) and the feed concentration within the fibrous thin film. This will increase the net driving pressure gradient which eventually led to an increased in the electric potential gradient between them [37]. With the elevated electric potential gradient, it enhanced fluoride removal performance by increasing the solution flux according to the extended Nernst-Planck equation [37]. The reducing effect of de-fluoridation efficiency with fibrous thin film which opposed against theoretical background suggested a possible inconsistence of pole size at the surface of fibrous thin film used for the study. Bowen *et al*. reported that the application of equations related to membrane separation such as Gouy-Chapman equation and Nernst-Planck equation required certain critical criteria and assumption, in which one of them is the size uniformity of the film capillary pores [100]. However, the limitation of this study was the inconsistency of the pore radius on the surface of the fibrous thin film surface upon evaluation. Therefore, such errors caused the results to deviate from the theoretical background of those related

equations. Mohammad *et al*. stated the pore size of the membrane used was one of the membrane structural parameters which provided the significant effect on the fluoride removal performance by affecting the ion rejection occurred within the permeate [38]. According to Nernst-Planck equation, the diffusion hindrance coefficients (H_{id}) would increase when pore size increased which eventually caused reduction in ion rejection and enhanced the effective diffusivity of anion through the film from bulk solution [38]. In other words, the lower rate of fluoride removal efficiency might occur because of the fibrous thin film used consisted of small pore sizes which reduced fluoride removal performance. Wang *et al*. claimed that the concentration polarization effect must be negligible before applying the theoretical explanation of Nernst-Planck equation as a significant concentration polarization effect would cause the ion concentration on the feed surface layer to be higher than in bulk solution [6]. As a result, the osmotic pressure difference was, hence results in lower solution flux to have such discrepancy according to Nernst-Planck equation [6]. Thus, it is clearly apparent that the inconsistency of pore radius on surface of fibrous thin film is the reason behind having concentration polarization effects which eventually influenced the fluoride removal efficiency.

3.6 Statistical Analysis

Statistical analysis was necessary to be conducted to evaluate how significant of the parameter affected the desired result. The study was focusing on the effect of coagulant dosage on fluoride removal performance and therefore, ANOVA one-way test was selected to verify the significance of only parameter, coagulant dosage on de-fluoridation efficiency. Results obtained for verifying the significance between parameter were presented as Table 7. below.

Table 7. Statistical Analysis of Respective Chemical Coagulant Dosage on De-Fluoridation Efficiency Using ANOVA-1 Way Test

Comparison between Chemical Coagulant Dosage, g/L	***p* value**	**Indication**
1 with 2	1.18×10^{-9}	$p < 0.05$
2 with 3	0.65	$p > 0.05$
1 with 3	1.5×10^{-9}	$p < 0.05$
All	5.53×10^{-12}	$p < 0.05$

The effect of chemical coagulant dosage on de-fluoridation efficiency was studied using ANOVA 1-way method. Referring to Table 7., it was observed that *p* value between chemical dosage of 1 g/L to 2 g/L and 1 g/L to 3 g/L were found to be 1.18×10^{-9} and 1.5×10^{-9} respectively. The *p* value for coagulant dosage between 1 g/L and 2 g/L as well as 1 g/L and 3 g/L were under the same category of $p < 0.05$. This indicated when the coagulant dosage increased from 1 g/L to 2 g/L, there was a significant effect and great impact on fluoride removal efficiency. This same applies to coagulant dosage of 1 g/L to 3 g/L. However, it showed *p* value of 0.65 when the coagulant dosage was increased from 2 g/L to 3 g/L which fall under the category of $p > 0.05$. This implied that there was no significant effect on fluoride removal performance when coagulant dosage was increased from 2 g/L to 3 g/L. This could be explained because the elevated coagulant dosage caused an increased trend of aluminium composition, which might inhibit the formation of aluminium-fluoride complex (Al-F), also known as flocs, for fluoride removal purpose [38]. Thus, the decreased in fluoride removing rate have less significant effect on de-fluoridation performance at coagulant dosage of 2 g/L to 3 g/L. In overall, the elevated coagulant

dosage from 1 g/L to 3 g/L brought significant effect on fluoride removal efficiency as the *p* value showed 5.53 x 10^{-12} which is less than 0.05 and hence, the effect of coagulant dosage range from 1 g/L to 3 g/L is worth to be studied and evaluated.

4.0 Conclusion

The above results gave a conclusive idea that physical parameters are crucial and the most effective factors on enhancing fluoride removal efficiency under specified circumstances. With respect to the above, it is important to comprehend the effect of chemical coagulant dosage and the type of coagulant on fluoride removal performance, along with the evaluation of de-fluoridation performance with fibrous thin film to improve the current existing technologies.

With the results obtained, the highest fluoride removal efficiency of 85.9 % was achieved when 3 g/L of chemical coagulant with formulation provided previously was used to treat 100.0 ppm of synthetic wastewater sample, HF at pH 7 in room condition. The study also stated that the higher the coagulant dosage, the higher fluoride removal performance could be accomplished but with a decreasing of elevation rate because of the inhibition of de-fluoridation efficiency by elevated aluminium composition. It was additionally to be observed that 65.8 % of fluoride removal rate was achieved using 2.5 g of natural coagulant, *Moringa oleifera* which was ground manually and operated at pH value of 4.0. With respect to that, natural coagulant provided lower fluoride removal efficiency compared to chemical coagulant. Besides, the results obtained showed pH value after coagulation with the use of *M. oleifera* with and without fibrous thin film was increased from 2.86 ± 0.04 to 3.15 ± 0.41 and 2.78 ± 0.12 to 3.0 ± 0.82 respectively due to the released of hydroxyl ion, OH^- from the amino acid within *M. oleifera* increased. In addition, the efficiency of fluoride removal with the fibrous thin film was reduced from 65.8 % to 42.6 %. This could be explained as the concentration polarization effect might existed during the de-fluoridation process due to inconsistent and small pore sizes of the fibrous thin film according to Nernst-Planck equation which inhibit fluoride removal performance. The coagulant dosage was proved to have significant effect on fluoride removal performance as the *p* value between the coagulant dosage is 5.53 x 10^{-12} which is less than 0.05 ($p < 0.05$).

While the results obtained display varying effects, datable results from numerous research have provide distinctive commentary which extend the limitation regarding the factors expatiated in this research. This also suggested the expansion of further aspect and other area of interest that contributes in improving the quality of freshwater such as:

1. Study effect of freshness of natural coagulant on de-fluoridation using coagulation
2. Study of other physical parameters (The effect of pH, temperature, Coagulant dosage at different range and film intrinsic properties) on de-fluoridation efficiency

As a primary conclusion for this research, the research objective of reducing the fluoride content to meet the standard of industrial effluent from wastewater (5.0 ppm for standard B) was not accomplished and the lowest fluoride concentration achieved through this study was 14.2 ppm. Figure 2 was presented to illustrate the findings of this research on different decisions and pathways to remove fluoride content from stock solution, HF using coagulation with specified condition and achievements.

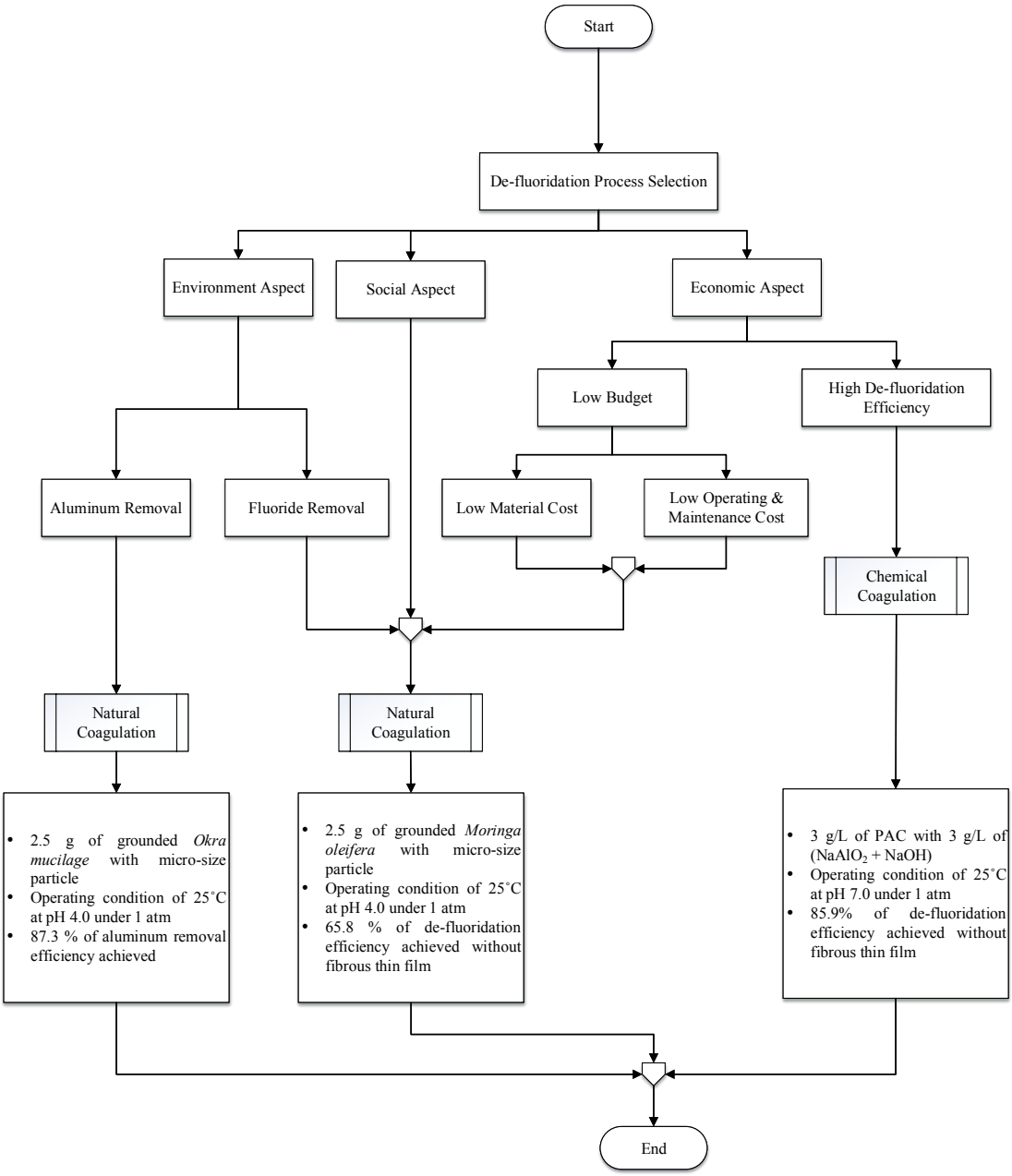


Figure 2. Decision Making on De-fluoridation process

Acknowledgement

The author would like to give thousands of thanks to Prof. Chong Chien Hwa and Dr. Rajesh Nithyanandam for their constant support and substantial guidance which led to successful and smooth progression of this research. The author would also like to express his token of appreciation to the team leader, Mr. Winston Lim Lik Khai, as well as the team members, Mr. Nicholas Ong Tze Kai, Mrs. Nurasatifah binti Kahar and Mr. Hew Wee Seong, for their team efforts, cooperation, and assistances upon performing experimental research which contributed to the completion of this research thesis.

References

[1] Rafique, A., Awan, M. A., Wasti, A., Qazi, I. A., & Arshad, M. (2013). Removal of fluoride from drinking water using modified immobilized activated alumina. *Chemical Engineering Journal, 1*, 1-7.

[2] Ayoob, S., Gupta, A. K., & Bhat, V. T. (2008). A conceptual overview on sustainable technology for de-fluoridation of drinking water and removal mechanisms. *Critical Revolution and Environmental Science Technology, 38*, 401-470

[3] Moussa, D. T., El-naas, M. H., Nasser, M., & Al-marri, M. J. (2017). A comprehensive review of electrocoagulation for water treatment: Potentials and challenges. *Journal of Environmental Management, 186*, 24-41.

[4] Apaydin, O., Kurt, U., & Gonullu, M. (2009). An investigation on the treatment of tannery wastewater by electrocoagulation. *Global Technology Journal, 11*(4), 546-555.

[5] Asia, U. N. E. (2003). Waste-water Treatment Technologies: A general review. Economic and Social Commission for Western Asia, United Nations.

[6] Bi, S. P., Wang, C. Y., Cao, Q., & Zhang, C. H. (2004). Studies on the mechanism of hydrolysis and polymerization of aluminium salts in aqueous solution: Correlations between the "Core-links" model and "Cage-like" Keggin-Al_{13} model. *Coordination of Chemical Revolution, 248*, 441-455.

[7] Matsui, Y., Yuasa, A., Furuya, Y., & Kamei, T. (2014). Dynamic analysis of coagulation with alum and poly-aluminium chloride. *Journal of Water Works Association, 90*, 96-106.

[8] Yang, Y. C., Abdul, T. S., Pei, L. Y., Ismail, M. S. N., Abdul, R. S. N. A, & Mohammad, A. M. (2007). A study on cactus *Opuntia* as natural coagulant in turbid water treatment. *Chemical Engineering Journal, 6*, 1-7.

[9] Yuliastri, I. R., Rohaeti, E., & Effendi, H. (2010). The use of *Moringa Oleifera* Seed Powder as Coagulant to improve the quality of wastewater and groundwater. *Chemical Engineering Journal, 2*(1), 25-34.

[10] Abidin, Z. Z., Ismail, N., Yunus, R., Ahamad, I. S., & Idris, A. (2011). A prelimary study on *Jatropha curcas* as coagulant in wastewater treatment. *Environment and Technology Journal, 32*(9), 971-977.

[11] Sowmeyan, R., Santhosh, J., & Latha, R. (2011). Effectiveness of herbs in community water treatment. *International Research and Journal in Biochemical, 1*(11), 293-303.

[12] Sutherland, J., Folkard, G., & Poirier, Y. (2011). *Moringa oleifera*, the constraints for commercialization. International Workshop: 29th October – 2nd November, Dar es Salaam, Tanzania, 2011.

[13] Shen, J., & Schäfer, A. (2014). Chemosphere Removal of fluoride and uranium by nanofiltration and reverse osmosis: A review. *Chemosphere Journal, 117*, 679-691.

[14] Jung, K., Hwang, M., Jeong, T., Minh, D., Kim, K., & Ahn, K. (2016). Journal of Industrial and Engineering Chemistry Entrapment of powdered drinking water treatment residues in calcium-alginate beads for fluoride removal from actual industrial wastewater. *Journal of Industrial and Engineering Chemistry, 39*, 101-111.

[15] Aoudj, S., Khelifa, A., Drouiche, N., Belkada, R., & Miroud, D. (2015). Simultaneous removal of chromium(VI) and fluoride by electrocoagulation with electro-floatation: Application of a hybrid Fe-Al anode. *Chemical Engineering Journal, 267*, 153-162.

[16] Kwaambwa, H., & Maikokera, R. (2007). A fluorescence spectroscopic study of a coagulating protein extracted from *Moringa oleifera* seeds. *Colloids and Surfaces B: Biointerfaces, 60*(2), 213-220.

[17] Aoudj, S., Drouiche, N., Hecini, M., Ouslimane, T., & Palaouane, B. (2012). Coagulation as a post-treatment method for the de-fluoridation of photovoltaic cell manufacturing wastewater. *Procedia Engineering Journal, 33*, 111-120.

[18] He, Z., Lan, H., Gong, W., Liu, R., Gao, Y., Liu, H., & Qu, J. (2016). Coagulation behaviours of aluminum salts towards fluoride: Significance of aluminium specification and transformation. *Separation and Purification Technology Journal, 164*, 137-144.

[19] Chen, Z., Fan, B., Peng, X., Zhang, Z., Fan, J., & Luan, Z. (2004). Evaluation of Al_{30} polynuclear species in poly-aluminum solutions as coagulant for water treatment. *Chemosphere Technology Journal, 6*, 912-918.

[20] Feng, C. H., Bi, Z., & Tang, H. X. (2015). Electrospray ionization time-of-flight mass spectrum analysis method of poly-aluminum chloride flocculants. *Environment and Science Technology Journal, 49*, 474-480.

[21] Tezcan, U. U., Koparal, A. S., & Bakir, O. U. (2013). Wastewater effluent standard in Malaysia [Online]. Viewed 2017 May 13rd. Available URL: http://www.doe.gov.my/eia/wp-content/uploads/2012/03/A-Guide-For-Investors1.pdf

[22] Bi, S. P., Wang, C. Y., Cao, Q., & Zhang, C. H. (2004). Studies on the mechanism of hydrolysis and polymerization of aluminum salts in aqueous solution: Correlations between the "Core-links" model and "Cage-like" Keggin-Al_{13} model. *Coordination of Chemical Revolution, 248*, 441-455.

[23] Liu, R. P., Zhu, L. J., Gong, W. X., Lan, H. C., Liu, H. J., & Qu, J. H. (2013). Effects of fluoride on coagulation performance of aluminum chloride towards Kaolin suspension. *Colloids Surface A: Physiochemical Engineering Aspects, 421*, 84-90.

[24] Ndabigengesere, A., Subba, N. K., & Talbot, B. G. (2011). Active agents and mechanism of coagulation of turbid waters using *Moringa oleifera*. *Journal of Water Research, 29*(2), 703-710.

[25] Choy, S. Y., Murthy, K., Prasad, N., Wu, T. Y., Raghunandan, M. E., & Ramanan, R. N. (2014). Utilization of plant-based natural coagulants as future alternatives towards sustainable water clarification. *Journal of Environmental Science, 26*(11), 2178-2189.

[26] Okuda, T., Baes, A. U., Nishijima, W., & Okada, M. (2001). Isolation and characterization of coagulant extracted from *Moringa oleifera* seed by salt solution. *Journal of Water Research, 35*(2), 405-412.

[27] McLachlan, D. R. (2012). Aluminum and the risk of Alzheimer's disease. *Environ-metrics Journal, 6*(3), 233-275.

[28] Anastasakis, K., Kalderis, D., & Diamadopoulos, E. (2009). Flocculation behaviour of *mallow* and *okra mucilage* in treating wastewater. *Desalination, 249*(2), 786-791.

[29] Mota, W. F., Finger, F. L., Cecon, P. R., Silva, D. J. H., Corrêa, P. C., Firme, L. P., & Neves, L. M. (2006). Study of natural coagulant, *Okra mucilage* for coagulation performance. *Chemical Engineering Journal, 24*(2), 255-258.

[30] Sher, F., Malik, A., & Liu, H. (2013). Industrial polymer effluent treatment by chemical coagulation and flocculation. *Journal of Environmental and Chemical Engineering, 1*, 648-689.

[31] Eckenfelder, W. W. (2006). Industrial Water Pollution Control. *Chemical Engineering Journal, 4*(2), 34-45.

[32] Freitas, T. K. F. S., Oliveira, V. M., Souza, M. T. F. D., Geraldino, H. C. L., Almeida, V. C., Fávaro, S. L., & Garcia, J. C. (2015). Optimization of coagulation-flocculation process for treatment of industrial textile wastewater using Okra (*A. esculentus*) mucilage as natural coagulant. Journal of *Industrial Crops & Products, 76*, 538-544.

[33] Miller, S. M., Fugate, E. J., Craver, V. O., Smith, J. A., & Zimmerman, J. B. (2008). Toward understanding of efficiency and mechanism of *Opuntia spp*. as natural coagulant for potential application in water treatment. *Environmental Science Technology, 42*, 4274-4279.

[34] Stephenson, R. J., & Duff, J. B. (2009). Coagulation and precipitation of a mechanical pulping effluent: Removal of carbon, colour and turbidity. *Water Resolution Technology, 30*,781-792.

[35] Parlikar, A. S., & Mokashi, S. S. (2013). De-fluoridation of water by *Moringa oleifera*- A Natural Adsorbent. *International Journal of Engineering Science and Innovative Technology (IJESIT), 2*(5), 245-252.

[36] Sutherland, J. P., Folkard, G. K., Mtawali, M. A., & Grant, W. D. (2007). *Moringa oleifera* as natural coagulant. *Journal of WEDC Conference.* University of Leicester, UK.

[37] Lhassani, A., Rumeau, M., Benjelloun, D., & Pontie, M. (2009). Selective demineralization of water by nanofiltration application to the de-fluoridation of Brackish water. *Journal of Water Research, 35*(13), 3260.

[38] Hu, K., & Dickson, J. M. (2006). Nanofiltration membrane performance on fluoride removal from water. *Journal of Membrane Science, 279*, 529-538.

eureca 2017 – Conference Paper
Paper Number 2CE08

Degradation Studies of Corn Husk-Filled Polylactic Acid Composites

Lee Kim Weng[1*], Pang Ming Meng[1], Koay Seong Chun[1], Albert Tshai Kim Yeow[2]

[1]*School of Engineering, Taylor's University, Lakeside Campus, No1, Jalan Taylor's, 47500 Subang Jaya, Malaysia*

[2]*University of Nottingham Malaysia Campus, Department of Mechanical, Materials and Manufacturing Engineering, Jalan Broga, 43500 Semenyih, Selangor Darul Ehsan, Malaysia*

[*]*Corresponding author: kimweng_lee@hotmail.com*

Abstract

Polylactic acid (PLA) is biodegradable aliphatic polyester, which is synthesized from lactic acid produced from agricultural products such as corn and sugarcane. However, brittleness and high cost limited the application of PLA. In this study, PLA/Corn husk (CH) composites with different corn husk content of 10%, 20%, and 30% were prepared using melt blending and compression molding process. Maleic anhydride grafted polypropylene (MAPP) was used as a compatibilizer to enhance the interfacial adhesion between corn husk and the PLA matrix. The degradation behaviors of PLA/CH composites were investigated by soil burial test, hygrothermal test, and thermal degradation test via TGA. Characterization analysis such as SEM was conducted to analyze the morphology of the composites. The results showed that the PLA/CH composites with 30% CH content has the highest weight loss in soil burial and hygrothermal test compared to composites with low CH content and neat PLA. This was because the natural fibers are lignocellulosic materials which easily attract microorganism to attack it. The weight loss increased with increase in fiber content. Therefore, the sample of 30% corn husk degraded rapidly. The weight loss for hygrothermal was higher than the soil burial test due to PLA was heated at 58^{o}C which closer to its glass transition temperature. The TGA results showed that the neat PLA has higher thermal stability compared to PLA/CH composites. The addition of corn husk decreased the thermal stability of the composites. This was due to the decomposition temperature of corn husk was occurred at 197^{o}C and thus caused an earlier thermal degradation occurring in PLA/CH composites. PLA/CH composite with MAPP shows faster degradation rate compared to the one without MAPP because the onset degradation temperature of MAPP occurred at 150^{o}C. The SEM images showed that the treated PLA/CH composites have good interfacial adhesion between corn husk and the PLA matrix compared to untreated composites. SEM micrographs for soil burial samples show rough areas and holes on the surface, indicates the sign of degradation.

Keywords: Polylactic acid, corn husk, maleic anhydride-grafted polypropylene, soil burial, hygrothermal

1. Introduction

Polymeric materials have gained high attention due to the structural versatility, excellent mechanical and thermal properties and high stability. Non-biodegradable polymer like plastic (eg., polypropylene, polyethylene) causes environment pollution because it is rarely consumed by bacteria. Therefore, they remain in nature without any degradation for a very long time [1]. Nowadays, most of the research is focused on biodegradable polymer because they have the potential to replace non-biodegradable polymer.

Polylactic acid (PLA) and polyvinyl alcohol (PVOH) are the most widely produced biodegradable polymers. PLA is a plant-derived biodegradable polymer whereas PVOH is petroleum-derived biodegradable polymer [2]. In general, PLA is polymerized from lactic acid which can be produced from different lignocellulosic biomass through fermentation. For example, lactic acid can be obtained from the fermentation of dextrose by bacteria and dextrose is derived from starch, sugarcane and corn [3-4]. Hence, PLA is a renewable biodegradable polymer. With the use of PLA, it can reduce dependence on conventional non-degradable plastics which made from petroleum-based resources [2]. Besides that, PLA has properties that are comparable to many commodity polymers (eg., polypropylene, polyethylene, polystyrene) such as high stiffness, clarity, gloss and UV stability [5]. PLA typically used as packaging material because it has high strength, thermal plasticity, and compostability [6]. However, PLA is brittle and high cost compared to most conventional plastic which causes PLA seldom been chosen by the manufacturer [7-8]. In order to reduce the cost of PLA, it can be combined with natural fiber.

Natural fiber reinforced polymer composites are widely used in many applications, but most of those composites are made from non-biodegradable polymers, like polyethylene and polypropylene. Recently, many research studies have focused on combining natural fiber obtained from agricultural waste and biodegradable polymer to produce composites. Natural fibers possess many advantages such as low density, low cost, high strength, stiffness, biodegradability, and renewability [5, 9]. There are many types of natural fibers that have been used as reinforcement in polymer composites such as bamboo, empty fruit bunch (EFB), ramie, coconut, and wood fiber [5, 7, 9-10].

In this work, corn husk (CH) was used as reinforcing filler in PLA composites since it is readily available and abundant in Malaysia. The production of the corn in Malaysia was about 58 metric tons in the year 2015 [11]. Corn husk is the outer protective covering of the corn and it comprised of 40% cellulose, 45% hemicelluloses, 7% lignin, 2% protein and 3% ash [12]. The composition of corn husk is similar to wood fiber; thus, it has great potential to use as natural fiber in PLA composites. The addition of corn husk in PLA composites could improve the mechanical properties and reduce the cost of PLA.

One of the disadvantages of natural fiber filled PLA composites is low compatibility between the hydrophilic character of the polar filler and hydrophobic character of the non-polar matrix polymer. Natural fiber does not disperse evenly in polymer matrix due to strong intermolecular hydrogen bonding between the natural fibers [13]. The mechanical properties of the composites were get affected due to low compatibility and interfacial adhesion. To overcome the low compatibility and improve

the interfacial adhesion of the natural fiber and polymer matrix, compatibilizer like maleic anhydride-grafted polypropylene (MAPP) can be introduced to composites. There are many studies showing the addition of MAPP increases the strength of composites by improving the filler-matrix adhesion [13-15].

The objectives of the study are to prepare the corn husk-filled PLA composites with different loadings of corn husk and study the degradation behavior of corn husk-filled PLA composites. Degradation of the polymer is defined as a process which deteriorates the polymer properties. A complete degradation is achieved over a period a time when there is no residue remains or when the polymer is completely converted into salts and gaseous products [15]. The degradation behaviors of corn husk-filled PLA composites were investigated by soil burial test, hygrothermal test, and thermal degradation test via Thermo Gravimetric Analysis (TGA). Characterization test such as Scanning Electron Microscopy (SEM) was carried out to investigate the surface morphology of the composites.

Soil burial is a traditional and standard method for degradation because of its similarity to the actual condition of waste disposal [1]. For soil burial test, the depth of burying of the samples varies for the different researcher. According to Obasi et al. [16], the samples were buried in boxes with tiny openings containing soil at a depth of 15 cm. Ainun et al. [17] put the samples at 10 cm depth in the compost soil. The degradation rate is dependent on the presence of the microorganism in the soil. Soil burial test was carried out for three months to study the weight loss. The weight loss was caused by the breakdown of the long polymer chain by microorganism inside the soil.

Hygrothermal aging is a degradation test that combines the effects of moisture and temperature [19]. This method was carried out to investigate the changes of PLA composites that affected by different temperature and humidity. PLA has a good degradation rate at 58^{o}C because this temperature is closer to its glass transition temperature which is between 60^{o}C to 65^{o}C [20].

2. Methodology

2.1 Materials

The materials used were polylactic acid 3051D (PLA), corn husk and maleic anhydride grafted polypropylene (MAPP). PLA was provided by Nature Work LLC with a melting temperature of 170^{o}C and a glass transition temperature range from 55 to 60^{o}C. MAPP used was supplied by Merck. The corn husks were obtained from the corn farm located in Cameron Highlands. The corn husks were prepared as filler in following sequences:

1. Collected corn husk was washed with water
2. The washed corn husk was cut into small pieces and dried in an oven at 80^{o}C for 8 hours.
3. The dried corn husks were ground into fine powder using grinder
4. Fine powder corn husk was passed through 100 mesh sized sieve to obtain homogenous size corn husk fiber.

2.2 Preparation of PLA/CH composites

The PLA/Corn husk composite was mixed using a Haake internal mixer (model: Polylab System E93) according to the formulation shown in Table 1. Prior to melt blending process, PLA and corn husk powder were dried at temperature 80^{o}C for 24 hours in an oven to remove moisture. The process temperature and rotor speed were 180^{o}C and 50 rpm respectively. The processing time was 10 minutes in order to obtain a homogenous compound. For treated PLA/CH composites, MAPP was mixed with PLA and corn husk with a processing time of 15 minutes. The processing method was referred to H. Salmah et al. [13], A. N. Borhan et al. [17], and P. Prahaladar et al. [21].

Table 1. Formulation of untreated and treated PLA/Corn Husk Composites

Designation of composites	PLA (wt%)	Corn husk (wt%)	MAPP (wt%)
Neat PLA	100	-	-
PLA/Corn Husk	80	20	-
PLA/Corn husk/MAPP	87	10	3
PLA/Corn husk/MAPP	77	20	3
PLA/Corn husk/MAPP	67	30	3

The PLA/Corn husk composites were molded into a sheet with a dimension of 12cm x 13cm size with 0.1cm thickness. The PLA/CH compound was compressed at a temperature of 180^{o}C and pressure of 150 bar by using a hot press machine (model: Moore E53). The compound was preheated for about 5 minutes to soft and then compressed for 2 minutes. Last, the sample was cooled under same pressure for 5 minutes until the temperature was dropped to 60^{o}C before taking out the sheet. The moulding procedure was done based on A. N. Borhan et al. [17] and P. Prahaladar et al. [21].

The polymer sheet was cut into a square shape with the dimension of 2cm x 2cm in order to conduct soil burial and hygrothermal test.

2.3 Soil Burial Test

Soil burial test was carried out to investigate the degradability of PLA/CH composites. The soil burial test method used in this experiment following method suggested by A. N. Borhan et al. [17] and H. C. Obasi et al. [16]. Three pieces of the sample of each formulation were used to conduct soil burial test to get an average reading. The initial weights of the samples were weighed using a weighing balance. The samples were buried in composted soil at a depth of 10 cm at room temperature. The soil was sprayed with water to maintain the moisture for a better microbial activity. Different time intervals were set which is 1st, 2nd, 3rd, 7th, 14th, 21st, 30th, 45th, 60th, 75th, and 90th day in order to investigate the degradation rate. The samples were wiped to remove any leftover soil and dried to a constant weight in the oven at a temperature of 50^{o}C to remove moisture after taking out from the soil. The percentage weight loss was calculated using equation (1):

$$weight\ loss\ (\%) = \frac{W_i - W_0}{W_i} \times 100\% \quad (1)$$

Where W_i is the initial weight (g) and W_o is the final weight (g)

2.4 Hygrothermal Test

The temperature of water bath used in the hygrothermal test was 58°C because PLA has the highest degradation rate at this temperature [21]. The temperature of 58°C was closer to PLA glass transition temperature which is between 60°C to 65°C. The samples of each formulation were immersed in the water bath. The initial weights of the samples were weighed using weighing balance. The samples were weighed at different time intervals which are 1st, 2nd, 3rd, 5th, 7th, and 14th day in order to investigate the degradation rate. The percentage weight loss was calculated using the equation (1).

2.5 Thermo Gravimetric Analysis (TGA)

TGA (Model: Perkin Elmer) was used to measure the degradation temperature of the PLA/Corn husk composites. The temperature range was set from 30°C to 800°C at a rate of 20°C/min under nitrogen environment.

2.6 Scanning Electron Microscopy (SEM)

A scanning electron microscope (model: Quanta 400 FEG) was used to investigate the PLA/CH composites morphology of different loadings of corn husk after degradation. It was operated at 20 kV.

3. Results and Discussion

3.1 Soil Burial

Figure 1 illustrates the weight loss trend of soil burial sample of neat PLA and PLA/CH composites. The sample of 30% corn husk has the highest weight loss compared to other formulation such as 10 and 20% corn husk loadings. The weight loss attained by the treated 30% corn husk was reported as 2.53% after 90 days. The weight loss of pure PLA was the lowest among others. The reason of PLA has the lowest weight loss is it having slow hydrolysis rate at ambient temperature [17]. Therefore, there was only a small change in weight loss. Lee et al. [22] studied the biodegradation of PLA/bamboo fiber and reported that the degradation rate of PLA was slow, but enhanced in the presence of bamboo fiber. The weight loss of the composites increased as the fiber content increased. The more the corn husk used, the higher is the weight loss. This is because the natural fibers are lignocellulosic materials which easily attract microorganism to attack it [18]. Thus, the higher corn husk content (30%) has faster degradation rate. This was due to the microorganism present in the soil consumed the corn husk filler and created pits and voids in the PLA matrix [23]. Yaacob et al. [18] studied the biodegradation of PLA/PSP and they reported that the weight loss of the composites increased as the PSP content increased. In general, faster degradation rate

achieved during the first 21 days, afterward, the degradation activity slowly reduced until all the carbon sources are utilized. The degradation was due to the invasion of microorganisms into the substrate and absorption of the moisture by the samples [24]. Based on the results, it was proved that the biodegradability of the composites can be enhanced with the addition of natural filler into PLA matrix. In addition, the difference in the degradation behavior of the composite with and without MAPP compatibilizer can be observed. At the beginning stage, the treated 20% corn husk showed slightly higher weight loss compared to the untreated 20% corn husk. However, once the soil burial test proceeded for a longer period, the weight loss between the treated and untreated composites is not varied much, both reported between 1.45 to 1.49%.

3.2 Hygrothermal

Figure 2 displays the weight loss of pure PLA and PLA/CH composites for the hygrothermal test. It can be seen that the weight loss of the composites increased as the fiber content increased. The more the filler content used, the higher is the weight loss. Thus, the sample of 30% corn husk degraded rapidly as compared to other composites. It had the highest weight loss of 15.92% at day 14 while pure PLA showed 4.4% at day 14. Therefore, it was proved that the addition of natural filler into PLA can accelerate the degradation process, and this is supported by previous research [16-18]. A comparison has been done on the sample of 20% corn husk with and without MAPP. It showed that the weight loss of the sample with MAPP was slightly higher than the one without MAPP. Besides that, the percentage weight loss for the hygrothermal test was higher than the soil burial test. This is attributed to the specimens were subjected to heat (high temperature at 58^{o}C) and also moisture attack in the hygrothermal test as compared to soil burial which is kept at indoor room temperature. The samples were broken into pieces after 2 weeks.

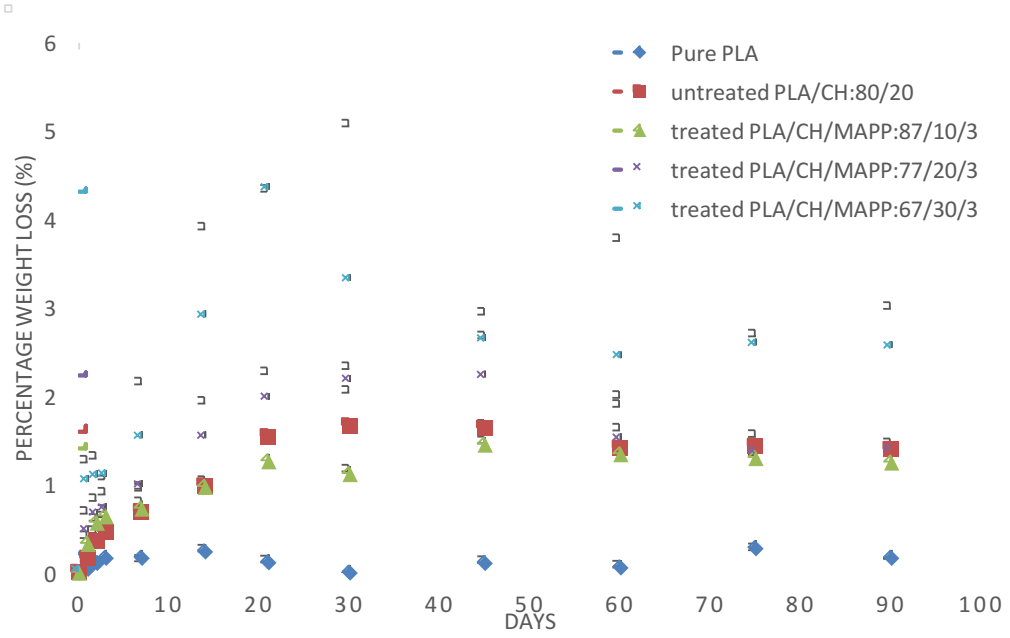


Figure 1 Percentage weight loss against days for soil burial test

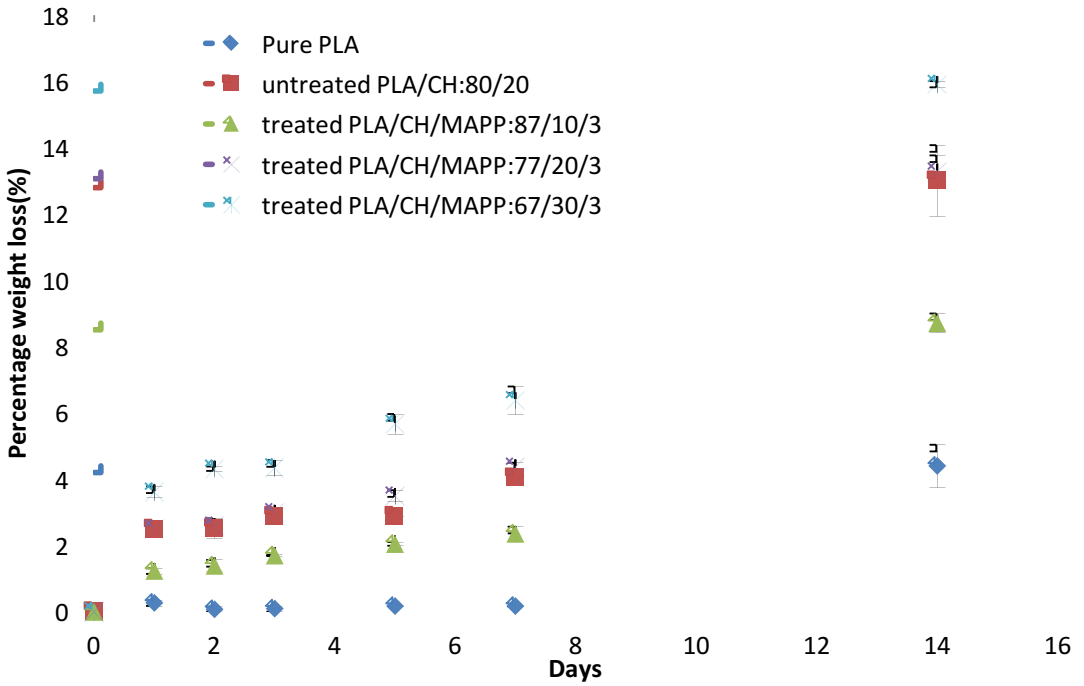


Figure 2 Percentage weight loss for hygrothermal test

3.3 Thermo Gravimetric Analysis (TGA)

Figure 3 shows the TGA curves of neat PLA and PLA/CH composites. The obtained results were tabulated in Table 2. From Table 2, it can be seen that neat PLA has higher onset degradation temperature (380^{o}C) compared to PLA/CH composites. The increase in CH content reduced the onset of degradation temperature of PLA/CH composites. According to Mendes et al. [25], the corn husk has lower thermal stability and it starts to decompose at a temperature of 197^{o}C. For this reason, the addition of corn husk caused an earlier thermal degradation occurring in PLA/CH composites. Moreover, the untreated PLA/CH composites showed higher onset degradation temperature than treated PLA/CH composites. The treated PLA/CH composites have lower PLA content compared to untreated PLA/CH, since part of the PLA resin had been replaced by the MAPP. In addition, the MAPP exhibited lower thermal stability compared to neat PLA where the onset degradation temperature of MAPP occurs at 150^{o}C [26]. Therefore, the thermal stability of the treated PLA/CH composites was lower than the untreated PLA/CH composites. It can be said that the addition of MAPP did not show improvement in thermal stability of PLA/CH composites. The residual weight indicated the total amount of the fiber was decomposed and become char [27]. Pure PLA has the 0% residual weight, thus it was fully decomposed under high temperature and become gaseous product [28]. The residual weights of the treated PLA/CH composites increased from 1.6% to 7.9%.

Table 2 Thermal properties of PLA/Corn husk composites

Samples	Degradation temperature, T_{onset} (^oC)	Residual weight, % at 800^oC
Pure PLA	380.21	0
PLA/corn husk 20%	341.45	0.03
PLA/corn husk 10%/MAPP 3%	345.45	1.60
PLA/corn husk 20%/ MAPP 3%	334.38	4.50
PLA/corn husk 30%/MAPP 3%	300.66	7.90

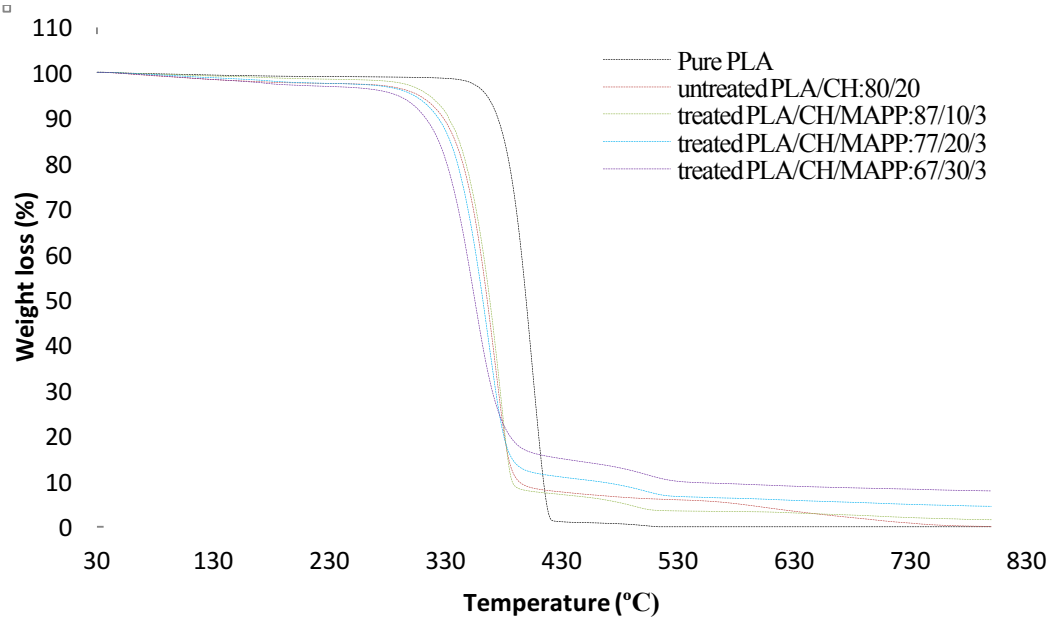


Figure 3 TGA curves of PLA and PLA/CH composites

3.4 Morphology Properties

Scanning electron microscopy (SEM) was conducted to observe the surface morphology of PLA/CH composites before and after soil burial. SEM analysis gives a better image about the fiber morphology and diameter. Figure 4 shows the SEM images of untreated and treated PLA/CH composites before soil burial test at different magnification whereas Figure 5 illustrates the SEM pictures of untreated and treated PLA/CH composites after burial test for 75 days.

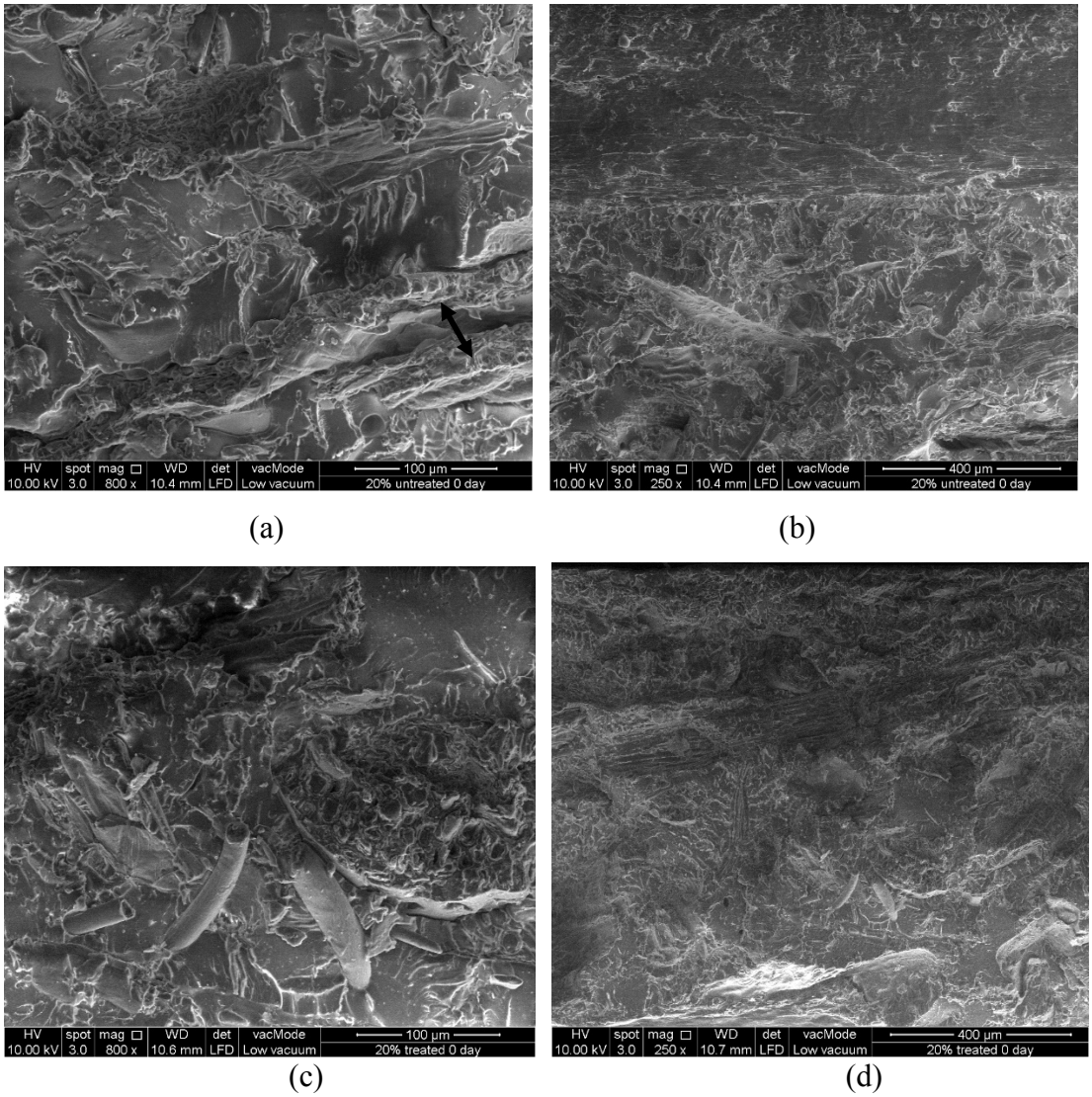


Figure 4. SEM images of untreated PLA/CH (20%) composites of (a) 100x; (b) 400x and treated PLA/CH composites of (c) 100x; (d) 400x, before soil burial

Figure 4(a) and (b) are the untreated PLA/CH composites and it shows poor interfacial adhesion between the PLA matrix and the corn husk due to weak dispersion in PLA matrix. From Figure 4(c) and (d), it can be seen that the interfacial adhesion of the treated PLA/CH composites was better than the untreated composites. However, there are some holes appeared on the surface of the sheet and this may be due to the corn fibers pulled out during the cutting process.

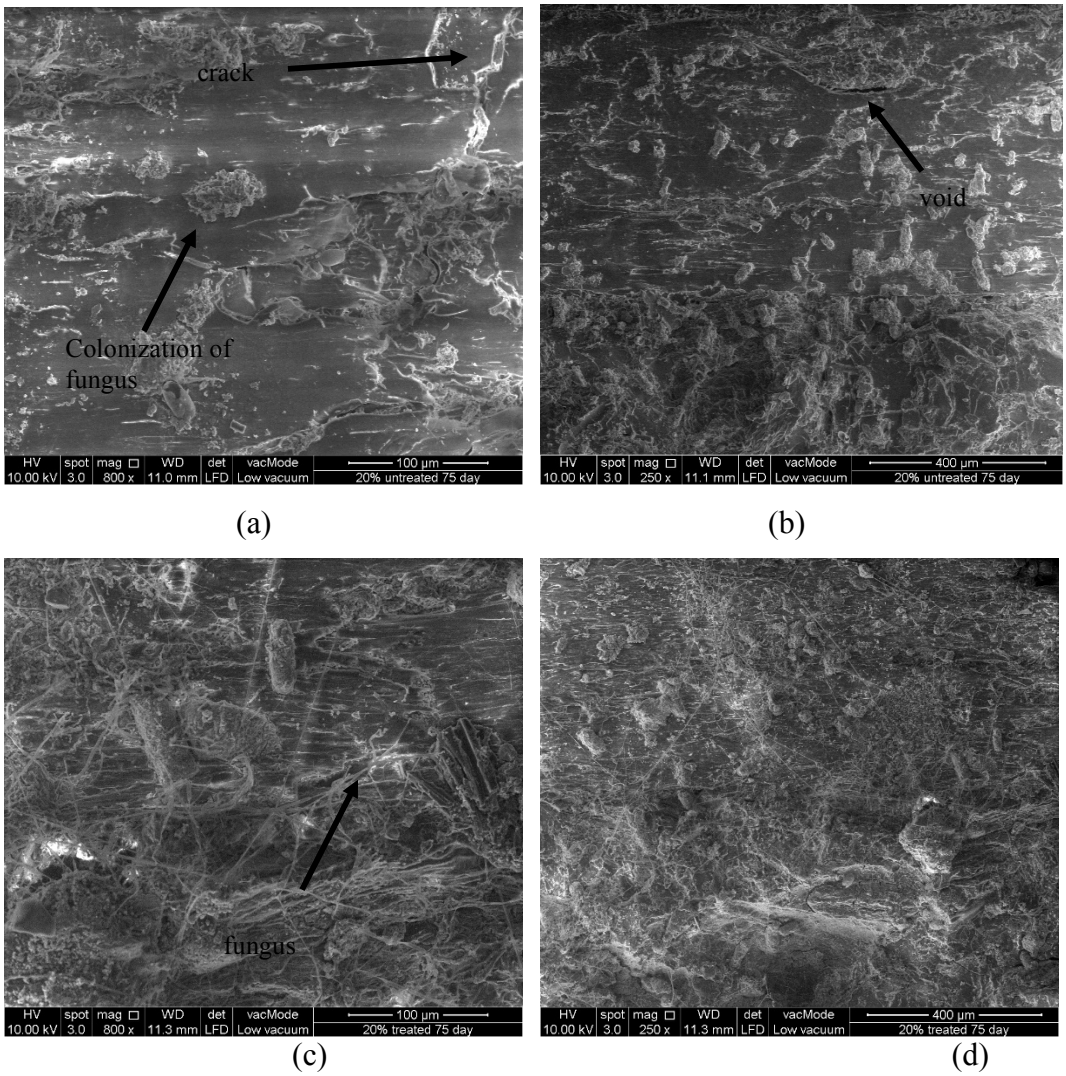


Figure 5 SEM images of untreated PLA/CH (20%) composites of (a) 100x; (b) 400x and treated PLA/CH composites of (c) 100x; (d) 400x, after burial test for 75 days

Figure 5 shows erosions on the surface of the PLA/CH sheets after buried in the soil for 75 days. It can be seen that the rough areas and the holes were appeared on the surface of the PLA/CH sheets by biodegradation. The fungi were distributed randomly on the surface of the sheet. The size of the cracks and pores were larger in the untreated PLA/CH sheet compared to the treated PLA/CH sheet. This is because MAPP increases the interfacial adhesion between the corn husk and PLA matrix, thus the treated PLA/CH sheet did not show many cracks and holes on the surface. However, the strength of the samples was decreased due to the invasion of microorganism. The diffusion of water caused swelling in the polymer which boosted the microorganism attack and improved the microbial activity [29]. A similar result was reported by Yaacob et al. [18] on the PLA/PSP bio-composite.

4. Conclusions

In conclusion, PLA/CH composites with different corn husk content were prepared using the melt blending and compression molding process. MAPP was used

as a compatibilizer to overcome the low compatibility and improve the interfacial adhesion of the composites. The degradation behaviors of PLA/CH composites were investigated by soil burial test and hygrothermal test, and the thermal degradation test via TGA. Characterization test such as SEM was conducted to observe the morphology in PLA/CH composites upon degradation. For soil burial test, the neat PLA showed small changes in weight loss because it had slow hydrolysis rate at ambient temperature. Besides that, the composite with high corn husk content showed the highest weight loss compared to other composites. The weight loss of the composites increased as the fiber content increased. This was due to the corn husks are lignocellulosic materials which easily attract microorganism to attack it. The biodegradability of the composites can be enhanced with the addition of natural filler into PLA matrix. The weight loss for the hygrothermal test was similar to soil burial test where the sample of 30% corn husk has the highest weight loss. The thermal stability of the PLA/CH composites was characterized using TGA. The thermal stability and degradation temperature were found to be high for the pure PLA when compared to the bio-composites because the decomposition temperature of corn husk was 197^{o}C. Hence, the addition of corn husk caused an earlier thermal degradation occurring in PLA/CH composites. The morphology of the PLA/CH composites was determined using SEM. The untreated PLA/CH composites showed poor adhesion between the PLA matrix and the corn husk. The treated PLA/CH composites had a slow degradation rate compared to untreated PLA/CH composites. With the addition of MAPP, the interfacial adhesion between the PLA matrix and the corn husk can be enhanced thus having slow degradation. The present of void for the sample after soil burial and suspected the present of fungus on the surface of the specimens.

References

[1] Kh. M. Siddiquee, Dr. M. M. Helali, Dr. Md. A. Gafur, S. Chakraborty. (2014). 'Investigation of an Optimum Method of Biodegradation Process for Jute Polymer Composites', *American Journal of Engineering Research.*

[2] T. S. Lee. (2012, October 19). *Polylactic Acid.* (1st edition). [On-line]. Available: https://www.elsevier.com/books/polylactic-acid/sin/978-1-4377-4459-0 [Nov 20, 2016].

[3] D. Y. Liu, X. W. Yuan, D. Bhattcharyya, A. J. Eateal. (2010). 'Characterisation of solution cast cellulose nanofiber-reinforced poly (lactic acid)', *eXPRESS Polymer Letters.*

[4] W. Jia, R. H. Gong, C. Soutis, P. J. Hogg. (2014). 'Biodegradable fiber reinforced composites composed of polylactic acid and polybutylene sucinante', *Plastic Rubber and Composites.*

[5] Y. Tao, L. Yan, R. Jie. (2009). 'Preparation and properties of short natural fiber reinforced polylactic acid composites', *Transactions of Nonferrous Metals Society of China.*

[6] Y. Tadashi, Y. Masayuki. (2008). 'Structure and properties of biomass-based polyester blends of PLA and PBS', *European Polymer Journal.*

[7] W. Sujaritjun, P. Uawingsuwan, W. Pivsa-Art, H. Hamada. (2013). 'Mechanical Property of surface modified natural fiber reinforced PLA bicomposites', *Energy Procedia.*

[8] D. Cohn, A. H. Salomon. (2005). 'Designing biodegradable multiblock PCL/PLA Thermoplastic Elastomers [J]', *Biomaterials.*

[9] W. L. Ngo, M. M. Pang, L. C. Yong, K. Y. Tshai. (2014). 'Mechanical Properties of Natural Fiber (Kenaf, Oil Palm Empty Fruit Bunch) Reinforced Polymer Composites', *Advances in Environmental Biology.*
[10] M. S. Huda, L. T. Drzal, A. K. Mohanty, M. Misra. (2015). 'Wood Fiber Reinforced Polylactic Acid Composites', *5th Annual SPE Automotive Composites Conference.*
[11] IndexMundi. (2016). *Malaysia Corn Production by Year* [online]. Viewed 2016 Dec 10. Available: https://www.indexmundi.com/agriculture/?country=my&commodity=corn&graph=production
[12] N. J. Chitra, R. Vasanthakumari. (2012). 'Studies on Polypropylene Bio-composites with Corn Husk Waste', *International Journal of Scientific & Engineering Research.*
[13] H. Salmah, M. Z. Marliza, E. Selvi. (2014). 'Biocomposites from Polypropylene and Corn Cob: Effect Maleic Anhydride Polypropylene', *Advances in Civil, Environmental, and Materials Research.*
[14] K. Jarukumjorn, W. Sutapun, Y. Ruksakulpiwat, J. Kluengsamrong. (2008). 'Effect of Silane Coupling Agent and Compatibilier on Properties of Short Rossells Fiber/Poly(propylene) Composites', *Macromolecular Symposia.*
[15] S. A. A. Ramazani, M. A. Valami, M. Khak. (2009). 'Effect of Poly(Propylene-g-maleic Anhydride) on the Morphological, Rheological, and Mechanical Properties of PP/HDPE Blend', *Journal of Thermoplastic Composite Materials.*
[16] H. C. Obasi, F. N. Onuoha, I. O. Ezo, S. C. Nwanonenyi, I. O. Arukalam, P. C. Uzoma. (2013). 'Effect of Soil Burial on Properties of Polypropylene (PP)/Plasticized Potato Starch (PPS) Blends', *The International Journal of Engineering and Science*, vol. 2, pp. 14-18.
[17] A. N. Borhan, M. M. Pang, K. Y. Tshai. (2016). 'Degradation Studies of Microcrystalline Cellulose Reinforced Polylactic Acid Composites', *5th Eureca Conference.*
[18] N. D. Yaacob, H. Ismail, S. S. Ting. (2016). 'Soil burial of PLA/Paddy Straw Powder Biocomposites', *BioResources*, vol. 11, no. 1, pp. 1255-1269.
[19] W. S. Chow, A. A. Bakar, Z. A. M. Ishak. (2005). 'Water Absorption and hygrothermal Aging Study on Organomontmorillonite Reinforced Polyamide 6/Polypropylene Nanocomposites', *Wiley InterScience*, vol. 98, no. 2, pp. 780-790.
[20] P. Stloukal, A. Kalendove, H. Mattausch, S. Laske, C. Holzer, M. Koutny. (2015). 'The influence of a hydrolysis-inhibiting additive on the degradation and biodegradation of PLA and its nanocomposites', *Elsevier*, vol. 41, pp. 124-132.
[21] P. Prahaladar, M. M. Pang, K. Y. Tshai. 'Preparation and Properties Study of PLA/Waste Tea Leaf Fiber Composites', presented at the 4th Eureca Conference, Malaysia, 2015.
[22] S-H. Lee, S. Wang. (2006). 'Biodegradable polymers/bamboo fiber biocomposite with bio-based coupling agent', *Elsevier*, vol. 37, no. 1, pp. 80-91.
[23] H. C. Obasi, G. C. Onuegbu. (2013). 'Biodegradability and Mechanical Properties of Low Density Polyethylene/Waste Maize Cob Flour Blends', *International Journal of Applied Sciences and Engineering Research*, vol. 2, no. 3.
[24] N. Gautam, I. Kaur. (2013). 'Soil burial biodegradation studies of starch grafted polyethylene and identification of Rhizobium meliloti therefrom', *Journals of Environment Chemistry and Ecotoxicology*, vol. 5, no. 6, pp. 147-158.

[25] C. A. D. C. Mendes, F. A. D. O. Adnet, M. C. A. M. Leite, C. R. G. Furtado, A. M. F. D. Sousa. (2014). 'Chemical, Physical, Mechanical, Thermal and Morphology Characterization of corn husk residue', *Elsevier*, vol. 13.
[26] H. S. Kim, B. H. Lee, S. W. Choi, S. Kim, H. J. Kim. (2007). 'The effect of types of maleic anhydride-grafted polypropylene (MAPP) on the interfacial adhesion properties of bio-flour-filled polypropylene composites', *Elsevier*, vol. 38, pp. 1473-1482.
[27] C. Lee, M. M. Pang. 'Preparation and Characterisation of Talc-filled Polylactic Acid Composites', presented at 7th Eureca Conference, Malaysia, 2016.
[28] G. R. Rajandran, M. M. Pang. 'Preparation and characterization of Bentonite-filled Polylactic Acid (PLA) Composites', presented at 7th Eureca Conference, Malaysia, 2016.
[29] R. H. Falk, C. Felton, T. Lundin. (2000). 'Effect of weathering on color loss of natural fiber thermoplastic composites', *International Symposium on Natural Polymers and Composites*, pp. 382-385.

Effect of Radiation Energy on Crystallization Behaviour of Ethylene-Vinyl-Acetate

Lim Khai Ming, Suganti Ramarad

School of Engineering, Taylor's University Lakeside Campus, Malaysia

limkhaiming@hotmail.com
Suganti.Ramarad@taylors.edu.my

Abstract

Ethylene-Vinyl-Acetate is a synthetic thermoplastic polymer that is flexible, possess high chemical resistance, tough and transparent. It has many applications from industrial to consumer products because of its properties. Many studies have been done on improving properties of EVA, including chemical and radiation crosslinking. Radiation crosslinking improve crystallinity of polymers up to an optimum radiation dose. Radiation sensitizers are added into polymers to improve the crosslinking process when polymers are exposed to irradiation. In this research, the main objectives of this study is to access the crystallization properties of EVA with and without electron beam irradiation, and also to study the effects of radiation sensitizers on EVA when exposed to EB irradiation. The samples are melt compounded and compression moulded for consistency, and are irradiated at 50 to 200 kGy radiation doses. The computerized differential scanning calorimeter is used to study the crystallization behavior of EVA when exposed to electron beam irradiation. Data comparison of effect of radiation dose and the heating and cooling rate was done. It can be concluded that the optimum condition for obtaining the highest percentage levels of crystallinity is 100 kGy radiation dose and 20 ºC/min heating and cooling rate based on the result obtained in this research. Comparison between EVA/TMPTA and EVA/TPGDA shows that the EVA/TPGDA blend is performing better with a significant 1.95% more crystallinity than the EVA/TMPTA blend at optimum conditions.

Keywords: Crystallization, Differential Scanning Calorimetry, EVA, Electron Beam Irradiation, Radiation Sensitizers.

1. Introduction

Ethylene Vinyl Acetate (EVA) is a synthetic polymer that is common in a lot of consumer products. The weight percentage of vinyl acetate in ethylene vinyl acetate ranges from approximately 10% to 40% depending on the application of the thermoplastic polymer. As such, the physical properties of ethylene vinyl acetate will change depending on the weight percentage of vinyl acetate. There are many applications of EVA; namely hot melt adhesives with the addition of petroleum wax and resin tackifier, a component in drug delivery services, padding for footwear and sportswear components, plastic parts in injection moulding, and a major component in packaging materials.

A polymer can be described simply as a big molecule that is consisted of numerous smaller structural units that are labeled as monomers, and they are bonded together mainly by covalent forces in all kinds of patterns. A molecule can only be labeled as a monomer when it contains two or more bonding sites which are used to link with other monomers. The process of changing the monomers into polymers are called polymerization, and the two main polymerization methods are called step-growth and addition [1]. In the case of EVA, it is a synthetic polymer in the category of thermoplastic.

There are two regions in solid state polymer that is important to note when studying the properties of a polymer, namely amorphous and crystalline region. The amorphous state of a polymer refers to randomly arranged polymer chains in a solid state. Whereas the crystalline state of a polymer refers to orderly arranged polymer chains in a solid state [2]. All crystalline polymers have a certain percentage of amorphous portion in it. It has been found that three parameters can be used to determine the crystalline properties of polymers. The first one is called Tg, the glass transition temperature. Tg is the temperature that differentiates the heat capacity of a polymer. If the temperature goes above Tg, the polymer has a higher heat capacity than below it. This glass transition process is called a second order transition [2]. Tc is the temperature that separates the amorphous and crystalline region. If the temperature is below Tc, it means the polymer would be in the amorphous region and it would be in crystalline region if temperature is above Tc. The third one is called Tm, the melting temperature. Tm is the temperature that separates the solid and liquid state of a polymer. If the temperature goes above Tm, the polymer would be in the liquid state [2]. The melting process is a called a first order transition [2].

In a general sense, crystallization is a process whereby a desired substance crystallizes or solidifies from a cooled saturated solution after heating a mixture, thus creating a separation process. There are two crucial steps in the crystallization process, nucleation and crystal growth. In order for the steps to happen, two requirements must be met. Firstly, is the polymer chains will only pack into a regular crystal lattice when the polymer chain itself is regular and ordered. Secondly, the forces that bind the polymer chains with each other in the crystal lattice must be strong enough to offset the disordering effect of thermal energy [2].

There are five main factors that affect the crystallinity of a polymer. First factor is the symmetry of the structure of the polymer chain. If the polymer chains tend to be symmetrical, this will increase the entropy and stabilize the crystal, thus increasing the

Tm value. Second factor is the forces that bind the polymer chains with each other. If the forces are strong, they will greatly increase crystal stability and increase Tm value as well. The third factor is the tacticity of a polymer. If a polymer chain has big pendant groups, it will be harder to form crystals. The fourth factor is the branching of the polymer chain. If the polymer chain branches a lot, the packing efficiency will decrease, which will also decrease the Tm and crystalline content. The fifth factor is the molar mass of the polymer. If the number of polymer chains are long, the energy required to melt is increased, thus Tm is increased [2].

In previous work [3] [4] [5] [6], it is found that when a polymer is cooled from the melt, it will form a crystalline structure that will affect certain properties such as toughness. In other words, the process to initiate and form crystallization will affect the crystallinity of the substance. Many studies have focused on how and what affects the crystallization of a polymer. The crystallinity of a substance can be observed and analysed by using the computerized differential scanning calorimeter. The DSC is used to measure and record the crystallization temperature and the melting temperature by producing a heat flow curve which highlights the melting peak Tm and the crystallization peak Tc.

Studies have shown that the physical and chemical properties of EVA can be enhanced by exposing it with electron beam irradiation [7] [8] [9]. This method of enhancing the properties of EVA is called radiation processing. The main focus of this report, the crystallization of EVA, is found to be affected due to exposure to irradiation, possibly by affecting one of the factors mentioned above. This can be seen from the changes in the crystallization and melting peaks when the polymer is exposed to electron beam irradiation. Treating EVA with ionizing radiation promotes crosslinking and chain scissions at molecular level of EVA, which will consequently affect the crystallinity of the EVA. While certain level of crosslinking is expected to increase crystallinity, chain scissions is expected to decrease crystallinity. On the other hand, irradiation can also cause severe degradation to polymers [10] [9]. One of the degradation effects is when oxidation occurs to polymers irradiated in air atmosphere [7]. Furthermore, when polymer is exposed to high levels of irradiation dosages, the chain scission effect will be dominant to the crosslinking effect which will consequently decrease the crystallinity of the EVA.

However, the degradation effect can be reduced or minimized with the addition of irradiation sensitizers [10] [8]. Irradiation sensitizers are essentially components that lowers the polymer absorbed dose requirement and maintain the desired amount of crosslinking. Their main purpose is to accelerate the crosslinking process of a polymer. In this project, the study focuses on the effect of electron beam irradiation and the addition of irradiation sensitizers on the isothermal and non-isothermal crystallization behaviour of EVA using differential scanning calorimetry.

In this project, the crosslinking method used is radiation crosslinking instead of the traditional chemical crosslinking. Type of radiation used is electron beam irradiation. EVA is chosen as the sample polymer for this research because EVA has a good crosslinking to scission ratio of 0.23, high tolerance dose of (100-3000) kGy and acceptable undesired side effect of discolouration [11]. Two types of radiation sensitizers are used in this research, which are trimethylol propane triacrylate (TMPTA) and tripropylene glycol diacrylate (TPGDA). They are used in this research with the

reason past studies have found that they improve effectiveness of EVA when exposed to radiation [12].

There are two main objectives that is achieved in this study. The first objective is to study the crystallization behaviour and kinetics of EVA with and without electron beam irradiation. The second objective is to study the effects of EB irradiation in the presence of radiation sensitizers on the crystallization behavior and kinetics of EVA.

2. Methodology

Methodology for this research is divided into three sections, which are the materials, the methods used, and the data analysis tools.

2.1 Materials

The main subject of study in this project is Ethylene vinyl acetate (EVA) with a 18% vinyl acetate content, a melt flow index (MFI) of 2.3g/10min and a density of 0.947 g/cm^3. EVA with low VA content is chosen for this project because research indicated at higher VA content the crystallization tendency of EVA would be decreased [13]. The irradiation sensitized crosslinking agents that are used in this project would be trimethylol propane triacrylate (TMPTA) and tripropylene glycol diacrylate (TPGDA). Studies have shown that the mentioned radiation sensitizers have shown positive effect in improving properties of polymers [12] [14].

2.2 Melt Compounding

The purpose of melt compounding is to properly blend two different substances together to form an evenly distributed blend. EVA and irradiation sensitized crosslinking agents is mixed in an internal mixer (Brabender Plasticoder PL2000-6 equipped with co-rotating blades and a mixing head with a volumetric capacity of 69cm^3). The rotor speed is set to 50 rpm and the blending temperature is set to 120ºC. EVA is fed into the internal mixer chamber and melting time is set to two minutes. The irradiation sensitized crosslinking agents are mixed into the internal mixer chamber at the third minute. The total mixing time for all designation of blends is ten minutes for consistent thermal history purpose. The solid taken out of the internal mixer is cut into tiny pieces and kept in clean sealed plastic bags before the next process to take place. Studies have shown that the optimal weight percentage of radiation sensitizers for crosslinking purposes tend to be 3 wt% [15].

2.3 Compression Moulding

The aim of compression moulding is to obtain a consistent size and shape of the solid from the melt compounding process. The tiny pieces from the internal mixer are placed with some excess into a steel frame flash mould (200mm x 200mm) covered by disposable polypropylene (PP) sheets (200mm x 200mm x 0.1mm) and aluminium plates (200mm x 200mm x 2mm) on both sides. In this way, the test specimens' length and width is determined by the cavity size of the flash mould. The disposable polypropylene sheets are used to prevent the slab from adhering to the aluminium plates.

The mould containing the tiny pieces are positioned directly in between the two press platens of an automated hydraulic heated press (LP-S-50 Scientific Hot and Cold Press). The heat of the press platens is set to 130ºC, which is sufficient for heat to be transferred via conduction from the plates to the specimen. Firstly, the specimen is preheated for three minutes without any pressure applied to it so that the specimen can melt. Secondly, the specimen is pressure cycled from 0 up to 10 MPa for twenty seconds to distribute the melted specimen evenly in the cavity. Lastly, the specimen is pressure cycled at 10 MPa for three minutes. The specimen is then subjected to cooling process by carefully removing the mould from the heated press to the adjacent cooling press equipped with water circulating channels pumped with chilled (20ºC) water. A cooling rate of 45ºC/min with 10 MPa holding pressure is applied to the specimen for two minutes to prevent non-uniform cooling and warping of the slabs [16].

2.4 Electron beam irradiation

The moulded slabs are irradiated with a 3 MeV electron beam accelerator at doses of 100, and 200 kGy. The settings of the beam accelerator is the acceleration energy of 2 MeV, beam current of 5 mA, and dose rate of 50 kGy per pass.

2.5 Crystallinity

The final procedure step is the crystallization study. The computerized differential scanning calorimeter (PerkinElmerDSC with STARe System) is used to determine the degree of crystallization and the heat of fusion by measuring and recording data of the crystallization and melting temperature. Before the crystallinity test is initiated, all specimens are subjected to a standard heat/cool/heat cycle in a covered aluminium pan.

For non-isothermal, the test is initiated by heating the specimens from room temperature to 140ºC with a heat rate of 50ºC/min followed by a cooling rate of 10ºC/min to achieve a temperature of 0ºC. The thermal history of the heat cycle is erased and the polymeric material is allowed to reach repeatable enthalpic state associated with the crystallization through the cooling process [28]. The second heating is performed to achieve temperature of 140ºC with heating rate of 5ºC/min, 10ºC/min and 20ºC/min from the starting temperature of 30ºC, and then three different cooling rates which are corresponding with the heating rate. The time to complete a single completed heat flow curve varies with the heating/cooling rate. After a heat flow curve is obtained, the program of DSC is used to process and analyze the kinetics data.

For isothermal, the test is initiated by erasing the thermal history mentioned above, and then heating the specimens from 30ºC to 140ºC with a heat rate of 50ºC/min and is held for 10 minutes, followed by a rapid cooling rate of 200ºC/min to achieve the crystallization temperature of 82 ºC, 84 ºC, and 86 ºC. The result is recorded and analysed with the STARe System software.

The normalized heat flow curve is smoothed using least squares averaging method before analysis. Based on the heat flow curve, T_c is the peak of crystallization temperature and T_m is the peak of melting temperature. ΔH_f is the heat of fusion of the specimen, and it can be calculated from the area under the peak of the melting curve. The percentage of crystallinity can be calculated based on this equation [28].

$$X_c = \frac{\Delta Hf}{\Delta H°f} \times 100 \quad (1)$$

Where ΔH_f is the heat of fusion of specimen, $\Delta H°_f$ is the heat of fusion of a pure crystalline polyethylene which is 295 J/g, and X_c is the percentage of crystallinity.

3. Results and Discussion

The results and discussion is divided into two sections, the non-isothermal crystallization analysis and isothermal crystallization analysis. The parameters that are studied in this research are the crystallization temperature, melting temperature, radiation dose, heating and cooling rate, and percentage levels of crystallinity.

3.1 Crystallization analysis

3.1.1 Effect of Radiation Dose

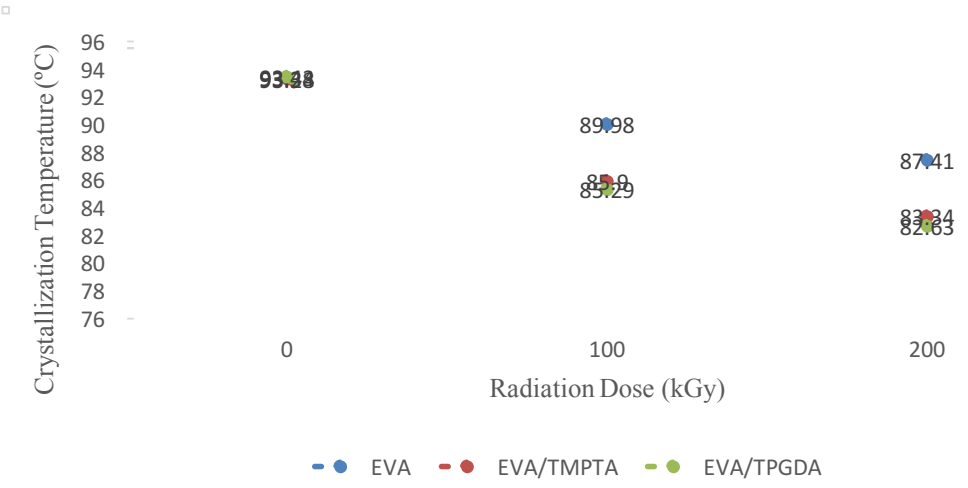


Figure 1. Effect of radiation dose on crystallization temperature of eva and blends at 20ºC/min heating and cooling rate.

Figure 1 shows that all three blends have almost similar starting crystallization temperature at 0 kGy radiation dose. This is expected as the radiation sensitizers only function when the blends are exposed to radiation, thus the big changes when radiation dose is applied. The figure also shows all three blends have a trend of decreasing crystallization temperature as the radiation dose increases. The EVA/TPGDA blend has the biggest crystallization temperature drop of 10.8 ºC, while EVA has the smallest drop of 5.93 ºC. However, it is clear that the performance of EVA/TMPTA and EVA/TPGDA in terms of the magnitude of the crystallization temperature is very similar. The result of the trend of crystallization temperature decreasing as radiation dose increases is expected as when blends are exposed to irradiation, the crystallites formed will be smaller in size, thus less energy are needed to create them [17].

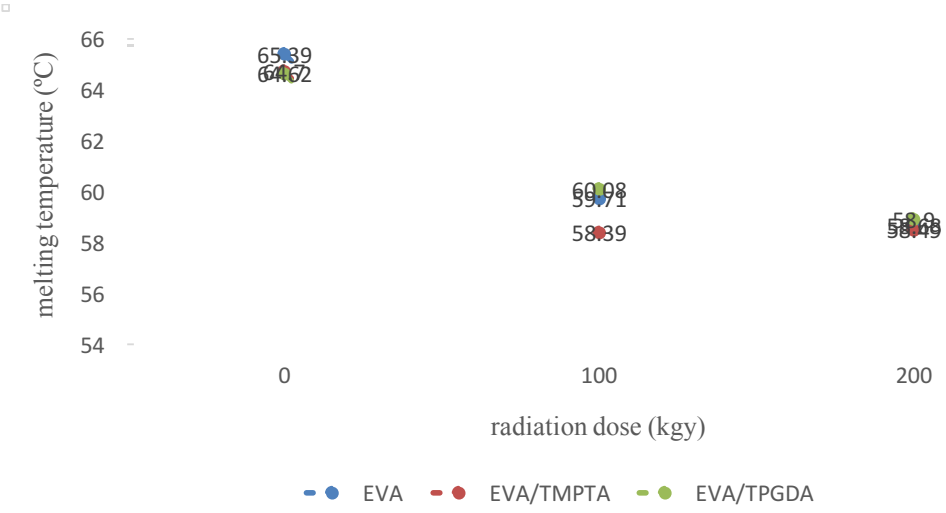


Figure 2. Effect of radiation dose on melting temperature of eva and blends.

Figure 2 shows that all three blends also have almost similar starting melting temperature at 0 kGy radiation dose. As mentioned earlier, this is expected as the radiation sensitizers do not affect or change the physical nature of EVA prior to irradiation. The figure also shows the blends have a trend of decreasing melting temperature as the radiation dose increases, with the exception of EVA/TMPTA blend. The magnitude of melting temperature has decreased as well when the radiation dose increases. The EVA/TMPTA blend has the biggest melting temperature drop of 6.31 ºC, from 0 to 100 kGy radiation dose. Thus, EVA/TMPTA seems to be performing better in terms of lower melting temperature than EVA/TPGDA at 100 kGy. This is also expected with similar reasoning as the crystallization temperature decreasing because the crystallites formed will be smaller in size, thus less energy to create them [17].

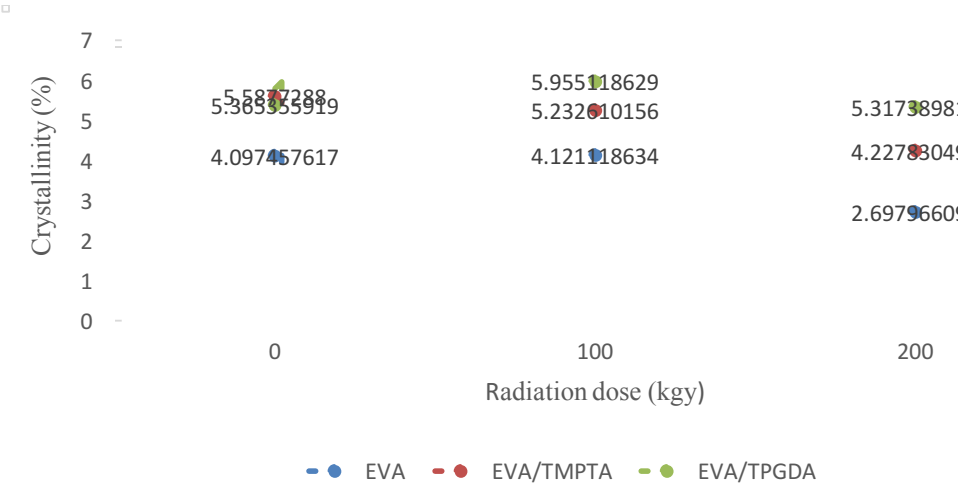


Figure 3. Effect of radiation dose on crystallinity of eva and blends.

Based on figure 3, the starting crystallinity levels of both the EVA/TMPTA and EVA/TPGDA are significantly higher than EVA at 0 kGy radiation dose. It can also be seen that both EVA and EVA/TPGDA have a similar trend of having slightly higher crystallinity levels at 100 kGy, which decreases at 200 kGy. The EVA/TPGDA blend seems to have a positive crystalline growth at 100 kGy. EVA has the most notable drop

of 1.4% crystallinity from 100 to 200 kGy. Irradiation is expected to improve the percentage of crystallinity up to a certain radiation dose as the exposure creates more functional groups that will generate defective crystals in the crystalline phase [18].

3.1.2 Effect of heating and cooling rate

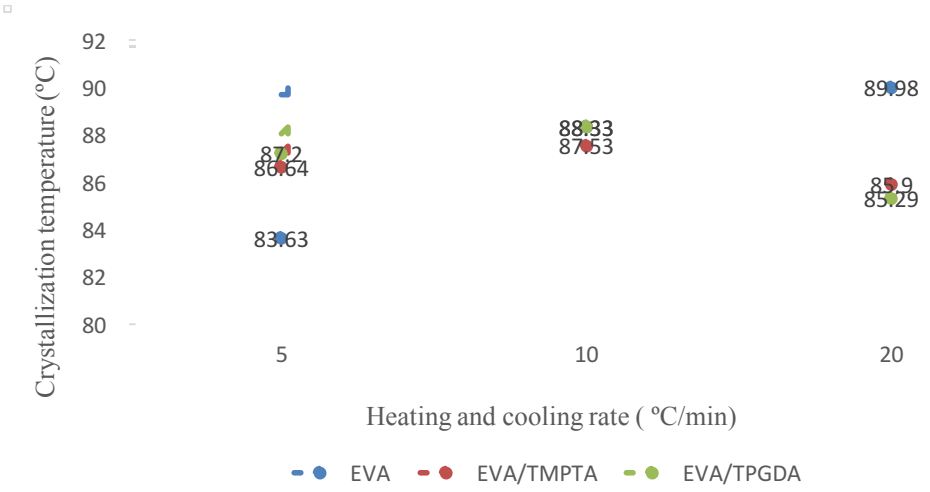


Figure 4. Effect of heating and cooling rate on crystallization temperature of eva and blends.

According to figure 4, it seems that the crystallization temperature of EVA that is in the presence of radiation sensitizers is not affected by the heating and cooling rate. This study is relatively new, and so far there are no studies that have been done to compare with this result. Thus, this relation needs to be studied further. EVA has a trend of increasing crystallization temperature as the heating and cooling rate increases. With this result, it is clear that 10°C/min heating and cooling rate is the optimum rate to have high crystallization temperature when radiation sensitizers are added into EVA. Past research has also shown setting 10°C/min as the default heating and cooling rate for their research in studying crystallization behavior [16].

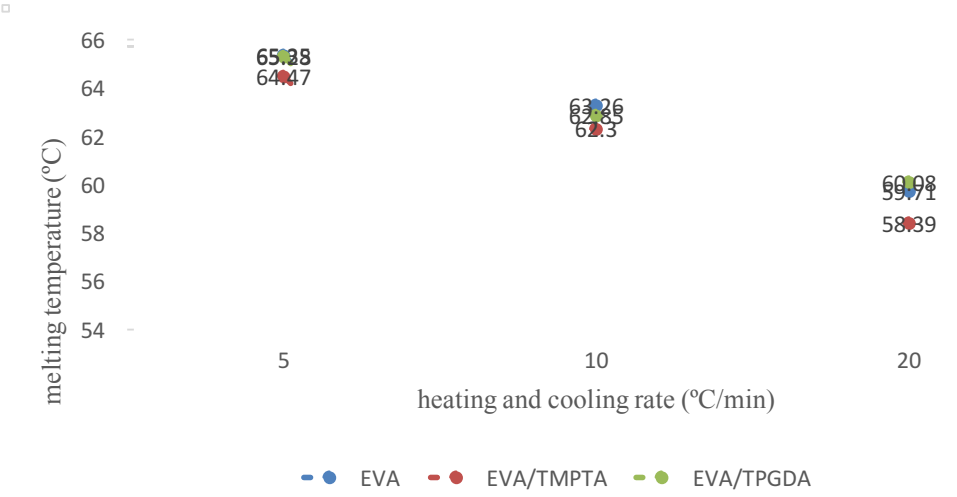


Figure 5. Effect of heating and cooling rate on melting temperature of eva and blends.

With the figure 5 in mind, there is a trend in all three blends in that the melting temperature decreases when the heating and cooling rate increases. The EVA/TMPTA blend has the biggest melting temperature drop of 6.08 ºC from 5 to 20 ºC/min. It is interesting to note that for effect of radiation dose, the crystallization temperature and melting temperature trends have a similar trend, however different trends were noted for effect of heating and cooling rate.

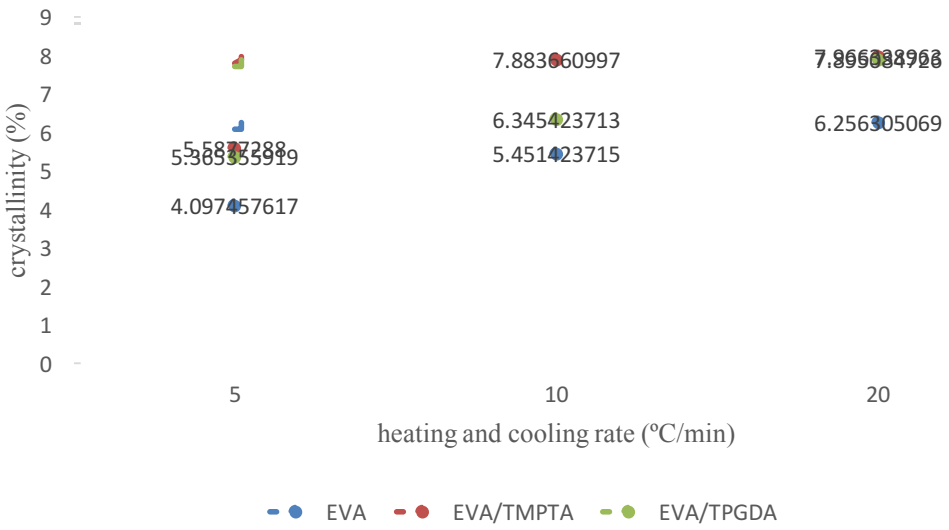


Figure 6. Effect of heating and cooling rate on crystallinity of eva and blends.

Figure 6 shows the crystallinity percentage of all three blends having the same trend of when heating and cooling rate increases, the percentage of crystallinity increases as well. The crystallinity behavior of the EVA/TMPTA and EVA/TPGDA can be seen to be different from each heating and cooling rate despite both of have increasing percentage levels of crystallinity. Past studies have found to be in opposite effect in the sense that the percentage of crystallinity decreases when the heating and cooling rate increases, although the polymer and blend is different from this research [19].

After collecting and analyzing the figures, a comparison is made between the optimum conditions for all the three blends to have highest percentage of crystallinity. From the data obtained, it can be deduced that the optimum radiation dose would be 100 kGy, and the optimum heating and cooling rate would be 20 ºC/min.

Table 1. Optimum Crystallinity Percentage of eva and blends.

Optimum Crystallinity Percentage (%)		
[1] EVA	[2] EVA/TMPTA	[3] EVA/TPGDA
[4] 6.835	[5] 6.308	[6] 8.248

The table above shows that the EVA/TPGDA has a remarkably higher percentage levels of crystallinity than the other two blends. The percentage value of

8.248% crystallinity is the highest amount obtained from this research. It is also unexpected that the EVA/TMPTA has a lower percentage level than EVA. The TMPTA radiation sensitizer should in theory promote higher amounts of crystallinity compared to pure EVA. Thus, it is clear that the EVA/TPGDA performs much better than the EVA/TMPTA blend in terms of crystallinity levels.

4.0 Conclusion

The main objectives of this project are achieved as radiation energy has affected the crystallinity, crystallization half-time and activation energy values of EVA. It is also proven that the addition of radiation sensitizers tend to improve the crystallization properties of EVA, with TPGDA blend obtaining the highest crystallinity, and TMPTA blend getting a lower activation energies when they are exposed to electron beam irradiation. In the dynamic crystallization behavior analysis, it is found that the crystallization temperature and melting temperature decreases when the radiation dose increases. It is also found that the percentage of crystallinity is optimum at 100 kGy. The combination of 100 kGy radiation dose and 20ºC/min heating/cooling rate produces the highest percentage of crystallinity at 8.248% with the TPGDA/EVA blend.

Acknowledgement

A token of appreciation is given to Dr. Rashmi G. Walvekar, Ms. Lithnes Kalaivani, Ms. Nur. Farihah and Ms.Sharon Wong for thier guidance, advices and support that made this study a successful one. Appreciation is also given to Taylor's University for providing the facilities and equipment to perform this study in an effective and proper manner.

References

[1] J. Cowie, Polymers: Chemistry and Physics of Modern Materials, International Textbook Company Limited, 1973.

[2] S. L.Rosen, Fundamental Principles of Polymeric Materials, John Wiley & Sons Inc., 1982.

[3] Y. Mubarak, E. Harkin-Jones, P. Martin and M. Ahmad, "Modelling of non-isothermal crystallization kinetics of isotactic polypropene," *European Polymer Journal,* p. 7, 2001.

[4] L. Valentini, J. Biagiotti, M. Lopez-Manchado, S. Santucci and J. Kenny, "Effect of carbon nanotubes on the crystallization behaviour of polypropene," *Polym Eng Sci,* 2004.

[5] M. Fujiyama and T. Wakino, "Structures and Properties of injection moldings of crystallization nucleator-added polypropylene," *Journal of applied science,* p. 42, 1991.

[6] J. Kim, M.-S. Kim and B.-W. Kim, "Study on isothermal crystallization behaviour and surface properties of non-oriented PLA film with annealing tempreature," *Korean Chemical Engineering Research,* vol. 49, no. 5, pp. 611-616, 2011.

[7] Makuuchi, K; Cheng, S; John Wiley & Sons, Inc., "Radiation Processing of Polymer Materials and its industrial applications," 2012.

[8] M. Zurina, H. Ismail and R. C.T., "Effect of Trimethylolpropane Triacrylate on properties of Irradiated epoxidixed natural rubber (ENR), ethylene vinyl acetate (EVA) copolymer and an ENR-50/EVA Blend," *Journal of Vinyl and Additive Technology,* vol. 15, no. 1, 2009.

[9] H. Abd El-Rehim and E. El-Nesr, "Radiation Induced Crosslinking of Ethylene Vinyl Acetate Copolymers Hosting Sulfonic Acid Groups and their potential applications," *Journal of Macromolecular Science,* vol. 43, no. 6, 2006.

[10] V. Mittal, "Functional polymer blends: synthesis, properties and performance," *CRC Press,* 2012.

[11] J.G.Drobny, Radiation Technology for Polymers, CRC Press LLC, 2003.

[12] Z. M, I. H and R. C, "Effect of Trimethylolpropane Triacrylate (TMPTA) on Properties of Irradiated Epoxidixed Natural Rubber (ENR-50), Ethylene-Vinyl-Acetate (EVA) and ENR-50/EVA blend," *Journal of Vinyl and Additive Technology,* 2009.

[13] X. M. Shi, J. Zhang and S. Chen, "Non-isothermal crystallization and melting of Ethylene-Vinyl-Acetate copolymers with different vinyl acetate contents," *Express Polymer Letters,* vol. 2, no. 9, pp. 623-629, 2008.

[14] W. Xinfeng, Z. Jianqiang, W.Chao, W. Genlin and J. PIngkai, "Study on tribological properties of UHMWPE irradiated by electron beam with TMPTA and TPGDA as crosslinking agents," *Wear,* vol. 297, no. 1-2, pp. 742-751, 2013.

[15] Y. Yin, Liu, Zheng, Shen and P. Deng, "Improvement of compatibility of polyethylene terephthalene and polyethylene octene blends by gamma irradiation," *Journal of Applied Polymer Science,* vol. 127, pp. 200-207, 2013.

[16] S. Ramarad, IMproving the properties of reclaimed waste tire rubber by blending with poly(ethylene-vinyl-acetate) and electron beam irradiation, 2015.

[17] H. Khonakdar, S. Jafari, M. Taheri, M. Wagenknecht, U. Jehnichen and L. Haussler, "Thermal and wide angle X-ray analysis of chemically and radiation-crosslinked low and high density polyethylenes," *Journal of Applied Polymer Science,* no. 100, pp. 3264-3271.

[18] Reyes-Labarta, J. Olaya and M. Marcilla, "DSC and TGA study of the transitions involved in the thermal treatment of binary mixture of PE and EVA copolymer with a croslinking agent," *Polymer,* no. 47, pp. 8194-8202, 2006.

[19] R. Wellen, M. Rabello, I. Junior, G. Fechine and E. Carnedo, "Melting and crystallization of poly(3-hydroxybutyrate): Effect of heating/cooling rates on phase transformation," *Polimeros,* vol. 25, no. 3, 2015.

Optimisation of Extraction Condition of Avocado Fruit using Response Surface Methodology

Nassor Ali Seif Hemed, Rajesh Nithyanandam & Ayu Haslija Bt Abu Bakar
School of Engineering, Taylor's University, Malaysia
No. 1 Jalan Taylor's, 47500, Subang Jaya, Selangor DE, Malaysia

nassorjamal1@gmail.com
Rajesh.Rajasekaran@taylors.edu.my
ayuhaslija@ucsiuniversity.edu.my

Abstract
Oxidative stress is a process which occurs in human bodies when subjected to environmental stress, Oxygen free radicals attack biological molecules such as lipids, proteins and DNA. Antioxidant quench the hydroxide radical oxidative stress in cells, therefore, are used to treat different kind of human diseases such as cardiovascular diseases, cancer and inflammatory diseases. The objective of the project is to determine antioxidant potential of inner pulp of avocado fruit and its peel. Previous researches shows the pharmacological and phytochemical abilities of the avocado but still not too much literature is available on the fruit. Avocado inner pulp and peels extract is spray dried using maltodextrin as a binding material (5 wt.%) at selected variable of temperature and *Mcore/Mwall.* Response surface methodology will be used to optimise the spray drying process for four response variables which are moisture content, DPPH radical scavenging activity, total phenolic content and total flavonoid. The expected outcomes of the project are that the avocado fruit and peel will have same or more antioxidant potential than literature finding, the spray dried avocado fruit and peel extract may be used as preventive medicine and can be used as an alternative on the available synthetic antioxidants such as butylated hydroxytoluene (BHT) and butylated hydroxyanisole (BHA) which have been reported to be carcinogenic, this has increased interest in using natural antioxidants. The project results suggest that avocado fruit and peels possess potent antioxidant activity and are reliable source of natural antioxidants. Future work of the project is to pelletize the bioactive compounds which will be found in the avocado fruit and peel extract and to be used as preventive medicines for different diseases after it has been scientifically proven.

Keywords: Antioxidant potential, spray drying. Response surface methodology, total phenolic content, total flavonoid content.

1. Introduction

Human bodies if subjected to daily environmental stress produces reactive oxygen species (ROS), ROS are chemically containing species which contain oxygen such as superoxide, peroxide, hydrogen peroxide, singlet oxygen and hydroxyl radical, in other meaning ROS are unstable molecules containing oxygen that can easily react to other molecules in the cell, accumulation of reactive oxygen species in the cell causes damage to DNA and protein and may lead to cell death [1]. Cell metabolism in our bodies produces free oxygen radicals as byproducts are part of our body biological body process. However excess of this free radicals is dangerous which damage lipids, nucleic acids, protein and membranes which could eventually lead to diseases such as Alzheimer's, cardiovascular, inflammatory or even cancer [2].

Human bodies detoxify these free oxygen radicals by producing antioxidants which neutralise the free oxygen radicals, however, the antioxidant produced is not sufficient therefore it must be applied in form of supplements or daily diet [2]. Reports have shown that food which contains high amount antioxidants will have an inverse relationship with incidence of different kind of human diseases. However synthetic antioxidants such as butylated hydroxytoluene (BHT) and butylated hydroxyanisole (BHA) have been reported to be unhealthy and even carcinogenic that is why there has been a high interest in using natural antioxidants [3].

Herbal medicines have gained high attention over the past decades' since many of the synthetic medicines have major side effect [3], but not too much information is available regarding their quality potency and safety. Therefore, before any herbal medicines have to be scientifically proven before being prescribed or consumed by humans. Avocado which is also known as Persea Americana and either apukado or avocado in Malay which belongs to the family lauraceae is widely grown in central America, Mexico tropical and subtropical countries all over the world. Avocado is recognised for its rich nutrients, unsaturated fatty acids, fibers, proteins, minerals, vitamins B and E and antioxidants [4]. In additional to that studies have shown that avocados are great cancer-fighting fruits containing multiplicity of nutrients and antioxidants [5]. Previous researches have been which are done on avocado but this research will focus on the amount of antioxidant present in the peels and the inner pulp of avocado fruit which will eventually lead to the insight of other medicinal properties of avocado and potential use of these compounds as an ingredient in food packing industry, the research gap below cover the difference on what is done previously and what is done now, Table 1.1 below shows scientific classification of avocado.

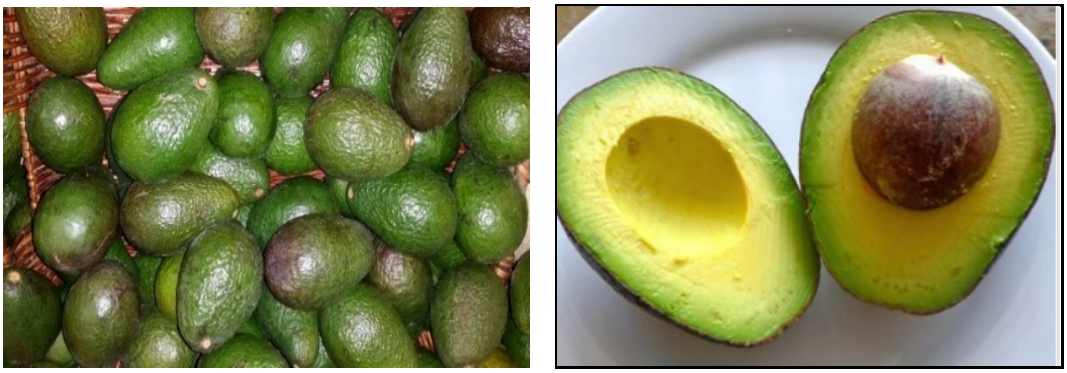


Figure 1.1: Avocado fruit

Table 1.1: Classification of Avocado

Avocado	
Scientific classification	
Kingdom	Plantae
Order	*Laurales*
Family	*Lauraceae*
Genus	*Persea*
Species	*P.Americana*

Avocado fruit will undergo several processes to study its antioxidant potency as it is claimed to have, bioactive component from the fruit pulp and peel will be extracted, spray dried and the powder characteristics will be studied, the whole process will be optimised using response surface methodology.

Spray drying Microencapsulation is a technique used to protect food ingredients against spoilage and unfavourable environmental condition such as light, moisture, and oxygen and hence increasing the life of the product[6]. The mechanism of microencapsulation is that it will cover all the particles of the food ingredient with a wall membrane protecting the useful material or eliminating useless properties to or from the original ingredient[6]. There are many ways that can be used for microencapsulation depending on the particle sizes and shapes however for the food and drug industry spray drying is still one of the most popular methods because it is easy to industrialise and allows continuous production [7].

2. Objectives and scope

The research is aimed at studying the optimum volume to weight ratio of extraction solvents i.e. ethyl acetate and water and avocado powder which can yield the maximum antioxidant potential between two extraction process: the first extraction process was a mixture of ethyl acetate and water with avocado (fruit and peel) powder, while the second extraction is water with avocado (fruit and peel) powder. RSM was used to find the number of experimental runs needed for both extraction process and the experiment was conducted accordingly. In addition to measuring the antioxidant parameters which are DPPH radical scavenging activity, total phenolic and flavonoid content the research also aims to determine storage capabilities and moisture content of the spray dried (Fruit and peel) extract.

The scope of the project will comprise extraction process which will be guided by RSM approach (for both ethyl acetate water mixture to avocado powder and water to avocado powder), extraction performed by water will be taken for spray drying and the encapsulated microparticles will undergo further analysis to measure the antioxidant potential of the powder, however for the extraction performed by ethyl acetate and water mixture the supernatant obtained from the extraction is the one which will be analysed for antioxidant potential this is because the spray dried used was specifically for only water-based solutions, The tangential output of the project is based on the pharmaceutical industry. After the powder from spray dryer is obtained further process is done to the powder to change it in the form of tablets, the process is known

as pelletization. Palletization is a method of formation of spherical beads or pellets with an average diameter ranging from 0.5 to 2.0mm[8]. the pellets are eventually coated and used in control release dosage as medicines. Pelletization leads to an improvement in the flowability, appearance and improving the physical and chemical properties of the powder. Pelletization is done to prevent segregation of the co-agglomerated components, which result in an improved uniform content, pelletization increases bulk density and decreases bulk volume, improves handling properties etc.[8]

3. Methodology

3.1 Experimental procedure

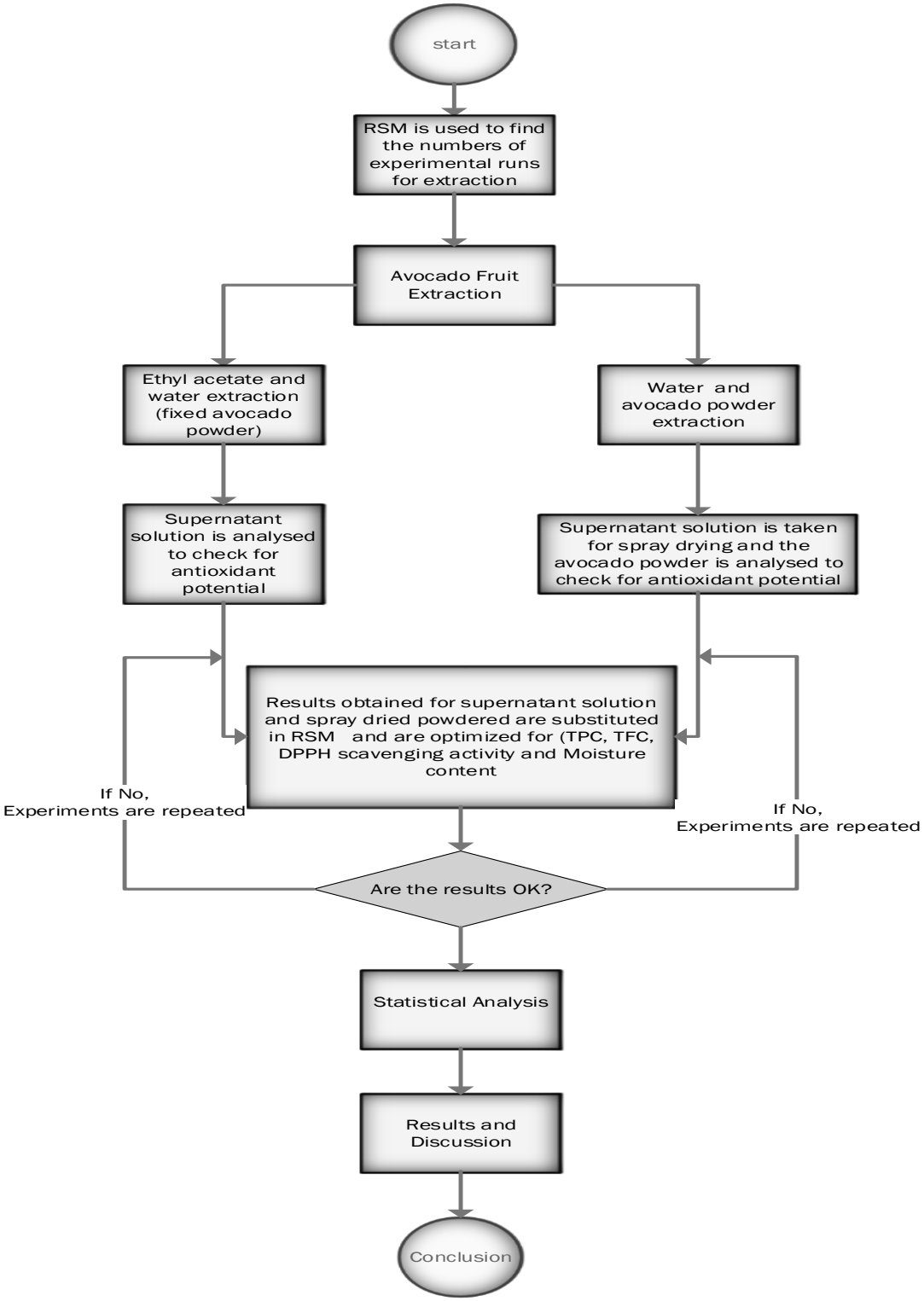


Figure 2.1: Experimental Procedure

3.2 Materials and chemicals

Chemicals such as ethyl acetate, methanol, sodium carbonate (and aluminium chloride were purchased locally from suppliers. Folin ciocalteua reagent, Tannic acid (TA) and2,2-diphenyl picryl hydrazyl (DPPH) were on from our chemical laboratory. A total of 6 kg of Avocado fruits which were close to ripe stage were purchased from a local market. All other chemicals used were of reagent grade which did not need any further purifications.

3.3 Preparation of Avocado fruit extracts

Avocado fruits were washed with tap water followed by distilled water. The fruit was peeled and the pulp and peels were cut into small pieces and oven dried at 50°C for three (3) consecutive days until the moisture content of the dried fruit and peels became constant. By using a blender, the dried avocado fruit and peels were powdered.

3.4 Extraction process of ethyl acetate and water (with fixed ratio of avocado powder) and water with avocado powder

Two extraction process were done: one was ethyl acetate and water to avocado powder and the other was water to avocado powder, RSM design of experiment software was used to obtained the number of runs needed to conduct the experiment for extraction process, the total number of runs from RSM was 12 with different ethyl acetate to water ratio. Solute to solvent ratio of ethyl acetate and water to avocado powder was a ratio of (1:10), the extraction of all 12 samples were performed in an orbital incubator shaker for three days continuously at 100 rpm and 35°C [9]. The filtrate is separated from the liquid using filter paper and the extracted solutions are stored in Schott bottles and refrigerated at 4°C [9].The same procedure was repeated for water with avocado extraction, however, for the second extraction the supernatant solution obtained is taken for spray drying and the spray dried powder is analysed.

3.5 Spray drying of the avocado fruit extracted by water

Maltodextrin (5wt. %) was mixed with avocado extract at a volume ratio of (1:2) and then stirred to form an aqueous solution [10]. The resulting mixture was then spray-dried using a Buchi spray dryer B-290 with co-current flow (the spray dried product and the drying air flow was in the same direction). the spray dryer sturdy glass apparatus provides a clear view of the process and can be easily cleaned and assembled by a single person. The main components of the system were the drying chamber, a peristaltic pump which pumps the extract solution to the spraying nozzle and an air compressor, there is also blower and an air filter to dry the inlet gas. In addition to that is the outlet temperature sensor, cyclonic separator and product removal flask to collect the spray dried sample. The inlet temperature of the spray dryer was set at 160°C and the outlet temperature was set at 70°C. The pump was set at 20% and the nozzle pressure was 1.1 bar. Several spray-drying runs were carried out as per the RSM experimental design, the microencapsulate powdered was collected and further analysis was performed to

determine the moisture content, total phenolic content, total flavonoid content and DPPH radical scavenging activity.

3.6 Moisture content

The moisture content of the spray-dried microparticles was determined using drying method. Samples of the microparticles were weighed prior to drying, the masses were recorded and the sample was kept in an oven (Memmert oven), heated to 105°C, and weighed again on an analytical balance until a constant mass was obtained. The moisture content of the powder was determined from weight loss by averaging three samples[7].

3.7 DPPH radical scavenging activity

DPPH is a free radical that has the ability to react with different compounds that can donate hydrogen atom. The hydrogen donating ability of the spray fried avocado fruit and peel extract was determined by measuring the absorbance of the samples at a wavelength of 515nm, the spray dried samples were measured to 10mg and dissolved to 30ml of methanol and centrifuged for 10 minutes. Aliquots of the samples (0.5ml) were added to 3ml of 0.0025g/l DPPH in methanol. The absorbance sample was measured after 40 minutes using a UV-VIS single-beam spectrometer and methanol was used as a reference, a standard calibration curve of DPPH in methanol in a range of (0-100mg/l) [11].

The DPPH radical scavenging activity was calculated using the formula:

$$DPPH\ radical\ activity\ (\%) = \left[1 - \frac{Abs515\ sample}{Abs515 DPPH\ solution}\right] \times 100 \ldots \quad (3.1)$$

3.8 Total phenolic content

The total phenolic content (TPC) was determined using Folin Ciocalteau (FC) method. TPC is estimated in terms of tannic acid equivalents. The spray dried samples were measured to 10mg and dissolved to 30ml of methanol and centrifuged for 10 minutes, aliquots of the samples (0.5ml) was added to 2.5ml of the 0.2N FC reagent and allowed to react for 5 min. Then, 2ml of 75g/l sodium carbonate was added to the mixture followed by 25ml of distilled water. The mixture was incubated for two hours at room temperature and the absorbance was measured at a wavelength of 760nm using a single beam spectrophotometer[7]. Methanol was used as a reference and a standard calibration curve was plotted using Tannic acid. The total phenolic content was expressed in TAE/g of the spray dried powdered [7].

3.9 Total flavonoid content

A total of 5ml of 2% alumi4ium chloride in methanol was mixed with the same volume of the extract solution. The absorption reading was taken after 15 minutes using a UV-Vis single-beam spectrophotometer at a wavelength of 415nm, the blank sample consists of a 5ml extract solution with 5 ml of methanol without aluminium chloride. The total flavonoid content is determined a standard calibration curve with quercetin at

a range of (0-100mg/l) the content is expressed as quercetin equivalent (QE/g of the spray-dried powder [7].

4.0 Results and Discussion

Response surface methodology (RSM) was applied using a commercial statistical package, Design- Expert version v10 to identify the optimum ratio of ethyl acetate to water for the first extraction process and water to avocado powder for the second extraction process, analysis of four response was performed (i.e. DPPH scavenging activity, Total phenolic content(TPC), Total flavonoid content (TFC) and moisture content (MC)). The order of experiments was randomized and all the data was analyzed by multiple regression using least-squares method. Quadratic equation will be used to express the responses as a function of independent variable where A and B will represent ethyl acetate and water for the first extraction process and water to avocado powder for the second extraction process. Confidence level of 95% is used and the significant terms of the response are found using one-way analysis of variance, ANOVA. The model adequacy is checked by calculating R^2, the numerical and graphical optimization technique of the software are used for optimization of the responses and the final preferable variable/ratios are chosen. Table 4.1 and 4.2 below show factors tested for both extraction process.

Table 4.1: Factors and levels tested for first extraction (Ethyl acetate- water extraction with fixed ratio of avocado powder)

Ethyl acetate and water		
Parameter	Ethyl acetate	water
Factor	A	B
Max. parameter	100	100
High level	+1	+1
Average parameter	50	50
Medium level	0	0
Min parameter	0	0
Low level	-1	-1

Table 4.2: Factors and levels tested for both extraction by RSM.

Water and avocado powder		
Parameter	Water	Avocado powder
Factor	A	B
Max. parameter	250	25
High level	+1	+1
Average parameter	125	17.5
Medium level	0	0
Min parameter	0	10
Low level	-1	-1

All the experiments for both extraction processes were done. The results are tabulated below. Table 4.3 shows the results for DPPH scavenging activity, TPC and TFC for the supernatant solution obtained from the first extraction (ethyl acetate water mixture with avocado powder) and Table 4.4 shows the result of DPPH scavenging

activity, TPC, TFC and moisture content for the spray dried avocado powder, here the supernatant solution obtained is taken for spray drying and the powder is analysed.

Table 4.3: Experimental design condition and results. (ethyl acetate water extraction)

S No.	Two Factors		Responsive value		
	Factor 1	Factor 2	DPPH scavenging activity %	TPC mg of TAE/g	TFC mg of QUE/g
	ethyl acetate	water			
1	66	82	88.8	0.047	0.086
2	17.5	37	81.24	0.034	0.015
3	33	100	78.58	0.038	0.006
4	57	45	77.6	0.039	0.08
5	57	45	88.12	0.058	0.07
6	33	100	43.41	0.04	0.068
7	100	100	86.84	0.025	0.09
8	46.5	0	67.38	0.028	0.082
9	0	73	9.8	0.0282	0.042
10	100	0	12.3	0.035	0.053
11	0	0	0	0	0
12	57	45	73.47	0.033	0.074

Table 4.4: Experimental design condition and results. (water extraction)

S No.	Two Factors		Responsive value			
	Factor 1	Factor 2	DPPH scavenging activity %	TPC mg of TAE/g	TFC mg of QUE/g	MC %
	water	Avocado powder				
1	137.5	16.3153	20.8	0.018	0.075	8.2
2	0	19.75	0	0	0	0
3	63.75	25	0	0	0	0
4	110	10	29.4	0.016	0.06	10.5
5	157.5	22.375	62.34	0.014	0.012	10
6	137.5	16.3153	31.11	0.015	0	14.2
7	137.5	16.3153	31.57	0.024	0	8.5
8	250	25	47.99	0.06	0.005	11.1
9	0	10	0	0	0	0
10	0	19.75	0	0	0	0
11	250	10	46.4	0.06	0.003	20.9
12	250	17.875	63.03	0.01	0.001	10.9

Experiments to analyze the antioxidant potential of avocado powder for both extraction were conducted and the responses of DPPH radical scavenging activity, TPC and TFC were recorded as seen in the tables above. Experiment results were used to calculate the coefficient of the quadratic equation and ANOVA results for the model. For the model with high value than p-value would indicate more significant effect on

the response variables. Coefficient of multiple determination of R^2 for the experimental data were 0.84, 0.82 and 0.6 for response of DPPH scavenging activity, TPC and TFC for the first extraction which was done using ethyl acetate water mixture, R^2 value for the second extraction done using water and avocado powder are 0.84,0.71 and 0.35 for response of DPPH scavenging activity, TPC and TFC respectively, when R^2 is greater than 80% the model is considered to be good-fitting model when the value of R^2 is close to unity (1) it indicates that the empirical model is suitable for fitting the actual data, the lower the R^2 shows the inappropriateness of the model to explain the relationships between two variables, however adding any other variable will increase the value of R^2 even if the variable is not of much importance, therefore this also indicates that a larger R^2 does not always imply the adequacy of the model, the experiments were done and data were collected and tabulated below:

4.1 Analyzation of supernatant solution (ethyl acetate-water mixture and avocado powder

First, the extraction process of ethyl acetate and water is explained below, RSM was used to find the number of experiment runs of ethyl acetate-water mixture as shown in Table 5.2. the avocado powder (non-spray-dried) was fixed at a ratio of 1:10 of the ethyl acetate-water mixture, extraction process was performed and the supernatant solution was analysed using standard procedures and the results are explained below.

4.11 Response surface analysis of DPPH scavenging activity for water-ethyl extraction.

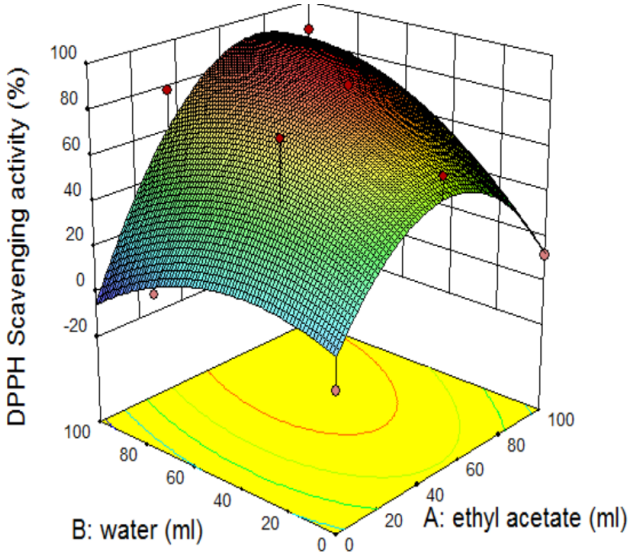
The data in Table 4.4 below shows the relationship between DPPH and the two variables which are ethyl acetate and water. Equation 4.1 below shows the relationship between the two variables, where A represents ethyl acetate and B represents water.

$$DPPH = 86.28 + 21.24A + 11.93B + 21.71AB - 44.14A^2 - 18.85B^2 \ldots\ldots \quad (4.1)$$

Table 4.4: Estimated coefficients for experimental design and their VIF(DPPH)

Ethyl water extraction						
	DPPH					
Factor	Coefficient Estimate	df	Standard Error	95% CI Low	95% CI High	VIF
Intercept	86.28	1	9.07	64.09	108.47	
A-ethyl acetate	21.24	1	8.57	0.26	42.22	1.04
B-water	11.93	1	7.23	-5.76	29.61	1.03
A*B	21.71	1	10.01	-2.78	46.19	1.04
A^2	-44.14	1	13.33	-76.75	-11.53	1.19
B^2	-16.85	1	12.72	-47.99	14.28	1.17
R^2= 0.84						

Figure 4.1 is response surface plot and 4.2 contour plot showing the effect of ethyl acetate and water ratio on DPPH scavenging activity. Both ethyl acetate and water showed a positive linear effect and a negative quadratic effect on the DPPH scavenging activity with the interaction variable remaining positive, the DPPH scavenging activity first increased and then it decreased when water volume increased which revealed the best water volume should be 58.3 ml, anything after that will decrease the DPPH scavenging activity, on the other hand as the volume of ethyl acetate increased the DPPH scavenging activity a volume of 75.95ml is favourable for obtaining high DPPH scavenging activity. From the results, high DPPH is obtained at low water volume and high ethyl acetate volume, this is because ethyl acetate facilitates to better extraction process, therefore the experimental ratio to obtain high DPPH scavenging activity was 58.3 ml of water and 75.95 ml of ethyl acetate which yield DPPH radical scavenging activity of 88% which is better than other findings [12], according to the research done on avocado to measure the phytochemical composition and antioxidant activity the seed extract demonstrated DPPH activity of 43% , skin had 35% and the pulp had 23% [12]. The reason of high DPPH in this research may be contributed by the extraction technique performed and the combination of fruit pulp and peels together may have boosted the DPPH scavenging activity.



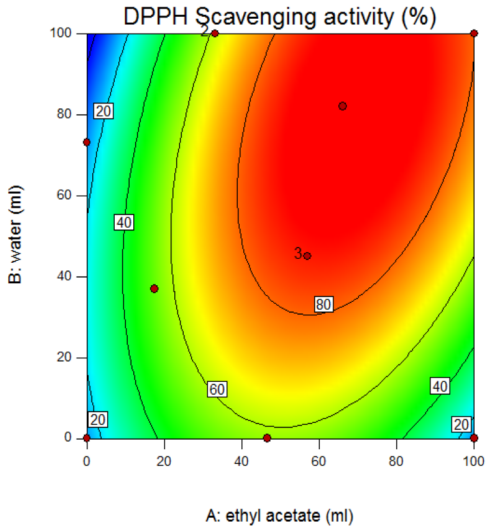


Figure 4.1 and 4.2: Response surface plot for DPPH activity (ethyl acetate-water extraction) and Contour plot for DPPH activity (ethyl acetate-water extraction)

4.2 Analyzation of the spray dried powder

Extraction was done using water and avocado powder the supernatant solution was filtered and taken for spray drying and the spray dried powder was analysed to measure the DPPH scavenging activity, TPC and TFC using standard procedures and the results are discussed below

4.2.1 Response surface analysis of DPPH activity for spray dried powder.

The data in Table 4.5 below shows the relationship between DPPH and the two variables which are water and avocado powder with a regression of 0.84. Equation 4.2 below shows the relationship between the two variables, where A represents water and B represents avocado powder.

$$DPPH = 86.28 + 21.24A + 11.93B + 21.71AB - 44.14A^2 - 18.85B^2 \ldots\ldots\ldots\ldots\ldots (4.2)$$

Table 4.5: Estimated coefficients for experimental design and their VIF (DPPH)

Water and avocado powder extraction only						
	DPPH					
	Coefficient		Standard	95% CI	95% CI	
Factor	Estimate	df	Error	Low	High	VIF
Intercept	32.79	1	6.64	16.54	49.05	
A-water	28.75	1	5.27	15.85	41.65	1.04
B-weight	-0.74	1	5.65	-14.58	13.09	1.03
A*B	5.53	1	7.27	-12.27	23.33	1.04
A^2	-3.44	1	8.18	-23.44	16.57	1.19
B^2	-6.84	1	8.79	-28.35	14.67	1.17
R^2= 0.84						

Figure 4.3 and 4.4 response surface and contour plot showing the effect of water and avocado powder on DPPH scavenging activity. Water showed a positive linear effect whereas avocado powder showed a negative linear impact, their interaction variable is positive and both variable showed negative quadratic effect. The reason of having negative linear effect on avocado powder is that if the mass of avocado to the volume of water is high it forms a thick solution to which proper extraction won't be achieved and eventually will lead to low DPPH scavenging activity. DPPH scavenging

activity first increased and then decrease when the avocado powder increased which indicates that 10g is the optimum avocado weight, on the other side water seemed to have a positive effect on DPPH activity which indicates that high volume will have better extraction on the avocado powder and will yield better results, from the experimental results, optimum water volume was 149.6 ml which achieved high DPPH activity of 31% when the mass of the powder was 10g. This clearly indicates that water to weight ratio should be balanced in a medium ratio to achieve better extraction which will have a better effect of DPPH scavenging activity. However, DPPH activity obtained from the spray dried avocado powder is low compared to the extraction done suing ethyl acetate. This shows the impact of solvent used for extraction, using of acid based solvents such as ethyl acetate, methanol and ethanol enhance the extraction activity and enables the powder to effectively dissolve in the solvents which result to higher antioxidant activity.

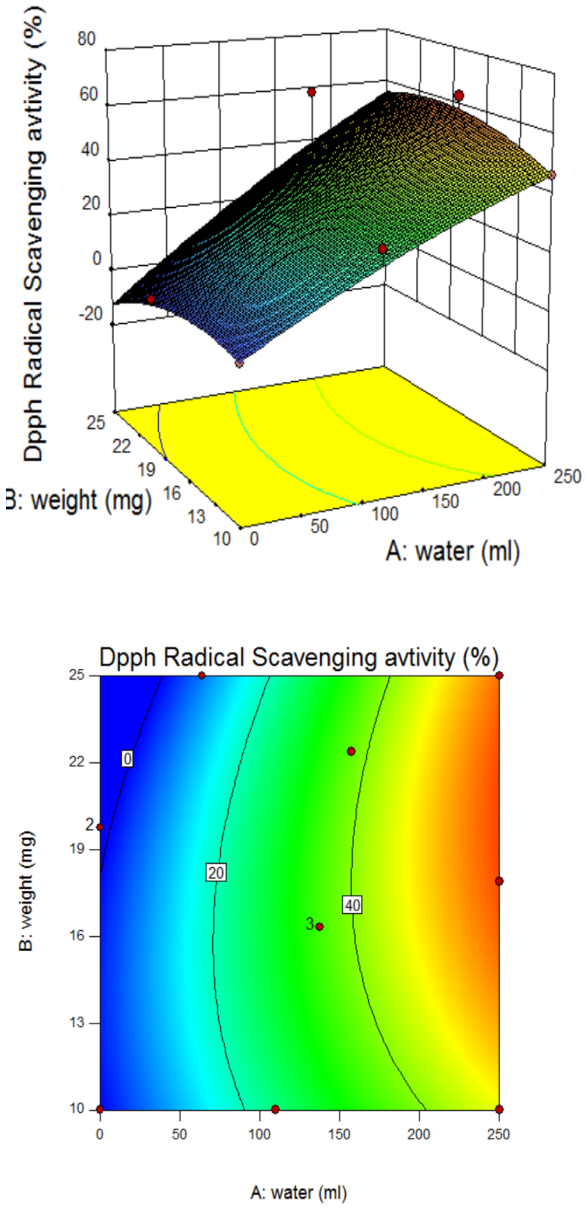


Figure 4.3 and 4.4: Response surface plot for DPPH (spray dried avocado powder) and Contour plot for DPPH (spray dried powder)

4. Conclusion and future work

Statistical techniques such as RSM and availability of software such as design of experiment has simplified complex calculations which allow process to be optimised fast, this is because of not only the advanced computer speed but the techniques reduce the number of experiment data required for analysis, in addition to that the results are represented in different forms of graphs such as contours and 3D model which gives the better understanding of the process.

All experimental runs for both extractions were conducted as per RSM in order to study DPPH scavenging activity, Total phenolic content(TPC) and Total flavonoid content (TFC). RSM was effective at determining the optimum zone within the experimental region, from response surface of quadratic models the results of DPPH scavenging activity, TPC, TFC was found to be 88.8%, 45mg of TAE/g and 85mg of QUE/g for ethyl water mixture and and 31.124%, 28mg of TAE/g, 37mg of QUE/g and 13.757 % of moisture ccontent for water and avocado powder extraction respectively, which reveals that avocado has good source of antioxidants, phenols, and flavonoid compounds.

Future work of the project is to extract the avocado peel and fruit powder by using ethyl acetate and the supernatant solution obtained after the filtration is to spray dried and analyzed, by doing so high antioxidant activity of the avocado fruit and peel might be achieved. In addition to that the bioactive found in avocado can be pelletized and used as medicines after it has been scientifically proven and replace synthetic antioxidants such as butylated hydroxytoluene (BHT) and butylated hydroxyanisole (BHA) are reported to be carcinogenic and cause liver damage.

References

[1] F. Moreira da Silva, A. Marques, and A. Chaveiro, “Reactive Oxygen Species: A Double-Edged Sword in Reproduction,” Open Vet. Sci. J., vol. 4, pp. 127–133, 2010.

[2] Sinha, S.K., “Trace elements deficiency & cancer,” J. Pharm. Biol. Sci., vol. 9, no. 4, pp. 21–32, 2014.

[3] D. Krishnaiah, R. Sarbatly, and R. Nithyanandam, “A review of the antioxidant potential of medicinal plant species,” Food Bioprod. Process., vol. 89, no. 3, pp. 217–233, 2011.

[4] M. D. K. M. Yasir, S. Dias, “The phytochemical and pharmacological profile of Persea americana Mill,” Pharmacogn. Rev., vol. 4, no. 7, pp. 77–84, 2010.

[5] W. Wang, T. R. Bostic, and L. Gu, “Antioxidant capacities, procyanidins and pigments in avocados of different strains and cultivars,” Food Chem., vol. 122, no. 4, pp. 1193–1198, 2010.

[6] A. Gharsallaoui, G. Roudaut, O. Chambin, A. Voilley, and R. Saurel, “Applications of spray-drying in microencapsulation of food ingredients: An overview,” Food Res. Int., vol. 40, no. 9, pp. 1107–1121, 2007.

[7] D. Krishnaiah, R. Sarbatly, and R. Nithyanandam, “Optimization of spray for drying Morinda citrifolia L. fruit extract,” J. Appl. Sci., vol. 11, no. 13, pp. 2276–2283, 2011.

[8] M. Hirjau, A. C. Nicoara, V. Hirjau, and D. Lupuleasa, “Pelletization Techniques Used in Pharmaceutical Fields,” Pract. Farm., vol. 4, no. 3–4, pp. 206–211, 2011.

[9] D. Krishnaiah, R. Sarbatly, S. Ram Mohan Rao, and R. Rajesh Nithyanandam, “Optimal operating conditions of spray dried noni frnit extract using K{green}-carrageenan as adjuvant,” J. Appl. Sci., vol. 9, no. 17, pp. 3062–3067, 2009.

[10] W. P. Batiston, S. A. Maruyama, S. T. M. Gomes, J. V. Visentainer, N. E. De Souza, and M. Matsushita, "Total phenolic content and antioxidant capacity of methanolic extracts of ten fruits - doi: 10.4025/actascitechnol.v35i3.18533," Acta Sci. Technol., vol. 35, no. 3, pp. 581–585, 2013.

[11] D. Krishnaiah, R. Sarbatly, S. R. Mohan Rao, and R. R. Nithyanand, "Optimal Operating Conditions of Spray Dried Noni Fruit Extract using κ-carrageenan as Adjuvant," J. Appl. Sci., vol. 9, no. 17, pp. 3062–3067, 2009.

[12] A. F. Vinha, J. Moreira, R. De Jorge, and V. Ferreira, "Physicochemical Parameters , Phytochemical Composition and Antioxidant Activity of the Algarvian Avocado (Persea americana," vol. 5, no. 12, pp. 100–109, 2013.

eureca 2017 – Conference Paper
Paper Number 2CE11

Ammoniacal Nitrogen Removal in Synthetic Wastewater using Seaweed-Based Ionic Liquid and *Bacillus spp.*

Nazween Adrynna binti Ahmad Nazri*, Chong Chien Hwa, Rajesh Nithyanandam
School of Engineering, Taylor's University, Malaysia

**nazweenadrynna@gmail.com*

Abstract
Ammoniacal nitrogen is considered a hazardous component and a pollutant in rivers that is a challenge to be removed. The purpose of the project is to remove ammoniacal nitrogen in wastewater using a seaweed-based ionic liquid and *Bacillus spp.* bacterium which is required to achieve the Department of Environment (DOE) environmental quality (industrial effluent) requirement 2009 of 20 ppm ammoniacal nitrogen based on Standard B. Standard B is the water quality index set by the DOE to ensure the effluent discharge from industry would not cause the rivers to be highly polluted which will cause environmental issues in a long run. A denitrification and ion exchange process occurs in the bioreactor that utilized the removal of ammonia ions. The process variables used to evaluate the removal efficiency are pH and temperature while taking into account the COD, BOD and sludge of the effluent. The pH used is between 6 to 8 and a temperature that varies between 30^{o}C to 40^{o}C. Furthermore, to evaluate the effect of pH and temperature during the biological treatment process of ammonia removal. It was found that the optimum pH is 7 and optimum temperature is 37^{o}C. The result is then used as a constant to study the optimum condition for the bacteria either in aerobic and anaerobic condition in which aerobic growth is the best condition. The ammonia removal rate was achieved at 94.173% with a final concentration of ammonia at 5.8270 ppm using 12 grams of bacteria for 24 hour in a bioreactor.

Keywords: Ammoniacal Nitrogen, Wastewater, Bacteria, Ionic Liquid, Denitrification process

1.0 INTRODUCTION

The demand for clean water has increased throughout the years which have revolutionized science and engineering in wastewater treatment to meet the demands of the society. Water demand is increasing every year due to the increasing population, rapid industrial development and climate change. Butler and Memon researched that the demand and usage of clean water increased in the past 31 years and has been forecasted to continuously increase in year 2025 to fulfil a population of 4800 million people but there is a decrease in water availability of 13,300 km^3/yr compared to year 1985 that only have a population of 2930 million people with water availability of 13,700 km^3/yr [1]. This data has shown how with an increasing population will require higher demand of clean water however the availability is drastically decreasing over the years.

With a continuous need of clean water, a better solution is required to meet the future demands. Wastewater has played a large contribution in providing water to the population and has a high potential to be further developed in providing further access to clean water in Malaysia [2]. Wastewater can be known as liquid wastes and wastes from households, commercial establishment, industries, storm water and other surface runoff water. Based on research, 43.02% of the water supply are from Malaysia rivers that originates from industrial wastewater [2]. The challenge is to provide access to clean water using wastewater to meet the Department of Environment (DOE) regulation based on the Environmental Quality Act 1974 which is the Environmental Quality (Industrial Effluent) Regulations 2009 as seen in Table 1. Referring to the DOE environmental report 2013, 72% of 473 rivers in Malaysia is found polluted and 25% were classified as highly polluted [3]. Furthermore based on the DOE environmental quality report 2014-2015, there was a decrease of ammoniacal nitrogen in polluted rivers from 151 in 2014 to 136 in 2015 [4]. The water pollution is classified in the form of Biochemical Oxygen Demand (BOD), ammoniacal nitrogen (AN) and suspended solids (SS). Ammoniacal nitrogen is a form of nitrogen when in contact with water and is a challenged to be removed in wastewater based on the DOE environmental report. This shows a high potential threat to the environment in terms of water quality and water pollution. Thus, further research is required to overcome this issue.

Table 1: Water quality standard in Malaysia [4].

Parameters	Unit	Standard	
		A	B
pH	-	6.0-9.0	5.5-9.0
BOD5 at 20^oC	mg/L	20	50
COD	mg/L	50	100
Ammoniacal nitrogen	mg/L	10	20

Wastewater is required to be treated before consumption. Based on the current wastewater treatment technology, ammoniacal nitrogen removal is not sufficient to meet the water quality index based on the environmental quality report 2015 [4]. The two types of treatment available for ammonia removal are biological treatment or chemical treatment but research has found that the biological has a better opportunity in terms of environmental and economical aspect [5]. Biological treatment involves utilizing the bacteria either aerobes or anaerobes to remove the ammonia through a

denitrification or nitrification process. Aerobic bacteria require the presence of oxygen while an anaerobic bacterium does not require oxygen to break down ammonia. Frostell and Cervantes et al., researched on the advantage of aerobic removal efficiency but has a larger sludge disposal compared to anaerobic treatment. It was suggested to use anaerobic-aerobic bioreactors to overcome the limitations but has only been tested on a small scale compared to a large-scale wastewater treatment [5].

Based on the bacteria used, it has the properties of aerobic *bacillus spp*. bacteria and is considered denitrifying bacteria. Denitrification is the reduction of ammonium nitrogen to nitrogen gas. Foglar et al., stated that denitrification is environmentally friendly and cost effective compared to nitrification which supports Soares assumption that it may be the most economical strategy for polluted water [6-7]. Zhou et al., and Ergas and Rheinheimer stated that denitrification has an advantage due to the nitrogen gas as the end product based on Van Der Hoek et al., research [8-10]. Also, Kim et al., and Yang et al., stated about the *Bacillus spp.* strain shows potential as a biological treatment bacteria to treat ammonia removal in soil and water based [11-12].Although ionic liquid and zeolite have been studied to remove metal ions from wastewater but there has not been a research on the removal of ammoniacal nitrogen. Thus, using ionic liquid to remove ammoniacal nitrogen in wastewater is rather scarce.

The project will be conducted based on a hybrid process which is a denitrification process as the first stage and then ion exchange process using seaweed-based ionic liquid to further remove ammoniacal nitrogen as a second stage. The first stage is by sterilizing the bioreactor with an autoclave then running the bioreactor for 24 hour using 100 ppm of ammoniacal nitrogen solution with Bacillus spp. A bioreactor is used to ensure that the bacterium is able to grow in a controlled environment and also in an enclosed environment to avoid pathogens from growing. Also, The bioreactor represents a smaller scale to the current technology used which is an aerated lagoon or tank. The second stage is to extract samples from the bioreactor after 24 hour using the sample syringe located in the bioreactor and is tested using different amount of ionic liquid to see if further ammonia removal is feasible. The significance of the seaweed-based ionic liquid is the ion composition that is similar to seaweed characteristic. The purpose of the project is to meet the DOE environmental quality (industrial effluent) requirement 2009 of 20 ppm using a bioreactor. A bioreactor is used due to easy use of controlling the growth or environment of the bacteria to achieve optimum growth which allows a higher percentage of ammonia removal. Furthermore, the key parameters such as pH and temperature are manipulated to optimize the ammonia removal rate. However, pressure is not able to be manipulated due to the characteristic of the equipment that is built to only withstand a neutral pressure which is 1 atm.

2.0 Methodology

A two-step process was applied to in the process of ammonia removal. Firstly, biological treatment using Bacillus spp. through denitrification process with an initial concentration of 100 ppm of ammonia solution in the bioreactor that was run for 24 hours. Secondly, 100 mL was extracted from the bioreactor into 4 sample sets that was used to improve the ammonia removal using ionic liquid. Other than that, pH and temperature were set as a manipulated parameter to understand further the effect of the parameters to ammonia removal. There are a few limitation to take note of, pH cannot be manipulated as the bioreactor is standardize at 1 atm and the volume of the solution

is required to be at 4 L in the bioreactor or there will be an error in data reading in the programme. This limitation was set due to the manufacture of the bioreactor but can be overcome by using a different type of bioreactor that enables pressure to be manipulated.

2.1 Material Preparation

Ammonia solution is prepared using Ammonia 53 wt% solvent from Merck by diluting the solvent until 100 ppm at 4L. The ammonia is then added into the bioreactor for autoclaving. NaOH and NaCl is prepared using 1500 ppm and 36000 ppm which is then diluted using distilled water until 2000 ppm at 2L which is then added into the bioreactor pH beaker storage. Other than that, ionic liquid and nessler reagent are not prepared since it comes in a bottle supplied by Platinum Strike Sdn Bhd.

2.2 Bioreactor Setup

The bioreactor was cleaned thoroughly and was filled with ammonia solution prepared beforehand. The bioreactor was changed from an open system to a closed system by closing all the openings with either a clip and was covered with an aluminum foil to avoid damage to the equipment .Furthermore, the bioreactor was added into an autoclave at 121^{o}C and 0.1 atm for 15 minutes based on ISO standard 17655 [13]. The purpose was to fully sterilize the bioreactor internally and externally to ensure no biohazard contamination occurs.

After sterilizing, the bioreactor was set up with the set parameters which were operated for 24 hours as a batch process. Each run consisted of different condition either an anaerobic and aerobic bacteria which was suspended in the bioreactor. The run was tested with 4 g, 8 g and 12 g of bacteria at a constant condition of 37^{o}C, pH 7, 100 rpm and an aerator at 7 L/s. Urea was added into the bioreactor as a nutrient source to the bacteria with a ratio of 1 gram of bacteria to 7 gram of urea. Between the range of 4 to 8 grams of urea is able to grow in an sustainable environment [14].

2.3 Improvement Ammonia Removal using Ionic Liquid

After the denitrification process, 4 samples were taken from the bioreactor after 24 hour through a sample syringe attached to the bioreactor. Each of the samples was collected at 50 mL and was placed into a beaker. After obtaining the 4 samples, 1 to 4 mL of ionic liquid is added into the samples with an interval of 1 mL. Each sample was then lightly shaken and closed using an aluminum foil. The samples were then left for 5 minutes. After 5 minutes, the samples were dropped into a clean cuticle using a pipette before measuring the ammonia concentration in the photometer.

2.4 Experimental Analysis and Test

There were a total of 4 testing methods which were ammoniacal nitrogen reading through American Standard Test Method (ASTM) using Merck Spectroquant Prove 700, chemical and biological oxygen demand using Merck Spectroquant Prove 700, jar test using Lovibond ET 750 and sludge volume index(SVI) using calculation. After collecting all the result and verification then the process of modification for further improvement will be done if necessary.

2.4.1 Ammoniacal Nitrogen

Ammoniacal nitrogen analysis methodology was adapted from ASTM D1426-08 [15]. A sample of 0, 10, 20, 30, 40 and 50 mL of the ammonia nitrogen standard was diluted using deionized water until 50 mL. However, if turbidity was present then the sample was required to be mixed with zinc sulfate ($ZnSO_4$) at 0.5 mL/L which was then left to settle for 5 minutes. The sample was then filtered using a filter paper to remove any sediment before adding 1 mL of Nessler reagent to avoid error in photometer reading. After 30 minutes, each samples were added into a cuvette which will be placed in the photometer (Merck Spectroquant Prove 300, Taylors University).The absorbance measurement was set at 425 mm according to the standard and was also tested using a blank (Nesslerized ammonia-free water) followed by each sample. Each sample data was recorded to create a calibration curve.

2.4.2 Chemical Oxygen Demand (COD) and Biological Oxygen Demand (BOD).

The method to analyze the COD and BOD was by using a test kit from Merck and was tested using a Photometer (Merck Spectroquant Prove 300, Taylors University). The COD test kit has a range of 15-300 mg/L while the BOD has a range of 0.5-3000 mg/L. Each test kit has a specific method of testing according to ASTM standard. The test method for COD was 2 mL of the sample was added to the Merck sample tube and was shaken at the cap until its mixed which was then heated in a thermoreactor for 2 hours at 150^{o} [16]. After 2 hours, the sample tube was then cooled down for 30 minutes on a rack and was then tested using the photometer. The test method for BOD was modified based on the winkler dissolved oxygen method [17]. There were 3 reagents which were SP 1, SP 2 and SP 3 . The sample was poured into an oxygenated bottle until its full and bubble free. 5 drops of SP1 and 10 drops of SP2 were added and slowly stirred for 10 seconds and was closed and set aside for 1 minute to react. SP 3 was then added at 10 drops and was stirred for another 10 seconds. The sample was then left for 5 minutes before taking the sample from the bottle into the sample tubes to be tested in the photometer.

2.4.3 Jar Test

The purpose of jar test was to know the amount of coagulant concentration needed for optimum sludge settlement which was based on the ASTM jar test of water [18]. This jar test was highly related to sludge volume index to determine the amount of sludge in the mixture. This was because the amount of sludge will determine the condition of the bacteria and also was considered a physical treatment before obtaining the final ammonia concentration. Lime will be used as the coagulant component. 1000 mL of six samples were taken after ammoniacal nitrogen removal. The jars were placed on a stirrer (Lovibond ET 750, Taylors University) with paddles positioned perpendicularly to each beaker. At 10-40 rpm with an interval of 10, the liquid was mixed for 30 seconds. The first beaker was left as a blank while the other 5 beakers were added with lime at different concentration. The samples were then stirred for 60 seconds at 75-300 rpm with 75 rpm interval. Then it was slowly reduced to 40 rpm for 160 seconds. Let the liquid settle for 15 minutes and record the appearance and time of settlement for each of the samples. Use Zinc Sulphate to reduce the turbidity in the

water. The steps were repeated at the intervals and the results were compared to know the amount of coagulant concentration needed for the sludge to settle.

2.4.4 Sludge Volume Index (SVI)

The SVI was used to determine and compare the mixed solution to know the settleability in the liquid which were based on the Wastewater and Water standard of America [19]. This was to determine the amount of sludge used before and after the denitrification process and the relation between denitrification process and sludge volume. The volume includes mixed liquor solid settleability (MLSS) concentration and the formula can be seen in Eq (1). The volume was in milliliters occupied by one gram of activated sludge that has settled within 30 minutes as was related to MLSS concentration in g/L. The MLSS concentration was approximately same with the amount of organism in the bioreactor. A good SVI is when it was in between 80-100 [16].

$$SVI = \frac{Mixed\ Liquar\ solid\ settled\ in\ 30\ minutes}{\frac{\left(MLSS\ concentration\ \frac{mg}{L}\right)}{1000}} \quad (1)$$

3.0 Results and Discussion

Aerobic and anaerobic test was carried out with 4 grams, 8 grams and 12 grams of bacteria with a constant parameter of pH 7 and a temperature of 37^{o}C for 24 hours. Further improvement of ammonia removal was also tested using ionic liquid at 1 mL to 4 mL using 100mL of each conditions sample. After determining the best condition for the bacteria growth then pH and temperature can be manipulated to determine the relationship between the parameters and ammonia removal rate.

3.1 Ammonia Removal based on Aerobic and Anaerobic Conditions

Two type of condition was applied to the bacteria in terms of aerobic condition or anaerobic condition and each conditions provides different in the sustainability of the bacteria that can result in a diverse difference in term of ammonia removal rate.

Table 2: Ammonia removal rate based on aerobic or anaerobic conditions.

Condition	Time	Bacteria (gram)	Concentration (ppm)		Ammonia removal rate (%)
			Initial	Final	
Aerobic	24 hour	4	100	43.969	56.031
		8	100	19.854	80.146
		12	100	5.8274	94.173
Anaerobic	24 hour	4	100	63.128	36.872
		8	100	59.235	40.765
		12	100	53.513	46.487

The two aerobic and anaerobic conditions inhibit different growth rate of the bacteria which were highly co-related to the ammonia removal rate. By comparing the results, aerobic bacteria has a higher removal rate of 56.031% to 94.173% while

anaerobic was only able to remove 36.872% to 46.4877%. This has shown that aerobic condition has a higher efficiency in ammonia removal compared to anaerobic bacteria. This could be highly due to the characteristic of ammoniacal nitrogen that were readily biodegradable and has a high oxygen demand. Oxygen shows to be a limiting factor in bacterial growth [20].

The results were tabulated in Table 2 in which the ammonia removal rate was higher in aerobic conditions. Even if aerobic bacteria show a more efficient result but anaerobic was also able to remove a certain amount of ammonia only. Thus, the growth of the bacteria was able to survive in both the condition but produces different ammonia removal rate. Based on the study conducted by Fuafo et al., the results of *Bacillus spp.* shows a similar growth trend in which the bacteria were able to grow in both aerobic and anaerobic conditions however it shows a higher growth rate in aerobic conditions [21]. There were two factors that affect the ammonia removal rate which were the bacteria growth in different conditions and the amount of bacteria added. Thus, based on the results 12 grams of bacteria in aerobic condition has the highest ammonia removal rate of 94.173% in the ammonia biodegration process. Furthermore, COD, BOD and sludge weight were required to be taken into account as well.

Table 3: COD, BOD and sludge weight in based on 12 grams of bacteria

Conditions	BOD (mg/L)		COD (mg/L)		SVI
	Initial	Final	Initial	Final	
Aerobic	9.6000	3.2000	1261.0	12.000	91.000

Aerobic condition shows a BOD of 3.2000 mg/L and COD of 12.000 mg/L with an SVI of 91. The BOD and COD were within the range for the DOE requirement standard B of 10 mg/L and 100 mg/L. However, the initial BOD was 8.9000 mg/L and dropped to 3.2 mg/L which has only achieved a removal of 66.667%. The results were considered to be poor and showed that there was still a certain amount of organic matter that requires to be removed in the solution as compared to Corsino et al.,. He was able to achieve 90% removal of BOD that was higher than the resulted outcome. This was due to the process difference used such as bacteria and wastewater composition. Furthermore, COD has an initial reading of 1261.0 mg/L and dropped to 12.000 mg/L that archived a 99.048% removal rate which was an excellent result compared to Corsino et al., that was only able to remove 90% of the COD. There can still be improvements to the BOD removal efficiency by using pretreatment methods or filtering methods as researched by Saad using activated carbon and sand filtration [22]. Based on the SVI at 91.000, there were still remaining organics suspended within the solution because it was above the range of 80 and states that there was still an amount of suspended organic that hasn't been removed yet [23]. This can be further improved by increasing the floc size of the sludge either by changing the coagulant or adding treatment beforehand as suggested by Rosman et al., [24].

3.2 Improving Ammonia Removal using Ionic Liquid

Ammonia removal rate was further improved using ionic liquid after the denitrification process in the bioreactor. The ionic liquid was based on the ion composition of 40:60 of negative to positive ions based on the ionic liquid characteristic provided by platinum strike Sdn Bhd. 100 mL of 4 samples from the reactor were taken to be tested. The results were compiled and obtained as seen in Table 3.

Table 4: Ammonia removal based on ionic liquid addition

Ionic liquid (mL)	Ammonia concentration (ppm)					
	Aerobic condition			Anaerobic condition		
	4 g	8 g	12 g	4 g	8 g	12 g
1	35.119	20.296	16.535	52.376	50.827	42.907
2	6.2260	19.544	11.137	37.022	38.792	20.606
3	6.8450	20.031	24.146	22.730	21.668	18.881
4	11.093	19.721	24.765	20.341	15.518	29.942

Table 4 shows the relationship of ionic liquid based on two conditions with different bacteria weight. For aerobic condition, 100 mL samples were tested using 1-4 mL of ionic liquid with 1mL interval which was set as a basis. 4 gram of bacteria resulted in a decrease in ammonia concentration of 6.8450 ppm based on 3 mL of ionic liquid and increases to 11.093 ppm with 4 mL of ionic liquid. 8 gram of bacteria resulted in a decrease in ammonia concentration up to 19.544 mg/L of 2 mL of ionic liquid then resulted in a slight variation of 20.031 mg/L of ammonia then 19.721 mg/L.12 grams resulted in a decrease of ammonia removal up to 11.137 mg/L using 2 mL then resulted in a slight increase up to 24.765 mg/L. There was a certain pattern based on the aerobic condition in which after a certain amount of ionic liquid added there would be a slight increase in ammonia concentration. After removing excess ammonia ions with ionic liquid there will be no ions left to be binded and will result in the excess ionic liquid to be in the solution. However, Fisher et al., was studying on the removal of metal ions in wastewater but shows similar reasoning based on her results that there was an excess of ions due to ionic liquid unable to bind with the metal ions.

For anaerobic conditions, with 4 grams of bacteria the concentration of ammonia decreases until 20.341 mg/L with the increase of ionic liquid added. For 8 grams of bacteria there concentration of ammonia was reduced until 15.518 mg/L and for 12 grams of bacteria the ammonia concentration was until 18.881 mg/L then increased slightly to 29.942 mg/L. Based on the decrease of ammonia concentration in each of the samples, there were more un-binded ions compared to aerobic which was due to the poor biodegration of ammoniacal nitrogen in anaerobic condition which was similar to Foresti et al., result [25-26]. Since the initial bacteria denitrification stage produces poor results, ionic liquid was able to remove the excess ions that the bacteria couldn't. This results in a higher removal rate during the second removal process using ionic liquid.

3.3 Effect of pH on Ammoniacal Nitrogen Removal Rate

Aerobic condition with 12 grams of bacteria has the highest ammonia removal rate which will be used as a constant to study the effect of pH. Based on Cheba et al., he studied that *Bacillus spp*. were highly stable between pH 7 and pH 8 and was able to sustain its growth. Also, Sabumon et al., studied on ammonia removal using batch process with a pH less than 7 and occurred poor ammonia removal rate of 44% [27]. The results was obtained and compiled in Table 5.

Table 5: Ammonia removal based on pH

pH	Concentration (ppm)	Ammonia removal rate (%)
6	50.296	49.704
7	5.8270	94.173
8	25.221	74.779

It has been identified that the highest ammonia removal was at pH 7 with a final concentration of 5.827 ppm with an ammonia removal of 94.173% while the lowest was at pH 6 with a final concentration of 50.296 ppm with an ammonia removal of 49.704%.There was still a slightly higher ammonia removal rate at pH 8 of 74.779% compared to pH 6 which states that there was a higher biodegration process of ammoniacal nitrogen in an alkaline environment compared to the acidic environment. This can be highly due to the characteristic of the bacteria to either be able to withstand an alkaline or acidic environment for the bacteria to fully function in a stressful growth environment.

A stressful growth environment can induce the bacteria into homeostasis mode in which the bacteria will stop multiplying and be in a standstill state to survive the harsh environment [28]. Thus, there was no biodegration of ammoniacal nitrogen due to the inactivity of the bacteria. A *bacillus spp.* bacterium optimally grows at a pH of 7 and was slightly tolerant to an alkaline environment which was in an agreement with Cheba et al., and Sabumon et al., results.

3.4 Effect of Temperature on Ammonia Removal Rate

Using the constant variables chosen which was in an aerobic condition with 12 grams of bacteria, temperature was considered a manipulated variable using temperature 30^{o}C, 35 ^{o}C, 37^{o}C and 40 ^{o}C. Table 6 shows the data obtained during experimentation.

Table 6: Ammonia removal based on the temperature.

Temperature (^{o}C)	Concentration (ppm)	Ammonia removal rate (%)
30	50.341	49.659
35	27.730	72.270
37	94.173	94.173
40	51.712	48.288

The ammonia removal rate was at 49.659% which slowly increased to 72.270% at 35^{o}C .However, the temperature of 37^{o}C was initially tested and found that the removal rate was at 94.173% and was then decreases at 40^{o}C with a removal rate of 48.288%. The temperature then drops as it slowly increases to 40^{o}C. *Bacillus spp*. has always been known as a thermophilic bacteria and a mesophilic bacteria depending on the genus [29]. For this experiment, the *Bacillus spp*. used was a mesophilic bacteria based on the bacteria characteristic. With this environment, the bacteria was not able to thrive beyond 40^{o}C and under 30^{o}C and has an optimum growth at 35-37^{o}C [29]. Lopex et al., also tested the removal of ammonia in industrial wastewater treatment using

various bacteria and found that all failed to show bacterial activity above 40^{o}C which results in poor ammonia removal rate [30]. Sudamo et al., also tested until a temperature of 40^{o}C in a similar test and found that it was optimal between 37^{o}C [31]. This shows that ammonia removal rate was highly dependent on the growth or condition of the bacteria.

4.0 Conclusion

Ammonia removal was conducted through biological treatment using bacteria with similar traits to *Bacillus spp* and further improvement of ammonia removal using ion exchange process using ionic liquid. Based on the two growth conditions which were aerobic and anaerobic, aerobic conditions provides the most suitable environment for denitrification process to take place. The amount of bacteria used in the aerobic conditions also was an important factor in which 12 grams of bacteria was able to remove 94.173%. Further ammonia removal was also highly dependent on the amount of ammonia ions that was inside the solution. Also, the pH and temperature was an up most important parameter to ensure smooth ammonia removal and bacteria growth. Thus, the optimum pH was 7 and temperature of 37^{o}C

Based on the research objective, 5.8730 ppm can be met under the aerobic conditions with 12 grams bacteria and also 19.859 ppm with 8 grams of bacteria that was able to meet standard B set by DOE of 20 ppm. Thus, anywhere between the range of 8 grams to 12 grams of bacteria in aerobic condition for 24 hours was able to achieve the DOE standard B also taking into account the BOD,COD and SVI at 3.2000 mg/L, 12.000 mg/L and 91.000. In conclusion, the results obtained have provided substantial result that is able to be used in the future for ammoniacal nitrogen treatment in Malaysia as well as it is able to meet the DOE requirement with a removal rate of up to 94.173%.

References

[1] D. Butler and F. a Memon, *Water Demand Management*, 1st ed. London: IWA publishing, 2006.
[2] Department of economic planning P, “Ensuring Quality and Efficient Water and Sewerage Services,” *Stratey. Paper*, no. 16, pp. 1–14, 2016.
[3] Department of Environment Malaysia, “Malaysia Environmental Quality Report 2014,” Malaysia, 2015.
[4] Department of Environment Malaysia, “Malaysia Environmental Quality Report 2015,” Malaysia, 2016.
[5] Y. J. Chan, M. F. Chong, C. L. Law, and D. G. Hassell, “A Review on Anaerobic-Aerobic Treatment of Industrial and Municipal Wastewater,” *Chemical Engineering Journal*, vol. 155, no. 1–2, pp. 1–18, 2009.
[6] L. Foglar, F. Briski, L. Sipos, and M. Vuković, “High nitrate removal from synthetic wastewater with the mixed bacterial culture,” *Bioresource Technology*, vol. 96, no. 8, pp. 879–888, 2005.
[7] M. I. M. Soares, “Biological denitrification of groundwater,” *Water Air Soil Pollution Journal*, vol. 123, pp. 183–193, 2000.
[8] W. Zhou, Y. Sun, B. Wu, Y. Zhang, M. Huang, T. Miyanaga, and Z. Zhang, “Autotrophic Denitrification for Nitrate and Nitrite Removal using Sulfur-Limestone,” *Enviromental Science Journal*, vol. 23, no. 11, pp. 1761–1769, 2011.
[9] S. J. Ergas and D. E. Rheinheimer, “Drinking water denitrification using a membrane bioreactor,” *Water Resource*, vol. 38, no. 14–15, pp. 3225–3232,

2004.
[10] J. Van Der Hoek, P. Van Der Ven, and A. Klapwijk, “Combined Ion Exchange / Biological Denitrification for Nitrate Removal from Ground Water under Different Process Conditions,” *Water Resource*, no. 22, pp. 679–684, 1988.
[11] X. P. Yang, S. M. Wang, D. W. Zhang, and L. X. Zhou, “Isolation and nitrogen removal characteristics of an aerobic heterotrophic nitrifying-denitrifying bacterium, Bacillus subtilis A1,” *Bioresource Technology*, vol. 102, no. 2, pp. 854–862, 2011.
[12] S. . Yang, S. . Wang, D. . Zhang, and L. . Zhou, “Aerobic nitrification–denitrification by heterotrophic Bacillus strains,” *Bioresource Technology*, 2011.
[13] International organization for standardization, “ISO-17665 : Steam sterilization for medical devices.” .
[14] J. Muhammad and Y. Namdar, “Nutritional optimization for anerobic growth of Bacillus steaothermophilus LLD-16,” *Radiation Resource Applied Science Journal*, vol. 9, pp. 170–179, 2015.
[15] ASTM Standard D1426, “Standard Test Methods for Ammonia Nitrogen In Water,” *ASTM International*, no. September, pp. 1–7, 2008.
[16] Standard methods for the examination of water and wastewater, “Method 5220 D,” vol. 18, 1998.
[17] Standard methods for examination of water and wastewater, “4500-O: Oxygen dissolved.”
[18] ASTM, “Standard Practice for Coagulation- Flocculation Jar Test of Water,” 2013.
[19] Water Environment Federation, “2710 D,” *Standard Methods Examination Water Wastewater*, vol. 20, 1997.
[20] A. O. Sliekers, N. Derwort, J. L. Campos Gomez, M. Strous, J. G. Kuenen, and M. S. M. Jetten, “Completely autotrophic nitrogen removal over nitrite in one single reactor,” *Water Resource*, vol. 36, no. 10, pp. 2475–2482, 2002.
[21] S. Fuofu, S. Elena, C. Ruth, B. Stephanie, D. Mary, S. Alexi, P. Petar, E. Dusko, and H. Marion, “Regulators of Aerobic and Anaerobic Respiration in Bacillus subtilis,” *Bacterology Journal*, vol. 178, no. 5, 1996.
[22] S. A. Al-Jlil, “COD and BOD reduction of domestic wastewater using activated sludge, sand filters and activated Carbon in Saudi Arabia,” *Biotechnology*, vol. 8, no. 4, pp. 473–477, 2009.
[23] D. Wei, L. Shi, T. Yan, G. Zhang, Y. Wang, and B. Du, “Aerobic granules formation and simultaneous nitrogen and phosphorus removal treating high strength ammonia wastewater in sequencing batch reactor,” *Bioresource Technology*, vol. 171, no. 1, pp. 211–216, 2014.
[24] N. H. Rosman, A. Nor Anuar, S. Chelliapan, M. F. Md Din, and Z. Ujang, “Characteristics and performance of aerobic granular sludge treating rubber wastewater at different hydraulic retention time,” *Bioresource Technology*, vol. 161, pp. 155–161, 2014.
[25] D. C. Rodríguez, O. Ramírez, and G. P. Mesa, “Behavior of nitrifying and denitrifying bacteria in a sequencing batch reactor for the removal of ammoniacal nitrogen and organic matter,” *Desalination*, vol. 273, no. 2–3, pp. 447–452, 2011.
[26] E. Foresti, M. Zaiat, and M. Vallero, “Anaerobic processes as the core technology for sustainable domestic wastewater treatment: Consolidated applications, new trends, perspectives, and challenges,” *Enviroment Science Biotechnology*, vol. 5, no. 1, pp. 3–19, 2006.

[27] P. . Sabumon, “Anaerobic ammonia removal in presence of organic matter: A novel route,” *Hazard Matter*, vol. 149, pp. 49–58, 2007.

[28] E. Padan, E. Bibi, M. Ito, and T. A. Krulwich, “Alkaline pH homeostasis in bacteria: New insights,” *Biochimican Biophysica Acta - Biomembrane*, vol. 1717, no. 2, pp. 67–88, 2005.

[29] C. Ben, Z. Taha, E.-M. Rafik, and E.-M. Hisham, “Effect of pH and Temperature on Bacillus sp. R2 Chitinase Activity and Stability,” *Procedia Technology*, vol. 22, pp. 471–477, 2016.

[30] C. . Lopex-Vaxquez, M. Kubare, D. . Saroj, C. Chikamba, S. J, D. H, and Crdjanovic, “Thermophilic biological nitrogen removal in industrial wastewater treatment,” *Enviromental Biotechnology*, 2013.

[31] U. Sudarno, J. Winter, and C. Gallert, “Effect of varying salinity, temperature, ammonia and nitrous acid concentrations on nitrification of saline wastewater in fixed-bed reactors,” *Bioresource Technology*, vol. 102, no. 10, pp. 5665–5673, 2011.

Primary Recovery of Amylase from Pitaya (*Hylocereus Polyrhizus*) Peels Using Alcohol/Salt Aqueous Two-Phase System (ATPS)

Ow Jun Leong[*], Chow Yin Hui[#]

Taylor's University Lakeside Campus, Jalan Taylor's, Subang Jaya, 47500, Selangor Darul Ehsan, Malaysia

[*]*junleong.ow@sd.taylors.edu.my*
[#]*yinhui.chow@taylors.edu.my*

Abstract
In this study, the alcohol-salt aqueous two phase system (ATPS) is used to recover the amylase from the red pitaya peel. Currently, the source is only limited to certain strains of microorganisms. Plant source like red pitaya peel can serve as a natural source to produce amylase with the Generally Recognized as Safe (GRAS) status for use in industries like the pharmaceutical industry as a digestive aid. Pitaya peel, which constitutes 33% of its total weight, is a fruit residue that usually thrown away from the food industry. The conventional chromatographic techniques such as precipitation and ion exchange to extract the amylase are not favourable because of low yield, multi-step and decrease of enzymatic activity. In this study, the ATPS is proposed as an alternative recovery method due to the advantage of one step, fast separation and no influence on the enzymatic activity. The ethanol and potassium phosphate are selected as the phase forming chemicals because of the efficient recovery, reusable and inexpensive constituents. The ATPS of 19 % (w/w) ethanol, 26 % (w/w) potassium phosphate (pH 7) and 5 % (w/w) NaCl has the optimum partition efficiency for the recovery of the amylase. The purified amylase had a purification factor of 5.8, a selectivity of 4.72 and a yield of 94.956 %. Therefore, the ethanol-potassium phosphate ATPS can serve as an easy and practical method in the recovery of the amylase from the red pitaya peel.

Keywords
Amylase, protein recovery, aqueous two-phase system, bio-separation, purification

1. Introduction

$\alpha-$amylase is a starch degrading enzyme that helps to break down the carbohydrates into the reducing group i.e. maltose [1]. This enzyme itself currently consumes 30% of the industrial enzyme production and is widely used in various industries to produce value added products [2]. Extraction of the amylase generally limited to the microorganism because of achievable economical production in a high reproduction rate [3]. However, amylase extracted from the microorganisms will cause allergic reaction when it is consumed by human being [4]. Based on Generally Recognized as Safe (GRAS) status, natural source i.e. plant peel is an alternative source to extract the industrial enzymes as no harmful residues should be found in the finished product. Recent biotechnology has enabled the plant to use the peel source to produce a variety of enzymes including amylase. One of the plant peels is red pitaya (*Hylocereus polyrhizus*) peel. The peel, which amounts to one-third of the total fruit weight, is usually disposed as waste material by the food and beverage industries. It can be beneficially utilized in the enzymes production [5].

Processes like precipitation, dialysis and chromatography are the conventional method to extract the amylase in the industries. But, disadvantages such as low stability, low reusability of organic solvent, multi-step and high investment cost are not feasible for the production. Aqueous two-phase system (ATPS) is a cost-effective purification that is proposed to replace the aforementioned techniques. This separation technique consists of two different immiscible aqueous phases that form under a critical concentration [6]. Advantages like simple and benign technique, rapid separation, short processing time and reusability of organic solvents have led to its wide application in the separation and purification of biomolecules [7]. Polymer-polymer and polymer-salt are the common ATPSs used to extract the biomolecules. The accompanied slow segregation phase forming, high viscosities and high polymer cost have however make them not feasible for the large-scale protein purification [8]. Alcohol-salt ATPS is another alternative system that can be applied in protein purification with the advantages of simplifying process recycling of organic solvents, low toxicity towards the environment, easy scalability, low viscosity and low investment cost [8,9]. However, there is a setback in using this ATPS which is target biomolecules are incompatible with the organic solvent phases. As a result, denaturation and inactivation of target enzymes occur [7]. Although alcohol-salt ATPS has its disadvantages, it has been applied for the recovery of protease [10] and lipase [7] by using low concentration of alcohol and high concentration of salt solution. The reason is to prevent the loss of enzyme partition to the bottom phase through precipitation.

In this study, purification and separation of amylase from pitaya peel is attempted for first time in literature by using the alcohol-salt ATPS to provide alternative amylase recovery techniques from pitaya peel with high yield. According to the study of M. Amid and Y. Manap [11], recovery of amylase from mango waste using ethanol-phosphate ATPS shown the highest partition coefficient and selectivity among all the alcohol-salt ATPS phase forming components (e.g. ethanol, 1-propanol, 2-propanol, sodium phosphate, ammonium sulphate & sodium citrate) investigated. In this study, the ethanol and phosphate salt were selected as the phase forming component on amylase partitioning.

The influence of ATPS parameters such as phase forming composition, pH & addition of sodium chloride on the partition efficiency of the amylase in the alcohol-salt ATPS is investigated in this study to determine the optimum condition of ATPS parameters for the recovery of amylase from the red pitaya peel. The research gap of this project is the extraction of amylase from natural source based on GRAS status using cost effective liquid-liquid separation method.

2. Methods and Materials

2.1 Chemicals and Materials

Red pitaya fruits were acquired from Pasar Borong Selayang (Kuala Lumpur, Malaysia). These fruits were picked depend on their grade and size uniformity at the phase of ripening and lack of visual defects on the peel surface. Sodium hydroxide was obtained from R & M chemicals (Essex, United Kingdom). Bovine Serum Albumin (BSA) and Pierce BCA Protein Assay Reagent A & reagent B were obtained from Thermo Scientific (Rockford, United States of America). Anhydrous sodium acetate (CH_3COONa) was obtained from Merck (Billerica, United States of America). Potassium dihydrogen phosphate ($KH_2PO_4 \cdot H_2O$), dipotassium hydrogen phosphate ($K_2HPO_4 \cdot 2H_2O$), glacial acetic acid (CH_3COOH), potassium sodium tartrate tetrahydrate ($NaKC_4H_4O_6 \cdot 4H_2O$) and soluble starch were obtained from Merck (Darmstadt, Germany). Sodium chloride (NaCl), 3, 5-dinitrosalicylic acid (DNS) and D (+) maltose monohydrate ($C_{12}H_{22}O_{11} \cdot H_2O$) were obtained from Sigma-Aldrich (St. Louis, Missouri, United States of America). Ethanol Absolute 99.8% (C_2H_5OH) was obtained from VWR Chemicals (Fontenay-Sous-Bois, France). All reagents and chemicals used in the experiment were of analytical grade.

2.2 Preparation of Crude Extract

Red pitaya fruits were rinsed and cleaned thoroughly with the deionised water. Dry tissue towel was used to drain the deionised water on the peel surface. Subsequently, peels were separated from the red flesh and carved into small pieces by using a stainless-steel knife. Then, the sliced peels and sodium acetate buffer (pH 5.0) were blended (Model Takada TK-350, Takada Corporation, Japan) at a sample: buffer ratio of 1:4 for 2 minutes at a temperature of 2.5 ℃. Next, the blended homogenate was filtered by using cheesecloth. Thereafter, the filtrate homogenate was centrifuged (Model G322511050059, Labogene, Denmark) at 4427 x g for 5 minutes at a temperature of 4 ℃. The crude load was collected and kept for overnight at a temperature of 4 ℃ to maintain the stability of the enzyme activity before the ATPS partitioning experiment [12].

2.3 ATPS Partitioning

Alcohol-salt ATPSs with a volume ratio, V_R of 1 were prepared in the 15ml centrifuge tube by mixing the ethanol, 50 % (w/w) phosphate buffer stock solution at desired pH, 10 % (w/w) crude load and sodium chloride (NaCl) at an appropriate ratio according to the ethanol-phosphate ATPS phase diagram reported by Ooi et al. [7]. Deionised water was added lastly until the final mass reached 5g. The 50 % (w/w) phosphate buffer stock solution at desired pH by mixing the different solution of monobasic potassium phosphate and dibasic potassium phosphate at appropriate

proportion. The resulted mixture was thoroughly mixed with vortex mixer (Model BV 1000, Benchmark Scientific, New Jersey, USA) and centrifuged (Model G322511050059, Labogene, Denmark) at 1968 x g for 10 min to achieve a total phase separation. The volume of both (top and bottom) phases was measured to determine the V_R. The samples were collected from top and bottom phases for amylase activity assay and BCA assay.

2.4 Amylase Activity Assay

Amylase activity assay was conducted according to the enzymatic assay of Bernfield [13] to measure the amylase enzymatic activity at both top and bottom phases. which contained. Firstly, 200 μl of 25 % (w/v) soluble starch solution prepared in the sodium acetate buffer (pH 5.0) that contained 10 mM sodium chloride was mixed with 200 μl of amylase extracting sample from top phase and bottom phase in the 2ml microcentrifuge tube. Next, the amylase sample was incubated in an incubator (Model BP120, Froilabo Firlabo, France) at a temperature of 37 ℃, for 20 mins. Once the incubation finished, 200 μL of 3,5-dinitrosalicylic acid (DNS) solution was added to the sample solution for determination of reducing sugar. The DNS solution was prepared by mixing 0.5 g of DNS, 15 g of potassium sodium tartrate tetrahydrate, 0.8 g of sodium hydroxide and 50 ml of deionised water. Then, the sample solution was heated at a temperature of 100 ℃, for 15 minutes. The heated sample solution mixture was then cooled for 5 mins and 900 μl of deionised water were added to the solution. The released reducing sugar was measured using the microplate reader (Model EPOCH2T, BioTek, Winnoski, VT, USA) at 540 nm. Maltose is used as the standard reducing sugar. One unit of α-amylase activity (U) was determined as the quantity of enzyme that produced 1 μmol of maltose per minute under the enzyme activity conditions [12]. A blank ATPS without the crude load was prepared to eliminate the interference from alcohol and salt phase-forming components.

2.5 Total Protein Determination

Total protein content in the top and bottom phase were measured using bicinchoninic acid assay (BCA) [12]. Bovine serum albumin (BSA) was used as the standard in this assay. Firstly, enzyme sample and working reagent solution were added into a microplate well with a sample: working reagent ratio of 1:8. The filled microplate wells were then shaken for 30 seconds on a microplate mixer. Next, the shaken samples were incubated in an incubator (Model BP120, Froilabo Firlabo, France) at a temperature of 37 ℃, for 30 mins. The solution was then measured using the microplate reader (Model EPOCH2T, BioTek, Winnoski, VT, USA) at 562nm. A blank ATPS without the crude load was prepared to eliminate the interference from alcohol and salt phase-forming component and then measured at 562 nm.

2.6 Calculation of Partition Parameters

Amylase partition coefficient (K_e) was defined as the ratio of amylase activity measured at the alcohol-rich top phase to the salt-rich bottom phases:

$$K_e = \frac{A_T}{A_B} \quad (1)$$

where A_T and A_B were the activity of amylase from ethanol and potassium phosphate phases, respectively.

Protein partition coefficient (K_P) was defined as the ratio of concentration of total protein measured at the alcohol-rich top phase to the salt-rich bottom phase:

$$K_p = \frac{P_T}{P_B} \tag{2}$$

where P_T and P_B were the total protein concentration measured in the ethanol and potassium phosphate phases.

Selectivity was defined as the ratio of the amylase enzyme partition coefficient (K_e) to the protein partition coefficient (K_P) and calculated using Eq. (3) [5]:

$$S = \frac{K_e}{K_P} = \frac{\frac{A_T}{A_B}}{\frac{P_T}{P_B}} \tag{3}$$

where Ke and K_P were the amylase enzyme partition coefficient and the protein partition coefficient, respectively.

Specific activity of amylase was determined using the following Eq. (4) [5]:

$$Specific\ activity\ \left(\frac{U}{mg}\right) = \frac{\text{amylase total activity (U)}}{Amount\ of\ total\ protein\ (mg)} \tag{4}$$

Purification factor was calculated using Eq. (5) and was defined as the ratio of amylase specific activity between the top phase and crude load [5]:

$$PF = \frac{Specific\ activity\ of\ amylase}{Specific\ activity\ of\ crude\ load} \tag{5}$$

Yield (%) was calculated using Eq. (6) and was determined based on the volume ratio of the ATPS (V_R, top phase to bottom phase) and amylase enzyme partition coefficient [5]:

$$Y_T = \frac{100}{1+\frac{1}{V_R K_e}} \tag{6}$$

where V_R is the volume ratio and K_e is the amylase enzyme partition coefficient.

3. Results and Discussions

3.1 Effect of Ethanol-Potassium Phosphate on Amylase Partitioning

Based on Figure 1, the partition coefficient (K_e) of the amylase increased when the phase forming components' concentration increased. The increment of phosphate concentration has strengthened the salting out effect and eventually increased the ethanol concentration in the alcohol phase [15]. The highest partition coefficient and selectivity of the amylase was measured at 19 % (w/w) ethanol - 26 % (w/w)

potassium phosphate ATPS, with the values of 8.529 and 3.168, respectively. However, the partition coefficient of the amylase decreased when the concentration of the ethanol exceeded 19 % (w/w). This result suggested that the increment of alcohol concentration lead to a reduction in the partitioning efficiency of amylase to the top phase. The amylase retention was not favoured in the top phase because of the gradual dehydration of potassium phosphate salt in the bottom phase [10]. Thus, the partition coefficient decreased at higher ethanol concentration. A similar style was noticed when the potassium phosphate concentration increased beyond 26 % (w/w). High concentration of phosphate will induce salting out effect, resulting in more proteins segregated towards the bottom phase [16]. The reason was the saturation of the phosphate salt concentration at the salt phase in which causing the phosphate salt cannot precipitate to the bottom phase anymore. This fact explained the lowest selectivity observed in the 25 % (w/w) ethanol – 30 % (w/w) potassium phosphate ATPS as shown in Figure 1. After reviewing the results from Figure 1, the optimum system which was 19 % (w/w) ethanol – 26 % (w/w) potassium phosphate ATPS was selected for further optimisation.

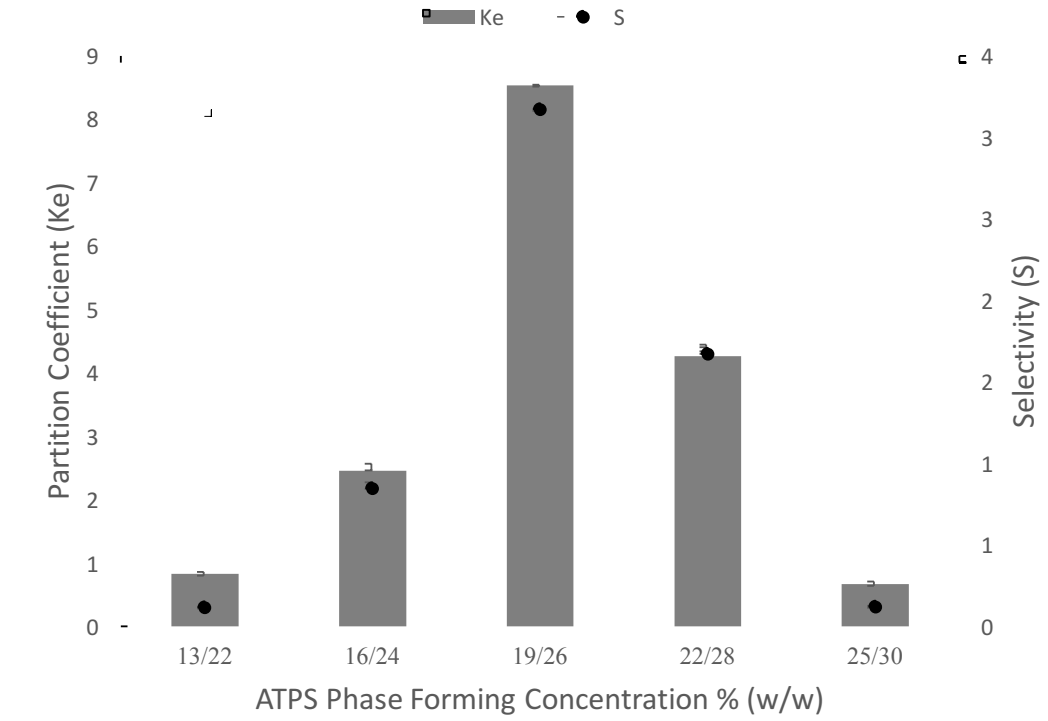


Figure 1. The amylase enzyme partition coefficient and selectivity of amylase in ethanol-potassium phosphate systems. This figure summarised the partitioning and selectivity of different phase forming components' concentration. The results were the means of triplicate readings, which has a standard error of $\pm$10%.

3.2 Effect of pH on Amylase Partitioning

Another important parameter that influences the biomolecules partitioning in the ATPS is the pH. The system pH in ATPS affects the target protein's surface properties and thus it's partitioning behaviour [17]. In this study, the effect of pH on partition coefficient, purification factor and selectivity on the partitioning of the

amylase in the 19 % (w/w) ethanol – 26 % (w/w) potassium phosphate ATPS was studied in the range of 7.0 to 9.0 at an interval of 0.5 (Figure 2). The pH below the range of 7.0 was not investigated because no phase forming of ATPS was visibly noticeable.

Based on Figure 2, the partition coefficient of the amylase decreased when the pH increased. The similar trend was also observed for the purification factor and selectivity. Amylase has an isoelectric point, pI of 5.0, in which the biomolecules carry no net electrical change. At system pH above the pI of the biomolecules, the biomolecules that were negatively charged therefore partitioned to the top phase, whereas the biomolecules that were positively charged therefore partitioned to the bottom phase [18]. Tentatively, the partition coefficient of the amylase should be increasing as the pH increased because of the higher positive charge density at the ethanol phase [19,20]. Thus, the negatively charged amylase favour a higher electrostatic interaction with the ethanol and partitioned to the top phase. This explained the highest amylase partition coefficient, purification factor and selectivity were observed at pH 7.0 because the electrostatic interactions of the amylase and the ethanol was the strongest. However, amylase partitioning decreased thereafter pH 7.0, which indicated there were possibility of the denaturation and precipitation of the amylase. The partition coefficient of the amylase at pH 9.0 was measured at 0.683. Due to the aforementioned possibilities, the pH above 7.0 were not feasible [21].

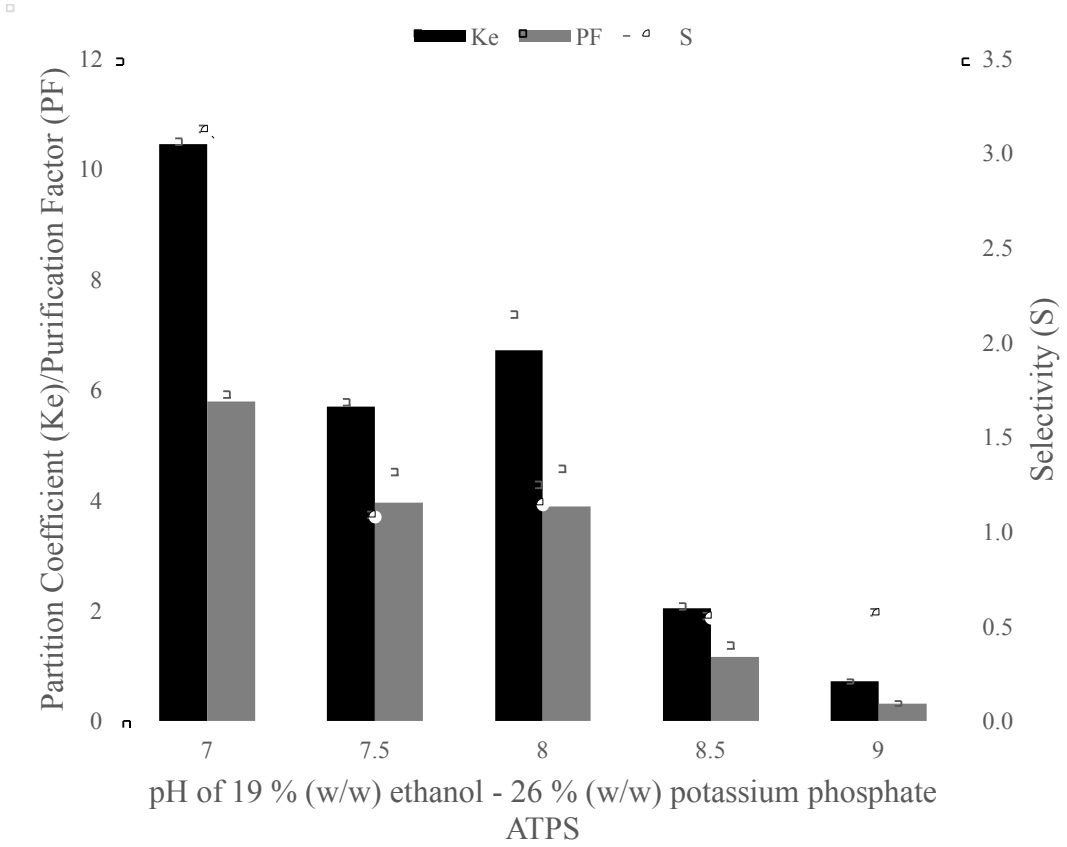


Figure 2. The amylase enzyme partition coefficient, purification factor and selectivity of amylase in different pH of ethanol-potassium phosphate systems. This figure summarised the partition coefficient, purification factor and selectivity

of different phase forming components' pH. The results were the means of triplicate readings, which has a standard error of ± 25 %.

3.3 Effect of Sodium Chloride (NaCl) on Amylase Partitioning

The addition of the salt generates the electrical potential difference between the phase forming and affects the biomolecules partitioning in ATPS [22]. By adding the NaCl, it generates the electrostatic potential that strongly expels the negatively charged amylase to the ethanol phase and further improves the amylase partitioning and the yield too [7]. Moreover, the non-toxicity property of NaCl does not affect the enzyme in any biological processes and aid the enzyme to partition towards the top phase efficiently [18]. Based on the result in Section 3.2, 19 % (w/w) ethanol- 26 % (w/w) potassium phosphate ATPS at pH 7 was chosen to study the effect of NaCl concentrations on the amylase purification factor, selectivity and yield and the results were shown in Figure 3. The concentrations were varied from 0 % (w/w) to 10 % (w/w) at an interval of 2.5 % (w/w).

Based on Figure 3, the trend of purification factor, selectivity and yield increased as the concentration of the NaCl increased. Generation of the electrostatic potential difference between the ethanol and potassium phosphate phases has strongly expelled the negatively charged amylase to the ethanol phase with the increment of the yield. In addition to that, the interaction of the amylase's hydrophobic surface area and ethanol's hydrophobic chain were enhanced by the hydrophobic interaction between the ethanol & the amylase as well as the effect of the salt added to the water solvent structure [6]. However, when the NaCl concentration exceeded 5 % (w/w), the purification factor, selectivity and yield decreased to a minimum of 1.096, 0.478 and 70.836 % at 10 % (w/w) NaCl. The significant decrease may be due to the precipitation and the denaturation of the amylase. Based on the obtained result, an optimum partition efficiency was achieved at 5 % (w/w) NaCl with selectivity of 4.72, purification factor of 5.8-fold and yield of 94.956 %.

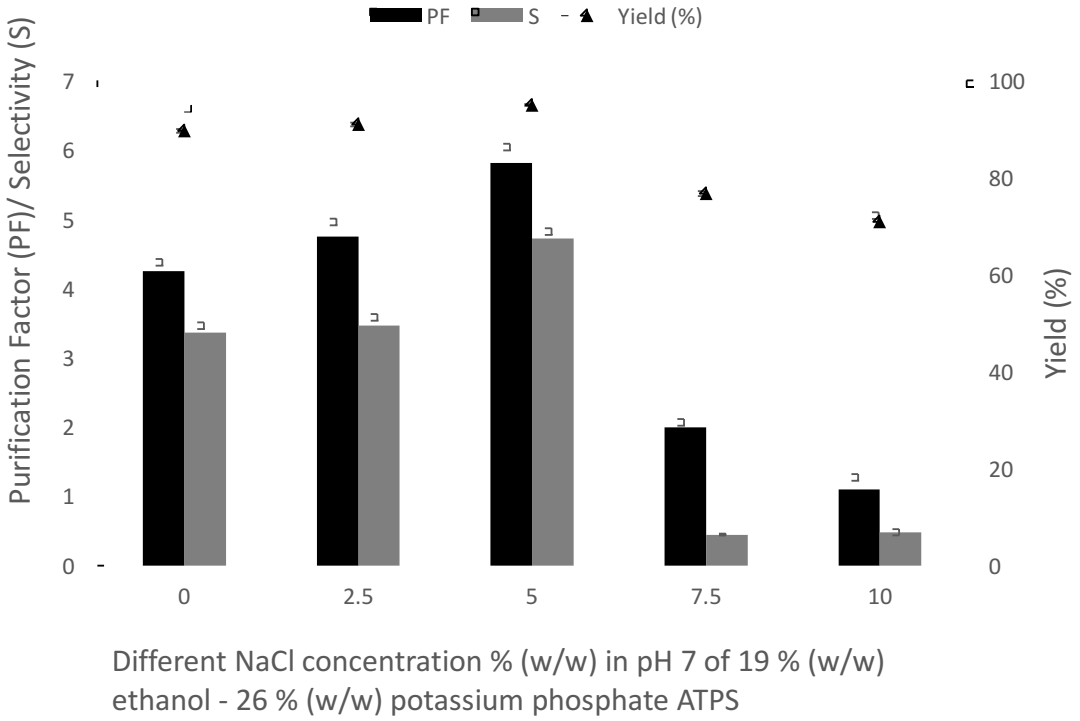


Figure 3. The purification factor, selectivity and yield of amylase at different NaCl concentration of ethanol-potassium phosphate systems. This figure summarised the purification factor, selectivity and yield of the amylase at different NaCl concentration. The results were the means of triplicate readings, which has a standard error of ± 10 %.

4. Conclusions

Amylase was successfully recovered from the red pitaya peel by using the ethanol-potassium phosphate ATPS. An optimum yield of 94.956 % and a high purification factor of 5.8 was achieved in an ATPS constituted of 19 % (w/w) ethanol, 26 % (w/w) potassium phosphate at pH 7 and 5 % (w/w) NaCl. Thus, alcohol-salt ATPS can serve as a rapid, biocompatible and cost effective alternative amylase recovery techniques for the recovery of amylase partitioning with high yield and purity.

References

[1] A. Sundarram and T. P. K. Murthy, "α-Amylase Production and Applications: A Review", *Journal of Applied & Environmental Microbiology*, Vol. 2, No. 4, pp. 166-175, 2014.

[2] P. M. de Souza and P. de Oliveira Magalhaes, "Application of Microbial a-Amylase in Industry- a Review", *Brazilian Journal of Microbiology*, Vol. 41, No. 4, pp 850-861, 2010.

[3] M. S. Tanyildizi, D. Ozer, M. Elibol, "Optimization of a-Amylase Production by *Bacillus Sp*. Using Response Surface Methodology", *Process Biochemical*, Vol. 40, No. 7, pp. 2291-2296, 2005.

[4] H. D. Shen, W. L. Lin, M. F. Tam, S. R. Wang, J. J. Tsai, H. Chou, S. H. Han, "Alkaline Serine Proteinase: A Major Allergen of *Aspergillus Oryzae* and its Cross-Reactivity with *Penicilium Citrinum*", *International Archives of Allergy and Immunology*, Vol. 1, No. 116, pp. 29-35, 1998.

[5] M. Amid, Y. Manap, N. Zohdi, "A novel Aqueous Two Phase System Composed of a Thermo-Separating Polymer and an Organic Solvent for Purification of Thermo-Acidic Amylase Enzyme from Red Pitaya (*Hylocereus Polyrhizus*) Peel", *Molecules*, Vol. 19, No. 5, pp. 6635-6650, 2014.

[6] P.A. Albertsson. *Partition of Cell Particles and Macromolecules*. New York: Wiley, pp. 309-341,1986.

[7] C.W. Ooi, B.T. Tey, S.L. Hii, "Purification of Lipase Derived from *Burkholderia Pseudomallei* with Alcohol/Salt-Based Aqueous Two-phase Systems", *Process Biochemistry*, Vol. 44, No. 10, pp. 1083-1087, 2009.

[8] T.W. Tan, Q. Huo, Q. Ling, "Purification of glycyrrhizin from *Glycyrrhiza Uralensis Fisch* with Ethanol/Phosphate Aqueous Two Phase System", *Biotechnology Letters*, Vol. 24, No. 17, pp. 1417-1420, 2002.

[9] W. Zhi and Q. Deng, "Purification of Salvianolic acid B from The Crude Extract of *Salvia Militiorrhiza* with Hydrophillic Organic/Salt-Containing Aqueous Two-Phase System by Counter-Current Chromatography", *Journal of Chromatography A*, Vol. 1116, No. 1-2, pp. 149-152, 2006.

[10] M. Amid, M. Shuhaimi, Z. Sarker, Y. Manap, "Purification of Serine Protease from Mango (*Mangifera Indica Cv. Chokanan*) Peel Using an Alcohol/Salt Aqueous Two-Phase System", *Food Chemistry*, Vol. 132, No. 3, pp. 1382-1386, 2012.

[11] M. Amid and Y. Manap, "Recovery of Amylase from Mango (*Mangifera Indica L. Cv. Chokanan*) Waste Using Organic Solvent/Salt Aqueous Two-Phase System: A Potential Low Cost Source of Enzyme and Purification Method", *Journal of Food, Agriculture and Environment*, Vol. 12, No. 2, pp. 259-262, 2014.

[12] M. Amid and Y. Manap, "Purification and Characterization of a Novel Amylase Enzyme from Red Pitaya (*Hylocereus Polyrhizus*) Peel", *Food chemistry*, Vol. 165, No. 47, pp. 412-418, 2014.

[13] P. Bernfield. "Amylases Alphas and Beta." *Methods in Enzymology*, Vol. 1, pp. 149-158, 1995.

[14] L. Jiang, L. He, M. Fountoulakis, "Comparison of protein precipitation methods for sample preparation prior to proteomic analysis", *Journal of chromatography A*, Vol. 1023, No. 2, pp. 317-320, 2004.

[15] S. S. Alumairi, M. S. Shawkat, M. A. Alaubydi, "Extraction of Aloin from Aloe Vera Plant and Study Its Effect in Micronucleus Formation in Acute Lymphoid Leukemia", *Iraqi Journal of Science*, Vol. 56, No. 1, pp731-737, 2015.

[16] R. C. F. Bonomo, L. A. Minim, J. S. R. Coimbra, R. C. I. Fontan, L. H. M. Silva, V. P. R. Minim, "Hydrophobic Interaction Adsorption of Whey Proteins: Effect of Temperature and Salt Concentration and Thermodynamic Analysis", *Journal of Chromatography B*, Vol 844, No. 1, pp. 6-14, 2006.

[17] R. Hatti-Kaul. *Methods in Biotechnology: Aqueous Two Phase System: Methods and Protocols.* New Jersey: Humana Press Inc, pp. 413-420, 1999.

[18] O. Aydogan, E. Bayraktar, U. Mehmetoglu, T. Kaeding, A. P. Zeng, "Selection and Optimization of an Aqueous Two Phase System for The Recovery of 1,3-Propandiol from Fermentation Broth", *Engineering in Life Sciences*, Vol.10, No. 2, pp. 121-129, 2010.

[19] L. Capezio, D. Romanini, G. Pico, B. Nerli, "Partition of Whey Milk Proteins in Aqueous Two Phase Systems of Polyethylene Glycol-Phosphate as A Starting Point to Isolate Proteins Expressed in Transgenic Milk", *Journal of Chromatography B*, Vol. 819, No. 1, pp. 25-31, 2005.

[20] J. -C. W. Lan, C. Y. Yeh, C. C. Wang, Y. H. Yang, H. S. Wu, "Partition Separation and Characterization of The Polyhydroxyalkanoates Synthase Produced from Recombinant Escherichia Coli Using an Aqueous Two-Phase System", *Journal of Bioscience and Bioengineering*, Vol. 116, No. 4, pp. 499-505, 2013.

[21] A. M. Azevedo, P. A. J. Rosa, F. Ferreira, M. R. Aires-Barros, "Chromatography-Free Recovery of Biopharmaceuticals through Aqueous Two-phase Processing", *Trends in Biotechnology*, Vol. 27, No. 4, pp. 240-247, 2009.

[22] B. Zaslavsky. *Aqueous Two-phase Partitioning: Physical Chemistry and Bioanalytical Applications*. New York: Marcel Dekker Inc, 1995.

eureca 2017 – Conference Paper
Paper Number 2CE13

Thermal Characterization of Recycled Waste Tire Rubber/EVA Blends

Siew Sue Ting[1]*, Suganti Ramarad[1#]

[1]School of Engineering, Taylor's University Lakeside Campus, Malaysia
**sueting.siew@sd.taylors.edu.my*
[#]*suganti.ramarad@taylors.edu.my*

Abstract
The rapid growth of automobile industry has a direct link to the increase in production of waste tire rubber. The growing number of waste tire generation has raised the environmental awareness. Waste tire rubber (WTR) has high thermal resistance as it contains natural rubber, fillers and additives to resist thermal degradation. To assess the feasibility of new application for the WTR, thermal properties of WTR and ethylene vinyl acetate copolymer (EVA) at different blend ratio was studied. The thermal degradation of WTR, EVA and blends were studied in a purified air atmosphere using thermogravimetric analysis (TGA). The degradation kinetic of dynamic samples with the different heating rate of 10, 20, and 30°C/min was studied using Kissinger model to determine the model fitting of the samples and the degradation activation energies of the blends. Oxidative degradation occurs in this case as purified air atmosphere was used. Two-step degradation was observed for all WTR, EVA and blends. Blends with higher EVA content showed better thermal stability. Kissinger model is used to undergo the degradation kinetic analysis by fitting the data collected from the TGA. From the kinetic analysis, the observed activation energy increased from the first step degradation to the second step of the degradation of the RTR/EVA blends. The 30RTR sample shows the highest thermal stability with the activation energy of 300kJ/mole at the second step of degradation as the EVA content increased.

Keywords: Waste Tire Rubber (WTR), Ethylene Vinyl Acetate (EVA), Thermogravimetric Analysis (TGA), Degradation Kinetic, Dynamic Response.

Introduction

In the world today, the utilisation of the tire increases as the manufacture of automobile industry increases. The main transportation such as cars, buses, transporting trucks and tankers, heavy duty vehicles and aeroplane are highly used, showing a rapid growth in automobile industry [1]. Hence, it is responsible for the tremendous amount of waste tire produced annually. Based on the annual report of the largest tire and rubber product manufacturers, the production of tires is approximated to be 1.4 billion units and estimated 14 million tonnes of waste tire is discarded [2]. Vulcanised tires, known as a thermoset, are highly resistant to high temperature degradation due to the cross-linked structure.

Waste tire rubber is commonly a blend of natural rubber, synthetic rubber, reinforcing fillers, carbon black, silica, metallic and reinforcement cables to achieve high grip, mechanical strength and durability [2-3]. Based on the application of tire rubber, the production of vehicle tires were enforced with chemical and additives in order to achieve the optimum mechanical and thermal properties. However, the disposal or degradation of the rubber has been a major challenge to date. Hence, methods such as devulcanisation and reclamation are done to break down the three-dimensional structure to attain the plasticity and the ability to reprocess while retaining the polymer backbone chain [4].

EVA is a combination of polymerisation of ethylene and vinyl acetate (VA). The application of EVA is commonly seen in insulation purpose for the rough environments such as moist and illumination and the additional feature of flame retardant properties [5]. Devulcanised and reclaimed rubber retained the processability and plasticity are able to be blended with EVA. The EVA has excellent thermal properties hoped to improve the thermal properties of the blend. The W. Chumeka [6], uses grafted poly(vinyl acetate) copolymer to enhance the miscibility of polymer and rubber blend.

In this paper, the thermal properties of RTR/EVA are ventured to search for a new route of application such as an electrical insulator. The major study on the influence of the blend ratio on thermal degradation properties and the degradation kinetics of reclaimed tire rubber/ethylene vinyl acetate copolymer (RTR/EVA) blends. Hence, this study will address the disposal issue of WTR as well as the study of thermal stability of polymeric material to assess the feasibility of new application for the WTR,

2.0 Methodology

2.1 Raw Materials

Waste tire rubber (WTR) used in this study is the reclaimed WTR supplied by Rubplast Sdn. Bhd.. The WTR is treated with chemicals in order to break down the crosslink, and known as reclaimed tire rubber (RTR). Ethylene co-vinyl acetate (EVA) is supplied by TPI Polena Public Limited Company. The properties of EVA is as shown in Table 2.1.

Table 0.1.Properties of ethylene vinyl acetate copolymer

PROPERTIES	
DENSITY	0.941 g/cm^3
SPECIFIC GRAVITY	0.92 to 0.96 g/cm^3
TENSILE STRENGTH (YIELD)	653 psi
TENSILE STRENGTH (BREAK)	3490 psi
TENSILE ELONGATION (BREAK)	820%
MELT PROCESSING TEMPERATURE	130-180°C

2.2 Preparation of Material: RTR/EVA Blends

2.2.1 Melt Compounding

Firstly, the EVA pellets are fed into the internal mixer (Machine Model: Brabender Plasticoder PL2000-6 equipped with co-rotating blades and a mixing head with a volumetric capacity of 69cm^3) to allow melting to occur for 2 minutes then followed by feeding the RTR pellets into the internal mixture chamber [7]. The blending temperature is set at 120°C and the rotor speed at 50 rpm. The RTR and EVA are melt mixed and a pressure transducer is used to detect and record the mixing torque using a built-in software. After the two materials are mixed by maintaining the torque speed for 10 minutes, it is kept constant to ensure the blends are well-melt mixed and the materials were immediately cut into smaller pieces for compression moulding process.

The study of the blends is selected as shown in Table 2.2. The two samples, 100% EVA and 100% RTR undergoes the same process in order to further study and compare with the RTR/EVA blends. The blend ratios of RTR/EVA are named over EVA, 30RTR, 50RTR, 70RTR, RTR.

Table 0.2. RTR and EVA blend ratio

SAMPLE DESIGNATION	EVA (WT. %)	RTR (WT. %)
EVA	100	0
30RTR	70	30
50RTR	50	50
70RTR	30	70
RTR	0	100

2.2.2 Compressing Moulding

After the blends are mixed cut into smaller pieces, the material is then placed within the cavity covered with the disposable polypropylene sheet for easy removal and the top plate will compress the material and mould it into the desired size and thickness. The mould is placed in between the top plate and the bottom plate of an automated hydraulic heated press (LP-S-50 Scientific Hot and Cold Press) [7]. The top plate is pre-heated to a temperature of 130°C. The preheating process takes up to 3 minutes without pressing to melt the material then followed by 20 seconds of venting between the pressure of 0 to 10 MPa in order to distribute the material evenly in the cavity and remove any air bubbles. The heating of the mould ended with a holding pressure at 10 MPa for 3 minutes then followed by the holding time to cool the mould. The cooling process required holding time of 2 minutes and holding pressure at 10 MPa to get rid of the non-uniform cooling. The ejection mould is then removed from the cavity.

2.3 Thermogravimetric Analysis (TGA)

The thermal stability of RTR/EVA blends is investigated using TGA (Perkin Elmer, TGA 8000). The samples are exposed to the temperature of 30°C to 600°C at three different heating rates at 10, 20 and 30°C/min in the purified air atmosphere. The RTR/EVA blends are placed under purified air condition to study under the oxidative degradation and thermal degradation. The purified air flow rate is fixed at 20 ml/min and the sample size is within 3 mg to 5 mg. The raw data of the weight loss against the degradation temperature was extracted from the software, Pyris Manager. The data analysis of the dynamic response is done using Pyris Manager.

2.4 Thermal Kinetic Analysis

The obtained thermal degradation data of each sample are used to obtain the activation energy of thermal degradation of RTR/EVA blends by using Kissinger method as shown in Table 2.3. Data from TGA was used to generate information for Kissinger plots (Table 2.3). Hence, using the linear equation, the plot of $ln\,\beta/T_P^2$ against $1/T_p$ can be generated. One of the important kinetic parameter, activation energies can be determined from the Kissinger method that is applied. The activation energies of the blend is will determine the thermal stability of the blend.

Table 0.3. Kinetic analysis model for evaluating activation energy

Method	Expression	Plots	Slope	Reference
Kissinger	$ln\frac{\beta}{T_P^2} = \ln\frac{AR}{E_a} + \left(\frac{1}{T_P}\right)\left(-\frac{E_a}{R}\right)$	$ln\frac{\beta}{T_P^2}$ against $\frac{1}{T_P}$	$-\frac{E_a}{R}$	[8]

Whereas,

β is the heating rate in $\frac{K}{min}$,

T_P is peak temperature in $Kelvin$,

E_a is the activation energies in $\frac{kJ}{mol}$,

A is the pre-exponential factor of decomposition reaction in $\frac{1}{min}$,

R is the gas constant, $8.314 \frac{J}{mol.K}$ [8].

3.0 Results and Discussion

3.1 Thermogravimetric Analysis

The samples were done by heating from the temperature of 30°C to 600°C. The graph of weight loss percentage versus the degradation temperature is obtained as shown in Fig. 3.1 below. It shows two degradation steps occurred (Fig. 3.1).

The first step degradation occurs due to the heating happens and break down the weak-link contains in RTR/EVA blends [6-7]. The first step degradation is the decomposed of the volatile or other low boiling point components which will be the natural rubber results in weight loss [11]. The second step degradation occurs as the continuous heating and breaking down the styrene-butadiene and nitrile-butadiene (SBR/NBR) at a high degradation temperature.

B. Wang et al. and H.C. Bidsorkhi et. al. [11-12] stated the two-step mechanism occurred for thermal degradation of EVA. In the first step of degradation, the acetic acid is broken down and forms the unsaturated polyenes. The following step is the random chain scission of the remaining material, polyethylene (PE) into unsaturated vapour species such as butane and ethylene. The gaseous product will then be purged out by constant air flow in the thermogravimetric analyser system.

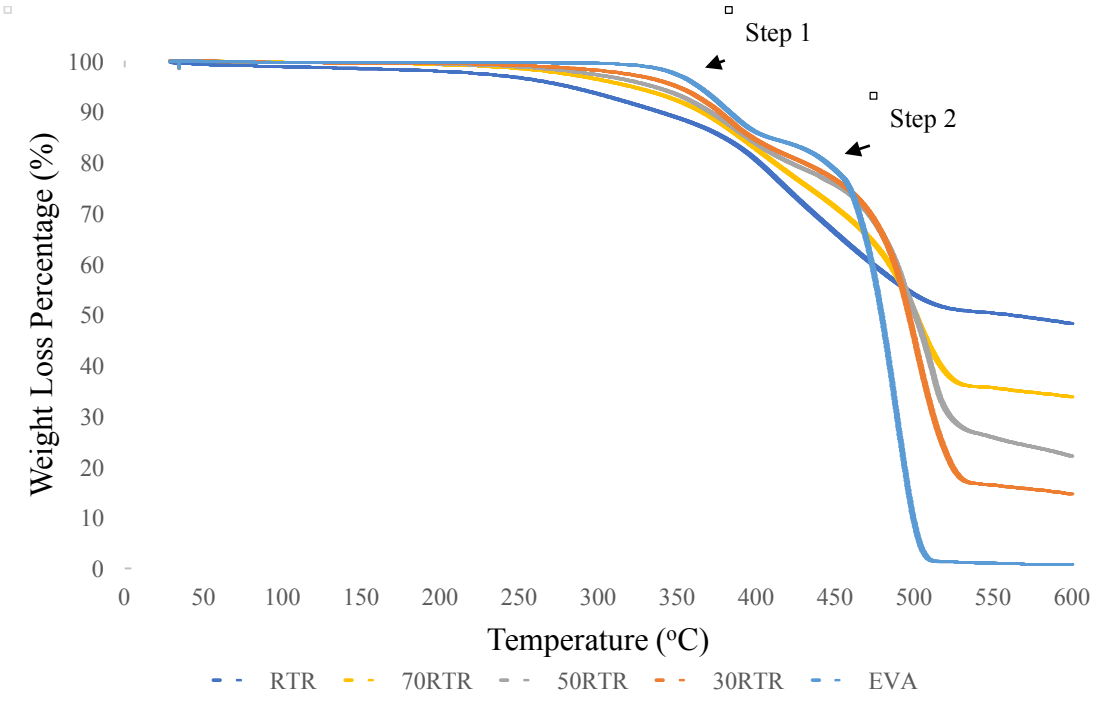


Figure 0.1. Dynamic response of RTR/EVA blends

Besides, from Fig. 3.1, the ethylene vinyl acetate copolymer (EVA) curve has the highest gradient as the second step degradation occurs, followed by 70RTR, 50RTR,

30RTR and RTR. This shows that the EVA has the best thermal stability. Whereas the RTR/EVA blends show improvement of the thermal stability as it increases the weight percentage of EVA. As for the heating rate of 20 and 30°C/min, both dynamic responses shows the exact trend as Fig. 3.1.

The degradation temperature at weight loss percentage of 10% and 25% ($T_{10\%}$ and $T_{25\%}$) shows an increase in temperature with increasing EVA content as shown in Table 3.1. The thermal stability is improved with an increase in EVA content. Thus, all three blends show a greater thermal stability as compared to RTR. However, at weight loss percentage of 50% ($T_{50\%}$), the degradation temperature decreases as the EVA content increases.

In the first step, the vinyl-acetate of the EVA with 18 wt% is degraded. The natural rubber for RTR degrades around 50%. The second step of EVA degradation is the polyethylene (PE) chain at 82 wt% whereas the styrene-butadiene and nitrile-butadiene rubber (SBR/NBR) at 50 wt%. The temperature decreases with the increase in EVA content as SBR/NBR has the higher thermal stabilities than PE.

Table 0.4. Degradation temperature at 10, 20 and 50% weight loss

SAMPLE DESIGNATION	**$T_{10\%}$ (°C)**	**$T_{25\%}$ (°C)**	**$T_{50\%}$ (°C)**
EVA	382.65	458.99	479.32
30RTR	376.48	456.98	496.04
50RTR	370.33	453.16	500.66
70RTR	364.97	433.31	500.97
RTR	337.93	418.77	558.27

Table 3.2 shows the residual weight of the blends decreases as the EVA weight percentage increases. The highest residual weight, RTR consist of carbon fillers during the manufacture for its use of the application. The residual weight shows incomplete combustion as the impurities and carbon fillers consist in the RTR require higher temperature heating in order to further break down the carbon chains [14]. Based on S. Ramarad's findings, the RTR sample with the highest residual of 48.20% due to the carbon fillers and impurities within the rubber content [7]. This further support the findings found in the degradation temperature at weight loss percentage of 50% ($T_{50\%}$).

Table 0.5. Residual weight of RTR/EVA blends

SAMPLE DESIGNATION	**RESIDUAL WT (%)**
EVA	0.77
30RTR	14.63
50RTR	22.10
70RTR	38.75
RTR	48.20

3.2 Thermal Degradation Kinetic of RTR/EVA Blends

The peak temperatures (known as the maximum temperature) obtained from the first and second peak of each blends using the Pyris Manager to generate the derivative curve of the raw data is obtained at each heating rate of 10, 20 and 30°C in order to generate the Kissinger Plot. Based on the heating rates and maximum degradation temperatures to generate the Kissinger Plot (ln ß/T_p^2 against 1/T_p) as shown in Table 2.3. The first and second peak temperature obtained from the derivative curve using the Pyris Manager is tabulated in a table as shown in Table 3.3. Generally, the peak temperatures increase along the increase of the heating rates. The collected peak temperatures are converted into Kelvin in order to generate the Kissinger plots. Hence, using the data in Table 3.3, the Kissinger plots using first and second peak temperature is generated as shown in Fig. 3.2 and Fig. 3.3.

Table 0.6. Tabulation of Data for Kissinger Plots

BLENDS	HEATING RATES, ß (K/MIN)	T_{peak_1} (K)	$\frac{1}{T_{peak_1}}$ (K^{-1})	T_{peak_2} (K)	$\frac{1}{T_{peak_2}}$ (K^{-1})
EVA	10	686.05	0.0014576	736.02	0.001359
	20	706.90	0.0014146	757.12	0.001321
	30	708.63	0.0014112	759.67	0.001316
30RTR	10	671.63	0.0014889	774.12	0.001292
	20	700.54	0.0014275	789.80	0.001266
	30	696.80	0.0014351	805.00	0.001242
50RTR	10	660.92	0.0015130	783.99	0.001276
	20	668.68	0.0014955	783.63	0.001276
	30	682.43	0.0014654	802.21	0.001247
70RTR	10	650.03	0.0015384	774.71	0.001291
	20	674.88	0.0014817	787.08	0.001271
	30	681.25	0.0014679	792.24	0.001262
RTR	10	651.33	0.0015353	761.84	0.001313
	20	666.75	0.0014998	768.44	0.001301
	30	686.30	0.0014571	787.47	0.001270

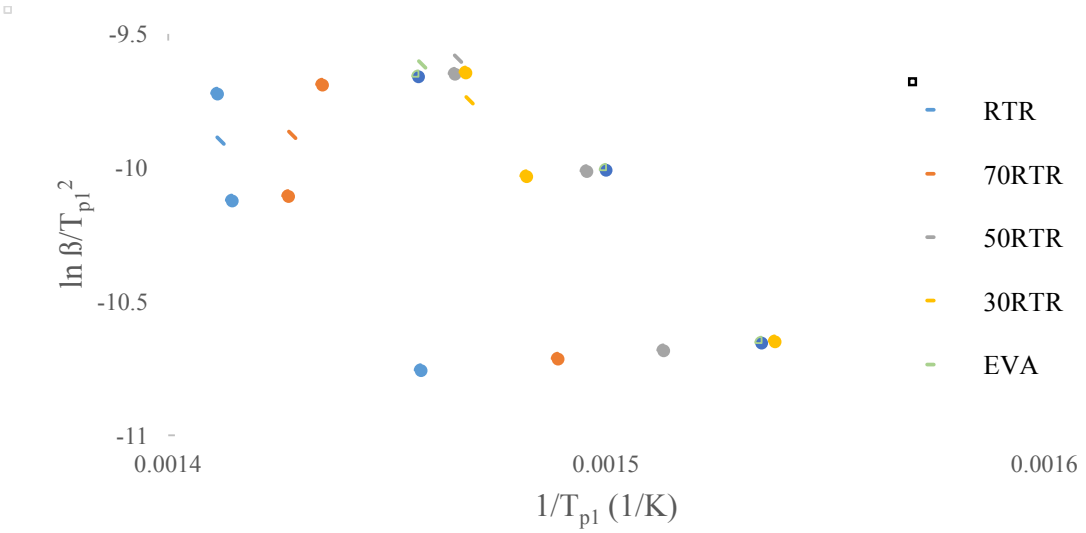


Figure 0.2. Kissinger plot to determine the activation energy, E_{a_1} at first peak temperature for non-isothermal thermal degradation of EVA/RTR blends

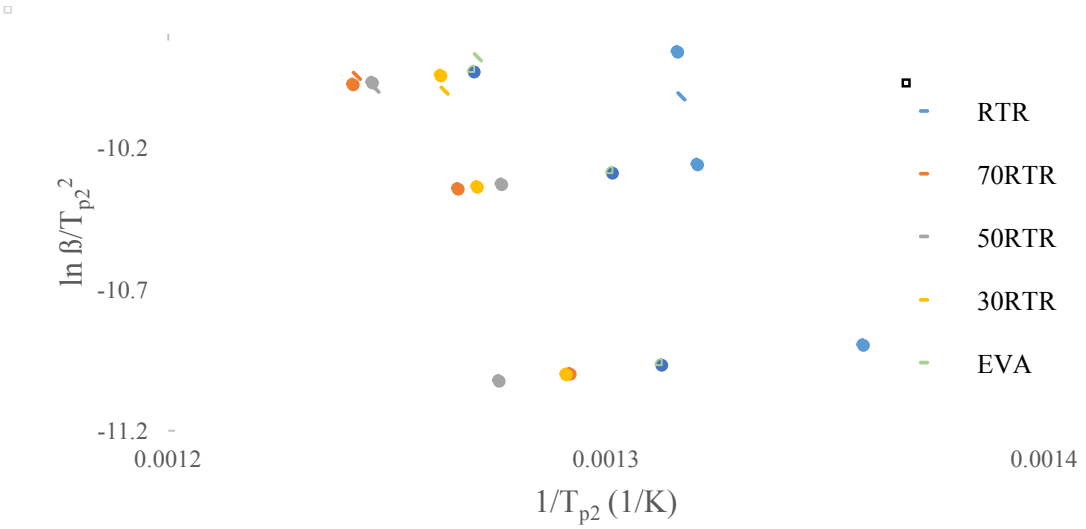


Figure 0.3. Kissinger plot to determine the activation energy, $\mathbf{E_{a_2}}$ at second peak temperature for non-isothermal thermal degradation of EVA/RTR blends

The information extracted from the Kissinger plot (Figs. 3.2 and 3.3) are as shown in Table 3.4. The R-squared (R^2) value shown in Table 3.4 demonstrates the fitness of the data. According to Fig. 3.2, the overall R_1^2 value is above 0.80 which is acceptable fitness to Kissinger model. However, the blend of 30RTR shows the insignificant R_1^2 value of 0.7443. On the other hand, the R_2^2 value has shown significant values for the model fitting of Kissinger but 50RTR R_2^2 value shows 0.5623, which is out of the acceptable range. The possible reason is that Kissinger may not be the best model fitting for sample 30RTR and 50RTR.

Table 0.7. Data and Activation Energy from Kissinger Plots

BLENDS	GRADIENT, M_1	R_1^2	E_{a_1} (KJ/ MOLE)	GRADIENT, M_2	R_2^2	E_{a_2}(KJ/ MOLE)
EVA	-19,073	0.8965	104.37	-21,486	0.9148	177.91
30RTR	-13,283	0.7443	110.45	-20,651	0.9805	300.05
50RTR	-20,652	0.9012	171.70	-23,750	0.5623	197.46
70RTR	-13,285	0.9586	110.45	-36,090	0.9916	171.69
RTR	-12,553	0.9502	158.57	-21,399	0.8163	178.63

The theoretical activation energies for the first peak (Table 3.4) shows that the RTR and EVA are 159kJ/mole and 104kJ/mole. Based on the weight percentage of RTR and EVA (Table 2.2) of each blend to calculate the activation energies for 30RTR, 50RTR and 70RTR, it is calculated to be 121, 132 and 143kJ/mole. Hence, the activation energy of 70RTR favours to RTR as the blend consist 70 wt% of RTR. As for the 30RTR will favours to EVA as the activation energy of 30RTR is close to the activation energy of EVA and the blend of 30RTR consist 70 wt% of EVA. The activation energies of the blend ratio of 50RTR and 70RTR in Table 3.4 tends to deviate from the activation energy of RTR, it does not favour to RTR. However, it shows that 30RTR activation energy favours more towards EVA due to the high weight percentage of EVA consist of the blend with 30% of RTR. Hence, it favours to the activation energy of EVA. The activation energy of 30RTR is higher than EVA is due to the existing 30% of RTR with the styrene-butadiene and carbon fillers content in the RTR, it required high activation energy to be degraded.

Moreover, the theoretical activation energies for the second step of degradation of RTR and EVA is 179 and 178kJ/mole. The calculated activation energies based on weight percentage, 30RTR, 50RTR and 70RTR are 178.1, 178.3, and 178.4kJ/mole. The second step degradation shows a very close value of both, EVA and RTR as the strong link structure that is being broken down with the heating process.

The highest activation energy of 30RTR at the second peak temperature shows the durability of the blend is thermally stable as it consists of 70% of EVA within the blend. This defines as the energy required to decompose the polymeric material, in this case, will be 30RTR sample will be higher. The blend consists of high cross-linked distribution and therefore, the higher the activation energy of decomposition, the higher the thermal stability [15]. The Kissinger is a method that is useful in the comparative studies, but overall the 50RTR blend does not favour to RTR and EVA based on the activation energies [8].

4.0 Conclusions

In conclusion, the thermogravimetric analysis (TGA) results obtained shows that the increase of EVA content of the blend will have an improvement in thermal stability which is comparable with EVA. Hence, the results are able to assess the feasibility of the alternative recycling method of WTR and a new application for the WTR. The first and second step degradation of RTR and EVA demonstrate the degradation of the weak link structure in the polymer chain, natural rubber and the vinyl

acetate content. Follow by the second step degradation will decompose the styrene-butadiene, nitrile-butadiene and polyethylene content in the RTR, EVA and the blends. Hence, the higher activation energy requires as the amount of stronger link structure are required to break down the polymer chain. Based on the fitness of the model, overall data are fitted into the Kissinger model but 50RTR at the first and second degradation step shows a significant difference with the other blend which does not favours to both EVA and RTR activation energy due to the unsuitable model for fitting. Additionally, the blend ratio can be further study under an isothermal condition with varies heating rate, the holding time varies from 15 minutes up to 60 minutes to venture into a new application using the blends. The degradation kinetic analysis can be further study using other methods such as Coats-Redfern and Friedman's method. Finally, the 30RTR at the second peak temperature obtained the highest activation energy. The high content of EVA in the blend gives a high thermal stability which is desirable for the venture into the future application based on its thermal properties.

Acknowledgement

I would like to express my gratitude to my project supervisor and laboratory officer, Suganti Ramarad and Lithnes Kalaivani Palniandy for the guidance, supervision and encouragement throughout the process of my final year project.

References

[1] L. Yung, W., Yung, L., Hua, 'A study of the durability properties of waste tire rubber applied to self-compacting concrete', *Constr. Build. Mater.*, vol. 41, pp. 665–672, 2013.

[2] B. Maciej, S., Justyna, K., Helena, J., Adolf, 'Progress in used tyres management in the European Union: A review', *Waste Manag.*, vol. 32, no. 10, pp. 1742–1751, 2012.

[3] S. Saiwari, 'Post-Consumer Tires Back Into New Tires: De-vulcanization and Re-utilization of Passenger Car Tires', p. 2, 2013.

[4] G. Tao, Q. He, Y. Xia, G. Jia, H. Yang, and W. Ma, 'The effect of devulcanization level on mechanical properties of reclaimed rubber by thermal-mechanical shearing devulcanization', *J. Appl. Polym. Sci.*, vol. 129, no. 5, pp. 2598–2605, 2013.

[5] B. Wang *et al.*, 'Cyclodextrin microencapsulated ammonium polyphosphate: Preparation and its performance on the thermal, flame retardancy and mechanical properties of ethylene vinyl acetate copolymer', *Compos. Part B Eng.*, vol. 69, pp. 22–30, 2015.

[6] W. Chumeka, 'Improvement of compatibility of poly(lactic acid) blended with natural rubber by modified natural rubber', *Univ. du Maine*, no. Prince of Songkla University, pp. 1–10, 2013.

[7] S. Ramarad, C. T. Ratnam, M. Khalid, and A. L. Chuah, 'Improving the properties of reclaimed waste tire rubber by blending with poly(ethylene-co-vinyl acetate) and electron beam irradiation', *J. Appl. Polym. Sci.*, vol. 132, no. 11, 2015.

[8] R. M. R. Wellen and E. L. Canedo, 'On the Kissinger equation and the estimate of activation energies for non-isothermal cold crystallisation of PET', *Polym. Test.*, vol. 40, pp. 33–38, 2014.

[9] J. D. Peterson, S. Vyazovkin, and C. A. Wight, 'Kinetics of the thermal and thermo-oxidative degradation of polystyrene, polyethylene and poly (propylene)',

Macromol. Chem. Phys., vol. 202, no. 6, pp. 775–784, 2001.

[10] K. Pielichowski and K. Flejtuch, 'Non-oxidative thermal degradation of poly(ethylene oxide): kinetic and thermoanalytical study', *J. Anal. Appl. Pyrolysis*, vol. 73, no. 1, pp. 131–138, 2005.

[11] X. Wang, N. Feng, and S. Chang, 'Effect of precured degrees on morphology, thermal, and mechanical properties of BR/SBR/NR foams', *Polym. Compos.*, vol. 34, no. 6, pp. 849–859, 2013.

[12] B. Wang *et al.*, 'Effect of vinyl acetate content and electron beam irradiation on the flame retardancy, mechanical and thermal properties of intumescent flame retardant ethylene-vinyl acetate copolymer', *Radiat. Phys. Chem.*, vol. 81, no. 3, pp. 308–315, 2012.

[13] H. C. Bidsorkhi, M. Soheilmoghaddam, R. H. Pour, H. Adelnia, and Z. Mohamad, 'Mechanical, thermal and flammability properties of ethylene-vinyl acetate (EVA)/sepiolite nanocomposites', *Polym. Test.*, vol. 37, pp. 117–122, 2014.

[14] K. A. Dubey *et al.*, 'Polychloroprene rubber/ethylene-propylene-diene monomer/multiple walled carbon nanotube nanocomposites: synergistic effects of radiation crosslinking and MWNT addition', *J. Polym. Res.*, vol. 19, no. 5, p. 9876, 2012.

[15] H. Nabil, H. Ismail, and A. R. Azura, 'Optimisation of accelerators and vulcanising systems on thermal stability of natural rubber/recycled ethylene–propylene–diene-monomer blends', *Mater. Des.*, vol. 53, pp. 651–661, 2014.

eureca 2017 – Conference Paper
Paper Number 2CE14

Life Cycle Assessment of Direct Carbon Fuel Cell Using Rice Husk as a Fuel Source

Tan Yong De[1*], Veena Doshi, Viknesh Andiappan Murugappan[1],
Edwin Chung Chin Yau[1],
[1]*Taylor's University Lakeside Campus, Subang Jaya, Selangor, Malaysia*

[*]*alonsotyd@hotmail.com*

Abstract
Nowadays in the developing 21st century, greenhouse gases (GHG) especially carbon dioxide (CO_2), sulphur dioxide (SO_2), methane (CH_4) and nitrous oxides (NO_x) are continuously released to the Earth's atmosphere since the Industrial Revolution in the 1750s due to heavy fuel usage. Among the ways to curb this subject is to use biomass as a fuel source for generating electricity in the direct carbon fuel cells (DCFC). In this study, rice husk was selected as fuel for DCFC experiment due to its high carbon content and abundance in Malaysia. Next, life cycle analysis (LCA) was conducted on the DCFC experiment to compare the amount of gaseous by-products liberated to the environment with that of coal power plants. In this study, the boundary for LCA was the *cradle-to-grave* method (from the production of rice husk to the final disposal of DCFC). This boundary consisted of stages such as rice husk production, pyrolysis and electricity generation in DCFC. Based on the results in the LCA assessment, coal power plant produced 99.3 wt.% CO_2 while rice husk emitted 92.2% CO_2 to the surroundings. Thus, rice husk emitted 7.1 wt.% CO_2 lesser than the coal power plants.

Keywords: Rice Husk, Greenhouse Gases, Direct Carbon Fuel Cell, Life Cycle Analysis

1. Introduction

In the current urbanising century, the greenhouse gases (GHG) like carbon dioxide, methane, sulphur dioxide and nitrous oxides are emitted continuously since the Industrial Revolution in the 1750s [1]. This problem is typically caused by heavy fuel burnings especially in the transportation, industrial and domestic sectors in terms of electrical household usage [2]. Moreover, agricultural activities have contributed the greenhouse gas emissions as many of the forests are cleared and burned for agricultural purposes [3]. Among the ways of curbing the air pollution calamities are to use biomass as a fuel source for generating electricity in the direct carbon fuel cells (DCFCs). It generates electricity by converting the chemical energy stored in carbon compounds directly to electricity via a chemical decomposition process without the needs of reforming process such as gasification [4]–[6].

The main reason for conducting the DCFC experiment was to compare the amount of GHGs emitted from the DCFC into the environment with the coal power plants. Hence, life cycle analysis or assessment (LCA) is the most common environmental management tool that assists in interpreting life cycle by allowing quantification measures of environmental burdens, sustainability of products, products or activities and their potential impacts on a life cycle basis [7]–[9]. There are three types of LCA methods that examine the performance of the environment of every product: the *cradle-to-grave*, *cradle-to-cradle* and *cradle-to-gate* methods [7]–[9]. LCA is commonly used as a tool for both environmental system management and reporting by calculating the environmental burdens, depending on the data availability using a formula:

$$B_j = \sum_{i=1}^{I} bc_{j,i} x_i \tag{1.1}$$

where $bc_{j,i}$ represents the burden j from subsystems or activities I and x_i is a mass or energy flow involved in that activity [7], [8]. In this project, the *cradle-to-grave* method was used to compare the performance and life cycle of electricity generation between rice husk and coal as fuels. There would be two system boundaries in this LCA study: the production of rice husk (from rice cultivation to milling) and the generation of electricity in DCFC (from its assembly to final usage and disposal) [10], [11].

1.1 Project Objectives

There were three main objectives in this paper. Firstly, this project was aimed to assess the life cycle of a direct carbon fuel cell (DCFC) using rice husk as a fuel source. Secondly, it was also executed to determine the content of fixed carbon present in rice husk in order to run the DCFC experiment effectively using thermogravimetric analysis (TGA) methods. Finally, the paramount of this project was to compare the life cycle assessment (LCA) of a DCFC cell with the conventional power generation methods by conducting calculations using Microsoft Excel spreadsheet.

2. Materials & Methodology

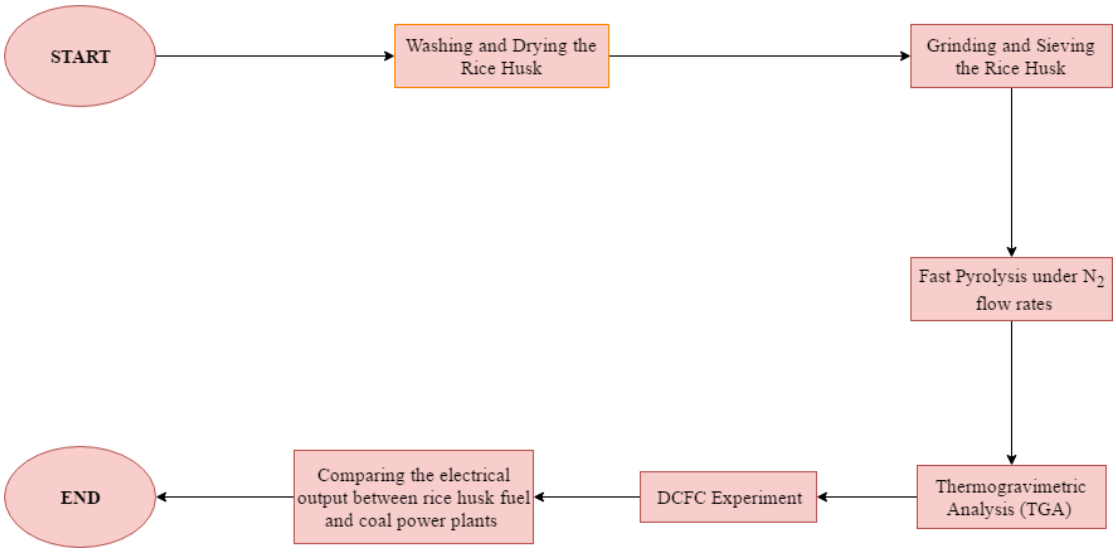


Figure 4: Flow Chart of the DCFC Experiment

2.1 Sample Preparation

200 g rice husk was obtained from PLS Marketing (M) Sdn. Bhd in Sekinchan, Selangor and weighed using an electronic balance. Later, it was washed inside a 5-litre measuring cylinder using distilled or purified water for at least thrice including its first wash which produced a very brackish solution. The aim of washing the sample was to remove the impurities such as dirt and adhering materials from the surface of the husk which might affect its fuel performance significantly [12].

The temperature of a forced convection furnace was set at a temperature of 105°C and the newly washed rice husk was dried for overnight to avoid further deterioration caused by the excessive moisture content [13], [14]. 24 hours later, the newly dried rice husk was cooled to room temperature and then taken out from the furnace followed by reweighing it.

The rice husk was placed inside an electrical grinder. After grinding the rice hull, the sample was placed inside an electrical sieve shaker and sieved into 4 different particle sizes i.e. 1 mm, 600 µm, 500 µm and less than 500 µm for at least an hour. Around 5 to 6 g 500 µm rice husk was placed onto two rectangular crucibles using a spatula and they were reweighed and recorded. The crucibles were placed inside a 1-metre glass tube using a long steel rod. The pyrolysis temperature and nitrogen (N_2) flow rate were set at 550°C and 150 ml/min respectively using a furnace controller. For the sake of producing the maximum bio-char yield, the heating rate of 10°C/min was set in order to coincide with the slow pyrolysis method [15]. Meanwhile, the dwelling or residence time was set for an hour [15].

The glass tube and crucibles were then washed thoroughly using detergent to remove the reminisces of the previous experiment as they might cross-contaminate with the new samples. The newly washed crucibles were then dried in an oven at the temperature of 65°C for at least one hour in order to remove the trapped moisture from

them. Otherwise, the trapped moisture would deliberately add more weight onto these two crucibles. The entire fast pyrolysis process was then repeated by heating the 600 μm rice husk sample at the temperatures of 650°C, 750°C and 850°C under same heat and N_2 flow rates and the residence period.

2.2 Sample Characterisation

The contents present in the rice husk biochar samples were analysed by PerkinElmer TGA 8000 analyser. Before the start of the experiment, a small sample pan was zeroed by the PerkinElmer software since a hook in the TGA device acted as a weighing machine [13]. 5 mg of RH 550 sample was measured by using the same electronic balance used in the fast pyrolysis experiment and later transferred into the pan carefully.

During the 3-hour operation, the RH 550 sample was heated inside an enclosed furnace from 30°C to 110°C at 10°C/min under inert N_2 conditions followed by a 20-minute hold-up at 110°C. The sample was then heated at the similar heating rate of 10°C/min from 110°C to 950°C followed by a 30-minute hold-up at 950°C. Finally, the gas was switched from N_2 to oxygen (O_2) and held for 20 minutes at 950°C. Simultaneously, a TGA graph of weight percentage vs. time was plotted by the PerkinElmer software. 3 hours, later the TGA device was cooled down to its initial temperature of 30°C and the entire experiment was repeated by analysing the contents present in the RH 650, RH 750 and RH 850 samples.

2.3 DCFC Experiment

A Ni-YSZ ring-shaped button cell with an area of 1.743 cm^2 was used as its reaction medium for the direct carbon fuel cell (DCFC) operations under high temperatures [5]. Before the beginning of the experiment, the button cell was activated by heating it inside the fuel cell's furnace from room temperature to 850°C under the heating rate of 10°C/min and 1-hour dwelling period without adding the rice husk samples onto it. This activation task was an important precautionary procedure in order to eliminate any abnormalities during the DCFC experiment.

About 0.1 g of 550°C rice hull sample was weighed using the same electronic balance containing 4 decimal places in gram scale as in the fast pyrolysis and TGA analysis segments. The silver wire was then readjusted until a proper contact with the rice husk fuel was achieved. Later, the furnace used in the fast pyrolysis experiment earlier was programmed by setting the temperature to 850 °C under the heating rate of 10°C/min and dwelling period of 2 hours. During the initial heating process to 800°C, an inert N_2 was purged into both anode and cathode chambers at 150 and 600 ml/min correspondingly. This precautionary action was to prevent an earlier oxidation process of the rice husk fuel sample from occurring inside the DCFC apparatus. Once the DCFC's temperature had reached 800°C, the purging gas at the cathode was immediately switched from noble N_2 to oxidising purified air under the similar flow rates as in the commencing heating process. The fuel cell apparatus was heated further to 850°C.

The output voltage at the anodic silver wire was measured by the potentiometer via the connecting crocodile clips under a scan rate of 10 mV/s. The furnace was then

switched off and the DCFC setup was cooled to room temperature. After cooling down the DCFC apparatus to room temperature, the rice husk fuel sample was taken out from the DCFC setup and its final mass was weighed and recorded. The entire DCFC experiment was repeated by adding the remaining 3 rice husk fuel samples into the button cell.

The data of the greenhouse gas (GHG) emissions from DCFC were collected and tabulated. Later, the DCFC's GHG emission data were compared with the data of greenhouse gas emissions from coal power plants based on the literature review by performing calculations using Microsoft Excel. Once the hypothesis was valid, the LCA study was officially ended.

3.0 Results And Discussions

3.1 TGA Analysis

Table 1 shows the TGA results for all the four rice husk samples. Based on this table, it is clearly seen that moisture, fixed carbon and ash contents increase while a number of volatile matters present in the sample drop as the pyrolysis temperature increases. The sample with the highest contents of moisture, ash and fixed carbon is the RH 850 sample with their respective values of 7.58 wt. %, 43.638 wt.% and 35.462 wt. %. In contrast, the RH 550 sample has the highest amount of volatile matters with its value of 30.874 wt. %. In conclusion, this thermal analysis aims not only to calculate these 4 contents in the rice husk samples but also to examine both the thermal and chemical stabilities of the rice hull fuels at the DCFC's operating temperatures [16].

Table 8: Thermogravimetric Analysis (TGA) Results

Samples	Amount of Contents (wt. %)			
	Moisture	**Volatile Matters**	**Fixed Carbon**	**Ash**
RH 550	3.163	30.874	19.828	32.636
RH 650	5.077	10.782	42.151	32.950
RH 750	6.929	10.016	43.000	34.983
RH 850	7.580	7.699	43.638	35.462

3.2 DCFC Experiment

Table 2 presents the amount of rice husk mass consumed for the electricity generation in the DCFC apparatus. As the pyrolysis temperature rises from 550°C to 750°C under a constant heating rate of 10°C/min, a huge mass in the rice husk samples drop has occurred. Beyond 750°C, the mass loss of rice husk fuel starts to drop drastically from 0.0726 g to 0.0377 in RH 850.

Table 9: Mass of Rice Husk Fuel Burnt for Electricity Generation in DCFC

Rice Husk Samples (°C)	Initial Mass (g)	Final Mass (g)	Consumed Mass (g)
550	0.1014	0.0886	0.0128
650	0.1022	0.0513	0.0509
750	0.1071	0.0345	0.0726
850	0.1096	0.0719	0.0377

Figure 2 displays the graph of the voltage produced in DCFC against the pyrolysis temperatures of the rice husk samples. It is noticeable that as the pyrolysis temperature increases, the voltage in the DCFC drops from 0.8685 V in RH 550 to 0.813 V in RH 750 and later rises to 0.8197 V in RH 850. It was suggested that as the pyrolysis temperature rose at a fixed heating rate, the biochar amount inside the sample dropped in virtue to more volatiles being vaporised in the secondary reactions [17]–[20]. Hence, it can be concluded that raising the pyrolysis temperature at a fixed heating rate decreases the amount of biochar content in rice husk and thus decreasing the voltage produced in DCFC.

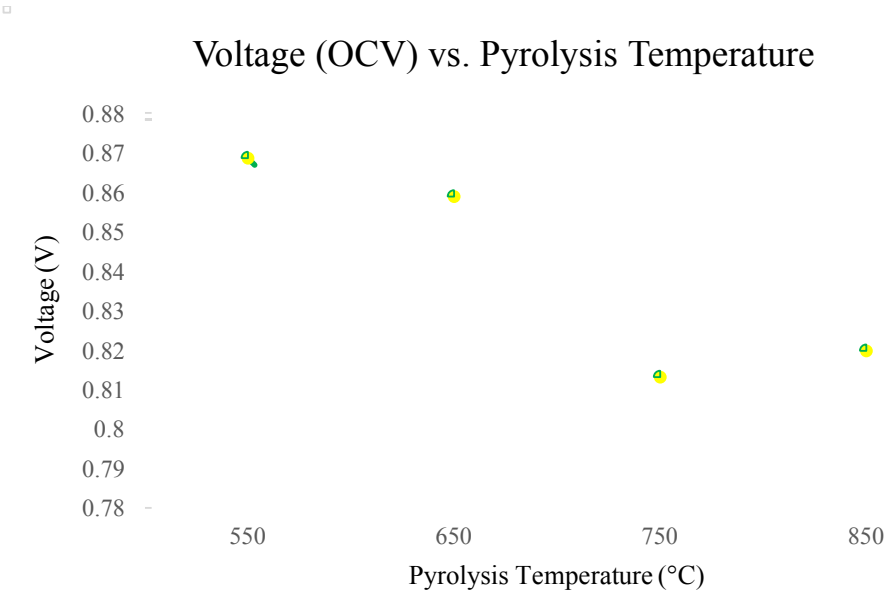


Figure 5: Graph of Voltage vs. Pyrolysis Temperature

Figure 3 displays the Nyquist plots for all the rice husk samples. It is noticeable that the RH 850 fuel produces the highest imaginary impedance of 1522 Ω under the real impedance of 2744 Ω followed by RH 550, RH 750 and RH 650 with their highest imaginary impedances of 894.1 Ω, 849.3 Ω and 744.8 Ω under the real impedances of 1284 Ω, 1909 Ω and 1928 Ω respectively. Besides that, two semicircles are shown in this diagram as well.

Figures 4 to 7 present the polarisation or I-V curves for RH 550, RH 650, RH 750 and RH 850 samples respectively. Using the second order polynomial trendline in the power density curve, RH 750 suits the best because of its highest R-squared value

of 0.9854 followed by RH 650, RH 550 and RH 850 which have their corresponding R-squared values of 0.9685, 0.9575 and 0.9564.

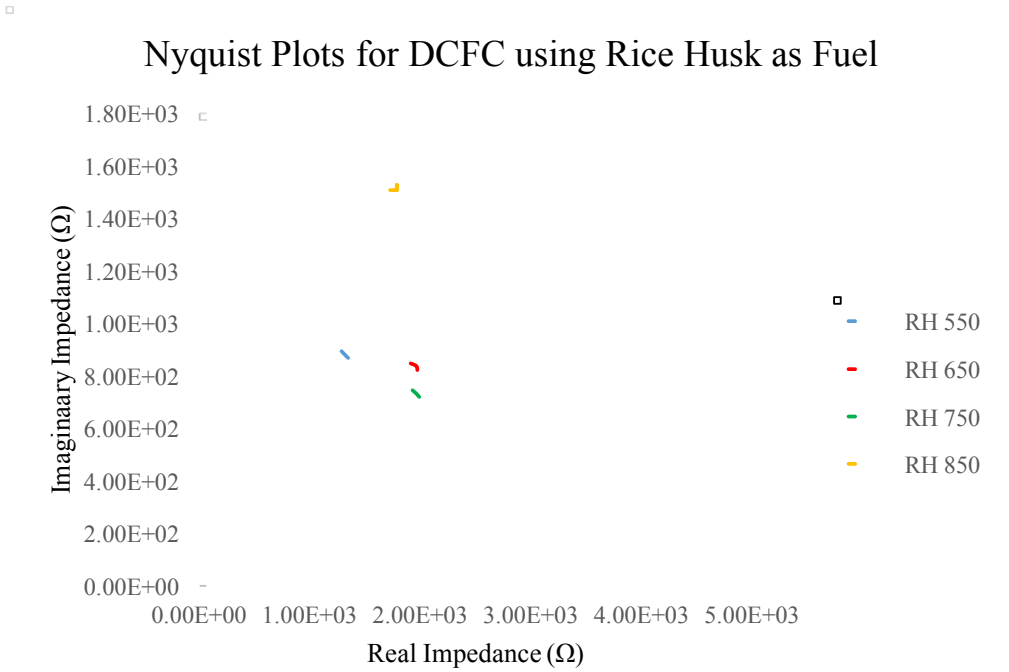


Figure 6: Nyquist Plot Diagram

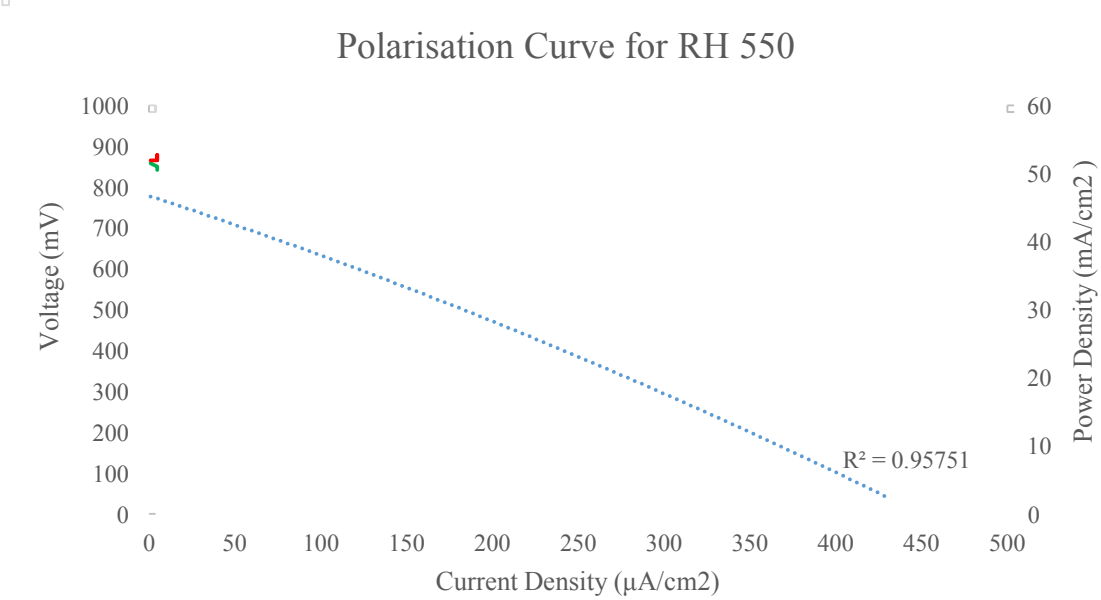


Figure 7: I-V Curve for RH 550

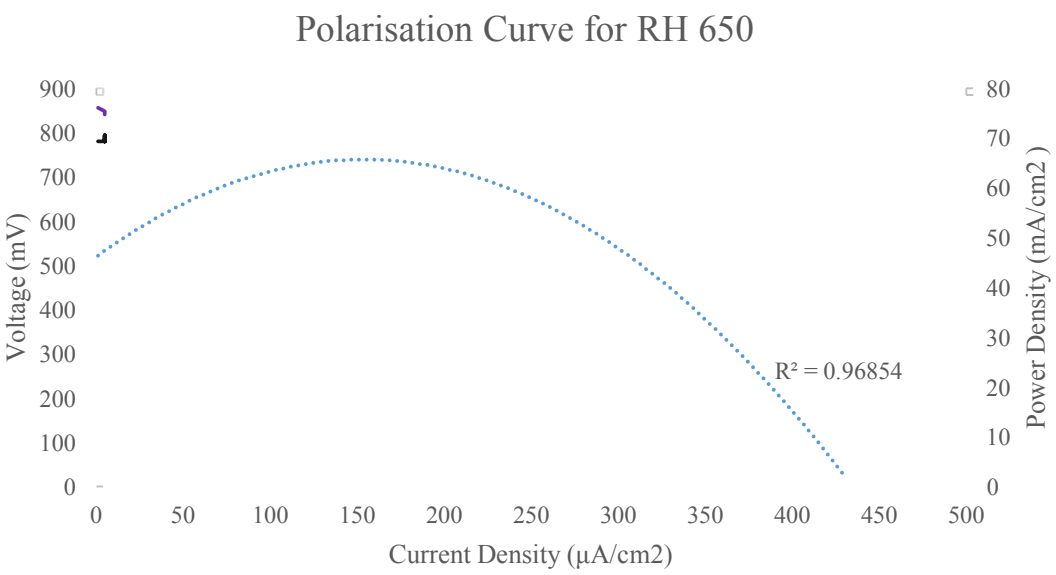


Figure 8: I-V Curve for RH 650

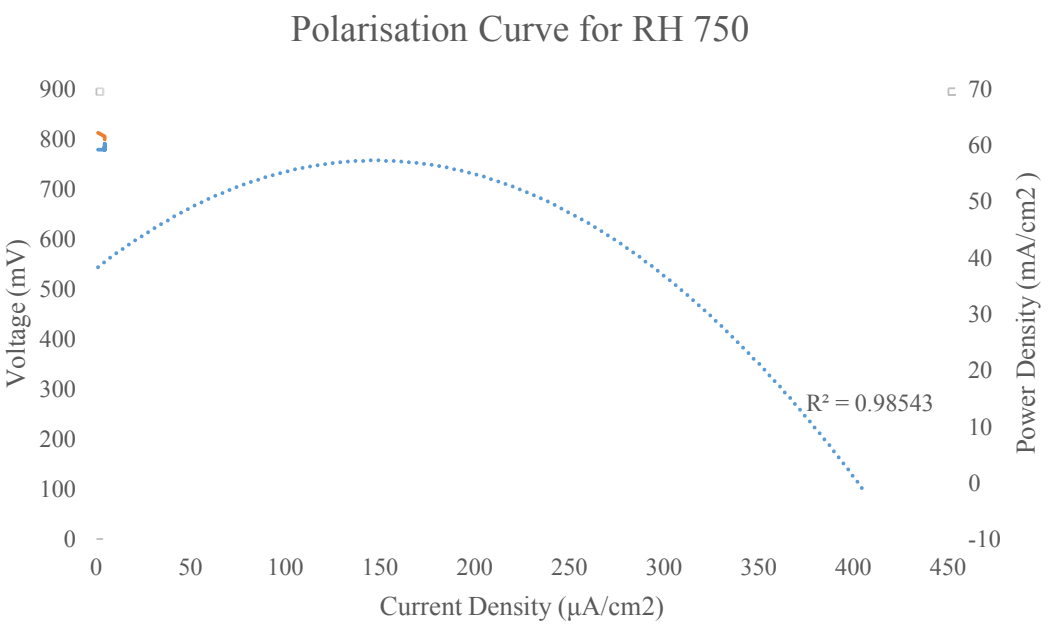


Figure 9: I-V Curve for RH 750

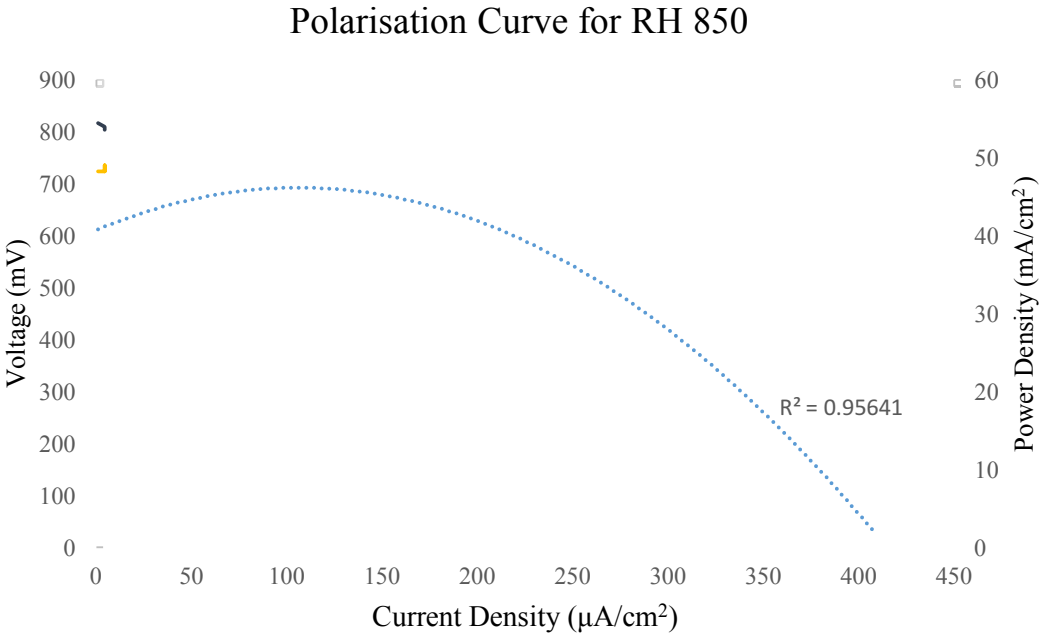


Figure 10: I-V Curve for RH 850

3.3 LCA Assessment

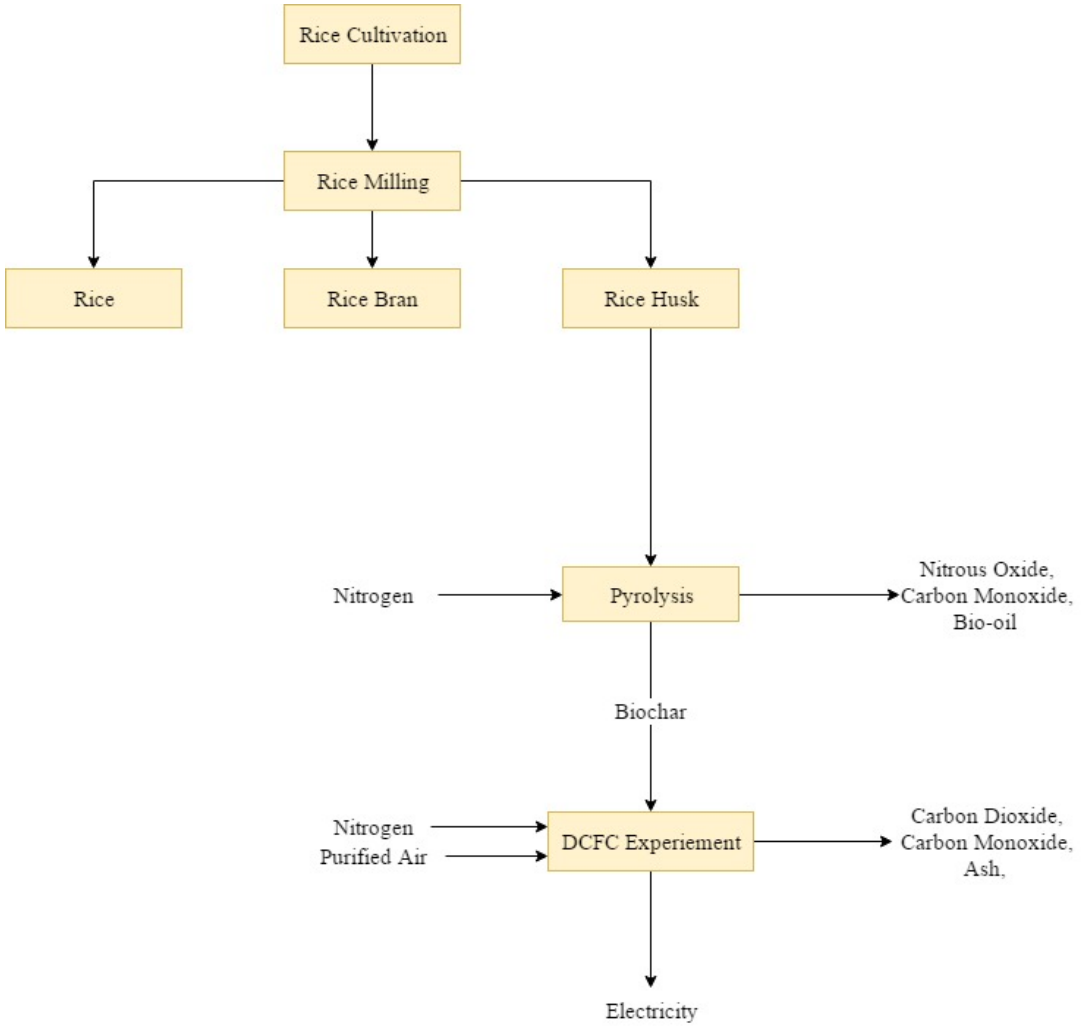


Figure 11: LCA Scope

The main goal of conducting this LCA study was to compare the amount of greenhouse gases (GHG) emitted to the environment between DCFC using rice husk as its fuel and conventional coal power plants. These two systems were evaluated from cradle to gate based on the environmental sustainability agenda. There were three main system boundaries in this LCA analysis as shown in Figure 8: rice husk production, pyrolysis and electricity generation in DCFC. Rice cultivation was excluded in the system boundary as it involved several processes such as rice transplant and harvest which are not related to this study. The functional unit for this assessment was the typical electrical power generated by both coal and rice husk based on the reports from the International Energy Agency (IEA) [21] and Anshar et al. [22] respectively. As stated earlier in the Project Objectives, a Microsoft Excel spreadsheet was used to calculate the GHG emissions from these two fuel sources.

Table 3 displays the data on GHG emissions from coal power plants and burning of rice husk in the electrical power generation sector In terms of emission percentage, rice husk and coal power plants emitted 92.21 wt.% and 99.27 wt.% CO_2 respectively. Thus, it was noted that rice husk liberated at least 7 wt.% lesser CO_2 than the coal power plants. This scene could be due to the recycling of CO_2 to the growing paddy seedlings.

Since methane (CH_4) was produced in an anaerobic soil, it was released to the surroundings during the ploughing period and hence it was not applicable in this LCA study [9].

Table 10: Amount of Greenhouse Gases Produced by Coal Power Plants and Burning Rice Husk [21]–[25]

Type of Fuels	**Coal Power Plants**	**Burning Rice Husk**
Typical Power Generated (kWh)	260,00	41,250
CO_2 Emission (kg CO_2/kWh)	1,008,610	17,160
SO_2 Emission (kg SO_2/kWh)	3,885	390
NO_X Emission (kg NO_X/kWh)	2,682	1,060
CH_4 Emission (kg CH_4/kWh)	820	Not Applicable
CO_2 Emission (wt.% CO_2)	99.27293	92.20849
SO_2 Emission (wt.% SO_2)	0.38238	2.09565
NO_X Emission (wt.% NO_X)	0.26398	5.69586
CH_4 Emission (wt.% CH_4)	0.00807	Not Applicable

4.0 Conclusions

In conclusion, rice husk emitted a lesser amount of greenhouse gases (GHG) than the coal power plant. This was because rice husk contains not only the high carbon content but the absence of the polluting elements such as sulphur and mercury. Besides that, the amount of carbon dioxide (CO_2) was recycled back to the plants including the growing paddies as part of the carbon cycle. Since methane (CH_4) was produced by anaerobic reactions in the soil and released during the ploughing season, the rice husk does not contain any amount of this GHG and hence there was no data emission of this gas from the rice hull combustion in DCFC.

In the future, this LCA study will be extended to rice cultivation including ploughing and irrigation of rice fields, transplant of rice seedlings using a mechanical rice transplanter and the rice harvest using a harvesting machine. Prasara-A [9] claims that GHGs especially CH_4 and nitrous oxides (NO_X) are contributed by the wetland rice system since CH_4 is produced by anaerobic reactions in the alluvial soil while NO_X is formed during the irrigation periods [9]. Besides that, this LCA study will also include the burning of rice stalks right after the bountiful harvest as well as energy loss to the environment from the rice husk during the fertilisation of farmlands [9], [12].

Next, a computational fluid dynamics (CFD) research will be conducted to determine an ideal DCFC performance by analysing its effects on temperature, pressure and gas flow rates as well as the fuel combustion performance inside the DCFC. This achievement is usually done by conducting several calculations using the fundamental equations (mass, momentum and energy equations) derived from the Navier-Stokes equations [26], [27]. Therefore, CFD will provide several useful information on the DCFC performance via numerous modelling such as the non-premixed model for the rice husk fuel combustion in DCFC [28].

Acknowledgement

I am grateful to my programme director, Miss Eunice Phang Siew Wei and also my supervisors: Dr. Veena, Dr. Viknesh and Dr. Edwin Chung; for giving me a special privilege to select one of the project titles earlier than other students based on their

recommendations as a result of my mild autism. Without their help, I would suffer several interest conflicts and also bear all the transportation costs to go elsewhere such as SIRIM Laboratories in Shah Alam and Nottingham University in Semenyih in order to use the experimental apparatus that are not available in Taylor's University Lakeside Campus for certain experiments.

References

[1] US EPA, "Overview of Greenhouse Gases," *US Environmental Protection Agency (EPA)*, 2016. [Online]. Available: https://www.epa.gov/ghgemissions/overview-greenhouse-gases. [Accessed: 08-Oct-2016].

[2] US EPA, "Sources of Greenhouse Gas Emissions," *US Environmental Protection Agency (EPA)*, 2016. [Online]. Available: https://www.epa.gov/ghgemissions/sources-greenhouse-gas-emissions. [Accessed: 08-Oct-2016].

[3] US EPA, "Global Greenhouse Gas Emissions Data," *US Environmental Protection Agency (EPA)*, 2016. [Online]. Available: https://www.epa.gov/ghgemissions/global-greenhouse-gas-emissions-data#Country. [Accessed: 08-Oct-2016].

[4] F. K. C. Goh, V. Doshi, and W. Y. Wong, "Effect of Pyrolysis Temperature on DCFC Performance of Rubber Wood Sawdust-derived Biochar," in *Eureca Conference 2016*, 2016, pp. 39–52.

[5] D. W. H. Thong and V. Doshi, "Effect of Torrefaction and Pyrolysis on the Electrochemical Reaction Mechanisms in Direct Carbon Fuel Cells," in *Eureca Conference 2016*, 2016, pp. 252–264.

[6] S. P. S. Badwal and S. Giddey, "The holy grail of carbon combustion - The direct carbon fuel cell technology," *Mater. Forum*, vol. 34, pp. 181–185, 2010.

[7] A. Azapagic, "Life Cycle Assessment and Its Application to Process Selection, Design and Optimisation," *Chem. Eng. J.*, vol. 73, no. 1, pp. 1–21, 1999.

[8] A. Azapagic and S. Perdan, *Sustainable Development in Practice: Case Studies for Engineers and Scientists*, 2nd ed. Wiley-Blackwell, 2011.

[9] J. Prasara-A, "Comparative Life Cycle Assessment of Rice Husk Utilization in Thailand," RMIT University, Melbourne, 2009.

[10] S. M. Shafie, T.M.I.Mahlia, H. H. Masjuki, and B. Rismanchi, "Life cycle assessment (LCA) of electricity generation from rice husk in Malaysia," *Energy Procedia*, vol. 14, pp. 499–504, 2012.

[11] S. M. Shafie, "Paddy Residue Based Power Generation in Malaysia: Environmental Assessment Using LCA Approach," *APRN J. Eng. Appl. Sci.*, vol. 10, no. 15, pp. 6643–6648, 2015.

[12] S. J. D. Hoh, V. Doshi, and W. Y. Wong, "Pretreatment of Rice Husk for Application as a Fuel Source in Direct Carbon Fuel," in *Eureca Conference 2015*, 2015, pp. 297–316.

[13] M. S. Abu Bakar, "Catalytic pyrolysis of rice husk for bio-oil production," Aston University, 2013.

[14] C. M. Chin, V. Doshi, and W. Y. Wong, "Rice Husk as a Fuel Source in Direct Carbon Fuel Cells," in *Eureca Conference 2014*, 2014, pp. 1–9.

[15] M. Sean and V. Doshi, "Palm Oil Waste as Fuel Source in a DCFC," in *Eureca Conference 2014*, 2014, pp. 1–2.

[16] M. Dudek, P. Tomczyk, R. Socha, M. Skrzypkiewicz, and J. Jewulski, "Biomass

fuels for direct carbon fuel cell with solid oxide electrolyte," *Int. J. Electrochem. Sci.*, vol. 8, no. 3, pp. 3229–3253, 2013.

[17] K. Crombie, O. Mašek, S. P. Sohi, P. Brownsort, and A. Cross, "The effect of pyrolysis conditions on biochar stability as determined by three methods," *GCB Bioenergy*, vol. 5, no. 2, pp. 122–131, 2013.

[18] K. Jindo, H. Mizumoto, Y. Sawada, M. A. Sanchez-Monedero, and T. Sonoki, "Physical and chemical characterization of biochars derived from different agricultural residues," *Biogeosciences*, vol. 11, no. 23, pp. 6613–6621, 2014.

[19] R. Z. Vigouroux, "Pyrolysis of Biomass," Royal Institue of Technology Stockholm, 2001.

[20] Q. M. K. Waheed, M. a Nahil, and P. T. Williams, "Pyrolysis of waste biomass: investigation of fast pyrolysis and slow pyrolysis process conditions on product yield and gas composition," *J. Energy Inst.*, vol. 86, no. 4, pp. 233–241, 2013.

[21] International Energy Agency, "Key Coal Trends," Paris, France, 2016.

[22] M. Anshar, F. N. Ani, and A. S. Kader, "Electrical energy potential of rice husk as fuel for power generation in Indonesia," *ARPN J. Eng. Appl. Sci.*, vol. 11, no. 6, pp. 3616–3624, 2016.

[23] C. Wang and D. Mu, "An LCA study of an electricity coal supply chain," *J. Ind. Eng. Manag.*, vol. 7, no. 1, pp. 311–335, 2014.

[24] R. Turconi, A. Boldrin, and T. Astrup, "Life cycle assessment (LCA) of electricity generation technologies: Overview, comparability and limitations," *Renew. Sustain. Energy Rev.*, vol. 28, pp. 555–565, 2013.

[25] T. Chungsangunsit, S. H. Gheewala, and S. Patumsawad, "Emission assessment of rice husk combustion for power production," *World Acad. Sci. Eng. Technol.*, vol. 53_, no. 5, pp. 1070–1075, 2009.

[26] N. Autissier, D. Larrain, J. Van Herle, and D. Favrat, "CFD simulation tool for solid oxide fuel cells," *J. Power Sources*, vol. 131, no. 1–2, pp. 313–319, 2004.

[27] D. H. Jeon, "A comprehensive CFD model of anode-supported solid oxide fuel cells," *Electrochim. Acta*, vol. 54, no. 10, pp. 2727–2736, 2009.

[28] F. Hashemi, S. Rowshanzamir, and M. Rezakazemi, "CFD simulation of PEM fuel cell performance: Effect of straight and serpentine flow fields," *Math. Comput. Model.*, vol. 55, no. 3–4, pp. 1540–1557, 2012.

Debottlenecking biofuel process plants via Simulation-based tool

Mark Leong Tin Wai*, Viknesh Andiappan, Eunice Phang Siew Wei

leong_tinwai92@hotmail.com
VikneshAndiappan.Murugappan@taylors.edu.my
SiewWei.Phang@taylors.edu.my

Abstract
As the amount of fossil fuel in the world depletes, biofuels can be used as an alternative to fossil fuels in everyday life. Production of bioethanol is a promising alternative as bioethanol can be produced from any lignocellulosic agricultural residue. This research is aimed to analyse and debottleneck a biofuel process plant using simulation-based tool and to perform cost analysis in order to determine the feasibility of the debottlenecking. The simulation tool used in this research is UNISIM and it is used to simulate the bioethanol production. Following this, data from UNISIM is extracted and analysed in a spreadsheet in order to determine the bottleneck. The equipment is further analysed and the cost for replacing the equipment is calculated. It is found that the debottlenecking technique is feasible in this research.

Keywords: Debottlenecking, Biofuel production plant, Bioethanol.

1. Introduction

As fossil fuels is not a renewable energy, it is estimated that fossil fuels will used up [1]. Since fossil fuels are a need in everyday life from cooking to vehicle usage, it is important to find an alternative source in order to move away from fossil fuel. Bioethanol can be considered as a good alternative from petroleum as it has a high octane value [1]. One of the leading countries in producing ethanol is the USA followed by Brazil and Asian countries are only producing 14% of the total ethanol production of the world [2]. Bioethanol can be produced by using sugar cane, empty fruit branches and soybeans etc. This is because the production of ethanol is based on fermentation of sugars using enzymes.

Previous researchers have found that bioethanol can be produced using algae by cultivating, harvesting, extracting and commercialization techniques. Results from the research show that to cultivate algae for biofuels, it would require a high capital cost [3]. Another research states that bioethanol can be produced by using the fermentation technique [4]. Bioethanol can be produced by using lignocellulosic agricultural residue that will undergo pretreatment, enzymatic hydrolysis, fermentation and dehydration [4]. However, focusing on the development of the bioethanol process alone is not sufficient for an optimised design. It is important to analyse the capability of the bioethanol process to adjust for potential increase in bioethanol demands. It is common for plants to increase the production of a certain product as the demand of the product increases. As the demand for a certain products increases in the market, the supply of said products has to meet the demands of the consumers. Since production has to increase, the production plant has to take in more input to produce more output. This can cause the plant capacity to be exceeded resulting in process equipment bottlenecks. An equipment is considered as bottleneck when the capacity of the equipment is exceeded and thus inhibiting the equipment from functioning. In this respect, as the demand of bioethanol begin to rise so will the production, hence, resulting in possible bottlenecks in a production plant. In order to debottleneck a production plant, it is important to determine the equipment of the plant that needs to be debottleneck. There are a few methods on debottlenecking an equipment. One of the methods to address increase in capacity is to build a new production plant [5]. This would be costly and would take a long time to achieve breakeven. Another way is to analyse each equipment, identify bottlenecks and determine a solution to debottleneck the equipment. Based on previous research, an approach to debottleneck a plant is to rerate the equipment. For example, if a distillation column has a bottlenecking problem, one can always increase the fractional tower capacity. Another example is for pumps where pumps can have the impeller changed if bottlenecking happens [5].

Many previous works focus on the design modification, operating condition change, catalyst replacement and so on. However, the propose actions are insufficient. In this work, UNISIM simulation package is used to simulate the plant for the increased output and to analyse the capacity from all equipment. Then the data is then analysed using a spreadsheet to determine the equipment that has bottleneck. The objective of this research is to analyse and debottleneck a biofuel process plant using simulation-based tool. To perform cost analysis in order to determine the benefit cost ratio of debottlenecking the biofuel process plant.

2. Methodology

This research is carried out using a simulation tool which is UNISIM. Empty Fruit Branch (EFB) is used as a feed into the bioethanol plant. The plant is simulated at the beginning and the values of the flow rates are transferred into a spreadsheet. Then a product increase of 25% is introduced and the flow rates of the inlet is recalculated. The values are then added into the simulation and the plant is simulated again. Table 1 shows the specifications in UNISIM used for the simulation and figure 1 shows the process flow diagram of the process plant.

Table 1: UNISIM Specifications

UNISIM Specifications	
Fluid Package:	NRTL
Inlet EFB composition	
Hemicellulose:	27%
Cellulose:	42%
Lignin:	31%

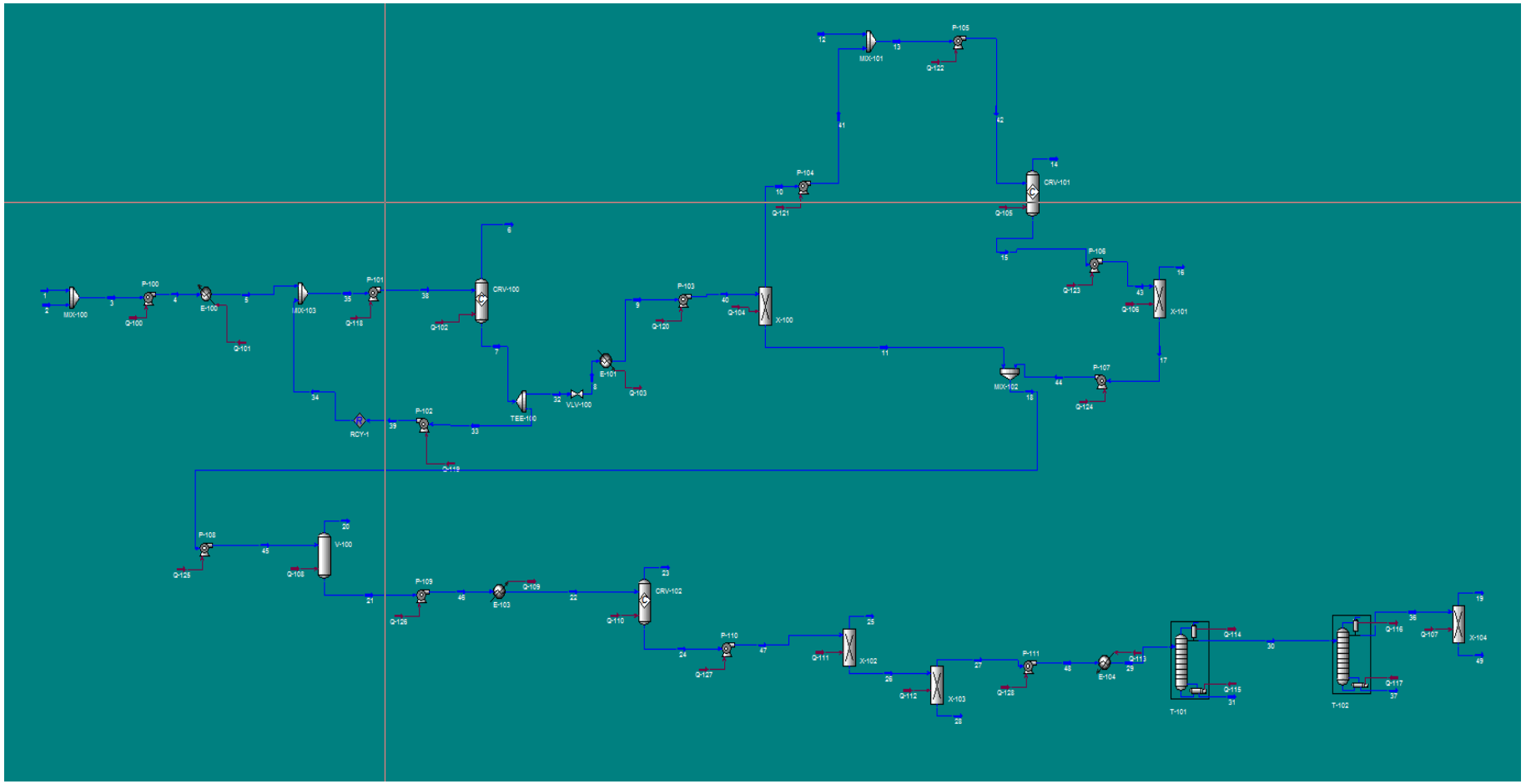


Figure. Simulation PFD of the biofuel plant

After the simulation is done, the flow rates are then transferred into the excel sheet. There the flow rates are cross-checked with the maximum capacity of each equipment and bottleneck is then determined. An equipment is considered bottleneck when the flow rate in that equipment exceeds the maximum capacity allowable.

Next, each equipment that has a bottleneck is analysed and a recommendation is given. The cost of the new equipment is then calculated with the equation:

$$Ce = a + bS^n \quad (1)$$

Ce is the estimated cost of an equipment in terms of USD. For pumps, a, b and n is a constant of 3,300, 4.8 and 1.2 respectively, S is the flow in the pump in L/s. For reactors, a, b and n are constants of 14,000, 15,400 and 0.7 respectively and S is the volume of the reactor in cubic metre [6].

$$\frac{Cost\ A}{Cost\ B} = \left(\frac{Capacity\ A}{Capacity\ B}\right)^{0.6} \quad (2)$$

Equation (2) is used to calculate the cost of the pumps and reactors if the values of the flow or volume are outside of the limitation range of equation (1) [8].

Then the cost for each newly acquired equipment are then added together and multiplied by the annualising cost factor of 0.13. Profit of the plant is then calculated by adding the selling price of ethanol and carbon dioxide per year. After that, the profit is divided with the annualised cost of the new equipment to obtain the benefit cost ratio (BCR) [8].

$$BCR = \frac{Incremental\ profit\ gained}{Total\ annualised\ cost\ of\ new\ equipment} \quad (2)$$

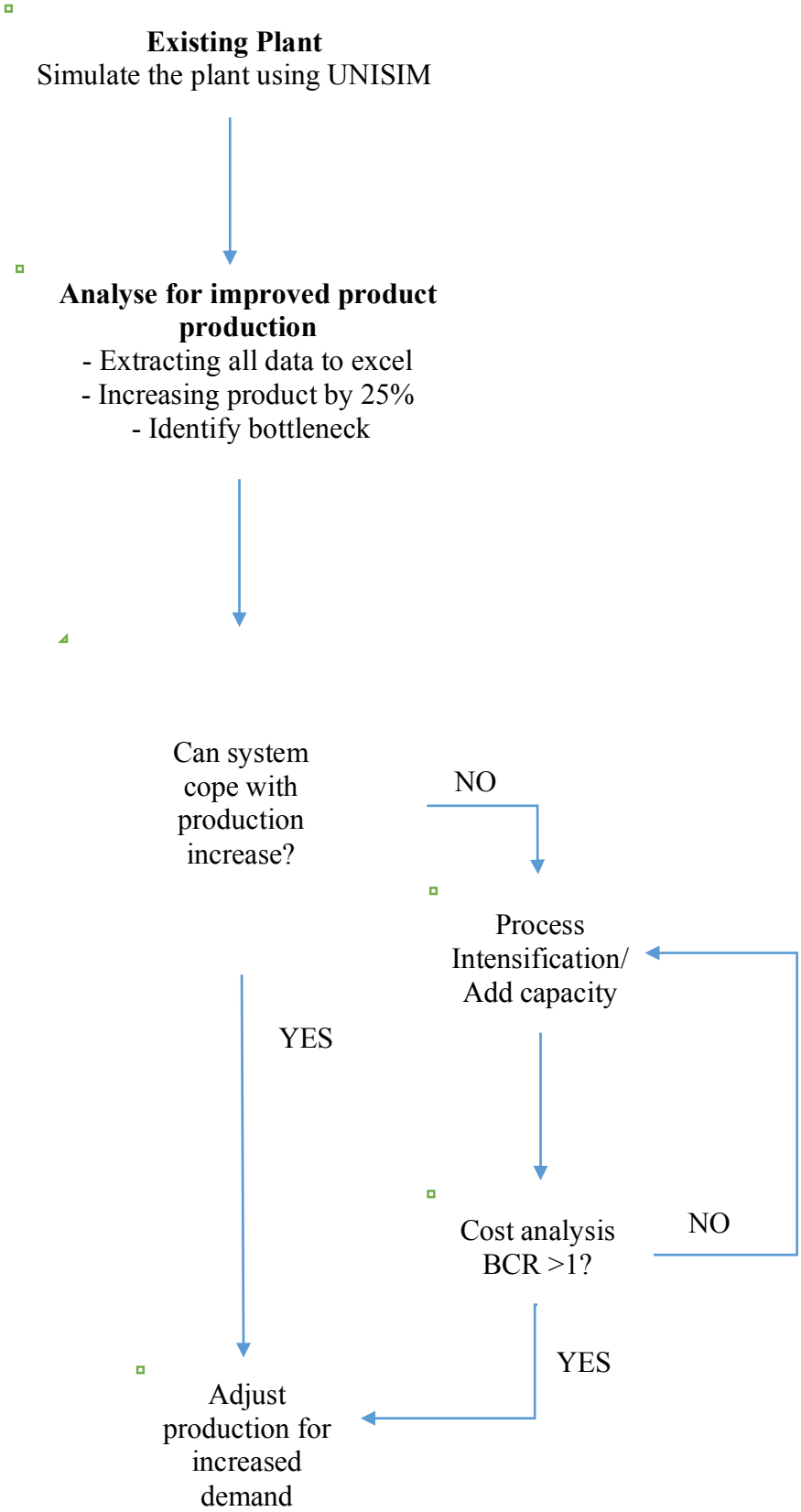


Figure 2: Methodology flowchart

3. Results and discussion

3.1 Results Analysis

Table 2 shows the list of equipment in the plant and the minimum and maximum allowable capacity. As long as the capacity of the new flow is over the maximum capacity of the equipment, it is bottleneck. Based on Table 1, pumps at the simultaneous saccharification co-fermentation production line is affected by the increase in production and therefore are considered as process bottlenecks.

In order to debottleneck the pumps, it is recommended to increase the capacity of the pump which results in purchasing a new pump. This is because the initial pump is already sized to fit the flow before the change. Hence, replacing any internal components of the pump for a higher flow is not feasible. So, the cost of the new pump is calculated using equation (1), resulting in a cost of $542.44 and $521.03 for the first and the second pump respectively. The pump is designed based on having a 25% allowance on the new flow rate. This is to ensure there is ample allowance in case the flow fluctuates or for future increases in the flow.

Next, for the reactor, there are a few ways to debottleneck the reactor. Firstly, changing the catalyst of the reaction to have a bigger yield. Since in this reactor there is a fermentation process going on, the only component that can be changed is the enzyme. In this reactor the two enzyme that is used is T. reesei and Zmymononas Mobilis 31821 (pZB5). However, based on previous researches, some enzymes have a higher yield of ethanol but has a side effect and some enzymes have a lower yield. For example, according to Seiborth. B, et al, T. reesei has a glycoside hydrolases (GH) of 193 whereas Aspergillus niger has a GH of 243, but Aspergillus niger has spores and pathogens that could ruin the reaction [7]. So, it is recommended to install an additional reactor to cater for the increased flow. The cost of the reactor is also calculated by using the equation (1).

Table 2: Bottleneck analysis

Equipment	Min capacity (kg/h)	Maximum capacity (kg/h)	Capacity after increase (kg/h)	Bottleneck?
Pump-101	112.500	468.750	468.750	No
Reactor	150.000	625.000	623.416	No
Pump-102	37.500	156.250	155.854	No
Pump-103	112.500	468.751	467.562	No
Pump-104	103.129	429.705	428.527	No
Pump-105	299.703	1248.762	1247.527	No
Reactor	299.703	1248.762	1247.527	No
Pump-106	299.703	1248.870	1247.526	No
Pump-107	237.692	990.383	989.395	No
Pump-108	247.063	1029.429	1028.431	No
Tank	247.063	1029.429	1028.431	No
Pump-109	9.897	41.239	41.240	Yes
Reactor	9.897	41.239	41.240	Yes
Pump-110	7.774	32.392	32.395	Yes
Pump-111	3.101	12.923	12.921	No
Distillation column	3.101	12.923	12.921	No
Distillation column	2.096	8.734	8.732	No

Table 3 shows the summary of cost of the pump and reactor. The ethanol profit is calculated by using the price of ethanol of RM2.31 per litre and price of Carbon dioxide of RM1 per litre [9]. It can be seen that the Benefit cost ratio (BCR) is more than 1. This shows that replacing the equipment is one way to debottleneck the plant and it is feasible. In addition from calculating the BCR, a sensitivity analysis is performed in order to determine the minimum price that can be set to sell a product in order to still gain a BCR of higher than 1.

Table 3: Summary of cost

Cost of new equipment	
Pump 109 (USD)	542.44
Pump 110 (USD)	521.03
Reactor (USD)	11,752.126
Annualizing factor	0.13
Total annualized cost (USD/yr)	15,416.01
Income gained	
Ethanol (USD/yr)	8,136.07
Carbon dioxide (USD/yr)	18,957.58
Total (USD/yr)	27,093.65
BCR	**1.76**

3.2 Sensitivity analysis

Since carbon dioxide is a major factor affecting the BCR, sensitivity analysis is done in order to determine the lowest price of carbon dioxide that can be sold in order to determine the feasibility of the project. Based on table 3, it is found that the BCR is lower than 1 when the price of carbon dioxide is about 30% of the initial price of RM 1 per litre and slightly above 1 when the price is 40% of the initial price. This shows that the project is feasible only if the price of carbon dioxide is more than or equal to 40% of the initial price.

Table 3: sensitivity analysis of Carbon dioxide

Percent of CO_2 price	Price of CO_2 (USD/l)	CO_2 profit (USD/hr)	Annual Profit (USD/yr)	BCR
0.9	0.207	2.13	17061.82	1.63
0.8	0.184	1.90	15166.06	1.51
0.7	0.161	1.66	13270.30	1.39
0.6	0.138	1.42	11374.55	1.27
0.5	0.115	1.18	9478.79	1.14
0.4	0.092	0.95	7583.03	1.02
0.3	0.069	0.71	5687.27	0.90

4. Conclusion

In conclusion, this research work presents a debottlenecking approach using UNISIM simulation based tool.. In this research based on the biofuel process plant, increasing the production by 25 percent will cause the pumps and reactor at the SSCF stage to achieve bottleneck status. This can be solved by replacing the equipment which will not cause any disturbances to the initial process. The benefit cost ratio of the process plant after debottlenecking is 1.76. It shows that the method of replacing the equipment is feasible.

References

[1] E. P. S. Bon and M. A. Ferrara, "Bioethanol Production via Enzymatic Hydrolysis of Cellulosic Biomass," *Biotechnology*, no. October 2007, pp. 1–11, 2010.

[2] B. Joshi, M. Raj, B. Dinita, S. Jarina, and J. Rajani, "Lignocellulosic ethanol production : Current practices and recent developments," *Biotechnol. Mol. Biol. Rev.*, vol. 6, no. November, pp. 172–182, 2011.

[3] R. Bibi, Z. Ahmad, M. Imran, S. Hussain, A. Ditta, S. Mahmood, and A. Khalid, "Algal bioethanol production technology: A trend towards sustainable development," *Renew. Sustain. Energy Rev.*, vol. 71, December 2016, pp. 976–985, 2017.

[4] K. Saha, U. M. R, J. Sikder, S. Chakraborty, S. S. da Silva, and J. C. dos Santos, "Membranes as a tool to support biorefineries: Applications in enzymatic hydrolysis, fermentation and dehydration for bioethanol production," *Renew. Sustain. Energy Rev.*, vol. 74, no. March, pp. 873–890, 2017.

[5] Schneider DF. Debottlenecking Options and Optimization 1997.

[6] R. Sinnott and G. Towler, *Chemical Engineering Design,* fifth edition, 2009, Oxford, Butterworth-Heinemann

[7] B. Seiboth, C. I. Verena, and S. Seibot, "Trichoderma reesei: A Fungal Enzyme Producer for Cellulosic Biofuels, Biofuel Production-Recent Developments and Prospects.," *Biotechnol. Biofuels*, vol. 6, no. 1, p. 127, 2011.

[8] M. S. Peters and K. D. Timmerhaus, *Plant Design and Economics for Chemical Engineers*, fifth edition, 2004, New York, McGraw-Hill, Inc.

[9] P. Luckow *et al.*, "2015 Carbon Dioxide Price Forecast," *Synap. Energy Econ. Inc.*, pp. 1–39, 2015

eureca 2017 – Conference Paper
Paper Number 2CE16

Integration of Pretreatment and *in Situ* Enzymatic Saccharification of Lignocellulosic Biomass for Sugar Production

So Khai Ang [1], Li Wan Yoon [1*], Teck Nam Ang [2]

[1] *School of Engineering, Taylor's University Lakeside Campus, Subang Jaya, Selangor, Malaysia*

[2] *Department of Applied Sciences, Faculty of Science and Technology, Nilai University, No 1, Persiaran Universiti, Putra Nilai, 71800, Nilai, Negeri Sembilan, Malaysia*

[2]*liwan.yoon@taylors.edu.my*

Abstract
With the rapid demand on the energy consumption of the fossil fuel, bioethanol and bioethanol are secondary fuel which is promising solution to decrease the dependency on fossil fuel and the waste of lignocellulosic biomass which is known as renewable materials and used for biofuel fermentation. Biofuel fermentation is widely applied in the industry, it increases indirectly on glucose and xylose demand which are essential substrates for microorganism. The performance of pretreatment methods on the coconut husks were investigated. Reagents (0.5% (w/v) of NaOH, NaCl and H_2SO_4) and hot water were used in the coconut husk pretreatment in the condition (solid-liquid ratio (1:15), 95℃, 2 hours) and compares to untreated coconut husk. The pretreatment reagent hydrolyses the cellulose and hemicellulose of coconut husk during the pretretment, the glucose and xylose were detected in the pretreatment reagent by using HPLC. The characterization study of pretreated and untreated coconut husks was conducted in SEM, it signified that the largest the porous sizes and volumes from NaOH pretreatment method. It was justified to produce the highest sugar yield from enzymatic saccharification among other coconut husks regardless pretreated or untreated. NaOH pretreatment method was used to compare untreated coconut husks for solid state fermentation with fungal strains, *Phlebia Radiata* which is commonly used for cellulase production on agriculture waste. On the other side, NaOH pretreated coconut husks were reported to be beneficial on growth of the fungal strain, *Phlebia Radiata* without providing sugar in the coconut husks. Glucose was consumed to sustain the growth and produce more cellulase to produce glucose. It was found maximum glucose production rate of 0.6% and suggested to extract out the glucose on day 2.

Keywords: Coconut Husk, Pretreatment, Enzymatic Hydrolysis, Solid State Fermentation (SSF), *Phlebia Radiata*.

1. Introduction

The global energy market increases rapidly in the large population in the world, second generation fuel is an alternative option in replacing fossil fuel when it is completely depleted. The examples of second generation fuel such as bioethanol and biodiesel can be produced by utilizing abandoned lignocellulose and starch components in biomass from agriculture and forest. These biofuels are blended with fossil fuel to promote cleaner combustion and lower toxic emission [1]. They are economical viable to be produced from low cost agriculture waste which turns waste into valuable products and declines the waste amount on the planet, independency on the fluctuation price of fossil fuel.

Glucose and xylose are derived from cellulose and hemicellulose respectively present in the lignocellulosic biomass [1-2]. Both are the essential substrates for bacteria/fungi to undergo biofuel fermentation process. Apart from producing biofuels through fermentation, the diversity of other high chemical valued products are achieved by applying other strains types and supplying sufficient nutrients and substrates. Coconut is high potential lignocellulosic biomass to be used for sugar production due to its high carbohydrate components (cellulose and hemicellulose) [2,3]. It is generally grown in the coastal area of the tropical countries around the world. In 2014, there were approximately 60.5 Mt and 0.6 Mt of coconuts produced in the worldwide and Malaysia respectively [5].

Coconut (Cocos nucifera L.) is disposed after the coconut water is extracted [6]. The coconut husks are mixed with different maturity during waste collection as shown as Table 1.

Table 1: Typical Components of Green Coconut Husk [7]

Green Coconut Husk Compounds	Mature Coconut Husks Dry Weight (%)	Green Coconut Husks Dry Weight (%)
Cellulose	31.60 ± 0.51	32.88 ± 0.88
Hemicellulose	26.33 ± 0.89	26.50 ± 0.45
Lignin	26.69 ± 0.97	26.88 ± 1.02
Ash & others	8.75 ± 0.56	7.61 ± 0.35

Attributing to absence hydrolysable linkages and complex 3D structure formed by phenyl moieties, lignin is recalcitrant barrier against enzymatic hydrolysis [8]. Therefore, various types of pretreatment methods are proposed to break down the lignin and provide better accessibility for enzymes to produce fermentable sugar. The benefits of doing pretreatment on substrates help to increase the porous size and volume when compares to untreated substrates [9].

Pretreatmet methods are categorized into physical, chemical and biological pretreatment. The physical pretreatment involves the milling, grinding and thermal treatment whereas chemical pretreatments involves the application on chemical solvent in dissolving of substrates components. On the other hand, microorganism is involved in hydrolyzing the lignin in biological treatment. White rot fungi is known as good ability of lignin degradation [10]. The selected white rot fungi strains, *Phlebia radiata* can secret three major types of ligninolytic enzymes for delignification such as: lignin

peroxidase, manganese peroxidase and laccase under normal room condition [9-10]. Although it is specific to lignin and saving up intensive energy used to destruct lignin, it contributes the loss of polysaccharides and slower destruction rate lignin framework than other delignification pretreatment methods [12]. The fungi consume nutrients in the wetted insoluble substrates and grow under low moisture content environment is known as solid state fermentation.

The term of "*in situ*" is referred as the original place where *Phlebia radiata* secrets enzymes and undergoes saccharification on coconut husks. Low cost single stage chemical pretreatment was compared to non-chemical pretreated coconut husks to study the significant of chemical pretreatment method. The morphology study on analyzing the structure of coconut husks was done through the observation of Scanning Electronics Microscope (SEM). The objectives of this research are as follow:

1. To examine the effect of pretreatment on coconut husks.
2. To evaluate the glucose and xylose production with the interaction of pretreatment reagent and coconut husks.
3. To investigate the glucose and xylose production with the integration of pretreatment and *in situ* saccharification of coconut husks.

2. Research Methodology

2.1 Coconut Husk Collection and Preparation

The disposed coconut was collected from the hawker center in SS14, Selangor. The coconut husk was cut out from coconut by removing the inter shell and outer layer. It was then flushed with distilled water to remove the ash on the surface before it was dried at temperature 60℃ for 24 hours. The samples can be taken out from drying until the weight of the coconut husk was measured to be constant for 3 times. It was grinded to particles size (<1.5mm) and used throughout whole project.

2.2 Untreated Coconut Husk Preparation

The dried and grinded coconut husks were washed until it reaches to pH 5 with 50mM acidic sodium acetate buffer solution (pH 5), the preparation of buffer solution is suggest by [13]. Washed coconut husks were dried at temperature 60℃ for 24 hours until it had reached to constant weight for 3 times measurements.

2.3 Alkaline Pretreated Coconut Husk Preparation

The dried and grinded coconut husks were pretreated with 0.5% (w/v) of NaOH (Merck) with solid liquid ratio (1:15) and heated at temperature 95℃ (±3 ℃) for 2 hours. The reagent was filtered out from pretreated coconut husks by using tea filter bag after it had cooled downed to room temperature. The filtered reagent was centrifuged at 4000 rpm for 20 minutes before it was extracted out by syringe. It was pumped through syringe filter and then stored into 2 ml HPLC vials (Agilent) for quantity measurement of glucose and xylose.

NaOH pretreated coconut husks were washed with 500 ml of distilled water by batch until the distilled water is not dyed by NaOH reagents and the pH of washed water become neutral (10g of pretreated coconut husk was washed with 10 batches of distilled

water). After that, pretreated coconut husks were rinsed with 50mM acidic sodium acetate buffer solution and adjusted to pH 5. It was filtered out by using tea filter bag and dried at 60℃ (±5℃) for 24 hours.

2.4 Acidic Pretreated Coconut Husk Preparation

The dried and grinded coconut husks were pretreated with 0.5% (w/v) of H_2SO_4 (Merck) with solid liquid ratio (1:15) and heated at temperature 95℃ (± 3 ℃) for 2 hours. The reagent was filtered out from pretreated coconut husks by using tea filter bag after it had cooled downed to room temperature. The filtered reagent was centrifuged at 4000 rpm for 20 minutes before it was extracted out by syringe. It was pumped through syringe filter and then stored into 2 ml HPLC vials (Agilent) for quantity measurement of glucose and xylose.

H_2SO_4 pretreated coconut husks were washed with 500ml of distilled water by batch until the distilled water is not dyed by H_2SO_4 reagents and the pH of washed water become neutral (10g of pretreated coconut husk was washed with 10 batches of distilled water). After that, pretreated coconut husks were rinsed with 50mM acidic sodium acetate tryhydrate buffer solution and adjusted to pH 5. It was filtered out by using tea filter bag and dried at 60℃ (± 5℃) for 24 hours.

2.5 Salt Pretreated Coconut Husk Preparation

The dried and grinded coconut husks were pretreated with 0.5% (w/v) of NaCl (Merck) with solid liquid ratio (1:15) and heated at temperature 95℃ (± 3 ℃) for 2 hours. The reagent was filtered out from pretreated coconut husks by using tea filter bag after it had cooled downed to room temperature. The filtered reagent was centrifuged at 4000 rpm for 20 minutes before it was extracted out by syringe. It was pumped through syringe filter and then stored into 2 ml HPLC vials (Agilent) for quantity measurement of glucose and xylose.

NaCl pretreated coconut husks were washed with 500ml of distilled water by batch, 5 Liter of distilled water was used to washed 10 grams of pretreated coconut husk. After that, pretreated coconut husks were rinsed with 50mM acidic sodium acetate tryhydrate buffer solution and adjusted to pH 5. It was filtered out by using tea filter bag and dried at 60℃ (± 5℃) for 24 hours.

2.6 Hot Water Pretreated Coconut Husk Preparation

The dried and grinded coconut husks were pretreated with distilled water with solid liquid ratio (1:15) and heated at temperature 95℃ (± 3 ℃) for 2 hours. The hot water was filtered out from pretreated coconut husks by using tea filter bag after it had cooled downed to room temperature. The filtered water was centrifuged at 4000 rpm for 20 minutes before it was extracted out by syringe. It was pumped through syringe filter and then stored into 2 ml HPLC vials (Agilent) for quantity measurement of glucose and xylose.

Hot water pretreated coconut husks were washed with 500ml of distilled water by batch, 5 Liter of distilled water was used to washed 10 grams of pretreated coconut husk. After that, pretreated coconut husks were rinsed with 50mM acidic sodium

acetate tryhydrate buffer solution and adjusted to pH 5. It was filtered out by using tea filter bag and dried at 60℃ (± 5℃) for 24 hours.

2.7 Enzymatic Hydrolysis

0.5 g pretreated and untreated coconut husks were used for enzymatic hydrolysis in triplicates. 30 FPU/g of cellulase (Trichoderma Longibrachiatum; Sigma-Aldrich) [14] was used in this experiment and preparation of buffer solution was suggested by [13]. 1.5 mg/ml of cellulase was only added into acidic sodium acetate tryhydrate buffer solution (pH 5) before enzymatic hydrolysis. 0.5 g substrates were mixed with 10 ml acidic sodium acetate tryhydrate buffer solution (pH 5). It was conducted in 250ml conical flask and incubated in orbital shaking incubator (150 rpm) at temperature 37℃ for 24 hours. The solvent in the conical flask was extracted out and centrifuged at 4000 rpm for 20 minutes. Supernatant was extracted out by syringe and pumped through syringe filter and then stored into HPLC vials for quantity measurement of glucose and xylose. The highest total fermentable sugar yield from pretreated coconut husks were selected and used to compare saccharification result from untreated coconut husk under solid state fermentation.

2.8 High Performance Liquid Chromatography (HPLC)

The deionized water was used as mobile phase to flow through Agilent Hi-Plex Column. It was vacuum filtered and degassed at temperature 37℃ with frequency of 80Hz for 25 minutes. Agilent Hi-Plex column was selected to determine the sugar varieties in the sample. The HPLC (Agilent 1260, USA) was equipped with Refractive Index Detector (RID) and Agilent Hi-Plex Column with 0.6ml/min flowrate of mobile phase. The temperature for RID and Agilent Hi-Plex Column were set to 55 ℃ and 65 ℃ respectively suggested by [14].

Xylose and glucose standard with different concentration (mg/ml) were prepared and used to generate calibration curves prior sugar analysis. The 20 μl of reagents was extracted from HPLC vials with the implementation of automation system. The injected reagent was purged out after every analysis and priming with mobile phase.

2.9 Morphology Study on the Coconut Husks

The dried pretreated and non-pretreated coconut husks were outsourced to Quantum Skynet Solutions Sdn. Bhd. (Nilai, Negeri Sembilan, Malaysia). The structures of coconuts husks were examined under low vacuum condition. It was analyzed by Quanta^{TM} 200 FESEM with accelerating voltage of 2-10 kV for scanning electron microscope visualization.

2.10 Solid State Fermentation

2.10.1 Inoculum Preparation of White Rot Fungi

Phlebia radiata (DSM 5111) was obtained from the German Collection of Microorganism and Cell Cultures (DSMZ, Braunschweig, Germany). The fungi strains were subcultured to new malt extract peptone agar plate [14].by transferring 6mm agar

plug into the center of agar plate in sterilized laminar hood. It was incubated at 30℃ for 2 weeks until its mycelium was fully grown and covered on the top of the agar plate.

2.10.2 Preparation of Substrates

Upon the completion growth of mycelium on agar plate, the substrates (selected pretreatment method and no pretreatment method) were measured to be 2 grams and placed into 100 ml conical flasks respectively. Both samples were covered with double layered of aluminum foil and sterilized at 121 ℃ for 2 hours.

2.10.3 Solid State Fermentation

Cotton ball was made of cotton gauze and cotton, it was designed to be slotted tightly into the neck of 100 ml conical flask. The cotton ball was placed into a beaker and then covered with double layers of aluminum foil. It was sent to autoclave together with glass rod and cork barrier which had covered with aluminum foils at temperature of 121 ℃ for 2 hours.

Sterilized glass rod and cork barrier were used to transfer 5 pieces of agar plugs from cultured agar plate into 100 ml conical flask. All agar plugs were smashed and distributed among substrates by using sterilized glass rod. 5 ml of sterilized water was poured on the substrates in 100 ml conical flask. The cotton ball was slotted into the neck of 100 ml conical flask after the neck had been flamed by Bunsen burner.

.

2.10.4 Fermentable Sugar Analysis

The investigation on the effect of solid state fermentation were carried for 14 days and in duplicates samples. The samples were kept in Styrofoam box under room temperature and dark condition. The fermentable sugar yield was measured with intervals 2 days. 30 ml acidic sodium acetate tryhydrate buffer solution (pH 5) was pour into 100 ml conical flask to washed out the fermentable sugars from the substrates at the end of solid state fermentation. It was kept in shaking incubator and agitated 150 rpm at temperature of 37 ℃ for 1 hour. The solvent in the conical flask was extracted out and centrifuged at 4000 rpm for 20 minutes. Supernatant was extracted out by syringe and pumped through syringe filter and then stored into HPLC vials for quantity measurement of glucose and xylose.

3.0 Result and Discussion

3.1 Screening to Characteristic of Coconut Husk

Based on the screening result with magnificiant 50μm resolution, the surface porous were blocked by silica component as shown as Figure 1. It is hardly observed the porous on the surface of the untreated coconut husks on Figure 1a. Compared among the various types of pretreatment methods, alkaline pretreatment method (Figure 1b) provided the largest porous size and most clear porous and on the coconut husks. It was reported that alkaline reagent caused structure swollen with the exposure to heat [15].

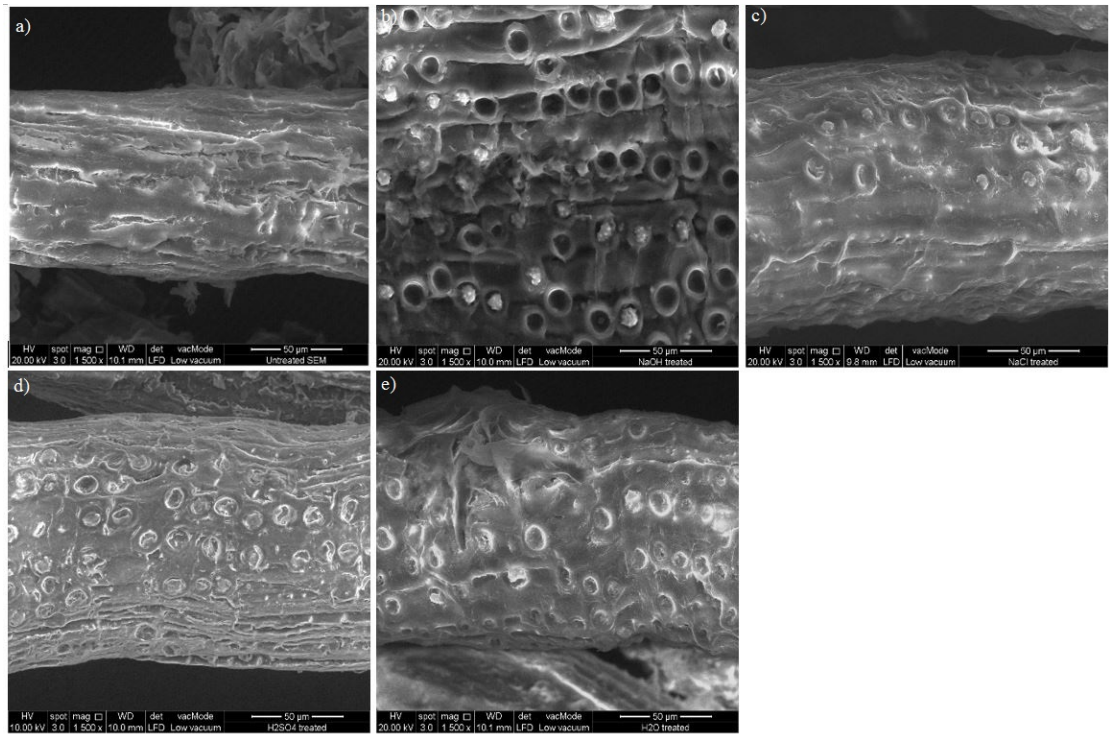


Figure 1. The characteristic of coconut husks: a) Untreated; b) NaOH pretreated; c) NaCl pretreated; d) H_2SO_4 pretreated and e) Hot water pretreated.

Pretreated reagents were collected after it had been used to pretreat 2g coconut husks at temperature of 95 ℃ (± 3 ℃) for 2 hours. It was sent for HPLC analysis once it had cooled down. The result of sugar analysis is shown as Table 2, H_2SO_4 exhibits its characteristic in hydrolyzing the structure of the coconut husks for sugar production, total fermentable sugar (22.85 ± 1.87 mg/g coconut husk) are produced in this experiment. The concentration of pretreatment reagent and temperature are the major parameters to maximize the sugar yield as reported by [9]. The mechanism of acid is to hydrolyze the structure with hydrogen bond present in the coconut husks. The total sugar yield is increased when the protons are active to disrupt the coconut husk structure. It is significant sugar loss to discard the H_2SO_4 reagents after pretreatment without recovering the total sugar in it. On the other side, NaOH reagent produces the least total sugar as it does the cleavage of the linkage between glycosidic bond [16].

The total sugar yield from hot water and NaCl reagents are almost identical, hot water pretreatment is more economical viable without dependency on the price of the NaCl. The selection of hot water and NaCl as pretreatment reagents is dependent on the accessibility of the reagent.

Table 2: Production of Fermentable Sugar from Pretreated Reagents

Characteristic of Samples:	**Produced Glucose (mg/g coconut husks):**	**Produced Xylose (mg/g coconut husks):**
NaOH Pretreated	4.55 ± 3.27	1.35 ± 0.78
H_2SO_4 Pretreated	15.35 ± 1.38	7.50 ± 0.49
Hot Water Pretreated	15.21 ± 3.84	6.65 ± 1.26
NaCl Pretreated	15.39 ± 1.36	6.38 ± 0.66

3.2 Analysis of Enzymatic Hydrolysis with Different Pretreated Coconut Husks

In this section, the control part was done by adding the distilled water to the coconut husks from each method to analyze the sugar amount prior enzymatic hydrolysis. There was significant amount of sugar residues in untreated coconut husks even though it had been washed with same amount of distilled water for pretreated coconut husks and neutralized to pH 5 with 50 mM sodium acetate tryhydrate buffer solution. The loading of enzymes (Trichoderma Longibrachiatum) was set as 1.5 mg/ml and sugar was produced from coconut husks. Glucose (44.37 ± 1.625 mg/g of coconut husks) and xylose (21.79 ± 2.38 mg/g coconut husks) were detected in untreated coconut husks while were no sugars were detected from pretreated samples before enzymatic hydrolysis.

The purpose of doing enzymatic hydrolysis is to select the pretreatment method based on the highest sugar yield and quality check on the handling procedures and preparations before going for solid state fermentation. Plenty of time would be wasted if it was caused by the quality of the procedures as fungi cannot grow on the toxic coconut husks and secrets enzymes to hydrolyze the coconut husks.

The highest sugar yield from enzymatic hydrolysis was found to be NaOH pretreated coconut husks (113.86 ± 8.35 mg/g coconut husks), followed by hot water pretreated coconut husks (13.25 ± 0.75 mg/g coconut husks) and NaCl pretreated coconut husks (10.44 ± 0.29 mg/g coconut husks), the result is shown as Table 3. The hot water is dissolving hemicellulose component to produce xylose [17]. The hot water pretreatment method on coconut husks feasible without considering on the chemical cost. However, glucose and xylose production from NaOH pretreatment method is (88.0 - 88.5 %) and (88.7 - 90.3%) higher than hot water pretreatment method. The advantages of the producing the coconut husks surface with large porous volume and size do help to increase the sugar yield from enzymatic hydrolysis part as screening from Figure 1 b).

Although H_2SO_4 reagent shows the great characteristic in hydrolyze the cellulose and hemicellulose, the H_2SO_4 pretreated coconut husks is not effective for enzymatic saccharification due to the inhibition of furfural produced from acid pretreated coconut husks. It is reported similar concentration (5% w/v of H_2SO_4) dissolve the monosaccharide and produces by-products (5-HMF, furfural levulinic acid and formic acid) to inhibit the fermentive organism [2]. For the untreated coconut husks consists the most lignin compares to others, lignin contributes black liquor and good absorption which is considered as hurdle for cellulase to hydrolyze cellulose [17] and bind with lignin [18]. Based on Table 3, xylose was produced by cellulase as the commercial cellulase was conjugated enzymes to prevent the inhibition from the end products [19]. The common types of cellulase are produced from white rot fungi, *Trichoderma ressei* [12]. The production of sugar is conducted in fundamental study, *in situ* saccharification by white rot fungi to produce suitable enzymes and eliminate uncertainty of inhibition from coconut husks.

Table 3. The Enzymatic Saccharification of Coconut Husks by Cellulase (*Trichoderma Longibrachiatum*)

Characteristic of Samples:	Produced Glucose (mg/g coconut husks):	Produced Xylose (mg/g coconut husks):
Untreated	0	0
NaOH Pretreated	104.35 ± 7.80	9.51 ± 0.55
H_2SO_4 Pretreated	2.34 ± 0.27	0
Hot Water Pretreated	12.21 ± 0.66	1.04 ± 0.09
NaCl Pretreated	9.44 ± 0.16	1.00 ± 0.13

3.4 Analysis of Solid State Fermentation with Selected Coconut Husks

3.4.1 Morphology Study on Selected Coconut Husks after Solid State Fermentation

The untreated coconut husks were selected to investigating the effect of *in situ* saccharification of white rot fungi, *Phlebia radiata* under solid state fermentation since it consisted sugar in the coconut husks. Pretreated coconut husks were selected for this research as it exhibited good characteristic on enzymatic saccharification. A small fraction of white spores was seen on NaOH pretreated coconut husks.

Figure 2 shows the SEM images with magnificent (40µm), it shows that the destruction of pretreated coconut husks is more severe and porous than untreated coconut husks under solid state fermentation after 14 days. In Figure 2 b), *Phlebia radiata* is scattered around the porous of pretreated coconut husks and higher intensity of fungal hyphae (white dot) when compares to Figure 2 a). As compared to both pictures, *in situ* saccharification of white rot fungi works with of NaOH pretreated coconut husks. This signifies that the white rot fungi grow better with larger porous sizes and volumes of coconut husks where it caused by NaOH pretreatment method. With the successful growth of *Phlebia radiata*, it secreted ligninolytic enzymes to penetrates the porous for structure delignification and depolymerization of coconut husks structure [10].

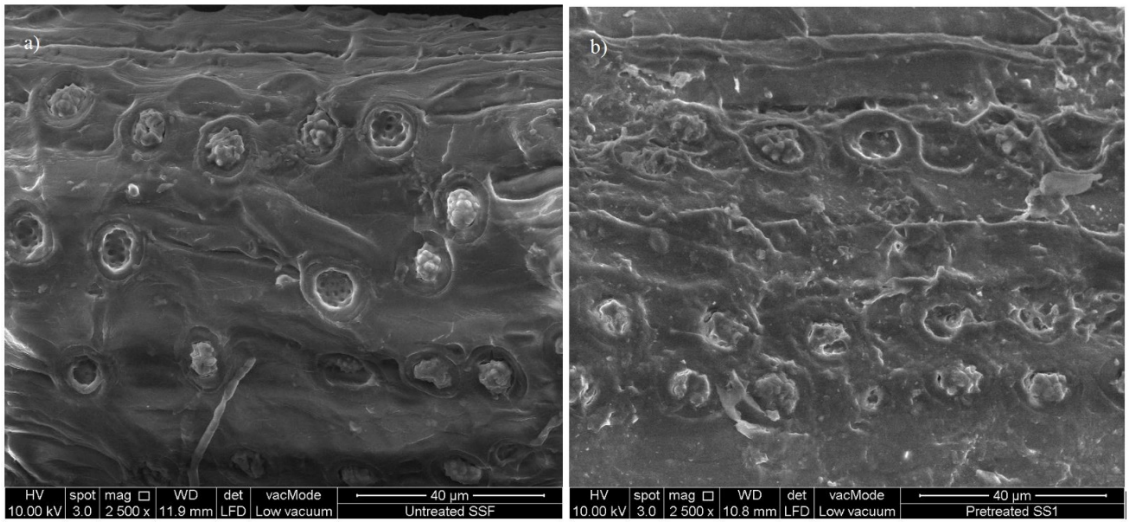


Figure 2. The Characteristic of Coconut Husks after 14 Days Solid State Fermentation: a) Untreated; b) NaOH Pretreated

3.4.2 Analysis on Sugar Production of Solid State Fermentation

The control sample was done to analyze the sugars residue before undergoing solid state fermentation. The glucose and xylose were detected as (68.86 ±2.20 mg/g coconut husks) and (44.45 ± 1.69 mg/g coconut husks) respectively. There was no sugar residue was reported in NaOH pretreated coconut husks.

Figure 3 shows that *Phlebia radiata* grows on the pretreated coconuts husks by utilizing the nutrients inside the pretreated coconut husks. It shows 2 mg of glucose per gram of pretreated coconut husks are produced from day 2. Refer to the fluctuation of glucose production, it signifies that glucose is the nutrients to sustain the growth of *Phlebia radiata* and produce cellulase. Therefore, it results the maximum sugar yield is found 6.86 mg/g of pretreated coconut husks on day 14. The amount of cellulase increases with the day of fermentation. However, the rapid growth of white rot fungi consumes more sugar with more time allocation.

To adapt the application of solid state fermentation for sugar production, it is suggested to the highest glucose production rate 0.6% occurs on day 2 to eliminate the uncertainty of sugar consumption by *Phlebia radiata.* The glucose production rate is increased 1% of the at the day 14. The glucose production rate is too low when compares to application of enzymes [15]. The disruption on lignin still not yet fully understood [8].

Based on Figure 3, the sugar residue in untreated coconut husks was fully consumed. The xylose was consumed and no production of xylose from NaOH pretreated coconut husks.

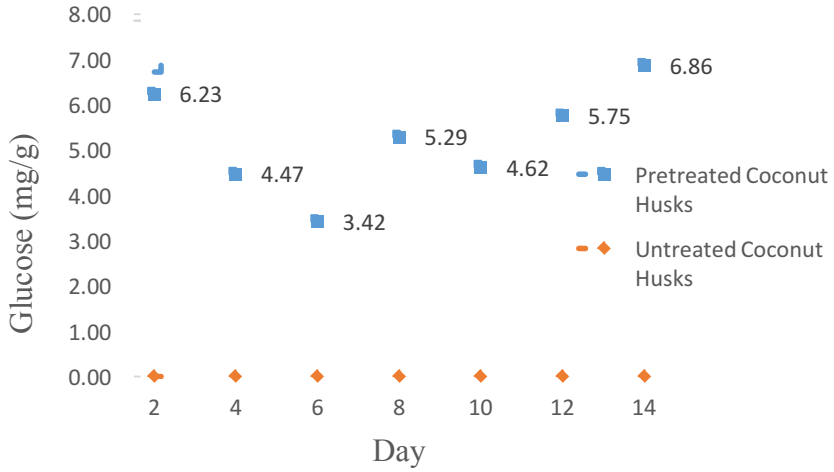


Figure 3 Glucose Production from Solid State Fermentation

4.0 Conclusions

In this experiment, 0.5 % (w/v) reagents are used to pretreat coconut husks at temperature of 95 ℃ (± 3 ℃) for 2 hours. Glucose and xyloses have been produced and found in pretreated reagents after pretreatment, especially H_2SO_4. It has been found to

be better performance on total sugar production than other pretreated reagents used in this study but it exhibits enzymatic saccharification even the substrates have been washed and neutralized.

NaOH pretreated coconut husks have displayed the great characteristic for enzymatic saccharification and increased significantly the structure porous size and volume. It has been discovered to produce glucose successfully without sugar residue from day 0 by using fungi strain, *Phlebia radiata*. Structure severity (larger porous sizes and volumes) of NaOH pretreated coconut husk is favorable for *Phlebia radiata* to produce glucose from nothing.

Despites the low sugar production rate and high sugar consumption by *Phlebia radiata*, it is applicable to extract out the produced sugar and enzymes. Compare to untreated coconut husks, pretreated coconut husks show the less sugar consumption and higher sugar production in short time. Therefore, for sugar production application, it is suggested to extract out glucose in day 2 where the glucose production rate is 0.06% per gram of NaOH pretreated coconut husks by using the fungi strain, *Phlebia radiata*.

Acknowledgment

The author would like to extend gratitude and thankfulness to project supervisor, Dr. Yoon Li Wan and co-supervisor, Dr. Ang Teck Nam for their patience and guidance to ensure the success of the project. The author also thanks the lab assistances to provide technical supports and trainings, especially to Ms. Lithnes Kalaivani and Ms. Nur. Farihah A. Malek.

References

[1] H. B. Aditiya, W. T. Chong, T. M. I. Mahlia, A. H. Sebayang, M. A. Berawi, and H. Nur, “Second generation bioethanol potential from selected Malaysia’s biodiversity biomasses: A review,” *Waste Manag.*, vol. 47, pp. 46–61, 2016.

[2] R. R. Gonzales, P. Sivagurunathan, and S.-H. Kim, “Effect of severity on dilute acid pretreatment of lignocellulosic biomass and the following hydrogen fermentation,” 2016.

[3] T. Y. Ding, S. L. Hii, and L. G. A. Ong, “Comparison of pretreatment strategies for conversion of coconut husk fiber to fermentable sugars,” *BioResources*, vol. 7, no. 2, pp. 1540–1547, 2012.

[4] M. K. D. Rambo, F. L. Schmidt, and M. M. C. Ferreira, “Analysis of the lignocellulosic components of biomass residues for biorefinery opportunities,” *Talanta*, vol. 144, pp. 696–703, 2015.

[5] Food and Agriculture Organization of the United Nations (FAOSTAT), “Coconut production in the world and Malaysia,” 2014. [Online]. Available: http://www.fao.org/faostat/en/#compare. [Accessed: 25-May-2017].

[6] M. DebMandal and S. Mandal, “Coconut (Cocos nucifera L.: Arecaceae): In health promotion and disease prevention,” *Asian Pac. J. Trop. Med.*, vol. 4, no. 3, pp. 241–247, 2011.

[7] F. A. Gonçalves, H. A. Ruiz, C. D. C. Nogueira, E. S. Dos Santos, J. A. Teixeira, and G. R. De Macedo, “Comparison of delignified coconuts waste and cactus for fuel-ethanol production by the simultaneous and semi-

simultaneous saccharification and fermentation strategies," *Fuel*, vol. 131, pp. 66–76, 2014.

[8] J. Ke, D. D. Laskar, D. Singh, and S. Chen, "In situ lignocellulosic unlocking mechanism for carbohydrate hydrolysis in termites: crucial lignin modification.," *Biotechnol. Biofuels*, vol. 4, no. 1, p. 17, 2011.

[9] T. N. Ang, G. C. Ngoh, and A. S. M. Chua, "Comparative study of various pretreatment reagents on rice husk and structural changes assessment of the optimized pretreated rice husk," *Bioresour. Technol.*, vol. 135, no. January, pp. 116–119, 2013.

[10] H. Meehnian, A. K. Jana, and M. M. Jana, "Pretreatment of cotton stalks by synergistic interaction of Daedalea flavida and Phlebia radiata in co-culture for improvement in delignification and saccharification," *Int. Biodeterior. Biodegrad.*, vol. 117, pp. 68–77, 2017.

[11] M. V. Bule, I. Chaudhary, A. H. Gao, and S. Chen, "Effects of extracellular proteome on wheat straw pretreatment during solid-state fermentation of Phlebia radiata ATCC 64658," *Int. Biodeterior. Biodegradation*, vol. 109, pp. 36–44, 2016.

[12] A. Várnai, M. R. Mäkelä, D. T. Djajadi, J. Rahikainen, A. Hatakka, and L. Viikari, *Carbohydrate-Binding Modules of Fungal Cellulases. Occurrence in Nature, Function, and Relevance in Industrial Biomass Conversion*, vol. 88. 2014.

[13] Sigma-Aldrich, "Enzymatic Assay of Cellulase," 2017. [Online]. Available: http://www.sigmaaldrich.com/technical-documents/protocols/biology/enzymatic-assay-of-cellulase.html. [Accessed: 26-Apr-2017].

[14] Sigma-Aldrich, "Cellulase from Trichoderma longibrachiatum powder, ≥1.0 unit/mg solid | Sigma-Aldrich," 2017. [Online]. Available: http://www.sigmaaldrich.com/catalog/product/sigma/c9748?lang=en&region=MY. [Accessed: 26-Apr-2017].

[15] Galbe M and Zacchi G, "Pretreatment of lignocellulosic materials for efficient bioethanol production," *Adv. Biochem. Eng. Biotechnol.*, vol. 108, no. July, pp. 41–65, 2007.

[16] Y. Chen, M. A. Stevens, Y. Zhu, J. Holmes, and H. Xu, "Understanding of alkaline pretreatment parameters for corn stover enzymatic saccharification," *Biotechnol. Biofuels*, vol. 6, no. 1, p. 8, 2013.

[17] X. Zhuang *et al.*, "Liquid hot water pretreatment of lignocellulosic biomass for bioethanol production accompanying with high valuable products," 2016.

[18] M. Kellock, J. Rahikainen, K. Marjamaa, and K. Kruus, "Lignin-derived inhibition of monocomponent cellulases and a xylanase in the hydrolysis of lignocellulosics," 2017.

[19] F. Asina, I. Brzonova, E. Kozliak, A. Kubátová, and Y. Ji, "Microbial treatment of industrial lignin_ Successes, problems and challenges," 2017.

Bentonite-Cement Mixes as Electrical Grounding Improvement Material

Andrew Yap Khin Mann[1], Mohsen Nabi Poor[1*], Koay Seong Chun[1], Siow Chun Lim[1]
[1]School of Engineering, Taylor's University, Malaysia.

[*]Mohsen.nabipoor@taylors.edu.my

Abstract
The scope of this paper is to study the bentonite mix with cement as an electrical grounding improvement material (GIM). The GIM used should possess the characteristics of having low and stable resistivity, as well as compactable and soil-compacting. Bentonite is found out to have very low resistivity with moisture, however as bentonite is a clay properties, the compression strength itself is very weak. Cement is known to be non-electrical conductive since the electrical conductive value is small, however cement has the abilities to form strong binding bond between cements and other material when reacted with water. As bentonite and cement are mixed together, the mixture with possess the ability of having low electrical resistivity and high compression strength. This research paper focuses on experiment based study, analysis and research on the characteristics bentonite-cement mixes for its electrical resistivity as well as their compression strength. Different chosen percentage of bentonite (20%, 30%, 40%, 50%, 60%, 70%, and 80%) are mixed with cement to produced various mixing ratio of bentonite-cement mix samples. The experiment is separated into two categories, electrical properties experiment to measure the resistivity and conductivity, and mechanical properties where measure of the compression strength is done. In electrical properties experiment, the different mixing ratio samples are measured using an LCR meter to determine the inductance, capacitance, and impedance value, and therefore determine the sample's electrical resistivity and conductivity. In mechanical properties experiment, the sample's compression strength is measured by using compression strength measurement test machine. The result in summary shows that as the percentage of bentonite increases in the mixing ratio, the resistivity decreases or the conductivity increases, and the compression strength decreases. The optimum or best mixing ratio of bentonite and cement is therefore being determined for electrical GIM

Keywords: GIM, resistivity, conductivity, compression strength.

1. Introduction

Electrical grounding system serves many application or purpose, but the primary function of this system is to discharge electric or lighting charge to earth in a short period of time. The efficiency of electrical grounding system is measured or depend on the low frequency grounding resistance. The grounding resistance however depend on the surrounding soil resistivity. Common practice to improve or obtain low resistance are deep installation of electrode, Ufer method, or backfilling with electrical grounding improvement material. Grounding improvement material (GIM), is an earthing backfill compound which consisting of conductive material. GIM able to increase the earthing system efficiency and is effective in area which have high soil resistance value. To classify backfilling material as a GIM, the GIM used should possess the following characteristic [1].

1. It has low and stable resistivity
2. It is compactable and soil-compacting

Bentonite is a natural clay which itself have low resistivity characteristics. The approximately resistivity value of bentonite is around 3Ω-m to 18Ω-m. However, the compactness of bentonite alone is very low [2]. One of the method which may solve these issues is to introduce cement to bentonite to form bentonite-cement mixes. Cement is known as a binder, which it used to bind material together and harden it. Most commonly used application of cement is to mix with concrete as it provides high compressive strength [3]. In other hands, studies show that cement is found out that it has a high resistivity which is around 8×10^4 Ω-cm [2]. In electrical grounding system, compressive strength is important for the sustainability of the system. Without reasonable or have low compressive strength, the GIM backfill compacted and crush due to the weight of the system, which result in crack in a matter of time. Therefore, the bentonite-cement mixes need to have high compressive strength for it to be a GIM [2].

2. Experiment Setup and Methods

2.1 Electrical properties experiment

In electrical properties experiment is to measure the sample's resistivity of different mixing ratio of bentonite with cement. A customize mould is constructed using thick acrylic, a material which has non-electrical conductivity properties. The mould will housed and hold the sample in place, and will produce the sample size of $4cm\times4cm\times4cm$. Two metal aluminum plates are placed at both end of the sample's compartment to provide electrical flow to the sample from both end-to-end. Figure 1 below illustrate the process.

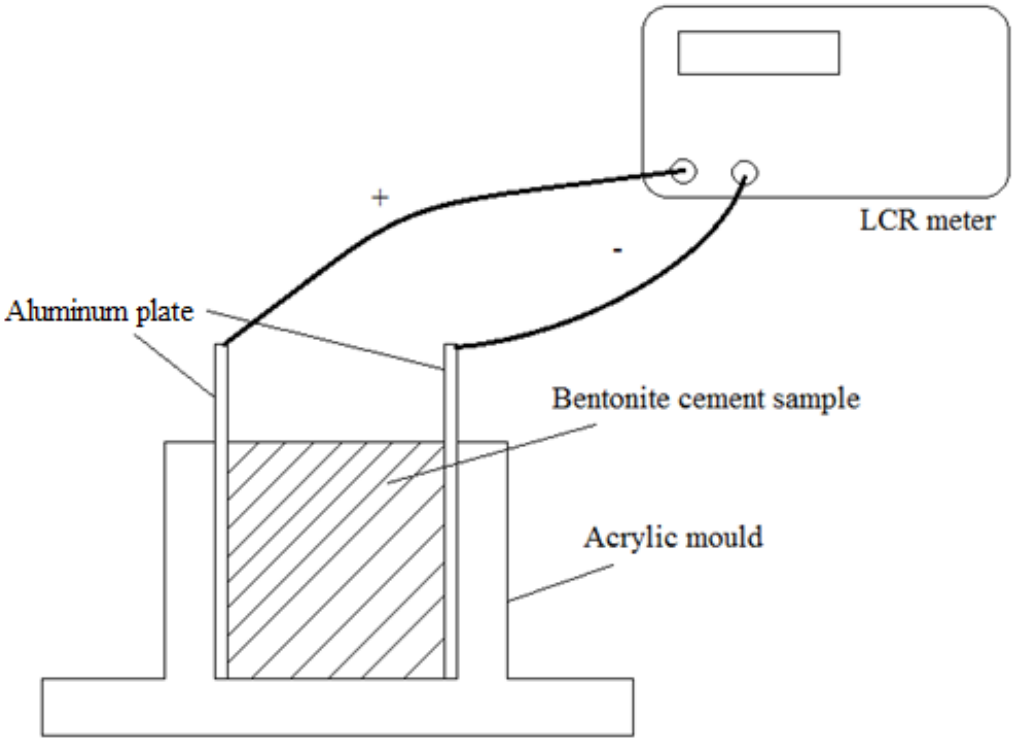


Figure 1. Electrical experiment setup

The mixing ratio of bentonite and cement is measured by their weight. Table 1 below shows the percentage (%) of bentonite mixes with cement in a total weight of 450g.

Table 1. Mixing ratio of bentonite percentage (%) with cement weight

Bentonite percentage (%)	**Bentonite weight (g)**	**Cement weight (g)**
20	90	360
40	180	270
60	270	180
80	360	90

Water is then added to the mix until an optimum saturation is achieved and stirred. The mixture is then poured into the mould and stored inside a room for 12 hours to undergo hardening process [4]. Water is known to have electrical conductivity properties, in which will contribute to the resistivity result of the samples. Therefore, during the 12 hours hardening process, it is crucial to store the samples in a constant room environment condition to prevent major water losses. After 12 hours, the sample is then being connected to the LCR meter on both metal aluminum plate. The impedance, capacitance, and inductance is then being recorded from the LCR meter at frequency of 200kHz and 1V. The procedure is then being repeated for each other different mixing ratio samples and the data is then obtained from the LCR meter for analyze.

2.2 Mechanical properties experiment

In this research, the mechanical properties of bentonite cement mixes were studied using Instron Universal Testing Machine, model 5569. The compression test was carried out according ASTM C39/C39M. Before test, all the specimens were prepared using an acrylic mold with dimension 4 cm x 4 cm x 4 cm. Table 3.2 below shows the percentage (%) of bentonite mixes with cement in a total weight of 450g. All the specimens were prepared according to formulation listed at Table 3.2. The load cell for the test was 50kN and the cross-head speed was 5 mm/min. The testing environment was at room temperature.

Table 2. Mixing ratio of bentonite percentage (%) with cement weight

Bentonite percentage (%)	Bentonite weight (g)	Cement weight (g)
0 (Pure cement)	0	450
20	90	360
30	135	315
40	180	270
50	225	225
60	270	180
70	315	135
80	360	90

Water is then added to the mix until an optimum saturation is achieved and stirred. The mixture is then poured into the mould and stored inside a room for 12 hour. During the 12 hour, the sample will undergo hardening process, which is when cement react with water molecules, it will bind together forming a bond with other cement and with bentonite as well [4]. Therefore, the room environment needed to kept in a room condition constant to prevent water loss from the sample. After 12 hour, the sample is then removed from the mould carefully and placed into a water container for 24 hour to undergo curing process. Curing process is to further enhance the compression strength of the sample [4]. After 24 hour, the sample is then removed from the water container and leave it to dry for less than an hour in a room. Next, the sample is placed into the compression measurement test machine and compressed. The procedure is then being repeated for each other different mixing ratio samples and the data is then obtained from the computer for analysis.

3. Result and Discussion

3.1 Electrical Properties

The measurement of impedance, inductance and capacitance of the sample is measured two times in two different set. The result and the average result of different percentage of bentonite are shown in Table 3, 4, 5, and 6 below.

Table 3. The impedance, inductance and capacitance of 20% bentonite

	20%		
	Sample 1	**Sample 2**	**Average**
Z	147.80 ohm; -4.12 deg	149.50 ohm; -4.18 deg	148.65 ohm: -4.15 deg

Lp	-1.63 mH	-1.67 mH	-1.65 mH
Ls	-0.86 µF	-8.93 µH	-4.89 µH
Cp	380.50 pF	378.20 pF	379.35 pF
Cs	72.40 nF	69.88 nF	71.14 nF

Table 4. The impedance, inductance and capacitance of 40% bentonite

40%			
	Sample 1	**Sample 2**	**Average**
Z	111.70 ohm; -4.97 deg	105.20 ohm; -4.88 deg	108.45 ohm; -4.93 deg
Lp	-1.04 mH	-0.99 mH	-1.01 mH
Ls	-7.72 µH	-7.23 µH	-7.48 µH
Cp	606.10 pF	639.70 pF	622.90 pF
Cs	81.01 nF	86.70 nF	83.86 nF

Table 5. The impedance, inductance and capacitance of 60% bentonite

60%			
	Sample 1	**Sample 2**	**Average**
Z	61.05 ohm; -3.26 deg	50.36 ohm; -2.08 deg	55.71 ohm; -2.67 deg
Lp	0.82 mH	-1.00 mH	-0.91 mH
Ls	-2.74 µH	-1.47 µH	-2.10 µH
Cp	771.50 pF	585.90 pF	678.70 pF
Cs	228.00 nF	415.20 nF	321.60 nF

Table 6. The impedance, inductance and capacitance of 80% bentonite

80%			
	Sample 1	**Sample 2**	**Average**
Z	40.94 ohm; -3.69 deg	47.30 ohm; -3.78 deg	44.12 ohm; -3.73 deg
Lp	-0.50 mH	-0.58 mH	-0.54 mH
Ls	-2.14 µH	-2.47µH	-2.30 µH
Cp	1.27 nF	1.03 nF	1.15 nF
Cs	295.50 nF	256.00 nF	275.75 nF

Table shows the impedance Z, inductance parallel L_P, inductance series L_S, capacitance parallel C_P, and capacitance series C_S, of 20%, 40%, 60%, and 80% of bentonite. The inductive reactance X_L, and capacitive reactance X_C, can be calculated using inductive reactance formula Eq. (1) and capacitive reactance formula Eq. (2). Total reactance X_T, can be calculated using formula Eq. (3). Assume the RLC circuit are to be in series configuration, the resistance R, can be calculated using impedance formula Eq. (4).

$$X_L = 2\pi fL \quad (1)$$

$$X_C = \frac{1}{2\pi fC} \quad (2)$$

$$X_T = |X_c - X_L| \quad (3)$$

$$Z = \sqrt{R^2 + {X_T}^2} \text{ or } R = \sqrt{Z^2 - {X_T}^2} \quad (4)$$

$$\rho = \frac{RA}{l} \quad (5)$$

From the resistance value R, the resistivity value ρ, can be then obtained using Pouillet's law of resistivity formula Eq. (5), with the sample size of area $A = 14cm^2$ and length $l = 4cm$. The total impedance, resistance, and the resistivity of 20%, 40%, 60% and 80% of bentonite result are shown and illustrate in Table 7 and Figure below.

Table 7. The total reactance, resistance, resistivity and the conductivity of different percentage of bentonite

Percentage of bentonite (%)	Total Reactance (Ω)	Resistance (Ω)	Resistivity (Ω-m)	Conductivity (S-m^{-1})
20	17.33	147.64	5.91	0.17
40	18.89	106.79	4.27	0.23
60	5.11	55.48	2.22	0.45
80	5.78	43.74	1.75	0.57

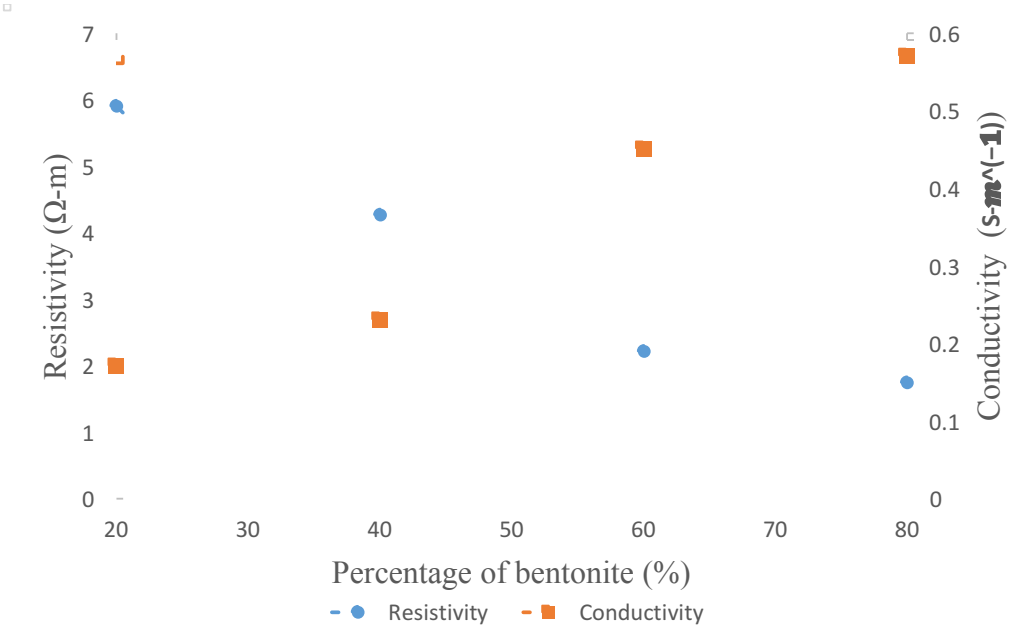


Figure 2. Resistivity (Ω-m) and conductivity (S-m^{-1}) against percentage of bentonite (%) graph

In Figure 2 above show the characteristic or the relationship between the resistivity or conductivity with the percentage of bentonite. It is observed that the resistivity value drop with further increment in percentage of bentonite. In another interpretation, the sample's electrical conductivity increases as the percentage of bentonite increases. Another observation is there is higher drop rate in resistivity, or higher rise rate of conductivity, in between the increment from 40 to 60 percent of bentonite. As mention, water has electrical conductivity properties, the sample's

resistivity factor might be mainly due to moisture content. Bentonite has attribution of absorbing tremendous amount of water [2][5], usually three times the amount of its original size. As percentage of bentonite increases, the bentonite ratio in the sample's increases, which provide higher surface area to bentonite in the sample for water absorption, and therefore further lowering the resistivity.

Cement is known to be non-electrical conductive as the electrical conductive properties of cement is very minor [6]. However, cement provide compactness to the sample which might contribute to the resistivity and conductivity. Compactness is to bind and hold all material and hold them as close as possible, higher compactness means more contact between bentonites molecules [7]. This might explain the drop rate of resistivity or rise rate for conductivity is faster during the increment of bentonite percentage from 40% to 60%. As cement ratio decreases, the compression strength decrease, as well as the compactness, therefore at more than 60% the drop or rise rate of resistivity or conductivity is not as fast as mention.

3.2 Mechanical properties

The compression strength measurement was performed three times, and the average value of those three measurements result are shown in Table below. A graph of relationship between percentage of bentonite and compression strength is then plotted as shown in Figure below.

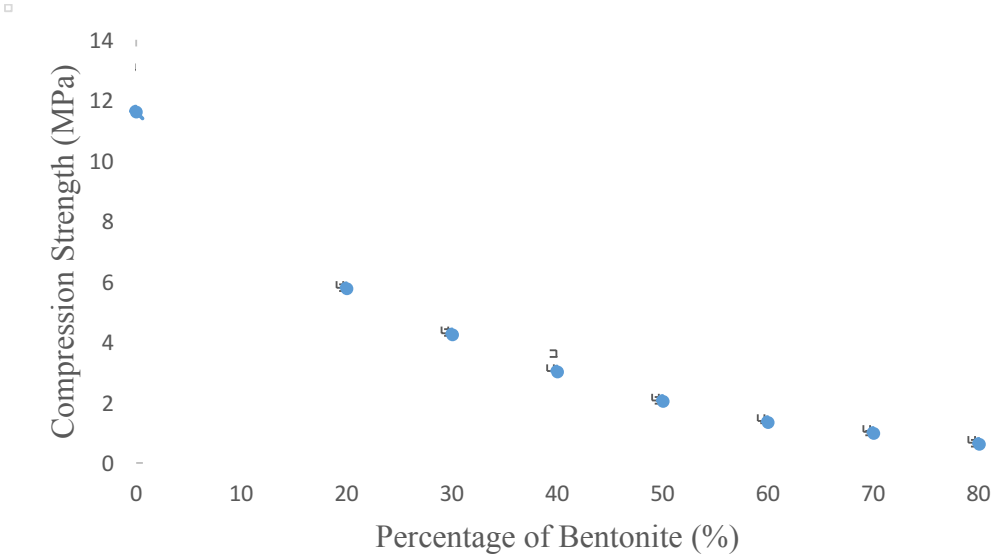


Figure 3. Compression Strength (MPa) against Bentonite Percentage (%)

From Figure 3 shows the compression strength of bentonite with cement content. It is observed that the compression strength of the samples reduced with increasing of bentonite content. Cement is the key ingredient of providing hardens strength and binding strength to the samples, therefore it explained that the reduction of cement contributes the decreases of compression strength of the samples.

From the result shows the pure cement has compression strength of 11.60 MPa. The main function of the cement is acts as a binder and providing strength to the bentonite-cement mixed. Moreover, the bentonite is acts as a fine aggerate in the

mixture and it typically lower compression strength compared to cement [8]. When mixing cement with component that lower strength, part of the cement is reduced. If the cement content reduced, the cement would not able contribute strength to bentonite cement mixed. Besides, the bentonite consists of mainly of montmorillonite clay and it will be absorbing tremendous amount of water. The water molecules will form hydrogen bonding and trapped between the montmorillonite clay layers and resulting the structure expended three times from this original size. This might also cause the compression strength of bentonite reduced. As bentonite content increases, this might cause the water content in bentonite cement mixed increased. The present of water weaken the structure of bentonite, which attributed to lowering the compression strength of the bentonite cement mixed.

Rafat et al. [9] also reported the similar result trend as in Figure 3 above on fly ash cement mix. The authors found the increases of fly ash content reduced the compression strength of cement mix. There is another research conducted on compression strength with sand-cement-clay by Bassam Z et al. [10] the result also report had a similar trend, as the sand content increase in cement, the compression strength decreases.

3.3 Electrical and mechanical properties

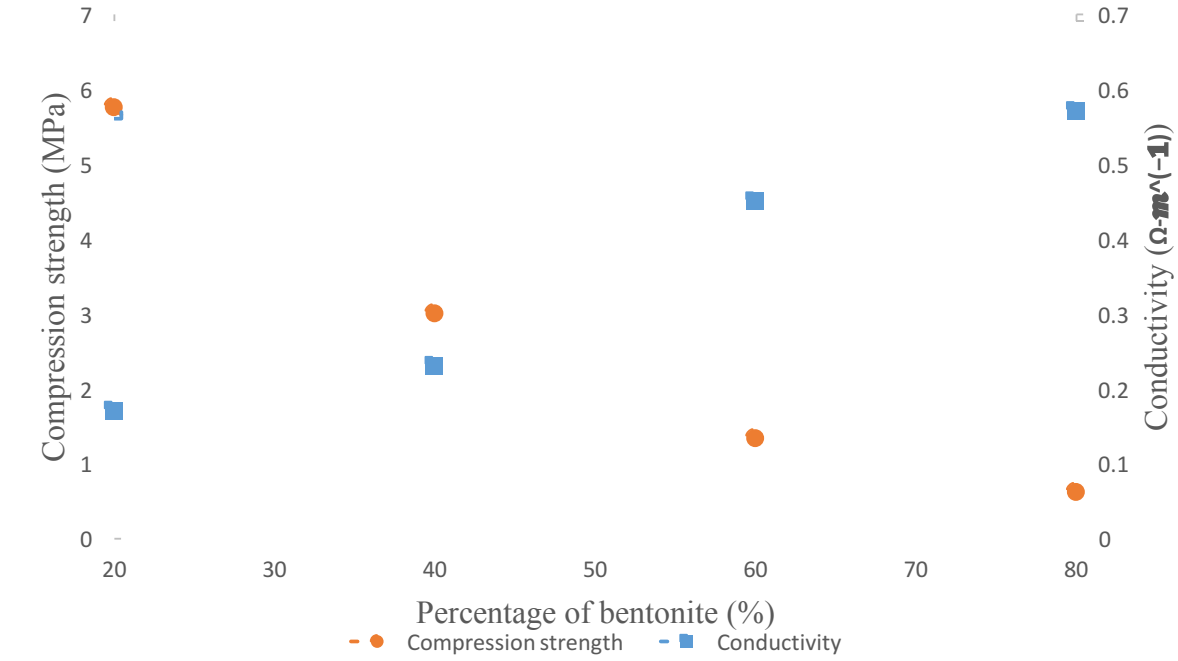


Figure 4. Compression strength and conductivity against percentage of bentonite

Figure 4 shown above shows the relationship between the compression strength with conductivity in respect of the bentonite percentage. As the bentonite percentage increases, the compression strength decreases, and the conductivity increases. Having high bentonite ratio proven to provide significant incrementation to the sample's electrical conductivity, however the drawback of having this ratio is the physical and structurer strength, or compression strength, is very weak. In vise versa, having high cement ratio provide low conductivity. At the conductivity curve point of view, it is observed that the increment rate is higher at 40% to 60% than at more than 60% onward.

This is due to the compactness of the samples as explained in Electrical properties discussion.

There requirement characteristics of electrical GIM is that it possesses low electrical resistivity and high compactness. In opinion, the best or optimum choice of mixing ratio to be chosen to be as electrical GIM is in the range between 45% to 55% of bentonite due to the higher increment rate of electrical conductivity at that range. In 45%, the electrical conductivity is 0.26 Sm^{-1} and the compression strength is 2.51 MPa. As for 55%, the electrical conductivity is 0.41 Sm^{-1} and the compression strength is 1.68 MPa.

Similar studies had been conducted of the electrical conductivity of bentonite-cement mixes, the author concluded that the best optimum mixing ratio, for electrical conductivity only, of bentonite and cement is at 60%. This value is chosen as it is at the highest rise time curve. However, in this percentage value without the consent of the mechanical properties, the compression strength of the samples is low. The compression strength in 45% to 55% range it is not severe when comparing to 60%. Therefore, personal opinion wise the best optimum mixing ratio of bentonite and cement to be used as GIM is within this range.

4. Conclusion and Future Work

As the percentage of bentonite increase in the bentonite-cement mix, the electrical resistivity value decrease and the compression strength decrease as well. Besides that, higher the percentage of bentonite shows that there's more water moisture content present in the mix. Higher water moisture content provides higher electrical conductivity, however lowering the compression strength. It is also noted that the conductivity rate is much higher at the incrementation of bentonite percentage from 40% to 60%, this might be due to the compactness properties as there is more contact between bentonite molecules. In opinion, the best or optimum choice of mixing ratio to be chosen to be as electrical GIM is in the range between 45% to 55% of bentonite due to the higher increment rate of electrical conductivity at that range.

For future work, in electrical properties experiment, as water moisture might be the factor or key ingredients of providing the electrical conductivity to the bentonite-cement mix samples, future research is needed to be done of studying various water moisture level content in the samples, as different water moisture level will result in different conductivity. For mechanical properties experiment, it is noted that the longer the samples are placed in curing process, the higher the compression strength it gains. The samples achieved maximum compression strength after 28 days of curing time, which indicate that the whole cement in the samples in fully reacted to water molecule. Therefore, the compression strength of the bentonite-cement mix samples with different curing time such as 1, 14, and 28 days needed to be conduct and measure as future work or research.

References

[1] C. Engineering, D. Eyl, B. Bulama, and E. Spektroskopileri, "Electrical Spectroscopy of Kaolin and Bentonite Slurries," vol. 25, pp. 345–354, 2001.

[2] S. C. Lim, C. Gomes, and M. Z. A. Ab Kadir, “Characterizing of bentonite with chemical, physical and electrical perspectives for improvement of electrical grounding systems,” Int. J. Electrochem. Sci., vol. 8, no. 9, pp. 11429–11447, 2013.
[3] I. Repository, “The prediction of shear strength in bentonite” Loughborough University Institutional Repository.
[4] C. Aggregate, S. Mixtures, C. S. Mixtures, and S. Cylinders, “Standard Practice for Making and Curing Soil-Cement Compression and Flexure,” pp. 1–6.
[5] A. International, “SODIUM BENTONITE: ITS STRUCTURE AND PROPERTIES GN-001.”
[6] S. Wen and D. D. L. Chung, “Cement-based controlled electrical resistivity materials,” Journal of Electronic Materials, vol. 30, no. 11. pp. 1448–1451, 2001.
[7] S. Xia, L. Hu, Z. Yang, Y. Bao, X. Zou, and H. Wang, “A Method of Rapid Compactness Inspection for Cement Stabilized Macadam,” no. Ictim, pp. 900–907, 2016.
[8] F. S. Khan, S. Azam, M. E. Raghunandan, and R. Clark, “Compressive strength of compacted clay-sand mixes,” vol. 2014, 2014.
[9] R. Siddique, W. Prince, and S. Kamali, “Influence of Utilization of High-Volumes of Class F Fly Ash on the Abrasion Resistance of Concrete.” pp. 1–24, 2011.
[10] E. Journal, G. Engineering, B. Zaal, and M. Mu, “Compressive Strength and Permeability of Sand- Cement-Clay Composite and Application for Heavy Metals Stabilization,” no. January, 2005.

eureca 2017 – Conference Paper
Paper Number 2EE02

Artificial Neural Network (ANN) Based Load Flow Method for Distribution Network with Distributed Generation

Mohammad Hafizuddin bin Ameruddin [*], Charles R. Sarimuthu [**], Aravind CV [***]

School of Engineering, Taylor's University, Malaysia
[*]hafizuddinameruddin@gmail.com,
***CharlesRaymond.Sarimuthu@taylors.edu.my,*
****ChockalingamAravind.Vaithilingam@taylors.edu.my*

Abstract
Load Flow analysis is important in power system operation planning which helped in optimizing the system. In the past, this analysis is done by calculations which involved iteration that took a long time to solve such as Newton-Raphson, Gauss-Seidel and Fast Decouple. Since load flow analysis is important in order to know whether the system is under load or overload, the analysis needs to be done accurately and fast. Artificial Neural Network (ANN) is proposed as an alternative solution in solving load flow which is believed it can solve load flow precisely in short duration. Few researchers had compared the results provided by ANN and solution gained from the calculation method and found that the difference between the two results was not very significant. However, none had used real or simulation data with ANN and compared the result with any of the conventional methods. For this research, the result produced by the ANN, coded in MATLAB which is trained with simulation data is compared with the result obtained from the one of the normal method, which is Newton-Raphson that proved to be more accurate compared to Gauss-Seidel and Fast-Decoupled method as to know, whether ANN can produce better results in terms of accuracy and computation time than Newton-Raphson method. The ANN is optimized by setting the parameter of the ANN such as the transfer function, training function and learning rate correctly and ensured that the ANN is trained with sufficient data. Finally, the result difference between the ANN and the Newton-Raphson is discussed. IEEE 14-bus system is simulated in Simulink where one of the load's (which connected to bus 6 for this research) real and reactive power is altered and the resulting bus voltage of all buses in the system is recorded and separated into two sets of data or case each for training and testing the ANN. Then, a set of the bus voltage data is used for the training of the ANN and another set of values is used to test the ANN to evaluate the performance of the ANN. The output of the ANN is compared with the output produced by Newton-Raphson method that is calculated using MATLAB software. The result showed that the difference of the output for the two methods was under tolerance which within 5% and the ANN able to display the result for all cases simultaneously in about one second while Newton-Raphson only able to show the result for a case one at a time instantaneously.

Keyword: Artificial Neural Network, IEEE 14-bus, MATLAB, Newton-Raphson, load flow analysis

1. Introduction

A power system should be within their own specified limit in all operation where the condition of the load inside the system whether under or overload need to be known for the system to maintain its stability [1]. This information is used for the purpose of planning the power system's operation [1].

The information regarding the system's performance and steady-state can be extracted by solving the load flow of the system [2]. Load flow can be calculated by identifying the transmission line's voltage reading and the power flow [2].

With the load flow analysis, the power system is able to be optimized since it is able to be identify whether the system operation is still under allowable tolerance or not. The power losses inside the system is able to be calculated using this analysis too [1].

Load flow is solved conventionally using these three methods which were named Fast-Decouple, Newton-Raphson and Gauss-Seidel method [3]. Although these three methods were widely used, problems are encountered when these methods were used to solve load flow. Firstly, the Fast-Decouple method is not able to provide good solution if any of the bus voltage is low [4]. Next, the Newton-Raphson method heavily depends on the initially guessed value as this method take time to solve load flow if the guessed value is far off with the answer [4]. Lastly, the Gauss-Seidel method used complex algorithm so it is not advisable to use it in a large system [4].

It is observable that today, the technology of Artificial Intelligence (AI) had improved remarkably. So, instead of using the previously mentioned method, AI might be able to be utilized to solve load flow [5]. Hence, a type of AI called Artificial Neural Network (ANN) is suggested to analyse and solve load flow.

As the brain had a neuron, the ANN had Processing Element (PE) since the structure of ANN is based on brain's structure [6]. Although their speed is still in the stage of discussion, it is said that the brain had a processing speed of 10-100ms while the ANN speed to process information is 10-100 nanoseconds [6].

AI is trained through the three types of machine learning named supervised, unsupervised and reinforcement training [6]. For the supervised training, the network analyses the data provided through regression [7]. Unsupervised training identifies the similarity of the provided data statistically and grouped them [8]. The last one which is the reinforcement learning is trained through the trial-and-error method where if the machine produced correct answer [9]. As ANN is also a type of AI, the learning method is also similar which utilized the previously mentioned type of learning for training.

Two sets of data were required when building the ANN where the first set is needed for the training while the second set is used for testing purpose. The configuration of ANN consisted of training function, transfer function, learning rate, error, iteration number and the number of nodes inside the input, output and hidden layer.

For this research, the ANN is tested to see the ANN performance when compared with one of the conventional methods used to solve load flow by comparing the output differences and time taken to produce results for both methods.

2. Concept

As previously mentioned, the regular methods used to solve load flow which were Newton-Raphson, Fast-Decouple and Gauss-Seidel method were tedious as the algorithms were complex and time-consuming. So, it is a good idea if an alternative method to solve and analyse load flow in faster and simpler manner been found.

The proposed method, Artificial Neural Network (ANN) is studied previously in the field of forecasting and in the electrical system too. However, not much is known how accurate ANN when real-time or simulation data is used [10] [11]. So, in this research, simulation of a distribution system is done where the output is recorded to be used with the ANN. Then, the ANN produces results that are compared with one of the conventional load flow solving method which is Newton-Raphson's output. The comparison is made in terms of output differences (error) and calculation time. The effect and function of the ANN parameters were studied too in this research. The basic framework of the research is shown in Figure 1 below.

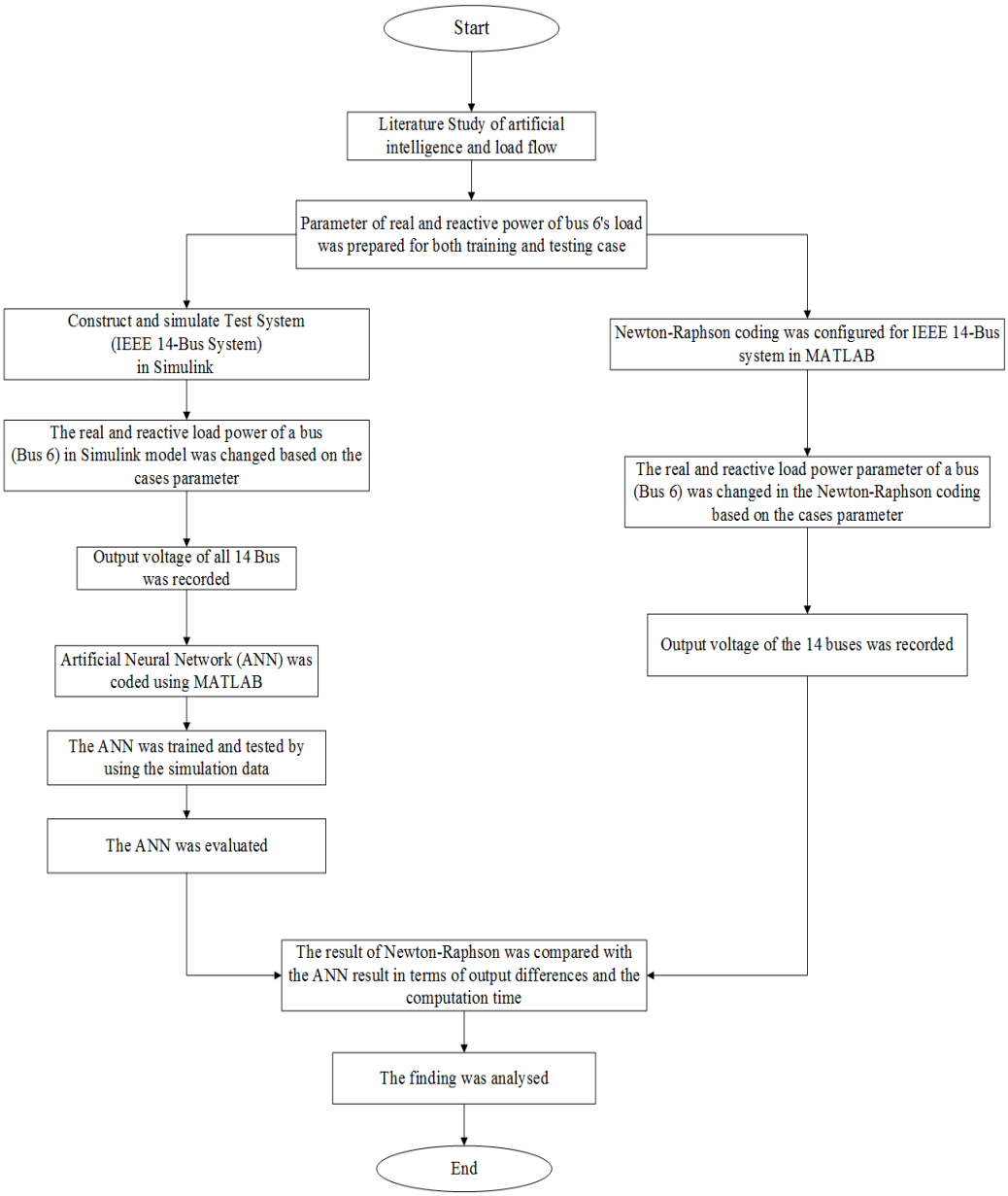


Figure 1: Basic Flowchart of the Research's Process

3. Research Methodology

3.1. Artificial Neural Network (ANN) Model

The Artificial Neural Network (ANN) basically have input, output and hidden layer [12]. Figure 2 below shows the basic modeling of the ANN.

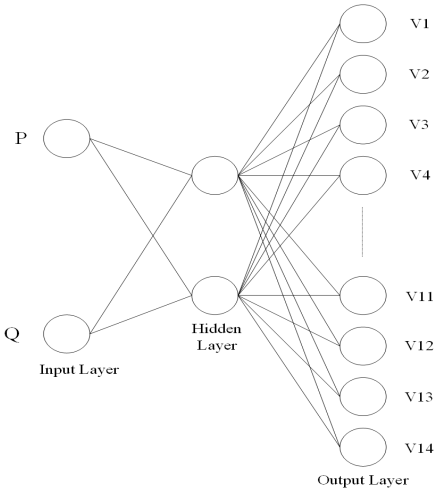


Figure 2: The Basic Model of an ANN [12]

The input layer can be more than one, depending on the input number which also is the same case for the output. However, as for the hidden layer, it is not known how much layer is accurately needed in order to work perfectly.

3.2. IEEE 14-Bus Model

For this research, the IEEE 14-bus system is paired with the ANN where ANN is used to solve the model's load flow. This bus system includes 5 generators, 14 buses and 11 loads and is based on the approximation of the American Power System where the diagram of the model is shown in Figure 3 [13].

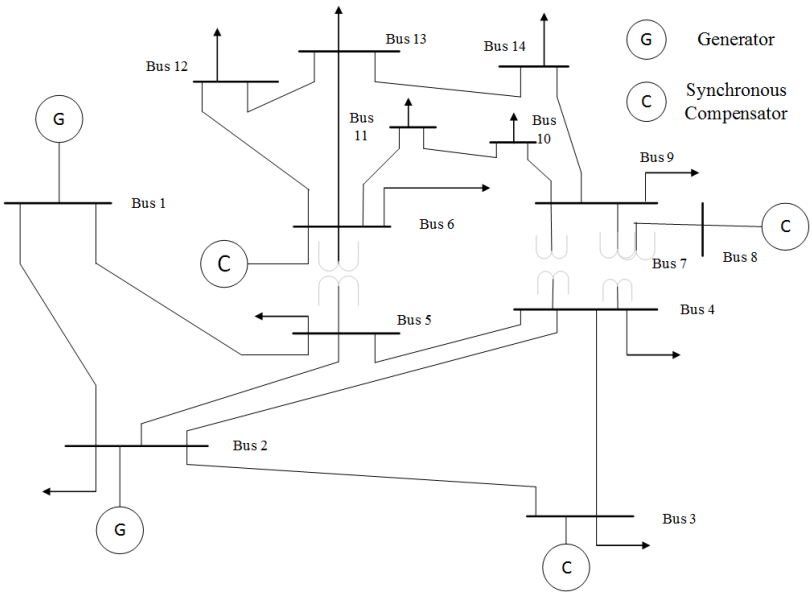


Figure 3: The Diagram of IEEE 14-Bus System [13]

The bus system's Simulink model which is built based on the IEEE 14-bus data sheet [14] and the model built by [15] is used for simulation purpose where the resulted voltage from the simulation is utilized by the ANN. This distribution model was used instead of other system because it is a radial system and compared to other distribution

model, the size is good enough for data collection to demonstrate the ability of ANN in solving load flow. For the purpose of authenticating the model's accuracy, the model is run and the output voltage in per unit (p.u) for all the buses were listed. Then, the recorded voltage is compared with the stated voltage in the IEEE 14-bus data sheet where the difference must be less than 5%.

3.3. Simulink Simulation

After the verification had been done, the simulation was further proceeded. Any one of the load's real (P) and reactive power (Q) is changed accordingly to see the changes in output voltage of all the buses. In this case, the load connected to bus 6 is selected where the real power is changed into 10MW and increased gradually until it reached 100MW and the reactive power is adjusted in order to maintain the power factor of 0.9. The P and Q of bus 6 is calculated by using the power triangle as shown in Figure 4 below.

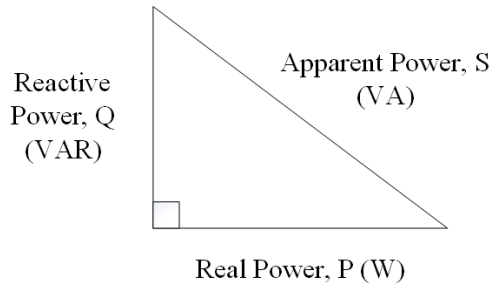


Figure 4: The Power Triangle

The recorded output voltage is separated into two different sets as mentioned earlier, one set of data is listed for the ANN training (training case) while another set is used for the ANN testing (testing case). The ANN is built through coding in the MATLAB software which the coding did include all the ANN parameters like the learning rate, training function and transfer function.

3.4. Artificial Neural Network (ANN)

For the ANN, Bus 6's real and reactive power is set as the ANN's input while the output voltage for all 14 buses is denoted as the ANN's output. After the code is completed, it is trained using the training case data then, it is run and the output is recorded. Both outputs from the simulation and the ANN is compared. More data is added for training and the parameters are reconfigured until the difference between the two results were little which must be as close to 0% difference. Then, the ANN is run using the testing case and similar with the previous step, the similarity between the results from the ANN is compared with the simulation result. The ANN configuration is stopped and finalized only after the difference is close to 0% which tells that the ANN training is successful.

Next, after the ANN had been done, the produced result is compared with the results given by the traditional load flow method. Newton-Raphson method is chosen for this comparison as this method is more universal compared to Gauss-Seidel and Fast-Decoupled method where the number of iteration is independent to the bus size and still gave accurate result [16].

3.5. Newton-Raphson

Just like the Simulink model, the bus parameters used for the purpose of the Newton-Raphson calculation by MATLAB software is adapted from IEEE 14-bus data sheet from [14]. In this case, bus 1 is set as the slack bus. Just as the previous method for the Simulink simulation, Bus 6's real and reactive power is changed based on the training and testing case parameters, and all of the 14 buses' output voltage is listed.

The output voltage obtained from both the ANN and the Newton-Raphson is compared and their difference is calculated and analyzed. The conclusion is made in terms of the output differences and the computation time.

4. Result and Discussion

4.1. Simulink Model Verification

The percentage difference between the output voltage shown in the simulation in default parameters (P=11.2 kW and Q=7.5 kVar for the load connected to bus 6) and the expected voltage gained from the IEEE 14-bus data sheet is shown in Table 1 below.

Table 1: The Percentage Difference of Simulated and Data Sheet Voltage in Default Parameters

Bus Number	Simulated Voltage (p.u)	Data Sheet Voltage (p.u)	% difference
Bus 1	1.012	1.06	4.53
Bus 2	1.004	1.045	3.92
Bus 3	0.978	1.01	3.17
Bus 4	0.99	1	1
Bus 5	0.995	1	0.5
Bus 6	0.997	1	0.3
Bus 7	0.994	1	0.6
Bus 8	0.984	1	1.6
Bus 9	0.981	1	1.9
Bus 10	0.978	1	2.2
Bus 11	0.978	1	2.2
Bus 12	0.981	1	1.9
Bus 13	0.975	1	2.5
Bus 14	0.986	1	1.4

It can be seen that, from Table 1, the maximum error shown is 4.53% which considered to be within tolerance level (5%), so the Simulink model is verified and the research is continued to the next stage.

4.2. The Parameters Used in the Research

The value of real (P) and reactive (Q) power for both training and testing case that is used in bus 6 is shown in Table 2 and Table 3 below. As mentioned previously, the value of Q is set by using the power triangle in order to maintain the power factor of the load by 0.9.

Table 2: Value of P and Q for Training Case

Training Case	P (MW)	Q (MVar)
1	10	4.8
2	20	9.7
3	30	14.5
4	40	19.4
5	50	24.2
6	60	29.1
7	70	33.9
8	80	38.8
9	90	43.6
10	100	48.4

Table 3: Value of P and Q for Testing Case

Testing Case	P (MW)	Q (MVar)
1	25	12.1
2	45	21.8
3	65	31.5
4	85	41.2

4.3. Simulation and Artificial Neural Network (ANN)

Figure 5 and 6 below shows the graph of the difference between the ANN output and the simulation output for both situations where the training and testing case is used. For this paper, three cases for each set is shown. Figure 5 shows the result for the training cases.

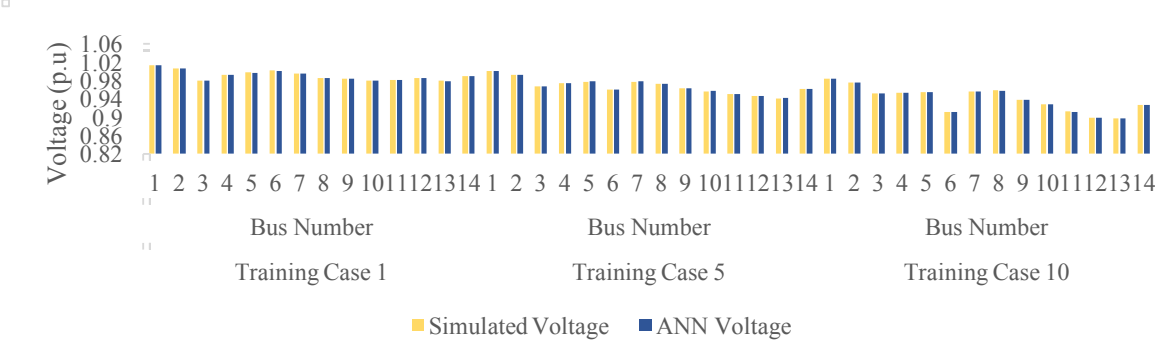


Figure 5: The Illustration of the Difference Between the Simulation and ANN Result for Training Cases

Figure 6 below shows the result for the testing cases.

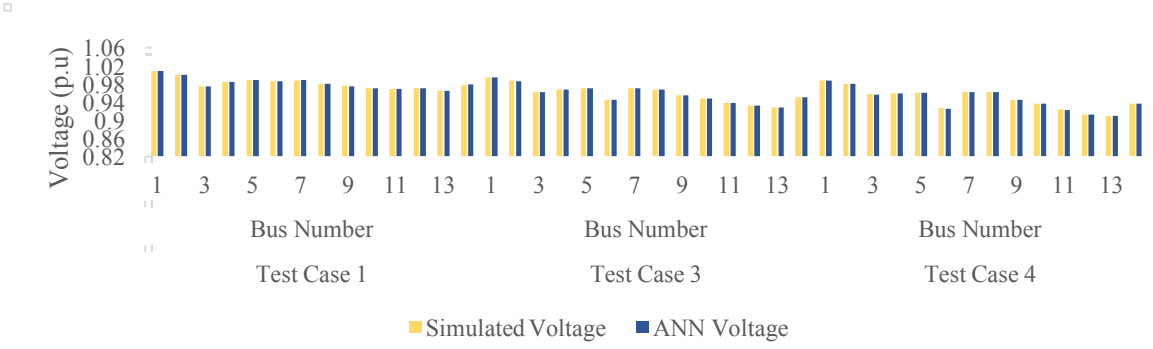


Figure 6: The Illustration of the Difference Between the Simulation and ANN Result for Testing Cases

It can be seen clearly that the difference between the two results were too close to each other and almost similar. The ANN coding is finalized and no more data is added to the ANN training since the difference between the two results (ANN and simulation) in both situation (training and testing case) showed that the difference ranged from 0% to 0.1% which very close to 0%. This showed that the ANN is coded and trained successfully.

4.4. Artificial Neural Network (ANN) and Newton-Raphson

To see the difference between the ANN and the Newton Raphson result, similar method is used in order to illustrate the difference clearly where the result when the training and testing case is used. Figure 7 below shows the results for the three training cases.

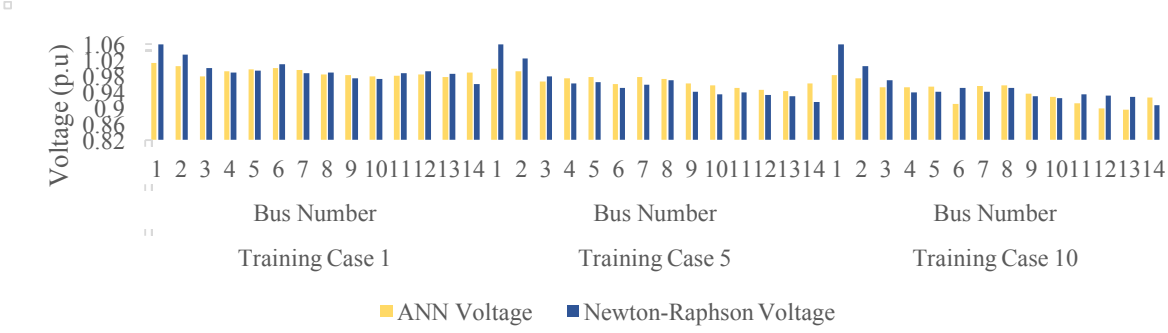


Figure 7: The Illustration of the Difference Between the ANN and Newton-Raphson Result for Training Cases

While Figure 8 below shows the results for the three testing cases.

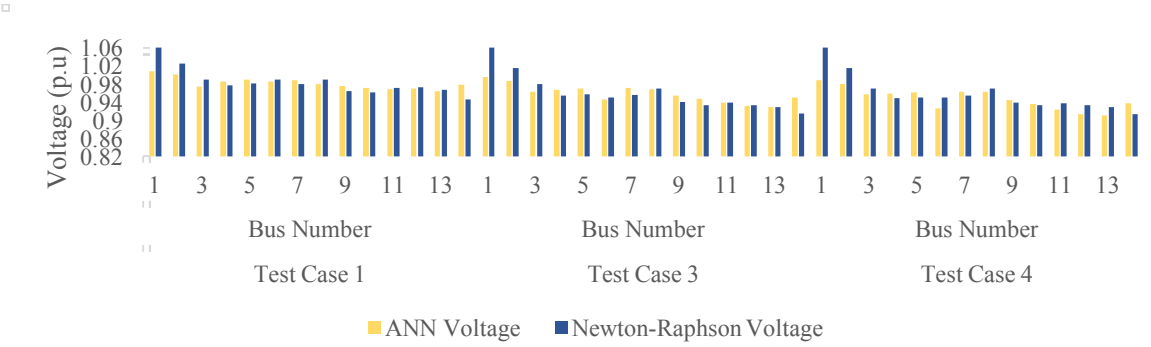


Figure 8: The Illustration of the Difference Between the ANN and Newton-Raphson Result for Testing Cases

From the recorded result, it is found that the highest error found is exactly 5% for overall cases in both set which covered both 10 training cases and 4 test cases where the highest error happened in bus 14 in Training case 5 followed by 4.31% (bus 14 in training case 6) while the lowest error found is 0.02% which for bus 6 in training case 4. Since Bus 1 is set as the slack bus, used for the Newton-Raphson calculation, the resulted bus 1's output is always 1.06, so the result for bus 1 is ignored for all the cases. The difference for all the cases is within tolerance level which is 5%, so the error is in acceptable range.

4.5. Analysis

Although the error for Newton-Raphson when compared with Artificial Neural Network (ANN) is in acceptable level, the error is quite significant. This happened due to the fact that the data that is used to train the ANN is obtained from the Simulink simulation, so it is natural that the ANN result is close to the Simulink result instead of Newton-Raphson. Besides that, Simulink result accuracy may be affected by the MATLAB's parameter such as the type of solver or even the code of the block used in the model. Besides that, Newton-Raphson utilized complex formula that leads to long calculation process and multiple iterations in the calculation which also contribute to the differences between the results. Due to these reasons, the Simulink model produced results slightly different with the Newton-Raphson. For clearer comparison between the three methods, Figure 9 below shows the comparison result of the three methods which are ANN, simulation and the Newton-Raphson for the training cases.

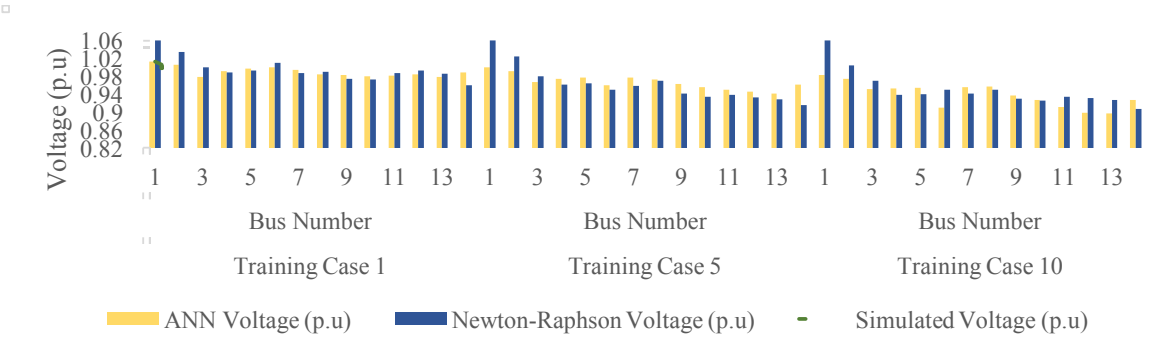


Figure 9: The Illustration of the Difference Between the ANN, Newton-Raphson and Simulation Result for Training Cases

Then, the Figure 10 below shows the comparison result of the three methods which are ANN, simulation and the Newton-Raphson for the testing cases.

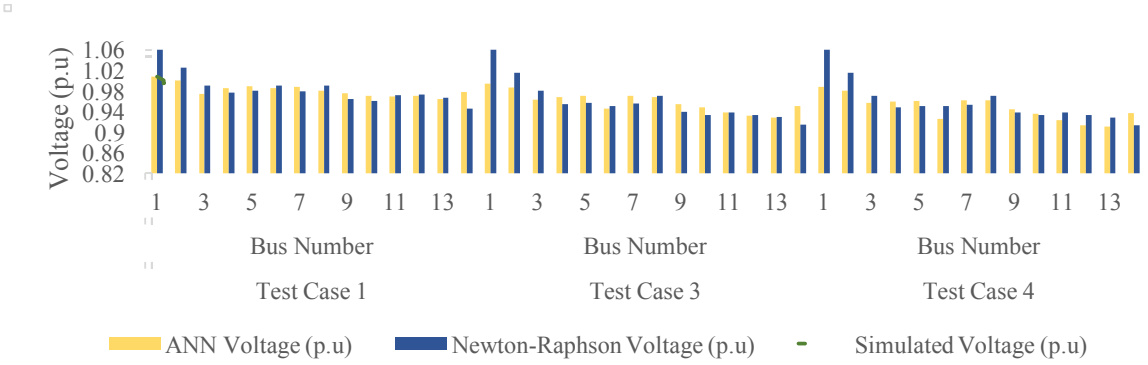


Figure 10: The Illustration of the Difference Between the ANN, Newton-Raphson and Simulation Result for Testing Cases

4.6. Artificial Neural Network (ANN) Parameters

The ANN parameter that is written in the code will bring impact on the result accuracy. However, not all give big difference as the sample used is small, there is only minor differences and it might be unnoticeable. Below showed the parameter of the ANN used in this research.

Input= 2
Output= 14
Number of node in first hidden layer= 48
Number of node in second hidden layer= 14
Iteration= 8000
Training Function= Trainlm
Transfer Function= Purelin
Error= 0.00001
Learning Rate=0.001

The epoch is set to 8000 but the training is done within 3 iterations as the sample is small, so it converged fast. For the learning rate, the optimized value can be found through trial and error method [17]. Again, as the sample used in this research is small, changing the learning rate did not affect the time taken for the ANN training. The ‘error’ denoted the acceptable accuracy of the ANN where the lower the ‘error’, the higher the accuracy of the ANN. The value of ‘error’ is set to 0.00001 in order to make it accurate to three decimal places, similar to the Simulink output which is set to three decimal points. Table 4 showed the difference when different ‘error’ value is used for the result of training case 5.

Table 4: Effect of Error Value Configured to the ANN Result

Bus Number	Error Set on ANN				Simulated Voltage (p.u)
	0.01	0.001	0.0001	0.00001	
1	0.9865	1.0120	0.9996	0.9997	1
2	0.9896	0.9920	0.9918	0.9918	0.992
3	0.9681	0.9727	0.9670	0.9670	0.967
4	0.9083	0.9829	0.9743	0.9743	0.974
5	0.9788	0.9598	0.9776	0.9775	0.977
6	1.0155	0.9038	0.9605	0.9605	0.96
7	0.9876	0.9922	0.9774	0.9774	0.977
8	0.9954	0.9780	0.9725	0.9725	0.972
9	0.9711	0.9791	0.9625	0.9626	0.962
10	0.9048	0.9453	0.9565	0.9564	0.956
11	0.9191	0.9806	0.9499	0.9499	0.95
12	0.9535	0.9240	0.9463	0.9464	0.946
13	0.8910	0.9246	0.9419	0.9419	0.941
14	0.9663	0.9700	0.9611	0.9612	0.961

Next, due to the small-scale system, trainlm is chosen for the training function as it gave low mean square error (MSE) and fit to use with the size of our sample [18]. Moreover, the produced output voltage with respect to the real and reactive power is linear (see Figure 11), so 'purelin' is used for the transfer function in the ANN.

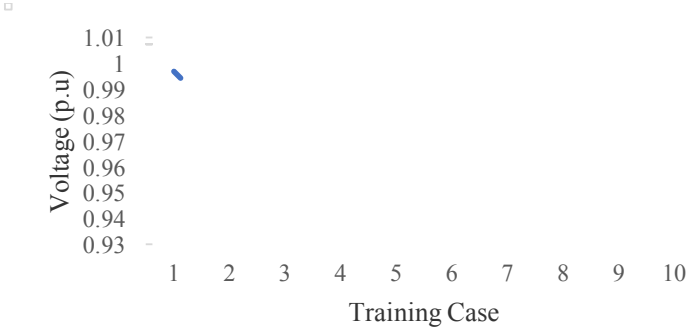


Figure 11: The Simulated Voltage of Bus 5 with Respect to the Parameter of Training Cases

The input and output layer is represented as the number of input and output of the system, so it is 2 inputs (real and reactive power of bus 6's load) and 14 outputs (bus voltage for all the 14 buses). Besides that, two hidden layers were used as it were more efficient than only using one hidden layer [10]. The number of the hidden node for the second layer must be equal to the output number or MATLAB give an error message while any number of the hidden layer can be used for the number of hidden node in the first layer. However, overfitting happens if the number of hidden layers is

too much and insufficient hidden node stop the ANN from learning [10]. Thus, trial-and-error method is suggested.

4.7. Accuracy and Computational Time Between Artificial Neural Network and Newton-Raphson

In term of accuracy, the ANN produced accurate results with error close to 0% only if it is trained with considerable amount of accurate data and suitable parameter the ANN is coded. For computation time, in this research, the ANN was able to produce output of the 14 buses for all cases (10 for training case or 4 for testing case) simultaneously within 1 second as measured in the MATLAB's Neural Network Toolbox, while Newton-Raphson can produce output of the 14 bus instantly but only for one case at a time in expense of long coding compared to the length of ANN code in the MATLAB.

5. Conclusions

It can be concluded that, Artificial Neural Network (ANN) can be utilized to solve load flow since the difference of the voltage output produced by one of the conventional method, Newton-Raphson and the suggested method, ANN is still within tolerance level which does not exceed 5%. ANN able to solve load flow and produce accurate result rapidly as long it is trained using accurate data sufficiently with correct parameters configured while coding the ANN. For the future work, more research regarding the ANN needs to be done especially regarding the parameters that required trial-and-error method as this method is not reliable in the engineering field. Finally, a database which contained bus data needs to be created where the database can to be utilized by anyone and able to be used for ANN training used to solve load flow problem.

References

[1] AVO Training Institute, "Go With the Flow the Importance of Load Flow Studies," 2016. [Online]. Available: http://www.avotraining.com/go-with-the-flow-the-importance-of-load-flow-studies/. [Accessed on November 18 2016].

[2] M. G. Lauby, P. Kundur and N. J. Balu, *Power system stability and control*. New York: McGraw-hill, 1994, pp. 255.

[3] K. Singhal, "Comparison between Load Flow Analysis Methods in Power System using MATLAB," *International Journal of Scientific & Engineering Research*, vol. 5, no. 5 pp. 1412, 2014.

[4] N. Bokka, "Comparison of Power Flow Algorithms for inclusion in On-line Power Systems Operation Tools," M.S. thesis, University of New Orleans, United States of America, 2010.

[5] A. Pannu, "Artificial intelligence and its application in different areas," *International Journal of Engineering and Innovative Technology (IJEIT)*, vol. 4, no. 10, 2015.

[6] R. C. Eberhart and Y. Shi. *Computational intelligence: concept to implementations.* Elsevier, 2007, pp. 2,6, 20-24.

[7] Mathworks, "Supervised Learning," *The MathWorks, Inc*, 2016. [Online]. Available: https://www.mathworks.com/discovery/supervised-learning.html?requestedDomain= www.mathworks.com&requestedDomain=www.mathworks.com. [Accessed on

November 18 2016].

[8] P. Dayan, M. Sahani and G. Deback, "Unsupervised Learning," *The MIT Encyclopedia of the Cognitive Sciences*, 1999.

[9] M. Lee, "Reinforcement Learning," 2005. [Online]. Available: https://webdocs.cs.
ualberta.ca/~sutton/book/ebook/node7.html. [Accessed on November 18 2016].

[10] G. Zhang, B. E. Patuwo, and M. Y. Hu, "Forecasting with artificial neural networks: The state of the art," *International Journal of Forecasting*, vol. 14, no. 1, pp. 35-62, 1998.

[11] S. B. Efe and M. Cebeci, "Power Flow Analysis by Artificial Neural Network," *International Journal of Energy and Power Engineering*, vol. 2, no. 6, p. 204, 2013.

[12] J. T. Burger, "A Basic Introduction To Neural Networks," *University of Winconsin-Madison*. [Online]. Available: http://pages.cs.wisc.edu/~bolo/shipyard/neural/local.
html. [Accessed on January 22 2017].

[13] S. Kodsi and C. Canizares, "Modeling and simulation of IEEE 14-bus system with FACTS controllers," 2003. [Online]. Available: https://www.researchgate.net/file.
PostFileLoader.%0Ahtml?id=57b2b0c493553b281e5076e6&assetKey=AS%3A395594351824896%401471328451959. [Accessed on May 22 2017].

[14] "Data Sheets for IEEE 14 Bus System." [Online]. Available: http://shodhganga.inflibnet.ac.in/%0Abitstream/10603/5247/18/19_appendix.pdf. [Accessed on May 22 2017] .

[15] Y. Bharath, "IEEE 14 bus system," *The MathWorks, Inc*, 2016. [Online]. Available: https://www.mathworks.com/matlabcentral/fileexchange/46067-ieee-14-bus-system. [Accessed on December 11 2016].

[16] A. K. Kailay, "Identification of Best Load Flow Calculation Method for IEEE-30 BUS System Using MATLAB," *International Journal of Electrical and Electronics Research,* vol. 3, no. 3, pp. 155–161, 2015.

[17] Y. Bengio, "Practical Recommendations for Gradient-Based Training of Deep Architectures," *Lecture Notes in Computer Science*, vol. 7700, pp. 437–478, 2012.

[18] "Summary," *San Diego State University*. [Online]. Available: http://www-rohan.sdsu.edu/doc/matlab/toolbox/nnet/backpr14.html. [Accessed on January 22 2017].

eureca 2017 – Conference Paper
Paper Number 2EE03

Controller Design for Load Frequency Control in Deregulated Environment

Ser Yi Heng[1], Aravind CV[1*], Charles R Sarimuthu[1]
[1]School of Engineering, Taylor's University, Malaysia.

[*]*aravindcv@ieee.org*

Abstract
The demand of load increases every year due to the rise of population around the world. One of the major challenges in power systems is the fluctuations in the supply frequency caused by the load variations within the interconnected system or due to the addition of new generators/supply sources. A number of studies have been in the area of interconnected systems with most of them focus on voltage balance solution. Other than that, the influence in power system dynamics in deregulated environments has not studied by most of the researchers. This paper investigated an interconnected network in a deregulated environment focusing on the addition of a generation unit. The modelling of the proposed two-area power system is performed using MATLAB/SIMULINK tool and various controllers are tested for their performance evaluations in terms of time-bound operations characteristics. Three different conditions of power systems in deregulated environment are tested which are load fluctuation in one area alone, load fluctuation in both areas under considerations and due to sudden load increase within the two area networks. The controller designed for load frequency control shows that there is more than 20% improvement in Area 1 and Area 2 by comparing the time bound operational characteristics with a further 80% improvement in tie-line in comparison with that of the existing conventional controller.

Keywords: Load Frequency Control (LFC), Deregulated Environment, Controller Design, Two-area System

1. Introduction

Malaysia is a developing country where the population is growing very fast which lead to increase in demand of electricity supply. The generation must be increased to meet the growing of population where efficient use of energy is important. The smart control on the demand side lowers down stress on the power system and energy losses such as distribution and transmission powers. The saving due to energy efficiency reduces the cost for the consumer. Besides that, the energy efficiency ensures that the power quality are maintained. In Malaysia, the government made some policies to promote the renewable energy (RE). The policy is to ensure that the power supply from RE increases from 5% (Year 2010) to 15% (Year 2020). Some researches focus on increasing awareness on energy efficiency while some others provide the knowledge on green building and subsidy on the equipment. The improvement on smart grid and control that help on energy efficiency.

In this paper, the power systems in Subang Jaya and Petaling Jaya are monitored and modelled as Area 1 and Area 2. The areas of Subang Jaya and Petaling Jaya are shown in Figure 1. Load Frequency Control (LFC) in power systems is important in maintaining the quality of power supply such as maintaining frequency and power interchange between any area in certain limit [1]. The main purpose of Load Frequency Load is to control the steady stage error to zero in deregulated interconnect power systems. The fluctuation of the load change in any area of interconnected power system lead to change of frequency and power interchange between areas [2-6].



Figure 1 Area of Subang Jaya and Petaling Jaya (source: https://www.google.com.my/maps)

In the past few years, many researchers focused on monitoring the load side and control the system [7-12]. This research focuses on the performance of the power system when additional generator is connected to the existing or conventional power system. The two-area interconnected power system in deregulated environment is modelled by using MATLAB/SIMULINK. The study focuses on the performance of the conventional power system and proposed power system. Besides that, study the performance of the system with and without controller.

In deregulated environments, the generation and distribution operate by different companies which can be represented as generation company (GENCO) and distribution company (DISCO). The DISCO can have contract with any GENCO in the same area or from other areas. Figure 2 shows the two area connected by tie-line [13-14].

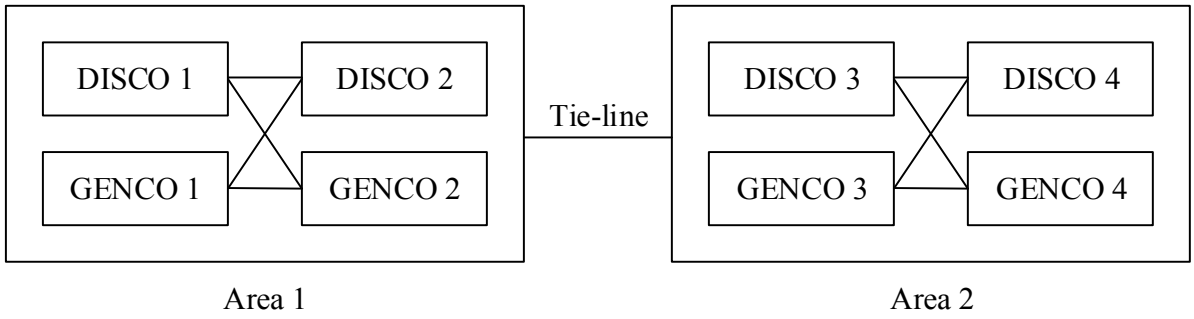


Figure 2 Two Area Connected by Tie-line

In the interconnected power systems, Area Control Error (ACE) is the input signal to the controller so that the controller can generate the control signal. ACE is the summation of vary frequency and vary tie-line power exchange between areas.

2. Research Framework

This research focuses on two-area interconnected power system in deregulated environment. The conventional power system and proposed design are modelled by using MATLAB/SIMULINK. Study the performance of the system with and without controller.

There are many areas in the interconnected power system and tie-line is connected between areas. A two-area interconnected power system is show in Figure 3.

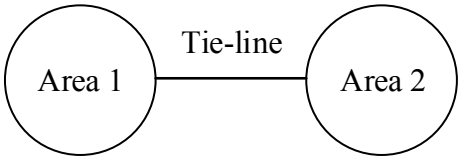


Figure 3 Two-Area Interconnected Power System

A deregulated environment, consists of many generation companies (GENCO) and distribution companies (DISCO), the DISCO has contract with GENCO from different area. DISCO Participation Matrix (DPM) is a method to represent the contract between DISCO and GENCO in interconnected power system as shown in Equation 1. In the matrix, the row and column represent the GENCO and DISCO respectively. Each element in the matrix is the fraction of total load contracted by distribution company j from generation company i, cpf_{ij} is the contract participation factor. The summation of all the element in one column is equal to one or unity.

$$DPM = \begin{bmatrix} cpf_{ij} & \cdots & cpf_{ij} \\ \vdots & \ddots & \vdots \\ cpf_{ij} & \cdots & cpf_{ij} \end{bmatrix}, DPM = \begin{bmatrix} cpf_{11} & cpf_{12} & cpf_{13} & cpf_{14} \\ cpf_{21} & cpf_{22} & cpf_{23} & cpf_{24} \\ cpf_{31} & cpf_{32} & cpf_{33} & cpf_{34} \\ cpf_{41} & cpf_{42} & cpf_{43} & cpf_{44} \end{bmatrix} \quad (1)$$

The two-area deregulated interconnected power system is shown in Figure 4 and the numerical parameter of the power system is shown in Table 1.

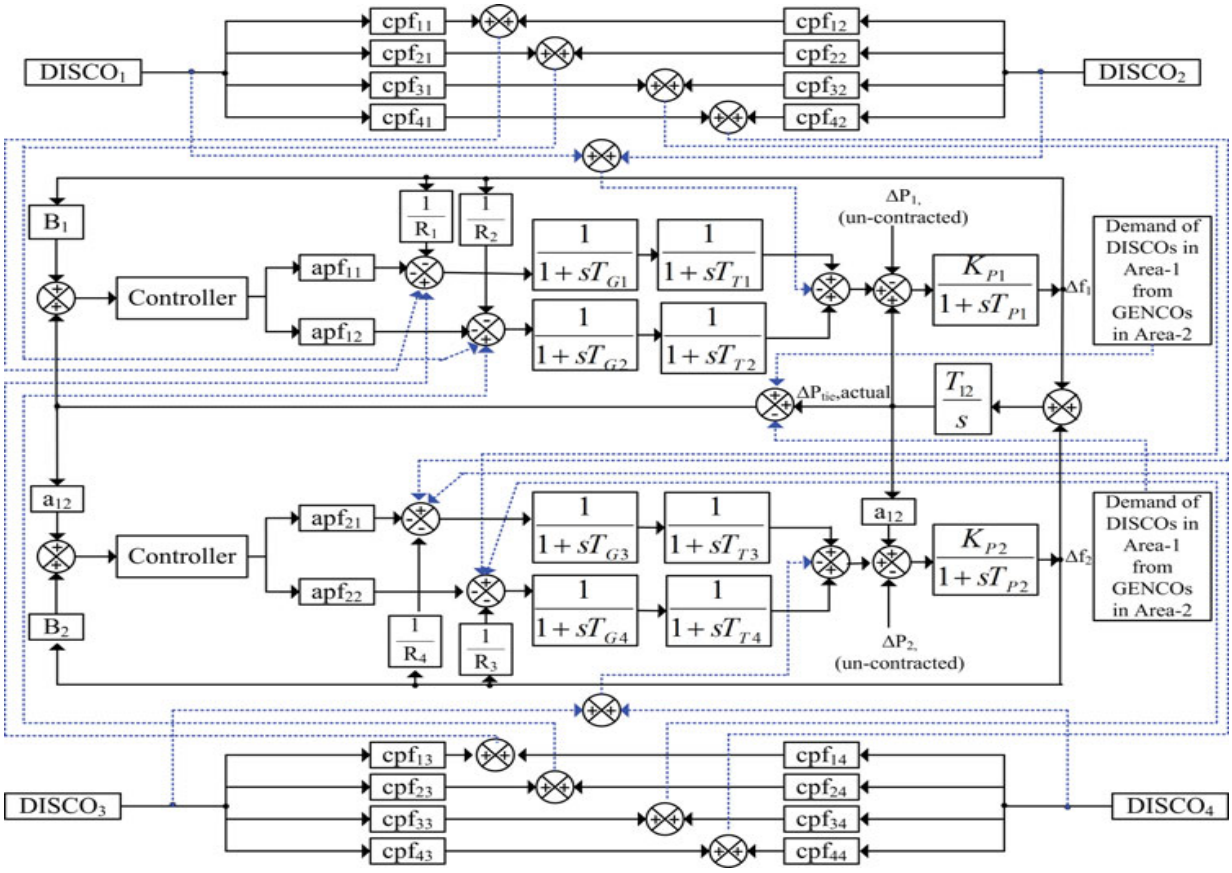


Figure 4 Two-Area Interconnected Power System in Deregulated Environment [4,15-16]

Table 1 Numerical Parameter of Power System [4,15-16]

Parameter	Value
$T_{G1}, T_{G2}, T_{G3}, T_{G4}$	0.08
$T_{R1}, T_{R2}, T_{R3}, T_{R4}$	5
$T_{T1}, T_{T2}, T_{T3}, T_{T4}$	10
T_{P1}, T_{P2}	20
K_{P1}, K_{P2}	120
T_{12}	3.424
R_1, R_2, R_3, R_4	2.4
B_1, B_2	0.4256
a_{12}	-1

There are four DISCOs in the system and two GENCOs in each areas. Both area are run by thermal power system. There is one Load Frequency Control (LFC) in each area. Design an adaptive scheduled controller for the system as LFC. The turbine produces the mechanical power to the generator. The generator generates the electrical power to the load. The variation of frequency and tie-line power exchange is the main issue of power quality in LFC.

Equation 2 and Equation 3 are the power balance equations of Area 1 and Area 2.

$$\Delta F_1(s) = [\Delta P_{G1}(s) - \Delta P_{D1}(s) - \Delta P_{tie,1}(s)] \times \frac{K_{ps1}}{1 + T_{ps1}s} \tag{2}$$

$$\Delta F_2(s) = [\Delta P_{G2}(s) - \Delta P_{D2}(s) - \Delta P_{tie,2}(s)] \times \frac{K_{ps2}}{1 + T_{ps2}s} \tag{3}$$

Area Control Error (ACE) is the input signal to the controller and the controller produces a control signal to the system. The ACE is given as Equation 4.

$$ACE_1 = B_1 \Delta F_1 + \Delta P_{tie12,error}, ACE_2 = B_2 \Delta F_2 + a_{12} \Delta P_{tie12,error} \tag{4}$$

Equation 5, Equation 6 and Equation 7 are the schedule steady state tie-line power flow, actual tie-line power, and the tie-line power error.

$$\Delta P_{tie12,sch} = (Demand\ of\ DISCOs\ in\ area\ 1\ to\ GENCOs\ in\ area\ 2) - (Demand\ of\ DISCOs\ in\ area\ 2\ to\ GENCOs\ in\ area\ 1) \tag{5}$$

$$\Delta P_{tie12,actual} = \frac{2\pi T_{12}}{s}(\Delta F_1 - \Delta F_2) \tag{6}$$

$$\Delta P_{tie12,error} = \Delta P_{tie12,actual} - \Delta P_{tie12,sch} \tag{7}$$

The component that ACE distributes to each participating GENCO, called as ACE Participation Factor (APF), is given as Equation 8. The summation of APF in each area must equal to unity or one.

$$APF_1 + APF_2 = 1, APF_3 + APF_4 = 1 \tag{8}$$

The proposed design of this research is adding generator into the conventional power system. The change of frequency in Area 1 and Area 2 area modified and given as Equation 9 and Equation 10.

$$\Delta F_1(s) = [\Delta P_{G1}(s) - \Delta P_{D1}(s) - \Delta P_{tie,1}(s)] \times \left(\frac{K_{ps1}}{1 + T_{ps1}s} + \frac{K_{ps,new}}{1 + T_{ps,new}s}\right) \tag{9}$$

$$\Delta F_2(s) = [\Delta P_{G2}(s) - \Delta P_{D2}(s) - \Delta P_{tie,2}(s)] \times \left(\frac{K_{ps1}}{1 + T_{ps1}s} + \frac{K_{ps,new}}{1 + T_{ps,new}s}\right) \quad (10)$$

The flow chart of the research is show in Figure 5 which included all the steps to conduct the research.

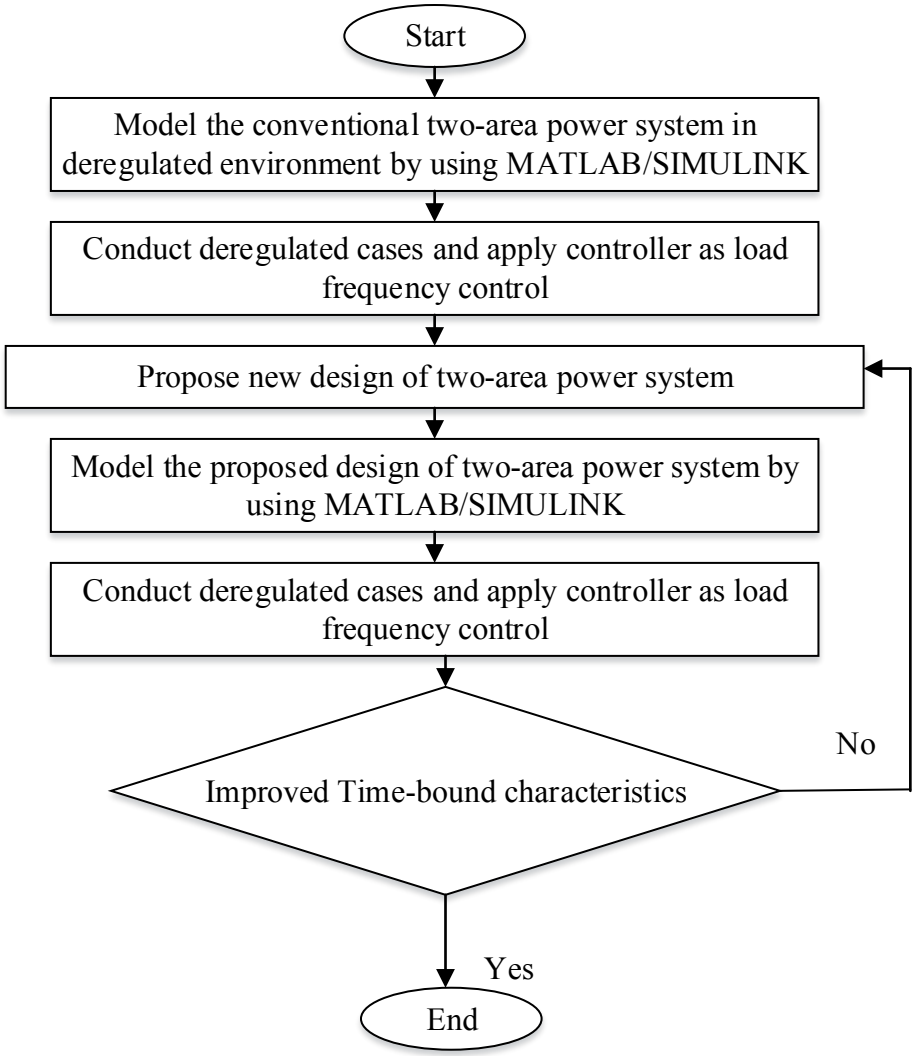


Figure 5 Flow Chart of the Research

3. Testing

The proposed design and the adaptive scheduled controller are tested on three cases.

Case 1

The values of all the GENCOs in each area are equal which is shown in Table 2. The summation of GENCOs in each area equals to one or unity.

In this case, the load fluctuations happen only in Area 1.Besides that, the load demand of each DISCOs is the same which equals to 0.1. The Contract Participation Factor (cpf) is show in DISCO Participation Matrix given as Equation 11.

In the DPM, it shows that $DISCO_3$ and $DISCO_4$ do no need power from any GENCO where cpf in Area 2 are equal to 0. The demand of $DISCO_1$ and $DISCO_2$ identical to the GENCO in Area 1.

Table 2 GENCOs in Each Area

Parameter	Value
GENCO 1 in area 1, apf_1	0.5
GENCO 2 in area 1, apf_2	$apf_2 = 1 - apf_1 = 0.5$
GENCO 3 in area 2, apf_3	0.5
GENCO 4 in area 2, apf_4	$apf_4 = 1 - apf_3 = 0.5$

$$DPM = \begin{bmatrix} cpf_{11} & cpf_{12} & cpf_{13} & cpf_{14} \\ cpf_{21} & cpf_{22} & cpf_{23} & cpf_{24} \\ cpf_{31} & cpf_{32} & cpf_{33} & cpf_{34} \\ cpf_{41} & cpf_{42} & cpf_{43} & cpf_{44} \end{bmatrix} = \begin{bmatrix} 0.5 & 0.5 & 0 & 0 \\ 0.5 & 0.5 & 0 & 0 \\ 0 & 0 & 0 & 0 \\ 0 & 0 & 0 & 0 \end{bmatrix} \quad (11)$$

Case 2

In this case, the load fluctuation happen in Area 1 and Area 2, all the GENCOs participate in Load Frequency Control. Each apf value is show in Table 3. The load demand of all the DISCOs are equal to 0.1. The cpf is show in DPM given as Equation 12. The DISCO in Area 1 and Area 2 have contract with the GENCO in their own area and GENCO from other area.

Table 3 apf of each GENCOs

Parameter	Value
GENCO 1 in area 1, apf_1	0.75
GENCO 2 in area 1, apf_2	$apf_2 = 1 - apf_1 = 0.25$
GENCO 3 in area 2, apf_3	0.5
GENCO 4 in area 2, apf_4	$apf_4 = 1 - apf_3 = 0.5$

$$DPM = \begin{bmatrix} cpf_{11} & cpf_{12} & cpf_{13} & cpf_{14} \\ cpf_{21} & cpf_{22} & cpf_{23} & cpf_{24} \\ cpf_{31} & cpf_{32} & cpf_{33} & cpf_{34} \\ cpf_{41} & cpf_{42} & cpf_{43} & cpf_{44} \end{bmatrix} = \begin{bmatrix} 0.5 & 0.25 & 0 & 0.3 \\ 0.2 & 0.25 & 0 & 0 \\ 0 & 0.25 & 1 & 0.7 \\ 0.3 & 0.25 & 0 & 0 \end{bmatrix} \quad (12)$$

Case 3

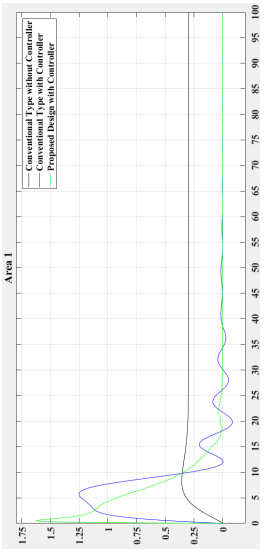
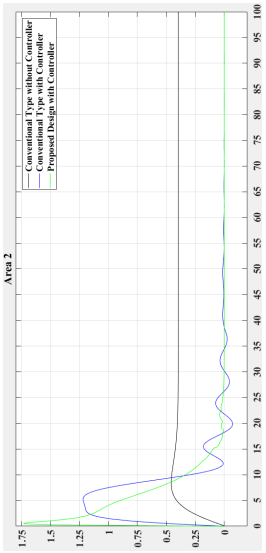
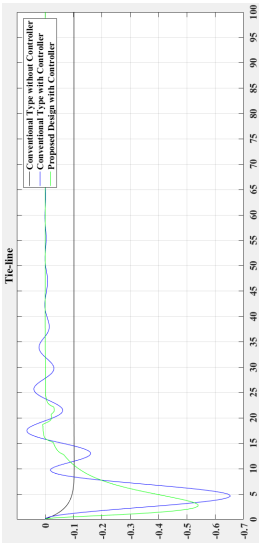
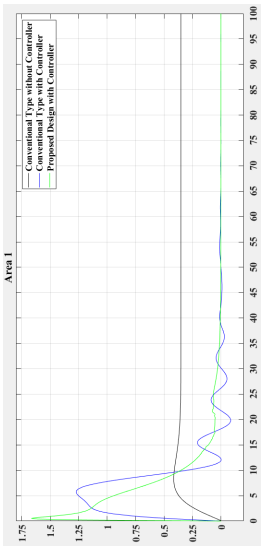
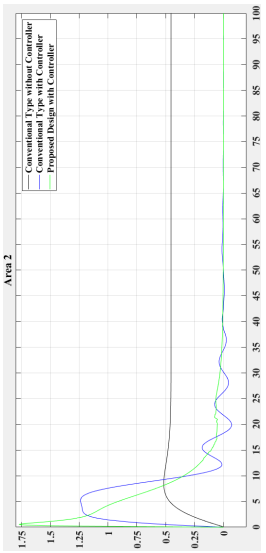
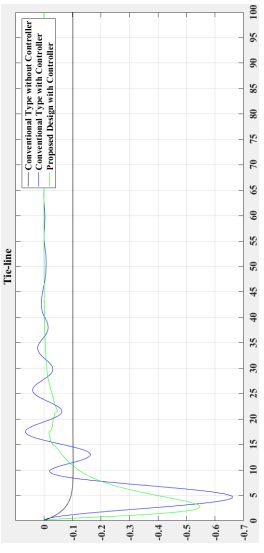
In this case, consider one of the DISCO require more power than the contract with GENCO, but the DISCO has no contract with other GENCO to provide extra power. In this condition, the power is to be provided in the same area and the GENCO as the load in that area. The value of each DISCO is show in Table 4. The GENCO and DPM condition area same as the environment in Case 2.

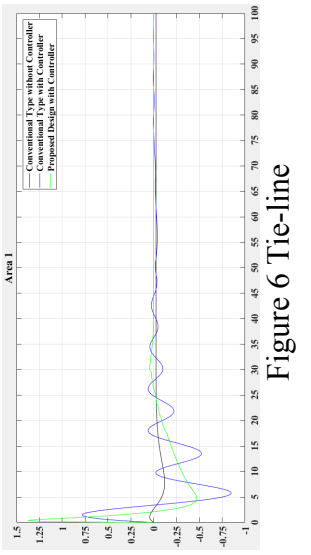
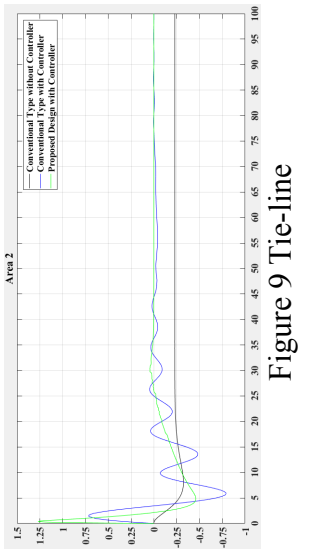
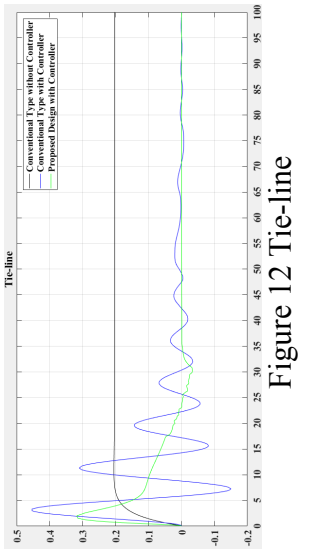
Table 4 DISCO in each Area

Parameter	Value
DISCO 1 in area 1, $DISCO_1$	$0.1 + 0.1 = 0.2$

DISCO 2 in area 1, $DISCO_2$	0.1
DISCO 3 in area 2, $DISCO_3$	0.1
DISCO 4 in area 2, $DISCO_4$	0.1

4. Result and Discussion

Case 3	 Figure 8 Area 2	 Figure 11 Area 2	 Figure 14 Area 2
Case 2	 Figure 7 Area 1	 Figure 10 Area 1	 Figure 13 Area 1

Case	Case 1
Area 1	 Figure 6 Tie-line
Area 2	 Figure 9 Tie-line
Tie-line	 Figure 12 Tie-line

Case 1
Figure 7 and Figure 8 show the frequency variation in Area 1 (Subang Jaya) and Area 2 (Petaling Jaya). Figure 6 shows the tie-line power exchange between areas. In the graph, it shows that the conventional model without controller has less overshooting and undershooting compare to conventional model with controller and proposed model with controller, but it never achieve steady state. Compare the model with controller, the proposed model has the better settling time and undershooting compare to conventional model which are 35% and 44% improvement, but the overshooting is increase 43% compare to conventional model.

Case 2
Figure 10 and Figure 11 show the frequency variation in Area 1 (Subang Jaya) and Area 2 (Petaling Jaya). Figure 9 shows the tie-line power exchange between areas. In the graph, it shows that the conventional model without controller has less overshooting and do not has undershooting compare to conventional model with controller and proposed model with controller, but it never achieve steady state. Compare the model with controller, the proposed model has the better settling time and undershooting compare to conventional model. In proposed model, there is no undershooting in Area 1 and Area 2, there is 17.4% improvement in tie-line. However, the overshooting is increase 23% and 30% in Area 1 and Area 2 compare to conventional model, but there is 85% improvement in tie-line power exchange. Besides that, there is 35.5% improvement on settling time compare to conventional model.

Case 3
Figure 13 and Figure 14 show the frequency variation in Area 1 (Subang Jaya) and Area 2 (Petaling Jaya). Figure 12 shows the tie-line power exchange between areas. In the graph, it shows that the conventional model without controller has less overshooting and do not has undershooting compare to conventional model with controller and proposed model with controller, but it never achieve steady state. Compare the model with controller, the proposed model has the better settling time and undershooting compare to conventional model. In proposed model, there is no undershooting in Area

1 and Area 2, there is 17.35% improvement in tie-line. However, the overshooting is increase 23% and 30% in Area 1 and Area 2 compare to conventional model, but there is no overshooting in tie-line power exchange. Besides that, there is 19.75% improvement on settling time in Area 1 and Area2 and 24.05% improvement for tie-line.

Table 5 Deregulated Power System

Operating Condition		Conventional without Controller			Conventional with Controller			Proposed Design		
		Settling Time (s)	Peak Overshoot	Peak Undershoot	Settling Time (s)	Peak Overshoot	Peak Undershoot	Settling Time (s)	Peak Overshoot	Peak Undershoot
Case-1	Area 1	-	0.0428	-0.121	77	0.7803	-0.8484	50	1.373	-0.4718
	Area 2	-	0	-0.3243	78	0.7136	-0.7922	55	1.269	-0.4604
	Tie-line	-	0.2051	0	78	0.4535	-0.1505	55	0.3179	-0.0338
Case-2	Area 1	-	0.3708	0	62	1.251	-0.08675	40	1.629	0
	Area 2	-	0.4727	0	62	1.218	-0.0734	40	1.735	0
	Tie-line	-	0	-0.1025	65	0.0648	-0.6531	40	0.0097	-0.5395
Case-3	Area 1	-	0.4298	0	81	1.271	-0.0863	65	1.665	0
	Area 2	-	0.5371	0	81	1.238	-0.0727	65	1.771	0
	Tie-line	-	0	-0.1025	79	0.0646	-0.6614	60	0	-0.5466

Although there is less overshooting and undershooting for conventional type power system without controller in all the cases, it never achieve steady state. By applying the controller, it increase the overshooting and undershooting, but it able to achieve the steady state. The proposed design has 17% increase in overshooting, but the undershooting and settling time improve more than 25%.

5. Conclusion

In this research, a new Load Frequency Control (LFC) method for two-area power system of Subang Jaya and Petaling Jaya in deregulated environment modelled and simulated by using MATLAB/SIMULINK. The DISCO Participation Matrix (DPM) presented to clearly describe the contract between DISCOs and GENCOs. Simulated the power system with three different deregulated environment and apply the controller as LFC. The new LFC method has the improvement on undershooting and settling time, but there is small number increase on overshooting. There is more than 20% improvement on settling time of the new LFC method and more than 40% improvement on undershooting. But, there is less than 30% increase on overshooting. It can conclude that new LFC method is better than conventional model.

References

[1] S. K. Pandey, S. R. Mohanty, and N. Kishor, "A literature survey on load-frequency control for conventional and distribution generation power systems," *Renew. Sustain. Energy Rev.*, vol. 25, no. October 2016, pp. 318–334, 2013.

[2] A. P. S. Meliopoulos, G. J. Cokkinides, and A. G. Bakirtzis, "Load-frequency control service in a deregulated environment," *Proc. Thirty-First Hawaii Int. Conf. Syst. Sci.*, vol. 3, no. C, pp. 1–8, 1998.

[3] S. Srikanth, "Load Frequency Control in Deregulated Power System using Fuzzy C-Means," vol. 74, no. 11, pp. 34–41, 2013.

[4] W. Tan, Y. Hao, and D. Li, "Load frequency control in deregulated environments via active disturbance rejection," *Int. J. Electr. Power Energy Syst.*, vol. 66, pp. 166–177, 2015.

[5] L. Dong, Y. Zhang, and Z. Gao, "A robust decentralized load frequency controller for interconnected power systems," *ISA Trans.*, vol. 51, no. 3, pp. 410–419, 2012.

[6] N. Hasan and S. Farooq, "Real Time Simulation of Automatic Generation Control For Interconnected Power System," *International Journal on Electrical Engineering and Informatics.*, vol. 4, no. 1, pp. 40–51, 2012.

[7] K. Das, P. Das, and S. Sharma, "Load Frequency Control Using Classical Controller in An Isolated Single Area and Two Area Reheat Thermal Power System," *International Journal of Emerging Technology and Advanced Engineering*. vol. 2, no. 3, pp. 403–409, 2012.

[8] S. Subha, "Load Frequency Control with Fuzzy Logic Controller Considering Governor Dead Band and Generation Rate Constraint Non-Linearities," *World Applied Sciences Journal*.vol. 29, no. 8, pp. 1059–1066, 2014.

[9] I. Kocaarslan, "Fuzzy logic controller in interconnected electrical power systems for load-frequency control," *International Journal of Electrical Power & Energy Systems*. vol. 27, pp. 542–549, 2005.

[10] K. R. Sudha and R. V. Santhi, "Electrical Power and Energy Systems Robust decentralized load frequency control of interconnected power system with Generation Rate Constraint using Type-2 fuzzy approach," *Int. J. Electr. Power Energy Syst.*, vol. 33, no. 3, pp. 699–707, 2011.

[11] F. Beaufays, Y. Abdel-Magid and B. Widrow, "Application of neural networks to load-frequency control in power systems", *Neural Networks*, vol. 7, no. 1, pp. 183-194, 1994.

[12] M. Pal and K. Kaur, "To Control Load Frequency by using Integral," *International Journal of Innovative Research in Science, Engineering and Technology.* vol. 3, no. 5, pp. 12502–12506, 2014.

[13] F. F. Wu, F. L. Zheng, and F. S. Wen, "Transmission investment and expansion planning in a restructured electricity market," *Energy*. vol. 31, pp. 954–966, 2006.

[14] T. S. Gorripotu, R. K. Sahu, and S. Panda, "Engineering Science and Technology , an International Journal AGC of a multi-area power system under deregulated environment using redox fl ow batteries and interline power fl ow controller," *Eng. Sci. Technol. an Int. J.*, vol. 18, no. 4, pp. 555–578, 2015.

[15] Akankshya Mishra, Minakhi Behera, "*Simulation and Modeling of Automatic Generation Control using PI and PID Controller in Deregulated Environment*", International Journal of Computer Application, 2014.

[16] D. Das, *Electrical power systems*. New Delhi: New Age International (P) Ltd., Publishers, 2006.

eureca 2017 – Conference Paper
Paper Number 2EE04

Assessment of Taylor's University Electrical Distribution System

Ting Yong Tee[1], Reynato Gamboa[*], Charles R. Sarimuthu
[1]School of Engineering, Taylor's University, Malaysia.

ReynatoAndal.Gamboa@taylors.edu.my

Abstract

Malaysia is a developing country where the application of software tools for power system studies are continuously expanding in size and growing in complexity due to the population is growing rapidly. The demand of power is increasing enormously day by day. So it has been difficult task to maintain the power quality. Electrical power Industries have always been concerned about power quality. In Engineering Procurement and Construction (EPC) industries, they plan new power system and the expansion of existing industry by several of analyses which is performed using ETAP software. There are many analysis of power system simulated by researchers, but most of them run the power assessment and analysis in the industries and sub stations. This paper is report deals with assessment of distribution system of Taylor's University. The simulation using ETAP software can show whether any part of the system is operating under abnormal condition such as under voltage of feeder buses, overloaded transformers and cables. It can further show when protective devices have low rated current and interrupting current capacities. From these alerts, recommendation and simulation of proposed solution were conducted to bring the system back to normal operating condition. Low Power Factor of electrical loads cause high current is drawn from power supply. The impact of this circumstance is influenced by impedance of electrical load. Conventional shunt compensation method is used by connecting capacitor in parallel to the bus. After compensation the system is simulated and under voltage in buses has solved and improved the power factor of buses. A number of contingencies (scenarios) were also simulated to check the system performance in case of emergency conditions and possible solution to avoid system collapse. Load shedding is proposed to prevent failure of the entire system when the demand strains the capacity of the system.

Keywords: Power Quality, Under Voltage, Power Factor Improvement, Compensation, Load Sheddings

1. Introduction

The application of software tools for power system studies are increasing over the years. After the development of powerful computer based software, the recent advances in engineering sciences have brought a revolution in the field of electrical engineering. Distribution system is an ultimate related part in power system which provides supply to the consumers from high voltage to low voltage transmission system.

Tenaga National Berhad (TNB) is a public listed company registered under Companies Act 1965 that owns and operates generating plants, transmission systems and distribution systems. TNB is mainly separated into three divisions which are generation, transmission, and distribution. TNB's distribution division is divided into two regional areas as shown in Table 1.1.

Table 1. Two Main Regional Operational Areas [1]

Regional Areas	Service Location
Region 1	Selangor, Putrajaya / Cyberjaya, Negeri Sembilan, Melaka and Johor
Region 2	Perlis, Kedah, Pulau Pinang, Perak, Pahang, Terengganu and Kelantan

Distribution Division is divided into two main regional operational areas as shown in Table 1. The TNB transmits, constructs, operates, and maintains transmission networks at voltage level of 500kV, 275kV and 132kV. TNB distribute the voltage to 33kV, 11kV and 415/240 Volts while certain parts of Johor and Perak are 22kV and 6.6kV [1].

The incoming power for Taylor's University would be 11kV with 50Hz frequency. The main focus for this eureca paper would is on the real-time data of Taylors University. There are various types of load that is connected with distribution system, therefore it is not constant. Also, many studies have shown that there are researchers had already done the simulation and analysis of power system simulation on large industrials[2]–[10]. The studies of load flow in university are not focus by most of the researchers. The main focus for this research paper is on the real-time data of Taylor's University Electrical Distribution System (TUEDS). Framework of schematic single-line diagram of Taylor's University is shown in Figure 1.

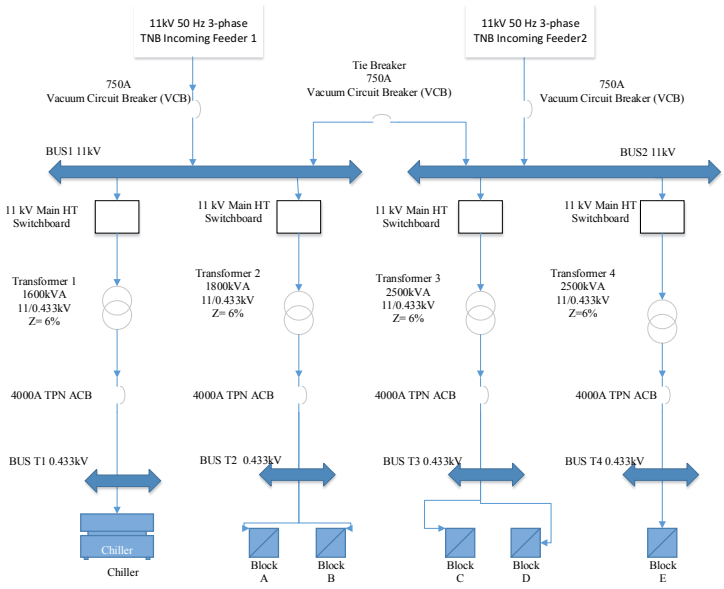


Figure 1. Schematic Single-line Diagram for Taylor's University

The incoming power supply of Taylor's University is connected to two 11kV TNB feeders. Each feeders are protected by a 750A Vacuum Circuit Breaker (VCB). The two feeders are connected to 1.6MVA, 1.8 MVA and 2.5MVA transformer respectively. The transformers are protected with Air Circuit Breaker (ACB).

The result of a power quality is difficult to be solved among the industries from offshore rigs to data centres because the sudden disconnection of loads might be happened. The power quality issues consist of single phase tripping, harmonic distortion, unbalance voltage and many more[6], [11], [12]. As for the low power quality, it will cause power lost and maintenance cost is high.

In this project the possible issues of TUEDS was assessed through ETAP software. TUEDS system was simulated by using load flow analysis (LFA) and three phase device duty check (DDC) through ETAP software. The system that operated under voltage on buses and low power factor of electrical loads will cause high current is drawn from power supply. The impact of this circumstance is influenced by impedance of electrical load. A low power factor draws a higher internal current and the excessive heat generated will damage and shorten equipment life. As system redesign is very costly so it is necessary to control power factor. Thus, a cost effective conventional shunt compensation method which connecting capacitor in parallel to the bus to ensure the TUEDS operated above 0.95 pu and the power factor at those buses are above 85%.

A number of contingencies (scenarios) were also simulated to check the system performance in case of emergency conditions and possible solution to avoid system collapse. Load shedding is proposed to prevent failure of the entire system when the demand strains the capacity of the system. DDC was conducted to evaluate the capability of protective devices under normal operation conditions by continuous current duty of the circuit breakers. It can determine maximum fault current in TUEDS. Human could be shocked or killed without tripping a circuit breaker. Overcurrent

wiring and equipment will overheating and fire. Thus, the circuit breakers had adequate rating and be able to trip during system configuration.

2. Methodology

The methodology has achieved the effective results based on the objective of the project. The methodology presented the method to construct the assessment of TUEDS. Figure 2 shows the flow chart of research methodology that narrows down the process of research and provides the explanation of each process. It included the discussion of simulation TUEDS in ETAP software.

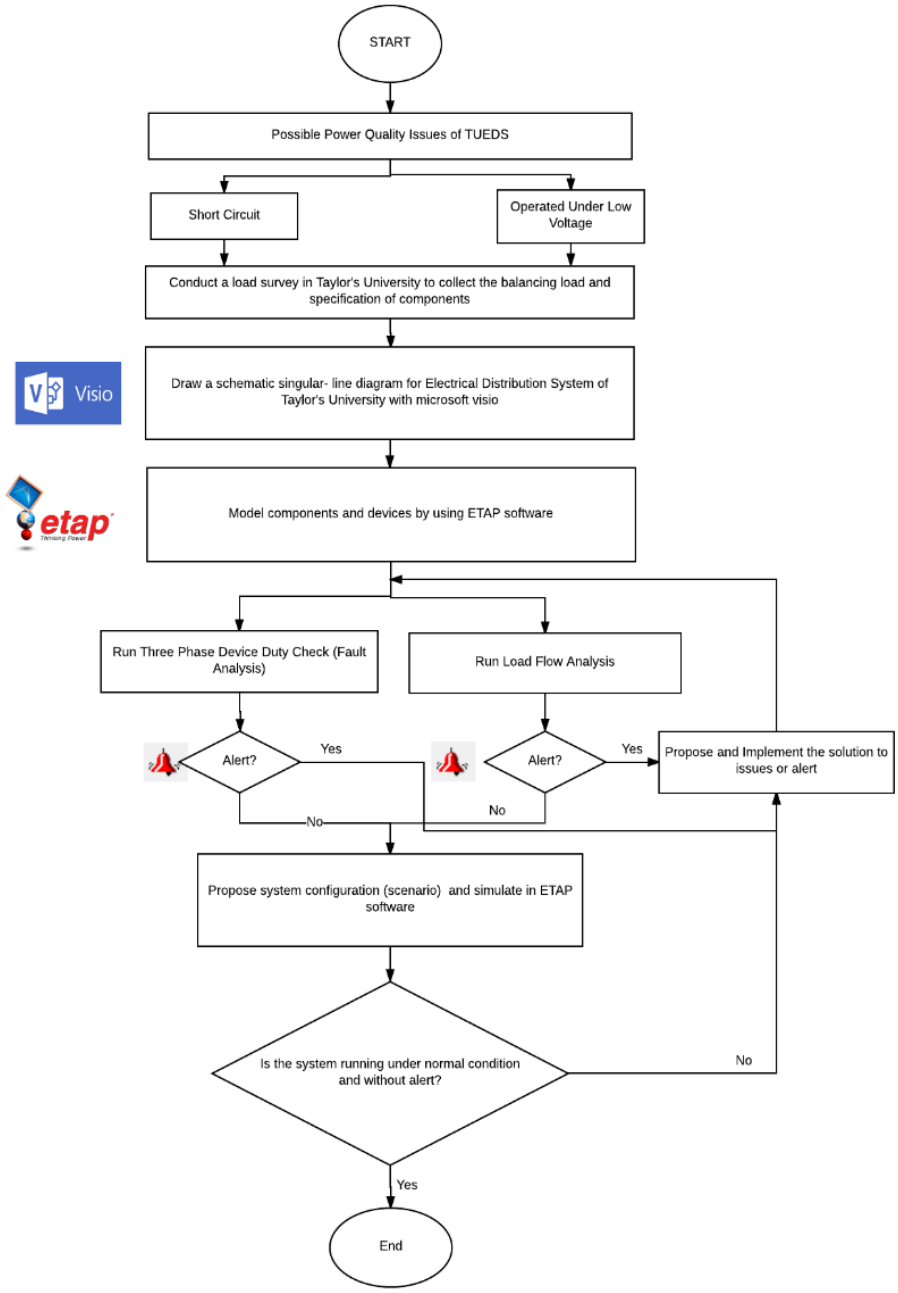


Figure 2. Research Methodology

The first stage in this research were conceived and designed. Literature review conducts the knowledge of power quality issues in power distribution system, load flow,

3 phase DDC and method of simulation. LFA and 3 phase DDC in different substation and distribution system were studied. This section conducted the theory and design of load flow and fault analysis. Power quality issues in electrical power distribution and the different type of simulations for load flow and fault analysis were studied.

The research trend and research gap were obtained after the literature review. The power qualities issues in electrical power distribution and the solution and type of simulations were analysed by researchers were shown in literature review. This research focused on assessment of TUEDS.

As a result of trade secret in Taylor's University, the actual balancing value is not provided. Due to limited information available in system particularly the details of the load schedule, this researcher conducted a load survey to ensure that system loading is appropriately balanced. The balancing of the static loads for four transformers were tabulated. The load description and location were collected by the load survey. The difference of the total lumped load /ph should not be more than 15% from the average in balance phase. The researcher used the maximum demand (MD) load for the static load. The MD is the total kW that actually contributes the total power used in one time and the capacity of electricity usage[13].

The balancing of load for four transformers are recorded. The difference of the total lumped load /ph in each transformer was less than 10% from the average load in balance phase which was acceptable. A load schedule was tabulated after the load survey which include the power transformers, current transformers and specification of devices used in TUEDS.

There were two type of CB which is main type of high voltage CB and low voltage. The cables were either single phase or three phase. The name of devices are name according to the results of load survey. Schedule of loads was conducted after the load survey. It had determined the size of conductors, the proper overload and other protection devices.

The next stage was constructed the summary of instrument elements and devices on the one-line diagrams by using Microsoft Visio. There were many analysis for power system simulated by the researchers but most of them using MATLAB instead of ETAP software. Thus, the researcher used ETAP software to construct the complete single line diagram (SLD) of TUEDS. The complete single line diagram (SLD) of TUEDS was recorded. It was simulated under normal condition that two supplying power to four power transformers of different ratings which were connected with 11 kV power distribution network. The loads connected with the system are static load. The load can also be classified as lights, fans, air conditioners, printers, computers, laboratory equipment.

There were couples of errors while constructing simulation such as lumped load rated kV is lower than the nominal voltage and the phase of the load is different with the buses. The errors could be solved by checking the specification for the specific feeders. The sizing of cables, sizing of transformers, sizing of circuit breakers and the value of the loads was selected according to the load survey.

The LFA button on the Mode toolbar was clicked to switch to LFA mode. When there is no error in the SLD of TUEDS, the LFA mode was simulated continuously.

There were few types of alerts such as cable and CB overload, the feeder or buses under voltage and so on. Normal operating condition is such that bus voltage should be within 0.95pu to 1.05pu of rated bus voltage while cables and equipment are operating within their rated capacities [14], [15].

In the real world scenario there may have some maintenance of the transformers, circuit breakers, and cables. Thus, system configuration was constructed to ensure the load flow in Taylor's University are operating in normal condition. Three cases were implemented in this paper which are:

1) Case 1-System Performance Check

TUEDS was simulated through ETAP. Operated voltage level and power factor of buses of were recorded and analysed. The solution in case 1 was implemented conventional shunt compensation method which connecting capacitor in parallel to the bus. After compensation the system is simulated and under voltage in buses has solved and power factor of buses is also improved.

%Power Factor (PF) was calculated by using the Eq (3.1).

$$\%PF = \cos\left[\frac{Active\ Power(MW)}{Apparent\ Power(MVA)}\right] * 100\% \quad (3.1)$$

The Power Quality improvement were calculated by using the Eqs (3.2), (3.3), (3.4) and (3.5) while the size of Capacitor bank was calculated by using the Eq (3.6).

$$Z = R + j\omega X_L + (-\frac{1}{j\omega X_c}) \quad (3.2)$$

Z=Total Impedance
R=Resistance
L=Impedance
C=Capacitance

$$V = I * Z \quad (3.3)$$

V=Voltage
I= Current

$$P = V * I * cos\theta \quad (3.4)$$

$$Q = V * I * sin\theta$$

Cosθ=Power Factor

$$S = \sqrt{P^2 + Q^2} \quad (3.5)$$

S=Apparent Power
P= Active Power
Q=Reactive Power

$$Q = P * (\tan\theta 1 - \tan\theta 2) \quad (3.6)$$

Cos(θ1) = Existing Power Factor
Cos(θ2) = Required Power Factor

$$\tan\theta 1 = cos^{-1}\ (\cos\theta 1)$$

$$\tan\theta 2 = cos^{-1}\ \ (\cos\theta 1)$$

A three phase DDC was studied by clicked on the Run 3-Phase DDC button after the singular diagram is constructed. The alerts could be solved by changing the specification for the specific CBs. The contact-parting (interrupting) network is used to calculate the contact-parting (interrupting) symmetrical rms current for medium-voltage circuit breaker minimum contact-parting times of 1.5 to 4 cycles after the inception of the short circuit fault. The bolted 3-phase fault represents the worst-case condition at every bus of this example, insofar as contact-parting (interrupting) short circuit current duty is concerned.

2) Case 2- Incoming feeder 1 down

System configuration (scenario) was proposed and implemented in the simulation. This scenario could be a result of equipment shut down due to maintenance or faulted system. Incoming feeder 1 serves transformer 1 and transformer 3. Under this configuration, these transformers will be switch off through their respond circuit breakers. In this configuration, incoming feeder 2 is expected to carry loads of incoming feeder 1.

Load shedding was proposed as a solution for buses operated under voltage condition. The deliberate shutdown of electric power in a part or parts of a power-distribution system to prevent the failure of the entire system when the demand strains the capacity of the system. The total static and motor load are decreased due to the shutdown power of some blocks or location in Taylor's University. The location suggested are block B, carpark, rooftop and the location with high power demand of air conditioner. Some blocks or location in Taylor's University were switched off in order to reduce the load. The LFA report for system configuration were recorded and tabulated.

3) Case 3- Incoming feeder 2 down

System configuration (scenario) was proposed and implemented in the simulation. This scenario could be a result of equipment shut down due to maintenance or faulted system. Incoming feeder 2 serves transformer 2 and transformer 4. Under this configuration, these transformers will be switch off through their respond circuit breakers. In this configuration, incoming feeder 1 is expected to carry loads of incoming feeder 2. The same method in case 2 was applied in case 3.

After the simulation, the LFA report and 3 phase DDC report were tabulated as results. The proposed solutions were implemented and the results were recorded when there was no alert. The implemented solution was simulated and analysed. The bus loading summary report LFA and complete three phase DDC report for three phase DDC.

3. Result and Discussion

3.1 Case 1-System Performance Check

3.1.1 Under Voltage and Low Power Factor on the Buses

The LFA gives the voltage, current and power flow of line, bus, transformer, circuit breakers and other components. The load flow standard output report was generated by ETAP enlists all input parameters like bus input parameters, cable

parameters and transformer parameters. It shows that two incoming power grids which supplies power to the 11 kV Bus 1 and 29. The incoming power grid 1 was connected to transformer 1 and transformer 2 while incoming power grid 2 was connected to transformer 3 and transformer 4.

While performing LFA in ETAP, it provides various alerts which need immediate attention for smooth running of the system. The summary of the load analysis were recorded Table 2, Table 3 and Table 4. Table 2 shows the under voltage alerts of buses in simulation while Table 3 shows the power factor of buses. Table 4 shows the summary of load flow results.

Table 2. Under Voltage Alerts of the Buses

Bus ID	Condition	Rated Voltage (kV)	Operated Voltage(kV)	%Operated Voltage
Bus T1	Under Voltage	0.433	0.411	94.9
Bus T2	Under Voltage	0.433	0.411	94.9
Bus4	Under Voltage	0.433	0.408	94.2
Bus5	Under Voltage	0.433	0.407	93.9

From the alerts of LFA, it can be seen that the Bus T1, Bus T2, Bus 4 and Bus 5 were operated under voltage condition. The normal operating condition in the bus voltage has to be within the range from 0.95pu to 1.05pu of rated bus voltage so that the cables and equipment are operated within their rated capacities [14], [15]. The operated voltage level of Bus T2 is 0.949pu and bus 5 the voltage level is 0.939pu which both are below 0.95pu which are under voltage. Specific buses are operated under voltage and low power factor condition.

Table 3. Summary of Results for Buses

Monitoring Part	MW	MVAR	MVA	%PF
Bus T2	0.457	0.315	0.555	82.34 Lagging
Bus4	0.076	0.053	0.093	81.72 Lagging
Bus5	0.046	0.030	0.055	83.64 Lagging

Table 3 shows that the specific buses were operated under low power factor. The power factor of buses and loads should be above 85%. If the power factor is below 85%, it will result in a more expensive system with equipment able to absorb internal loads and larger load requirements. Low power factor of buses will cause high current is drawn from power supply. The impact of this circumstance is influenced by impedance of electrical load. A low power factor draws a higher internal current and the excessive heat generated will damage and shorten equipment life.

Table 4. Summary of LFA Results

Monitoring Part	MW	MVAR	MVA	%PF
Swing buses	8.951	4.883	10.196	87.79 Lagging
Total Demand	8.951	4.883	10.196	87.79 Lagging
Total Motor Load	6.397	2.816	6.989	91.53 Lagging
Total Static Load	2.426	1.244	2.726	88.98 Lagging
Apparent Losses	0.128	0.823		

Table 4 shows the demand and losses summary report which include the total demand and the losses of the system with power factor that occurs in simulation. The active power of swing buses are 8.951MW while the apparent power are 10.196MVAR.The reactive power of swing buses are 4.883MVAR. The %Power Factor (%PF) is determined by using Eq (3.1). There are some apparent losses due to the non-physical losses that occur in simulation.

Figure 3 shows the sectional views of LFA which was connected to feeder one which was connected to transformer 2 while Figure 4 and Figure 5 show the bus T2 and bus 4 which were connected from transformer 2. By analysing the results of simulation, the Bus T2, Bus 4 and Bus 5 which were operated under voltage condition showing the sectional view of the feeders. The operated voltage level of Bus T2 was 0.949pu and Bus 4 the voltage level was 0.942pu.

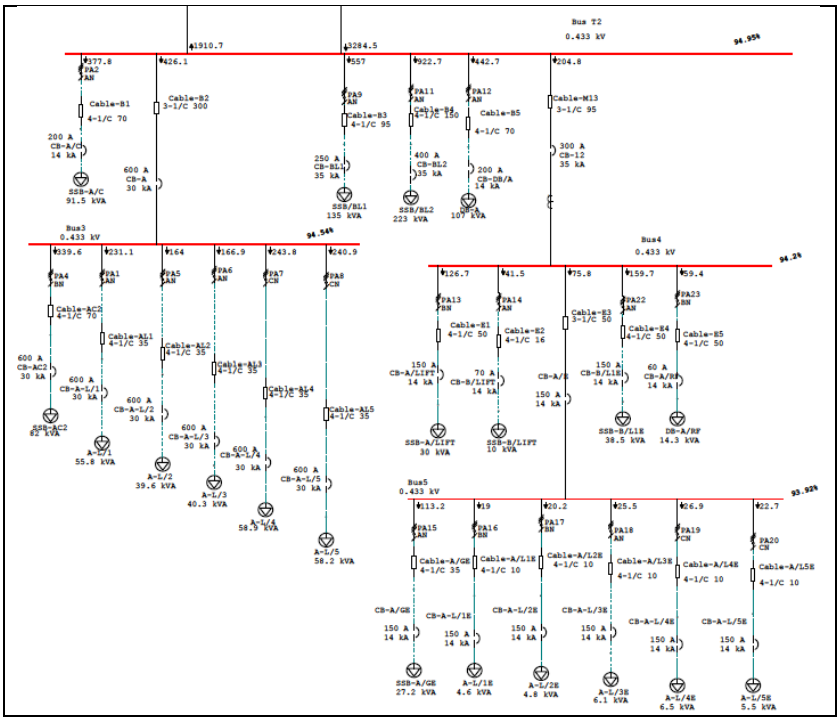


Figure 3. Sectional View of Buses for LFA

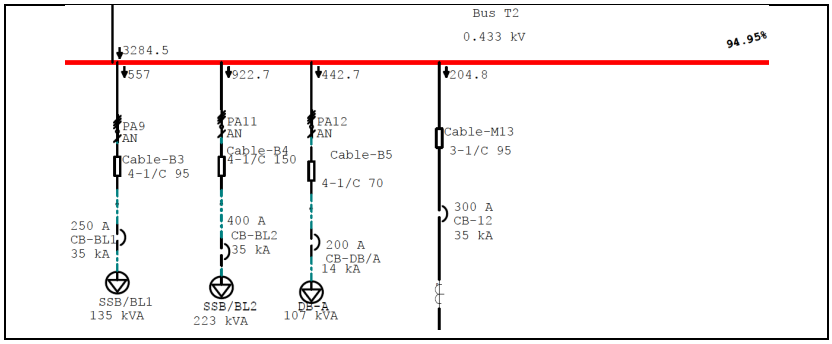


Figure 4. Under Voltage in BusT2

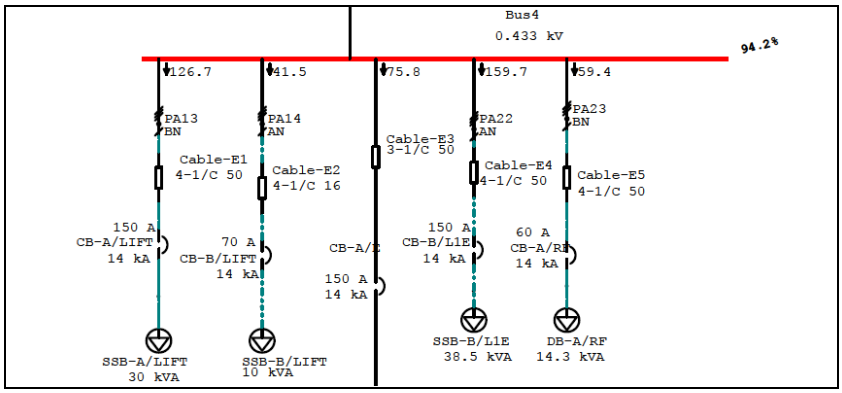


Figure 5. Under Voltage in Bus 4

3.1.2 Solution to Under Voltage and Low Power Factor on the Buses

The issue of the under voltage for buses can be solved by using conventional shunt compensation method which connecting capacitor in parallel to the bus. After compensation the system is simulated and under voltage in buses has solved and power factor of buses is also improved by placing the capacitor banks in parallel with the three phase feeders. The capacitor banks can increase the leading current and reduce the reactive power of the bus as shown in Eq. (3.2). Table 5 shows the results of buses after the solution was implemented solution while Table 6 shows the summary of power factor of buses after the solution were implemented.

Table 5. Comparison of Results for Buses Before and After the Simulation for Proposed Solution

Bus ID	Rated Voltage (kV)	Before		After		Condition
		Operated Voltage (kV)	% Operated Voltage	Operated Voltage (kV)	% Operated Voltage	
Bus T2	0.433	0.411	94.9*	0.417	96.39	Normal
Bus4	0.433	0.408	94.2*	0.415	95.74	Normal
Bus5	0.433	0.407	93.9*	0.413	95.49	Normal

*Under Voltage Condition

According to the Table 6, the results show that the %Operated Voltage of buses are increased and operated under normal condition due to the installation of Capacitor. With this result, the improvement of this simulation in terms of capacitor banks is verified or justified. The calculation can be checked by using Eq. (3.3). The operated voltage are increased due to the increase of total impedance. Therefore, this simulation is performed to ensure that the improvement of % operated buses voltage level obtained in Table 5 is valid. The size of capacitor were small because the price of 1MVAR Capacitor is much higher if compare to 100x 10kVAR capacitors.

Table 6. Summary of Results for Buses

Monitoring Part	Previous MVAR	New MVAR	New MVA	Capacitor (kVAR)	%PF	New %PF
Bus T2	0.315	0.030	0.466	75/ph	82.34 Lagging	98.07 Lagging
Bus4	0.053	0.023	0.079	10/ph	81.72 Lagging	96.20 Lagging
Bus5	0.030	0.015	0.048	5/ph	83.64 Lagging	95.83 Lagging

The power factor should be above 85%. The implemented capacitor bank was connected parallel with the three phase feeders in the simulation. The size of capacitor bank were determined by using Eqs (3.5) & (3.6). This calculation above is performed to ensure that power quality results of LFA in Table 6 is valid.

Table 7. Summary of LFA Results

Monitoring Part	MW	MVAR	MVA	%PF
Swing buses	8.946	4.120	10.196	90.83 Lagging
Total Demand	8.946	4.120	10.196	90.83 Lagging
Total Motor Load	6.397	2.816	6.989	91.53 Lagging
Total Static Load	2.432	0.536	2.452	97.66 Lagging
Apparent Losses	0.118	0.768		

Table 7 shows the improvement in the buses' power factor and reduction in the buses' reactive power when compared with Table 4. The reactive power is produced losses and leading the buses to operate under voltage condition. Table 7 shows that apparent losses are far less as compared to the losses shown in Table 4 due to increase of capacitance.

Figure 6 and Figure 7 illustrate that Bus T2 and Bus 4 which were connected from transformer 2 and were operated under normal condition after the solution was implemented in the simulation. The operated voltage level of Bus T2 was 0.9639pu and the voltage level of Bus 4 was 0.9574pu which both were increased if compare to Figure 4 and Figure 5.

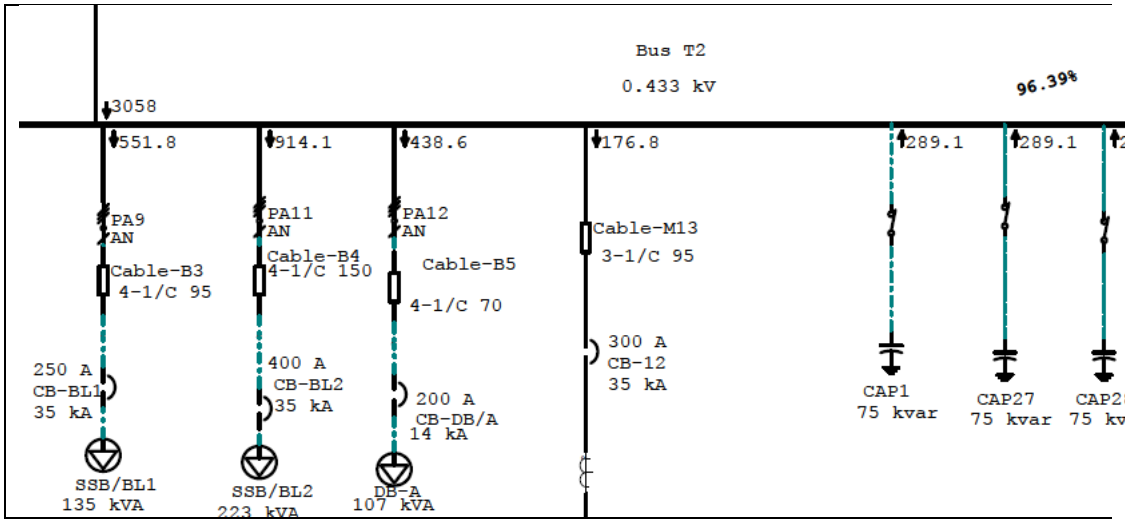


Figure 6. Improvement of %Operated Voltage Level in Bus T2

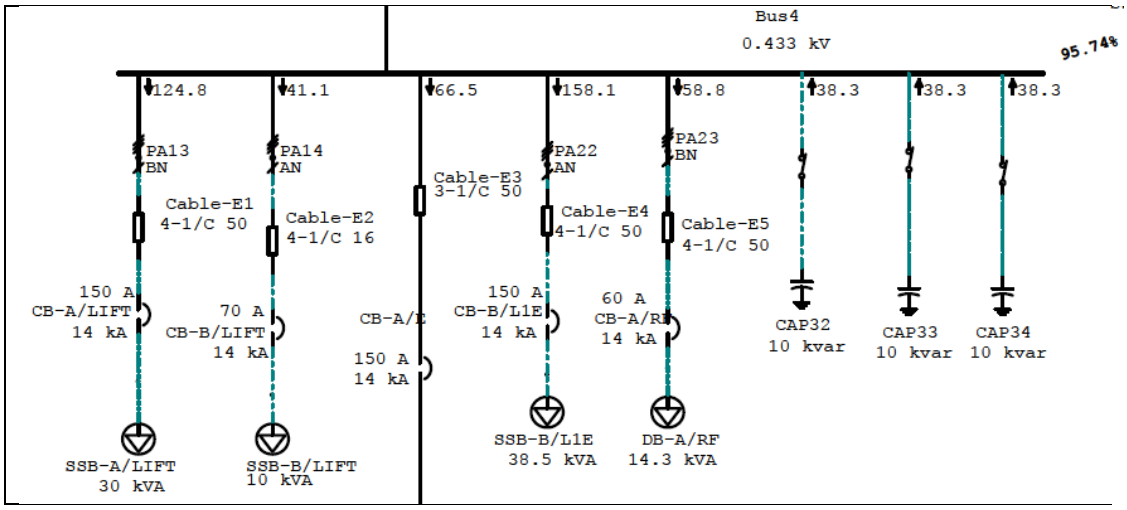


Figure 7. Improvement of %Operated Voltage Level in Bus 4

3.1.3 Three Phase Device Duty Check (DDC)

In order to check momentary & interrupting device duty, a three phase DDC check which is fault analysis for TUEDS was simulated in ETAP. The maximum short circuit fault current were determined through DDC. Table 8 shows the interrupting duty summary report in three phase DDC that was simulated by using ETAP.

Table 8. Interrupting Duty Summary Report in Three Phase DDC

ID	Condition	Rated Maximum Current(kA)	Operated Interrupting Current (kA)	Operating %
CB-1	Interrupting	36	37.056	102.9
CB-2	Interrupting	36	37.056	102.9
CB-D1	Interrupting	30	49.066	163.6
CB-D2	Interrupting	30	49.066	163.6

The alerts of three phase DDC was analysed by using results interrupting duty summary report in Table 9. According to the Table 9, it shows that specific circuit breakers are operated over 100 percentage which are operated under interrupting condition because the operated interrupting current were higher than the rated maximum current available in TUEDS. Interruption may occur several cycles after the fault to allow for downstream device to open.

3.1.4 Solution for Interrupting Condition in Circuit Breaker

The maximum short circuit fault current were determined through DDC. The single line diagram of three phase DDC simulation for TUEDS with proposed recommendation were saved. The new rating of circuit breakers with higher rated maximum which able to trip during system fault condition in TUEDS was proposed. It can avoided the significant damage of system by detected a fault condition and shut off the electric current.

Table 10. Comparison of Interrupting Duty Summary Report

ID	Operating Interrupting (kA)	Before		After	
		Rated Maximum current(kA)	Operating %	New Rated Maximum current(kA)	New Operating %
CB-1	37.056	36	102.9*	48	77.2
CB-2	37.056	36	102.9*	48	77.2
CB-D1	49.066	30	163.6*	65	75.5
CB-D2	49.066	30	163.6*	65	75.5

*Interrupting condition

Faults could cause the three phase system to become unbalanced with the result that three phase equipment. Thus, the specific circuit breakers with new rated maximum current is recommended as shown in Table 10 to avoid the circuit breakers in Taylor's University operate under interrupting capacity. According to the Table 10, it shows that specific circuit breakers are operated below 100 percentage which are operated under normal condition by open the circuit automatically on a predetermined overcurrent without damage to itself.

Figure 8 shows the operated current in CB-D1 was 49.1kA while the rated maximum current of that CB was 30kA which was 63.6% more than the rated maximum

current. It also shows the CB-D1 was operated under normal condition when the new CB 65kA rated maximum current was implemented.

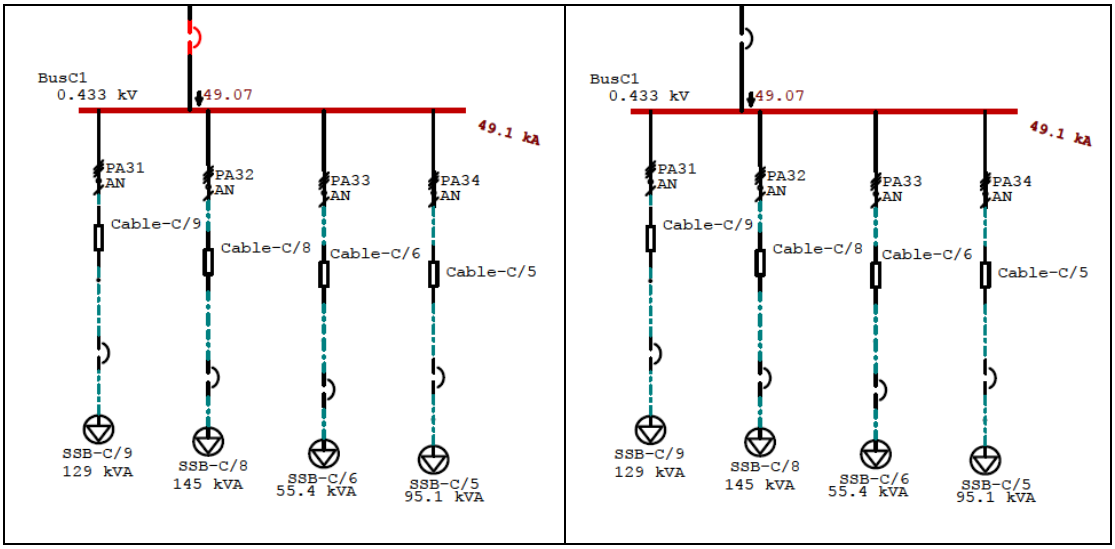


Figure 8. Operation of CB under Interrupting Condition and Normal Condition

3.2 Case 2 Incoming Feeder 1 Down

3.2.1 Under Voltage on the Buses

System configuration (scenario) was proposed and implemented in the simulation. This scenario could be a result of equipment shut down due to maintenance or faulted system. Incoming feeder 1 serves transformer 1 and transformer 3. Under this configuration, these transformers will be switch off through their respond circuit breakers. In this configuration, incoming feeder 2 is expected to carry loads of incoming feeder 1. Simulation of system performance was simulated. Table 11 shows the summary alerts during simulation while Table 12 shows the summary of LFA results when the incoming feeder 1 down.

Table 11. Under Voltage Alerts of the Simulation.

Bus ID	Condition	Rating/ Limit	Operated	%Operated Voltage
Bus T2	Under Voltage	0.433 kV	0.400 kV	92.3
Bus4	Under Voltage	0.433 kV	0.397 kV	91.7
Bus5	Under Voltage	0.433 kV	0.396 kV	91.4
CB-T2	Overload	4000Amp	5944.0Amp	148.6
T2	Overload	2.588MVA	4.153MVA	160.5

From the alerts of LFA, it can be seen that the Bus 4, Bus 5 and Bus T1 to T4 were operated under voltage condition. The normal operating condition in the bus voltage and equipment has to be within the range from 0.95pu to 1.05pu of their rated values so that the cables and equipment are operated within their rated capacities [14],

[15]. Specific cables, CBs, and transformers that were connected to transformer 2 and transformer 4 were operated under overload condition because the incoming feeder 2 was expected to carry loads of incoming feeder 1. When the carried loads in buses were increased, the specific buses that were connected from incoming feeder 2 were faced under voltage condition.

Table 12. Summary of LFA Results.

Monitoring Part	MW	MVAR	MVA	%PF
Swing buses	8.835	4.827	10.067	87.76 Lagging
Total Demand	8.835	4.827	10.067	87.76 Lagging
Total Motor Load	6.397	2.816	6.989	91.53 Lagging
Total Static Load	2.214	0.484	2.267	97.79 Lagging
Apparent Losses	0.224	1.527		

Table 12 shows the demand and losses summary report which include the total demand and the losses of the system with power factor that occurs in simulation. The active power of swing buses are 8.834MW while the apparent power are 10.196MVAR.The reactive power of swing buses are 4.585MVAR. The %Power Factor (%PF) is determined by using Eq. (3.1). There are some apparent losses due to the non-physical losses that occur in simulation. Figure 9 and Figure 10 show the buses that were connected from incoming feeder 2. By analysing the results of simulation, the Bus T2 and Bus 4 were operated under voltage condition.

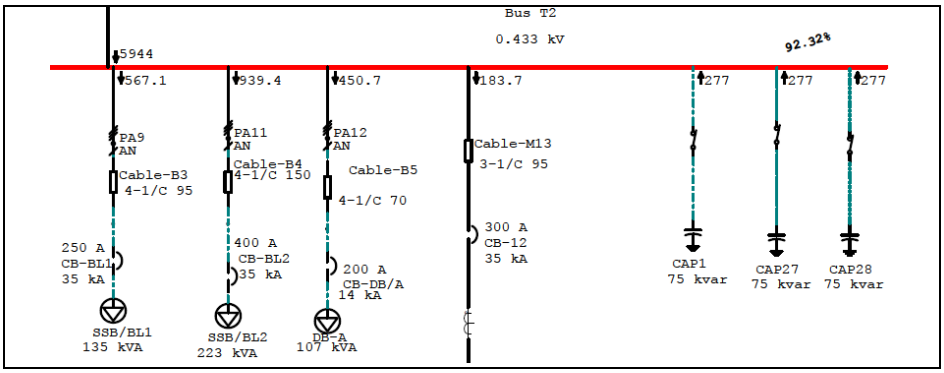


Figure 9. Under Voltage in Bus T2

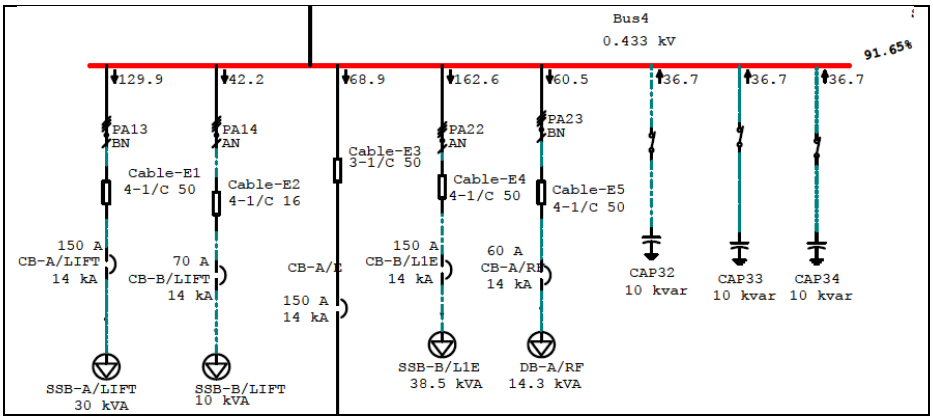


Figure 10. Under Voltage in Bus 4

3.2.2 Solution to Under Voltage Problem at the Buses for System Configuration

The easiest way to solve the overload condition in equipment is to change the size of the affecting equipment. Unfortunately the equipment in Taylor's University had already installed and the cost will be high if it needs to change to a new equipment. Thus, the issues of the under voltage for buses and overload equipment can be solved by using load shedding. The deliberate shutdown of electric power in a part or parts of a power-distribution system to prevent the failure of the entire system when the demand strains the capacity of the system. Simulation of system performance after load shedding was simulated. Table 13 shows the comparison of values of buses and equipment after the solution was implemented solution while Table 14 shows the summary of load flow results after the solution were implemented.

Table 13. Comparison of Values for Buses and Equipment Before and After the Simulation of Proposed Solution

Bus ID	**Rated Value**	**Before**		**After**		
		Operated Value	**%Operated Value**	**Operated Value**	**%Operated Value**	**Condition**
Bus T2	0.433 kV	0.400 kV	92.3*	0.428 kV	96.94	Normal
Bus4	0.433 kV	0.397 kV	91.7*	0.425 kV	94.44	Normal
Bus5	0.433 kV	0.396 kV	91.4*	0.424 kV	96.32	Normal
CB-T2	4000Amp	5944.0Amp	148.6**	2758.6Amp	47.42	Normal
T2	2.588MVA	4.153MVA	160.5**	2.160MVA	83.5	Normal

*under voltage condition **overload condition

According to the Table 13, the results show that the %Operated Voltage of buses the operated values for equipment are increased due to load shedding by reduced the demand to bring the system back into balanced. The total static and motor load are decreased due to the shutdown power of some blocks or location in Taylor's University. The location suggested are block B, carpark, rooftop and the location with high power demand of air conditioner. With this result, the improvement of this simulation in terms of capacitor banks is verified or justified. The calculation can be checked by using Eq. (3.4). The %operated voltage level are increased due to the decrease of total impedance. Therefore, this simulation is performed to ensure that the improvement of buses voltage obtained in Table 13 is valid.

Table 14. Summary of LFA Results

Monitoring Part	**MW**	**MVAR**	**MVA**	**%PF**
Swing buses	4.572	2.014	4.996	91.52 Lagging
Total Demand	4.572	2.014	4.996	91.52 Lagging
Total Motor Load	3.587	1.653	3.950	90.82 Lagging
Total Static Load	0.923	-0.029	0.923	99.95 Lagging
Apparent Losses	0.062	0.389		

Table 14 shows the improvement in the buses' power factor and reduction in the buses' reactive power when compared with Table 12. The reactive power is produced losses and leading the buses to operate under voltage condition. Table 14 shows that apparent losses are far less as compared to the losses shown in Table 12 due to reduce demand of loads by using load shedding. The Power Factor of total demand were determined by using Eq. (3.1) Figure 11 to Figure 12 show that Bus T2 and Bus 4 which were connected from incoming feeder 2 and were operated under normal condition after the solution was implemented in the simulation. The operated voltage level of Bus T2 was 0.9694pu and the operated voltage level of Bus 4 was 0.9644pu which both were increased if compare to Figure 11 and Figure 12.

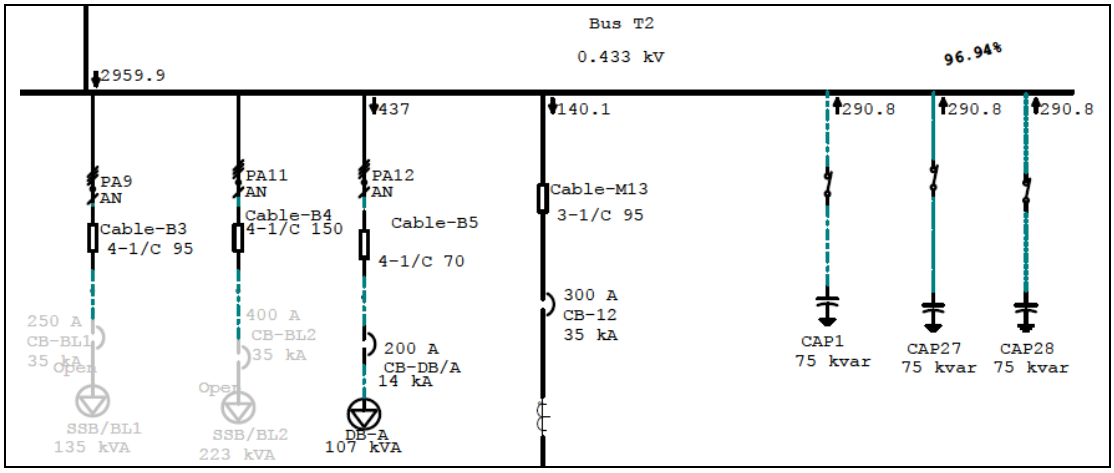


Figure 11. Improvement of %Operated Voltage Level in Bus T2

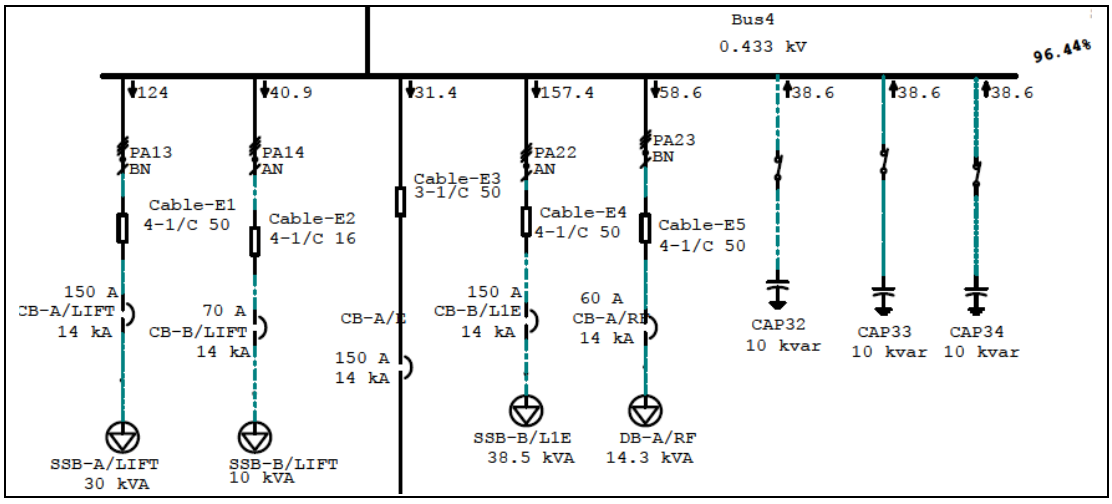


Figure 12. Improvement of %Operated Voltage Level in Bus 4

3.2.3 Three Phase Device Duty Check (DDC)

The single line diagram of three phase DDC simulation for TUEDS in case 1 was used to simulate the system configuration. When the configuration, these transformers will be switch off through their respond circuit breakers. There are no alerts in the simulation which mean the operated current is lower than the maximum

short circuit fault current of the equipment. Thus, the system is operated under normal condition and the recommendation in case 1 is acceptable. The single line diagram of three phase DDC simulation for TUEDS is recorded.

4 Conclusion

The TUEDS was simulated to determine the performance of the electrical network under normal, faulted, and contingency conditions. Upon simulation of the whole system, it was found out that certain load buses operated under 0.95 pu and the power factor at those buses are below 85%. To mitigate under voltage and low power factor conditions, sets of capacitor banks were proposed to be installed at specific locations where the respective capacitor sizes are selected with due economic consideration. This also solved the issue of system power factor. Contingency situations like Feeder 1 down, or Feeder 2 down were also simulated and system performance are checked to ensure normal operating conditions. With the load shedding scheme as solutions implemented, the system now runs under normal operating conditions. The rating of protective devices were also analysed through three phase DDC simulation. The specific circuit breakers with rated maximum current was proposed in situations where cables, equipment, and circuit breakers are experienced overloading.

References

[1] Tenaga Nasional Berhad (TNB), "Distribution Division" 2016. [Online]. Available:https://www.tnb.com.my/about-tnb/our-business/core-business/distribution-division/. [Accessed: 14-Sep-2016].

[2] N. K.Lal & D. S. E.Mubeen, "A Review on Load Flow Analysis," Vol. 3, no. 11, pp. 337–341, 2014.

[3] K. Rajesh, A. Arjunamuthu, M. Karuppasamypandiyan, & A. Bhuvanesh, "*Power Flow Analysis of 230 / 110 kV Substation using ETAP*," Available: https://www.researchgate.net/publication/260041388_Power_Flow_Analysis_of_230110_kV_Substation_using_ETAP [February, 2014].

[4] Dharamjit & D.K.Tanti, "Load Flow Analysis on IEEE 30 bus System," Int. J. Sci. Res. Publ., Vol. 2, no. 11, pp. 1–6, 2012.

[5] R. Alqadi & M. Khammash, "An Efficient Parallel Gauss-Seidel Algorithm for the Solution of Load Flow Problems," *Int. Arab J. Inf. Technol*., Vol. 4, no. 2, pp. 148–152, 2007.

[6] A.von Jouanne, "Assessment of Voltage Unbalance," *IEEE Trans. Power Deliv*., Vol. 17, no. 4, pp. 1176–1177, 2002.

[7] J. A. Jaleel and S. S. Shabna, "Load Flow Analysis and Reliability Evaluation of 220kV Kerala Power system," Vol. 3, no. 2, pp. 558–563, 2013.

[8] R. Kapahi, "Load Flow Analysis of 132 kV substation using ETAP Software," Vol. 4, no. 2, pp. 2–6, Available: https://www.ijser.org/researchpaper/Load-Flow-Analysis-of-132-kV-substation-using-ETAP-Software.pdf [2013].

[9] B. Md. Asaduzzaman Nur, M. Hasan Sourov, M. S. Muhit, M. Khaled Hossain, M.Asaduzzaman Nur, M.Hasan Sourov, M. S.Muhit, & M. Khaled Hossain , "Fault Analysis and Electrical Protection of Distribution Transformers," *Glob. J. Res. Eng*., Vol. 14, no. 3, 2014.

[10] C. J. Soni, P.R. Gandhi, & S. M. Takalkar, "Design and Analysis of 11 KV Distribution System using ETAP Software," pp. 451–456, Available:

https://www.researchgate.net/publication/305390637_Design_and_analysis_of_11_KV_Distribution_System_using_ETAP_Software [2015].

[11] R. M. Cheney, J. T. Thorne & G.Hataway, "Distribution single-phase tripping and reclosing: Overcoming obstacles with programmable recloser controls," April, pp. 238–247, 2009.

[12] M. H. BinBakar, "Design of Harmonic Filters using MATLAB," Vol. 16, no. [April, 2010].

[13] P.Dhabai, D.S. Kumari, S. Kumari, & N. N. Ghuge, "Forecasting Maximum Demand And Loadshedding," Vol. 4, no. 5, pp. 62–65, 2014.

[14] R. B. Epili & K. Vadirajacharya, "Performance Analysis of Transient Stability on a Power System Network," pp. 37–44, 2014.

[15] M. N. Malik, A. I. Toor, & M. A. Siddiqui, "Load Flow Analysis of an EHT Network using ETAP," Vol. 3, no. 6, pp. 4979–4984, 2016.

eureca 2017 – Conference Paper
Paper Number 2ME01

Effects of Manganese Oxide on the Sintered Properties of Alumina Ceramics

K.W. Andrew Ng[1*], W. J. Kelvin Chew[1], S. Ramesh[2]
[1]*Department of Mechanical Engineering,*
School of Engineering, Taylor's University, 47500 Subang Jaya, Selangor, Malaysia.
[2]*Centre of Advanced Manufacturing & Material Processing (AMMP), Department of Mechanical Engineering, Faculty of Engineering, University of Malaya, 50603 Kuala Lumpur, Malaysia.*

[*] andrewngkwongweng02@sd.taylors.edu.my

Abstract
The purpose of this current study is to improve the mechanical properties (density, hardness and fracture toughness), as well as the sinterability of alumina ceramics, through the addition of manganese (IV) oxide (MnO_2) dopants. Transitional metal dopants (including MnO_2) have been proven to be beneficial to the sintering process of alumina, as well as its mechanical properties. Thus, this project aims to investigate if this trend is recurring, as well as to establish parameters in experiments such as the optimal doping amount as well as their ideal sintering temperature in order to produce a dense alumina compact with high hardness and fracture toughness. This experiment was conducted by doping alumina with various amounts of MnO_2 dopants (0, 0.01, 0.1 and 0.5 wt%). The mixtures were then pressed and shaped, followed by sintering at four different temperatures (1250°C, 1300°C, 1400°C, and 1500°C). Next, the samples are grround and polished, before it can undergo Vicker's hardness testing. Density of samples was measured using the Archimedes principle. The density as well as fracture toughness of doped alumina is higher than that of the undoped samples. At 1300°C, the alumina sample doped with 0.01 wt% MnO_2 achieved a relative density of 96% when sintered at 1300°C, which is higher than the relative density of the undoped alumina sample sintered at 1500°C. Besides that, the sample of alumina doped with 0.5wt% MnO_2, sintered at 1400°C shows a higher fracture toughness value (7.37 $MPa.m^{1/2}$) compared to the undoped sample sintered at 1500°C (4.03 $MPa.m^{1/2}$). The hardness of alumina increases with increasing sintering temperature and dopant amount, resulting in a maximum hardness of 12.8 GPa for the sample doped with 0.5 wt% MnO_2 (sintered at 1500°C). These results indicate that doping alumina can in fact improve its sinterability, as well as its mechanical properties.

Keywords: Sintering, Relative density, Manganese (IV) Oxide, Fracture toughness, Hardness.

1. Introduction

A majority of people have always associated ceramics with pottery making, and has a brittle characteristic to it. It is however, not the most accurate denotation to the word ceramic. Ceramics obtain their properties through high temperature firing, as they are usually formed from separated solids such as powders and granules [1]. Ceramics can be categorized into two groups, the traditional ceramics, and advanced ceramics. Traditional ceramics have an inferior mechanical property, as well as poor manufacturability when compared to advanced ceramics [2]. Alumina is just one of the many examples of advanced ceramics, as they comprise of various non-metallic, polycrystalline material [1].

Alumina has many applications in the industry, such as being made into insulators in spark plugs, and as a material used to create artificial bone and joint replacements, due to its toughness, high resistance to wear and high strength [1, 2]. There are many ways that alumina can be shaped and manufactured from its powders form. Referring to the scope of this current study, the alumina will first undergo a cold isostatic press in order to give shape to the green sample (alumina powders before heating). After that, it will undergo pressureless sintering in order to allow the atoms of each divided solid to diffuse into grain boundaries, fusing with the localized particles, melding into a bigger object. By sintering the alumina, the powders will adhere with each other forming a finished solid with more ideal mechanical properties than before (state of sample after cold isostatic press).

However, it is difficult to sinter alumina to high relative density, while keeping the grain size small, in order to maintain the desired toughness as well as hardness of the material. This is because at high sintering temperature will induce grain growth in the material [3]. Although it is the easiest way to achieve a high relative density, it will however, reduce the initial hardness and toughness of the material that is exhibited by the material before grain growth. Besides that, the difficulty to obtain alumina powder size of less than 20 nm with a narrow size distribution and weak agglomeration also contributes to the difficulty of preparing the bulk nanocrystalline alumina ceramic [3].

In hopes of avoiding the aforementioned difficulties from occurring, different weight percent of dopants (MnO_2) will be tested in order to determine if it will have any effects on the mechanical properties of alumina ceramics, as well as to compare and confirm the optimal sintering temperature and the best amount (wt%) of dopants to add to the mixture to yield the best mechanical properties (density, toughness and hardness).

2. Research Methodology

In order to determine how varying concentrations of manganese (IV) oxide (MnO_2) dopant will influence the characteristics of the alumina, the samples were first prepared, before having its mechanical and physical properties tested. α-Alumina powder (Nabalox No. 713-10) with a purity of 99.7% with a specific surface area of 5-9 m^2/g with an average grain size of 0.8 μm was used in this study.

2.1 Sample Preparation

A specific order of steps was followed, when preparing the doped and undoped alumina samples. The steps below indicate the required processes needed to fabricate these samples from separated solids. Steps 2.1.1 - 2.1.3 were only carried out on the doped alumina mixture.

2.1.1 MnO_2 Doping in Alumina and Ultrasonification

First, the powders were measured up to 50 g, as each alumina disc will only weigh around 2.5 g. This guarantees that there is sufficient alumina powder, in case the samples fabricated are flawed. MnO_2 was then added to alumina in concentrations of (0.01, 0.1 and 0.5 wt%). After this, to ensure that both separated solids (alumina and MnO_2) were mixed thoroughly, an ultrasonic bath was used. The powder mixture was put into a beaker, and was mixed with 200 ml of ethanol. Next, the beaker was placed into the ultrasonic bath, with a water level that slightly exceeds the height of ethanol in the beaker.

The intensity of the ultrasonic bath was turned up to 40 kHz for 20 minutes. The mixture in the beaker was stirred every 5 minutes while the ultrasonic bath was still running. It is important to ensure the spoon was washed with ethanol to remove any agglomerates (alumina or MnO_2) that might be adhering to the surface of the spoon, and return them back into the beaker, so that the amount of dopant and alumina powders can be maintained.

2.1.2 Ball Milling

After adding the dopant into the alumina powder, and thoroughly mixing them in the ultrasonic bath, the doped mixture of alumina underwent ball milling, to break down the powders, as well as any agglomerates, in order to facilitate the sintering process of alumina to a high relative density [3]. The slurry contained in the beaker was poured into the ball milling machine, followed by the ball mills. The ball milling process ran at 500 rpm for 30 minutes.

After it was done, the mixture of slurry and ball mills was sieved, in order to separate the slurry from the ball mills. Ethanol was used to remove any agglomerates of concern (alumina and MnO_2) from the sieve and the ball mills until the solution dripping from the sieve becomes colourless.

2.1.3 Grinding and Sieving

The slurry (alumina doped with 0.01, 0.1 and 0.5wt% of MnO_2) as mentioned previously in 2.1.2 were collected in a bowl, and was left in a convection oven in order to vaporize all the alcohol from the solution, thus leaving behind only the solid constituents of the slurry. Next, the doped alumina of were ground and sieved up to 212 microns. This step was imperative, as finer alumina powders will result in a better sintered product (less porosity).

2.1.4 Green Sample Preparation

In this stage, the alumina powders were subjected to a uniaxial press using a Clarke CSA10BB Hydraulic Bench Press that shaped each sample by pressing them at 750 psi for 10 seconds. Next, the alumina powder compact underwent a cold isostatic press using the MTI Corp CIP 50A Cold Isostatic Press machine in order to compact the sample in all directions, thus reducing distance of diffusion among each separated solid, thus increasing diffusion rate of the sample, which will result in better densification of the finished product.

2.1.5 Sintering Process

Each green specimen has undergone 2 hours of sintering in the Furnace model XY-1200N at 1250°C, 1300°C, 1400°C, and 1500°C with a ramp rate of 10°C/min. By sintering at different temperatures, the author will be able to study the effects of different temperatures on both doped and undoped samples. This is a form of presureless sintering, as pressure sintering would cost a lot more, and would result in a higher budget.

2.1.6 Grinding and Polishing

The alumina samples that has undergone sintering at 1400°C and 1500°C was grinded using SiC (silicon carbide) grinding paper of (120, 240, 600, 800 and 1200 grit size). For the samples that were sintered at 1250°C and 1300°C, SiC paper of 120 and 240 grit were not used, as it has caused the sample to slope on one side. This slope is present in samples sintered only at low temperatures as they lack the hardness as compared to the samples that were sintered higher temperatures (1400°C and 1500°C). Thus, only SiC papers of 600, 800 and 1200 grit were used for the samples that were sintered at 1250°C and 1300°C. The wet grinding process was carried out at 50 rpm at 2 minutes for each sample.

After finishing the grinding of the samples, diamond based polishing was carried out in order to attain a polished finish. Diamond paste of 6 microns and 1 micron grades were applied onto the polishing cloth, and spread using lubricant. The polishing process was carried out at 20 rpm for 2 minutes. The grinding rate as well as duration was determined by means of trial and error. The grinding rate was set as such (50 rpm for wet grinding and 20 rpm for diamond based polishing), as the sample had to be held in place by hand. If the grinding speed was increased any more, increase the risk of damaging the alumina sample, as it may fly off the revolving plates.

2.2 Determination of Physical and Mechanical Properties

Once the sample preparations were completed, measurement of the mechanical properties for each sample was made.

2.2.1 Bulk Density Analysis

Bulk densities of the sintered compacts (≥ 95% theoretical density) were determined through a water immersion technique based on the Archimedes principle

using a Mettler Toledo Balance AG204 densi-meter while adhering to the ASTM C-29 standard. The bulk density was calculated using equation 1 below.

$$\rho = \frac{W_a}{W_a - W_w} \rho_w \quad (1)$$

ρ = Bulk density of sample
W_a = Weight of the sample in air
W_w = Weight of sample in water
ρ_w = Density of distilled water

2.2.2 Vicker's Hardness and Fracture Toughness Test

The Vicker's hardness and fracture toughness test was conducted using MV-01 machine manufactured by Matsuzawa. The indentation was made using a pyramidal diamond indenter with an applied load of 10 kg. The load was applied slowly (without impact) and was held in place for 10 seconds. All parameters of the experiment adhered to the ASTM E384-99 and ISO 14705 standards in order to get an accurate result. Once indentation was made, the crack length (L_1, L_2, L_3, L_4) as well as the length of indentation (D) was measured using a filar micrometer attached to a microscope. The hardness value was obtained from equation 2, and the fracture toughness value was obtained from equation 3. Illustrations for the hardness and fracture toughness calculations are in Figures 1 and 2 respectively.

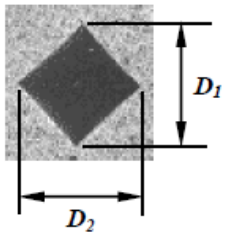


Figure 1. Values needed to determine hardness value

$$H_v = \frac{1.854\,P}{D^2} \quad (2)$$

P = Applied Load (N)
D = Average Diagonals = $\frac{D_1 + D_2}{2}$

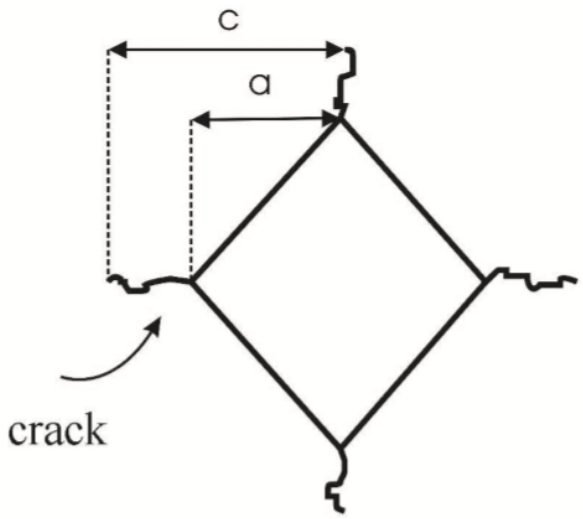


Figure 2. Illustration of indentation for fracture toughness determination [4]

$K_{IC} = 0.16 \times \left(\frac{c}{a}\right)^{-1.5} \times (H \times a^{0.5})$ [5] (3)

K_{IC} = Fracture toughness (MPa·m1/2)
H = Vickers hardness (MPa)
P = Test load in Vickers hardener (MPa)
c = Average length of the cracks obtained in the tips of the Vickers marks (microns)
a = Half average length of the diagonal of the Vickers marks (microns)

3. Results and Discussion

After subjecting each sample (total of 16 samples) to tests, results of the mechanical properties were obtained. These results are the bulk density analysis, as well as the hardness and fracture toughness derived from the Vicker's indentation method.

3.1 Bulk Density

The bulk density of each sample with varying dopant amount and sintering temperature were plotted on a graph shown in figure 3. At the sintering temperature of 1250°C, the undoped alumina sample exhibits the highest relative density of 94.72%, as compared to the doped samples. However, at sintering temperatures of 1300°C and 1400°C, the undoped sample displays a reduced bulk density, and finally it increases to a relative density of 95.69% at 1500°C. The samples doped with 0.01wt% shows the most benefit in the densification of the compact during sintering, as it has the highest bulk density at 1300°C, 1400°C and 1500°C. It was able to aid the densification of alumina up to a relative density of 96% when sintered at 1300°C, which is higher than the relative density of the undoped alumina sample sintered at 1500°C. The same trend was also observed by Ramesh et al., as the sample doped with 0.05wt% MnO_2 exhibits higher bulk density than the other samples [6]. Since both dopant concentrations in alumina are relatively similar, and yield maximum theoretical density compared to other samples, the optimal dopant concentration range for fabricating alumina to a high bulk density was found (0.01wt%-0.05wt%).

Table 1. Relative density of the MnO_2-doped alumina samples.

Sintering temperature (°C)	Theoretical density (%)			
	0 wt% MnO_2	0.01 wt% MnO_2	0.1 wt% MnO_2	0.5 wt% MnO_2
1250	94.72	93.99	93.09	92.24
1300	92.31	96.00	94.36	91.35
1400	92.97	95.30	94.84	94.98
1500	95.69	96.94	96.38	96.03

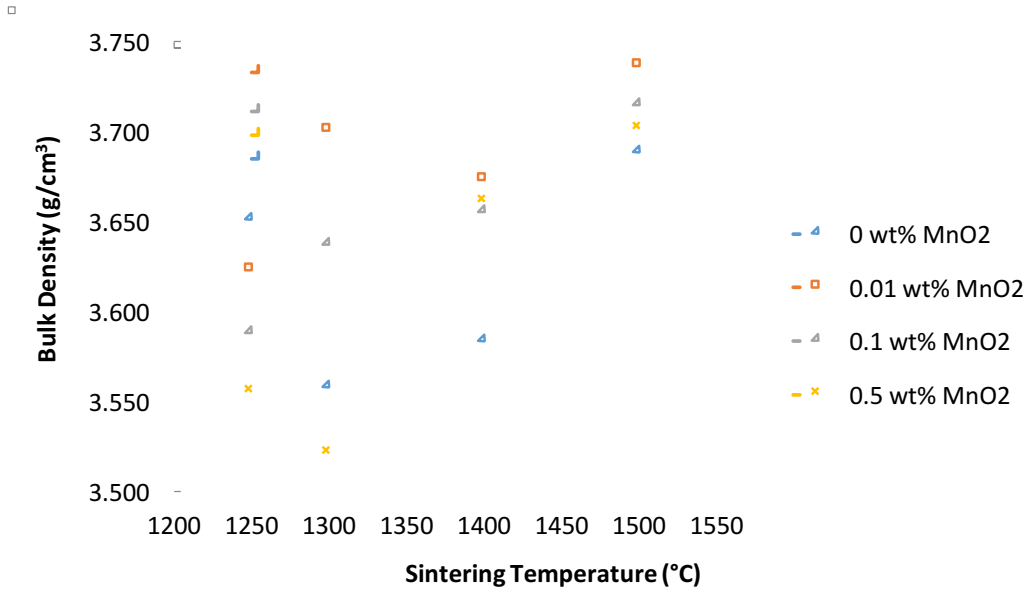


Figure 3. Graph of bulk density of samples against sintering temperature

This is evident that the addition of MnO_2 into alumina enhances the consolidation process at lower sintering temperatures. The sample doped with 0.1wt% of MnO_2 has a bulk density that increases steadily with sintering temperature. The alumina specimen doped with 0.5wt% MnO_2 had a decreasing bulk density when sintered at 1250°C and 1300°C. However, at sintering temperatures of 1400°C and 1500°C, the sample (0.5wt% doped alumina) attained a relative density of 94.98% and 96.03%. This is abnormal, as the bulk density of the undoped sample was supposed to increase with increasing sintering temperature as observed by the sample that is doped with 0.1 wt% of MnO_2 [6, 7]. This error may have been induced into the experiment during the sample preparation phase, when minute amounts of alumina powder spillage occurred as it was poured into a cast in order to undergo hydraulic pressing. As a result of the aforementioned error, it was possible that the non-linear relation of temperature was caused by coarsening of the sample, most likely due to a more dominant sintering mechanism that causes coarsening, instead of densification such as surface diffusion, lattice diffusion and vapour transport, leading to the fabrication of an alumina specimen with low bulk density. Figure 4 shows the difference in surface microstructure of a

dense alumina specimen, compared to one that is porous, caused by a dominating coarsening mechanism [8].

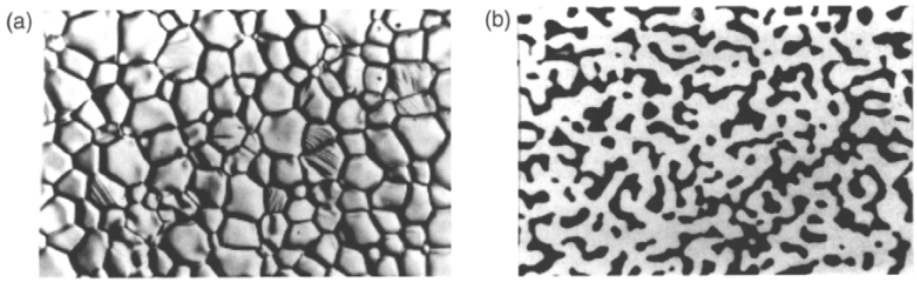


Figure 4. Surface of (a) dense alumina and a (b) porous alumina [8]

3.2 Vicker's Hardness

Figure 5 shows the effects of sintering temperature and the addition of MnO_2 dopants, and how it affects the hardness of alumina.

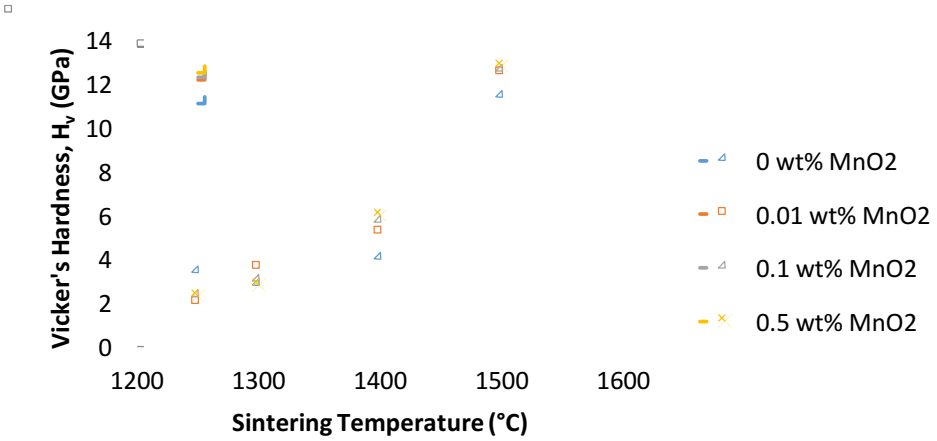


Figure 5. Graph of hardness of samples against sintering temperature

At the lowest sintering temperature (1250°C), the undoped sample had the highest hardness of 3.4 GPa. This was contrary to what was reported by Ramesh et al.[7], as at 1250°C, the hardness of samples should increase with increasing dopant amount. The hardness of the undoped sample dropped, and is the lowest (2 GPa) as compared to the doped samples at a sintering temperature of 1300°C, which should not happen, as the hardness of undoped alumina specimen should have increased with an increase in sintering temperature, as observed by Ramesh et al. [7] in Y-TZP. This irregularity in hardness readings of the sample have been caused by coarsening of the sample which have led to the reduction in hardness of the specimen. At the aforementioned sintering temperature (1300°C), the hardness of the 0.01wt% alumina sample was the highest (3.6 GPa), as it has the highest bulk density compared to the other specimens that were sintered at the same temperature. The higher degree of

densification of the aforementioned sample resulted in a specimen with maximum hardness. When sintering temperature was increased to 1400°C and 1500°C, the hardness of all samples increased, with the alumina sample doped with 0.5wt% having the highest hardness of 6 GPa and 12.8 GPa respectively. All doped samples exhibited higher hardness as compared to the undoped sample at sintering temperatures of above 1250°C. The hardness of each sample increased with increasing sintering temperature. A rapid increase in hardness of all samples occurred when sintered at 1500°C (increased from a range of 4-6 GPa until 11.4-12.8 GPa). This trend of increase in hardness of doped samples proves that MnO2 dopant was capable of increasing the hardness of fabricated alumina parts. It should also be noted that at sintering temperatures of 1400°C and 1500°C, the hardness of all samples increased with increasing dopant amount.

In a study conducted by Erkalfa et al. [9] on how MnO2 affected the microstructural development of alumina, it was reported that the hardness of undoped alumina sintered at 1350°C, 1450°C and 1550°C are 18.24 GPa, 20.59 GPa and 22.56 GPa respectively [9]. These values were significantly higher than the values of hardness of the undoped alumina obtained from this experiment. This difference in reading may have been caused by the difference in the average particle size of alumina powder used. In this experiment, alumina powder with an average particle size of 0.9 μm was used, whereas the alumina powder used by Erkalfa et al. [9] was much finer, with an average particle size of 0.37 μm. The reduction of hardness value obtained from this experiment, as compared to the values obtained from literature review may have been caused by excessive grain growth, as samples with an overall smaller average grain size will exhibit higher hardness (refer to figure 6). The hardness of the sample is sensitive to alumina with finer grain sizes but is not really affected by larger grain sizes, as it reaches a hardness stabilizing point after the grain of the alumina exceeds 9 μm. Therefore the critical grain size lies in between the range of 3 to 9 μm [9]. Therefore, in order to fabricate an alumina part with high hardness, it is imperative to keep the grain sizes close to the range of the identified critical grain size (3 to 9 μm).

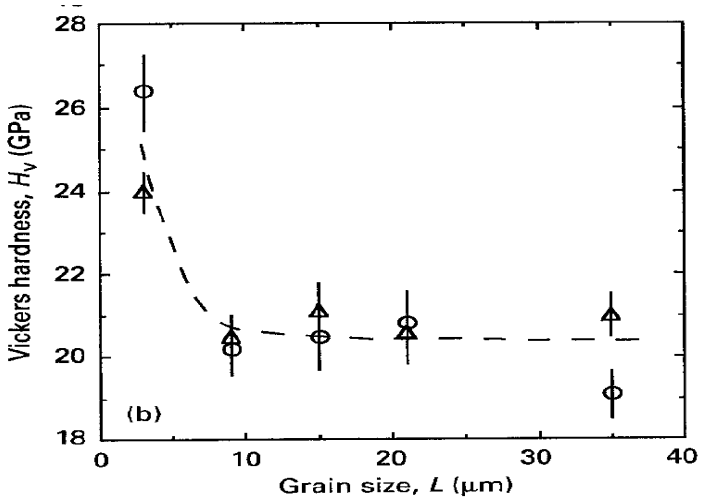


Figure 20. Effect of grain size on the hardness of samples [9]

3.3 Fracture Toughness

The effect of doping alumina with MnO_2, and how it affects the fracture toughness of the samples are shown in Figure 6.

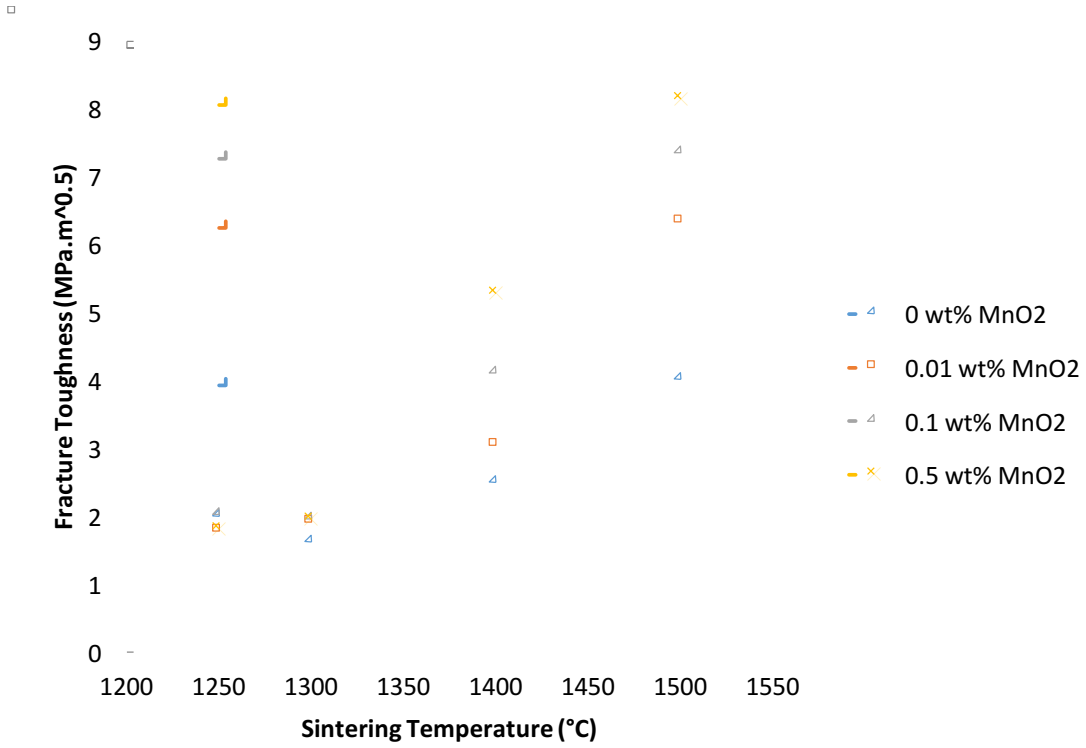


Figure 5. Fracture toughness of samples against sintering temperature

Samples sintered at 1250°C and 1300°C had a fracture toughness ranging from 1.63 to 2.04 MPa.m$^{1/2}$ for all samples. However, once the sintering temperature was increased to 1400°C and 1500°C, the fracture toughness of all samples increased. This degree of increase in fracture toughness of samples rises with higher amounts of dopant concentration at higher sintering temperatures (sample doped with 0.5wt% MnO_2 sintered at 1500°C in this study has the highest fracture toughness) [7, 10, 11]. This however was not observed at 1250°C where the sample doped with 0.1 wt% MnO_2 showed the highest fracture toughness followed by the undoped sample, then, followed by samples doped with 0.05 wt% and 0.01 wt% MnO_2 respectively. This irregularity was caused by the low bulk density of samples caused by coarsening of the sample after sintering. The sample of alumina doped with 0.5wt%, sintered at 1400°C showed a higher fracture toughness value (7.37 MPa.m$^{1/2}$) compared to the undoped sample sintered at 1500°C (4.03 MPa.m$^{1/2}$). This observation is critical, as it proves that when MnO_2 was used as a sintering additive in alumina, it was capable of improving fracture toughness at a lower temperature. At 1500°C, the fracture toughness of the sample with 0.5wt% of MnO_2 attained the highest fracture toughness of 8.16 MPa.m$^{1/2}$.

In this study, at 1400°C, the sample doped with 0.5 wt% MnO_2 had a fracture toughness of 5.29 MPa.m$^{1/2}$, whereas the undoped sample had a fracture toughness of only 2.51 MPa.m$^{1/2}$. This showed that by doping alumina with only 0.5 wt% MnO_2, its fracture toughness when sintered at 1400°C could be increased by more than two times. This was also observed by Vishista et al. [10] where fracture toughness of alumina (sintered at 1400°C) was increased from 3.7 MPa.m$^{1/2}$ (undoped alumina) to 5 MPa.m$^{1/2}$

(alumina doped with 0.5 wt% AgO). Wang and Huang [11] also made similar observations, as fracture toughness of alumina (sintered at 1450°C) was increased from 4.4 MPa.$m^{1/2}$ (undoped alumina) to 5.2 MPa.$m^{1/2}$ (alumina doped with 0.5 wt% TiO2). Although the increase in fracture toughness in both studies were not as significant as the one in this particular study, the trend still remains quite similar, as in all cases, fracture toughness increased up to a fracture toughness around 5 MPa.$m^{1/2}$ from a lower value obtained from the undoped alumina.

4. Conclusion

The sintering property of alumina ceramics, with the addition of MnO_2 has been investigated. By adding the sintering additive into alumina, it was able to improve the densification, as well as the hardness and fracture toughness of the alumina ceramics. The optimal sintering temperature in order to obtain high density and fracture toughness has been effectively reduced to 1300°C and 1400°C respectively.

At 1300°C, the alumina sample doped with 0.01 wt% MnO2 achieved a relative density of 95.37% when sintered at 1300°C, which was higher than the relative density of the undoped alumina sample sintered at 1500°C. Besides that, the sample of alumina doped with 0.5 wt% MnO_2, sintered at 1400°C shows a higher fracture toughness value (7.37 MPa.$m^{1/2}$) compared to the undoped sample sintered at 1500°C (4.03 MPa.$m^{1/2}$). As for the hardness of the samples, it increases with sintering temperature and, dopant amount. This resulted in the achievement of maximum hardness of 12.8 GPa for the sample doped with 0.5 wt% MnO2 (sintered at 1500°C).

Thus, it was concluded that for densification, the optimal dopant amount that should be added is 0.01 wt% with an ideal sintering temperature of 1300°C, as the sample has a high theoretical density of 95.37%. However, if a higher density alumina is required, the sintering temperature can be increased up to 1500°C for maximum densification (96.3%). As for hardness, the optimal dopant amount needed to fabricate alumina of high hardness was 0.5 wt% sintered at 1500°C, as this sample exhibited the highest hardness (12.8 GPa) compared to other alumina samples with lesser amount of dopant and lower sintering temperature. Lastly, the ideal sintering temperature and dopant concentration to create alumina with a high fracture toughness is 1500°C and 0.5 wt% respectively. This specific specimen exhibits the highest fracture toughness (8.16 MPa.$m^{1/2}$).

Acknowledgement

This final year project would not have been successful without the help of Ms. Hartini from University of Malaya.

References

[1] D. Salamon, *Advanced Ceramics*. Elsevier Inc., 2014.
[2] M. Mohanty, “Medical Applications of Alumina Ceramics,” *Trans. Indian Ceram. Soc.*, vol. 54, no. 5, pp. 200–204, 1995.
[3] J. Li and Y. Ye, “Densification and grain growth of Al2O3 nanoceramics during pressureless sintering,” *J. Am. Ceram. Soc.*, vol. 89, no. 1, pp. 139–143, 2006.
[4] E. Rocha-rangel, “Fracture Toughness Determinations by Means of Indentation

Fracture," no. c, 2003.
[5] A. G. E. and E. A. Charles, "Fracture Toughness Determination by Indentation," *J. Am. Ceram. Soc.*, vol. 59, no. 7–8, pp. 371–372, 1976.
[6] S. Ramesh, K. L. Aw, C. H. Ting, C. Y. Tan, I. Sopyan, and W. D. Teng, "Effect of Copper Oxide on the Sintering of Alumina Ceramics," *Adv. Mater. Res.*, vol. 47–50, pp. 801–804, 2008.
[7] S. Ramesh, W. J. Kelvin Chew, C. Y. Tan, J. Purbolaksono, A. M. Noor, M. A. Hassan, U. Sutharsini, M. Satgunam, and W. D. Teng, "Influence of manganese on the sintering properties of tetragonal zirconia," *Ceram. - Silikaty*, vol. 57, no. 1, pp. 28–32, 2013.
[8] M. Sciences, "4.1 Sintering of Ceramics," in *Handbook of Advanced Ceramics*, 1st ed., vol. i, S. Sōmiya, Ed. Academic Press, 2003, 2003, pp. 187–222.
[9] H. Erkalfa, Z. Misirli, and T. Baykara, "The Effect of TiO2 and Mn02 on Densification and Microstructural Development of Alumina," *Ceram. Int.*, vol. 8842, no. 97, pp. 81–90, 1998.
[10] K. Vishista, D. D. Jayaseelan, F. D. Gnanam, K. Vishista, D. D. Jayaseelan, and F. D. Gnanam, "Densification and Mechanical Properties of Sol-Gel Alumina : Effect of Sinter Additives Densification and Mechanical Properties of Sol-Gel Alumina : Effect of Sinter Additives," *Trans. Indian Ceram. Soc.*, no. January 2015, pp. 37–41, 2014.
[11] C. Wang and C. Huang, "Effect of TiO 2 addition on the sintering behavior , hardness and fracture toughness of an ultrafine alumina," *Mater. Sci. Eng. A*, vol. 492, pp. 306–310, 2008.

Upper Limb Tracking System

Arif Akmal Bin Kamarudin*, Mr. Mohd Farid Bin Aladdin
School of Engineering, Taylor's University, Malaysia

* *arif_akmal@hotmail.com*

Abstract
The objective of this research is to conceive, design, integrate and operate an upper limb motion tracking system. Quantification of movement using sensors to track the affected area enables physiologists and patients to compare, understand and visualize therapy progress. One of the method used for visualization is to use a robotized prosthetic arm that mimics movement of the upper limb using data obtained from the sensors. This research is carried out to develop motion tracking technology for medical and for human-machine interaction. An array of conductive ink based flex sensors are sewn along the finger region of a glove to measure the bending of the finger during flexion motion. Potentiometers are placed parallel to the wrist to measure the degree of rotation of the hand during palmar and dorsal flexion, and radial and ulnar abduction. Resistive flex sensors (RFS) and potentiometers can measure bending and flexing with relatively low budget. Holders and enclosure of the electronic parts are 3D printed and attached to the forearm. Gestures initiated by fingers and wrist will cause variations in the value of voltage in the electronic circuit. A programmed microcontroller interprets and process the data before transferring it to computer for data analysis or to a robotized prosthetic arm for movement simulation. Data analysis allows collection data such as the angle of fingers flexion and angle of flexion and abduction of the palm can be used to gauge recovery process of a patient. The motion tracking system can also be programmed as a controller for robotic arm consisting of servos for articulation to mimic flexing of fingers and flexion and abduction of palm. Results obtained from the research were validated as the motion tracking system able to approximately measure the degree of angle during flexion of fingers and both palmar and dorsal abduction and radial and ulnar abduction with an acceptable degree of repeatability in both grip and flat position of hand. As a conclusion, measurement of ambulation of body parts enables quantification of movement important for data collection and for potential future robotic purposes.

Keywords: Robotics, Rehabilitation, Medical Informatics, 3D printing, Prosthetic Hand

1. Introduction

Mobility and movement to perform activities of daily living (ADL) are made possible by musculoskeletal system working in an ideal condition. However, any impairment in the system by internal or external causes will contribute to the severe impairment to movement and function of limbs and joints. A person who have the system compromised must undergo rehabilitation with treatments varying depending on the affected areas. Joint range of motion (ROM) is a go-to measure used for hand rehabilitation. Invasive techniques used in the diagnosis includes x-rays, Health Assessment Questionnaire (HAQ), traditional measurements using measuring tape and specialized angle-measuring instruments, and grip strength apparatus [1]. Research has shown that with correct modifications, the number of activities in the diagnosis can be greatly reduced [2].

Quantification of movement from articulation of joints enables deeper understanding of patients' recovery by comparing data accumulated throughout the duration of rehabilitation or kinesiology sessions. Furthermore, it provides a convincing evidence to back the results gathered from questionnaires which are mostly qualitative. This can be achieved using electronic that can measure mechanical, analogue movements to form of data that can be interpreted by computers. With proper programming, data received can be visualize effectively using graphs. In addition to data visualization, quantification enhances rehabilitation through gamification. By incorporating gaming into rehabilitation, it enables acceleration of physical recovery process while helps to reduce stress that is often experienced by patients undergoing medical treatment.

Flexion and extension can be measured using different kind of sensors such as accelerometers [3], gyroscopes [4] or magnetometers but often suffers problems from crosstalk [5] or integration drifts along the vertical axis, requiring additional processing of data. In this case, resistive flex sensors (RFS) represent a lucrative alternative as it can be applied into not only as a tool to measure angle of flexion by joints but also to measure shapes or wide variety of surface geometry [6, 7]. RFS allows for tracking segments of body while being unobtrusive, LIGHT WEIGHT, easy-to-operate, cost effective and requires a relatively low power consumption even when use continuously over extended period.

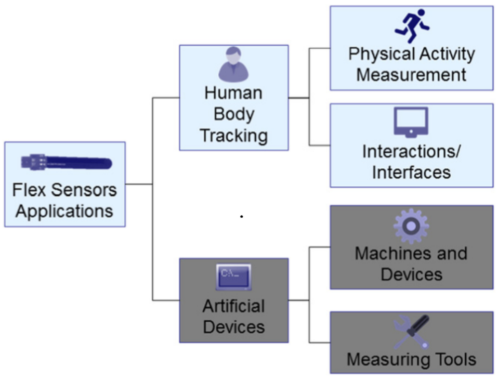


Figure 1. Tree diagram representing possible use of flex sensors [8]

Thanakodi [9] conducted a research of using conductive ink based flex sensors to measure flexion of the fingers to wirelessly control a robotic hand as an alternative to a very simple 2 or 3-fingers gripping tool of an Explosive Ordnance Disposal (EOD) robot. The testing shows that it is possible to use the method of measuring finger flexion to control a robotic hand to mimic hand movement. However, the angle of movement of middle and index finger does not translate well to the robotic hand due to rough joints caused by error during 3D printing and assembly. Moreover, lagging between the flexion of a user finger and flexion of robotic hand is present and increases from 0.5 second to 1 second when both system is increasingly moving apart from each other from 0 to 10 metres.

2. Research Methodology

In this section, methods that are involved in the researched are discussed and its justifications are provided.

2.1 Assembly

2.1.1 Flex Sensor

To measure degree of flexion of fingers, a conductive ink based RFS will be placed at each finger. RFS does not require source power to change its resistance value and is considered as a passive device. It contains resistive ink laid on a flexible plastic substrate that is shaped in a thin strip with varying length. Conductive ink is present within the layers of flex sensor substrate. When it is laid flat (at rest), it is characterized by its intrinsic resistance. As it is bent inward, conductive ink inside the strip stretches causing fewer adjacent resistive particles to come into contact which in turn, causing resistance to increase [10]. The sensors will continuously change its resistance depending on the bending therefore making it possible to acquire continuous data of flexion of fingers.



Figure 2. FLX-01 (Spectra Symbol)

Table 1. Mechanical and Electrical Specifications

Mechanical	Electrical
-Life cycle: >1 million -Height: ≤0.43mm -Temperature range: -35°C to +80°C	-Flat Resistance: 10K Ohms ±30% -Bend Resistance: minimum 2 times greater than the flat resistance at 180° pinch bend -Power Rating: 0.5 Watts continuous; 1 Watt Peak

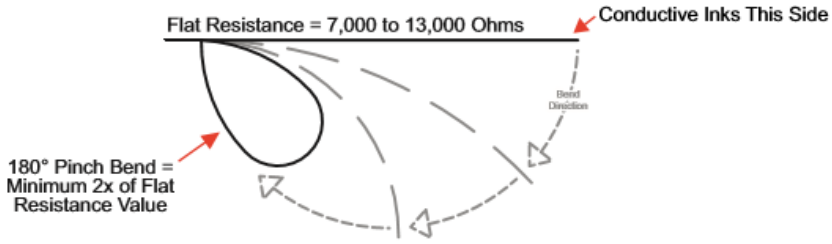


Figure 3. Angle of bending and resistance specifications for flex sensor [11]

The sensors will vary its resistance value depending on the angle of pinch bend when a finger is bent towards the palm (gripping action). At rest, the plastic strip that contains the inductive ink will have an intrinsic resistance. From the batch of RFSs obtained for this research, it measures value of resistance ranging at 10K Ohms when it is laid rest and maximum resistance value of 110K Ohms when fully bend inwards. They are placed along fingers in such a way that whenever a flexion motion is executed by each finger, the bending will be transferred to the sensors and therefore, bending along the fingers can be measured.

A voltage divider configuration is used to connect the RFSs to the Arduino board. Using this configuration, the relation of resistance due to flexing the RFS and the voltage reading across it can be visualize.

V=IR [1]

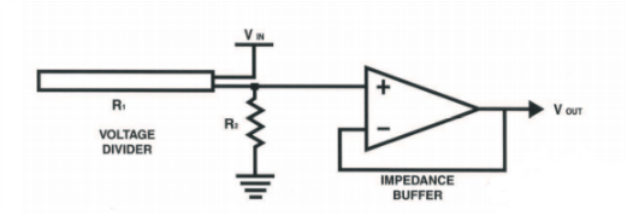


Figure 4. Voltage divider circuit of the flex sensor [12]

$$V_{out} = V_{in}\left(\frac{R_1}{R_1+R_2}\right) \quad [2]$$

where V_{out} = Voltage flowing out of voltage divider (5V)
V_{out} = Voltage flowing out of voltage divider
R_1 = resistance value of RFS
R_2 = resistance value of fixed resistor (10K Ohms)

All RFSs are connected to the 5V output of the Arduino, the V flowing into each RFS circuit is constantly at 5V. As resistance R increases, the current I of the voltage divider decreases and vice versa. RFS characteristics are measured in terms of voltage output V (instead of resistance R) against bending angle ϑ. [13-19]. Output V values for 5 RFSs are analogue and are attached to analogue pin A0 to A4 of the Arduino microcontroller.

2.1.2 Potentiometer

Rotary potentiometers are used to measure the angle of flexion and reduction of the hand. Two rotary potentiometers are placed near the wrist to measure the rotation and enclosed in a casing. For this research, 2 rotary potentiometers with maximum resistance of 500k Ohms

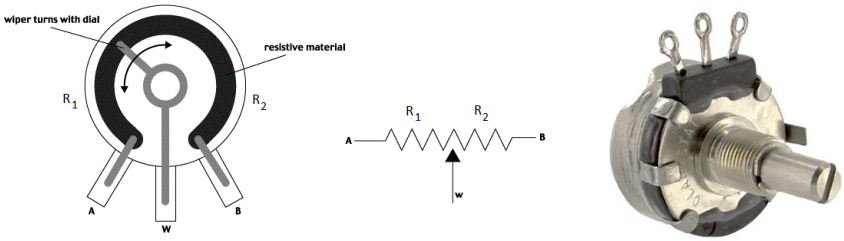


Figure 5. From left, how rotary potentiometer works, circuit diagram of a potentiometer [20] and an actual rotary potentiometer [21]

Rotary potentiometers are used as rotary angle sensors, measuring the angle difference between the palm and wrist of the wearer. Angle is measured by the rotation of the knob of the potentiometer with maximum angle of 300°±5° based on simple testing to the potentiometers used in this research. Potentiometers are suitable to be used in this case as the maximum angle of rotation along the wrist from neutral position is 60° for both hyperextension and flexion, 20° for radial flexion and 30° for ulnar flexion.

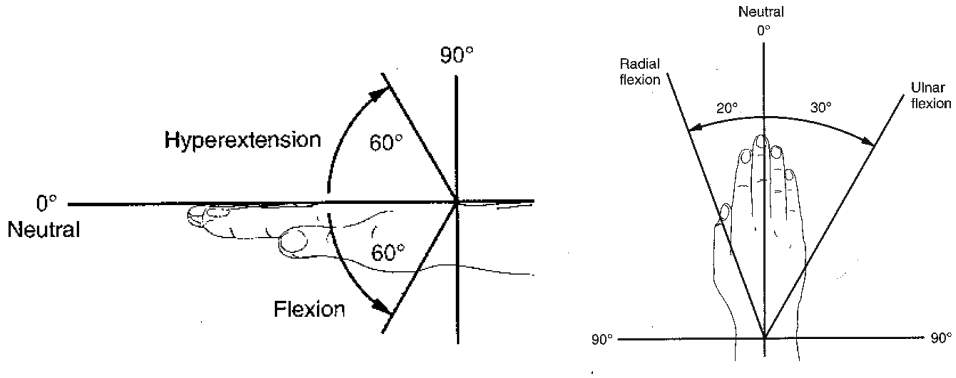


Figure 6. Wrist Joint Motions [22]

2.1.3 Connection

Arduino microcontroller is used to detect readings obtained from the sensors and output data required for measurement by articulation of hand parts. The microcontroller will be programmed for two purposes: a) converting and mapping voltage changes to value that represent degree angle of movement of fingers and palm, b) send the data through serial port for data analysis and c) enabling control of robotic prosthetic arm through direct connection to the output pins of the Arduino Mega board.

When a variable resistor is connected to analogue pin of an Arduino microcontroller, the code needs to specifically state the location of the analogue input using analogRead(pin) syntax where pin is the number of pin in which a variable resistor is connected. This analogRead library will automatically map the value of 0 to 5 volts into 0 to 1023 integer or 0.0049 volts for each unit thanks to the 10-bit analogue to digital converter in the microcontroller. Coding is done through Arduino Integrated Development Environment and the language used is C++. The following is flow of process that occurs in the microcontroller during operation.

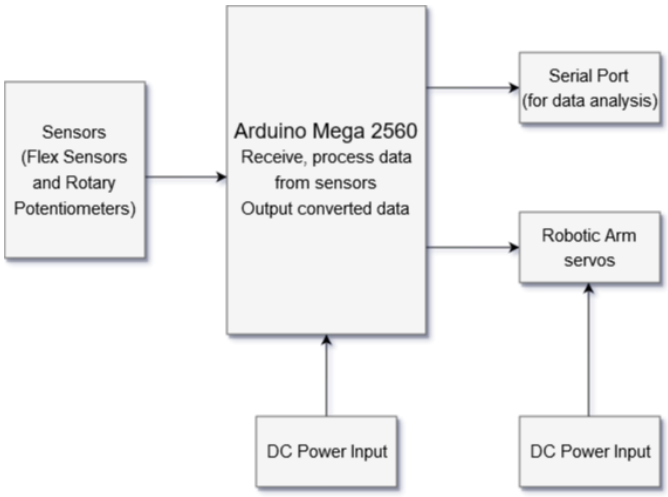


Figure 7. Process flow of the motion tracking system

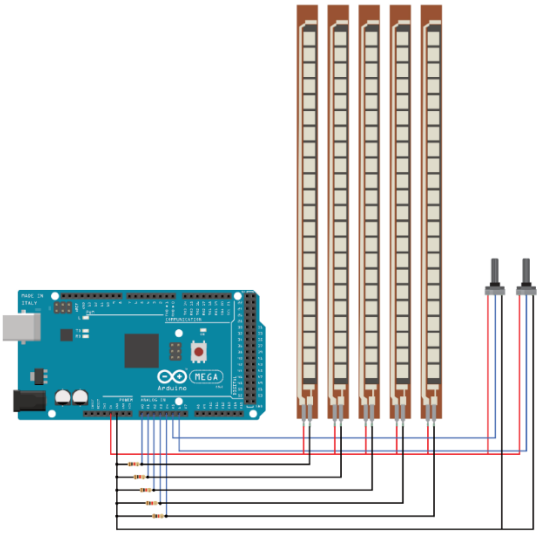


Figure 8. Connection diagram of the setup consisting of Arduino Mega microcontroller, RFSs with each connected to one 10K Ohms fixed resistor and 2 rotary potentiometers.

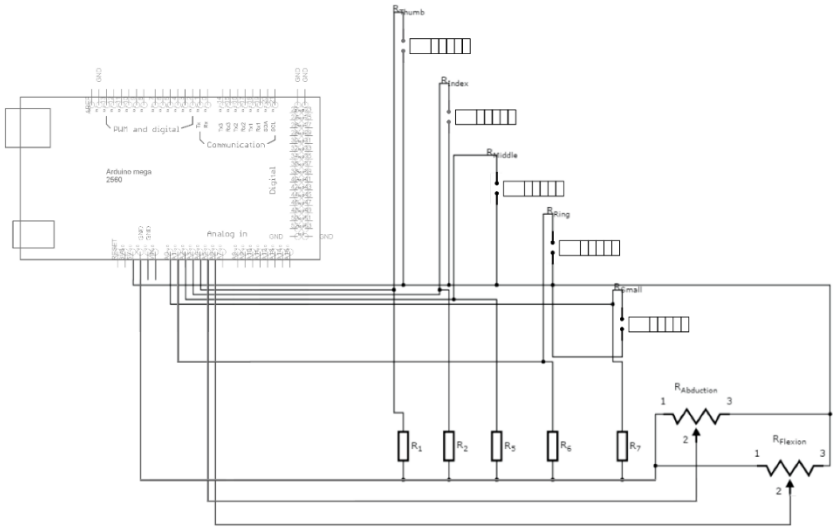


Figure 9. Circuit diagram of the setup.

2.1.4 Glove and enclosure construction method

One of the design goal is to make the motion tracker assembly to be easy to use as possible, it is designed to be easy to wear, remain comfortable during long uses and durability. For the glove construction, a sports cycling glove is used as it provides breathe-able mesh panelling for great ventilation for the fingers and palm of the user. The RFS are slide into sleeves made using felt fabric that is sewn to each finger pockets of the gloves. As a result, this ensures a snug fit of the RFSs to reduce measurement errors [23] and reduce likelihood of external damages to the RFSs.

Using Computer Assisted Drawing software Autodesk Fusion 360, mounting parts for rotary potentiometer and others can be designed. On the glove region of the

motion tracker, a part is 3D printed acts as a mounting point for a potentiometer and is sewn at the back of the hand. This enables mounting of potentiometers to the glove to measure radial and ulnar flexion. It also designed to be sturdy and lightweight while routing the wires from RFSs in a tidy manner. This helps the wearer to not feel tired or fatigue when donning the motion tracker during prolonged use.

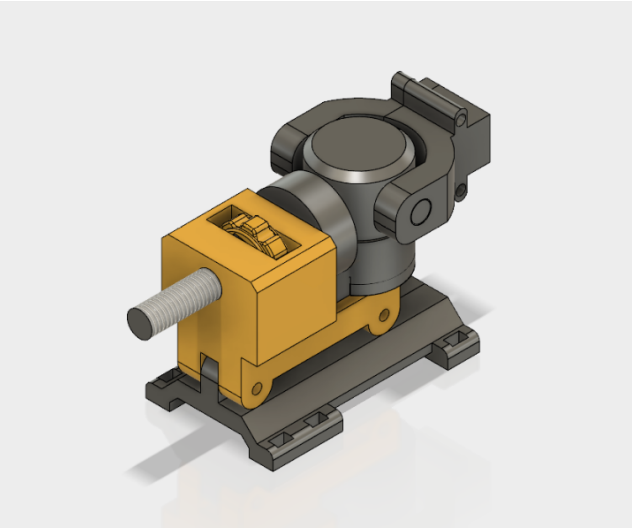


Figure 10. Rotary potentiometer mounting with adjustable length

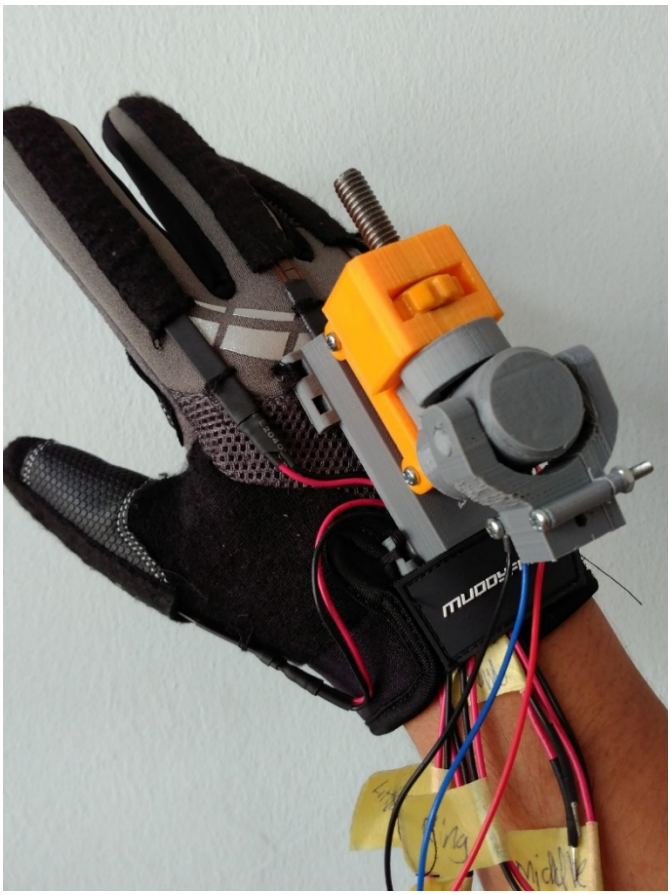


Figure 11. Glove assembly

Another potentiometer is placed at the region near the wrist to measure hypertension and flexion of the palm. Rotary potentiometers are mounted near the axis of rotation around the wrist, like a gimbal of a camera stabilizer. An L connector is used to connect the two potentiometers. This setup enables the system to measure 2 degrees of freedom (deviation and flexion) for movement around wrist region.

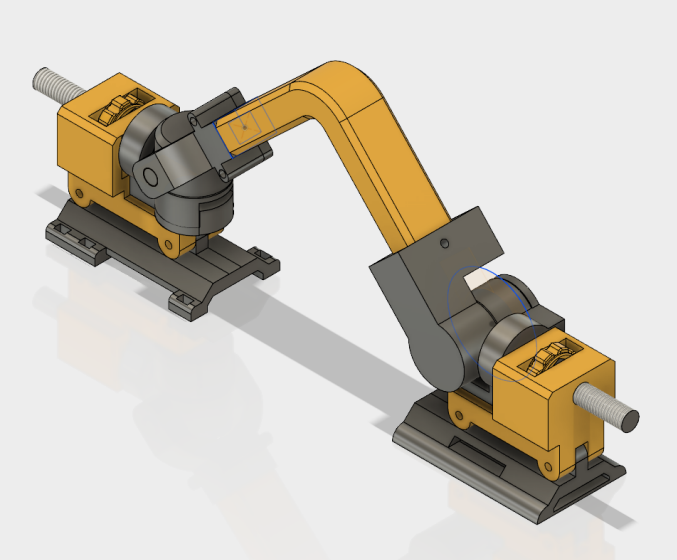
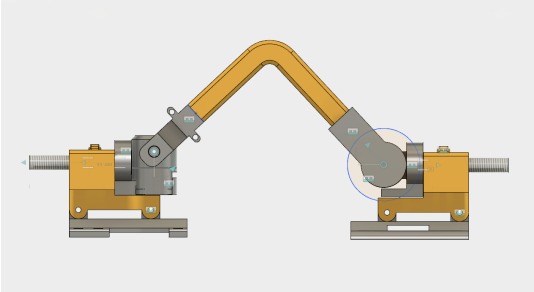
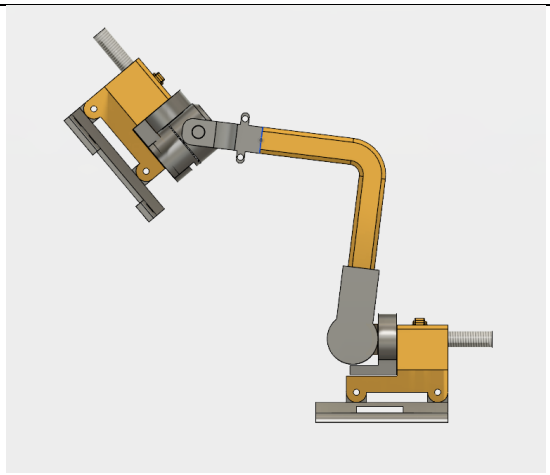
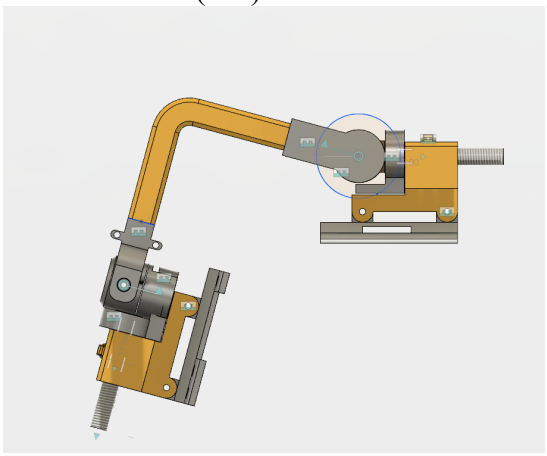
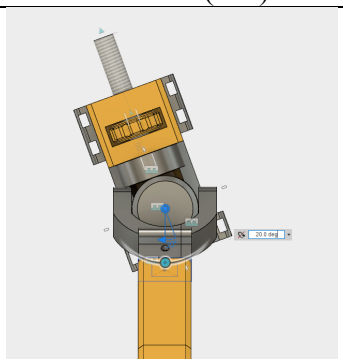
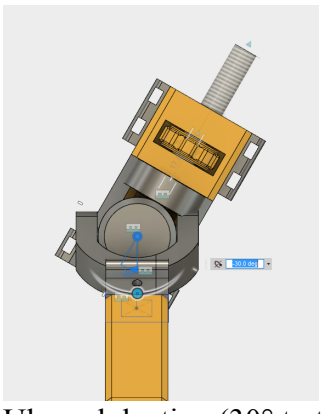


Figure 12. Overall view of the flexion and deviation angle measuring component.

Table 2. Motion study of motion tracker

	Type of wrist movement (Right Handed)	**Diagram**
1.	Flexion	 Neutral Position (0°)

		 Dorsal flexion (70°)  Palmar flexion (80°)
2.	Abduction	 Radial abduction (20° to the left)  Ulnar abduction (30° to the right)

2.2 Testing Method

After assembly, two tests are carried out to ensure that the motion tracker can function as per objective. One of many tests that will be done is motion tracking of hand. In this experiment, two persons will be instructed to perform bending of their fingers at a certain percentage of bending condition. The procedures will be repeated 3 times for each finger to obtain an average reading from RFS and potentiometers. Sensor repeatability will be commented at the end of this test.

Second test will be focused around controlling a robotic prosthetic hand for mimicking movement by wearer of the motion tracker. Subject were asked each finger and the corresponding finger on the robotic hand movement angles are measured. Qualitative and quantitative data is obtained: determined whether the parts are functional and measuring the angle of movement of various parts of the robotic hand.

3. Results and Discussion

3.1 Motion Tracking of Hand

Bending Condition	Sensor reading value (0-1023)									
	Person A					Person B				
	Thumb	Index	Middle	Ring	Little	Thumb	Index	Middle	Ring	Little
0%	560	540	532	572	551	530	545	531	580	549
25%	615	630	624	611	632	593	625	622	615	634
50%	654	666	681	653	650	664	651	692	650	659
75%	723	750	762	745	699	715	732	751	772	704
100%	764	802	830	790	750	795	810	842	801	747

Table 3. Average data from motion tracking using RFSs

Table 6 represents the average RFSs reading value ranging from 0 to 1023 for each finger the RFS is measuring. The sensor reading value is attributed to how Arduino perceives changes in voltage due to the 10-bit analogue to digital signal converter. The sensor reading increases as the bending condition increases as shown in the table and later in the graphs. Due to use of 4.5k Ohms resistor in the voltage divider circuit, the sensor reading value ranges from the 500 to the highest of 842. As it can be seen in the table, both person records slightly different average sensor reading value even when the bending condition is at 0%. This erratic behaviour can be caused by several factors such as microcontroller not providing enough voltage for all sensors in the circuit. Another possible factor is the inaccuracy of the flex sensor used, specifically the Spectra Symbol FLX-01 used in the experiment as stated by Saggio [8]. Nevertheless, preventative actions such as making two different power distribution circuits for servo and sensors have been taken prior to the tests and the error that could be present during the experiment is alleviated by taking average reading of each values.

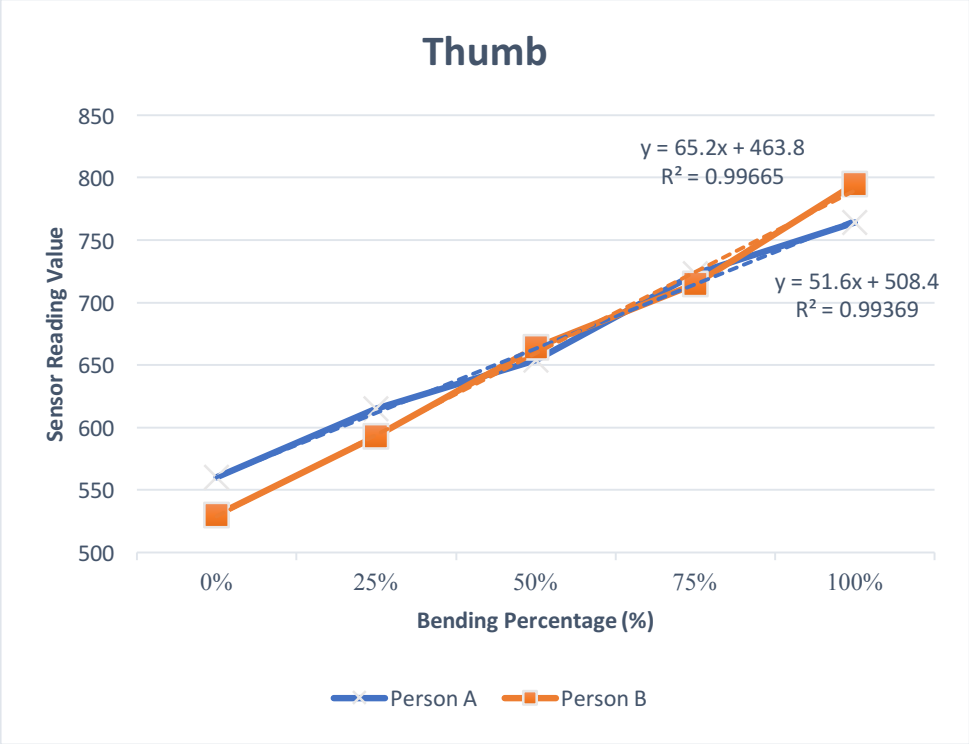


Figure 13. Thumb Finger RFS linearity study

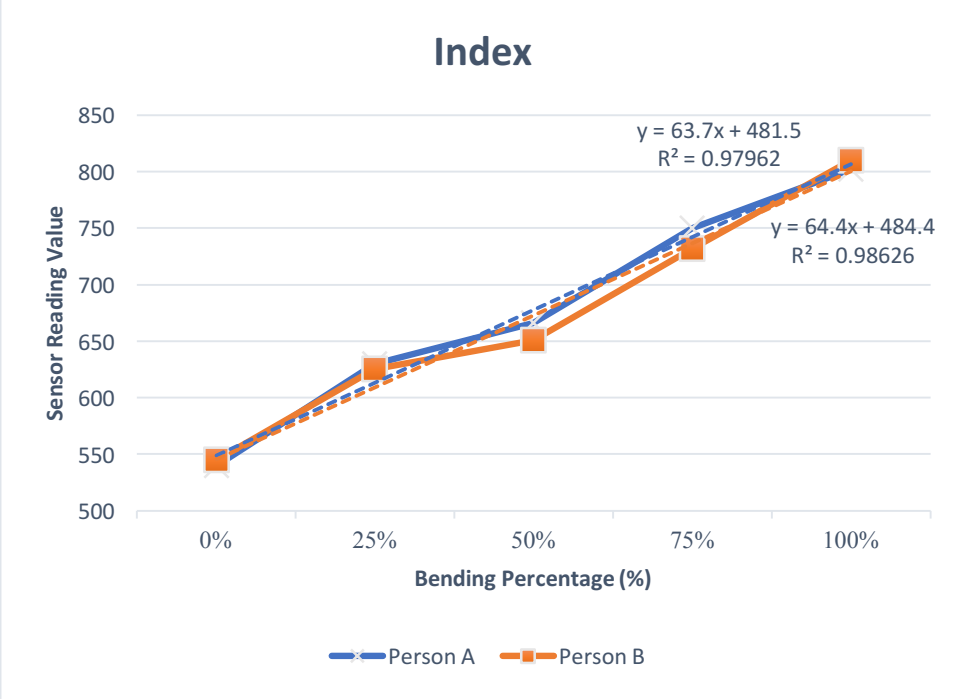


Figure 14. Index Finger RFS linearity study

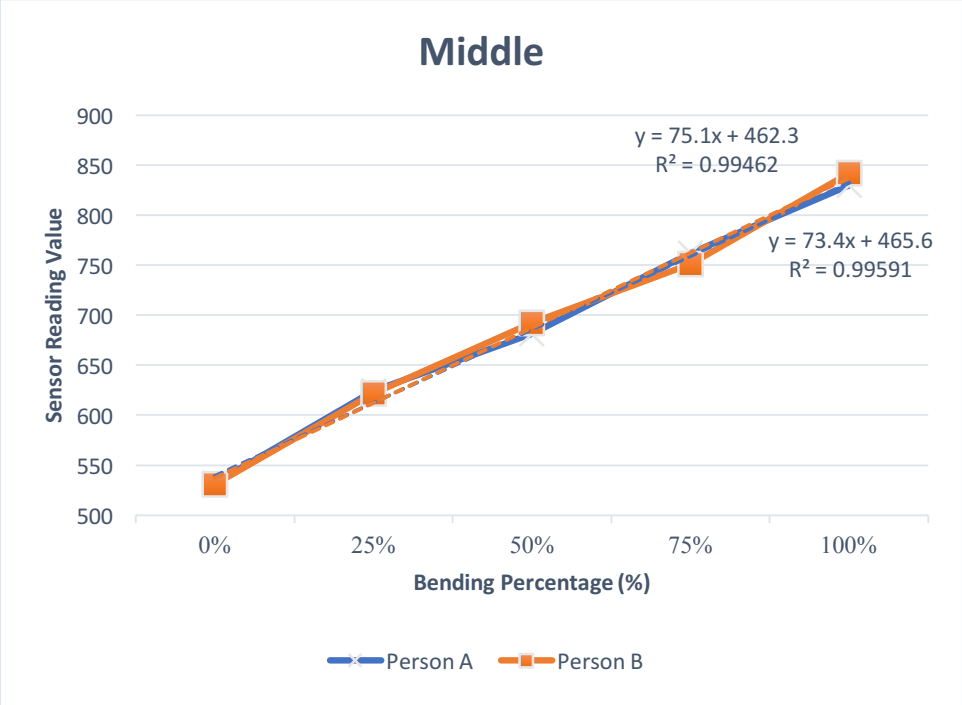


Figure 15. Middle Finger RFS linearity study

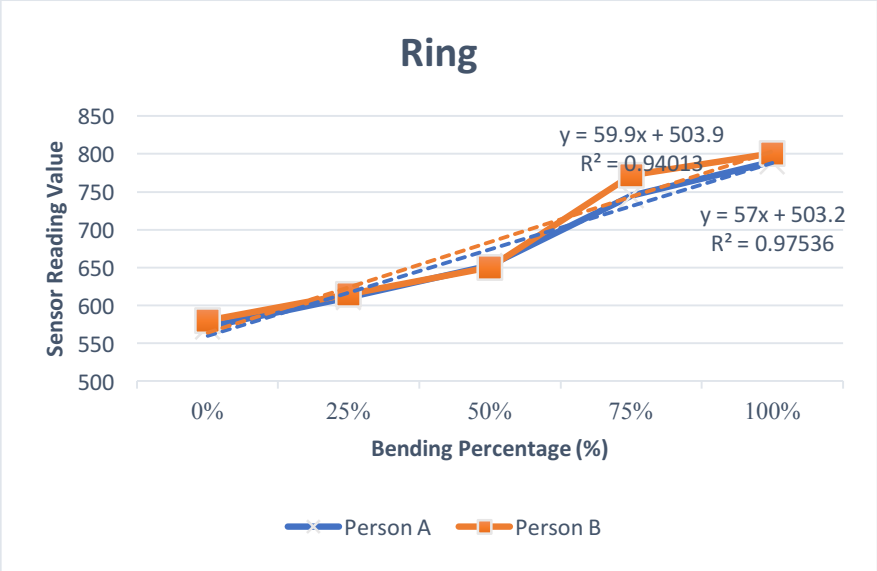


Figure 16. Ring Finger RFS linearity study

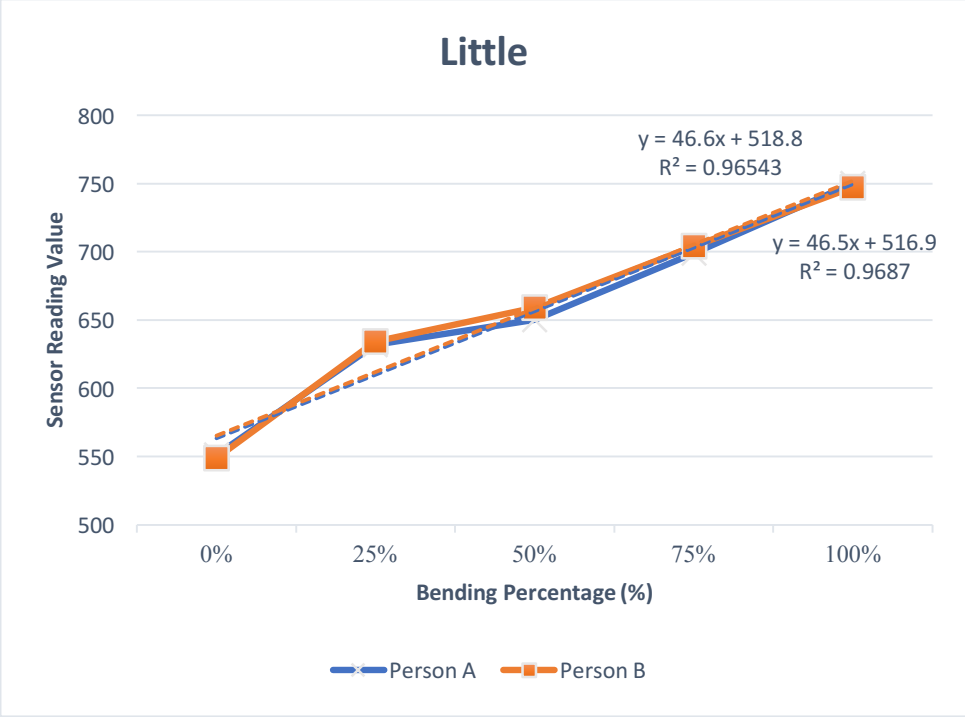


Figure 17. Little Finger RFS linearity study

3.2 Interface with Robotic Arm

Table 7 shows the data and observations from the test. Data includes finger movement corresponding to bending of finger of the motion tracker wearer and the angle of movement of the robotic hand.

Table 4. Test results of robotic hand movement

Parts	Movement	Angle of movement (°)		Comment
		Max	Min	
Thumb	Yes	54	0	Screw getting in the way of movement
Index	Yes	75	0	-
Middle	Yes	74	0	-
Ring	Yes	76	0	-
Little	Yes	74	0	-
Deviation	Yes	+30	-20	-
Flexion	Yes	50	-30	The hand is too heavy for the servo

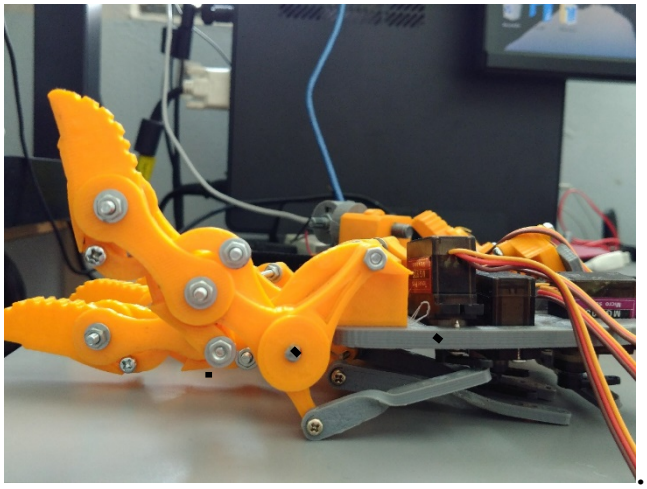


Figure 18. Angular measurement of robotic hand.

Based on the results obtained from the test, it proves that the motion tracker can provide a simple method of controlling a robotic hand by measuring the different segments of a finger and treating them as one. This is enough for the goal of this experiment: to prove that the motion tracker can be used to control a robotic prosthetic, enabling it to mimic movement of the wearer. From here, limitations on the design and build quality can be seen in the case of thumb and flexion part of the robotic hand. In the case of thumb, one of the screw head is getting in the way of movement of the finger, causing obstruction and therefore limiting its angle of movement. It can be rectified by using screw with flat head. For flexion, it is caused by servo that can only handle stall torque of 1.8kg/cm on a 4.8V circuit. From MG90S servo specification, it can handle a maximum stall torque of 2.2kg/cm if 6.0V is provided to it but it could probably be caused by poor design of the additional part that enables flexion movement of the robotic hand.

4. Conclusion

As a conclusion, the glove that is developed from this research is sufficient as a novel method on evaluating the health of body parts through measurement of the fingers and hand ability to fulfil characteristics of a normal, healthy joints. Bend sensors and rotary potentiometers are selected for their cost effectiveness, lightweight and easy integration through existing Arduino libraries. The total cost of the motion tracking system is low (<RM500) which is cost effective with most of the cost contributed by the resistive flex sensors. Easy integration with robotic arm is also achievable which is crucial for future development in medical, robotics and education sector.

Future improvements that can be ventured at the completion of this study is to add more rotary potentiometers to measure angular movement of more body joints. It is also suggested to add a wireless capability to the motion tracker either through Xigbee or Bluetooth module to enable true mobility of the motion tracking system.

Acknowledgement

I would like to express thanks to my supervisor, Mr. Farid Aladdin for taking the responsibility of becoming an acting supervisor for this project and to help me complete this thesis. Also, I would love to further my appreciation to my parents

Kamarudin Bin Kamilin and Sabaria Bt. Darut for helping me both moral and financial support throughout the project and it would be impossible without their help.

References

[1] M. Fransen, “When is physiotherapy appropriate?” Best Practices Res Clinic Rheumatology, pp. 18:477–89, 2004.
[2] A. Hammond, “When is physiotherapy appropriate?”Arthritis Care Res,pp. 7:5–9, 1994.
[3] Luinge H J, Veltink P H and Baten C T M 2007 Ambulatory measurement of arm orientation J. Biomech. 40 78–85
[4] Williamson R and Andrews B J 2001 Detecting absolute human knee angle and angular velocity using accelerometers and rate gyroscopes Medical and Biological Engineering and Computing 39 294–302
[5] Hansson G A, Balogh I, Ohlsson K, Rylander L and Skerfving S 1996 Goniometer measurement and computer analysis of wrist angles and movements applied to occupational repetitive work J. Electromyography and Kinesiology 6 23–35
[6] Khor J M, Tizzard A, Demosthenous A and Bayford R 2014 Wearable sensors for patient-specific boundary shape estimation to improve the forward model for electrical impedance tomography (EIT) of neonatal lung function Physiol.Meas. 35 1149–61
[7] Starck J R, Murray G, Lawford P V and Hose D R 1999 An inexpensive sensor for measuring surface geometry Med. Eng. Phys. 21 725–9
[8] Saggio, Giovanni et al. "Resistive Flex Sensors: A Survey". Smart Materials and Structures 25.1 (2015): 013001. Web.
[9] Thanakodi, S. Azhar and A. Miskon, "Prosthetic Hand Controlled by Wireless Flex Sensor on EOD Robot", International Conference for Innovation in Biomedical Engineering and Life Sciences, pp. 1-6, 2015.
[10] Sensorwiki.org. (2016). sensors:flexion · SensorWiki.org. [online] Available at: http://www.sensorwiki.org/doku.php/sensors/flexion [Accessed 6 Oct. 2016]
[11] SYMBOL, S. (2016). Flex Sensor Manufacturers | Spectra Symbol. [online] Spectrasymbol.com. Available at: http://www.spectrasymbol.com/flex-sensor [Accessed 3 Oct. 2016].
[12] A. Syed, Z. Agasbal, T. Melligeri and B. Gudur, "Flex Sensor Based Robotic Arm Controller Using Micro Controller," Journal of Software Engineering and Applications, Vol. 5 No. 5, 2012, pp. 364-366. doi: 10.4236/jsea.2012.55042.
[13] G. Saggio, F. Riillo, L. Sbernini and L. Quitadamo, "Resistive flex sensors: a survey", Smart Materials and Structures, vol. 25, no. 1, p. 013001, 2015.
[14] Simone L K and Kamper D G 2005 Design considerations for a wearable monitor to measure finger posture J. Neuroeng. Rehabilitation 2 5.
[15] Kaczmarek A S 2006 Sensing bending in a compliant biomimetic fish MS Thesis (Massachusetts Institute of Technology).
[16] Orengo G, Sbernini L, Di Lorenzo N, Lagati A and Saggio G 2013 Curvature characterization of flex sensors for human posture recognition Universal J. Biomed. Eng. 1 10–5.
[17] Srinivasan C R, Sen S, Kumar A and Saibabu C 2014 Measurement of flow using bend sensor Advances in Energy Conversion Technologies (ICAECT), 2014 Int. Conf. on: IEEE pp 27–30.

[18] Setiawan I and Iswara S 2012 Electric Air Ukulele (Champaign: University of Illinois at Urbana).

[19] Oess N P, Wanek J and van Hedel H J A 2010 Enhancement of bend sensor properties as applied in a glove for use in neurorehabilitation settings Engineering in Medicine and Biology Society (EMBC), 2010 Annual Int. Conf. of the IEEE: IEEE pp 5903–6

[20] S. Erik Cheever, "Electromechanical Systems", *Lpsa.swarthmore.edu*, 2017. [Online]. Available: http://lpsa.swarthmore.edu/Systems/Electromechanical/SysElectMechSystems.html. [Accessed: 25- Apr- 2017].

[21] "Potentiometer - Physical Programming", Openobject.org, 2017. [Online]. Available: *http://www.openobject.org/physicalprogramming/Potentiometer*. [Accessed: 15- Apr- 2017].

[22] Luttgens, K., & Hamilton, N. (1997). Kinesiology: Scientific basis of human motion. Madison, W: Brown & Benchmark.

[23] Dipietro L, Sabatini AM, Dario P: Evaluation of an instrumented glove for hand-movement acquisition. Journal of Rehabilitation Research and Development 2003, 40: 179-190. 10.1682/JRRD.2003.03.0181

Autonomous Water Quality Monitoring Unit for Autonomous Lake Improvement System (ALIS)

Chua Yong Hong[1]*, Mohammad Taghi Hajibeigy[2], Dr. Se Yong Eh Noum[2], Dr. Shirley Ch'ng[1]
[1]*Department of Mechanical Engineering*
[2]*Department of Electrical Engineering*
School of Engineering, Taylor's University, Malaysia

* *yonghong.chua@sd.taylors.edu.my*

Abstract
This paper presents the design of the autonomous mobile water quality measurement unit as part of the autonomous lake improvement system, ALIS. The water monitoring system measures turbidity, temperature and dissolved oxygen, DO and upload real-time measured data to an online platform, ThingSpeak. Users are able to access and view the recorded data in a timely manner. The water monitoring system operates on an Arduino platform and its positioning is traced by a GPS module as it moves on a fixed path. It relies on solar energy as the main source of energy throughout the day. The solar charging rate is estimated to have a minimum of 2 hours to charge the LiPo battery from a low voltage of 9.4V to 11.25V. The operating voltage range for the dual 12 V DC motors relying on solar energy is 10.94 V to 11.25 V which lasts 2 hours and 15 minutes. The system is 4.3 kg and operates at a speed of 0.41 ms^{-1}. The angle of turn per second to the left is 18.67 and 23.92 for the right. It contains three HC-SR04 ultrasonic sensors to detect frontal obstacles and act as the assistive navigator for the system to avoid obstacles in its path. The working principle of the prototype of the autonomous mobile water quality measurement unit for the system are well explained in this paper.

Keywords: Autonomous, Water Monitoring, Wireless Data Collection, Solar Powered, Real time monitoring

1. Introduction

Bartram et al. [1] have estimated that the freshwater quality deterioration at the global level for lake waters ranges from occasional deterioration to severe deterioration, in which it is no longer able to hold any living fishes. In addition, Bartram et al [1] also pointed out that the residence time of closed lake waters, that is, the time taken for recovery from a water pollution, are approximately 100 years depending on the depth of the lake. This pollution includes human-induced eutrophication, sedimentation and acidification. Jeremy [2] added that common human-induced eutrophication is caused by partially treated sewage in addition to agriculture fertilisers. The rapid buildup of nitrogen and phosphorus from these wastes led to an unnatural increase in algae growth. This, in turn will decrease the level of light absorbed as well as minimizing oxygen content within the lake.

In Malaysia, the National Hydraulic Research Institute of Malaysia [3] reported that more than 60% of the 90 lakes reviewed in 2005 are experiencing eutrophication. Sharip and Zakaria [4] identified that the deterioration of water quality and quantity was reported in all three biggest natural lakes in Malaysia, that is, Lake Bera, Lake Chini, and Loagan Bunut Lake. The degradation includes surface runoff containing nutrient-rich water from nearby plantations, sewage from communities living around the lake, logging activities and oil discharges from motorboats. All of which has led to a decrease of aquatic organisms such as fishes and reduction of agriculture.

Therefore, maintaining water quality on precious fresh lake water is desired. However, accurate measurements and reading of water quality is required beforehand to monitor on which level is considered healthy or in dangerous level. Sharon [5] states that the few important water quality parameters that define the healthiness of fresh water are pH, turbidity, conductivity, dissolved oxygen, temperature and nutrient ions.

To date, large corporations such as Libelium, YSI and Stevens Water have come up with several water quality measurement devices. However, the drawback of these devices is that it is intended to measure in static mode, at a specific location at one time and mostly off-site analysis is required. Once measured, the water quality of that single data captured is assumed to be for the entire lake. However, Dlamini et al [6] and Amarjeet Singh et al [7] argued that water quality parameters differ in a different location in addition to the depth of the lake. In order to address this shortfall in all the commercially available devices, a mobile water monitoring system is greatly desired.

Currently, one of the latest development of mobile water measurement system is by Hitz et al [8] where their team designed a catamaran boat equipped with a GPS system to maneuver around the ocean autonomously on designated location. Nonetheless, the drawback of this design compared to lake water is that it is only suitable for wide-open areas such as an ocean and thus, does not have obstacle detection. In addition, the design requires 2 large acid batteries which need maintenance over time and also poses a potential threat to the environment should it leak or even during disposal.

Furthermore, Hudson [9] stated that the frequency of measurement should be recorded at least once every month with several samples from different locations on a lake if the purpose is to generally characterize the lake quality and identify potential problems.

As such, this paper aims to present the autonomous water quality monitoring unit as part of the Autonomous Lake Improvement System (ALIS), of which it is able to maneuver on the lake autonomously through a fixed pattern and is capable of measuring the water quality, and uploading these data onto the online platform real time. In addition, the system will be self-sustainable and could last on the lake as long as it is able to re-charge its battery from sunlight. The design and manufacturing of the system will be briefly explained, which is then followed by the mechanism and integration of software such as programming and GPS. The water qualities parameters that will be discussed in this project are dissolved oxygen, temperature and turbidity. Furthermore, Taylor's lake water will be used as the sample in this project to test the prototype.

2. Methodology

2.1 Water monitoring system design

Before considering the design stage of the system, several conditions must be identified and taken into account beforehand. These desired conditions are:

1. The system does not need to move faster than 15 $cm.s^{-1}$, as its positioning is the main concern rather than its fast movement.

2. Requires large area of inner space that is isolated from water to place electricals and electronic components such as batteries, distribution boards, wirings, motors, sensors and micro-controllers.

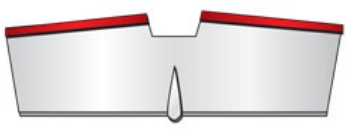
3. Requires large surface area on the deck to place solar panels so as to allow absorption of sunlight. In addition to spaces to place sensors and probes.

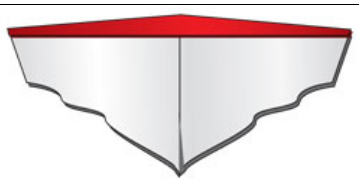
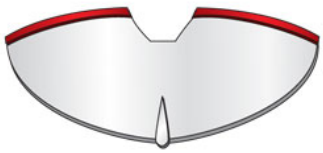
4. It is feasible from the manufacturability and economical perspectives.

It is of big concern that the electronic components are required to be stored internally and is completely isolated from lake water. Several designs were considered based on the 4 conditions mentioned earlier.

Table 1 shows the summary of the designs considered that could possibly fit with all 4 conditions mentioned earlier along with its advantages and disadvantages noted down.

Table 11. Hull types with advantages and disadvantages [10]

Hull Shapes	Hull Illustrations	Advantages	Disadvantages
Flat Bottom Hull		• Planing hull with a shallow draft • Useful for fishing in small lakes and rivers.	• Rides roughly in choppy waters.

Deep Vee Hull		• Planing hull with a V-shape • Smooth movement in the rough water.	• Consume more power to move at the same speed as flat bottom hulls. • May roll or bank in sharp turns due to less surface contact with the water.
Round Bottom Hull		• Displacement hull • Moves easily through the water even at slow speeds.	• Has a tendency to roll over.
Multi-Hull		• Displacement hull • The multi-hull has greater stability because of its wide beam.	• Needs a large area when turning due to its wide area.

Through careful consideration, Deep Vee Hull appears to be a good choice in terms of mobility. However, installing water quality probes would be an issue as it requires some parts to be submerged in the water. The next feasible choice comes with multi-hull while the other two design contains similar risks, which is less stable as compared to the Deep Vee Hull. Hence, multi-hull design is selected to be used as the platform to maneuver around the lake. Theoretically, the disadvantages of the multi-hull can be mitigated by allowing a larger limit of turning when integrating the coding into the system.

Therefore, the final design modelled through Solidworks as shown in Figure 1.

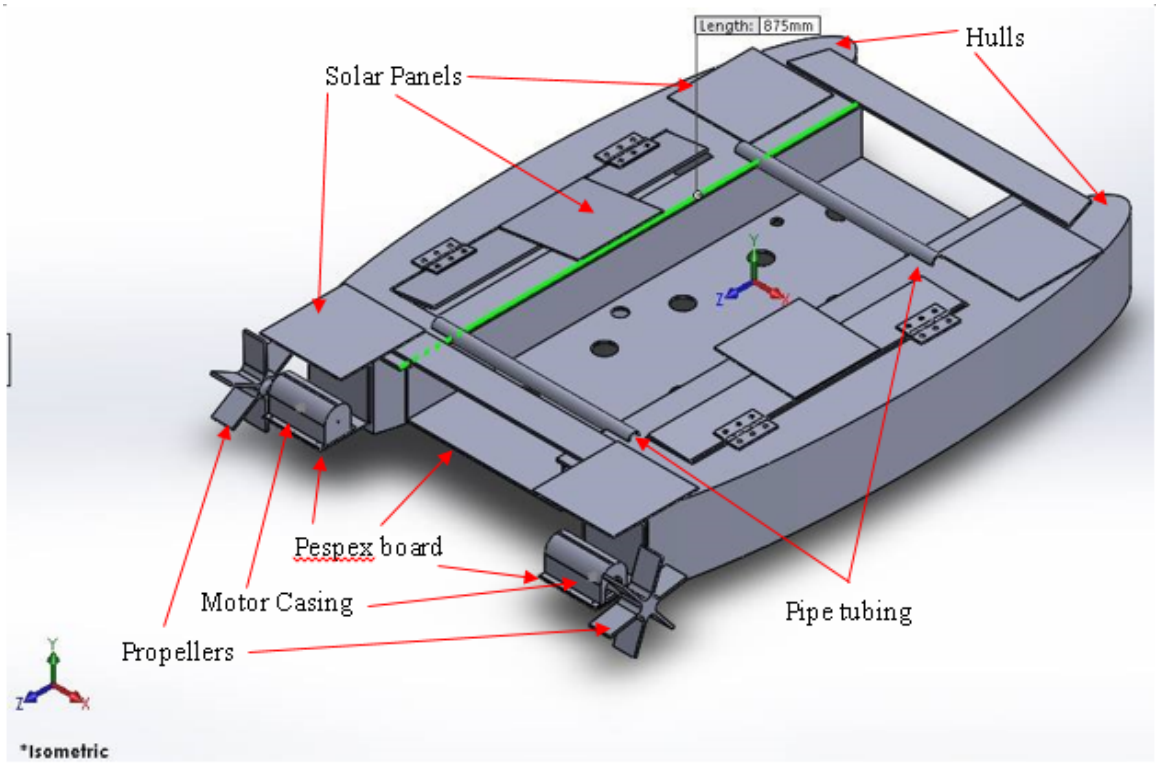


Figure 14. Initial design of water monitoring system in Solidworks

The 2 hulls side by side were planned to be hollow where all the electronic and electrical components will be stored within. These 2 hulls will be connected through the middle Perspex board platform along with the pipe tubing as shown in Figure 1. The pipe tubing is to allow wires to be passed in between in addition to enhancing the stability to prevent the 2 hulls from bending inward towards the middle platform. On the other hand, the middle platform that consists of 13 circular holes, 10 of which are for vegetative plants; which are spaces reserved for the vegetative plants for the water quality correction system, which will be reported in a separated paper in the future, and 3 for the measurement probes.

This platform connects the two hulls by means of nuts and bolts through the sides with the help of L-brackets. As for the housing of each hull, it is made of polyester resin, tissue fiberglass as filler and primer. The Styrofoam were used as the inner source of buoyancy.

Two 12 V DC motors with no load specifications of 111 rpm and 92 mA are used to power the propellers; one on each side of the hulls within the motor casing as illustrated in Figure 1 [11]. Since a high torque and low-speed motor are desired and the maximum estimated weight of the system is 5 kg, the 12 V DC motor with 3 kg.cm torque is selected based on the calculation from Martenhoff's Powerboat Handbook [12] on the power to weight ratio for an average drive 13m.s^{-1} is:

$$\frac{54.82\ W}{kg} \equiv 13\ m.s^{-1} = 1300\ cm.s^{-1}$$

The maximum desired speed is 15 cm.s^{-1}. Therefore, the power to weight ratio of a motor to drive 15cm.s^{-1} is:

$$\frac{54.82\ W}{kg} \times \frac{15cm.s^{-1}}{1300cm.s^{-1}} = \frac{0.633\ W}{kg}$$

Since the system has a maximum weight of 5kg, the power of the motor to drive 15cm.s^{-1} including a safety factor of 20% is:

$$\frac{0.633\ W}{kg} \times 5\ kg \times 120\%\ Safety\ Factor = \mathbf{3.8\ W}$$

From the technical specifications of the motor provided [11], the maximum power of the motor provided at stall condition with a safety factor of 20% less is:

$$12V \times 1.2A \times 80\% = \mathbf{11.5\ W}$$

With two of the same motor, it is expected that the motor will be able to drive the system forward to at least 10cm.s^{-1} of speed without reaching stall condition. The motors will be controlled by a motor controller, L298N that interfaces with Arduino Mega.

The motor casing, shafts connecting the motor to the propeller and the propeller were 3D-printed. These 3D printed components will be placed on top of Perspex block as shown in Figure 1.

2.2 Software system

This section will further breakdown to several sub-sections that encompass the coding, sensors and online platform.

2.2.1 Microcontroller

The microcontroller that was used is the Arduino Mega 2560. This is due to the advantage of Arduino Mega 2560 has 50 more pins and 96 Kb more memory spaces for programs to be stored as compared to the more common option in Arduino Uno. An Arduino WiFi shield is attached to equip the unit with WIFI capability that connects to the internet.

2.2.2 Navigation System

The idea to navigate the system autonomously is for the system to move in a fixed cycle pattern. The program will loop continuously for the system with the ultrasonic sensors acting as the top priority when obstacles are detected. The system will be tracked by a GPS module to know where the system is. The turning of the system relies on the delay function of the program within the ultrasonic sensor and motor movement. As a result, it is required to identify the angle per turn of the system. This can be done by investigating the total time used to turn a complete 360° clockwise and anti-clockwise. Program interfacing is done by using PlatformIO Atom IDE. It is selected due to its simplicity and various support on certain languages.

The GPS module VK2828U7G5LF will be used. It was selected due to its low-cost available online with an accuracy sensitivity of 2.5 m and operating speed of 1 Hz as desired.

2.2.3 Sensors and Probes

The HC-SR04 ultrasonic sensors are used to detect obstacles up to a range of 4 m in front. On the other hand, the probes used to measure the water qualities are Turbidity Sensor, Dissolved Oxygen (DO) and LM35 Temperature probe. pH value was not measured due to a limitation in the availability of a suitable probe at the time when this report was prepared.

It has a measuring angle of 15° [13] and hence, 3 ultrasonic sensors are used to detect obstacles up to 45° of frontal cone area. Electronics Hub [14] states that Ultrasonic sensor is better than IR sensor as the latter has a risk of not able to detect the emitted radiation if the surface is not reflective enough as well as only measures up to the 1 m maximum range.

The turbidity probe used to measure the cloudiness or haziness of the water due to individual particles such as sands and dirt will be SEN0189. The sensor is operated by comparing the data collected with the standard results and referring it to the datasheet available online [15]. It has an Analog output of 0 to 4.4 V where 0 V is the most turbid and 4.4V is the least turbid. The operating voltage for SEN0189 is 5 V with a weight of 30 g. Supplementary to that, the DO probe - Atlas Scientific's EZO DO probe is used to measure dissolved oxygen, has a reading range of 0.01 to 35.99 mg/L with an operating voltage of 3.3 V to 5 V based on datasheet and a total weight of 52.77g. It has a response time of 0.3 mg/L and therefore requires a brief amount of time for the reading to be stabilized. Last but not least, the temperature probe is the LM35. It has an operating voltage of 3.3 V to 5V and a weight of 5 g. LM35 is protected with heat-shrink tubing to prevent water from entering the pin as it will fluctuate the voltage reading.

2.2.4 Online Platform

Once the water quality data are collected, Arduino Mega 2560, along with an equipped WiFi Shield is used to upload these data to an online platform. The platform used is ThingSpeak as it holds up to a maximum of 8 data channels to be displayed simultaneously in terms of graphs over time.

Figure 3 portrays an example of data uploaded to a public channel on ThingSpeak. A total of 5 data channels will be expected to be used namely temperature, turbidity, dissolved oxygen and the location of the system through latitude and longitude. With that, users are free to access and view the recorded water quality data from the public channel. The process flow on the collection of data is summarized in Figure 2.

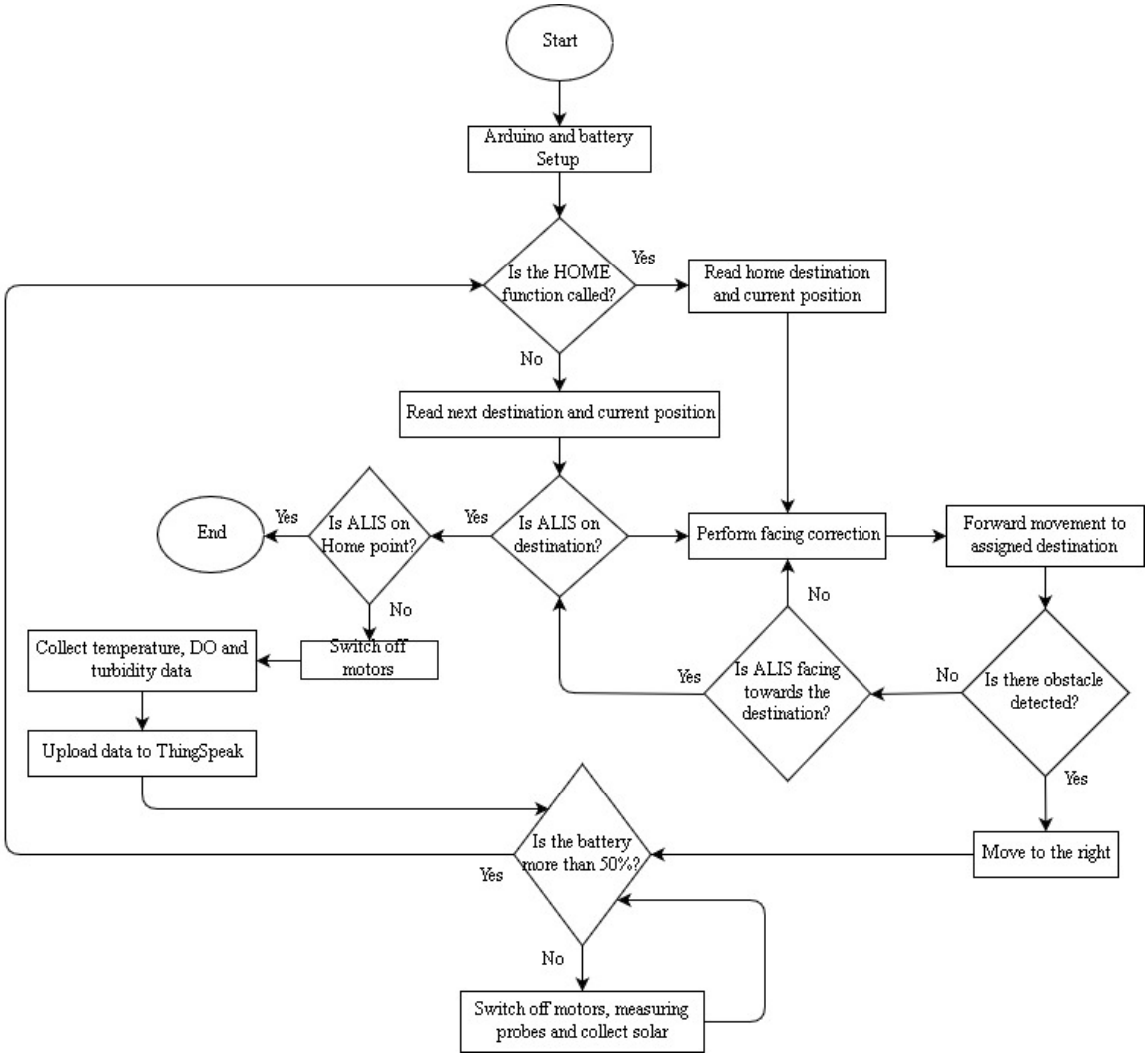


Figure 13. Process flow chart of system's algorithm

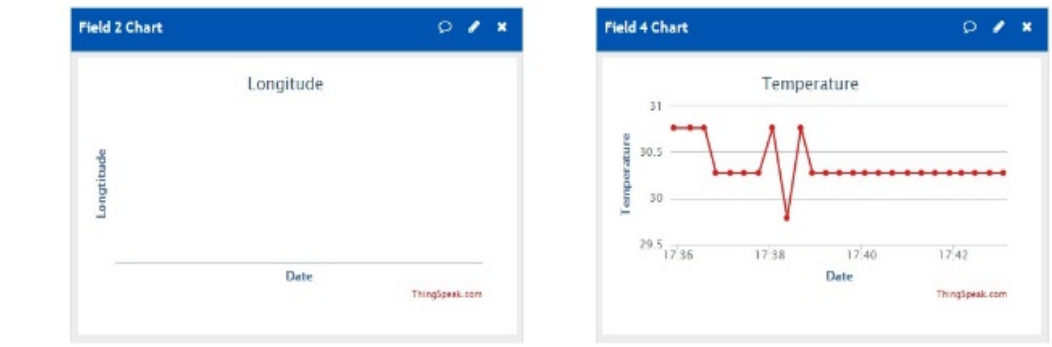


Figure 16. Temperature test data uploaded to ThingSpeak

2.2.5 Solar Energy

Two choices of different solar panels are provided. The big solar panel has a size of 62 cm by 33 cm whereas the small solar panel has a size of 16 cm by 15 cm.

With spaces constraint as one of the main concern, it was decided that the small solar panels were used. A total of 6 solar panels were used to power the unit and were positioned as in Figure 1. The connection schematic is summarized in Figure 4. Converted electrical energy will first be controlled with solar charger controller before channelled and stored in the battery. The controller ensures that there is no backflow current from the battery to the solar panel due to a condition where the voltage of the solar panel is lower than the voltage of a battery.

The battery used is Lithium Polymer (LiPo) battery. It is rechargeable and consists of 2200 mAh with a rated voltage of 11.1 V. It was selected due to its capability to recharge and high discharge which is sufficient enough to power 2 DC motors, sensors, probes and microcontrollers.

To test the charging rate of the battery with 6 solar panels connected in parallel as to allow larger current flow to the battery, the battery is first discharged by connecting it to several running loads until it is stopped. The reading recorded is 9.4 V. It is then placed outdoor and the time taken to obtain a constant reading are recorded.

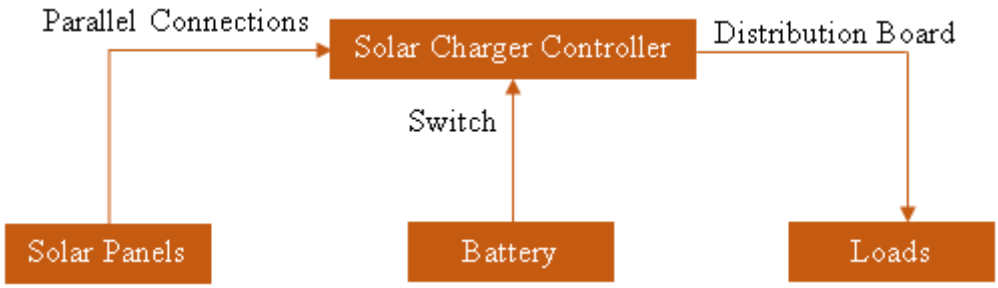


Figure 17. Connection schematic of solar panels, charger, battery and loads

3. Results and Discussion

3.1 Product and Mobility

The water monitoring system has a dry weight of 3 kg excluding motors, propellers, Arduino Mega, sensors and probes. Figure 5 shows a weight test on the system with 2 kg on each hull giving a total of 4 kg to test the buoyancy of system. From the result of the test, it is able to float with all the components stored inside.

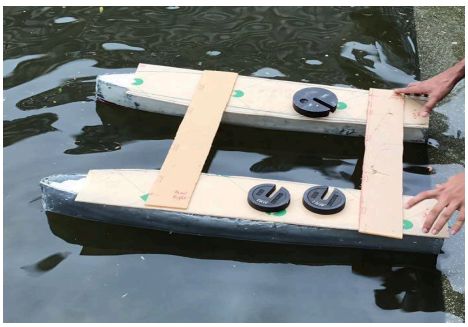


Figure 18. Weight test on first prototype of water monitoring system, 2 kg on each hull

The final prototype of the system is depicted in Figure 6 where the measured 3D printed motor casing, shafts and propellers are tested with the motor on the system. The final weight is roughly measured to be 4.3 kg.

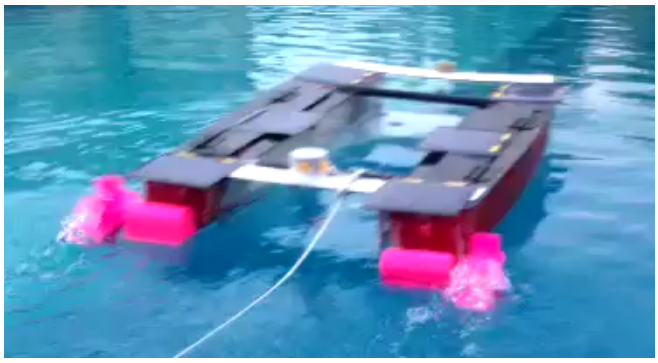


Figure 19. Motor and 3D printed tests on water monitoring system

In addition, the time taken for the system to move over a distance of 7.5 m is 18.4 seconds. Hence, the speed of the system is:

$$Speed = \frac{Distance}{Time} = \frac{7.5\ m}{18.4\ s} = 0.408\ m\ s^{-1} = 40.8\ cm\ s^{-1}$$

This is faster than the desired speed. In addition, the turning angle per second of the system is also identified by measuring the time taken for the system to turn 360° with one of the motor moving forward and the other moving backward. The results are summarized in Table 2 below.

Table 12: Movement result of water monitoring system

Variable	Result
Speed (m/s)	0.408
Left turn (°/s)	18.672
Right turn (°/s)	23.920

From Table 2 above, it is observed that the right turn is faster than the left turn. This is due to the reason of the right motor is slightly more submerged into the water than the left motor. The error alignment arise when the Perspex blocks are installed as the left and right blocks are not equally aligned. As a result, the right motor spins slower than the left motor due to the increased drag by the water.

3.2 Solar Charging Rate and Power Consumption

The charging rate in voltage on the LiPo battery with 6 solar panels connected in parallel in a typical day time is shown in Figure 7.

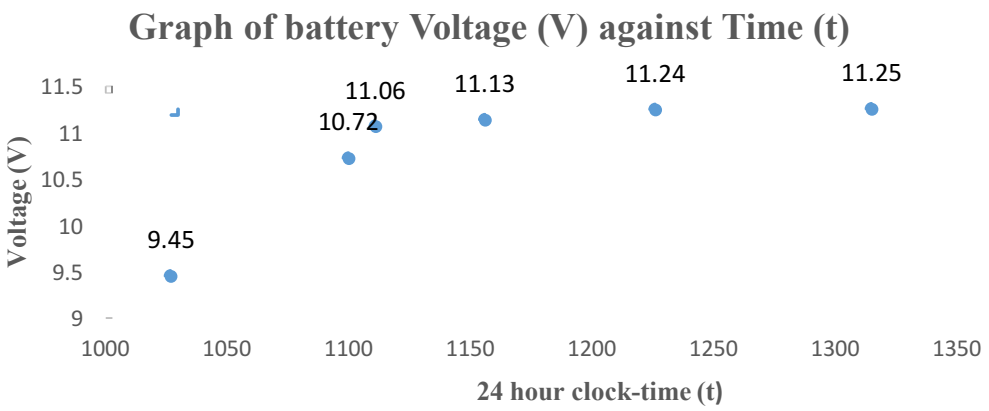


Figure 18. Charging of battery with 6 parallel solar panels in voltage with time

From Figure 7, it is observed that the voltage stabilizes to 11.25V after 2 hours of charging from 9.45 V. The constant trend of 11.25 V is due to the maximum voltage it can receive from the sunlight during that day. However, the voltage gain is not expected to be above the rated voltage of the small solar panel which is 11.74 V as that is the maximum voltage gain available for the solar panel. This infers that the maximum voltage for the battery to be charged from the solar panel is 11.74 V under the best condition provided by the sunlight. This is satisfactory as the system does not require to continuously move and measure the water quality throughout the entire day.

However, 11.25 V is not the maximum power capacity of the battery. By charging electrically, it can rise up to 12.5 V. This implies that the battery will never be able to be fully charged through the use of solar panels. Figure 8 below shows the discharge rate of battery by running the two 12V DC motors only on dry air.

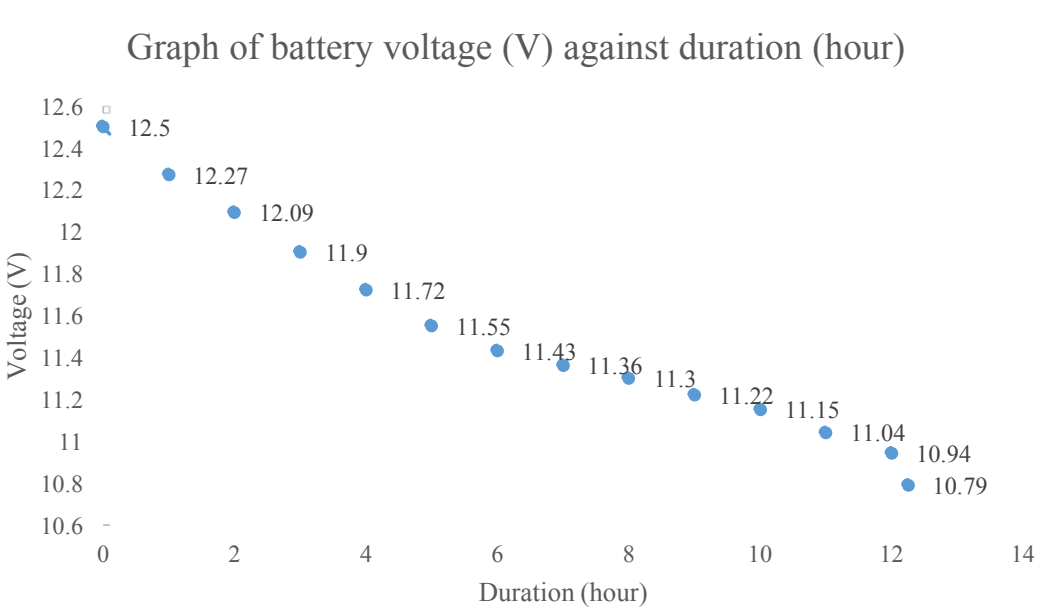


Figure 19. Discharge rate of LiPo battery on two 12V DC motors

From Figure 8 above, it can be understood that the complete discharge duration from a fully charged LiPo battery until the motor stops operating is 12 hours 15 minutes with a voltage reading of 10.79 V. However, it is noted that 10.79V is not the end capacity of the LiPo battery as it is still sufficient to power the sensors and probes. This is due to the reason that the 12 V DC motors requires a minimum of 10.79 V so that it can draw sufficient enough current to operate.

In addition, it can also be inferred that the voltage drop ranges from 0.23 V to 0.06 V per hour. The decrement of voltage slows down to a minimum between 11.55 V and 11.22 V. Despite that, the voltage decreases tremendously from 10.94 V to 10.79V within 15 minutes.

By combining Figure 7 and Figure 8, since the DC motors are only operational above 10.79 V, it can be implied that the duration of motor is operational when using solar to charge is about 2 hours and 15 minutes, from 11.25 V of maximum charged of solar to 10.94 V. In other words, the motors are expected to be able to operate for 2 hours and 15 minutes if the system is fully charged using solar instead. In addition, the charging duration from 10.94 V to 11.25V is about 1 hour 30 minutes. This signifies that the charging rate from solar is more than the discharge rate by the dual DC motors within the range of 10.79 V to 11.25 V during the peak of the day.

This is only true if it is during the peak of the day in addition to the sensors, probes and microcontrollers as well as the additional force due to drag by the water are not included. As a result, a safety factor is needed to compensate for the extra charging time for the system to be equal to the discharge rate. Table 3 below summarizes the power consumption of all components.

Table 13: Power usage of each component except motor based on technical specifications

Components	Power usage (W)
GPS	0.1500 [16]
3 Ultrasonic sensors	0.2250 [13]
Temperature probe	0.0500 [17]
Dissolved Oxygen probe	0.0675 [18]
Turbidity Probe	0.2000 [15]
Arduino Mega	0.2500 [19]
Motor Controller	0.1800 [20]
Total	**1.1225**

Assuming each motor consumes 4 W as calculated in the methodology. Therefore, the power consumption of all other components relative to the motors are:

$$\frac{1.1225\ W}{8\ W} \times 100\% = 14.03\%$$

This means that the power consumption of all other components other than the 2 motors consumes about 14% of the power consumed by the two motors at the same amount of time. As a result, by including the additional drag force by the water and possible low peak day, it is safe to assume to have a safety factor of 25% of the charging time for on top of the movement duration. In other words, for every hour the motors are switched on, it is recommended to have

an additional charging time of 1 hour and 15 minutes when the system comes to a halt and charges while it is performing its measurements.

4. Conclusion

The final prototype of the system has an estimated weight of 4.3kg. Electronic components are stored within the 2 hulls moulded through Styrofoam. Two 12V DC gear motor with 111 RPM high torque is used to drive the system. Motor casing, propeller shaft and propellers are 3D-printed based upon design on Figure 1 assembly. 6 Solar Panels are placed on top of the system along with 3 HC-SR04 ultrasonic sensors to detect frontal obstacles. Measuring probes are placed on the middle platform. The water monitoring system moves in 0.41 ms^{-1} and has a left turning of 18.67 and right turning of 23.92 degree per second. It requires a minimum of 2 hours to charge from 9.4V to 11.24V under a typical day using 6 solar panels connected in parallel. The minimum operating voltage for the 12V DC motor is 10.49V and has a total discharge time of 2 hours 15 minutes from 11.25 V to 10.49 V. A safety factor of 25% additional charging time is applied when the system is in idle after it performs it data measurement and upload for every time the motor is switched on.

Acknowledgement

Much appreciated to Mohammad Taghi Hajibeigy, Dr. Se Yong Eh Noum and Dr. Shirley Ch'ng for their supervision and guidance throughout the project development, Dr Dennis McMahon for the sponsorship of this project, Taylor's Mechanical Engineering batch August 2012 for assisting in various sections and Mr. Lai in assisting the code.

Abbreviations

ALIS	Autonomous Lake Improvement System
GPS	Global Positioning System
IR	Infrared Ray
DO	Dissolved Oxygen
LiPo	Lithium Polymer

References

[1] J. Bartram, R. Ballance, M. Meybeck, E. Kuusisto, A. Mäkelä, and E. Mälkki, "Water Quality Monitoring -A Practical Guide to the Design and Implementation of Freshwater Quality Studies and Monitoring Programmes Edited Chapter 2 -WATER QUALITY," pp. 0–419.

[2] J. Mack, "Eutrophication - Lake Scientist," *Miami University*. [Online]. Available: http://www.lakescientist.com/eutrophication/. [Accessed: 02-Oct-2016].

[3] NAHRIM, "A Desktop St udy on the Status of Lake Eutrophication in Malaysia."

[4] Z. Sharip and S. Zakaria, "Lakes and Reservoir in Malaysia: Management and Research Challenges," pp. 1349–1355, 2008.

[5] Sharon Behar. Montpelier, "Water Quality Parameters," *River Watch Network*. [Online]. Available: http://fosc.org/WQData/WQParameters.htm. [Accessed: 02-Oct-2016].

[6] S. Dlamini, I. Nhapi, W. Gumindoga, T. Nhiwatiwa, and T. Dube, "Assessing the feasibility of integrating remote sensing and in-situ measurements in monitoring water

quality status of Lake Chivero, Zimbabwe," *Phys. Chem. Earth*, vol. 93, pp. 2–11, 2016.
[7] A. Singh, M. J. Stealey, C. Victor, W. J. Kaiser, M. Batalin, Y. Lam, B. Zhang, A. Dhariwal, C. Oberg, A. Pereira, G. S. Sukhatme, B. Stauffer, S. Moorthi, D. Caron, and M. Hansen, "Human assisted robotic team campaigns for aquatic monitoring," *J. F. Robot.*, vol. 24, no. 11–12, pp. 969–989, 2007.
[8] G. Hitz, F. Pomerleau, M.-E. Garneau, C. Pradalier, T. Posch, J. Pernthaler, and R. Y. Siegwart, "Autonomous inland water monitoring: Design and application of a surface vessel," *Robot. Autom. Mag. IEEE*, vol. 19, no. 1, pp. 62–72, 2012.
[9] H. Hudson, "Monitoring-Lake-Quality."
[10] Boat Pennsylvania Course, "Hull Types and How They Operate | Pennsylvania Boating License Study Guide for Online Boating Safety Course." [Online]. Available: https://www.boat-ed.com/pennsylvania/studyGuide/Hull-Types-and-How-They-Operate/101039_101039011/. [Accessed: 25-May-2017].
[11] QQ Online Tradings, "DC Geared Motor GB37 [12V] Speed 17rpm ~ 500rpm." [Online]. Available: http://qqtrading.com.my/dc-geared-motor-gb37?search=12V Dc motor. [Accessed: 21-May-2017].
[12] J. Martenhoff, *The Powerboat Handbook*. Winchester Press, 1975.
[13] ElecFreaks, "Ultrasonic Ranging Module HC -SR04." [Online]. Available: http://www.micropik.com/PDF/HCSR04.pdf. [Accessed: 26-May-2017].
[14] Electronics Hub, "IR (Infrared) Obstacle Detection Sensor Circuit." [Online]. Available: http://www.electronicshub.org/ir-sensor/#Principle_of_Working. [Accessed: 21-May-2017].
[15] DFrobot, "Turbidity sensor SKU: SEN0189." [Online]. Available: https://www.dfrobot.com/wiki/index.php/Turbidity_sensor_SKU:_SEN0189. [Accessed: 21-May-2017].
[16] V. ke. Electronics, "Vk2828U7G5Lf." [Online]. Available: https://github.com/CainZ/V.KEL-GPS/blob/master/VK2828U7G5LF Data Sheet 20150902.pdf. [Accessed: 25-May-2017].
[17] T. Instrument, "LM35 Precision Centigrade Temperature Sensors," 2013. [Online]. Available: http://www.ti.com/lit/ds/symlink/lm35.pdf. [Accessed: 26-May-2017].
[18] Atlas Scientific Environment, "Dissolved Oxygen Probe." [Online]. Available: https://www.atlas-scientific.com/_files/_datasheets/_probe/DO_probe.pdf. [Accessed: 21-May-2017].
[19] Arduino, "Arduino Mega," 2017. [Online]. Available: https://www.arduino.cc/en/Main/arduinoBoardMega. [Accessed: 26-May-2017].
[20] STMicroelectronics, "L298N Motor Controller Datasheet," 2000. [Online]. Available: http://www.geeetech.com/Documents/L298N datasheet.pdf. [Accessed: 26-May-2017].

Properties of Differently Sintered Commercial Y-TZP Ceramics

R. Dharuna Raj[1*], W. J. Kelvin Chew[2*], S. Ramesh[3]
Department of Mechanical Engineering,
School of Engineering, Taylors University, 47500 Subang Jaya, Selangor, Malaysia
Centre of Advanced Manufacturing & Material Processing (AMMP),
Department of Mechanical Engineering, Faculty of Engineering, University of Malaya, 50603 Kuala Lumpur, Malaysia.

**dharunarajrajandran@sd.taylors.edu.my*

Abstract
In this research paper, the aim is to improve the mechanical properties of advance ceramic yttria-stabilized tetragonal zirconia polycrystals (Y-TZP). Advanced ceramic is a form of non-metallic polycrystalline material that has very high mechanical properties. Due to its high mechanical properties, Y-TZP main application is in the bio-medical division. It is mainly used for hip- replacement or knee replacement surgery. Two different Y-TZP brands were used in this research, samples Daichi and Tosoh. Both brands have very similar initial mechanical properties. Both have a density of 6.05 g/cm3 and a maximum bending strength of 1200 MPa is. Despite already having an existing high mechanical properties, it can still be improved. One of the ways of improving the properties is by carrying out sintering process. Sintering is a form of heat treatment that is exposed to the Y-TZP material while still in powder form. By carrying out the sintering process, it will fuse the small grains with other particles together to form a large grain. Four different range of temperatures were selected for the sintering process (1250^{o}C, 1300^{o}C, 1400^{o}C and 1500^{o}C). When the sintering process has been completed, the samples will undergo several test (bulk density measurement. Vicker's Hardness, and Fracture toughness) in order to determine whether the mechanical properties have been improved and what is the optimum sintering temperature. Based on the test carried out, it shows that the 1400^{o}C is the most optimum sintering temperature that will improve the mechanical properties of the Y-TZP. However, when the samples were exposed to 1500^{o}C, the test showed that the mechanical properties of the Y-TZP samples began to decrease.

Keywords: Y-TZP, Advance Ceramic, Sintering Process, Mechanical Properties, Optimum Temperature

1. Introduction

Ceramics are divided into two different categories which are the traditional and advanced ceramics. The difference between these two categories are the mechanical properties and the applications of the ceramics. Traditional ceramic is usually used to manufacture simple items such as pots due to its relatively low mechanical properties. However, advanced ceramic is non-metallic polycrystalline material with very high mechanical properties. One example of advanced ceramics is yttria-stabilized tetragonal zirconia polycrystals (Y-TZP). One of the main applications of Y-TZP is in the medical and bio-science division [1]. It is mainly used for hip-replacement surgery The comparison between advanced ceramic with metals and engineering plastic is shown is table 1 below.

Table 1. Comparison of Advanced Ceramics with Metals and Engineering Plastic [11]

Property	Metals	Engineering Plastics	Advanced Ceramics
Maximum Temperature for Typical Use (°C)	1500	350	2500
Hardness	Medium-High	Low-Medium	High
Corrosion Resistance	Low-Medium	Medium	High
Coefficient of Thermal Expansion	High	Medium	Low

Advanced ceramics have the mechanical and biological properties that can perform well under certain extreme conditions such as high temperature (more than 2500^{o}C), high pressure, high radiation and corrosion exposure [3]. Zirconia has a density of 6.0 g/cm2, the average grain size is 0.25 μm. young modulus of 2.1 × 105MPa and thermal conductivity of 0.009 cal/cm.s [9]. In order to obtain yttria-stabilized tetragonal zirconia polycrystals (Y-TZP), zirconia is blended with yttria. Y-TZP is a metastable state and it has a density of 6.05 g/cm3, bending strength at 1200 MPa and a Vicker hardness of 12.26 GPa [11].

There was a study done by Singh et al. [7] that focus on how the sintering parameters will affect the mechanical properties of the Y-TZP. The experiment was carried out with three samples. One sample is a standard 'Tioxode' that are coated with 2.5%mole of Y-TZP and the other two samples are Tosoh (Zirconia powder), but is coated with 2.5% and 3% mole of Y-TZP respectively. The proposed sintering temperature is set in between 1320 and 1600^{o}C. After the sintering process is carried out, the graph shows that the vicker hardness of each samples increases to maximum at 1400^{o}C then it will decrease and remains constant.

Another study was conducted by Matsui et al. [9] to show the effects of sintering parameter on the microstructure of the Y-TZP. The author conducted the experiment using two different sintering temperature (1300^{o}C and 1500^{o}C) and two different holding period (2 hours and 50 hours) using 3% mol (Y-TZP). When the samples are exposed to sintering temperature of 1300^{o}C with holding time of 2 hours and 50 hours, there is no significate increase the grain size. However, when the samples are exposed to 1500^{o}C with holding time of 2 hours and 50 hours, the grains have increased

remarkably. In this particular research paper, the objectives are to determine how did the sintering parameters affect the mechanical properties (density, hardness, toughness and phase content) of the commercial Y-TZP ceramics and what are the optimum range of sintering parameters for each type of Y-TZP ceramic.

2.0 Research Methodology

In this section, the methods and steps of carrying out the experiment is discussed and explain.

2.1 Preparation of Samples

2.1.1 Y-TZP Samples

Initially the samples will be in powdered form. Two different types of Y-TZP brand will be used in this experiment, Tosoh and Daichi. Both of the brands have very similar mechanical properties. Both brands have density of 6.05 g/cm3 and a maximum bending strength of 1200 MPa [11]. Before the experiment is carried out, the samples must be shaped into a circular shape. In order to achieve that, the Y-TZP must undergo two pressing process.

2.1.2 Pressing Process

Before the Y-TZP is pressed, the powder is dried in a vacuum chamber to remove all the moisture that may be present. The first pressing process is carried out using a device called the RMS Hydro Hydraulic Bench Press that has a capacity of 10 tones. After pressing, the powder will be compacted into a circular shape weighing in around 2.5 grams and 2 cm in diameter. After the using the hydraulic press machine, the samples undergo a second pressing process using a Cold Isostatic Press (CIP) machine (MTI Corp CIP 50A) to give its green sample. This machine uses water as compacting device. The reason the Y-TZP material has to undergo the pressing method is to ensure the molecules of the Y-TZP are compacted together leaving minimum gaps in between. Total of 16 green samples are produced. (8 Samples are reserved for the accelerated aging test that will be carried out in the future).

2.1.3 Sintering Process

The green samples will undergo a sintering process in a furnace model (XY-1200N). Different samples will be sintered at different temperatures ranging from 1250°C, 1300°C, 1400°C, and 1500°C with a ramp rate of 10°C/min. The reason this process is carried out is to manipulate the properties of the Y-TZP material by making it harder so that the samples will not rupture easily. The samples will undergo a single stage sintering temperature which means the starting temperature will be constant which is the room temperature. The reason for different temperature is selected is to determine which temperature will be the optimum sintering temperature for that will manipulate the mechanical properties of the Y-TZP to its extreme.

2.1.4 Accelerated Aging Test

After 16 green samples have undergone the sintering process, 8 samples are then separated and out of the 8 samples, one sample from each brand which is exposed to the most optimum sintering temperature will be chosen to undergo aging test. After that, the samples are placed in the machine called the acid digestion bomb from parr instrument. In the machine, it will be filled with distilled water and the device is placed in the oven at 180°C and 10 bar for increasing durations until all the water has been converted into superheated steam. This test is a carried out to prove that aging does change the mechanical properties of Y-TZP.

2.1.5 Grinding and Polishing

Out of the 16 Y-TZP samples, 8 samples that did not undergo the accelerated aging test will be proceeded to grinding and polishing. The Y-TZP samples was grinded using SiC (Silicon Carbide) grinding paper with 5 different grit sizes (120, 240, 600, 800 and 1200 grit). The wet grinding process was carried out at 50 rpm at 2 minutes for each sample. After the samples have finished grinding, the samples are polished to obtain that shinny polished look. This process if carried out by using a diamond based paste of 6 microns and 1 micron. The paste is applied onto the polishing cloth, and spread throughout using lubricant. The polishing process was carried out at 20 rpm for 2 minutes.

2.2 Measurement of Mechanical Properties

After 8 samples have undergone the grinding and polishing process, the sample are then exposed to three different tests in order to determine whether the mechanical properties of the samples have been changed.

2.2.1 Bulk Density Measurement

Bulk density measurement is a technique done based on the Archimedes principle which is using water immersion. An Analytical Balance (Model AG204, Mettler Toledo Balance densi-meter) is used to determine the density measurement. The bulk density was calculated using equation 1 below.

$$\rho = \frac{W_a}{W_a - W_w}\rho_w \qquad \text{Eqn.(1)}$$

ρ = Bulk density of sample
W_a = Weight of the sample in air
W_w = Weight of sample in water
ρ_w = Density of distilled water

2.2.2 Vicker's Hardness and Fracture Toughness Test

The vicker's hardness and fracture toughness test is carried out using a machine model MV-01 from Futuretech Japan. In the test, a fixed load of 10kg is applied onto the samples slowly to avoid any sudden impacts, after the load is on the sample, it is

placed there for 10 seconds. After the load is removed, it will form two diagonal indentations and fracture lines (L1, L2, L3, L4) on the edges on the indentations. The length of the indentations and the fracture lines are measured using a filar microscope attached to a microscope. The Vickers hardness (H_v) and the fracture toughness (K_{IC}) values are determined using equation 2 and equation 3.

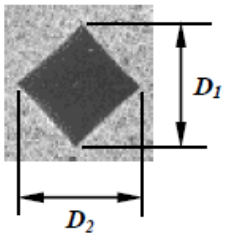


Figure 1. Indentation and Measurements needed to determine hardness value

$$H_v = \frac{1.854\,P}{D^2} \tag{2}$$

P = Applied Load (N)
D = Average Diagonals = $\frac{D_1+D_2}{2}$

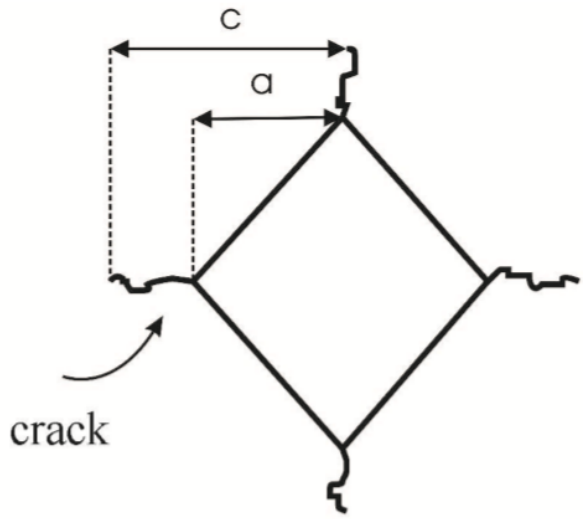


Figure 2. Measurements needed to determine the fracture toughness

$$K_{IC} = 0.16 \times \left(\frac{c}{a}\right)^{-1.5} \times (H \times a^{-0.5}) \text{ [5]} \tag{3}$$

K_{IC} = Fracture toughness (MPa·$m^{0.5}$)
H = Vickers hardness (MPa)
P = Test load in Vickers hardener (MPa)
c = Average length of the cracks obtained in the tips of the Vickers marks (μm)
a = Half average length of the diagonal of the Vickers marks (μm)

3.0 Results and Discussion

After the tests have been carried out on the samples, the results of the mechanical properties have been determined and shown in the tables and graphs below.

3.1 Bulk Density Measurements Results.

In order to determine the dense compacts ($\geqslant$ 95% theoretical density), the samples are first weighed in air and then water. The density of the distilled water remains at constant, 1g/cm^3 because the test was carried out under room temperature. Using equation (1) stated above, the bulk density of the samples was determined. Table one shows the values of the bulk density and the relative density of each samples the sintering temperature that each samples had undergone.

Table 2. Bulk Density Measurement of Samples

Samples	Sintering Temperature (°C)	Density of Distilled water (g/cm^3)	Weight in air (g)	Weight in water (g)	Bulk Density(Mg/m^3)	Relative Density (%)
X1	1250	1	2.433	2.025	5.96	98.5
X2	1300	1	2.451	2.02	5.68	93.9
X3	1400	1	2.446	2.041	6.03	99.8
X4	1500	1	2.41	2.007	5.98	98.8
Y1	1250	1	2.432	2.02	5.90	97.5
Y2	1300	1	2.446	2.036	5.96	98.6
Y3	1400	1	2.436	2.03	6.00	99.1
Y4	1500	1	2.445	2.039	6.028	99.5

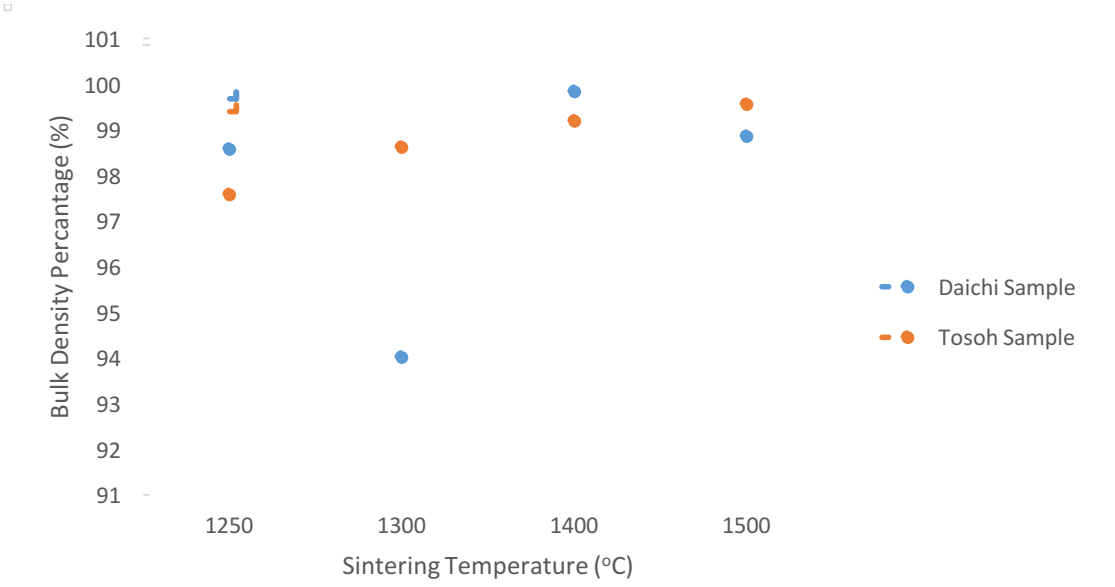


Figure 3. Graph of Bulk Density Against Sintering Temperature

Figure 3 shows the graph of the bulk density against sintering temperature between samples Daichi and Tosoh Samples. Based on the graph it shows Tosoh brand samples relative density gradually increases as the sintering temperature increases. However, for the Daichi samples, the relative density decreases at sintering temperature 1300°C and 1500°C. Similar trend was seen in study done by Dehestani [2].

3.2 Vickers Hardness Results

In order to determine the vicker's hardness, indentations are first made on the samples. Based on the indentation as shown in Figure 1, the average length of indentations (D) are determined and using equation (2), the vicker's hardness of the samples are determine.

Table 3. Vickers Hardness (H_V) Results of Samples

Samples	Sintering Temperature (°C)	D (µm)	L1 (µm)	L2 (µm)	L3 (µm)	H_V (GPa)
X1	1250	169.5	47.6	53.3	46.7	6.45
X2	1300	137.4	58.5	56	49.35	9.82
X3	1400	121.7	70.35	68.85	52.75	12.52
X4	1500	127.2	62.15	51.7	44.05	11.46
Y1	1250	126.5	61.55	56.75	55.5	11.59
Y2	1300	125.4	64.95	68.8	61.3	11.79
Y3	1400	128.1	68.9	50.55	49.25	11.30
Y4	1500	128.4	65.05	53.85	54.35	11.25

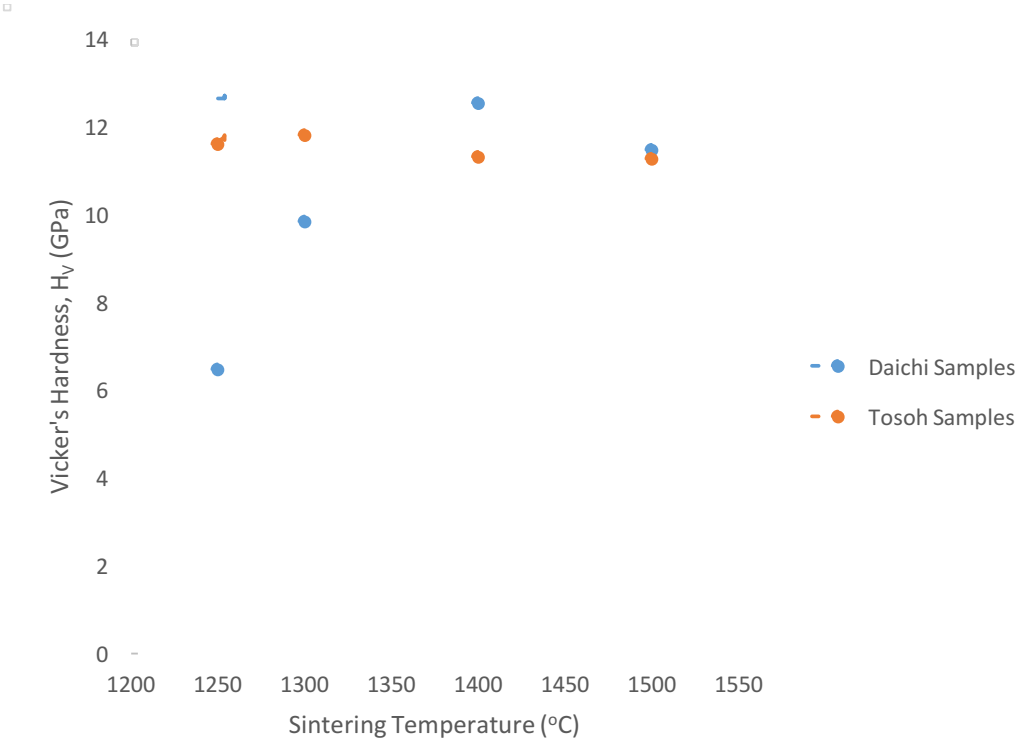


Figure 4. Graph of Vicker's Hardness (H_V) against Sintering Temperature (°C)

Figure 4 shows the graph of the Vicker's Hardness against sintering temperature between Daichi and Tosoh Samples. Based on the graph, it shows that the Daichi samples vicker's hardness have increased gradually as the sintering temperature increases. It shows that the samples reached its maximum hardness when is exposed to 1400^{o}C. However, the hardness begins to decrease when is exposed to the highest temperature which is 1500^{o}C. For the Tosoh samples, the graph shows that the sample reaches its maximum hardness at 1300^{o}C and then begins to decrease when the samples are exposed to higher temperature. It shows then when the samples are exposed to very high temperature, the vicker's hardness of the samples decreases. Therefore, it can be assumed that the mechanical properties of the samples with different brands can only be manipulated when exposed to certain range of temperatures. It also shows that Tosoh brand have a much higher initial vicker's hardness value when compared with Daichi brand. Similar study was done by Singh to determine the optimum sintering temperature of different brand of Y-TZP. In that study, it also shows that if the samples are exposed to very temperature, the mechanical properties decreases and will remain constant [7].

3.3 Fracture Toughness Results

After the indentation are made on the samples, fracture lines are seen on the edges of the indentations (L1, L2, L3). The lines are then measured and the average L is determined. Using equation (3), the value of the fracture toughness, K_{IC} is determined.

Table 4. Fracture Toughness (K_{IC}) Results of Samples

Samples	Sintering Temperature (^{o}C)	Half average length of indentation, a (μm)	Average length of the cracks, c (μm)	D(μm)	K_{IC} (MPa·m$^{-0.5}$)
X1	1250	24.6	49.2	169.5	1.81
X2	1300	27.3	54.6	137.4	2.91
X3	1400	31.9	63.9	121.7	4.02
X4	1500	26.3	52.6	127.2	3.31
Y1	1250	28.9	57.9	126.5	3.54
Y2	1300	32.5	65.0	125.4	3.81
Y3	1400	28.1	56.2	128.1	3.39
Y4	1500	28.8	57.7	128.4	3.44

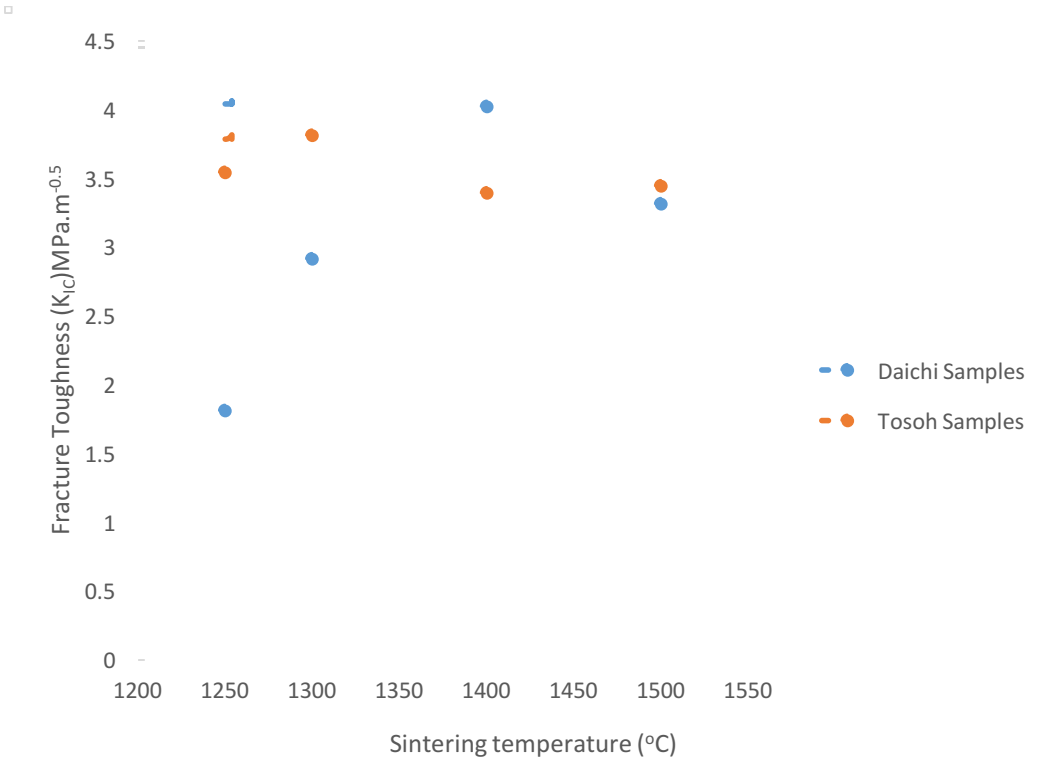


Figure 5. Graph of Fracture Toughness, K_{IC} against Sintering Temperature

Figure 5 shows the graph of the fracture toughness against sintering temperature between Daichi and Tosoh samples. Based on the graph it shows that Daichi samples have a lower fracture toughness compared with Tosoh. Despite that, the fracture toughness has increased gradually as the sintering temperature increases. It reaches it maximum toughness at 1400°C then began to decrease when exposed to 1500°C. It also shows similarity to the data collected from the vicker's hardness test, the Tosoh samples reaches its maximum toughness at 1300°C and then begins to decrease when the samples are exposed to higher temperature. the fracture toughness value decreases when exposed to the highest sintering temperature of 1500°C. This could be due to the different of grain sizes and particle sizes between the two brands. Similar results were seen in research paper done by Borrell, E. Rocha-rangel and R. Singh [2, 4, 7].

4.4 Aging Resistance Results

In order to determine the resistance of the Y-TZP samples of both brands from the undesired ageing or low temperature degradation (LTD) phenomenon when exposed to humid environments [27,28], selected samples were subjected to an accelerated ageing test. In general, the samples were exposed to superheated steam at 180°C and 10 bar for increasing durations and the phase content of the samples were periodically monitored via XRD analysis to determine the monoclinic zirconia (m-ZrO_2) phase content. Figure 4.4 shows the development of the monoclinic phase of zirconia in the Y-TZP samples after different ageing intervals between zero to 24 hours. The Y-TZP samples of both brands from the sintering temperature of 1400°C were chosen for the ageing treatment as these samples attained the highest mechanical properties among the range of sintering temperatures investigated.

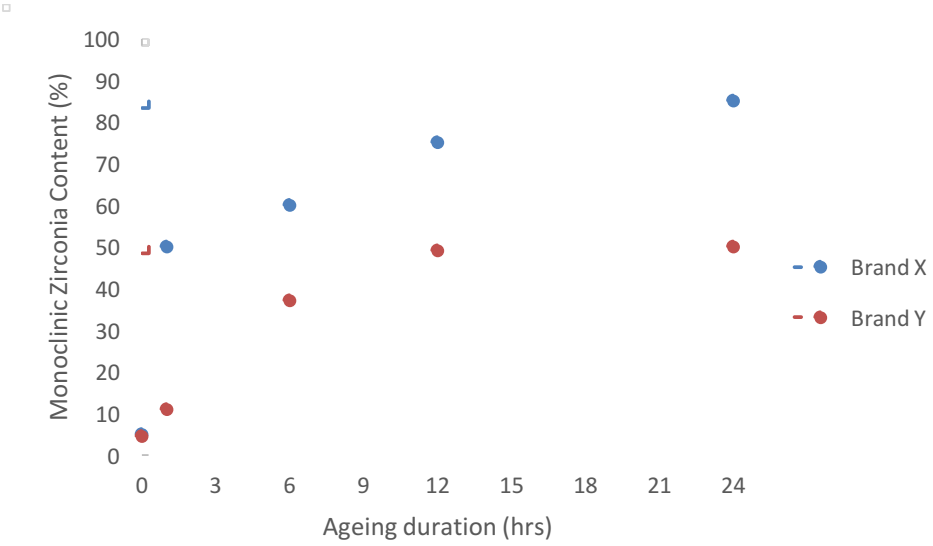


Figure 6. Monoclinic phase content in the Y-TZP samples after various accelerated ageing intervals.

In general, the tetragonal to monoclinic phase transformation of zirconia in the Y-TZP sample brand Y was found to occur at a slower rate as compared to that of brand X. The monoclinic phase content for Y-TZP brand X increased rapidly to the 50% mark after 1 hour of exposure and continued at a slower rate before reaching close to 90% after 24 hours' exposure. Visual inspection of the sample showed development of cracks apart from surface spalling with progressive ageing exposure. On the other hand, the Y-TZP brand Y showed better ageing resistance with the formation of monoclinic phase zirconia appearing to remain at 50% after aging beyond 12 hours. The better ageing resistance shown by sintered Y-TZP sample of brand Y could possibly be attributed to finer grain sizes attained after sintering [16,17,18].

4.0 Conclusion

In conclusion, the based on the experimental data and results, its shows that by carrying out the sintering temperature process, it will affect the mechanical properties of the Y-TZP. The tests also show that as the temperature increases, the mechanical properties (bulk density, vicker hardness and fracture toughness, aging resistance) is improved. However, only certain range of temperatures will improve the mechanical properties. The suitable and most optimum range of temperature that should be used is ranging from 1250^{o}C -1400^{o}C If the samples are exposed to very high temperature such as 1500^{o}C, the mechanical properties will decrease due to the sample being damaged at high temperature. If comparing which brand of Y-TZP (Daichi and Tosoh) is better, the results shows that the Tosoh brand is better. This could be due to the difference in particle size between the two brands (Tosoh having smaller particle size compared to Daichi). This shows that the smaller the particle size, the better the Y-TZP material will be

Acknowledgement

I would like thank the lab technicians from University Malaya who aided me in the vicker's hardness and the fracture toughness via Vickers indentation method and Andrew Ng for being my research partner.

References

[1] Egilmez, Ferhan Ergun, Gulfem, Cekic-Nagas, Isil Vallittu, Pekka K. Lassila and Lippo V J, "Factors affecting the mechanical behavior of Y-TZP", Journal of the Mechanical Behaviour of Biomedical Materials, vol. 37, pp 78-87, 2014.

[2] Borrell, Amparo, Salvador, María Dolores, Rayón, Emilio, Peñaranda-Foix and Felipe L, "Improvement of microstructural properties of 3Y-TZP materials by conventional and non-conventional sintering techniques", Ceramics International, vol. 38, pp 39-43, 2012.

[3] Dehestani, Mahdi and Adolfsson, Erik, "Phase stability and mechanical properties of zirconia and zirconia composites", International Journal of Applied Ceramic Technology, vol. 10, pp 129-141, 2013.

[4] E. Rocha-rangel, "Fracture Toughness Determinations by Means of Indentation Fracture," no. c, 2003.

[5] A. G. E. and E. A. Charles, "Fracture Toughness Determination by Indentation," *J. Am. Ceram. Soc.*, vol. 59, no. 7–8, pp. 371–372, 1976.

[6] M. Inokoshi, Masanao, Zhang, Fei, De Munck, Jan Minakuchi, Shunsuke, Naert, Ignace, Vleugels, Jozef, Van Meerbeek, Bart and Vanmeensel Kim, "Influence of sintering conditions on low-temperature degradation of dental zirconia", Dental Materials, vol. 30, ppl 669-678,2014.

[7] Singh. R, Gill. C, Lawson. S and Dransfield. G P "Sintering, microstructure and mechanical properties of commercial Y-TZPs", Journal of Materials Science, vol 31, ppl 6055-6062, 1996.

[8] Heimann, Robert B, "Introduction to Advanced Ceramics:", Classic and Advanced Ceramics, ppl 157-175, 2010.

[9] Matsui, Koji Yoshida, Hidehiro Ikuhara and Yuichi "Isothermal sintering effects on phase separation and grain growth in yttria-stabilized tetragonal zirconia polycrystal", Journal of the American Ceramic Society, vol 92, ppl 467-475,2009.

[10] D. Salamon, Advanced Ceramics. Elsevier Inc., 2014.

[11] Heimann, Robert B, "Introduction to Advanced Ceramics:", Classic and Advanced Ceramics, ppl 157-175, 2010.

[12] Tholey, Michael J. Swain, Michael V and Thiel, Norbert "SEM observations of porcelain Y-TZP interface", Dental Materials, vol 25, ppl 857-862, 2009.

[13] N. Amat, Noor Faeizah Muchtar, Andanastuti Yahaya, Norziha Ghazali and Mariyam Jameelah, "Effect of Sintering Temperature on the Mechanical Properties of Nanostructured Zirconia Fabricated via Colloidal Processing", Advanced Materials Research, vol 686, ppl 44-48, 2013.

[14] Lee, M.-C and Ahn, J.-W, "Ceramic Femoral Prosthesis in TKA – Present and Future", BIOLOX Symposium, vol 12, ppl 123, 2007.

[15] Clarke, I C, Green, D D, Pezzoti, G, Donaldson, D, "20 Year Experience of Zirconia Total Hip Replacements", Bioceramics and Alternative Bearings in Joint Arthroplasty, pp 67-78, 2005.

[16] Y. F. Yi, N. Wen, X. L. Wang, L. Q. Shao, and C. Wang, "Comparison of the

Low Temperature Degradation Properties of Two Y-TZP Ceramics for Dental Applications," *Key Eng. Mater.*, vol. 492, pp. 107–111, 2011.

[17] L. Hallmann, P. Ulmer, E. Reusser, M. Louvel, and C. H. F. Hämmerle, "Effect of dopants and sintering temperature on microstructure and low temperature degradation of dental Y-TZP-zirconia," *J. Eur. Ceram. Soc.*, vol. 32, no. 16, pp. 4091–4104, 2012

[18] M. Inokoshi *et al.*, "Influence of sintering conditions on low-temperature degradation of dental zirconia," *Dent. Mater.*, vol. 30, no. 6, pp. 669–678, 2014.

eureca 2017 – Conference Paper
Paper Number 2ME05

Improving the accuracy of Taylor's wind tunnel measurements

Hutomo Wibowo, Abdulkareem Sh. Mahdi Al-Obaidi
School of Engineering, Taylors University, Malaysia

Abdulkareem.Mahdi@taylors.edu.my

Abstract
This paper aims to improve the accuracy of Taylor's wind tunnel measurement. During the operations of the Taylor's wind tunnel, it was found that the wind tunnel has slight deviation in the measurement in terms of the lift and drag measurement. The study focused on the quantification of the wind tunnel sources of errors experimentally. 4 different experiments were considered identify the errors under 4 parameters which are the effect of air leak, flowrate, test rig and size of the model in the wind tunnel. Based on the experiments, the contribution of the errors percentages is quantified as 1.23%, 0.65%, 24.87%, and 20.18% respectively. the results obtained from the experiments are compared with the published paper. Errors contributed by the air leak and flowrate can be corrected by including the percentage error contribution during the experiment as tolerance values that can either be subtracted from the results. For test rig, the error contribution can be corrected by implementing the Eq. (1) to obtain the true drag and lift coefficient. Lastly the error contributed by the size of the model can be minimized. The percentage error contribution in the wind tunnel can be further identified by conducting other experiments involving the drag and lift such as the effect of angle of attack on the drag and lift measurement of NACA 0012 in the wind tunnel, the effect of shapes on the drag and lift measurement in the wind tunnel, the effect of lab conditions in the wind tunnel, the effect of rigidity of the connections of test rig with the load cell

Keywords: Experimental, Wind tunnel, sources of error, Drag, lift,

1.0 Introduction

Taylor's wind tunnel is an open-section wind tunnel that was initially created by former student of Taylor's University located in Malaysia. Taylor's wind tunnel is built for education and research purposes. A number of students have used the wind tunnel for different purposes. Taylor's wind tunnel specifications can be referred to S. Eftekhari, [1].

Wind tunnel is a useful tool to study the aerodynamic characteristics of different objects with various shapes and sizes. The accuracy of the subsonic wind tunnel which is located in Taylor's University laboratory will have a great impact on the understanding of aerodynamic and fluid mechanics. Methodology is conceived based on the DOE approach [2], these errors are then classified in 3 different categories. However, it is important to determine the potential error sources in the wind tunnel to improve the data accuracy of the wind tunnel. This paper has listed several experiments that was conducted and validated to determine the potential error sources in the wind tunnel.

According to the study of the summary of experimental uncertainty, Stern, et al. [2] pointed out that in experiments, the true values of measured variables are usually difficult to be determined since experiments tends to always have errors given by the instrumentations, facility data acquisition and environmental and data acquisition and reduction limitations. Mills and Chang [3], also pointed out that physical quantities such as velocity, flowrate, temperature that are measured in experiment are subject to errors. There are 2 types of errors. these errors are precision errors and bias errors.

Precision errors can be called random errors which can be associated with instruments such as hot wire probe which is used to measure various parameters such as velocity, flowrate and temperature. According to Mills and Chang [3], precision errors can be treated through statistical analysis. On the other hand, bias errors can also be called systematic errors which can be associated with calibration error such as zero-offset errors for example zero-offset error of Vernier caliper which causes a constant absolute error in all the readings [3]. However, accuracy is defined on how close is the measured value to the true value and is usually in terms of percentage errors. Accuracy increases as errors approaches zero [2].

According to Lombardi et al. [4], stated that the wall interference effect in the wind tunnel test section is considered to be one of the main sources of error that affects the accuracy of the results. They conducted a study of correction of the wall interference effects in wind tunnel experiments numerically under two conditions. Free air flow over the model and measured pressure values over the wind tunnel walls are used as boundary conditions.

Rhode and Oberkampf [5], conducted a study of estimation of uncertainties for a model validation experiment in a wind tunnel. The author studied the source of

uncertainties in the wind tunnel by implementing DOE strategy in order to categorized the error sources into 3 classes which are

- Random uncertainty
- Flow field non-uniformity uncertainty
- Model and instrumentation uncertainty

The author concluded that the major contributor to the uncertainty in wind tunnel falls under the flow field non-uniformity to the total uncertainty.

S. Lai, [6] performed a study in the effect of size and shape of side mirrors on the drag of a personal vehicle. The study focuses to calculate the drag contributions of the side mirrors. The author demonstrates a calculation formula to calculate the coefficient of drag in Taylor's University wind tunnel since the results obtained from the wind tunnel is in drag force. Therefore, Eq. (1) was developed to estimate the coefficient of drag of the model only.

$$C_{D(model)} = C_{D(total)} \frac{S_{total}}{S_{ref}} - C_{D(Rod)} \frac{S_{Rig}}{S_{ref}} \quad (1)$$

where,

- $C_{D(Model)}$ is the coefficient of drag of the model.
- $C_{D(total)}$ is the total coefficient of drag.
- S_{total} , which is the total frontal area of the model and test rig.
- S_{ref} is the frontal area of the model without the test rig.
- $C_{D(rig)}$ is the coefficient of the test rig.
- S_{rig} frontal area of the test rig.

This project was offered for the final year project in Taylor's University. The purpose of this project is to quantify the sources of error that can be identified in the Taylor's wind tunnel and if possible propose and engineering solutions to improve the wind tunnel. In this paper, there are four effects that are considered to determine the error sources such as:

- The first is the effect of the air leak on the velocity of the wind tunnel test section. This test is to assess the wind tunnel flow quality due to holes since flow quality may affects the wind tunnel results, accuracy [7].
- The second is the effect of the flowrate in the test section at different frequency ranging from 0 to 40 Hz. This study is to ensure that the accuracy of the flowrate at different frequency from the theoretical calculation wind tunnel flowrate. By knowing the difference, the experimenter will be able to make a correction in order to run at a desired speed and flowrate by taking into the consideration of the difference.
- The third is the effect of test rig/support system of the model on the drag and lift measurement. The study of the test rig interference is very important among the aerodynamic testing due to it adverse effects that it brings to the results [8]. The effect of the test rig can be calculated using Eq. (1) from the study conducted by S. Lai [6]
- The fourth is the study of the effect of the size of the model on the drag and lift measurement [9,10]. The present paper aims to to identify what are the sources

of errors in measuring the aerodynamic characteristics and analyze and assess the contribution of each error source. The project is limited at low subsonic speed in the range of 0 m/s to 38 m/s and at 5 different angle of attack range from 0 to 20 at the interval of 5 degrees. Errors sources is also limited under 3 different categories and human errors are not included. As for the model, NACA 0012 Finite wings airfoil will be used.

2.0 Research Methodology

The sources of error are identified through the observations of doing the experiments in Taylor's wind tunnel. The errors are then classified under 3 different categories which are the instrumental errors, environmental errors and test rig errors. 10 different sub-categories are conceived and 4 different sub-categories which are the effect of air leakage, effect of the support, effect of the flowrate and lastly effect of size of the model.

2.1 Data Extraction

All of the published paper data were extracted using the WebPlotDigitizer v3.12 that is able to automatically follow and acquire data points from a given high resolution image of C_D-AOA or C_L-AOA curve, to extract the digitized drag and lift coefficient at different AOA information (refer to Figure 6). Before obtaining the Published data [20], the two axis limits are initially set. Then, individual data points were selectively chosen. The accumulated data is compiled in the excel spreadsheets. The procedure was conducted three times to take the average. Once the average extracted data have been compiled, the author performed interpolations for the desired data points such as angle of attack of 0, 5, 10, 15, and 20 from the extracted data. After the desired data has been acquired, the author can finally conduct a comparison with the experimental data obtained from the TUWT.

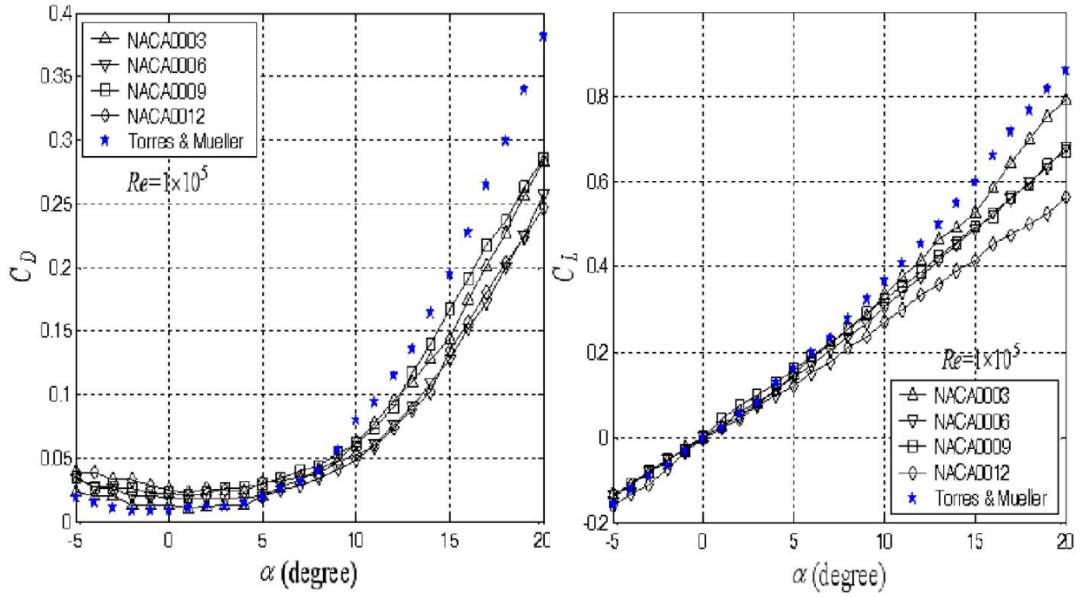


Figure 20. Drag and lift coefficient w.r.t AOA [9]

2.2 Calibrations

Before starting any experiment, calibrations are an important part of the experiment to achieve an accurate result. The focus of this project is to improve the accuracy of Taylor's wind tunnel. Therefore, it is important to know about the losses in each section in the wind tunnel.

Table 14: Taylor's Wind Tunnel Specifications [1]

Taylor's Wind Tunnel Specifications	
Type	Open-circuit or Eiffel
Test Section Cross-sectional area	0.303 m by 0.303 m
Geometrical shape of the test section	Rectangular
Length of the test section	0.885 m
Contraction ratio	3:4:1
Fan Speed	3.33 m/s – 38.85 m/s
Fan diameter	0.63 m
Output torque of a motor	415 V/50 Hz
Motor Horsepower	3 HP

2.3 Velocity distribution along the centerline in Test Section

The purpose behind this study is to ensure the consistency of the velocity along the centerline. Hot wire anemometer was used and positioned at three positions along the centerline in the test section which is shown in Figure 3 and Figure 4. Wind tunnel velocity was initially set at frequency input of 5 Hz which is 3.23 m/s. in order to record the velocity, hotwire anemometer was connected to the datalogger (DO2003) [11]. After the results has been recorded, the experiment was repeated at five operational frequency input of 10, 15, 20, and 25 Hz. The results were then tabulated.

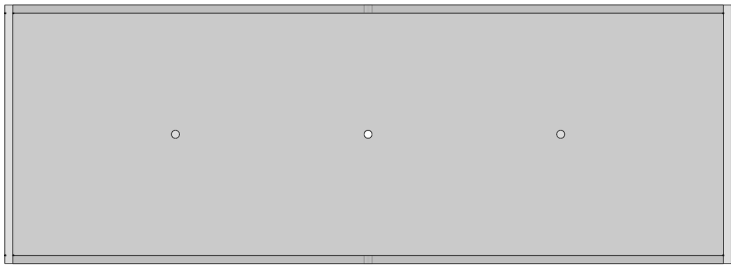


Figure 21. Test Section with 3 centerline holes

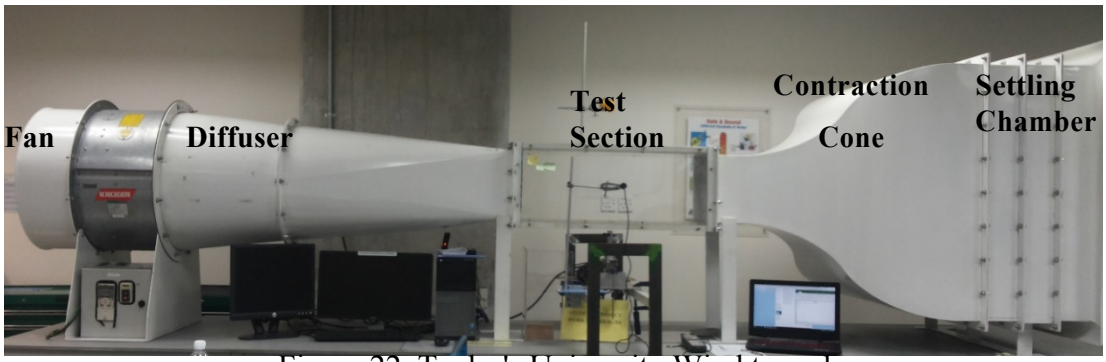


Figure 22. Taylor's University Wind tunnel

2.4 Effect of air leakage at 3 different position

The purpose of this experiment is to determine the error contributed on through the air leakage in the test section with or without model. Two condition are created for the purpose of this experiment. The first condition is to create some holes on the walls of the test section. There are total 7 holes on each walls of the test section. One on the top-center, bottom-center, back-center and 4 holes on the front where 3 holes are scattered on the center line and another one is placed above the hole in the center. The test section with holes is illustrated in Figure 11 at Appendix 1. A hot wire anemometer is used to obtained the velocity reading for 3 different position of the front acrylic on 3 different center line positions.

2.5 Effect of the flowrate

On the third experiment in this methodology was conducted in order to identify the how much the experimental flowrate differs from the theoretical values. The experiment was run using different frequency ranges from 5 Hz to 40 Hz with the interval of 2.5 Hz. The flowrate at different frequency is then recorded for 30 second interval for each frequency.

2.6 Effect of the test rig/support system of the model

The experiment is designed for the purpose of measuring the drag and lift on the test rig and to determine how different model affect the support. The outcome of the experiment is that the drag and lift data of the model only should be able to be calculated. The model that were used in this experiment are NACA 0012 finite wing with an aspect ratio of one with test rig and test rig only which are shown Figure 9 and 10 respectively along with the dimensions. The experiment set-up is illustrated in Figure A.2 in Appendix A. Equation (3) will be adopted which was studied by S. Lai [6] as the following:

$$C_{D(model)} = C_{D(total)} \frac{S_{total}}{S_{ref}} - C_{D(Rod)} \frac{S_{Rig}}{S_{ref}} \quad (3)$$

where,
$C_{D(Model)}$ is the drag coefficient of the model.
$C_{D(total)}$ is the total coefficient of drag.
S_{total} , is the total frontal area of the model and test rig.
S_{ref} is the frontal area of the model without the test rig.
$C_{D(rig)}$ is the drag coefficient of the test rig.
S_{rig} frontal area of the test rig.

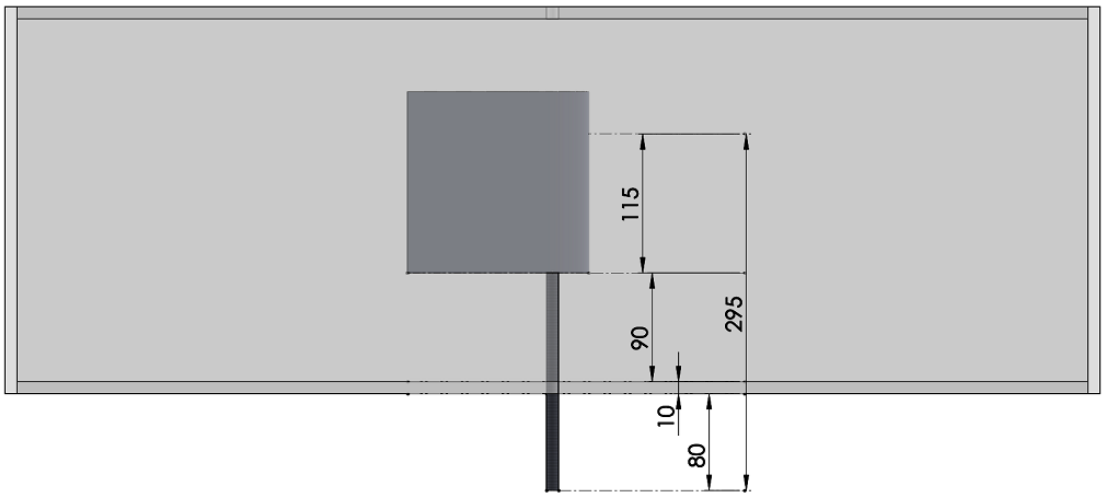


Figure 23. Test Section setup of model with test rig

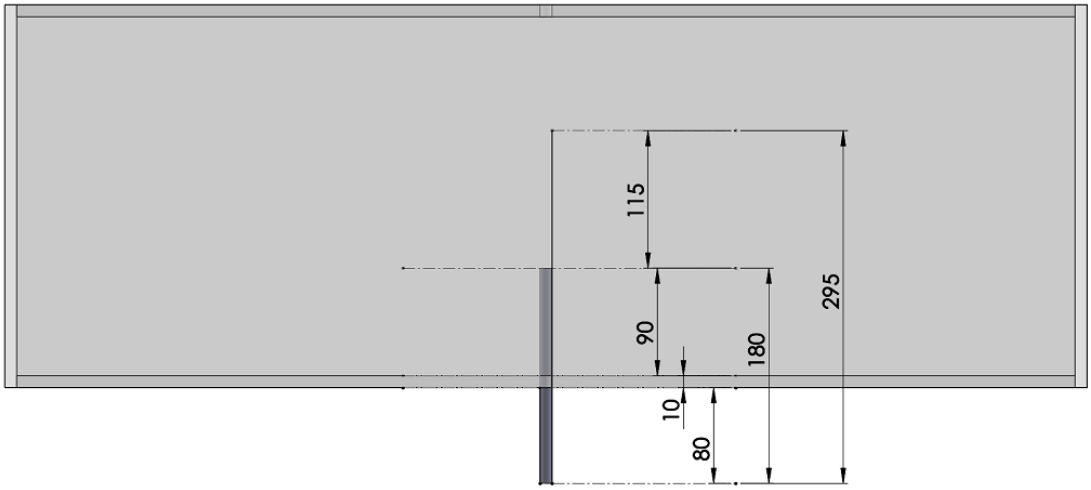


Figure 24. Test section setup only Test rig

2.5 Effect of size of the models

In this last experiment that was conducted was to study on how the effect of size of the model affect the drag and lift measurement in Taylor's University wind tunnel. The models that were used for this experiment are three aspect ratios of NACA 0012 profile which are 0.5, 1.0 and 1.5 and the experiment is run at five angle of attack. Both the drag and lift results on each aspect ratio were recorded and compared with the published paper [9]. From the Figure 7 shown three different aspect ratios of the finite wings of NACA 0012. The chord length for all three airfoils are the same only the span of the airfoil that were modified. In the figure 8, 9, 10 shows the experiment set up of each airfoil according to the aspect ratio. Detailed drawing of each airfoil aspect ratios can be referred at appendix.

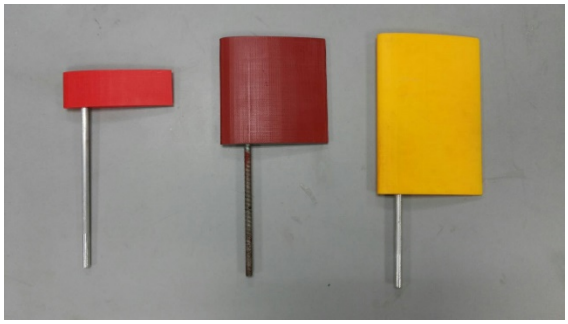


Figure 25. Different aspect ratio of NACA 0012

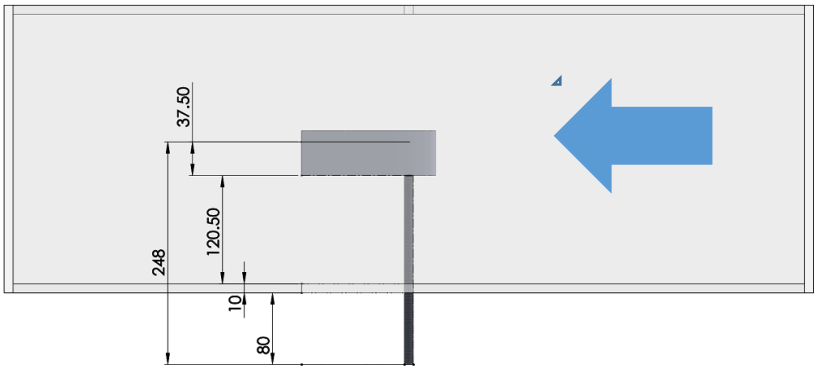


Figure 26. NACA 0012 with AR 0.5 in the Test section

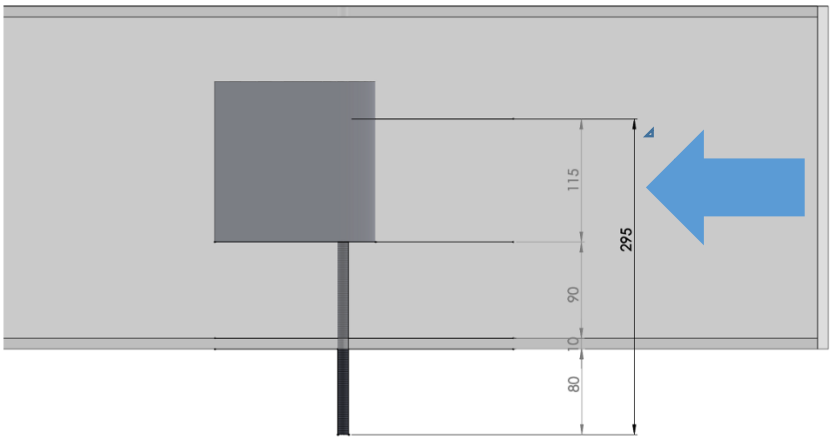


Figure 27. NACA 0012 with AR of 1.0 in the Test section

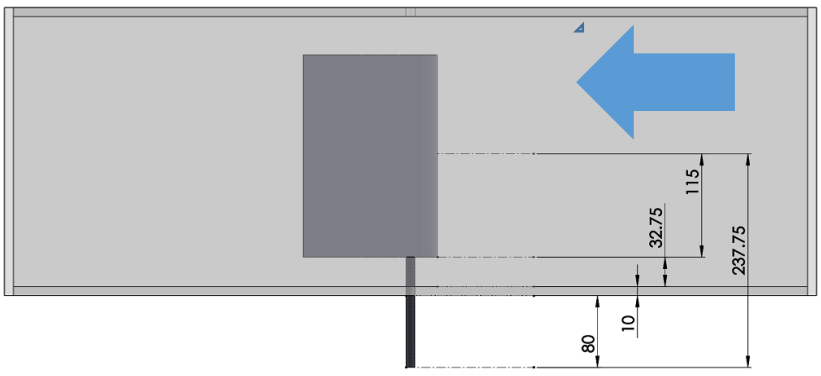


Figure 28. NACA 0012 with AR of 1.5 in the Test Section

3.0 Results and Discussion

This section discusses the experimental results obtained throughout this research. The effects of air leak to the velocity under three different positions, the effects of the test rig to the drag and lift of NACA 0012 with aspect ratio of 1, the effects of size of NACA 0012 on the drag and lift measurement and the effect of flowrate in the test section. The experimental results obtained are validated from the published paper.

3.1 Effect of air leak on the velocity along the center line in the test section under three positions

From the data shown in the Table 2, there are two conditions under the effect of air leak which are with holes and sealed. It can be observed that there is an increase of velocity as the frequency increases. Similar trend can be observed from the three positions where for each the velocity at the same frequency among the positions has not much of a difference.

Table 2. Air leak under 3 different position

	Distance (cm)	Position	5 Hz	10 Hz	15 Hz	20 Hz	25 Hz
with holes	-12	Left	3.39	6.8	10.63	14.25	17.72
	0	Center	3.3	6.63	10.58	13.97	17.12
	12	Right	3.31	6.69	10.28	13.71	16.84
sealed	-12	Left	3.48	6.79	10.62	14.02	17.22
	0	Center	3.38	6.66	10.32	13.76	17.06
	12	Right	3.34	6.74	10.43	13.76	16.77

Moreover, from the Table 3, shows the percentage error distribution between the sealed and leaks conditions in three positions along the centerline of the test section. Table 3 also shows the maximum error percentage is at 2.90% where the minimum goes down to 0.09%.

Table 15. Percentage error distribution of air leak in different positions

	% diff b/n sealed and holes		
Frequency	Left	Center	Right
5	2.59	0.90	2.37
10	0.15	0.74	0.45
15	0.09	1.44	2.52
20	1.64	0.36	1.55
25	2.90	0.42	0.33

In Table 4 shows the summarization of the whole results tabulated from Table 2 and 3, by taking the average of each position of the error percentage contribution and adding each average for three positions to find the average of the average to obtain the final percentage contribution on the overall error contribution of the effect of air leak on the wind tunnel velocity measurement.

Table 16. Average error of air leak in different positions

	Left	Center	Right
Average error	1.47	0.77	1.44
Average of average errors	1.23		
Range error	0.09 - 2.9	0.36 - 1.44	0.33 - 2.52

From the graph shown on Figure 23, there are three positions that are shown in the graph. It can be observed that the error percentage distribution given by air leakage has a higher contribution in the first three frequency which shows that lower speed is prone to air leakage. As the frequency increases shown in the graph, the error distribution decreases.

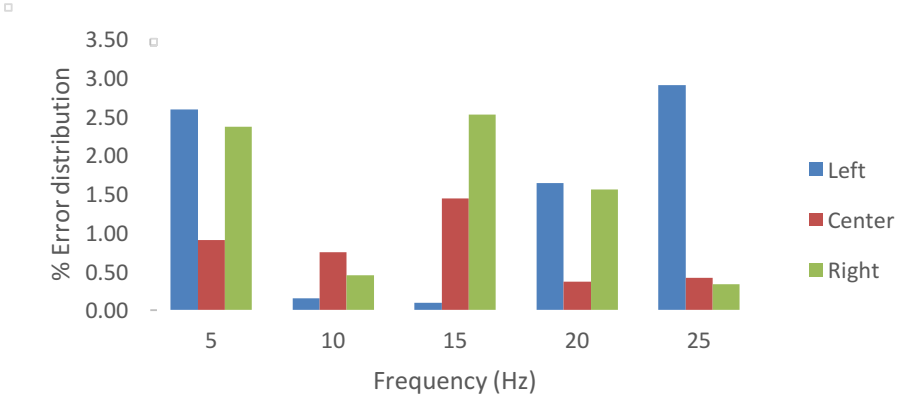


Figure 29. Percentage error distribution of the air leak in.

3.2 Analysis and calculation of the experiment of the effect of flowrate

Table 5 shows the frequency range of 0 to 40 Hz at the interval of 2.5 Hz. In this Table, there are two methods that are used to obtain the flowrate. The first is the theoretical flow rate in which the flowrate is calculated with respect of the desire velocity corresponds to the frequency. The area that is used in the calculation is the cross-sectional area of the test section measured. The second method is the experimental flowrate in which the wind tunnel is run in the range of the desire frequency and the flowrate is measured using the hotwire that is connected to the data logger under 30 second interval for every frequency. It can also be seen from Table 5 that the theoretical flowrate is very close with the experimental flowrate which shows that the flowrate has very little effect on the performance of the wind tunnel. Table 5 also shows that the results of the experimental flowrate have lower values compared theoretical results.

Table 17. Flowrate distribution

Frequency (Hz)	Avg velocity (m/s)	Experimental Flowrate (m^3/s)	Theoretical flowrate (m3/s)	% error difference

5	3.38	1089.70	1095.12	0.49
7.5	4.80	1566.00	1556.28	0.62
10	6.66	2153.30	2157.84	0.21
12.5	8.48	2770.00	2748.60	0.78
15	10.32	3340.00	3343.68	0.11
17.5	12.07	3906.70	3911.76	0.13
20	13.76	4453.30	4457.16	0.09
22.5	15.42	4976.70	4997.16	0.41
25	17.06	5526.70	5528.52	0.03
27.5	18.68	6063.30	6052.32	0.18
30	20.37	6586.70	6598.80	0.18
32.5	22.10	7153.30	7160.40	0.10
35	24.40	7776.70	7905.60	1.63
37.5	25.90	8370.00	8391.60	0.26
40	26.60	9010.00	8618.40	4.54

Table 6 shows the percentage error distribution between the theoretical and experimental values obtained. The error percentage distribution between two methods have mostly lower than one percent of difference except for two values that are highlighted in yellow. The minimum and maximum range of error percentage contribution is from 0.09 to 4.54 percent respectively. The average of average error is 0.65 percent.

Table 18. Error percentage distribution of Flowrate distribution

Range of errors	Average % error difference
0.03 - 4.54	0.65

In Figure 11, the percentage of error contribution can be seen more clearly showing that for most flowrate is lower than one percent. Due to the low percentage contribution, the effect of flowrate can be neglected. However, for better accuracy in using the Taylor's wind tunnel, it is best to include the average of average error percentage for flowrate measurement purpose.

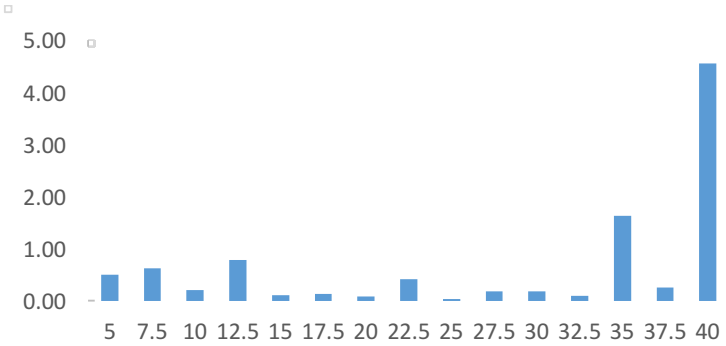


Figure 30. Percentage error distribution of flowrate under different frequency

The theoretical flowrate calculation is calculated as the following:

$$\dot{V} = A \cdot \mathrm{v} \tag{4}$$

$$\dot{V} = (0.0303 \times 0.303)\mathrm{m}^2 \cdot 3.38\ \mathrm{m/s} \cdot \frac{3600\ \mathrm{s}}{1\ \mathrm{h}}$$

$$\dot{V} = 1095.12\ \mathrm{m}^3/\mathrm{h}$$

3.3 Effect of test rig/support system on drag and lift measurement

Table 6, summarizes the result of measurement of drag and lift of the model with the support. Whereas Table 7 shows results of the measurement of drag and lift of the model without the support. Table 8 shows the summary of the error difference obtained from table 6 and 7. The range of the error found in the effect of the test rig on the lift and drag measurement were found to be 1.43% - 32.13%, 11.85% - 41.24% respectively. The support interference on the drag coefficient is found to be more profound than coefficient of lift shown in Figure

Table 19. Effect of model support on the drag and lift measurement with rig

w/h rig	Published paper [9]		Experimental Data		% Error difference	
AR 1	CL	CD	CL	CD	CL	CD
0	0.000	0.025	0.050	0.041	4.984	64.770
5	0.122	0.031	0.161	0.049	32.129	59.925
10	0.271	0.051	0.268	0.068	1.433	33.312
15	0.413	0.136	0.355	0.102	13.963	25.211
20	0.561	0.251	0.469	0.214	16.342	14.706

Table 20. Effect of test rig on the drag and lift measurement without rig

w/o rig	Published paper [9]		Experimental Data		% Error difference	
AR 1	CL	CD	CL	CD	CL	CD
0	0.000	0.025	0.040	0.017	3.97	30.98
5	0.122	0.031	0.165	0.025	35.09	18.19
10	0.271	0.051	0.275	0.045	1.46	11.85
15	0.413	0.136	0.367	0.080	11.21	41.24
20	0.561	0.251	0.485	0.196	13.50	21.63

Table 4 shows the summary of the error percentage found in the effect of test rig experiment. It can be observed that the average errors of condition with rig has a higher lift and drag coefficient error percentage difference compare with condition of without rig at Reynold's number of 1.0 x 10^5; hence model without rig will be closer to the true value compare the model with rig. The method to determine the coefficient of

drag and lift with and without rig can be refer using Equations (3) shown in section 3.5 from the study conducted S. Lai [6].

Table 21. Range of errors and average errors of effect of test rig

Conditions	Range of errors		Average errors	
AR 1	CL	CD	CL	CD
w/h rig	1.43 - 32.13	14.71 - 64.77	13.77	39.58
w/o rig	1.46 - 35.09	11.85 - 41.24	13.05	24.78

Moreover, from Figure 11, it is shown that the difference between the percentage error distribution under two conditions such as condition with rig and without rig. For the first two angles, the percentage errors on the model with rig is higher compared to the percentage errors on the model without rig. As the angle increases, it can be seen that the percentage error starts to shift sides especially at the last two angles which are at the angle of 15 and 20 which shows the percentage error of the model without the without rig has a higher error compare to the model with rig.

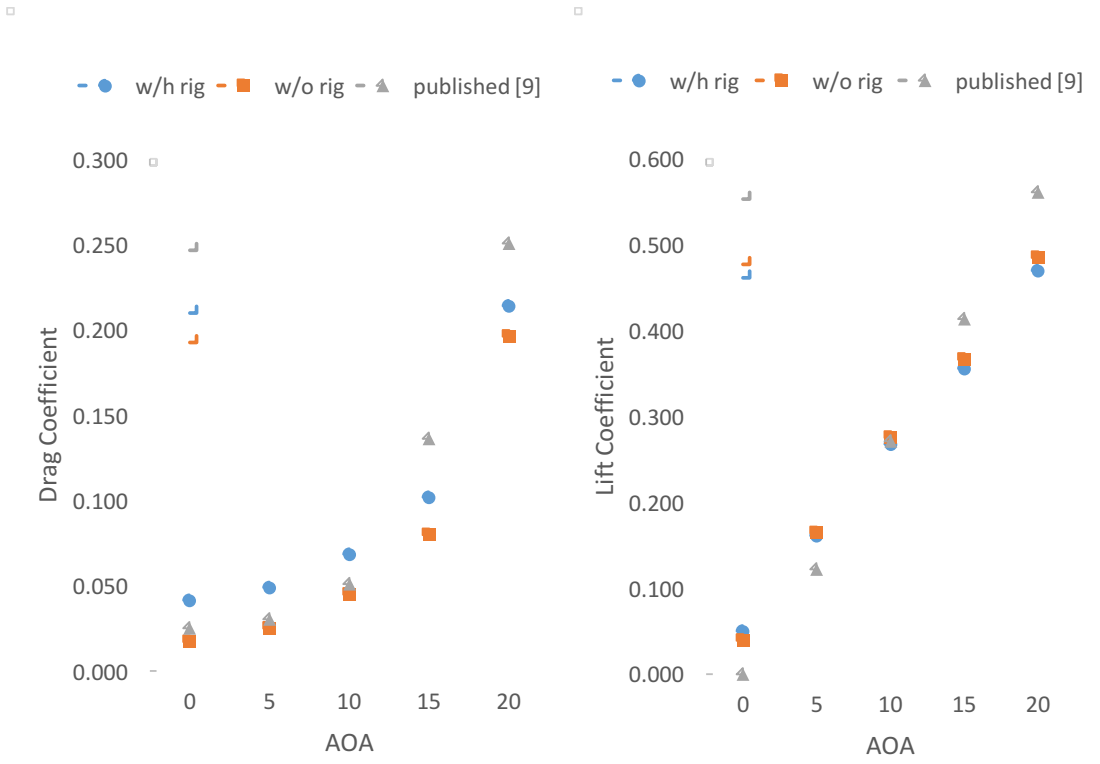


Figure 312. Comparison of drag and lift distribution between with rig, without rig and published paper [9].

3.4 Effect of size of the models on the drag and lift measurement

The purpose of the study of the effect of size initially conceived in order to investigate the effect of the difference of aspect ratio of the same model. Study shows that for streamlined shapes that higher aspect ratio has will have a higher stall angle. Three model were used to investigate on the effect of size on the airfoil with three aspect ratios of 0.5, 1.0 and 1.5. Table 26 shows the percentage error difference of the effect of size of three aspect ratios. It can be observed that the error percentage differences increase with the aspect ratios on the drag and lift coefficient at various angle of attack shown in Table 9.

Table 22. Percentage error differences of different aspect ratio

AOA	% error differences					
	AR 0.5		AR 1		AR 1.5	
	C_D	C_L	C_D	C_L	C_D	C_L
0	28.49	1.76	30.53	0.02	42.30	0.02
5	24.51	57.68	10.27	48.02	58.93	27.85
10	27.27	26.97	42.03	46.47	64.97	2.43
15	37.46	18.81	44.44	38.04	63.12	11.07
20	38.40	6.75	24.54	22.18	31.47	26.80

Figure 13 - 15 shows the drag and lift distribution under the aspect ratio of 0.5, 1.0, and 1.5 the drag distribution deviated more profound as the angle of attack increase.

- At zero AOA, percentage error differences of drag coefficient of AR 0.5 amount to 28.49% with AR 1 of 30.53% and AR 1.5 at 42,30%.
- At AOA of five, percentage error differences of drag coefficient of AR 0.5 amount to 24.51% with AR 1 of 10.27% and AR 1.5 at 58.93%.
- At AOA of ten, percentage error differences of drag coefficient of AR 0.5 amount to 27.27% with AR 1 of 42.03% and AR 1.5 at 64.97%.
- At AOA of 15, percentage error differences of drag coefficient of AR 0.5 amount to 37.46% with AR 1 of 44.44% and AR 1.5 at 63.12%.
- At AOA of 20, percentage error differences of drag coefficient of AR 0.5 amount to 38.40% with AR 1 of 24.54% and AR 1.5 at 31.47%.

Figure 13 - 15 also shows that both lift and drag coefficient under three aspect ratios have a gradual increase of deviation as the aspect ratio increases with an increase of AOA. Higher aspect ratio leads to a higher error contributions. Therefore, future user who will be using the TUWT at higher aspect ratio will have to expect that high error percentage will occur especially when measuring drag coefficient.

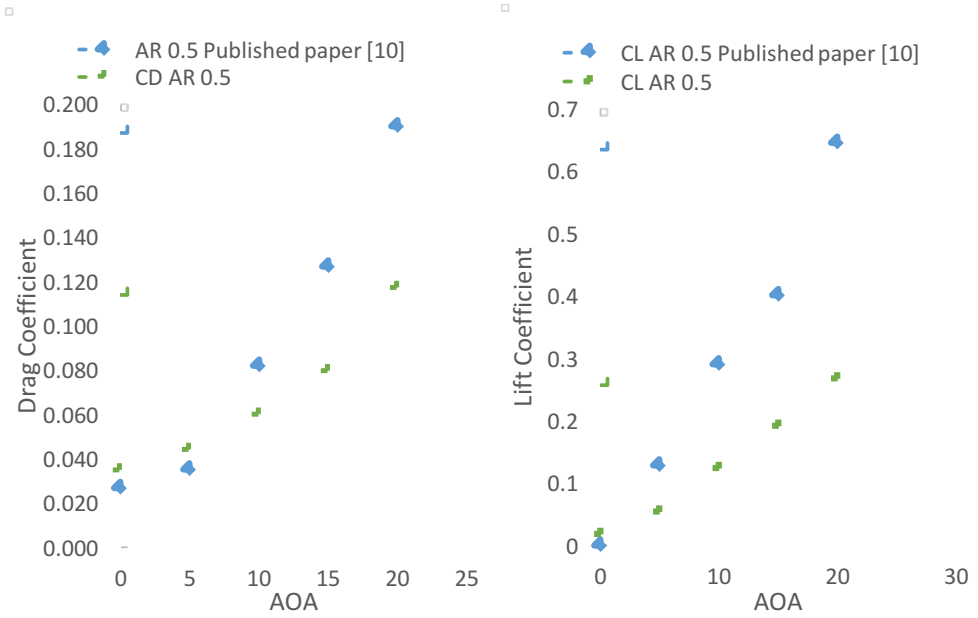


Figure 13. Drag and Lift distribution under aspect ratio of 0.5 at various angle at Re no of 1.23 x 10^5

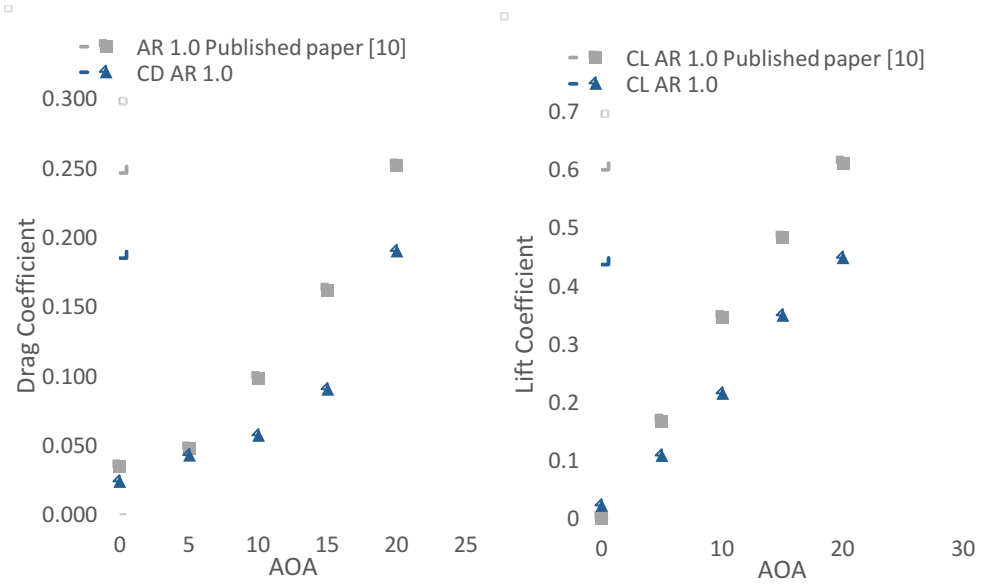


Figure 32. Lift distribution under aspect ratio of 1.0 at Re no of 1.0 x 10^5 at Re no of 1.23 x 10^5

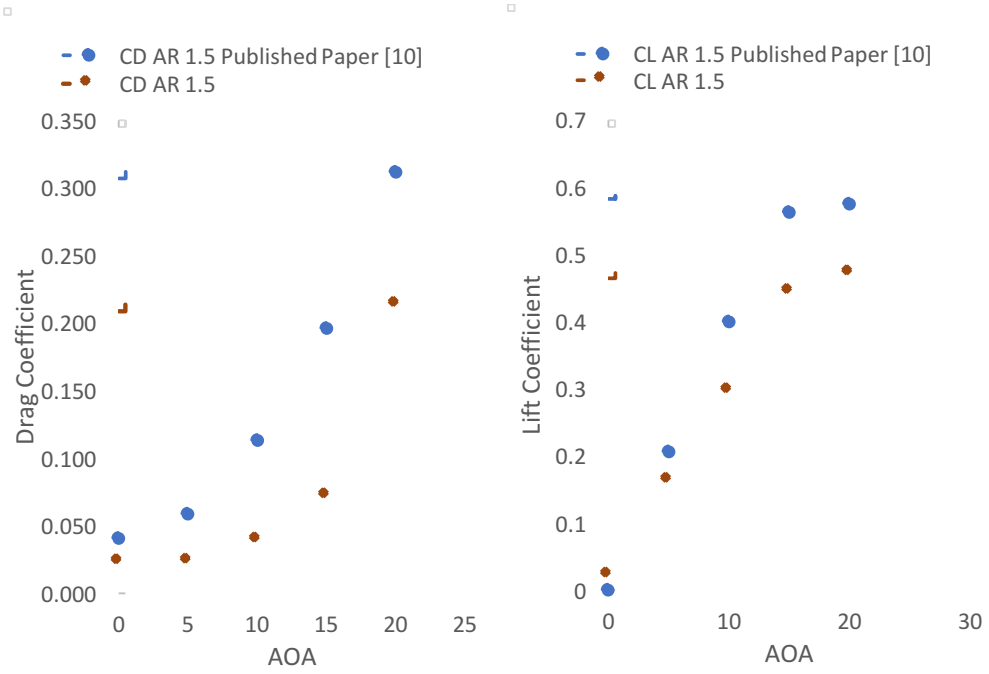


Figure 33. Lift distribution under aspect ratio of 1.5 at Re no of 1.23 x 10^5

3.5 Summary of sources of errors

From the Table 10, shows the sources of error percentage of error from minimum to maximum of the 4 effects studied in the wind tunnel. This table helps to provide insight for the students or experimenter to take into consideration of the errors that they may encounter throughout the wind tunnel test.

Table 23. Sources of errors summarized

Experiment no:	**Sources of error**	**Parameters**	**Range of errors**				**Average errors**		**Average of average errors**	
1	**Airleak**	Velocity	Min		Max					
Positions		Left (-24 cm)	0.09		2.90		1.47		1.23	
		Center (0)	0.36		1.44		0.77			
		Right (24 cm)	0.33		2.52		1.44			
2	**Flowrate**	Flowrate	0.10		4.50		0.65		0.65	
3	**Test rig**	Lift and Drag	CD	CL	CD	CL	CD	CL	CD	CL
Conditions		With Rig	14.71	1.43	64.77	32.13	39.58	13.77	32.18	13.41

		Without Rig	11.86	1.46	41.24	35.09	24.78	13.05		
4	**Model size**	Lift and Drag	CD	CL	CD	CL	CD	CL	CD	CL
Aspect Ratio		AR 0.5	24.51	1.83	38.40	57.68	31.64	24.69	46.76	23.04
		AR 1.0	28.69	0.47	63.36	44.20	49.94	28.38		
		AR 1.5	30.66	2.32	69.93	32.55	58.69	16.06		

4.0 Conclusion

In the study of improving the accuracy of Taylor's wind tunnel measurement experimentally. Four types of experiments were conducted. Four different parameters were considered in identifying the error sources in the Taylor's wind tunnel. The effect of these parameters is summarized as follows

- The effect of air leak on the velocity along the center line is very small which almost can be neglected. However, for better accuracy, the experimenter may be able to take into consideration of the errors by estimating the errors at 1.23%.
- The effect of flowrate in the wind tunnel test section at different frequency average of average errors is at 0.65%
- The effect of test rig which are conducted in the wind tunnel contributes major amount of average of average errors of drag and lift measurement of 32.18% and 13.41% respectively which means the drag and lift measurement are 32.18% and 13.41% lesser than the obtained result.
- The effect of model size on the lift and drag measurement in the wind tunnel have average of average errors of drag and lift measurement of 46.76% and 23.04% respectively which means the drag and lift measurement are 46.76% and 23.04% lesser than the obtained result for different aspect ratios.

The percentage error contribution in the wind tunnel can be further identified by conducting other experiments involving the drag and lift such as

- The effect of angle of attack on the drag and lift measurement of NACA 0012 in the wind tunnel
- The effect of shapes on the drag and lift measurement in the wind tunnel
- The effect of lab conditions in the wind tunnel
- The effect of rigidity of the connections of test rig with the load cell

Acknowledgement

This research study will not be possible without the participation and guidance and assistance whose contributions are sincerely appreciated and gratefully acknowledged. Special thanks to Shahrooz Eftekhari and Stephanie Lai Shen Ai for the great input as research colleagues.

References

[1] S. Eftekhari, “Numerical and Experimental Investigation of a Cruising Fixed Wing Mini-Unmanned Aerial Vehicles Performance Optimization,” Taylor’s University, 2017.
[2] F. Stern, M. Muste, M. Beninati, and W. E. Eichinger, “Summary of Experimental Uncertainty,” no. 406, p. 37, 1999.
[3] A. Mills and B. Chang, “Error analysis of experiments,” UCLA, Los Angeles, CA, pp. 12–16, 2004.
[4] G. Lombardi, M. V. Salvetti, and M. Morelli, “Correction of the wall interference effects in wind tunnel experiments,” Comput. Eng., vol. 30, pp. 75–84, 2001.
[5] M. N. Rhode, “Estimation of Uncertainties for a Supersonic Retro-Propulsion Model Validation Experiment in a Wind Tunnel,” 42nd AIAA Fluid Dyn. Conf. Exhib., vol. 54, no. June, pp. 1–28, 2012.
[6] S. Lai, “Thesis Effect of Size and Shape of Side Mirrors on the Drag of a Personal Vehicle,” Undergraduate, Taylor's University, Selangor, Malaysia, 2016.
[7] F. K. Owen and A. K. Owen, “Measurement and assessment of wind tunnel flow quality,” Prog. Aerosp. Sci., vol. 44, no. 5, pp. 315–348, 2008.
[8] B. Rašuo, M. Kozi, and G. Ocokolji, “Supporting system interference on aerodynamic characteristics of an aircraft model in a low-speed wind tunnel,” vol. 64, pp. 133–146, 2017.
[9] F. B. Hsiao, C. Y. Lin, Y. C. Liu, D. B. Wang, C. C. Hsu, and C. H. Chiang, “Thickness Effect on Low-Aspect-Ratio Wing Aerodynamic Characteristics at a Low Reynolds Number,” J. Mech., vol. 24, no. 3, pp. 223–228, 2008.
[10] J. H. Chen, S. S. Li, and V. T. Nguyen, “The Effect of Leading Edge Protuberances on the Performance of Small Aspect Ratio Foils,” 15th Int. Symp. Flow Vis. June 25-28, 2012, Minsk. Belarus, pp. 1–16, 2012.
[11] DO 2003 HVAC Multifunction datalogger: Delta Ohm Srl, Padova, ITALY, Portable and industrial instruments for measuring physical quantities", Deltaohm.com, 2016.

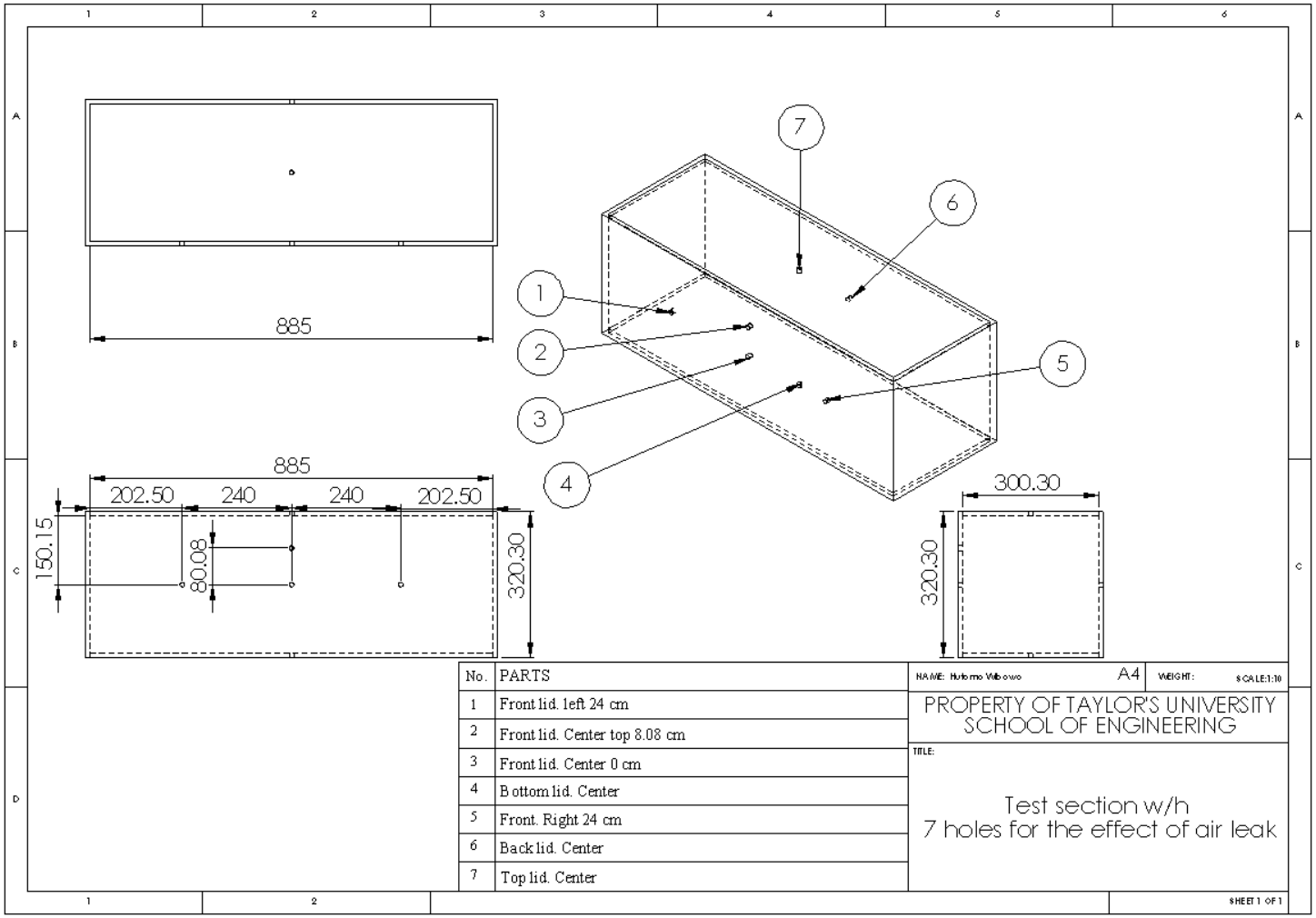


Figure 341. The effect of air leak experimental set-up

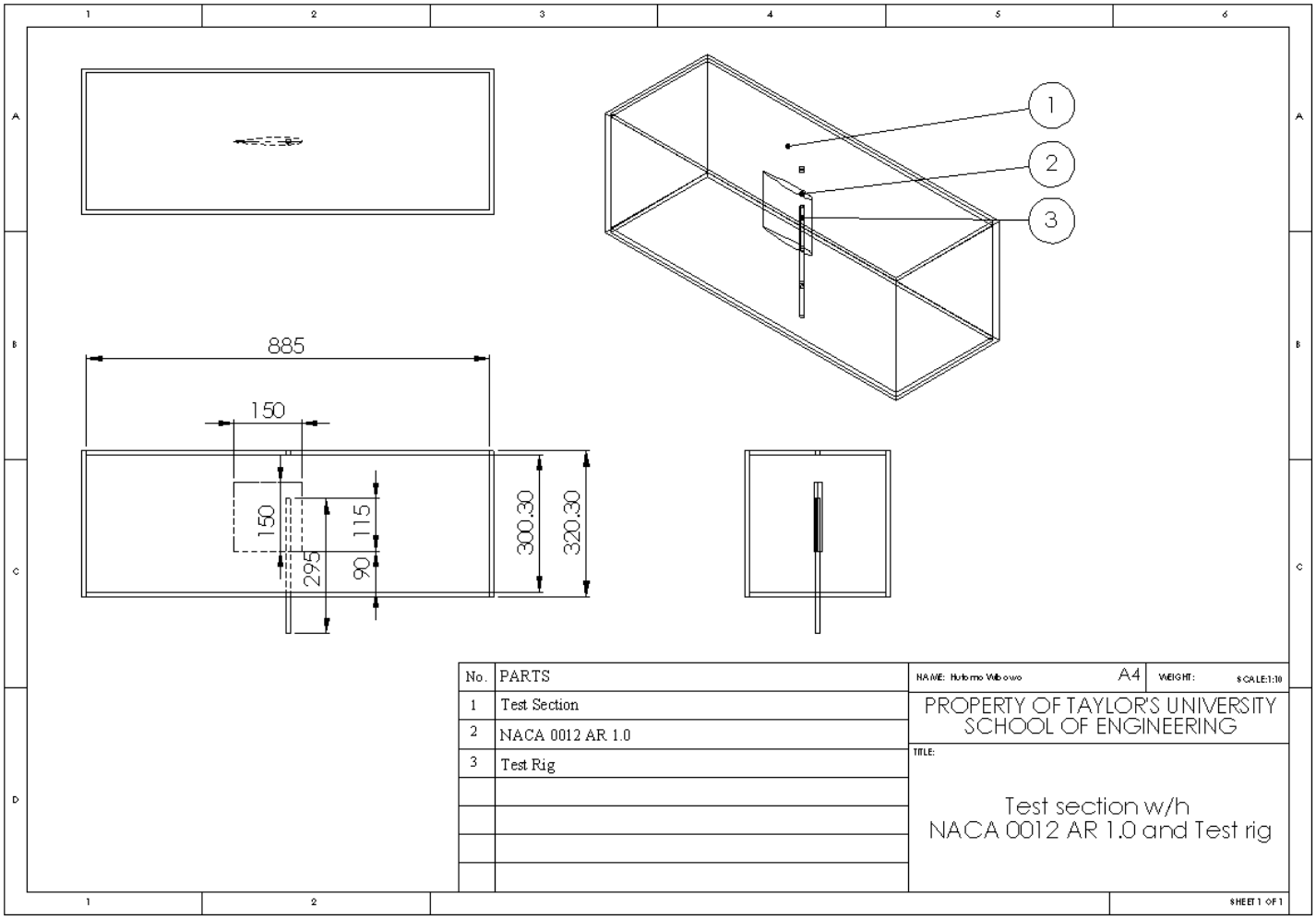


Figure 135. The effect of test rig experimental set-up

EURECA 2017 – Conference Paper
Paper Number 2ME06

Numerical Investigation on Two-Wheeler Bias Tyre Impact Using Various Material Models

Jane Lee Song Ern[1*], Felicia Wong Yen Myan[1], Ch'ng Shiau Ying[2]
[1]*Taylor's University Lakeside Campus, Subang Jaya, Selangor, Malaysia*
[2]*University of Southampton Malaysia Campus, Nusajaya, Johor, Malaysia*

[*]janesongern.lee@sd.taylors.edu.my

Abstract
Radial and bias ply is the two most common used two-wheeler tyre available in the market yet current research found is mainly focused on radial tyre instead of bias ply tyre. Hence, bias-ply two-wheeler tyre is focused on throughout this research. In bias-ply tyre, there are total of five layers each with different material properties. Two approaches therefore are introduced in this research. Firstly, simulation is conducted by considering the tyre as a single layer model. It is found that majority of simulation conducted with only single layer model. The results obtained are not as accurate as compare to measurement data and is due to the lack of consideration of material properties for each tyre layer components. Hence, second simulation model with tyre layers components and specific material properties respectively are presented. Considering rubber as the major materials in a tyre, hyperelastic material model is chosen as the simulation model throughout the research. In this research, the simulation is carried out based on Mooney-Rivlin with 5 parameters, Yeoh 3rd order and Neo-Hookean model only. These three are able to obtain results with stress strain at low, medium and high range, hence it is chosen in this research. Furthermore, material parameters that are originally curve fitted with wide range are improved and fitted with smaller range. It is due to the large error gap, approximately with average of 2-5%, obtained when simulation is first conducted with wide range fitted parameters. Hence, second set of parameters constant is curve fitted with smaller range and significant improvement is noticed on Mooney-Rivlin and Yeoh material model, with the lowest error percentage of 0.15% for Yeoh model. It is found at the end of this research that simulation with multi layer tyre model and small range fitted parameters possess the highest results accuracy. Mooney-Rivlin with 5 parameters is sufficient enough for simulation with wide range fitted parameters whereas higher number of parameters is needed if simulation is conducting with smaller range fitted parameters.

Keywords: Hyperelastic material model, two-wheeler bias-ply tyre, ANSYS, inflation pressure

1. Introduction

Tyres are always the main parts of any vehicle that stays in contact with the ground. Hence, it is important to ensure that the tyres are always in good condition. A report on Malaysia vehicle fatalities shows that motorcyclists constitute the highest number of fatalities and this number was predicted to increase in future years. Among the number of fatalities, up to 8% of it were caused by vehicles factors. If these vehicles factors could be prevented beforehand, it is believed to have a good effect on reducing the number of fatalities for motorcyclist [1].

Oftenly, industry tends to conduct experiment yet it is time and cost consuming [2]. Finite element analysis (FEA) always is an ideal approach to predict performances of an object. Though best method based on each different conditions is necessary to be determined for results realiablity. Therefore, this research is aimed to identify the most suitable material method for a two-wheeler bias-ply tyre. In this research, the model of an 80/90-17 bias-ply two-wheeler tyre is chosen to examine the effect of inflation pressure on the tyre.

Two different types of methodology are introduced in this research to verify and compare results accuracy. In current studies, majority of FEA on two-wheeler bias ply tyre was conducted by considering the tyre just as a single layer model [3]. However, a tyre actually consists of five different layers; each layer with unique material properties that exhibits unique behaviour [4]. Ignoring the individual layers of the tyre is believed to have affected the accuracy of current simulation results found in the market [5]. Therefore, first part of this research is to conduct FEA just as the majority, which was considering the tyre model as single body layer. Secondly, a new method is presented by modelling the tyre layer by layer as according to two- wheeler bias-ply geometry layer components.

It is well-known that the majority of a tyre is made from rubber material. Material model used in this research for any simulation therefore must then be fitted to rubber behaviour in any circumstances [6]. Hyperelastic material model is the most well known material model that regularly utilized for any rubber-like material simulation [7]. The hyperelastic material models mentioned in the literature includes the Mooney-Rivlin model, the Yeoh model, the Odgen, Arruda-Boyce model, and the Neo-Hookean [8]. The three material models that possess low, medium and high strain ranges are chosen in this research, which was Neo-Hookean, Yeoh 3rd order, and Mooney-Rivlin with 5 parameters.

Layer components of the bias-ply tyre include tread, tread base, cord-ply, and inner liner as shown in Figure 1.1. Tread is found to be the thickest layers of these components [9]. It was presume that tread is the most affected layers for a tyre performances. Since only a single layer was consider in the first approach, tread layer material was assign as the material in this particular simulation. As for multi-layer approach, individual material properties are assigned to each layer of the tyre. Materials constants of each layer were obtain using the curve-fitting method [10]. However, details of materials constants are not presented in this paper due to confidential information.

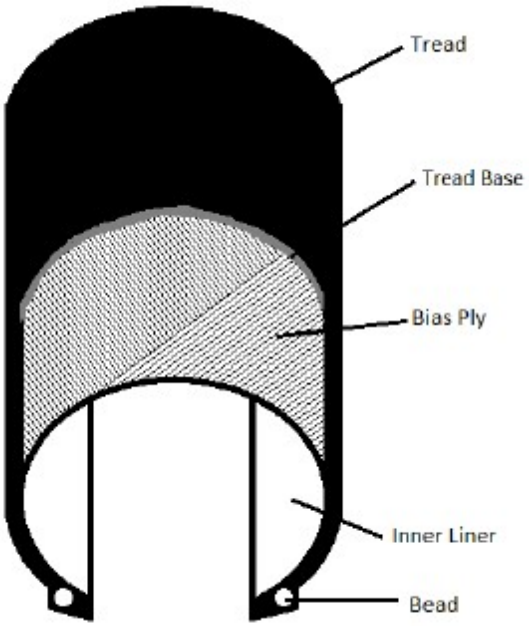


Figure 1.1. Bias Ply Tyre Layer Components [11]

Numerous finite element analysis simulations are carried out in this research. Two approaches with completely different simulation models are conducted and five sets of internal pressure tested on each model. The five internal pressure utilized in this research were 0.19 MPa, 0.21 MPa, 0.23 MPa, 0.25 MPa, and 0.27 MPa [3].

On the other hand, this is an integrated research with previous paper titled Parametric Study of a Bias Two-Wheel Tire [11]. From previous research, Mooney-Rivlin 5 parameters was the only hyperelastic material model tested in the paper. Besides, a three-dimensional, multi layer tyre model was used in the previous work. Hence, this research is conducted with single and multi layer two-dimensional models. Comparison is conducted to validate the feasibility two-dimensional model in this field of research. Moreover, Neo-Hookean and Yeoh 3rd order material model are introduced in this research to compare the results from different hyperelastic material models, as previous work was aimed just to validate the FEA results with experimental data obtained in the particular paper. Hence, as a summary, this research paper is conducted with:

1. Two 2-dimensional FEA models; single layer and multi layer tyre model,
2. Three hyperelastic material model; Mooney-Rivlin 5 parameters, Yeoh 3rd order and Neo-Hookean, and
3. Two curve-fitted parameters; wide range and small range fitted parameters.

2. Methodology

In this section, the model used for both single and multi-layer tyre simulation will be introduced. Next, the material parameters based on chosen model will be briefly discussed and meshing method will then be presented. Lastly, boundary conditions were discussed in details for the simulation of tyre inflation.

2.1 Tyre Model

By utilizing the symmetrical geometry of a tyre, the model in the simulation was simplified to the two-dimensional cross sectional area of a tyre. Two different approaches were used for the simulation: by considering the tyre as a whole part and by considering the individual layer which makes up the tyre.

2.1.1 Single Layer Tyre Model

A single-layered, two-dimensional tyre model was generated for single-layer tyre simulation. A cross-sectional geometry for an 80/90-17 bias two-wheeler tyre was drawn. Dimensions of the outermost shell of the tyre were fully utilized for the drawing of single-layer tyre simulation model. The stress-strain relationship of the tyre was assumed to be controlled mainly by the thickest layer of the tyre. Detail discussion will be given in the following section. Figure 2.1 shows the details of the model for single-layer tyre model simulation.



Figure 2.1. Single-layer Tyre Model Based on 80/90-17 Bias-Ply Tyre

2.1.2 Multi Layer Tyre Model

The actual tyre is made up from the combination of multiple layers, which includes tread, tread base, two cord-ply layers and inner liner. Each layer of the tyre has different material properties. In order to achieve better accuracy of the simulation result, a two-dimensional model based on the actual dimension of each layer was generated as shown in Figure 2.2. From Figure 2.2, it was obvious that tread occupies the thickest layer. Therefore, it was assumed that in the case of single layer tyre the material properties of the tyre were based on the material properties of tread.

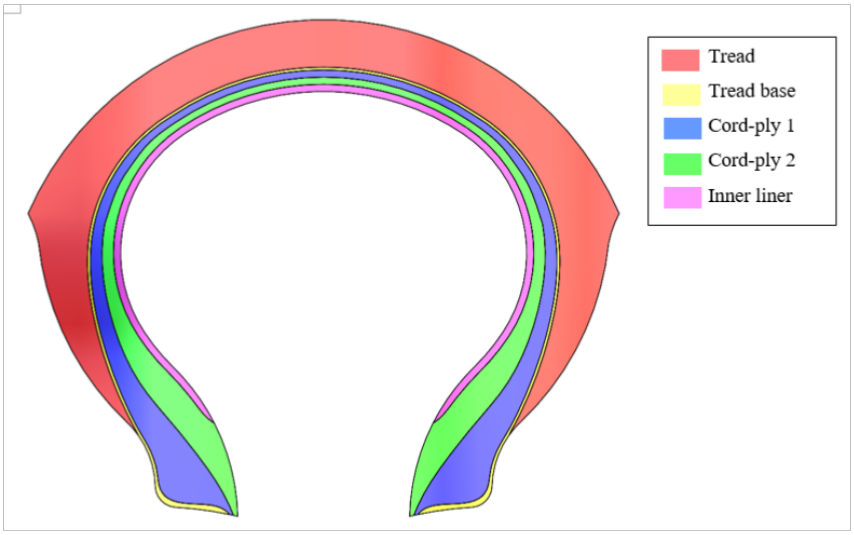


Figure 2.2 Multi Layer Tyre Model

2.2 Material Parameters

The tyre is made up of rubber compound which is a hyperelastic material. Stress-strain response of a hyperelastic material can be described using various hyperelastic material models by considering rubber compound to be incompressible and isotropy. Three hyperelastic material models were selected in this study, which includes Neo-Hookean, Yeoh, and Mooney-Rivlin. The strain energy density and material parameters of each model are shown in Table 2.1.

Table 2.1. Summary of strain energy density and material parameters for each model

Model	Strain energy density	Material parameters
Neo-Hookean	$W = C_{10}(I_1 - 3)$	C_{10}
Yeoh	$W = C_{10}(I_1 - 3) + C_{20}(I_1 - 3)^2 + C_{30}(I_1 - 3)^3$	C_{10}, C_{20}, C_{30}
Mooney-Rivlin	$W = C_{10}(I_1 - 3) + C_{01}(I_2 - 3) + C_{20}(I_1 - 3)^2 + C_{11}(I_1 - 3)(I_2 - 3) + C_{02}(I_2 - 3)^2$	C_{10}, C_{01}, C_{20}, C_{11}, C_{02}

where I_1 and I_2 is the first and second deviatoric strain invariants of the stress tensor. The material parameters were obtained using curve fitting feature in ANSYS based on uniaxial tensile testing data of each layer.

As mentioned in the previous section, cross-sectional model of the tyre show that the thickest layer found in a tyre was the tread layer. Material parameters of tread layer was therefore taken into consideration for single-layer tyre model, as it was assumed to be the most affected layer towards the results due to its thickest layer dimension in the bias-ply tyre. In the multi-layer model, there were a total of five layers with their corresponding material parameters. For each layer, the particular material parameters were assigned to it. The simulation was repeated for three different models and the results were compared to measurement data.

2.3 Mesh Convergence Study

In order to verify the accuracy of the obtained results, a mesh convergence study was necessary to determine the most suitable mesh size for both simulation methods. Initially, simulation with the default meshing done by ANSYS was conducted to obtain the result as the comparison value, as it possesses the coarsest sizing. Then, simulation with finer mesh size was repeated and the percentage difference between results of each mesh size was calculated. The most suitable mesh
size was determined when the simulation result approaches stable level.

2.4 Boundary Conditions

To simulate the inflation process, pressure was applied normal to the inner surface of the tyre. This represents the inflation pressure of a bias-ply tyre in real-life situations. Then, fixed support was secured on the edge where the tyre was attached to the rim. Details of boundary conditions for both models were presented in Figure 2.3.

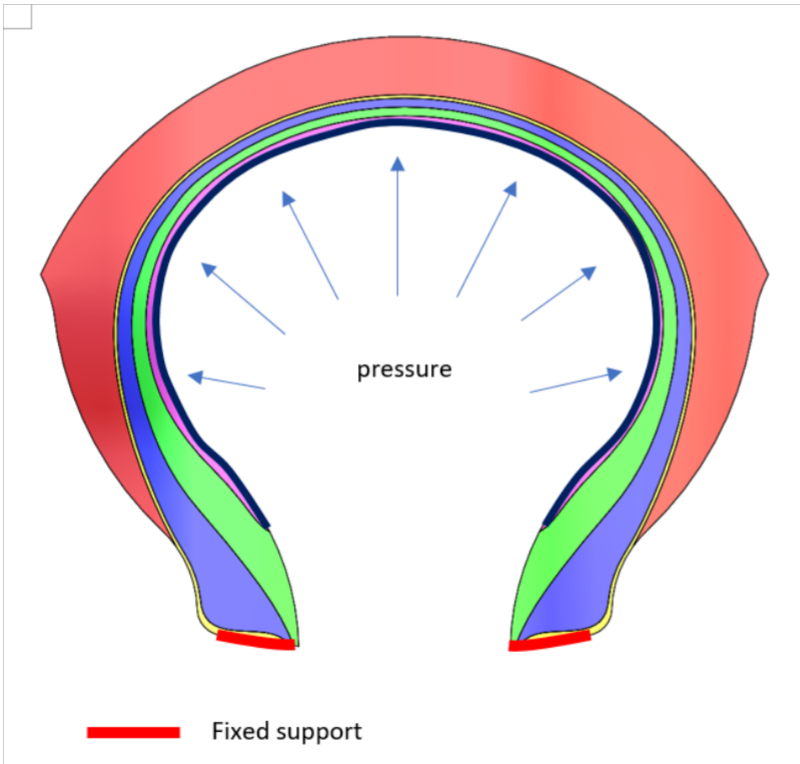


Figure 2.3 Boundary Conditions Applied on Both Tyre Models

3. Results and Discussions

In this section, the mesh size determined from mesh convergence study was presented. Directional deformation in Y-axis was extracted in this study to determine the circumference of the tyre under different inflation pressure. Results obtained for both models were then compared with actual measurement data.

3.1 Mesh Convergence Study

The results for single layer tyre model using different mesh size are tabulated in Table 3.1. The number of element increases as finer element size is used. To obtain high accuracy simulation results, it is important to achieve low skewness and high mesh quality. As shown in Table 3.1, skewness and mesh quality for all three meshing method are qualified for high accuracy results. Besides, percentage difference for extracted from total deformation are significant low as well. Hence, considering the time constrains and refering to results obtained from Table 3.1, auto meshing is utilised in this project for single layer tyre model. Figure 3.1 shows the single layer tyre model meshed with auto meshing method.

Table 3.1 Mesh Convergence Study for Single Layer Tyre Model

No.	Mesh Method	Number of Node	Number of Element	Skewness	Mesh Quality	Total Deformation (mm)	Percentage Difference (%)
1.	Auto meshing	464	127	0.247	0.912	10.146	-
2.	Face sizing with 4.5 mm	522	143	0.248	0.910	10.147	0.1
3.	Face sizing with 1.5 mm	2943	904	0.105	0.977	10.148	0.1

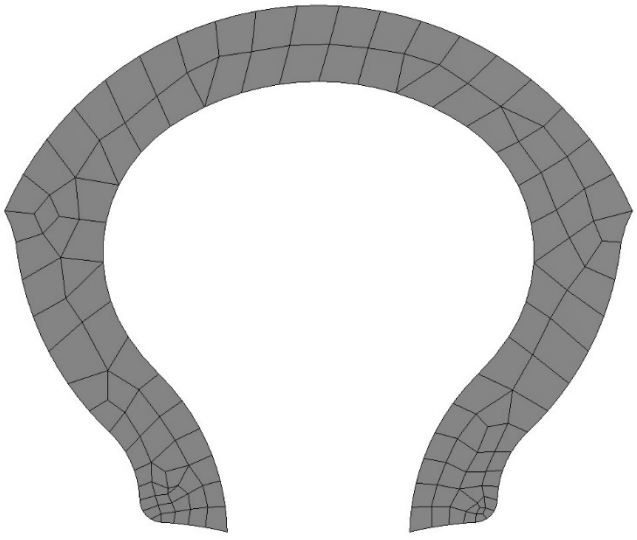


Figure 3.1 Single Layer Tyre Model with Auto Meshed Element

Similarly to single layer tyre model, mesh convergence study is conducted first with auto meshing then repeated with with finer mesh size for multi layer tyre model. Table 3.2 shows the mesh convergence study for multi layer tyre model. Based

on Table 3.2, it is noticed that again, all meshing method carried out for the model are fulfilling the requirement for high accuracy results. Auto meshing is sufficient to provide reasonable accurate as well as observed from the skewness and mesh quality it possesses. Percentage difference in this case are way lower as compared to single layer tyre model. Hence, auto meshing once again is chosen for multi layer tyre model for its finite element analysis as shown in Figure 3.2.

Table 3.2. Mesh Convergence Study for Multi Layer Tyre Model

No.	Mesh Method	Number of Node	Number of Element	Skewness	Mesh Quality	Total Deformation (mm)	Percentage Difference (%)
1.	Auto meshing	26695	7824	0.092	0.977	6.179	-
2.	Face sizing with 4 mm	40465	12162	0.074	0.981	6.176	0.04
3.	Face sizing with 3 mm	69101	21274	0.059	0.984	6.176	0

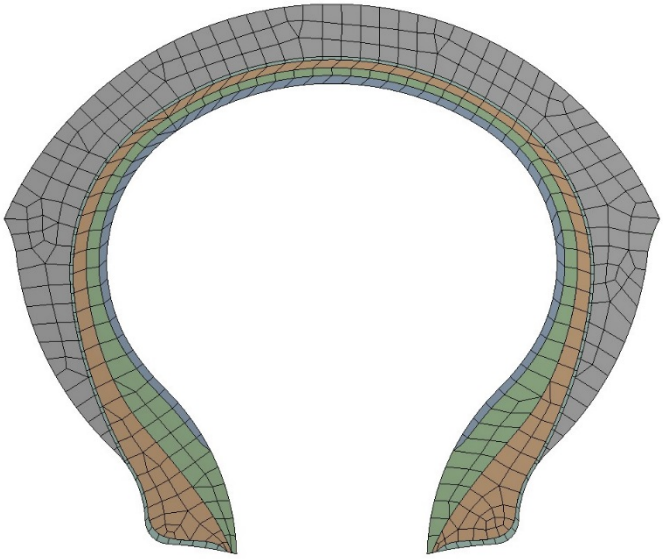


Figure 3.2. Multi Layer Tyre Model with Auto Meshed Element

3.2 Determination of Material Parameters

The material parameters for different models were curve-fitted using the data from uniaxial tensile testing for each layer. Using the obtained material parameters, the stress-strain response from uniaxial tensile testing for tread and the prediction from various models were plotted in Figure 3.3. For fitting purpose, the engineering strain was converted to stretch following Eq. (3.1),

$$\lambda = \varepsilon + 1 \tag{3.1}$$

where λ=stretch and ε=engineering strain.

The comparison of stress-strain response from uniaxial tensile testing and the prediction from various material models for tread layer are plotted in Figure 3.3. From Figure 3.3, it is obvious that the prediction from Neo-Hookean model shows a large deviation from the experimental data. The result is expected since Neo-Hookean is the simplest material models for hyperelastic material and it is only accurate at low strain. As for Yeoh and Mooney-Rivlin, both models give a very good prediction as compared to the experimental data. Thus, it is estimated that the simulation results using these two models would be more accurate. Similar procedures are repeated for other layers and the similar trend is observed. The curve fitting for other layers are shown in Appendix section.

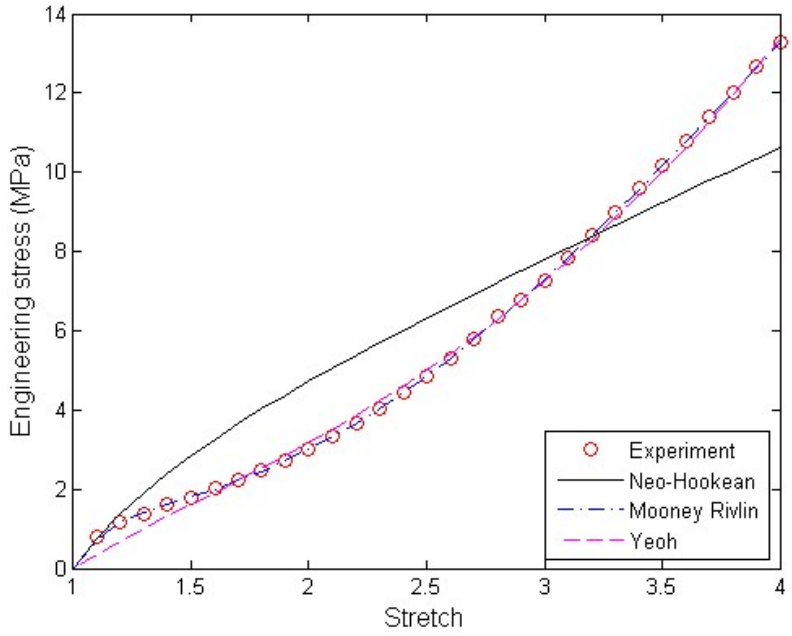


Figure 3.3. Comparison of Stress-Strain Response from Uniaxial Tensile Testing and Prediction from Material Models for Tread

In real situation, the deformation experienced by the tyre under full inflation as observed from the measurement is rather small. Therefore, the accuracy of model prediction using material parameters fitted based on wide strain range might not be applicable to the real situation. Hence, material parameter is again fitted but with smaller strain range which is more relevant to the actual application. As shown in Figure 3.4, Neo-Hookean again has the largest deviation due to its simplest material model as compared to Mooney-Rivlin and Yeoh. The curve fitting for other layers with small strain range are shown in Appendix section.

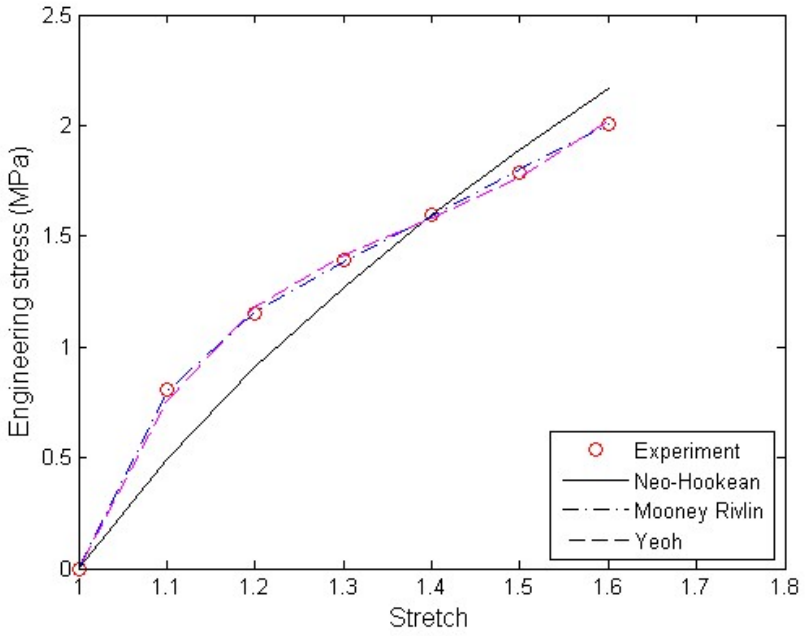


Figure 3.4. Comparison of Stress-Strain Response from Uniaxial Tensile Testing and Prediction from Material Models for Tread at Small Strain Range

3.3 Inflation Results for Single Layer Tyre Model

As inflation pressure is applied, tyre is deformed and affected the tyre performances. The data obtained from experimental results were measured based on the largest deformation found in the study as well [11]. Hence, in this project, total deformation of tyre is extracted as the simulation results. Total deformation obtained from the simulation results are in the unit of millimeter, as the deformation found is reasonably small. Figure 3.5 shows the example of tyre before and after deformation, where wireframe represented the undeform model and solid colour shows the deformed model when 0.19 MPa pressure applied and simulated with Neo-Hookean material model.

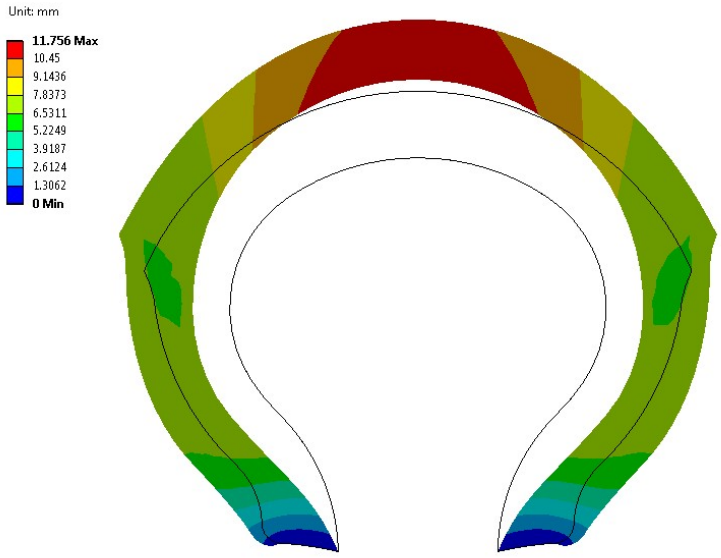


Figure 3.5. Tyre Model Before and After Deformation

Using the approach mentioned above, the inflation results for single-layer tyre model under different pressures using wide range fitted parameters are shown in Figure 3.6. From Figure 3.6, it is observed that Neo-Hookean possesses the lowest accuracy among the simulation model followed by Yeoh. It was noticed that Mooney-Rivlin provided the highest accuracy results as validated with measurement data. This phenomenon can be explained as Neo-Hookean was the lowest order of material model utilized in this project. Result of Neo-Hookean in this simulation model was well expected beforehand. On the contrary, results for Yeoh and Mooney-Rivlin are closer to measurement data. However, Mooney-Rivlin is more accurate than Yeoh as it possesses a smaller error gap. It was expected as Mooney-Rivlin had higher order than Yeoh material model used in this project. Despite the low accuracy results, Neo-Hookean material model is utilized throughout the project as comparison basis since it is the most basic material model and has the lowest order among the material models simulated in this project.

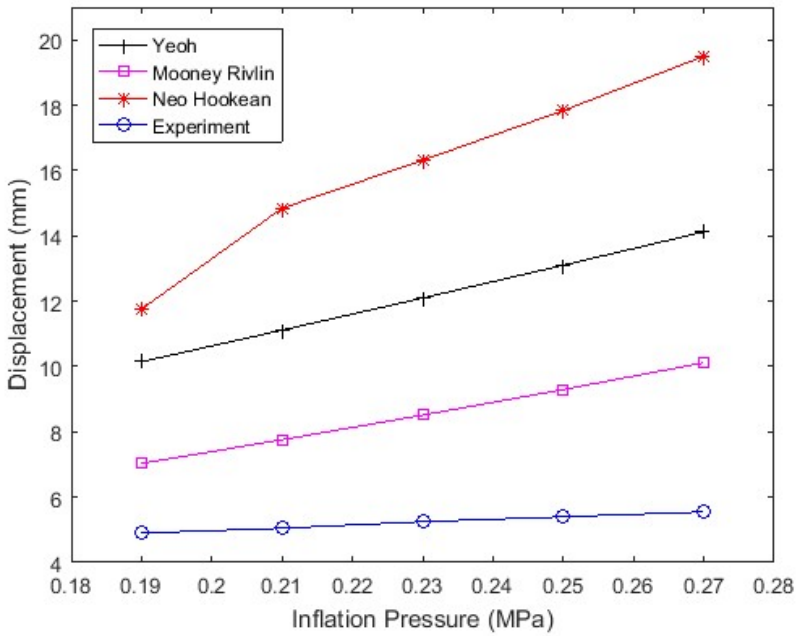


Figure 3.6. Comparison of Displacement with Various Material Models for Single Layer Tyre Model with Wide Range Fitted Parameters

Similarly, Figure 3.7 shows the inflation results for single-layer tyre model under different pressure but with small range fitted parameters. As shown in figure, accuracy of results for Yeoh and Mooney-Rivlin are well improved, whereas Neo-Hookean has poorer accuracy as compared to Figure 3.6. Notice that results of Neo-Hookean are only available for inflation pressure with 0.19, 0.21, 0.23 and 0.25 MPa. It is due to the poorer accuracy and highly distorted of the model where finer meshing is needed. However, ANSYS Workbench available in Taylor's University is limited with maximum number of element due to the student license it has. Therefore, simulation for 0.27 MPa using Neo-Hookean with small range fitted parameters is unable to conduct and complete.

Based on both figures, it is notice that results for Yeoh and Mooney-Rivlin material model are almost identical. Nonetheless, Mooney-Rivlin still is having slightly higher accuracy than Yeoh model. Besides, the error gap between both models and the experimental results decreases as compared to previous work with wide range fitter parameters. Hence, it can be concluded that small range of fitted parameters are more suitable to predict inflation results for bias-ply tyre.

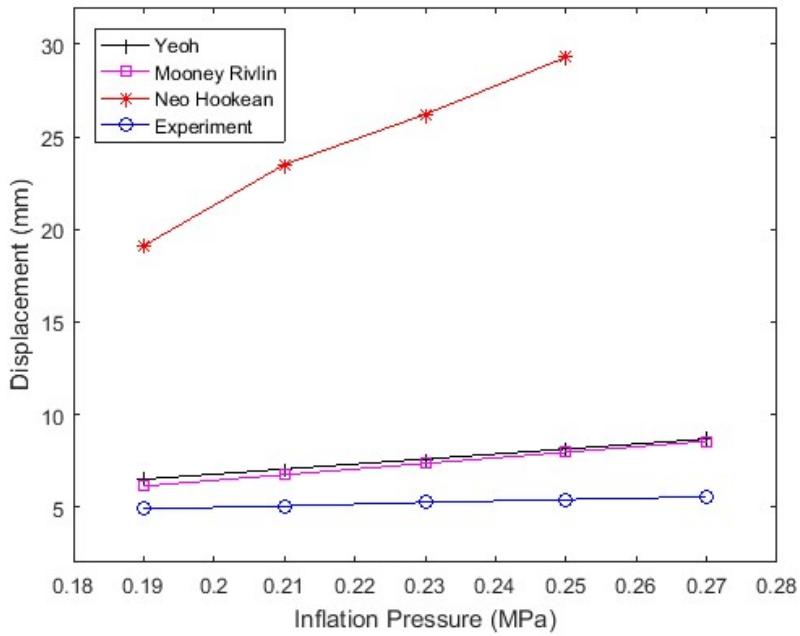


Figure 3.7. Comparison of Displacement with Various Material Models for Single Layer Tyre Model with Small Range Fitted Parameters

Nevertheless, it is notice that the error gaps between all simulation results and the experimental data increases as the pressure applied increases. It is therefore suggested to utilize a higher order hyperelastic material model, such as Mooney-Rivlin 9 parameters if higher pressure is to be applied.

3.4 Inflation Results for Multi Layer Tyre Model

Similarly to single-layer tyre model, simulation for multi layer tyre model are conducted with both wide and small range fitted parameters to compare the results. Figure 3.8 shows the results for multi layer tyre model with wide range fitted parameters. Based on the figure, is it observe that results for Neo-Hookean material model had improved significantly as compared to Figure 3.6 and 7. This improvement is believed due to the consideration of each tyre layers in the simulation. It is also notice that results for all material models in this case are almost identical. However, Mooney-Rivlin is found to have higher gradient as compared to Neo-Hookean and Yeoh model. It is most likely due to the higher order of Mooney-Rivlin material model and simulation is carried out with more prediction as number of parameter increases.

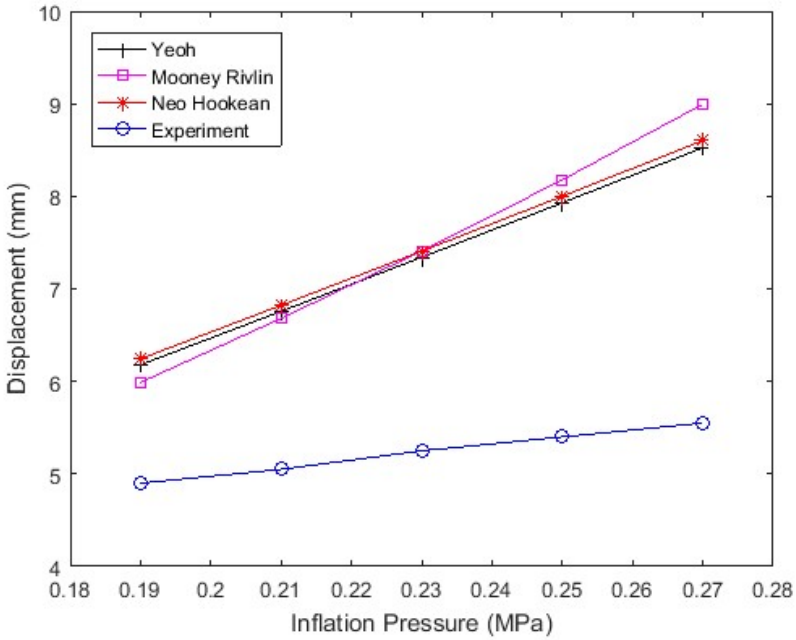


Figure 3.8. Comparison of Displacement with Various Material Models for Multi Layer Tyre Model with Wide Range Fitted Parameters

From the Figure 3.9, it can be seen that Neo-Hookean again decreases the results accuracy for multi layer tyre model with small range fitted parameters. As parameters are fitted with smaller strain range, the constant obtained are more accurate as compared to wide range fitted parameters. Hence, low order of material model, such as Neo-Hookean is insufficient to provide the relatively accuracy in the results. In contrast, Yeoh and Mooney-Rivlin can be seen to have significant improvement in Figure 3.9. Yeoh material model in this case possesses higher accuracy than Mooney-Rivlin as it is coincide with experimental results. It is unexpected, as Yeoh 3rd order possesses lower order than Mooney-Rivlin 5 parameters. However, this phenomenon might again due to the small range fitted parameters where higher order of Mooney-Rivlin material model, such as Mooney-Rivlin with 7 or 9 parameters is necessary. As Yeoh 3rd is the highest order in its material model category, hence, results obtained in this case is more accurate than Mooney-Rivlin 5 parameters.

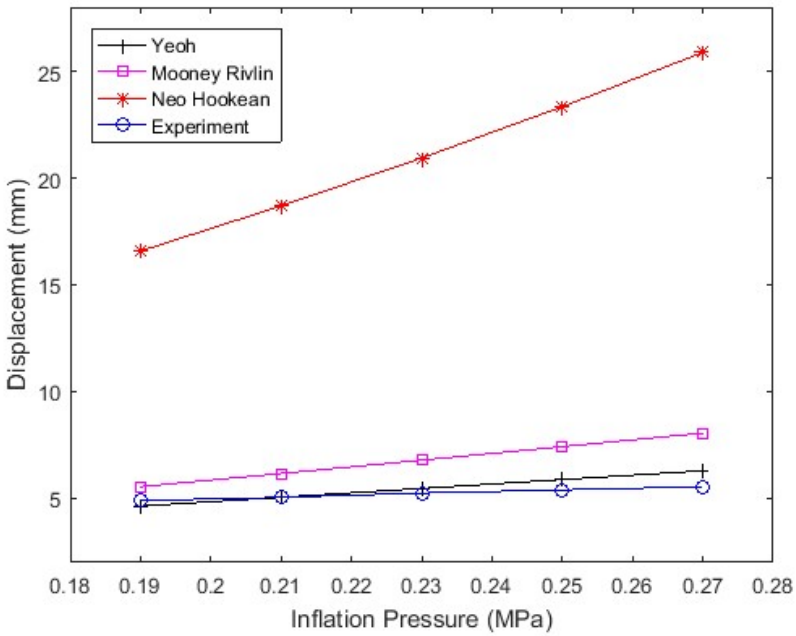


Figure 3.9. Comparison of Displacement with Various Material Models for Multi Layer Tyre Model with Small Range Fitted Parameters

Based on Figures 3.8 and 3.9, it is realized that wide range fitted parameters are not suitable to be used in simulation for multi layer tyre model. It can be explained as parameters fitted using wide range are rather suitable for larger strain range material model. As multi layer tyre model is simulated with each layer material accordingly, hence, precise parameters constant fitted with smaller range is needed to support with respective simulation. Therefore, wide range fitted parameters is not recommended for simulation conducted with multi layer tyre model.

Comparing the results between single and multi layer tyre model, it is noticeable that Neo-Hookean always is the lowest accuracy for all cases. In summary, small range fitted parameters are suitable to be used in this project for both single and multi layer tyre models. Yeoh 3rd model is suitable for small range fitted parameters simulation. Besides, Mooney-Rivlin with 5 parameters is sufficient to predict relatively accurate result in all cases. However, higher order of Mooney-Rivlin material model is needed if small range fitted parameters are utilized in the simulation. Based on the results, the most recommended bias ply tyre simulation due to inflation pressure is concluded to be multi layer tyre model with small range fitted parameters. Suitable material model vary based on the requirement of results and the type of fitted parameters utilized in the particular simulation.

3.5 Error Analysis

Error analysis is necessary to provide a better insight to the analysis of simulation results. The error was calculated using the Eq. (5.1) for the whole tyre diameter. As observed from previous sections, small range fitted parameters for both tyre models are in better agreement with the measurement data. Error analysis is therefore only conducted for small range fitted parameters for both tyre models.

$$\text{Error Percentage} = \frac{|\text{Simulation result} - \text{Measurement data}|}{\text{Measurement data}} \times 100\% \quad (5.1)$$

Based on Figures 3.10 and 3.11, it is noticed that Neo-Hookean possessed the highest percentage difference among all simulations and it is fitted to the results as shown in previous discussion. Comparing Yeoh and Mooney-Rivlin for single layer model simulation, both material models have nearly identical percentage error for single layer but not for multi layer tyre model. Reason for Yeoh having lower percentage errors than Mooney-Rivlin in multi layer tyre model is as mentioned in previous discussion. Yeoh is the highest order in its particular material model, and Mooney-Rivlin 5 parameters is insufficient to support small range fitted parameters constant to have relatively accurate results as it is not the highest order in its material model.

Error percentage found for both Yeoh and Mooney-Rivlin models are significantly low, which are less than 2%. In addition, it is observed that percentage errors for Mooney-Rivlin model is consistent at both single and multi layer tyre model. It is therefore can be said that Mooney-Rivlin 5 parameters model is able to provide relatively accurate results if only quick prediction is needed. Yeoh 3rd model with small range fitted parameters however is suggested if precise results are needed.

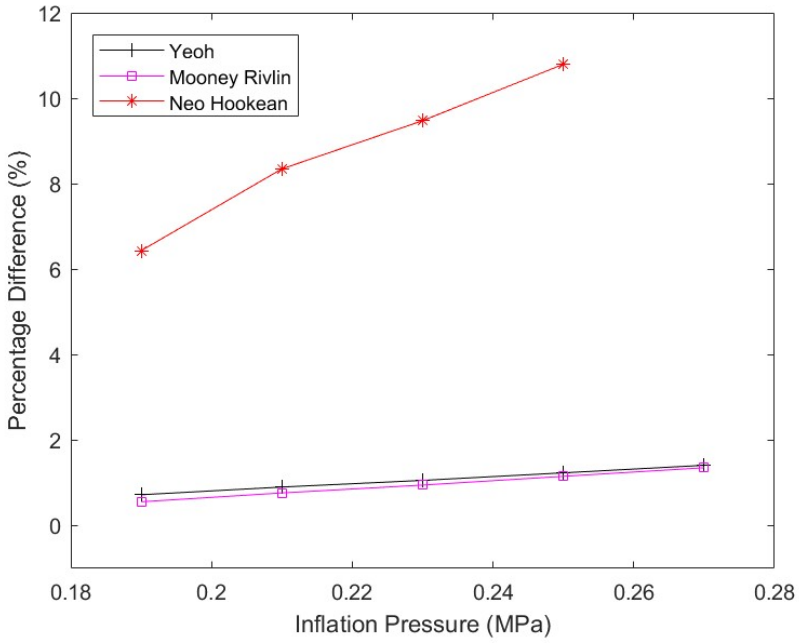


Figure 3.10. Comparison of Error Percentage with Various Material Models for Single Layer Tyre Models

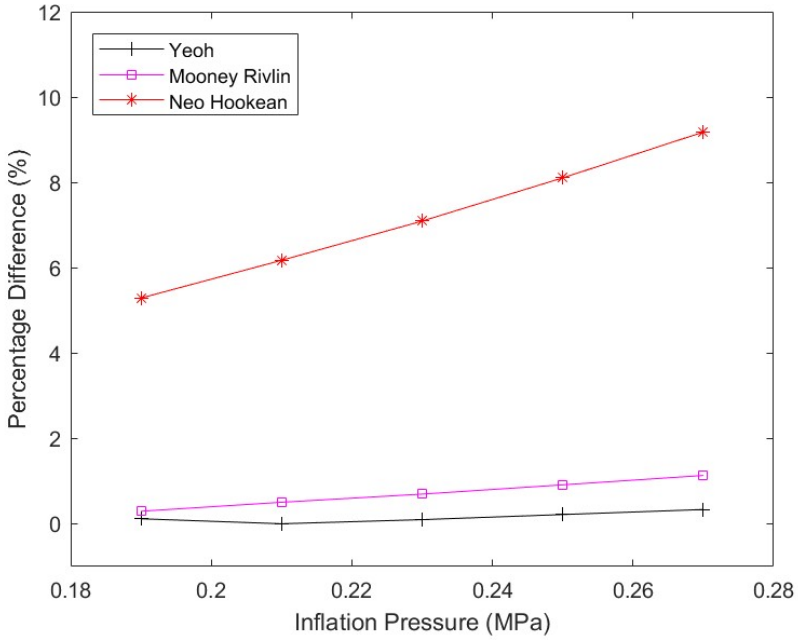


Figure 3.11 Comparison of Error Percentage with Various Material Models for Multi Layer Tyre Model

The obtained results were further verified with findings from a study conducted by Baranowski *et al.* [12]. It was found that results attained in this project matched the outcome presented in the paper. As pressure applied in a tyre increases, the deformation of tyre increases as well. A separate study by Polasik *et al.* [2] that conducted the same experiment also obtained results that are similar to the finding in this paper. However, results from the multi layer simulation were more likely similar to [2,12] as compared with single layer simulation. These validations proved that the multi layer tyre model is highly recommended over single layer simulation.

4. Conclusions

Based on the discussion in previous chapters, the curved fitting method is critical for results accuracy. The wide and small range of the curved fitted method is suitable for different hyperelastic material models. As shown by the result, the accuracy of simulation results depends highly on the chosen material model and also on the range of strain used for curve fitting purpose. There is no certain recommendation for which hyperelastic material model and curved fitting method should be applied, as it depends strongly on the conditions of the actual application. Small range curved fitted parameters is more appropriate in this research since in the actual case the inflation deformation is rather small, as a majority of high order material models, Yeoh 3rd order and Mooney-Rivlin 5 parameters, are used for analysis.

Results proved that a 2-dimensional model is sufficient to obtain simulation results which show good agreement to actual measurements. The 2-dimensional model is advantageous because it requires less time for simulations and requires less computational resources which has been beneficial to the research timeline. The small range curved fitted method is suitable for the single layer tyre model simulation to obtain reasonable results. This model is recommended if only a quick estimation is

required. Mooney-Rivlin with 5 parameters is sufficient in this model. If precise outcomes are required, multi layer tyre model with small range fitted parameters model are recommended. However, higher order material models such as Yeoh 3rd order or Mooney-Rivlin with 7 or 9 parameters are necessary for this FEA model.

Lastly, results obtained are verified with results in published papers. Similar outcomes were observed from multi-layer tyre model with small range fitted parameters in published studies [5]. Tyre deformation increases as inflation pressure increases. A higher order hyperelastic material model is necessary for higher inflation pressure simulation. In a nutshell, research outcomes satisfied and achieved project objectives.

References

[1] Sultan, Z., Ngadiman, N.I., Kadir, F.D.A., Roslan, N.F. (2016). Factor Analysis of Motorcycle Crashes in Malaysia. *Journal of the Malaysian Institute of Planners,* 4, 135–146.

[2] Polasik, J., Walu, K.J.,Wargu, Ł. (2017). Experimental Studies of The Size Contact Area of A Summer Tire as A Function of Pressure and The Load. *XXI International Polish-Slovak Conference "Machine Modeling and Simulations 2016"*, 177, 347–351.

[3] Huang, J.L., Xie, G.J., Liu, Z.W. (2008). FEA of Hyperelastic Rubber Material Based on Mooney-Rivln Model and Yeoh Model. *China Rubber Industry,* 55(8), 467-471.

[4] Xiong, Y., Tuononen, A. (2015). Rolling Deformation of Truck Tires: Measurement and Analysis Using A Tire Sensing Approach. *Journal of Terramechanics*, 61, 33–42.

[5] Yang, X., Olatunbosun, O., Bolarinwa, E. (2010). Materials Testing for Finite Element Tire Model. *SAE International Journal of Materials and Manufacturing*, 3(1), 211–220.

[6] Ogden, R.W., Saccomandi, G., Sgura, I. (2004). Fitting Hyperelastic Models to Experimental Data. *Compound Mechanics,* 34(6), 484-502.

[7] Ali, A., Hosseini, M., Sahari, B.B. (2010). A Review of Constitutive Models for Rubber-Like Materials. *American Journal of Engineering and Applied Sciences,* 3(1), 232-239.

[8] Boyce, M.C., Arruda, E.M. (2000). Constitutive Models of Rubber Elasticity: A Review. *Rubber Chemistry and Technology,* 73(3), 504-523.

[9] Evans, M.S. (2002). *Tyre Compounding for Improved Performance*, 12th ed. Shrewsbury: ISmithers Rapra Pub.

[10] Fu, Y.B., Ogden R.W. (2001) *Nonlinear Elasticity: Theory and Applications* (Vol. 283). Cambridge: Cambridge University Press.

[11] Tan, H.M. (2015). *Parametric Study of a Bias Two-Wheel Tyre.* Degree thesis, Taylor's Univeristy, Malaysia.

[12] Baranowski, P., Malachowski, J., Janiszewski, J., Wekezer, J. (2016). Detailed Tyre FE Modelling with Multistage Validation for Dynamic Analysis. *Materials and Design*, 96, 68–79.

Appendixes

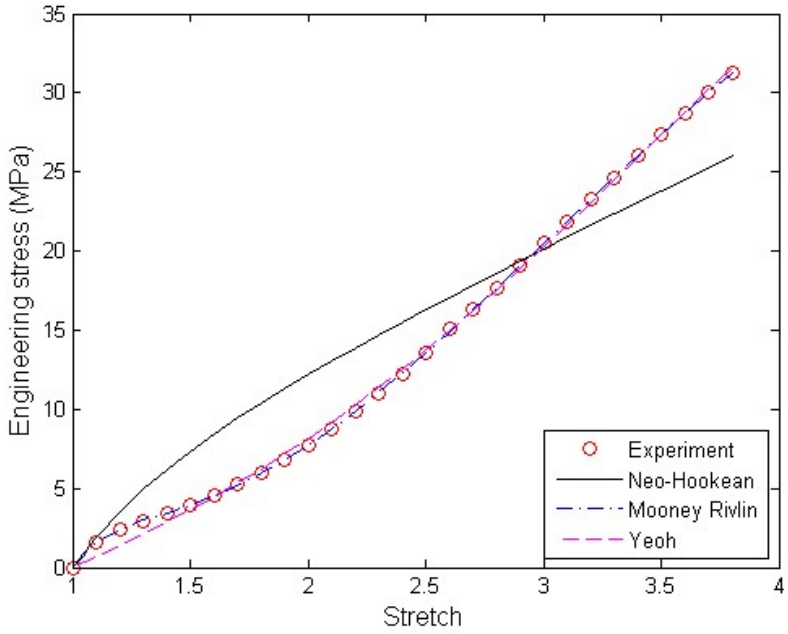


Figure A1. Comparison of Stress-Strain Response from Uniaxial Tensile Testing and Prediction from Material Models for Tread Base

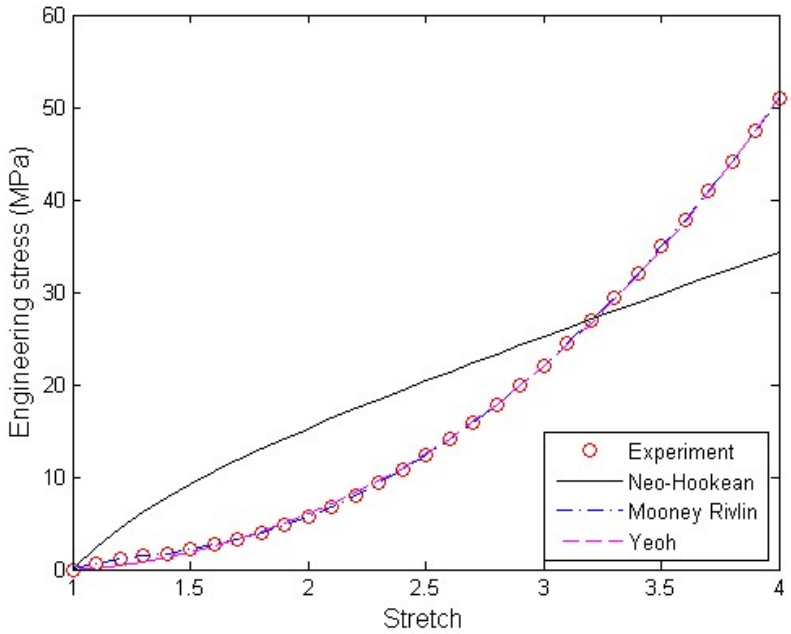


Figure A2. Comparison of Stress-Strain Response from Uniaxial Tensile Testing and Prediction from Material Models for Cord Ply

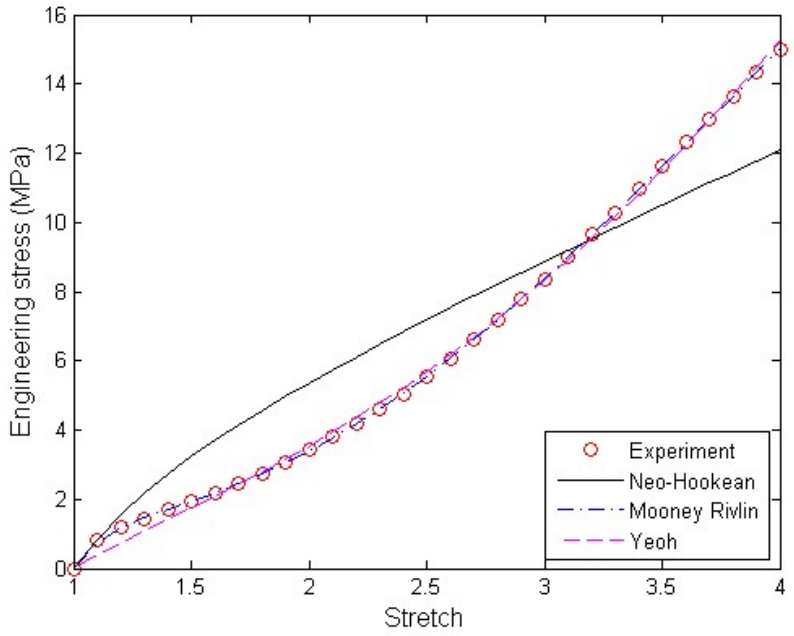


Figure A3. Comparison of Stress-Strain Response from Uniaxial Tensile Testing and Prediction from Material Models for Inner Liner

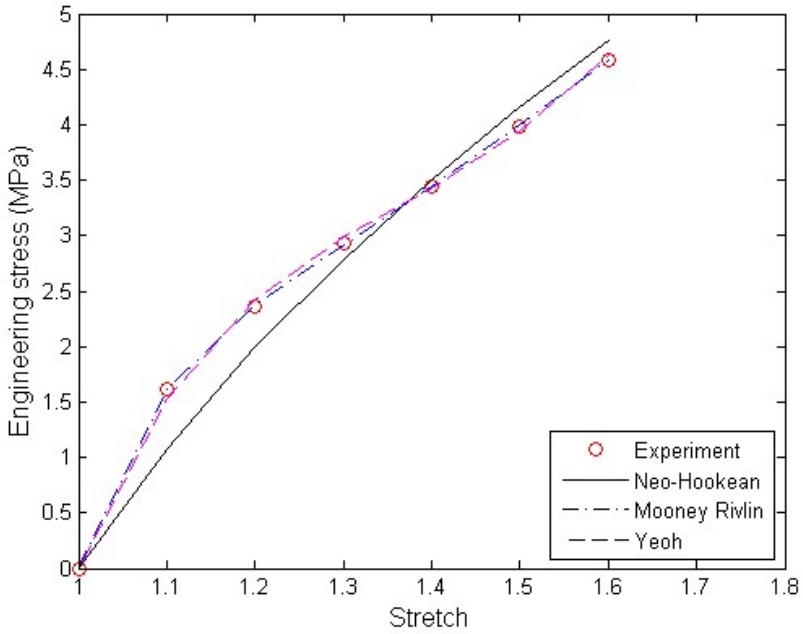


Figure A4. Comparison of Stress-Strain Response from Uniaxial Tensile Testing and Prediction from Material Models for Tread Base at Small Strain Range

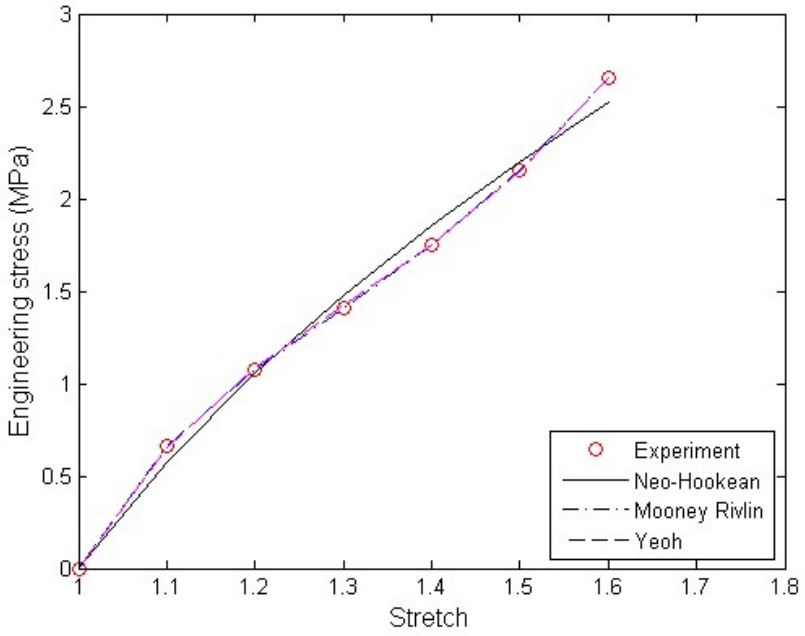


Figure A5. Comparison of Stress-Strain Response from Uniaxial Tensile Testing and Prediction from Material Models for Cord Ply at Small Strain Range

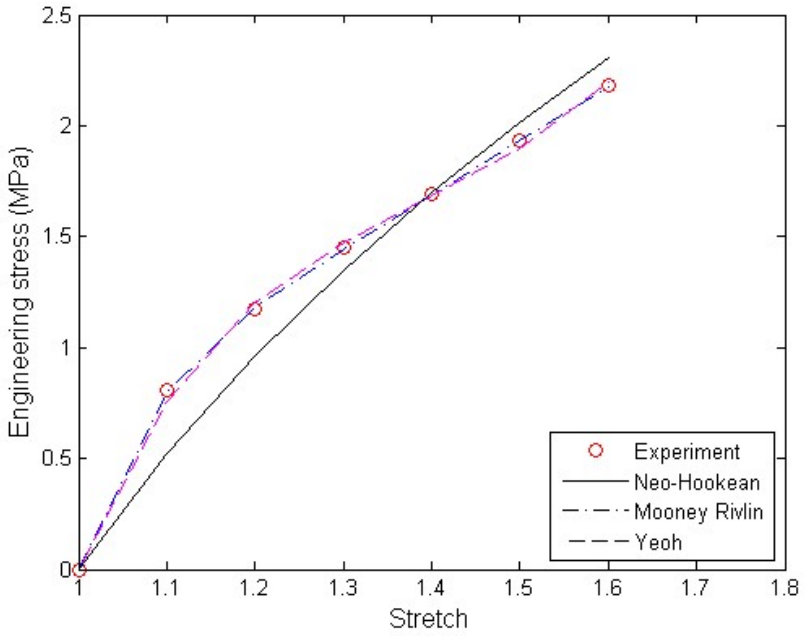


Figure A6. Comparison of Stress-Strain Response from Uniaxial Tensile Testing and Prediction from Material Models for Inner Liner at Small Strain Range

eureca 2017 – Conference Paper
Paper Number 2ME07

Oil Soluble Graphene for Thermal Conductivity Enhancement of Phase-Change Materials

Jeremy Fernandez[1*], Azadeh Ghadimi[1], Henk Metselaar[2], Amir Reza[3]
[1]*School of Engineering, Taylor's University, Malaysia*
[2]*Faculty of Engineering, University of Malaya, Malaysia*

[*]*Azadeh.ghadimi@taylors.edu.my*

Abstract
A phase-change material (PCM) is considered to be a great solution for thermal energy management. Since these materials contains a relatively high heat of fusion, it provides the ability for these materials to store and release a large amount of energy during the process of melting and solidifying at certain temperature programs. In this study, the main focus is on enhancing the thermal conductivity of phase-change materials by adding functionalized GNPs into the composite. The phase-change material that is selected is called paraffin which is an organic PCM. The hypothesis that is deduced based on the research question is that by dispersing functionalized GNPs into paraffin, the thermal conductivity of the composite phase-change material will increase. The functionalization process is done by chemically bonding the GNPs to 4-nitroaniline and sodium nitrate. This is done as the GNPs have to be oil soluble or in other words hydrophobic in order to react with the paraffin. Hence, the 4-nitroaniline will bind to the GNPs and a long hydrophobic tail will be attached to the structure of the GNPs through this reaction with sodium nitrate. This process will convert the hydrophilic GNPs into functionalized hydrophobic GNPs. The functionalized GNPs are then added in the paraffin wax to produce a composite phase-change material. In order to identify the chemical structure, peaks and microstructure of the composite phase-change material, apparatus such as scanning electron microscope (SEM), X-ray Diffractometer (XRD) and fourier transform infrared spectroscope (FT-IR) can be used. The thermal properties are determined by using a differential scanning calorimeter (DSC) and the thermal stability is measured using the thermogravimetric analyser (TGA). Next, the thermal conductivity of the composite is measured by using an apparatus called the KD2 pro. At the end of the experiment, the thermal conductivity of the composite should increase and hence prove that this composite is highly functional towards the application of thermal energy storage (TES).

Keywords: Phase-Change Material (PCM), Graphene Nanoplatelets (GNPs), 4-Nitroaniline, Sodium Nitrate, Thermal Energy Storage.

1.0 Introduction

A Phase change material (PCM) is amongst the most frequently discussed topic in the field of energy storage and can be used as an extensive solution for thermal management. As a result of their ability to release and absorb a great capacity of latent heat in regards to the surrounding temperature difference, PCMs can be used in a variety of applications [2]. Some of the applications in which PCMs are used includes sodium acetate heating pad, solar power plants, lighting strike protection, thermal protection for electronic devices, cold energy batteries and many more [2]. Generally, in the midst of the material's freezing process there is an immense amount of energy that consists of latent heat of fusion which is released. Similarly, during the melting process there will be an equal amount of energy that is absorbed in reference to the adjacent environment as there is a shift in the phase of the material from solid to liquid. PCMs come in a wide range of melting/freezing points and the shifting of the material's state is identified as latent heat of storage. Moreover, the phase change of PCMs are extensively from liquid to solid and vice versa as it is practical for it to shift within those phases. There are three groups in which PCMs can be classified into which includes organic compounds, inorganic compounds and eutectic compounds [3]. Figure 1 shows the classification of energy storage materials.

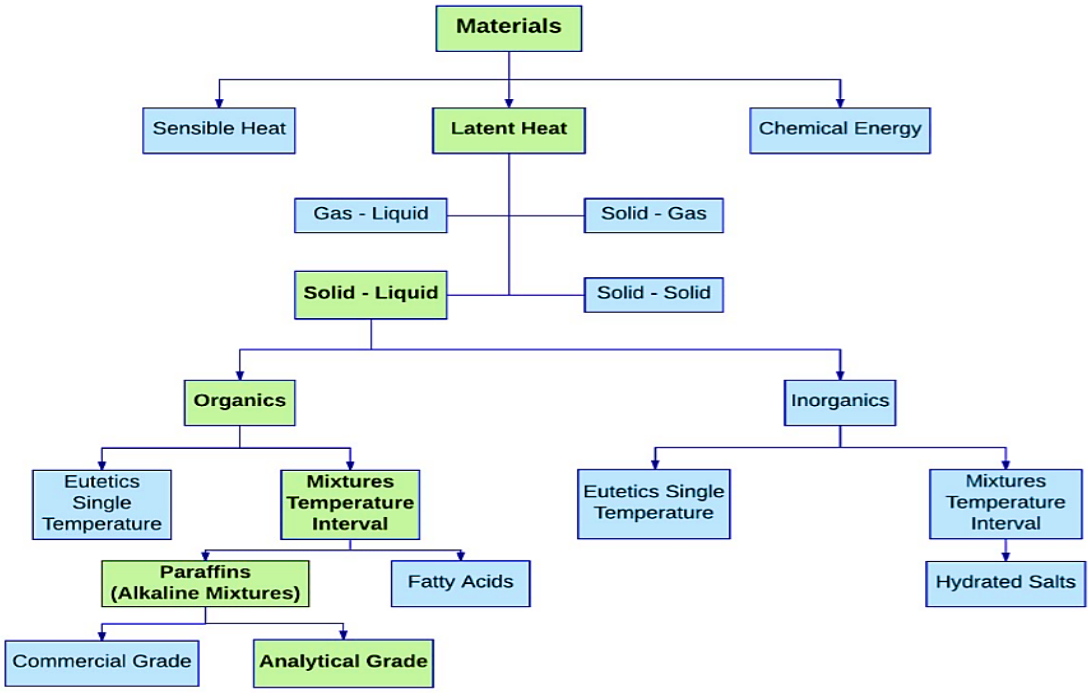


Figure 1: Classification of energy storage materials [3]

In this study paraffin wax is used as an organic PCM because, it retains a high energy storage capability as well as possesses certain properties such as good thermal stability and little supercooling. However, due to the low thermal conductivity during the cooling process, below 0.4W/(m.K), the heat storage and utilization efficiency will be reduced simultaneously [4]. Therefore, studies on the various methods to enhance the PCMs thermal conductivity is currently being researched upon. Some of the suggested solutions in enhancing the PCMs thermal conductivity include contaminants which are highly-conductive to produce a composite PCM that in return will be able to

improve its thermal conductivity. Thermal conductive fillers were initially used at a micro scale, however recent studies has proposed that nano-composite PCMs with ultrafine fillers would be a better option [5].

In order to improve the thermal conductivity of the composite PCMs, graphene oxide (GO) will be used as the supporting material. However, recent studies shows a drastic difference between graphene oxide (GO) and graphene nanoplatelets (GNPs) essentially based on their electrical and thermal conductivities that is rather intriguing and can illuminate the phenomena for a nanoscale transfer of heat between the graphene flakes and composite PCMs [5]. In this study, GNPs will be used as the supporting material for the composite PCM. The reason GNPs are selected is due to the many beneficial like properties that the GNPs possess which are ideal for the application of PCM.

Identical to the carbon-based systems, the nanoplatelets are composed of graphene sheets that are thermally and electrically conductive. In addition, the GNPs possesses a large specific surface area which is desirable during the transition of solid-liquid of PCMs as it aids the grasping liquid by means of surface tension [3]. To determine the chemical properties and microstructure of the GNPs composite, various apparatus such as Differential Scanning Calorimeter (DSC), Thermogravimetric Analyzer (TGA), Sonicator (Ultrasonic Liquid Processor), Scanning Electron Microscope (SEM), Field Emission Scanning Electron Microscopy (FESEM), X-ray Diffractometer (XRD), and Fourier Transform Infrared Spectroscope (FT-IR) were applied.

2.0 Research Methodology

2.1 Characterization of objective properties

Based on the research question that was developed, this study was conducted to enhance the thermal conductivity of PCM by means of using f-GNPs. All numerical as well as experimental results will be verified and validated. To be able to apply PCMs for the design of efficient energy systems, it is important to choose the best material that suits the purpose. The thermal properties of the PCM have to be measured at an initial stage and must be prioritized because elements such as their chemical and physical properties can be determined with an adequate accuracy based on the manufactures [6]. Basically, the thermophysical property is known to be the property of a material which influences the storage and transfer of heat which changes with certain variables such as pressure, temperature and composition, but does not change the chemical identity of the given material. Based on previous conducted studies, it was proven that the phase change material's thermal conductivity, latent heat, temperature and heat capacity are amongst the most vital parameters that should be prioritized in the experiment [7].

2.2 Selection of GNPs

GNPs come in a wide range of specifications which varies in terms of bulk density, relative gravity, specific surface area and peaks in UV-vis spectrophotometer. Table 1 shows all the specifications of GNPs.

Table 1. Specification of nanoparticle [8]

Properties	Specifications
Particle	GNPs
Colour	Black granules/powder
Carbon Content	>99.5
Bulk Density	0.2 to 0.4 g/cm^3
Relative gravity	2.0 to 2.25 g/cm^3
Specific Surface Area	300, 500, and 750 m^2/g
Particle Diameter	2μm
Peak in UV-vis Spectrophotometer	265 to 270 nm
Thickness	2nm

Based on Table 1, GNPs come in three different specific surface areas. For this experiment, the specific surface area of GNPs that is selected is 750 m^2/g as it is the highest specific surface area compared with the other two. Hence, when the GNPs are to be dispersed into the PCM composite, it will show the best dispersion property in comparison with the GNPs with smaller specific surface areas.

2.3 Preparation of Functionalized GNPs

Firstly, 1.84 grams of 4-nitroaniline is dissolved in a beaker of warm solution which consists of 4 ml of hydrochloric acid and 16 ml of water. The mixture then undergoes stirring and is cooled in an ice-bath to a temperature of about 2-4^{o}C. Then, 1.08 gram of sodium nitrate is added into a separate beaker containing 10ml of water and is cooled below a temperature of 5^{o}C. After stirring the 4-nitroaniline solution for 15 minutes, the sodium nitrate solution is slowly added into the 4-nitroaniline solution and the new solution is stirred for 30 minutes under an ice-bath. This reaction has to be conducted under an ice-bath as diazonium salts are unstable at temperatures above 5^{o}C [9]. While the 4-nitroaniline/sodium nitrate solution is being stirred, 400 mg of GNPs are measured and is added into a beaker containing 100 ml of ethanol and 10 0ml of water. The GNP solution is then sonicated for 20 minutes. After this process, the GNP mixture is slowly added into the 4-nitroaniline/sodium nitrate solution and is stirred under an ice-bath for 12 hours to ensure a complete reaction takes place. The temperature of the solution is measured using a thermometer from time to time to ensure that the temperature range stays within 2-4^{o}C. If the temperature increases, more ice is added into the ice-bath.

Once the reaction has been completed, the solution is transferred to four 50ml tubes and it is placed in the centrifuge for washing. The solution is washed with water for 15 minutes and this process is repeated 3 times. On the fourth time, the solution is washed with ethanol to completely clean the functionalized GNPs. When the functionalized GNPs are washed from the centrifuge, it is transferred to a petri dish and placed in the oven at 90^{o}C for drying. After 30 minutes, the functionalized GNPs are removed and the amount is measured. About 0.4 grams of f-GNPs we produced in the end of this process. Figure 2 shows the process of producing the functionalized GNPs.

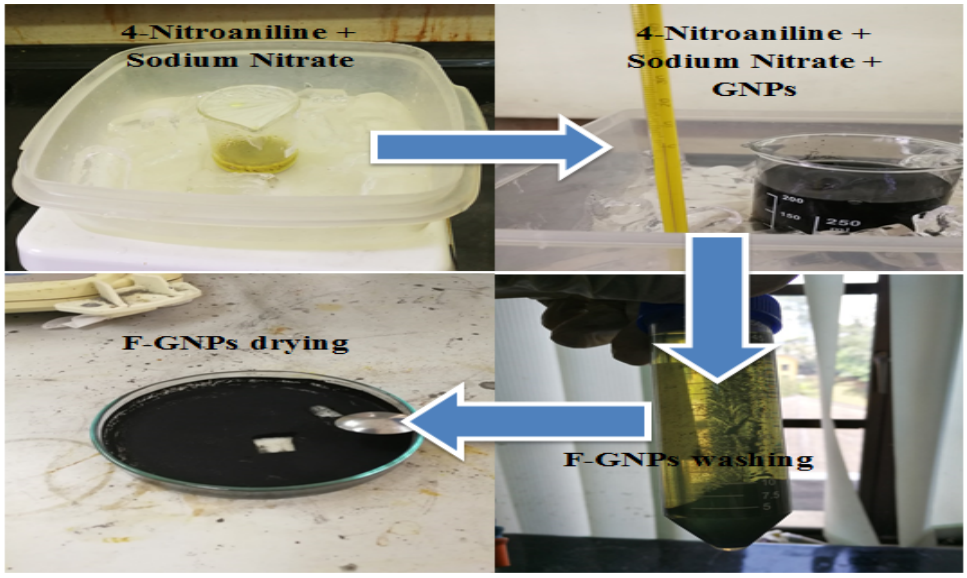


Figure 2. Preparation of f-GNPs

2.4 Preparation of PCM

The PCM that is used in this study is an organic PCM called paraffin. This paraffin that is selected is high temperature paraffin wax with melting point of above 70°C. Five samples are prepared in this study and the paraffin wax is cut and measured into five different tubes. Each tube contains six grams of paraffin wax. Once the five tubes of paraffin wax are prepared, it is placed in the oven at a temperature of 90°C. Since the melting point is above 70°C, any temperature above that can be set as the main purpose of placing the five samples in the oven is only to melt the paraffin wax before creating the PCM composite. Figure 3 shows the readings of all the paraffin samples that were measured.

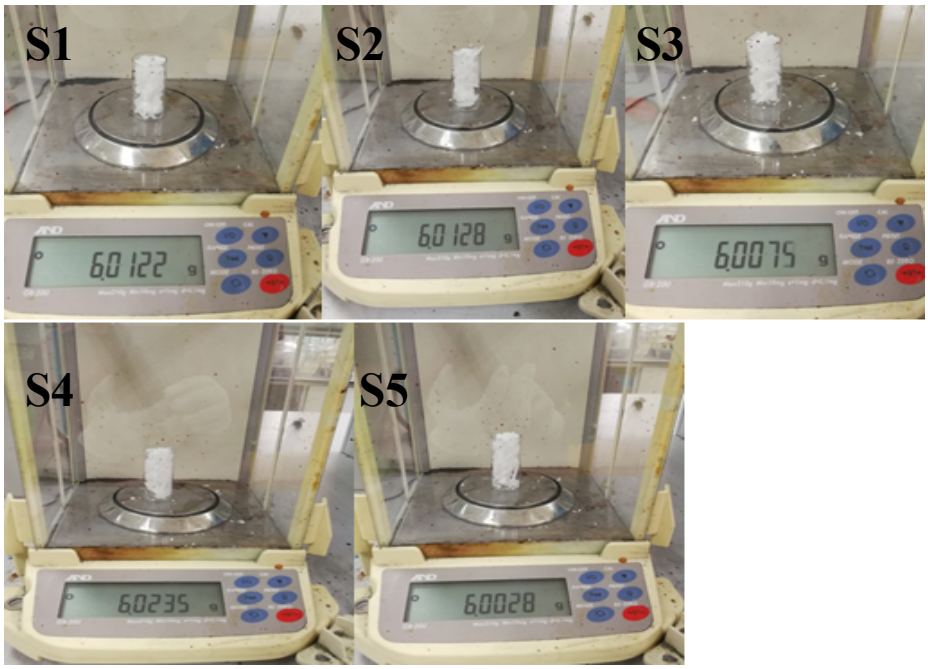


Figure 3. Readings of the paraffin samples

2.5 Preparation of composite PCM

Once the functionalized GNPs and PCM has been prepared, the next stage is to add them together to produce a composite PCM. The functionalized GNPs are added into the 5 tubes that contain 6 grams of paraffin wax each, by means of different concentration levels. The first sample will be pure paraffin, the second sample will be paraffin with 0.5 wt% of f-GNPs, the third sample will be paraffin with 1.0 wt% of f-GNPs, the fourth sample will be paraffin and 1.5 wt% of f-GNPs and the final sample will be paraffin with 2.0 wt% of f-GNPs. Table 2 shows the different sample concentrations of composite PCM that is produced.

Table 2. Concentration of samples

Samples	Amount of paraffin	Concentration of GNPs (wt%)	Total weight of samples
S1	6g	0	6g
S2	6g	0.5	6.03g
S3	6g	1.0	6.06g
S4	6g	1.5	6.09g
S5	6g	2.0	6.12g

Based on Table 2, four samples of composite PCMs and one sample of pure PCM is produced. Once all the samples are ready, it will undergo various analysis that includes the differential scanning calorimeter (DSC), thermogravimetric analyzer (TGA), scanning electron microscope (SEM), x-ray diffractometer (XRD) and fourier transform infrared spectroscope (FT-IR). These experiments will be conducted in University Malaya. Further explanation on these apparatus will be provided in the following section. All these apparatus that are used is for the purpose to study the chemical, physical and thermal characterization of the composite PCM. Figure 4 shows the five samples of the composite PCM that were produced.

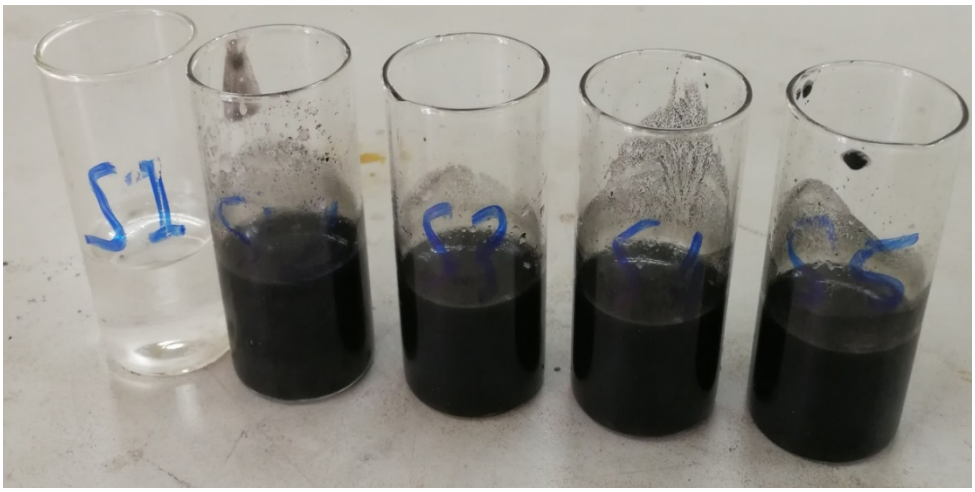


Figure 4. Composite PCM samples

3.0 Results and Discussion

3.1 Energy Storage Properties

This analysis was conducted by means of using the differential scanning calorimetry (DSC) to investigate the thermal energy storage properties of pure paraffin which in this case is sample 1 and the respective composite PCMs which is denoted as sample 2, sample 3, sample 4 and sample 5. Figure 5 shows the results of the DSC analysis that was conducted on all the 5 samples.

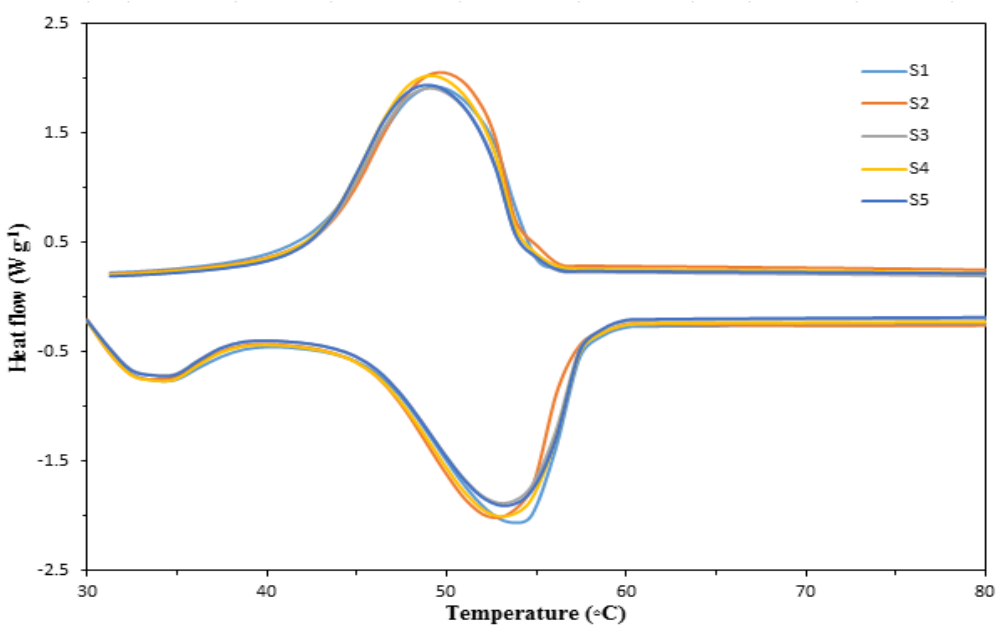


Figure 5. Melting and solidification curves for all the 5 samples

Based on Figure 5, the two main transition peaks can clearly be observed, by which the main peak attributed towards the heterogeneous nucleated rotator-liquid phase transition illustrates the solid-liquid phase change of the sample 1 which is pure paraffin. The minor peak that is located towards the left of the sharp peak at the homogeneous nucleated crystal-rotator phase transition illustrates the solid-solid phase transition of the pure paraffin in sample 1. The pure paraffin's thermal properties as well as the other 4 composite PCMs are summarized in Table 3. Based on table 3, the phase change temperature, transition temperature and latent heat can be seen. The melting and solidifying temperature of pure paraffin wax is determined to be 49.35^{o}C and 53.78^{o}C respectively. As for the sample 5 which has the highest concentration of GNPs in the paraffin wax was determine to be 48.88^{o}C for the melting temperature and 53.28^{o}C for the solidification temperature.

Table 3. DSC results of the 5 samples

Sample name	Paraffin (Wt %)	Melting			Solidification		
		$T_{t,m}$ (°C)	T_m (°C)	ΔH_m (Jg^-1)	$T_{t,f}$ (°C)	T_f (°C)	ΔH_f (Jg^-1)
S1	100	54.72	49.35	177.67	45.47	53.78	161.11
S2	99.5	54.42	49.62	175.42	45.21	52.88	159.33
S3	99	54.36	49.03	166.62	45.20	53.21	156.47
S4	98.5	54.29	49.04	165.90	45.36	53.03	154.20
S5	98	54.26	48.88	161.33	45.29	53.28	152.69

$T_{t,m}$: Melting transition temperature ; $T_{t,f}$: Freezing transition temperature

T_m : Melting Temperature ; T_f : Freezing temperature

ΔH_m : Melting latent heat ; ΔH_f : Freezing latent heat

3.2 Thermal Reliability of Composite PCM

The main challenge in thermal energy storage of materials is the stability of the chemical and thermal properties after a long period of utility for the respective materials. Hence, to test the thermal reliability of the composite PCM, a thermal cycling test is conducted to investigate the difference in properties of the material after undergoing a large number of freezing and melting cycles. The thermal cycling test that was conducted was performed up to 1000 cycles and DSC analysis was conducted at the end to compare the results before and after the thermal cycling test. Figure 6 and figure 7 shows the cycling test that was conducted on sample 5 which is the composite PCM that possesses the highest concentration of functionalized GNPs.

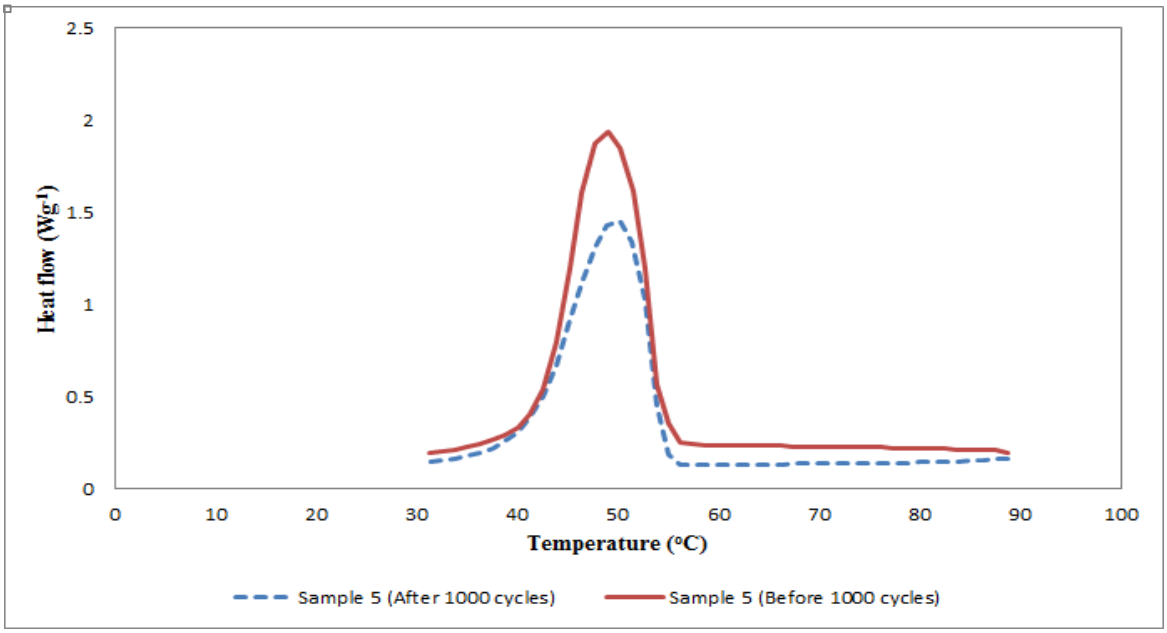


Figure 6. Melting curve of sample 5 before and after thermal cycling

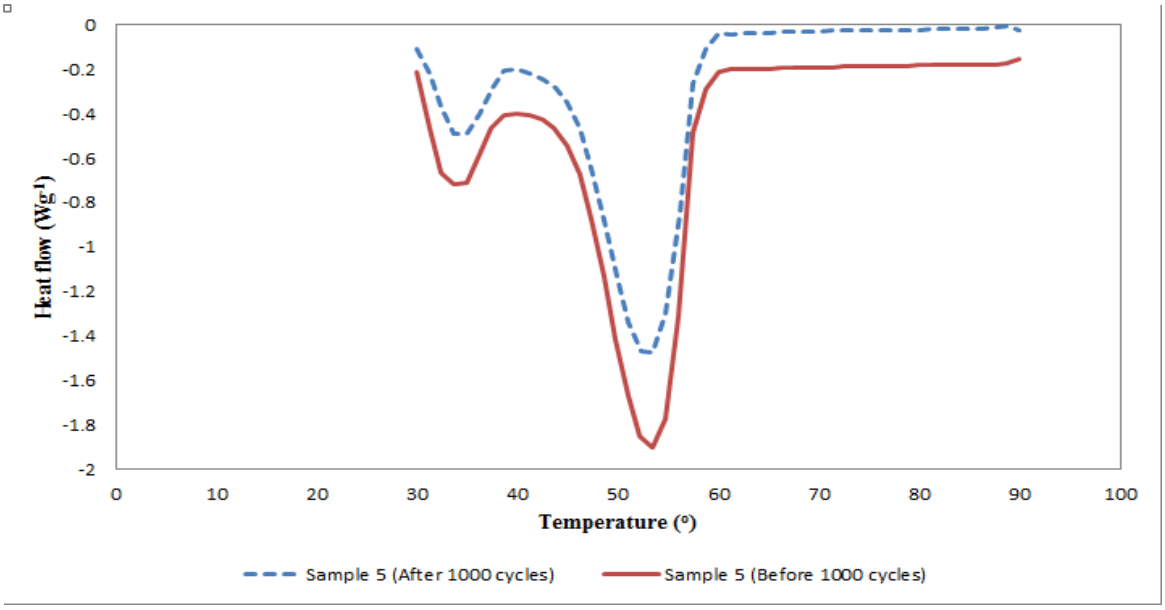


Figure 7. Solidifying curve of sample 5 before and after thermal cycling

Based on Figure 6 and Figure 7, the solidification and melting temperature of sample 5 after 1000 cycles was changed as the initial melting temperature before cycling was 48.88°C and the melting temperature after cycling was 49.81°C. This shows that the change in melting temperature before and after the thermal cycling was performed is -0.93°C. As for the freezing temperature before cycling was 53.28°C and 53.01°C after cycling for sample 5. This shows that the change in freezing temperature before and after cycling was performed is 0.27°C. The thermal cycling test was performed for all the 5 samples and the results are shown in Table 4.

Table 4. DSC results after cycling test

Sample name	Paraffin (Wt %)	Melting			Solidification		
		$T_{t,m}$ (°C)	T_m (°C)	ΔH_m (Jg^-1)	$T_{t,f}$ (°C)	T_f (°C)	ΔH_f (Jg^-1)
S1	100	54.89	49.79	145.04	45.52	53.85	141.33
S2	99.5	54.18	50.15	145.85	45.04	52.76	142.93
S3	99	54.45	49.98	151.71	45.19	52.98	150.80
S4	98.5	54.33	49.73	150.16	45.16	53.16	147.36
S5	98	54.23	49.81	143.75	45.06	53.01	138.68

$T_{t,m}$: Melting transition temperature ; $T_{t,f}$: Freezing transition temperature

T_m : Melting Temparature ; T_f : Freezing temperature

ΔH_m : Melting latent heat ; ΔH_f : Freezing latent heat

3.3 FT-IR Analysis

Figure 8 shows the results that was obtained from the FI-IR analysis for sample 1 that is pure paraffin and the balance 4 samples of the composite PCM. From figure 8, the peaks that are located at 2916.01cm^{-1} and 2852.56cm^{-1} is the vibration peaks of the symmetrical stretching of $-CH_2$ in sample 1. The peaks that are located at 1458.16cm^{-1} and 725cm^{-1} are the bending vibration peaks for the CH_3 in sample 1. From the FT-IR spectrum which is obtained, it can be clearly seen that there is no shifting in the above primary absorption peaks. Hence, from these results it shows that there is no chemical reaction of the samples of paraffin and GNPs with the functional group.

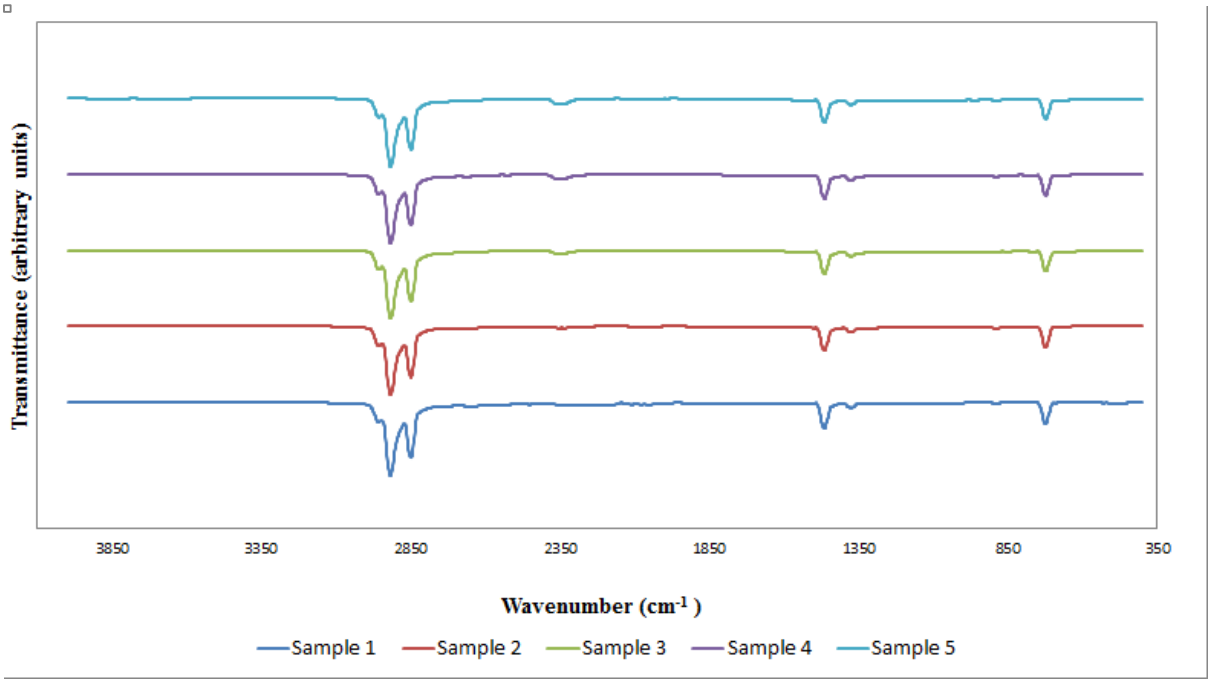


Figure 8. FT-IR spectra of the 5 samples

3.4 Thermal Conductivity and Thermal Resistivity

The thermal conductivity and thermal resistivity of pure paraffin and the composite PCMs samples were measured using a thermal conductivity apparatus called KD-2 pro which is done by means of using a hot wire method. Both the thermal conductivity and thermal resistivity was measured initially at solid state (30^{o}C) which is before its melting temperature and at molten state (80^{o}C) above its melting temperature in a thermal equilibrium condition. Table 5 shows the results of the thermal conductivity and thermal resistivity. Based on table 5, it is observed that the thermal conductivity at molten state for the composite PCMs is higher than that of the pure paraffin in sample 1. The thermal conductivity of the sample 1, sample 2, sample 3, sample 4 and sample 5 is 0.293 W/m·K, 0.406 W/m·K, 0.416 W/m·K, 0.420 W/m·K and 0.533 W/m·K respectively for solid state at 30^{o}C and 0.277 W/m·K, 0.563 W/m·K, 0.560 W/m·K, 0.556 W/m·K and 0.630 W/m·K repectively for molten state at 80^{o}C. The PCM that is used in this experiment is a high melting point paraffin wax which has a melting point of above 70^{o}C, hence all the samples were placed in a water bath at a fixed position at a temperature which is higher than its melting point so that is the reason a 80^{o}C temperature was selected for the molten state. From the results that are obtained,

it shows that the thermal conductivity of the composite PCM at both regions of solid and molten state is higher than that of the pure paraffin which is denoted as sample 1.

Table 5. Results of thermal conductivity and thermal resistivity of the 5 samples

Samples	*Thermal Conductivity (W/m·K)*		*Thermal Resistivity (C·C$_m$/W)*	
	Solid State (30^{o}C)	*Molten State (80^{o}C)*	*Solid State (30^{o}C)*	*Molten State (80^{o}C)*
Average, ΔS1	**0.293**	**0.277**	**3443.67**	**3656.67**
Average, ΔS2	**0.406**	**0.563**	**3360.67**	**3840.67**
Average, ΔS3	**0.416**	**0.560**	**3299.33**	**3883.33**
Average, ΔS4	**0.420**	**0.556**	**3218.67**	**3923.00**
Average, ΔS5	**0.533**	**0.630**	**3199.33**	**4312.00**

4.0 Conclusion

In this research, the composite PCMs are fabricated and characterizad to produce a new composite material for thermal energy storage. The thermal conductivity is enhanced by using applied composite technology to produce stable properties of organic PCMs by means of carbon nanofillers. For this study the nanofiller that is selected is GNPs as they exhibit a relatively high thermal conductivity capabilities. The GNPs are then functionalized with 5-nitroaniline and sodium nitrate to convert the GNPs to become hydrophobic for it to reactive with the PCM which is oil soluble to form a composite PCM that has an increased in thermal conductivity. Based on the results that was obtained from various analyses that were conducted, the composite PCM shows a success in enhancing its thermal conductivity that was analysed using the KD2-pro apparatus. Moreover, the chemical, physical and thermal properties of the composite PCM were analysed based on different concentration levels to identify the best composite PCM that can be applied towards the field of thermal energy storage and the best composite PCM that yields the best thermal conductivity enhancement is sample 5 which consists of the highest concentration of functionalized GNPs that is 2wt%.

Acknowledgement

Through this process of research, the author of this research would like to show gratitude towards all the support that was given by Dr. Azadeh Ghadimi, Assoc. Prof. Dr. Henk Metselaar, Mr Amir Reza and Dr. Mohamed Mehrali for their guidance and assistance that aided this research to achieve its completion

References

[1] M. Liu, W. Saman, and F. Bruno, "Review on storage materials and thermal performance enhancement techniques for high temperature phase change thermal storage systems," *Renewable and Sustainable Energy Reviews*, vol. 16, no. 4. pp. 2118–2132, 2012.

[2] M. Silakhori, M. S. Naghavi, H. S. C. Metselaar, T. M. I. Mahlia, H. Fauzi, and M. Mehrali, "Accelerated thermal cycling test of microencapsulated paraffin wax/polyaniline made by simple preparation method for solar thermal energy storage," *Materials (Basel).*, vol. 6, no. 5, pp. 1608–1620, 2013.

[3] M. Mehrali, S. T. Latibari, M. Mehrali, T. M. Indra Mahlia, H. S. Cornelis Metselaar, M. S. Naghavi, E. Sadeghinezhad, and A. R. Akhiani, "Preparation and characterization of palmitic acid/graphene nanoplatelets composite with remarkable thermal conductivity as a novel shape-stabilized phase change material," *Appl. Therm. Eng.*, vol. 61, no. 2, pp. 633–640, 2013.

[4] B. Zalba, "Review on thermal energy storage with phase change: materials, heat transfer analysis and applications," *Appl. Therm. Eng.*, vol. 23, no. 3, pp. 251–283, 2003.

[5] F. Perrozzi, S. Prezioso, and L. Ottaviano, "Graphene oxide: from fundamentals to applications," *J. Phys. Condens. Matter*, vol. 27, no. 27, p. 13002, 2015.

[6] Z. Yinping and J. Yi, "A simple method , the T -history method , of determining the heat of fusion , specific heat and thermal conductivity of phase-change materials," *Meas. Sci. Technol.*, vol. 10, no. 3, pp. 201–205, 1999.

[7] B. Xu, P. Li, and C. Chan, "Application of phase change materials for thermal energy storage in concentrated solar thermal power plants: A review to recent developments," *Applied Energy*, vol. 160. pp. 286–307, 2015.

[8] M. Mehrali, E. Sadeghinezhad, S. T. Latibari, S. N. Kazi, M. Mehrali, M. N. B. M. Zubir, and H. S. C. Metselaar, "Investigation of thermal conductivity and rheological properties of nanofluids containing graphene nanoplatelets.," *Nanoscale Res. Lett.*, vol. 9, no. 1, p. 15, 2014.

[9] G. Fabrizi, A. Goggiamani, A. Sferrazza, and S. Cacchi, "Sonogashira cross-coupling of arenediazonium salts," *Angew. Chemie - Int. Ed.*, vol. 49, no. 24, pp. 4067–4070, 2010.

eureca 2017 – Conference Paper
Paper Number 2ME08

Reduction of Artefacts Caused By Implant in a 3D Model

Karthik Mayakrisenan*, Cheah Kean How, Mohan Kumar
School of Engineering, Taylor's University, Malaysia

** jmt.karthikmaya@gmail.com*

Abstract
Scoliosis is a disease that affects the vertebra of a human body. This disease can be cured by executing an operation which includes the insertion two metal implants through the affected curvature bone in the vertebra. This operation would help the bones in the vertebra to reinstate its normal position of 90 degrees. After the surgery, the individual will have to undergo several computerized tomography (CT) scans to aid the orthopaedic surgeons to monitor the patient's recovery progress. Unfortunately, the captured CT scans will have several artefacts present which hinder the orthopaedic surgeons' view of the scan. As for this project, the author observes and study each artefact present in the scans thus selecting the ideal artefacts which relates to metal implants in the bone and removed the artefacts form the bones in the form 3D model. The second part of this research is to determine the artefacts' impact in Finite Element Analysis (FEA). After selection, the author would delegate certain scans to be processed by software named as InVesalius. The InVesalius software is widely used by the medical bodies to convert CT-scans to 3-Dimensional (3D) model conveniently. Since there many models for this project, the author will choose an ideal model which has the best 3D specifications such as the view of the noises and the efficient scan of the complete spine. The selected model was removed from the noises with Space Claim and Mesh Mixer. Both pre-and post-refined models were experimented with parameters such as the volumetric and cross-sectional area. A relative error analysis to determine the most efficient software. As for a result, the Mesh Mixer has the best accuracy as it does not have any error whereas Space Claim had an error percentage of 35.7%. For the second part of this research, the refined models produce an increase in tensile and compressive forces. The data of both parts are tabulated and discussed.

Keywords: Scoliosis, CT Scans, Refinement, Software, Noises, FEA.

1. Introduction

1.1 Background

Vertebra is a structure that is made up of calcium consisted bones, muscles, tendons and has also has coverage range from the skull to the tail bone the spinal cord or the backbone has different adverbs such as spinal cord, spine and vertebral column [1]. Scoliosis is a phenomenon that has the spine or the backbone in a twisting and curved manner [1] as shown in Figure 1.0. The curvatures of scoliosis are categorized in many groups as the Table 1.0.



Figure 1.0. An example of Scoliosis Case [1].

Table 1.0. Groups of Scoliosis

NO	GROUP	CURVATURE PATTERN
1	Levoscoliosis	Letter ‘C’ Shaped
2	DextroScoliosis	Mirror of Letter ‘C’

Both groups are the primary types that are common nowadays. In the later stage of the spine, a secondary curve will develop thus providing a mirror of letter ‘C’. After undergoing an operation, the curves tend to resemble a normal person’s posture of spine as shown in Figure 1.1. In the treatment’s progress, the surgeons face a challenge to examine the Computerized Topography Scan (CT-Scan) as the implants fitted in the spine interferes the rays emitted by CT-Scan and generates noises in the scan file.

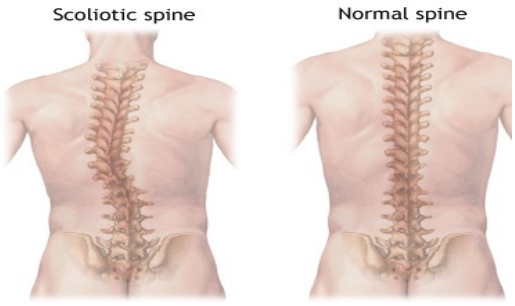


Figure 1.1. A post scoliotic operative result

Bone is a rigid body tissue consisting of cells embedded in an abundant of hard intercellular materials [3]. The major functions of a bone are to support the movements and protection for the important organs. Several factors such as the age, gender, location in the body, mineral content and diseases affects the density of the bone.

Bones are made up of collagen fiber, proteins, and minerals such as calcium phosphate and calcium carbonate [3]. These contents provide the bone strength and toughness. Another advantage of possessing these contents would be the versatility of the bone in adapting to a load. This adaptability is very helpful in primary bones such as the femur, tibia and fibula. These two bones are responsible for being the neutral for load bearing part. The characteristics of the cancellous bone would be highly porous and non-isotopic. Each bone in the spine are separated by a disc which allows movements between the bones and acts as a shock absorber. The disc or the vertebral disc are made up of fibrocartilage material [3].

It possesses two layers which is the outer and the inner layer. Outer layer is called as annulus fibrosis [3] and the inner layer is called as the nucleus pulpous. In the disc, both layers have fibers that distribute pressure evenly throughout the vertebral disc to avoid damage to the bones and the nerves surrounding it.

1.1.1 Types of Scoliosis

Scoliosis are categorized into four- types which are idiopathic, congenital, neuromuscular and miscellaneous. All the mentioned types above have an origin point. They are mentioned in the Table 1.2.

Table 2.0. Origins' of Scoliosis according to their Age Group

TYPES	ORIGIN	AGE GROUP
Idiopathic	Infant	(0-3) years
	Juvenile	(3-10) years
	Adolescent	(>10) years
Congenital	Forms at birth	-
Neuromuscular	Forms at tumor	-
Miscellaneous	Forms at accidents	-

Scoliosis can be detected via utilizing the Adams' Forward Bend Test, Reiser's Sign, Lenke system and Cobb Angle Measurement [3]. It can be also verified by X-ray, CT-scans, ultrasound imaging and surface topography [5][6][7] [9] [16]. As for Cobb angle, an angle more than 10° or higher as in Figure 1.3 is diagnosed as scoliosis [10].

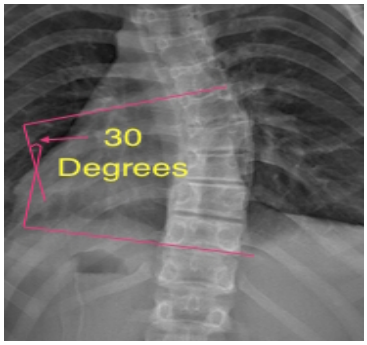


Figure 1.3. Cobb Angle of a Patient

1.1.2 Available Treatments

Scoliosis can be cured by using surgical, cast and braces. Casting are mainly used for infantile patients. Braces are mainly used for children as their bone growth is still available. Surgical method is executed in adults and only if the Cobb Angle is 40° or higher. The main goal of these treatments is to avoid lower back pains, and aid the patients to normally perform their daily activities just like a normal person. According to a survey performed by T. Maruyama, nearly 76% of curvatures in spine can be reduced via braces and the effectiveness of those braces increases significantly [11]. The common brace used to treat scoliosis will be the Thoracolumbosacral Orthosis (TLSO). TLSO includes Boston brace, Charleston brace and Providence brace. These braces are shown in Figure 1.4.

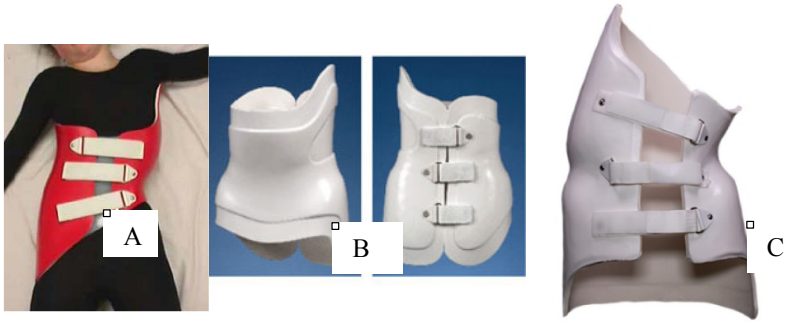


Figure 1.4 (A) Providence Brace, (B) Boston Brace, (C) Charleston Brace

T. Maruyama also claims that by using the OSAKA Medical College's braces can decrease the progression of the curvature present in the spine [11]. To have an optimal result, the braces must be worn for a duration of two (2) years and periodically monitoring the progress every two to four months.

1.1.3 Surgical methods

Surgical methods are classified into four categories as anterior, posterior, combined anterior and posterior and minimal invasive approach (MIS). Among the methods mentioned, posterior and minimal invasive approach are the most preferable methods to treat scoliosis. Posterior approach enables the surgeon to approach the spine without the disruption of organs as in anterior approach. In MIS, the amount of blood loss, hospitality days and mobility of the patient after post operation are less compared to the other approaches.

1.1.4 Surgical techniques

There are three techniques followed to treat Scoliosis which are growing rods, guided growth systems and compression based systems. Growing rods apply internal force to the curvature. guided growth systems are basically devices planted with implants to ensure a significant amount of force applied on the curvature and later diminishing the curvature [12] [13]. The implants are usually made up of titanium, titanium-alloy, non-metallic and steel. Currently, implants are created by polymers which syncs with the biological properties of the bone [14]. Among these materials, titanium based implants are used frequently as it has less interference with the MRI scan [15].

2.0 Theoretical Literature

Since the creation of CT-scan machines in the year 1972, numerous cases on orthopedic sector have been easily diagnosed by medical profession all around the globe. Unfortunately, the scan images that were produced have noises that can corrupt the data at any point during the CT process [16]. The term; Noise has many categories such as random, statistical, electronic, round off errors. artefactual and structural.

Random is a noise that has fluctuations in image density that varies randomly from an image to another. Statistical noise is the transmission of X-radiation energy in a chunk where it is called as quanta. The counter-measure taken for this noise will be detecting a finite number of X-ray quanta [16]. The statistical noise has another alias as Quantum noise. The reduction of statistical noise is to increase the number of detected X-ray quanta [16]. Detected X-ray quanta works directly proportional to the relative accuracy of the scan. As an example, in Figure 2.1 portrays a series of images taken by GE CT/T 7800 scanner machine using phantom specifically designed to experiment contrast sensitivity [16].

As can be observed from the Figure 2.1, increasing X-ray exposure (milliampere-second) can reduce the noise [16].

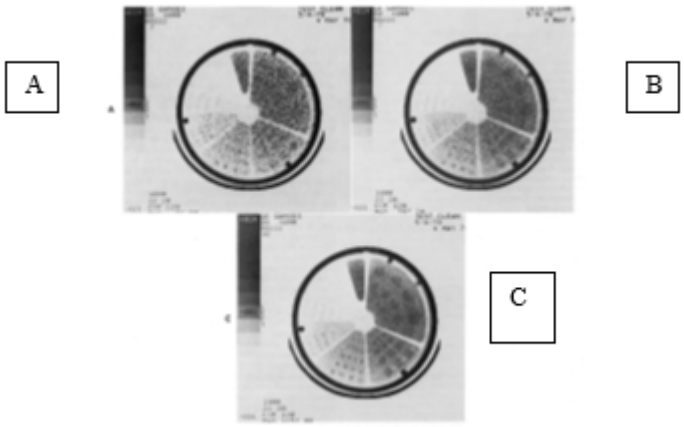


Figure 2.1. Three scans of a contrast sensitivity phantom taken on a GE CTIT 7800 scanner at various milliampere-second values: A, 77. B, 307. C, 1152. For this scanner, higher dose leads to lower noise and improved contrast sensitivity [16].

Electronic noises are developed in scan images via electric signals, electronic circuits and analog circuits in the machine. Analog circuits are the major cause of this noise as it always processes varying signals throughout the CT-process. A work breakdown of CT-process has been shown as in Figure 2.2.

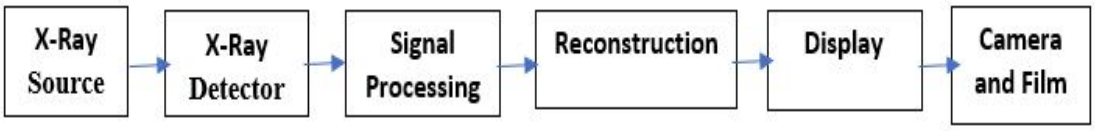


Figure 2.2. Work Breakdown of a CT-Process

As for the study performed by Cohen,1979 [16], many commercially available CT-scanners are designed efficiently to reduce the contribution of electronic noise under normal operating machine.

Round Off Errors are noises that aren't generated by X-radiation but it is created by the computer which only possess a limited number of bits [16]. For an example, the output of a product has two significant numbers but the computer rounds off the last number only. This will produce different result compared to other machines. Round errors occur in the display stage shown in work breakdown above as only a fixed number of discrete brightness levels are displayed at the end [16].

Structural noise is an occurrence that happens when different densities of an object interferes with the diagnosis in a CT scan [16]. As an example, when the rib-cage overlaps the lungs in a CT process, it exceeds the superposition of the lungs whereas the same scan with the liver can't be exceeded as the liver and other organs in the body have different densities in nature.

Artefactual noise is basically a misinterpretation of the scan image with a surrounding shape exist after the scan process. Their existences can be read or studied with a trend or pattern that appear in the scans [16]. This artefact can interfere the surgeons' interpretations of the patients' progress in the post-operative period. Not only that, these artefacts can be reduced using several methods as it has a huge scope of artefacts in this category.

2.1 Noise selection

Among the listed noises in section 2.0, the artefact that is very prone to CT scan images will be the Artefactual noise. Artefactual noise consists of four major groups of artefacts which are physics-based, patient-based, scanner-based and helical and multi section [17]. In physics-based group; Beam hardening, cupping artefact and Streaks and Dark bands are included whereas in patient-based group; Metallic and motion artefact are included. In scanner-based group, ring artifact is included and finally helical and multi-section group; helical and cone beam artefacts are included. With all these information, the identification of the most prone artefacts to the CT scan image will be the metal artefact. This was justified with a research conducted by F. Edward Boas, twenty-one percent of CT scans are affected by metal artefacts and it is very common in CT images to have the artefacts. [18]. Metal artefacts also influences other artefacts such Beam Hardening, Compton Scatter, Under sampling, Cone Beam, Motion and Windmill.

2.2 Metal artefact

Metal artefact occurs when the density of the metal implant is higher than the computer can handle resulting in different attenuation profiles [17]. Metals implants with high atomic number such as steel and titanium interferes with the X-radiation emitted from the CT machine providing an output as in Figure 2.3.

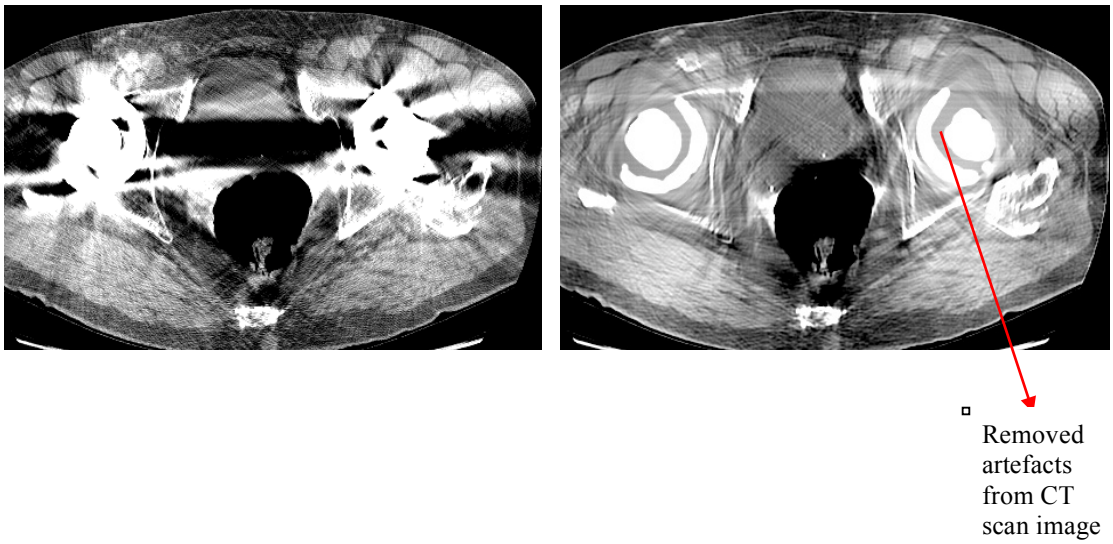


Figure 2.6 Comparisons between an original image and a MDT processed image [18].



Figure 2.3 Metal artefact affected CT scan image

As can be observed from Figure 2.2, the streaks are caused by under sampling, motion, cone beam and windmill artefacts [18]. With Filtered Back projection (FBP) filter the chunk of discontinuities of electron number can be detected and amplified. To eliminate the edges from the metal, an accurate data with an infinite resolution is required. According to F. Edward Boas [19], many reduction techniques are suggested such as metal deletion technique (MDT), selective algebraic reconstruction technique (SART), FBP and Linear Interpolation (LI) [19]. Among the four techniques suggested, the most efficient technique is the MDT.

This is justified with MDT producing the lowest average error (76 % less than FBP, 42% less than LI and 17% less than SART) [19]. MDT starts with a raw projection

data from scanner, then it uses high quality non-metal data to reconstruct the metal positions of the CT images [18].

In selective cases, MDT has drawbacks as it decreases the resolution of the image and introduces several new artefacts to the image. To achieve an efficient CT-scan image, the MDT processed images must be compared with the original images; as shown in Figure 2.6.

Improved in ≥ 75% of cases		Improved in < 75% of cases
aneurysm clip (brain)	shoulder replacement	pedicle screws
aneurysm coil (brain)	unilateral hip replacement	depth electrodes (brain)
dental fillings	bilateral hip replacements	cryoablation probes
pacer wire	knee replacement	iodinated contrast
ventricular assist device	orthopedic plate(s)	
surgical clip(s) (abdomen)	femoral neck screw	
embolization coil(s) (abdomen)	spinal rods	
bullet(s) / schrapnel / lead shot		

Figure 2.5 (A) Metal implants that undergoes MDT in an efficient manner, (B) Metals that does not perform well in MDT process [18].

2.3 3D Modelling

Three-dimensional (3D) modelling are widely used by many professions in engineering, medicine architecture etc. In engineering, 3D modelling is considered an essential tool for graduates' technical skill. 3D modelling skill has evolved to be a mandatory requirement for employers especially in the designing sector. Private and government institutions have made compulsory for graduates gain the skill of 3D modeling by running classes. There are many types of 3D modelling software as Space Claim, Auto Cad, GeoMagicX etc.

3D modelling of an object starts from data acquisition and ends with a 3D virtual model visually interactive on a display in a computer [19]. 3D modelling can be also called as computer aided drawing (CAD). It is also a process which converts a cloud point on object to a triangular shaped network called as "Mesh". CAD models achieve a significant demand in preserving heritage locations around the globe for virtual tourism, reverse engineering, documentation in case or loss damage. Therefore, the scope of the CAD is huge and wide, it is not an easy task to select an appropriate software without any comparisons thus not forgetting the cost involved to purchase those software.

CAD products and measurement can be divided into two methods which is contact and non-contact. Contact methods uses conventional methods as coordinate measuring machine, calipers and ruler or bearings. In non-contact methods, machines as X-ray, CT-scan and laser scanning are included [19]. In current trend, all the CAD software are developing models utilizing the non-contact methods as it is based on light-waves using active and passive sensors as. In passive and active sensors, four alternative methods are distinguished which are image-based rendering (IBR), image-based

modelling (IBM), range-based modelling and combination of image and range based modelling [19].

To achieve the "Mesh", polygons are used as they are accurate to represent the results of 3D geometries and providing an optimal surface profile [21]. For applications as building reconstruction, only small number of points are required as the planes or the surface of the building is flat and surface generation is achievable with few triangular patterns. As for objects which has irregular surfaces such as bones requires a "smart algorithms" to convert the cloud pints to triangular points to generate a surface that resemble 90 % of the original surface.

Smart algorithm which is meant by Fabio Remondino, is Kaczmarski methods. It is an iterative algorithm for solving linear equations systems. It is also called as Algebraic Reconstruction Technique (ART).
It is formulated as:

$$\boldsymbol{x^{k+1}} = \boldsymbol{x^{k}} + \boldsymbol{\lambda_k} \frac{\boldsymbol{b_i} - (\boldsymbol{a_i}, \boldsymbol{x^k})}{||\boldsymbol{a_i}||^2} \boldsymbol{a_i} \quad (1)$$

where i = k mod m+1, ai is the ith row of the matrix A, bi is the ith of the component vector b, λk is a tolerance parameter [21].

The conversion of the measured 3D point clouds is summarized into four steps as Pre-processing, Determination of the global topology, Generation of the polygonal surface and post-processing [21]. Pre-processing executed to eliminate corrupt data and noise present in the models. The data may also rework the data to develop to create a much better model than the previous model. Determination of the global topology is a process to determine the adjacent parts of the surface to eliminate possible constraints such as break lines.

4.1 Refinement process

The results from both software; Mesh Mixer and Space Claim are portrayed as following and their breakdown will be discussed later at section 5.0.

Mesh Mixer
MODEL A- High level of noise

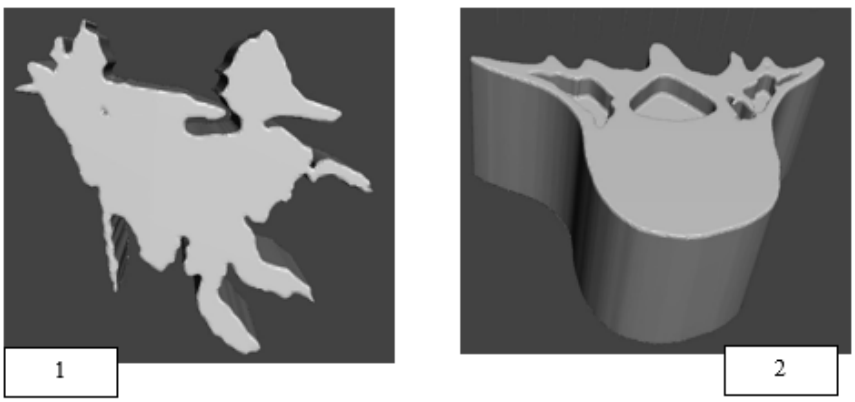


Figure 4.4 (1). Pre-refined sample of Model A, (2) Post-refined sample of Model A

MODEL B- Medium level of noise

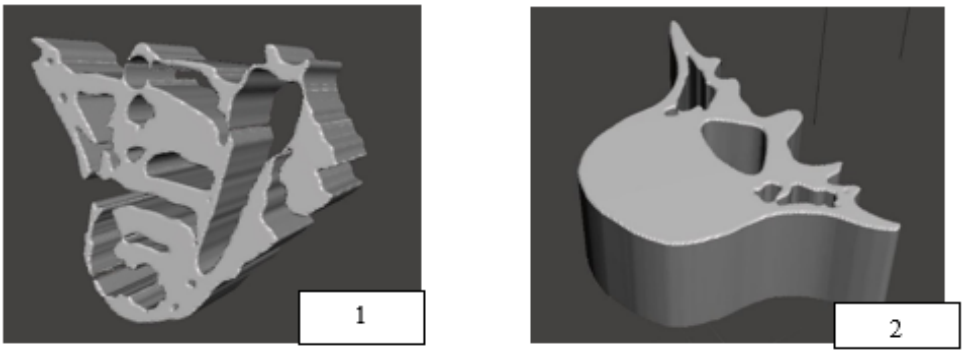


Figure 4.5 (1). Pre-refined sample of Model B, (2) Post-Refined sample of Model B



Figure 4.6 A good sample of model C-it is used as a reference and a constant in this research.

Space Claim

MODEL A- High level of noise

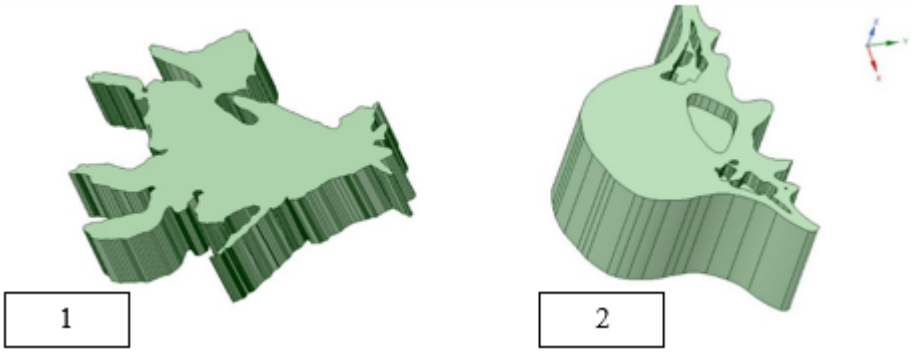


Figure 4.7 (1) Pre-refined sample of Model A, (2) Post-refined sample of Model A

MODEL B – Medium level of noise

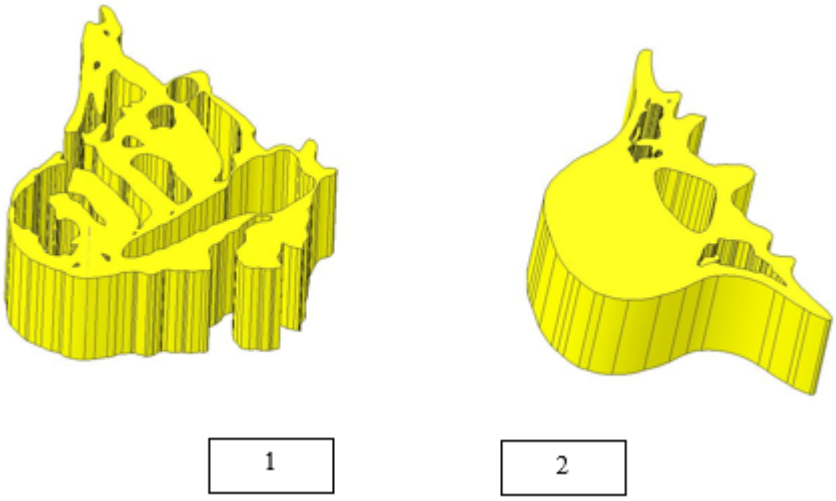


Figure 4.8 (1) Pre-refined sample of Model B, (2) Post-refined sample of Model B

MODEL C- No Noise

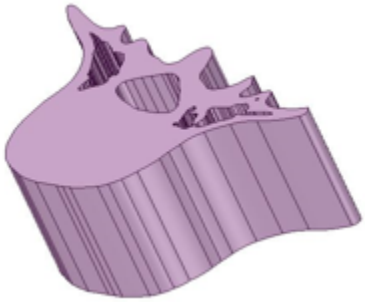


Figure 4.9 Model C without any noises and used as a constant, a reference for refinement and analysis.

DISCUSSION

Refinement Process

In Mesh Mixer, solid 3D models are generated in a smooth surface manner (refer to Figure 4.5,4.5 and 4.6). These 3D models are perfect to be exercised in FEA because it does not create any miscalculations by the FEA software thus enabling it to produce an efficient result. In a study conducted by the Institute of Structural Engineering, a 3D model must be developed with a correct geometry such as thickness, break line etc. and without any interference of other solids in the model [31]. In Space Claim, it is nearly impossible to remove all the break lines on the model as shown in Figure 4.7, 4.8 and 4.9. These break line has its own functions which is to aid the author to trace back the history of the CAD model to modify in future. As calculated from section 4.5, the relative error analysis of Mesh Mixer is 0% whereby Space Claim is 36%. Space Claim's values deviates from Mesh Mixer in a range of 0.002 to 0.005. From this result, Mesh Mixer is justified as an efficient basic analytical software compared to Space Claim. As for Computer Aided Drawing (CAD) processes, Space

Claim provides better features and functions as other professional CAD software such as SolidWorks and AutoCAD.

An added advantage in Space Claim is its ability to export 3D models to all types of file formats such as STL, OBJ, STP etc. Unfortunately, Mesh Mixer does not have that capability and it exports 3D models in MIX file format which is not compatible in FUSION 360 software as it only imports models in STL, OBJ and STP format. To counter this challenge, the MIX file must be imported in Space Claim an exported back to FUSION 360 as STL file format and had to be saved as mesh to avoid any break lines in the models.

Removing noises from models are achievable with ease with Space Claim than Mesh Mixer. This was justified as Space Claim uses an essential tool which is "Planes" feature. This feature enables the author to insert planes in various angles in the model to eliminate the noises in the pre-refined models of A and B. Finally, Mesh Mixer also removes noises but it does not provide an accuracy when eliminating the noises as the might remove parts of the bone.

Finite Element Analysis

In FEA, models A and B shows a significant increase in the tensile and compressive forces as evaluated in section 4.5, As taking the study of Institute of Structural Engineering, a model's geometry influences the performance of the model in FEA [24]. Noises creates unnecessary shapes on the model's structure and thickness of the model also varies. For instance, in pre-refined model A; tensile force is 0.472 MPa at maximum whereas in the post-refined model it is at 2.707 MPa. It shows an increase of 17 % in strength to withstand the pressure input of 1.72 MPa. With this information, the model won't able to collapse under failure. In pre-refine model B, the tensile stress is at 0.1990 MPa. After undergoing refining, the tensile stress is increased to 0.281 MPa. An increase of 70.8 % can be seen. As for compressive stress, models A and B has an increase of 17% and 16.5% respectively. With this data, a justification can be drawn whereby removal of noises can introduce an impact on the FEA 3D models and by improving models in geometry can provide an efficient performance in Finite Element Analysis.

References

[1] D. T. Derrer, "Scoliosis," WebMD, May. 23, 2014. [Online]. Available: http://www.webmd.com/osteoarthritis/guide/arthritis-scoliosis.

[2] J. D. Lewin, "Are you suffering from degenerative Scoliosis?," The Center for Spinal Disorders, Jan. 3, 2015. [Online]. Available: http://www.njspinaldisorders.com/suffering-degenerative-scoliosis/

[3] Y. Abe, M. Ito, K. Abumi, and H. Sudo, "Scoliosis corrective force estimation from the implanted rod deformation using 3D-FEM analysis," BioMed Central, vol. 10, no. 2, pp. 10-22, 2015.

[4] P. N. Soucacos, and E. Beris, "School-Screening for Scoliosis. A Prospective Epidemiological Study," The Journal of Bone and Joint Surgery, vol. 10, no. 79, pp. 1498-1503, 1997.

[5] The Luklinski' Spine Care, "Structural Defects - Scoliosis," The Luklinski' Spine Care, May.8,2014. [Online] http://www.theluklinskispineclinic.com/backrack/en/conditions/scoliosis.
[6] P. Agrawal, A. Kajla and M. N. Raverkar, "Different methods of detection of scoliosis - a Review," International Journal of Innovative Science, Engineering & Technology, vol. 1, no. 9, pp. 246 - 248, November 2014.
[7] A. Gardner, "Clinical assessment of scoliosis," in Mini-Symposium: Spinal Deformity, 2011.
[8] H. Kim, H. S. Kim, E. S. Moon, C.-S. Yoon, T.-S. Chung, H.-T. Song, F.-S. Suh, Y. H. Lee and S. Kim, "Scoliosis Imaging: What Radiologists Should Know," RSNA, vol. 30, pp. 1823 - 1842, 2010.
[9] T. Amaral, A. L. Wollowick, S. Moghtaderi, B. Thornhill and V. Sarwahi, "The Usefulness and limitations of the Nash and Moe Rotational Grading Method in Predicting Vertebral Rotation," Lippincott Williams & Wilkins, Inc, San Antonio, 2009.
[10] W. Chen, L. H. Le and E. H. M. Lou, "Ultrasound Imaging of Spinal Vertebrae to Study Scoliosis," Open Journal of Acoustics, vol. 2, pp. 95 - 103, September 2012.
[10] BOUGHERARA ET AL., "NEW PREDICTIVE MODEL FOR MONITORING BONE REMODELING,"
[11] T. Maruyama, Y. Kobayashi, M. Miura and Y. Nakao, "Effectiveness of brace treatment for adolescent idiopathic scoliosis," *Scoliosis Journal,* pp. 1 - 4, 2015.
[12] E. Jazini, T. Raman, J. Bressner, K. M. Kebaish and P. D. Sponseller, "Adolescent idiopathic scoliosis: Considerations for the transition to adulthood," *Seminars in Spine Surgery,* vol. 27, pp. 62 - 69, 2015.
[13] H. Kuroki, N. Inomata, H. Hamanaka, K. Higa, E. Chosa and N. Tajima, "Efficacy of the Osaka Medical College (OMC) brace in the treatment of adolescent idiopathic scoliosis following Scoliosis Research Society brace studies criteria," *Scoliosis Journal,* vol. 10, no. 12, pp. 1 - 9, 11 April 2015.
[14] F. Miyanji and S. Desai, "Minimally invasive surgical options for adolescent idiopathic scoliosis," *Seminars in Spine Surgery,* vol. 27, pp. 39 - 44, 2015.
[15] J. M. Highsmith, "What Is Spinal Instrumentation and Spinal usion?," 23 March 2015. [Online]. Available: http://www.spineuniverse.com/treatments/surgery/what-spinal-instrumentation-spinal-fusion.
[16] L.Letko, R. G. Jensen and J. Harms, "The Treatment of Rigid Adolescent Idiopathic Scoliosis: Releases, Osteotomies and Apical Vertebral Column Resection," in *Idiopathic Scoliosis - The Harms Study Group Treatment Guide*, 1st ed., P. O. Newton, M. F. O'Brien, H. L. Shufflebarger, R. R. Betz, R. A. Dickson and J. Harms, Eds., Thieme, 2010, pp. 188-199.
[17] Elke Van de Casteele, "A bimodal energy model for correcting beam hardening artefacts in X-ray tomography''. doi:0-7803-7767-2/03/$17.00 02003 IEEE
[18] Bal, M., & Spies, L. (2006). Metal artifact reduction in CT using tissue-class modeling and adaptive prefiltering. Medical Physics, 33(8), 2852-2859. doi:10.1118/1.2218062
[19] Boas FE, Fleischmann D: Evaluation of two iterative techniques for reducing metal artifacts in computed tomography. Radiology 259(3), 894-902 (2011).
[20] De Man B, Nuyts J, Dupont P, Marchal G, Suetens P: Metal streak artifacts in X-ray computed tomography: a simulation study. IEEE Transactions on Nuclear Science 46(3), 691-696 (1999).

[21] Feldkamp LA, David LC, Kress JW: Practical cone-beam algorithm. J. Opt. Soc. Am. A 1(6), 612-619. (1984).
[22] Yanna, R., Lei, X., & Qiang, W. (2011). Research on the 3D visualization modeling technique of complex underground Chambers. 2011 3rd International Conference on Computer Research and Development. doi:10.1109/iccrd.2011.5763876
[23] Chiu, L. N., Falzon, B. G., Boman, R., Chen, B., & Yan, W. (2015). Finite element modelling of composite structures under crushing load. Composite Structures, 131, 215-228. doi:10.1016/j.compstruct.2015.05.008
[24] Slambrouck, K. V., & Nuyts, J. (2012). Metal artifact reduction in computed tomography using local models in an image block-iterative scheme. Medical Physics, 39(11), 7080-7093. doi:10.1118/1.4762567

A Numerical Assessment of Microtopographies with Varied Geometries in Relation to Biofouling Control

Lam Kuo Min*, Felicia Wong Yen Myan, Lim Chin Hong
Department of Mechanical Engineering,
School of Engineering, Taylor's University, Malaysia.

*Corresponding author: kuomin.lam@sd.taylors.edu.my

Abstract
Biofouling is the unwanted attachment of organisms and microorganisms to a submerged surface. Biofouling of organisms promotes mechanical interference, physical damage to infrastructures and biological competition in aquaculture. Numerous studies have shown that the application of surface topography with varied geometries and sizes are effective in preventing biofouling. Hence, the current research aims to study and assess microtopographies of varied geometries in relation to biofouling control. This research will strictly focus on controlling surface topography by using a fixed optimum topography size and manipulating the shape and geometry. This research is fully computational where simulations of flow over three-dimensional (3D) models will be carried out with Computational Fluid Dynamics (CFD). With the aid of CFD, numerical methods can be used to solve governing equations that describe the fluid flow of predefined models of varied geometries and boundary conditions which will tremendously save time and cost for this research. Parameters that will be studied includes hydrodynamic variations such as wall shear stress and velocity. In general, hydrodynamic variations with the largest magnitude among the different topography geometries will exhibit the best antifouling performance. The greater the magnitude of the parameters, the higher the hydrodynamic disturbance and the better the antifouling efficacy. Topography geometries of pillars, octagons and squared grooves were studied, compared and analyzed to determine their respective hydrodynamic variations and antifouling efficacy. It was concluded that pillar topography exhibits the highest magnitude of wall shear stress and velocity as compared to other topography. It was also found that topography peaks, regardless of topography geometries, make better defensive stances against fouling due to its higher hydrodynamic changes.

Keywords: Biofouling control, Antifouling, Topography geometries, Wall shear stress, Velocity

1. Introduction

Biofouling is the unwanted attachment of organisms and microorganisms to a surface. It usually starts within minutes after a surface is in contact with water. Biofouling starts with the formation of biofilms, which include proteins, polysaccharides, both dead and living bacteria encased in extracellular polymeric substances (EPS) [1]. Biofilms may seem harmless, but it actually brings more harm than good affecting parts and systems of various industries. The cost of antifouling equipment for the oil and gas sector alone have been estimated to be USD 960 to 1280 million in the United States during 1982 [2]. To date, this amount could have escalated to billions of dollars. This illustrates the need to implement innovative methods and intensive research on the subject to prevent and mitigate biofouling.

Numerous approaches have been used to tackle biofouling with limited success. One of these approaches involved the use of toxic biocides such as Tributyltin (TBT) which was frequently used due to its high efficacy at deterring biofouling. However, this method has been eliminated and prohibited due to its detrimental effects on the environment [3].

Using copper-nickel alloys for ships and aquamarine structures mitigated biofouling to a degree but were not as effective in freshwater environments [4]. Over an extended period, biofouling may eventually build up anyway. Fortunately, there are also non-toxic alternative coatings used for antifouling applications which are specially grouped and catered around specific performance requirements to provide optimal solutions to clients in the market nowadays. These coatings, often called foul release coatings, include silicone based coatings, hydrogel coatings, thermo-responsive hydrogel coatings and hydrolysis binder coatings. Nevertheless, these coatings sold by companies like Pittsburgh Plate Glass (PPG) Industries are very costly.

Current research to develop new solutions for biofouling control aims to be non-toxic, requires little or no power consumption with small energy footprint, has a long lifecycle and requires low maintenance [5].

Aside from foul-release coatings, another non-toxic antifouling approach is the application of surface topography. Many studies have investigated surface topographies of various shapes and sizes in their efforts to reduce or prevent biofouling. The design, developments and fabrication of such surfaces usually require extensive lab experiments that can be time-consuming and costly.

This led to recent research which applied Computational Fluid Dynamics (CFD) to assess the antifouling characteristics of microwell arrays arranged in a channel that was 1 mm in width and 0.11 mm in height [6]. The application of CFD is still a relatively new approach to understand the antifouling properties of a surface topography. Nonetheless, this approach is advantageous because it permits the analyses of flow characteristics over such surfaces. Such observations would otherwise be challenging to do with lab experiments or field tests.

The goal of this research is to study and assess microtopographies of varied geometries in relation to biofouling control. Larger magnitude of hydrodynamic variations (i.e. wall shear stress, velocity) creates higher hydrodynamic disturbance

towards microorganisms and unwanted surface inhabitants, therefore exhibits better antifouling efficacy for biofouling control [7]. This paper presents results of CFD simulations carried out to compare and analyze hydrodynamic variations over microtopographies that are uniform in size but varied in geometry.

2. Research Methodology

This section presents and explains methods applied to conduct this research. There are a total of three models, each a microtopography array with physical dimensions that are fixed but varied in geometry. The microtopography geometries with fixed sizes were selected to be compared and analyzed.

2.1 3D Topography Geometry Modelling

3D models of patterned surfaces with varied microtopography geometries and fixed sizes were modeled utilizing computer aided design (CAD) software SOLIDWORKS 2015 Student Edition.

Myan et al [7] conclude that microtopography sizes of 64-256 μm significantly reduced cyprids settlements on a submerged surface. It could be argued that 64-256 μm were too small to accommodate cyprids with body widths of 500 μm or larger. Sizes of 64 μm and below, however, promotes biofouling of cyprids, which might be due to its antennal discs (approximately 30 μm) being compatible with the topography size.

It is challenging to simulate dynamic conditions of a field test site especially with the presence of various types of microorganisms in the water. In addition to that, researchers and engineers have yet to determine a fixed optimum microtopography size that exhibits optimum antifouling efficacy. Thus to simplify and make simulations easier for this research, patterned surfaces with microtopography size of 150 μm (approximately average the size of 64-256 μm range) were chosen as a fixed size (constant variable) for all three models. It is again emphasized that the objective of this research places priority on varying the topography geometries.

Fig. 1 below shows the three models with different topography geometries, namely pillars, octagons and squared grooves. All pillars and octagons have a diameter, height and distance apart of 150 μm with a 10 x 20 topography array. Squared grooves have a height, width and distance apart of 150 μm. However, each groove was modeled to have a length of 2.85 mm so that it is equivalent in length when compared to pillar and octagon arrays.

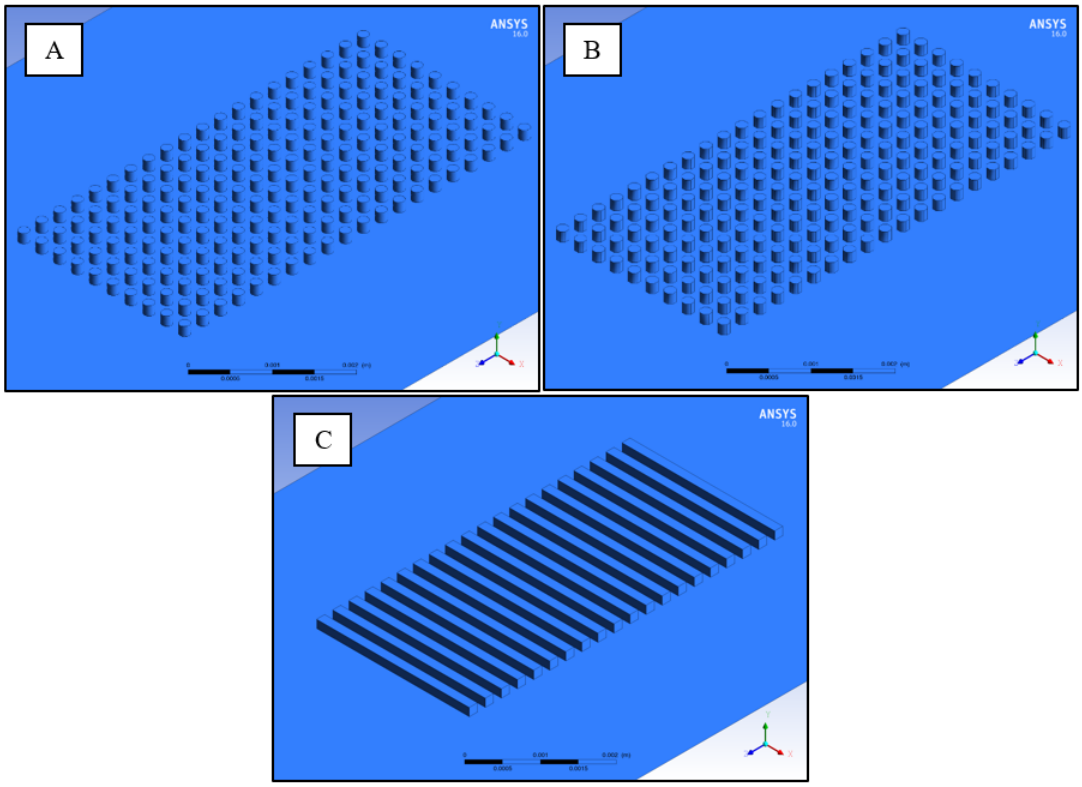


Figure 1. (A) 150 µm pillar model, (B) 150 µm octagon model, (C) 150 µm squared groove model

The three geometries were chosen for this research due to its relation to studies that have been published by Petronis et al. [8] and Won et al. [9]. Their findings act as a good baseline for the author to achieve the objectives of this project. These two published journal articles studied geometries that consisted of pyramids, prisms and V-shaped grooves that are similar to the three chosen models in this research. The author would like to correlate and seek improvements from the chosen models.

2.2 Mesh Convergence Analysis

The 3D models were meshed with ANSYS Meshing. Fig. 2 below shows an example of the fluid domain model that is 8 mm in width and height, with a length of 80 mm. This fluid domain will be fixed in size for all three models.

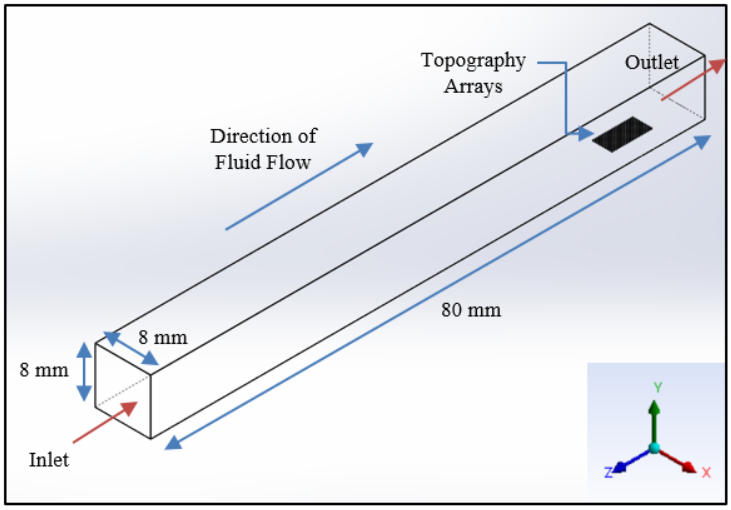


Figure 2. 3D model of 150 µm pillar fluid domain with dimensions and topography placement

According to Hagen-Poiseuille's Flow law, pressure drop will occur when an incompressible fluid flows through a channel with constant cross-section and a length longer than its diameter. Likewise, steady and laminar flow will be induced within such channel. Thus to ensure that the flow in this study is steady, laminar flow is fully induced and a good velocity profile is achieved, the length of the channel is thus set at 80 mm for the channel to be long enough to avoid velocity interference at the inlet [10].

Fig. 3 below presents an example of a fully meshed fluid domain model and a zoomed-in topography array of 150 µm pillars with refined meshes. All three models were meshed with tetrahedral elements.

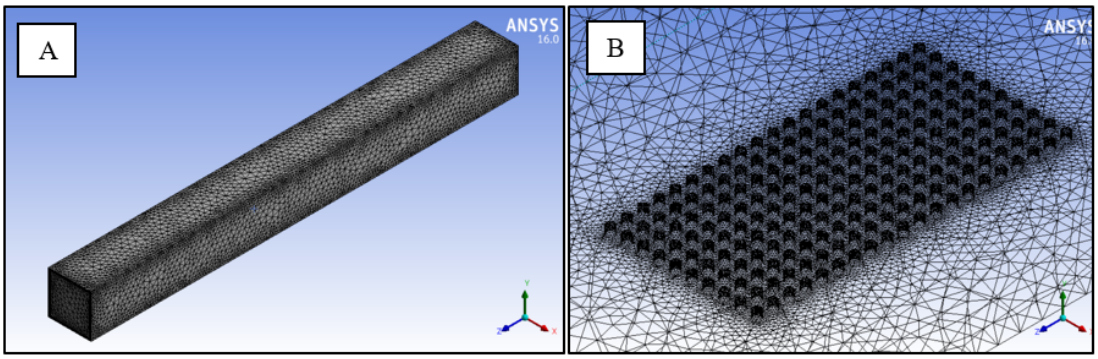


Figure 3. (A) Fully meshed 150 µm pillar fluid domain model, (B) Refined meshes of 150 µm pillar topography array

For every model, a mesh convergence analysis was performed to optimize the number of mesh elements. This method reduces computational time for simulations while maintaining the quality of the results. A study done by Halder et al. [11] refined mesh elements in consecutive models and performed respective simulations for each mesh refinements. Mesh convergence was considered satisfied when the difference of wall shear stress between each mesh refinements was less than 5%. The model with the least mesh elements and with a relative error percentage of less than 5% will then be

chosen as the optimum model. Table 1 below presents the results of mesh convergence analysis for the three models.

Table 1. Mesh convergence analysis result for three models

3D Model	Number Of Elements	Relative Error (%)	Optimum Number of Elements
Pillars	924,118 → 1,200,500	4.5	924,118
	1,200,500 → 1,840,829	3.7	
Octagons	316,799 → 445,993	12.9	445,993
	445,993 → 1,147,121	4.9	
Squared Grooves	254,743 → 429,454	8.6	429,454
	429,454 → 1,006,071	3.5	

2.3 CFD Fluent

All three models with the optimum number of meshed elements were then exported to the CFD software ANSYS Fluent. The flow model used in ANSYS Fluent is the standard k-omega turbulence model. This is because the k-omega model is a suitable model for low Reynolds number flow and transitional flow scenarios. The quantitative variables that the author is interested from the simulations include wall shear stress and velocity. Since the k-omega model is commonly used for shear-driven flows, this turbulence model is suitable for the purpose of this research.

Cell zone conditions with liquid water (H_2O) as material was used as the main fluid inside the model. No-slip boundary conditions were fixed on all four walls of the fluid domain, specifically the top, bottom, and the side walls. The boundary condition for inlet was applied with mass flow rate of 0.001 kg/s, which was reasonably proportioned in relation to Halder's study [11] where inlet flow rate was set at 0.000001 kg/s for a fluid domain of 1 mm width and 0.11 mm height. Fig. 4 shows the side view of the fluid domain model with its respective boundary conditions.

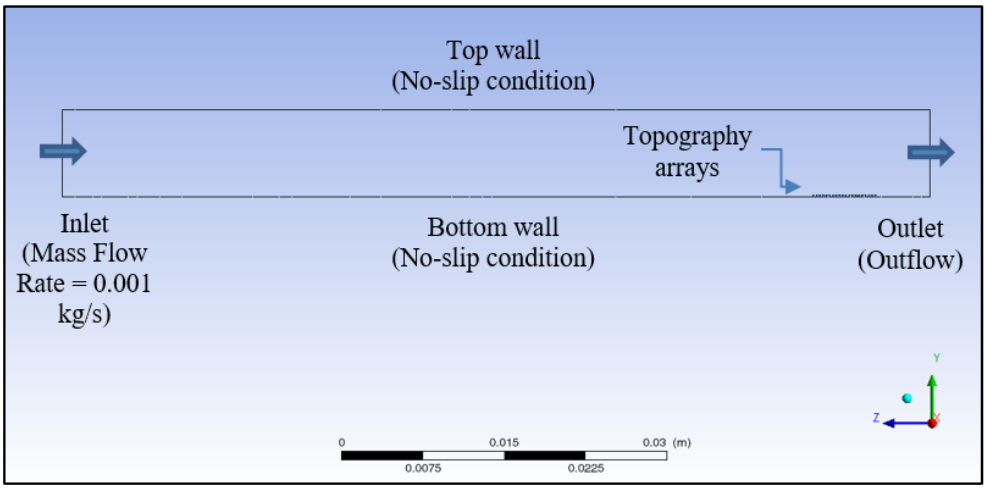


Figure 4. Side view of fluid domain with boundary conditions of inlet, outlet, top and bottom wall

3. Results and Discussions

An optimum topography geometry exhibits the largest magnitude of hydrodynamic variations. The greater the magnitude of the variables, the more "volatile" the flow is in a particular region. In another context, the higher the hydrodynamic disturbance towards microorganisms and unwanted surface inhabitants, therefore exhibit better antifouling efficacy for biofouling control.

The hydrodynamic variables that were analyzed in this study were velocity and wall shear stress. Velocity streamlines represent how fluid flows inside the channel over the arrays of topography geometries whereas wall shear stress exhibits the shear stress induced by solid boundaries of the patterned surfaces.

Fig. 5 below shows an illustration of how velocity was measured for the pillar topography model. Average velocities were measured at the peaks of the topography arrays (red line) and at 30 µm above the base of the wall surface (blue line). Average velocities were also measured at similar positions for the remaining two topographies: octagons and squared grooves.

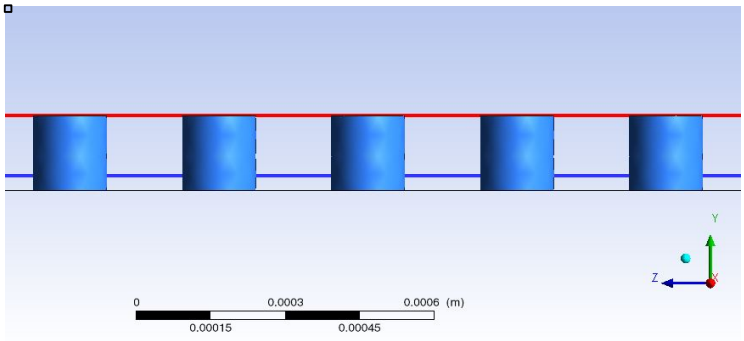


Figure 5. Side view of pillar topography with red and blue lines where average velocity was measured

Fig. 6 below depicts an illustration of how wall shear stress was measured for the pillar topography model. Average wall shear stresses were measured at the peaks of the topography arrays (red line) and at the base of the wall surface (orange line). Average wall shear stresses were also measured at exact positions for the other topographies.

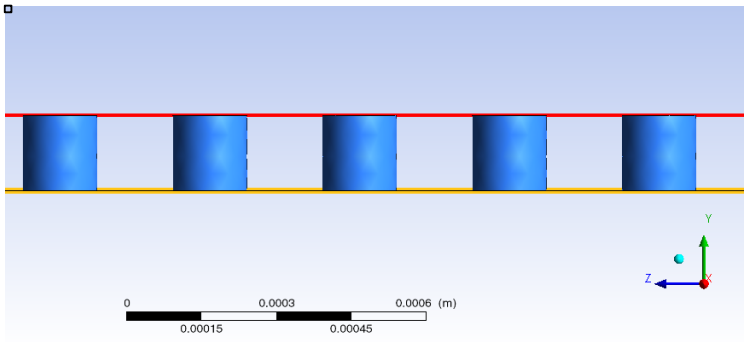


Figure 6. Side view of pillar topography with red and orange lines where average wall shear stress was measured

The positions were chosen at the peaks and base to calculate average wall shear stress because these are the positions that are experiencing the highest and the lowest shear stresses respectively. The average values for velocity and wall shear stress were calculated and compared between the various topography geometries.

3.1. Velocity

3.1.1 Pillar Topography

Fig. 7 below shows the velocity streamline of fluid flow over pillar topography.

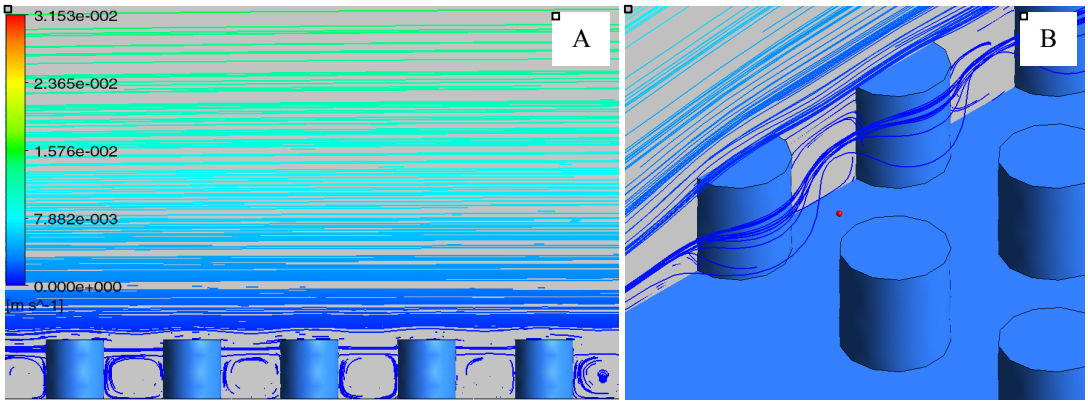


Figure 7: Velocity streamline with fluid flow from left to right at (A) side view and (B) isometric view

Streamlines show that fluid flow is uniformly distributed across the channel. The nearer the streamlines were to the base of the wall surface, the lower the velocity of the fluid flow until it reaches 0 m/s. This is because no-slip boundary condition has been applied at bottom wall surface. Vortices can be seen at all gaps between the pillars. Average velocities at the peaks of the pillars and at the height of 30 µm above the base are 2.322×10^{-4} m/s and 8.76×10^{-6} m/s respectively.

Fig. 7(B) depicts how fluid flows over the side wall surface of the pillars. This change in flow direction reduces the velocity of fluid. Fluid flow at the peaks of the pillars will then create a slipping force over fluid that is in the vicinity of the gaps between pillars [12]. Slip forces promote the formation of vortices, which will encourage the formation of biofouling since the velocities of vortices are at its minimum level. Besides, vortices also carry biofouling organisms from the flow stream to accumulate in the gaps. Microorganisms and biofouling materials will tend to accumulate and settle at areas with lower fluid flow velocity.

3.1.2 Octagonal Topography

Fig. 8 below shows the velocity streamline of fluid flow over octagonal topography.

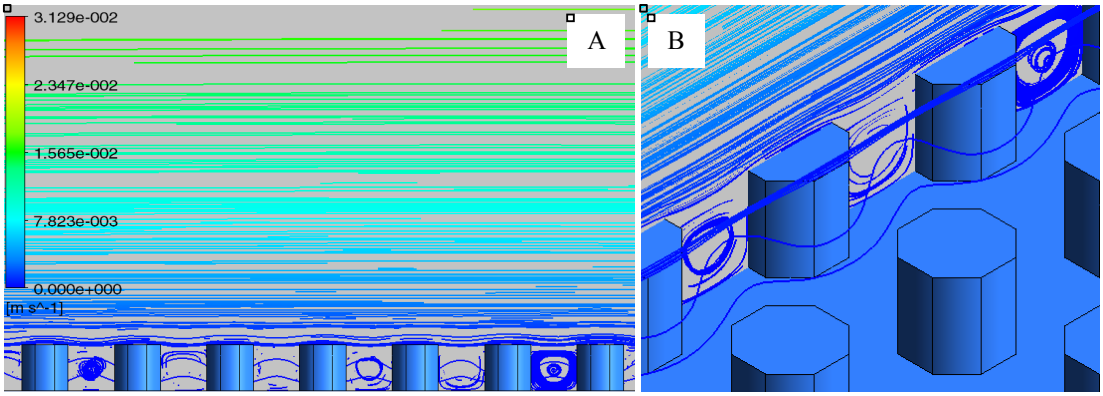


Figure 8: Velocity streamline with fluid flow from left to right at (A) side view and (B) isometric view

Streamlines show that fluid flow is uniformly distributed. The nearer the streamlines were to the base of the wall surface, the lower the velocity of the fluid flow due to no-slip boundary condition applied at bottom wall surface. There were more vortices in the gaps between the octagons as compared to pillar topography. Average velocities at the peak of the octagons and at the height of 30 µm above the base are 2.03×10^{-4} m/s and 8.69×10^{-6} m/s respectively.

Fig. 8(B) shows how fluid flows over the side wall surface of the octagons. This change in flow direction reduces velocity of fluid. Comparing to pillar topography, it can be seen that the change in flow direction at the side walls of octagons is much lesser despite having more vortices in between the gaps.

3.1.3 Squared Grooves Topography

Fig. 9 below shows the velocity streamline of fluid flow over squared grooves topography.

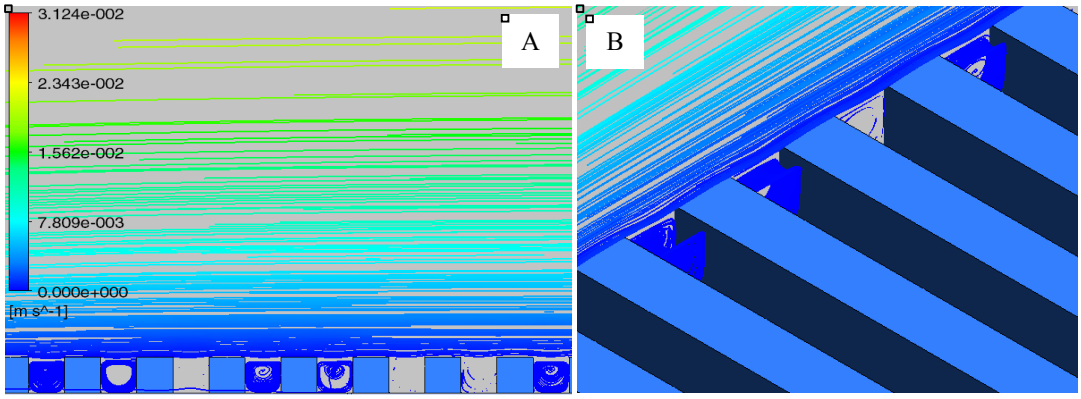


Figure 9: Velocity streamline with fluid flow from left to right at (A) side view and (B) isometric view

Fluid flow above the grooves was distributed uniformly and velocity decreases as the height from the base decreases. The nearer the streamlines were to the base of the wall surface, the lower the velocity of the fluid flow due to no-slip condition. Vortices can be seen in between gaps of the grooves. The magnitude of vortices

increased significantly as compared to the pillar and octagonal topographies. Average velocities at the peak of the squared grooves and at the height of 30 µm above the base are 1.39×10^{-4} m/s and 7.28×10^{-6} m/s respectively.

3.1.4 Average Velocity Analysis

Fig. 10 below summarizes the average velocity at the peaks and at 30 µm above the base surface of all topographies.

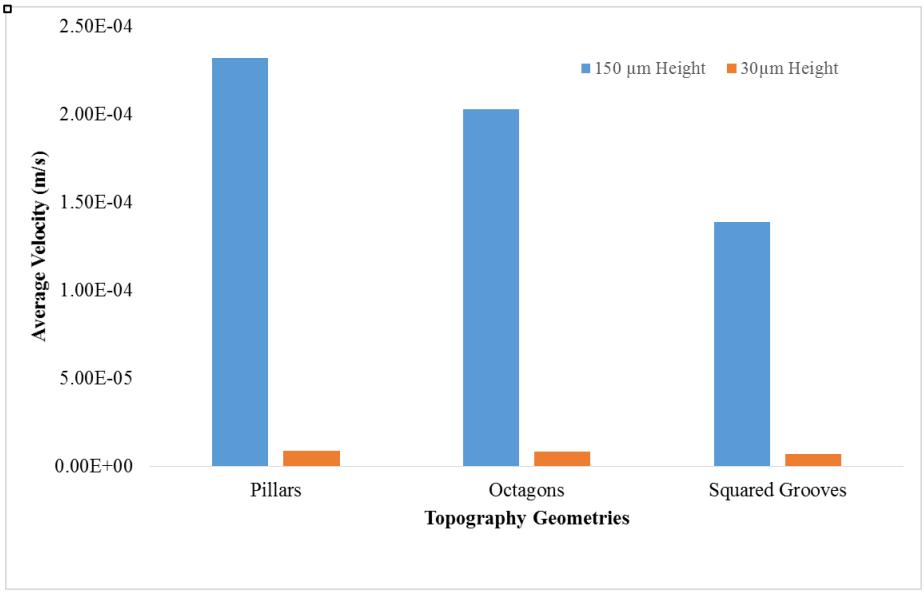


Figure 10: Average velocities at 150 µm peaks and 30 µm above base surface for all three topography geometries

Fig. 10 shows a histogram of average velocities over two separate heights of three different topography geometries. It can be seen that pillars have the highest average velocities for both heights, followed by octagons and lastly squared grooves. Average velocities at 150 µm height decrease significantly from pillars to octagons and squared grooves. Unlike the peaks, average velocities at 30 µm heights only experience slight difference when comparing all 3 topographies.

For all topography geometries, the average velocity at 150 µm height is at least 19 times greater of that at 30 µm height. This is because topography geometries act as a hurdle towards fluid flow which significantly reduces flow velocities. The nearer the distance towards the base, the lower the fluid velocity until it reaches 0 m/s at base Y=0.

From Fig. 10, it can be assumed that pillars exhibit the best antifouling efficacy among all topography geometries. This is because average velocity at both 150 µm and 30 µm height above the base is the highest compared to octagons and grooves. It can also be seen that the amount of vortices in the gaps between pillars from Fig.7 is the lowest amongst the topographies. It is not conducive for microorganisms or biofouling materials to settle at areas with high velocities and small amount of vortices.

3.2 Wall Shear Stress

3.2.1 Pillar Topography

Fig. 11 below shows the contour plot of wall shear stress exerted on pillar topography in isometric view.

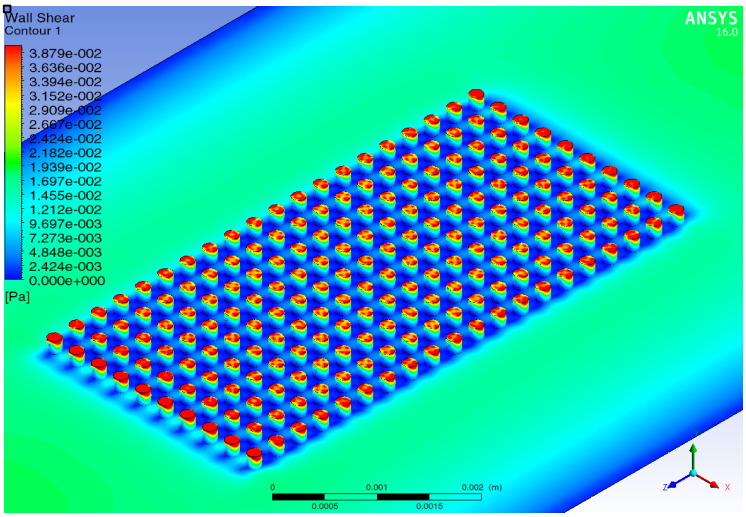


Figure 11: Wall shear stress contour plot over pillar topography in isometric view

Fig. 11 shows that the higher wall shear stresses are condensed at the peaks of the pillar topography. Wall shear stresses are at its lowest near the base of the topography, especially in gaps between the pillars. The average wall shear stresses at the peaks and at the base of the topography is 3.33×10^{-2} Pa and 7.86×10^{-4} Pa respectively.

3.2.2 Octagonal Topography

Fig. 12 below shows the contour plot of wall shear stress exerted on octagonal topography in isometric view.

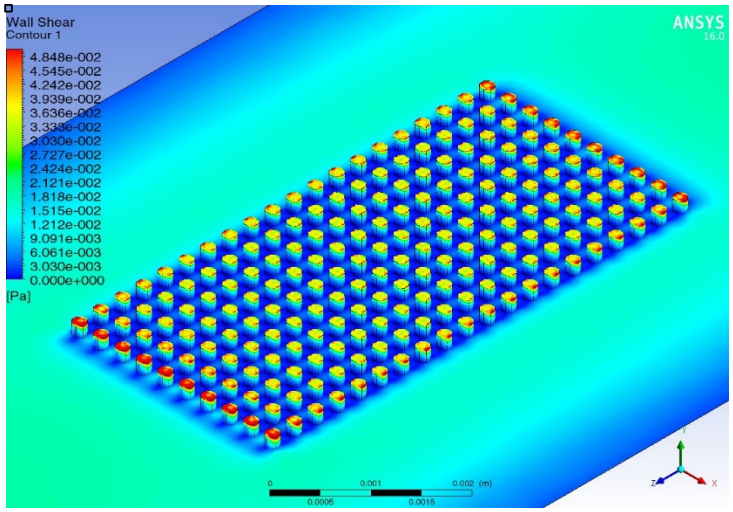


Figure 12: Wall shear stress contour plot over octagonal topography in isometric view

The contour plot in Fig. 12 shows that the higher wall shear stresses are concentrated at the peaks of the octagonal topography. Wall shear stresses are at its lowest near the base of the topography and in the gaps between octagons. The average wall shear stresses at the peaks and at the base of the topography is 3.23×10^{-2} Pa and 5.76×10^{-4} Pa respectively.

3.2.3 Squared Grooves Topography

Fig. 13 depicts the contour plot of wall shear stress exerted on squared grooves topography in isometric view.

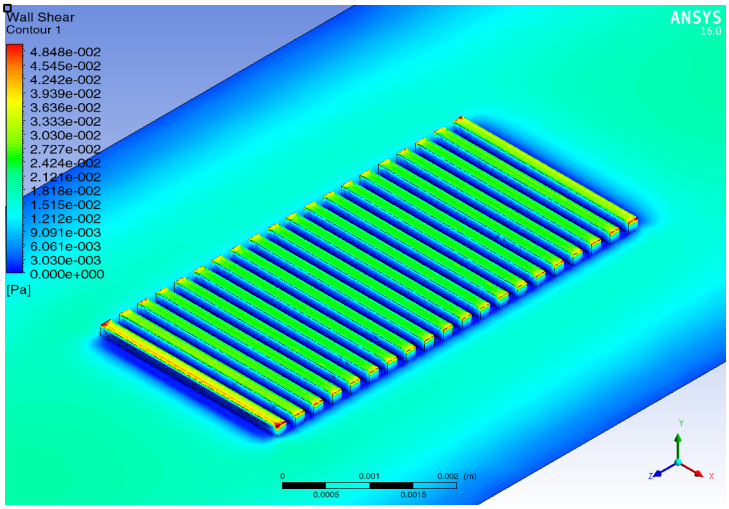


Figure 13: Wall shear stress contour plot over squared grooves topography in isometric view

Fig. 13 shows that the higher wall shear stresses are focused at the peaks of the squared grooves topography, specifically at the edges of the grooves. Wall shear stresses are at its lowest near the base of the topography, especially in gaps between the grooves. The average wall shear stresses at the peaks and at the base of the topography is 2.31×10^{-2} Pa and 3.26×10^{-4} Pa respectively.

3.2.4 Average Wall Shear Stress Analysis

Fig. 14 below summarizes the average wall shear stress at the peaks and base of all topographies.

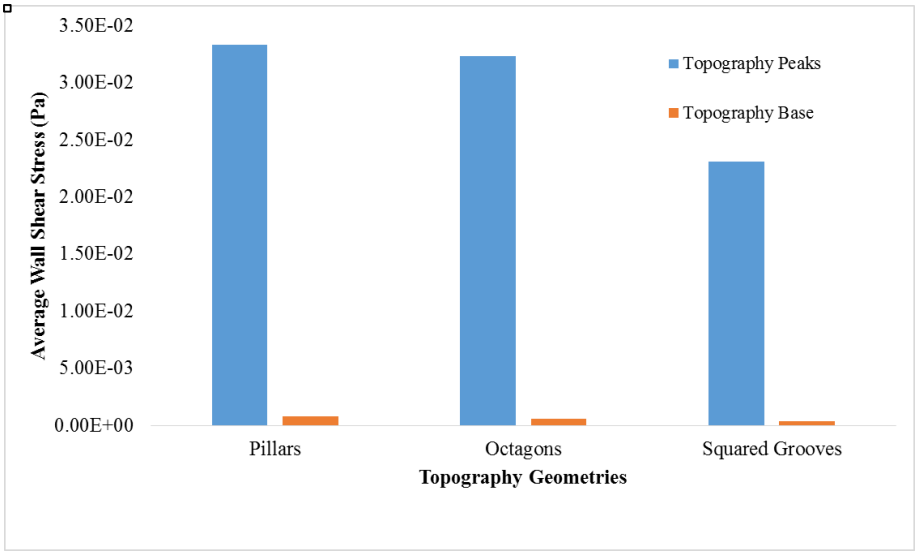


Figure 14: Average wall shear stresses at peaks and base for all three topography geometries

Fig. 14 shows a histogram of average wall shear stresses over two separate heights of three different topography geometries. It can be seen that pillars have the highest average wall shear stress for both peaks and base, followed by octagons and then squared grooves. Average wall shear stress at peaks decreases slightly from pillars to octagons and then decreases greatly for squared grooves. Unlike the peaks, average wall shear stresses at all three topography bases only experience slight differences.

For all topography geometries, the average wall shear stresses at the peaks are at least 42 times greater of that at the base. This is because fluid flows through the peaks at a higher velocity with potentially larger contact area, thus creating higher shear stresses compared to the base and the gaps between topography geometries.

From Fig. 14, it can be assumed that pillars exhibit the best antifouling efficacy among all topography geometries. This is because average wall shear stresses at both its peaks and base are the highest compared to octagons and grooves. According to Myan et al. [7], the higher the wall shear stresses, the higher the resistance of that topography towards fouling of microorganisms. The results obtained from this section further back and support the conclusion attained from section 3.1.4 where pillar topography was also assumed to exhibit the best antifouling performance amongst all topography geometries studied.

4. Conclusions

Microtopographies of varied geometries and fixed sizes were assessed numerically in relation to biofouling control. Larger magnitude of hydrodynamic variations creates higher hydrodynamic disturbance towards microorganisms and unwanted surface inhabitants, therefore exhibits better antifouling efficacy for biofouling control.

Based on the comparisons of velocity and wall shear stress of three different topography geometries, it was found that pillars displayed the largest magnitude of both said variables. It was also found that topography peaks, regardless of topography geometries, make better defensive stances against fouling due to its higher hydrodynamic changes. On the other hand, it can be concluded that topography base regions promote fouling activities due to lower hydrodynamic variations.

For future improvements, topographies can be designed with smaller gaps between geometries to minimize the potential areas for biofouling. Furthermore, designs can also consider smaller scaled geometries (nanotopographies) that promote higher hydrodynamic variations around the vicinity of the topography.

Acknowledgment

The author would like to extend his utmost gratitude to Dr. Felicia Wong Yen Myan for her continuous support and encouragements throughout the duration of this study.

References

[1] J. M. Willey, L. M. Sherwood, and C. J. Woolverton, *Prescott, Harley, Klein's Microbiology*, 7th ed. New York: Colin Wheatley/Janice Roerig-Blong, 2008.

[2] H. M. Steinhagen, *Heat exchanger fouling: mitigation and cleaning technique*. Rugby: Institution of Chemical Engineers, 2000.

[3] L. D. Chambers, K. R. Stokes, F. C. Walsh, and R. J. K. Wood, "Modern approaches to marine antifouling coatings," *Surf. Coatings Technol.*, vol. 201, no. 6, pp. 3642–3652, 2006.

[4] C. Development Association, "Copper-nickel alloys, properties and applications," CDA Publication, 1982.

[5] P. J. Earley, B. L. Swope, K. Barbeau, R. Bundy, J. A. McDonald, and I. Rivera-Duarte, "Life cycle contributions of copper from vessel painting and maintenance activities," *Biofouling*, vol. 30, no. 1, pp. 51–68, Jan. 2014.

[6] P. Halder *et al.*, "An assessment of the dynamic stability of microorganisms on patterned surfaces in relation to biofouling control.," *Biofouling*, vol. 30, no. 6, pp. 695–707, 2014.

[7] F. W. Y. Myan, J. Walker, and O. Paramor, "The interaction of marine fouling organisms with topography of varied scale and geometry: a review.," *Biointerphases*, vol. 8, no. 1, p. 27, 2013.

[8] Š. Petronis, K. Berntsson, J. Gold, and P. Gatenholm, "Design and microstructuring of PDMS surfaces for improved marine biofouling resistance," *J. Biomater. Sci. Polym. Ed.*, vol. 11, no. 10, pp. 1051–1072, Jan. 2000.

[9] Y.-J. Won *et al.*, "Correlation of membrane fouling with topography of patterned membranes for water treatment," *J. Memb. Sci.*, vol. 498, pp. 14–19, 2016.

[10] N. A. Mortensen, F. Okkels, and H. Bruus, “Reexamination of Hagen-Poiseuille flow: Shape dependence of the hydraulic resistance in microchannels,” *Phys. Rev. E*, vol. 71, no. 5, p. 57301, May 2005.

[11] P. Halder *et al.*, “A novel approach to determine the efficacy of patterned surfaces for biofouling control in relation to its microfluidic environment,” *Biofouling*, vol. 29, no. April 2016, pp. 697–713, 2013.

[12] E. Friedmann, J. Portl, and T. Richter, “A Study of Shark Skin and Its Drag Reducing Mechanism,” in *Advances in Mathematical Fluid Mechanics*, Berlin, Heidelberg: Springer Berlin Heidelberg, 2009, pp. 271–285.

eureca 2017 – Conference Paper
Paper Number 2ME10

Energy Harvesting of Air Conditioning Outdoor Unit

Lee Kian Leng*, Wincent Lie, G. A. Mahdiraji
School Of Engineering, Taylor's University, 47500 Subang Jaya, Selangor, Malaysia

** kianleng8@gmail.com*

Abstract
This study aims to determine whether thermoelectric generators (TEG) and piezoelectric generators would be able to harvest enough energy from the air conditioning (AC) outdoor unit to light up a light bulb. The test is first done by testing one under different conditions to determine the best mode of operation such as with or without heat paste and whether the combination of heat paste and heat sink is better. Three and five TEGs are then connected in series to determine whether there is any scaling of power with the increased number of TEG(s). This would allow us to determine the number of TEG actually needed to generate more power for future applications. Five TEGs are placed on a perspec board such as way that only the heat sink of the TEG is exposed to the hot air from the outdoor unit. The TEG would have heat sink attached to both side to ensure one side would absorb heat efficiently whereas the other side would dissipate heat easily. The maximum temperature difference have been achieved in this study was 2.87°C which results in an average power of around 116.89 μW. On the other hand, five piezoelectric have been connected in series and tested to see the significance of energy that can be harvested from the AC vibration. The results show that the amount of power generated by five piezoelectrics are about nano-Watt, which is relatively lower than what TEGs generated.

Keywords**:** Thermoelectric Generator, Piezoelectric, Air conditioning system, Energy harvesting, Wasted heat and vibration.

1.0 Introduction

One very unique energy that had been discovered by Thomas Johann Seebeck in 1821 is the conversion of heat energy to electrical energy through the Seebeck effect. The Seebeck effect states that when the joints have a temperature difference, electricity would be produced due to how electron in each materials shifted differently [1]. The discovery of Seebeck effect created thermoelectric generator (TEG) which operates using the Seebeck effect.

We know that energy cannot be created nor destroyed, they can only change from one form to another. As we operate our machineries, factories and cars, we convert energies from one form to another. Through these conversion, we also have loss of energy in the form of heat and sometimes vibration. These energies are wasted as they are dissipated to the surrounding. TEGs and piezoelectric generators could be added to these situations to convert the wasted heat and vibration into usable electricity. One such machinery that we use on a daily basis consist of losses from both heat and vibration and that is the outdoor unit of our air conditioning (AC) system.

The AC unit consist of 4 components called evaporator, compressor, condenser and expansion valve [2]. The usual household installs the split AC unit where the evaporator and the expansion valve are located on the inside of the house whereas the compressor and condenser is located on the outdoor unit. Since the compressor's function is to compress the refrigerant to raise its temperature and pressure and this refrigerant exits the compressor as hot, high-pressure gas, most of the heat generated and heat loss would be located there. The fan is located in the outdoor unit as well hence most of the vibration from the mechanical movement is again located in the outdoor unit. Chow et al. (2002) had shown that the exhaust of the outdoor unit is the hottest point of the outdoor unit [3].

This raises the question on whether the heat and vibration wasted in air conditioning system would generate enough usable electricity to be used in lighting system. There is also a need to determine whether vibration or heat waste alone would be sufficient to support the lighting system. The module cost is also needed to be taken into consideration and compared with the energy saved in order to justify whether it was economically feasible. This in turn requires research on the most optimal condition and location on the air conditioning unit to gather the most heat and vibration possible for power generation.

The main objective of this study is to develop a hybrid system for harvesting electrical energy from the waste heat and vibration of an air conditioning system. The data collected from the hybrid and stand-alone devices would also be analysed to determine the best method for energy generation. The energy generated would then be used to compare with the system cost to determine whether it would be economically feasible when energy is harvested from the outdoor air conditioning system.

2. Research Methodology

This section explains the method and procedure of the experiments along with providing justifications for each task used in the study. The framework of the experiment is adopted from [4]. The flowchart of the project can be seen in Figure 1.

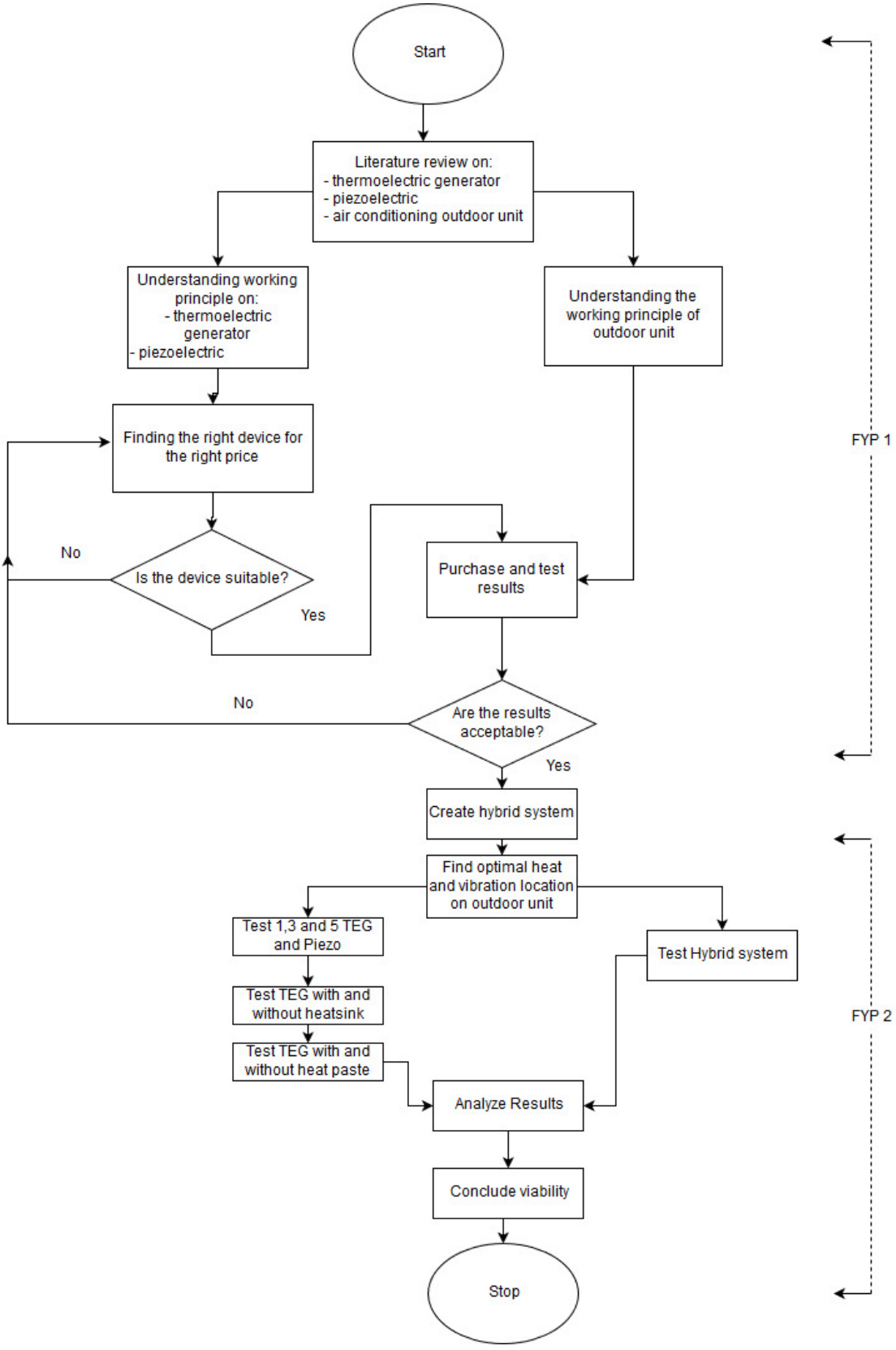


Figure 1. Flowchart of the project

The TEG is tested on the outdoor unit for the air conditioning system. This is to investigate the amount of power generated would justify the feasibility of TEG used on

the outdoor unit. The initial test for the TEG was to determine the optimal condition of the TEG. Figure 2 shows the TEG used with heat sink.

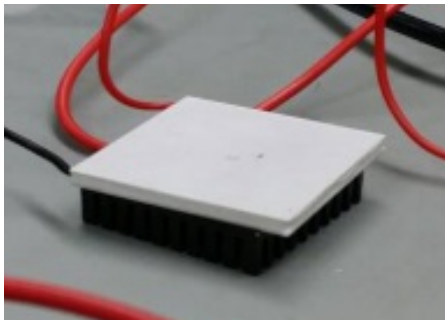


Figure 2. TEG with heat sink

The TEG is first used on top of the air conditioning outdoor unit to determine the amount of power that could be generated. A heat sink is then added to the TEG in order to cool one side of the TEG to create a larger temperature difference. Since the power generated is dependent on the temperature difference, heat paste and heat sink is used in an effort to create a larger temperature difference by cooling one side. The heat sink is later added with heat paste to allow better heat conduction. The heat paste is also placed between the contact surface (top of the outdoor unit) and the TEG to allow better heat conduction which would heat one side more.

The next step was to test 5 TEGs together to determine whether it would produce sufficient power to achieve the goal of lighting the light bulb. The TEG is connected in series to generate a larger voltage whereas the current would remain the same. Research has been done as seen in Figure 3 that shows the hottest region of the outdoor unit.

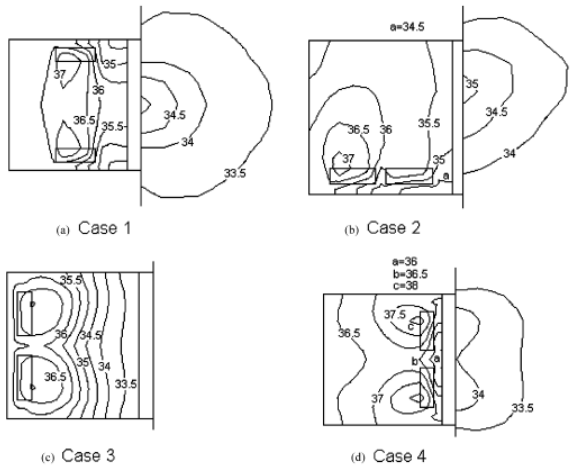


Figure 3. Hottest region on outdoor unit [3]

The research done by Chow[3] on the region that dissipates the most heat on the outdoor unit can be seen in Figure 3. The image shows that the most heat comes from the exhaust of the outdoor unit. It also shows that the most heat was generated from close proximity of the outdoor unit and slowly becomes cooler as it moves away from the outdoor unit. This information was used when conducting the experiment on TEG in order to harvest the most power from the outdoor unit.

Since the hottest region of the outdoor unit is seen to be the exhaust, a perspec board is used to prevent too much heat conduction which would heat up the TEG quickly. The TEG has heat sink attached onto it on each side with heat paste in between, which would allow better heat conduction at the side that is exposed to the exhaust and cooling for the other side as adopted from [4]. A fixture with perspec material is developed to hold five TEGs such a way that one side of the TEG can be exposed to the heat whereas the other side is shielded from it as shown in Figure 4. After the TEGs fixed in the holder, it is placed in front of the air conditioning exhaust hot air and tilted to a certain angle to ensure that most of the exhaust air flow from one side of the TEGs and directed to upward and not flow to the other side of the TEG, while the cold side of TEG is facing the ceramic tiles which is cooler in temperature.

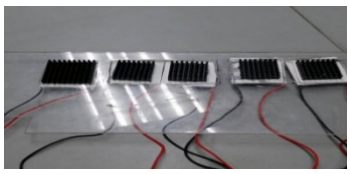


Figure 4: Fixture developed to hold five TEGs

Figure 5 shows experimental set up for current and voltage measurements. In this measurement, a 1Ω resistor is used to enable the current measurement using an ammeter connected in series. The voltmeter however, is connected parallel to the load, 1Ω resistor, or otherwise directly connected to the output of individual TEG. The current and voltage of the load are recorded every 5 minutes for a duration of 1 hour to make sure the stability of the power generation. An optical temperature sensor is used to determine the temperature difference in the hot and cold side of the TEGs.

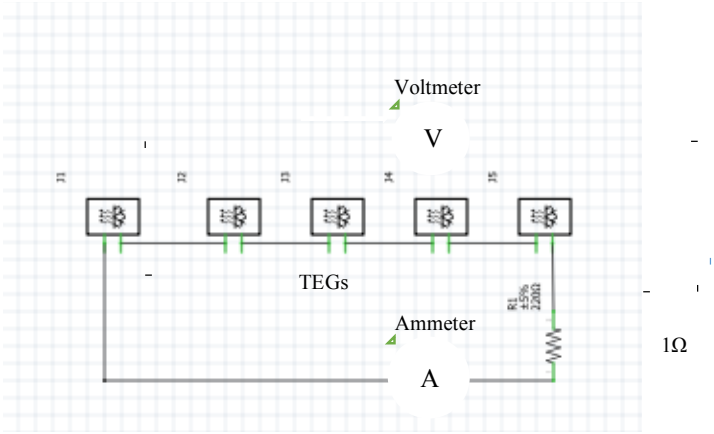


Figure 5: Schematic Diagram of Experimental Set up

Similar current and voltage measurement set up shown in Figure 5 is used for piezoelectric too. The piezoelectric is placed on top of the outdoor unit as we require the vibration to generate the power. 100 g weights are placed on top of each piezoelectric as seen in Figure 6 to ensure the piezoelectric does not move about too much which would disrupt the data collection. Duration of data collection along with the intervals are the same with TEG.



Figure 6: Experimental setup of piezoelectric generator

3. Results and Discussion

3.1 Results

The initial test on the TEG on the outdoor unit without any heat sink or heat paste produces an average power of 5.83 µW. When a heat sink is applied onto the TEG with heat paste in between, the average power produced is increased to 8.04 µW. The result suggested having heat sink connected to TEG with heat paste in between would be more optimized for generating higher electricity.

Figure 7 shows the graph obtained from the experiment of testing 5 TEGs. The maximum output of the power obtained is 116.89 µW with a temperature difference of 2.87˚C and the smallest output power is 66.54 µW with a temperature difference of 1.73˚C. The general trend from the graph shows that when there is a larger temperature difference, more power would be generated.

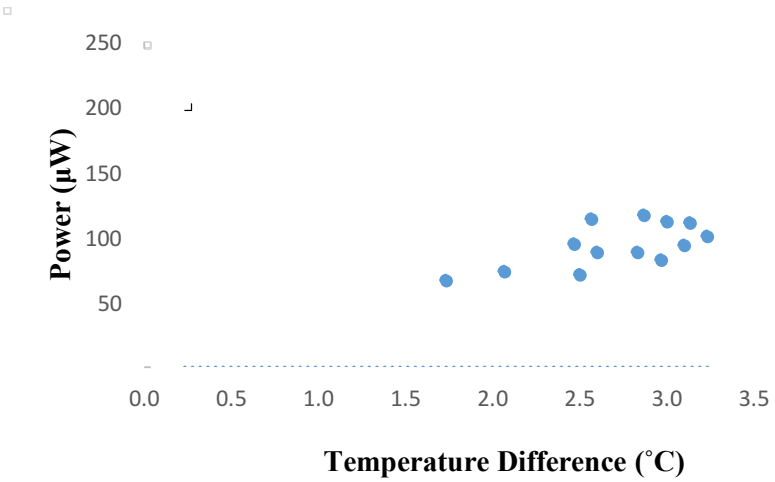


Figure 7. The graph of power output against temperature difference for 5 TEGs

Further testing is done on TEGs by using a combination of 3 TEGs and 1 TEG. The results obtained are used to be compared with 5 TEGs as shown in Figure 9. The results show an exponential scaling as seen in Figure 8.

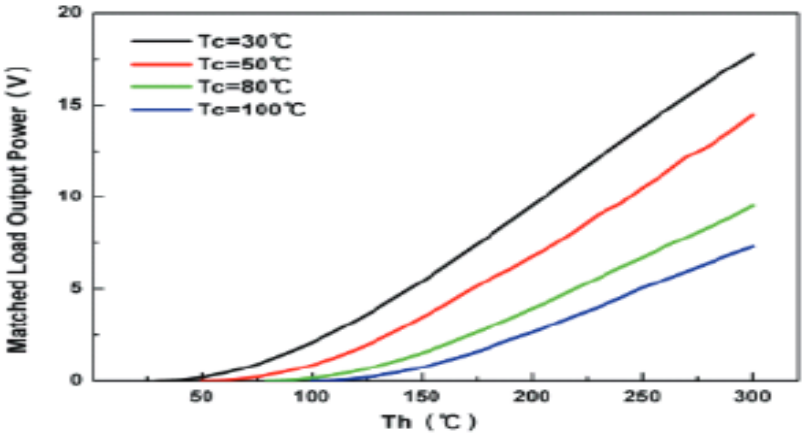


Figure 8. Datasheet of TEG [5]

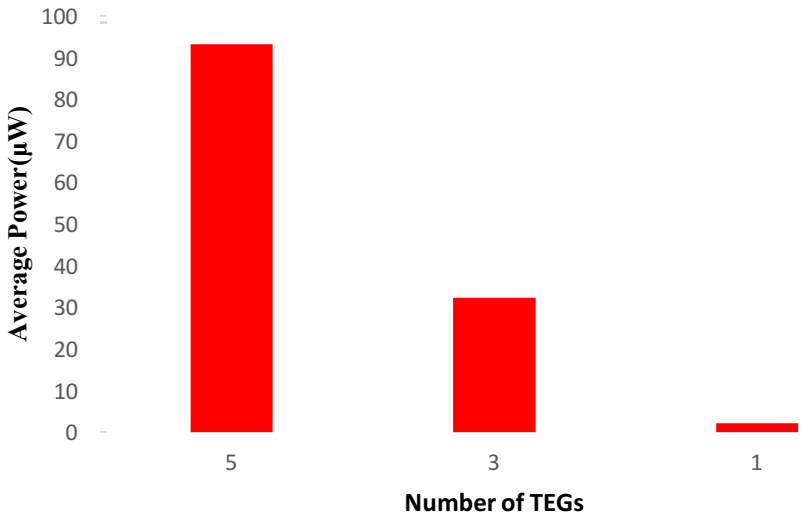


Figure 9: Comparison on average power based on the number of TEG

The study is extended to investigate electricity generation when the temperature difference between two sides of a TEG is increased. In this experiment, 5 TEGs are subjected to high temperature using a stove. In this set up, the temperature difference has been increased up to 18.57˚C, which could result in thermal electric generation of 2873.15μW. The lowest power output observed is 82.41μW with a temperature difference of 2.83˚C. Figure 10 shows the comparison between the power output obtained from stove compared with the outdoor unit. The graph shows a clear indication that the power output produced from the stove is significantly larger than the power output of outdoor unit. The heat from stove also has a steeper gradient which indicates that the power output increases greater when temperature difference is higher. This is well agreed with the graphs shown in Figure 8 that the rate of thermal energy generation exponentially increased with temperature.

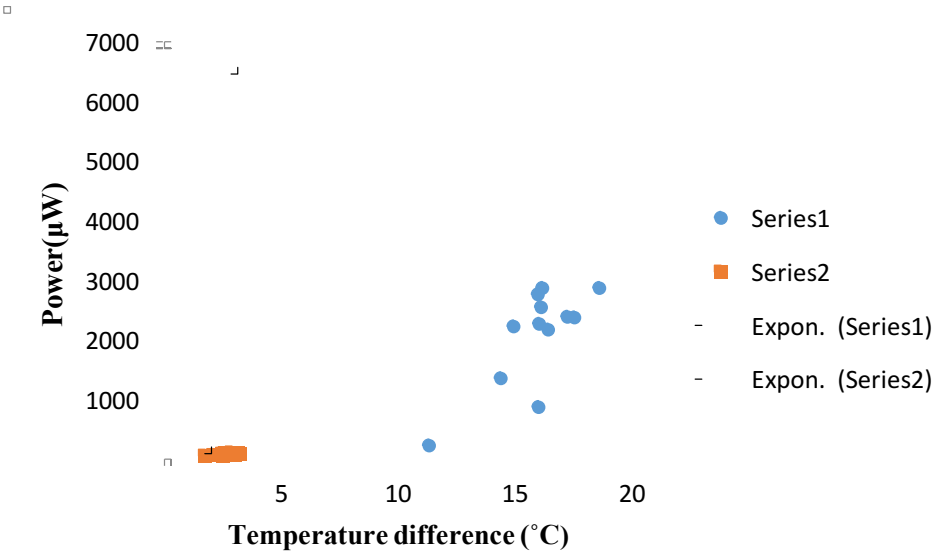


Figure 10. Comparison of power output between Series 1(Heat from stove) and Series 2 (Heat from Outdoor Unit) against temperature difference.

The power output from five piezoelectric connected in series is recorded with an average power of 19.94 mV for the first set, 19.23 mV for the second set and 16.68 mV for the third set with a very low current of around micro-ampere.
A hybrid system was also experimentally developed and tested in this study. However, due to very low power generation from the piezoelectric, a hybrid system was not economical in terms of efficiency in electric generation. \

3.2 Discussion

The results obtained through changing the location of the application of heat paste have shown that the presence of heat paste would boost the power output. This is due to the heat paste allowing better heat conduction which can either be used to conduct heat to the TEG or remove the heat from the TEG via heat sink. When five TEGs are combined together, the highest power generated was 116.89 μW with the temperature difference of 2.87˚C. Even at the highest power output, five TEGs are proven to be insufficient in lighting one LED. Through calculations, it can be seen that about 2700 number of TEGs needed to power up one 65 mW LED [6] purely from the outdoor unit. Besides, the cost of TEG, which would be around RM 2,700 for RM 1 per TEGs, 2,700 TEG required lots of space.

These analysis shows that using TEG for harvesting waste heat from air conditioning is not economical and practically feasible. The positive side of the findings would be the power produced scales greatly with an increase in the temperature difference. As seen in Figure 7 and 8, greater temperature difference would generate a much larger power output since the graph scales exponentially.

The TEG proves to be more effective where there is a larger temperature difference which in turn produced a power output of 2,873.15 μW at a temperature difference of 18.57˚C. This finding proves that TEG is more suitable for situations

where the temperature difference on the TEG plates is higher. Considering this amount of power generated by five TEGs, a 65 mW LED can be turned on by about 23 TEGs. The power generated per TEG is expected to be increased by further optimizing the system towards higher temperature difference.

The temperature difference has shown to play a very significant role in the production of power in TEG. Aside from that, Figure 7 shows that with higher temperature, the power generated scales better compared to the low temperature situations. Comparing the measurements performed on air conditioning with the one on stove, the temperature difference increased by about 9 times, however, the power generated is increased by about 25 times.

On the other hand, the power generated by piezoelectric is shown to be very low and fluctuates rapidly. Refer to literature, piezoelectric can generate in the range of micro-Watt [7] with extremely low current of nano-Ampere [8].

4. Conclusions

The average power generated from five TEGs at a temperature difference of around 2°C is 93.12 μW when using the air conditioning outdoor unit. This power is increased by about 25 times when the temperature difference on the TEG plates are increased by 9 times. This result shows that TEG is highly dependent on temperature difference and its efficiency can be increased significantly at higher temperature difference. Through preliminary observations, it can be concluded that by producing about 18 °C temperature difference on the TEG plates, a thermal electricity up to around 0.6 mW can be generated per TEG. This initial observation suggests feasibility of using TEGs in harvesting waste heat where such temperature difference can be produced. Temperature difference on TEG plates can be increased further by optimizing the TEG position around the heat source and introducing insulator to reduce the heat transfer from the heat source to the other plate of TEG (i.e., cold plate).

Acknowledgement

The authors would like to acknowledge School of Engineering, Taylor's University for financially supporting this project.

References

[1] S. B. Riffat and X. Ma, "Thermoelectrics: A review of present and potential applications," *Appl. Therm. Eng.*, vol. 23, no. 8, pp. 913–935, 2003.

[2] "How Does An Air Conditioner Work?," 2016. [Online]. Available: http://www.energyquest.ca.gov/how_it_works/air_conditioner.html. [Accessed: 20-Nov-2016].

[3] T. T. Chow, Z. Lin, and J. P. Liu, "Effect of condensing unit layout at building re-entrant on split-type air-conditioner performance," *Energy Build.*, vol. 34, no. 3, pp. 237–244, Mar. 2002.

[4] R. Y. Nuwayhid, A. Shihadeh, and N. Ghaddar, "Development and testing of a domestic woodstove thermoelectric generator with natural convection cooling," *Energy Convers. Manag.*, vol. 46, no. 9–10, pp. 1631–1643, 2005.

[5] TEGproT M, "Module Performance Recycling waste heat for a cooler tomorrow

Recycling waste heat for a cooler tomorrow."
[6] "Everlight LED 6325K 2SMD Datasheet."
[7] T. Dikshit and D. Shrivastava, "Energy Harvesting via Piezoelectricity.," *BVICAM's ...*, vol. 2, no. 2, pp. 265–270, 2010.
[8] "CMOS_Circuits_for_Piezoelectric_Energy_H-1." Springer, Netherlands, Freiburg, p. 160, 2015.

eureca 2017 – Conference Paper
Paper Number 2ME11

Design and Development of a Multi-Element Active Aerodynamic Package to Enhance the Performance of Taylor's Formula SAE Car

Lee Wen Yew*, Abdulkareem Sh. Mahdi Al-Obaidi, Satesh Narayana Namasivayam
Department of Mechanical Engineering,
School of Engineering, Taylor's University, Malaysia.

* *wenyew.lee@gmail.com*

Abstract
This study aims to provide an initial prediction on the effects of an aerodynamic package in affecting the performance on Taylor's Formula SAE race car. A downforce of 90.830 N and drag of 186.018 N for the simplified Taylor's Racing Team TR 16 race car was identified through a 3D CFD simulation using the Reynold's Averaged Navier-Stokes k-ε model at a velocity of 17.88 m/s. The lift-drag ratio of the car was calculated and the corresponding lap time recorded for the four dynamic events in the Formula SAE competition was taken as the benchmark. The lift-to-drag ratio of 0.488 for the TR 16 race car indicated that the race car is aerodynamically efficient which contributes to a slower lap time and higher fuel consumption. The diffuser was analyzed and a 3D CFD simulation concluded that at an inlet angle of 3° and outlet angle of 22°, the highest downforce of 253.628 N and drag of 49.651 N was recorded. The results were input to the lap time simulator and it recorded the fastest lap time as compared to the other configurations. The two element front wing with configuration of pitch of 13° for the main element and pitch of 30° for the flap recorded the highest downforce of 131.165 N and drag of 37.504 N. The results were input to the lap time simulator and configuration mentioned above recorded the fastest lap time. Both the diffuser and front wing produced a downforce higher than the race car as well as a higher lift-to-drag ratio of 5.108 and 3.497 respectively as compared to 0.488 for the TR 16 race car. Consequently, by manipulating only the downforce and lift-to-drag ratio produced, the lap time recorded by the diffuser and two-element front wing was faster than the car with no aerodynamic package. This proves the initial prediction that adding an aerodynamic package to the TR 16 race car will enhance its performance.

Keywords: FSAE Car, Multi-element front wing, Diffuser, Computational Fluid Dynamics, Reynold's Averaged Navier-Stokes k-ε model

1. Introduction

When vehicles travel at high speeds, the airflow passing along the geometry of the car will generate lift and a nose-up pitching moment [1]. The lifting force reduces the tyre contact patch of the vehicle, leading to lesser traction and lower lateral stability. This can be countered by the introduction of an aerodynamic package that generates negative lift or downforce. Katz [2] mentioned that race car designers only understood the importance of vehicle aerodynamic by the late 1960s. This led to the advent of incorporating aerodynamic packages to race cars and later shaped the future of the motorsports scene.

In the context of Formula Society of Automotive Engineers (FSAE) races, Wordley [3] conducted an initial prediction study and found that the incorporation of an aerodynamic package improves the overall performance of the a race car. An aerodynamic package consists of a diffuser, front wing or rear wing. The front wing consists of endplates and an airfoil that acts as the element that produces the majority of downforce as well as drag. Merkel [4] conducted a study to analyze the effects of a multi-element wing specifically on the vehicle's aerodynamic downforce. This study determined that multi-element wings produced more significant downforce as compared to a single element wing. Zhang [5] identified ground effect as a major factor that increases downforce. It can be said that the diffuser which functions using a difference in pressure as well as ground effect contributes the most significant downforce in an aerodynamic package.

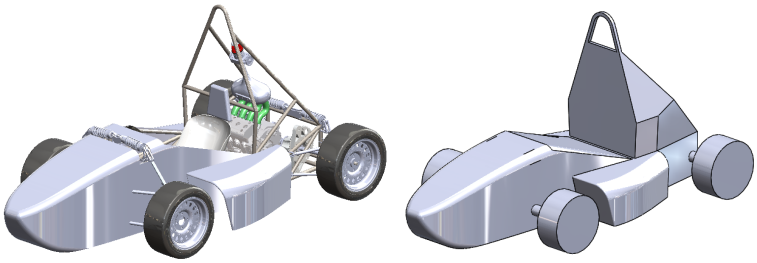
This paper aims to provide an initial prediction of the downforce and drag produced by the Taylor's Racing Team 2016 FSAE race car TR 16. Furthermore, this paper aims to investigate if the addition of an aerodynamic package to the race car will enhance its performance. First, the parameters of the TR 16 race car will be determined and a 3D computational fluid dynamic (CFD) analysis will be conducted to analyze the downforce as well as the lift-to-drag ratio, $\frac{L}{D}$, produced. A lap time simulator will be used to identify the lap time the TR 16 race car records based on the four separate dynamic events in the FSAE racing competition. An aerodynamic package, namely the diffuser and front wing will be designed and a 3D CFD simulation will be conducted as well. The inlet as well as the outlet angle of the diffuser will be manipulated and the effects will be compared. A Selig S1223 airfoil is chosen to be the main airfoil to be used in the design of the front wing. The pitch or angle of attack of the airfoil and its corresponding effect on the downforce and drag produced will be analyzed. A two element front wing will be designed based on the results obtained from the single element front wing. The downforce and $\frac{L}{D}$ obtained from the diffuser and front wing will be input to the lap time simulator as well to determine which configuration yields the best results in terms of lap time reductions. This also serves as an initial prediction that by increasing the downforce produced as well as $\frac{L}{D}$, the lap time recorded for each dynamic event will be reduced.

2. Research Methodology

2.1 3D Geometry Modelling

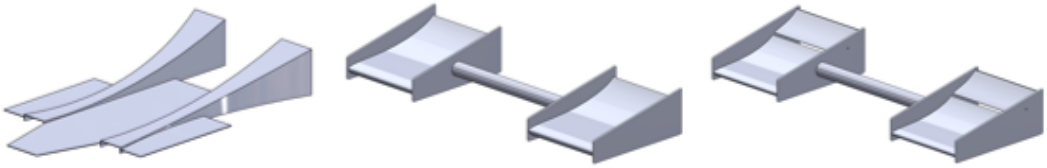
TR 16 was chosen for this study as a means of continuous improvement in the design and performance of the car. The race car was designed in Solidworks and further

simplified using surface modelling. Fig. 1 depicts the model of the car as well as the simplified version taken for 3D CFD analysis. The vehicle was modelled with a height, length, width and ground clearance of 1.45 m, 2.845 m, 1.375 m and 0.08m. Fig. 2 shows the model for the aerodynamic package that will be analyzed individually as well as incorporated into TR 16 for analysis. The diffuser is designed with a dimension of 2.3 m in length and maximum height of 0.322 m with a thickness of 0.005 m. The front wing endplate configuration is designed to be 0.5 m in length, front height of 0.1 m and rear height of 0.2 m with a thickness of 0.005 m.



(a) **(b)**

Figure 1. (a) Model of TR 16 Race Car (b) Simplified model of TR 16 Race Car



(a) **(b)** **(c)**

Figure 2. (a) Proposed Diffuser Model (b) Single Element Front Wing (c) Two Element Front Wing

2.2 Numerical Method

2.2.1 Model and Meshing Setup

An enclosed boundary domain was created to simulate the airflow along the geometry of the car body as well as the aerodynamic package. The model is sliced in half and assumed to be symmetric with a steady flow. An inlet, outlet, symmetry and wall regions were created to emulate real life conditions as closely as possible. In efforts to reduce the computational time, the dimensions of the enclosed unit for the TR 16 race car was referenced from Lai [6] as can be seen in Fig. 3. Similarly, the enclosed domain for the diffuser and front wing is shown in Fig. 4 and Fig. 5 respectively.

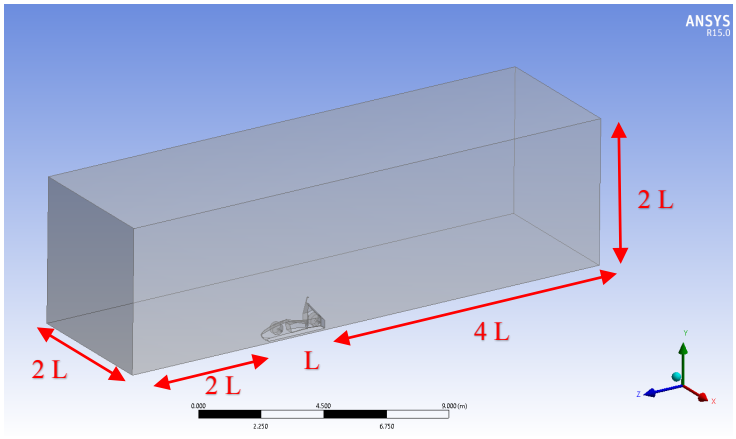


Figure 3. Enclosed Domain for TR 16 Race Car

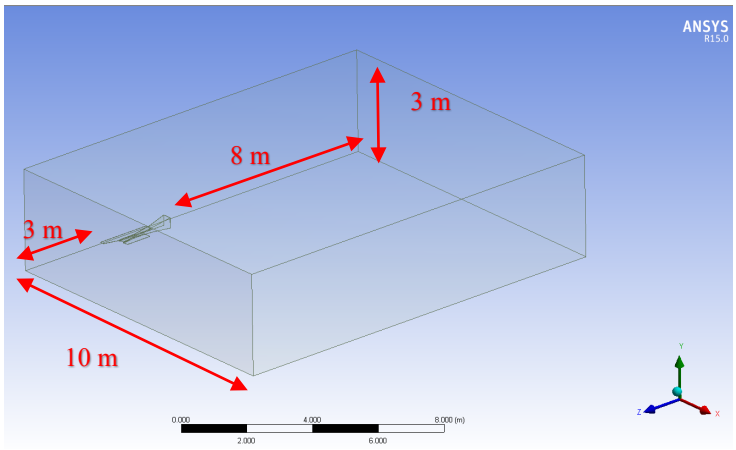


Figure 4. Enclosed Domain for TR 16 Race Car

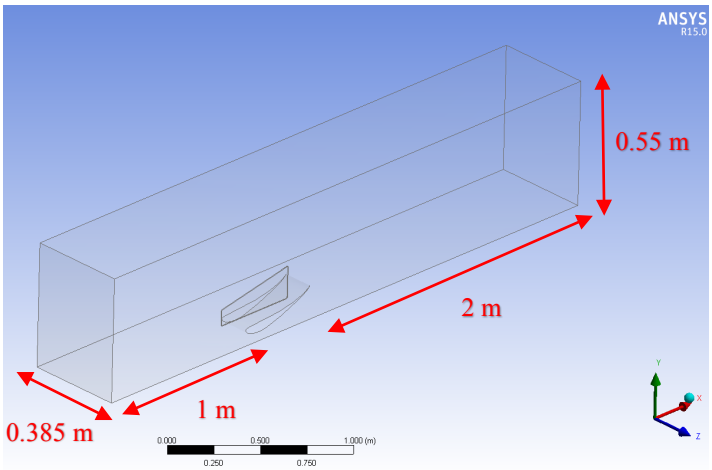


Figure 5. Enclosed Domain for TR 16 Race Car

Due to the complexity of the geometry of the race car as well as the aerodynamic package, a tetrahedral mesh was incorporated. A coarse global mesh sizing relevance center which produces a finer mesh surrounding the geometry of the model and enlarges as the mesh moves further away from the model helps in reducing the overall number

of elements for efficient computational time. The meshing result for the race car, diffuser and front wing can be seen in Fig. 6, Fig. 7 and Fig. 8 respectively.

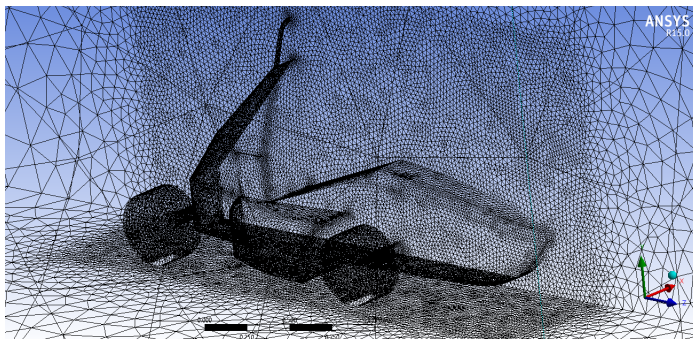


Figure 6. Coarse Mesh Sizing Relevance with Enclosed Body of 0.03 m Finer Mesh

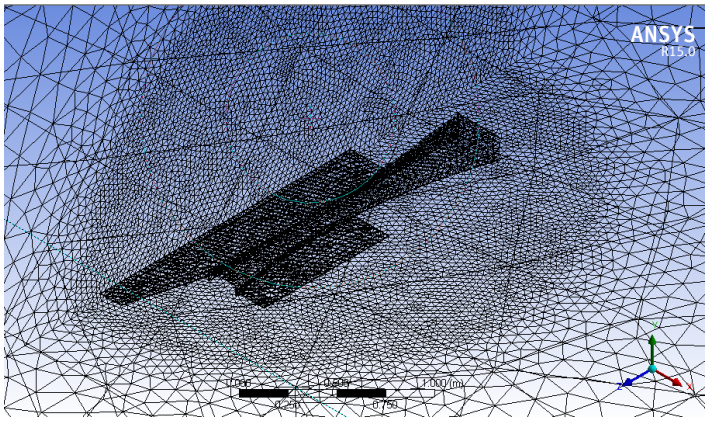


Figure 7. Coarse Mesh Sizing Relevance with a Sphere of Influence of 0.035 m Finer Mesh

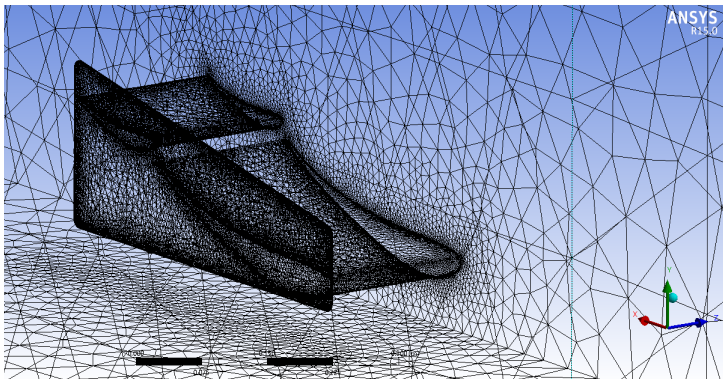


Figure 8. Coarse Mesh Sizing Edge Sizing of 0.00075 m and Seven Layer Inflation of 0.00075 m

2.2.2 Numerical Method and Cases

The Reynold's Averaged Navier-Stokes (RANS) k-ε realizable turbulence model with enhanced wall treatment was selected to simulate TR 16 as well as the aerodynamic package. The k-ε turbulence model is a suitable model as it can predict

the recirculation and boundary layers under strong adverse pressure gradients or separation caused by the geometry of the race car. The body of the TR 16 race car and aerodynamic package and walls of the enclosed domain were set to no slip wall condition whereas the symmetry plane was set to a symmetry condition. The inlet speed was fixed at 17.88 m/s as the average speed of a Formula student race car across its circuit is approximately 60 km/h. The outlet of the enclosed domain was set to an outlet pressure of 0 Pa. The pressure far field option was not selected due to the intersection between the wheels and bottom of the enclosed domain as configured by Lai [6].

There were three cases that were analyzed namely case 0, case 1 and case 2 which correspond to the non-aero assisted race, the diffuser and the front wing. In this preliminary study, these are the cases that are concerned and the inclusion of the aerodynamic package into the race car will be incorporated later as cases 01 with the race car and the diffuser and case 012 with the race car, diffuser and front wing. Table 1 depicts the parameters concerned for case 1 and case 2.

Table 1. Parameters of Case Study

Case	Parameter	
0	Simplified TR 16 Race Car Model	
1	Inlet (◦)	Outlet (◦)
	5	10
	5	16
	5	22
	3	22
	7	22
2	Pitch of Single wing Element	
	-3	
	8	
	13	
	Pitch of 2 wing elements	
	Main element (◦)	Flap(◦)
	0	10
	0	30
	12	10
	12	30

2.2.3 Lap Time Simulator

To translate the performance of the TR 16 race car into quantifiable measures, an online lap time simulator, namely FSAESim, is used to identify the lap times it can record based on the four dynamic events. The four events are autocross, skidpad, acceleration and endurance as well as its fuel consumption. The software utilizes the input of the race car vehicle parameters to simulate a vehicle going around a track. Table 2 illustrates the TR 16 vehicle parameters that are input into the online lap time simulator to compute the results of the lap time.

Table 2. Vehicle Parameters of TR 16 Race Car for Lap Time Simulation

Vehicle Parameters	Details
Tyre choice	Hoosier 13” Large
Vehicle Weight (lb)	656.978
Wheel Base (in)	64.567
Wheel Radius (in)	6.5
Track Width (in)	50
Centre of Gravity (in)	12.992
Weight Distribution (%)	0.52
Shift RPM	11000
Final Drive Ratio	4.1
Engine / Curve	Yamaha R6 – TU Graz Curve
Forced Induction	Naturally Aspirated (o hp)
Aero Downforce at 40 mph	20.419
Lift/Drag Ratio	0.488

The results obtained from the lap time are set as a benchmark. The final configuration of the race car with the aerodynamic package will be compared with the benchmark to determine whether its performance will improve. The downforce and lift-to-drag ratio of the diffuser and two element front wing will be input into the software without changing the other parameters as seen in Table 2. This is to determine the effects of the downforce and lift-to-drag ratio on the lap time recorded. This will serve as the initial prediction that a higher downforce and increased lift-drag ration will improve the recorded time.

3. Results and Discussion

3.1 TR 16 Race Car

The negative lift, or downforce and drag produced by the TR 16 race car is summarized in Table 3. The $\frac{L}{D}$ indicates that the race car has a relatively poor aerodynamic design in which the amount of drag produced is almost twice as much as the downforce produced at a speed of 17.88 m/s. This not only affects the fuel efficiency of the race car, it also increases the time required to complete a lap.

Table 3. Summary of Results for TR 16 Race Car

Downforce (N)	Drag (N)	$\frac{L}{D}$
90.830	186.018	0.488

Fig. 9 shows that most of the induced drag is formed due to the frontal area of the race car exposed to the airflow as well as the tyres. By further analyzing the velocity vector of the airflow along the surfaces of the race car, Fig. 10 indicates that there exists a recirculation zone after the air passes the front and rear tyres which contribute to the formation of wake and turbulence, and consequently induces more drag.

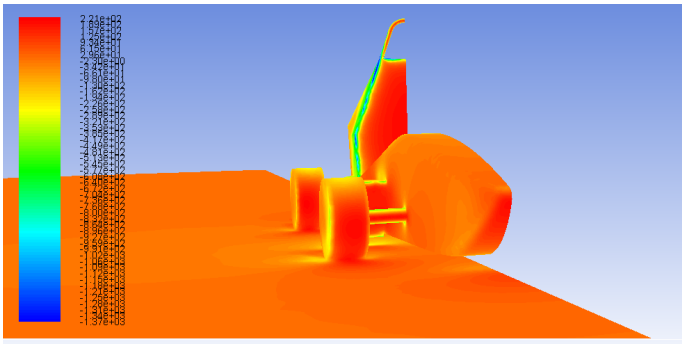


Figure 9. Static Pressure Distribution over the TR 16 Race Car

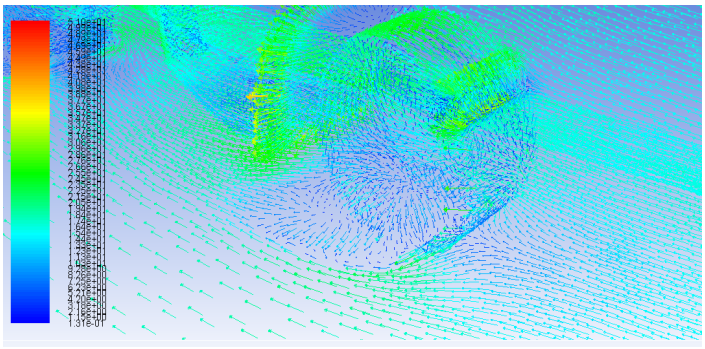


Figure 10. Velocity Vector around the Tyre of TR 16 Race Car

The effect of the downforce and drag acting on the race car is translated to a more comprehendible manner in terms of lap time. Table 4 depicts the lap time recorded based on each dynamic event by the TR 16 race car. Having identified the downforce and drag produced especially the main areas which contribute to the drag of the car, a suitable aerodynamic package can be designed to further increase the amount of downforce produced whilst optimizing the drag. The lap time recorded as depicted in Table 4 will act as the benchmark to determine whether the addition of an aerodynamic package enhances the performance of the race car in terms of lap time reduction and improved fuel consumption.

Table 4. TR 16 Race Car Recorded Lap Time Based on Dynamic Events

Downforce at 40 mph (lbf)	$\frac{L}{D}$	Dynamic Event Lap Time (s)				Endurance Event Fuel Consumption (gallons)
		Autocross	Skidpad	Acceleration	Endurance	
20.419	0.488	76.398	5.057	5.06	1512.389	2.44

3.2 Front Wing

3.2.1 Single Element Front Wing

Fig. 11 shows the results obtained for the downforce and drag values at different airfoil pitch or angle of attack. It can be seen as when the pitch of the airfoil increases, the downforce and drag also increases. The flow velocity of air passing through the bottom of the inverted Selig S 1223 airfoil is higher than the upper surface of the airfoil. As a result, a difference of pressure is formed as can be seen in Fig.12. Hence, downforce is produced. From the results obtained, the pitch of the airfoil that produces the least drag, which is -3°, and the most downforce, which is 13°, is selected in designing a two element front wing.

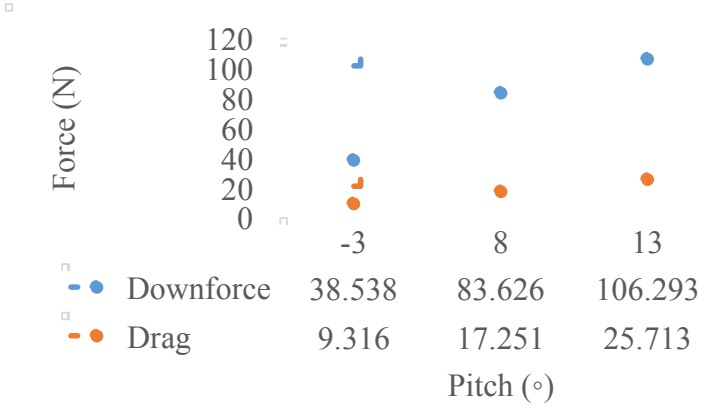


Figure 11. Downforce and Drag Produced on Different Airfoil Pitch

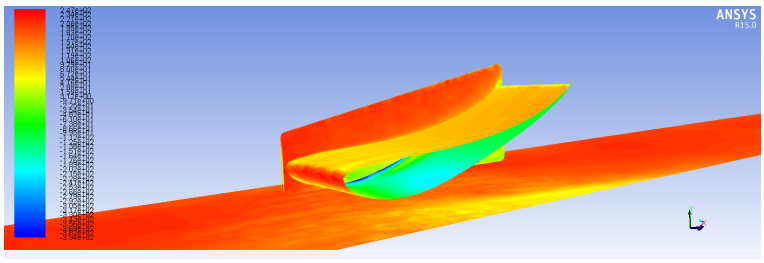


Figure 12. Pressure Contour Acting on the Single Element Front Wing with a Pitch of 13°

3.2.2 Two Element Front Wing

The addition of a front wing not only produces downforce, it also serves to direct the airflow above and away from the front tyres, thereby reducing the drag induced by the tyres. A multi-element front wing consists of a main element and a flap. The option of being able to manipulate the pitch of the flap enables a multi-element front wing to produce more downforce as compared to a single element front wing.

Fig. 13 depicts the downforce and drag produced based on the various configurations (main element_flap) of the two element front wing. It can be seen that as the pitch of the main element increases from -3° to 13°, the downforce as well as drag increases. The same can be said for the flap when the pitch increases from 10° to 30°. The obtained downforce and drag results are then input into the lap time simulator to identify which configuration requires the least time to complete a dynamic event.

From Table 5, it is evident that the front wing with a 13° main element pitch and 30° flap pitch produces the best lap time in all dynamic events.

Although this configuration produces the most drag, the effect of the downforce is more significant. This is validated through Table 5 where it is observed that the lap time recorded for each dynamic event reduces with an increase in downforce across each different configuration. Therefore, the front wing with configuration main element pitch of 13° and flap pitch of 30° is selected to be incorporated to the TR 16 race car.

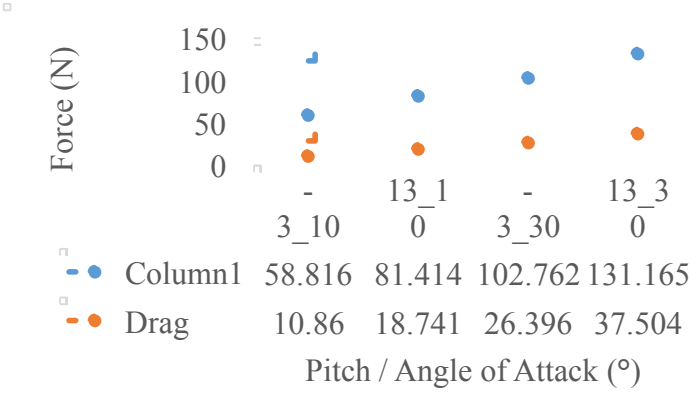


Figure 13. Downforce and Drag Produced on Different Two Element Front Wing Setup

Table 5. Lap Time Recorded Based on Two Element Front Wing Configuration Downforce and $\frac{L}{D}$ Ratio

Two Element Front Wing Configuration	Dynamic Event Lap Time (s)				Endurance Event Fuel Consumption (gallons)
	Autocross	Skidpad	Acceleration	Endurance	
-3_10	76.837	5.093	5.070	1521.158	2.450
13_10	76.571	5.067	5.070	1515.840	2.430
-3_30	76.320	5.043	5.070	1510.818	2.440
13_30	75.995	5.012	5.060	1504.325	2.420

3.3 Diffuser

3.3.1 Diffuser Outlet Angle

Fig. 14 depicts the downforce and drag produced when the inlet angle of the diffuser is fixed at 5°. When the outlet angle is 22°, maximum downforce and drag is produced. This is a result of negative pressure being formed near the rear of the diffuser as seen in Fig. 15. As air enters the inlet of the diffuser, it is accelerated through the throat. The sudden decrease in velocity of the air when it starts to exit the throat towards the outlet of the diffuser causes a drastic decrease in pressure. An area of vacuum starts to form, causing turbulence and thereby producing drag. However, Fig. 16 shows that flow separation does not occur until the airflow leaves the diffuser, ensuring that drag

does not occur within the diffuser. Hence, the configuration of the diffuser outlet is set at 22°.

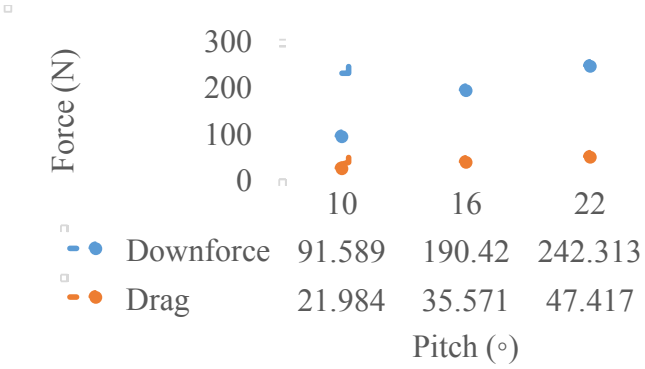


Figure 14. Downforce and Drag Produced against Varying Diffuser Outlet Angle When Inlet Angle is Constant at 5°

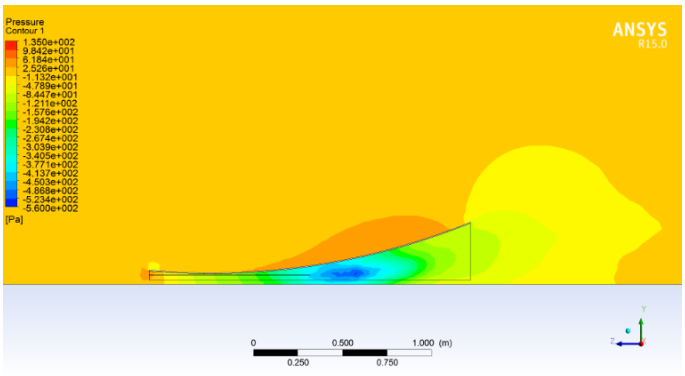


Figure 15. Pressure Contour along Diffuser Model with Outlet Angle of 22° and Fixed Inlet Angle of 5°

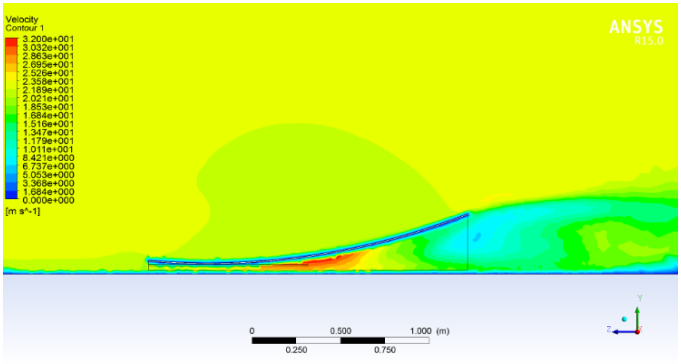


Figure 16. Velocity Contour along Diffuser Model with Outlet Angle of 22° and Fixed Inlet Angle of 5°

3.3.2 Diffuser Inlet Angle

Fig. 17 depicts the downforce and drag produced at varying diffuser inlet angles when the outlet angle is fixed at 22°. When the inlet angle is 3°, maximum downforce

and drag if produced. This is due to the bigger gap in pressure between the top and bottom layer of the diffuser as seen in Fig. 18. A decrease in velocity as the air exits the throat to the outlet of the diffuser created a large recirculation zone. This produced higher a drag as compared to the case when the inlet is 5°. However, according to Jensen [7] and Khokhar [8], if the inlet angle is too small, there will be no increment in the airflow speed thus downforce is significantly reduced. Therefore, the inlet angle of 3° is the most optimum configuration for this case.

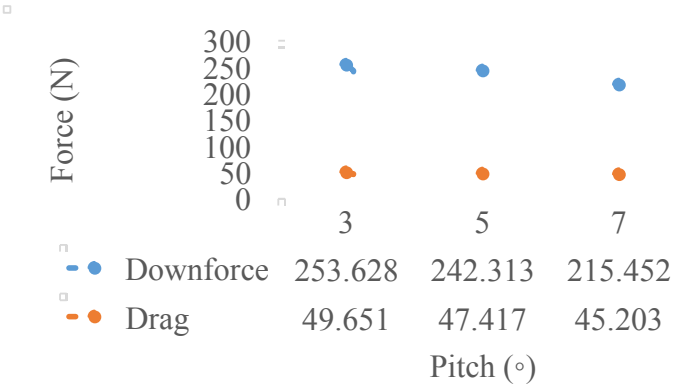


Figure 17. Downforce and Drag Produced against Varying Diffuser Inlet Angle When Outlet Angle is Constant at 22°

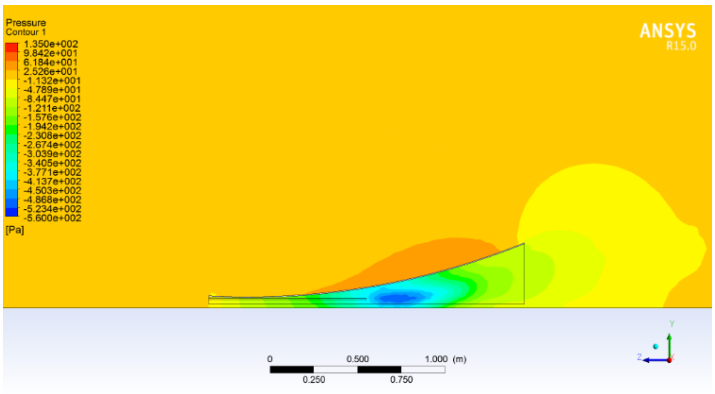


Figure 18. Pressure Contour along Diffuser Model with Inlet Angle of 3° and Fixed Outlet Angle of 22°

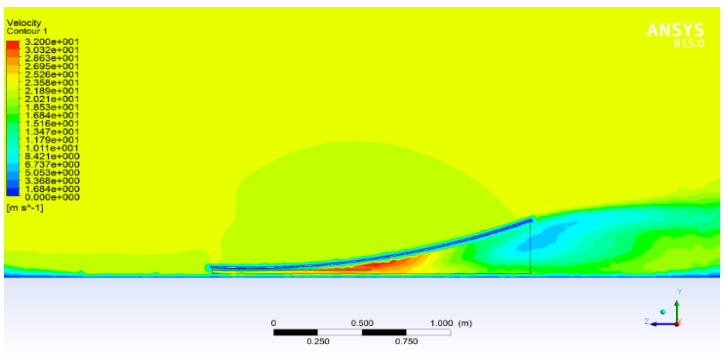


Figure 19. Velocity Contour along Diffuser Model with Inlet Angle of 3° and Fixed Outlet Angle of 22°

The diffuser configuration that produces the best result is when the inlet is 3° with an outlet of 22°. This diffuser configuration recorded the least time taken to complete all dynamic events except for the acceleration event. This is due to the increase in drag as a result of the formation of wake and turbulence when the air exits the diffuser. Hence, the diffuser configuration of inlet angle 3° and outlet angle 22° is selected to be incorporated to the TR 16 race car.

Table 6. Lap Time Recorded Based on Diffuser Inlet Outlet Angle Configuration Downforce and $\frac{L}{D}$ Ratio

Diffuser Inlet Outlet Angle Configuration	Dynamic Event Lap Time (s)				Endurance Event Fuel Consumption (gallons)
	Autocross	Skidpad	Acceleration	Endurance	
3_22	74.880	4.833	5.08	1482.028	2.41
5_22	74.920	4.899	5.08	1482.811	2.41
7_22	75.174	4.992	5.07	1487.904	2.41

4. Conclusion

The TR 16 race car was identified to have a relatively poor aerodynamic design. The effects of an aerodynamic package, namely the diffuser and multi-element front wing was studied numerically as well This is to enhance its performance in terms of reducing the overall lap time of the race car and to increase its fuel efficiency. The multi-element front wing produces more downforce as compared to a single element front wing. When the pitch of the element increases, downforce and drag is also increased. Furthermore, the multi-element front wing serves an additional function of directing the airflow away from the tyre, thereby reducing the drag induced by the tyre of the race car. The diffuser's capacity to produce downforce depends heavily on the inlet and outlet angle of the diffuser. A smaller inlet angle and larger outlet angle corresponds to both a higher downforce and induced drag. This preliminary study shows promise that when the diffuser and multi-element front wing is added to the TR 16 race car, a significant amount of downforce can be produced whilst maintaining an acceptable drag limit. As a result, a better lap time can be recorded.

Acknowledgement

Throughout the duration of this research process, various guidance, help and supervision was offered. A whole hearted gratitude and appreciation goes out to Tan Zhe Xin, Muhammad Ammar Zulsyahmi and Farah Danial Rahman for their support and assistance.

Nomenclatures

$\frac{L}{D}$	**Lift-to-drag Ratio**

Abbreviations

FSAE	**Formula Society of Automotive Engineers**
CFD	**Computational Fluid Dynamics**
RANS	**Reynold's Averaged Navier-Stokes**

References

[1] Walter, D.J., (2007). *Study of Aerofoils at High Angle of Attack , in Ground Effect.* Master's Thesis, RMIT University, Australia.
[2] Katz, J., (1995). *Race Car Aerodynamics : Designing for Speed*. Cambridge, Massachusetts: Bentley Publishers.
[3] Wordley, S., Saunders, J., (2006) Aerodynamics for Formula SAE: Initial Design and Performance Prediction. *SAE World Congr., (1)724, 0806*
[4] Merkel, J.P., (2013) *Development of Multi-Element Active Aerodynamics for the Formula Sae Car.* Master's Thesis, University of Texas, USA.
[5] Zhang, X., Toet, W., Zerihan, J., (2006) Ground Effect Aerodynamics of Race Cars, *Annu. Rev. Fluid Mech.*, *1*(38) ,27–63.
[6] Lai, S.A., (2016, December). *Effect of Size and Shape of Side Mirrors on the Drag of a Personal Vehicle.* Paper presented at Taylor's University EURECA Conference, Subang Jaya, Selangor.
[7] Jensen, K., (2010) *Aerodynamic Undertray Design for Formula SAE*. Master's Thesis, Oregon State University, USA.
[8] Khokhar, A.A.S., Shirolkar, S.S., (2015). Design and Analysis of Undertray Diffuser for a Formula Style Racecar. *International Journal of Research in Engineering and Technology*, *4*(11), 202–210

eureca 2017 – Conference Paper
Paper Number 2ME12

Modification and Validation of Tensile Testing Method for Biaxial Loading on Cord Ply Layer in Two-wheeler Bias Tire

Mah Weng Onn[1*], Koay Seong Chun[1], Ch'ng Shiau Ying[2], Thien Chung Ket[3]
[1]*Taylor's University Lakeside Campus, Subang Jaya, Selangor, Malaysia*
[2]*University of Southampton Malaysia Campus, Nusajaya, Johor, Malaysia*
[3]*Heriot-Watt University, Putrajaya, Wilayah Persekutuan Putrajaya, Malaysia*

[*]*wengonn.mah@sd.taylors.edu.my*

Abstract
A cord ply layer is a composite material that consists of twisted Nylon cord arranged at an angle within the range of 30° to 35° in the rubber matrix. This study focuses on the mechanical behavior and properties of the cord ply layer using a modified biaxial tensile test. Two variations of specimens were tested, including the i) single layered cord ply layer with unidirectional nylon cord, and the ii) double layered cord ply layer with bidirectional nylon cord. The stress versus strain curves showed that the failure behavior of both cord ply layers can be categorized into four failure modes which are the i) failure within the cord, ii) cord breakage, iii) shearing on the interface between cord and rubber and iv) mixed mode failure. To validate the experimental data, the 2D static sutural analysis is selected. The Mooney Rivlin model with 2 parameters is chosen for the simulation of a hyperelastic material. By comparing initial stage of both stress strain curves, the deviation is shown to be caused by the shortcomings of the clamping mechanism of the proposed biaxial tensile test.

Keywords: Cord ply layer, Fiber and matrix, Anisotropic material, Young's modulus, Failure mode, Hyperelastic model

1. Introduction

According to Malaysian Institute of Road Safety (MIROS), the number of motorcycle accident has increased from 97,072 cases in year 2005 to 120,156 cases in 2010 which is a significant increment of 23.78 percent [1]. Based on the investigation, tire failure was reported as one of the main factors that causes the motorcycle accidents. This incident has alerted tire manufacturers to enhance the quality of tires.

Motorcycle tire, which also known as two-wheeler tire, can be mainly categorized into two types – radial and bias ply tire. Both types of tires cater to different applications based on the inner structure that consists of various type of material. A radial ply tire is multilayered to provide good stability for the vehicle especially while cornering or passing through road bumps. This feature make this type of tire look bulky. The bias ply tire consists of a few layers of composite materials overlapped at specific arrangements which makes this type of tire tough and able to carry high loads [2]. The bias ply tire is also more economical in comparison to the radial ply tire. Therefore, most motorcycles use bias ply tires unless the cyclist emphasizes on the performance of motorcycle like sportbike.

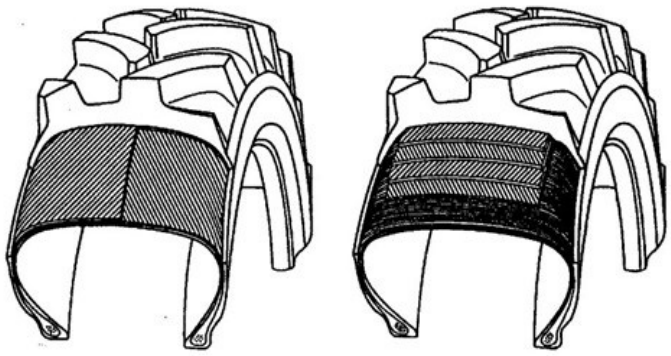


Figure 36. Structure of bias and radial ply tire [3]

In terms of analyzing the performance of the tire, Baranowski *et al*. [4] investigated the contour deformation of a bias ply tire. The results found that in reality, the footprint test was significantly different in comparison to simulation results. The main reason why the footprint test and simulation result show great difference was because the tire was modelled as a a single rubber model. However, the tire actually consists of different layers of material such as thread, thread base, inner layer, bead and cord ply layer (as illustrated in Figure 2). Each layer is made of different materials with their own mechanical properties. To improve the studies done by Baranowski *et al.* [4] , it is suggested to consider mechanical properties of each layer in the bias ply tire during the simulation.

Of the different layers of materials in tires, the cord ply layer is the most complex material due to its structure. The cord ply layer is considered to be a composite material, since it comprises of thin textile nylon fibers that are embedded in a rubber matrix. The nylon fibers are mainly responsible for the strength reinforcement of the tire. Furthermore, the cord ply layer is anisotropic behavior due to the textile nylon fiber are either unidirectional or bidirectional and orientation of fiber is not perpendicular to direction of stress. For this reason, there are many limitations on studying the

mechanical properties of cord ply layer using conventional uniaxial tensile test method. In addition, a biaxial tensile testing is recommended for composite material investigation due to anisotropic behavior. In general, the specimen is prepared as cruciform shaped specimen that use on standard biaxial tensile testing (as displayed in Figure 3). However, biaxial tensile test still has limitation on testing cord ply layer. This is because a cruciform shaped specimen is not able to ensure every single nylon fiber is subjected to the tension load, such as the edges region. Therefore, the data from conventional biaxial tensile test is not able to express the actual mechanical behavior of cord ply layer.

The present research is mainly focused on studying mechanical behavior and properties cord ply layer with a modified biaxial tensile test method that referring to Mullen burst test. The experiment is carried out on single layered with unidirectional nylon cord and double layered cord ply layer with bidirectional nylon cord. For the validation of experiment data, 2D static structural analysis is carried out to compare the stress strain behavior of specimen.

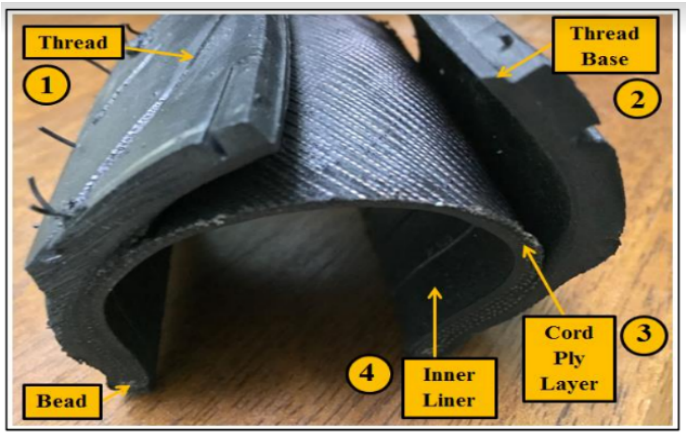


Figure 37. Dissection of bias ply tire

2. Research Methodology

2.1 Material and Specimen

The cord ply layer consists of rubber and Nylon 6-6. The dimensions of the specimen is 200 mm x 200 mm square shape with the thickness of 1.5 mm. Two different types of cord ply layers were tested in this experiment. The first is a cord ply layer with a single layer,32^{o} orientated nylon cord and the second is a cord ply layer with double layers of the 32^{o} orientated nylon cord as shown in Figure 3. All specimens were supplied by Continental Malaysia Sdn. Bhd.

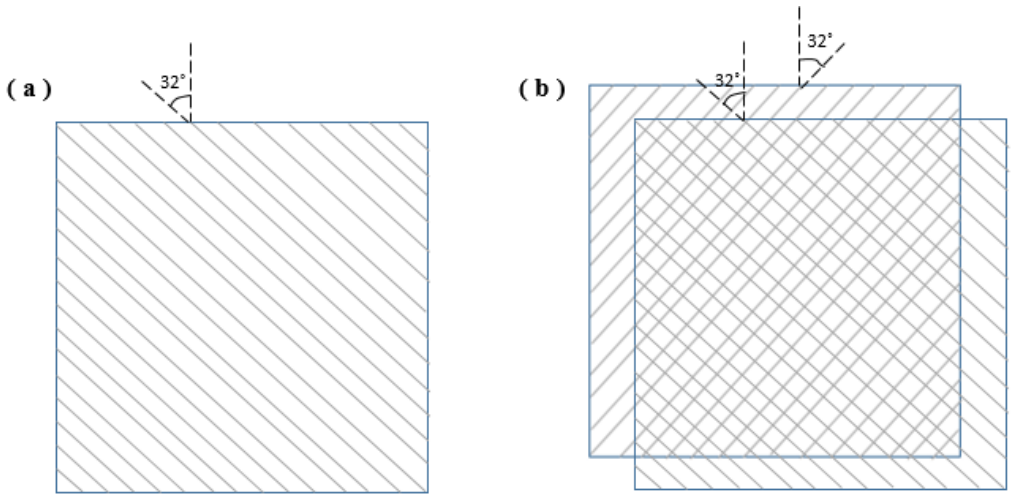


Figure 38. Cord ply layer with (a) single layered and (b) double layered 32^{o} oriented nylon Cord

2.2 Modification of Biaxial Test

The main concept is to simulate the experiment process of the Mullen burst test which is categorized under biaxial tensile testing. It has a different working principle as compared with conventional biaxial tensile tests. By using the annular clamp to hold the specimen, air is inserted into the specimen until it bursts. Similarly, all specimens were tested for its mechanical properties following a method suggested by Koutiri *et al.* [6]. and Brugger *et al*.[7]. The biaxial test was carried out using the Instron universal testing machine, model 5596. An indenter was attached on the moving crosshead and a jig was fixed on the bottom base. The dimension of the indenter was made according to the dimensions of the tire according to the shape of bias ply tire sample (as illustrated in Figure 5). The setup of the indenter and jib were shown in Figure 4. According to the R&D Department of Continental Sdn. Bhd, the uniaxial tensile result of the cord ply layer showed 300% of elongation. Thus, the jig was designed to have the height of 40 cm which allows the specimen to extend 300 times. Whereas the base is supported by a thin aluminum in order to lock the entire jig on the tensile machine. Furthermore, the shaft that attached with the indenter was designed to have similar length as the height of the jig.

The specimen was placed on the top of jib and fixed with mini G-clamps, as shown in Figure 4. Then, the indenter was moved downwards with a crosshead speed of 50 mm/min and the specimen was punched until fracture. The data was recorded by the computer and a stress versus strain curves were plotted by the Bluehill software. The experiment was carried out at a temperature of approximately 25^{o}C and a minimum of 10 specimens were tested for two different samples as mentioned.

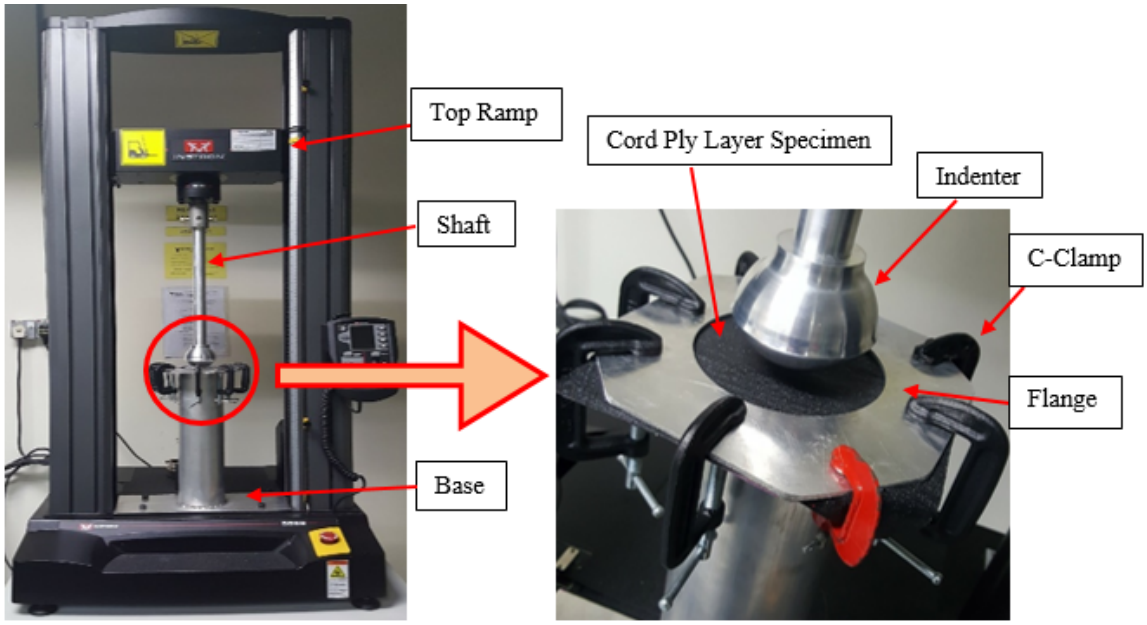


Figure 39. Allocation of indenter and jig on Instron machine

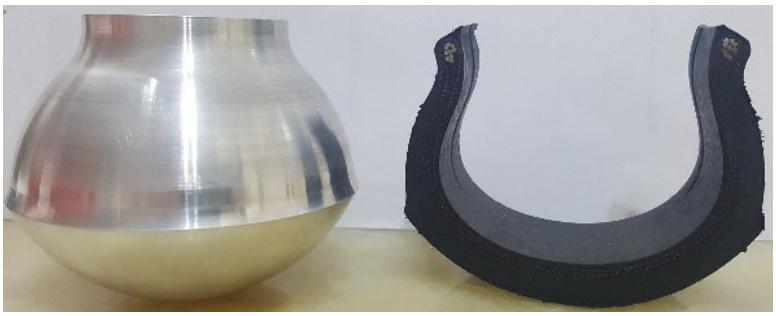


Figure 40. Indenter and bias ply tire sample

2.3 Calculation of Stress Strain Data

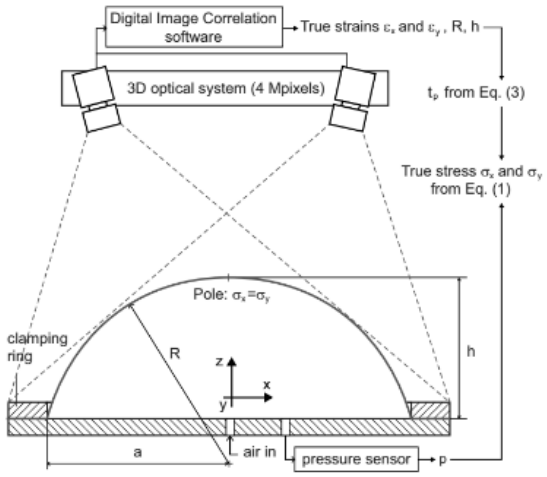


Figure 41. Setup of Mullen Burst Test [8]

Figure 6 shows the typical setup of Mullen Burst test. Pole is used to denote the peak region on top of the specimen which will deform the most during the inflation. All the stresses at the pole were estimated by pressure vessel theory. However, the extension of the entire specimen is unpredictable because the specimen is free to deform in any direction. This means that many aspects have to be taken into consideration making data calculation complicated. In order to simplify all calculations, the bubble shape was assumed to be spherical in shape and the material is defined to be incompressible. The biaxial stresses on the pole is given as below:

$$\sigma_x = \sigma_y = \frac{p\,R}{2\,t_p} \quad (1)$$

Where p = pressure at pole
R is the bubble radius
t_p is the thickness of specimen at the pole

Due to the complexity of measuring the thickness of the specimen at the pole which the dimension is varied based on time, an optic system is applied in this experiment to estimate the thickness from the biaxial true strain at the pole in order to get ε_x and ε_y. The incompressibility assumption is defined as

$$\varepsilon_x + \varepsilon_y + \varepsilon_z = 0 \quad (2)$$

Where ε is the strain and depends on the x, y and z directions

Equation 3 below is derived to calculate the pole thickness of the specimen:

$$t_p = t_o \exp^{\varepsilon_z} = t_o\, exp^{-\varepsilon_x - \varepsilon_y} \quad (3)$$

where t_o is the initial thickness of specimen.

Technically, the radius of bubble (R) is obtainable by using the optic system. To compare the accuracy of the result from the optic system, there is an analytical method that was proposed by Charalambides [9] to calculate the radius of bubble every single time. The investigation of his paper was to study the inflation of a flour/water dough. Similarly, the bubble size from his experiment is also idealized to be spherical. Based on his findings, he concluded that the radius can be calculated by using the equation below:

$$R = \frac{a^2 + h^2}{2h} \quad (4)$$

where a is the radius of flat circular specimen and h is the height of bubble which is also the extension of specimen.

As for the estimation of material thickness, Bloksma who extended the previous study on the dough extension measurement has proposed another method to estimate the distribution of the membrane thickness [10]. To summarize the entire research, he mentioned that there is another method to estimate the thickness at pole which the equation has shown below.

$$t_p = t_o \left(1 + \frac{h^2}{a^2}\right)^{-2} \quad (5)$$

By combining all the related studies together, a new equation is derived to describe the biaxial true strain at the pole. This equation assumed that strain on the x and y axis experience the same deformation.

$$\varepsilon_x = \varepsilon_y = -\frac{1}{2}\varepsilon_z = -\frac{1}{2}\ln\left(\frac{t_p}{t_o}\right) = \ln\left(1 + \frac{h^2}{a^2}\right) \quad (6)$$

In this research paper, the engineering stresses and strains were obtained by using equations 1 and 6.

2.4 Setup of Simulation

To validate the experimental data, the ANSYS software package was used to conduct 2D static structural simulations.

2.4.1 Material Engineering Data

The indenter is assigned as AL T6061 which is the actual material that was used to manufacture the apparatus, while the specimen is assigned as a Mooney Rivlin model with two parameters. The material parameters for Mooney Rivlin model are obtained using engineering stress equation for biaxial condition as shown below:

$$\mathrm{P} = 2C_{10}\left(\lambda - \frac{1}{\lambda^5}\right) + 2C_{01}\left(\lambda^3 - \frac{1}{\lambda^3}\right) \quad (7)$$

where C_{10} and C_{01} are material constants obtained from curve fitting and

λ represents stretch in principal direction ($\varepsilon + 1$).

2.4.2 Boundary Condition

Since the indenter and rubber are highly symmetrical, the entire model was simplified to be 2-dimensional as shown in Figure 7. Displacement control was imposed to the indenter to observe the stress and strain behavior of the contacted specimen in the x axis. The displacement was set from 1 mm to 10 mm for each simulation. Fixed support was set around the edges of circular specimen as the case is idealized that the remaining part of the actual specimen is tightly clamped on the flange which assumes that slip does not occur. The obtained stress strain response from the rubber was compared against experimental data for validation purposes.

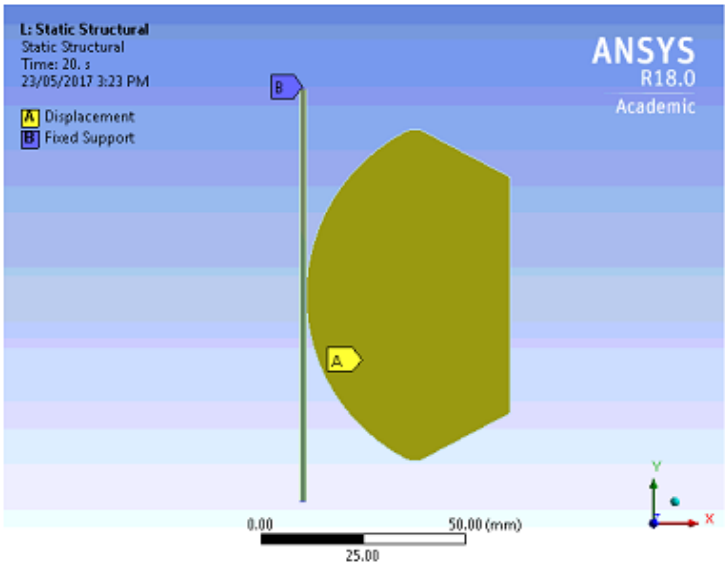


Figure 42. Setup of boundary condition. (A) Displacement (B) Fixed Support

3. Result and Discussion

3.1 Initial Nonlinear Behavior

Figure 10 and 11 shows the stress strain curve that is plotted by averaging the experimental data. Both stress strain curves show a common sigmoidal shape characteristic of rubber. Based on a research study by Rao *et al.* [11], the nonlinear behavior can be differentiated by three stages :

Stage 1: Nonlinear deformation with increasing stiffness
Stage 2: Linear Stress Strain Behavior
Stage 3: Linear deformation with decreasing stiffness

During the first stage, the single layer and the double layer experiences a strain of up to 0.52 and 0.56 respectively. The phenomena is explained due to the facts that wires composing the cord do not come into contact with each other until subjected to a higher degree of stress . Melerose [12] also explained that the shortcomings of the apparatus is also a possible factor. These shortcomings include the “settling down” duration of the specimen in the grips, machine backlash being taken up and slippage. Moreover, the specimen preparation process has also been considered as a factor.

During the curing process, the cord was not ensure to experience high tension behavior which cause the cord stay relax on the rubber matrix.

The second stage shows that the composite material exhibits a linear stress strain behaviour. This is the most suitable region to calculate the slope which is also known as the Young's modulus. Both point A and B represents the start and end of stage 2 respectively on the initial nonlinear behavior of a single layer and double layer specimen.

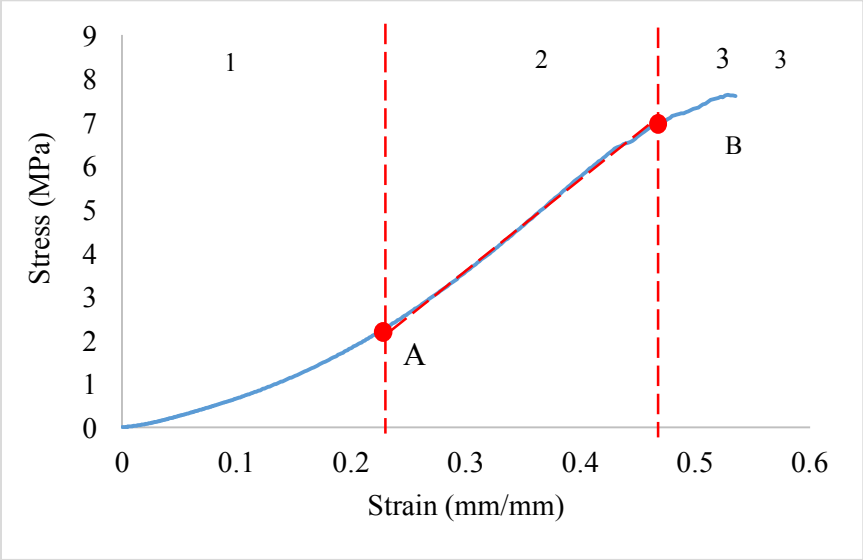


Figure 43. Initial nonlinear behavior for single layer specimen

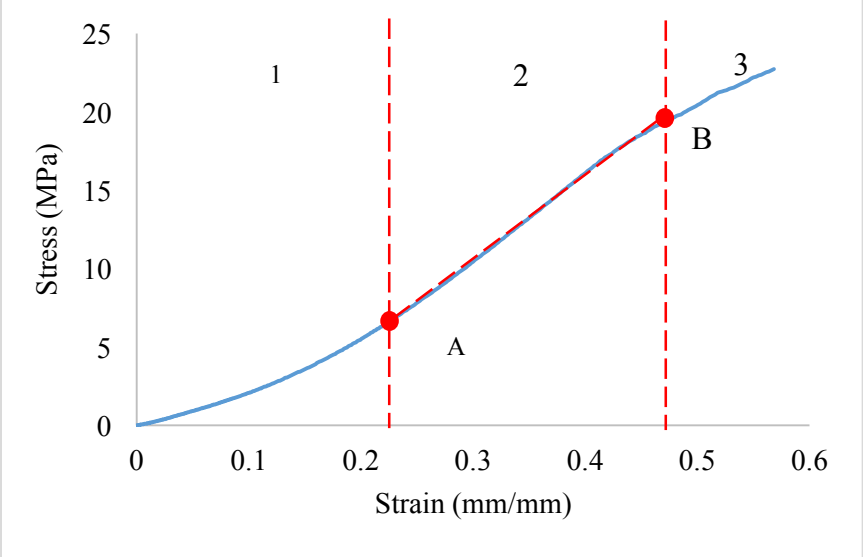


Figure 44. Initial deformation behavior for double layer specimen

The last stage corresponds to the nonlinear behavior of the Nylon cord which indicates that every strain that happens on the material requires higher stress applications. The ending point of this stage also represents the maximum tensile

strength that the cord ply layer is able to withstand. The mechanical properties for each type of specimen are tabulated below. Overall, the mechanical properties of the double layer specimen is higher than the single layer specimen, especially the Young's modulus of double layer is doubled of the single layer's Young's modulus.

Table 24: Mechanical properties of cord ply layer specimen

Specimen	Young's modulus (MPa)	Ultimate tensile strength (MPa)	Elongation (%)
Single Layer	18.72(±5.36)	9.14 (±1.62)	54.23
Double Layer	39.62(±1.94)	32.05 (±3.83)	56.56

3.2 Failure Mode

As an observation from the graph trend as well as the tested specimen, different failure modes of cord ply layer are observed as proposed failure mechanism (Figure 10) and concluded as following:

i) Failure mode 1 : Failure within the cord

This failure happens when the force applied was parallel to the direction of the nylon fibers and causes the separation of a single Nylon fiber as shown in Figure 11(a). Figure 10 illustrates the proposed mechanism of failure mode 1. Initially, the microcrack starts from flaws during the manufacturing process, otherwise it will self-generated by coalescence of voids. This stage has higher chance to start on the fiber surface, but occasionally from internal flaw. Then, the following stage is the microcrack propagation through the cord. When the microcrack has reached a certain stage, it will cause the separation within a single cord. The separation leads the macrocrack initiation and subsequently propagates to the surface of cord caused the total failure within the cord.

ii) Failure mode 2: Cord breakage

This failure mode is also happened on the Nylon cord and the failure stages are similar to the previous failure mode which firstly initiated by micro crack from the outer surface and slowly propagate to center of cord. The fracture section on Figure 11(b) shows irregular break points. In fact, the specimen fractures due to it originates from the extension and accumulation of the micro flaws on the rubber matrix. This causes the neighboring fibers in weaker spot fractures and induces the crack on both specimens.

iii) Failure mode 3: Shear failure of the interface between cord and fiber

This stage is also known as delamination where happens due to the weak adhesive bonding between rubber matrix and fiber cords. This particular failure mode consists of five different stages. Firstly, the micro crack initiates at the interface between rubber and cord near the edge. As the loading keeps increasing, the density of

microcrack increases at the same time until the macrocrack is formed on the interface. Then, the macrocrack will propagate slowly to region nearby which eventually the shearing occurs on a particular region. Therefore, Figure 11(c) shows that the Nylon cords are completely pull out from the rubber matrix.

iv) Failure mode 4 : Mixed Mode of Shearing and Cord Breakage

The failure mode is the most common failure that can be observed on every tested specimen regardless of the type of specimen. The damage evolution is also combined from both failure mode 2 and 3. Firstly, the microrack within the cords, macrocrack through each particular cord, wire breakage, macrocrack initiation at the interface between Nylon and rubber and lastly shearing occurs. As the observation from typical failure of both type of material, single layer specimen shows more uniform fracture section (Figure 121(e)) as compared to double layer (Figure 11 (f)) due to the angle orientation of allocation of Nylon cords. With uniform allocation of fiber, the shearing of rubber tends to occur in between cords, otherwise the fracture sections would appear randomly.

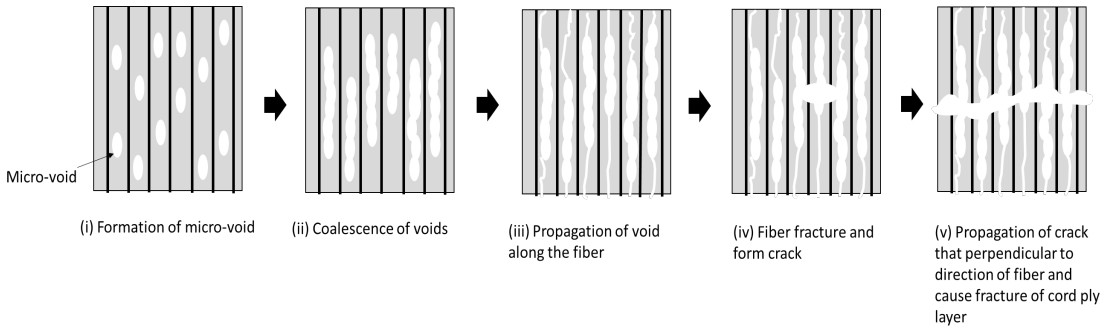


Figure 45. Proposed mechanism failure mode of cord ply layer.

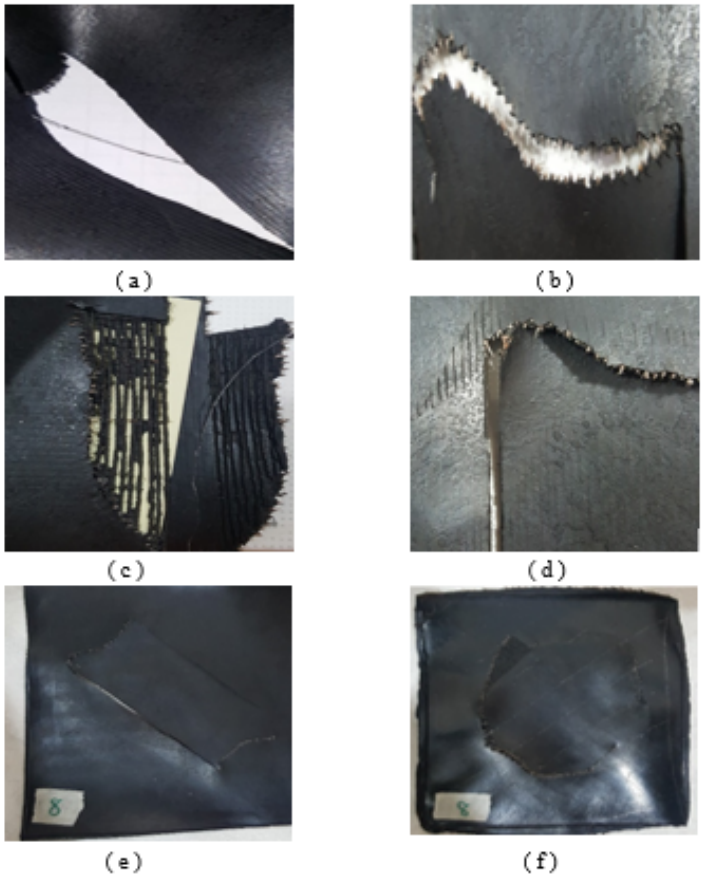


Figure 46. Fracture section of specimen (a) Failure within cord (b) Cord breakage (c) Delamination (d) Shearing on rubber matrix (e) Typical failure of single layer (f) Typical failure of double layer

Initially, both types of cord ply layers experienced a non-linear deformation due to the deformation of the rubber component in the cord ply layer. Then, the stress of both samples exhibits an erratic trend that decreases with continuous increase in strain. This erratic stress strain curve is shown in Figures 12 and 13 below.

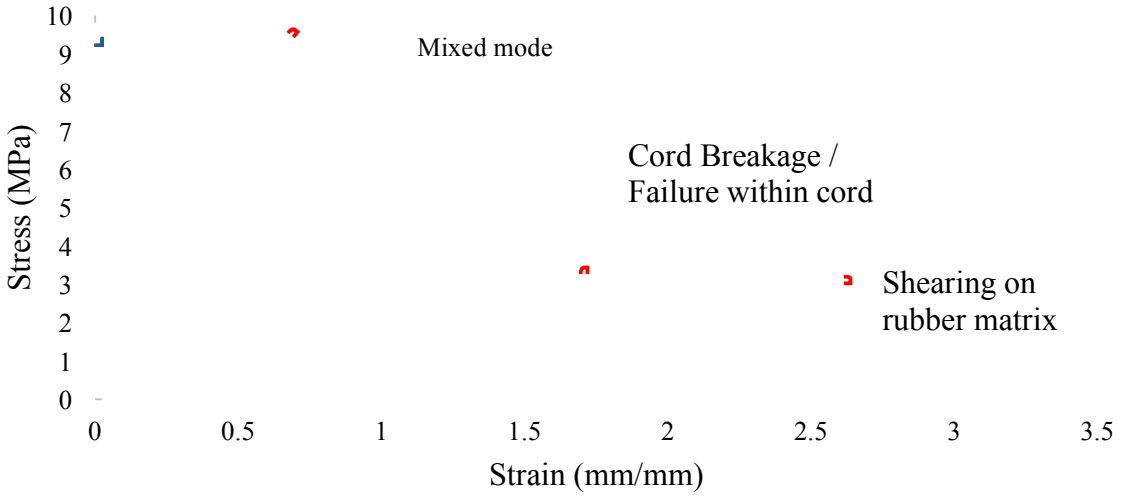


Figure 47. Stress Strain Curve of Single Layer

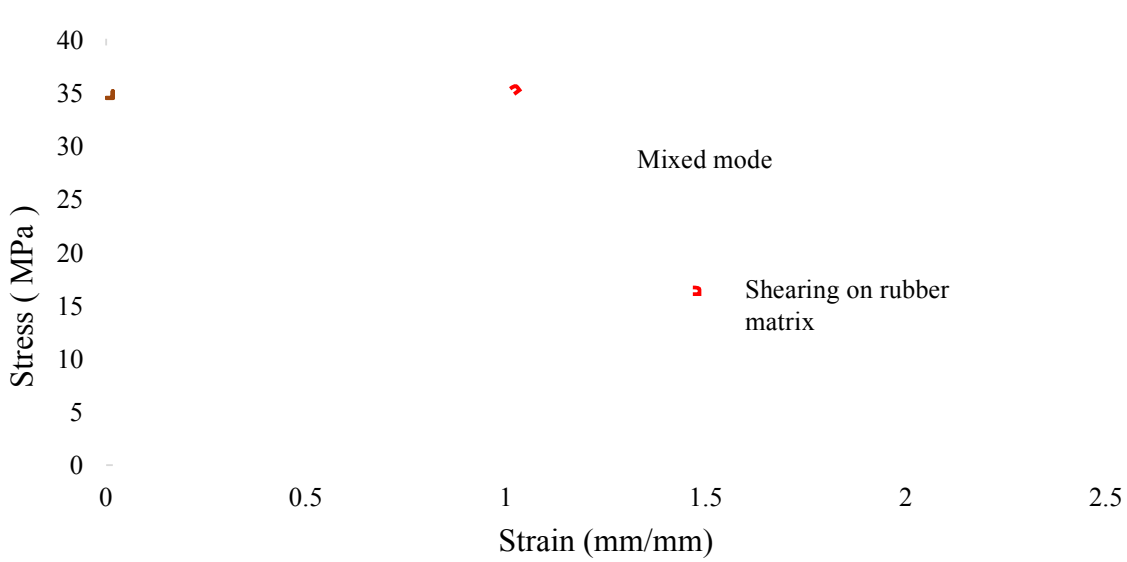


Figure 48. Stress Strain curve for double layer

3.3 Simulation Result

3.3.1 Parameter

The two parameters of the Mooney Rivlin model obtained from curve fitting are tabulated in Table 2. These material constants were applied in the software for numerical analysis. The double layer specimen showed higher material constants values in comparison to the material constants of the single layer specimen.

Table 25. Mooney Rivlin Parameter

Specimen	**Mooney Rivlin Strain Energy (MPa)**	**Potential Constants**
	C_{10}	C_{01}
Single layer	-1.6325	1.9742
Double layer	-3.2030	4.7658

3.3.2 Stress Strain Data from Simulation

In real application, a cord ply layer will never exceed deformation of 5mm when the tire is fully inflated. Therefore, both results illustrate the comparison of stress strain curve up to 10mm extension. Both graphs (Figure 14 and 15) show that experimental data (solid line) has higher strain value as compared to simulation results (dotted line). This phenomena is due to the slippage in between the specimen and the flange. This indicates that the clamping mechanism is not able to secure the rubber piece in place. This results in the specimen being pulled out from the flange when the indenter is moving downwards which causes excessive extension of the specimen.

A steeper slope is observed in the result of the double layer specimen as compared to single layer specimen. The steeper the slope indicates the tougher the material. This can be explained by the structure of the specimen. Unlike single layer specimen that the rubber matrix has space between two Nylon cords, the void between two Nylon cords in double layer specimen is supported by another direction of Nylon cord, therefore it results in requiring higher force from the indenter to punch through the specimen.

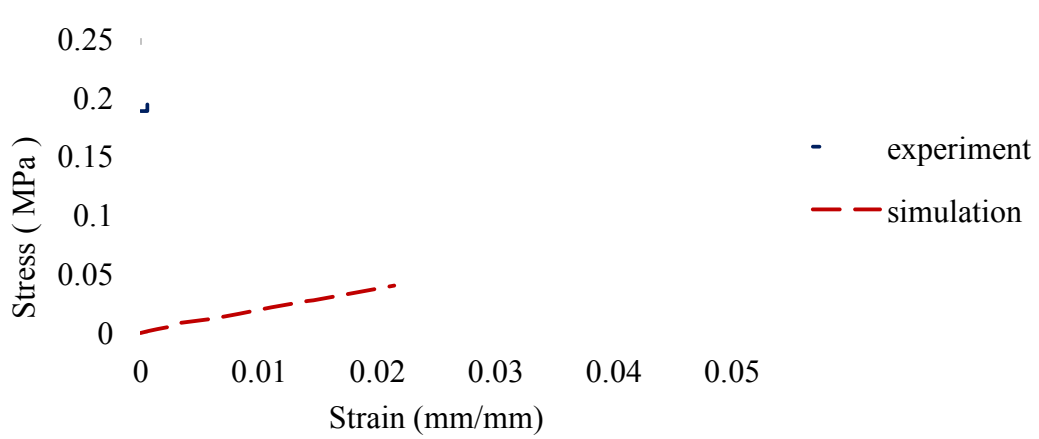


Figure 49. Initial stress strain stage of the single layer specimen

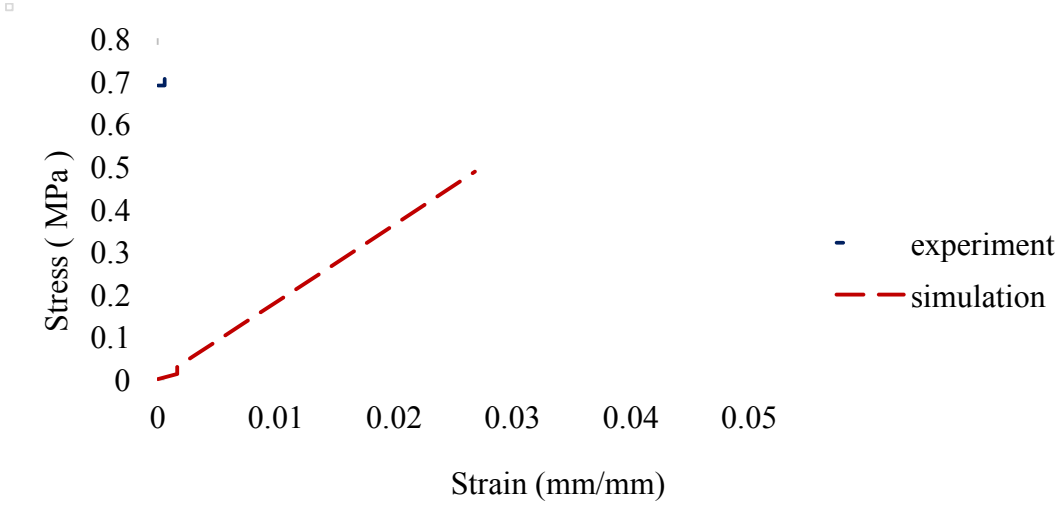


Figure 50. Initial stress strain stage of the double layer specimen.

4. Conclusion

By referring to the working principles of the Mullen Burst Test, the modification of a conventional biaxial loading has been carried out with an Instron universal testing machine. The setup showed some flaws such as slippage on the clamping region, but still proves that the experimental setup is suitable for observing the mechanical properties and the failure behavior of the cord ply layer. Others than the higher Young's modulus and maximum tensile strength observed from the double layer specimen, both specimens are generally similar in behavior. Both specimens typically display three deformation stages which are the initial nonlinear behavior with decreasing stiffness,

followed by the linear stress strain behavior and lastly, the nearly linear deformation with increasing stiffness. As the tensile load exceeds the limitation of the specimen, it leads to a zig zag decreasing stress strain behavior that is caused by four possible failure modes on the cord ply layer material. The four failure mechanism includes failure within the cord, cord breakage, shear failure of the interface between cord and fiber and mixed mode last two failure modes. Based on the comparison between experiment and simulation result, modifications of the proposed biaxial tensile testing is necessary to ensure the clamping mechanism can be function properly.

References

[1] A. Roslan, R. Sarani, H. H. Hashim, and N. Saniran, "Motorcycle ADSA Fact Sheet Vol. 2," Malaysian Inst. Road Saf. Res., vol. 2, no. December, pp. 1–4, 2011.
[2] B. Rodgers and W. Waddell, Tire Engineering, Fourth Edi. Elsevier Inc., 2013.
[3] M. Blundell and D. Harty, 5 - Tyre characteristics and modelling. 2004.
[4] P. Baranowski, J. Malachowski, and L. Mazurkiewicz, "Numerical and experimental testing of vehicle tyre under impulse loading conditions," Int. J. Mech. Sci., vol. 106, pp. 346–356, 2016.
[5] E. Mtcanique and M. Anisotropes, "Optimal design of biaxial testing specimen," vol. 41, 2000.
[6] I. Koutiri, D. Bellett, F. Morel, L. Augustins, and J. Adrien, "High cycle fatigue damage mechanisms in cast aluminium subject to complex loads," Int. J. Fatigue, vol. 47, pp. 44–57, 2013.
[7] C. Brugger, T. Palin-luc, P. Osmond, and M. Blanc, "A new ultrasonic fatigue testing device for biaxial bending in the gigacycle regime," Int. J. Fatigue, 2017.
[8] C. Galliot and R. H. Luchsinger, "Uniaxial and biaxial mechanical properties of ETFE foils," Polym. Test., vol. 30, no. 4, pp. 356–365, 2011.
[9] M. N. Charalambides, L. Wanigasooriya, and J. G. Williams, "Biaxial deformation of dough using the bubble inflation technique . I . Experimental," pp. 532–540, 2002.
[10] J. B. B. Launay, "A calculation of the shape of the alveograms of some rheological model substances." 2003.
[11] S. Rao, I. M. Daniel, and E. E. Gdoutos, "Mechanical properties and failure behavior of cord/rubber composites," Applied Composite Material, vol. 11, no. 6, pp. 353–375, 2004.
[12] J. Melorose, R. Perroy, and S. Careas, Mechanical testing of Advance fibre composites, vol. 1. 2015.

eureca 2017 – Conference Paper
Paper Number 2ME13

Finite Element Analysis on Human Spine Drawing

Melvin Mok Poh Chuen*, Cheah Kean How, Leong Wai Yie
Department of Mechanical Engineering
School of Engineering, Taylor's University, Malaysia.

melvinpohchuen.mok@sd.taylors.edu.my

Abstract
Finite element analysis is the analysis of the effect of an object under stress. Scoliosis is a disease that frequently occurs during childhood and adolescence stage. This disease will cause the spine of the patient to curve to one side, the deformed spine will greatly affect the daily life of the patient and more serious case of deformation of spine will even affect the functionality of the lungs and heart of the patient. Scoliosis can be either congenital where the patient suffers from this disease since birth or idiopathic where the disease arises spontaneously with the cause remains unknown. Scoliosis affects 2% of females and 0.5% of males, thus it is safe to say that scoliosis happens more frequently for female than male. As for the range of the age most scoliosis to happen is at the age of 9-15 years old. Besides that, people with family members with scoliosis have a higher chance of getting scoliosis as scoliosis is an inherited disease. The project aims to study the effect of conversion of files to the fine structure of the model. Other than that, this project also compares the results of FEA generate by different software using the same model. The FEA results obtained were validated with other results published by different researcher. The model generated will be evaluated based on the quality of meshing of the generated model and the numbers of element under the same meshing setup. The software for FEA is also evaluated based on the result generated that will be verified with the results of other researcher. The result obtained for generating spine model is the slicer software is capable of generating better fine structure model than the Invesalius 3.0 software. From the meshing of the model generated the number of elements obtained by Slicer is 38190 while the meshing of the model generated by InVesalius 3.0 consists of 30175 elements. The FEA results of strain and deformation generated by ANSYS and SolidWorks are relatively similar, for the force of 30N, the max deformation and max strain results generated by ANSYS is 3.2271x10^-8m and 5.8022x10^-7, while the result generated by SolidWorks is 4.2178x10^-8m and 2.907x10^-5.

Keywords: Finite element analysis, Scoliosis, Spine, Fine structure, Software

1. Introduction

Scoliosis is an abnormal curvature of spine that can be cause by birth defects, infections, tumors and various genetic conditions. This deformation of spine will cause the spine of the patient to curve more than 10 degrees, this abnormal curvature will results in many inconvenience in the daily life of the patient. Scoliosis affects 2% of the female and 0.5% of males, this research shows that scoliosis affect female more than male.

Finite Element Analysis is prediction of how an object will react to external element. Finite element is the isolation of an object into multiple element and formulas are applied on to each one of the element with the final solution to be the sum of the result of the entire individual element. The application of FEA on spine can be used to determine the effect on the spine when external element is applied on to the spine. To use FEA, a solid model have to be generated, for this study to generate the model, the DICOM files of a scoliosis patient is used to generate the model needed for the Finite element analysis.

This research focuses on the effect of the fine structure of model on FEA and the difference in the model generated by different software. The result of FEA will also be compared by using different software.

The reason that the scoliosis spine is used as the model of FEA is to obtain the result on the scoliosis, so that the result obtained can be used to evaluate the condition of the spine after surgery, the information can help the doctor to plan the treatment earlier and come out with a better treatment for the patient.

The technique used to compare the model result obtained the difference of the model obtained is by comparing the plan view of the model on certain layer, by comparing the quantity of element on each model can be used evaluate the quality of the model generated. The 2 plan view of the model generated by 2 separate software will be compare with the original DICOM files as the based. The 2 software used to generate the surface model from DICOM files is Invesalius 3.0 and Slicer, both of this software is capable to generate the solid model needed for the Finite Element Analysis, after the model is generated, the model is moved to solidworks for easier viewing.

The FEA analysis is done on 2 different software to compare the results generated, the 2 software is solidwork and ANSYS, the analysis result will be evaluated with similar result obtained by other researcher. The setting for the analysis is the spine will be set to be upright and the pressure applied on top of the spine, the stress and strain of the spine will be analyzed. Different types of methods are used for the analysis of the spine, M J Fagan, P.Lebrogne and W.Skali uses a 3D FE model of the spine of a scoliosis patient obtained through stereo radiographs according to Dansereau method. While the geometric characteristic of the spine is obtained from database following Guise method. With the model they obtained, they compare the lateral bending of the spine of the scoliosis patient against a healthy spine. The results shows that the healthy spine have better adequation of the model than the scoliosis spine. [1]

A. Rohmann, T.Zander did a FEA to study the scoliosis correction by orthotic and by surgical treatment. Their study include the analysis of the behavior of the spine

after the implant component is mounted on to the patient spine. They obtained the geometry of the spine model from CT scan preprocessed with MSC/PATRAN program to combine the image of the spine with the implant components, while the analysis of the combine model is undergone using program ABAQUS. [2]

S Julian and AM Mohsen work on finite element analysis on spine, and they model the whole human spine with just few element, the model they did include discs with shear and bending resistance, for this model they assumed the simple whole spine components were rigid bodies. Each vertebra is model using only one rigid element. The limitation of this method is that it will not produce accurate data as the model is too simple. Slight change in the reading will greatly affect the results of the analysis.[3]

N. Yoganandan, S. Kumaresan did a FEA on human lower cervical spine, the lower cervical spine from section C4 to C6 is used for this analysis, the model is made based on the CT scans. The CT scans is then digitized and processed using an edge-detection algorithm using NIH-image to determine the border of the of the actual CT image. A graphic software I-DEAS to convert the images to a geometric elements and for the analysis of the model, they chose to use NASTRAN program to analyses the behavior of the lower spine by applying force on to the model. [4]

V Divya and M Anuburajan work on the FEA of human lumbar spine by using the MIMICS to create the model of the lumbar spine using the image of the lumbar spine obtained from a CT scan, crop mask is used to manipulate the boundaries of the mask to fix the desired region, the entire spine is cropped and removed to focus on the lumbar spine. The 2D medical data image of the focus lumbar spine is then converted to surface mesh using MIMICS software. With the surface mesh obtained, the model is moved into ANSYS for the FEA analysis. This method manage to produce model with nice meshing, but if the same method is applied while using full spine as a model, the meshing of the model will take too long to generate for ANSYS.[5]

M.Alizadeh, J.Kashani work on a FEA on the spine to determine the influence of cancellous bone existence in human lumbar spine. For the modelling of the spine, they choose to use the CT dataset of a patient and the images obtained is import to MIMICS where it is convert to a 3D model, while the fixation used to mount on the spine is made using solidworks. The 3D model spine generated by MIMICS is then imported to solidworks and combined with the fixation model made. The assembly is then imported into CosmosWorks 2009 to undergo meshing and analysis. [6]

Young Kim and Ray Vanderby perform a FEA on human spine to analyze the effect of an innovative technology call interbody cage which allow the separation, stabilization and fusion of intervertebral bodies, they claim that this method is less invasive and will allow patient to recover faster. They model the human lumbar spine by using ABAQUS to compute the model of the cage, while the preprocess and post processing of the intervertebral spine is done by using ANSYS before converting it into ABAQUS file for analysis. [7]

2. Research Methodology

Based on the scope of this project, this research project is separated into 3 parts which is the conversion of the DICOM files to model files, model pre-processing and the FEA of the generated spine model. This section will discuss about the software used for each part and the configuration used for each analysis.

2.1 Conversion of DICOM files to model files

For this project, the solid model for analysis will be generated by using DICOM files. The DICOM files are obtained from Mr. Mohankumar Palaniswamy who is currently working on similar topic. The model chosen for analysis is the model of a spine of a scoliosis patient post operation, DICOM files generated using the CT-scan contained some noise due to the metal implant onto the spine, the DICOM file consists of 481 layers for the whole spine CT-scan. For converting DICOM files to solid model, the software used is Invesalius3.0 (version 3 released at 2015) and Slicer (version 4.6.2). The generated model of both softwares will be compared and evaluated to determine which software has bigger effect on the fine structure of the model.

The 481 layers of DICOM files takes a long time to be converted into solid model file, to reduce the time taken to convert the DICOM files and ease the process to produce the specific part needed for the analysis, instead of processing all 481 layers, the DICOM files for the specific part is isolated to be used to generate the model. In this project, the specific part is L1 to L4 part of the spine. Hence, layers 250 to 380 are isolated to be used to generate the model. After the model is generated on both the software, it is then converted into STL files. Figure 1 shows the Lumbar spine L1 to L5.



Figure 1. Lumbar Spine L1 to L5

2.2 FEA on Spine mode

For the comparison of the software used for FEA on the spine model, the software used is solidworks (version 2015) and ANSYS (version 18). The FEA perform is to generate the deformation and strain of the spine model when force is applied on to the spine. The setup for the force and fixed support of the spine model is shown in figure 2 and figure 3 respectively.

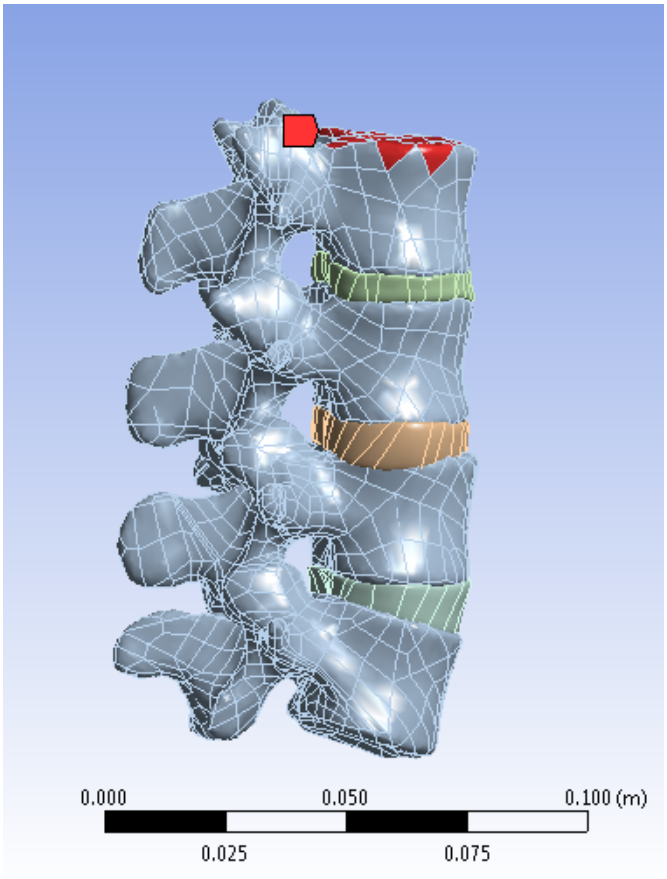


Figure 2. Force applied onto the spine model

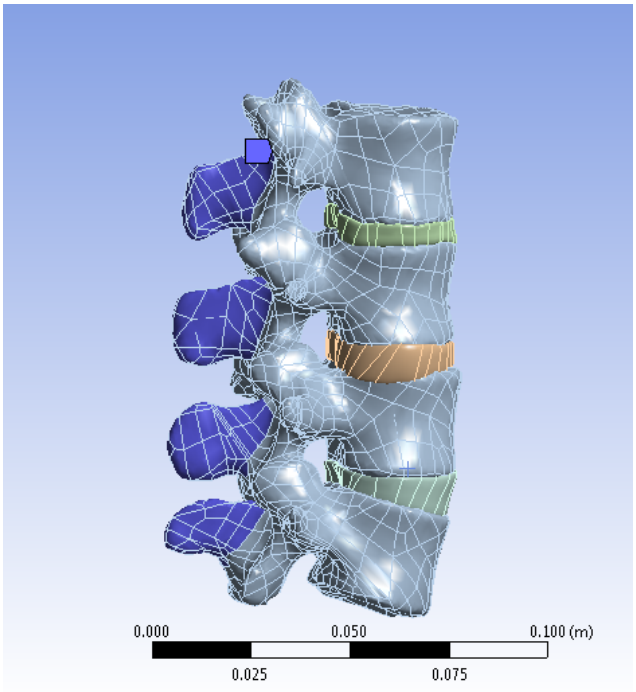


Figure 3. Fixed support of spine

The properties of the spine will be input into ANSYS to generate the result. Before running the analysis, the model have to undergo meshing, the sizing of the meshing is set to be 15mm and the mesh method used is the tetrahedron method. Figure 4 shows the meshing of the spine model generated.

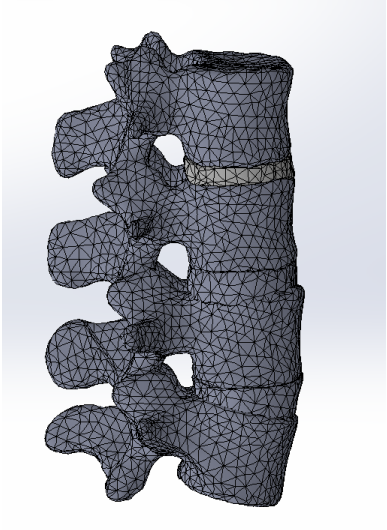


Figure 4. Meshing of spine model generated

3. Results and Discussion

This part will discuss about the difference in the model generated by 2 software and determine which software affects the fine structure more. Other than that, the results generated by ANSYS and solidworks will also be discussed.

3.1 Model Generated

The software used for converting DICOM files to solid model is Invesalius 3.0 and Slicer, the model generated by both softwares are shown in Figure 5 and Figure 6 respectively.



Figure 5. part model generated by Invesalius 3.0

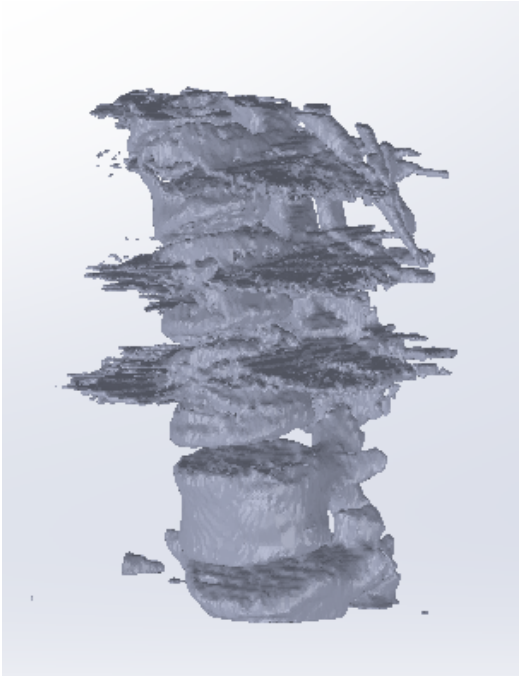


Figure 6. part model generated by Slicer

The model generated is then imported into ANSYS to undergo meshing. The type of meshing used is tetrahedron and at a sizing of 15mm. The result generated is shown in table 1.

Table 1. Results of meshing generated by ANSYS for both model

Software used	Numbers of element	Number of nodes	Skewness (min)	Element Quality (max)
Slicer 3D	38190	65504	7.337 x 10^-3	0.89
InVesalius 3.0	30175	59844	9.226x10^-3	0.76

From the results generated, we can conclude that the model generated by Slicer 3D have more numbers of element which suggested that the model of Slicer 3D have better details in model and manage to preserve a better fine structure during file conversion. Other than that, the model of Slicer 3D also manage to produce a better mesh quality than InVesalius 3.0.

3.2 FEA of spine model

FEA is apply on to the spine model by using both solidwork and ANSYS. For both software the setup for force and fixed support and the meshing method is the same. Figure 7 and 8 shows the image of FEA for deformation and strain generated by solidworks and ANSYS respectively.

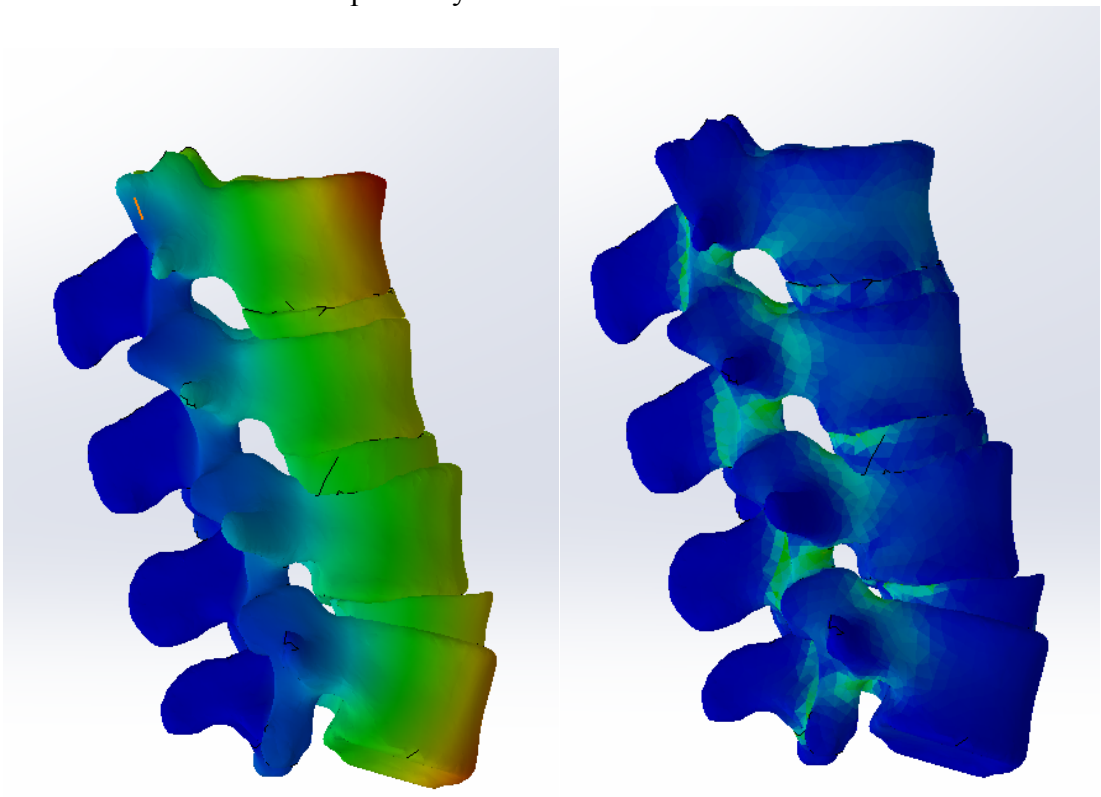


Figure 7: Image of FEA for deformation (left) and strain (right) generated by SolidWorks

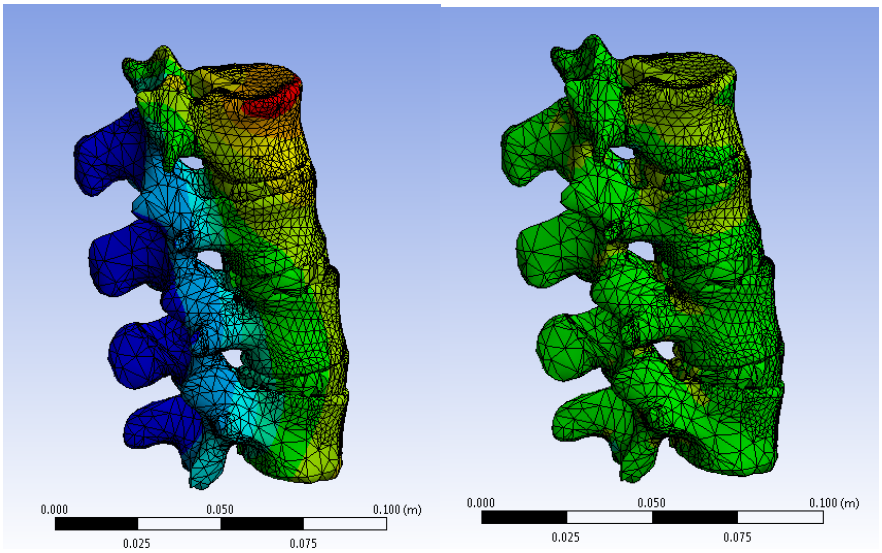


Figure 8: Image of FEA for deformation (left) and strain (right) generated by ANSYS

The total deformation and strain results obtained by ANSYS and Solidworks are shown in table 2 and 3 respectively.

Table 2: Total Deformation

Deformation	Solidworks		ANSYS	
Force	max	min	max	min
10 N	1.6547x10^-8m	0	1.0757x10^-8m	0
20N	2.7845x10^-8m	0	2.1514x10^-8m	0
30N	4.2178x10^-8m	0	3.2271x10^-8m	0

Table 3: Strain

Strain	Solidworks		ANSYS	
Force	max	min	max	min
10 N	9.689x10^-6	-1.4384x10^-7	1.9341x10^-7	-2.1814x10^-7
20N	1.938x10^-5	-2.6792x10^-7	3.8682x10^-7	-4.3629x10^-7
30N	2.907x10^-5	-4.5467x10^-7	5.8022x10^-7	-6.5443x10^-7

From the results obtained, we can concluded that the results generated by solidworks and ANSYS are very similar. The slight difference in the result might be generated by the difference in mathematical calculation or formula used.

4. Conclusion

The conclusion of this project is that the software Slicer can generate better model compare to the InVesalius software because Slicer have lot more module that can identify and separate the noise with the actual spine model.

The FEA results obtained from ANSYS and solidworks are similar as both software used the same input of data which is the same geometry model, the same mechanical properties the same force and fixed support applied and the same meshing method and sizing. This shows that both software uses similar formula and method to generate the data.

Through this project, I can conclude that the most important phase for generating an accurate FEA results are the model pre-processing phase, this phase is important because the quality of the refine model will directly affect the time taken for generating the result and also the accuracy of the results. The setup and meshing of the FEA phase also play a crucial parts in generating accurate result, as the smaller the mesh sizing, the higher number of element will be generated, hence resulting is a more accurate result.

5. References

[1] P.LeBorgne, W. Skalli, “Global Finite Element Model of the Spine Dedicated to Biomechanical Scoliosis Analysis”, 11th Conference of the ESB, July 8-11 98, Toulouse, France 1998.

[2] A. Rohlmann, T.Zander, “Flexible non-fusion scoliosis correction system reduce intervertebral rotation less than rigid implants and allow growth of the spine: a finite element analysis of different features of orthobiom”, European Spine Journal 17 issue 2 2008, pp. 218-223.

[3] M J Fagan, S Julian, A M Mohsen, “Finite element analysis in spine research”, Proceedings of the Institution of Mechanical Engineering Part H Journal of Engineering in Medicine Volume 216 issue 5 2002, pp. 281- 298.

[4] N. Yoganandan, S. Kumaresan, “Finite Elment Model of Huamn Lower Cervical Spine: Parametric Analysis of C4-C6 Unit”, Journal of Biomechanical Engineering Volume 119 issue 1 1997, pp. 87-92.

[5] V Divya, M Anburajan, “Finite Element Analysis of Human Lumbar Spine”, IEEE 2011 3rd International Conference on Electronics Computer Technology (ICECT)- Kanyakumari, India, pp. 350-354.

[6] M. Alizadeh, J. Kashini, “Influence of Cancellous Bone Existence in Human Lumbar Spine: A Finite Element Analysis”, [IFMBE Proceedings] 5th Kuala Lumpur International Conference on Biomedical Engineering 2011 V, pp. 439-442.

[7] Young Kim, Ray Vanderby, “Finite Element Analysis of Interbody Cages in a Human Lumber Spine”, Computer Methods in Biomechanics and Biomedical Engineering, 3:4, 257-272, 2011.

[8] A. Laville, S. Laporte, “Parametric and subject-specific finite element modelling of the lower cervical spine. Influence of geometrical parameters on the motion pattern.”, Journal of Biomechanics Volume 42 issue 10 2009, pp. 1409-1415.

[9] J. Paige Little, Clayton Adam, “Towards determining soft tissue properties for modelling spine surgery: current progress and challenges”, Medical and Biological Engineering and Computing Volume 50 issue 2 2012, pp. 199-209.

[10] F. Nabhani, M.Wake, “Computer modelling and stress analysis of the lumber spine”, Journal of Materials Processing Technology Volume 127 issue 1 2002. pp. 40-47.

eureca 2017 – Conference Paper
Paper Number 2ME14

Studying the Effect of Pitch Ratio on Sheet Cavitation in Marine Propellers

Mohamed Abdou*, Abdulkareem Al-Obaidi
Department of Mechanical Engineering,
School of Engineering, Taylor's University, Malaysia.

* *mohamed_ihab96@live.com*

Abstract
Cavitation is a phenomena that occurs when the pressure of a fluid drops below its saturated vapor pressure. Even though cavitation could be used in some applications in a beneficial way, it poses serious adverse effects in the marine propulsion field. The explosion of formed cavitation bubbles in the wake field of the propeller puts large stresses on the propellers blade causing blade erosion in the long term, costing the marine industry millions of dollars annually for maintenance. It also causes vibrations and noise in ships which are some effects propulsion system designers have to minimize during the propeller design stages. Non cavitating flow and cavitating flow are studied in the research, using a common CFD tool that uses the RANS approach. The effects of altering the pitch ratio on sheet cavitation is studied in cavitating flow using the INSEAN E779A propeller. The study used ANSYS Fluent for the simulation and only one blade is considered in the simulation. Periodic boundary conditions are applied for the 4 bladed propeller. The propeller is simulated in conditions set by the Wageningen worksop and the domain size is based on the cavitation tunnel size used in the measurements of the torque and thrust. The flows considered is uniform and has a speed of V = 5.808 m/s and propeller rotational speed n = 36.0 rps, advance coefficient J = 0.71; cavitating flow at cavitation number σ = 1.763. For the cavitating flow the Zwart-Gerber-Belamri cavitation model along with the k-ε turbulence model are used. Pitch ratios of 0.8, 1.0 and 1.5 are studied and the results showed an increase of the extent of sheet cavitation on the blade surface with an increase in pitch ratio.

Keywords: Cavitation, ANSYS Fluent, Numerical simulation.

1. Introduction

The shipping industry has always had a major role in the world trade, around 90% of the world trade is carried by the international shipping industry. This have had a large impact on the marine industry in terms of technological development and sustainability. This meant producing propulsion systems which are more economical and has a lesser impact on the environment. This drove propulsion system technologies into greater improvement and the introduction of new technologies which had a positive impact on performance including lesser use of fossil fuels, less noise and vibration which have had an impact on the marine life and also a better user comfort and safety. The technological surge in computational technologies have helped the marine propulsion industry in this improvement. As numerical simulations have replaced expensive and time consuming experimental testing with a constant improvement in accuracy and ease of use.

Propulsion efficiency is mainly judged based on the force output considering the work input by the engine. The force output is the thrust generated by the propeller, which is equivalent to the lift force in aerodynamics, and it is generated due to the difference in pressure between the suction side and the pressure side of a propeller blade. In addition to the thrust, torque is also an important factor considered in propulsion systems. Thrust and torque coefficients are calculated using the thrust and torque measurements and they describe the efficiency of a propulsion system.

Therefore designers seek to increase thrust and torque coefficients while reducing losses in operation caused by friction and cavitation. Cavitation bubbles form during the operation of marine propellers at a high RPM due to a drop in pressure. The drop in pressure puts the liquid under tension, which when reaches a tension high enough it causes nucleation and subsequently bubble formation [2]. These bubbles subsequently collapse and place a large amount of stress on the propeller blades, which has many detrimental effects including noise generation and a drop in performance displayed by a decrease in thrust and torque in addition to vibration. Many factors have a direct effect on cavitation and propeller performance which makes it a complex area to study. Propeller performance studies were always previously based on tow tank and cavitation tunnels results but due to the high costs of building such facilities and the improvement displayed in computational results the marine industry is moving towards computational simulations which is continuously improving its results accuracy and shortening the time taken in generating the simulation results.

Another factor that is very critical to be considered in propellers is the blade pitch ratio which is the ratio of the pitch to the diameter of the propeller. As pitch has a direct effect on thrust and torque generation it is very important for a designer to determine the most suitable pitch ratio in the design stage based on a number of factors.

Controllable pitch propellers are a relatively new propulsion system technology compared to the commonly used fixed pitch propellers that have been in use for hundreds of years. Most ships use fixed pitch propellers but in the recent years an increase in the use of controllable pitch propellers is seen. It has a number of advantages over fixed pitch propellers including generating a larger torque and thrust. It also enable ships to move both back and forth without a need to change the direction of rotation of the engine, which results in using a smaller engine subsequently resulting in a reduction

in cost. It also enables a faster change in ship speed as it stops the need to send a command to the marine engineer on board. Even though the ability to control the pitch of a propeller gives flexibility to the user in terms of thrust and speed control, it is important to understand the effects of change in pitch on the extent of the cavitation on blades, as to make sure the propeller has the longest usage lifespan and maximize rider comfort in ships.

The objective of the study is to find the relationship between pitch ratio and cavitation formation on propellers blades. This will enable controllable pitch propellers designers to find the optimal range of the pitch ratio for the propellers. Possibly increasing usage life and enhancing propellers performance. Three different pitch ratios were used in the study including pitch ratios of 0.8, 1.1 and 1.5. Prior to studying the cavitating flow of the propellers, non cavitating flow was simulated and compared to the experimental results to ensure accurate simulations.

2. Research Methodology

ANSYS Fluent CFD software was used in the simulations presented in the following paper. The INSEAN E779A propeller model was used the study, and only one blade was considered for the simulation. The case presented is a low Reynold number turbulence, cavitating flow. The k-ε turbulence model was used along with the Zwart Gembali cavitation model.

2.1 Geometry

The INSEAN E779A propeller was selected as reference for the study. Due to the wide availability of tests and research performed at INSEAN over the last decade. Description of the INSEAN E779A experimental data is done by Pereira et al. in a paper in early 2004 [2] and one later in the same year [3].

The INSEAN E779A propeller is a four blade, right handed, fixed pitch propeller with a diameter of 0.227m and a fairly small rake and skew angle. It has a constant pitch ratio of 1.1 along the blade diameter. Fig. 1 shows the INSEAN E779A propeller.

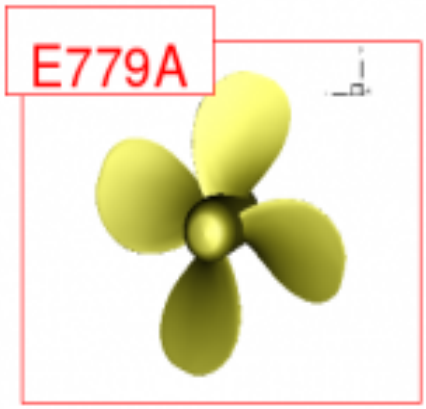


Figure 1. INSEAN E799A Propeller [3]

The propeller specifications are listed in Table 1.

Table 1. INSEAN E779A propeller specifications

	E779A
Blades	4
P/D	1.10
Skew	4.5
A_p/A_0	0.69
Diameter (mm)	227.27

Prior to the simulations, the geometry of the propeller was modified. These modifications included simplifications, drawing of the fluid domain and changing the pitch of the propeller. In order to reduce the computational duration and resources only one blade was considered in the simulation and periodic boundary conditions were applied. The domain size was based on the domain size proposed in the Wageningen Workshop in 2007 [4]. The ideal tunnel size that is used as the fluid domain in the simulation is shown in Fig. 2. Where R_{tun} =1.471 D, where D is the diameter of the propeller.

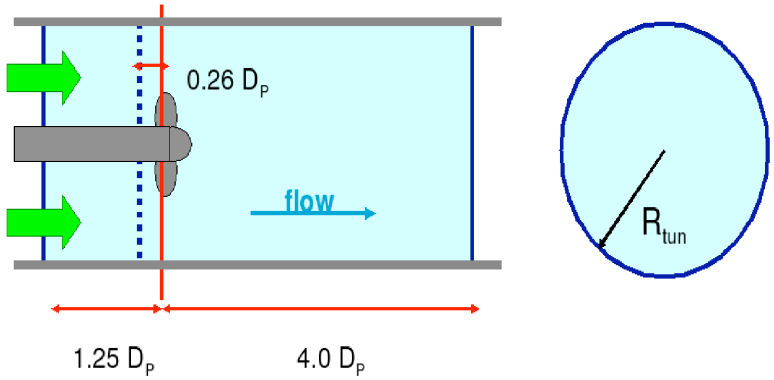


Figure 2. Idealized tunnel size [5]

2.2 Mesh

Since only one blade was used in the simulation the domain cylinder was divided by 4 and the simulated domain was only a 90^o section. This reduced the element count by 4 times. An unstructured grid was used for the simulation using the default mesh interface for ANSYS Fluent. The domain consisted approximately of 700000 elements compared to more than 2 million elements in a full cylindrical domain. The elements had an average skewness of 0.28 with a maximum skewness value kept below 0.85 in order to ensure accurate results generation. The mesh mainly consists of tetrahedrons with a small percentage of wedges used in the inflation around the blade surface. The inflation was applied around the blade in order to capture the boundary flows more accurately around the blade tip. 10 layers of inflation was used with a growth rate of 1.4. In addition to that proximity and curvature based meshing was used to automatically set the element size around hard curves and thin edges. The mesh of the blade and domain is shown in Fig. 3.

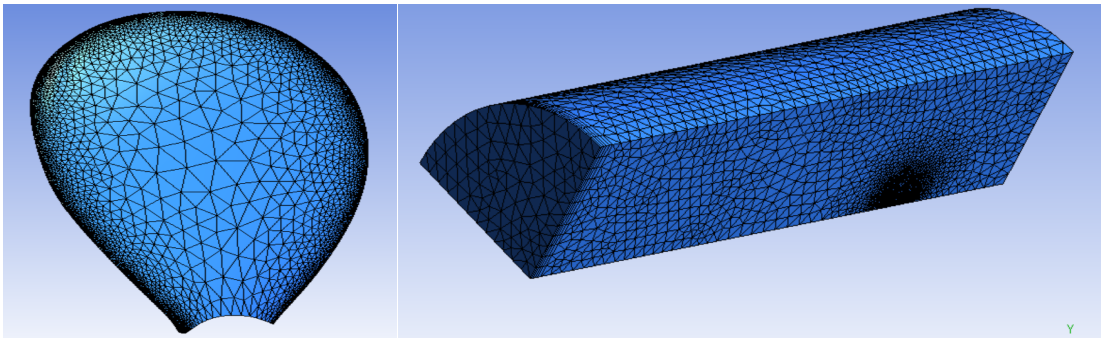


Figure 3. Mesh for blade and domain.

2.3 Numerical Setup

Initially non cavitating flow is considered and compared to the benchmark results database of the INSEAN E799A propeller. After the results had an acceptable accuracy comparing it to the experimental results, cavitating flow was considered and the vapor fraction on the blade surface was shown.

For a given advance coefficient J, defined in Eq. (1) below;

$$J = \frac{U}{nD} \tag{1}$$

where U is the advance speed, n is the rotational speed of the propeller, and D is the diameter of the propeller.

A specific cavitating flow was applied according to the flow cavitation number defined in Eq. (2).

$$\sigma_n = \frac{P - P_V}{0.5\rho_L(nD)^2} \tag{2}$$

where P is the outlet pressure, P_V is the vapor pressure and ρ_L is the density of the liquid.

The flows considered is uniform and has a speed of V = 5.808 m/s and propeller rotational speed n = 36.0 rps, advance coefficient J = 0.71; cavitating flow at cavitation number σ = 1.763. The flow conditions were based on the reference benchmark databse conditions set at the Wageningen 2007 Workshop [4].

The flow is considered a steady turbulent flow. Realizable k-ε turbulence model was used, with standard wall function which is a common turbulence model shown to give accurate results for cavitating flows along with the k-ω turbulence model. A turbulence intensity of 2% and a turbulence viscosity ratio of 10 is used in the computation which were also specified in the Wageningen Workshop along with the tunnel size. Zwart gembali cavitation model was used in calculating the cavitating flow as it was shown to give reliable results in a study by Heinke H. in 2011. [6]

The factors considered were the thrust and torque generated by the propeller. The thrust and torque coefficients were calculated using Eq. (3), and Eq. (4) respectively and compared with the experimental data.

$$K_T = \frac{\mathrm{T}}{\rho \mathrm{n}^2 \mathrm{D}^4} \tag{3}$$

$$K_Q = \frac{Q}{\rho n^2 D^5} \tag{4}$$

where
T is the thrust
Q is torque.

For the non cavitating flow the solver used was SIMPLE, with the standard pressure solver and the second order upwind for the turbulence factors and momentum. As for the cavitating flow the solver used was COUPLED, with PRESTO pressure solver and second order upwind for turbulence and momentum. Due to the quick nature of cavitation formation, a very small time step had to be used for the simulation or else divergence occurs. After multiple trials with the most suitable time step, a time step of 0.00002 was used, as a time step larger than that caused a divergence.

2.3.1 Parametric Study

Following the verification of the accuracy of the flow using both cavitating and non cavitating flow. The effect of pitch on cavitation on the propeller blade surface was considered. The effect of pitch on thrust and torque generation have been thoroughly studied in the past decade and their relationship is shown in Fig. 4.

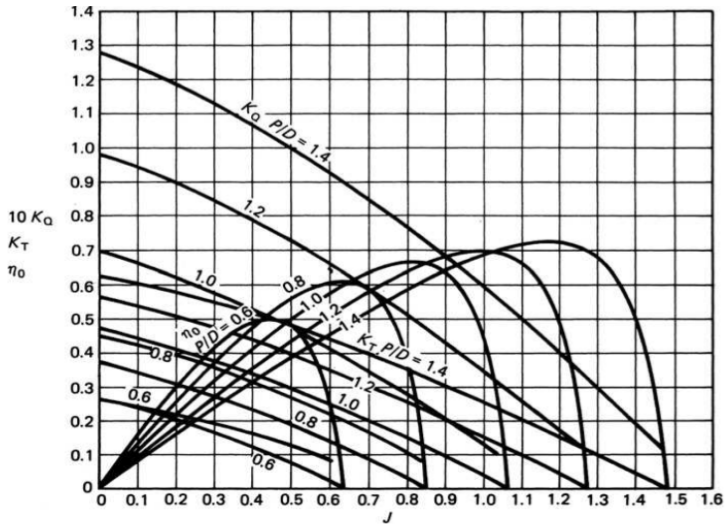


Figure 4. Open water diagram for wageningen propeller [7]

It is seen that with an increase in pitch ratio, there is an increase in both thrust and torque coefficients and subsequently an increase in torque and thrust. But on the other hand, the extent of the formation of cavitation bubbles on the blade surface is not well studied and therefore the detrimental effects of cavitation on the propeller at higher pitch ratios is not known. With the increase in use of controllable pitch propellers it is necessary to know the optimal operating pitch ratios for both thrust and torque generation along with the minimal cavitation in order to enhance the operation of a propulsion system.

Three different pitch ratios are considered in the study, including a pitch ratio of 0.8, 1.1 and 1.5. The following pitch ratios were chosen based on the advance coefficient used in the study. The study wanted to consider the minumum and maximum pitch ratios that could be used at the following advance coefficient. As seen in Fig. 4 at a pitch ratio lower than 0.8 the thrust and torque coefficients are nearly equal to zero and at a pitch ratio of 1.4 torque measurements start increasing which causes a drop in a propellers efficiency, therefore the maximum pitch was not recommended to be 10% higher than 1.4. The thrust and torque coefficient is calculated for the three cases and the extent of the cavitation on the blade surface is visually observed.

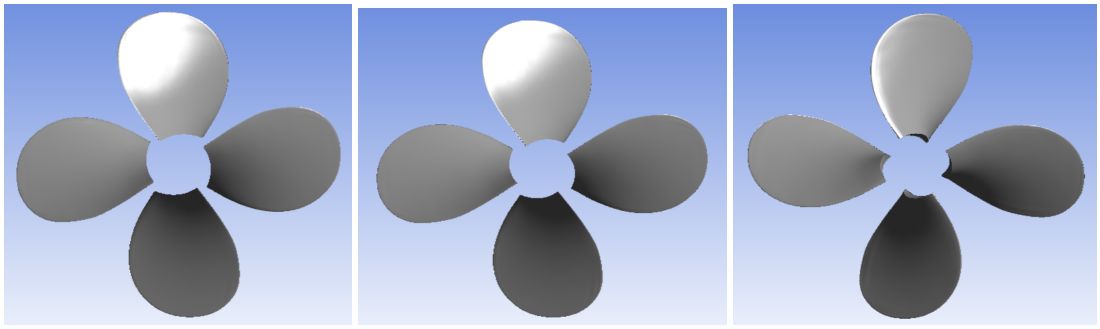


Figure 5. Pitch ratios used in the study

Additional factors could be considered in the study in the future including varying the rake and skew angles and studying their effect on thrust and torque generation along with cavitation formation.

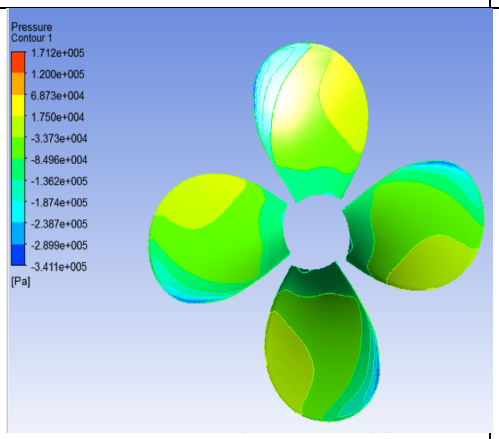
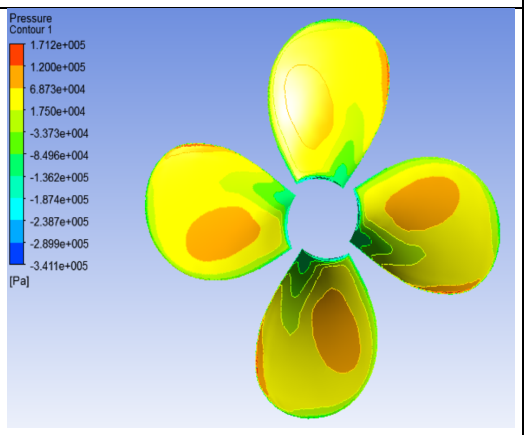
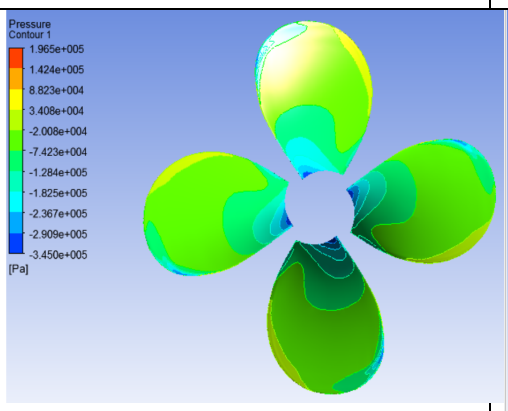
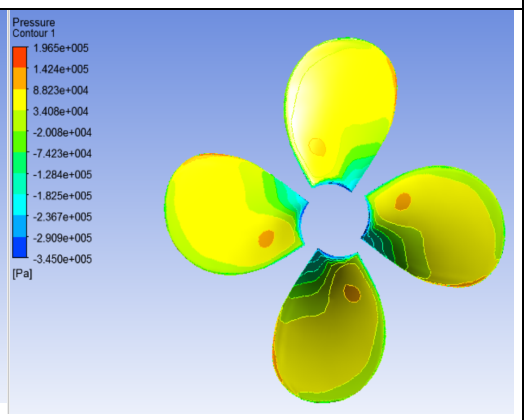
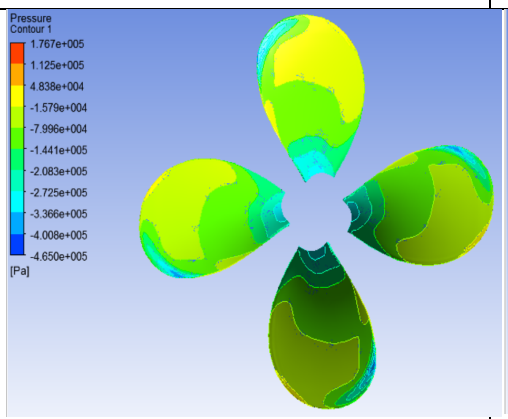
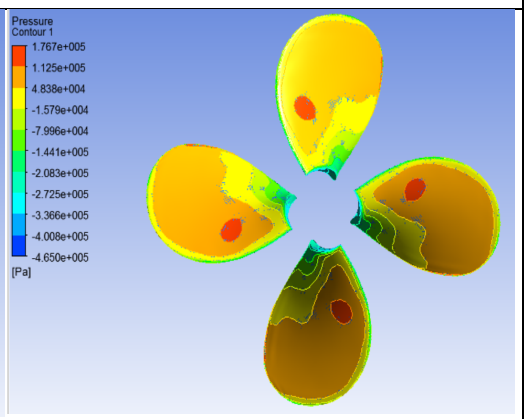
3. Results and discussions

3.1 Uniform Non cavitating flow

In order to ensure correct simulation setup and accurate results a uniform non cavitating flow was done prior to completing the parametric study. The flow conditions specified in the Wageningen Workshop was applied and results were compared to the results published by Subhas in 2012 [8]. Results also published by Watanabe, 2003 was used for reference. [9]

Only one blade was modeled in a 90^{o} periodic domain, in order to reduce the computational time. In order to view the four blades, 4 graphical instances were set up to complete the 4 blades of the propeller. The pressure contours of the blade surface suction and pressure sides were set up and the torque and thrust generated were calculated using ANSYS CFD POST. Subsequently the thrust and torque coefficients were calculated and compared to the experimental results. The pressure contours of the 3 pitch ratios of 0.8, 1.0 and 1.5 are shown in Table 2.

Table 2. Pressure contours of different pitch ratios

Pitch Ratio	Suction side	Pressure side
0.8		
1.1		
1.5		

As shown by the pressure contours results, as the pitch ratio increases, there is an increase in pressure on the blade surfaces. This is seen in the pressure distribution on the blade. At a pitch ratio of 0.8 and 1.1 it is seen that the pressure is highest towards the tip of the blade which slightly moves inwards towards the blade surface with an

increase in the pitch ratio. This is due to the increase in area of the blade surface that is in contact with the fluid. This increase in pressure on the pressure side creates an increase in the generated thrust and torque as calculated in Table 3.

Table 3. Calculated torque and thrust values

Pitch Ratio	Thrust (N)	Torque (N.m)
0.8	612.31	20.82
1.1	760.48	34.67
1.5	832.66	43.73

The thrust and torque coefficients were then calculated and compared to the experimental results of the INSEAN E779A propeller which has a pitch ratio of 1.1. The results are listed in Table 4 below.

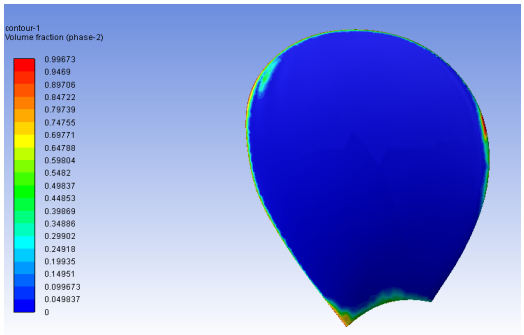
Table 4. Comparison between calculated and experimental K_T and K_Q values

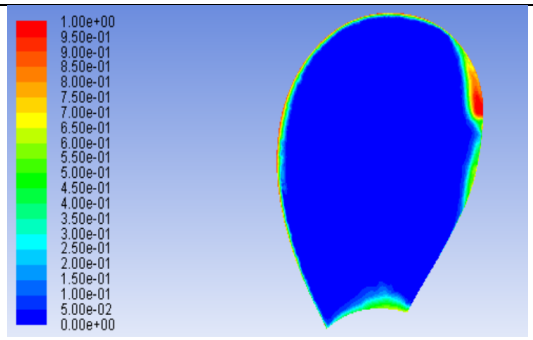
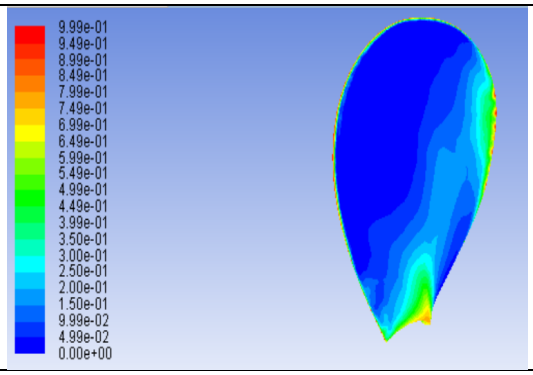
Coefficients	Measured (tunnel)	Calculated (Simulation)	Percentage difference (%)
K_T	0.256	0.221	13.67
K_Q	0.464	0.445	4.09

3.2 Cavitating flow

Uniform Cavitating flow using the same conditions as the non cavitating flow was simulated in order to find the relationship between pitch ratio and cavitation area on the blade surface. Three pitch ratios were used including a pitch ratio of 0.8, 1.1 and 1.5. The vapor formation on the blade surface is shown in Table 5.

Table 5 Cavitation formation on the blade with different pressure ratios

Pitch ratio	Blade contours
0.8	

1.1	
1.5	

The results in Table 5 shows that as the pitch ratio increases, sheet cavitation on the blade surface increases. This is caused by the increased pressure difference between the suction and the pressure sides of the blade. As the pressure difference increases the negative pressures that build up on the suction side increases causing the formation of bubbles on the suction side and therefore an increase in cavitation. Which could lead to adding large loads on the blade surface leading to blade erosion in the long term usage.

Despite the positive effects the pitch ratio has on torque and thrust generation, it also increases deteriorative effects such as cavitation and blade contact area with the water which increases friction and causes losses in the work input, therefore causing a drop in propulsion efficiency. Therefore in order for a propeller designer to choose an optimum propeller pitch, those number of factors have to be taken into consideration.

4. Conclusion

The effect the pitch ratio has on sheet cavitation in marine propellers was studied. Both non cavitating and cavitating flow were simulated using the same conditions previously set in the Wageningen in 2007. The pitch ratios that were used in the study were 0.8, 1.0 and 1.5. Initially the non cavitating flow was used to ensure the accuracy of the simulations and the torque and thrust for the different pitch ratios were measured using ANSYS Fluent. The thrust and torque coefficients were then calculated and the results showed a difference between measured and calculated torque and thrust coefficients that were within acceptable range.

The cavitating flow used the same pitch ratios used in the study, with the Zwart Gerber Gembali cavitation model used in the simulation. The results of the cavitation on the blade surface showed that as the pitch ratio increased the cavitation formation on the blade increased significantly.

References

[1] Brennen, C.E., “An Introduction to Cavitation Fundamentals” *WIMRC Forum*, University of Warwick, UK, pp. 1–17, 2011.

[2] Salvatore, F., Pereira, F., Felli, M., Calcagni, D., Di Felice. “Description of the INSEAN E779A Propeller Experimental Dataset*”. Technical Report INSEAN 206-085*, Rome, Italy, 2006.

[3] Pereira, F., Salvatore, F., Di Felice, F., Soave M., “Experimental Investigation of a Cavitating Propeller in Non-Uniform Inflow” *Proceedings of the twenty-fifth ONR Symposium on Naval Hydrodynamics*, St. John's, Newfoundland, Canada, 2004.

[4] Streckwall, H., Salvatore, F., “Results from the Wageningen 2007 Workshop on Propeller Open Water Calculations Including Cavitation” *Proceedings of the RINA Symposium on CFD Models*, London, UK, 2008.

[5] Salvatore F., Streckwall H. and van Terwisga T., “Propeller Cavitation Modelling by CFD - Results from the VIRTUE 2008 Rome Workshop ,” *First International Symposium on Marine Propulsors,* Trondheim, Norway, Jun. 2009.

[6] Heinke, H. J., “Potsdam Propeller Test Case (PPTC), Cavitation Tests with the Model Propeller VP1304,” Schiffbau-Versuchsanstalt, Potsdam, Report 3753, Apr. 2011.

[7] Carlton, J. S., *Marine propellers and propulsion*. Burlington: Butterworth-Heinemann Second Edi. 2007. pp. 11-219.

[8] Subhas S., Saji V. F., Ramakrishna S. “CFD Analysis of a Propeller Flow and Cavitation” *International Journal of Computer Applications,* vol. 55, no. 16, Oct. 2012.

[9] Watanabe T., Kawamura T., Takekoshi Y., Maeda M. and Rhee S. “Simulation of Steady and Unsteady Cavitation on a Marine Propeller Using a RANS CFD Code ” *Fifth International Symposium on Cavitation,* Osaka, Japan, Nov. 2003.

eureca 2017 – Conference Paper
Paper Number 2ME15

Reduction of Local Pressure Loss at 90° Bend Using Swirl Generator

Mohanad Mohammed Bajunaid, Abdulkareem Sh.Mahdi Al-Obaidi , Chong Chien Hwa
School of Engineering, Taylor's University, Malaysia.

* *Abdulkareem.Mahdi@taylors.edu.my*

Abstract
The piping network system has been implemented in houses, buildings, and industries so it is important to increase the efficiency of this system. This paper illustrates the concept of improving the piping network system by reducing the pressure loss in 90° bend. Losses are the main problems for piping as it consumes energy and increase the cost and among these losses is the pressure loss inside 90° bend which occurs due to the pressure eddies that happen inside the pipe. These pressure eddies happen due to change of direction of the fluid flow. Swirl flow is the fluid rotates around an axis that is in the same direction of flow and produces the vortex. In this project, a swirl flow generation will be used to reduce the pressure loss in **90°** bends. There are several types of swirl generation such as rotating pipe, tangential, guided swirler and axial swirler. The guided swirler technique is used to evaluate the effectiveness of axial swirler in experiment setup that have been built and used. an guided swirl generator is used to generate the swirl flow and pump the fluid in the **90°** bends as well. The purpose of conducting experiment to assess effectiveness of the swirl flow in reducing the pressure loss in **90°** bend. Based on the results obtained that the swirl generator with 60° angel is reducing the pressure loss in **90°** bend the most.

Keywords: Pressure loss, 90° bend, Swil flow generation, guided swirler technique

1. Introduction

Fluid is a substance that has no specific shape and is able to flow under applied shear stress such as liquid and gas. The science that studies behavior of fluid in stationary (statics) or moving (dynamics) is called fluid mechanics.

As this science deals with flowing fluid, there is a classification for fluid as well as the flow. Compressibility is one of the classifications of fluid which means the changing in density when the working medium flowing. Viscosity is another classification of fluid, which is a quantitative measure of fluid's resistance. This means if the fluid is less viscous, the fluid will flow faster. On the other hand, there are two different types of flows which are laminar and turbulent. Laminar flow is a flow where the particles of fluid are moving smoothly at low velocity and turbulent flow is flow where the particles are not moving in a line and have random velocities. The type of flows can be determined by a dimensionless number the Reynolds number which describes the properties of flow of viscous fluid for a flow in pipes. If Reynolds number is less than 2100, it is considered as laminar flow however if it is greater than 4000, it is considered as turbulent flow. If the Reynolds number is between 2100 and 4000, the flow called a transitional flow with development of society, piping system is extremely important field as it is available in the houses, industries, and building and used for different purposes such as continues transportation of product, materials or medium from one process to another. Therefore, a total understanding of the details of piping system is needed. The main problem that reduces the efficiency of this system are the losses that happen inside the pipe. The accurate prediction of the losses across the piping system is in relation with choosing the accurate pump. In other words, the calculations of the losses in the pipe system are the initial steps for choosing the most suitable pump. Purchasing a pump without calculating the losses will lead to a failure in providing water for the whole piping system due to less energy supply by the pump which result in loss of money and buying a powerful pump when having a small amount of losses compared to pump's power will result in energy consuming and increase unnecessary cost. There are two different types of losses; major losses and minor losses. Major losses happen due to viscosity and the roughness of the inner walls of the pipes which produce friction that decreases the pressure along the pipe (pressure loss). Minor losses occur due to different fittings such as valves, elbows or changing in the pipe circuit. Generally, we have the head loss, energy loss, and pressure loss.

Pipe Fitting is utilized as a part of pipe frameworks to interface straight pipe and adjusted to various sizes or shapes and for different purposes, for example, controlling the flowing fluids. Fittings are used in different systems like HVAC and manufacturing. There are several types of fittings that used in pipe network systems such as valve, bends. 90° bends in pipe network aims to change the flow direction of the fluid. However, this changing in direction results in producing a separation in flow and a pressure loss in the pipe [1].

Based on Dutta et al. [2], when the fluid flows in a curved path, the fluid experiences a centripetal force which means that the fluid has force vector acted toward the center of that circle. As result of the centripetal force, the fluid at the center of the pipe moved toward the outer wall and came back toward the inner wall. This means the pressure would increase at the outer wall of the bend and reduced at the inner wall, therefore, the fluid would experience an adverse pressure gradient. In addition, the fluid particles

in this region have low velocities and could not defeat the adverse pressure gradient which resulted in a separation of flow from the boundary and pair of counter-rotating vortices. These rotating vortices led to a loss of energy and increase pressure loss. There are several methods used to reduce the pressure drop in bends.

Beij et al. [3] tested nine pipe bends that have the same diameter but different curvature radius. The author took the relative radius of each pipe bends at the same fluid, surface roughness, and viscosity. The relative radius defined as the radius of curvature divided by the diameter of the pipe. The results show that when the relative radius increases, the pressure loss coefficient (ξ) decreases which result in decreasing the total pressure loss according to the formula of the pressure loss.

Another method that can be used to reduce the pressure loss is swirl flow. Based on S.Sujoy [4] swirl flow described as the fluid rotates around an axis that is in the same direction of flow and produces the vortex. "Physically, the swirl flow is a conservation of angular momentum results in the creation of a free vortex flow in which circumferential velocity increases as the radius decreases". Mixing, separation, and stabilization are several industrial processes that swirl flow is used to approach it.

In Chen et al. [5] mentioned that there are several ways to produce swirling flow. The first method was the rotating pipe (Taylor coquette flow) where either the inner and outer pipes or one of them rotated to generate a swirler flow. Tavener et al. [6] had conducted an experiment and numerical study of the rotating pipe by rotating the inner cylinder and the swirl flow was produced. The result showed that the rotational speed (ω) would determine the Reynolds number of the swirling flow. The second method was tangential where the fluid injected from the top of the pipe and went in the circular motion between the inner and outer diameter of the pipe. Neto et al. [7] have investigated the tangential inlets method to produce swirler flow. The advantage of this method was it is an economical way to generate swirl flow, on the other hand, the disadvantage was the decay of swirling flow that will appear due to lack of active source to sustain the swirl along the flow path. The third method was guided swirler where the swirl flow was produced by a coil that attached to the inner diameter along the flow path not only in the inlet. Sivashanmugan and Suresh. [8] tested this method by using helical screwtape and the swirl was produced. The outcomes showed that guided swirler consumed more power source than other swirler. The fourth method was axial or radial swirler where the fan or propeller was placed at the inlet and produce the swirl flow in ducts. Yilmaz et al. [9] have tested this method and concluded that the swirl momentum would decrease along the flow path until flow one-dimensional axial flow, however, axial swirler could produce flows with high swirl numbers and nonintrusive.

Moreover, Zhang et al. [10] investigated the pressure drop effect of turning vanes in 90° duct elbow. A numerical investigation was done at $1x10^5$ Reynold number(R) for air duct with a diameter of 5 cm and curvature radius ratio of 1.5. The length of the inlet duct before the elbow was 5 cm and the outlet duct length of the duct was 10 cm. In addition, the guided vanes that were used in this experiment has an angle of 60 degree. k-epsilon (k-ε) turbulence model chose for this study with second order upwind differences scheme and the pressure and velocity was solved by using SIMPLEC algorithm. The experiment started by testing the normal flow without the guided vanes in the 90° duct elbow then testing the swirl flow that generated by the guiding vanes. From Figure 1and 2, it was observed that the pressure at the outer wall

of the elbow of the duct has the highest pressure in the elbow and the inner wall has the lowest pressure. Also, there was a massive decreasing in the velocity at the outer and inner wall of the. However, when the guided vane was placed at the inlet of the pipe, the pressure at the outer wall reduced and increased at the inner wall. In addition, the velocity at the outer wall is the same as the velocity of the flow before entering the elbow but the velocity still less at the inner wall. According to Moujaes et al. [11] the reason that velocity at the inner wall was reduced to almost to zero is due to the velocity changing its direction rapidly when it enters the elbow which results in a sudden impact at outer wall and secondary motion occur.

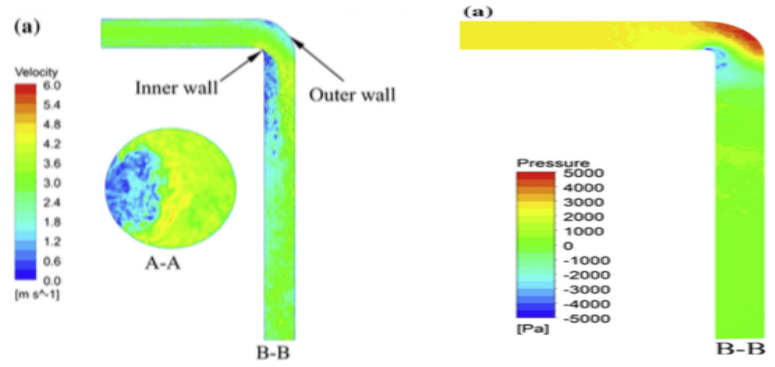


Figure 1. Velocity & pressure distribution on the elbow without the guided vane [22].

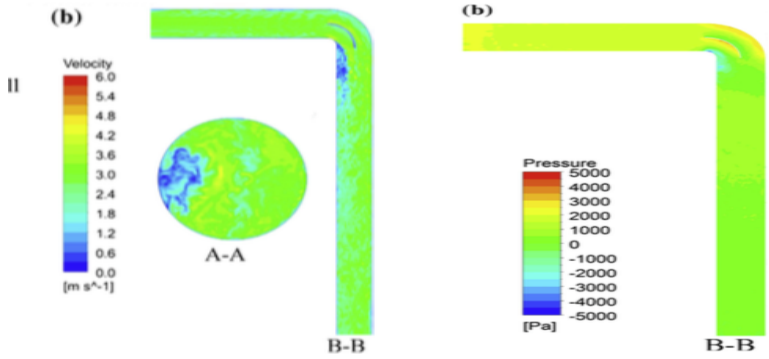


Figure2. Velocity & pressure distribution on the elbow with the guided vanes [10].

The aim of this paper is to reduce the local pressure loss at 90° bend using swirl generator. First, a study of how the 90° bend affect the pressure will conducted by understanding the fluid mechanics and piping system by doing experimental analysis. The design of the experiment setup and the swirl generator will be designed in software to be visualized. Then the swirl generator will be 3D printed and experimental setup will be build. The research parameters considered in this research were static temperature and no bubbles formation in the pipes during flow.

2. Research methodology

In this section, the producer that has been used to conduct the research will be discussed and justified.

2.1 Geometry Modeling

the experiment setup was designed in the Solidworks software with dimensions shown in table 1 to visualize it and have a clear idea about it as shown in figure 1

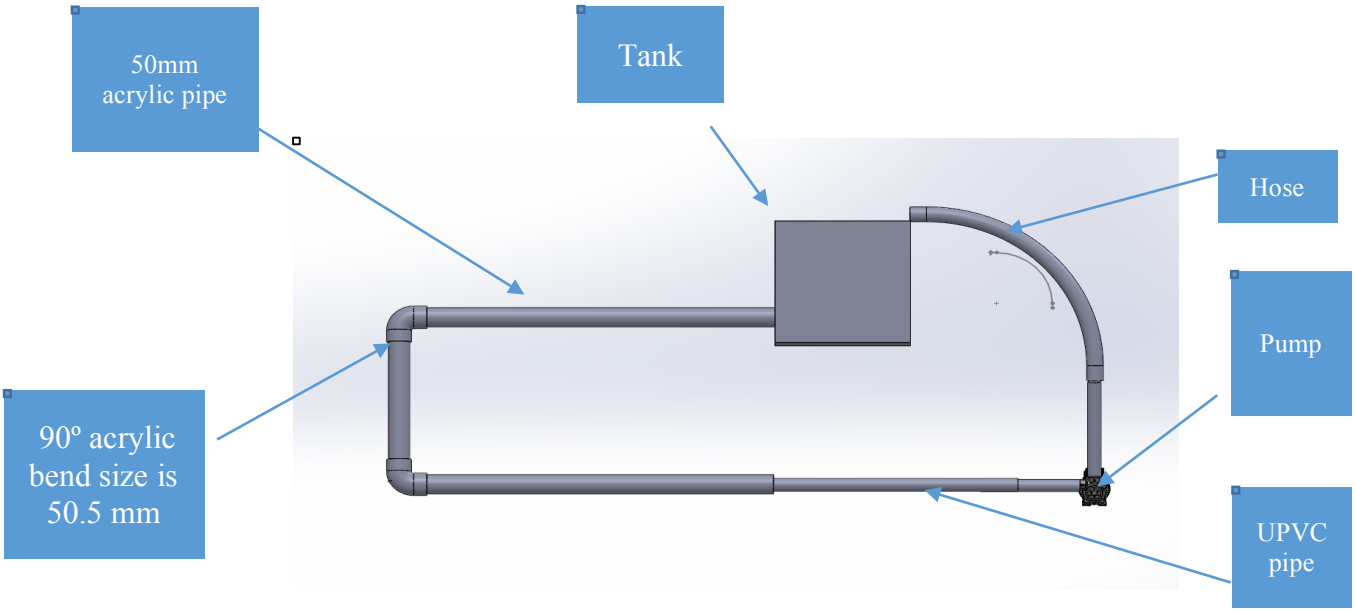


Figure 3. 3D model of the experiment setup

The setup consists of one tanks with capacity of 0.0687 m^3 at constant temperature.it used to store the flow that comes from the system and resupply it again to the system at constant temperature 20°. The tank is connected to 1000mm long acrylic pipe with outer diameter of 50mm and inner diameter of 46mm this connected to 90º bend. The 90º acrylic bend size is 50.5 mm and has curvature radius of 30mm and width and length of 15mm.the outlet of the bend is connected to another acrylic pipe with length of 30mm and it is connected to 90º bend with the same dimensions as the previous bend. At the outlet of the bend, 1000mm acrylic pipe is connected and it connected to UPVC pipe with dimeter of 38mm and length of 50mm. then the UPVC is connected to PPR pipe with diameter of 34mm with length of 50mm.Next, the PPR is connected to pump has volume flow rate (**Q**) capacity of 60 $^{l}/_{s}$ and pressure of 4 bar max and power of 650w max. the pump is connected to a tube with 20mm diameter and length of 1500mm and then submerge the tube inside the tank. Next, three swirl generators that is shown in figure 4 was designed with dimensions according to literature reviews which that shown in table 1. According to In Chen et al. [12] these swirl generators with different angles were used to investigate the fluid dynamics and heat transfer in an annular. The results show that swirl number depends in the Reynold

number Therefore, these swirl generators with be used in this research to check the effectiveness of it to reduce the pressure drop in 90-degree elbow.

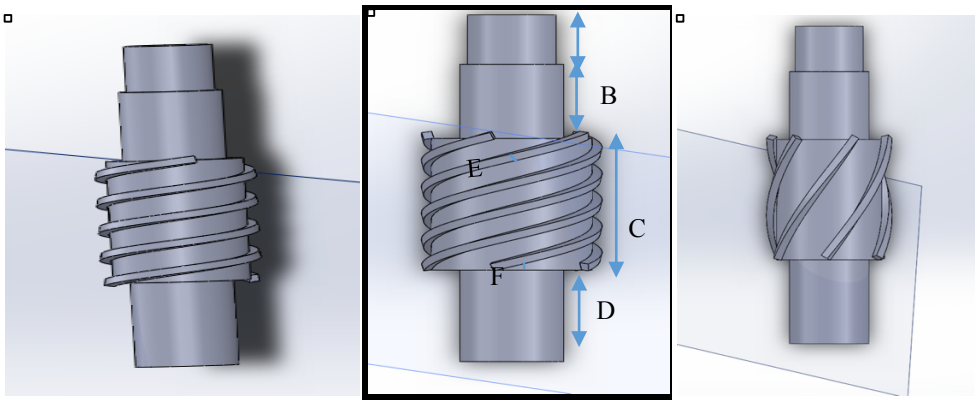


Figure 4. swirl generators with 30. 45.60 degree angels

Table 1: Dimensions used to design the swirl generators (all unties are mm)

vane	**Length**						**Diameter**			
	A	B	C	D	E	F	A	B	C	D
30°	20	30	53.2	37	6	2.8	25.8	30.2	43	30.2
45°	20	30	50.2	40	6.7	2.8	25.8	30.2	43	30.2
60°	20	30	50.6	39.4	8.4	2.8	25.8	30.2	43	30.2

2.2 Experiment Setup

An experiment setup was built to visualize the flow and understanding the calculations of the pressure loss as shown in figure 5. The materials need to be determined from the design of the experiment setup such as the tank, pipes and 90 degree elbows and the length of pipe as well. Two 90 degree elbows were purchased as it not available in the lab as well as the acrylic pipes. the UPVC pipe, PPR pipe, pump and hose were collected from the lab. Then, the components were assembled together and test to check if there is a leakage when the water flow or pressure loss inside the experiment setup. Then, the swirl generators were 3D printed in Taylors' lab and test it in the experiment set up.

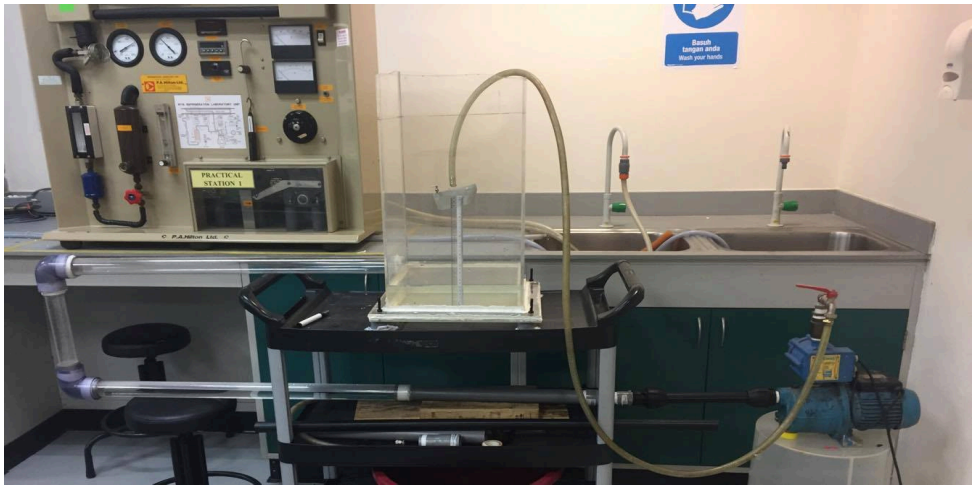


Figure 5. Experiment setup

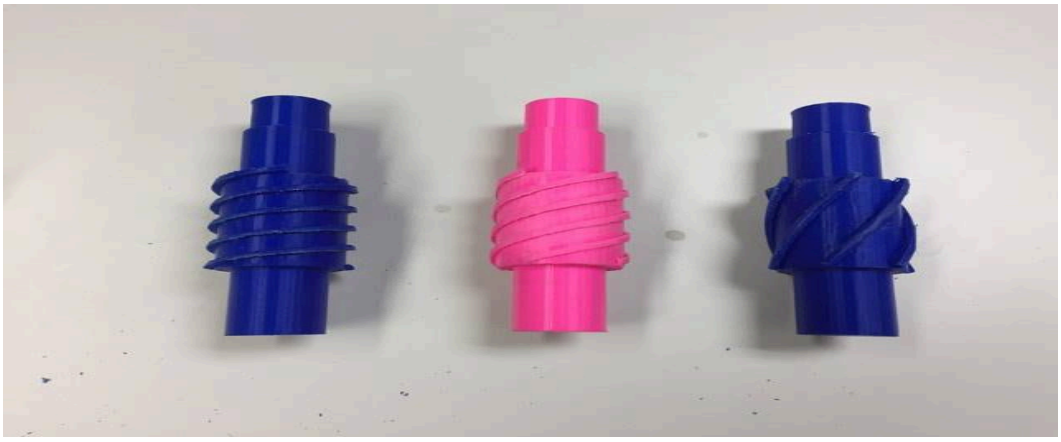


Figure 6. The 3D printed swirl generators (From the left 30º, 45º.60º)

2.3 Experimental Execution

2.3.1 case 1 (Normal flow)

The experiment starts by filling the tank from the tape water to 30 cm height and after the tank is filled with water, the hose that coming from the pump is inserted inside the tank and it is switched on. When the pump is switched on, the water is left to flow through the system for 10-15 minutes to ensure that there are no bubbles inside the system. Next, the velocity of the water before entering the bend is measured by using a pitot static tube with manometer that is shown in figure 7 as well as the velocity of water just after leaving 90º bend. Next, the reading was tabulated and calculation is applied to measure the pressure drop before and after 90º bend

2.3.2 case 2 (swirl flow)

The experiment starts by filling the tank from the tape water to 30 cm height and after the tank is filled with water, the hose that coming from the pump is inserted inside the tank and the swirl generator is placed at the inlet of the pipe that is connected to the tank as shown in Figure then it is switched on. When the pump is switched on,

the water is left to flow through the system for 10-15 minutes to ensure that there are no bubbles inside the system. Next, the velocity of the water before entering the bend is measured by using a pitot static tube with manometer as well as the velocity of water just after leaving 90º bend. Next, the reading was tabulated and calculation is applied to measure the pressure drop before and after 90º bend.

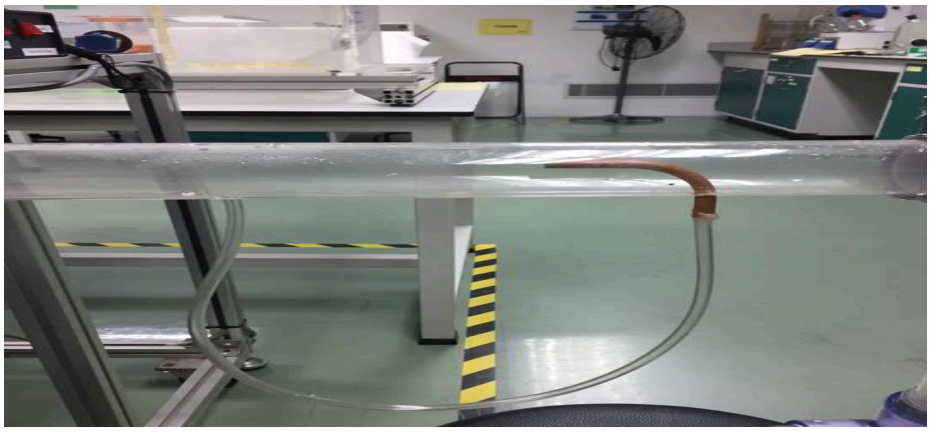


Figure 7. pitot static tube with manometer.

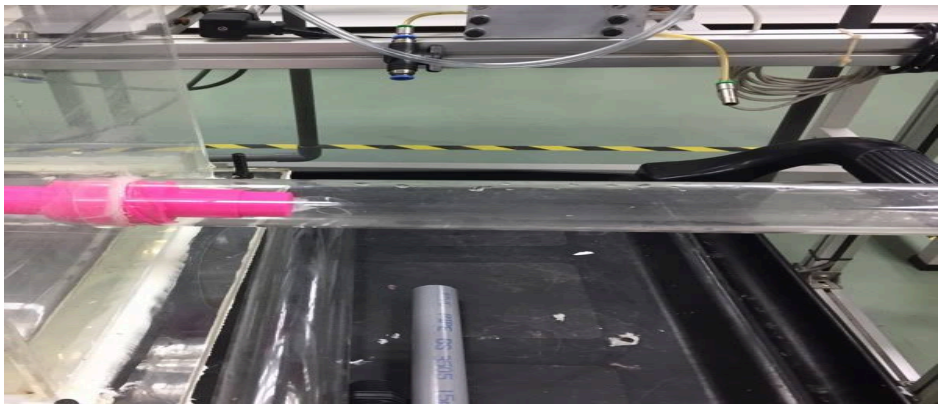


Figure 8. swirl generator placed at the inlet of the pipe

2.4 Governing equations

Most of the fluid that flow in pipe and pressure drop can be mathematically calculated by using several equations. The first equation was Volume flow rate (Q). Volume flow rate of the fluid identified as the volume of the fluid flowing through a cross section area per unit time.in this experiment the volume flow rate was calculated by using Eq. (1).

$$\text{Volume flow rate (Q)} = \frac{volume\ (V)}{time\ (t)} \quad (1)$$

In order to know the volume flow rate, the time needed to fill tank was measured and the volume of the tank was calculated by using Eq. (2).

$$\text{Volume of tank (V)} = (L^2 + W^2 + H^2) \quad (2)$$

where,

L = length of the tank, cm
W = width of the tank, cm
H = height of the tank, cm

In order to identify the velocity of the fluid at the inlet of the pipe, the area of the pipe was calculated by using Eq. (3).

Area of a pipe (A) = $\pi \times r^2 \times h$ (3)

where,

R = radius of the pipe diameter, cm
h = height of the pipe, cm

Next the velocity at the inlet was calculated by Eq. (4).

Velocity = $\frac{Q}{A}$ (4)

After that the velocity at the outlet was calculated by using the Continuity Equation the Continuity equation defined as mass flow rate (ṁ) entering the system is equal to mass flow rate (ṁ) exiting as shown below in Eq. (5)

Mass flow rate ($\dot{m}_{in}$) = Mass flow rate ($\dot{m}_{out}$) (5)

The continuity equation can be derived as follow:

$(\rho \; x \; Q)_{in} = (\rho \; x \; Q)_{out}$ (6)

$A_1 \times v_1 = A_2 \times v_2$ (7)

where,

A_1 = Area of the inlet, cm
v_1= Velocity at the inlet, $^{m}/_{s}$
A_2 = Area of the outlet, cm
v_2 = Velocity at the inlet, $^{m}/_{s}$

Then the velocities before entering the bend and after leaving were calculated by using pitot static tube with manometer by using Eq.7.

Velocity (v)= $\sqrt{\frac{2(p-p_s)}{\rho}}$ (8)

where,

p= total pressure, pa
p_s= static pressure, pa
ρ= Density of the water, $^{kg}/_{m^3}$

In order to calculate the velocity before and after the bend, the density was calculated by Eq. 8:

Density at specific temperature (ρ) = $\frac{\rho_0}{(1+\beta\,(t_1-t_0))}$ (9)

where,

ρ_0 = Density at the initial temperature
β = Volumetric temperature coefficient
t_1= Final temperature
t_0= Initial temperature

Therefore

t_0= 0°, t_1= 20°

Next, the pressure before and after the bend was obtained by using Bernoulli equation which is shown below:

$p_1+\frac{1}{2}\rho v_1^2+\rho g z_1= p_2+\frac{1}{2}\rho v_2^2+\rho g z_2$ (10)

The Reynold number was calculated by using Eq. 11.

Reynold number = $\frac{\rho\ x\ v\ x\ D}{\mu}$ (11)

The pressure drop was calculated for different cases by using Eq.12.

Pressure drop (Δp) = $(f\ \frac{L}{D}+\ K_L)\ \frac{\rho\ V^2}{2}$ (12)

where,

f= Friction factor
L = Pipe length, m
K_L= Minor head loss coefficient for 90° elbow
ρ = Density, $^{kg}/_{m^3}$
V = Velocity of the fluid, $^{m}/_{s}$

Finally, the swirl number (s) was calculated through the whole pipe for every swirl generators by using the equations below.

$S=\frac{\sigma\ R}{2B}[1-(^{R_h}/_{R})^2$ (13)

$\sigma=\frac{\tan(\propto)}{(1-\psi)[1+\tan(\propto)\tan(^{\pi}/_{z})}$ (14)

$\psi=\frac{zt}{2\pi R_1\cos(\propto)}$ (15)

where,

Z =Number of vanes
t= Vane thickness, mm
B= Height of the vane, mm
R_1= Distance from axis to vane, mm
R = outer diameter of exit pipe, mm
R_h= inner diameter of exit pipe, mm
S = Swirl number

4. Results and Discussion

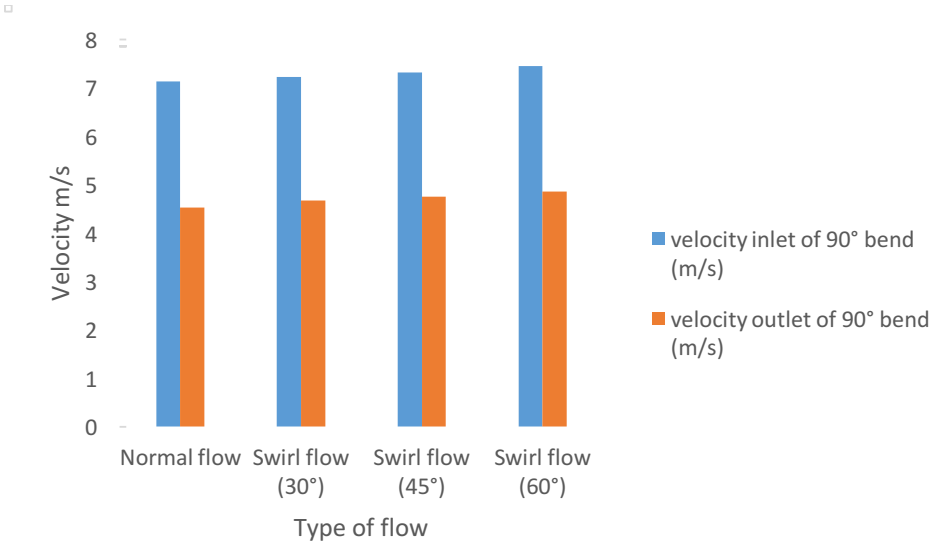


Figure 9. The velocity of different flow before and after the bend at Re= 25449

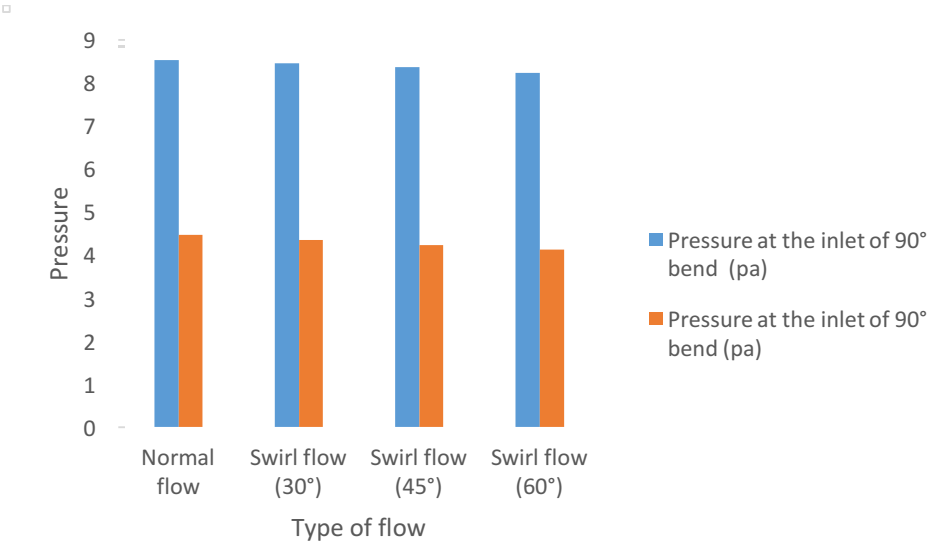


Figure 10. The pressure drop (Δp) of different flow before and after the bend at Re= 25449

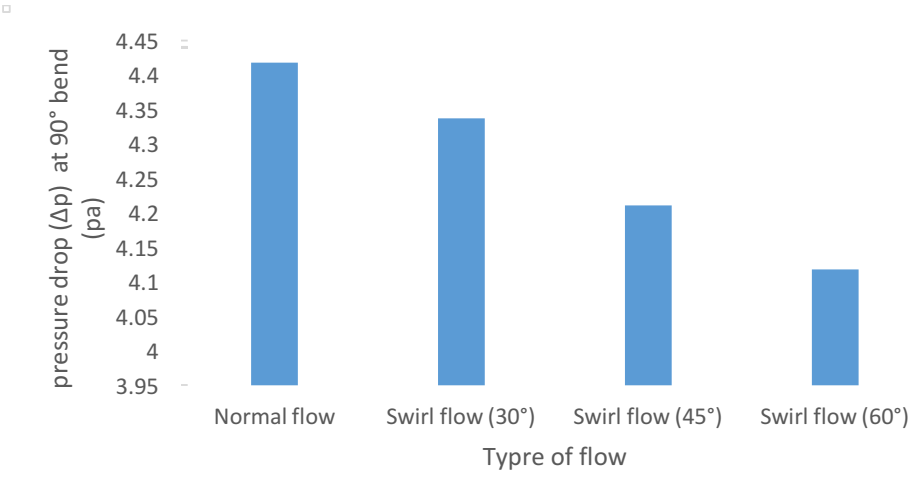


Figure 11. The pressure drop of different flows at 90 degree bend (Re=25449)

The results obtained for velocity for different types of flow and the pressure different flow before and after the bend are shown in Figure 9 and Figure 10 it is observed that the velocity decreases after the bend and this happen due to centripetal force which result in separation of flow. Moreover, when the normal flow is compared with swirl flow, the normal flow has some differences in velocity before and after entering the 90 degree bend however the swirl flow has less differences in velocity as the separation of flow is less in the swirl flow. Also, the results show that the swirl flow with 60 degree angle has the less velocities differences between the before inlet and after the outlet of the 90 degree bend compared with swirl with 30 and 45 degree angles. In addition, the swill flow with 60 degree has the highest velocity before entering the bend because the swill number of it is less showing as shown in Figure 12 When the vane angle decreases, the swirl number increases at the inlet of the vane which result in increasing of the velocity however the velocity after the 90 degree bend decreases.

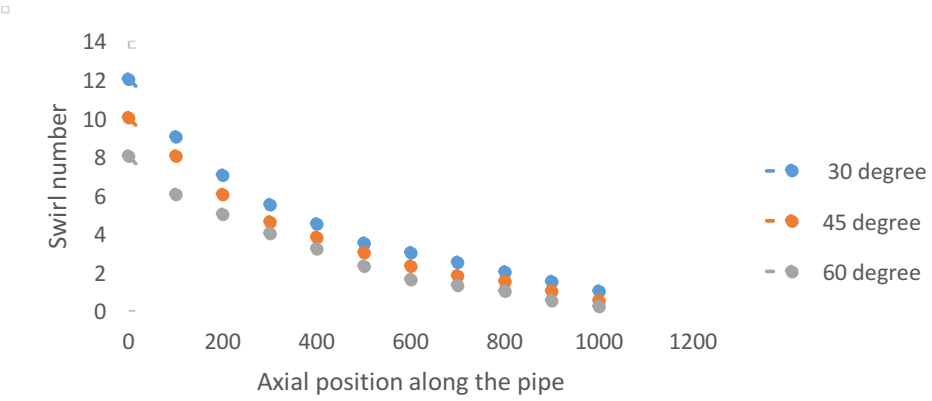


Figure 12. Variation of swirl number through the axial pipe for different swirl generator (Re= 25449)

From Figure 11 it observed that the pressure drop after the 90 degree is higher for the normal flow due to loss of energy. On the other hand, the swirl flow has less pressure drop at elbow. In addition, the swirl flow with 60 degree angle has the least pressure drop differences compared with the other swirl flows as the swirl generator with 60 degree angel has a highest vane angle and less swirl number before entering the 90 bend Also, it was observed from Figure 4.7 that the pressure drop for normal flow was 4.4 and swirl flow of 60 degree angle has pressure drop of 4.1 which mean that pressure drop decreases by 9% compared with normal flow.

.

7. Conclusions

Reduction of local pressure at 90° bend using swirl generator was studied experimentally. An experiment setup was build and three swirl generators with different angles (30°, 45°, 60°) were designed and 3D printed. Then, the velocities before and after the 90 bend were measure and the pressure drop was calculated from normal flow and swirl flow. The results show that the swirl generator with 60° angle has the less pressure drop in the 90° bend compared to other normal flow and other swirl generators due to less swirl number that it has before entering the 90 degree bend

References

[1] F. M.White, "Viscous Flow in Ducts," in *Fluid Mechanics,* 7th. New York, USA, 2010, ch.6, pp. 357–418.

[2] P. Dutta, S. K. Saha, N. Nandi, and N. Pal, "Numerical study on flow separation in 90° pipe bend under high Reynolds number by k-ε modelling," *Engineering Science and Technology, an International Journal*, vol. 19, no. 2, pp. 904–910, 2016.

[3] G. H. Keulegan and K. H. Beij, "Pressure losses for fluid flow in curved pipes," *Journal of Research of the National Bureau of Standards. (1934).*, vol. 18, no. 1, p. 89, 1997.

[4] S. Sujoy."Swirl Flow," in *Twisted-Tape-Generated Single-Phase Swirl Flow Through Ducts*. Saarbrücken, Germany, 2010.

[5] B. Chen, K. Ho, Y. Abakr and A. Chan, "Fluid dynamics and heat transfer investigations of swirling decaying flow in an annular pipe Part 1: Review, problem description, verification and validation", *International Journal of Heat and Mass Transfer*, vol. 97, pp. 1029-1043, 2016.

[6] S. Tavener, T. Mullin and K. Cliffe, "Novel bifurcation phenomena in a rotating annulus", *Journal of Fluid Mechanics*, vol. 229, no. 1, p. 483, 1991.

[7] S. de Farias Neto, P. Legentilhomme and J. Legrand, "Finite element simulation of mass transfer in laminar swirling decaying flow induced by means of a tangential inlet in an annulus", *Computer Methods in Applied Mechanics and Engineering*, vol. 190, no. 35-36, pp. 4713-4731, 2001.

[8] P. Sivashanmugam and S. Suresh, "Experimental studies on heat transfer and friction factor characteristics of laminar flow through a circular tube fitted with helical screw-tape inserts", *Applied Thermal Engineering*, vol. 26, no. 16, pp. 1990-1997, 2006.

[9] M. Yilmaz, O. Comakli, S. Yapici and O. Sara, "Heat transfer and friction characteristics in decaying swirl flow generated by different radial guide vane swirl generators", *Energy Conversion and Management*, vol. 44, no. 2, pp. 283-300, 2003.

[10] T. Zhang, Y. Zhang and H. Ouyang, "Structural vibration and fluid-borne noise induced by turbulent flow through a 90° piping elbow with/without a guide vane", *International Journal of Pressure Vessels and Piping*, vol. 125, pp. 66-77, 2015.

[11] S. Moujaes and S. Aekula, "CFD Predictions and Experimental Comparisons of Pressure Drop Effects of Turning Vanes in 90° Duct Elbows", *Journal of Energy Engineering*, vol. 135, no. 4, pp. 119-126, 2009.
[12] K. Ho, Y. Abdalla Abakr and A. Chan, "An experimental set-up for investigating wirling decaying flow in an annular pipe", *International Communications in Heat and Mass Transfer*, vol. 38, no. 9, pp. 1253-1261, 2011.

eureca 2017 – Conference Paper
Paper Number 2ME16

Electrical Conductivity Enhancement of Graphene Oxide Nanofluid

Muhammad Affiq bin Mohd Isa*, Dr. Azadeh Ghadimi, Mr. Taghi Hajibeigy
Department of Mechanical Engineering, School of Engineering, Taylor's University, Malaysia.

* *achicohebat@gmail.com*

Abstract
The nanofluid technology has been one of the most evolving areas in nanotechnology industry. The technology can be applied in a wide variety of applications. Nanofluid is fluid that has suspension of nanomaterial properties within them. Graphene also has been chemically modified to alter some of its inferior properties especially hydrophobic its nature but still retain the capability of graphene. This Chemically Modified Graphene (CMG) has several features that differentiate them from graphene such as specific surface area and hydrophilic properties. The main focus in this study is to know the most appropriate selection of electrolyte such as reduced Graphene Oxide (rGO) nanofluid or Graphene Nanoplatelets (GNP) nanofluid which can provide higher power generation in a flow battery. The optimum level of concentration is the other important criteria that need to be identify in this study in order to reduce the cost as well as to increase the efficiency of the battery. Apart from that, this study also conducted to measure the amount of the electrical output produced when variable external load being used in which this finding is not achieved in previous study. The finding of this research will revolutionize flow battery technology with the use of nanofluids as its electrolytes. Besides that, this study also focuses on the effect of stability improvements on the electrical conductivity and the optimum weight percentage (wt.%) of nanoparticles in the electrolyte. There is no literature that support the use of nanofluid in flow battery. The rGO nanoparticles was prepared using simplified Hummer's method while GNP nanoparticles was purchased from manufacturer. The nanofluids was prepared by using two step preparation method. The used of Design Expert version 10.0.6 software aids in analyzing and designing the experimental model. The concentration and volume of electrolyte was the deciding factor for the total amount of energy that can be stored in the electrolyte.

Keywords: nanofluid, reduced graphene oxide, graphene Nanoplatelets, electrical, energy.

1. Introduction

The rapid developments and advancements of technology lead to abundance of solutions in every field for various challenges in the present and also the future which occurs due to increase in demands to fulfil life. Recently, a particular field of nanomaterials that suspend in fluid which called nanofluids has find its way into the applications of technology called nanotechnology. The term 'nanofluids' was originally founded by Choi and Eastman [1 – 3], which referred to fluids that contain dispersion of nanoparticles with the notable characteristic of high thermal conductivity and thermal management. The nanofluids uniqueness in term of chemical and physical properties made the technology become attractive to be applied in the numerous applications within the industries. Nanofluid will retain some of the properties of their nanomaterials which allow the nanomaterials application in technology in liquid state. The preparation method of nanofluids is important as it will affect the homogeneity of nanofluid. In this study, the preparation method involve two-step, which are the first step is the base fluid and the nanoparticle are synthesis separately. Then, the second step is where the nanoparticles and base fluid are mixed together and in this particular study the suspension is ultrasonicated. The suspension is ultrasonicated to ensure the dispersion of the nanoparticles is uniform throughout the base fluid by putting immense force on the nanoparticle to ensure it is well dispersed.

Graphene is considered two dimensional as the material itself is very thin which is Nano scale region as the thickness of graphene is only one atom thick [4, 5]. The arrangement of graphene is 2D sp^2 which shows that the graphene atom is bonded and surrounded with each other by sp^2 and each of these molecules display a full planar shape while a single graphene sheet is considered to be one molecule. The structure of graphene is shown in Figure 1. Zhang *et al.* [6] also suggest that the relation between specific surface area and electrical conductivity, in order to achieve the higher electrical conductivity, the surface area of material has to be increase.

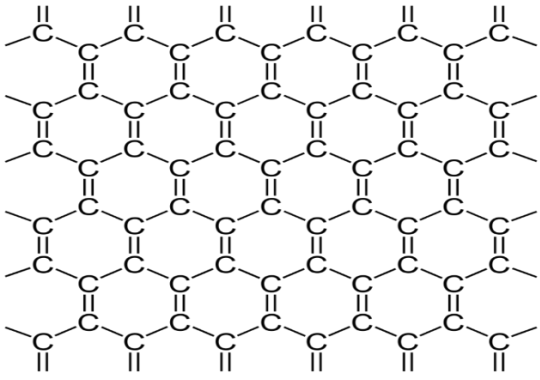


Figure 1. Structure of graphene

Graphene can be modified to alter some of the inferior characteristics to fit into particular application. Graphene itself is hydrophobic by nature means it cannot form colloidal suspension when mixed with water. Thus, graphene has to be functionalised further for application in nanofluid. Reduced Graphene oxide (rGO) is one of the chemically modified graphene (CMG). The use of rGO is driven by Graphene Oxide (GO) nature of naturally electrical insulating and thus cannot be used without further processing [7]. Reduced Graphene Oxide is hydrophilic which means it can create a

stable nanofluids reacting with water due to the existence of hydroxyl group (OH) in the structural formula and thus GO is readily forms colloidal suspensions in thin sheets of water [7 – 9]. The GO itself can be prepared by oxidizing graphene using modified Hummer's which can be adapted for large scale productions [10]. The produced GO nanoparticles are reduced by addition of hydrazine hydrate solution (H_6N_2O).

Another emerging CMG is Graphene Nanoplatelets (GNP) which has different physical and chemical properties than rGO. GNP also has high surface area since the material is in sheet form. GNP is an excellent thermal and electrical conductor as stated by Zhang *et al.* [6], which the conductivity increases as the surface area increase. Graphene sheet in the form of Nanoplatelets is highly conductive as it has the effective conducting network at low loading levels [11 – 12]. Figure 2 shows that GNP is hydrophilic material at low loading levels due to the naturally formed oxygen groups such as hydroxyl, carboxyl and ethers groups at the edges of the nanoparticles and it varies with particle size. This grant GNP the ability to disperse in water as one of the important characteristic of nanofluids. As stated by Biswas *et al.* [11] the homogeneous dispersion and strong interaction of the graphene basal plane and polymer matrices are essential in order to achieve the desired nanomaterial properties. GNP have wide variety of applications, its multi-functionality includes increasing thermal conductivity and stability, increasing electrical conductivity, improves barrier properties, increasing stiffness and toughness and increasing flame retardance [13]. GNP are available in various sizes up to 25 microns with average thickness of 5 – 15 nm.

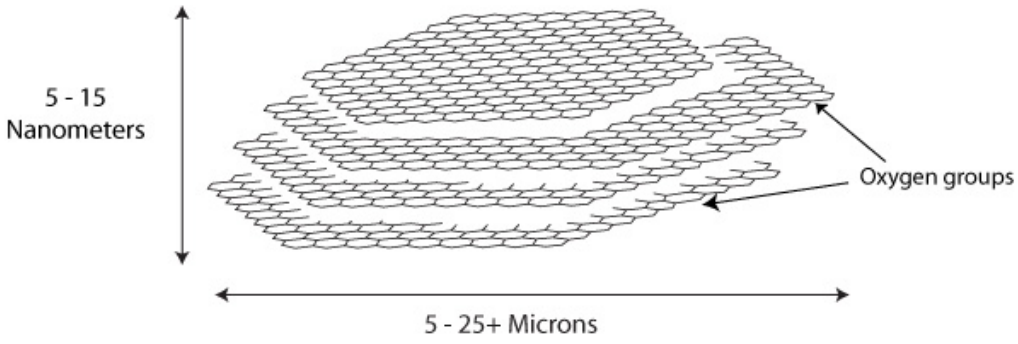


Figure 2. Structure of GNP

The numerous applications of nanofluids have made it found its way into flow batteries applications which still a new concept in this technology. Flow batteries have many applications in which generally it is used to store energy generated by renewable power source, load balancing in an electrical grid, electric vehicles and stand-alone power system [14 - 15]. Flow batteries differ from the other types of electrochemical energy storage unit such as nickel batteries, lithium ion batteries and supercapacitors. The natural features of flow batteries allow it to charge and discharge heavily without affecting their cycle life limitations [13 – 14]. The flow batteries differ from the conventional batteries as the energy is stored by the separate electrolytes which stored in the reservoirs, the electrolytes are constantly pumped through power converting components during charging or discharging, [14]. The storage capacity of the batteries is determined by concentration and volume of the electrolytes. The batteries convert the

chemical energy to electrical energy by the exchange of ion that occurs between anode and cathode electrolytes [16].

Even though there are numerous researches conducted regarding to reduced Graphene Oxide (rGO) nanofluid and Graphene Nanoplatelets (GNP) nanofluid which has high electrical conductivity, which also important properties for flow battery electrolyte to store and discharge electricity [2, 7, 10]. These properties have made both nanofluid suitable and potentially to be used as an electrolyte in the flow battery. Nonetheless, there are still no conclusive literature review that supports the use of rGO nor GNP nanofluid in a flow battery that can have the performance equivalent to other flow batteries.

The aims of this research are to achieved an understanding regarding the electrical conductivity properties of rGO and GNP nanofluids. This research will determine which nanoparticles is best suited for flow battery electrolyte and the optimum level of concentration of nanofluid to achieve higher efficiency of flow battery. The objectives of this research are as follows:

1. To prepare stable nanofluid of rGO and GNP nanoparticles.
2. To increase the efficiency of the nanofluid flow battery by varying the concentration of electrolytes.
3. To test the manufactured nanofluid flow battery by an external load (from LED to small motor).

2.0 Research Methodology

This particular research requires some procedures to be completed in order to achieve the research objectives. The research aims to study and create a higher efficiency of flow battery compared to previous design. There are two types of nanoparticles to be tested in this research. The experiment will be optimized using Design Expert version 10.0.6 (DE) statistical software to determine the optimum weight percentage (wt.%) of nanofluid. Then, a flow battery prototype will be produced at the end of this research.

2.1 Preparation of Reduced Graphene Oxide (rGO) Nanofluid and Graphene Nanoplatelets (GNP) Nanoparticles

The rGO nanoparticles is produced while GNP 300 nanoparticles is purchased from Sigma-Aldrich Corporation to ensure the purity and quality (5 – 15 nm average thickness) of the material itself and avoid any contaminations of the sample, especially for the experimental purposes. GNP nanoparticle is not produced by the author as it does not include in the scope of study due to limitations of time. GNP nanoparticles is available widely in the market and cheaper than rGO nanoparticle. 10g of GNP nanoparticles is purchased from the supplier for this study.

The production of GO nanoparticles can be done using simplified Hummer's method. The graphite obtained from Sigma-Aldrich Corporation. Initially the 3g of graphite powder is treated with 360 ml of sulphuric acid (H_2SO_4) with 98% concentration and 40 ml phosphoric acid (H_3PO_4) with 98% concentration. The treated

solution will be stirred constantly using magnetic stirrer at 355 rpm while gradually adding 18g potassium permanganate ($KMnO_4$) with 99.9% purity. After three days of stirring, the solution is put into an ice bath and add 350ml hydrogen peroxide (H_2O_2) with 30% concentration. The ice bath cooled down the solution as the addition of hydrogen peroxide will increased the temperature. Then the solution leaved to be stirred at 650 rpm for another 10 minutes. After that, the solution was washed using multipurpose centrifuge (Scanspeed 1236MG/1248) at 9000 rpm with 1 mole of hydrochloric acid (HCl) with 37% concentration 3 times then with distilled water until the solution has pH level of around 6 or 7 to avoid agglomeration. The solution has turned into suspension and colour change from bright yellow to light brown and to dark brown. The solution became more viscous. Lastly, the suspension was placed into oven for 24 hours at 50°C to remove the water molecules, the composition left will be the GO nanoparticle [17]. The temperature of the oven must not be more than 50°C because it will denature the existing functional group in GO and may be reduced thermally. The produced GO nanoparticle was dispersed in 100 ml of water forming inhomogeneous yellow-brown mixture and then ultrasonicated until stable and homogenize forming GO nanofluid. The addition of 1 ml of 32.1 mmol hydrazine hydrate was done then the mixture heated in oil bath at 100 °C under a water-cooled condenser for 24 hours. The rGO gradually precipitated and producing black solid. The black solid was filtered over a medium fritted glass funnel and washed 5 times with 100 ml water and 100 ml methanol. The washed product was dry under continuous air flow. The dried product is the rGO nanoparticle [7].

2.2 Preparation of rGO and GNP Nanofluid

Three small batches (20 ml each sample) of rGO nanofluid and GNP nanofluid was prepared using two-step preparation method process in which the materials mixed with base fluid (distilled water) for both nanofluids [1]. These mixtures were ultrasonicated using ultrasonic bath (Elmasonic P120H/1013777) at 37 kHz for 70 minutes and pH value of these nanofluids was controlled by pH control method (addition of sodium hydroxide). The rGO nanofluid pH value was set to pH 8 while the GNP nanofluid was set to 10 pH which are the determined stable pH value for each nanofluid respectively [10]. The prepared nanofluids obtained used for experimental purposes as there are no conclusive literature review of comparing between rGO nanofluid and GNP nanofluid in terms of electrical conductivity and their application in flow battery. The rGO nanofluid produced was started with 0.03 wt.% and gradually increased in concentration of nanoparticle as at 0.03 wt.% was the highest electrical conductivity from previous literature [17]. The GNP nanofluid was produced with a concentration start with 0.03 wt.% as well for direct comparison.
Equation 1 shows the formula used to determine the volume fraction of nanofluid for both nanoparticles.

$$vol\ \% = \frac{\frac{M_{particles}}{\rho_{particles}}}{\frac{M_{particles}}{\rho_{particles}} + \frac{M_{water}}{\rho_{water}}} \times 100\% \quad (1)$$

2.3 Measuring Electrical Conductivity of rGO Nanofluid and GNP Nanofluid

A multipurpose bench meter (Eutech PC 700) that has temperature compensation features was used to measure the electrical conductivity of the nanofluids

and their pH value. This instrument has the ability to accurately measure the electrical conductivity, pH value and the temperature simultaneously of the fluids when disperse completely in the solution. The instrument also has to be calibrated separately for electrical conductivity and pH value. The electrical conductivity function was calibrated using de-ionized water up to 5 times while the pH measure function the device has to be calibrated with standard solution of pH 4.01 and 7.00. This instrument has conductivity range of 0 μScm^{-1} - 200 $mScm^{-1}$ And has temperature compensation of 0 - 100°C. The important factor of this instrument is the accuracy of $\pm$1% at full scale for temperature and electrical conductivity function with $\pm$0.01 pH accuracy for pH mode [18]. The concentration of nanofluids are set to be between 0.03 - 5 wt.% and temperature between 25 – 50 °C. The best nanofluid (rGO or GNP nanofluid) is chosen to be implemented in the flow battery.

2.4 Optimization of The Design

Further optimization can be conducted using Design Expert version 10.0.6 (DE) software which used to design the experimental model. With the obtained results, the software can be used to optimized the results. The design used is Response Surface Methodology (RSM) with Central Composite Design (CCD). The experimental design consists of two factors and multiple levels. DE was used to determine the optimum level of concentration and temperature of the nanofluid so it can maximize the electrical conductivity of nanofluid.

2.5 Measurement of Current and Power Generated

The optimized nanofluid combination (concentration and temperature) was selected as one of the electrolyte in the flow battery prototype which served as test bench as shown in Figure 3 so the results obtained directly compared to the previous research results. The selected nanofluid was produced at 300ml and served as the cathode electrolyte. The anode electrolyte was 300ml of 0.5 mole sodium chloride (NaCl). The NaCl was used due to the reason of direct comparison with the previous research which one of the foundation for this research. NaCl was stated to have good electrical conductivity and also used as electrolyte in existing Aluminium-air battery [19]. The two electrolytes were separated by Nafion Proton Exchange Membrane (PEM) which also allowed the exchange of ions while separating the electrolytes physically. The area of contact of PEM with electrolytes was kept constant for direct comparison and reducing number of factors affecting the results. The voltage was measured using digital meter across a circuit with a 1K Ω resistor due to the small value of current. The power output will be used to operate external load ranging from and Light Emitting Diode (LED) to small motor.

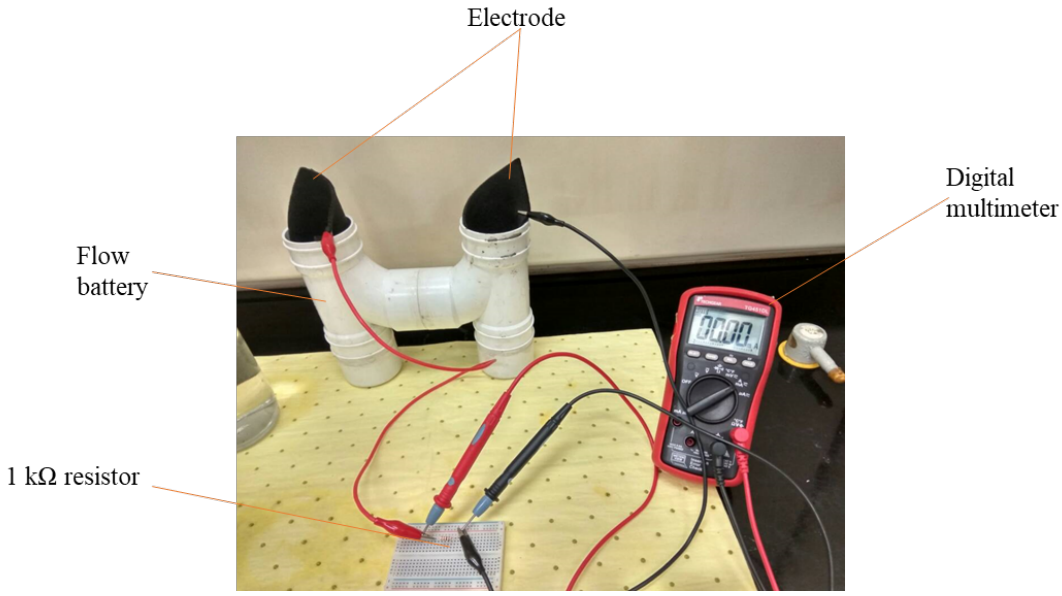


Figure 3. The experimental setup to measure the current output

Current and power generated by the battery is calculated using Equation 2 and 3. Where V is the voltage, I is current and P is the power.

$$I = \frac{V}{R} \quad (2)$$

$$P = VI \quad (3)$$

3.0 Result and Discussion

3.1 Electrical Conductivity

The electrical conductivity of rGO and GNP nanofluids was measured to determine which nanoparticles is best suited for flow battery. The concentration of both nanofluids is set to be 0.03 wt.% at 25°C. The temperature is kept constant to compare the electrical conductivity of the nanofluid without affected by temperature which allow direct comparison of the nanoparticle ability to enhance the electrical conductivity of base fluid. The first sample is set to 0.03 wt.% is due to this concentration is the last known highest electrical conductivity of Graphene Oxide (GO) nanofluid from previous research [6]. The distilled water electrical conductivity @ 25°C is 10 μScm^{-1} while de-ionised water @ 25 °C has electrical conductivity of 4 μScm^{-1}. The value of electrical conductivity of GO nanofluid obtained in the previous research is also included to demonstrate the enhancement value by reducing the GO to rGO.

$$\text{Enhancement over base fluid (\%)} = \frac{EC_{Nanofluid} - EC_{Base\ fluid}}{EC_{Base\ fluid}} \times 100\% \quad (4)$$

Table 1. The comparison of nanofluids

Nanofluid (0.03 wt.%)	Electrical conductivity @ 25 °C (Scm^{-1})	Enhancement over base fluid (%)
GNP	2.47×10^{-3}	24600
rGO	1.03×10^{-3}	25650
GO [17]	161.44×10^{-6}	3936

Based on Table 1 the highest nanofluid electrical conductivity is GNP based nanofluid followed by rGO nanofluid and GO nanofluid respectively. Electrical conductivity enhancement percentage is calculated using Equation 4. The electrical conductivity enhancement percentage over base fluid shows the rGO gives the highest enhancement percentage at 25650% followed by GNP and GO nanofluid with 24600% and 3936% respectively. The use of rGO over GO in this study is driven by GO nature of hydrophobic and need to be further reduced.

The temperature effect on electrical conductivity is not taken into consideration at this concentration because at low concentration (0.03 wt.%) of nanofluid the temperature effect is insignificant. Although, the effect of temperature rises when the concentration increased as higher temperature will decrease the viscosity of nanofluid which promotes electrophoretic mobility [20]. This results also supports Zhang *et al*. [6] claims that higher surface area of nanoparticles the higher the electrical conductivity. GNP nanoparticles used in this experiment is GNP 300 which means that it has 300 m^2 /g specific surface area. Thus, the nanosheets surface is bigger and longer than of graphene which has 2630 m^2 /g theoretical specific surface area. A smaller specific surface area means that the nanosheets is bigger than nanosheets that has higher specific surface area. To put this into perspective, a sugar cube of 5 g takes more time to dissolve in solution whereas sugar in granules form with same mass takes less time to dissolve due to higher specific surface area. GNP nanoparticles has larger surface area which contributing to better electrical conductivity. Based on colloidal suspension theory, the properties of nanofluid especially electrical conductivity depends on formation of dielectric layer on the surface and net electric charge of the nanoparticles. Besides that, nanofluid has Electrical Double Layer (EDL) around the particle surfaces. EDL is the surface charge of the particle with ion clouds encircle it. EDL formations primarily depends on the size, volume fraction of particle in dispersed in fluid and the surface charge. When electrical energy is applied the EDL will travel towards the oppositely charge region where the electrical conductivity of the mixture is determined by the mobility of particles [21].

3.2 Selection of GNP Nanofluid as The Electrolyte

From Table 1, GNP nanofluid is proven to be the superior nanofluid in terms of electrical conductivity. The GNP nanofluid is prepared for further experimentation to determine the optimum level of concentration to achieve the maximum value of electrical conductivity. For this part of the experimentation three small batches of GNP nanofluid of 20 ml with three levels of concentration which is 0.03, 2.52 and 5.00 wt.% were prepared. These samples were prepared for additional data for DE software to analyse and optimize.

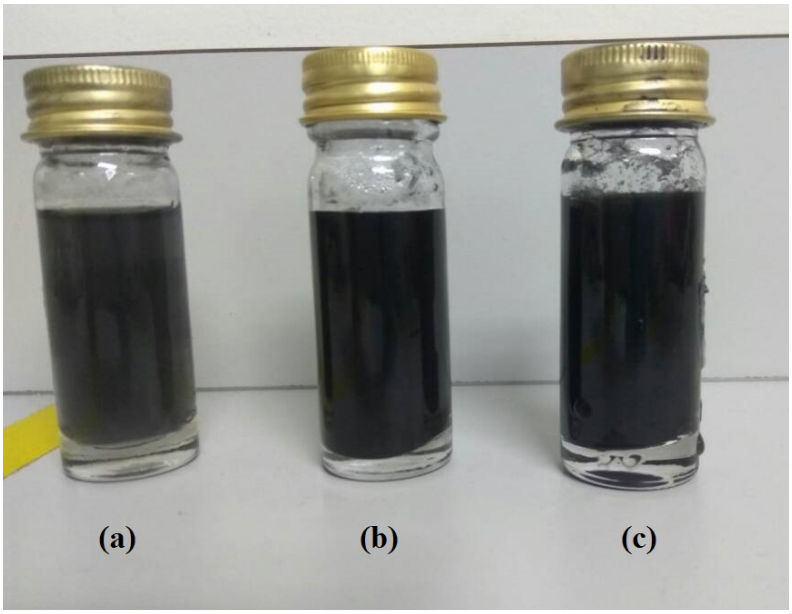


Figure 4: Nanofluid samples after prepared as (a) 0.03 wt.%, (b) 2.52 wt.% and (c) 5.00 wt.%

The RSM and CCD experimental design function of DE software requires sets of data from three different level of concentration at various temperature. In Figure 4(a), the colour intensity of the solution is the lowest compared to the others due to low concentration of nanoparticles and shows a good dispersion of nanoparticles. Figure 4(b) represent the sample for 2.52 wt.% concentration show a good dispersion of nanoparticles and uniformly dark colour intensity observed. However, in Figure 4(C) which shows the 5 wt.% of concentration appears to be homogenous at first but later the nanoparticles sediment which is shown in Figure 5. Figure 5 shows that the nanofluid is non-homogenous as it forms two-layered solutions. The fact that the suspension immediately sediment few minutes after ultrasonicated proves that the sample can be neglected. This requires a new upper limit to be set in order to produce reliable results.

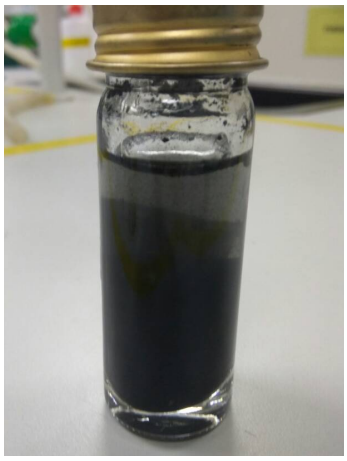


Figure 5. The 5 wt.% sample forms two-layered solution minutes after ultrasonicated

In order to get a significant input into the DE software the upper limit has to be reduced. The duration of stability of nanofluid also an important factor in the experiment. Even though the 2.52 wt.% nanofluid concentration shows a good

dispersion and stability after prepared, it loses the stability after 14 days which is less the intended duration of 30 days' stability required to determine whether the nanofluid is stable for the study. Figure 6 shows the two-layered solution formed after 14 days by the 2.52 wt.% GNP nanofluid. It is to be noted that all of the nanofluids pH level is adjusted by pH control by addition of few drops of 1 mole of sodium hydroxide. Both samples of 2.52 and 5 wt.% GNP nanofluid is determined to be too high and neglected.



Figure 6. The 2.52 wt.% GNP nanofluid after 14 days- two-layered solution clearly seen

In order to get a new reliable upper limit, the nanofluid concentration is halved from the previous concentration. This means that 2.52 wt.% nanofluid concentration is halved. Thus, a nanofluid with concentration of 1.27 wt.% is produced. The nanofluid shows good stability and dispersion up to more than 30 days. An upper limit of 1.27 wt.% is selected for the new upper limit with 0.03 wt.% lower limit.

3.3 GNP Nanofluid Samples Data

Table 2. The results of the experiment (GNP nanofluid)

Run	Concentration (wt.%)	Temperature (°C)	Electrical Conductivity (Scm^{-1})
~~1~~	~~0.65~~	~~55.2~~	-
~~2~~	~~0.23~~	~~37.5~~	-
3	0.65	30.9	$3.41x10^{-3}$
4	1.27	50.0	$1.67\ x10^{-3}$
5	0.03	25.0	$2.47\ x10^{-3}$
~~6~~	~~0.65~~	~~19.8~~	-
~~7~~	~~1.53~~	~~37.5~~	-
8	1.27	25.0	$1.55\ x10^{-3}$
9	0.03	50.0	$2.67\ x10^{-3}$
10	0.65	35.4	$3.67\ x10^{-3}$
11	0.65	25.4	$3.36\ x10^{-3}$
12	0.65	33.4	$3.52\ x10^{-3}$
13	0.65	37.5	$3.70\ x10^{-3}$

Based on Table 2, there are four runs (1, 2, 6 and 7) that were ignored due to exceeding the parameters scope. The scope of the parameters is the concentration is between 0.03 – 1.27 wt.% and the temperature between 25 – 50°C. The highest electrical conductivity for GNP nanofluid is at 0.65 wt.% @ 37.5 °C with 3.7 x10^{-3} Scm^{-1} whereas the lowest electrical conductivity is at 1.27 wt.% @ 25°C with 1.55 x10^{-3} Scm^{-1}. These data represent actual experimental values of these nanofluids. 0.65 wt.% nanofluid is used to determine the centre point for optimization.

3.4 Analysis by Design Expert

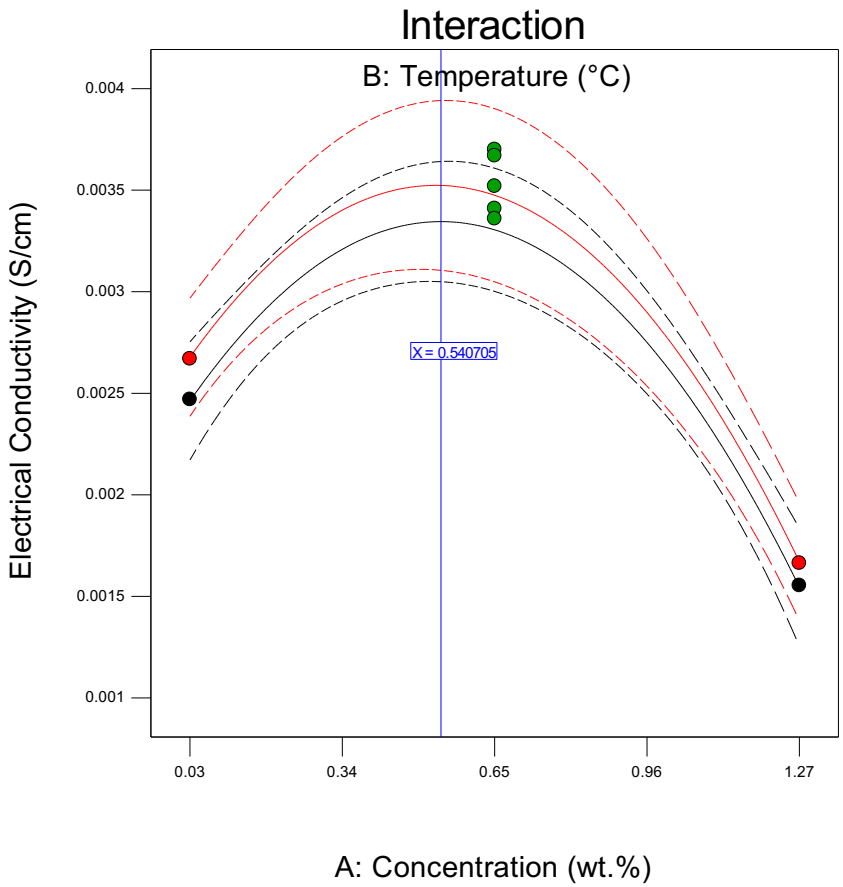


Figure 7. The interaction between the two factors and electrical conductivity

RSM is used to obtain precise and accurate results in both magnitude and direction of the factors that were affecting the experimental model. Based on Figure 7 the electrical conductivity increases exponentially from 0.03 wt.% to around 0.54 wt.% and then decreases exponentially to 1.27 wt.%. The figure shows the existence of interaction between the two factors which is concentration and temperature relative to electrical conductivity. From the same figure, it can be deduced that the electrical conductivity starts to decreases as the concentration past 0.54 wt.%. This determines the maximum loading levels of GNP nanoparticles in distilled water. The formation of agglomeration in nanofluid will destroys reduce the performance as the nanoparticles restacked together and decreasing the total surface area drastically. Agglomeration also will form big clump and sediment agglomeration therefore they can be observed with naked eye when it forms two-layered solution as shown in Figure 8.

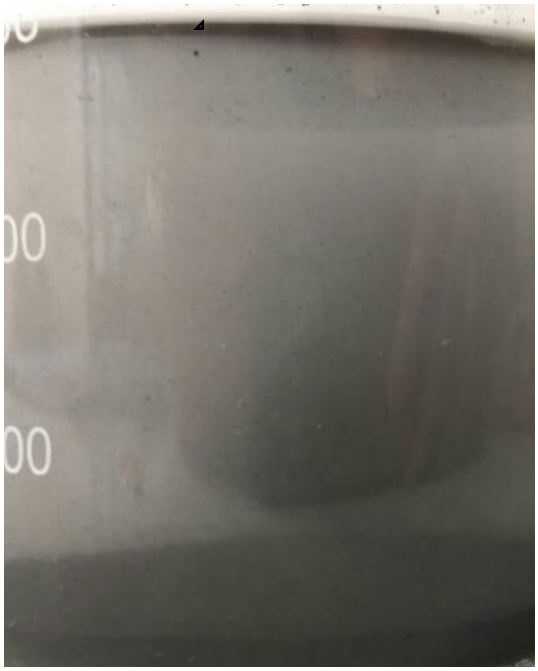


Figure 8. Agglomeration observed in circled area

Based on Figure 8, the nanoparticles clump observed is considered big as the size or nanoparticles is very small. Agglomeration occurs in GNP nanofluid is due to flat surfaces of the nanoparticles that make it tends to restack together [22].

3.5 Design Expert Optimization

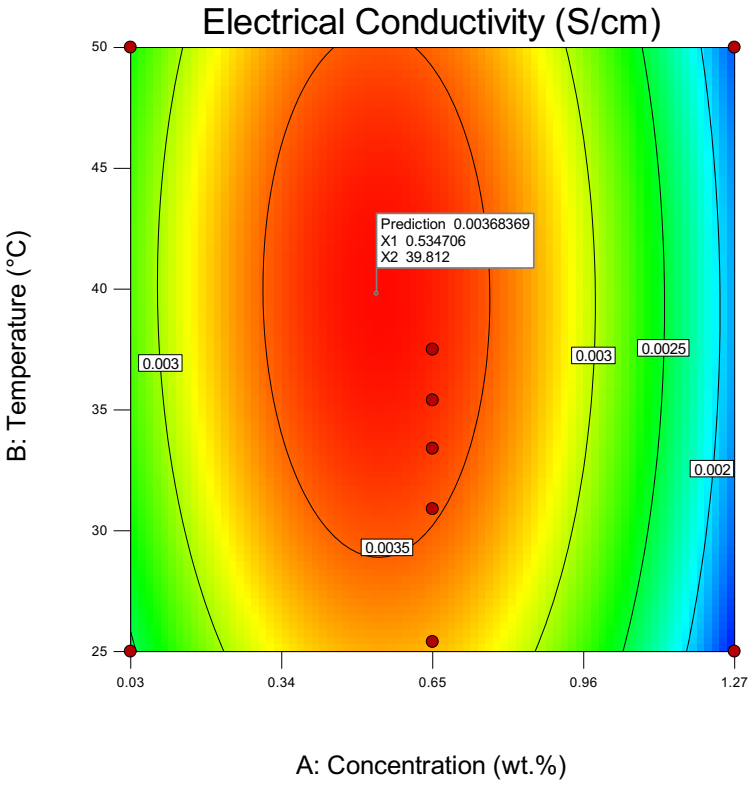


Figure 9. The contour shows the prediction of the optimized experimental design

One of the outcomes of this project it to further enhance and optimize the nanofluid using statistical software. This step mainly aims to optimize the electrical conductivity of nanofluid to achieve an efficient enhancement. The optimization involves maximizing the electrical conductivity while keeping the concentration between 0.03 – 1.27 wt.% and temperature between 25 – 50°C. Figure 18 shows the desirability of the optimization generated.

Based on Figure 9, the optimized design can create GNP nanofluid that has electrical conductivity of 3.68×10^{-3} Scm^{-1} with nanofluid concentration of 0.53 wt.% @ 40°C. The maximum electrical conductivity achieved in the experimental runs is 3.70×10^{-3} Scm^{-1} @ 35. 4°C. The optimized value is slightly lower than maximum electrical conductivity achieved but with less concentration and slightly higher temperature. The optimization produces 99.2% desirability and it lowers the concentration by 18%. It is to be noted that the cost of GNP nanoparticles is considered very high which one the reason it barely crosses the concept stage in development. Thus, the optimized design will have lower cost to produce and will promote the technology into industry

4.0 Conclusion

In this study, the GNP nanofluid is proved to be superior than rGO and GO nanofluid in terms of electrical conductivity. Based on the data obtained, it can be deduced that larger surface area can create better conducting network as the gap between nanoparticles in nanofluid is reduced. This study also determines the previously unknown maximum loading level of GNP nanoparticles in distilled water. The optimum concentration of nanofluid to maximize electrical conductivity also generated by DE software. The optimized design will result in lower cost of flow battery due to less nanomaterials used for the nanofluid.

References

[1] R. Saidur, K. Y. Leong, and H. A. Mohammad, “A review on applications and challenges of nanofluids,” Renew. Sustain. Energy Rev., vol. 15, no. 3, pp. 1646–1668, 2011.

[2] T. T. Baby and S. Ramaprabhu, “Synthesis and nanofluid application of silver nanoparticles decorated graphene,” J. Mater. Chem., vol. 21, no. 26, pp. 9702, 2011.

[3] S. U. S. Choi, “Nanofluids: From Vision to Reality Through Research,” J. Heat Transfer, vol. 131, no. 3, pp. 33106, 2009.

[4] R. R. Nair et al., “Fine Structure Constant Defines Visual Transperency of Graphene,” Science (80-.)., vol. 320, no. June, pp. 2008, 2008.

[5] F. Ban and S. Majid, “Graphene oxide and its electrochemical performance,” J. Electrochem., vol. 7, pp. 4345–4351, 2012.

[6] Z. J. Li, B. C. Yang, S. R. Zhang, and C. M. Zhao, “Graphene oxide with improved electrical conductivity for supercapacitor electrodes,” Appl. Surf. Sci., vol. 258, no. 8, pp. 3726–3731, 2012.

[7] S. Stankovich et al., “Synthesis of graphene-based nanosheets via chemical reduction of exfoliated graphite oxide,” Carbon N. Y., vol. 45, no. 7, pp. 1558–1565, 2007.

[8] L. T. Le, M. H. Ervin, H. Qiu, B. E. Fuchs, and W. Y. Lee, "Graphene supercapacitor electrodes fabricated by inkjet printing and thermal reduction of graphene oxide," Electrochem. commun., vol. 13, no. 4, pp. 355–358, 2011.

[9] W. Gao, "The chemistry of graphene oxide," Graphene Oxide Reduct. Recipes, Spectrosc. Appl., vol. 1, no. 1, pp. 61–95, 2015.

[10] M. Mehrali et al., "Investigation of thermal conductivity and rheological properties of nanofluids containing graphene nanoplatelets.," Nanoscale Res. Lett., vol. 9, no. 1, pp. 15, 2014.

[11] S. Biswas, H. Fukushima, and L. T. Drzal, "Mechanical and electrical property enhancement in exfoliated graphene nanoplatelet/liquid crystalline polymer nanocomposites," Compos. Part A Appl. Sci. Manuf., vol. 42, no. 4, pp. 371–375, 2011.

[12] M. Rashad, F. Pan, A. Tang, M. Asif, and M. Aamir, "Synergetic effect of graphene nanoplatelets (GNPs) and multi-walled carbon nanotube (MW-CNTs) on mechanical properties of pure magnesium," J. Alloys Compd., vol. 603, no. October 2016, pp. 111–118, 2014.

[13] J. Shen, Y. Hu, C. Li, C. Qin, and M. Ye, "Graphene nanoplatelets," Strem Chem., vol. 1, no. 978, pp. 3–6, 2008.

[14] M. Skyllas-Kazacos, M. H. Chakrabarti, S. a. Hajimolana, F. S. Mjalli, and M. Saleem, "Progress in Flow Battery Research and Development," J. Electrochem. Soc., vol. 158, no. 8, pp. R55, 2011.

[15] M. H. Chakrabarti, R. A. W. Dryfe, and E. P. L. Roberts, "Evaluation of electrolytes for redox flow battery applications," Electrochim. Acta, vol. 52, no. 5, pp. 2189–2195, 2007.

[16] L. Joerissen, J. Garche, C. Fabjan, and G. Tomazic, "Possible use of vanadium redox-flow batteries for energy storage in small grids and stand-alone photovoltaic systems," J. Power Sources, vol. 127, no. 1–2, pp. 98–104, 2004.

[17] K. Saktiyaramana, G. Azadeh, M. T. Hajibeigy, L. Campus, and S. Jaya, "Graphene Oxide Nanofluids Characterization and Electrical Conductivity," J. Eng. Sci. Technol., vol. 1, no. 1, pp. 62–72, 2015.

[18] B. Meter, "Instruction Manual: PC700 pH/mV/Conductivity/C/F," Thermo Fisher Scientific, vol. 2, no 1, pp. 1-32, 2010.

[19] Smoljko, S. Gudić, N. Kuzmanić, and M. Kliskić, "Electrochemical properties of aluminium anodes for Al/air batteries with aqueous sodium chloride electrolyte," J. Appl. Electrochem., vol. 42, no. 11, pp. 969–977, 2012.

[20] M. Hadadian, E. K. Goharshadi, and A. Youssefi, "Electrical conductivity, thermal conductivity, and rheological properties of graphene oxide-based nanofluids," J. Nanoparticle Res., vol. 16, no. 12, pp. 1, 2014.

[21] H. Setia, R. Gupta, and R. K. Wanchoo, "Stability of nanofluids," Mater. Sci. Forum, vol. 757, pp. 139–149, 2013.

[22] C. Liu, Z. Yu, D. Neff, A. Zhamu, and B. Z. Jang, "Graphene-Based Supercapacitor with an Ultrahigh Energy Density - SI," Nano Lett., vol. 10, no. 12, pp. 4863–4868, 2010.

eureca 2017 – Conference Paper
Paper Number 2ME18

Preparation and Characterization of Plastic Wood Composite from Recycled Polystyrene Foam and Corn Husk Fiber

Nur Muhammmad Yusuf Fahmy Bin Idzehar[1*], Koay Seong Chun[1], Pang Ming Meng[1], Tsai Kim Yeow[2]
[1] *School of Engineering, Taylor's University, Malaysia.*
[2] *Faculty of Engineering, The University of Nottingham, Malaysia.*

[*] *yusuf.fahmy93@gmail.com*

Abstract
This research focuses on the preparation of wood plastic composite (WPC) from corn husk fiber (CHF) and recycled polystyrene foam (rPSF). The effect of rPSF/CHF ratio and alkaline treatment on tensile, thermal, and water absorption properties of rPSF/CHF composites were investigated. The rPSF was dissolved in acetone and mixed with CHF to produce composite. Later the composites were tested using Instron universal testing machine, Thermogravimetric Analysis (TGA) and Fourier transform infrared spectroscopy (FTIR). The results show the increases of rPSF content increases the tensile strength and modulus while reducing the thermal stability of rPSF/CHF composite. However, the water absorption of rPSF/CHF composite dropped as the rPSF content increases. The alkaline treatment has improved the tensile strength, modulus, thermal stability (Td10%), and also water absorption. The WPS prepared from rPSF and treated CHF shows better tensile and thermal properties with lower water absorption. FTIR result also evidenced the alkaline treatment removed some components in CHF. As result, the surface roughness of fiber was increased and enhanced strong mechanical interlock at interfacial region. This due to significant improvement on properties of composites.

Keywords: Wood Plastic Composite (WPC), Corn Husk Fiber (CHF), Recycled Polystyrene Foam (rPSF), Thermogravimetric Analysis (TGA), Fourier transform infrared spectroscopy (FTIR)

1. Introduction

Wood-plastic composite (WPC) is a combination of wood waste and recycled plastics [1-2]. WPC is an alternative way of reusing sawing wood and plastics and the fiber raw material can be collected from plywood mills, sawmills and wood product mills [3-4]. In addition, being the fastest growing and largest market make the demand on WPC to be high [5]. The market of WPC is projected to increase from 1046.1 kilo tonnes to 1728.9 kilo tonnes from year 2014 to 2019 with compound annual growth rate of 10.5% [6]. Besides, WPC have a lot of application range from industrial products, commercial building and home construction, such as fencing in construction, cladding and decking [7-8]. Previously, WPC was made from wood fiber and plastic materials but now WPC can be made from natural fiber obtained from agricultural waste and recycled plastic materials thus WPC is considered as a sustainable material [9].

Fillers are additives that were added to a plastic material in order to enhance the properties of the plastic or partial replace part of plastic in order to reduce the cost. In the past, mineral filler (e.g, calcium carbonate and kaolin) was commonly used as filler for plastic material. Nowadays, natural fiber or filler are widely used in plastic industry to produce composite materials. This is because natural filler exhibited some advantages compared to mineral filler such as biodegradable, from renewable resource, less abrasive to compounding machine, low density and cost [10-13]. Furthermore, natural filler or fiber can be obtained from agricultural industry by-product and crop wastes for example, rice husk [14], coconut shell [15-17], palm kernel shell [18], palm oil empty fruit bunch [19], sugarcane bagasse [20], and corn cobs [21]. Natural fibers are widely used in almost everywhere in modern industries to biodegradability and minimize production costs [22]. One example of WPC composite that can be found in the market is the IKEA furniture which was made from polypropylene/wood flour composite through injection-moulding process [23].

Corn or maize is the most widely planted crop in the world. Corn husk is the leafy shell covering the corn (as shown in Figure 1). In general, corn husks are the leftover after the corns were harvested and corn husk is the non-food part of the corn and it usually left as waste material in corn field. The corn husk waste accumulated to about 45 million tons per year in the whole world. In additional, corn husk consists high content of lignocellulosic fiber (e.g, 1.9% protein, 2.8% ash, 6.6% lignin, 38.2% cellulose, 44.5% hemicellulose and some other undetermined materials) [24]. For this reason, the corn husk can be utilized as natural fiber in plastic wood composite. Besides, corn husks fiber also shows an outstanding strength, high elongation, good pliability, moderate durability and ready biodegradability [25].

Polystyrene is a thermoplastic mostly used for storage and packaging in food industry but it is also used in other industries such as foam, appliances and automotive industry. Polystyrene has a few good characteristics for example it is non-toxic, has good machinability, good process ability, high strength, stiffness as well as transparency [26]. Polystyrene foam (PSF) has a lot of advantages such as light weight, low cost, moisture resistance, high energy absorbing efficacy and good heat insulator [27]. It is reported that more than 1000 tons of PSF disposed into environments waste material and the amount is increasing annually [28]. PSF are seldom recycled because it is made of 98% air and has high size to weight ratio [29]. Recycling rate of PSF is low, due to it is bulky, EPS foam takes up storage space and costs more to transport and

yet yields only a small amount of polystyrene for re-use or remolding. Most of the time, PSF will ended up as landfills and it easily fill up the landfill site in a short time since its non-biodegradable [30]. Thus, this research is proposing to recycle the PSF and compound with CHF to produce WPC.

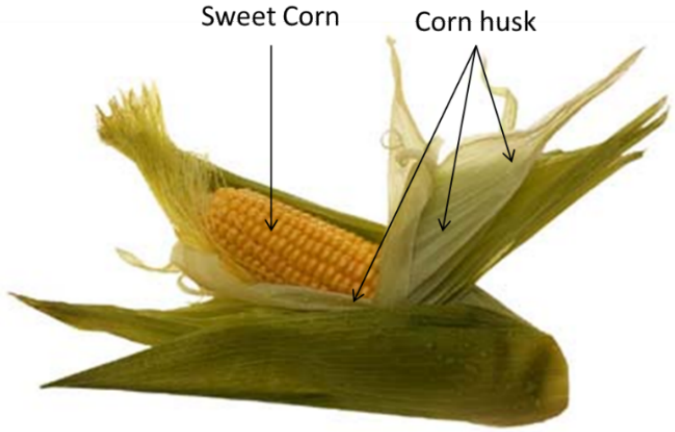


Figure 1. Corn

This research focuses on the preparation of wood plastic composite (WPC) from corn husk fiber (CHF) and recycled polystyrene foam (rPSF). The study also focuses on the effect of rPSF content and alkaline treatment on tensile, thermal, and water absorption properties of rPSF/CHF composites.

2. Research Methodology

2.1 Raw Material

In this research, the main components to produce WPC are corn husk and recycled polystyrene foam. The recycled polystyrene foam (rPSF) is mainly used as packaging material for electronic product. Thus, the rPSF was collected from an electrical shop. The corn husk was obtained from sweet corn store. The chemical used in this experiment (such as sodium hydroxide (NaOH) and acetone) were supplied by Evergreen Engineering & Resources.

2.2 Preparation of Corn Husk Fiber

First, the corn husks (CH) were washed to remove any dirt and then cut into small pieces. Next, CH was dried in oven at 60^{o}C until it fully dried. At this temperature, the CH moisture will be removed. The dried CH were further ground into short fiber using a surface grinder. The corn husk fiber (CHF) was later sieved using 100 mesh stainless steel sieve to obtain homogenous size of CHF.

Part of the CHF was further treated with sodium hydroxide (NaOH) solution using method suggested by Reddy & Yang [25]. The CHF were immersed in 1 mole of NaOH solution for 1 hour at room temperature. Then, treated CHF were filtered and washed using distillate water until the pH became neutral. Last, the treated CHF were dried in oven at 60^{o}C until it fully dried.

2.3 Preparation of Composites

The rPSF was dissolved in acetone solvent and the CHF was transferred into rPSF-acetone solution with weight ratio 1:10. Then, rPSF and CHF was mixed using mechanical stirrer for 15 minutes. The mixture was transferred into a stainless steel mould and compressed using hydraulic press for 15 minutes under pressure 1.5 bar. After molding, the rPSF/CHF composite were left in oven at temperature of 60^{o}C to evaporate the acetone solvent. The rPSF/CHF composite will became a hard solid sheet after acetone solvent was completely removed. The untreated and treated rPSF/CHF composites were prepared with different ratio according to Table 1.

Table 1. Formulation of untreated and treated rPSF/CHF

Ratio	**Untreated rPSF/CHF composites**	**Treated rPSF/CHF composites**
rPSF/untreated CHF	50/50, 45/55, 40/60, 35/65	-
rPSF/treated CHF	-	50/50, 45/55, 40/60, 35/65

2.4 Testing and Analysis

The mechanical testing of rPSF/CHF composites are carries out following ASTM D638 standard. The composites are test for its' tensile properties using Instron universal testing machine (model 5596). A 15 kN of load cell and cross-head speed of 5 mm/min will be used for tensile test. 4 different ratios of rPSF/CHF composites will be tested with a minimum of 5 samples for each ratio.

The tensile strength (σ) of specimen can be determined using Eq. (1). Where, F is applied load from equipment and A is cross-section area of tensile specimen.

$$\sigma = \frac{F}{A} \tag{1}$$

Eq. (2) was used to determine the strain (ε), where ΔL is the extension of specimen that measured by equipment and L_0 is the initial length. After determined the strain, the tensile modulus (E) can be calculated using Eq. (3).

$$\varepsilon = \frac{\Delta L}{L_0} \tag{2}$$

$$E = \frac{\sigma}{\varepsilon} \tag{3}$$

Moreover, the thermal analysis of neat rPSF, rPSF/CHF composites, untreated and treated CHF at selected ratio were studied using thermogravimetric analysis (TGA). The weight of the specimens for TGA is about 5 mg. The specimens were undergone thermal scan at a heating rate of 10^{o}C/min and range of thermal scan from 30 to 700^{o}C under nitrogen atmosphere. The nitrogen gas flow rate was fixed at 50 mL/min. Then, the weight loss against the temperature data was obtained from TGA. The heating rate was selected to allow the samples to react slowly towards the temperature change. Nitrogen was used due to its property as an inert gas so that it can eliminate the chances of oxidation reaction.

The water absorption test of rPSF/CH composites was performance according to ASTM D570 standard. All rPS/CHF composites samples with dimension 30 mm x 25 mm x 2 mm were immersed in distilled water at room temperature. The water absorption was determined by the record the weight change for 24 hours. A mass balance with the precision of ± 1 mg was used to measure the sample weight. The percentage of water absorption (W_a) at time (t) was calculated by using Eq. (4). Where W_d and W_n are the original dried sample weight and weight of sample after absorb water.

$$W_s = \frac{W_n - W_d}{W_d} x100\% \quad (4)$$

In addition, Fourier transmission infra-red (FTIR) was used to analyzed the chemical components in untreated and treated CHF. The FTIR spectra of specimens were recorded with 16 scans in the wavenumber (cm^{-1}) range from 4000-600 cm^{-1}. A resolution of 4 cm^{-1} was used for the FTIR analysis.

3. Results and Discussion

3.1 Tensile properties

Figure 2 illustrates the tensile strength of untreated and treated of rPSF/CHF composite. The rPSF was used as matrix to bind the CHF together to become composite and serves to transfer load to CHF. The result shows the increases of rPSF content increased the tensile strength of both composites. The similar result trend as obtained by Leu et al. [31] and Adhikary et al. [32]. At low rPSF content, the rPSF was insufficient to bind all the CHF together. Thus, the stress transfer within rPSF and CHF was limited. The rPSF/CHF achieved higher tensile strength when they have more rPSF to bind the CHF together and more stress can be transferred to CHF. However, the untreated rPSF/CHF composite still exhibited average of 46 % lower tensile strength compared to treated rPSF/CHF composite. Mohammed et al. [33] also found the alkaline treatment was improved the strength of composites. For treated CHF, part of the hemicellulose and lignin were removed and it causes the surface roughness of the CHF to increase. The rougher fiber surface allows the CHF to have better adhesion with rPSF. For this reason, the treated rPSF/CHF composite had higher strength than untreated rPSF/CHF composite.

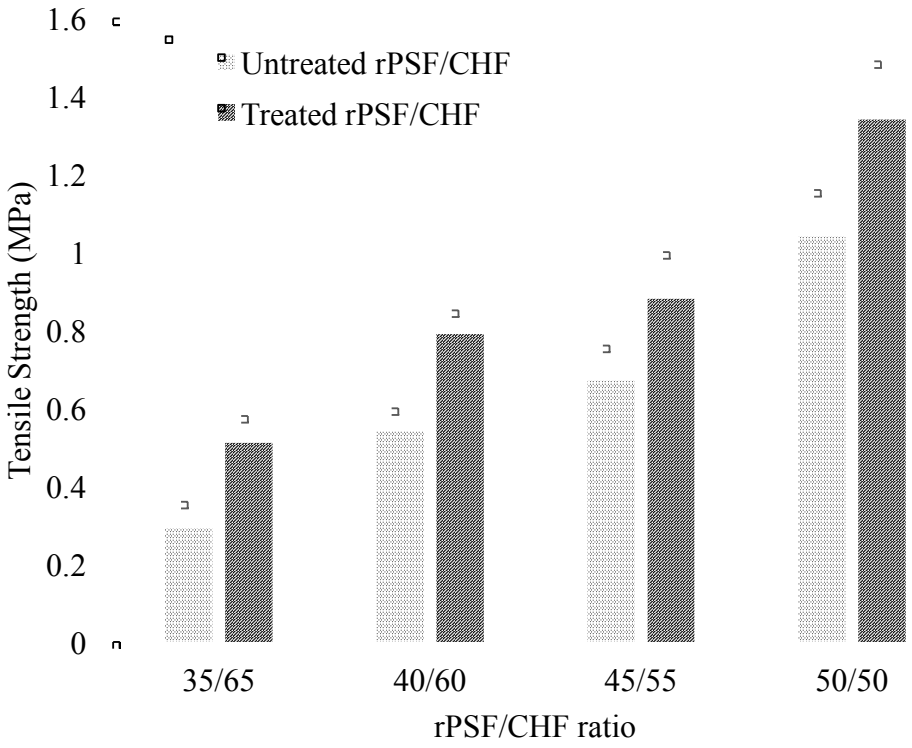


Figure 2. Tensile strength of untreated and treated rPSF/CHF composite.

The tensile modulus of untreated and treated rPSF/CHF composites are showed in Figure 3. The tensile modulus of rPSF/CHF composite increased as rPSF content increases in composite. The similar result trend also observed by Adhikary et al. [32] and Cerqueira et al. [20]. As mention earlier, this is due to the stress transfer was more efficient if the CHF can be bind together by sufficient amount rPSF matrix. Moreover, the natural fiber usually exhibited greater modulus than polymer matrix [34]. At higher rPSF content, there are more CHF covered by rPSF matrix and part of the tension stress was transferred from matrix to fiber. As result, the rPSF/CHF composite with 50/50 ratio shows higher tensile modulus. On the other hand, the treated rPSF/CHF composite shows an average of 13% higher tensile modulus than untreated rPSF/CHF composite. This is because the alkaline treatment increased the surface roughness of CHF, since part of the components have been removed. Then, this enhanced the fiber-matrix adhesion and resulting a better stress transfer at the interfacial region between fiber and matrix. These results of tensile modulus affected by the alkaline treatment are following the same trend as observed by Mohammed et al. [33] in his research. Therefore, the tensile modulus of rPSF/CHF composite improved with alkaline treatment.

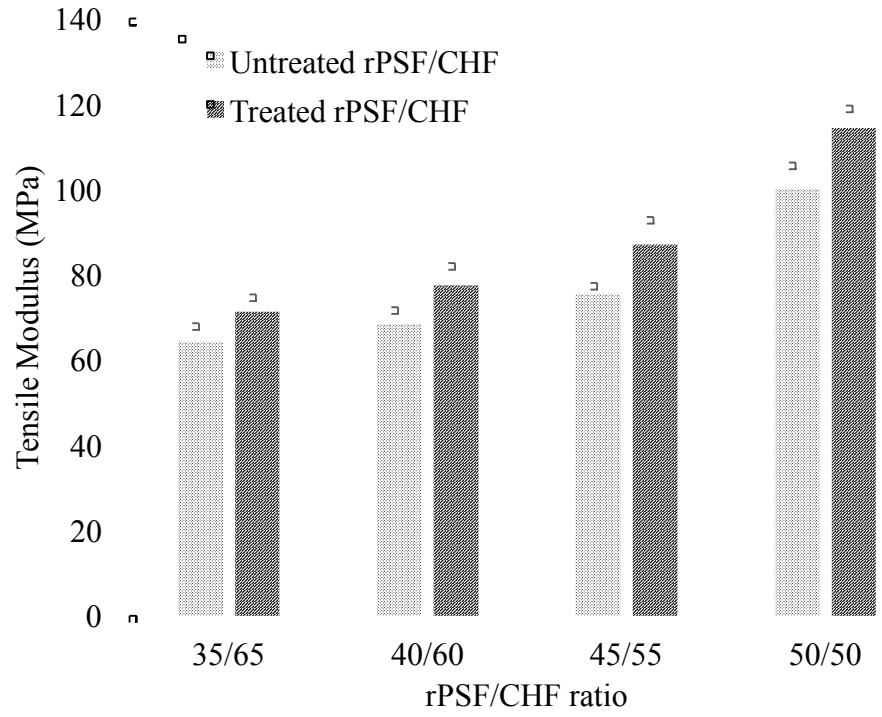


Figure 3. Tensile modulus of untreated and treated rPSF/CHF composite.

3.2 Thermal properties

Figure 4 displays the TGA curves of untreated and treated rPSF/CHF composites. The residue weight at 800°C, decomposition temperature at 10% ($T_{d10\%}$) and 50% ($T_{d50\%}$) obtained from TGA curves are listed in Table 2. The result found that the $T_{d10\%}$ and $T_{d50\%}$ of rPSF/CHF composite decreased as rPSF content increases. The major component of CHF was cellulose and it typically decomposes at temperature above 350°C. However, CHF also consists of minor components such as hemicellulose and lignin which have lower thermal stability and decompose start at temperature above 250°C [15-16]. Regarding to Jiao & Sun [35], the PSF undergone thermal decomposition within temperature 215°C to 470°C. The CHF exhibited overall better thermal stability compared to rPSF. Thus, the rPSF/CHF composites with high ratio of CHF displayed better thermal stability. Furthermore, the residue weight of rPSF/CHF composites increased as increases of rPSF content. The residue weight was referring to the char content after thermal decomposition of composite. The rPSF is a thermoplastic comprised plenty of aromatic molecules in structure which promoting the char yield of rPSF [35]. Besides, the natural fiber itself also contains a lot of aromatic molecules that can be found in lignin. The lignin also causes the formation of char during thermal decomposition of natural fiber [10]. In this case, the residue weight of composites was influenced by the content of rPSF. As comparison, the untreated rPSF/CHF composite shows lower $T_{d10\%}$ than treated rPSF/CHF composite. This indicates the untreated rPSF/CHF composite have lower thermal stability because it undergoes an earlier thermal decomposition. This earlier thermal decomposition is attributed by the thermal decomposition of hemicellulose and lignin in CHF [21]. During the alkaline treatment, most of the hemicellulose and lignin were removed from CHF. Thus, the treated rPSF/CHF composite has better thermal stability at $T_{d10\%}$. Moreover, the thermal decomposition of lignin promoting the formation of char. The char acts as thermal

barrier for the composite that improved the thermal stability of composite [13]. For this reason, the $T_{d50\%}$ of untreated rPSF/CHF composite were higher compared to treated rPSF/CHF composite due to the effect of char formation. The residue weight of treated rPSF/CHF composite was lower than untreated rPSF/CHF composite. This evidence supports the formation of char was less in treated rPSF/CHF composite.

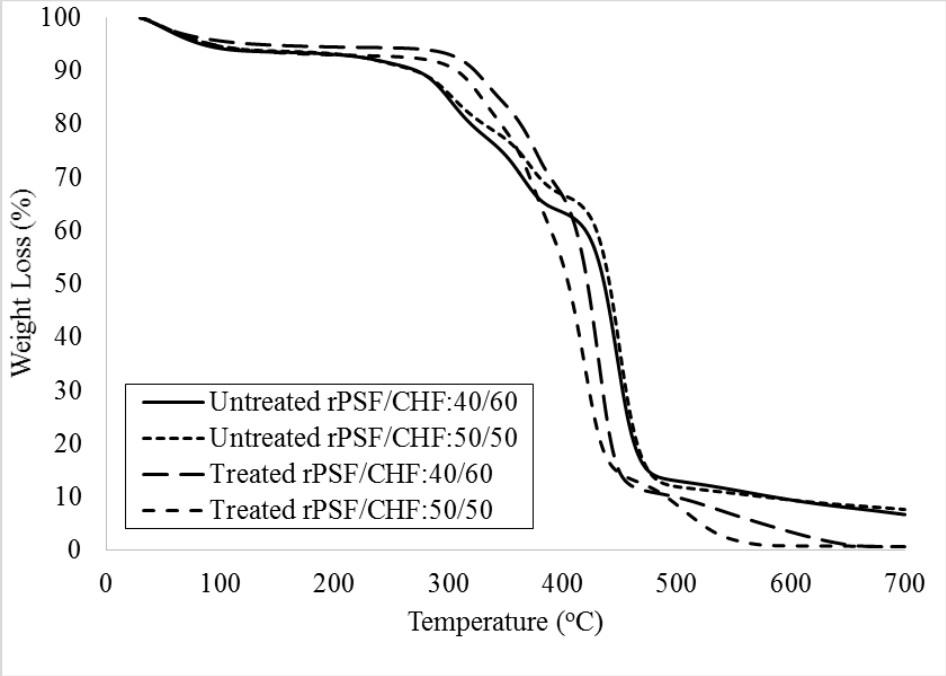


Figure 4. TGA curves of untreated and treated rPFS/CHF composites.

Table 2. TGA data of untreated and treated rPFS/CHF composites

Composites	$T_{d10\%}$(°C)	$T_{d50\%}$ (°C)	Residue weight (%)
Untreated rPSF/CHF:40/60	273	436	6.72
Untreated rPSF/CHF:50/50	268	431	7.64
Treated rPSF/CHF:40/60	324	422	0.65
Treated rPSF/CHF:50/50	308	405	0.70

3.3 Water absorption properties

The water absorption of untreated and treated rPSF/CHF composites are showed in Figure 5. The water absorption of rPFS/CHF composite was significantly reduced as the rPSF content increased. Same result trend is also obtained by Adhikary et al. [32]. The CHF naturally absorb water due to structure of cellulose, hemicellulose, and lignin consist plenty of hydroxyl groups. These hydroxyl groups from fiber can easily form hydrogen bonding with water molecules [10]. However, the present of rPSF blocked the fiber from forming hydrogen bonding with water molecules, since the rPSF is hydrophobic behavior. In the other ways, the treated rPSF/CHF shows lower water absorption than untreated rPSF/CHF composite. A similar observation also reported by Bisanda et al. [36]. This is because the NaOH reacted with hydroxyl group in CHF which causes the number of hydroxyl groups that available to form hydrogen bonding

with water molecules reduced. Thus, the treated rPSF/CHF absorbed less water than untreated rPSF/CHF.

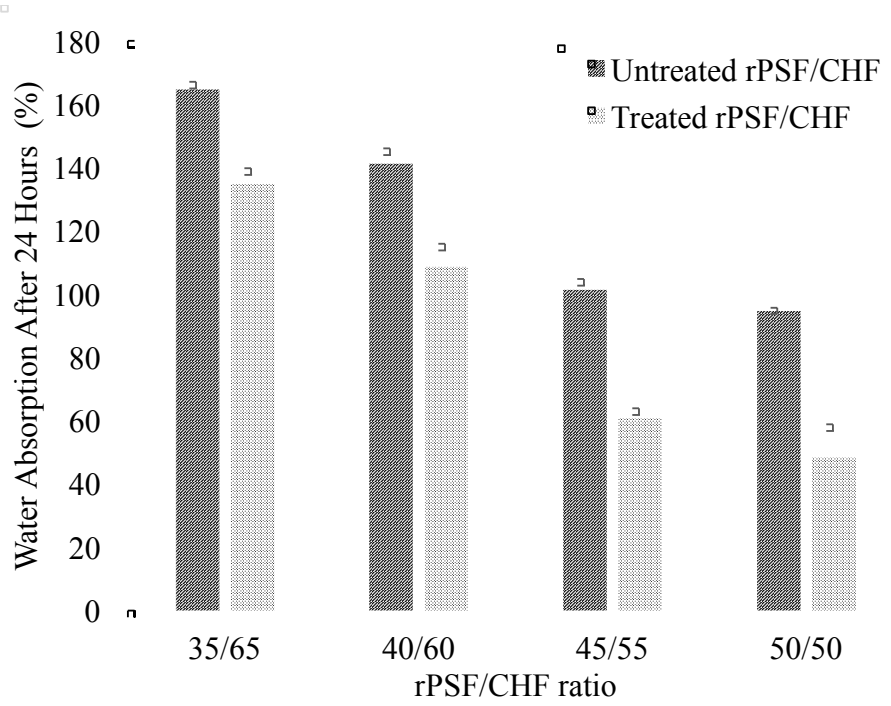


Figure 5. Water absorption of rPSF/CHF composites after 24 hours.

3.4 FTIR analysis

Figure 6 shows the FTIR spectrum of untreated and treated CHF. For untreated CHF, the wide peak recorded at 3381.5 cm-1 is due to the stretching of O-H which belongs to hydroxyl groups in fiber. In the 3000-2800 cm-1 range, the peaks are caused by the stretching of C-H. Peak measured at 1727.1 cm-1 is related to ester carbonyl vibration in lignin. As can be seen this intensity of peak reduced and the peak value shifted to 1714.6 cm-1 after the treatment indicating that the part of lignin has been removed from CHF. Then, carbonyl group in hemicellulose and carbonyl aldehyde in lignin is represented by the peak at 1638.4 cm-1. After treatment, the peak shifted from 1638.4 cm-1 to 1641.5 and the peak intensity is slightly reduced. This indicated the content of hemicellulose and lignin are reduced. The peaks at 1427.5 cm-1 is attributed by CH2 stretching from cellulose. While the peak at 1370.4 cm-1 and 1320.5 cm-1 are assigned to C-H group vibration from cellulose. The C-O groups from acetyl group of lignin found at peak 1245 cm-1. The intensity of peak at 1245 cm-1 reduced which indicates some of the lignin has been removed during the alkaline treatment. The broad peak ranging from 1000 to 1150 cm-1 is corresponding to anti-symmetrical vibration of C-O-C groups from cellulose. The last peak at 903.18 cm-1 is due to C-H stretching of lignin. After alkaline treatment, the peak reduced from 903.18 cm-1 to 894.27 cm-1 and the peak intensity also decreased. This also evidences the part of the lignin is removed from CHF.

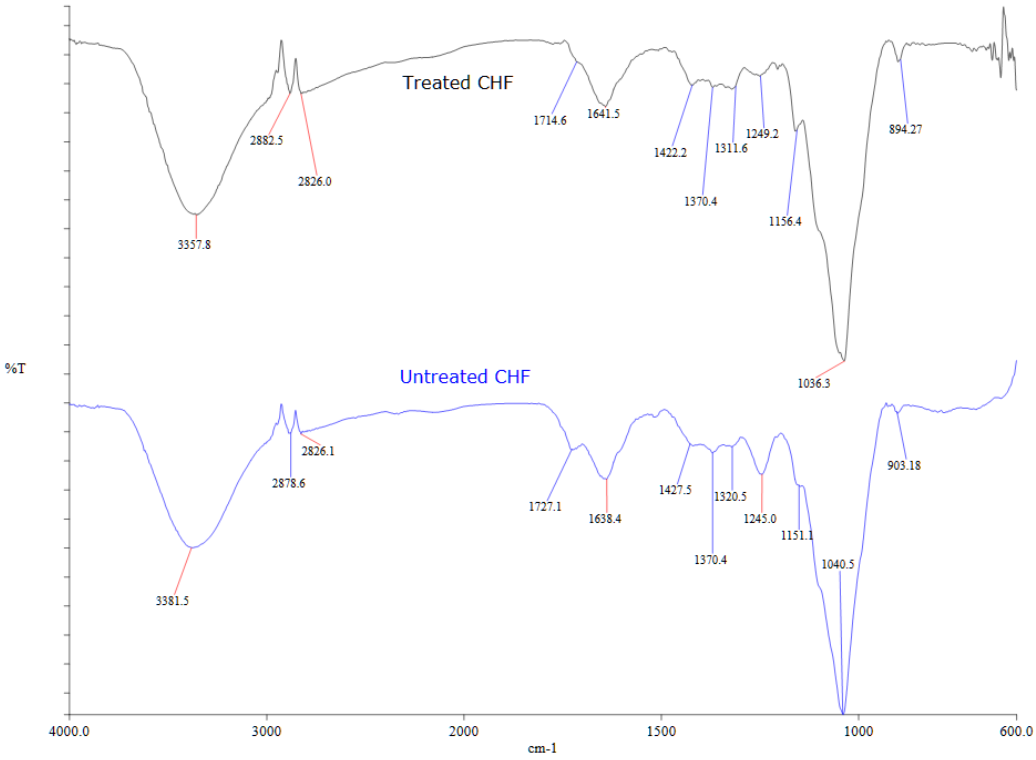


Figure 6. FTIR spectra of untreated and treated CHF

4.0 Conclusion

In short, the tensile strength and modulus of rPSF/CHF composites increased with the increases of rPSF content. The increases of rPSF content reduced the thermal stability and the rate of water absorption of rPSF/CHF composite. Overall, the treated rPSF/CHF composite shows improvement in term of tensile strength, modulus, and thermal stability (Td10%), with lower water absorption rate in comparison to untreated rPSF/CHF composite. FTIR analysis also evidenced that part of hemicellulose and lignin have been removed from CHF after the alkaline treatment.

References

[1] A. A. Klyosov, Wood-plastic composites, India: Wiley-Interscience, 2007.

[2] K. K. Jin and K. Pal, Recent Advances in the Processing of Wood-Plastic Composites, Berlin: Springer, 2010.

[3] S. Butylina, O. Martikka and T. Karki, "Physical and mechanical properties of wood polypropylene composites made with virgin and/or recycled polypropylene," *Polymer Plastic Technology,* vol. 50, pp. 1040-1046, 2011.

[4] S. Butylina, O. Martikka and T. Karki, "Properties of wood fibre-polypropylene composites: effect of wood fibre source," *Application of Composite Material,* vol. 2, pp. 101–111, 2011.

[5] J. M. Pilarski and L. M. Matuana, "Durability of wood flour-plastic composites exposed to accelerated freeze-thaw cycling. part I, rigid PVC matrix," *Journal of Vinyl Additives and Technology,* vol. 11, pp. 1-8, 2005.

[6] "Wood-plastic composite market to reach 1728.9 kilotons," *Reinforced Plastic,* vol. 59, pp. 72, 2015.

[7] S. G. Bajwa, D. S. Bajwa, G. Holt, T. Coffelt and F. Nakayama, "Properties of thermoplastic composites with cotton and guayule biomass residues as fillers," *Industrial Crops and Products,* vol. 33, pp. 747-755, 2011.

[8] D. R. Carroll, R. B. Stone, A. M. Sirignano, R. M. Saindon, S. C. Gose and M. A. Friedman, "Structural properties of recycled plastic/sawdust lumber decking planks," *Resources, Conservation & Recycling,* vol. 31, pp. 241-251, 2011.

[9] S. Gibson, "Synthetic Decking," *Remodeling Magazine,* 2008.

[10] K. S. Chun, S. Husseinsyah and F. N. Azizi, "Characterization and properties of recycled polypropylene/coconut shell powder composites: effect of sodium dodecyl sulphate modification," *Polymer-Plastics Technology & Engineering,* vol. 52, pp. 287–294, 2013.

[11] S. Husseinsyah, K. S. Chun and H. Osman, "Surface modification of coconut shell powder filled polylactic acid biocomposites," *Journal of Thermoplastic Composite Materials,* vol. 52*,* pp. 287-294, 2013.

[12] K. S. Chun, S. Husseinsyah and H. Osman, "Properties of coconut shell powder-filled polylactic acid ecocomposites: effect of maleic acid," *Polymer Engineering & Science,* vol. 53, pp. 1109–1116, 2013.

[13] K. S. Chun, S. Husseinsyah and H. Osman, "Mechanical and thermal properties of coconut shell powder filled polylactic acid biocomposites: effect of filler content and silane coupling agent," *Journal of Polymer Research,* vol. 19, pp. 1-8, 2012.

[14] H. S. Yang, H. J. Kim, J. Son, H. J. Park, B. J. Lee and T. S. Hwang, "Rice husk flour filled polypropylene composites: mechanical and morphology study," *Composites Structures,* vol. 63, pp. 305-312, 2004.

[15] K. S. Chun, S. Husseinsyah and H. Osman, "Modified cocoa pod husk-filled polypropylene composites by using methacrylic acid," *BioResources,* vol. 8, pp. 3260-3275, 2013.

[16] K. S. Chun, S. Husseinsyah and H. Osman, "Utilization of cocoa pod husk as filler in polypropylene biocomposites: effect of maleated polypropylene," *Journal of Thermoplastic Composite Materials,* vol. 28, pp. 1507-1521, 2015.

[17] A. K. Bledzki, A. A. Mamun and J. Volk, "Barley husk and coconut shell reinforced polypropylene composites: the effect of fibre physical, chemical and surface properties," *Composites Science and Technology,* vol. 70, pp. 840-846., 2010.

[18] R. Ahmad, S. Husseinsyah and A. Hadi, "Tensile properties of low density polyethylene (LDPE)/ palm kernel shell (PKS) biocomposites: the effect of acrylic acid," *Journal of Material Science and Engineering,* vol. 11, pp. 1-7, 2010.

[19] N. L. I. Zailuddin and S. Husseinsyah, "Tensile properties and morphology of oil palm empty fruit bunch regenerated cellulose biocomposite," *Procedia Chemistry,* vol. 19, pp. 366-372, 2016.

[20] E. F. Cerqueira, C. A. R. P. Baptistab and D. R. Muliari, "Mechanical behavior of polypropylene reinforced sugarcane bagasse fibers composites," *Procedia Engineering,* vol. 10, pp. 2046-2051, 2011.

[21] C. M. Yeng, S. Husseinsyah and S. S. Ting, "Chitosan/corn cob biocomposite films by cross-linking with glutaraldehyde," *Bioresources,* vol. 2, pp. 2910–2923, 2013.

[22] D. Dai and M. Fan, "Wood fibres as reinforcements in natural fibre composites: structure, properties, processing and applications," in *Natural fibre composites*, Sawston:Woodhead Publishing, 2014.

[23] K. Niskanen, Mechanics of Paper Products., Deutsche: Walter de Gruyter GmbH & Co. KG, 2011.

[24] B. Barl, C. G. Biliaderis, E. D. Murray and A. W. Macgregor, "Combined chemical and enzymic treatments of corn husk lignocellulosics," *Journal of the Science of Food and Agriculture,* vol. 56, pp. 195-214, 1991.

[25] N. Reddy and Y. Yang, "Properties and potential applications of natural cellulose fibers from corn husks," *Green Chemistry,* vol. 7, pp. 190-195, 2005.

[26] W. F. Smith, Polymeric Materials, Principles of Materials Science and Engineering, New York: McGraw-Hill, 1996.

[27] J. Schellenberg and M. Wallis, "Dependence of properties of expendable polystyrene particle foam on degree of fusion," *Journal of Applied Polymer Science,* vol. 115, pp. 2986-2990, 2010.

[28] R. Francis, Recycling of polymers: methods, characterization and applications, India: Wiley, 2016.

[29] S. W. Lye, H. S. Aw and S. G. Lee, "Adhesives for bead fusion of recycled expandable polystyrene," *Journal of Applied Polymer,* vol. 86, pp. 456-462, 2002.

[30] N. Chaukura, W. Gwenzi, T. Bunhu, D. T. Ruziwa and I. Pumere, "Potential uses and value-added products derived from waste polystyrene in developing countries: a review," *Resources Conservation and Recycling*, vol. 107, pp. 157-165, 2016.

[31] S. Y. Leu, T. H. Yang, S. F. Lo, T. H. Yang, "Optimized material composition to improve the physical and mechanical properties of extruded wood–plastic composites (WPCs), *Construction and Building Materials*, vol. 29, pp. 120-127, 2011.

[32] K. B. Adhikary, S. Pang, M. P. Staiger, "Dimensional stability and mechanical behaviour of wood–plastic composites based on recycled and virgin high-density polyethylene (HDPE)," *Composites: Part B Engineering*, vol. 34, pp. 897-815, 2008.

[33] A.A. Mohammed, D. Bachtiar1, J.P. Siregar and M.R.M. Rejab, "Effect of sodium hydroxide on the tensile properties of sugar palm fibre reinforced thermoplastic polyurethane composites," *Journal of Mechanical Engineering and Sciences*, vol. 10, pp. 1765-1777, 2016.

[34] H. Ku, H. Wang, N. Pattarachaiyakoop, and M. Trada, "A review on the tensile properties of natural fiber reinforced polymer composites," *Composites Part B*, vol. 42, pp. 856-873, 2011.

[35] L.L. Jiao and J. H. Sun, "A thermal degradation study of insulation materials extruded polystyrene," *Procedia Engineering*, vol. 71, pp. 622-628, 2014.

[36] E. T. N. Bisanda, "The effect of alkali treatment on the adhesion," *Applied Composite Materials*, vol. 7, pp. 281–289, 2000.

eureca 2017 – Conference Paper
Paper Number 2ME19

Development of an Airborne Traffic Monitoring System

Aaron Gayvin*, Dr Chech Kean How
Department of Mechanical Engineering, School of Engineering, Taylor's University, Malaysia

* aarongayvin.peterfrancisxavier@sd.taylors.edu.my

Abstract
This study focuses on the development of an airborne system that can monitor traffic using an aerial camera. Traffic congestion is a problem faced by many, especially in Malaysia. This study is done to create a system which would provide an aerial view of a traffic congestion, thus identifying the root-cause of the congestion. The airborne system has an airship and a payload, whereas the ground system has a monitor connected to an AV module. The electrical connections are shown using a schematic diagram. The approach taken to this study was through simulation. Using MATLAB, the range of radius and length for the airship was identified and a 3D model was created. The model underwent simulation to provide proof of feasibility. The aerial camera was tested to provide feedback from the electrical connection. The results obtained are tallied using graphs to show if the study provides proper understanding and contribution to the body of research. The study also focuses on the improvement of human life when a problem such as traffic congestion is provided with a solution from the study.

Keywords: Traffic monitoring, Traffic data, Airborne vehicles, Drones, Monitoring system.

1. Introduction

Traffic congestion is a problem faced by many. Long stretches of road with vehicles back-to-back is a sign of congestion. Both time and fuel are spent in excess by motorist daily due to poor road designs thus leading to traffic build-ups. International Business Machines Corporations (IBM) conducted a survey for three years to identify if traffic congestion increases drivers commute time. The survey shows that 87% of drivers have increased their commute time by an hour [1]. ASI Almselati et al. (2011) state that the number of vehicles here in Malaysia has increased exponentially since the 2000s.

Vehicle movement patterns, crucial to road planning, can be obtained from Closed-circuit television (CCTV)s and traffic cameras. Highway developers require traffic data to ensure the road they built meets certain requirements. Traffic data includes peak hours, traffic flow patterns, and the growth of the vehicle fleet [2]. With traffic data, developers make predictions as to the problems that may arise before opening the road to the public. With predictions, smart solutions can be implemented to the planning before work begins.

Global Positioning System (GPS) is an existing solution to traffic congestion. It is commonly found in smartphones whereby applications such as Waze use it to provide temporary solutions to the public. The system allows the application to identify alternative routes for drivers to avoid traffic congestion. The traffic data obtained from GPS is fed to the application in real-time, therefore drivers are able to reduce their commute time. The application provides color indication to identify the level of congestion. Red for very congested, orange for mildly congested and purple for no or less congested.

Unmanned Aerial Vehicle (UAV)s or drones can be used to identify the root cause of a traffic congestion. UAVs comes with aerial viewing camera systems that can be controlled remotely. Currently drones are widely used in many different areas. Amazon uses it for their delivery system and the army uses it for surveillances. Quick assessment and fast response are provided for congestions as UAVs give an edge by monitoring the root problem of it (Coifman et al., 2004). The duration and distance drones cover are limited by its batteries. Batteries can only be used for a period before recharging is required, meaning they can only achieve a short distance of a road.

The objective of this project is to develop an airborne system which will provide an aerial view of a traffic congestion and identify the root-cause of the congestion. The data collected by the camera will then be transferred to a ground system for analysis. The scope of the project includes up until the collection of data. The traffic data obtained can be used for multiple reasons including urban planning. As mentioned earlier, road planning is important to reduce and possibly eliminate traffic congestion, therefore preliminary data obtained from the airborne system should help. This project can ultimately provide useful data for road management and include benefits to the environment and improves road safety [3].

.

2. Research Methodology

2.1 Project Setup

The project is divided into two system, an airborne system and a ground system. The airborne system has the lifting mechanism and payload. The lifting mechanism used for this project is an airship. An airship is chosen due to its long endurance towards usage. The payload is made up of the aerial camera system.

Using MATLAB, the radius and length of the airship was calculated before modelling the geometry. The script for the calculation are shown in equations Eq. (1-4). The thickness of mylar film used is 12.5 µm, the radius of the airship are between 0.1 m to 0.5 m, and length of the mid-section is 1 m.

$$Buoyancy\ force\ (lifting\ force) = Weight\ of\ airship + payload\ mass \quad (1)$$

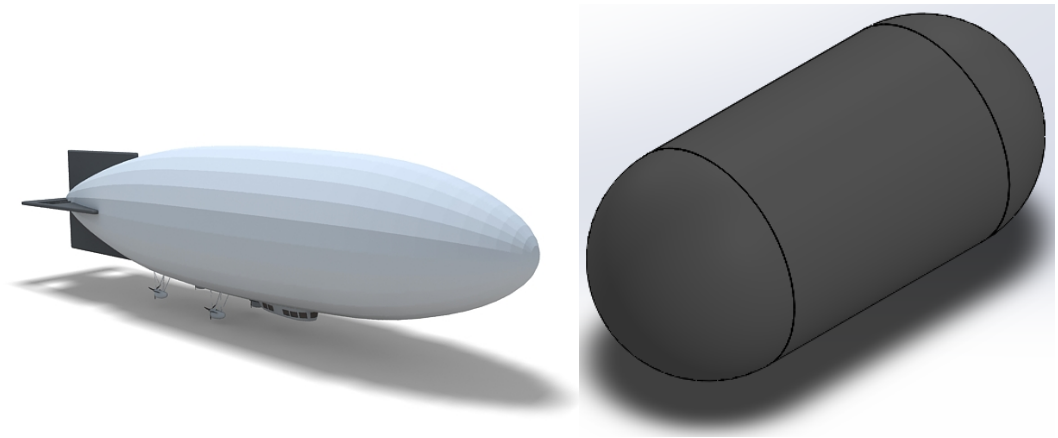
$$Volume\ of\ gas\ (V_{gas}) = \left[\frac{4}{3}\times\pi\times r^3\right] + [\pi\times r^2\times h] \quad (2)$$

$$Volume\ of\ airship\ (V_{airship}) = \left[\frac{4}{3}\times\pi\times r^{2\times t}\right] + [2\times\pi\times r\times t] \quad (3)$$

$$Mass\ of\ payload = \left[(\rho_{air} - \rho_{helium})\times V_{gas}\right] - (\rho_{mylar}\times V_{airship}) \quad (4)$$

2.2 Geometry Modelling

Unlike drones, airships shown in Fig. 1(a) are powered by helium gas, thus the prolonged airtime. The airship was designed using Solidworks with the blimp design in mind as shown in Fig. 1(b). The airship is made of two hemispheres and a cylinder. Both shapes share similar radius which is 0.4 m and the height of the cylinder is 1 m. The total length of the blimp is 1.8 m. The airship is not modelled with the payload due to complexity of shape. This airship is designed with simple shapes rather than the actual blimp size due to manufacturing time.



(a) (b)

Figure 1. Blimp Design (a) Complex (b) Simplified

2.3 Simulation Analysis

Simulation is done to determine the feasibility of the modelled airship. Solidworks has a feature whereby flow simulation can be used to graphically show pressure and velocity distribution around the model. The data obtained can then be used to determine if the model is feasible for the real world. The process of creating the flow simulation starts by creating a boundary for the model to be placed in. Next, initial conditions such as air speed and force hitting the front side of the model is added. Fig. 2 shows the set-up of the simulation before meshing and calculation.

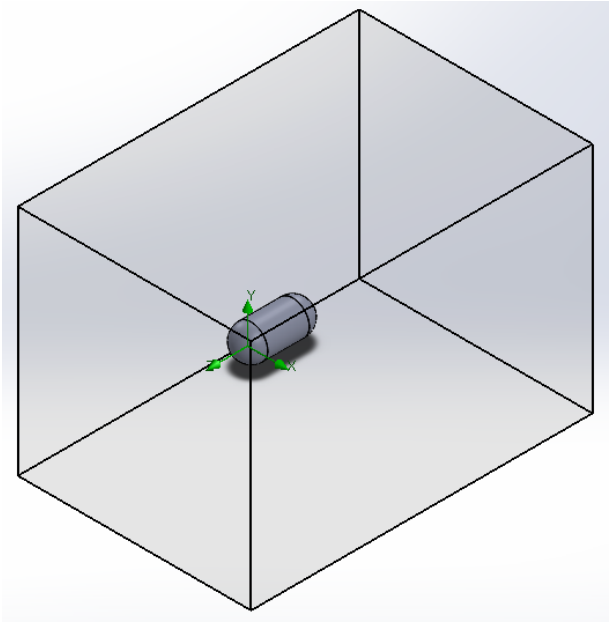
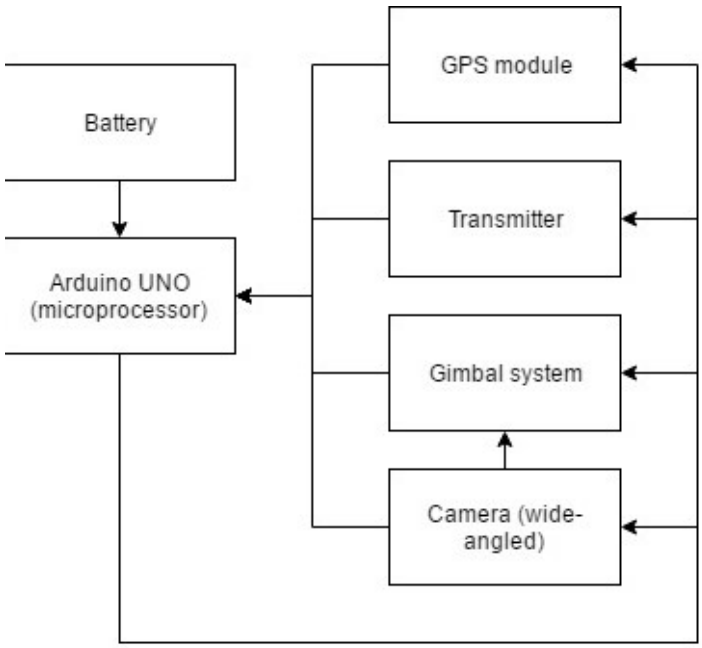


Figure 2. Boundary Domain

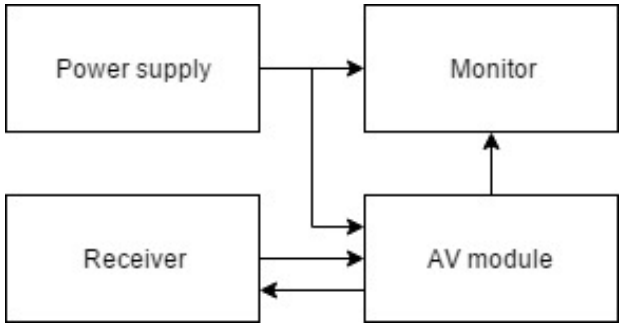
The initial condition used for the simulation is air velocity of 3 m/s at 30 m above ground. Since the airship will be anchored to the ground with strings, the stability of the airship was negated during the simulation.

2.4 Electrical System

The electrical components used for this project are selected based on the budget set for the project. The system is made up of a wide-angled camera, a gimbal system, an aerial antenna, wireless audio-video (AV) module, AV cables, GPS module for Arduino, transceiver module, Arduino UNO microcontroller and battery. Fig. 3(a) shows the connection of the system in an electrical schematic diagram. The diagram was created using Microsoft Paint to indicate the connection between the components. Fig. 3(b) shows the setup for the ground system.



(a)



(b)

Figure 3. Schematic Diagram (a) Payload (b) Ground System

The arrows drawn that connects the boxes are the wires and cables used. The Arduino UNO controls most of the component while distributing current from the battery properly back to the components. The aerial camera connects to both the microprocessor and the gimbal system. As the camera captures images of the ground, it is sent to the Arduino and in turn sent through the transmitter. The GPS module is connected to provide location data back to the ground system. Data obtained from the components can be used for multiple purposes which is explained in the discussion section.

3. Results and Discussion

3.1 Airship

Using the boundary conditions mentioned in section 2.1, the flow simulation done on the airship geometry model can be seen in Fig. 4. The simulation shows the movement of air flow when air encounters the airship. The distribution of pressure among the front of the airship to the back indicates minor changes, meaning the airship will most likely be stationary. The theoretical reason behind this is because of the anchoring strings attached to the airship, thus the speed of air at 30 m above ground should be negligible.

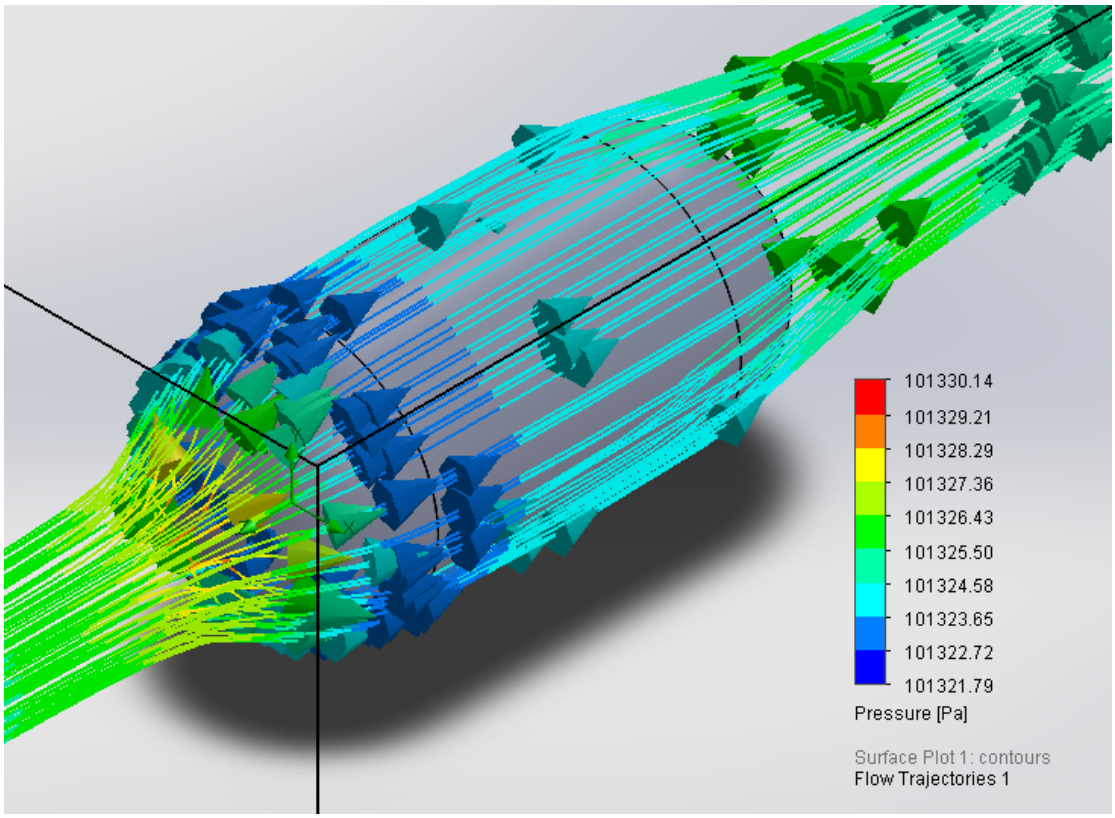


Figure 4. The air flow movement (pressure distribution)

The highest pressure can be found at the center point of the front hemisphere, which is 101.33 kPa. The lowest pressure is distributed around the edge of the front hemisphere which is 101.32 kPa. The difference between the highest and lowest pressure is very minimal which means the airship will experience similar pressure all around. This is because of the anchoring points placed on the airship which replicates the attachment using strings. Another information that can be extracted here is the stability of the airship. Due to even pressure distribution, the airship will be stable for the aerial camera to capture proper image without the need of a servo motor to control the camera.

3.2 Aerial Camera Testing

The testing procedure taken here is to compare the resolution of the camera with distance. The images taken are transferred to the receiver and screenshots of the images received are taken. Fig. 5(a) shows the image at 1 m, Fig. 5(b) shows the image at 2 m and Fig. 5(c) shows the image at 3 m. The resolution of the image changes with the distance due to the quality of the camera. However, the transmitted images are also affected by the distance between the transmitter and the receiver as during testing, the receiver was placed at the same distance as the object while the camera is moved away from the object.



(a)



(b)



(c)

Figure 5. Different image resolution (a) 1 m (b) 2 m (c) 3 m

The duration taken for each image to be transmitted was too short to differentiate, therefore no record of time was taken for this study. The success of image transfer indicates that the ground system works properly. As these are preliminary testing results, there is no confirmation that both the airborne and ground system should

work properly after manufacturing. The testing for both system after manufacturing will be the final outcome of the study.

4. Conclusion

The development part of the study is not complete, however with these preliminary data obtained from analysis, it can be concluded that the study has potential to be much more than a traffic monitoring system. The air flow simulation has shown that the design used for the airship is sufficient for the study. As discussed earlier, the design experiences equal pressure surrounding it, therefore it will be stable as it hovers on top of a road. Furthermore, the images obtained from the camera shows that all the electronic components work correctly as set-up.

References

1. "IBM Global Commuter Pain Study Reveals Traffic Crisis in Key International Cities", www-03.ibm.com, 2016. [Online]. Available: https://www-03.ibm.com/press/us/en/pressrelease/32017.wss. [Accessed: 04- May- 2016].
2. Road Planning Process, 1st ed. 2010.
3. D. Rosenbauma, Charmettea, F. Kurza, S. Suria, U. Thomasa, P. Reinartza, "AUTOMATIC TRAFFIC MONITORING FROM AN AIRBORNE WIDE ANGLE CAMERA SYSTEM", Remote Sensing Technology of the German Aerospace Center (DLR), pp. 557-562, 2008.
4. ASI. Almselati, Riza Atiq, O.K. Rahmat, and Othman Jaafar, "An Overview of Urban Transport in Malaysia", Medwell Journals, pp. 24-33, 2011.
5. Benjamin Coifman, Mark McCord, Rabi G. Mishalani, Keith Redmill, "Surface Transportation Surveillance from Unmanned Aerial Vehicles", International Applications of Advanced Technologies in Transportation Engineering, 2003.
6. Anuj Puri, "A Survey of Unmanned Aerial Vehicles (UAV) for Traffic Surveillance", Department of Computer Science and Engineering, University of South Florida, 2003.
7. E. Sofge, "4 New 'Blimp' Designs Bring Return of the Airship", Popular Mechanics, 2009. [Online]. Available: http://www.popularmechanics.com/flight/a2445/4242974/. [Accessed: 16- Jun- 2016].
8. "Ailerons", Grc.nasa.gov, 2016. [Online]. Available: https://www.grc.nasa.gov/www/k-12/airplane/alr.html. [Accessed: 16- Jun- 2016].
9. Gell´ert M´attyus, Franz Kurz, Dominik Rosenbaum, and Oliver Meynberg, "A real-time optical airborne road traffic monitoring system", Remote Sensing Technology of the German Aerospace Center (DLR), pp. 645-656, 2013.
10. P. Reinartza, T. Kraussa, M. Pötzscha, H. Rungea, S. Zuevb, "TRAFFIC MONITORING WITH SERIAL IMAGES FROM AIRBORNE CAMERAS", Remote Sensing Technology of the German Aerospace Center (DLR), 2005.
11. Casey Stockbridge, Alessandro Ceruti, Pier Marzocca, "Airship Research and Development in the Areas of Design, Structures, Dynamics and Energy Systems", International Journal of Aeronautical and Space Science, pp. 177, 2012.

eureca 2017 – Conference Paper
Paper Number 2ME20

Airflow study of a Split-Type Outdoor unit subjected near wall effect using Computational Fluid Dynamic (CFD) simulation

Syed Ahmad Fahmi Bin Syed Ibrahim[*1], Douglas Tong Kum Tien[1], Dr. Chin Wai Meng[2]

[1]*Department of Mechanical Engineering, School of Engineering, Taylor's University, Malaysia.*
[2]*Research & Application Department, Daikin R&D Malaysia Sdn. Bhd. (DRDM)*

[*]*syedahmadfahmibinsyedibrahim@sd.taylors.edu.my*

Abstract
The effectiveness of the split-type air conditioner which consists of indoor and outdoor units is determined by the effectiveness of its condensation, compression and evaporation cycles. The key factors that affect the performance of the outdoor unit are the air flow profile and the pressure discharge at the compressor. If the air flow rate decreases, the pressure discharge of the compressor increases. This will cause the power consumption to increase and overall efficiency to drop. One of the factors affecting the air flow profile is the distance between the outdoor unit and the wall. The distance of this wall gap is crucial because it affects the static pressure in the gap. This static pressure interferes with the air flow towards the outdoor unit. Therefore, the smaller the gap, the higher the static pressure and hence less air will flow through the outdoor unit. The purpose of this research is to study the air flow of a split-type outdoor air conditioner unit when it is placed near the wall and investigate its optimum placement from the wall. For the first stage of this investigation, the 3D CAD modeling of the DAIKIN outdoor unit of 5SL15F SERIES was completed using ANSYS SPACECLAIM software. The meshing was done using SnappyHexMesh code. Next, the simulation was conducted using OPENFOAM software to determine the air flow profile. The air flow profile was input into the CoilDesigner software. Then, the CoilDesigner software was used to create the heat exchanger condition for the condenser and evaporator prior to transferring this condition to the VapCyc software. The VapCyc software is a refrigerant cycle programme and it was used to predict the pressure discharge at the compressor based on the obtained air flow profile. The input for the VapCyc software comprises of the conditions at four air conditioner components, namely the condenser, evaporator, expansion device, compressor. The results show that optimum distance is at 200mm for x-axis and y-axis while 1000mm for the z-axis. It has the highest CFM and low-pressure discharge at the compressor.

Keywords: CFD simulation, Split-type, CFM, OpenFOAM.

1. Introduction

Usage of a split-type air conditioner units is common in Malaysia as it is located at the equatorial line and experiences tropical climate for the entire year with high temperatures and the humidity[1]. This makes the air conditioner important as it helps maintain low temperature and low humidity indoor. Most of the residential area uses split-type air conditioner units because they are smaller than another type of air conditioner units[2].

A split-type air conditioner unit consists of two different parts which are an indoor unit and an outdoor unit. The indoor unit contains an evaporator while the outdoor unit contains a compressor and a condenser. The indoor unit absorbs heat inside the room while the outdoor unit releases the heat into the air through a heat exchange process inside the unit. This research will focus mainly on the outdoor unit as tasked by the industrial partner. In the process of designing the outdoor unit, there are certain conditions that must be applied, one of which is that the heat exchanger inside the outdoor unit must not be congested by other parts so that the air may flow through it. The flow of the air is created when the surrounding air is extracted from the fan and discharged into the surroundings. In order to quantify the air passing through the heat exchanger, air volumetric flow rate is used.

There are many factors affecting the performance of the outdoor unit and one of them is the distance between the wall and the outdoor unit[3]. The wall gap distance is closely related to the air flow and it is necessary for the heat exchange process. Hence, the wall gap affecting the performance of the outdoor unit and the performance of the air conditioner system can be calculated using the Coefficient of Performance (COP) formula[2, 4].

Essentially, temperature and the flow rate affect the performance. Avara et al. stated that for every 1°C increment in temperature, there will be a 3% of the COP value[5]. Furthermore, when the temperature reaches beyond 45°C, the entire air conditioning system will fail due to extreme conditions at the condenser and the evaporator[6]. This may be caused by the wall gap distance of the outdoor unit. An inappropriate wall gap distance could contribute to increasing the temperature and decreasing the air flow rate of the heat exchanger.

Chow et al.[7] studied the effect of the of the placement and re-entry of the outdoor unit. The author stated that the placement of the outdoor unit for all kinds of re-entrant played an important role in the performance. Also, that in increasing the number of the outdoor units placed together at tall buildings, the heat rejected will accumulate and cause a mass of heat around the system and hence affect the performance of the outdoor unit.

Avara et al. conducted a simulation using the k-epsilon model to search on the optimum placement of the outdoor unit. The relationship between the temperature and the placement are shown in Figure 1 and Figure 2. The author stated that at a certain distance, there is no change in flow rate. However, there will be hot air recirculation occurring that will result in temperature increase. When the distance of the installation is too near to the wall, the air flow will be low. Accordingly, the hot air recirculation affected the air flow rate due to the static pressure.

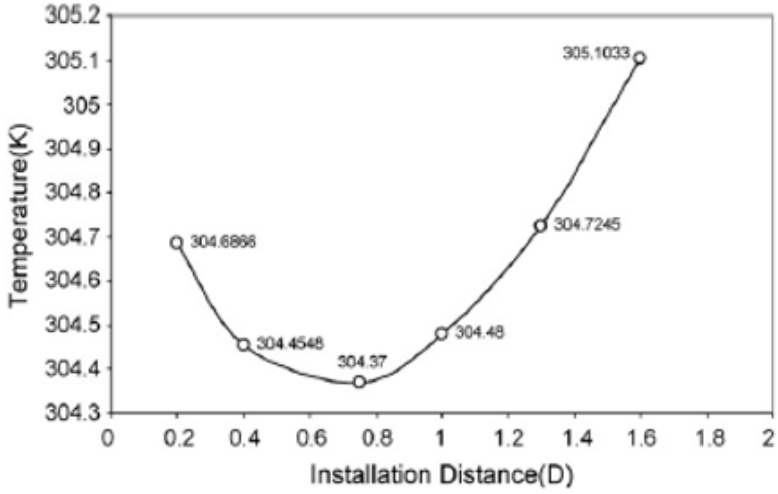


Figure 1. Graph of temperature against the installation distance[5]

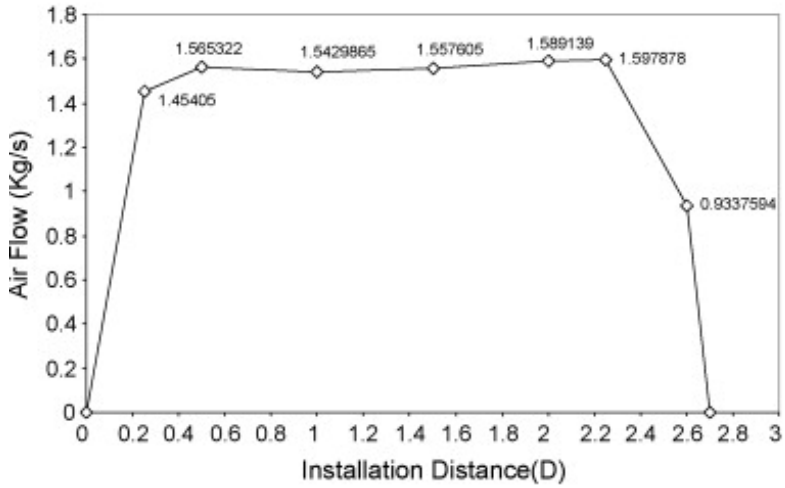


Figure 2. Graph of air flow against the installation distance[5]

To analyze the flow and velocity of a fluid, Computational Fluid Dynamic (CFD) simulation is one of the best ways to identify the air flow around the outdoor unit. Chow and Avara et al.[5] conducted research using CFD simulation with the k-epsilon model being chosen to identify the turbulence flow created near the wall condition and high rpm fan blade. Furthermore, k-ε aims for higher quality and stable flow rate. It is also supported by Q. Chen [8] in the research about the comparison of the k-ε model for an indoor flow. On the other hand, few other methods of heat transfer such as radiation and convection were neglected due to complex calculation and simulation[3].

This research's objectives are to investigate the relation between the air flow rate measured in cubic foot per minute (CFM), with the distance of the outdoor unit from the wall and to predict the operating pressure of the compressor. CFD simulation is carried out to investigate the air flow rate when outdoor unit is applied to a certain wall gap distance. The distance should be measured using the x-axis, y-axis, and z-axis. These parameters were constructed referring to the research by Avara et al[5]. However,

the research was lacking in another parameter which is z-axis. Therefore, z-axis was manipulated in this paper. Based on the air flow profile produced in the simulation, VapCyc software will be used to predict the temperature and pressure discharge at the compressor. Lastly, this paper aims to determine the optimum placement of the outdoor unit when it is subjected near a wall condition.

2. Research Methodology

The methodology employed for this study is discussed below. Each stage is explained with the help of relevant figures. The stages start with creating the model in ANSYS version 15.0, CFD simulation using OPENFOAM software version 3.4, analysis using Coil Designer software and VapCyc software. There will be further information on Coil Designer and VapCyc software in each stage.

2.1 Stage 1

2.1.1 CAD drawing of the outdoor unit

The drawing of the outdoor unit 5SLY15F SERIES that are provided by DAIKIN which is the original model is complicated. Hence, a simplified version is done using ANSYS SPACECLAIM where the important components are separated and the rest are removed (de-featured). This process will create a simpler mesh and save a lot of time for simulation. The important parts left is the fan blade, the casing of the outdoor unit, the grill, the bell mouth and the heat exchanger (condenser). The drawings for each part is shown in Figure 3.

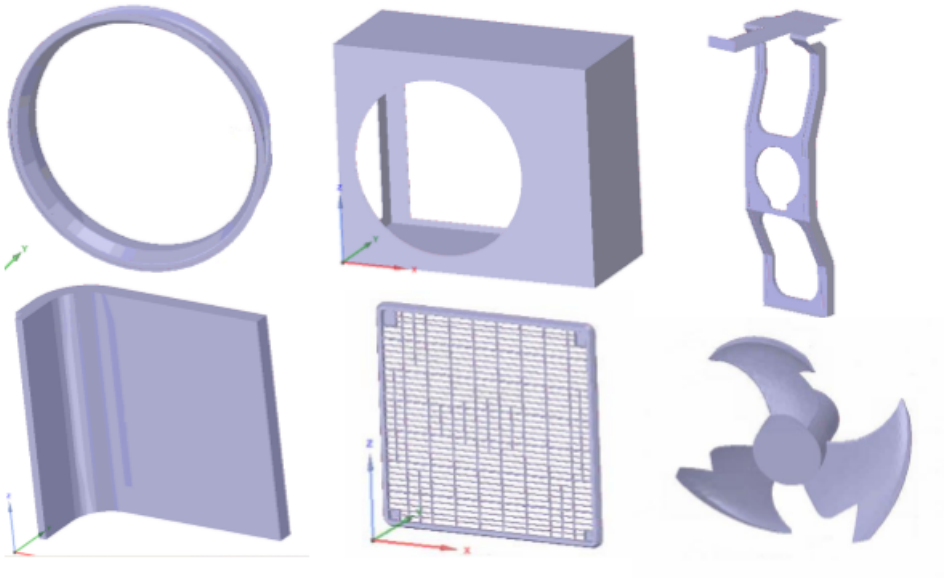


Figure 3. CAD drawing of the parts for the outdoor unit

Based on Figure 3, the drawings are in a simplified version where all the complex geometry is being removed. These simplified drawings produce a lesser number of mesh elements and eliminate error during meshing. An assembly drawing is shown in Figure 4 which is the exact drawing used in the simulation.

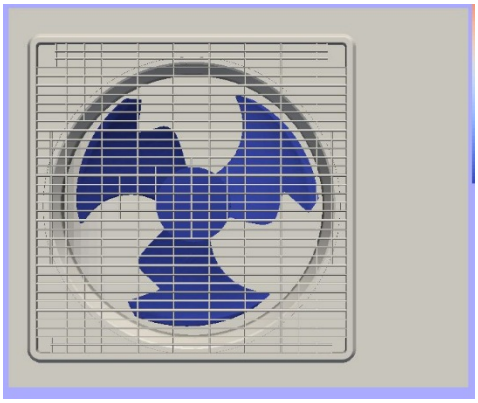


Figure 4. Assembly drawing of the outdoor unit

Subsequently, the simulation has to correspond with the real case where the fan blade rotates at a certain speed (rpm). To ensure that the process is similar, Multiple Reference Frame (MRF) zone were created. During the simulation, OPENFOAM Software was used to create a boundary around the fan blade which allows it to rotate inside the MRF zone itself. Since the MRF zone was assigned differently, it can perform different speed (rpm) during simulation. The MRF zone created were shown in Figure 5 below.

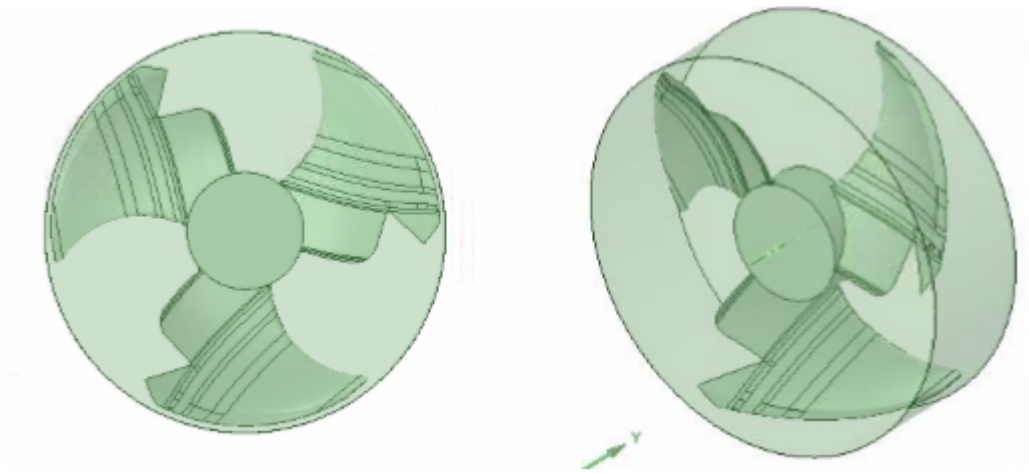


Figure 5. Multiple Reference Frame zone

The purpose of adding the MRF zone into the fan blade was to ensure that the software will recognize which parts were moving (rotating) and which part is stationary.

2.1.2 Case Studies

Before proceeding towards the simulation, there are a few parameters that need to be manipulated in order to compare the results and analyze the optimum placement. The speed for every case will be constant whereas the manipulated variables are the distance of the outdoor unit from the wall in term of x, y, and z-axis as shown in Figure 6.

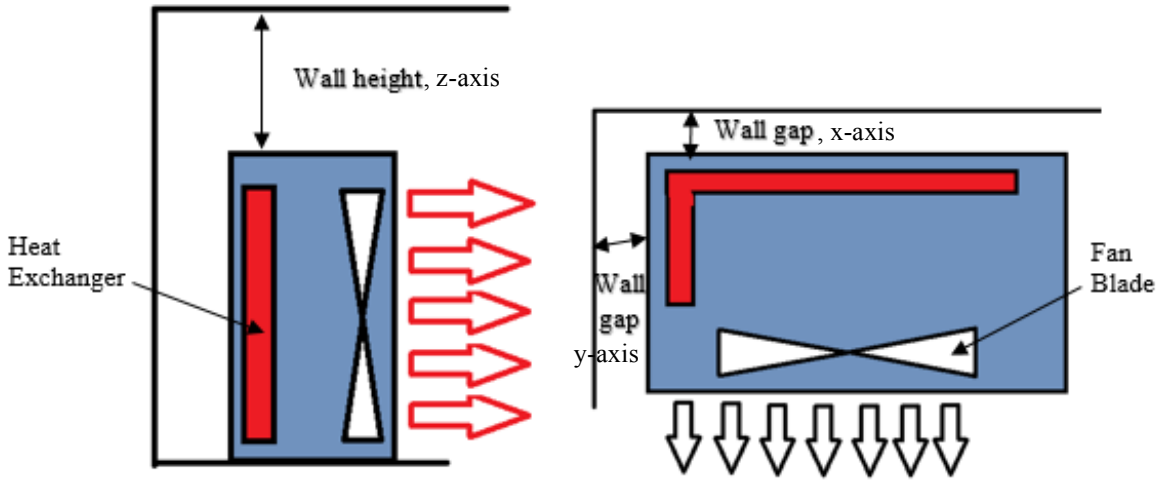


Figure 6. Manipulated variables

Table 1 represents the cases for the simulation where three different wall distances are manipulated. There was a total of 6 simulations conducted throughout the research and the parameters were set regarding the smallest range until the highest range which is from 60mm and 200mm. For any distance lower than 60 mm, the simulation produces an error due to this small gap. According to Avara et al.[5] for a distance more than 200mm, the temperature will remain nearly unchanged. Therefore, the range chosen was between 60mm to 200mm.

Table 1. Parameters of Case Study

	Wall Distance		
Case Studies	**x-axis(mm)**	**y-axis(mm)**	**z-axis(mm)**
Case 1	60	60	500
Case 2	60	60	1000
Case 3	150	150	500
Case 4	150	150	1000
Case 5	200	200	500
Case 6	200	200	1000

2.2 Stage 2

2.2.1 Meshing of the model

After the first part was completed, the model was meshed inside the OPENFOAM software using a SnappyHexMesh method where it created a fine mesh. Since the software uses the C++ language, all the information and editing are in coding form as shown in Figure 7. On the other hand, Figure 8 shows the sample of a refined mesh created on the fan blade using the SnappyHexMesh.

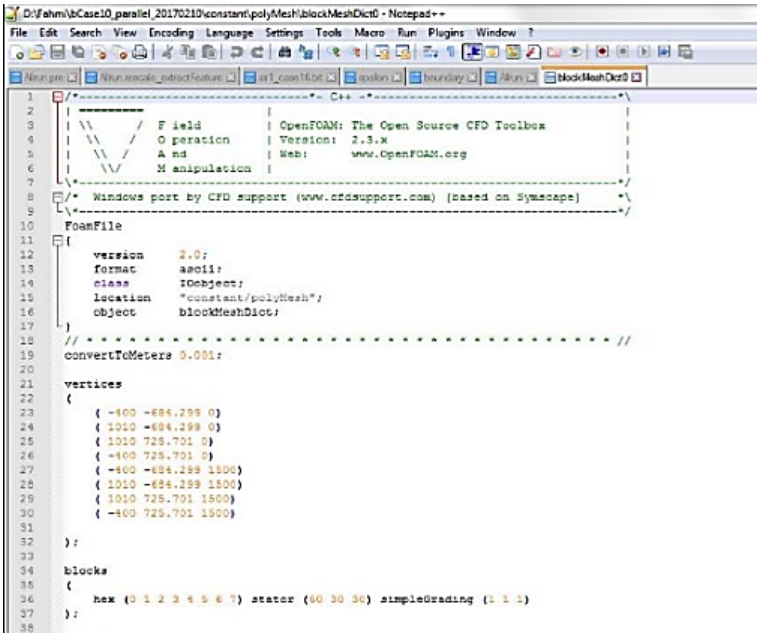


Figure 7. OPENFOAM Software coding

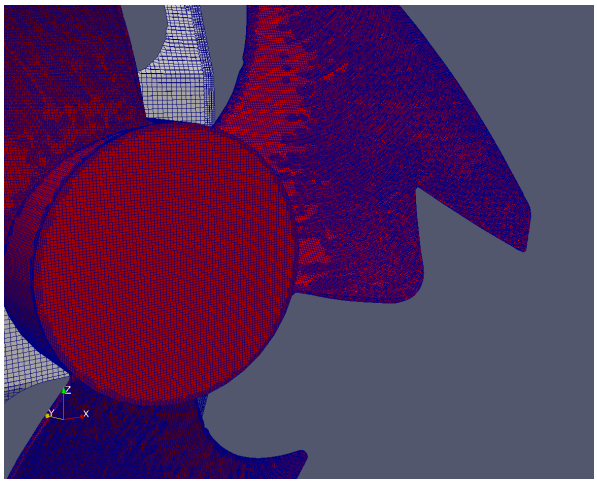


Figure 8. Refined mesh at the fan blade

The purpose of doing the simulation is to investigate the air volume flow rate through the heat exchanger. Once the meshing is done, the simulation process started for wall gap starting from 60mm, 150mm, and 200mm for the x-axis and y-axis while z-axis varied between 500mm and 1000mm. A total of 6 cases were tested. The air volume flow rate (air flow profile through the heat exchanger coil) is extracted from the simulation and the result was analyzed.

2.2.2 CFD Simulation

CFD simulation was completed using OPENFOAM software which consists of multiple solvers. However, this research uses incompressible flow which narrows down the list of solvers. The simpleFoam solver was chosen as the type of solver due to its characteristic which is a steady state solver and a turbulent flow was created around the

fan blade. OPENFOAM is an open source software whereby it does not come with the user guide. There are few commands were used in performing the simulation which is shown in Table 2.

Table 2. Commands used in OPENFOAM

Command	*Execute*
blockMesh	Applying the basic mesh into the 3D-model.
snappyHexMesh	Refining the mesh.
simpleFoam	Run the simulation.
Allrun	Run all the commands according to the sequent that is set.

All the executed commands were recorded and saved in a log file which can be viewed during the process. Figure 9 below shows the sample of the command and Figure 10. shows the data recorded in the log file.

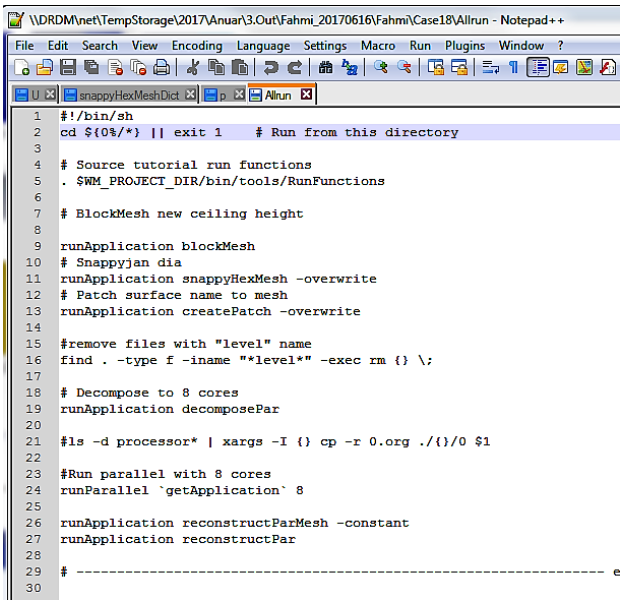


Figure 9. Allrun command script file

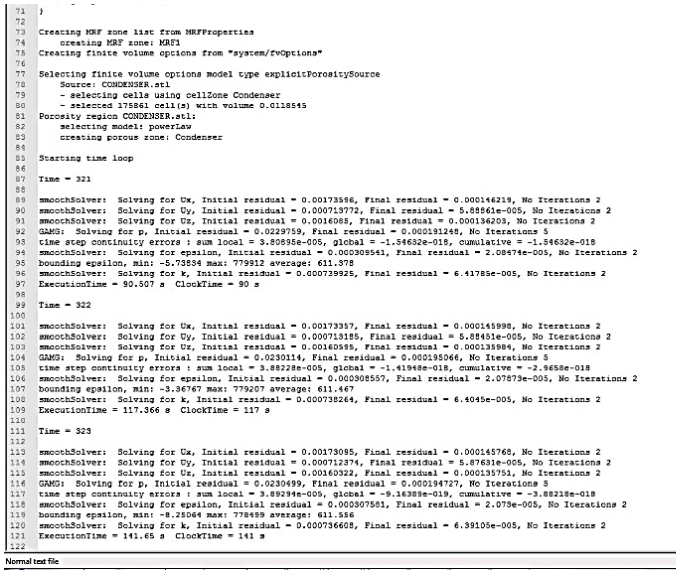


Figure 10. Sample of a running simulation in a log file

2.3 Stage 3

2.3.1 Coil Designer software

Another software which called CoilDesigner were used to identify the on-coil temperature. The actual heat exchanger or also known as coil were drawn and used in this particular software. Since an air conditioner system consists of two units which are the indoor(evaporator) and the outdoor(condenser), both of the units use a different design of coil. Figure 11 shows the drawing of the condenser coil.

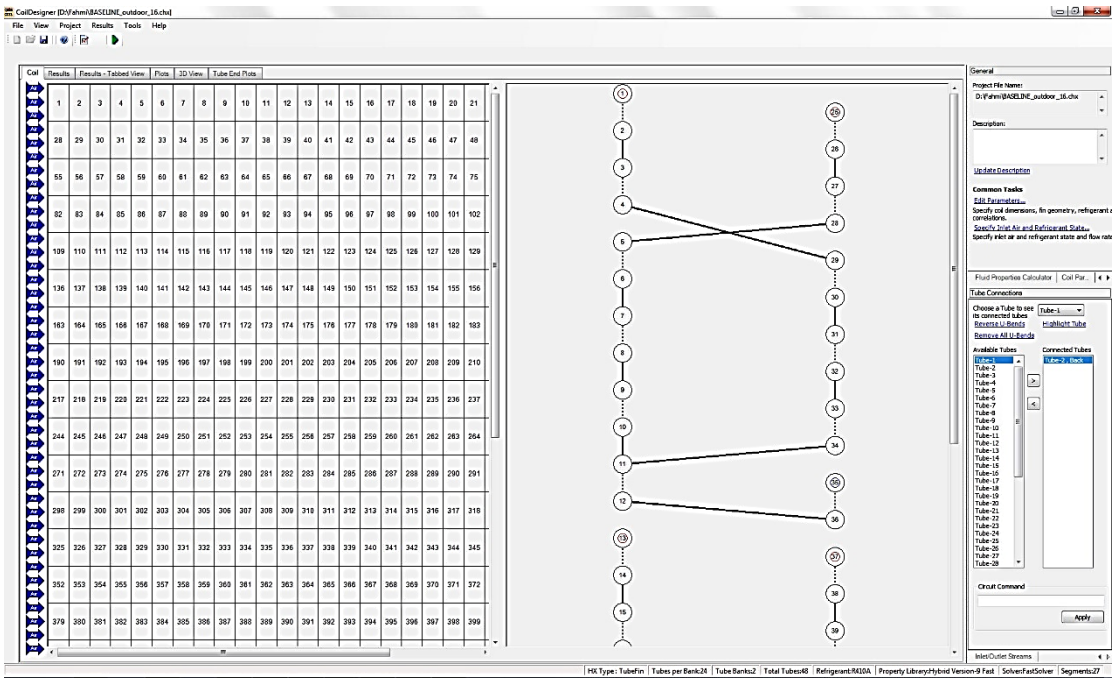


Figure 11. Drawing of the condenser coil using CoilDesigner

The air flow profile achieved from the CFD simulation was registered and divided into different coil numbers which followed the actual design and is divided into 27 segments for a more accurate result. This is because each of the coil levels has different air flow went through it. The outcome of this software is to obtain the on-coil temperature at the condenser unit and evaporator unit which are the input for the VapCyc software.

2.3.2 VapCyc software

Using the information given from the CoilDesigner software, it is then recorded into VapCyc software which consists of the refrigerant cycle. Data from condenser, evaporator, and compressor were applied accordingly to Figure 12.

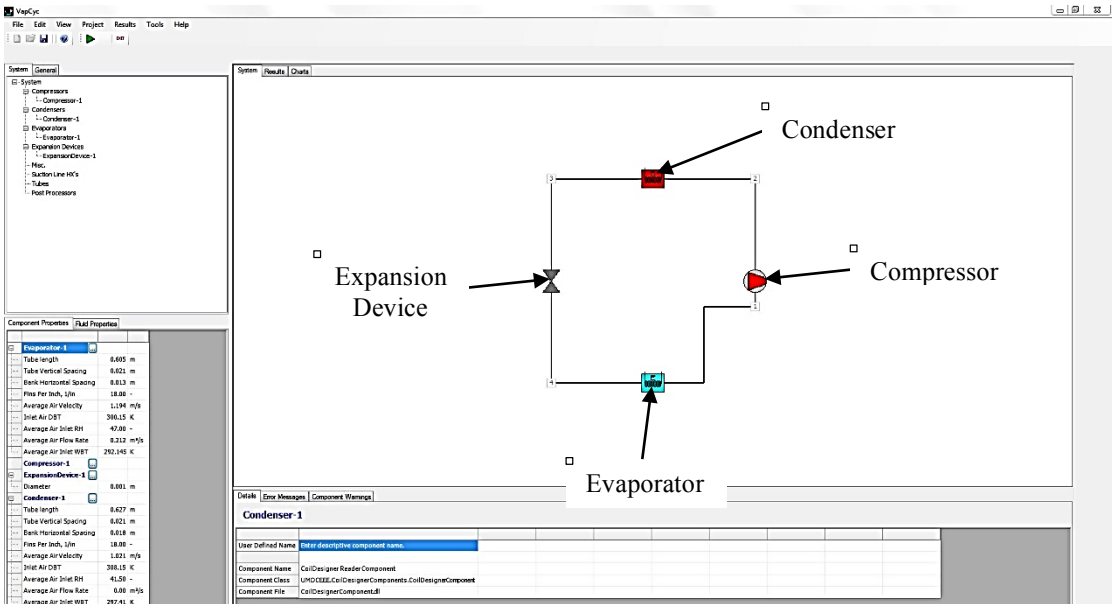


Figure 12. Refrigeration Cycle in VapCyc software

The purpose of using VapCyc software is to get the predicted value of the pressure discharge at the compressor according to the CFM when it is subjected near the wall. Then, the result was recorded into a table at the result and discussion part whereby comparison was made to determine the optimum placement.

3. Results and Discussion

3.1 Air Flow Profile

The air flow profile is shown in Figure 12. It revealed that a few important factors influence the CFM value. Firstly, there was pressure change at some certain places which affect the flow profile. Therefore, the velocity decrease. This is due to the static pressure that occurred when there is a blockage on a confined space.

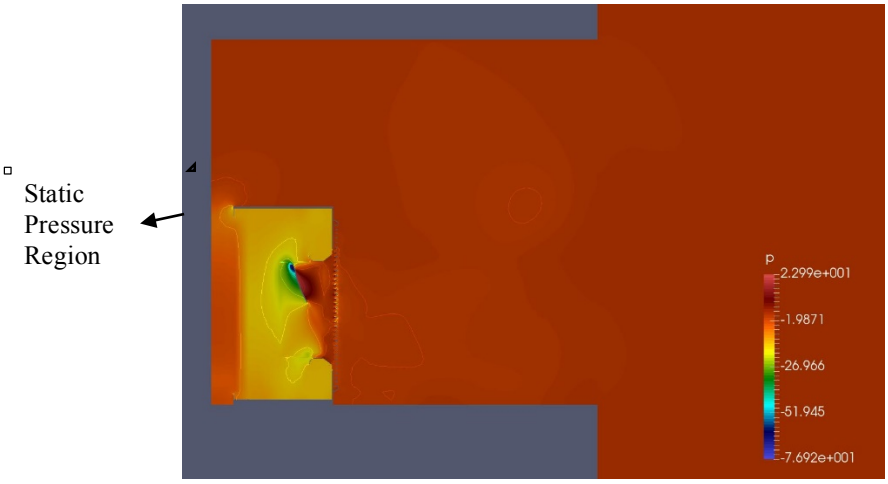


Figure 12. Static Pressure behind the outdoor unit

Based on the Bernoulli's Principle stated that high pressure will result in a low velocity simultaneously. Therefore, when there is a smaller gap between the outdoor unit and the wall, the pressure will increase at the same time causing the CFM to decrease. Secondly, the air flow profile shows a backflow or a heat recirculation due to the suction from the rotating fan which is shown in Figure 13 below.

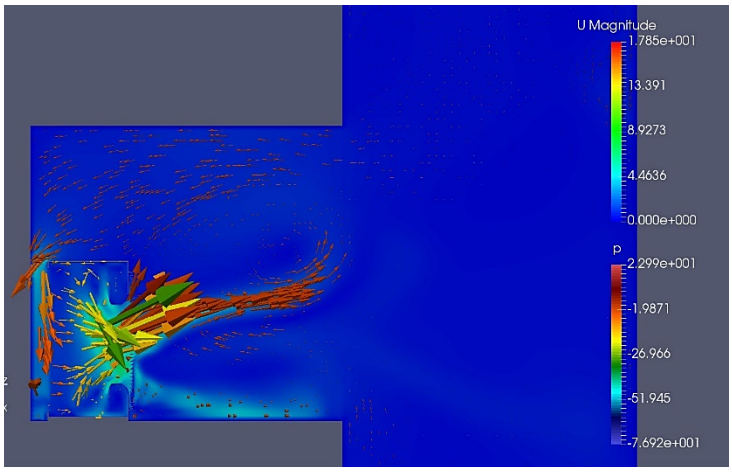


Figure 13. Hot air recirculation flow profile

The hot air recirculation is the backflow of the hot air that is blown out. This is due to the suction from the rotating fan and no air flowing from other directions. The hot air increases the on-coil temperature of the condenser. Therefore, the pressure discharge at the compressor is affected as well.

3.2 CFM Result and Pressure Discharge Result

Figure 14 shows the graph of CFM value and pressure discharge (MPa) of the compressor for each of the case studies. The graph line shows that CFM is inversely proportional with the pressure discharge of the compressor. When the CFM value is low, the pressure discharge at the compressor becomes high.

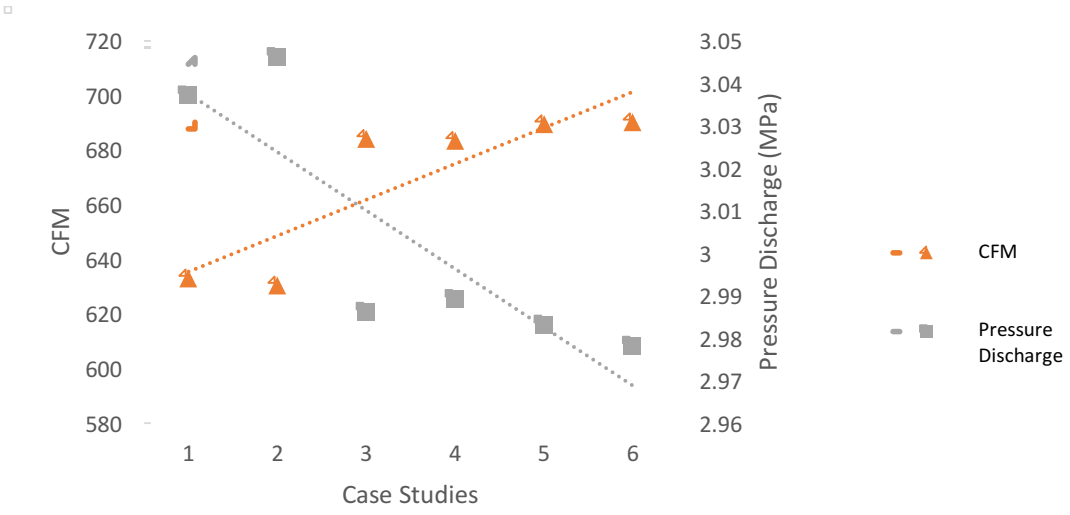


Figure 14. CFM and Pressure Discharge (MPa) of the Compressor

This situation occurred due to the restricted air flow. Plus, the pressure is inter-related with the area. Since case 6 has the biggest wall gap, the CFM value is high and there is a higher amount of area for the heat transfer. There were also some other factors that might affect the pressure discharge such as subcooled liquid and superheat liquid. However, for this study, these were fixed as constant throughout the entire process.

Referring to the Table 3, it is clear that the minimum wall gap of 60mm produces a very low value of CFM where on the other hand, wall gap of 200mm produce a high value of CFM. Besides, the CFM value remains nearly unchanged between 150mm to 200mm. However, the manipulated z-axis does not produce significant value for each case.

Table 3. CFM Results

Case Studies	*Power Consumption (W)*	*CFM*
1	1078.91	630.31
2	1076.77	632.98
3	1063.92	683.40
4	1063.17	683.97
5	1062.42	689.48
6	1062.31	690.05

In summary, for every increment of the wall gap, there is a significant change in the CFM value and pressure discharge value. This shows that CFM is correlated to the pressure discharge at the compressor. When the pressure discharge value is high, the power consumption of the compressor will increase too. Although the difference in power consumption is small, it will still affect the cost. In other words, the cost of the electricity will increase due to the extra workload at the compressor. In some cases, it will cause the entire system to fail due to the extreme condition. Therefore, it is important to place the outdoor unit at a proper distance due to the effect of the pressure discharge at the compressor.

4. Conclusion

The methodology of analyzing the performance of compressor using CFD (ANSYS-SpaceClaim version 16, SnappyHexMesh, OpenFoam version 3.0) and system simulation (CoilDesigner, VapCycle) has been demonstrated. It is shown that smaller wall gap at constant fan speed produces high flow resistance due to higher static pressure. Hence, the air flow rate (CFM) becomes less. The optimum placement of the outdoor unit from this study was 200mm for x-axis and y-axis coordinates. For z-axis, which is the top wall height, the minimum effect is observed up to a minimum distance of 500mm. Based on the CFM value, the pressure discharge at the compressor has been predicted. It is demonstrated that at lower values of CFM produced, higher pressure discharge is observed at the compressor, which in turn will further push the compressor to exceed its safe operating envelope.

Acknowledgement

This research was a collaborative project with DAIKIN Industries. DAIKIN provided all the guidance and supervision throughout the entire process. Appreciation and gratitude go to Mr. Mohd Anuar Bin Abd Aziz as a supervisor provided by DAIKIN Industries.

References

[1] N. Jamaludin, N. I. Mohammed, M. F. Khamidi, and S. N. A. Wahab, "Thermal Comfort of Residential Building in Malaysia at Different Micro-climates," *Procedia - Soc. Behav. Sci.*, vol. 170, pp. 613–623, 2015.

[2] Y. A. Çengel and M. A. Boles, *Thermodynamics : an engineering approach*. McGraw-Hill, 2011.

[3] K. Ryu, K.-S. Lee, and B.-S. Kim, "Optimum placement of top discharge outdoor unit installed near a wall," *Energy Build.*, vol. 59, pp. 228–235, 2013.

[4] W. Jin, Y. Zheng, Y. Zhang, and Y. Jiang, "Experimental Study of Factors Affecting the Performance of a Semi-enclosed Outdoor Air-conditioning Unit," *Procedia Eng.*, vol. 121, pp. 1713–1720, 2015.

[5] A. Avara and E. Daneshgar, "Optimum placement of condensing units of split-type air-conditioners by numerical simulation," *Energy Build.*, vol. 40, no. 7, pp. 1268–1272, 2008.

[6] T. T. Chow, Z. Lin, and X. Y. Yang, "Placement of condensing units of split-type air-conditioners at low-rise residences," *Appl. Therm. Eng.*, vol. 22, no. 13, pp. 1431–1444, 2002.

[7] T. T. Chow, Z. Lin, and J. P. Liu, "Effect of condensing unit layout at building re-entrant on split-type air-conditioner performance," *Energy Build.*, vol. 34, no. 3, pp. 237–244, 2002.

[8] Q. Chen, "COMPARISON OF DIFFERENT k-ε MODELS FOR INDOOR AIR FLOW COMPUTATIONS," *Numer. Heat Transf. Part B Fundam.*, vol. 28, no. 3, pp. 353–369, Oct. 1995.

eureca 2017 – Conference Paper
Paper Number 2ME21

Design and Development of EEG Controlled Robotic Prosthetic Arm

Tan Zhe Xin*, Hoo Choon Lih, Chew Wei Jen
School of Engineering, Taylor's University

* *adamzxtan@gmail.com*

Abstract
Prostheses has been around for a long time to replace missing human body parts. They are mostly powered by human body or purely for appearance purpose. Integration of electronic components and microprocessors into prosthetics that operates based on human thoughts has led to the development of smart prosthetics, called "Neuro-prosthetics". This enhancement has greatly improved the integration of prosthetics onto the human body. In terms of control for neuro-prosthetics, Brain-Computer-Interface (BCI) is getting more attention, as it allows direct extraction of brain signal from the patient to perform certain tasks. The non-invasive BCI method, the electroencephalogram (EEG) approach currently is highly favoured among most researcher due to its simplicity of implementation. This research project will utilize the simplicity of the consumer EEG headset, Emotiv Insight to develop a portable EEG-enabled robotic prosthetic arm that has 6 Degree-of-Freedom (DoF), by implementing a practical EEG control system onboard. This research project aims to develop an EEG-enabled prosthetic which its size is suitable for children. The whole research project is separated into two stages, which first stage will be developing a robotic prosthetic arm according to the anthropometry data of a 9 years old child, while the second stage of the research project will be focusing on designing a circuit that controls the prosthetic arm with an EEG headset. At completion, the user is able to control the prosthetic arm using Emotiv Insight to carry a 1.5kg load.

Keywords: Brain-Computer-Interface, EEG, Prosthetic arm, Emotiv Insight

1. Introduction

Prosthetic limbs have been around for ages to replace the missing limbs on human bodies, tracking back to the time of ancient Egypt. It is believed that ancient Egyptians are the early inventors of prosthetic limbs, though the prostheses at that time is more towards aesthetic rather than functionality. They would use it to substitute the missing body part of the dead, so that they can come and leave the world in "one piece" [1]. As time moves on, a great demand in prosthetics happened during the World War I and World War II, as most of the surviving war veterans were suffering from limbs loss. However, as the technology at that time was very limited, most war veterans were fitted with prosthetics that can only perform very basic functions and lacks any aesthetic design.

With the advancement of science and technology in the 20th century, more functions have been added into the prosthetics. Integration of electronics components and microprocessors into the prosthetics that operates based on human thoughts and muscle has breed a new kind of smart prosthetics, called "Neuro-prosthetics". In terms of control for neuro-prosthetics, Brain-Computer-Interface (BCI) is getting more attention, as it allows direct extraction of brain signal from the patient to perform certain task. There is numerous research being done on bridging the gap between implementation of BCI onto neuro-prosthetics. Some researchers uses mental states of the mind to determine the action on the neuro-prosthetics [2], [3], while others uses motor-imagery method for controlling the neuro-prosthetics [4], [5]. Different approach for utilizing BCI to control neuro-prosthetics has been established with mixed results. In some cases, the user can adapt and learn fast using the neuro-prosthetics with EEG headset, while some users found that it's easier to control their prosthetics manually.

As for the design of the prosthetic arm, it was observed that most of them are made for adults. This leaves not much of options for children with deformed limbs. Although there are researches being done on designing a prosthetic hand, there is little attention given on the design and development of actuators for the finger mechanism. Most of the current 3D printed prosthetic are actuated by strings which connects directly to a servo motor [6], [7]. The size of the 3D printed prosthetic hand is limited by the smallest size of servo motor that we can find in the market, as most hobby servo motor is intended for robotics, remote control (RC) car and RC plane application. Furthermore, the string actuation method will also require a lot of maintenance and adjustment, as the string will lose tension over time.

Therefore, this project aims to design and develop a small size actuator for robotic prosthetic arm which is intended for children who has transhumeral (above-elbow) amputation, aging between 8 - 11 years old. The robotic prosthetic arm is designed as per the anthropometry data of 8 - 11 years old kids, with a feedback control for controlling the position of the fingers, forearm, and elbow. The prosthetic arm has 6 Degree-of-Freedom (DoF) and is controlled using a consumer type EEG headset, Emotiv Insight.

2. Methodology

2.1 Mechanical System

2.1.1 Anthropometry data of 8 – 11 years old kid

The robotic prosthetic arm is aimed to be worn by a 9 years old kid, who was born without any limb. There is only a small stump extended from both her left and right shoulder. Table 1 shows all the necessary body measurement to fit a prosthetic arm onto the kid's body taken in January 2017.

Table 1. Upper body measurement of the 9 years old kid

Body section	Measurement (mm)
Right stump	164
Left stump	175
Right stump (circumference)	240
Left stump (circumference)	215
Shoulder width	300

As the kid was born without any upper limb, reference measurement cannot be taken from the kid's body for the robotic prosthetic arm's design. Hence, the dimension of the robotic prosthetic arm must be taken from the anthropometry database of children that aged between 8 - 11 years old [8].

2.1.2 Finger Mechanism Design

The human hand has a total of 23 DoF, allowing a wide range of motions and actions. Among those 23 DoF, each of the four fingers have 4 DoF while the thumb has a total of 5 DoF [9]. The fingers can be treated as 2 rigid links. The Distal phalanx and Middle phalanx is connected and treated as 1 rigid link, while the Proximal phalanx is treated as another rigid link. These 2 rigid link is connected to the metacarpal, with only 1 DoF.

The finger mechanism is constructed from the most common mechanism that can be found in mechanical design: the 4-bar linkage mechanism. Two different variation of finger mechanism design is proposed in the designing stage. Design A utilizes the Crank-Rocker 4-bar linkage design, while Design B uses the Reverse 4-bar linkage design. These 2 different variation of 4-bar linkage design results in different actuating motion to perform opening action for the finger. Design A utilizes pushing motion, while Design B uses pulling motion for the finger to perform opening action. The kinematic models of the proposed finger mechanism design can be seen in Figure 1. After considering the mounting point of the linear actuator that will move the fingers in latter stages, Design A is chosen for the finger mechanism design. The thumb has a similar design as Design A as well.

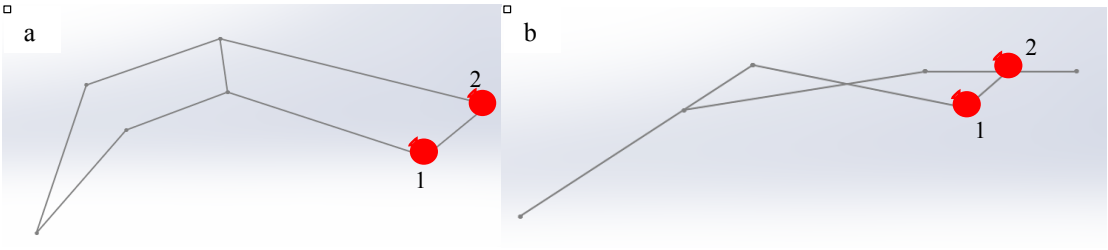


Figure 1. Proposed finger mechanism design, with a) Crank-Rocker 4-bar linkage; b) Reverse 4-bar linkage. Point 1 is the actuation point, while point 2 is the fixed point of the mechanism.

2.1.3 Mini Linear Actuator Design

The mechanism that is involved in designing the linear actuator is the screw mechanism. By combining the screw and nut with a mini DC geared motor, linear motion is achieved when the motor shaft rotates the screw, while the nut is prevented from rotation motion. The screw mechanism also has self-locking feature, in which applying torque to the screw shaft will allow it to do work against the load, yet axial load will not cause the screw shaft or nut to turn backwards. This feature is crucial to the mini linear actuator design, as this will save energy when the prosthetic arm is required to stay locked at certain position. Figure 2 shows a sketch of the proposed mini linear actuator design that will be installed in the prosthetic arm.

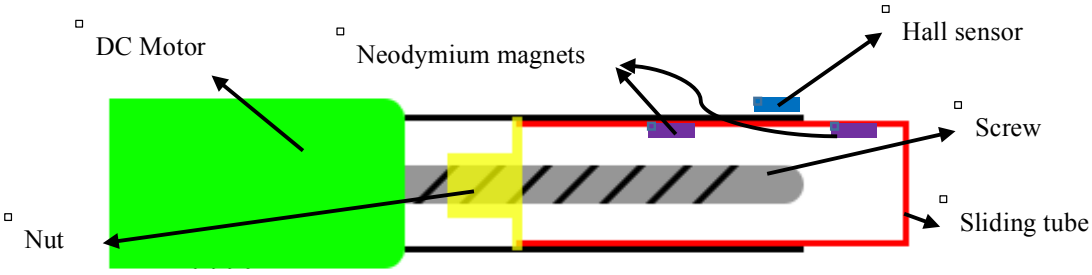


Figure 2. Illustration sketch of mini linear actuator

This linear actuator provides gripping force for the prosthetic hand. According to research, the peak gripping force that can be generated by a 9 years old girls is 127.4N, irrespective of hand [10]. Hence, the linear actuator that is actuating the finger must be able to provide similar gripping force. The equation that governs the selection of motor torque required for the linear actuator are Eq. (1), Eq. (2) and Eq. (3). The size of screw and nut chosen for all linear actuator is M5 ACME screw. By substituting the relevant information into all three equations, the torque needed for the motor to do lifting and lowering work on the prosthetic arm can be calculated. Same equations are applied to calculate the motor torque needed for the linear actuator in the elbow section.

$$T = \frac{Wd_m}{2}\left(\frac{f\pi d_m \pm L\cos\alpha_n}{\pi d_m \cos\alpha_n \mp fL}\right) + \frac{Wf_c d_c}{2} \quad (1)$$

where, T = torque, W = load, which is the gripping force, d_m = mean diameter of thread contact, d_c =thrust collar diameter, L = lead, f = coefficient friction of thread, f_c = coefficient friction of thrust collar, α_n = thread angle measured in normal plane

$$\tan \alpha_n = \tan \alpha \cos \lambda \quad (2)$$

where, α_n = thread angle measured in normal plane, α = thread angle, λ = helix angle

$$\tan \lambda = \frac{L}{\pi d_m} \quad (3)$$

where, λ = helix angle, L = lead, d_m= mean diameter of thread contact

2.1.4 Forearm Rotation Mechanism

To achieve rotational movement in the forearm, the direct method will be using gearing system, by combining a spur gear and an internal gear. As the forearm circumference dimension is taken from the anthropometry database [8], the gear tooth of the internal gear can be calculated using Eq. (4) and Eq. 5. The module (m) of every gear is fixed at 1.0, so that all the gears can be mated together and big enough for 3D printing prototyping in later stage. As the spur gear will be the driver gear, the number of teeth of spur gear is set to be at 10T. With all these information, the gear ratio and gear tooth of the internal gear can be calculated. The objective is to get the gear ratio that allows moderate rotation speed at the forearm. The spur gear and internal gear is then designed in SolidWorks.

$$m = \frac{d}{T} \quad (4)$$

where, m = module, d = pitch circle diameter of gear, T = number of tooth

$$\frac{d_2}{d_1} = \frac{T_2}{T_1} \quad (5)$$

where, d_1 = pitch circle diameter of driver gear, d_2 = pitch circle diameter of driven gear, T_1 = number of tooth of driver gear, T_2 = number of tooth of driven gear

2.1.5 Design Validation through FEA (Finite-Element-Analysis)

FEA simulation for testing the prosthetic arm's components are done using SolidWorks. Although it offers lesser features and controls over the simulation comparing with ANSYS, yet it still provides core simulation tools that is necessary to test the design. The area of interest on the prosthetic arm when it is being loaded is the forearm and the linear actuator at the bicep area. The forearm section of the prosthetic arm is basically a cantilever beam being loaded at one end. The linear actuator at the bicep area will need to sustain the amplified loading due to lever effect, whenever the hand is holding onto certain object. The free-body-diagram (FBD) of the prosthetic arm when its holding an object in the hand with the elbow in 90° position, can be seen in Figure 3. The prosthetic arm model is simplified for reducing the simulation time.

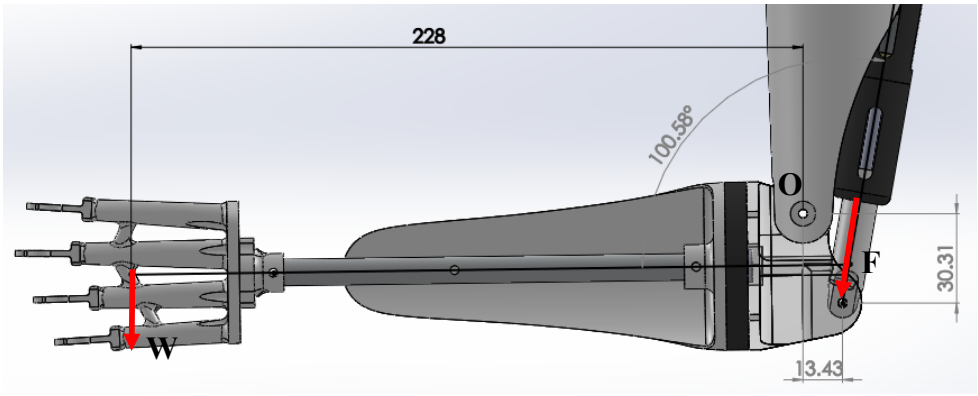


Figure 3. The FBD of the prosthetic arm when its holding an object in the hand. Point O is the pivot point.

According to a pediatric research, the safe weight that pre-teen children can carry is 10% of their body weight. As the average weight of 9-years-old girl is 29kg, therefore the maximum weight that the girl should carry is only around 3kg [11]. However, considering that the girl who is going to use the prosthetic arm have limited mobility (she's born without any limbs), will mainly manipulates everyday household objects (a mug, bowl, pencil, plastic bottles), therefore the weight of the object that the prosthetic arm will mainly manipulate is under 3kg. Considering a design safety factor of 3.0, the load that the hand will carry is 1.5kg, which is 3X the weight of an average 500mL plastic bottle. Together with FBD of the prosthetic arm, Eq. (6), Eq. (7) and Eq. (8) are used for finding out the force input for simulation on the forearm section and the linear actuator at elbow section.

$$\sum F_x = 0 \tag{6}$$

$$\sum F_y = 0 \tag{7}$$

$$\sum M_O = 0 \tag{8}$$

The meshing setting for both forearm section and linear actuator is curvature based meshing, which can provide a better meshing quality. The maximum meshing size of both model is set to be at 3mm. Meshing control is applied on the suspected critical region in the model for better accuracy of the simulation result.

2.2 Electronics System

2.2.1 The Control Circuit

The electronics are the heart and mind of the prosthetic arm. There is a total of 6 DC geared motors which will be controlling each section of the prosthetic arm, giving it 6 DoF. Instead of an open-loop control system, the approach taken for designing the control system of the prosthetic arm is a closed-loop system, with sensors providing feedback to a microcontroller to monitor the movement of the prosthetic arm. Figure 4 shows the block diagram of a normal closed-loop system.

A proper motor driver must be chosen to control each 6 DC geared motor in the prosthetic arm. L293D is selected due to its availability and price. Each L293D motor driver chip has 2 channels of H-bridge, which can drive a high impedance load on each channel with 0.6A at normal operation. Although there is a huge voltage drop between supply voltage and output voltage (V_{ss}-1.4V at max), yet it is the most common and easy to be implemented motor driver. A total of 3 pieces of L293D motor driver chip is needed to control 6 DC geared motor, therefore requiring a total of 12 inputs to control each 6 motor rotation direction.

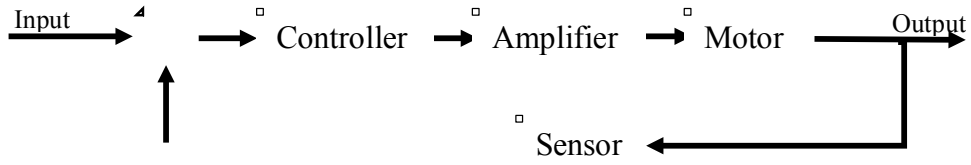


Figure 4. Closed-loop control system of the DC geared motor

On each motor, there is a feedback sensor to identify the current position of the motor and actuators. A latching-type hall effect sensor is installed on each of the linear actuator that controls the finger movement. This hall effect sensor has bipolarity feature, which can be used to tell the north or south pole of the magnet. It will stay at high/low state until it senses a different polarity of the magnet facing it. Potentiometer is installed at section which involves rotational movement, such as thumb, forearm, and elbow. A simple gearing system is installed between the potentiometer and the motor in each of these sections so that the potentiometer will change it resistance according to the rotation motion of those section. The controller will be able to tell the current position of the thumb, forearm, or elbow according to the resistance value of the potentiometer.

The controller that will be monitoring the Input/ Output (I/O) of the prosthetic arm is Arduino Pro Mini. It is chosen due to its ease of implementation and having a great online community. The Arduino Pro Mini is chosen as it suits the application of this project, which required 18 I/O from the microcontroller, in which 3 of them requires analog input. The Arduino Pro Mini that has 20 I/O, which 5 of them are analog input, operates at 5V 16MHz, has 32Kb of flash memory, is more than enough for this project.

2.2.2 EEG Headset and Control

The prosthetic arm is controlled using a consumer type (EEG) headset, Emotiv Insight. Instead of having a bunch of wires and electrodes sticking on the user head, Emotiv Insight only has 5 electrodes with Bluetooth® capability. The 5 electrodes are positioned on certain spots of the user's head, as per the International 10-20 System.

The control flow for using Emotiv Insight to control the prosthetic arm can be seen in Figure 5. First, the user will need to train the Emotiv Insight to recognize certain brainwave pattern, which is dependent on the user's emotion state. Then, the training that has been done on Emotiv Xavier will be used to activate certain keystroke when the user's thinking gives the same brainwave signal. This is done through another

software called EmoKey. The keystrokes that is activated will be sent to the Arduino Serial Monitor, which will be sent to Arduino Pro Mini wirelessly using 434MHz radio frequency module. Then, the prosthetic arm will perform pre-set actions according to the user's intention.

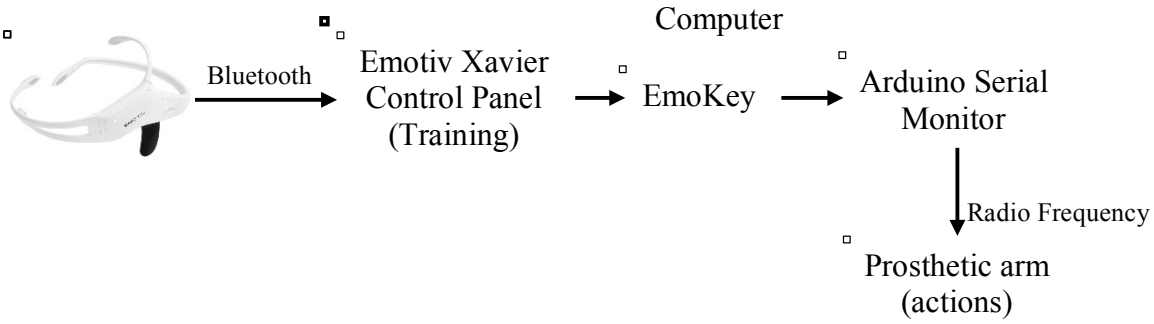


Figure 5. Control flow of EEG controlled prosthetic arm using Emotiv Insight

3. Results and Discussion

All the mechanical components in the robotic prosthetic arm are designed in SolidWorks. Each component is then exported into .stl format to be imported back into 3D printer slicing software for 3D printing. Most of the parts on the robotic prosthetic arm are printed in Polylactic acid (PLA) material, with 20% - 50% infill, depending on whether the part will be heavily loaded during operations. Mechanical components such as the linear actuator body are printed using Acrylonitrile-Butadiene-Styrene (ABS) material, which is more heat resistant compared with PLA material. Those parts are printed with ABS, as the linear actuator body is the housing for the 6V DC geared motor, which will heat up during operation. However, the gears and fingers are printed with ABS material only for aesthetic purposes on the prosthetic arm. The full design of the robotic prosthetic arm can be seen in Figure 6. The overall weight of the arm is 380g.

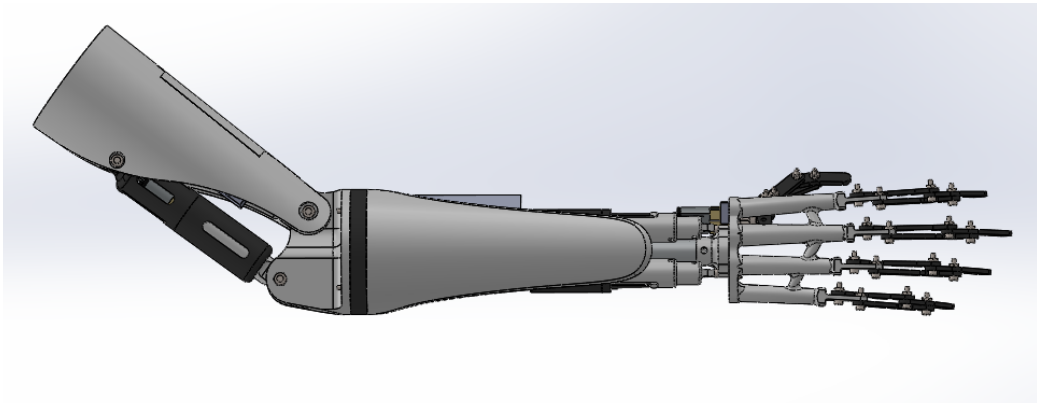


Figure 6. The robotic prosthetic arm for transhumeral amputee

3.1 Hand and Fingers Design

The hand section is modelled in a natural way of representing the human hand shape and geometry. The fingers are modelled in different length as per the 9-years-old kid anthropometry data [8]. The palm section of the hand is also modelled according to

the anthropometry data, with added slight curvature curving towards the metacarpal section of little finger. This added curvature will gives a more natural shape and look of the prosthetic hand. In addition to that, all fingers of the prosthetic hand are slightly offset by 3° - 5° from the middle finger to give a more natural look when the prosthetic arm is at resting position. This can be seen in Figure 7. The final design of finger mechanism can be seen in Figure 8. The prosthetic hand is intended to be designed as human's hand skeletal model for adding another layer of silicone skin on top of it.

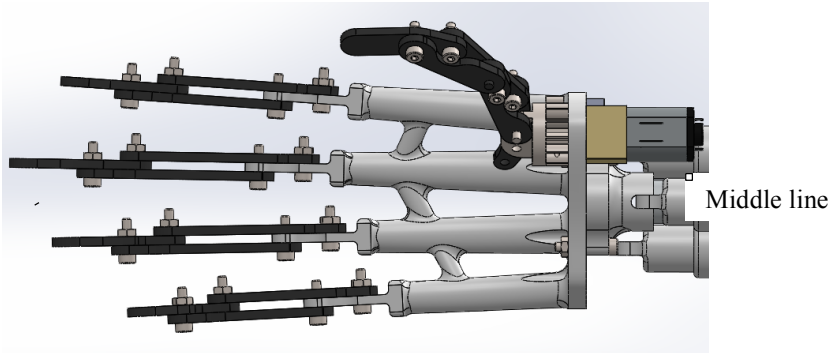


Figure 7. Fingers are offset slightly from the middle for a more natural resting look

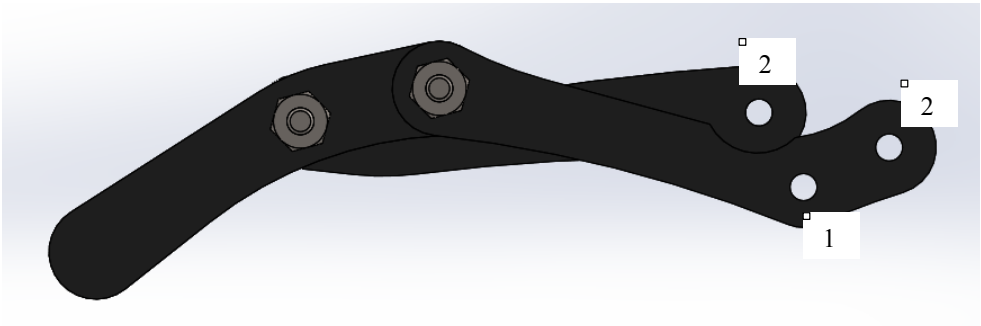


Figure 8. Final design of finger mechanism, with point 1 showing the actuation point and point 2 showing the fixed point of the mechanism

3.2 Linear Actuator for Fingers and Elbow

The linear actuator is designed according to Eq. (1) - Eq. (3). For the linear actuator that is connected with the fingers, the load that is applied onto the linear actuator is equal to the gripping force that can be produced by the hand, which is around 130N for a 9-years-old female child [10]. There is a total of 3 linear actuators positioned in the forearm section of the prosthetic arm. There are 2 linear actuators controlling 4 fingers, with 2 fingers connected to each one of them, while the other linear actuator is controlling the thumb. This is done to provide sufficient control and DoF for the fingers with just 3 linear actuators. Figure 9(a) shows the linear actuator position in the prosthetic arm, while Figure 9(b) shows the connection of each finger to its corresponding linear actuator, which located in the forearm section.

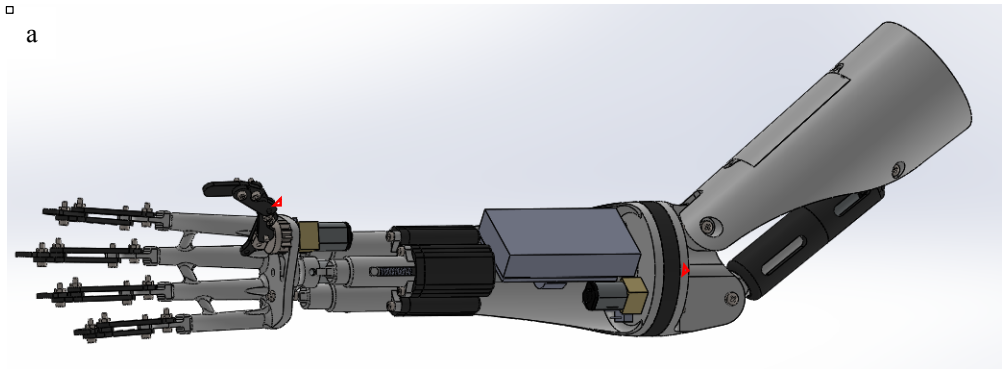


Figure 9(a). The red circle shows the linear actuators position in the prosthetic arm

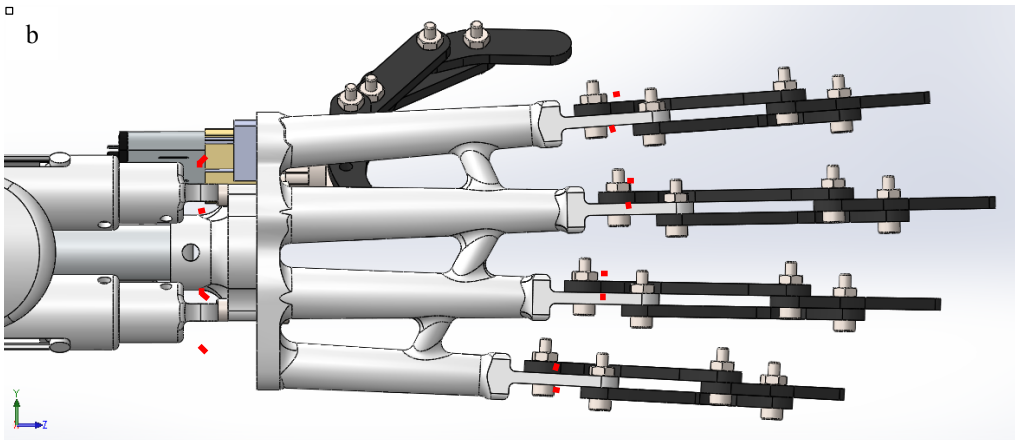


Figure 9(b). The red line represents a small metal wire loop that connects 2 fingers to each linear actuator in the forearm section

3.2.1 Finger Section Linear Actuator

For the linear actuator that controls the fingers and thumb, as most of the gripping force comes from the fingers, therefore the linear actuator that controls the fingers is loaded with 75N each. Hence, using Eq. (1) to Eq. (3), the torque needed can be calculated. Assumptions that are being made are the friction coefficient and collar friction coefficient to be 0.05, with starting friction of 0.067 (as starting friction coefficient is 1/3 higher than running). The nut and screw dimension is M5 ACME type, having 0.8mm pitch and mean diameter of 5mm. The thrust collar diameter is assumed to be the mean diameter of the nut body, which d_c= 7mm. As M5 ACME screw and nut is being used, therefore $L = 0.8\times10^{-3}m$, $d_m = 0.5\times10^{-3}m$. With all these parameters, using Eq. (2) and Eq. (3), the value of $\alpha_n = 30°$. Substitute $\alpha_n = 30°$ into Eq. (1) together with all known factors, the starting torque needed for the finger section linear actuator is 0.0423Nm. Based on this required torque, a 6V DC geared motor, with 200rpm at free rotation, has 360mA stall current was chosen. The motor has a dimension of 10x12x26mm, which is much smaller than the micro RC servo motor. Figure 10 shows the fingers' linear actuator that is positioned in the forearm section of the prosthetic arm. This packaging method can utilize all available space in the forearm.

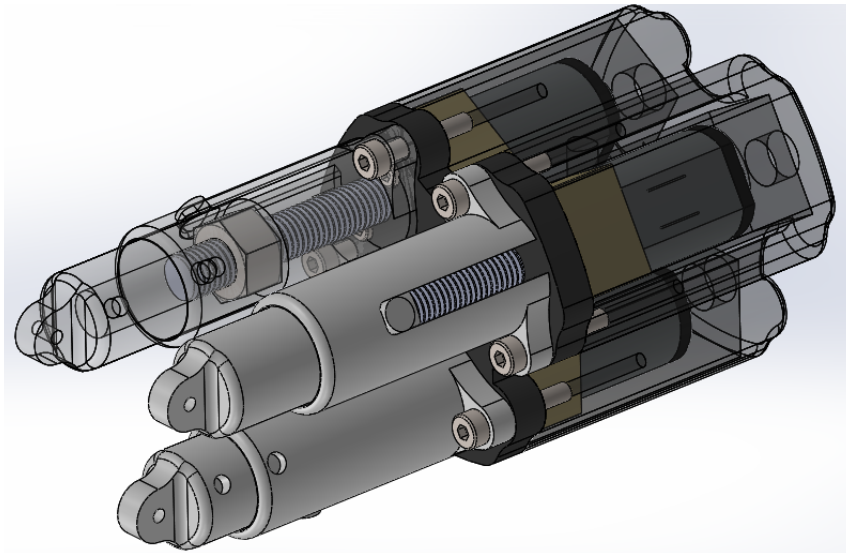


Figure 10. The linear actuator for finger section. There are 3 linear actuators in this single package. The mini DC geared motor is visible in this figure.

3.2.2 Elbow Section Linear Actuator

The linear actuator that is located at the triceps area of the upper arm is responsible for lifting the rest of forearm section of the prosthetic arm. Static analysis is done to find out the force needed at the elbow to keep the forearm stable in 90° position while holding a 1.5kg item on the hand. As the linear actuator in the triceps still uses M5 ACME screw and nut, therefore the normal thread angle (α_n) is still 30°. Using Eq. (1) together with all known parameters, the starting torque needed for linear actuator to lift the rest of forearm of the prosthetic arm is 0.0645Nm. Therefore, a 6V DC geared motor, with free rotation of 100rpm, stall current of 360mA was chosen for the elbow section linear actuator. Figure 11 shows the linear actuator design for the elbow section of the prosthetic arm.

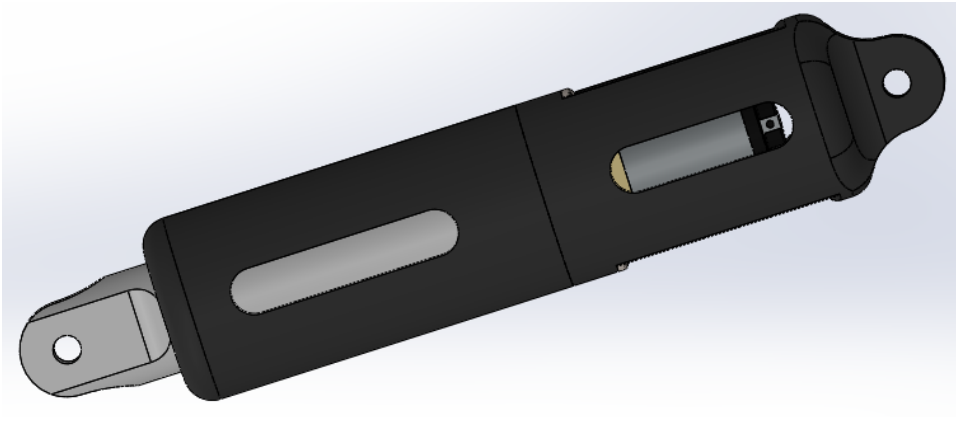


Figure 11. The linear actuator at the elbow section of the prosthetic arm

3.3 Forearm Rotation Mechanism

The forearm rotation mechanism is designed according to Eq. (4) and Eq. (5). The forearm biggest diameter is 57mm, which is taken from a research [8]. Since all

gears have a fixed module, which m = 1.0 to ensure meshing, the pitch diameter (*d)* of the internal gear must be smaller than 57mm. It is also known that the driving spur gear has a tooth number of 10 and the middle of the internal gear need to install a ball bearing with 9mm internal diameter (ID), 16mm outer diameter (OD). Hence, the smallest pitch diameter (*d)* for the internal gear must be bigger than 42mm.

The final gear ratio for the forearm gearing system is 4.5:1. The driving spur gear has 10 tooth, while the internal gear has 45 tooth. This gear ratio is found to be able to give the highest gear ratio while still reserving some space for mounting points on the internal gear to the elbow part of the prosthetic arm. The motor that is used for driving the forearm rotation is a 6V DC geared motor, with 200rpm free rotation speed and 360mA stall current. This makes the forearm rotating at 40rpm. The final design of the forearm rotation mechanism can be seen in Figure 12. Since the forearm will not perform 180° rotation due to limitation of the sensor used for position feedback, only some teeth on the internal gear are visible. This can reduce 3D printing time as well.

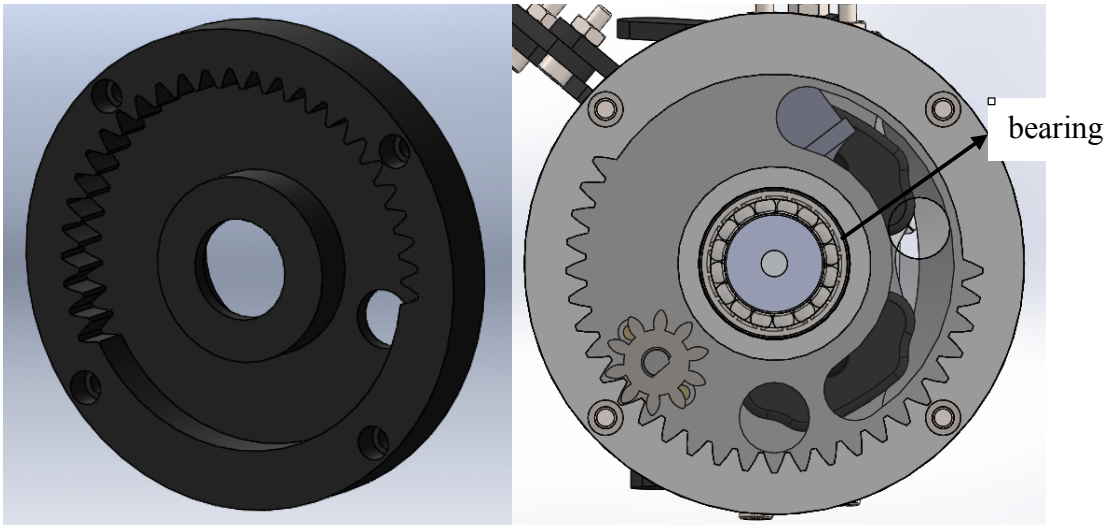


Figure 12. The final design of the internal gear for forearm rotation mechanism. The internal gear is fixed to the elbow and prevented from rotation

3.4 Simulation Results

For the FEA simulation on the forearm section, the upper arm section of the prosthetic arm is excluded from analysis to further reduce the simulation time. A load of 14.7N is applied on the middle section of the prosthetic hand section, to simulate the hand holding onto a 1.5kg object. The end of the forearm is treated as fixed point, with appropriate materials applied onto each section of the forearm assembly. The simulation result of the forearm section can be seen in Figure 13. The simulation shows that the maximum deflection exists at the palm section, with deflection of 2.29mm. Most of the load is taken by the aluminum shaft, which acts as the backbone of the forearm. The simulation result also shows that the minimum safety factor of the forearm section is 7.3. Although the safety factor is much higher than usual, yet aluminum shaft is still chosen as the main structure for the forearm section due to its availability and cheap cost of material.

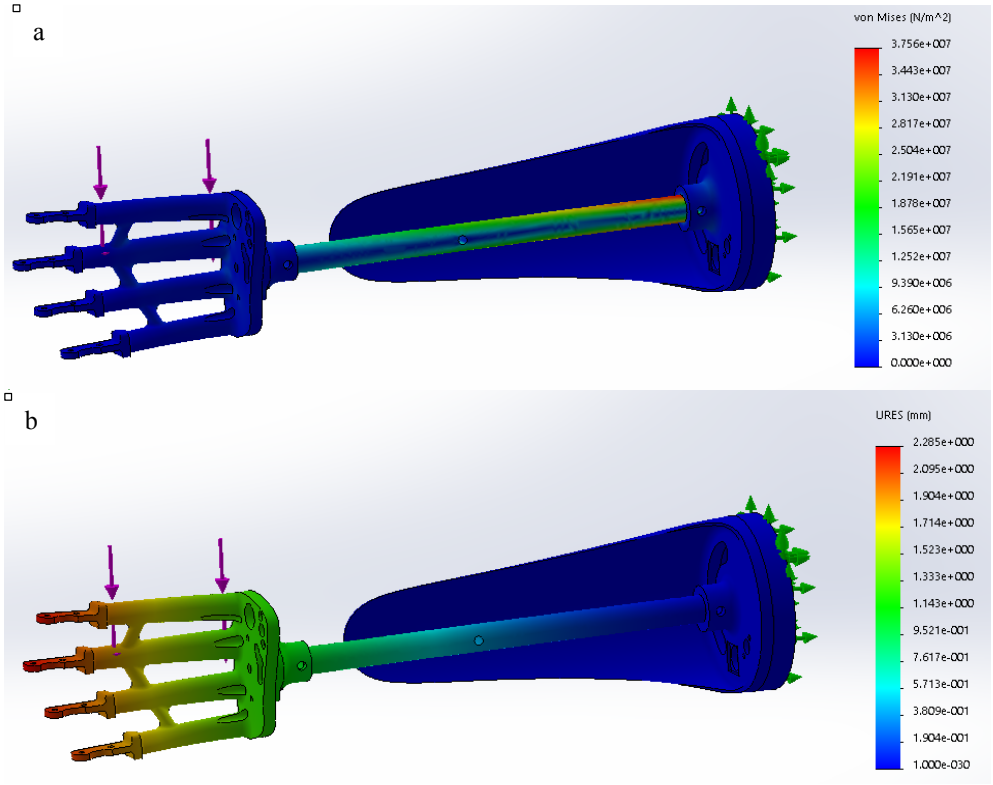


Figure 13. Simulation result of the forearm section, which a) stress plot on the forearm section, b) maximum deflection on the model

For the linear actuator on the elbow section, with W = 14.7N, using Eq. (6) to Eq. (8), the force input for the linear actuator is found to be 172.2N. The DC geared motor is treated to be rigid body as the stiffness of the DC motor is much higher compared with the material of the linear actuator body. By applying appropriate materials and boundary conditions onto the linear actuator, the simulation result can be seen in Figure 14. The maximum stress on the linear actuator exists in the screw section, with 20.87MPa. The deflection on the linear actuator is only 5.56×10^{-2}mm. The simulation result also shows that safety factor of the linear actuator is 11.0. The high value of safety factor is expected as the 3D printed parts of the linear actuator has a compressive strength of 93.7MPa. Hence, the linear actuator body will be able to handle much higher axial load before it fails mechanically.

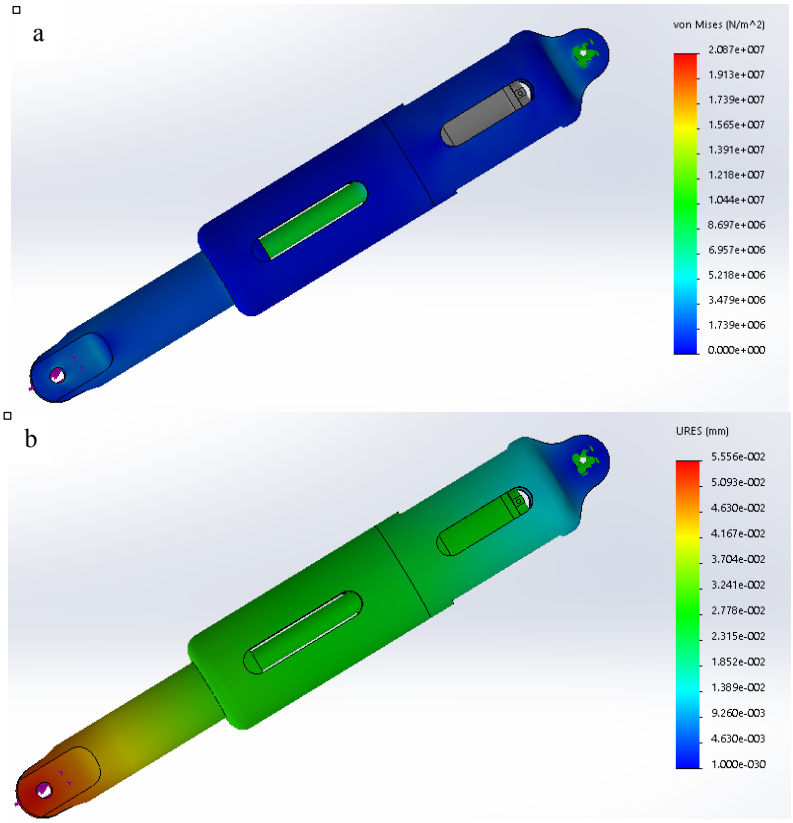


Figure 14. Simulation result of elbow section linear actuator, which a) stress plot on the linear actuator, b) deflection plot on the linear actuator

3.5 Electronics and Controls

The printed circuit board (PCB) design is designed using EAGLE, a free PCB design software by Autodesk. All components that are used on the circuit board are through-hole type, which is much easier to be soldered than surface mounted device (SMD) IC chip. However, the tradeoff would be the size of the PCB is much bigger, due to the size limitation of through-hole components. The final PCB is a two-layered design, with board thickness of 1.2mm, trace width of 0.6mm. The circuit board is manufactured by SeeedStudio, a PCB manufacturing company located at China.

There are 2 types of sensor installed in the prosthetic arm for position feedback to Arduino Pro mini, which are the hall-effect sensor and trimmer. The hall-effect sensor, SS460S, is installed on the fingers' linear actuator. It is digital latching type hall-effect sensor, which will stay in high/low state until a different external signal is given to the sensor. On the linear actuator, a 1mm neodymium magnet is installed on the actuator body, with different polarity facing upwards. The polarity of the magnet will tell whether the linear actuator is at full extension or full retraction. Figure 15 shows the hall-effect sensor on the fingers' linear actuator. A trimmer is a smaller type of potentiometer, which is suitable to be soldered onto small sized circuit board. Three 10KΩ trimmers are each installed at thumb, forearm, and elbow section. The position feedback is achieved by the changing value of resistance when the motor starts rotating either one of these parts. The value is absolute and the position of either of these parts is always known even when the Arduino Pro Mini restarts. Figure 16 shows the installation of trimmer location in the prosthetic arm for position feedback.

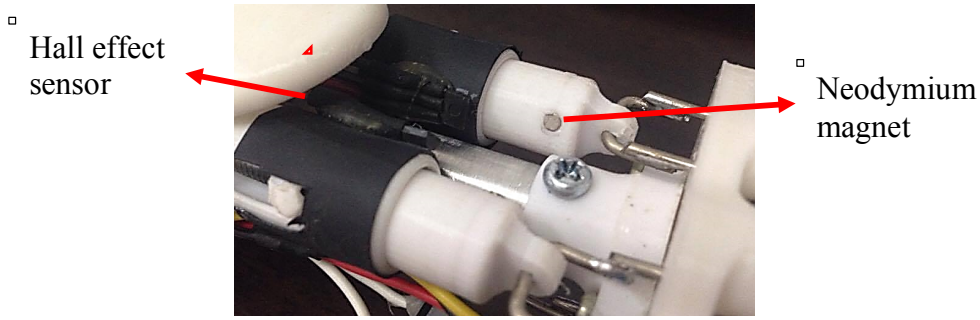


Figure 15. The position feedback setup on the finger linear actuator

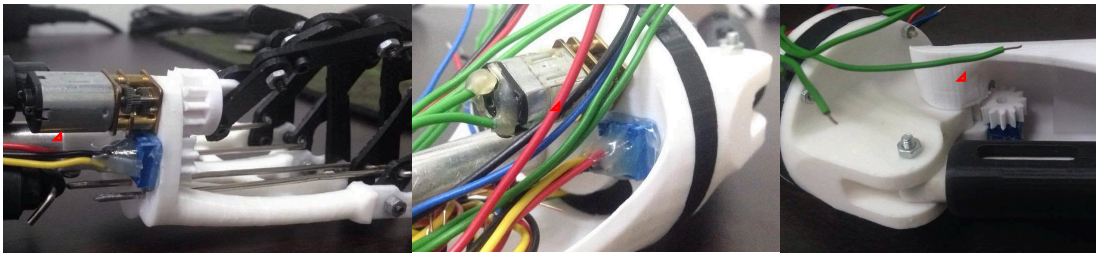


Figure 16. Trimmer installation location (red circle) on the prosthetic arm for position feedback control at a) thumb, b) forearm, c) elbow

Using Emotiv Insight, after the user has undergone a certain training on using thoughts command together with Emotiv Xavier Control Panel, certain hand actions can be performed as per the user training. As the fingers are not fully independent, only certain actions can be done, such as gripping a pencil, power grip, precision grip, and thumbs up. Pointing action can only be achieved with index and middle finger pointing together, as these two fingers are connected to the same linear actuator. Using thoughts command on Emotiv Xavier Control Panel, the user is able to control the prosthetic arm to grab onto a 1.5kg item and lift it with the elbow sustaining in 90°. Table 3 shows the list of hand actions that is achievable for the 3D printed prosthetic arm.

Table 3. Hand actions that is achievable for the hand section of prosthetic arm

Hand actions	Achievable?
Open Palm	✓
Power Grip	✓
Hook Grip	✓
Mouse Grip	✓
Tripod Grip	✓
Active Index (Pointing)	✗
Pinching	✗
Precision Grip	✗

4. Conclusions

In conclusion, a small size linear actuator that has position feedback feature has been successfully developed and implemented. The linear actuator that is developed is highly compact and able to perform as expected. The transhumeral prosthetic arm that is developed has 6 DoF, with an overall weight of 380g including all electronics components such as battery pack and the control circuit board. The user is able to

control the prosthetic arm to carry a 1.5kg weight using Emotiv Insight EEG headset after some period of training.

The future work of this project includes adding a layer of silicone skin onto the transhumeral prosthetic arm to give it a more user-friendly appearance. As the Emotiv Insight comes together with a software development kit (SDK), the software for decoding the brainwave pattern coming from Emotiv Insight can be implemented onto a single-board-computer (SBC) such as Intel Edison and Raspberry Pi. This would make the prosthetic arm to be a fully self-contained system, rather than needing an external computer for processing the brainwave pattern. Besides, the possibility of using micro stepper motor for the linear actuator that controls the finger movement can be investigated, enabling the fingers to move into different position rather than only fully opening or closing position.

Acknowledgment

The author would like to thank Mr. Ahmad Hilmi and Mr. Ahmad Hafez from Pebble3D Sdn. Bhd. for partially sponsoring and giving the author the opportunity to help the girl to develop a fully 3D printed prosthetic arm. The author is also grateful for friends and family that never stop encouraging author to complete this project.

References

[1] K. Norton, “A brief History of Prosthetics,” *InMotion*, vol. 17, no. 7, pp. 1–3, 2007.

[2] D. Salvekar, A. Nair, D. Bright, and P. S. A. Bhisikar, “Mind Controlled Robotic Arm,” *IOSR J. Electron. Commun. Eng.*, pp. 36–44, 2015.

[3] J. R. Millán, F. Renkens, J. Mouriño, S. Member, and W. Gerstner, “Noninvasive Brain-Actuated Control of a Mobile Robot by Human EEG,” *IEEE Trans. Biomed. Eng.*, vol. 51, no. 6, pp. 1026–1033, 2004.

[4] Y.-N. Li, X.-D. Zhang, and Z.-X. Huang, “A practical method for motor imagery based real-time prosthesis control,” in *2012 IEEE International Conference on Automation Science and Engineering (CASE)*, 2012, pp. 1052–1056.

[5] A. R. Murguialday, V. Aggarwal, A. Chatterjee, Y. Cho, R. Rasmussen, B. O’Rourke, S. Acharya, and N. V. Thakor, “Brain-Computer Interface for a Prosthetic Hand Using Local Machine Control and Haptic Feedback,” in *2007 IEEE 10th International Conference on Rehabilitation Robotics*, 2007.

[6] K. F. Gretsch, H. D. Lather, K. V. Peddada, C. R. Deeken, L. B. Wall, and C. a. Goldfarb, “Development of novel 3D-printed robotic prosthetic for transradial amputees,” *Prosthet. Orthot. Int.*, vol. 1, no. 4, pp. 3–6, 2015.

[7] P. H. Wu and J. S. Shieh, “3D printed prosthetic hands,” *2016 Int. Conf. Commun. Probl.*, pp. 1–2, 2016.

[8] R. Snyder, M. Spencer, C. Owings, and L. Schneider, “Physical Characteristics of Children,” 1975. [Online]. Available: http://ovrt.nist.gov/projects/anthrokids/child.html. [Accessed: 01-May-2017].

[9] K. Li, I.-M. Chen, S. H. Yeo, and C. K. Lim, “Development of finger-motion capturing device based on optical linear encoder.,” *J. Rehabil. Res. Dev.*, vol. 48, no. 1, pp. 69–82, 2011.

[10] C. Häger-Ross and B. Rösblad, “Norms for grip strength in children aged 4-16 years.,” *Acta Paediatr.*, vol. 91, no. 6, pp. 617–625, 2002.

[11] J. Whittfield, S. J. Legg, and D. I. Hedderley, “Schoolbag weight and

musculoskeletal symptoms in New Zealand secondary schools," *Appl. Ergon.*, vol. 36, no. 2, pp. 193–198, 2005.

eureca 2017 – Conference Paper
Paper Number 2ME22

Design of an Air Blower Mechanism for the Cassette Air Conditioner

Wen Yong Xiang*, Azadeh Ghadimi, Chin Wai Meng
Department of Mechanical Engineering, School of Engineering, Taylor's University, Malaysia.

* *yongxiang.wen02@sd.taylors.edu.my*

Abstract
This research study aims to design an air blower mechanism for the cassette air conditioner to improve the thermal comfort in an enclosed area. As there are a lot of parameters of thermal comfort, the air velocity and air temperature are taken into account for this study. To achieve satisfactory thermal comfort of the users, the fan mechanism to be implemented to the cassette air conditioner was studied. This is done numerically by using CFD software. The fan mechanism's design includes the number of blades and the angle of attack as these parameters had proven by other researches that it affects the performance of the fan mechanism in terms of volumetric flow rate, mass flow rate and energy consumption. In numerically modelling, ANSYS FLUENT was used together with Moving Reference Frame (MRF) method. Several turbulence models were analysed to determine the best option and it was found that k-epsilon turbulence model provides better results than the rest. The results of air flow, air velocity and air temperature were studied and compared with conventional air blower in the cassette air conditioner to prove that the air blower mechanism could improve the thermal comfort of the users. It was found that the implementation of the air blower mechanism has slightly improved the satisfaction of thermal comfort.

Keywords: Thermal comfort, Cassette air conditioner, Air blower mechanism, Computational Fluid Dynamic, SolidWorks

1. Introduction

The air conditioning system has been a necessity to the society and there are varieties of air conditioning system in recent years. The main purpose of this system is to provide thermal comfort to the users in a closed environment. In a case of failure to provide satisfactory thermal comfort would result in illness and discomfort of the users [1]. Therefore, a few studies have been conducted to understand the state of the office buildings as well as the residential buildings where most users spend most of the time [2 , 3].

The fundamentals of thermal comfort has been researched carefully. According to the American Society of Heating, Refrigerating and Air-Conditioning Engineers (ASHRAE), thermal comfort is the fulfillment of the people towards the thermal surrounding because there are many variations in satisfying every person in a room in terms of physiologically and psychologically [4]. The ASHRAE has identified the six primary elements that contributed to the thermal comfort in a room which are the air humidity, air velocity, air temperature, radiant temperature, metabolism of a person and the insulation supplied by the clothes [4]. However, Hensel claimed that the thermal comfort state is defined as there are no driving urge in regulating the environment by behaviour [5]. Moreover, Fanger stated that thermal comfort is affected by the thermal condition of the body [6]. Therefore, there are various forms to define thermal comfort because every person has different preferences towards the satisfaction of thermal comfort.

In this modern era, thermal comfort studies have been a lot easier with the help of computational fluid dynamics (CFD). Awbi has proven that CFD could be a good use to estimate the air flow and thermal comfort in a closed environment [7]. As more large enclosed areas require air conditioning system, the cassette air conditioner has been very popular among offices, universities, shopping malls and other more. Therefore, a study was conducted by Kwang and the team, Kwang claimed that primary factor that causes the unsatisfactory thermal comfort is the discharge angle of the blower in the 4-way cassette air conditioner [8]. This is meant by setting the discharge angle of the blower to supply satisfactory thermal comfort to the users. Despite the study on the 4-way cassette air conditioner, companies have come out with the new cassette air conditioner that has a round flow but still uses the discharge angle of the blower. Therefore, this only minimizes the dissatisfaction of thermal comfort and there are still room for improvements.

To improve the thermal comfort, mixing the air in an enclosed environment is necessary. This came out with an idea of adding a fan mechanism to the cassette air conditioner. This is because the fan mechanism provides axial air flow that would circulate the cold air around the enclosed environment. In order to prove that this method would work, a study must be conducted carefully. Bassiouny stated that the air flow from the ceiling fan has different attributes as it separated from the blades and move downwards to the floor [9].

Adeeb claimed that the mass and volumetric flow rates are maximized for six blade design and energy efficiency is maximized for two blade design [10]. In another journal, Adeeb stated that the root and tip angle of attack played a huge role in the volumetric flow rate, torque and energy efficiency whereas the tip width has the least

effect on all response results [11]. According to Mahlia, the ceiling fan with aerodynamic blade profile has better effectiveness than the conventional design. The new design increase the volumetric of the fan [12]. In a study conducted through experimentally and numerically by Rajapakshe, investigating the air flow distribution around the ceiling fan. Rajapakshe concluded that the blade design has a notable effect on the performance of the fan [13].

In this research study, there are three objectives to achieve. Firstly, select the primary parameters that contribute to thermal comfort. Then, design an air blower mechanism of a cassette air conditioner to improve the thermal comfort of the users. Finally, simulate and validate the design of the air blower mechanism.

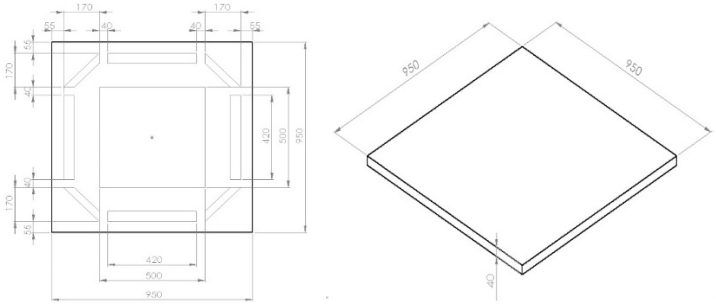
2. Research Methodology

In this segment, it contains the discussions on the procedures in managing this research. It includes justifications and configurations of every work undertaken in this study. All the three-dimensional geometry models were constructed using the SolidWorks (Version 2016) and simulations were performed using the ANSYS FLUENT (Version 18.0).

2.1 Three-Dimensional (3D) Geometry Model

2.1.1 Air Conditioner

The 3D model of the cassette air conditioner was required to simulate the condition of with and without the implication of the fan mechanism to compare both results. It was constructed based on the reference of the Daikin specification sheet as well as the research study by Ken Fukada [14, 15]. The Daikin cassette air conditioner (round flow) with indoor model of FCQ60KAVEA was selected in this study. The outer dimension of the cassette air conditioner was specified in the Daikin specification sheet which has 950 mm in length and 950 mm in width whereas the dimensions for the supply air and return air were not included. Therefore, the dimensions were assumed based on Ken Fukada research study. The height of the 3D model was set at 40 mm because this is the dimension that can be used when there is a minimal space between drop ceilings and ceiling slabs. Fig. 1 (a) shows the bottom view of the cassette air conditioner (round flow) with dimensions whereas Fig. 1 (b) shows the isometric view with dimensions. The cassette air conditioner was constructed by SolidWorks.



(a) (b)

Figure 1. Cassette Air Conditioner with Dimensions (a) Bottom View (b) Isometric View

2.1.2 Fan Mechanism

The fan mechanism for the cassette air conditioner was designed based on the reference of the available airfoils and the conventional ceiling fan. The conventional ceiling fan that was selected is the Panasonic BAYU 3 Blade Ceiling Fan F-M12D2VBHH which has an overall diameter (hub and blade) of 1 200 mm, hub diameter of 170.3 mm and blade's length of 514.85 mm. This ceiling fan was selected as the study model due to its dimension that was closely fitted to the dimension of the Daikin's round flow cassette which has the width of 950 mm and the length of 950 mm.

As for the available airfoils, according to Mahlia's research, the conventional ceiling fan runs in low Reynolds number which the air velocity around the fan's blades is low [12]. Therefore, the Gilbert Morris GM15 F1C class free flight flapper airfoil (GM15) is suitable for creating the fan mechanism for the cassette air conditioner as it provides extraordinary climb, glide and endurance abilities. Fig. 2 shows the GM15 airfoil that was used to construct the blades.

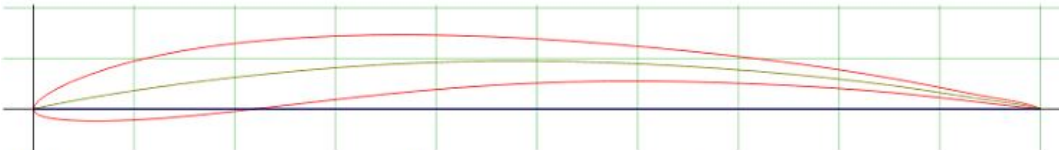


Figure 2. The Gilbert Morris GM15 Airfoil (GM15)

Fig. 3 shows the fan mechanism was modeled with total diameter, hub diameter, blade's length, angle of attack at the root, angle of attack at the tip, root's width and tip's width of 1 200 mm, 170 mm, 515 mm, 12˚, 6˚, 100 mm and 50 mm. The 12˚ angle of attack at the root and the 6˚ angle of attack at the tip were used because Adeeb has experimented these angles and claimed that the root and tip angle of attacks are the contribution of volumetric flow rate, torque and energy efficiency [11].

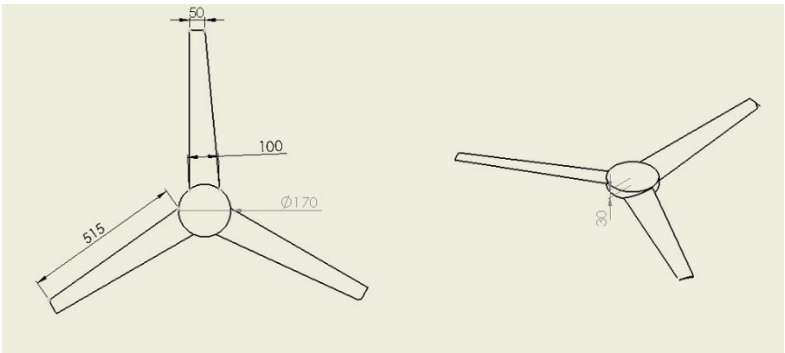


Figure 3. Dimensions of the Overall Fan Mechanism

2.2 Numerical Method

2.2.1 Geometry Modelling

To simulate the cassette air conditioner, an enclosure domain was created to prevent any flow interruption from outside. The 3D model of the cassette air conditioner was placed on the ceiling and in the middle of the enclosure domain. The enclosure domain imitates a classroom in Taylor's University (D4.04) which has dimensions of 7 850 mm in length, 7 150 mm in width and 2 800 mm in height. Fig. 4 shows the isometric view of the cassette air conditioner in an enclosure domain.

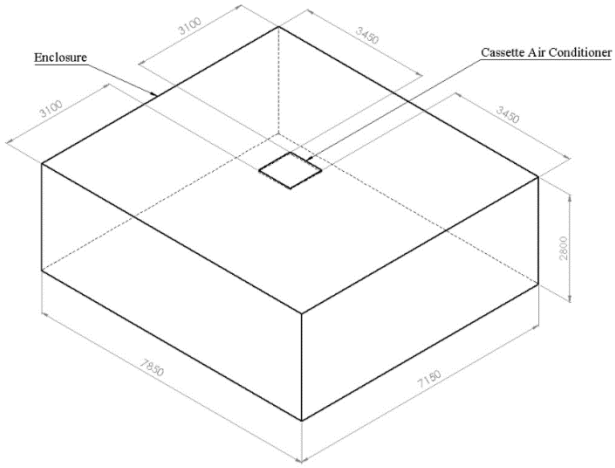


Figure 4. Isometric View of Cassette Air Conditioner in an Enclosure Domain

Besides that, a rotating domain with slightly larger dimensions of the fan mechanism was constructed to simulate the rotating fan mechanism with fluid flow. The dimensions of the rotating domain are 1 250 mm in diameter and 50 mm in height as shown in Fig. 5.

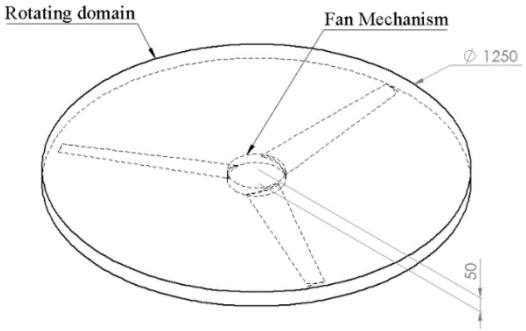


Figure 5. Rotating Domain

Then, an enclosure domain was created around the rotating domain and fan mechanism to prevent any flow interruption from outside. The rotating domain and fan mechanism are placed in the middle of the enclosure domain with a height tolerance of 240 mm from the ceiling of the enclosure domain. The enclosure domain has the same dimensions as the cassette air conditioner in an enclosure domain. Fig. 6 show the isometric view.

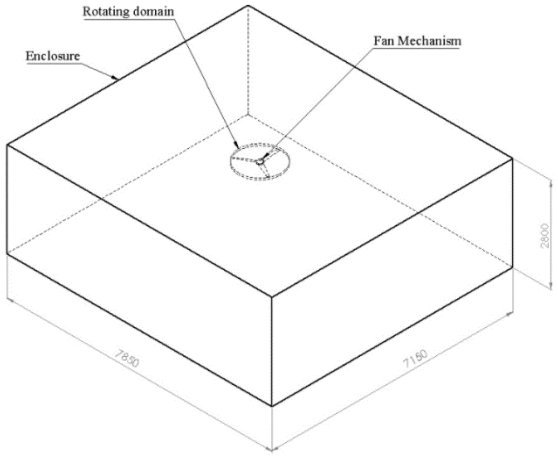


Figure 6. Isometric View of Fan Mechanism together with Rotating Domain in an Enclosure Domain

Furthermore, the combination of cassette air conditioner and fan mechanism with the rotating domain in an enclosed domain was created to simulate the condition of having a fan mechanism as the air blower mechanism to assist the cassette air conditioner in conditioned air flow distribution. All the dimensions from the previous cases are similar for this case, one thing to emphasize on is the distance between the cassette air conditioner and the fan mechanism which is 200 mm away from each other. Fig. 7 show the isometric view of the combination of cassette air conditioner and fan mechanism with the rotating domain in an enclosed domain respectively.

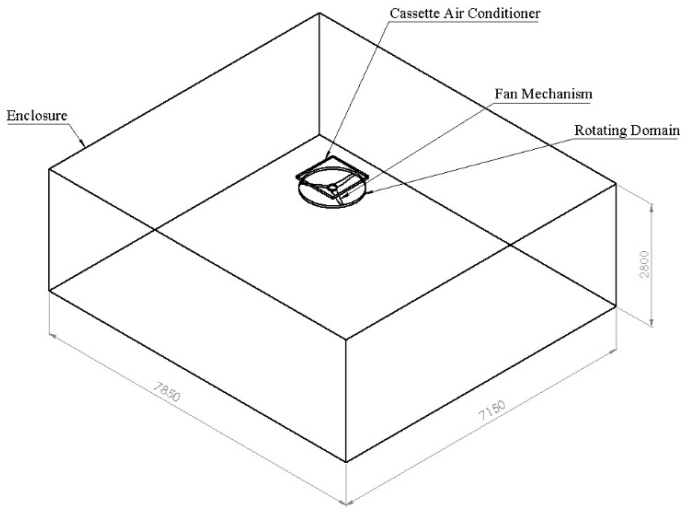


Figure 7. Isometric View of Combination of Cassette Air conditioner and Fan Mechanism with the Rotating Domain in an Enclosed Domain

2.2.2 Meshing

Meshing is the most vital step to produce precise results. Two quality measures were used to determine a decent mesh of the geometry which are the skewness and the orthogonal quality [16]. To have the best mesh, the skewness need to be near to zero whereas the orthogonal quality need to be near to one. The ANSYS Fluent Mesh is used to generate the mesh on the geometry. Therefore, the mesh dependency analysis of the cassette air conditioner and the fan mechanism were conducted separately to validate the mesh before combining both together. The primary aim of this analysis is to obtain the ideal mesh settings in order to produce precise results. The ideal mesh settings will be recognized when the mesh delivers same result.

2.2.3 Numerical Setup

The Reynolds Averaged Navier-Stokes (RANS) equations were used to find the airflow in the room. The equations are composed of continuity equation Eq. (1) and momentum equations for x-component, y-component and z-component Eq. (2-4).

$$\frac{\partial \rho}{\partial t} + \nabla \cdot (\rho V) = 0 \tag{1}$$

$$\frac{\partial \rho u}{\partial t} + \nabla \cdot (\rho u V) = -\frac{\partial P}{\partial x} + \nabla \cdot (\mu \nabla u) + S_{m,x} \tag{2}$$

$$\frac{\partial \rho v}{\partial t} + \nabla \cdot (\rho v V) = -\frac{\partial P}{\partial y} + \nabla \cdot (\mu \nabla v) + S_{m,y} \tag{3}$$

$$\frac{\partial \rho w}{\partial t} + \nabla \cdot (\rho w V) = -\frac{\partial P}{\partial z} + \nabla \cdot (\mu \nabla w) + S_{m,z} \tag{4}$$

where u, v and w are the velocity vectors for the respective x, y and z-components. ρ is the density of air, P is the static pressure whereas $S_{m,x}$, $S_{m,y}$ and $S_{m,z}$ are the source terms of x, y and z-components.

In the air conditioner simulation, the flow was treated as incompressible as the Mach number is less than 0.3. The material of the fluid used is air with default density and viscosity. The standard k-ε with standard wall function was chosen to follow the state of the airflow. The turbulence model was chosen based on the reviewed papers by Ooi Yongson and Ken Fukada [14, 17]. The k-ε turbulence model is suitable for this case because the airflow in the air conditioned room is mostly turbulent flow where turbulence model has advantage of this. This model also leads to stable calculation and has reasonable predictions for many flows in the air conditioned room.

In the fan mechanism simulation, the flow was treated as incompressible as well. The material of the fluid used is air with default density and viscosity The Spalart Allmaras turbulence model, k-ε turbulence model and k-ω turbulence model were studied with different mesh settings to obtain the best result.

2.2.5 Assumptions

At the beginning of this research study, a few assumptions were clarified as indicated below.

1. The parameters of thermal comfort such as air temperature and air velocity are only studied.
2. The domains are to recreate the setup of the rotating fan mechanism and the enclosed space.
3. The fan mechanism is simplified to reduce the complication of the 3D geometry.
4. The cold air that is discharged from the cassette air conditioner is at 6 m/s.
5. The discharge angle of the air blower at the cassette air conditioner is fixed at 30°.
6. The discharge air flow from the cassette air conditioner is at 20°C.

2.2.6 Calculation

The Draft Rate (DR) is the percentage of the dissatisfied users which is caused by the draft. Draft is the undesirable cold air of the air velocity. The draft's satisfaction is relied on the air velocity, air temperature, turbulence intensity and clothing. Hence, the higher the DR, the higher the dissatisfaction of thermal comfort of the users. In order to have a satisfied thermal comfort in an enclosed environment, the DR have to be lower than 20% [2]. Eq. (5) is the equation for calculating the DR.

$$DR = ([34 - t_a] * [v - 0.05]^{0.62}) * (0.37 * v * Tu + 3.14) \quad (5)$$

where;

t_a = air temperature (°C)

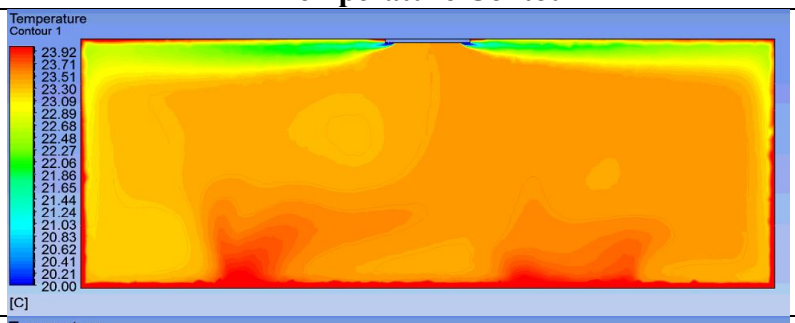
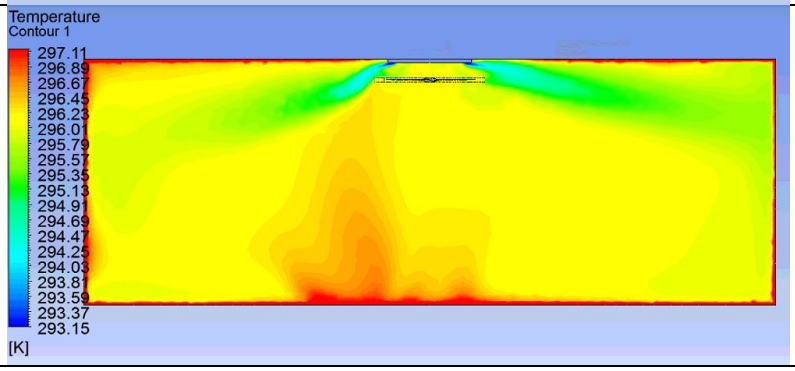
v = mean air velocity (m/s)

Tu = turbulence intensity (%)

3. Results and Discussion

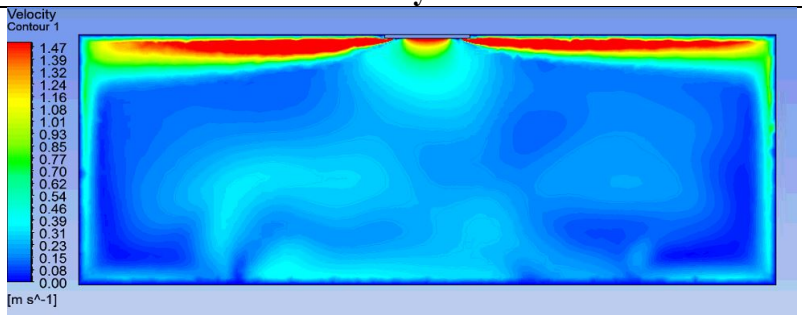
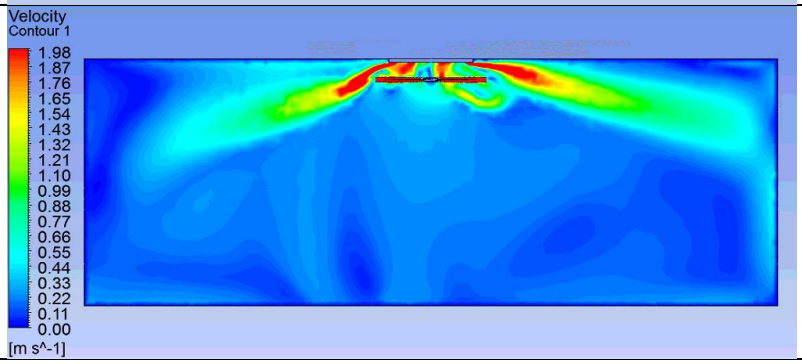
The k-ε turbulence model is a better option as it captures turbulence flow from the cassette air conditioner as well as from the fan mechanism which are important to identify the thermal comfort of the air conditioned room. This is because the distribution of air velocity and air temperature depend on the flow circulation in the enclosed space. Table 1 and Table 2 show the comparisons of temperature and velocity contours respectively. According to Table 1, the air temperature becomes colder with the addition of the fan mechanism.

Table 1. Comparison between Temperature Contours

Condition	Temperature Contour
Cassette air conditioner	
Cassette air conditioner and fan mechanism	

Besides that, the implementation of fan mechanism has pull the conditioned air downwards which slightly improves the air velocity in an enclosed space.

Table 2. Comparison between Velocity Contours

Condition	Velocity Contour
Cassette air conditioner	
Cassette air conditioner and fan mechanism	

A simple validation calculation is applied to determine the thermal comfort level in the enclosed space. The DR equation is used in this process.

Cassette air conditioner

$$DR = ([34 - 23.51] * [0.23 - 0.05]^{0.62}) * (0.37 * 0.23 * 5 + 3.14)$$
DR = 2.5%

Cassette air conditioner with fan mechanism

$$DR = ([34 - 23] * [0.22 - 0.05]^{0.62}) * (0.37 * 0.22 * 5 + 3.14)$$
DR = 2.4%

From the calculations, the difference is only 0.1%. Both falls in the satisfied thermal comfort as both values are below 20% [2]. However, the implementation of the fan mechanism has improved the thermal comfort in the enclosed space.

4. Conclusions

This research study aims to design an air blower mechanism for the cassette air conditioner to improve the thermal comfort in an enclosed area. The studies on the thermal comfort were conducted carefully as there are too many parameters of thermal comfort available. Air temperature and air velocity were selected as the primary parameters for this research study. As the primary parameters were selected, design research on the air blower mechanism was conducted. The concept of the air blower mechanism came from the inspiration of ceiling fan. Further research were conducted on the design of it. Then, the air blower mechanism was modelled by using SolidWorks. Then numerical studies were conducted by using ANSYS Fluent with several turbulence models such as Spalart Allmaras, k-ε and k-ω turbulence models to compare which turbulence model provides the most accurate results. According to the simulation results, the k-ε turbulence model is the best option to study the air velocity as well as the air temperature as this model captures the turbulent air flow. Furthermore, comparison between with and without the air blower mechanism were examined. The implementation of the fan mechanism has provide colder air and better air velocity distribution in an enclosed space. The DR equation was used to determine the satisfaction of thermal comfort in the enclosed space. It was found that with the implementation of the air blower mechanism to the cassette air conditioner, the DR value has decreased by 0.1%. This means that the air blower mechanism has slightly improved the thermal comfort in the enclosed space. However, there are still room for improvements to validate this further.

Errors could be seen in the simulation of the fan mechanism as the results show uneven air velocity flow. This could be done better by refining the model further. Besides that, experimental studies could be conducted to validate the simulation. Other than that, come out with more designs of the fan mechanism to further research the possibilities of improving the thermal comfort.

Acknowledgment

First and foremost, with my sincere appreciation and warmest thanks to everyone who had helped and lead me throughout this research study. I want to specially thank Dr. Azadeh Ghadimi for her supervision, knowledge and most importantly support that had given me during this research. I am so thankful for her commitment to assist me in completing this study. Besides that, I also want to thank Dr. Chin Wai Meng as well as Mohd Anuar Bin Abd Aziz from Daikin for assisting me in terms of knowledge and guidance. It was wonderful that they could me even though they are busy with their work. Furthermore, I want to also thank Madushi Rajapakshe for replying my e-mails, your feedbacks and suggestions had helped me a lot. Last but not least, I would like express my gratitude to my family and friends for their kind souls in encouraging me.

References

[1] K. W. D. Cheong *et al.*, "Thermal comfort study of an air-conditioned lecture theatre in the tropics," *Build. Environ.*, vol. 38, no. 1, pp. 63–73, 2003.

[2] D. B. Jouini, M. N. Saïd, and E. G. Plett, "Measurements of room air distribution in a ventilated office environment," *Build. Environ.*, vol. 29, no. 4, pp. 511–521, 1994.

[3] N. Baker and M. Standeven, "Thermal comfort for free-running buildings," *Energy Build.*, vol. 23, no. 3, pp. 175–182, 1996.

[4] Ansi/Ashrae, "ANSI/ASHRAE 55:2004 Thermal Environmental Conditions for Human Occupancy," *Ashrae*, vol. 2004, p. 30, 2004.

[5] H. Hensel 1981. Thermoreception and temperature regulation, Academic Press, London. (Monographs of the physiological society ; nr. 38)

[6] K. E. Charles, "Fanger's Thermal Comfort and Draught Models Fanger ' s Thermal Comfort and Draught Models IRC Research Report RR-162," *October*, p. 29, 2003.

[7] Awbi HB, Gan G. Predicting air 6ow and thermal comfort in oHces. ASHRAE Journal, February 1994;36(2):17–21

[8] K. C. Noh, J. S. Jang, and M. D. Oh, "Thermal comfort and indoor air quality in the lecture room with 4-way cassette air-conditioner and mixing ventilation system," *Build. Environ.*, vol. 42, no. 2, pp. 689–698, 2007.

[9] R. Bassiouny and N. S. Korah, "Studying the features of air flow induced by a room ceiling-fan," *Energy Build.*, vol. 43, no. 8, pp. 1913–1918, 2011.

[10] E. Adeeb, A. Maqsood, and A. Mushtaq, "Effect of Number of Blades on Performance of Ceiling Fans," *Eff. Number Bl. Perform. Ceil. Fans*, vol. 28, no. July, p. 2002, 2015.

[11] E. Adeeb, A. Maqsood, A. Musthaq, and C. H. Sohn, "Parametric Study and Optimization of Ceiling Fan Blades for Improved Aerodynamic Performance," *J. Appl. Fluid Mech.*, vol. 9, no. 6, pp. 2905–2916, 2016.

[12] M. M. Rahman, H. Y. Rahman, M. U. Maniam, and Y. S. Visvanathan, "Theoretical and Experimental Investigation of Energy Efficiency Improvement of the Ceiling Fan by Using Aerodynamic Blade Profile," no. M, pp. 14–17, 2011.

[13] P. D. M. P. Rajapakshe, M. H. H. G. Mapa, and R. Thanushan, "Investigating aerodynamic performance of a ceiling fan," *Annu. Sess. IESL*, no. April 2016, pp. 1–10, 2015.

[14] K. Fukada, K. Sakai, and H. Ono, "STUDY ON MODELING METHOD IN

MODULARIZING HVAC ELEMENTS FOR CFD SOFTWARE Research & Development Center , Shinryo Corporation , Tsukuba , Japan School of Science & Technology , Meiji University , Kawasaki , Japan Environmental Science Research Lab ., Centra," *Build. Simul. Conf.*, pp. 850–856, 2015.

[15] C. No, "R410A Energy saving Throughout the cooling season , reduce energy consumption."

[16] A. Bakker, "Meshing – Applied Computational Fluid Dynamics", Dartmouth College, Haover, New Hampshire, 2006.

[17] O. Yongson, I. A. Badruddin, Z. A. Zainal, and P. A. Aswatha Narayana, "Airflow analysis in an air conditioning room," *Build. Environ.*, vol. 42, no. 3, pp. 1531–1537, 2007.

eureca 2017 – Conference Paper
Paper Number 2ME23

Optimization of torsional thrust stand for sub-micronewton thrust measurement

Wong Shin Chien, Cheah Kean How
[1]*School of Engineering, Taylor's University, Malaysia*

Abstract
Nanosatellites orbiting Earth and has many applications on human activities on Earth such as telecommunications, broadcasting, *Global Positioning System* (GPS), etc. A calibration of its micro-propulsion system was carried out. A torsional thrust stand is one of the high accuracy tools used for micro-propulsion engine calibration [3]. This project is aimed to optimize the performance of a torsional thrust stand. The aim is to improve performance in several areas such as improving the resolution of the force reading taken in micronewton range, and also to reduce the uncertainty of readings obtained when measuring the displacement of the thrust stand by reducing the vibration from the surroundings. The most suitable magnet is selected from 6 different samples, which the selected one ranges from 0 μN to 912.33 μN while current is applied from 0 A to 1.0 A. The magnet is used for electromagnetic force generation which acts as a thrust force. A self-designed thrust stand is fabricated and force reading was calibrated. The reading shows that for every 4.799 μN generated, the displacement is increased by 1 μm. The resolution of the force based on smallest current generated is to be 3.36 μN, which is improved from old thrust stand (50 μN). Vibration reduction combination is most effective when applying vibration reduction mountings and protective casing only. The vibration shielded thrust stand shows results from the laser displacement sensor with uncertainty of ± 0.5μm compared with thrust stand without anti-vibration system installed (± 0.9559 mm). Maximum experimental error is calculated to be 11.41%, which is in an acceptable range. This research concludes the improvement in force calibration based on improved resolution and low uncertainty. This research proved to be useful when used to determine the accuracy of future nanosatellites navigations.

Keywords: Thrust stand, Resolution, Nanosatellite, Micronewton, Vibration.

1. Introduction

Satellites are devices that orbit around the earth, moon, or another planet transmitting data to Earth[1]. Nanosatellites orbiting Earth and has many applications on human activities on Earth such as telecommunications, broadcasting, *Global Positioning System* (GPS), etc[2]. Nanosatellites are small satellites that have wet mass less than 10 kg [3]. These satellites have their own micro-propulsion system which generates thrust force using their own micro-propulsion engine (thruster) [5].

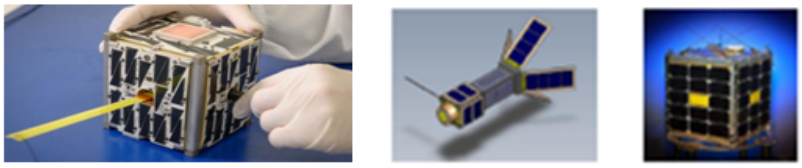
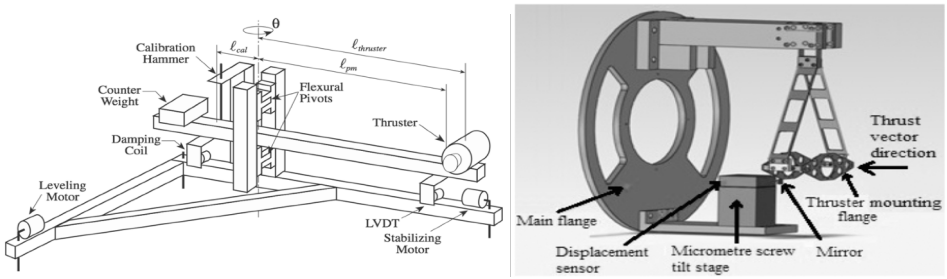


Figure 1. Boeing CSTB1, Nanosail-D2, and AprizeSat (from left to right) [4]

The purpose of a thrust stand is to calibrate the displacement value that corresponds to force applied. Firstly, a solenoid (voice coil) in is used as a force generator to deflect the thrust stand. We know how much displacement a certain force can produce after calibration. Hence, when a thruster is installed on the beam of thrust stand and produce thrust force, the thrust force is known based on the displacement of beam according to the calibration data from the voice coil calibration.

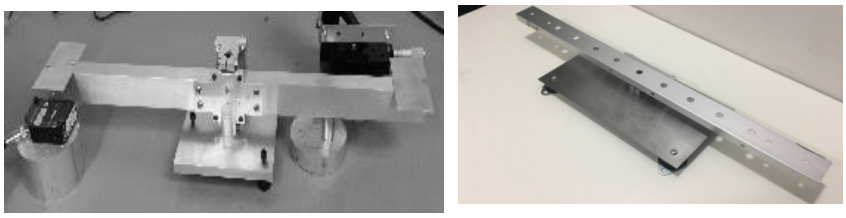
There are several sub-micronewton thrust stand. A torsional thrust stand oscillates around its axis of rotation in a harmonic motion when force is applied on it [6,7]. A hanging pendulum thrust stand uses pendulum concept with a weight hanging from a flange. The thruster is attached to it to generates deflection when thrust force is applied.



(a) (b)

Figure 2. Types of thrust stand (a) torsional and (b) hanging [8].

The aim of this research project is to optimize the performance of thrust stand by improving the resolution of the force calibration and reduce uncertainty error. Hence, a new thrust stand is designed and fabricated. New methods to improve accuracy are applied such as using current sensor to control the current to the voice coil, using vibration reduction mountings, protective casing, etc.



(a) (b)

Figure 3. Torsional thrust stand of (a) another project (b) this project

2. Research Methodology

2.1 Design & Fabrication of Thrust Stand Components

The thrust stand that used in this research is a torsional thrust stand that deflects its beam when the magnet attached to the beam is exerted a force by a solenoid (voice coil) near to it. To conduct the experimental studies needed to achieve a higher resolution compared to previous studies from other researchers, a new thrust stand was designed and fabricated with improved features as shown in figure 4.

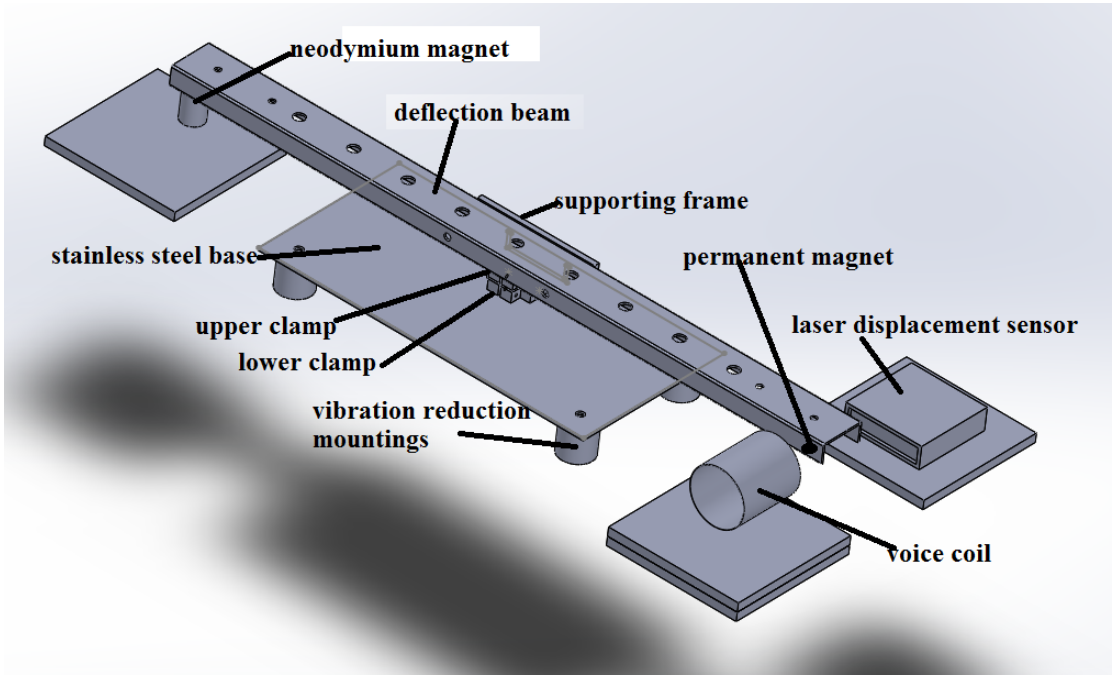
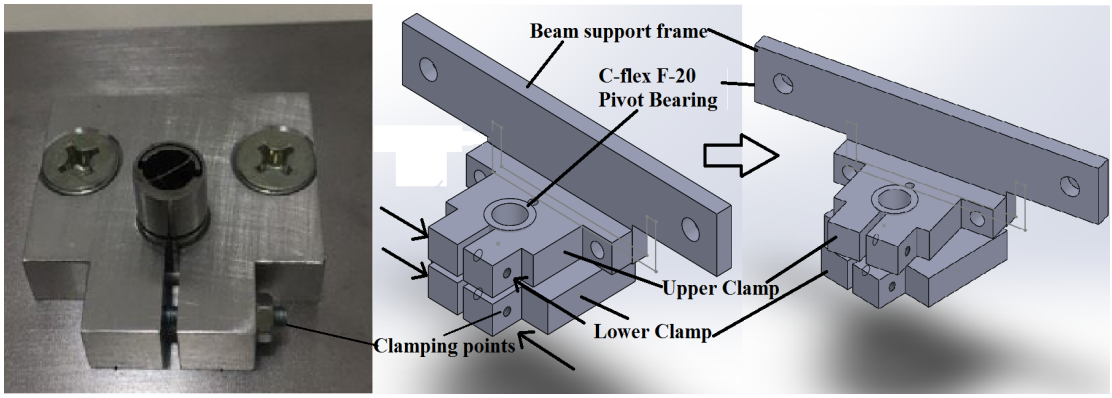


Figure 4. CAD drawing of new sub-micronewton thrust stand

To allow the U-shaped deflection beam in figure 4 to rotate on its axis, a sensitive component which responds force change is required. A C-flex F-20 pivot bearing is clamped between the lower and the upper clamp. This allow the deflection beam which is clamped to the upper clamp to rotate along with as shown in figure 5. Clamps, deflection beam, and its support frame are made of aluminium to reduce weight.



(a) (b)

Figure 5. (a) Actual C-Flex F-20 pivot bearing clamped & (b) CAD illustration

Besides, the stainless steel foundation provides a lower centre of gravity to the whole body and increase stability. It also allows 4 mounting points for vibration reduction mountings to be mounted beneath it. The U-shaped beam has relatively low weight compared to old thrust stand. A permanent magnet attached to the end of the beam. An electromagnetic voice coil is placed in front of it to produce electromagnetic force on the beam to allow deflection. The laser displacement sensor is placed behind it to record displacement changes. A strong neodymium magnet is placed underneath another end of the beam to act as a damper to the beam. This allows the beam to back to resting position faster. Table 1 summarize the improvement made when design a new thrust stand.

Table 1. Micronewton thrust stand components and its function

Component	Function
Long deflection beam	Made of aluminium, it amplifies the effect of angular displacement of pivot bearing and has relatively light weight.
Beam support frame	Holds upper clamp and deflection beam together.
Lower clamp	It is fixed to the stainless steel base amd also clamps the lower part of pivot bearing (C-Flex F-20)
Upper clamp	Free to rotate and clamps the upper part of pivot bearing (C-Flex F-20)
Stainless steel foundation	A stable foundation with high weight, and allows vibration absorption mountings, lower clamp to be mounted.
Vibration absorption mountings	Absorbs vibration energy that comes from the surface of the contact points to reduce experimental error.
Electromagnetic voice coil	Generates electromagnetic force that pushes the beam away to produce deflection needed for force calibration.
Neodymium magnet	Act as a damper to allow the beam to oscillates back to rest faster to carry out next data extraction.
Laser displacement sensor	A displacement sensor that has a sensitivity of ± 0.5μm. Reflects laser back to receiver and analyzes the distance.

2.2 External Vibration Reduction

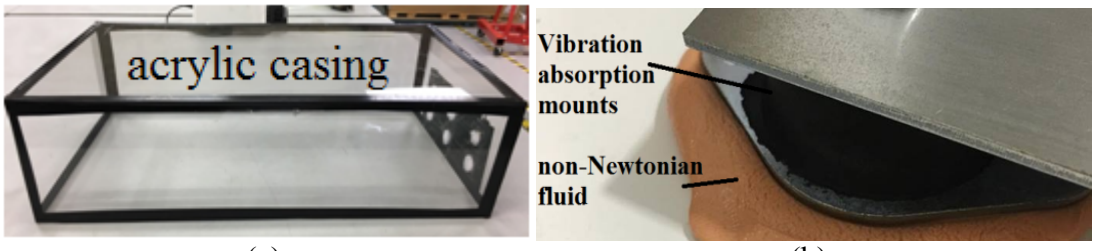
Vibration reduction is an important aspect that should be considered when designing a new thrust stand research. Displacement of thrust stand deflection beam is obtained through laser displacement sensor. It is important to reduce the vibration level lower than the minimum value of deflection of beam. For example, if the laser displacement sensor has a resolution of 1 μm, but the vibration level is 0.5 μm, the final resolution will not be affected by the vibration. In contrary, if vibration level is higher than sensor resolution, the results will be affected.

Eq. (1) shows the vibration of a mass-damper system similar to a torsional thrust stand. A spring vibration reduction system has to be introduced to reduce the amplitude of the vibration more effectively. The main vibration reduction variable is governed by w_d, which the effect is small when w_n value is high, which in our case is high for the natural frequency of thrust stand.

$$x(t) = [x_o e^{-\zeta w_n t} . cos(w_d t - \emptyset_o)] + [x. cos(wt - \emptyset)] \quad (1)$$

where x = displacement
x_o = original amplitude of displacement
w_d = damped frequency
w = external harmonic vibration frequency
w_n = natural frequency
$\emptyset_o$ = initial angular displacement
$\emptyset$ = angular phase lag
ζ = damping constant

Different approaches have been made to reduce the vibration level to an acceptable range which gives consistent result to the result obtained during experiment. Firstly, an acrylic casing is built as shown in figure 6 to isolate the system from high speed moving air surrounding it. Air particles often knock on the deflection beam and generates random deflection. Besides, vibration reduction mountings are mounted beneath the stainless steel base to absorb vibration coming from the surface. An addition of non-Newtonian fluid is added to improve the vibration reduction further as shown in figure 6.



(a) (b)

Figure 6. Acrylic casing & vibration absorption mounts with non-Newtonian fluid

To determine which vibration reduction approach is effective, different combinations of vibration reduction approaches are experimented. The combinations are shown in figure 7. The combination that gives the lowest vibration level will be chosen for the final calibration stage.

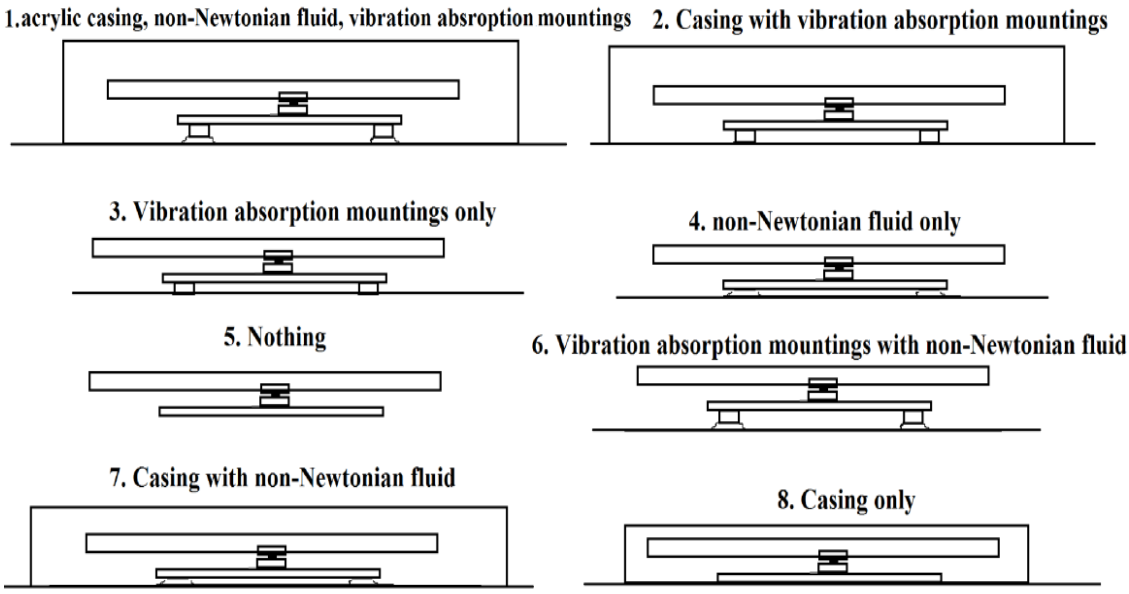


Figure 7. Different combinations of vibration reduction approaches

2.3 Selection of Suitable Magnet for Force Generation

Electromagnetic force is generated when a current passes through a solenoid. When the current increases, the force generated increases in proportion with it. In this research, voice coil acts as a solenoid that generates electromagnetic force which exerts force on permanent magnet attached to the beam. Eq. (2) shows the strength of electromagnetic force generated. The increases in current in the voice coil will increase the magnitude of force generated.

$$B = \mu NI \tag{2}$$

where B = magnetic field strength,

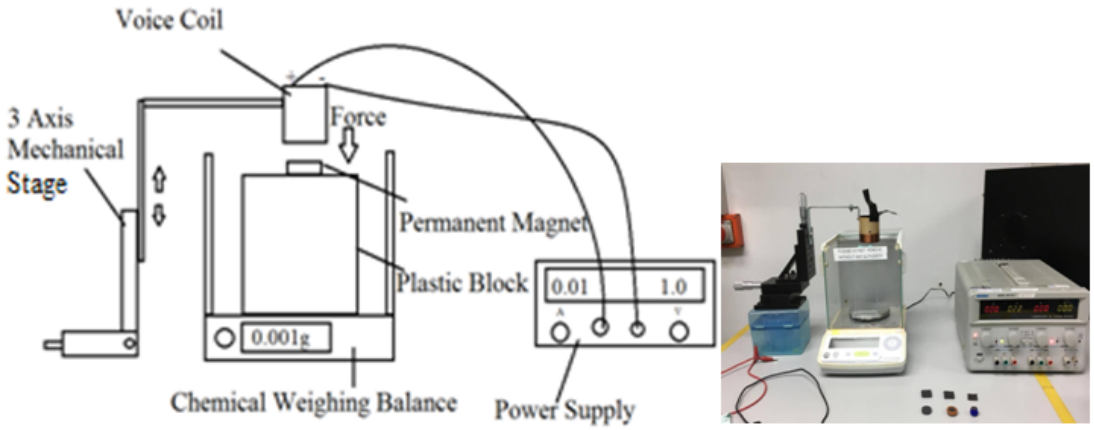
μ = permeability of vacuum,

N = number of turns of wire,

I=amount of current flow

Electromagnetic force can be determined by using a chemical weighing balance with a permanent magnet attached on top of it. The weight change is the force produced when current passes through the voice coil. Experimental setup is shown in figure 8.

To select a suitable magnet which is in desirable range for the research, 6 different magnets (figure 9) are tested. A mechanical stage is used to accurately position the magnets to hover just above the block with permanent magnet attached to it. Each magnet is placed on the block on top of the weighing balance as shown in figure 5 to determine the range of force that is produced when passing currents from 0 A to 1.0 A. The weight change is multiplied by gravity (9.81 ms^{-1})and is converted to force in micronewton (μN) units.



(a) (b)

Figure 8. Magnet selection with (a) schematic diagram, (b) actual experimental

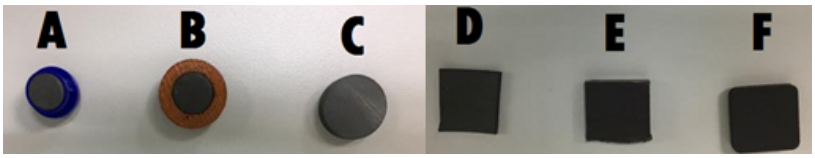


Figure 9. Different types of magnets with different magnitude of force

2.4 Constant force calibration of thrust stand

After suitable magnets and vibration level reduced to an acceptable level. The next step is to proceed with force calibration. The setup is shown in figure 10. The thrust stand is fixed inside a protective casing along with neodymium damper, laser displacement sensor, and voice coil. The voice coil is powered by a digital power supply with a current sensor hooped around its conducting wires for accurate current discharge. An oscilloscope reads the current signals supplied to the voice coil. A laptop with H1G1-SMI software installed helps to retrieve displacement graph data from laser displacement sensor.

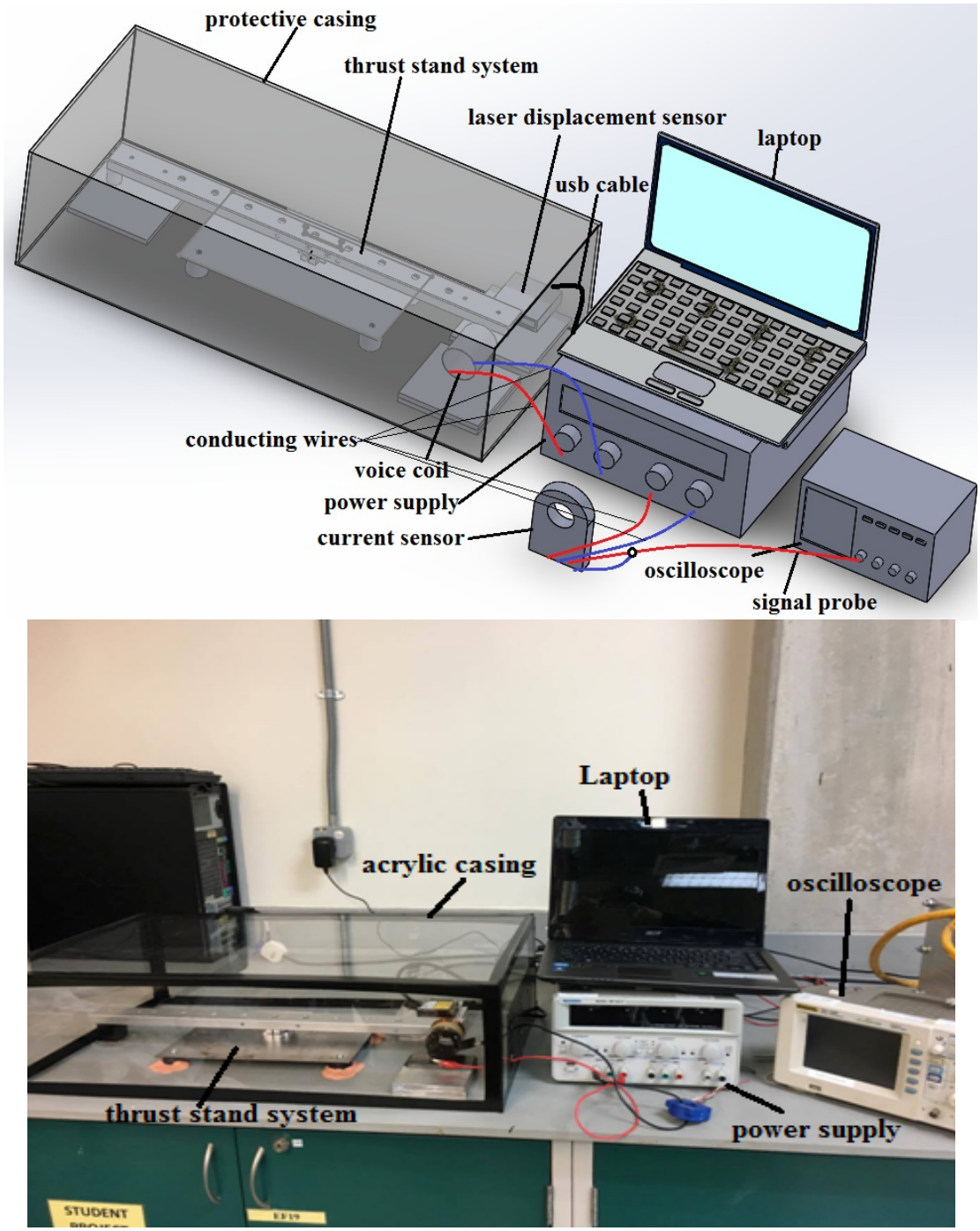


Figure 10 Schematic & actual force-displacement calibration experimental setup

Linear displacement measurement is carried out using a laser displacement sensor. The sensor projects laser that reflects back to its receiver as shown in figure 11. The time travels between from the emitter to the receiver is calculated automatically in the sensor firmware and is displayed using its relevant software on a laptop. Figure 11 also shows a displacement-time graph for the deflection beam.

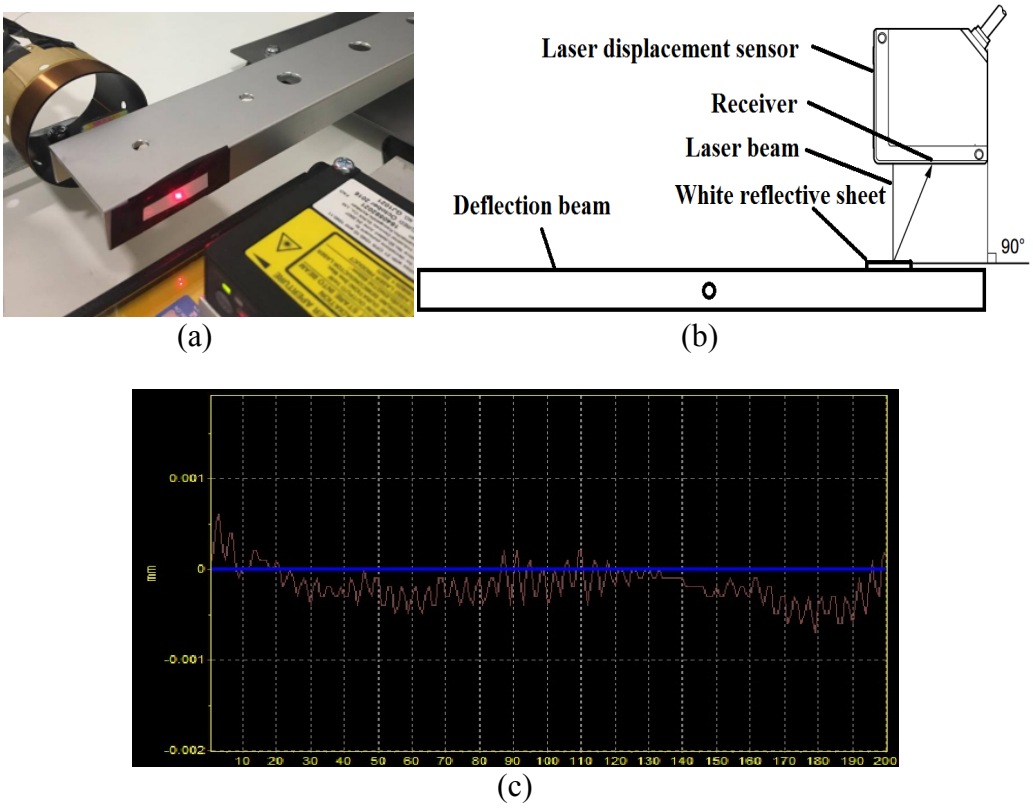


Figure 11. (a) sensor device, (b) technical diagram, (c) software generated graph

3. Results

3.1 Force generation of magnets

After running current through the voice coil starting from 0 A with an increment of 0.2 A until the current reaches 1.0 A, the weight change in milligrams displayed on the weighing balance is converted to force reading. 6 different magnets are tested in this experiment (Magnet A, B, C, D, E, F). Results are plotted in the graph shown in figure 12. Different magnets has different strength of magnetic field. Hence, when an electromagnetic field is generated, different forces are produced correspond to the strength of the magnet used.

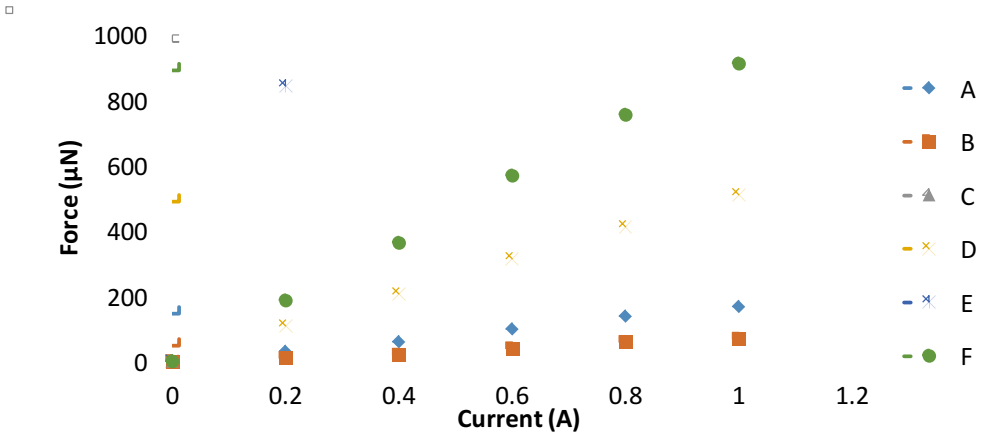


Figure 12. Graph of force vs current in the range of 0 to 1000 µN

From the graph, both magnet D & F are in the range of suitable force for calibration (0 μN - 1000 μN). The magnet that is suitable to be use is magnet F because at 0.5A (4.3V) it is able to supply a range between minimum and maximum of 0 μN - 568.98 μN. Magnet D might not be suitable because it runs at 1 A to produce 510.12 μN. This will make the voice coil very hot due to heat generated from eddy current. Next, a more refined reading is taken again with smaller increment (0.05 A) and graph was plotted as shown in figure 13. From the graph, the force (μN) increases linearly along with the increase in current (A). It has a gradient of 937.4 with R^2 value of 0.998, which is a very consistent result.

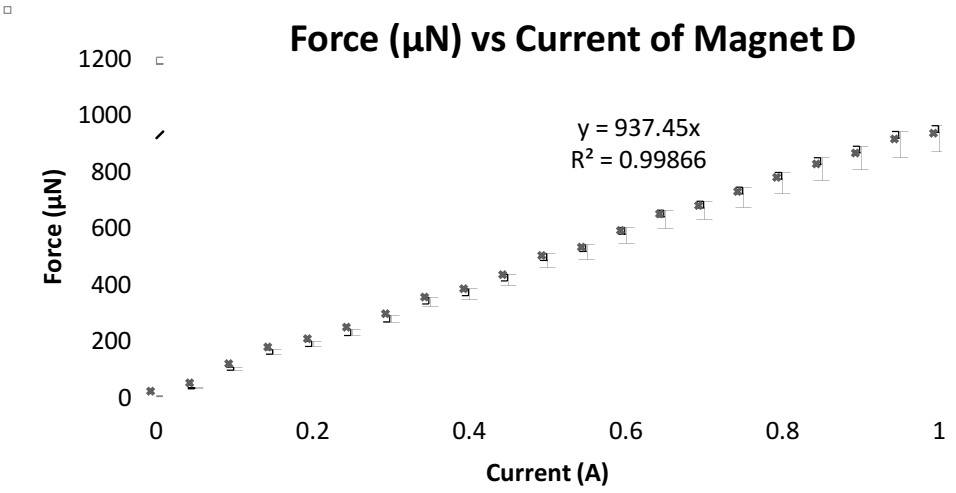


Figure 13. Graph of force vs current of magnet D (refined)

3.2 Vibration reduction

8 different scenarios as shown in figure 10 are tested using laser displacement sensor to obtain their resting vibration level. The maximum vibration levels are recorded and is converted to a bar chart as shown in table 2.

Table 2. Vibration levels of 8 different scenarios

Case	Vibration Reduction approach	Maximum Deviation (μm)	Minimum Deviation (μm)
1	Casing/non-Newtonian materials/vibration absorption mountings	-0.1	-1.6
2	Casing / vibration absorption mountings	0.6	-0.7
3	Vibration absorption mountings only	848.5	-1008.6
4	Non-Newtonian materials only	825.2	-853.8
5	Nothing	845.4	-955.9
6	Vibration absorption mountings / non-Newtonian materials	725.8	-796.5
7	Casing / non-Newtonian materials	12.3	0.3
8	Casing only	1.3	-3.5

From table 1, casing plays an important role as it isolates 99% of the vibration that causes the deflection beam to deflect randomly. Case 3, 4, 5, and 6 are the cases that have high distortion due to absence of casing. For case 1, 2, 7, and 8. the vibration level are much more lower as the casing is present. The deflection values of the beam are constructed with a bar chart in figure 14, which shows the significant of using an acrylic protective casing.

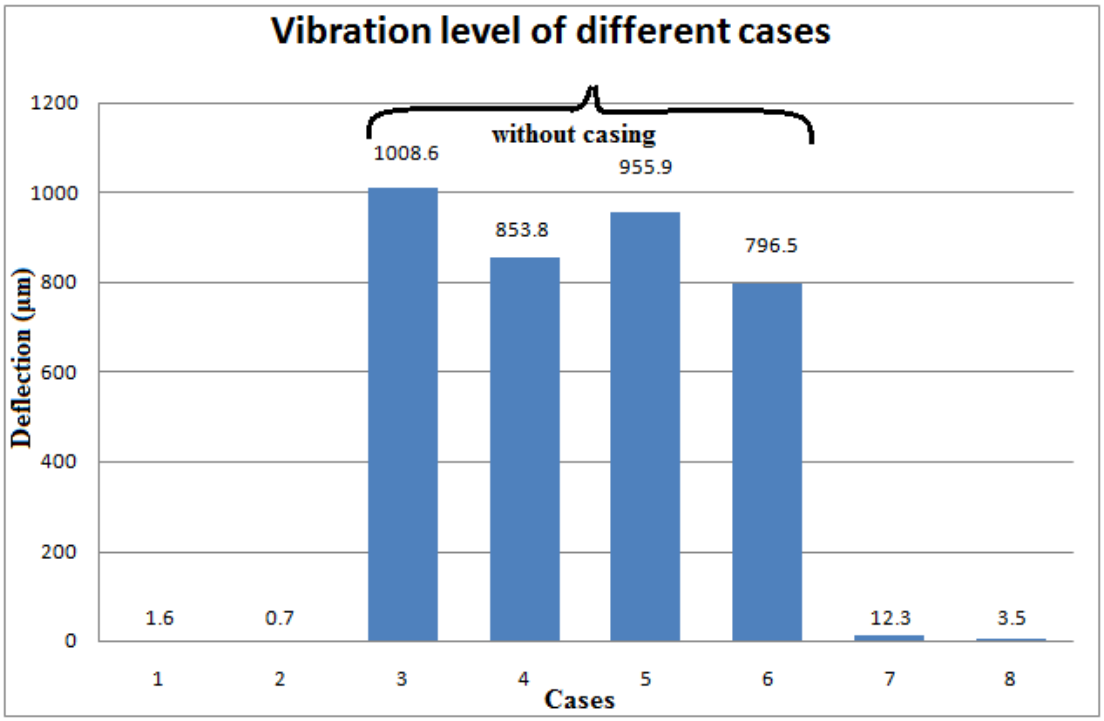


Figure 14. Vibration level of different cases

Besides, by analyzing the maximum and minimum deviation of the deflection beam of the thrust stand, we can see that vibration level that involves non-Newtonian fluid is always either positive or negative with the presence of casing. This is due to the shape of the non-Newtonian fluid changes over time, causes the thrust stand position to slightly move due imbalance mounting. Hence, non-Newtonian materials are not suitable for use at the base of the thrust stand.

Based on figure 15, a refined chart is constructed because values of case 3, 4, 5, and 6 are too big. This chart compares cases 1, 2, 7, and 8 based on maximum magnitude of vibration. The most suitable option among the 4 vibration approach combination is Case 2, which is using casing and vibration absorption mountings. This option provides the lowest ambient vibration level to the thrust stand system.

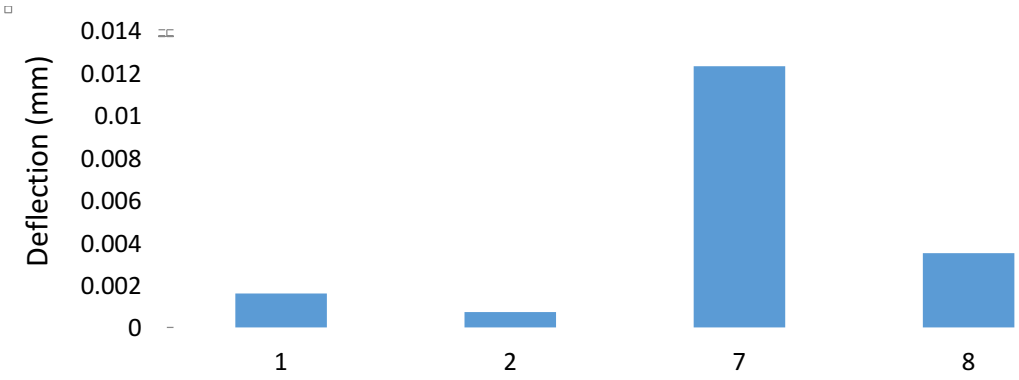


Figure 15. Maximum vibration levels of Case 1, 2, 7 and 8

3.3 Force calibration of thrust stand

Figure 16 shows a displacement-time graph response of the beam of a thrust stand when is 'pushed' by electromagnetic force. The beam is deflected to the maximum point at first and slowly oscillates to a constant deflection with the presence of a damper. The current used is 0.25 A with a time span of 30 seconds and the response is a deflection of 51 µm.

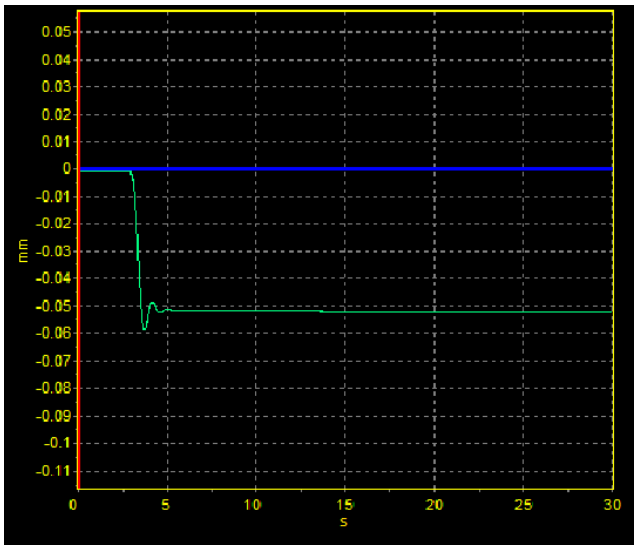


Figure 16 Displacement-time graph of deflection beam at 0.25 A in 30 s

Experiment was carried out using current supplied to the voice coil with an increment of 0.05 A starting from zero. The displacement reading picked up by laser displacement sensor was recorded. Since the ultimate purpose is to plot a graph of displacement versus force supplied. The current reading is converted to force reading based on data obtained in figure 13. In figure 17, the force calibration graph is plotted to understand the trend changes of displacement with force applied.

The force calibration graph in figure 16 above is analyzed. From the graph, the gradient of the calibration curve is 0.0002, with a fairly small y-intercept value of 0.0036. This is probably due to minor random error when taking readings from the displacement sensor as a result of vibration disturbance from the surroundings. The R^2

value of the graph is 0.9985, which shows good consistency in the experimental results taken. As the force exerted on the beam increases, the displacement of the beam increases linearly.

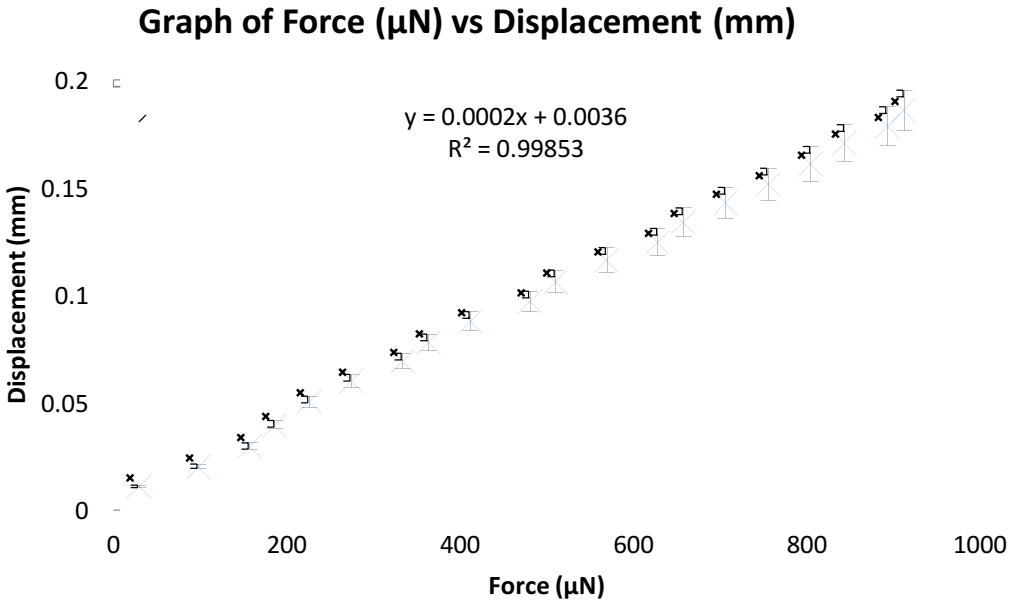


Figure 17. Graph of displacement of beam vs constant force applied to the beam.

3.5 Resolution of the optimized thrust stand

Laser displacement has a sensitivity of 0.0001 mm, which converts to 0.1 µm. When 510.12 µN is applied, there is a 0.1063 mm (106.3 µm) deflection. Hence, to find the sensitivity of the thrust stand system, one could use the ratio of force applied and displacement of the beam.

Sensitivity of the thrust stand is given by:

$$sensitivity = \frac{510.12\ \mu N}{106.3\ \mu m} = 4.799\ \mu N/\mu m$$

Also, by using the combination of vibration reduction approach of case 2 in figure 10, the vibration level is ± 0.7 µm, which is higher than the sensor smallest unit (±0.1 µm). Hence, the resolution in micronewton (µN) unit can be calculated as:

$sentivity$ x $vibration\ level = 4.799$ x $0.7 = 3.3593$ µN

The smallest force that has been used in the experiment is 29.43 µN. Therefore, a 29.43 µN force with an uncertainty of ± 3.3593 µN can be calculated to be:

$$uncertainty\ error = \frac{3.3593}{29.43} \times 100\ \% = 11.41\ \%$$

According to uncertainty error calculated, the force calibration results generated by carrying out thrust stand experiment is very promising, with an uncertainty of 11.41 % only. This is in an acceptable range (< 15%) and a nominated force between 0 μN to 1000 μN can be safely assumed to be reliable. A comparison with other research projects is also shown in table 3.

Table 3. Comparison of performance of thrust stand based on resolution

Author	Resolution (μN)	Reference
Allen H. Yan	~ 10	[13]
Yang, Yuan-Xia	~ 90	[14]
K H Cheah, K S Low	~ 40	[6]
J.K. Lam, K.H. Cheah	~ 50	[12]
S.C. Wong (This project)	~ 4 (3.36)	-

Finally, a summary of the technical specification of thrust stand built in this project is shown in table 4 below.

Table 4. Specification of torsional thrust stand of this project

Type of thrust stand	Torsional
Calibration type	Electromagnetic voice coil
Vibration attenuation	Up to 99.93 %
Force measuring range	3.36 μN - 912.33 μN
Resolution	3.36 μN
Weight	**~ 2kg**
Material	Steel & Aluminium
Torsional rate of pivot bearing	0.00545 N-m/degree

4.0 Conclusion

In conclusion, the objectives of optimizing of calibration of sub-micronewton thrust stand are met. This thrust stand components are designed using Solidwork 2015 and is fabricated accordingly. The methods are carefully followed based on the planned routines in research methodology. After obtaining datas from the well executed experiments, a force-displacement graph has been plotted. The resolution has been improved from 50 μN[12] to 3.36 μN, with an uncentainty error of 11.41%. Improved resolution and low uncertainty errors proves that the methods used are effective and successful.

References

[1] Anir Kumar Yadav. (2013). Nano-satellite, Micro electromechanical system.1 (1), p3.
[2] Professor Justin Dillon. (2014). Sputnik and the 'scientific revolution'. what happened to social justice?. 1 (1), p1.
[3] J. Li, M. Post, T. Wright, R. Lee.(2013).Design of Attitude Control Systems for CubeSat-Class Nanosatellite, Journal of Control Science and Engineering.1(1) p1
[4] R. Cannon. Nanosatellites.(2012). Educational Launch of Nanosatellites. Accessed on:7 May 2017.

[5] T. Morris, M. Jugroot. (2011). Study of an electrostatic micropropulsion system for nanosatellites, Canadian Aeronautics and Space Journal. 57(1), p99.
[6] K.H. Cheah, K.S. Low. (2016). Torsional thrust stand for characterization of microthrusters. Innovation in Aerospace Engineering and Technology, p1.
[7] A. Pancotti, T. Haag, S. King, and M. Walker. (2013) "Recommended Practices in Thrust Measurements," in 33rd International Electric Propulsion Conference
[8] J. K. Ziemer. (2001) "Performance Measurements Using a Sub-Micronewton Resolution Thrust Stand," in 27th International Electric Propulsion Conference
[9] Z. He, J. Wu, D. Zhang, G. Lu, Z. Liu, and R. Zhang. (2013)"Precision electromagnetic calibration technique for micro-Newton thrust" Rev. Sci. Instrum., vol. 84, no. 055107
[10] H. Koizumi, K. Komurasaki, and Y. Arakawa, (2004) "Development of thrust stand for low impulse measurement from microthrusters," Rev. Sci. Instrum., vol. 75, no. 3185
[11] J. Soni and S. Roy. (2013) "Design and characterization of a nano-Newton resolution thrust stand," Rev. Sci. Instrum., vol. 84, no. 095103
[12] J.K. Lam, K.H. Cheah. (2016) "Development of Torsional Thrust Stand that Resolves Micronewton Force," in 6th The European Educators' Christian Association Conference.
[13] Allen H. Yan, Bradley C. Appel, Jacob G. Gedrima. (2009) "MilliNewton Thrust Stand Calibration Using Electrostatic Fin," 47th AIAA Aerospace Sciences Meeting Including The New Horizons Forum and Aerospace Exposition
[14] Yang, Yuan-Xia; Tu, Liang-Cheng; Yang, Shan-Qing; Luo, Jun. (2012) "A torsion balance for impulse and thrust measurements of micro-Newton thrusters" Rev. Sci. Instrum., vol. 83, no. 015105

AUTHOR(S)

eureca 2017 – Conference Paper
Paper Number 2ME24

Assessing Flow Over Patterned Surfaces of Varied Sizes in Relation to Biofouling Control

Yap Yi Wei*, Felicia Wong Yen Myan, Lim Chin Hong
School of Engineering, Taylor's University, Malaysia

*yapyiwei@sd.taylors.edu.my

Abstract
Biofouling is the unwanted growth on submerged surfaces triggered by the surfaces' organic conditioning and has caused serious problems for underwater structures. Several studies have shown that biofouling can be prevented by the application of microtopographic features. Researchers have noticed that the geometries and sizes of the microtopographies play a role in affecting the antifouling performance. Thus, the objective of this study is to identify an optimum size of a suitable microtopography geometry with promising antifouling potential. These topographies are hypothesised to induce hydrodynamic changes that contribute to the mitigation of biofouling. In this study, a microchannel will be modelled as fluid domain with the pattered surface. Computation Fluid Dynamics (CFD) is employed in assessing the flow to show a better understanding on the flow characteristics over patterned surface. The flow assessments were carried out by altering the topographies' sizes. Data such as wall shear, velocity, shear strain rate and vorticity are analysed to evaluate the antifouling performance. This study considered wall shear distribution pattern as the significant aspect towards antifouling potential. The enclosed pattern such as circle, rectangular and hexagonal wells are effective in biofouling control. The effective range for the microtopography's sizes are around 50 μm to 500 μm. Pits with diameter, spacing and depth of 250 μm exhibited the best antifouling potential, whereas pits with diameter of 250 μm, spacing of 500 μm and depth of 125 μm demonstrated the least effective antifouling potential. Microstructures arranged with smaller spacing have higher shear stress developed at their edges. Comparisons between topographies with pits that are spaced 250 μm apart showed high fluctuating in the wall shear results. The sharply fluctuating shear stress along the peripheral of the topographies has presented an unfavourable environment for microorganisms' settlement. As for pits that were spaced 500 μm apart, alterations in depth showed insignificant difference in wall shear.

Keywords: Biofouling, Antifouling, Microtopography, CFD Simulation, Microorganisms

1. Introduction

Biofouling is a hierarchical process, scaled in length and time, where microorganisms grow and attach on the submerged surfaces. This has been an issue to the marine industry, as the biofilms formed on the ship hulls has actually increased the hydrodynamic drag and friction, which in turn increased the ship's fuel consumption [1,2]. Likewise, biofouling also has significant impact to filtration membranes in water treatment plants. The accumulation of biofouling results in an increase in the transmembrane pressure, which increases the operational costs of the plant [3].

To control the development of biofilms and the settlement of microorganisms, well-known approaches were to apply toxic antifouling coatings or fouling release coatings on the target surface. Apart from that, unique surface topographies can also be one of the application towards antifouling. This is a bioinspired approach, where there are surface designs that mimic natural surfaces that were found to demonstrate foul free properties of their own. Examples of these natural surfaces include, sharks skin, pilot whale skin, mussel shells, lotus leaves among many others [4,5]. Researchers have developed many synthetic surfaces mimicking the microtopographical arrangement of these natural surfaces in hopes of replacing metal-based antifouling coatings on underwater structures [6].

However, this approach is still the most challenging among other approaches due to difficulties develop and fabricate such patterned surfaces. Based on previous studies, several surface patterns such as channels, pits, riblets, ridges, pillars and pyramids have shown antifouling capabilities in different laboratory experiments and field studies [6,8]. The antifouling capabilities of these surfaces were found to be antifouling (i.e. width, length, height/depth, inclination, hierarchy, space apart and shape geometry).

Many studies have emphasized that size is the physical attribute which is contributing in antifouling properties of the topographies. However, these are mostly lab tests and field tests which are costly and time consuming to produce. The optimum range of the topographies' sizes which possessed high antifouling properties was 50 μm to 500 μm [2]. Based on studies, Ulva spores with diameter of 5 μm showed active settlement on substrates with uniform topography of 5 μm in width, length, height and space apart. This is due to the high contact area between the spores and topographies, decreased the energy required to adhere and increased the effectiveness of the spores' adhesive. Thus, topographies of this dimension are more favourable by the spores and seems more likely to provide refuge to the spores from flow shear. Only approximately half of the settled spores were removed when exposed to high hydrodynamic stresses [2,9].

Halder *et al.* 2013 performed a research that applied a novel approach to determine the efficacy of patterned surfaces for biofouling in a microfluidic environment. He conducted a study of patterned surfaces of different geometric features concurrently under the same experimental conditions. Experimental results were qualitatively observed with a light microscope (LM). Last, CFD analysis was perform to gain an insight into the microfluidic environment and validates with the experimental results [6].

Halder *et al.* 2013 found that cell-cell signalling processes (quorum sensing) were interrupted by wall shear. While circular shape microwells produced a strong influence on the interruption by developing higher shear bounded zones along the peripheries of the wells. When the microwells were arranged in smaller spacing, higher shear stress was developed at their edges. Sharply fluctuations in shear stress in this small area presented an unfavourable environment for the bacteria settlement. On the other hand, microwells with larger diameters developed higher shear stress at their edges, as well as the bottom compared to the microwells with smaller diameter [6].

This present study aims to assess flow over patterned surfaces of varied sizes in relation to biofouling control while the assessments were carried out through CFD simulations. This study will first consider how do the topographies' characteristic and sizes contribute to the antifouling potential and how do the flow over patterned surfaces affected the antifouling properties. First, a suitable geometry was identified as the surface topographies. Then, flow assessments of different topographies' sizes were carried out to choose an optimum size for antifouling potential. Finally, identified the flow characteristics induced by the surface topography which contributed to the mitigation and discouragement of biofouling.

2. Research Methodology

Despite many approaches in developing antifouling technologies, foul inhibiting surface is still the preferred non-toxic approach for antifouling applications. Most studies on antifouling topography were lab experiments and field studies. However, these approaches were time consuming and costly. Thus, in this research, CFD software was used to simulate and compare the flow over patterned surfaces of varied sizes in relation to biofouling control.

The following section describes the methods to assess the flow over several microtopographies with geometries that are varied in size. Each task and configurations used in this study are justified in details.

2.1 Geometry Modelling

In this study, the three-dimensional (3D) models of the fluid domain were generated using the 3D design software, Solidworks (Figure 1). The fluid domain was modelled as a rectangular block with a length of 80 mm and a square cross-section that is 8 mm by 8 mm in width and height. The topography array is placed 65 mm away from the inlet of the fluid domain. The placement of the topography array is to comply with Hagen-Poiseuille's flow theory; an incompressible Newtonian fluid flowing through a duct of constant cross-section and a length which is substantially longer than its diameter, there will be a laminar flow induced by the pressure drop along the flow. To ensure that fluid flow is fully developed (i.e. parabolic in nature), the length of flow of the fluid domain needed to be long enough so that the entrance and exit effects are negligible [10]. This is the reasoning for the length of the fluid domain and the placement of the topographies nearer to the outlet of the fluid domain

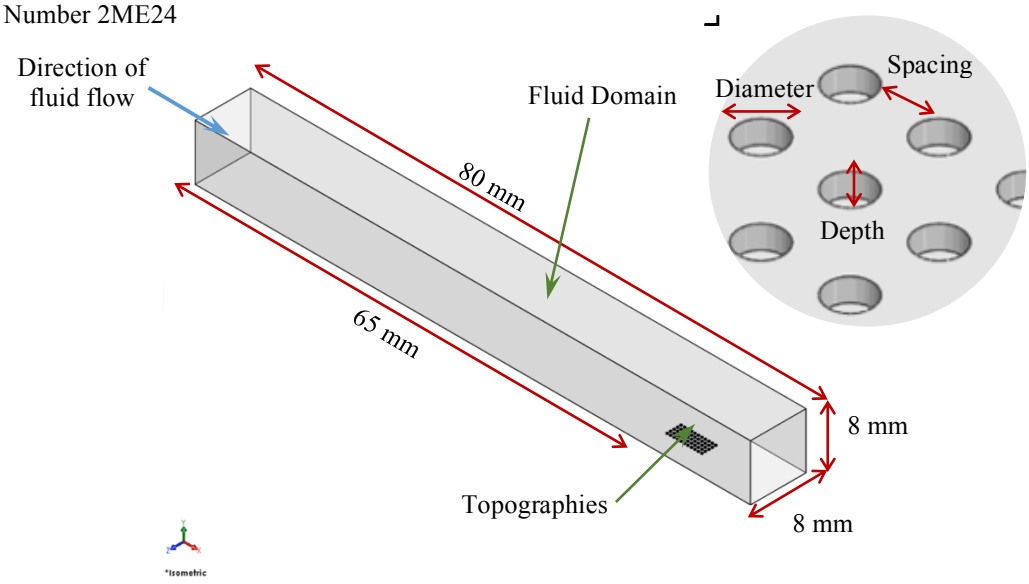


Figure 1. Dimensions of the fluid domain and the placement of the topography array in the fluid domain.

The topography consists of 55 pits, arranged in an array of 5 rows and 11 columns. The topography sizes were varied while keeping the topography's geometry constant. According to previous research conducted by [2], the effective topography sizes for antifouling ranged from 50 µm to 500 µm. Hence, the pits are circular in shape with diameter range of 125 µm to 500 µm. The dimensions of the pits' depth and space apart from each other were varied for all the six models along with the diameter. The sizes of the pits for each model is presented in Table 1 and Figure 2 illustrates the 3D models of all six topographies.

Table 1. Topographies' Sizes

Model	**1**	**2**	**3**	**4**	**5**	**6**
Diameter (µm)	250	250	250	250	125	500
Spacing (µm)	250	250	500	500	125	500
Depth (µm)	125	250	125	250	125	500

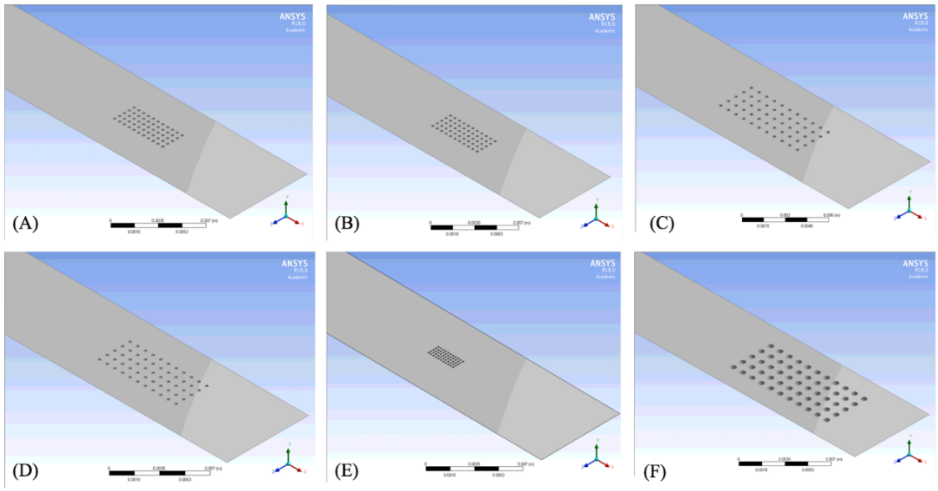


Figure 2. Topography for: (A) Model 1; (B) Model 2; (C) Model 3; (D) Model 4; (E) Model 5; (F) Model 6

2.2 Meshing Method

Mesh quality is important to ensure that the results are accurate. The model was then imported to ANSYS Workbench meshing module. Basically, the interior of the model was meshed with tetrahedral shape elements. The default mesh setting has produced finer mesh around the curvatures of the pits and larger mesh further from the pits. However, the mesh at the edges of the model, as well as the pits were improved and resized. A seven-layer inflation was applied to the walls of the model with hexahedral shape elements of 0.1 mm (Figure 3). Inflation was used for near wall refinement, especially when wall shear was focused.

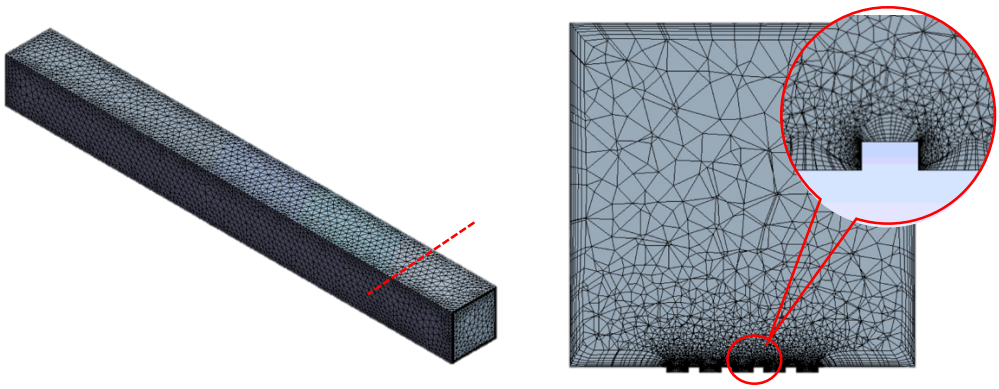


Figure 3. Inflation layers

From the convergence study (Table 2), the wall shear stress of Model 1 and 2 starts to approach stability and converges to within 5% around 0.1437 Pa and 0.2485 Pa with 2,338,194 and 2,757,990 of mesh elements. For the third and fourth model, the average wall shear converged at 0.0691 Pa and 0.0772 around 2,581,534 and 2,880,841 of mesh elements. Last, the average wall shear approach stability at 0.2422 Pa and 0.1201 Pa with 1,362,794 and 3,973,290 of mesh elements for Model 5 and Model 6.

Table 2. Optimum No. of Mesh Elements

Model	No. of Elements	Wall Shear (Pa)	Percentage Difference (%)
1	2,338,194	0.1437	2.42
2	2,757,990	0.2485	4.69
3	2,581,534	0.0682	2.52
4	2,880,841	0.0760	3.87
5	1,362,794	0.2422	4.92
6	3,973,290	0.1201	3.35

The optimum number of mesh elements is achieved when the variation in average wall shear drops below 5% (i.e., below the red line) (Figure 4). The mesh quality is considered acceptable when the minimum orthogonal quality value of mesh elements for each model was more than 0.01 and when the maximum skewness value was less than 0.9.

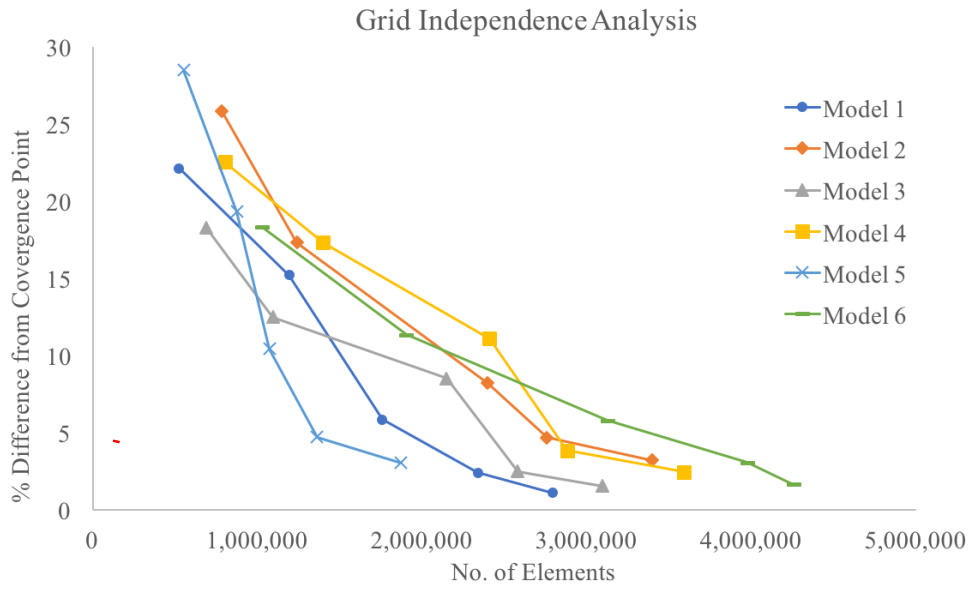


Figure 4. The mesh convergence analysis of the six topographies in this study

2.3 Numerical Setup

The CFD-software package ANSYS Fluent, version 18 was used for simulations in this study. The Navier-Stokes equations (Eqns. 1 to 3) and the continuity equation (Eqn. 4) ensured the conservation of mass and momentum. The k-ω model was selected as the turbulence model for this research because it switches from the normal wall function to a low-Reynolds number formulation.

$$\frac{\partial \rho u}{\partial t} + \nabla \cdot \rho u V = -\frac{\partial \rho}{\partial x} + \nabla \cdot (\mu \nabla u) + S_{m,x} \quad (1)$$

$$\frac{\partial \rho v}{\partial t} + \nabla \cdot \rho v V = -\frac{\partial \rho}{\partial y} + \nabla \cdot (\mu \nabla v) + S_{m,y} \quad (2)$$

$$\frac{\partial \rho w}{\partial t} + \nabla \cdot \rho w V = -\frac{\partial \rho}{\partial z} + \nabla \cdot (\mu \nabla \mathrm{w}) + S_{m,z} \quad (3)$$

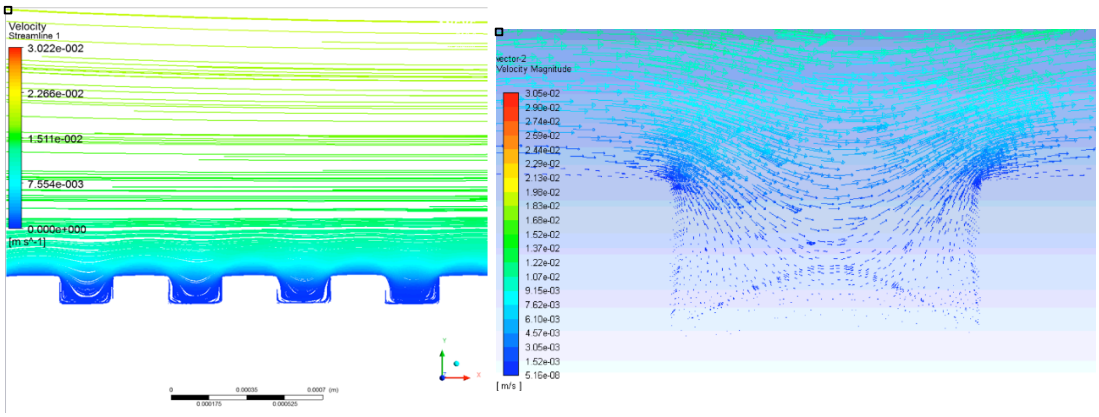
$$\frac{\partial \rho}{\partial t} + \nabla \cdot (\rho V) = 0 \quad (4)$$

where u, v, and w represented the velocity in x, y, and z directions. ρ is the fluid density, μ is the dynamic viscosity, P is the static pressure, while $S_{m,x}$, $S_{m,y}$, and $S_{m,z}$ are the source terms for x, y, and z components.

Fluid flow is Newtonian and incompressible. The density ρ, and dynamic viscosity μ, of the fluid is 1000 $kgms^{-3}$ and 0.001 $kgm^{-1}s^{-1}$ respectively. The k-ω turbulence model was employed to solve the flow, as wall shear was the main focus in this study and k-ω turbulence model is able to provide higher accuracy of wall shear results. The no-slip boundary condition was applied to the walls of the fluid domain. The mass-flow rate at the-inlet is 0.001 kgs^{-1}, while the outlet was set to outflow at x-direction.

3.0 Results and Discussions

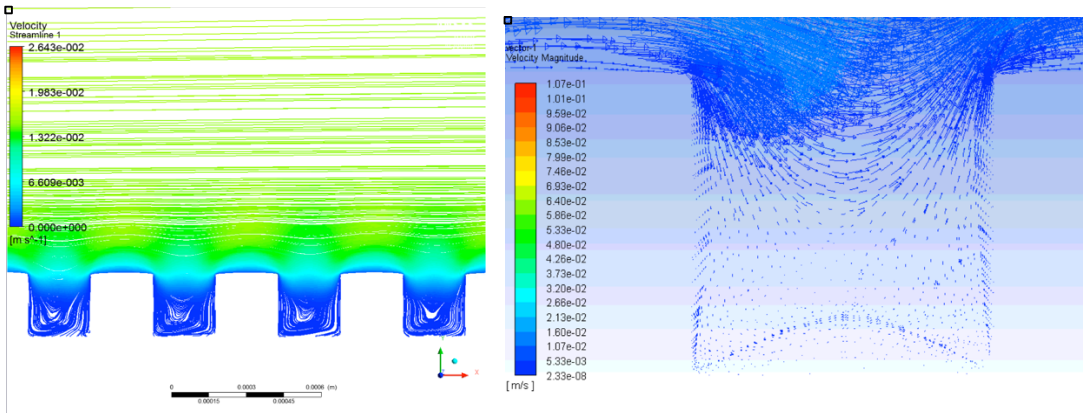
Figure 5 presents velocity streamlines and vector plots for Model 1, where fluid flows over pits with a diameter of 250 µm, spacing of 250 µm and depth of 125 µm. These streamlines (Figure 5A) showed that the fluid flowing above the pits has higher speed. The fluid right above the pits was then redirected into the pits, and brought out from the pits at a low velocity. The average velocity right above the pits was 1.649×10^{-6} ms^{-1}. From the vector profile (Figure 5B), the fluid flow into the pits at its lowest velocity and vortices were absent. The flow could possibly bring the microorganisms to settle in the pits, or the microorganisms might have brought out from the pits along the flow.



(A) (B)

Figure 5. Velocity (A) Streamlines over topographies; (B) Vector plot of flow in the pit for Model 1

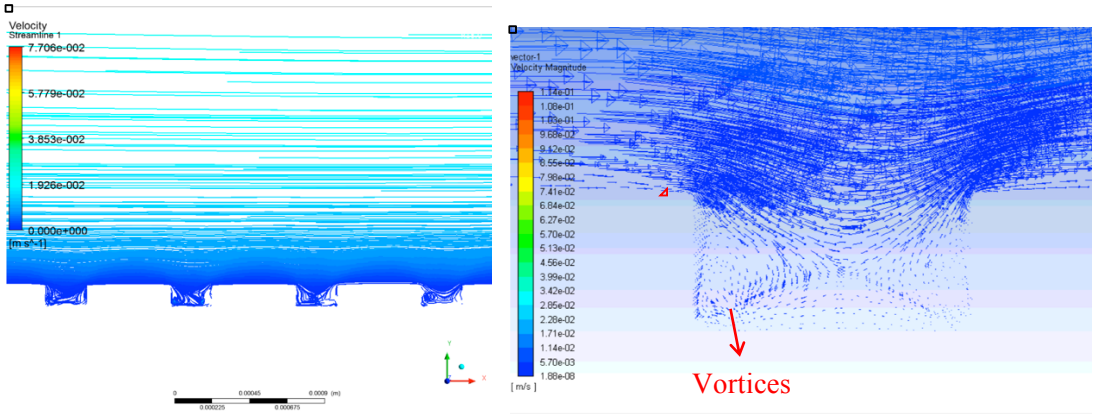
Figure 6 illustrates the velocity streamlines and vector plots for model 2, which has the diameter, distance apart and depth of 250 µm. These streamlines (Figure 6A) showed that the velocity increased as distance from the base of the topographies increases till a certain height of the model. The velocity decreased to the minimum as it entered and exit from the pits. The average velocity right above the pits was 3.241×10^{-5} ms^{-1} and was almost double compared to model 1. The vector plot (Figure 6B) has showed that vortices were not formed in the pits. This indicates that the chance for the microorganisms to be brought out from the pits is higher, since the velocity is higher.



(A) (B)

Figure 6. Velocity (A) Streamlines over topographies; (B) Vector plot of flow in the pit for Model 2

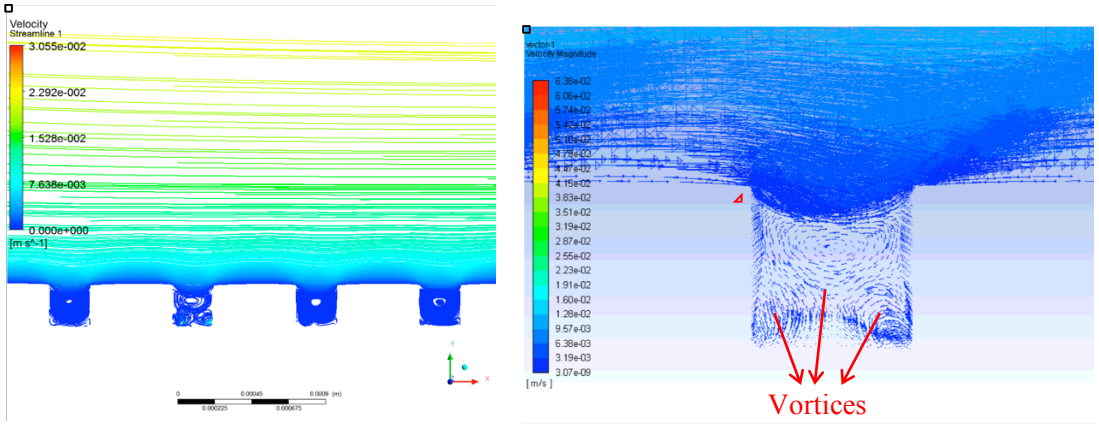
Similarly, velocity streamlines and vector plot for Model 3 were showed in Figure 7. The pits were 250 µm in diameter, 500 µm in spacing and 125 µm in depth. The average wall shear was found to be 5.216×10^{-7} ms^{-1}. Figure 7A showed the velocity was small around the topographies and vortices were formed in at the bottom of the pits. The vortices were rotating in clockwise direction in the pits, as shown in Figure 7B.



(A) (B)

Figure 7. Velocity (A) Streamlines over topographies; (B) Vector plot of flow in the pit for Model 3

For Model 4, the velocity streamline and vector plot was shown in Figure 8. The pits in model 4 were 250 µm in diameter, 500 µm distance apart and 250 µm in depth. The average wall shear would be 5.886×10^{-7} ms^{-1}. The velocity around the pits were slightly higher than model 3 and several vortices were formed in the pits, as shown in Figure 8A. The vector plot showed that the vortices were rotating in clockwise direction (Figure 8B). Since the flow velocity is low and circulating, there was a chance for the microorganisms to be trapped and settle down in the pits.

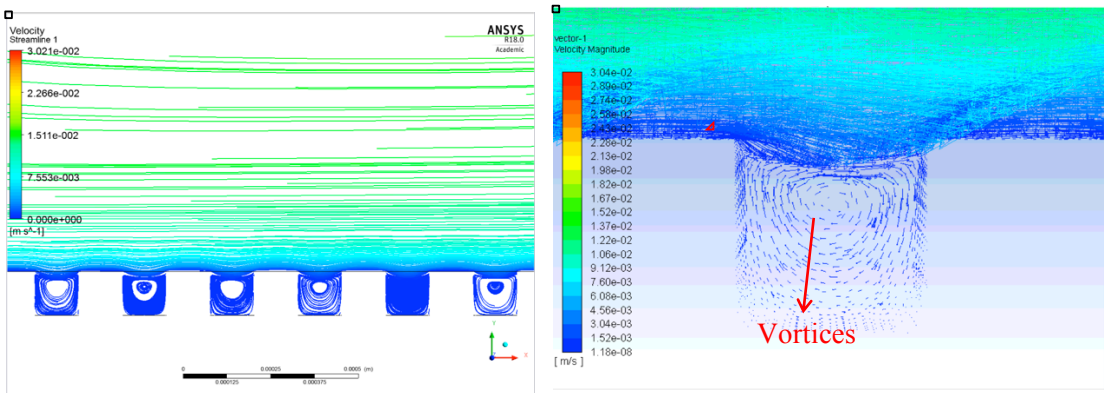


(A) (B)

Figure 8. Velocity (A) Streamlines over topographies; (B) Vector plot of flow in the pit for Model 4

For Model 5, the pits are in uniform dimensions, where the diameter, distance apart and the depth are 125 µm. The average velocity on the topography is 4.483×10^{-5} ms^{-1}, which is almost the same with model 2. Similar flow pattern as previous model was observed in Figure 9A. The fluid flows into the pits at a low velocity and exits also

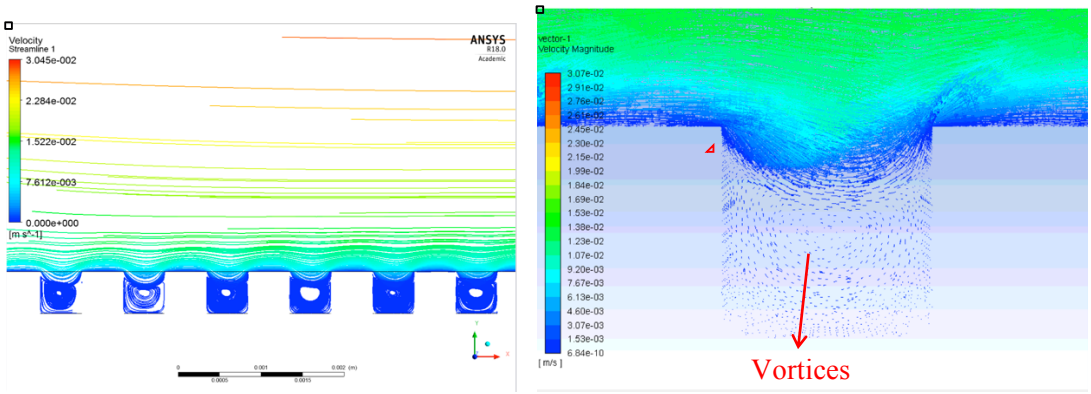
at a low velocity. The flow velocity increases when it is approaching to the central of the flow. Figure 9B showed that there are vortices formed in the pits and it is rotating in a clockwise direction.



(A) (B)

Figure 9. Velocity (A) Streamlines over topographies; (B) Vector plot of flow in the pit for Model 5

Figure 10 showed another model with topographies of uniform dimensions in 500 µm. The average velocity is 4.067×10^{-6} ms^{-1}, which is significantly lower as compared to model 2 and model 5. The fluid enters and exits the pits at a low velocity. Streamlines indicate that fluid flow above pits are distributed uniformly with velocity increasing as distance from the base of the topography increases (Figure 10A). Vortices are present in the pits and they rotate in a clockwise direction (Figure 10B).



(A) (B)

Figure 10. Velocity (A) Streamlines over topographies; (B) Vector plot of flow in the pit for Model 6

Streamlines and vector plots of velocity show that vortices are formed in the pits for model 3, 4, 5 and 6. In the past, Friedmann *et al.* 2010 has conducted a numerical study that investigated flow over riblets and also observed that vortices formed between the riblets. When fluid passed through the riblets, some fluid is redirected to flow into the gaps between the riblets. The change in direction of flow has significantly reduced fluid velocity in the area. Friedmann explained that the fluid is translating at high velocities around the peaks of riblets and slips over fluid in between the riblets. The fluid in between the riblets is then forced to rotate and results in the formation of vortices.

In this study, the formation of vortices in the pits is slightly similar to Friedmann's study. When the flow passes through the pits, some fluid is redirected to flow into the pits. This sudden change in flow direction interrupts and causes drop in velocity significantly. Difference in velocity between the fluid layer caused slips to occur. Thus, vortices were formed when the slips forced the fluid in the pits to rotate [11]. Figure 11 illustrates the locations of where the slip occurred.

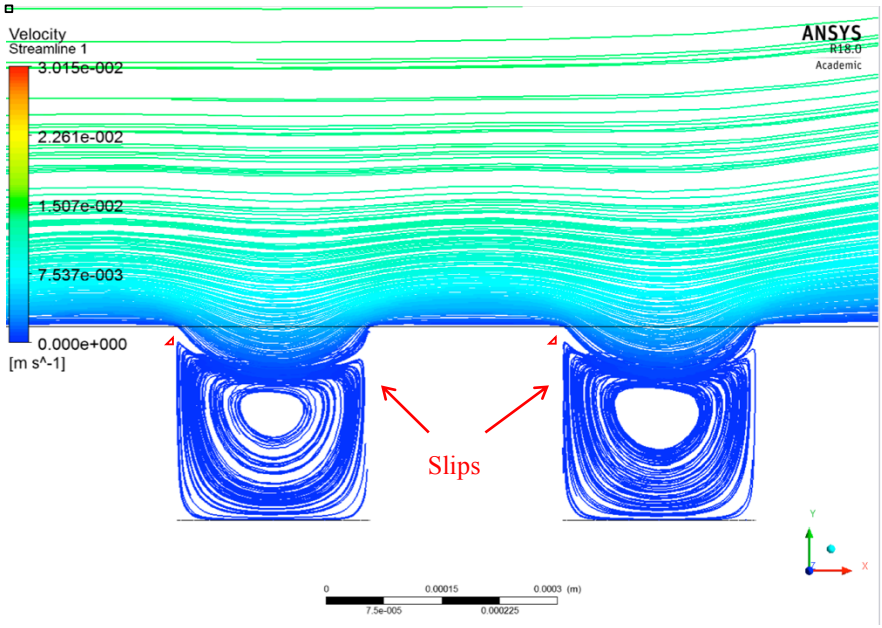


Figure 11. The location of slips occurred

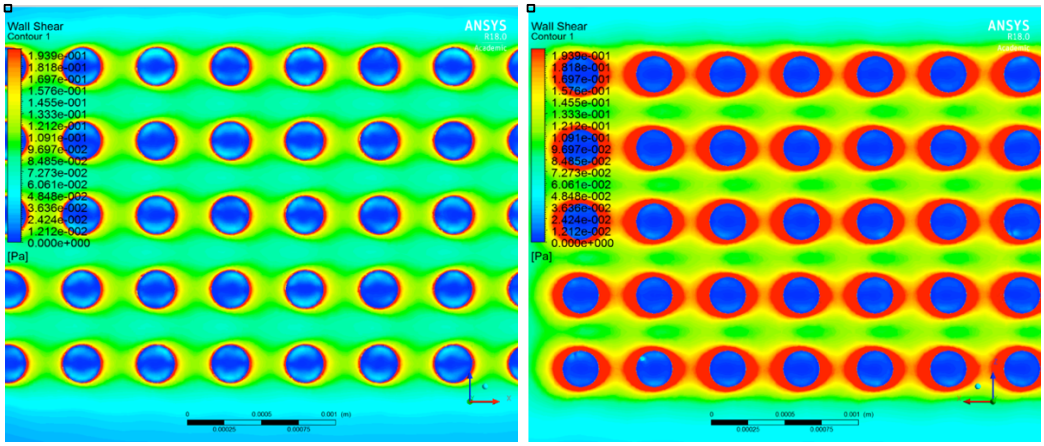
Slips and vortices could have contributed to the formation and increase of biofouling by carrying the biofouling materials into the pits. Since the vortices are rotating at a low velocity, it could be conducive for the collected biofouling materials and microorganisms to settle and accumulate with time in the pits. The enclosed area of the pits could have trapped some portion of fluid in the pits along with the microorganisms and biofouling materials and sheltered them within the pits. However, despite the velocity is very low, it is still possible for the microorganisms to be brought out along with the flow that exits the pits. Hence, future designs of the antifouling topographies should try to minimize the formation of vortices to increase the performance of antifouling.

Studies determined that microorganisms tend to explore substrates which are suitable for settlement and attachment. For example, algae spores adhere temporarily on a surface and spins in place to determine the strength of adhesion for permanent attachment [1,12]. Thus, reducing opportunities for microorganisms to establish initial contact with surfaces should discourage biofouling.

The antifouling potential was evaluated by analyzing the wall shear induced by the flow onto the topography and velocity of fluid flow over the topography. Shear stress in the fluid layer next to the wall of the model is measured by wall shear stress. This is important to determine the likelihood for the microorganisms to be detached from the substrates. Based on the study by Halder *et al.* 2013 [6], wall shear stress is a parameter that can be analysed to gauge the antifouling potential of the surface.

Velocity streamlines and vector profiles illustrate the direction and magnitude of the fluid flow over the topographies.

Models 1 and 2 consist of arrays of pits with a fixed in space apart (i.e., 250 µm) but varied in depth. Figure 12 presents the pattern distribution of wall shear stress for the two models. For both models, the shear stresses were highly concentrated around the edges of the pits, while the shear stresses were less concentrated at the bottom of pits. This means that the edges of the pits experienced higher shear stress compared to the bottom of the pits. Model 2 with pits of 250 µm in depth induced higher wall shear compared to model 1 with pits of 125 µm in depth.



(A) (B)

Figure 12. Wall Shear Contour Plot for (A) Model 1 (depth = 125 µm); (B) Model 2 (depth = 250 µm)

Since pits in model 2 have the higher shear stress, it is likely that these pits would have higher antifouling potential, as microorganisms have a higher chance to be sheared off from the substrates. This result can be corroborated by findings from a separate study which investigated micro-sized prisms by applying the CFD approach as well [3]. Lee *et al.* 2013 found that the peaks of prisms that were less fouled in lab experiments also experienced greater shear stresses in CFD simulations. Therefore, it can be surmised that the edges of the pits in this study will be areas with better antifouling properties as well.

Figure 13 shows a comparison of wall shear over the pits of different depths with spacing of 125 µm. From the graph, the wall shear of model 2 was highly fluctuating at the edge of the pits, compared to the wall shear of model 1. The average wall shear of model 1 and model 2 were 0.1437 Pa and 0.2485 Pa. These fluctuating shear stresses could help in repelling organisms and biofouling material from settling on the surface. The results in Figure 13 indicated that Topographies in model 2 exhibits better antifouling potential in comparison to the topographies on model 1.

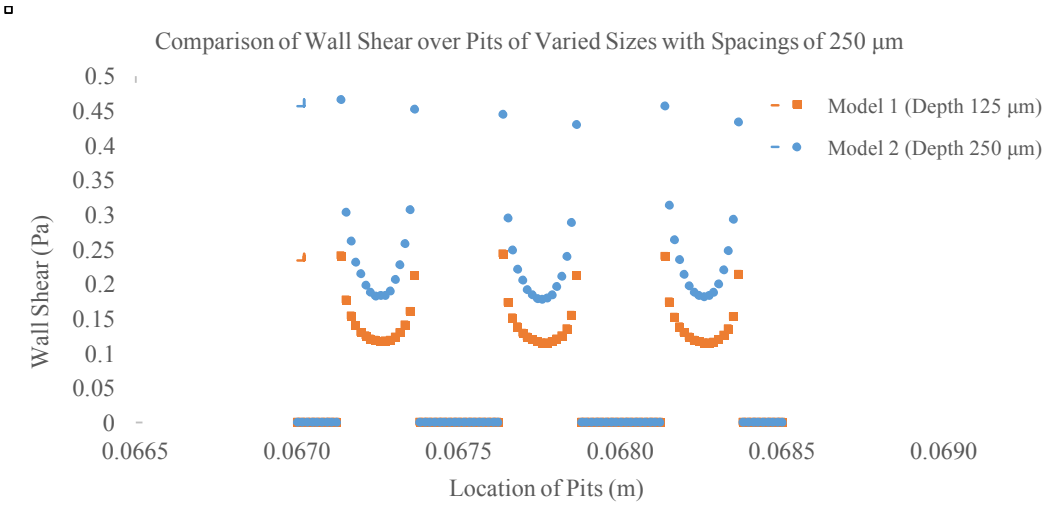
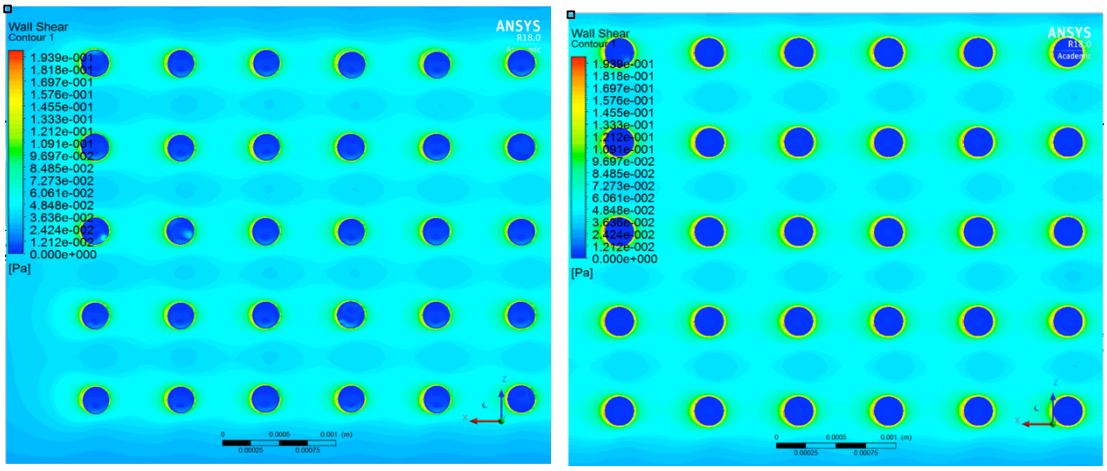


Figure 13. Wall shear over pits with varied depths of 125 µm (Model 1) and 250 µm (Model 2)

Model 3 and model 4 are micro-pits that with fixed spacings between pits of 500 µm but varied in depth of 125 µm and 250 µm. Figure 14 illustrates the wall shear distribution for the two models. Same observation was found where the edges of the pits have experienced higher shear stress compared to the bottom of the pits. Model 4 with deeper pits has induced wall shear which is slightly higher compared to model 3. However, the difference is insignificant compared to the previous two models. Despite the difference in wall shear was small, the pits still possessed antifouling properties, the microorganisms were still possibly to be sheared off from the substrates but with reduced efficacy.



(A) (B)

Figure 14. Wall Shear Contour Plot for (A) Model 3 (depth = 125 µm); (B) Model 4 (depth = 250 µm)

From Figure 15, the wall shear of the two models fluctuated around the edges of the pits. The average wall shear for model 3 and model 4 were 0.0682 Pa and 0.076 Pa. The wall shear produced by model 4 was slightly higher than model 3 and were nearly similar. This meant that varying the pits in terms of depth at the spacing of 125 µm is not encouraged. Hence, the antifouling performance for model 3 and model 4 were less effective compared to model 1 and model 2.

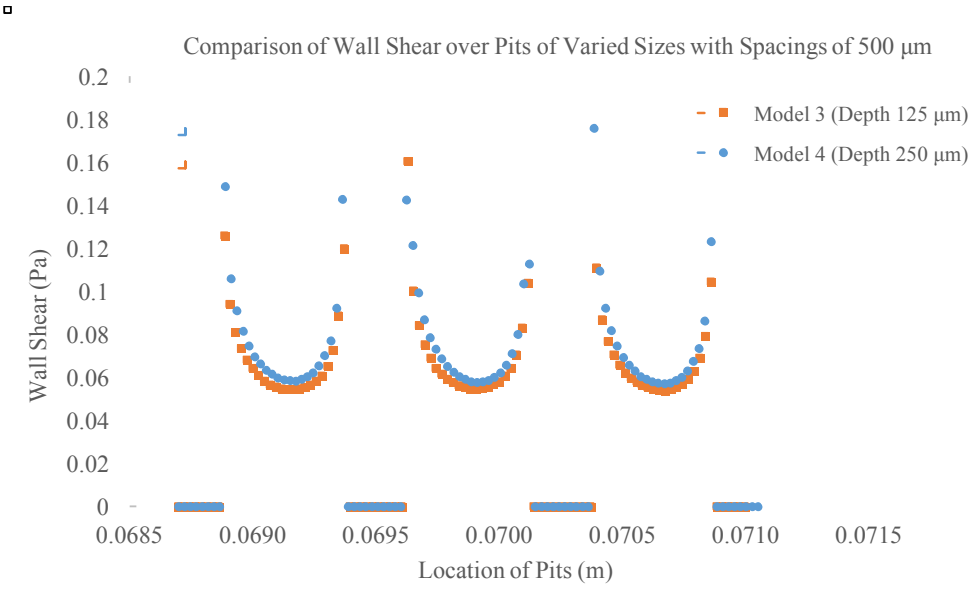


Figure 15. Wall shear over pits with varied depths of 125 µm (Model 3) and 250 µm (Model 4)

By comparing space between the pits, the pits for model 1 and model 3 (Figure 16) had the same depth of 125 µm but varied in space between the individual pits, 250 µm and 500 µm. It showed high difference between the wall shear induced by the two models. Pits arranged with lower spacing has induced higher wall shear than the pits with larger spacing. The difference in wall shear was significant. This results can be validated with Halder's studies which investigated varied sizes of microwells with the application of CFD as well [6]. Halder *et al.* 2013 found that microwells arranged with smaller spacing developed higher shear stress at the edges. Thus, it can be presumed that topography arranged with smaller spacing will promote better antifouling properties.

Same goes to the model 2 and model 4, which were fixed with depth of 250 µm and varied in spacing of 250 µm and 500 µm. The difference in wall shear induced by the two models were high. The antifouling potential of model 3 and model 4 were less effective compared to model 1 and model 2. Hence, the physical aspects such as the spacing (distance apart from the pits) were more effective in influencing the antifouling performance compared to the depths of the pits.

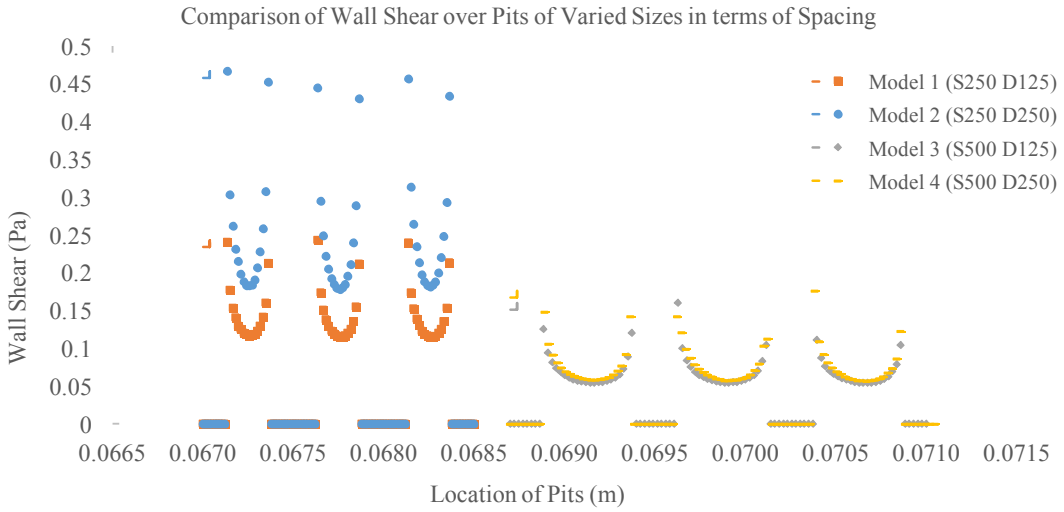
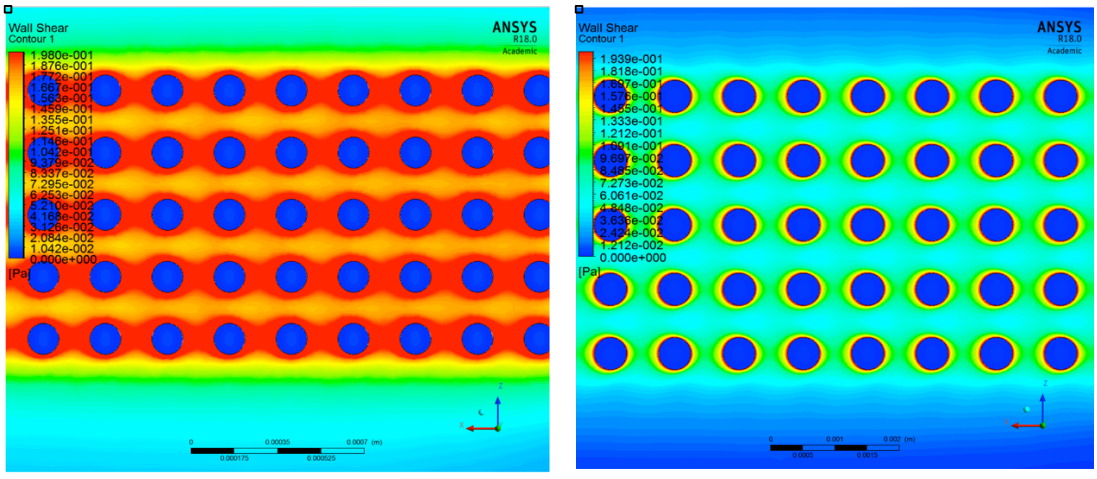


Figure 16. Wall Shear over the pits of varied spacing and depth

Model 2, 5 and 6 are micro-pits that with uniform sizes (same in diameter, distance apart and depth) in 125, 250 and 500 µm. Figure 17 illustrates the wall shear contour plot for model 5 and 6. Model 2 (Figure 17B) and model 5 (Figure 17A) are having almost the similar wall shear distribution. The wall shear stresses are highly concentrated around the edges of the pits compared to the bottom of pits. For model 6, pits with dimension of 500 µm induced lower shear stress around the edges of pits compared to model 2 and 5 with 125 and 250 µm pits. This shows that microorganisms are more unlikely to settle on pits with 125 and 250 µm compared to 500 µm, as chances to be sheared off from the substrates are higher.



(A) (B)

Figure 17. Wall Shear Contour Plot for (A) Model 5 (125 µm in dimension); (B) Model 6 (500 µm in dimension)

Figure 18 shows the wall shear distribution graph for the 125, 250 and 500 µm pits. The average wall shear for 125 µm, 250 µm and 500 µm are 0.2422, 0.2485 and 0.1201 Pa. Among the three dimensions, pits with measuring at 250 µm experienced the greatest wall shear. The wall shear stresses around 250 µm pits are highly fluctuating around the edges compared to 125 and 500 µm pits. This results shows that

pits with 250 µm in dimension are likely to exhibit the best antifouling properties in comparison to pits that are 125 and 500 µm. Simulation results also indicated that pits with 500 µm experienced the lowest shear stresses in comparison to the pits that were 125 and 250 µm in size. This indicates that 500 µm pits are likely to have the poorest antifouling properties among the 3 pit sizes.

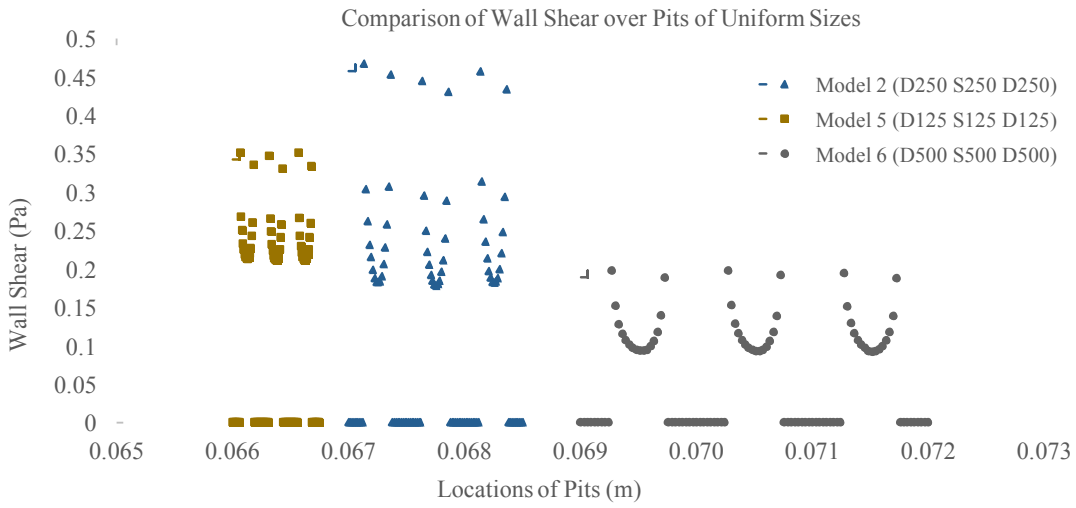


Figure 18. Wall shear distribution for pits with uniform sizes

These simulation results are complied with the studies which field tests or lab experiments were conducted. Aldred *et al.* (2010) discovered that topographies that were approximately 250 µm were less fouled by microorganisms in comparison to topographies that were 500 µm in size. Carl *et al.* 2012 also determined that topographies that were 400 µm (i.e., close in size to the 500 µm pits in this study) were the most fouled by the young of mussel clams. The same study (i.e., Carl *et al.* 2012) also determined that topographies that were exactly 250 µm were the least fouled among a range of topographies that ranged from 40 µm to 1000 µm. Results from these public studies therefore validate the simulation results that were obtained in this study [13-16].

As for pits with mixed dimensions (different diameter, distance apart and depth), any pits configuration that was 500 µm in size (Model 3, 4 and 6) resulted in lower wall shear stresses in comparison to pit configurations that did not have dimensions of 500 µm. This indicates that future designs of topographies should not be 500 µm in dimension. Simulation results also shows that pits that are uniform in size results in higher wall shear as compared to pits with mixed dimensions. In Figure 19, model 5 exhibits the highest fluctuation in wall shear. Likewise, in Figure 20 and 21, model 2 and 6 induced highest wall shear in comparison to others. This results show that future designs of topographies should have dimensions (i.e., length, width, depth, diameter, height, etc.) that are uniform.

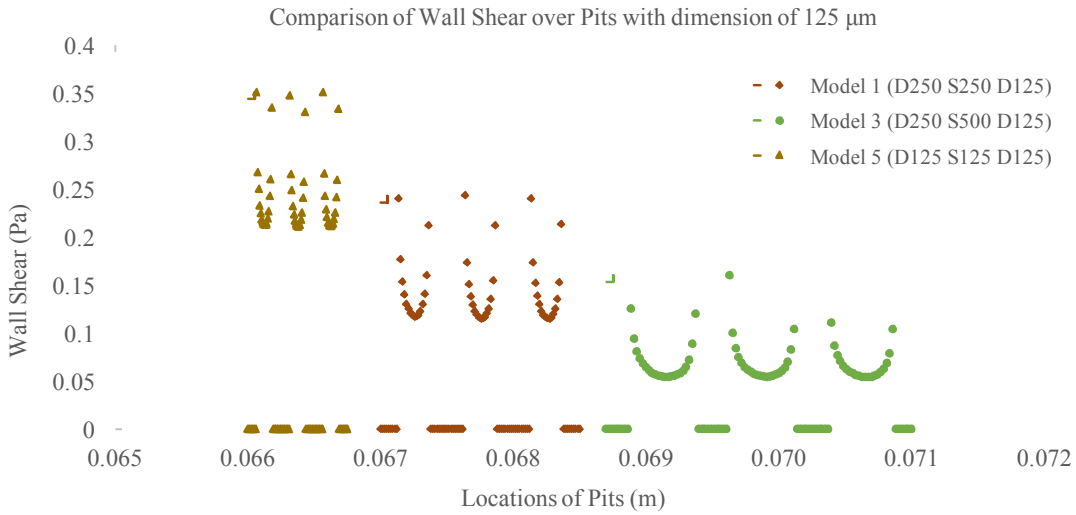


Figure 19. Wall shear distribution for pits with dimension of 125 µm

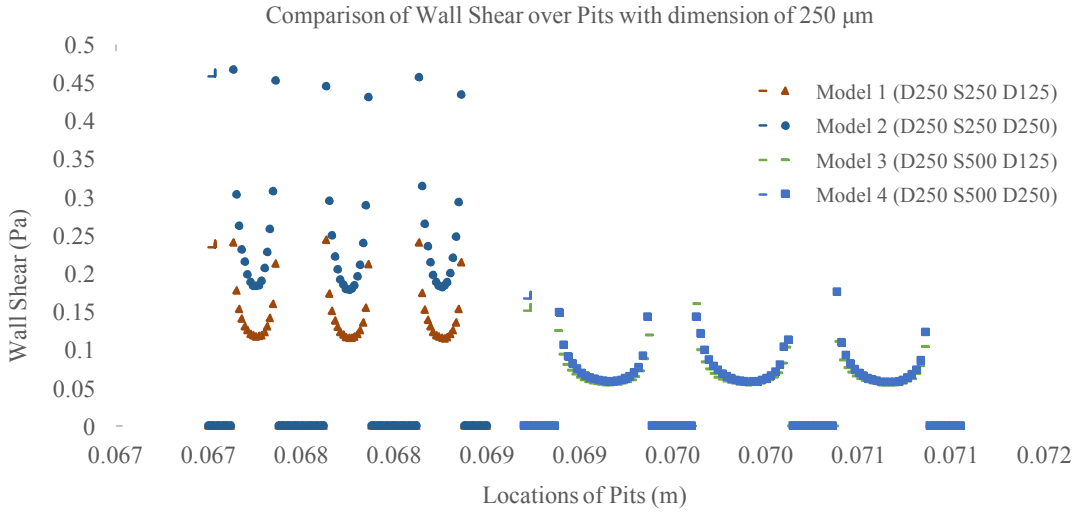


Figure 20. Wall shear distribution for pits with dimension of 250 µm

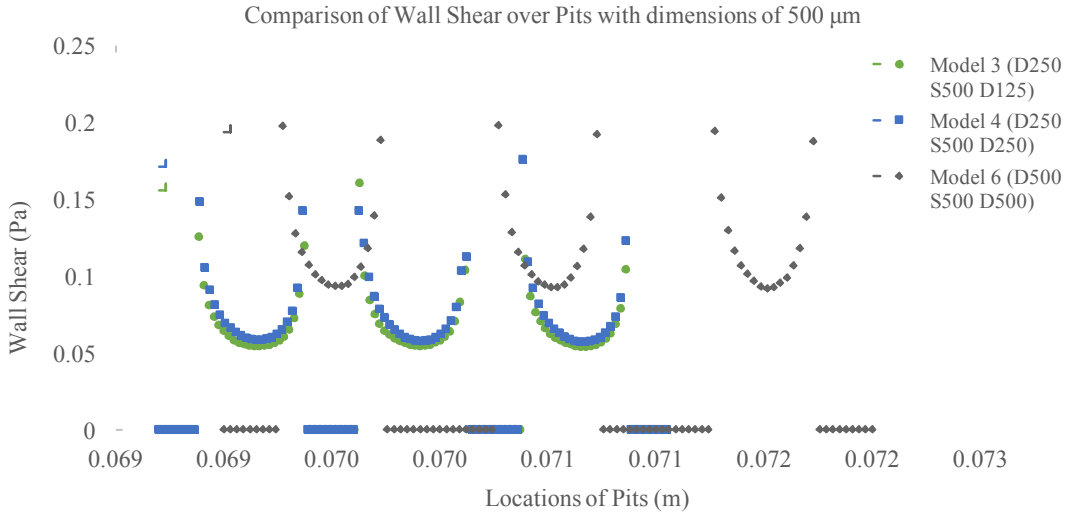


Figure 21. Wall shear distribution for pits with dimension of 500 µm

4.0 Conclusions

This research aimed to identify a suitable topography's geometry for antifouling potential through literature review, numerically identify the optimum size of topography for the best antifouling properties and identify the flow characteristic induced by the surface topography that contribute to the mitigation of biofouling. The numerical model was solved using the ANSYS Fluent with k-ω model. Simulations showed that the presence of topographies induced hydrodynamic variations to the flow with shear stresses fluctuating along the peripheral of pits. The shear stresses at the edge of the pits were higher compared to the bottom of the pits. The possibility for the microorganisms to be sheared off at the edge of the pits was higher, which highlights the possibility that the edges of pits have good fouling resistance. However, the microorganisms could settle down in the pits, since the velocity at the bottom of the pits was low. The possibility would increase with the presence of vortices. The criteria for topographies with promising antifouling properties would be topographies with geometries that are able to produce high hydrodynamic changes in the fluids in the topographies surroundings.

The physical aspects of antifouling topographies such as size, geometry, height, spacing and etc. have been emphasized in many studies. This study shows that topographies' sizes (distance apart and depth/height) influence the fouling resistance of the surface. By comparing within pits with diameter of 250 μm, Model 2 produced the highest wall shear and the lowest was Model 3. Physical aspect such as distance apart was effective in influencing the fouling resistance of the topographies. Besides, for pits with uniform dimensions, 125 and 250 μm have induced higher wall shear compared to 500 μm pits. This mean that pits with dimensions 500 μm is less effective in the mitigation of biofouling. Furthermore, pits with uniform dimensions have a greater impact at foul resisting in comparison with pits with mixed dimensions. However, different sizes of pits exhibited different antifouling potential.

The numerical method employed in this study was adequate in understanding flow characteristics over the patterned surfaces. This also proved that numerical analysis is a good approach in investigating the flow patterns around the topographies. Aside from this studies, there are still lots of sizes and geometries that possess a degree of antifouling potential. Hence, further studies on the topographies should be carried out, and include numerical studies to understand the flow patterns and the possible effects of such flow effects on the microorganisms' settlement.

References

[1] Rosenhahn, A., Sendra, G.H. (2012). Surface sensing and settlement strategies of marine biofouling organisma. *Biointerphases,7*(1-4), 1-13.

[2] Myan, F.W.Y., Walker, J., Paramor, O. (2013). The interaction of marine fouling organisms with topography of varied scale and geometry. *Biointerphases, 8*(1), 1-13.

[3] Lee, Y.K., Won, Y.J., Yoo, J.H., Ahn, K.H., Lee, C.H. (2013). Flow analysis and fouling on the patterned membrane surface. *Journal of Membrane Science, 427*, 320-325.

[4] Salta, M., Wharton, J.A., Stoodley, P., Dennington, S.P., Goodes, L.R.,

Werwinski, S., Mart, U., Wood, R.J.K., Stokes, K.R. (2010). Designing biomimetic antifouling surfaces. *Philosophical transactions. Series A, Mathematical, physical, and engineering sciences*, *368*, 4729-4754.

[5] Singh, A.V., Rahman, A., Kumar, N.V.G.S., Aditi, A.S., Galluzzi, M., Bovio, S.B., Montani, E., Parazzoli, D. (2011). Bio-inspired approaches to design smart fabrics. *Materials and Design, 36*, 829–839.

[6] Halder, P., Nasabi, M., Lopez, F.J.T., Jayasuriya, N., Bhattacharya, S., Deighton, M., Mitchell, A., Bhuiyan, M.A. (2013). A novel approach to determine the efficacy of patterned surfaces for biofouling control in relation to its microfluidic environment. *Biofouling*, *29*(6), 697-713.

[7] Petronis, S., Berntsson, K., Gold, J., Gatenholm, P. (2000). Design and microstructuring of PDMS surfaces for improved marine biofouling resistance. *Journal of biomaterials science. Polymer edition*, *11*(10), 1051–72.

[8] Carman, M.L., Estes, T.G., Feinberg, A.W., Schumacher, J.F., Wilkerson, W., Wilson, L.H., Callow, M.E., Callow, J.A., Brennan, A.B. (2006). Engineered antifouling microtopographies - correlating wettability with cell attachment. *Biofouling*, *22*(1–2), 11–21.

[9] Hoipkemeier-Wilson, L., Schumacher, J.F., Carman, M.L., Gibson, A.L., Feinberg, A.W., Callow, M.E., Finlay, J.A., Callow, J.A. (2004). Antifouling potential of lubricious, micro-engineered, PDMS elastomers against zoospores of the green fouling alga Ulva (Enteromorpha). *Biofouling*, *20*(1), 53–63.

[10] Mortensen, N.A., Okkels, F., Bruus, H. (2005). Reexamination of Hagen-Poiseuille flow: Shape dependence of the hydraulic resistance in microchannels. *Physical Review E - Statistical, Nonlinear, and Soft Matter Physics*, *71*(5), 1–4.

[11] Friedmann, E., Portl, J., Richter, T. (2010). A study of shark skin and its drag reducing mechanism. In Rannacher R., Sequeira, A. (Ed.), *Advances in mathematical fluid mechanics* (pp. 271-285). Berlin, Heidelberg: Springer-Verlag.

[12] Cao, X., Pettitt, M. E., Wode, F., Arpa Sancet, M. P., Fu, J., Ji, J., Callow, M. E., Callow, J. A., Rosenhahn, A., Grunze, M. (2010). Interaction of Zoospores of the Green Alga Ulva with Bioinspired Micro- and Nanostructured Surfaces Prepared by Polyelectrolyte Layer-by-Layer Self-Assembly. *Advanced Functional Materials, 20,* 1984-1993.

[13] Aldred, N., Scardino, A., Cavaco, A., de Nys, R., Clare, A.S. (2010). Attachment strength is a key factor in the selection of surfaces by barnacle cyprids (Balanus amphitrite) during settlement. *Biofouling, 26*, 287–299.

[14] Bers, a.V., Wahl, M. (2004). The influence of natural surface microtopographies on fouling. *Biofouling, 20*(1), 43-51.

[15] Carl, C., Poole, A.J., Vucko, M.J., Whalan, S. (2012). Enhancing the efficacy of fouling-release coatings against fouling by Mytilus galloprovincialis using nanofillers. *Biofouling, 28*(10), 1077-1091.

[16] Carl, C., Poole, A.J., Vucko, M.J., Whalan, S. (2012). Enhancing the settlement and attachment strength of pediveligers of Mytilus galloprovincialis bychanging surface wettability and microtopography. *Biofouling, 28*(2), 175-186.

eureca 2017 – Conference Paper
Paper Number 2ME25

A Numerical Study on Examining the Effects of Flooding on Train Tracks

Sathveer Roopah*, A/ P. Ir. Dr. Satesh Namasivayam.
Department of Mechanical Engineering, School of Engineering, Taylor's University, Malaysia.

* *sathveer.roopah@sd.taylors.edu.my*

Abstract
This study aims to evaluate the effects of flood on train tracks. Since the very early ages, train transport system has been one of the most important mode of transport and still today it is used widely around the world to commute or transport goods and materials. This study aims to evaluate the effects of the flood around the track structure and as well as the train boggy in an open land area. Not many numerical studies have been carried out on this type of situation as the computational knowledge and power required are immensely huge. Thus, by using computational fluid dynamics tools, 3D models will be created and flooding situations will be re-produced on a scaled level. A review of current practices carried out in the industry have been discussed in previous reports and solutions such as structural and non-structural have been identified by the industry. Most of the structural solutions found have not been validated as hence non-structural methods are the most common used solutions in the event of flood. This study will focus on the use of Navier-strokes equations used in the CFD tool to calculate for the hydro pressures and fluid velocity and fluid viscosity round the track. the tools use the RANS method of fluent to perform the calculations based on the conservations of momentum along with the turbulence methods. Data gathered for this study will be evaluated and intends to review the current operations of trains on inundated tracks. Boundary conditions to be applied are varied to get better view of the fluid characteristics around the structures. 2d models have also been created to analyze fluid inside the track ballast.

Keywords: Railway track, Ballast, Sub-ballast, Hydro-effects, Contamination Void Index, Fouling, Drainage capacity, Computational Fluid Dynamics.

1 INTRODUCTION

During the period of extreme rainfall, it is very common for railways tracks to inundate and be exposed to dangerous flooding. Structural solutions methods are being less trusted by the population and the commuters. Thus, this study will prove the effects of flooding on the structures, then using the results, the structural solutions proposed can be evaluated for its intended purpose and base whether it is acceptable for the current problems. Under severe flood conditions all traffic should come to a halt, except for some critical situations where the train might be stuck on track and even worse would be a train travelling on a damaged track. the train operator barely sees the conditions of the rails ahead and severe damages can be caused if the flooding situation is not fully understood.

As for the ballast part, water infiltrations inside the ballast and sub-ballast can cause detrimental damages to the track. water infiltration inside the track is very common and hence the track needs to be able to discharge the water in a certain given amount of time. This is known as track drainage capacity or hydraulic conductivity of the track. The effect of minimum track drainage capacity occurs when the track is contaminated with dust particles trapped inside the void areas between the granules inside the ballast and hence blocking all passages for proper water evacuation.

Hydro-dynamic pressure, fluid viscosity and velocity were gathered through an extensive set of Computational Fluid Dynamics(CFD) calculations and information regarding the forces of water due to the wheels were also obtained through a turbulence analysis of the CAD model scaled down to 1/10 to make sure the calculation process can be quick with keeping an efficient meshing setup for the study. These CFD studies have been based on the fact that the water impact due to the flood vary from different train designs. The models of trains used in the simulations are the dual axis boggy with one wagon attached. The level of the flood was varied as well to study the effect of the fluid around the boggy/bogeys., with notable 3m/s and 5m/s which are normal velocity for flood..

Previous studies have showed the effect of structures around the track can damage track parts. A study by Pams Cappoccioni et al, revealed that the drainage structure around the track can cause turbulent water hence in turn affecting the track. The purpose of the study was to replicate flood situations where the water is not opaque and the water flow can be properly visualized with its adverse effects on the track. Their lab experiment was set on a small-scale model to verify the data of hydraulic conductivity.

A study run by the university of Wollongong has showed that the major cause for track deterioration was mainly caused by the fouling which occurred in the ballast. The track drainage capacity or the hydraulic conductivity of the track decreases dramatically as the level of fouling increases. This proved to be a good tool for analysis as the fouling variable has a direct relation to the role of track drainage. The study also made use of the Void Contamination Index which is the ratio of unclean voids volumes over the clean void volume in the ballast.

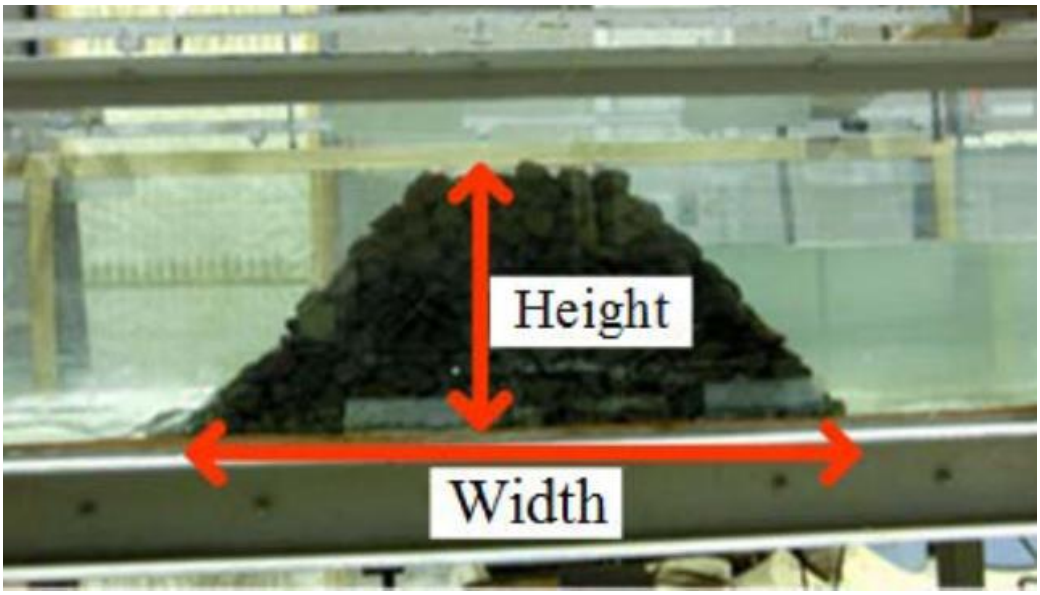


Figure 1. Water tank model. [1]

Indraratna et al carried-out studies on a flood specimen of ballast which was submerged in water for a period of 24 hours and observed gradual deformation occurring in the ballast particles. The study then showed a general displacement increment of the track as the water flow increased over time as chipping of the granules occurred during the process.

2 RESEARCH METHODOLOGY

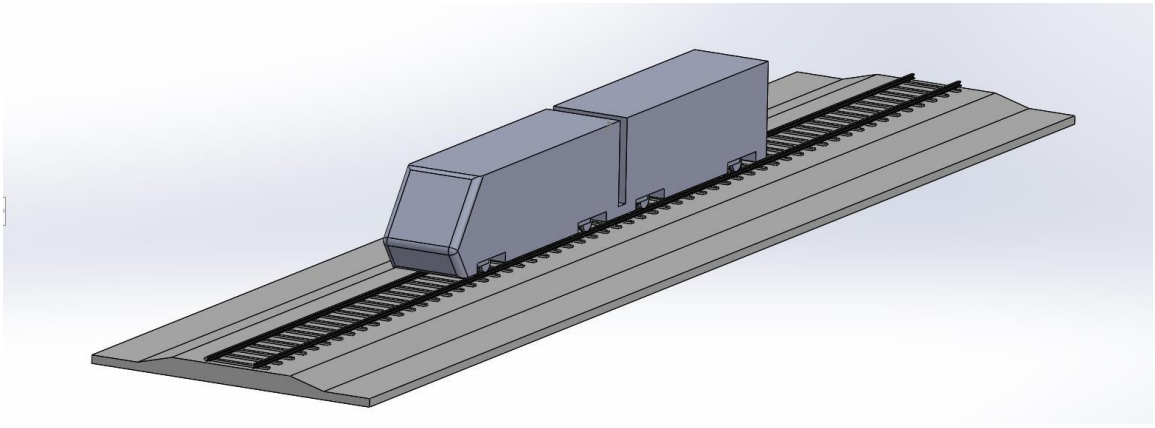
This section will review the steps and procedure in making a Fluent study. The processes are in the following order,

- Design of geometry based on track dimensions.
- Simplification of the geometry.
- Apply fluid domains such as inlet outlets and interiors.
- Transfer the geometry to the fluent solver.
- Apply boundary conditions
- Apply solving methods
- Calculations
- Results rendering.

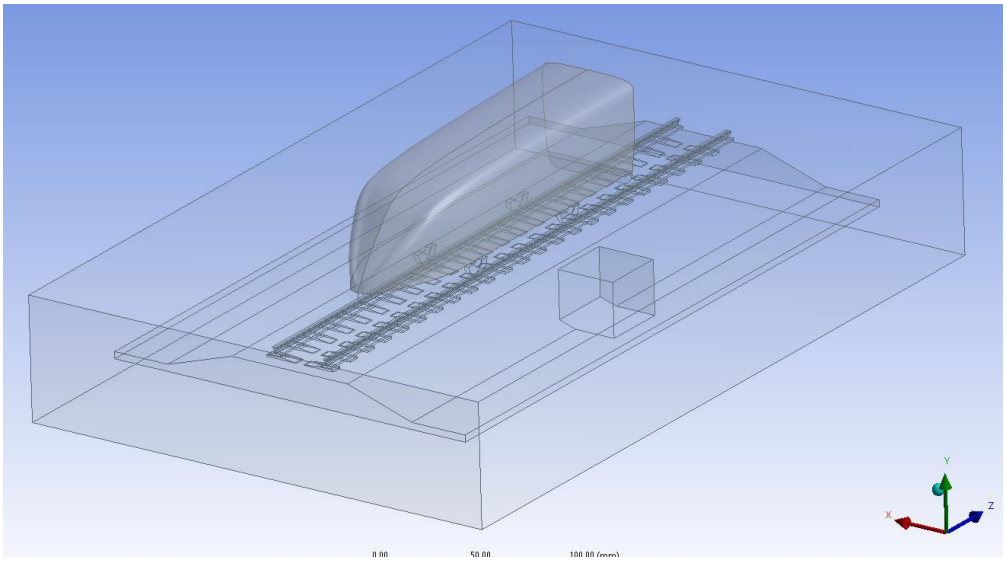
2.1 Geometry

The train geometries used in the research was the class 43 locomotive and Mk 3 passenger coach. These models were chosen based on the largest vehicle nose and underbody shapes. The trains have been modelled with one single bogie with addition of more wagons at the back to get more data sets. The model has also been scaled down to 1/10 to make maximum use of computational power available. At model scale the total length of the train was set around 10m and after scaling down, the geometry has a maximum length of 0.1m. however due to complexity of the shape and limitation of computational power, the model had to be simplified to make better use of mesh to be

generated. The model was created using Solidworks as shown in the pictures below.



Picture 1. Final model for train bogy and track. case D.

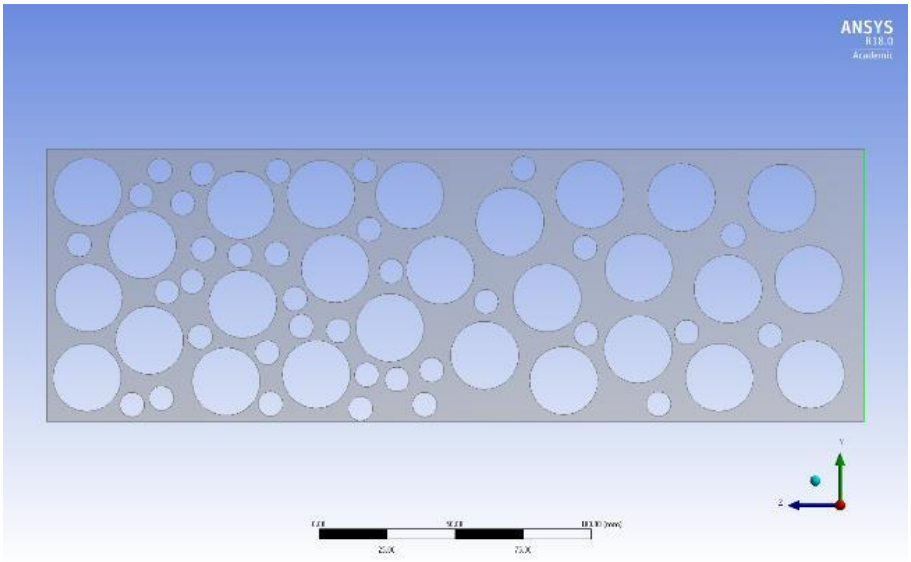


Picture 2. Fluid domain fort the 3d case E.

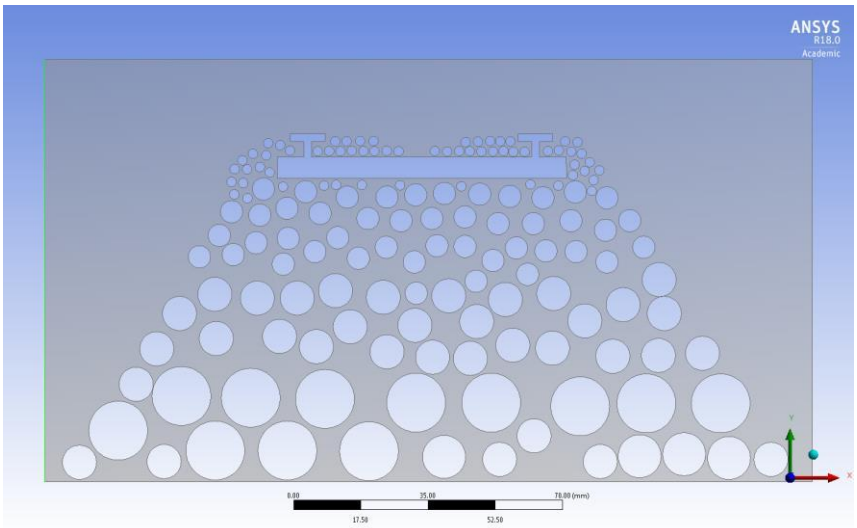
The wheel has a frontal area of 0.02 m^2. The dimensions of other components are neglected as the study focuses more on the wheel to track effect and the turbulence model based upon the rules of operation. As for the fluid domain, Boolean methods of subtraction is used to erase the solid track from the fluid domain created.

For the 2D simulations, the geometry was designed on a surface plane. Random ballast particles have been placed randomly around the fluid domain. The granules sizing and track dimensions are based upon the local data in Malaysia. The ballast in the first model concentrate on the microscopic area of the ballast with part contaminated and part non-contaminate. The second geometry represents a ballast on the side partition and the simulations will run on the hydraulic conductivity of the track.

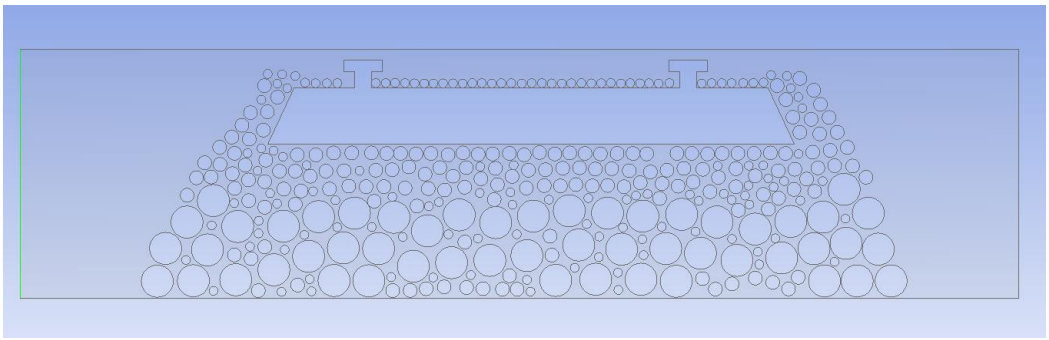
The 3D geometries shave been simplified as well. All fillet corners were erased from the design as this would help in achieving a better mesh data on a limited time period.



Picture 4. Part of ballast with partial contamination. Case A



Picture 5. ballast structure for hydraulic conductivity. Case B



Picture 6. ballast structure for hydraulic conductivity. Case C

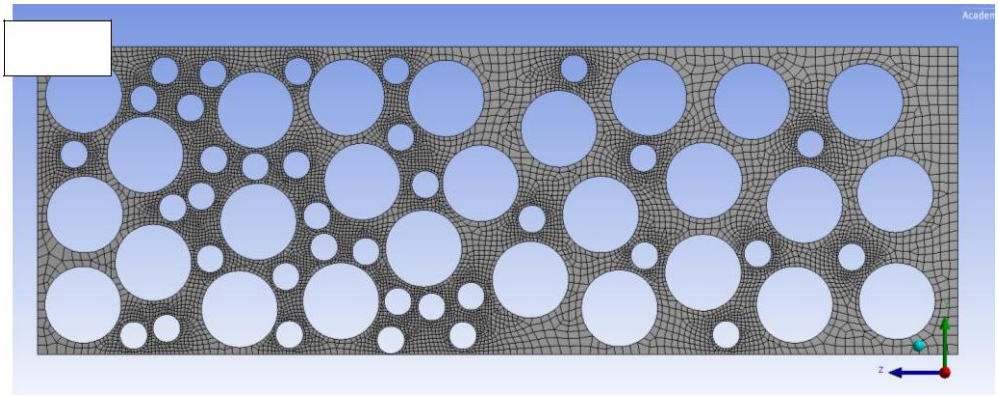
2.2 MESHING

The mesh setup in the solving for fluent case is a very important aspect of the setup. The mesh quality generated will be based on the orthogonal quality ad maximum skewness of the generated mesh. The geometry will be broken down into series of small

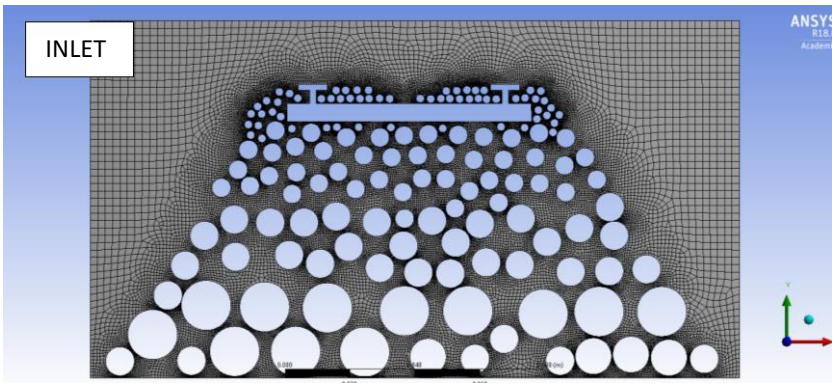
nodes and elements to be used by the finite volume method which is used across the whole domain.

The computational meshes used in the CFD analysis were generated using the different method found in the Ansys Workbench. The setup makes use of Tetrahedral, Hex-Quads and multizone to analyses the best mesh setup to be used in the fluent case. By refining the mesh quality and sizes, the accuracy of the simulations can significantly change. The use of tetrahedral mesh type proved to be the most efficient mesh with orthogonal quality of more than 0 and a maximum skewness of 0.88 was achieved. These mesh data can be checked in the statistics and changes can be made to achieve a better mesh using hexahedral mesh. Hexahedral mesh is usually more accurate than tetrahedral, but the generation of hexahedral mesh is mostly time consuming and with limited computational power the hexahedral mesh was discarded as the time was a constraint.

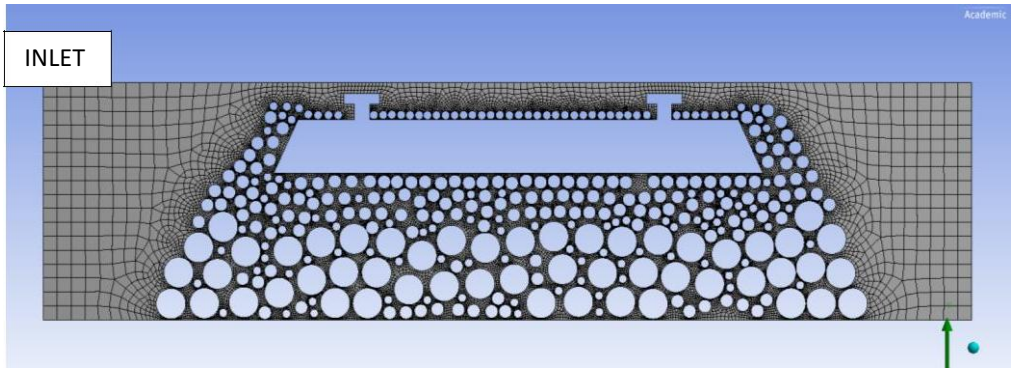
The mesh resolution as mentioned is a very important aspect in the simulation. For the turbulent model study the boundary layers, i.e. the flow gradient near the wall requires very flat cells such as prisms to ensure a good capture of the fluid flow. The model used a Y+ function of 25 to 100 to ensure that the logarithmic mesh cell of the profile so the wall function could be applied properly. Computational costs can significantly reduce based on such setups, but although the method does add further uncertainties and perhaps less accuracy in the data results.



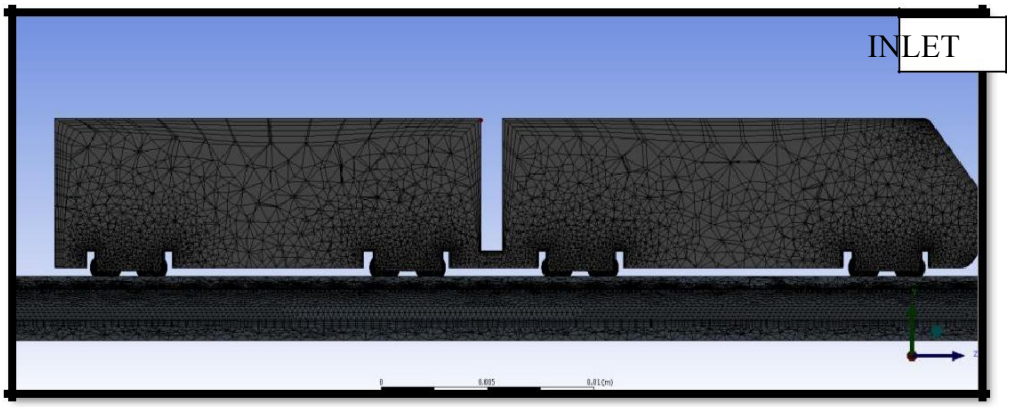
Picture 7.Mesh data for case A



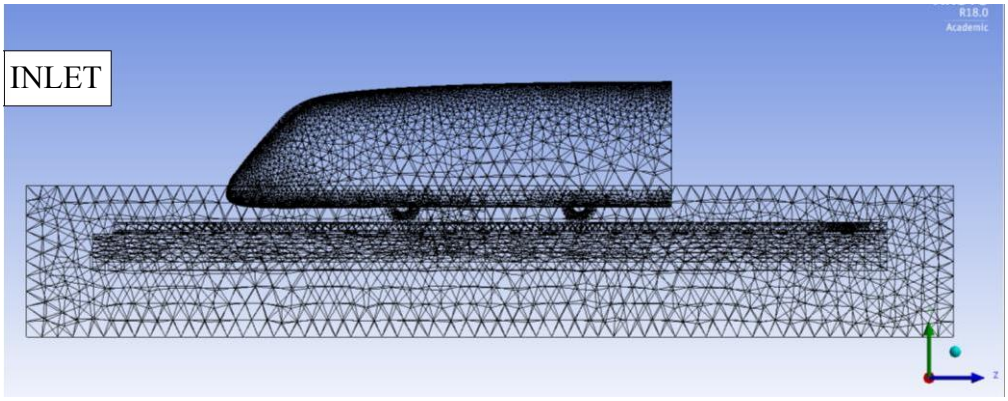
Picture 8. Mesh data for case B.



Picture 9. Mesh data for case C.



Picture 10. Mesh data with advance sizing and inflation case D.

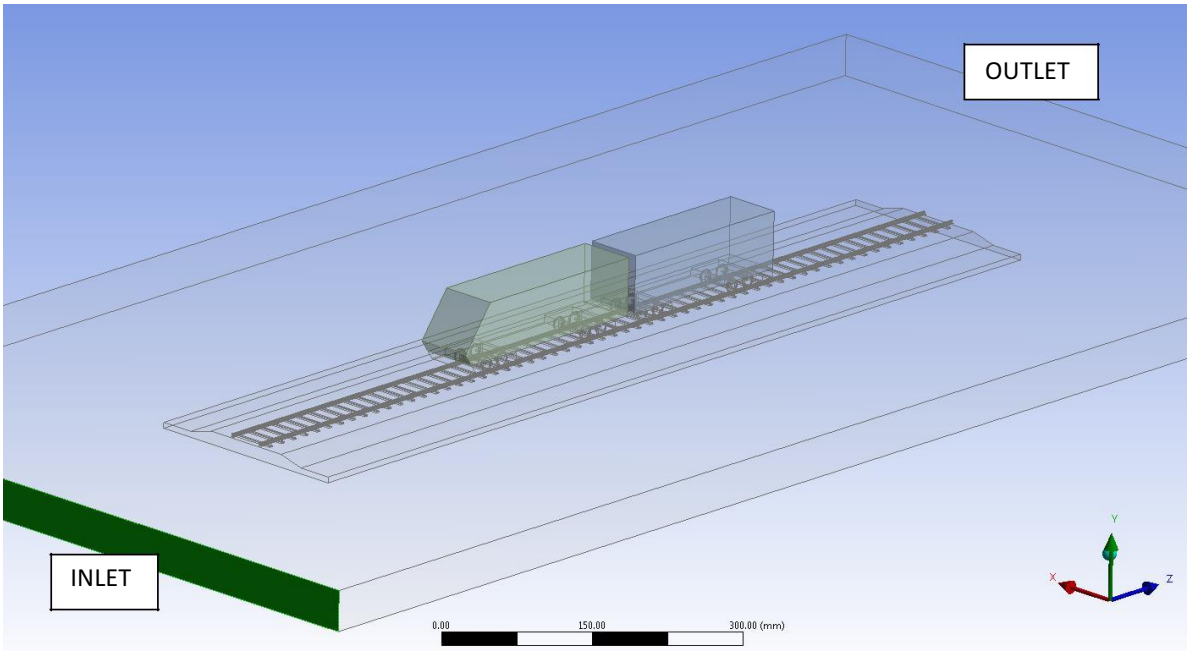


Picture 11. Mesh data case E.

2.3 COMPUTATIONAL DOMAIN AND BOUNDARY CONDITIONS

The boundary conditions used in the CFD simulation define the flow conditions inside the fluid domain, with having wrong boundary conditions the simulation can have detrimental effect on the solution output. For the simulation, the motion of the train was replicated by applying the same velocity as the inlet to the plane. This method is referred as the train fixed frame of reference and has been used in many simulation projects during the past few years. The inlet domain is set as fixed velocity inlet and

the outlet was defined as zero pressure outlet.



Picture 12.Fluid domain example for 3D analysis.

The computational domain used in the simulation was carried out at the scale of 1/10 and the inlet was positioned 75m before the nose head and 100m at least behind the train body. The model setup consisted of the energy equations along with the K-W and K-e models with enhanced wall function to capture the wall effect and wall shear stresses around the ballast based on the velocity of the train and level of flood water. After several mesh setups were carried out, thee best mesh were selected and imported into the fluent case.

As for the 2D simulations, the track drainage capacity was based on a semi-porous structure that represents the microscopic inside of the ballast. The case study was focused on achieving the most reliable data for turbulence effect and pressure effect on the track particles. The model is based upon the standard data for ballast granules which can be found from online sources. The mesh setup uses the best meshing options available to capture the curvatures and proximity effects of the shape. The geometry is part of the ballast structure where the granules have been randomly placed to create the small voids. This will also replicate the laboratory simulation of a reviewed paper and the data will be evaluated against. The mesh was also carried out using the workbench software from ANSYS, using methods of sizing on curvatures and proximities. The mesh geometry is shown below

This 2-dimensional study was carried out using different models available in the ANSYS Fluent. The best one will be chosen based upon the best data output. The cases involved using;

- Spallart Almaras
- K-omega
- K-epsilon
- Realizable k-epsilon

As for the numerical caclculations, the Navier-strokes equations, which consists of the governing equation and equations such as continuity and momentum which mentioned below.

$$\frac{\delta \rho}{\delta t} + \nabla . (\rho V) = 0 \qquad (1)$$

$$\frac{\delta \rho u}{\delta t} + \nabla . (\rho u V) = -\frac{\delta P}{\delta x} + \nabla . (\mu \nabla u) + S_{mx} \quad (2)$$

$$\frac{\delta \rho v}{\delta t} + \nabla . (\rho v V) = -\frac{\delta P}{\delta y} + \nabla . (\mu \nabla v) + S_{my} \quad (3)$$

$$\frac{\delta \rho w}{\delta t} + \nabla . (\rho w V) = -\frac{\delta P}{\delta z} + \nabla . (\mu \nabla w) + S_{mz} \quad (4)$$

where *u*, *v* and *z* is the component of velocity vector in *x*, *y* and *z*-components. 2 is the fluid density, *P* is static pressure and Sm,x, Sm,y , Sm,z are source terms for *x*, *y* and *z*-components.

Table A. boundary conditions for the 2D geometry.

Case	Width	Height	Length	Dry Density	Porosity	Slope angle	Velocity magnitude m/s
A	0.1 m	0.40m	0.6 m	1.60 g/cm^3	0.4	45	3
B	1m	0.25m					3
C	1.5m	0.25m					5

The 3D case had the following conditions;

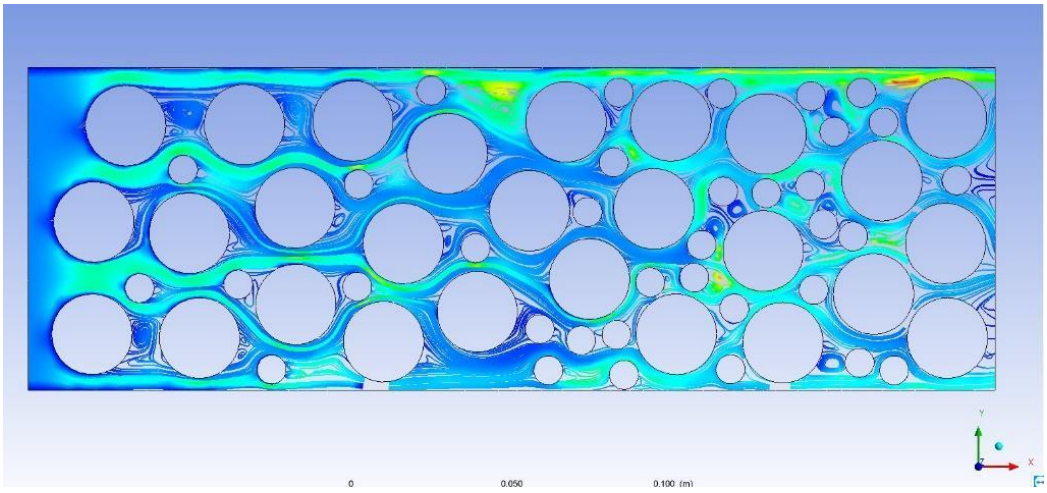
Table B. 3D cases parameters.

Case	Length	Fluid (flood) density	Velocity of flood	No of wagons
D	10m	1.60 kg/m^3	5m/s	2
E	5m		3m/s	1

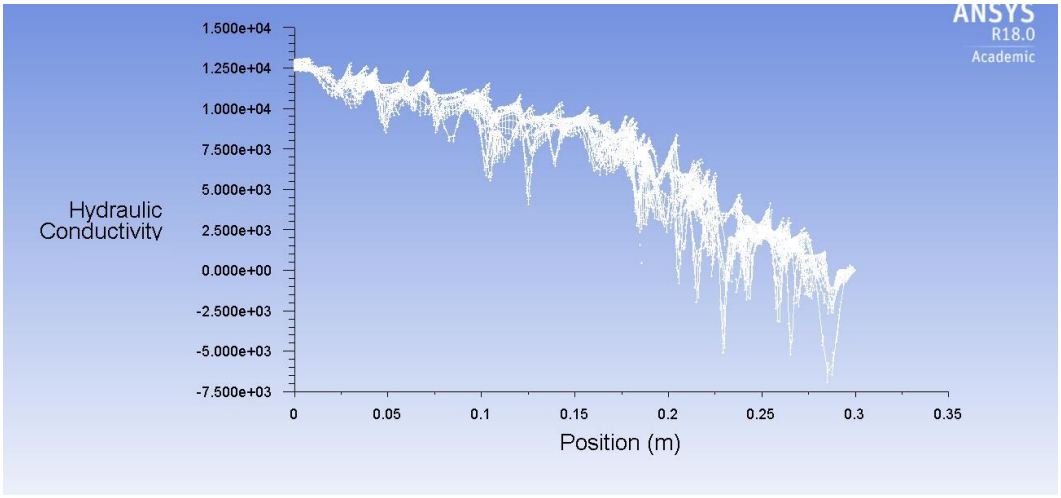
3 RESULTS AND DISCUSSION

In relation to the results found based on the research carried out, the data sets will be evaluated and used to predict the structural solution effectiveness. As mentioned the cases analyzed had relations to some laboratory experiments, which can be more precise with the use of computational tools such as ANSYS. The results display the hydraulic conductivity of the ballast and part of the ballast structure as the flood and contamination is varied. The pressure effect or hydro effects will damage the track structure in a way or another. Thus, from the data, the solutions suggested will be evaluated and help in restoring the sustainability of the railway industry through structural solutions as their efficacity can be rarely proven based on numerical solutions.

CASE A



Picture 13. K-3 enhanced wall function



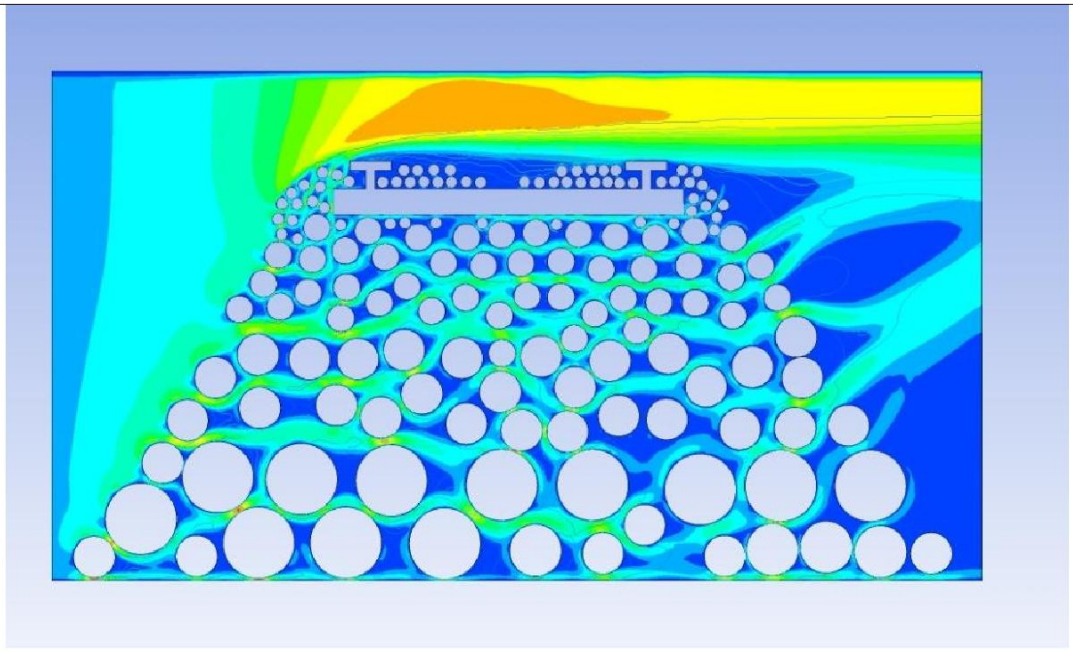
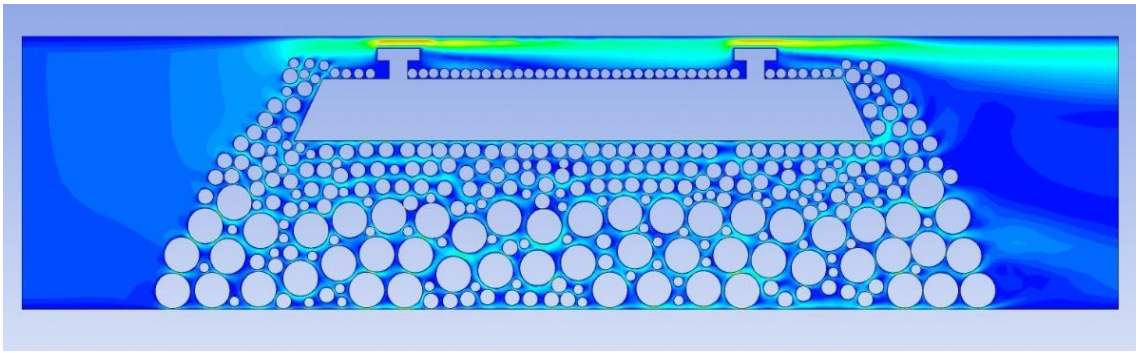
Graph 1. Drainage capacity for the track.

The case A clearly shows a fouled track on the half right side of the structure and on the left half side, the unfouled ballast structure has a good drainage capacity and decreases gradually to poor as it flows through the structure. This case shoes that fouled

ballast and unfouled ballast plays a great role in the structural dynamics of the track as loadings are applied upon a cyclic period of time. This can gradually cause chipping of the granules and create water puddles inside the structure which also leads to an effect known as mud pumping. This effect is a very common case in India as of their frequent monsoon seasons. Hence with the solution of geo-grids and geo-textiles, the granules can be prevented from chipping as the geo-technology is known to keep the structure in secured way to avoid destruction or damages.

Table C. rendering of fluid turbulence kinetic energy based on velocity fluctuations.

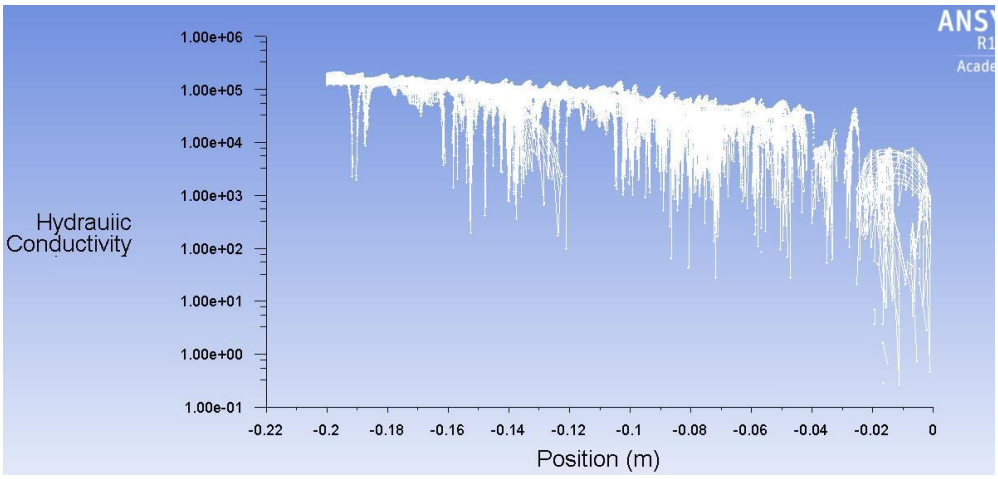
CASE B & C

C velocity	
D velocity	

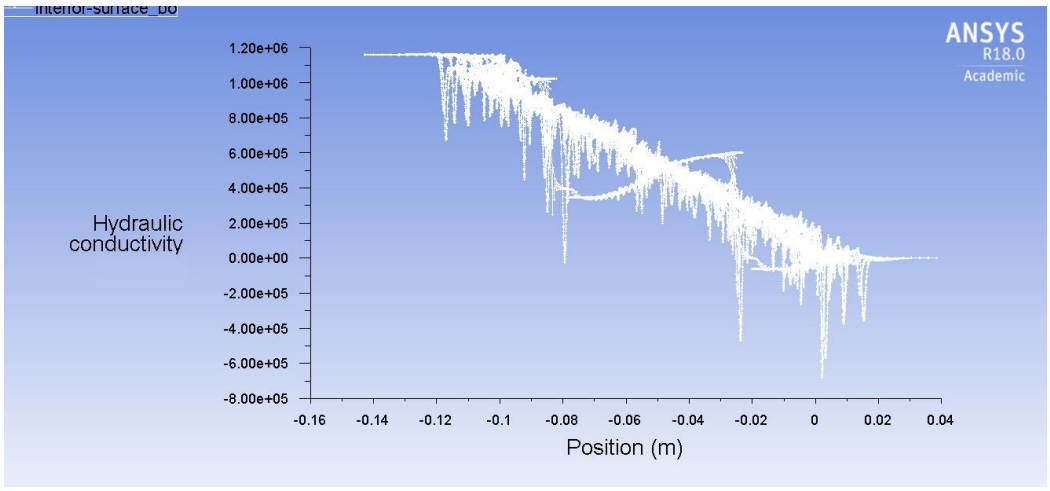
The results above describe the case where the water level is just above the rail level. The results demonstrate that the ballast having a poor drainage capacity as it does not evacuate the water in time to avoid buildup of pressure at the entry side of the structure for case C. The downstream side of the ballast has a high velocity exit on the top and at the middle and the ballast can be seen to be washed away at any point in both cases. The structural solution to be implemented here can be of several types.

The graph below shows the decrease in the drainage capacity of the track as the fluid passes through it for case C. The decreasing slope shows that the drainage capacity of the track is very poor and below average compared to case B where the graph has

barely a high gradient value. This suggest that the track has a good drainage capacity and can be considered to be an unfouled track. Hence this also suggest that the ballast needs to be refreshed with new granules. This can be also detected by the GPR (Ground Penetrating Radar) which is used in the industry to find fouled section of the ballast. Thus using such approach can easily solve for critical fouling on track length and help in saving the damage costs which will take place after the flood.



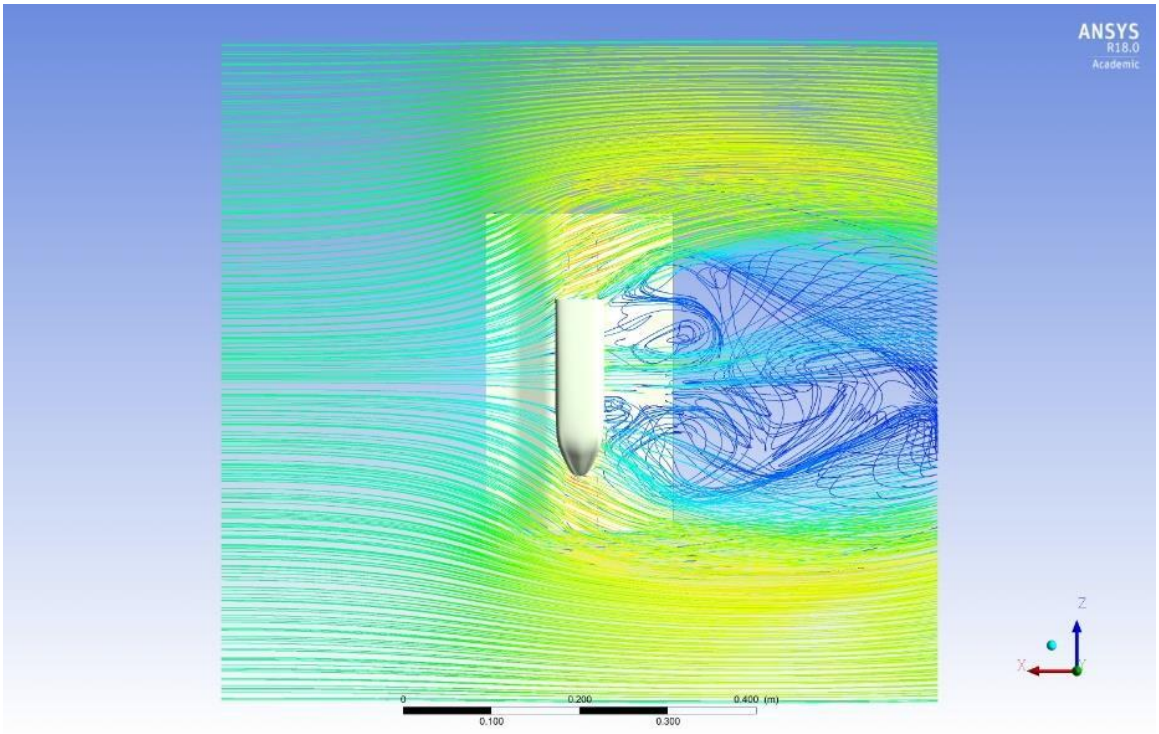
Graph 2. Drainage capacity for the track case B.



Graph 3. Drainage capacity for the track case C.

CASE C

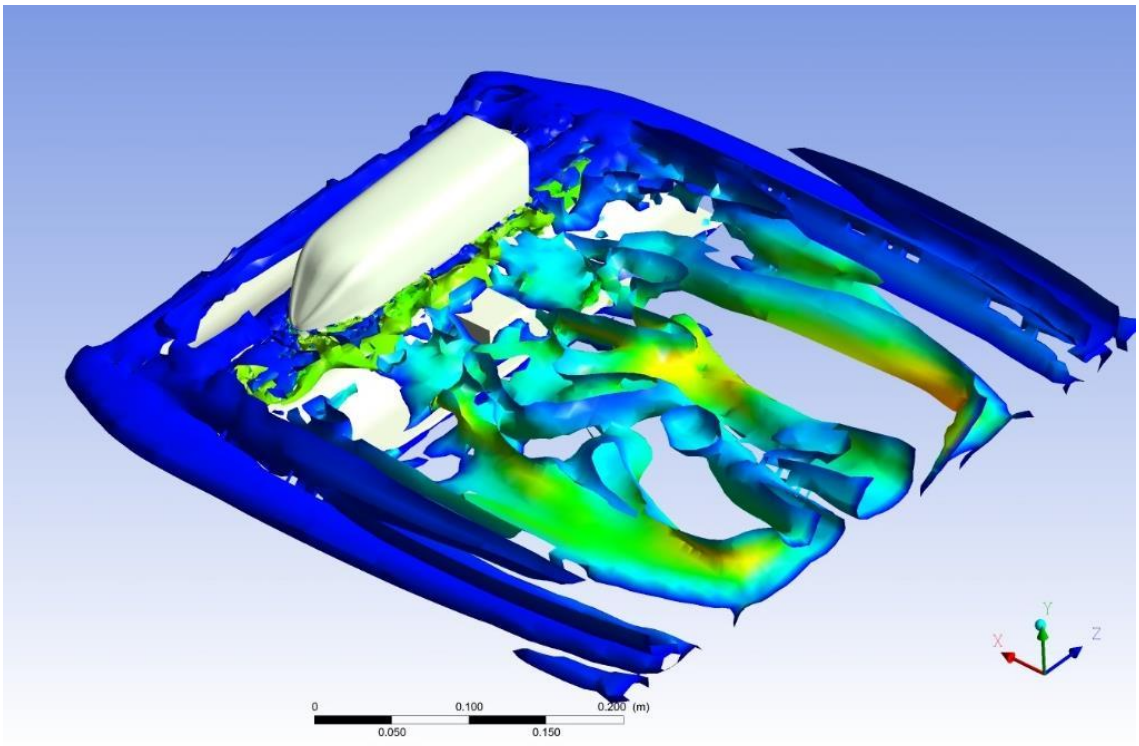
For the case of the 3d models, the results generated are a series of laboratory experiment carried out mainly by Pams and Cappoccioni [2] due to the events of ballast transport. These results demonstrate the other effect which is manhole clogging due to ballast wash away. The structural design around the track also needs to be considered when placed around a track as it can cause serious damage to the surroundings. The simulations represent a sideways flow perpendicular to the side of the track. This will show the effects of the multiple track damage caused by sideways erosion.



Picture14. Velocity streamlines. 3m/s.

The data shows the stream from left to right, thus not creating any major damages on the track. But if the stream was on the opposite ends, the track damages would be much considerable. This explains the reason for millions of cash being invested into the maintenance of the track after floods. The manhole structure does create very turbulent streamlines around the track. This data also is based on normal flood conditions which allow trains to operate on the track as the flood level is still below the rail head.

The picture above demonstrates the velocity streamlines just at the rail head. Solutions such as fenced retaining walls can be implemented in the case of critical areas of damage to prevent erosion. This technique is commonly used near beaches to prevent soil erosion into the sea and this technique can help in sustaining the railway tracks.

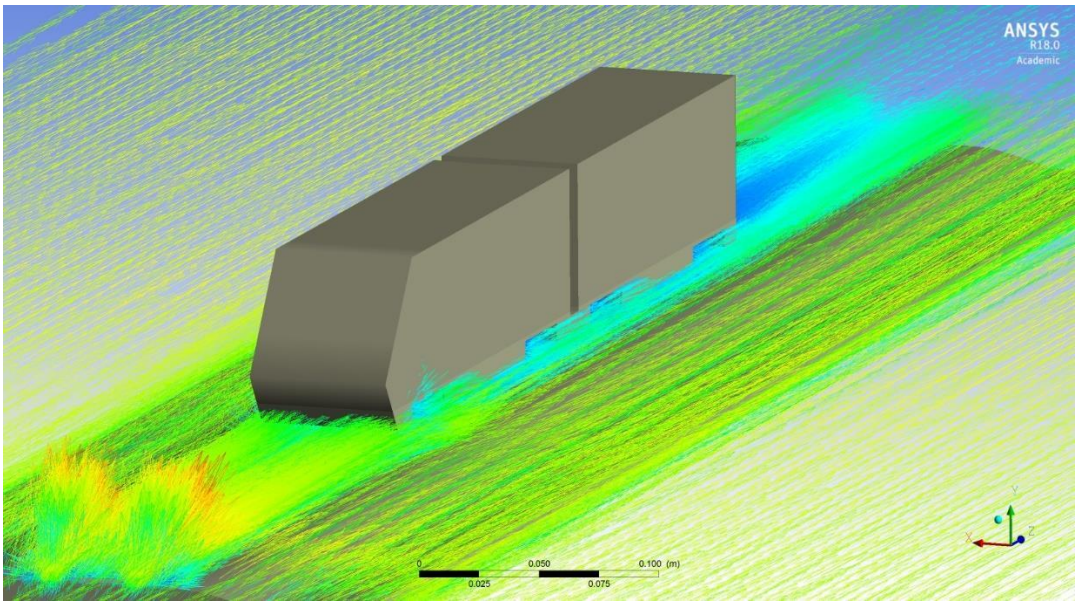


Picture 15. Vortex core regions at 1m/s to 3m/s.

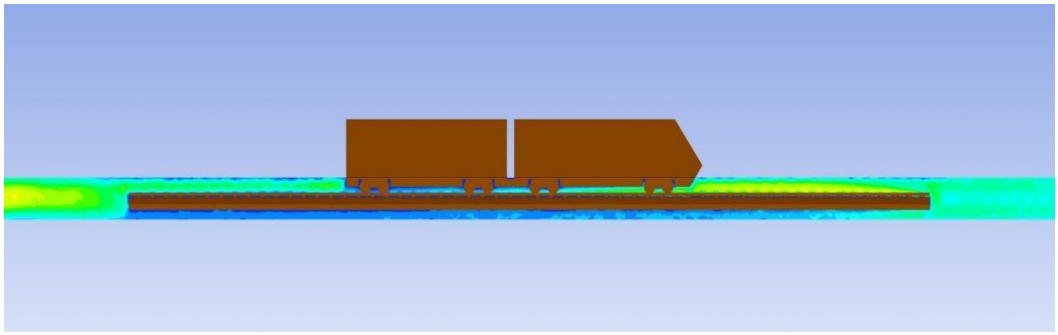
The vortex core regions also demonstrate the transport of granules from the ballast and the granules can definitely clog the manhole. The erosion is also demonstrated as the particles trajectory can be tracked and most of them will get washed away.

CASE D

This set of simulation represents the laboratory experiment carried out at the RSSB (Rail safety and Standard Boards) in UK to assess the current rule book of operations for trains on flooded tracks. The experiment demonstrates the fluid splashing around the damaged front section of the track and also around the train boggy. The simulation represents the train travelling on flooded track on extreme conditions and with permission to operate at 5m/s. this can be a very dangerous situation as the operator does not see ahead of him and operating along a flooded track can be very destructive as water splashing around the track causes high pressures and thus leading to track damage ahead of the nose of the train and below the train body. The vectors representation below shows this effect, which shows the fluid splashing.



Picture16. Velocity vectors.



Picture 17. Velocity around track.

Acknowledgements

Throughout this research process I would like to express my gratitude towards my supervisor, Dr. Ir. Satesh Namasivayam, Dean school of engineering who kept guiding me on the right track of the research till the end. I would also like to thank the SOE for having the necessary tools for Computational Fluid Dynamics tools as without these told, this research would have been difficult to put forward.

References

[1] K. Hayano, "Model tests and numerical analyses on the mechanism of flow-out of railway ballasts induced by flood inundation," pp. 1–4, 2013.

[2] C. Pams Capoccioni, D. Nivon, J. Amblard, G. De Cesare, and T. Ghilardi, "Analysis of ballast transport in the event of overflowing of the drainage system on HSL," *RTSE – Int. Work. Ballast Issues Challenges*, vol. 4, no. DECEMBER, 2013.

[3] N. Tennakoon, B. Indraratna, C. Rujikiatkamjorn, S. Nimbalkar, and T. Neville, "The role of ballast-fouling characteristics on the drainage capacity of rail substructure," *Geotech. Test. J.*, vol. 35, no. 4, pp. 1–4, 2012.

eureca 2017 – Conference Paper
Paper Number 2ME26

Numerical Modal Analysis and Design of Piezoelectric Energy Harvester

Shaun Tan Soon Xie*, Mohammad Hosseini Fouladi
School of Engineering, Taylor's University, Malaysia.

* *shauntan290993@hotmail.com*

Abstract
Energy is consumed all around us but we are bound to lose energy in the form of heat or vibrations; one way to reduce these losses is to convert said energy into electricity via a process known as energy harvesting. The aim of the research is to optimize the natural frequency, and therefore its maximum output, of a piezoelectric energy harvester (PZH) by implementing design modifications to a hypothetical model of a PZH with the aid of numerical modal analysis. The intended scope of the research is to design a PZH with the human body as an input and since the maximum frequency of any human movement can be assumed to be about 5 Hz, the objective frequency range set for this research is that as close as possible to 5 Hz. Literature research has been conducted; several possible design parameter changes have been tested and verified experimentally and analytically in the past. Various design modifications are modelled in this paper and then tested for their natural frequencies; their values then compared between one another. The design which yielded the lowest result is found to reduce the natural frequency of the PZH down to a minimum of 47 Hz from an initial 191 Hz; justification however needs to be provided to ensure viability of the modification. Further research needs to be done to identify other methods which can be compared to existing methods, and to potentially optimize the existing design even further.

Keywords: Piezoelectric, energy harvesting, modal analysis, design optimization

1. Introduction

Energy harvesting has been of great interest over the past decade as a means of an alternative wireless electrical power supply. Most interests focus in the use of a piezoelectric device to extract, or harvest the aforementioned energy from its surroundings. Piezoelectric devices for this purpose are commonly made of a piezoelectric compound known as lead zirconate titanate, otherwise known as PZT, with a chemical formula of $Pb[Zr_xTi_{1-x}]O_3$ where x is a value between 0 and 1. Piezoelectric materials generate electricity when said material is deformed by a small percentage of its original shape.

PZHs have recently been implemented in ways that are not only creative, but are also effective in that they reduce the need for replacement, an issue commonly found in installing power supplies in remote or hard-to-access areas. Dikshit et al. [1] have noted several existing applications of these PZHs.

Patel and Dewangan [2] have listed several benefits in energy harvesting. The most apparent benefit is the reduced dependency on battery power. They also directly reduce costs as harvesting systems allow devices to function while eliminating the need for any service visits. Energy harvesters are also great for long-term monitoring and will continue to operate as long as the ambient energy is still available. They also eliminate the need for millions of batteries and other energy costs associated with battery replacements.

Early developments show that vibration as an energy source is successfully converted into electrical energy but is only fully efficient when the vibration source operates at resonance; that is the efficiency of these harvesters suffers a huge drop if the input frequency does not match its natural frequency. Hence, the resonant frequency of the device has to be reduced. The research scope is to use human movement as input to the harvester and since the human is assumed to only be able to produce an average frequency of about 5 Hz through any kind of movement, the PZH needs to be optimized to harvest energy at much lower frequencies in order to be useful for this particular application.

It is hypothesized that the resonant frequency of PZHs can be reduced to that of human level movements through several design modifications; these can be modeled with software and subsequently analyzed numerically. Through modeling and simulation software, it is possible to design a PZH that caters to specific needs, as well as to avoid incurring additional costs from experimental methods.

Cornwell et al. [3] introduced an auxiliary structure on their model, which is essentially a location on the beam where a tip mass could be fitted. Their model managed to achieve a reduction in frequency (about 2 Hz) and also achieved a greater power output; no theoretical study on the relationship between resonant frequency and mass was performed however. Wu et al. [4] proposed that shifting the center of gravity of the system is yet another feasible method of lowering the resonant frequency of a system and as such built a prototype to verify their proposal. They applied the principle that states, the closer the center of gravity to the free end of the cantilever, the greater its effective mass. Ibrahim and Ali [5] suggested that the resonant frequency can also

be adjusted by altering the physical dimensions of the cantilever, although they also mentioned that due to real-time limitations, only length can be considered.

This paper aims to determine the effects of various design modifications on the natural frequency of a PZH. The research parameters are based on a small PZH constructed in the form of a bilayer cantilever beam using a stainless steel beam measuring 35mm x 10mm x 0.3mm and a piezoelectric strip (lead zirconate titanate, commonly known as PZT) layer measuring 30mm x 10mm x 0.2mm; any changes to these parameters are communicated accordingly. The PZH is supported on one end and all tests are aimed towards determining natural frequencies through numerical modal analysis. The effect of mass change will also be considered in this paper.

2. Methodology

This section outlines the methodology performed in this research. Each subsection also discusses any justifications to the tasks performed throughout this study.

2.1 Geometry Model

An initial model is first produced using Solidworks with the nominal dimensions listed in the preceding section. All modifications use the same nominal parameters of 35mm x 10mm x 0.3mm for the main beam and 30mm x 10mm x 0.2mm for the PZT layer. The PZT layer is joined to the stainless steel layer at the free end of the cantilever. Any changes to these initial parameters will have a separate model file created respectively for ease of analysis.

2.1.1 Base Model

Fig.1 shows the base model with the nominal parameters. The model is essentially the two strips of material joined together at the right side (free) end when viewed as shown. The left (fixed) end is designated as a fixed support during simulation. This model will be used as the primary reference for all other design changes performed in this study.

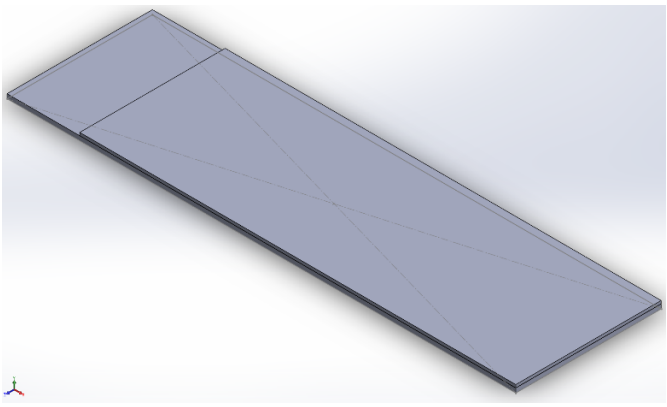


Figure 1. Base model

2.1.2 Modified model – Adding tip mass

Fig. 2 shows the base model modified to contain a mass block added at the tip of the cantilever. This configuration uses block dimensions measuring 10mm x 10mm x 5mm. Fig. 3 shows configurations tested using block heights of 2.5 mm, 5.0mm, 7.5mm and 10.0mm while maintaining the other dimensions. The respective mass changes will be highlighted in the discussion.

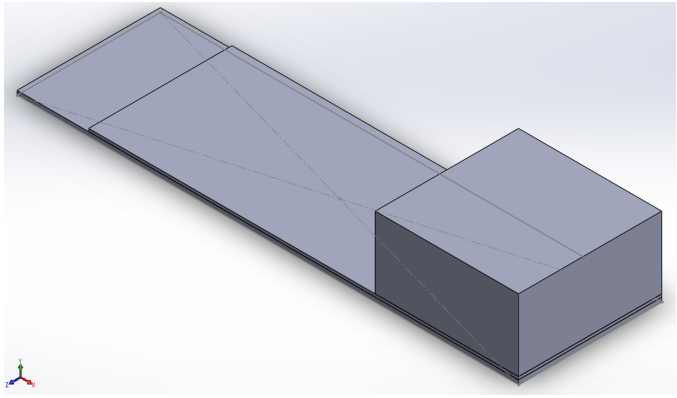


Figure 2. Base model with tip mass of height 5 mm.

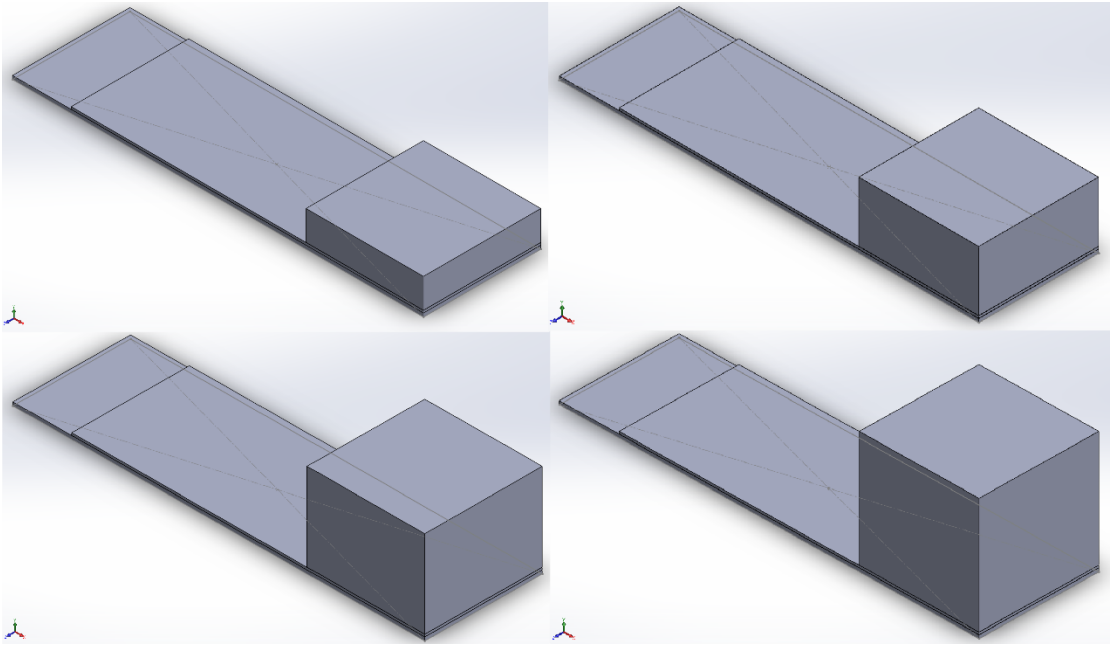


Figure 3. All tested configurations (2.5mm to 10.0mm block height).

This design change aims to investigate the effects of directly adding mass to the system and to determine its impact on the natural frequency on the system. The masses are modeled as cuboids bound to the tip of the beam with only varying thicknesses in an attempt to keep every other variable constant.

2.1.3 Modified model – Changing center of gravity

Fig. 4 shows the base model modified to have an additional fixed mass on a point along the beam. For this model, the additional mass is located 5 mm away from the tip of the cantilever, measured from the nearest edge of the mass.

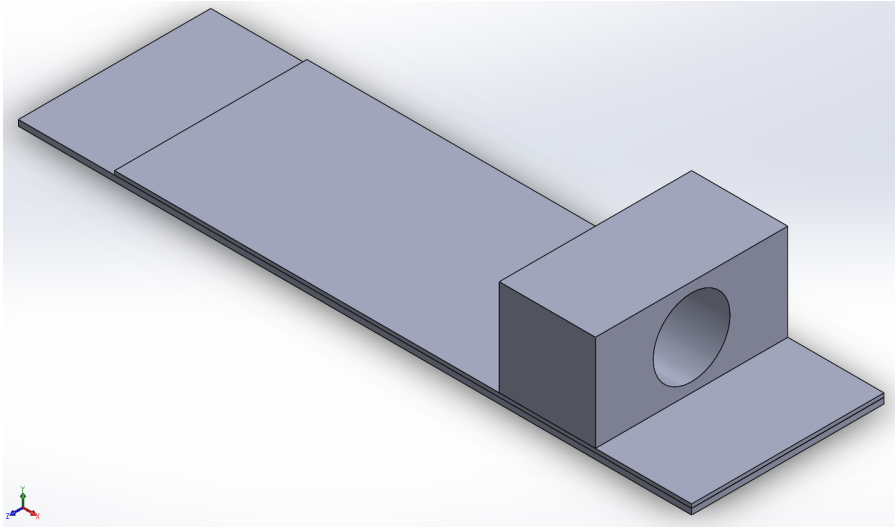


Figure 4. Base model with fixed mount.

The mass has dimensions measuring 5 mm x 10mm x 5mm and has a circular cut section measuring 4 mm in diameter. The width of the mass is simply set as the width of the beam itself to provide ease of modeling whereas the length, height and cutout size are all based on a preferred screw size of diameter 4 mm. This additional mass serves as a mount for an object (such as a screw) that can be fitted through the cutout.

For this study, although no treads were modeled, a screw modeled as a cylinder will be used as the sample object as screws can be locked in place. In theory, any object which can be repositioned along the mounting point without slipping can be used as a test object. The idea behind this design change is to allow the overall center of gravity of the system to be shifted freely without changing its overall mass. This method aims to determine the effects of shifting the center of gravity of the system on the natural frequency without changing its mass.

Fig. 5 shows the modified models fitted with a “screw” measuring 4 mm in diameter and 20 mm in length positioned to the far inward side, the far outward side, and the middle position. The screw is assumed to be even throughout its entire length and has a center of gravity located at its center.

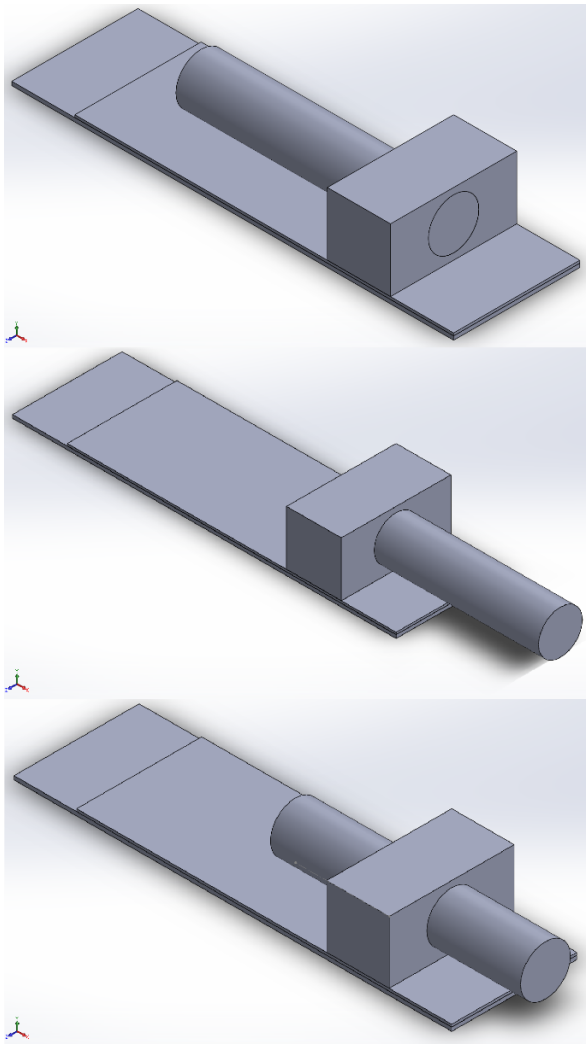


Figure 5. Model with “screw” fitted in various positions.

For this design, analysis consists of an extra section detailing the effects of having the additional fixed mass being added in the first place. Results are then compared relative to it.

2.1.4 Modified model – Changing overall dimensions

The base model is modified with the stainless steam beam component lengths adjusted to 40 mm, 45 mm, 50 mm and 55 mm respectively. The PZT layer remains bonded at the free end of the cantilever and keeps the same dimensions. This method aims to determine the effects of any physical dimension change (mainly length) on the natural frequency of the PZH.

Conversely, another configuration is also tested using the base model by instead having the PZT layer component lengths adjusted to 27.5 mm, 25.0 mm, 22.5mm and 20.0 mm respectively while maintaining the stainless steel beam length. Similarly, the PZT layer remains bonded at the free end of the cantilever.

2.2 Numerical Modal Analysis

2.2.1 Overview

Following the production of all geometric models, numerical modal analysis is employed with the aid of ANSYS software to determine their natural frequencies.

To initiate this process, the assembly file created using Solidworks needs to be exported into a compatible file format; the .IGES extension is used in this study. The model is then loaded into the modal component within ANSYS Workbench for analysis. For all models, simulation is performed using ANSYS R18.0 Academic and therefore carry their version-specific limitations.

Materials need to be defined within ANSYS with their appropriate parameters and each part of the model will need to be designated the correct material. The following subsection indicates the materials used throughout the simulation. Contact points then need to be defined based on their type and meshing settings need to be performed; all to ensure the accuracy of the results. ANSYS is then able to produce the desired number of mode shapes as well as their corresponding natural frequencies (starting with the lowest). All models are tested under two conditions, fully undamped and with damping ratio of 0.25 introduced to the system. The latter is conducted to investigate the impacts of damping on the natural frequency of the PZH.

2.2.2 Material Properties

Table 1 shows the properties of stainless steel and PZT used in the simulation.

Table 1. Properties of stainless steel and PZT layer.

Material	Density (kgm^{-3})	Elastic modulus (GPa)	Poisson's ratio
Stainless steel	7750	193	0.31
PZT	7500	63	0.31

2.2.3 Settings and Conditions

The following conditions are applied throughout the course of the simulation:

- All models have a fixed support on the left edge
- All contact points are set to "bonded" except for that between the screw mount and screw, of which it is set to "rough"
- All contact stiffness is set to 1 to prevent inaccuracy with results
- All meshing will attempt to use the maximum number of elements and/or nodes available, whichever is greater, limited to 32000 (ANSYS R18.0 Academic limits)
- Where damping is applicable, all damping ratios are set to 0.25

Due to limitations within the software itself, grid convergence tests using ANSYS' convergence feature is not performed. This is due to the test itself exceeding the numerical limits of the software, which is capped at 32000 elements or nodes for any given model, whichever is greater. Instead, the meshing setup uses element sizes rounded to the nearest 0.05 mm. An initial value (in this study, 0.75 mm) is first tested

and is gradually reduced in 0.05 mm decrements until the number of elements or nodes exceeds 32000, at which the last applicable size is used for meshing.

Since the design of all models is relatively simple, there are no issues regarding computational time despite using a very small element size for meshing. As a result, the study attempts to gain maximum accuracy while sacrificing little to no computational time by using the most number of elements possible, reaching the limit of 32000 units where applicable. Reasonable element sizes (i.e. rational numbers) will sometimes produce a quantity that may be far off the limiter, but will be given priority for easier understanding.

3. Results and Discussion

3.1. Overview

According to simulation, the base model has an overall mass of 1.264 g and a natural frequency of 191.34 Hz; these mass and frequency values are used as a reference to all other data, particularly mass where comparison is performed to determine if a mass change has any impact on the natural frequency of each design modification. All mass values obtained are based on ANSYS Design Modeler's internal calculator. Table 2 shows all key results pertaining to the suggested design modifications. Table 3 shows the information related to meshing. Fig. 6 shows the first mode shape of the base model.

Table 2. Frequencies and mass changes obtained across all models.

Model type	**Mass (g)**	**Mass chg. (%)**	**1st mode freq. (Hz)**	**Frequency chg. (%)**
Base model	1.264	N/A	191.34	N/A
Mod1 – 2.5mm block	3.201	+153.24	88.70	-53.64
Mod1 – 5.0mm block	5.139	+306.57	65.92	-65.55
Mod1 – 7.5mm block	7.076	+459.81	54.38	-71.58
Mod1 – 10.0mm block	9.014	+613.13	46.94	-75.47
Mod2 – No screw	2.714	+114.72	107.20	-43.97
Mod2 – Screw far in	4.662	+268.83	88.86	-53.56
Mod2 – Screw middle	4.662	+268.83	75.99	-60.29
Mod2 – Screw far out	4.662	+268.83	64.23	-66.43
Mod3a – Beam 40mm	1.380	+9.18	133.32	-30.32
Mod3a – Beam 45mm	1.496	+18.35	100.74	-47.35
Mod3a – Beam 50mm	1.613	+27.61	79.77	-58.31
Mod3a – Beam 55mm	1.729	+36.79	65.17	-65.94
Mod3b – PZT 27.5mm	1.226	-3.01	178.84	-6.53
Mod3b – PZT 25.0mm	1.189	-5.93	170.82	-10.72
Mod3b – PZT 22.5mm	1.151	-8.94	165.69	-13.41
Mod3b – PZT 20.0mm	1.114	-11.87	162.64	-15.00

Table 3. Number of nodes and elements of each model.

Model type	Element size (mm)	n(Nodes)	n(Elements)
Base model	0.40	29596	4075
Mod1 – 2.5mm block	0.50	28947	4600
Mod1 – 5.0mm block	0.60	25968	4454
Mod1 – 7.5mm block	0.60	31008	5610
Mod1 – 10.0mm block	0.65	30768	5712
Mod2 – No screw	0.50	27248	4200
Mod2 – Screw far in	0.60	31267	5560
Mod2 – Screw middle	0.60	31267	5560
Mod2 – Screw out	0.60	31267	5560
Mod3a – Beam 40mm	0.40	31756	4375
Mod3a – Beam 45mm	0.45	27958	3841
Mod3a – Beam 50mm	0.45	29950	4117
Mod3a – Beam 55mm	0.45	31776	4370
Mod3b – PZT 27.5mm	0.40	28516	3925
Mod3b – PZT 25.0mm	0.40	27436	3775
Mod3b – PZT 22.5mm	0.40	26356	3625
Mod3b – PZT 20.0mm	0.40	25096	3450

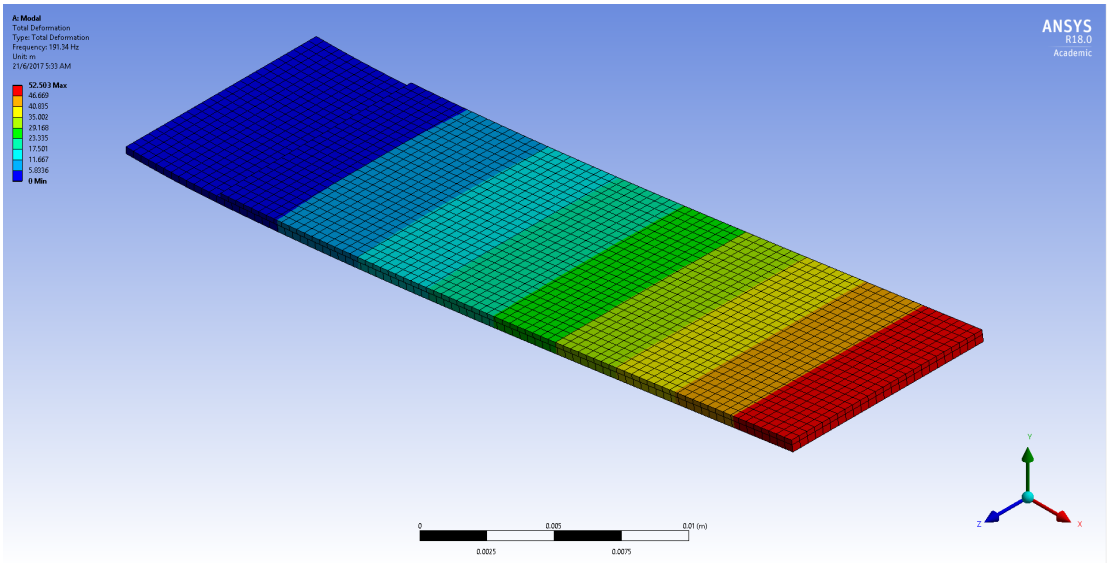


Figure 6. Mode shape (base model) at 191.34 Hz

3.1.1 Adding Tip Mass

Table 4 shows the data obtained by varying the size of the additional tip mass. Four different masses are tested with their lengths and widths fixed, while varying their heights. The mass is assumed to be made of stainless steel.

Table 4. Frequency data from adding tip mass

Model type	Mass (g)	Mass chg. (%)	Undamped freq. (Hz)	Damped freq. (Hz)	ΔUndamped freq. (%)
Base model	1.264	N/A	191.34	185.27	N/A
+2.5mm block	3.201	+153.24	88.70	85.88	-53.64
+5.0mm block	5.139	+306.57	65.92	63.83	-65.55
+7.5mm block	7.076	+459.81	54.38	52.66	-71.58
+10.0mm block	9.014	+613.13	46.94	45.45	-75.47

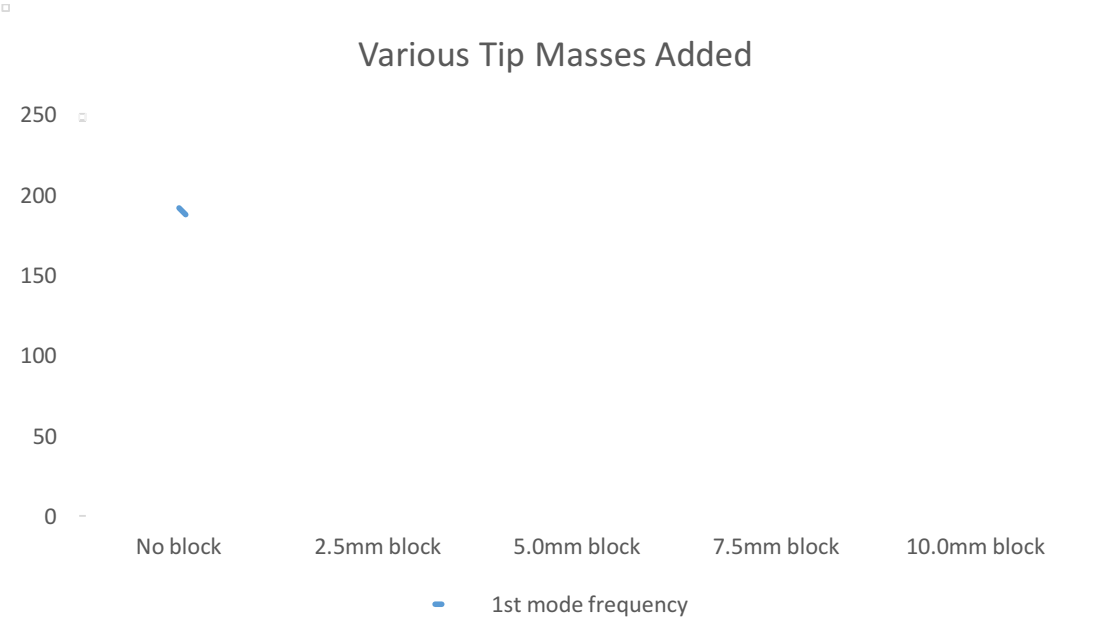


Figure 7. Graph of natural frequency against mass added to system.

Fig. 7 shows the graph of natural frequency against mass added to the system. Adding a tip mass yields positive results and by far is the simplest modification that can be performed on a PZH. This design shows that a high increase in mass (up to 613% tested) can provide very high reductions in frequency (up to 75% decrease). The drawbacks however depend on the intended scale and form factor of the system; dimensions may or may not need to be changed to accommodate any physical constraints. The lowest natural frequency observed using the tested conditions is found to be 46.94 Hz with an observed increase in mass of approximately 613%.

One weakness of directly adding a mass and only adding a mass is the selection of the material itself. As seen from the collected data, changing the mass alone for the purpose of reducing the natural frequency of any system requires a significant increase to obtain the desired frequency. If the material has a relatively low density, a large amount of the material (in terms of volume) will be required to compensate for the mass; this results in a much larger form factor, which can be a disadvantage depending on the intended use of the PZH. To rectify this, a much denser material may have to be selected during the fabrication of the PZH. The following section details a method that can be employed to reduce the natural frequency of a PZH without adding excessive amounts of mass.

3.1.2 Changing Center of Gravity

Table 9 shows the data obtained by varying the position of the mounted mass. Three positions are tested during the simulation; closest to the fixed end of the cantilever, positioned at the center of the housing, and closest to the free end of the cantilever. This method also ensures that the overall mass of the system remains constant. Both the housing and the mounted mass are assumed to be made of stainless steel.

Table 5. Frequency data from changing center of gravity

Model type	**Mass (g)**	**Mass chg. (%)**	**Undamped freq. (Hz)**	**Damped freq. (Hz)**	**ΔUndamped freq. (%)**
Base model	1.264	N/A	191.34	185.27	N/A
No screw (mount only)	2.714	+114.72	107.20	103.79	-43.97
Screw far in (nearest)	4.662	+268.83	88.86	86.04	-53.56
Screw middle	4.662	+268.83	75.99	73.58	-60.29
Screw far out (furthest)	4.662	+268.83	64.23	62.19	-66.43

Fig. 8 shows the graph of natural frequency against the relative position of the "screw" in the system.



Figure 8. Graph of natural frequency against position of the screws.

From Fig. 8, the method in which an additional housing is added supports the theory of adding a mass to reduce natural frequency as shown in the result where only the housing is modeled. With a 115% increase in mass, a reduction of 44% in natural frequency is observed with just the housing alone. The lowest natural frequency observed using the tested conditions is found to be 64.23 Hz with an observed increase in mass of approximately 269%.

The housing allows you to further add a mass and provides the ability to fine-tune the natural frequency of the PZH even further. This however may or may not pose construction problems in reality the nominal dimensions of the system are already very small. This design also proves that the addition or removal of a mass is not necessary to adjust the natural frequency of a system. The nearer the center of gravity of the system is to the free end, the lower its natural frequency. This is very likely due to the mass shifting towards the free end and therefore increasing the effective mass and reducing the natural frequency of the system. Conversely, the nearer the center of gravity is to the fixed end, the lesser the effective mass and the greater the natural frequency of the system.

3.1.3 Changing Overall Dimensions

Table 6 shows the data obtained by varying the lengths of the stainless steel layer while maintaining the length of the PZT layer and vice versa. The data shown lists the frequencies when the stainless steel layer is extended from the fixed end and when the PZT layer is extended from the free end of the cantilever.

Table 6. Frequency data from changing dimensions

Model type	**Mass (g)**	**Mass chg. (%)**	**Undamped freq. (Hz)**	**Damped freq. (Hz)**	**ΔUndamped freq. (%)**
Base model	1.264	N/A	191.34	185.27	N/A
Beam 40mm, PZT fixed	1.38	+9.18	133.32	129.08	-30.32
Beam 45mm, PZT fixed	1.496	+18.35	100.74	97.54	-47.35
Beam 50mm, PZT fixed	1.613	+27.61	79.77	77.23	-58.31
Beam 55mm, PZT fixed	1.729	+36.79	65.17	63.10	-65.94
PZT 27.5mm, beam fixed	1.226	-3.01	178.84	173.16	-6.53
PZT 25.0mm, beam fixed	1.189	-5.93	170.82	165.40	-10.72
PZT 22.5mm, beam fixed	1.151	-8.94	165.69	160.43	-13.41
PZT 20.0mm, beam fixed	1.114	-11.87	162.64	157.47	-15.00

Fig. 9 shows the graph of natural frequency against the length of the stainless steel layer, whereas Fig. 10 shows the graph of natural frequency against the length of the piezoelectric strip.

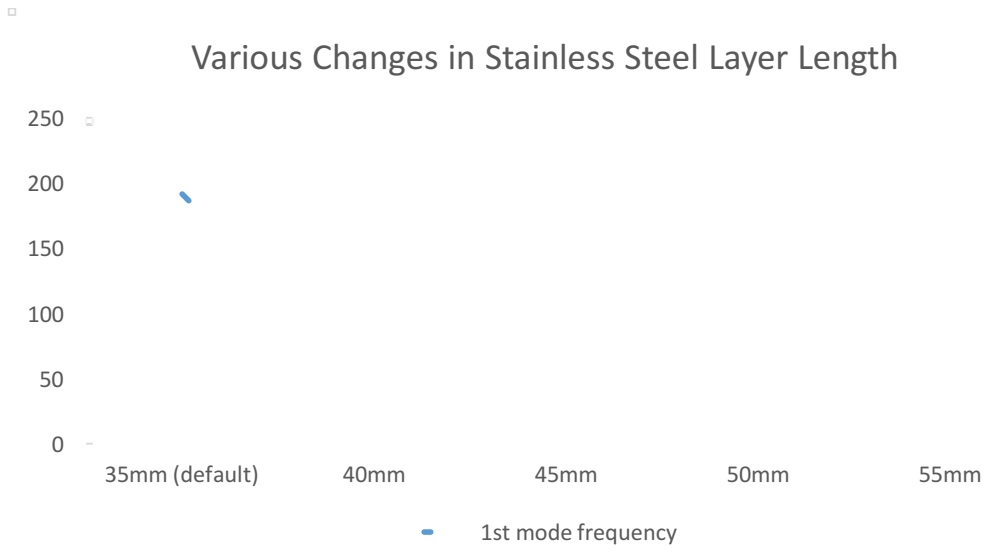


Figure 9. Graph of natural frequency against length of stainless steel layer.

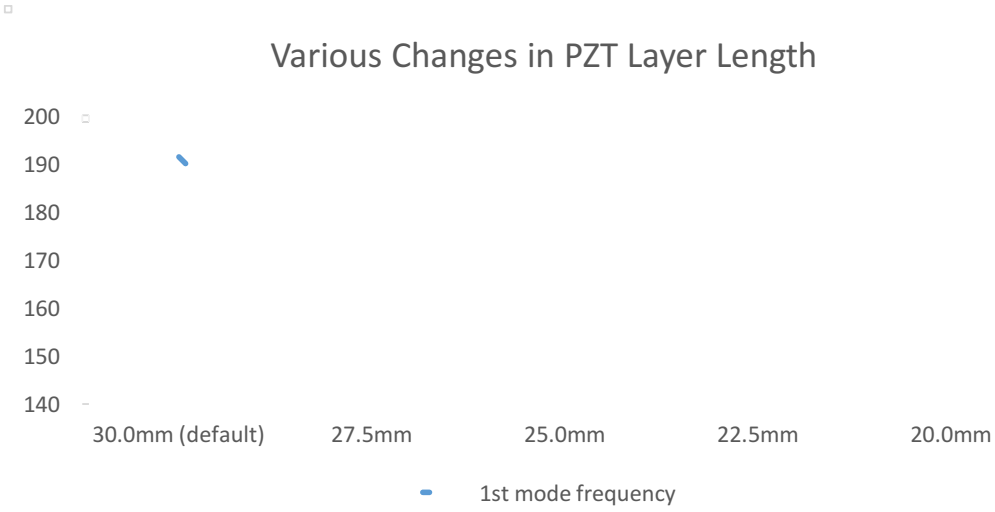


Figure 10. Graph of natural frequency against length of PZT strip.

Changing the dimensions on the structure yields mixed results. Extending the length of the cantilever has two effects, namely increasing the mass by a small margin as well as offsetting the center of gravity away from the fixed end; this results in the reduction of the natural frequency of the system depending on how the extension was performed. Extending the length of the system from the free end will yield different results when compared to extending from the fixed end; this is mainly due to the difference in the overall center of gravity of both designs. Despite having only a small mass gain (up to 36.79% tested), this design change is still able to provide a relatively beneficial frequency reduction (up to 65.94% decrease). The effective limits are essentially the physical constraints of the PZH itself.

Conversely, from Fig. 10, reducing the length of the PZT layer proves to be less useful, although some positive change has been recorded. Gradually shortening the PZT layer has the effect of shifting the center of gravity away from the fixed end similar to

extending the length of the cantilever. Another effect however is also the gradual reduction in mass, which appears to oppose the benefits of the former, leading to an overall positive but rather small change in natural frequency (up to 11.87% mass reduction, up to 15% frequency decrease). This design change is particularly useful to fabricate harvesters which demand a less complicated form factor and still require a lower natural frequency.

3.1.4 Effect of Damping

Table 7 shows the data obtained by introducing damping into the system. All tested systems have a damping ratio of 0.25 for consistency of collected data.

Table 7. Comparison between undamped and damped frequencies across all models

Model type	**Undamped frequency (Hz)**	**Damped frequency (Hz)**	**Frequency change (Hz)**
Base model	191.34	185.27	6.07
+2.5mm block	88.70	85.88	2.82
+5.0mm block	65.92	63.83	2.09
+7.5mm block	54.38	52.66	1.72
+10.0mm block	46.94	45.45	1.49
No screw (mount only)	107.20	103.79	3.41
Screw far in (nearest)	88.86	86.04	2.82
Screw middle	75.99	73.58	2.41
Screw far out (furthest)	64.23	62.19	2.04
Beam 40mm, PZT fixed	133.32	129.08	4.24
Beam 45mm, PZT fixed	100.74	97.54	3.20
Beam 50mm, PZT fixed	79.77	77.23	2.54
Beam 55mm, PZT fixed	65.17	63.10	2.07
PZT 27.5mm, beam fixed	178.84	173.16	5.68
PZT 25.0mm, beam fixed	170.82	165.40	5.12
PZT 22.5mm, beam fixed	165.69	160.43	5.26
PZT 20.0mm, beam fixed	162.64	157.47	5.17

Damping is able to reduce the natural frequency of any given system further, but is limited in that the reduction becomes less apparent with already low frequencies. The greatest observed change was that of the base model, indicating a reduction of 6.1 Hz due to its already high natural frequency. The smallest observed change was that of the modified block with the 10-mm high tip mass, indicating a reduction of only 1.5 Hz. Since a damping ratio of only 0.25 is used, it is possible to gain greater damping by increasing this value during simulation. In actual cases however, attempting to introduce a significantly greater damping element may introduce unwanted complications during the fabrication of the PZH.

3.1.5 Effect of Additional Mass

As seen from all the methods tested, any direct increase in mass will result in a lower natural frequency. Taking the preceding sections into consideration, the effect of adding mass can be magnified depending on the position of the added mass. Positioning

the mass closer to the free end of the system will result in an increase in natural frequency.

While adding additional mass is straightforward, it may produce complications in that the overall form factor of the system may be compromised depending on how it is performed. One other method of adding mass to a system is by using materials of greater density. This allows the PZH to be identical in size but carry a larger overall mass. Main drawbacks from this design change are potential increase in costs due to material availability as well as changes in mechanical properties of the material. Stainless steel was selected as the main beam layer for its high strength; other materials may not have the same strength required to prevent failure.

For designs that feature a mount such as the one detailed in this paper, additional masses can be further added by introducing more mounting points. Since the effective limit of the design is the overall height of the system itself, it is possible to introduce additional masses to the design by utilizing the space below the maximum point of the system.

Using the idea as just described, it is also possible to add additional mass by using a thicker stainless steel beam in place of a thicker tip mass. This allows the system have its mass increased without affecting the effective height of the PZH. Naturally, the tip mass will need to have its thickness reduced to compensate for the increase in thickness of the beam.

4. Conclusion

All of the tested methods proved to be useful one way or another, in that they have successfully brought down the natural frequency of the system in each of their own tests. While the research has not successfully reached the target frequency of 5 Hz, it has determined various methods that can be implemented in conjunction with one another to reduce the natural frequency nonetheless.

In addition to improving, or in this study, reducing the natural frequency of the system, these methods can also be employed in reverse, that is, the findings from this study can be employed to raise the natural frequency of a system where necessary. The best result achieved from the study is approximately 47 Hz, and this comes with a sacrifice of increasing the overall size of the system. The result represents a 75.47% reduction in natural frequency from 191 Hz, and although it is not too close to the target of 5 Hz, it is found to be the greatest improvement over the initial model based on the tested conditions. Other methods have been proposed to modify the system without compromising its form factor.

Mass, and by extension effective mass, remains a determinant of the natural frequency of the PZH. Mass directly affects the natural frequency in an inverse manner, that is the greater the mass of any system, the lower its natural frequency. However, changing the mass of the system is not the only method available for changing the natural frequency of a PZH. Effective mass refers to the overall center of gravity of the system. For a greater effective mass, the center of gravity needs to be concentrated towards the free end of the PZH to increase the excitation force and vice versa. This

results in greater overall inertia of the system and therefore a reduction in natural frequency.

Based on the research of others, it is found that there are also other methods that can be modeled such as adding magnetic forces and even using additional actuators, both of which also alter the natural frequencies of an oscillating system. Other physical parameters that are not covered in this study may also be tested. These however are more difficult to model both in terms of resources and accuracy, and will be designated as future work.

References

[1] T. Dikshit, D. Shrivastava, A. Gorey, A. Gupta, P. Parandkar and S. Katiyal, "Energy Harvesting via Piezoelectricity," *BVICAM's International Journal of Information technology (BIJIT)*, Vol. 2, No. 2, 0973-5658, 2010.

[2] N. Patel and S.K. Dewangan, "Piezoelectric Energy Harvesting," *International Conference of Advance Research and Innovation (ICARI-2015).*

[3] P. J. Cornwell, J. Goethal, J. Kowko, and M. Damianakis*, J. Intell. Mater. Syst. Struct. 16(10*), 825–834 (2005).

[4] X. Wu, J. Lin, S. Kato, K. Zhang, T. Ren, and L. Liu, "A frequency adjustable vibration energy harvester," in *Proceedings of PowerMEMS*, Sendai, Japan, 2008.

[5] S.W. Ibrahim and W.G. Ali, "A review on frequency tuning methods for piezoelectric energy harvesting systems," *Journal of Renewable and Sustainable Energy*, Vol. 4, 062703, 2012.

eureca 2017 – Conference Paper
Paper Number CE-UG001

Batch Removal of Manganese Using Modified Palm Kernel Shell

Ayu Haslija A.B[1*], Trilokesh R.M[2], Rajesh Nithyanandam[3]

[1,2] *Dept. of Chemical and Petroleum Engineering, UCSI University Kuala Lumpur, Malaysia*
[3]*School of Engineering, Taylor's University, Taylor's Lakeside Campus, No. 1 Jalan Taylor's, 47500, Subang Jaya, Selangor DE, Malaysia*

[*]chik_ija@yahoo.com

Abstract
In this study, palm kernel shell modified with task- specific ionic liquid, (3-chloro-2-hydroxypropyl trimethylammonium chloride) (CHMAC) was used as a novel composition for the removal of manganese from aqueous solutions in water samples through a batch-adsorption technique. The effect of pH and adsorbent dosage of manganese ions removal efficiency were examined. The maximum percentage removal of manganese was 97.95% using 10 mg/L concentration of $KMnO_4$ solution with an adsorbent dosage of $10gL^{-1}$ at the pH 5. The experimental data were fitted well with the linear form of Langmuir model, conforming that the monolayer adsorption capacity of manganese ions onto modified palm kernel shell.

Keywords: Adsorption, Batch, Manganese, Isotherms, Palm Kernel Shell, Langmuir

1. Introduction

The pollution by heavy metal ions is one of the most serious environmental problems. Effluents resulting from daily domestic and industrial activities may induce considerable changes in the physical and chemical properties of the river water. These changes may greatly alter the environmental characteristics of river[1].

This study focused on one of the heavy metal which is Manganese. The most common health problems in workers exposed to high levels of manganese involve the nervous system. These health effects include behavioral changes and other nervous system effects, which include movements that may become slow and clumsy. This combination of symptoms when sufficiently severe is referred to as "manganism." Other less severe nervous system effects such as slowed hand movements have been observed in some workers exposed to lower concentrations in the work place. The inhalation of a large quantity of dust or fumes containing manganese may cause irritation of the lungs which could lead to pneumonia.

Many studies have been conducted to determine the best methods for the removal of metal ions from water namely: chemical precipitation, ion-exchange, electrochemical deposition, solvent extraction and adsorption. Among these methods, adsorption has been shown as the most appealing in terms of economic and an environmental friendly procedure to remove heavy metals in wastewater [2].

Palm oil mills in Malaysia produce about 4.3 million tonnes of shell annually [3]. One of the significant problems in the palm fruit processing is managing of the wastes generated during the process [4]. Many palm oil mills burn the biomass in incinerators which creates serious environmental pollution and also offers small value to the industry. In order to make better use of this cheap and abundant agricultural waste, the palm kernel shell can be used as an absorbent in heavy metal removal.

Many of the residues of oil palm harvesting and processing are valued for various applications. Palm kernel shell has been laid on roads to improve vehicular traction along plantation farms where there are no tarred roads [5]. Street making is another application that can possibly advantage after utilizing palm kernel shell as material filler. It is prescribed that for vigorously trafficked streets, palm portion shell can supplant totals of stone dust and bitumen in 10% mixes with asphalt. Complete substitution of conventional totals is workable for daintily trafficked streets in rural settings. Indeed, even the halfway removal of bitumen will decrease human and biological system poisonous quality levels connected with roadways, as bitumen contains polyaromatic hydrocarbons, a few of which known as cancer-causing agents [6].

Malaysia accounts for 39% of the world's palm oil production and is the world's second biggest palm oil exporter, after Indonesia. Malaysia planted a total area of 5.03 million hectares of oil palms in June 2012 [22], and produced 17 million tons of palm oil from January 2012 to November 2012 [23]. The process of crude palm oil extraction from fresh fruit bunches produces few types of agricultural waste, namely empty fruit bunch (EFB), palm kernel shell (PKS), fiber, and palm oil mill effluent (POME). The estimated percentage of palm oil mill waste produced is 14.6% of EFB, 10.4% PKS, 15.4% of fiber, and 6.3% POME on the basis of dry weight of fresh fruit bunch (FFB)

[24] (Yusoff 2006). Ng et al. (2012) reported that in the year 2010, Malaysia produced a total of 86.90 million tons of palm oil biomass and 5.2 million tons of palm kernel shell (PKS). PKS is a more suitable adsorbent material than other palm oil waste because of its high mechanical strength, porous surface, chemical stability, variable surface functional groups, and insolubility in water [20].

The aim of this paper is to assess the ability of modified palm kernel shell to adsorb manganese ions from aqueous solutions. The effect of initial pH of the solution and dosage of the adsorbents on the removal of manganese ions were studied. The equilibrium data of adsorption process were then analyzed to study the adsorption isotherms of manganese ions on modified palm kernel shell.

2.0 Experimental Procedure

2.1 Preparation of $KMnO_4$ Stock Solution

The stock solution of $KMnO_4$ was prepared in the university laboratory. 0.2877g of $KMnO_4$ was carefully weighted and mixed with 1L of distilled water. The stock solution was prepared for 100ppm concentration in 1L volumetric flask and then poured inside a 1L stock solution bottle. The stock solution bottle was kept away from the sunlight to avoid colour degradation.

2.2 Preparation of PKS

The raw PKS was collected from Seri Ulu Langat Palm Oil Mill in Dengkil, Selangor. (Fig. 1) The PKS was left to dry under the sun for several days. The fibers of the PKS were then removed, washed and was placed in a closed container and kept at room temperature. The PKS were dried in oven for 24 hours at the 60°C to remove excess moisture [20].



Figure 1. Raw palm kernel shell

2.3 Modification of PKS

The PKS was washed with acetone for to remove the excess oil. Then, the PKS was dried in oven for 24 hours at the 60 °C. The dried PKS was grinded and sieved to size between 1mm to 600µm. The granular PKS was mercerized with 60 wt.% of NaOH and was left for 24 hours to let the PKS fiber to swell. (Fig. 2) The mercerized PKS

was washed with distilled water repeatedly until the pH reaches 7. Then, the PKS were dried in oven for 24 hours at the 60°C [20].



Figure 2. Palm kernel shell mercerized with 60 wt.% NaOH

The dried mercerized PKS was weighted. Each gram of the PKS was reacted to a solution consisting of 1.5: 4 w/w ratio of NaOH and (3-chloro-2-hydroxypropyl) trimethylammonium chloride (CHMAC) respectively. The mixture was kept in sealed container at room temperature for 24 hours. Then the PKS was mixed with 0.2 wt.% acetic acid solution to stop the reaction. The PKS was then washed with distilled water until the pH of the solution reaches 7. The modified PKS were dried in oven for 24 hours at the 60°C (Fig. 3) [20].



Figure 3. Modified Palm kernel shell

2.4 Point of Zero Charge (pH_{PZC})

1 gL^{-1} of modified PKS was added into 5 Erlenmayer flasks containing 100mL $NaNO_3$. The initial pH of the solutions was set to 2, 4, 6, 8, and 10 by using either 0.1M HCl or 0.1M NaOH. The solutions were stirred for 24 hours to reach equilibrium. The pH of the solutions was noted. The difference the initial and final pH values was plotted against the initial pH to determine the point of zero charge.

2.5 Batch Sorption Studies

The effect of initial pH of solution on equilibrium uptake on manganese ions was analyzed. 1 gL^{-1} of modified PKS was added into 6 Erlenmayer flask containing 100ml $KMnO_4$ solution of 10mg/L concentration. The initial pH of the solutions was adjusted from the pH 3 to pH 8 by using either 0.1M HCl or 0.1M NaOH. The solutions were stirred at 150rpm for 2 hours using orbital shaker. After the adsorption, the pH value providing the maximum manganese removal was determined.

For the effect of adsorbent dosage, a selected dosage of the modified PKS (1, 1.5, 10 and 15 gL^{-1}) was added into 4 Erlenmayer flask containing 100ml $KMnO_4$ solution of 100mg/L concentration. The pH of each solutions was set to pH 5. The solutions were stirred at 150rpm for 2 hours using orbital shaker. After the adsorption, the dosage value providing the maximum manganese removal was determined.

The percentage of manganese removal was calculated using Eq. (1):

$$Removal\ \% = \frac{C_o - C_e}{C_o} \quad (1)$$

where C_o and C_e are the initial and equilibrium concentrations of manganese ion (mg/L) in the solution.

2.6 Adsorption Isotherms

Adsorption properties and equilibrium parameter indicate the nature of the adsorbate adsorbents indication. Three different isotherms such as Langmuir, Freundlich and Temkin models were applied in this study for analyzing experimental sorption parameter so get some important information on the surface properties of the adsorbent and its affinity to the adsorbate.

3.0 Results & Discussion

3.1 Point of Zero Charge

The value of the pH needed to influence a net zero charge on as solid surface in the absence sorption is called the point of zero charge. Theoretically, if the pH value is less than the pH_{PZC} value, the surface of the adsorbent is positively charged. On the contrary, if the pH value is more than the pH_{PZC} value, the surface of the adsorbent is negatively charged [20][21]. The effect of pH on the adsorption of manganese ions on modified PKS has been studied by varying it in the ranges of 3-8 as shown in Fig. 5.

From the graph (Fig. 4), the point of zero charge was determined to be at pH 7. At this pH the modified palm kernel shell was at neutral charge. When the pH is more than 7, the surface of the adsorbent will be negatively charged. This is due to the OH^- ions presents at the adsorbent surface. The OH^- ions will attract all the cations on its surrounding to the active side. This site of adsorbent is more suitable to attract positive charged material [20][22].

On the contrary, when the pH is less than 7, the surface of the adsor bent will be positively charged. This is due to the H^+ ions present at the adsorbent surface. The H^+ ions present will attract the all the anions on its surrounding to the active site. This site of adsorbent is more suitable to attract negative charged material.

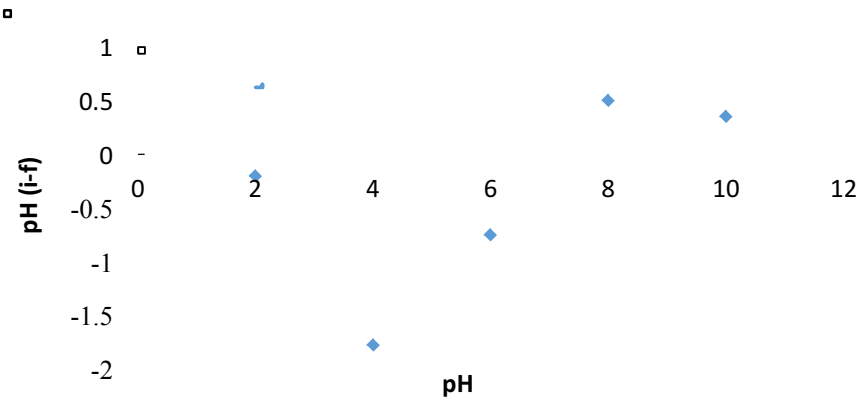


Figure 4. Point of zero charge (pH_{PZC}) of modified PKS

Since the manganese in the $KMnO_4$ solution is negatively charged, the modified PKS below the pH 7 is suitable to carry out the experiment as the adsorbent aids anion adsorption. From the graph, the most positive surface at pH 4 and most negative surface at pH 8.5.

3.2 Effect of Initial pH

Adsorption capacities of the adsorbents are strongly dependent on the initial solution pH. Initial pH has been shown to affect the magnitude of negative and positive charge on the adsorbent surface and the adsorbent capacities [7]. The effect of pH on the adsorption of manganese ions on modified PKS has been studied by varying it in the ranges of 3–8 as shown in Fig. 5. Fig. 5 shows the adsorption capacity of the modified PKS on the solution increased rapidly from the pH 3 to pH 5. It was found that the percentage removal of manganese was 71.5% at pH 3, 74.4% at pH 4 and 86.2% at pH 5.

Maximum adsorption at acidic pH indicates increased in H+ ions on the adsorbent surface at the low pH. This results in strong electrostatic attraction between positively charged modified PKS and manganese ions.

The adsorption capacity of the modified PKS on the solution decreases rapidly from the pH 6 to pH 8. It was found that the percentage removal of manganese was 77.4% at pH 6, 74.4% at pH 7 and 71.5% at pH 8. This adsorption capacity decrease is due to adsorbent surface attracts cations to the active sites. Therefore, the manganese removal decreases as more cations such as potassium are adsorbed into the adsorbent. The manganese ion was repelled from attaching to the adsorbent as the pH increases as the OH^- ions start to attach to the active sites of the adsorbent. This also might be caused by partial hydrolysis of Mn(II) ions with increasing pH, formations of complexes with OH^- such as $Mn(OH)^+$, Mn(OH)2, $Mn2(OH)3^-$, $Mn2OH^{3+}$ and $Mn(OH)4^{2-}$ species in solution.

Consequently, Mn-hydroxyl species might participate in the adsorption and/or precipitate onto the adsorbent structure. From Fig. 6, the optimum removal of manganese was found to be at the pH 5 which was 86.2%. The modified PKS adsorbed

best at pH 5. A similar phenomenon was observed for the adsorption of manganese from aqueous solution from activated carbon Ziziphus seed [8].

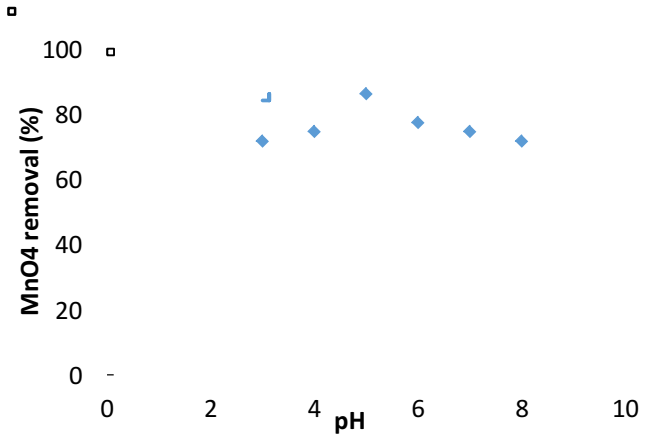


Figure 5. Effect of initial pH on manganese removal

3.3 Effect of Adsorbent Dosage

The adsorption studies on manganese ions on modified PKS by varying the quantity of adsorbent of 1, 1.5, 10 and 15 gL^{-1}. The influence of adsorbent dosage in adsorption of manganese ions is shown in Fig. 6 which can be observed that manganese removal percentage increases as the dosage increases. From the experiment; the percentage removal was increased from 56.7% to 97.8% with the increase of 1gL^{-1} to 10 gL^{-1}. This positive relationship between the adsorbent dosage and the manganese removal due to the number of active sites available for the adsorption of manganese ions presents in the solution increases and subsequently the removal capacity increases [9]. Yet, further increase in the adsorbent dosage results the removal of remaining manganese was remained constant. This could due to the saturation of the binding sites in the adsorbent [10]. Therefore, the optimum dosage for manganese removal was 10 gL^{-1}. The modified PKS adsorbed maximum manganese at 10gL^{-1}.

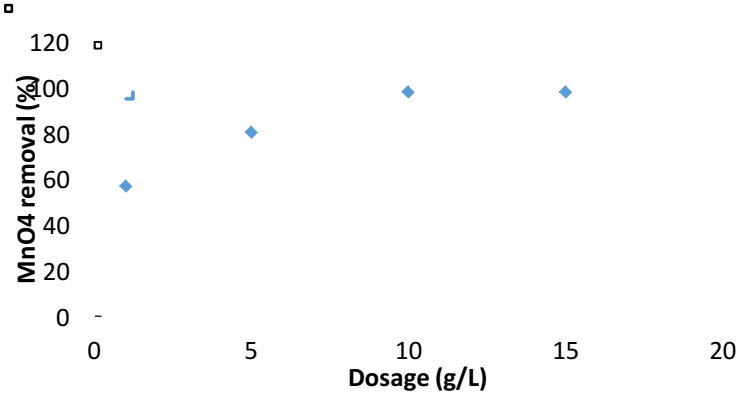


Figure 6. Effect of adsorbent dosage on manganese removal

3.4 Adsorption Isotherm

The adsorption isotherms reveal the specific relation between the concentration of the adsorbate and its adsorption degree onto adsorbent surface at a constant temperature. To quantify the adsorption capacity of modified PKS for the removal of manganese ions from aqueous solution, the Langmuir, Freundlich and Temkin isotherm models were used.

3.4.1 Langmuir Isotherm Model

This model assumes that the adsorption occurs at specific homogeneous sites on the adsorbent. The Langmuir model was used successfully in many monolayer adsorption process [11]. The linear equation of the Langmuir isotherm model is shown by Eq. (2) [12].

$$\frac{C_e}{Q_e} = \frac{1}{b\,Q_m} + \frac{C_e}{Q_m} \qquad (2)$$

where q_e is the amount of manganese adsorbed on modified PKS (mg/g), b is the adsorption equilibrium constant (L/mg) and Q_m is the maximum adsorption capacity.

A plot of C_e/q_e against C_e gives the adsorption coefficient. (Fig. 7). The related parameters were calculated and reported in Table 1. The correlation coefficient, R^2 value of 0.997 indicated the adsorption data of manganese ions onto modified PKS was well fitted to the Langmuir isotherm model.

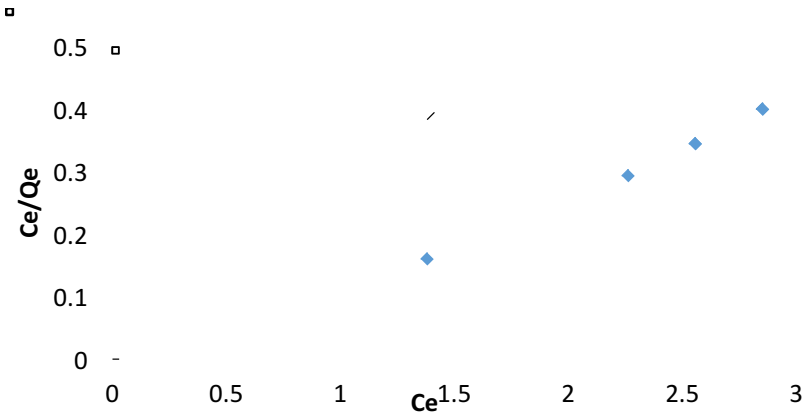


Figure 7. Langmuir isotherm model plot for manganese ions adsorption

3.4.2 Freundlich Isotherm Model

The Freundlich isotherm model can be applied for non-ideal adsorption on heterogeneous surfaces and multilayer adsorption [13]. The linear equation of the Freundlich isotherm model shown by Equation (3) [14].

$$\log q_e = \log K_f + \frac{1}{n}\log C_e \quad (3)$$

where K_F is Freundlich equilibrium constant and n is an empirical constant. A plot of log q_e against log C_e gives the adsorption coefficient. (Fig. 8). The related parameters were calculated and reported in Table 1. Freundlich type adsorption isotherm is an indication of surface heterogeneity of the adsorbent while Langmuir type isotherm hints towards surface homogeneity of the adsorbent.

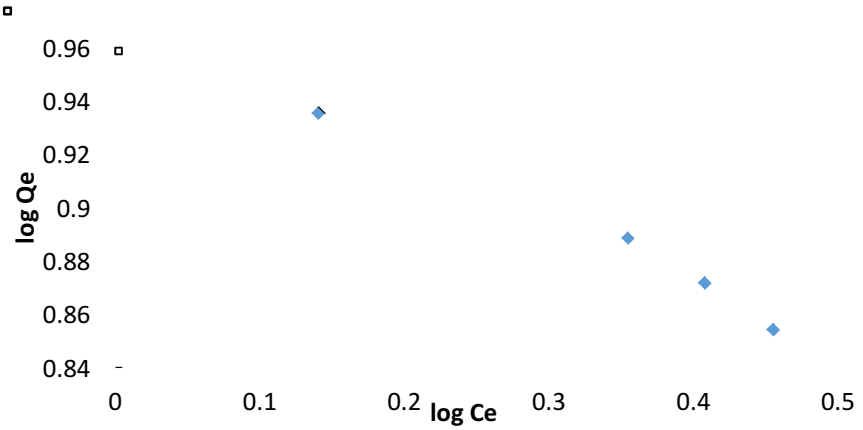


Figure 8. Freundlich isotherm model plot for manganese ions adsorption

3.4.3 Temkin Isotherm Model

Temkin and Pyzhev [15], suggests the effects of indirect adsorbate or adsorbate interaction on adsorption isotherms. The Temkin isotherm model assumes the due to adsorbent and adsorbate interaction, the heat of adsorption for all the molecules in the layer decreases proportionally with coverage. The adsorption is portrayed by a constant distribution, of binding energies [16]. The linear equation of the Temkin isotherm model shown by Eq. (4) [17].

$$q_e = B \ln K_t + B \ln C_e \quad (4)$$

where B=RT/b, K_t is the equilibrium binding constant (L/mg) and B is the heat of adsorption. A plot of q_e against ln C_e gives the adsorption coefficient. (Fig. 9). The related parameters were calculated and reported in Table 1.

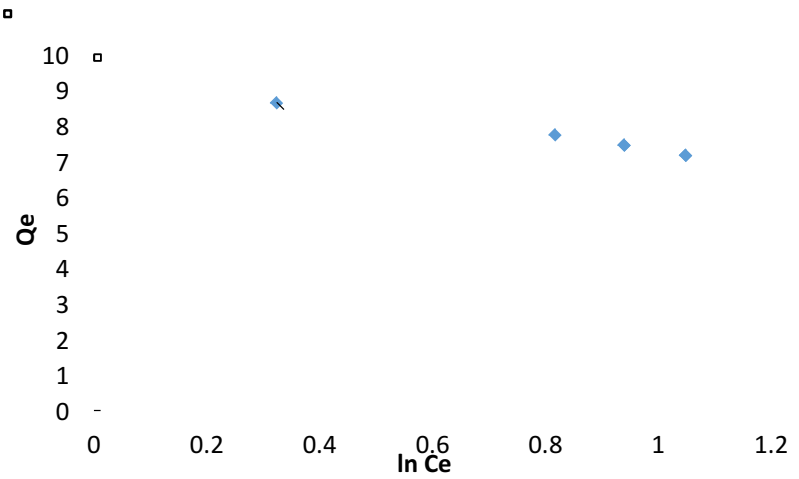


Figure 9. Temkin isotherm model plot for manganese ions adsorption

Table 1 shows the related parameters for the adsorption of manganese ions on modified PKS. From Table 1, the Langmuir adsorption model produce the best fit for the adsorption based on the highest R^2 value among the three isotherm models.

Table 1: Langmuir, Freundlich and Temkin Isotherm Models Parameters for the Adsorption of Manganese ions on Modified PKS.

Isotherm's Parameters	Parameter's Value
Langmuir	
Q_m (mg/L)	6.238
K_L (L/mg)	2.451
R^2	0.997
Freundlich	
K_F (mg/g)	9.407
n	3.39
R^2	0.986
Temkin	
K_T (L/mg)	0.001
B	-2.007
R^2	0.991

Table 2 shows the comparison of manganese adsorption results of modified PKS with other adsorbent.

Table 2: Comparison of Manganese Removal by Modified PKS with Other Adsorbent

Adsorbents	***Percentage Removal (%)***	***Fitted Isotherm Model***	***Reference***
Granular activated carbon	79.05	Langmuir	**[1]**
Amberlite IR-120H	96.65	Langmuir	**[1]**

Ziziphus spina-christi seeds activated carbon	93.12	Langmuir	**[8]**
Microporous chitosan	87.5	Freundlich	**[18]**
Polyethylene gycol	85.71	Freundlich	**[18]**
Clinoptilolite natural zeolite	81.5	Langmuir	**[19]**
Modified palm kernel shell	97.95	Langmuir	**This study**

4.0 Conclusion

In this study, the palm kernel shell was modified with using (3-chloro-2-hydroxypropyl) trimethylammonium chloride solution. The modification was huge success as the adsorbent able to remove the manganese ion from the aqueous solution prepared which was potassium permanganate, $KMnO_4$. A maximum removal of 97.95% was achieved using the 10 mg/L concentration of $KMnO_4$ solution with an adsorbent dosage of $10gL^{-1}$ at the pH 5. For the adsorption isotherm study, three isotherms were studies. They were Langmuir isotherm model, Freundlich isotherm model and Temkin isotherm model. Equilibrium data fitted very well in the Langmuir isotherm model equation, conforming that the monolayer adsorption capacity of manganese ions onto modified palm kernel shell.

Future work is recommended to adsorb different type of heavy metal or pollutants using the modified palm kernel shell.

Acknowledgement

Authors are grateful to UCSI University for the financial support of this research.

References

[1] Mohamed E. Goher, A. M.-M.-s. (2015). Removal of aluminum, iron and manganese ions from industrial wastes using granular activated carbon and Amberlite IR-120H. Egyptian Journal of Aquatic Research, 1-10.

[2] B.M. Richard, Heavy Metals, Introduction to Environmental Toxicology, Elsevier,New York, 1980.

[3] Z.Husain, Z. Z. (2003). Analysis of biomass-residue-based cogeneration system in palm oil mills. Biomass and Bioenergy 24 , 117 – 124.

[4] Tan, I. A. (2008). Adsorption of basic dye using activated carbon prepared from oil palm shell: batch and fixed bed studies. Desalination 225, 13–28.

[5] Okoroigwe, E. C. (2014). Characterization of palm kernel shell for materials reinforcement and water treatment. Journal of Chemical Engineering and Materials Science, 1-6.

[6] Ndoke, P. (2006). Performance of palm kernel shells as a partial replacement for coarse aggregate in asphalt concrete. Leonardo Electronic J. Pract. Tech., 145-152.

[7] Ho, Y. (1994). The adsoption of divalent copper ions from aqueous solution by sphagnum moss peat. Process Saf. Environ. Prot., 185-104.

[8] Omri, A. (2012). Removal of manganese(II) ions from aqueous solutions by adsorption on activated carbon derived a new precursor: Ziziphus spina-christi seeds. Alexandria Engineering Journal 51, 343–350.

[9] Casqueira, R. (2006). The removal of zinc from liquid streams by electroflotation. Minerals Engineering, 1388–1392.

[10] Mohan, S. (2009). Removal of heavy metal ions from municipal solid waste leachate using coal fly ash as an adsorbent. Journal of Hazardous Materials, 351–359.

[11] Langmuir, I. (1918). The adsorption of gases on plane surfaces of glass, mica and platinum. J. Am. Chem. Soc. 40, 1361–1403.

[12] Homagai, P. G. (2010). Adsorption behavior of heavy metals onto chemically modified sugarcane bagass. Bioresour Technol. 101, 2067–2069.

[13] Freundlich, H. (1907). Ueber die adsorption in Loesungen. Z. Phys. Chem. 57, 385–470.

[14] Feng, N. G. (2009). Adsorption study of copper(II) by chemically modified. J. Hazard. Mater.164, 1286-1292.

[15] Pyzhev, M. J. (1940). Recent Modifications to Langmuir Isotherms. Acta Physical Chemistry, Vol. 12, 217-222.

[16] Angın, D. (2014). Utilization of activated carbon produced from fruit juice industry solid waste for the adsorption of Yellow 18 from aqueous solutions. Bioresour. Technol. 168,, 259–266.

[17] Cheng, Z. Z. (2015). Adsorption behavior of direct red 80 and congo red onto activated carbon/surfactant: Process optimization, kinetics and equilibrium. Spectrochimica Acta Part A: Molecular and Biomolecular Spectroscopy, 1126–1143.

[18] Neama A. Reiad, O. E. (2012). Adsorptive removal of iron and manganese ions from aqueous solutions with microporous chitosan/polyethylene glycol blend membrane. Journal of Environmental Sciences, 1425–1432.

[19] M.A. Shavandi, Z. H. (2012). Removal of Fe(III), Mn(II) and Zn(II) from palm oil mill effluent (POME) by natural zeolite. Journal of the Taiwan Institute of Chemical Engineers, 750–759.

[20] Abu Bakar, A., Koay, Y., Ching, Y., Abdullah, L., Choong, T., Alkhatib, M., Mobarekeh, M., & Mohd Zahri, N. (2016). Removal of Fluoride using Quaternized Palm Kernel Shell as Adsorbents: Equilibrium Isotherms and Kinetics Studies. BioResources, 11(2), 4485-4511. doi:10.15376/biores.11.2.4485-4511

[21] I. D. Smičiklas, S. K. Milonjić, P. Pfendt, and S. Raičević, "The point of zero charge and sorption of cadmium (II) and strontium (II) ions on synthetic hydroxyapatite," *Sep. Purif. Technol.*, vol. 18, pp. 185–194, 2000.

[22] T. Nur, P. Loganathan, T. C. Nguyen, S. Vigneswaran, G. Singh, and J. Kandasamy, "Batch and column adsorption and desorption of fluoride using hydrous ferric oxide: Solution chemistry and modeling," *Chem. Eng. J.*, vol.

247, pp. 93–102, Jul. 2014.

eureca 2017 – Conference Paper
Paper Number PG01

Effective extraction of natural antioxidants from *Piper betle* with the aid of ultrasound: Temperature extraction kinetics

Ameena Ali[1]*, Bee Lin Chua[1], Chien Hwa Chong[1], Siau Hui Mah[2],
[1]*School of Engineering, Taylor's University, Lakeside Campus, Malaysia*
[2]*School of Biosciences, Taylor's University, Lakeside Campus, Malaysia*

ameenaali@ymail.com

Abstract

Medicinal herbs are rich source for natural antioxidants that can serve as excellent alternative to synthetic counterparts. Present study involves the recovery of natural antioxidants from the medicinal herb, *Piper betle* with the aid of ultrasound. The extraction kinetics for the parameter of temperature (50, 60 and 70^{o}C) was investigated. Experimental data were obtained in the form of extraction yield, total phenolic content and DPPH (1,1-diphenyl-2-picrylhydrazyl) antioxidant activity. Highly negative influence on the final outcomes by temperature was observed that were consequence of thermal degradation. The best results were acquired at 50^{o}C extraction temperature. Kinetic modelling was done by fitting the extraction curves to three different models to best describe the solid-liquid extraction of the antioxidants. The three models of interest for this study included the two site kinetic model, page's model and logarithmic model. Based on the statistical analysis, high coefficient of determination and low root mean square error for two site kinetic model (R^2≥0.98 and RMSE≤0.30) confirms it to be the best suited model to express the extraction of antioxidants from *Piper betle*.

Keywords: Piper betle, Ultrasound, Antioxidants, Modelling

1. Introduction

Chronic diseases are identified as prolonged diseases effecting one's health over long period of time. Upsurging chronic health complications including cardiovascular diseases, diabetes and various forms of cancer are result of oxidative stress, a term used to define the potential damage caused by reactive oxygen species (ROS) or free radicals [1]. Free radicals are highly unstable molecules generated as byproduct of metabolism. Nonetheless, certain risk factors such as pollution, cigarettes smoking and radiation may result to the overproduction of these free radicals. As a result, excessive oxidative stress caused by the free radicals can cause cellular as well as physiological damage [1], [2]. The intake of antioxidants is one preventative method of counteracting the free radicals, as they scavenge and react with the ROS species and even enhancing their decomposition. Damaging oxidation reaction to macromolecules such as DNA, lipids and protein can be inhibited by antioxidants [3]. Thereby, the ever growing drive by researchers to identify natural antioxidants from safer sources as alternatives.

Throughout the years, medicinal herbs and herbal extracts have been identified to posses numerous medicinal and nutritional properties in the prevention and treating of diseases due to the presence of natural bioactive compounds named phenolic compounds. These secondary metabolites are responsible for the organoleptic properties together with providing protection and defence to the plants [4]. Present not only in herbs, but also in fruits and vegetables in abundance, these bioactive compounds have been found to be excellent natural antioxidants that have piqued the interests of food and pharmaceutical industries [5], [6]. *Piper betle* is such a medicinal herb known to have demonstrated high antioxidant potential *via* multiple radical scavenging activities [7], [8]. Widely cultivated in Asian regions, this indigenous plant has been proven to inhibit and reduce lipid peroxidation together with enhancing the levels of natural antioxidants [9].

Typically, the natural antioxidants from *Piper betle* would be recovered using conventional extraction techniques involving such as maceration and soxhlet extraction [10], [11]. As effective as they may be, there are some disadvantages associated to them including prolong extraction period, high energy usage and solvent consumption makes them unattractive from economic point of view, particularly in industrial applications [12]. Recent times, research has involved the application of more greener techniques that can counter balance the disadvantages with equal effectiveness. Ultrasound-assisted extraction (UAE) is among the numerous emerging techniques that relies on the mechanism of acoustic cavitation for extraction. High frequency ultrasound waves generate cavitational bubbles in the medium that disrupts the cell wall. Ultimately, mass transfer is enhanced with the increased penetration of the solvent into the plant matrix and accelerated release of the targeted components from the plant cell [13]. To the best of author's knowledge, there is sparse literature involving the application of UAE for the recovery of antioxidants from *Piper betle*. This paper aims to fill that void by investigating the influence of UAE and its respective parameter on the extraction of antioxidants through mathematical modeling.

Mathematical modeling is an effective engineering tool vital for the understanding, designing, simulation, optimizing and controlling of processes that contribute to the utilization of time, energy, solvent and raw material [14]. Solvent extraction is a solid-liquid extraction that includes highly complex mass transfer

process severely driven by extraction parameters. The application of kinetic modelling is a swift and inexpensive method of determining the kinetics of the extraction process. They can also be very useful in providing invaluable information for industrial applications. Several empirical, semi-empirical and theoretical models have been employed in the past for the extraction of bioactive compounds from different plants and herbs. Some of them include Peleg's model [15], second-order rate model [16], two site kinetic model [17], Page model [15] and Fick's law of diffusion [17] to name a few. Current study aims to study the impact of extraction temperature on the recovery of antioxidants by utilizing three kinetics models. This study also aims to determine the model among the three that best describes the extraction of antioxidants from *Piper betle.*

2. Materials and methods

2.1 Plant materials

Fresh *Piper betle* leaves were bought from Chow Kit market, Kuala Lampur, Malaysia. The leaves were washed to rid of the dirt particles. Pre-treatment of the plant include drying of the leaves at 50^{o}C for 2 days followed by grinding and sieving to obtain uniform powdered leaf samples that were used for extraction.

2.2 Chemicals

The reagents used were Fast blue BB (FBBB) and DPPH (1,1-diphenyl-2-picrylhydrazyl), both purchased from Sigma-aldrich (Sigma-aldrich GmbH, Steinheim, Germany). The solvents used include 95% ethanol, 99.9% methanol and chloroform (HPLC grade) and are of analytical grade. The remaining chemicals used include Gallic acid standard and sodium hydroxide pellets. All of the chemicals mentioned with the exception of the reagents were purchased from Sigma-aldrich (Sigma, St. Louis, MO, USA).

2.3 Ultrasound-assisted extraction procedure

For kinetic modelling, powdered leaf samples (1g) was taken in schott bottles and 30 mL of 90% ethanol solution was subjected into it. The sample was placed in an ultrasonic bath (P120 H, Elmasonic, Germany) where extraction was carried out at temperatures of 50^{o}C, 60^{o}C and 70^{o}C to investigate the influence of temperature. The range of temperature were based on existing literature for conventional means of extraction [11], [18], [19]. Samples were retained every 5 mins for a time frame of 80 mins for all respective levels. The samples were subjected to vacuum rotary evaporator (Hei-VAP Platinum 3, Heidolph, Germany) to obtain crude extract which were stored at 4^{o}C for analysis purpose.

2.4 Analysis

The extraction yield was obtained by using Eq. (1). The total phenolic content (TPC) was carried out as explained by Medina (2011) [20].

$$Extraction\ yield\ (\%) = \frac{W_c}{W_r} \times 100\% \quad (1)$$

Where W_c is the weight of the crude extract and W_r is the weight of the powdered sample. The DPPH antioxidant activity was determined as described by Pin *et al.* (2010) with the equation presented in Eq. (2) [11].

$$DPPH\ inhibition\ (\%) = \frac{Abs_{control} - Abs_{sample}}{Abs_{control}} \times 100\% \quad (2)$$

Where $Abs_{control}$ and Abs_{sample} denotes the absorbance of blank solution containing DPPH solution only and absorbance of extract sample solution with DPPH respectively. All of the analysis were carried out in triplicates and the results expressed in this paper are mean of the triplicated experimental data.

2.5 Kinetic modelling for extraction temperature

To investigate the kinetics of the extraction of the solid-liquid extraction, mathematical modelling was carried out. The three models applied in current research were two site kinetic model, Page's model and logarithmic model. The two site kinetic model is given in Eq. (2) [17].

$$\frac{M_t}{M_\infty} = 1 - Fe^{-k_1 t} - (1 - F)e^{-k_2 t} \quad (2)$$

Where M_t and M_∞ are the concentration of the phenolic compounds extracted from the raw material at any given and infinite time respectively. *F* and (1-F) represents the fraction of the solute released during the fast and slow extraction stages. k_1 and k_2 are the first order rate constants. Page's model can be expressed as Eq. (3) [15].

$$c(t) = e^{-kt^n} \quad (3)$$

Where *k* and *n* are the Page model's constants and *c(t)* represents the concentration of the phenolic compounds at any given time. The logarithmic model can be written as Eq. (4) [21].

$$c(t) = alogt + b \quad (4)$$

Where *a* and *b* are Logarithmic model's constants and *c(t)* represents the concentration of the phenolic compounds at any given time. The Arrhenius equation was used to further investigate the influence of temperature which is expressed in Eq. (5).

$$k = k_o\, exp\left(-\frac{E_a}{RT}\right) \quad (5)$$

Where k_o and E_a are the temperature-independent factor and activation energy whereas *T* and *R* are the extraction temperature and gas constant respectively.

2.6 Statistical analysis

The kinetic coefficients was determined by fitting the experimental data to the general models using Matlab 2017a (The MathWorks Inc., USA). The predicted

coefficients were analysed based on two statistical criteria, coefficient of determination (R^2) and root mean square error (RMSE) given in Eqs. (6) and (7) respectively.

$$R^2 = \frac{\sum_{i=1}^{n}(y_i - \hat{y}_i)^2}{\sum_{i=1}^{n}(y_i - \bar{y})^2} \quad (6)$$

$$RMSE = \sqrt{\frac{\sum_{i-1}^{n}(y_i - \hat{y}_i)^2}{n}} \quad (7)$$

Where y_i and $\hat{y}_i$ predicted and experimental values of TPC respectively. *n* denotes the number of experiments carried out.

3. Results and discussion

3.1 Ultrasound-assisted extraction of phenolic compounds

Present study involves the extraction of antioxidants from *Piper betle* with the aid of ultrasound. The application of ultrasound saw a major difference in the final outcomes in comparison to conventional extraction techniques. The experimental data revealed the best results to be extraction yield of 17.75% with TPC and DPPH antioxidant activity of 307.18 mgGAE/gDW and 98.21% inhibition respectively within 30 minutes into extraction. Nouri *et al.* reported a TPC of 203 mgGAE/gDW from *Piper betle* using the maceration extraction method with the same solvent concentration [22]. However, different other extraction parameters were used including the solute to solvent ratio of 1:100 g/mL with an extraction period of 24 hours. That being said, even with such high solvent amount and extraction period still recovered lesser phenolic compounds than current study. Despande and Kadam (2013) applied the soxhlet extraction method on *Piper betle* with the parameter of 1:10 g/mL ratio to report findings of only 9% extraction yield with an extraction duration of 6 hours [23]. The author Pin *et al.* (2010) used extraction parameters of ratio 1:30 g/mL for an hour of extraction time with maceration method that is highly similar to current research [11]. In spite of that, the author reported an average extraction yield of 11% for ethanolic *Piper betle* extracts. The major difference in the findings of the studies mentioned above can be attributed to the different extraction techniques applied.

Maceration is an extraction technique that involves the dissolving of the plant material in the desired solvent for the extraction of the targeted materials. Soxhlet extraction involves the vaporisation of the extracting solvent that passes through the plant material to dissolve the targeted compounds [24]. Both of these extraction techniques are driven by some form of disadvantages as previous studies have shown both techniques to involve high solvent usage and tedious extraction periods. The use of ultrasound can counteract the undesired drawbacks with its cavitation mechanism. The disruption of the plant cell wall that is the result of the imploding cavitational bubbles releases the contents from within the plant material with much ease. Furthermore, the mechanical and thermal effects improves the penetration of solvent into the plant matrix making it comparatively easier for the solvent to dissolve the phenolic compounds. Thereby, with enhanced overall mass transfer, the recovery of the phenolic compounds is much more efficient and effective in shorter period without the usage of excess solvent. Jovanović *et al.* (2017) reported the recovery of TPC from the herb *Thymus serpyllum* L. using UAE for 5 mins which was more than the TPC recovered using maceration for 60 mins [25]. The author also reported that the TPC

obtained with the lowest ratio of 1:10 g/mL for UAE was marginally lesser than the TPC recovered with 1:30 g/mL for maceration. The results by Jovanović *et al.* are alignment with present research that the use of ultrasound garnered better TPC with lesser solvent usage and reduction of extraction period from hours to mere minutes.

3.2 Effect of extraction temperature on yield, total phenolic content and DPPH antioxidant activity

In this research, the influence of the parameter temperature on extraction kinetics was investigated. Three different temperature levels were chosen based on existing literature for conventional extraction techniques. An interesting observation was made as the experimental data revealed the highest extraction yield of 17.75% for the extraction temperature of 70^{o}C. Contrary to this, the best TPC and DPPH activity of 307.18 mgGAE/gDW and 98.21% inhibition respectively were obtained for 50^{o}C extraction temperature instead. Literature supports the fact that increase in temperature facilitates the extraction process as reported by Tuˇsek *et al.* (2016) in the extraction of polyphenols from Asteraceae plants. The author reported that the best results obtained on an average was with extraction temperature of 80^{o}C [15]. The application of high temperature facilities the mass transfer process and the extraction of desired compounds regardless of the extraction method used [12]. Therefore, the maximum extraction yield at 70^{o}C was no surprise. However, the high yield does not correspond with the TPC and DPPH as the best results for these two outcomes were recovered at 50^{o}C. Two possible explanations can explain this behaviour conveyed by this parameter.

One of the possible explanation is the release of other cellular components from the plant material with increasing temperature as reported by Shi *et al*. (2003) [26]. The author reported that the high extraction yield with increasing temperature was a result of enhanced protein and polysaccharides recovery as extreme temperature would weaken the bonds of the said compounds. Thus, the extraction of other undesired compounds would also enhance which is the most likely scenario behind the high extraction yield at 70^{o}C indicating the presence of compounds other than phenolics. The second explanation is behind the high TPC and DPPH at 50^{o}C could be the consequence of thermal degradation at high temperature. The sensitivity of the phenolic compounds to high temperature was reported in the past by Pin *et al.* (2006) [27]. The author saw decrease in one of the phenolic compound's concentration beyond extraction temperature of 60^{o}C which is in alignment with current study as the best outcomes were obtained at 50^{o}C. Therefore, this solidifies that an extraction temperature of 50^{o}C is the optimum temperature of the extraction of antioxidants from *Piper betle*.

3.4 Modeling of the kinetic parameters

Three models, two site kinetic model, Page's model and logarithmic model, were applied to understand the kinetics of the solid-liquid extraction process. In reference to the kinetic parameters in Table 26, both of the first order rate constants k_1 and k_2 gave maximum values at 70^{o}C in an increasing manner which corresponds to the presence of other components from *Piper betle*. On the otherhand, the equilibrium concentration M_∞ of the phenolic compounds were the lowest at the same temperature in a decreasing manner which corresponds to the degradation of the phenolics at 70^{o}C.

The experimental and predicted extraction curves for the total phenolic content of two site kinetic model is provided in Figure 2.

Table 26. Parameters of two site kinetic law for different extraction temperature, ratio and concentration.

Variable	Level	F	1-F	M_∞ (mg/g)	k_1 (min^{-1})	k_2 (min^{-1})	R^2	RMSE
Temperature (°C)	50	0.16	0.84	8.73	0.06	0.05	0.99	0.29
	60	0.15	0.85	6.72	0.06	0.06	0.99	0.24
	70	0.14	0.86	6.43	0.07	0.07	0.98	0.30

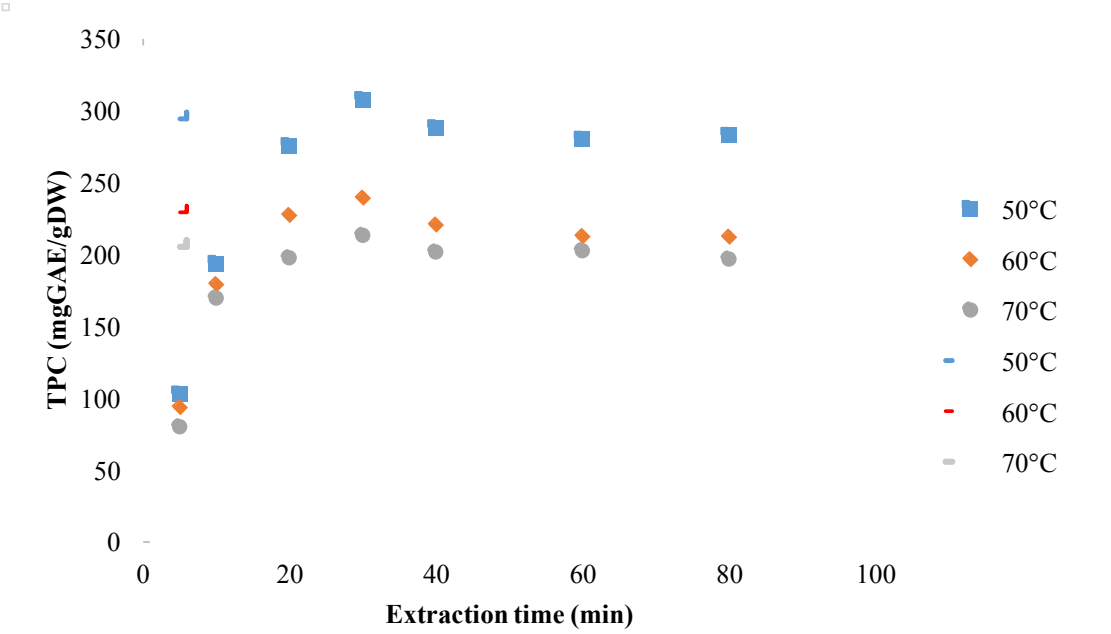


Figure 2. Experimental and predicted TPC extraction curves for Two site kinetic model

Taking Table 27 and Table 28 into consideration, vice versa results were obtained for the logarithmic and Page's model. The constant *a* for the logarithmic model gave the maximum value at 50°C while the constant *b* was the highest for 70°C. Likewise, the constant *k* for the Page's model was highest at an extraction temperature of 50°C with *n* being the highest for extraction temperature of 70°C. It is quite evident that all the models took into account of the extraction of other components as well as consequent degradation of phenolic compounds at high temperatures. The experimental and predicted extraction curves for the total phenolic content of logarithmic and Page's models are provided in

Figure *3* and Figure 4.

Table 27. Parameters of logarithmic model for different extraction temperature, ratio and concentration.

Variable	Level	*a*	*b*	R^2	RMSE
Temperature (°C)	50	2.83	4.75	0.88	0.29
	60	0.84	5.89	0.88	0.24
	70	0.94	5.13	0.95	0.30

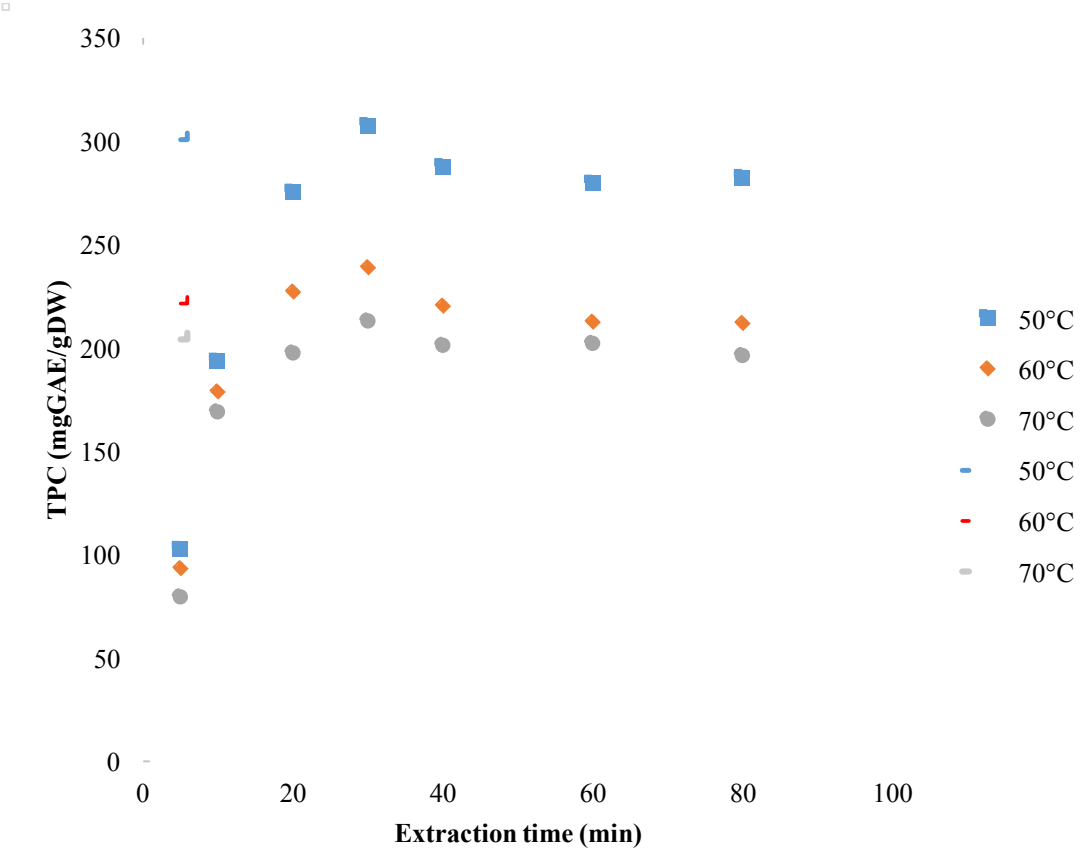


Figure 3. Experimental and predicted TPC extraction curves for the logarithmic model

Table 28. Parameters of Page's model for different extraction temperature, ratio and concentration.

Variable	Level	*k*	*n*	R^2	RMSE
Temperature (°C)	50	-1.47	0.11	0.78	5.13
	60	-1.41	0.09	0.72	3.17
	70	-1.27	0.10	0.79	2.44

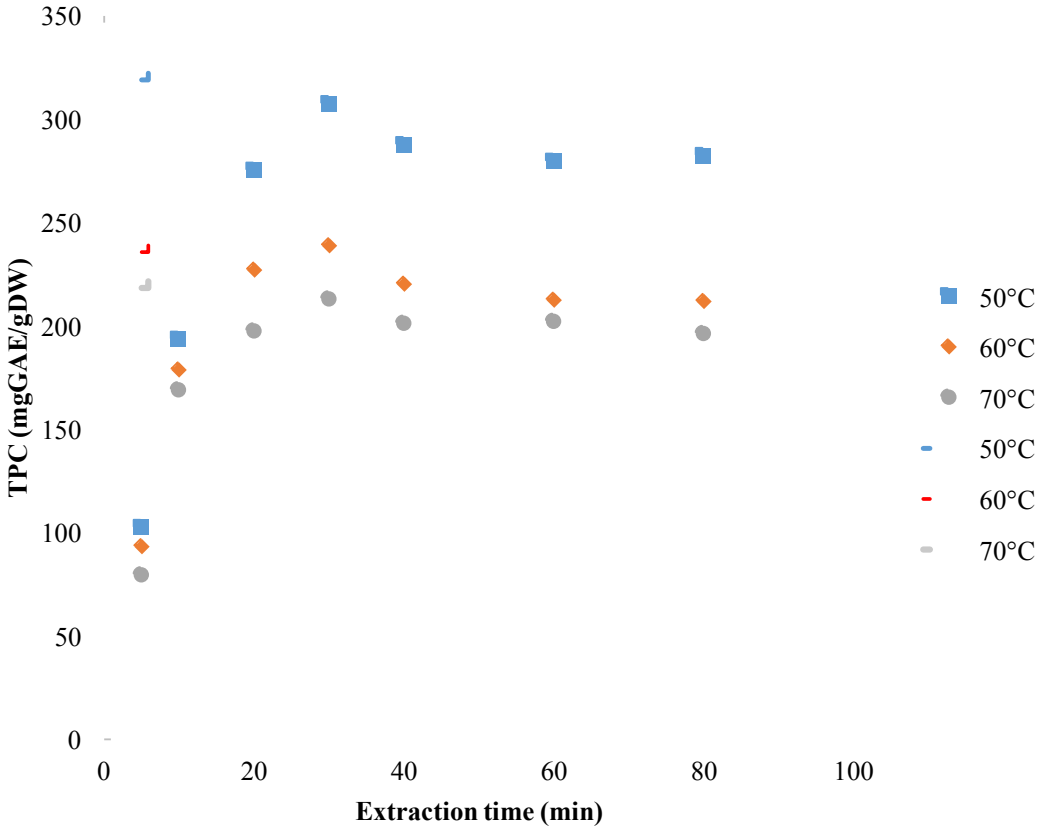


Figure 4. Experimental and predicted TPC extraction curves for Page's model

Based on the correlation coefficients from all the tables, the highest R^2 and low Root mean square error (RMSE) values ranging in between 0.98-0.99 and 0.24-0.30 were obtained for the two site kinetic models validating its accuracy. To further investigate the influence of extraction temperature, the Arrhenius law was applied to the same model to determine the two coefficients, E_a (activation energy) and k_o (temperature-independent factor). The two activation energies determined for fast and slow stages of extraction were 12.83 and 11.35 kJ/mol respectively. Positive values denotes the extraction process to be endothermic. Furthermore, the temperature dependent factor for the two stages were determined to be 6.74 and 3.65 min^{-1} respectively. González-Centeno *et al.* (2015) reported activation energies ranging in between 4.6 to 11.7 kJ/mol respectively for the extraction of phenolics from grape pomace [12]. The authors also reported activation energies for the conventional method of maceration to be in the range of 12.5 to 48.3 kJ/mol. It is evident in this case that the application of ultrasound drastically reduced the amount of energy required for effective extraction to take place. The study is in agreement with current research as very low activation energies were also obtained in this case. Similar observations were also made by Chemat *et al.* (2004) during the ultrasound-assisted extraction of carvone and limonene from caraway seeds [28].

4.0 Conclusion and future works

Present research involves the application of ultrasound-assisted extraction technique for the recovery of natural antioxidants from *Piper betle*. The kinetics of the extraction were investigating by studying the influence of temperature on the recovery

process. Experimental data were collected in the form of extraction yield, TPC and DPPH inhibition activity. Experimental data were fitted to three models: two site kinetic model, Page's model and logarithmic model to determine the kinetic coefficients that gives better understanding of the extraction process and can be employed in the future applications. Based on the analysis of the experimental results, low extraction temperature favoured the extraction of antioxidants with the best results at 50^{o}C. Two site kinetic model showed the best fit to the experimental data confirming its ability to express the extraction mechanism. The activation energies obtained were 12.83 and 11.35 kJ/mol for the washing and slow diffusion stage respectively.

In future research, the influence of more extraction parameters can be studied as literature has shown, together with temperature, the extraction process is also driven by other parameters. To take a step further, process optimizations could also be done as kinetic modelling allows to investigate the influence of one parameter as a time. Process optimization would involve the combined impact of multiple parameters at a time. Successful optimization of the extraction process could prove to be even more valuable in identifying the best combination of parameters for the recovery of phenolic compounds if they are to be utilized in food and pharmaceutical industries.

References

[1] A. Rahal, A. Kumar, V. Singh, B. Yadav, R. Tiwari, S. Chakraborty, and K. Dhama, "Oxidative stress, prooxidants, and antioxidants: The interplay," *Biomed Res. Int.*, vol. 2014:76126, pp. 1–19, 2014.

[2] D.-P. Xu, J. Zheng, Y. Zhou, Y. Li, S. Li, and H.-B. L, "Ultrasound-assisted extraction of natural antioxidants from the flower of Limonium sinuatum: Optimization and comparison with conventional methods," *Food Chem.*, vol. 217, pp. 552–559, 2017.

[3] I. S. Young and J. V Woodside, "Antioxidants in health and disease," *J. Clin. Pathol.*, vol. 54, no. 3, pp. 176–186, 2001.

[4] R. Nicholson and W. Vermerris, *Phenolic Compound Biochemistry*. Springer Netherlands, 2008.

[5] C. Kaur and H. C. Kapoor, "Antioxidants in fruits and vegetables ± the millennium's health," *Int. J. Food Sci. Technol.*, vol. 36, pp. 703–725, 2001.

[6] J. Dai and R. J. Mumper, "Plant phenolics: extraction, analysis and their antioxidant and anticancer properties," *Molecules*, vol. 15, no. 10, pp. 7313–7352, Jan. 2010.

[7] N. N. Sazwi, T. Nalina, and Z. H. A. Rahim, "Antioxidant and cytoprotective activities of Piper betle, Areca catechu, Uncaria gambir and betel quid with and without calcium hydroxide," *BMC Complement. Altern. Med.*, vol. 13, no. 351, pp. 1–12, 2013.

[8] S. G. Jaiswal, M. Patel, D. K. Saxena, and S. N. Naik, "Antioxidant properties of Piper Betel (L) leaf extracts from six different geographical domain of India," *J. Bioresour. Eng. Technol.*, vol. 2, no. 2, pp. 12–20, 2014.

[9] R. Saravanan, A. Prakasam, B. Ramesh, and K. V. Pugalendi, "Influence of Piper betle on hepatic marker enzymes and tissue antioxidant status in ethanol-treated wistar rats," *J. Med. Food*, vol. 5, no. 4, pp. 197–204, 2004.

[10] D. Chakraborty and B. Shah, "Antimicrobial, antioxidative and antihemolytic activity of piper betel leaf extracts," *Int. J. Pharm. Pharm. Sci.*, vol. 3, no. 3, pp. 192–199, 2011.

[11] K. Y. Pin, A. L. Chuah, A. A. Rashih, M. Mazura, J. Fadzureena, S. Vimala, and M. Rasadah, "Antioxidant and anti-inflammatory activities of extracts of betel leaves (Piper betle) from solvents with different polarities," *J. Trop. For. Sci.*, vol. 22, no. 4, pp. 448–455, 2010.

[12] M. R. González-Centeno, F. Comas-Serra, A. Femenia, C. Rosselló, and S. Simal, "Effect of power ultrasound application on aqueous extraction of phenolic compounds and antioxidant capacity from grape pomace (Vitis vinifera L.): Experimental kinetics and modeling," *Ultrason. Sonochem.*, vol. 22, pp. 506–514, 2015.

[13] E. Espada-Bellido, M. Ferreiro-González, C. Carrera, M. Palma, C. G. Barroso, and G. F. Barbero, "Optimization of the ultrasound-assisted extraction of anthocyanins and total phenolic compounds in mulberry (Morus nigra) pulp," *Food Chem.*, vol. 219, pp. 23–32, 2017.

[14] D. Đ. Paunović, S. S. Mitić, D. A. Kostić, M. N. Mitić, B. T. Stojanović, and J. L. Pavlovic, "Kinetics and thermodynamics of the solid-liquid extraction process of total polyphenols from barley," *Adv. Technol.*, vol. 3, no. 2, pp. 58–63, 2014.

[15] A. J. Tuˇsek, M. Benkovi´c, A. B. Cvitanovi´c, D. Valinger, T. Jurina, and J. G. Kljusuri´, "Kinetics and thermodynamics of the solid-liquid extraction process oftotal polyphenols, antioxidants and extraction yield from Asteraceae plants," *Ind. Crops Prod.*, vol. 91, pp. 205–214, 2016.

[16] L. Lazar, A. I. Talmaciu, I. Volf, and V. I. Popa, "Kinetic modeling of the ultrasound-assisted extraction of polyphenols from Picea abies bark," *Ultrason. Sonochem.*, vol. 32, pp. 191–197, 2016.

[17] Y. Tao, Z. Zhang, and D.-W. Sun, "Kinetic modeling of ultrasound-assisted extraction of phenolic compounds from grape marc: influence of acoustic energy density and temperature.," *Ultrason. Sonochem.*, vol. 21, no. 4, pp. 1461–1469, 2014.

[18] L. S. R. S. R. Arambewela, L. D. A. M. D. a M. Arawwawala, and W. D. D. Ratnasooriya, "Antidiabetic activities of aqueous and ethanolic extracts of Piper betle leaves in rats," *J. Ethnopharmacol.*, vol. 102, no. 2, pp. 239–245, Nov. 2005.

[19] A. Datta, S. Ghoshdastidar, and M. Singh, "Antimicrobial property of Piper betel leaf against clinical isolates of bacteria," *Int. J. Pharma Sci. Res.*, vol. 2, no. 3, pp. 104–109, 2011.

[20] M. B. Medina, "Determination of the total phenolics in juices and superfruits by a novel chemical method," *J. Funct. Foods*, vol. 3, no. 2, pp. 79–87, 2011.

[21] J. S., V. D., B. M., B.-K. A., P. M., and T. S, "Modelling of the process of solid-liquid extraction of total polyphenols from soybeans," *Czech J. Food Sci.*, vol. 28, no. 3, pp. 206–212, 2010.

[22] L. Nouri, A. M. Nafchi, and A. A. Karim, "Phytochemical, antioxidant, antibacterial, and α-amylase inhibitory properties of different extracts from betel leaves," *Ind. Crops Prod.*, vol. 62, no. 47–52, 2014.

[23] S. N. Deshpande and D. G. Kadam, "GCMS analysis and antibacterial activity of piper betle (linn) leaves against streptococcus mutans," *Asian J. Pharm. Clin. Res.*, vol. 6, no. 6, pp. 99–101, 2013.

[24] A. NN, "A review on the extraction methods use in medicinal plants, principle, strength and limitation," *Med. Aromat. Plants*, vol. 4, no. 3, pp. 1–6, 2015.

[25] A. A. Jovanovića, V. B. Đorđević, G. M. Zdunić, D. S. Pljevljakušić, K. P. Šavikin, D. M. Gođevac, and B. M. Bugarski, "Optimization of the extraction process of polyphenols from Thymus serpyllum L. herb using maceration, heat-

and ultrasound-assisted techniques," *Sep. Purif. Technol.*, vol. 179, pp. 369–380, 2017.

[26] J. Shi, J. Yu, J. Pohorly, J. C. Young, M. Bryan, Y. Wu, and 1, "Optimization of the extraction of polyphenols from grape seed meal by aqueous ethanol solution," *Food, Agric. Environ.*, vol. 1, no. 2, pp. 42–47, 2003.

[27] K. Y. Pin, T. G. Chuah, A. A. Rashih, M. A. Rasadah, C. L. Law, and T. S. Y. Choong, "Aqueous extraction of hydroxychavicol from Piper betle L. leaves," in *Natural Resources Engineering and Technology*, 2006, pp. 146–152.

[28] S. Chemat, A. Lagha, H. AitAmar, P. V. Bartels, and F. Chemat, "Comparison of conventional and ultrasound-assisted extraction of carvone and limonene from caraway seeds," *Flavour Fragr. J.*, vol. 19, no. 3, pp. 188–195, 2004.

eureca 2017 – Conference Paper
Paper Number PG02

Acoustic Absorption Performance of Coir Fiber- Rice Husk and Coir Fiber-Polystyrene Fibro-Granular Composites

Hasina Mamtaz[1*], Mohammad Hosseini Fouladi[2], Satesh Narayana Namasivayam[3]

Taylor's University, School of Engineering, Subang Jaya, Selangor 47500, DE Malaysia.

[*]hasina_ctg@yahoo.com

Abstract

Coir fiber and rice husk are two cost effective, abundant, sustainable and eco-friendly natural waste materials. Both of these natural waste substances have potential to be utilized as effective acoustic absorbers for various building and automotive applications. Polystyrene is also an eligible conventional sound absorbing material, which are identical and spherical shaped. The influence of granular materials on the acoustic absorption performance of a natural fiber composite was investigated in this study. This paper aimed to discuss the sound absorption properties of two innovative fibro-granular composites composed of natural fibers combined with natural and conventional granular materials. The fibrous and the granular components of one composite are pure natural which are fresh coir fiber and rice husk. On the other hand, the fibrous component of other composite is natural coir fiber and granular part is expended polystyrene beads. The amount of binder additive and grains added during composite preparation were compensated by reconstructing the equations using fiber diameters as new parameters in the case of both composites. The compensation was also considered for other two geometrical parameters such as porosity and viscous characteristic length, in order for the formulation of analytical model. The prediction of the sound absorption coefficient was performed in terms of developed analytical model by employing rigid frame Johnson-Champoux-Allard model. The experimental analysis was conducted through impedance tube measurement in order to support the analytical outcomes. Both analytical and experimental analyses were performed at different thicknesses for each composite sample. Results confirmed the potential of the coir fiber-rice husk composite as a better and promising acoustic absorber than the coir fiber-polystyrene in the low-frequency region (less than 1 kHz).

Keywords : Sound absorption, Natural and Conventional Acoustic Materials.

1. Introduction

The abundance of many agricultural and natural substances are common in most of the developing countries. The major part of these natural waste are being used as a fuel or burned to dispose in every year. For example, Bangladesh as a developing country, alone produces more than 200 million tonnes of agricultural wastes every year. The country produces a noticeable percentage of the total world production of jute, rice husk and coconut fiber. All these natural substances have potential to be used as efficient acoustic materials for sound absorption purpose.

Natural substances such as coir fiber [1], tea leaf fiber [2], bamboo fiber [3], date palm fiber [4, 5], rice straw [6, 7], rice husk [8], oil palm fiber [9], jute fiber [10], *Arrenga Pennata* fiber [11], kenaf fiber [12], kapok [13], grass and corn fiber [14] have already been reported as promising and efficient alternatives of synthetic fibers. These natural fiber composites have the potential to be used as sound absorber due to their biodegradability, renewability, abundance in nature, reduced cost and low health risk during the processing and handling[15].

But natural fibers have some extra moisture content which makes it unsuitable for commercial use. Therefore the fresh natural fiber is needed to be pretreated to replace the conventional acoustic materials. It was found that the chemical treatment of fresh natural fibers results in the reduction of extra moisture contents, leading the absorption performance to downwards[1]. At the response of this fact, the current research believes that the removal of the moisture content from the fresh natural fiber can be replaced by the granular materials.

Following the Johnson-Champoux-Allard-Pride-Lafarge model a good agreement between the theoretical and experimental method was reported by Zieliński [16] for sound absorption by spherical granular media with rigid frame. The author confirmed, the layer of identical spherical glass beads as a potential acoustic absorber when randomly packed in the measurement tube.

Sakamoto *et al.* [17] investigated the sound absorbing characteristics of two natural granular materials, rice and buckwheat husks. They revealed the effectiveness of rice husk and buckwheat husk as sound absorbing materials. They found the value of the sound absorption coefficient of rice husk is 0.5 and buckwheat husk is 4.5 at 500 Hz and 40 mm thickness.

A comparison study was made by Mahzan *et al.* [8] among rice husk, rubber granulate and woods shaved materials to validate the effectiveness of rice husk as an acoustic material. Their result demonstrated that the acoustic performance of 25% rice husk together with a polyurethane binder is superior to rubber and woods shaved material.

In recent years, many researchers [18-20] started working on the fabrication of fiber composites with the combination of plastic and rubber based granular materials. The incorporation of granular materials such as rubber crumb increases the flow resistivity and tortuosity of the composite material, which have significant effects in enhancing low frequency acoustic absorption.

The experimental examinations on the acoustic absorption performance of single fiber, grain and fiber- grain composite were reported by Turkiewicz and Sikora [21]. Results showed the acoustic absorption performance of the fibro-granular composite was better among simple rubber granulates, cotton fiber and cotton fiber–rubber granulate composites.

An encouraging performance of some sustainable eco-friendly composites with the combination of natural fiber and conventional granular materials was reported by a few researchers [17, 22-24] for low frequency acoustic absorption purpose.

Application of natural fiber reinforced with waste materials has shown its effectiveness as sustainable acoustic absorbers. The current research aims to study the two advantages of such materials utilization for the sake of environment and health issues. One advantage is to use this material for low frequency acoustic absorption purpose and the second one is the superior use of natural waste granular material for making new fibro granular composite.

2. Materials and Methods

2.1 Materials

The main materials used in this study were pure waste materials, such as fresh coir fiber, rice husk and expended polystyrene beads. The binder which was used for the necessary cohesion between the fibrous and granular components is 'Elmer's extra strong spray adhesive'.

2.2 Composite Preparation

The common fibrous component coir fiber of both composites and granular component rice husk grain for the first composite were collected from the local market. Both components were cleaned by spraying water and dried in open sunlight for one week. For conventional granular material, polystyrene beads were collected from the super market. The necessary cohesion between the composite components was facilitated by a spray binder adhesive purchased from a hardware shop. Afterwards, 20 samples were randomly chosen from each collected material to measure their physical characteristics such as, average diameter and density. The physical characteristics of the coir fiber, rice husk and polystyrene beads granulates are fabricated in Table 1.

Table 1. Physical characteristics of fresh coir fiber, rice husk and polystyrene beads.

Materials	Average Density kg/m^3	Average Diameter mm
Coir fiber	632	0.2
Rice husk	569	0.8
Polystyrene beads	40	5.2

The random mixing of both granular and fibrous components were performed manually and the ratio of the fiber and grain was fixed at 50:50 to prepare the composite samples with varying thickness. Plastic molds with four different thicknesses were prepared to shape the composite samples. The stated ratio was found the best for shaping the sample in the prepared mold. Thereafter, the composite samples with 20, 30 and 40 mm thicknesses were prepared using the collected materials and plastic molds shown in Figure. 1. below.



(a) (b) (c)

Figure 1. a) Plastic molds b) Coir fiber-Rice husk composite and c) Coir fiber-Polystyrene beads composite.

Two samples of 28 and 100 mm diameters were prepared for each thickness to measure the acoustic properties of the composites using the impedance tube. The masses of 100mm diameter coir fiber-rice husk composite samples with 20, 30 and 40 mm thicknesses were measured as 30.15, 46.29 and 61.68g, respectively. On the other hand, the masses of 100mm diameter coir fiber-polystyrene composite samples with 20, 30 and 40 mm thicknesses were measured as 29.25, 40.45 and 55.15g respectively.

2.3 Experimental Method

The acoustic absorption test of all the samples from both the composites were performed on a set of two impedance tubes SCS9020B/K, which was manufactured according to ISO 10534-2 and ASTM E1050-98 standards[25]. The set consisted of one high- frequency and one low-frequency impedance tubes with diameters of 28 and 100 mm, respectively, two channel data acquisition system 01dB Symphonie, two 1/2" microphone types GRAS-40BP in each tube and a random G10 noise generator. Calibration of the microphones' sensitivity was performed, by utilizing the calibrator type GRAS-42AB at 114dB level and 1kHz. The acoustic absorption coefficients were determined independently in the low-frequency range (0–1600 Hz) and high-frequency range (1600–5000 Hz), and the results are presented by a combined plot in Figures 4 to 10. Both frequency ranges were linked by the user-friendly SCS8100 software to measure the acoustic absorption coefficient through the overall frequency pattern. The equipment for the measurement of sound absorption coefficient is shown in Figure. 2. below.

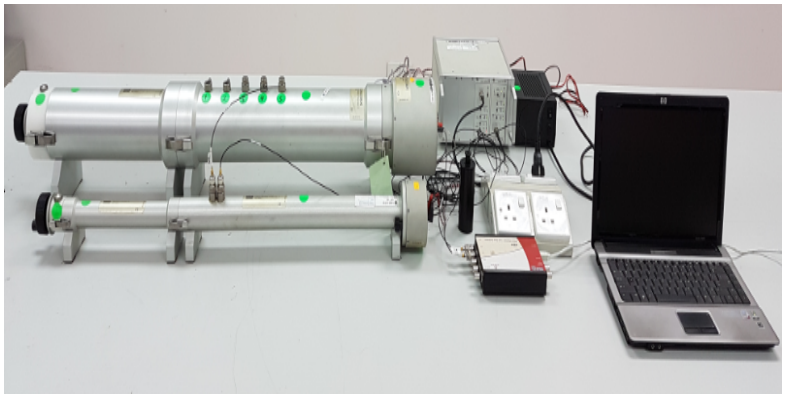


Figure 2. Experimental set up of fibro-granular acoustic absorption measurement. The equipment is composed of two tubes, a noise generator and two channel data acquisition system 01dB

The air flow resistance of each sample was measured using the ASTM C522 air flow resistance test system[26]. The test system package consisted of a sample holder, data acquisition system with vacuum pump and software package C522. The average value of flow resistivity from three repeated tests was considered for every sample. The equipment utilized for the measurement of the air flow resistance of both the composites is shown in Figure. 3. below.



Figure 3. Equipment and experimental set up for flow resistivity measurement. The equipment is composed of data acquisition system including vacuum pump, software package C522 and sample holder.

2.4 Theoretical Method

The theoretical method employed for the analytical prediction of both coir fiber-rice husk and coir fiber-polystyrene composites, is the well-known Johnson-Champoux-Allard Model. This is a rigid frame model, where the solid phase of the frame remains motionless. Five geometrical parameters, which are involved in this technique are – flow-resistivity, porosity, tortuosity, viscous characteristics length and thermal characteristics length. Later two parameters relate the viscous and thermal losses respectively.

According to Johnson[27], Allard and Champoux[28], the viscous characteristic length (Λ) characterizes the low frequency behavior of the effective density (ρ_ω) and thermal characteristic length (Λ')characterizes the high frequency behavior of the bulk

modulus $K(\omega)$. In the case of fibrous materials with porosity close to 1, the viscous characteristic length Λ and the thermal characteristic length Λ' can be stated as Eqs (2) and (3) respectively [29]:

$$\Lambda = 1/2\pi rl \tag{1}$$

$$\Lambda' = 1/\pi rl = 2\Lambda \tag{2}$$

According to Johnson [30], the expression of the effective density (ρ_ω) of rigid framed porous materials, is stated in Eq. (3) below:

$$\rho(\omega) = \alpha_\infty \rho_o \left[1 + \frac{\sigma\phi}{j\omega\rho_o\alpha_\infty}\sqrt{1 + \frac{4\,\alpha_\infty^2\eta\rho_o\omega}{\sigma^2\Lambda^2\omega^2}}\right] \tag{3}$$

The expression of the bulk modulus $K(\omega)$ of rigid framed porous materials which was proposed by Allard and Champoux [28, 29], is stated in Eq. (4) below:

$$K(\omega) = \frac{\gamma P_o}{\gamma-(\gamma-1)\left[1-j\frac{8\eta}{\Lambda'^2 N_p\rho_o\omega}\sqrt{1+j\frac{\Lambda'^2 N_p\rho_o\omega}{16k}}\right]^{-1}} \tag{4}$$

Where,

η = Viscosity of air
ω = Angular frequency
γ = Ratio of specific heat at constant pressure to specific heat at constant volume
P_0 = Atmospheric pressure
N_p= Prandtl number
ρ_o= Density of air

The expression for characteristic impedance $Z_c(\omega)$, the complex wave number $k_c(\omega)$, and surface acoustic impedance Z can be estimated by the equations below [29, 31]:

$$Z_c(\omega) = \frac{1}{\phi}\sqrt{\rho(\omega).K(\omega)} \tag{5}$$

$$k_c(\omega) = \omega\sqrt{\rho(\omega)/K(\omega)} \tag{6}$$

$$Z = Z_c(\omega).\coth(k_c(\omega)) \tag{7}$$

Having the surface acoustic impedance (Z), the absorption coefficient (α) at a normal incidence of the porous layer while backed with a rigid wall can be calculated as:

$$\alpha = 1 - \left|\frac{Z - Z_0}{Z + Z_0}\right|^2 \tag{8}$$

Where,
$Z_0 = \rho_0 c_0$ = Impedance of the air.

The effectiveness of any porous material depends on the value of its sound absorption coefficient which is close to one, with an absorption plane over a large frequency range.

4. Results and Discussion

A noticeable amount of binder is always needed when preparing any composite. This binder additive has an undoubted effect on the sound absorption performance of the composite. In the current paper, some compensations were considered due to the introduction of rice husk granular material and the binder additive in the developed composites. Hence, the formulation of the analytical model was done by developing the equations for few physical parameters of the composites which are shown below.

It was assumed that binder became the part of the fiber and grain and filled the porosity between them. In the case of coir fiber-rice husk composite, the effect of the amount of binder was compensated by reconstructing the fiber diameter of the as a new parameter in the following equation:

$$d_{fiber(mix)} = d_{fiber} + d_{fiber}\frac{\rho_{bulk(binder)}}{\rho_{bulk(s)}} \tag{9}$$

On the other hand, in the case of coir fiber-Polystyrene composite the effect of binder additive was neglected. This is because during this composite preparation a small amount of binder was utilized by spraying over the materials. Hence, the equation of fiber diameter as a new parameter was developed for this composite by considering the effect of the introduction of granular materials as follows:

$$d_{fiber(mix)} = d_{fiber} + d_{fiber}\frac{\rho_{bulk(grain)}}{\rho_{bulk(s)}} \tag{10}$$

Where,

$d_{fiber(mix)}$ = diameter of fiber with binder additive.

d_{fiber} = diameter of natural fiber

$\rho_{bulk(binder)} = \frac{\text{mass of binder additive}}{\text{volume of the sample}}$ = density of binder additive

$\rho_{bulk(grain)} = \frac{\text{mass of grain}}{\text{volume of the sample}}$ = density of grain

$\rho_{bulk(s)}$ = The bulk density of the composite sample.

Following the idea of Kino *et al.* [31], the current research developed the equation of the porosity (φ), for both natural fiber composite materials as follows:

$$\varphi_{mix} = 1 - \frac{\rho_{bulk(s)}}{\rho_f + \rho_g} \tag{11}$$

Where,

ρ_f = The average density of the fiber
ρ_g = The average density of the grain

The pore shape in a fibro-granular composite is controlled by the binder additive, fiber and grain size and amount of the grains. Hence, in the current paper the equation of viscous characteristic length was developed as a new pore shape factor which is stated as below:

$$\Lambda_{mix} = (1/2\pi r_{mix} l_{mix}) \times \varphi \quad (12)$$

The analytical and experimental estimation of the sound absorption coefficients of coir fiber-rice husk and coir fiber-polystyrene composites at three different thicknesses of 20, 30 and 40mm samples were performed. The results are plotted in Figures. 4-7. in terms of the developed analytical model employing Johnson-Champoux-Allard technique.

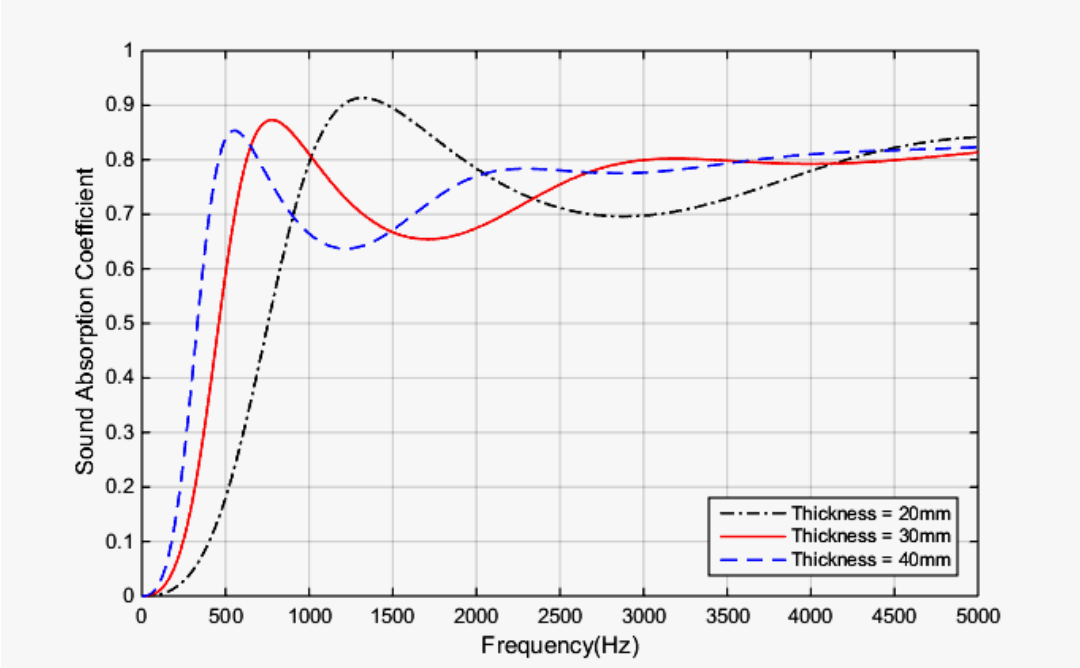


Figure 4. The acoustic absorption coefficients of coir fiber-rice husk composite at varying thicknesses in terms of Johnson-Champoux-Allard model

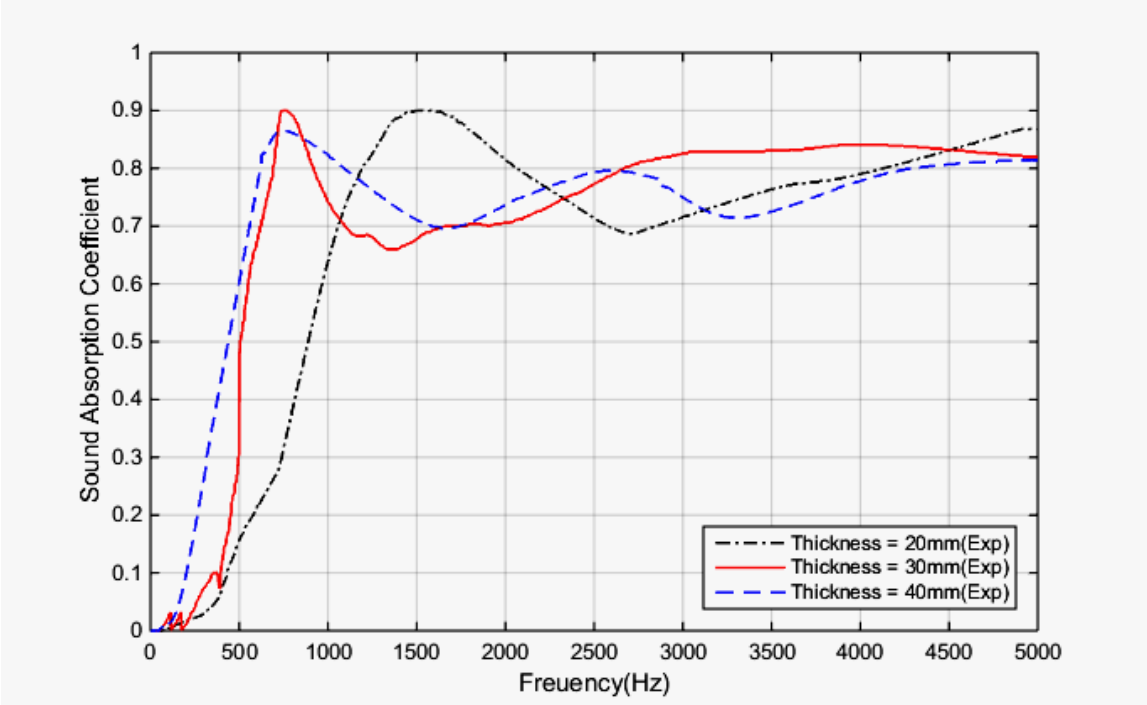


Figure 5 The acoustic absorption coefficients of coir fiber-rice husk composite at varying thicknesses in terms of impedance tube measurement.

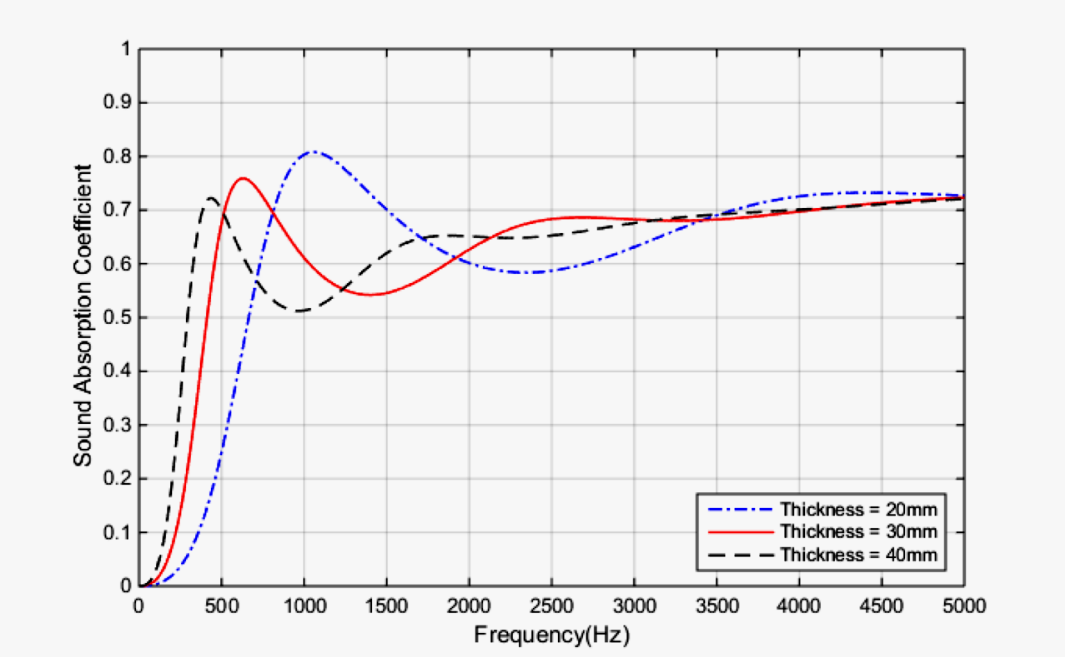


Figure 6. The acoustic absorption coefficients of coir fiber-polystyrene composite at varying thicknesses in terms of Johnson-Champoux-Allard model.

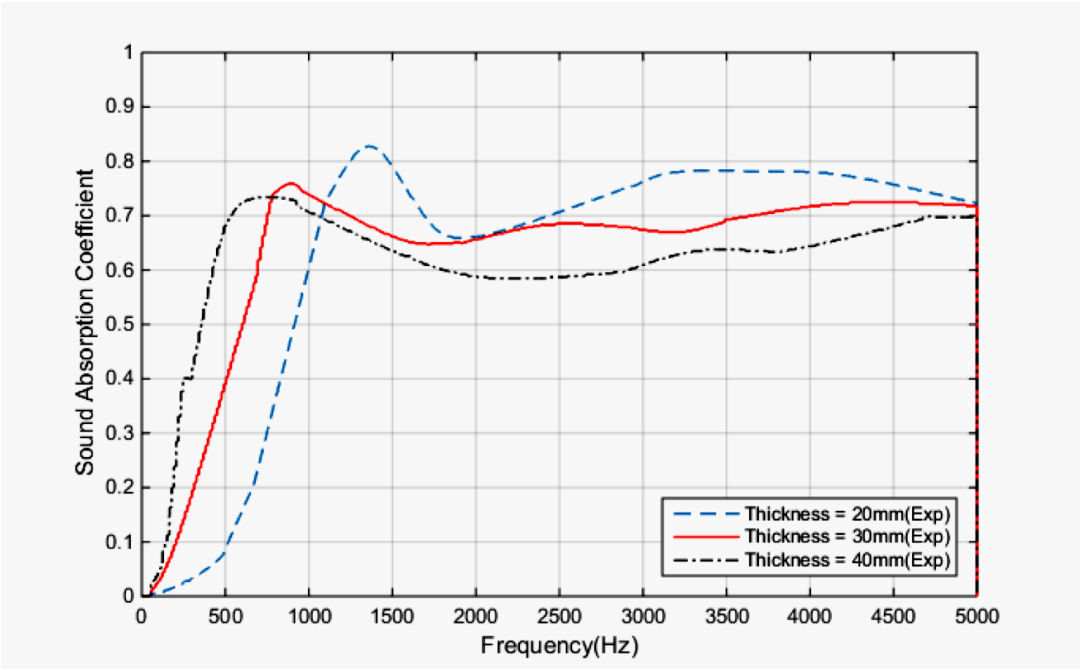


Figure 7. The acoustic absorption coefficients of coir fiber-polystyrene composite at varying thicknesses in terms of impedance tube measurement

In the case of coir fiber-rice husk composite the average predicted value of the acoustic absorption coefficient was found to be 85% at $f < 1321$Hz, $f < 777$Hz and $f < 578$Hz, while the average peak value of the sound absorption coefficient from impedance tube measurement was found 87% at $f < 1493$Hz, $f < 741$Hz and $f < 736$Hz at thicknesses of 20, 30 and 40mm respectively.

On the other hand, for the coir fiber-polystyrene composite the average peak value of the acoustic absorption coefficient was found 72% for the Johnson-Champoux-Allard model at $f < 1056$Hz, $f < 629$Hz and $f < 435$Hz while from the impedance tube measurement it was found 73% at $f < 1356$Hz, $f < 74$Hz and $f < 685$Hz at three thicknesses of 20, 30 and 40mm respectively.

Therefore, in the case of both composite, a propitious alignment of the acoustic absorption performance was observed between the experimental and analytical outcome of the developed Johnson-Champoux-Allard models. The findings indicate that increased sample thickness enhanced the acoustic absorption at the low-frequency region. Gradual shifting of the peak value of sound absorption coefficient was observed with increased sample thickness toward the low-frequency region. In the first instance, the results were due to the reduced average pore size and increased surface area, flow resistivity, and tortuosity.

The coir fiber–rice husk fibro-granular composite shows improved result at increased thickness compared with single coir fiber composite. Fresh coir fiber showed an average absorption of 0.8 for frequencies of $f > 1360$, $f > 940$, and $f > 578$ at sample thicknesses of 20, 30, and 45 mm, respectively. Similar to fresh coir fiber, industrial coir fiber with less moisture contents showed an average absorption 0.8 for frequencies $f > 3190$ and $f > 1300$ at sample thicknesses of 20 and 50mm, respectively[32, 33].

It should worth to mention that the coir fiber-rice husk composite material is superior to the simple coir fiber composite for commercial application, especially for low-frequency acoustic absorbent material. The reason can be attributed to the fact that in a fibro-granular composite, there is a good potential in filling the small pores by the granular component and the formation of bridges between the fibers as well. This contributes a higher surface area and more interaction of air molecules with the enlarged surface area within the composite, which leads higher sound absorption.

5. Conclusions

In the current study, the analytical experimental analyses were conducted on a layer of each developed composite while backed by a rigid wall. Analysing the results of prediction and measurements, this research concluded that coir fiber-rice husk composite was exhibited as a better acoustic absorber than the coir fiber-polystyrene composite. Hence, the current research is an expansion of the field of acoustic absorption from conventional fibro-granular composites to natural fibro-granular composites. Johnson-Champoux-Allard model can be accepted as an accurate and reliable analytical tool for the accurate resonance prediction of the developed composites, in the overall frequency range.

In conclusion, the materials made using the developed formulation proved to be competitive against the existing conventional acoustic products. the current investigation reports the potential of coir fiber composite with the combination of rice husk. The conducted analyses provide reliable guidance and knowledge to manufacture the product by fitting the chosen standardized parameters. This study facilitates the use of agricultural waste residues as acoustic absorbent material with low manufacturing cost. However, the influence of the varying ratio and size of fiber–grain components should be investigated further to achieve the acoustic absorption performance at a desired level. In addition, rather than the manual way, the current study recommends the alternate efficient way for the granular components to be uniformly mixed with the fibrous component in order to avoid any negative effect on the acoustic absorption performance of the fibro-granular composite.

References

[1] Fouladi M.H., Ghassem M., Ayub M., Nor M.J.M.(2011). Implementation of coir fiber as acoustic absorber material. *Noise & Vibration Worldwide*, 42(9). 11-16.

[2] Ersoy S., Küçük H. (2009). Investigation of industrial tea-leaf-fibre waste material for its sound absorption properties. *Applied Acoustics*, 70(1), 215-220.

[3] Koizumi T., Tsujiuchi N., Adachi A. (2002). *The development of sound absorbing materials using natural bamboo fibers. High performance structures and composites Book*. UK., (pp 157-166), WIT Press.

[4] Rahman L.A, Raja R.I., Rahman R.A., Ibrahim Z. (2012). Acoustic Properties of Innovative Material from Date Palm Fibre. *American Journal of Applied Sciences*, 9(9), 1390-1395.

[5] Elwaleed A., Nikabdullah N., Nor M., Tahir M., Zulkifli R.(2013). Experimental investigation of sound absorption properties of perforated date palm fibers panel. *IOP Conference Series: Volume.46. Materials Science and Engineering*, (pp 1-8). IOP Publishing.

[6] Yang H.S., Kim D.J., Kim H.J. (2003). Rice straw–wood particle composite for sound absorbing wooden construction materials. *Bioresource Technology*, 86(2). 117-121.

[7] Abdullah Y., Putra A., Efendy H., Farid W., Ayob M.(2013). Investigation on sound absorption coefficient of natural paddy fiber. *International Journal of Renewable Energy Resources*, 3(2013), 8-11

[8] Mahzan, S., Zaidi, A., Mujahid, A., Ghazali, M.I., Yahya, M.N., Ismail, M. (2009). Investigation on sound absorption of rice-husk reinforced composite, *Proceedings of Malaysian Technical Universities Conference on Engineering and Technology(MUCEET)* (pp. 19-22), MS Garden, Kuantan, Pahang, Malaysia.

[9] Zulkifli R., Nor M.J.M., Ismail A., Nuawi M., Abdullah S., Tahir M.M. Comparison of acoustic properties between coir fiber and oil palm fiber.(2009). *European Journal of Scientific Research*, 33(1), 144-152.

[10] Fatima S., Mohanty A. (2012). Noise control of home appliances-the green way. *Noise & Vibration Worldwide*, 43(7). 26-34.

[11] Ismail L., Ghazali M.I., Mahzan S., Zaidi A.M.A. (2010). Sound Absorption of Arenga Pinnata Natural Fiber. *World Academy of Science, Engineering and Technology* , 67(7), 804-806.

[12] Jayaraman K.A.(2005). *Acoustical absorptive properties of nonwovens*. Doctoral dissertation, North Carolina State University, North Carolina, USA.

[13] Veerakumar A., Selvakumara N.A.(2012). A preliminary investigation on kapok/polypropylene nonwoven composite for sound absorption. *Indian Journal of. Fibre & Textile Research*, 37(12), 385-388.

[14] Fouladi M.H., Nassir M.H., Ghassem M., Shamel M., Peng S.Y., Wen S.Y., Xin P.Z., Nor M.J.M. (2013). Utilizing Malaysian Natural Fibers as Sound Absorber. http://dx.doi.org/10.5772/53197, 161-170

[15] Zhu X, Kim B.J., Wang Q., Wu Q. (2013).Recent advances in the sound insulation properties of bio-based materials. *BioResources,* 9(1). 1764-1786.

[16] Zieliński T.G. (2014). Microstructure-based calculations and experimental results for sound absorbing porous layers of randomly packed rigid spherical beads. *Journal of Applied Physics,* 116(3), 1-17.

[17] Sakamoto S., Takauchi Y., Yanagimoto K. (2011). Watanabe S. Study for Sound Absorbing Materials of Biomass Tubule etc. *Journal of Environment and Engineering*, 6(2), 352-364.

[18] Maderuelo S.R, Barrigón M.J.M, Martín C.M., Gómez E.V., Rey G.G. (2013). Acoustical performance of porous absorber made from recycled rubber and polyurethane resin. *Latin American Journal of Solids and Structures(LAJSS),*10(3). 585-600.

[19] Maderuelo S.R., Nadal G.A.V., Crespo A.J.E., Parres G.F. (2012). A novel sound absorber with recycled fibers coming from end of life tires (ELTs). *Applied Acoustics,* 73(4). 402-408.

[20] Pfretzschner J. (2002). Rubber crumb as granular absorptive acoustic material, *PACS: 43.50.Rq, 43.55.Ev,* (pp 1-6), Instituto de Acústica, Serrano 144. 28006 Madrid, Spain.

[21] Turkiewicz J,Sikora J. (2013). Sound absorbing materials from recycled rubber products. *Mechanics and Control*, 32(3). 117-121.

[22] Mahzan, S., Ahmad Zaidi, M.A, Arsat, N, Hatta, M.N.M, Ghazali M.I. and Rasool Mohideen, S. (2010). Study on sound absorption properties of coconut coir fibre reinforced composite with added recycled rubber, *International Journal of Integrated Engineering* , 2(1), 29-34.

[23] Borlea A., Rusu T., Vasile O., Gheorghe A. (2012).Sound proofing materials with recycled rubber particles and sawdust. *Session of the Commission of Acoustics, (SISOM),* 291-296. Bucharest 30-31 May.
[24] Ekici B., Kentli A., Küçük H. (2012). Improving sound absorption property of polyurethane foams by adding tea-leaf fibers. *Archives of Acoustics*, 37(4). 515-520.
[25] Kundt tube Technical notes. (1998.)
[26] *http://www.scs-controlsys.com/systems/pdf/SCS-MT-PRO-KIT-ABSORPTION.pdf.* 1-2.
[27] ASTM C522. (2003). Standard test method for airflow resistance of acoustical
[28] material.
[29] Johnson D.L., Koplik J., Schwartz L.M. (1986). New pore-size parameter characterizing transport in porous media. *Physical review letters*, 57(20). 2564-2567.
[30] Champoux Y.,Allard J.F. (1991). Dynamic tortuosity and bulk modulus in air-saturated porous media. *Journal of Applied Physics*, 70(4). 1975-1979.
[31] Allard, J.F. (1993). *Propagation of sound in Porous media, Modelling sound absorbing materials,* New York and London: Elsevier Application Science, 284, 1-351.
[32] Johnson D.L, Koplik, J. and Dashen, R. (1987). Theory of dynamic permeability and tortuosity in fluid-saturated porous media, *Journal of fluid mechanics*, 176(3), 379-402.
[33] Kino N., Ueno T., Suzuki Y., Makino H. (2009). Investigation of non-acoustical parameters of compressed melamine foam materials. *Applied Acoustics*, 70(4). 595-604.
[34] Fouladi M.H., Ayub M, Nor M.J.M. (2011). Analysis of coir fiber acoustical characteristics. *Applied Acoustics*, 72(1), 35-42.
[35] Nor M.J.M, Ayub M, Zulkifli R, Amin N, Fouladi M.H. (2010). Effect of different factors on the acoustic absorption of coir fiber. *Journal of Applied Sciences*,10(22), 2887-2892.